12th Biennial SGA Meeting
12–15 AUGUST 2013, UPPSALA, SWEDEN

Mineral deposit research for a high-tech world

Proceedings

VOLUME 2

12th Biennial SGA Meeting
12–15 AUGUST 2013, UPPSALA, SWEDEN

Mineral deposit research for a high-tech world

Proceedings

Volume 2

Edited by
Erik Jonsson et al.

The 12th Biennial Meeting was organised by the Geological Survey of Sweden with assistance from Uppsala University, Stockholm University, the Geological surveys of Finland and Norway, Luleå University of Technology and the Swedish Museum of Natural History.

Suggested citation for entire volume:
Jonsson, E. et al. (ed.), 2013: Mineral deposit research for a high-tech world. Proceedings of the 12th Biennial SGA Meeting, 12–15 August 2013, Uppsala, Sweden. ISBN 978-91-7403-207-9. 1882 pp.

Suggested citation for an individual paper:
Sundberg, N. & Karlsson, E., 2013: Metallogeny of the Fennoscandian Shield. Mineral deposit research for a high-tech world. Proceedings of the 12th Biennial SGA Meeting, 12–15 August 2013, Uppsala, Sweden, ISBN 978-91-7403-207-9, 1450–1452.

A digital version of these volumes is available from the SGA website at www.e-sga.org

Cover photograph: View of the Aitik open pit copper mine in the very north of Sweden. Mining operations started in 1968 and the current mining depth is 430 m. The open pit is c. 3 km long and 1.1 km wide. The production in 2012 was 34,3 million tonnes of ore containing 67 100 tonnes of copper, 51 700 tonnes of silver and 1,9 tonnes of gold. Photo: Olof Martinsson, Luleå University of Technology.

ISBN 978-91-7403-207-9 set of 4 volumes

Layout: Jeanette Bergman Weihed, Kerstin Finn, Rebecca Litzell, SGU
Print: Elanders Sverige AB

VOLUME 2

S 2.7:

Predictive modelling

Convenor:
John Carranza

KEYNOTE SPEAKER

Uncertainty in GIS-based prospectivity mapping in greenfields and undercover terranes

Arianne Ford
Centre for Exploration Targeting, University of Western Australia, Crawley WA 6009, Australia

Abstract. Given the potential for the discovery of significant mineral deposits in greenfields terranes, as well as undercover, the methods used for GIS-based prospectivity mapping must be examined and adapted to address the challenges faced with exploration in these regions. As the quality of a prospectivity map can be dependent on both the understanding of a mineral system as well as the quality and quantity of the input datasets, the issue of how to quantify uncertainties must be addressed. Uncertainties may arise from the mathematical models used, data quality issues, and human bias. While mathematical uncertainties can generally be quantified using different statistical measures, it is more difficult to quantify the uncertainty related to human bias and data quality. Different methods for data interpretation and analysis are investigated to reduce the degree of uncertainty and to measure this value in a quantitative way when undertaking a prospectivity mapping exercise.

Keywords. GIS; greenfields exploration; prospectivity mapping; spatial statistics; uncertainty; undercover exploration.

1 Introduction

GIS-based prospectivity mapping involves the development of a mineral systems model from which spatial proxies can be extracted using available geoscience datasets. These proxies map the physical processes critical in a mineral system. The spatial proxies interpreted and mapped from the data are then analysed and integrated using one of a variety of prospectivity mapping methods, and targets generated that help reduce the exploration search space. There are several techniques available for integrating different datasets, including the data-driven weights of evidence (Agterberg et al., 1993; Bonham-Carter, 1994; Ford and Hart, 2013), evidential belief (An et al., 1994; Moon, 1998; Carranza, 2009) and neural network (Brown et al., 2000; Bougrain et al., 2003; Porwal et al., 2003) methods, or knowledge-driven methods such as fuzzy logic (Bonham-Carter; 1994; Knox-Robinson, 2000; Brown et al., 2003).

Each of these methods of data analysis and integration has its benefits and pitfalls. As such, the individual circumstances for each prospectivity mapping case study must be assessed carefully to determine which methods are the most appropriate to use (Figure 1). The method chosen for analysis is largely dependent on the degree of understanding of a mineral system, and the availability and quality of geoscience data. This study presents an overview of where things stand in GIS-based prospectivity mapping for exploration target generation and the challenges that need to be addressed going forward into the future in terms of uncertainty and exploration undercover.

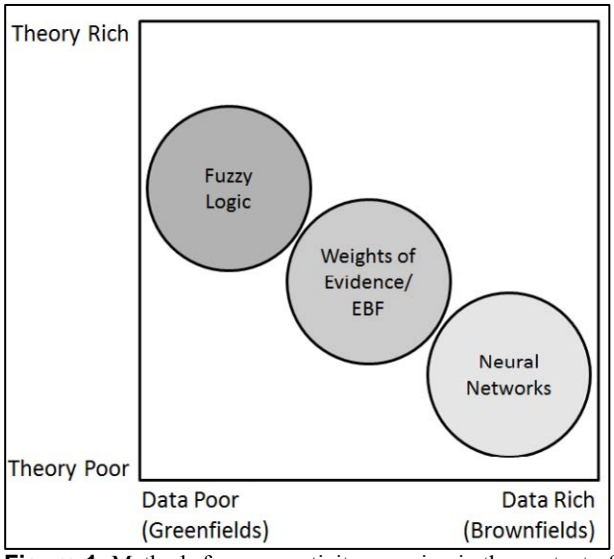

Figure 1. Methods for prospectivity mapping in the context of data availability and understanding of the mineral system.

2 Prospectivity mapping uncertainties

Both data-driven and knowledge-driven approaches for prospectivity mapping exist and are applied depending on the circumstances for each case study. An abundance of data, including a robust mineral deposit dataset may be required for the data-driven methods, while a comprehensive understanding of the mineral system may be considered more critical for knowledge-driven methods.

One must then consider the uncertainties associated with the prospectivity mapping. Mathematical uncertainties may exist due to the methodology chosen for the data interpretation and analysis, stochastic uncertainties commonly arise from data quality issues, and systemic uncertainties can result from human bias and an incomplete understanding of the mineral system being investigated (e.g. Figure 2).

As such, careful consideration must be given to the method of data interpretation and analysis chosen, data quality, and the development of a conceptual mineral systems model when undertaking a prospectivity analysis study.

Mathematical uncertainties exist for each of the data analysis and integration methods in terms of assumptions made and model parameters used. For example in weights of evidence analysis, we must assume that there is no violation of conditional independence, although it is noted there are tests that can

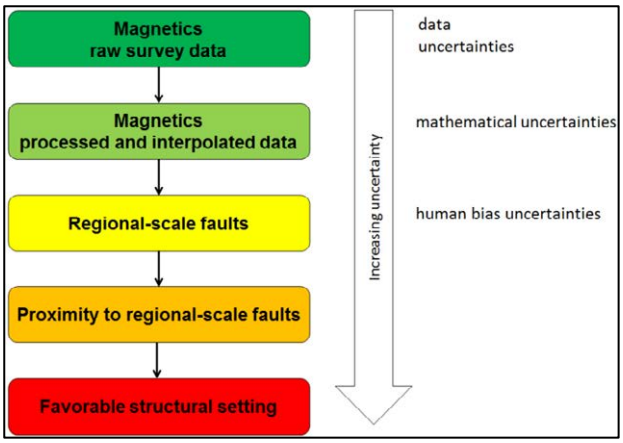

Figure 2. Compounding uncertainties in prospectivity mapping: (1) Start with an initial raw geophysical dataset containing data acquisition uncertainties, (2) raw data is processed to produce derivative geophysical images (e.g. analytic signal) which results in mathematical uncertainties, (3) regional scale structures are interpreted from derivative images introducing human bias, (4) human bias is compounded by selection of a favourable structural setting from the interpreted structural map, (5) map of favourable structural setting is integrated with other datasets into a prospectivity map.

be run to test the degree of dependence between the input layers (Agterberg and Cheng, 2002; Zhang et al., 2008). By integrating layers using fuzzy logic with the fuzzy GAMMA operator (Bonham-Carter, 1994), the value of the gamma parameter must be subjectively assigned. The processing of raw aeromagnetic data to produce total magnetic intensity or reduced to pole maps, which may subsequently be used to create new structural maps, also involves mathematical uncertainties relating to the processing methods used. In most cases, these mathematical uncertainties can be readily quantified using statistical measures and as such are of less concern.

Uncertainties relating to data quality and human bias are however less easy to quantify in an unbiased way. Traditionally, common methods for prospectivity mapping such as weights of evidence, neural networks and fuzzy logic have been applied to well explored and data rich terranes in a two-dimensional spatial context (e.g. Knox-Robinson, 2000; Billa et al., 2004; Mustard et al., 2004; Cassard et al., 2008; Nykänen et al., 2008; Fallon et al., 2010). While these are important case studies, the methods and assumptions used may be of limited practical use to mineral exploration companies that are working in greenfields terranes, or in terranes where there is little outcrop necessitating interpretation under potentially hundreds of meters of surficial cover.

A limited number of prospectivity mapping studies have been undertaken in greenfields terranes or those where the surficial cover is significant and these have endeavoured to address challenges relating to data availability, data quality and interpretation undercover (e.g. Partington, 2010; Ford and Hart, 2013; Joly et al., 2012). However, a number of concerns remain.

Addressing stochastic uncertainties relating to data quality remains a significant issue. Currently, the degree of uncertainty in the quality of a dataset can be subjectively assigned when undertaking a fuzzy logic prospectivity mapping exercise (cf. Joly et al., 2012). However as this is a subjective quantification, systemic biases are also introduced into the analysis (e.g. preferring one method of interpretation over another, who did the interpretation, etc.).

Specific challenges relating to quantifying data quality and uncertainty include the absence of evidence vs. evidence of absence problem and being able to use knowledge about the statistical distribution of mineral deposits and other geoscience data in a predictive capacity. The absence of evidence vs. evidence of absence problem relates to discontinuous data types such as structural maps or geochemical data points. If a structure is not shown on a map over a certain area, does this mean that there is no structure there, or is there a structure present that cannot be mapped from the available data? Progress towards addressing this problem may be made through investigating the spatial distribution of structures (or other discontinuous data) from multiple similarly mineralized terranes in order to understand what the background spatial distribution of the feature should be and comparing it to existing mapping. This may assist in predicting the localities of "missing" structures.

Additionally, one can address stochastic uncertainties by implementing automated methods for data interpretation. For example, the level of detail is often inhomogeneous on regional geological and structural maps, with a higher degree of detail in areas of outcrop. As areas of outcrop are often the initial focus for exploration efforts, mineralization is usually found in areas where mapping is in more detail. In order to be consistent with map detail, geophysical and remote sensing data can be interpreted using automated methods (e.g. Holden et al., 2008; 2011; 2012). Using an automated edge detection algorithm may produce a more consistent structural map than a geologist manually interpreting faults from an aeromagnetic image or aerial photograph on a computer screen. A more homogeneous map would be produced, it limits the human bias factor, and mathematical uncertainties for the processing method used can be quantified.

Interpretation of geology and structures undercover for use in a prospectivity map presents challenges in multiple ways. Without drillhole data, or an existing mine site that has been mapped in detail at depth in an area with which to constrain any geophysical or remote sensing interpretations, a high degree of uncertainty remains over the quality of an interpretation. As previously mentioned, the use of automated methods for interpreting undercover may reduce this uncertainty. Additionally, the use of 3D models to understand the geology at depth can be of practical use for prospectivity analysis studies over smaller areas where there is enough additional data to constrain the model (e.g. deep drillholes or deep seismic lines). However at larger regional- to craton-scales, this is often impractical due to the lack of additional data with which to constrain 3D models. By restricting prospectivity mapping case studies to areas over which such additional data exist the uncertainty may again be reduced.

Once uncertainties relating to data processing and interpretation have been addressed and quantified, the

different geoscience datasets must be integrated to generate a prospectivity map from which exploration targets can be delineated. Weights of evidence and evidential belief are data-driven prospectivity mapping techniques that assesses the strength of the spatial relationship between a series of known geological features (e.g. lithology, structures, style of alteration) and a set of known mineral deposit/occurrence locations using statistical measures. Consequently, both of these methods are dependent on the region being investigated having some degree of exploration history in order to derive a robust mineral deposit dataset for use in the analysis. A basic understanding of the mineral system processes is also necessary in order to derive the relevant spatial proxies and determine whether the statistics generated are geologically meaningful. Although these methods depend on the quality of the data used as inputs, Ford and Hart (2013) show that a modified weights of evidence technique can be applied in cases where the data quality is questionable.

The use of neural networks for data-driven prospectivity mapping is also critically dependent on access to a robust mineral deposit dataset. As neural networks do not provide the user with an indication of the relative merits of each of the input geological datasets (cf. weights of evidence statistics), but only the output prospectivity map, a high degree of confidence in the data quality is necessary.

The knowledge-driven fuzzy logic approach however, does not require a mineral deposit dataset as with the data-driven methodologies for prospectivity mapping. Although a comprehensive understanding of a mineral system and the proxies used to map these processes is necessary. The presence of any known mineral deposits may not be enough for a statistically significant data-driven analysis, however these deposits may be used as a verification tool for knowledge-driven techniques.

3 Conclusions

Although many challenges remain in undertaking GIS-based prospectivity mapping in greenfields and undercover terranes, a number of approaches have been suggested for quantifying and minimizing the degree of uncertainty involved. Using a combination of these approaches when interpreting different geoscience datasets and integrating such datasets to produce prospectivity maps and exploration targets is currently the best practice approach.

Acknowledgements

The author would like to acknowledge discussions with Cam McCuaig, Alok Porwal and Aurore Joly on data uncertainty. I would also like to thank Troy Resources for supporting the research project that raised many of the questions discussed in this paper.

References

Agterberg FP, Bonham-Carter GF, Cheng Q, Wright DF (1993) Weights of evidence modeling and weighted logistic regression for mineral potential mapping. In: Davis J, Herzfeld UC (eds) Computers in Geology - 25 Years of Progress. Oxford Univ. Press, New York, pp 13-32

Agterberg FP, Cheng Q (2002) Conditional independence test for weights-of-evidence modeling. Natural Resources Research 11: 249-255

An P, Moon WM, Bonham-Carter GF (1994) Uncertainty management in integration of exploration data using the belief function. Nonrenewable Resources 3: 60-71

Billa M, Cassard D, Lips ALW, Bouchot V, Tourliere B, Stein G, Guillou-Frottier L (2004) Predicting gold-rich epithermal and porphyry systems in the central Andes with a continental-scale metallogenic GIS. Ore Geology Reviews 25: 39-67

Bonham-Carter G (1994) Geographic Information Systems for Geoscientists: Modelling with GIS. Pergamon Press, Oxford

Bougrain L, Gonzalez M, Bouchot V, Cassard D, Lips ALW, Alexandre F, Stein G (2003) Knowledge recovery for continental-scale mineral exploration by neural networks. Natural Resources Research 12: 173-181

Brown W, Groves D, Gedeon T (2003) Use of fuzzy membership input layers to combine subjective geological knowledge and empirical data in a neural network method for mineral-potential mapping. Natural Resources Research 12: 183-200

Brown WM, Gedeon TD, Groves D, Barnes RG (2000) Artificial neural networks: a new method for mineral prospectivity mapping. Australian Journal of Earth Sciences 47: 757-770

Carranza EJM (2009) Controls on mineral deposit occurrence inferred from analysis of their spatial pattern and spatial association with geological features. Ore Geology Reviews 35: 383-400

Cassard D, Billa M, Lambert A, Picot J-C, Husson Y, Lasserre J-L, Delor C (2008) Gold predictivity mapping in French Guiana using an expert-guided data-driven approach based on a regional-scale GIS. Ore Geology Reviews 34: 471-500

Fallon M, Porwal A, Guj P (2010) Prospectivity analysis of the Plutonic Marymia Greenstone Belt, Western Australia. Ore Geology Reviews 38: 208-218

Ford A, Hart CJR (2013) Mineral potential mapping in frontier regions: A Mongolian case study. Ore Geology Reviews 51: 15-26

Holden E-J, Dentith M, Kovesi P (2008) Towards the automated analysis of regional aeromagnetic data to identify regions prospective for gold deposits. Computers & Geosciences 34: 1505-1513

Holden E-J, Fu SC, Kovesi P, Dentith M, Bourne B, Hope M (2011) Automatic identification of responses from porphyry intrusive systems within magnetic data using image analysis. Journal of Applied Geophysics 74: 255-262

Holden E-J, Wong JC, Kovesi P, Wedge D, Dentith M, Bagas L (2012) Identifying structural complexity in aeromagnetic data: An image analysis approach to greenfields gold exploration. Ore Geology Reviews 46: 47-59

Joly A, Porwal A, McCuaig TC (2012) Exploration targeting for orogenic gold deposits in the Granites-Tanami Orogen: Mineral system analysis, targeting model and prospectivity analysis. Ore Geology Reviews 48: 349-383

Knox-Robinson CM (2000) Vectorial fuzzy-logic: a novel technique for enhanced mineral prospectivity mapping, with reference to the orogenic gold mineralisation potential of the Kalgoorlie Terrane, Western Australia. Australian Journal of Earth Sciences 47: 929-941

Moon WM (1998) Integration and fusion of geological exploration data: a theoretical review of fuzzy logic approach. Geoscience Journal 2: 175-183

Mustard R, Blenkinsop T, McKeagney C, Huddleston-Holmes C, Partington G (2004) New perspectives on IOCG deposits, Mt Isa Eastern Succession, northwest Queensland. In: SEG 2004 Predictive Mineral Discovery Under Cover: Extended

Abstracts, University of Western Australia, Perth, 2004. Centre for Global Metallogeny, pp 281-284
Nykänen V, Groves DI, Ojala VJ, Eilu P, Gardoll SJ (2008) Reconnaissance-scale conceptual fuzzy-logic prospectivity modelling for iron oxide copper-gold deposits in the northern Fennoscandian Shield, Finland. Australian Journal of Earth Sciences 55: 25-38
Partington G (2010) Developing models using GIS to assess geological and economic risk: An example from VMS copper gold mineral exploration in Oman. Ore Geology Reviews 38: 197-207
Porwal A, Carranza EJM, Hale M (2003) Artificial Neural Networks for Mineral-Potential Mapping: A Case Study from Aravalli Province, Western India. Natural Resources Research 12: 155-171
Zhang S, Cheng Q, Chen Z (2008) Omnibus weights of evidence method implemented in GeoDAS GIS for information extraction and integration. Journal of China University of Geosciences 19: 404-409

NMDS scaling in classification of ore potential black shales in Finland

Airo, M.-L., Arkimaa, H., Loukola-Ruskeeniemi, K.
Geological Survey of Finland, P.O. Box 96, FI-02151 Espoo, Finland

Hyvönen, E.
Geological Survey of Finland, P.O. Box 77, FI-96101 Rovaniemi, Finland

Lerssi, J., Vanne, J.
Geological Survey of Finland, P.O. Box 1237, FI-70211 Kuopio, Finland

Abstract. Paleoproterozoic metamorphosed black shales in Finland are known for their ore potential for base-metal sulphides and graphite. All drill cores from which graphite or black shale has been reported, were reinvestigated and altogether 800 black shale samples from drill cores all over the country were selected for the purpose of a comparative black shale study. The distribution of black shales in Finland was mapped based on airborne geophysical interpretation verified by information from drill cores and outcrops. All the datasets were gathered into a black shale database updated by new laboratory measurements of petrophysical properties and results of geochemical analysis. Preliminary integration of the geochemical and rock physical datasets classifies black shales into five distinctive categories, one of them displaying high concentrations of base metals. Although black shales are characteristically rich both in organic C and S, the concentration of S, i.e. sulphides, correlates with their high electrical conductivity which is also typical for their airborne geophysical signatures.

Keywords. Black shale, susceptibility, remanence, resistivity, sulphur, carbon, iron

1 Black schist database

1.1 Introduction

Metamorphosed sedimentary rocks rich in organic C and S, known as 'black schists', are encountered in units of Paleoproterozoic supracrustal rocks all over Finland and they have long been known for their ore potential. The regional distribution of black schists was mapped by correlating airborne magnetic and electromagnetic data by Arkimaa et al. (1999, 2000). Integration of petrophysical and geochemical data with airborne geophysical data has been presented by Airo and Hyvönen (2008) and Airo et al. (2009). Now we updated the black schist map and created new database by reinvestigating all drill cores from which graphite or black shale had been reported (Loukola-Ruskeeniemi et al. 2011a,b, 2013, Hyvönen et al. 2013). Black schist units as inferred from airborne geophysical data were verified with drill-core and outcrop information (Fig. 1).

Altogether 800 black shale samples from drill cores all over Finland were selected for analysing textures, mineralogy, geochemistry and petrophysical properties. Statistical analysis and interpretation of airborne geophysical, geochemical and petrophysical data are used to characterize and classify black schists.

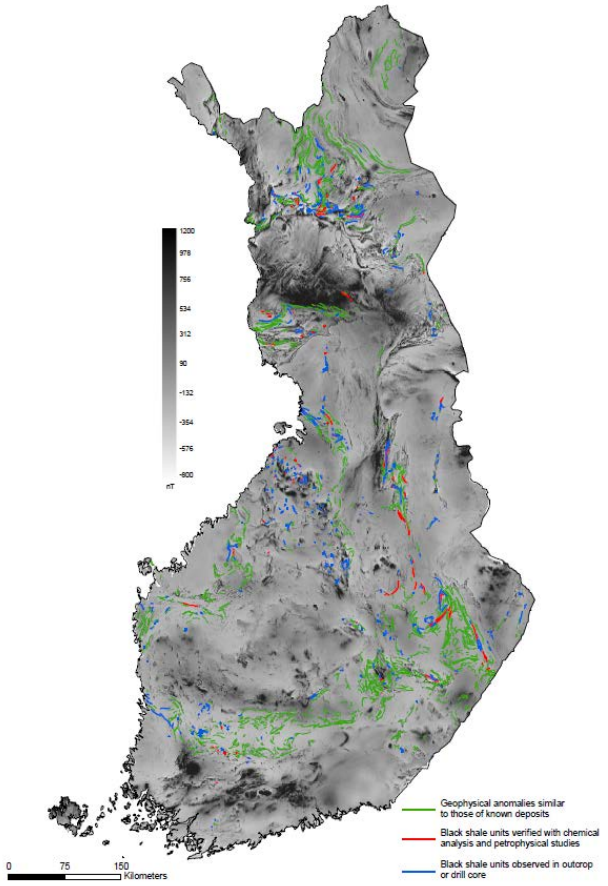

Figure 1. Aeromagnetic map of Finland with distribution of black shales as an overlayer, updated from Arkimaa et al. (2000). For airborne geophysical survey details, see Hautaniemi et al. (2005).

1.2 Datasets

Petrophysical data includes density, magnetic susceptibility, intensity of remanent magnetization, galvanic and/or induced resistivty. The petrophysical properties of black shales depend on their mineral composition and the abundance of graphite and sulphides in particular, with considerable differences being observed from site to site (Airo and Loukola-

Ruskeeniemi 2004). The mean density for "average" black shale is about 2800 kg/m^3 where graphite reduces and sulphides increase the density. Mean susceptibilities are about 6000 x10^{-6} SI-units and depend directly on the abundance of ferrimagnetic pyrrhotite. Consequently, the intensity of remanent magnetization is about 3 A/m. Königsberger ratios (the ratio of remanent to induced magnetization) for ordinary black shales range between 10 and 100. The high Q-ratios discriminate pyrrhotite-bearing rocks from magnetite-bearing sedimentary rocks, in which Königsberger ratios typically are much lower. Black shales are highly conductive electrically and their resistivity values are mainly below 1 Ohm-m.

Chemical analysis was subjected to the same samples from which petrophysical determinations were made. In the present sample set, represented by 800 samples from all over Finland, high concentrations of organic C and S were encountered in many localities in eastern and northern Finland. These values resemble those in the Talvivaara deposit in Sotkamo, eastern Finland (e.g., Loukola-Ruskeeniemi and Lahtinen 2012), but the Ni, Cu, Co, Zn, and Mn concentrations are lower than in Talvivaara. Indications of high Pd abundances were noted from some prospects, whereas U-rich black shale units were not encountered.

Black schists are easy to recognize on airborne geophysical maps because of their stratigraphy-related, coupled magnetic and conductive patterns. The magnetic anomalies are caused by ferrimagnetic, monoclinic pyrrhotite. Locally these anomalies may show strong magnetic intensities, and the crystal anisotropy of pyrrhotite introduces a high magnetic anisotropy which affects the aeromagnetic signatures producing irregular banded anomalies consisting of magnetic highs and lows. Correlation of drill core data with petrophysical and airborne geophysical data indicates that the geophysical responses of black shales are related to variation in concentrations of C, S and Fe. Increased S-content in geochemical data is connected to increased conductivity (high Re/Im ratio).

2 Statistical analysis

2.1 NMDS scaling

Petrophysical and geochemical data (428 drill core samples) were analyzed by using non-metric multidimensional scaling (NMDS). NMDS is an unconstrained ordination technique that represents samples in clusters with similar properties in a few ordination dimensions. Its application in this work led to the recognition of five black schist classes (Fig. 2), whose main characteristics are shown in Table 1.

Table 1. Characteristics of NMDS-classes.

Class	High values	Low values
Black	Na_2O, Al_2O_3, SiO_2, K_2O	CaO, P_2O5, MnO, Fe_2O_3, S, density, susceptibility, remanence, conductivity
Blue	CaO, Carbonate C	
Green	MgO, TiO_2	Carbonate C
Magenta	P_2O_5, MnO, Ni, Cu, Zn	Na_2O, MgO, Al_2O_3
Red	Fe_2O_3, V,C, S, susceptibility, remanence, conductivity	SiO_2, K_2O

The 'black' class corresponds to black shales rich in Na, Al, K and Si refering to rocks originally having detritus-fraction, clay and sand. Geophysically these are low in density, magnetic susceptibility and high electrical resistivity. In the 'blue' class the Ca and carbonate-C concentrations are typically high. The 'green' class is distinguished by high Mg, Ti and Cr and lowest organic C concentrations. Ca-content of the green class resembles that of the blue class. The 'magenta' class can be characterized by its high P and Mn concentrations refering to specific redox-conditions. It is likely that pulses of oxygen have affected the sedimentary basin. Ni, Cu and Zn concentrations are typical to the magenta class. The 'red' class is geophysically most distinctive with high density, magnetic properties and conductivity. The Fe, S and C concentrations are high, but Si and K concentrations low. Figure 2 illustrates the result of NMDS scaling and the division of samples into five classes. The longer the vector the more significant each variable is in its class.

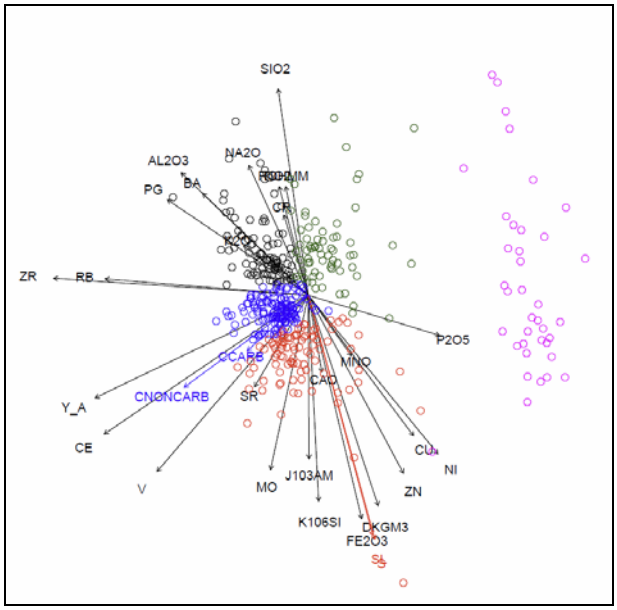

Figure 2. Result of NMDS scaling for petrophysical and geochemical data. Density and magnetic properties correlate with concentrations of Fe_2O_3 and S.

2.2 Comparison of NMDS classes

The 'blue' class is the largest in number samples, and exhibits a wide variation in concentrations and properties. The 'green' and 'black' classes resemble each other with their commonly poor physical properties compared with the red and magenta classes. The highest iron and sulphur concentrations appear in the 'red' and 'magenta' classes (Fig. 3). These classes also are characterised by high susceptibility (Fig. 4) and low resistivity (Fig. 5). Electrical conductivity correlates only poorly with concentration of organic C (Fig. 6). Depending on the Fe/S- ratio, the geophysical properties in these classes are controlled by pyrite / pyrrhotite.

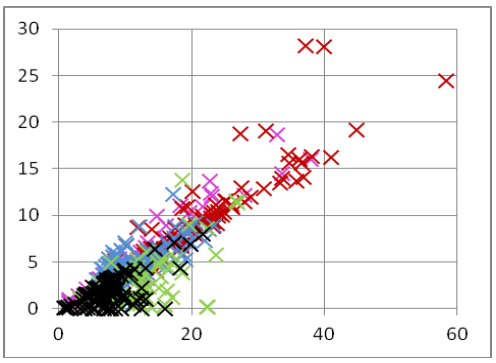

Figure 3. NMDS classes for concentrations (in %) of Fe_2O_3 (x-coord) and S (y-coord).

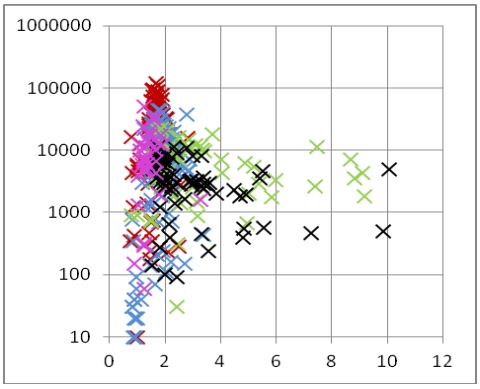

Figure 4. NMDS classes for concentrations (%) of Fe/S (x-coord) and magnetic susceptibility (y-coord).

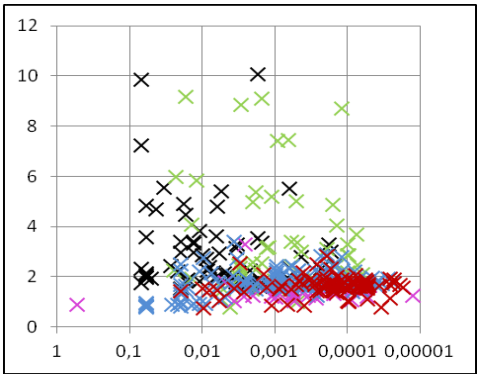

Figure 5. NMDS classes for concentrations of resistivity (x-coord, reversed scale) and Fe/S (y-coord) (%).

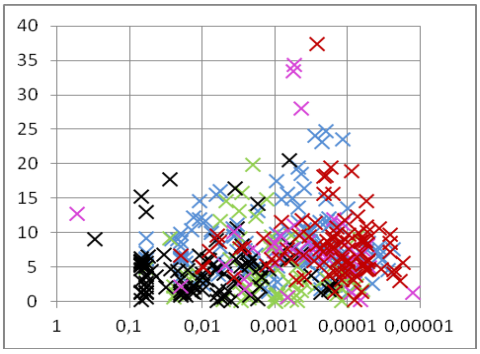

Figure 6. NMDS classes for concentrations of resistivity (x-coord, reversed scale) and C (y-coord) (%).

2.3 Individual drill cores

The regional distribution of the five classes partly reflects different depositional and deformational conditions (Fig. 7). The green class is characteristic to northern and western Finland, whereas the red and blue classes dominate in southern and eastern Finland. However, within most of the studied drill cores many of the five classes are represented in the sedimentary record. These relationships will be the subject of future studies.

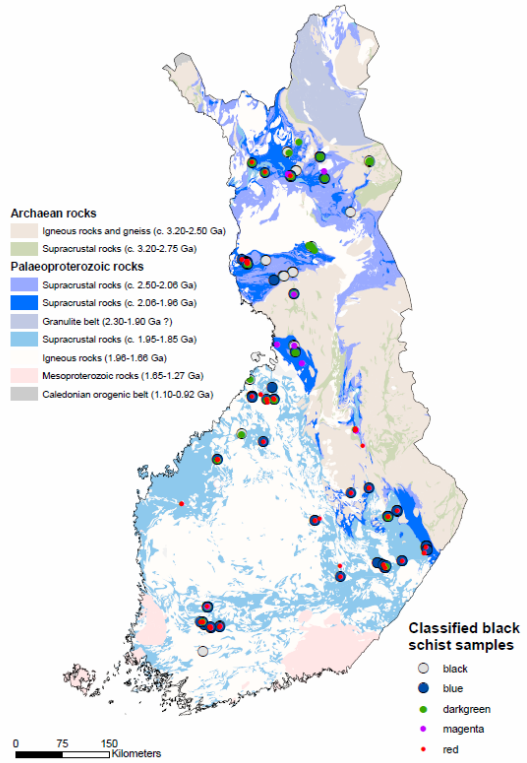

Figure 7. Result of NMDS scaling for petrophysical and geochemical data. Density and magnetic properties correlate with concentrations of Fe_2O_3 and S.

In southern Finland a group of nine investigated drill cores containing black schist units are located in an area rich in magnetic and conductivity surface anomalies (Fig. 8). The folded geological structure with a gradual reduction in anomaly intensity is pierced by a northwest-southeast trending shear zone of declined magnetic properties. The investigated samples belong mainly to groups 'red' and 'blue' but also 'green' and 'black' classes are represented. An example of the variation of the class characteristics in one of the drill cores is shown in Fig. 9.

The black shale layer at ~20 m depth belongs to the red class with strong magnetic properties. The susceptibilities vary between 30 000 and 110 000 ($x10^{-6}$) and the intensities of remanence are between 28 and 120 A/m. The concentrations of Fe are > 14 % and of S are > 5 %. The black shale at the depth of 42.4 m belongs to the green class and at 51.8 to the blue class. Fig. 9 compares the Al, Ca and Si concentrations of the black shales at different depths. The green class differs from the others by its low Ca concentration. The magnetic

properties of this sample are extremely weak and its concentration of C ~13 %. Although the very intense magnetic properties are found closest to surface, the magnetic anomalies related to this site are subtle as well as the electrical conductivity is not pronounced.

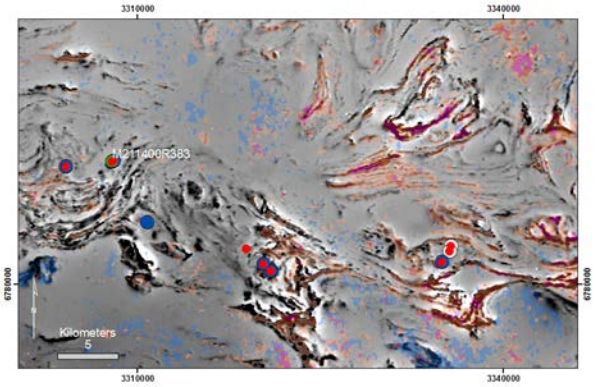

Figure 8. Combined airborne electromagnetic (orange to red indicating conductivity) and magnetic total field (greyscale, black is high intensity) anomalies typical to black shales. Blue denotes magnetite effect interpreted from EM data. Circles show 9 locations of re-investigated drill cores, drill hole M211400R383 is marked.

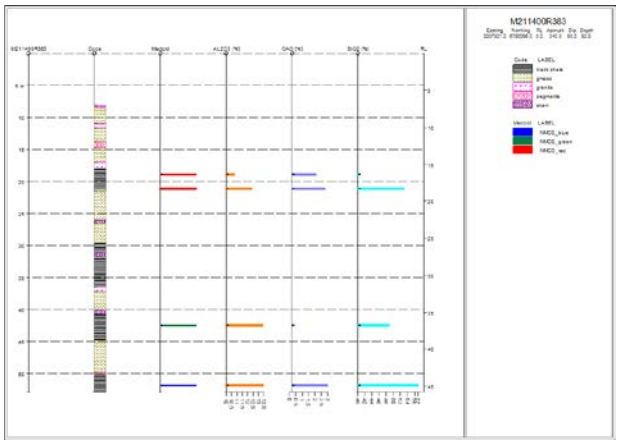

Figure 9. Classified black shales in drill hole M211400R383. Concentrations of Ca, Al and Si (%).

3 Discussion

Even though black shales are easy to identify in airborne geophysical data, their interpretation is challenging: their geophysical properties vary from site to site and within individual lithostratigraphic units. The example of correlating geophysical surface anomalies with the variable geophysical properties measured from the drill core explains the difficulty of this kind of correlations. The surveyed airborne geophysical responses are controlled by bedrock geology and structure, overburden and conductivity structures and texture.

The black schist database composed of airborne geophysical, geochemical and rock physical data sets facilitates data integration, statistical analysis and interpretation. These results integrated with magnetic structural analysis provide a good tool for investigation, characterization and classification of black schists in Finland. They can be used both in predicting mineralized areas in regional context and also be applied in detailed geological and geophysical studies.

Acknowledgements

We thank Satu Vuoriainen for carrying out the petrophysical determinations and preparing the petrophysical data set. We also thank Paavo Närhi for carrying out the statistical NMDS clustering and Hanna Leväniemi for AEM classification in Fig. 8.

References

Airo, M.-L. & Loukola-Ruskeeniemi, K. 2004. Characterization of sulfide deposits by airborne magnetic and gamma-ray responses in eastern Finland. Ore Geology Reviews 24:67-84.

Airo, M.-L. & Hyvönen, E. 2008. Petrophysical data coupled with airborne magnetic, conductive and radiometric signatures identifying bedrock conductors. Proceedings of the 5th International Conference on Airborne Electromagnetics, Porvoo Haikko, Finland, 28-30 May 2008.

Airo, M.-L., Loukola-Ruskeeniemi, K. ja Hyvönen, E. 2009. Geophysical databases supporting large- and detailed scale mineral exploration: black shale formations in Finland. In: Smart science for exploration and mining: proceedings of the 10th Biennial SGA Meeting, Townsville, Australia, 17th-20th August, 2009. Townsville: James Cook University, 781-783.

Arkimaa, H., Hyvönen, E., Lerssi, J., Loukola-Ruskeeniemi, K. and Vanne, J. 1999. Compilation of maps of black shales in Finland: applications for exploration and environmental studies. In Autio, S. (ed.), Geological Survey of Finland. Special Paper 27:111-114.

Arkimaa, H., Hyvönen, E., Lerssi, J., Loukola-Ruskeeniemi, K. and Vanne, J. 2000. Proterozoic black shale formations and aeromagnetic anomalies in Finland 1 : 1 000 000. Geological Survey of Finland.

Hautaniemi, H., Kurimo, M., Multala, J., Leväniemi, H. and Vironmäki, J. 2005. The 'three in one' aerogeophysical concept of GTK in 2004. In Airo, M.-L. (ed.), Aerogeophysics in Finland 1972-2004: Methods, System Characteristics and Applications, Geological Survey of Finland, Special Paper 39:21-74.

Hyvönen, E., Airo, M.-L., Arkimaa, H., Lerssi, J., Loukola-Ruskeeniemi, K., Vanne, J., Vuoriainen, S., 2013. Airborne geophysical, petrophysical and geochemical characteristics of Palaeoproterozoic black shale units in Finland: applications for exploration and environmental studies. Geological Survey of Finland, Special Paper (in press).

Loukola-Ruskeeniemi, K. & Lahtinen, H. 2012. Multiphase evolution in the black shale-hosted Ni-Cu-Zn-Co deposit at Talvivaara, Finland. Ore Geology Reviews (in press).

Loukola-Ruskeeniemi, K., Arkimaa, H., Airo, M.-L., Hyvönen, E., Lerssi, J., Vanne, J., Vuoriainen, S., 2013. Genetic models for the Talvivaara Ni deposit and ore potential of Palaeoproterozoic black shale units in Finland. SGA abstracts, Uppsala 2013 (submitted).

Loukola-Ruskeeniemi, K., Hyvönen, E., Airo, M.-L., Arkimaa, H., Eskelinen, J., Lerssi, J., Vanne, J., Vuoriainen, S., 2011a. Evaluation of the ore potential of black shale units in Finland - preliminary results of a geophysical and geochemical study. Geologi 63 (3), 68-79.

Loukola-Ruskeeniemi, K., Hyvönen, E., Arkimaa, H., Airo, M.-L., Vanne, J., Lerssi, J., Vuoriainen, S. 2011b. Talvivaara Ni deposit and ore potential of Palaeoproterozoic black shale formations in Finland. In: Goldschmidt abstracts 2011. Mineralogical Magazine 75 (3), 1357.

Data integration for interpretive bedrock mapping in the Giyani area (South Africa)

Emmanuel John M. Carranza
School of Earth and Environmental Sciences, James Cook University, Townsville, Queensland, Australia

Martiya Sadeghi
Geological Survey of Sweden, Uppsala, Sweden

Alazar Y. Billay
Council for Geoscience, Pretoria, South Africa

Abstract. The Giyani greenstone belt is situated in the Limpopo province of South Africa. All previous maps, field observations and available geo-data sets were integrated using image fusion to recognise lithological variations. Mafic and granitic rocks showed strong contrast in DEM. Single images of airborne radiometric data as well as composite maps of U showed very good correlations with lithology. Soil geochemistry data were interpolated, and principal components analysis was applied for major and trace elements, as well as ratio maps of geochemical data were used for interpretive bedrock mapping. All useful fused images were interpreted to compile a new bedrock map for follow-up fieldwork.

Keywords. Predictive mapping, Giyani, South Africa, GIS, remote sensing.

1 Introduction

The Archaean Giyani Greenstone Belt (GGB) in South Africa is known for its gold mineralization. There are 44 known deposits/prospects in GGB, hosted by mainly mafic metavolcanic rocks and iron-formations. No attempt has been made to establish a uniform stratigraphy across the belt due to the poor outcrop, and no accurate geological map could be produced.

The main aim of this work is to integrate all available data (e.g. previous bedrock maps, soil geochemistry, geophysics, etc.) to provide best estimate bedrock map of the GGB. The final integrated map will be used in the future for gold prospectivity mapping.

2 Geology

The GGB with age of 3203 ± 0.2 Ma (Brandl and Kröner 1993; Kröner et al., 2000) is situated at the north-eastern edge of the Kaapval craton (Figure 1). Towards its southwestern end it bifurcates into the Khavagari and Lwaji arms. The belt is dominated by ultramafic and to a lesser extent, mafic rocks with rare iron-formations, felsic schists and metasediments (Brandl et al. 2006). The GGB is flanked by migmatized tonalitic gneisses (Klein Letaba Gneiss and at places by younger granitoids of 2632 ± 53 Ma (Pretorius, et al. 1988).

On regional scale, the GGB is characterized by SW to NE prograde metamorphism (Lourence 1983). Parts of the Lwaji and Khavaqari arms are of greenschist metamorphic grade. The remaining parts of the belt, with a few exceptions, are of lower amphibolite grade. The GGB is generally characterized by a S-to-N increase in the metamorphic grade with higher grade zones being localized to high strain D_2 deformation zones (McCourt and van Reenen 1992). They are best developed along the northern margin of the GGB close to the Southern Marginal Zone of the Limpopo Belt.

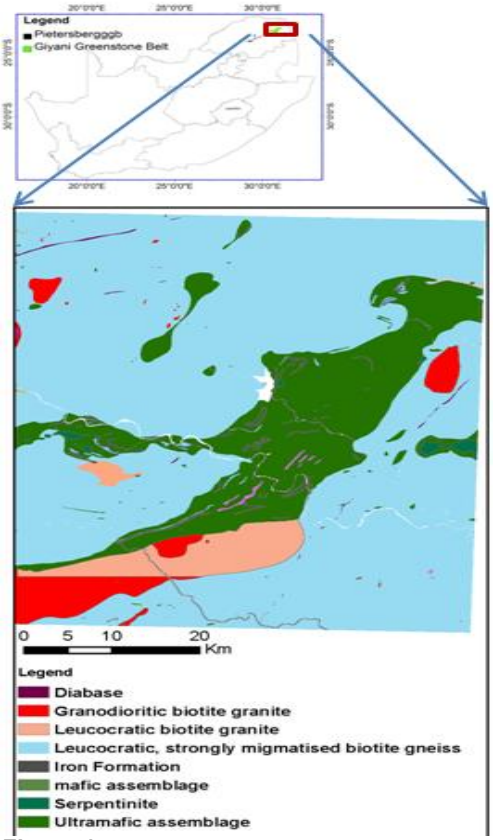

Figure 1. The present geological map of the Giyani area

Three ductile-deformation phases have affected the rocks of the GGB (McCourt and van Reenen 1992). An older penetrative deformation (D_1) and a younger non-penetrative (D_2) and a youngest (D_3) characterized by discrete strike-slip shear zones. D_1 gave rise to the N-trending regional schistocity and was responsible for the ENE-WSW and E-W-trending and north dipping oblique to reverse shear zones as well as the associated reclined sheath folds and well developed mineral lineation. The non-penetrative D_2 was superimposed on D_1 structures and can be recognized by either eastward plunging folds of the regional foliation or related horizontal crinkle lineation. Discrete strike-slip shear zones at the margins of the GGB post dating the granitoid intrusion are

attributed to the third phase (D_3) event.

There are 44 known gold deposits/prospects in the GGB. Six of these deposits contributed 97% of the total 10t gold recovered from the GGB (Ward and Wilson 1998). Gold-bearing quartz veins is hosted by mainly mafic metavolcanics and iron-formations and are controlled by north-dipping oblique to reverse sense ductile D_2 shear zones (McCourt and van Reenen 1992).

3 Data set and data processing

3.1 Image fusion for sharpening images

The method of image fusion used here was proposed by Chavez et al. (1991). This method is effective in integrating details from a high spatial resolution image while minimizing data distortions among lower spatial resolution images giving signals related to lithological composition. The method involves adding equal amounts of spatial information (SI) from a high spatial resolution image to each of three low spatial resolution 'compositional information' (CI) images in order to create new inputs to a colour composite:

Red input data $= (a \bullet CI_1 + b \bullet SI)/c$
Green input data $= (a \bullet CI_2 + b \bullet SI)/c$
Blue input data $= (a \bullet CI_3 + b \bullet SI)/c$

where a and b are weights to balance intensity sharpening from the SI image versus the hue and saturation from the CI images; c=a+b. By setting a=1, b can be determined as the ratio of the smallest maximum value among the three CI images to the maximum value in the SI image. For this project, we used the shaded-relief image of a digital elevation model (DEM) as SI and used various datasets as CI images.

3.2 DEM

The main lithologies in the area, which are granitic and ultrabasic-basic rocks, have strong contrasts both in chemical compositions and resistance to weathering. This implies that contrasts in topographic relief and 'texture' could be useful in bedrock mapping. Therefore, we used a DEM and created a shaded-relief image.

3.3 Airborne radiometric data

The airborne radiometric data were subjected to principal components analysis (Table 1).

Table 1. Summary of the principal component analysis on airborne radiometric images.

	K	Th	U	Variance	% Total variance
PC1	0.994	0.009	0.052	1509.89	96.30
PC2	-0.111	0.928	0.355	50.78	3.24
PC3	0.013	0.358	-0.934	7.21	0.46

PC1 reflects mostly K-rich and K-poor rocks. The former are likely to be granitic rocks including their metamorphosed equivalents, whereas the latter are most likely ultrabasic to basic rocks. PC2 reflects Th-rich rocks with moderate U contents, which are likely to be granites. PC3 reflects U-poor rocks with moderate Th contents, which are likely ultrabasic to basic rocks.

Aside from using single radioelement images, we used composite images of U (Duval 1983) by combining the data of U (in red) with the ratios U/Th (in green) and U/K (in blue) (Figure 2). The choice of these ratio images is based on the results of PCA (Table 1).

3.4 Magnetic field total intensity

The aeromagnetic data of the GGB are not useful for lithologic mapping but are useful for mapping structures.

3.5 Soil geochemistry

3.5.1 Trace element soil geochemical data

We interpolated trace element point data, using inverse distance moving average method to derive continuous geochemical maps. Then, we applied PCA to the element maps. To avoid data dimensionality problems in the PCA and interpretation of the results, we excluded some elements with similar information. Among the PCs of the element data, the first three PCs represent element associations that can reflect certain lithologies.

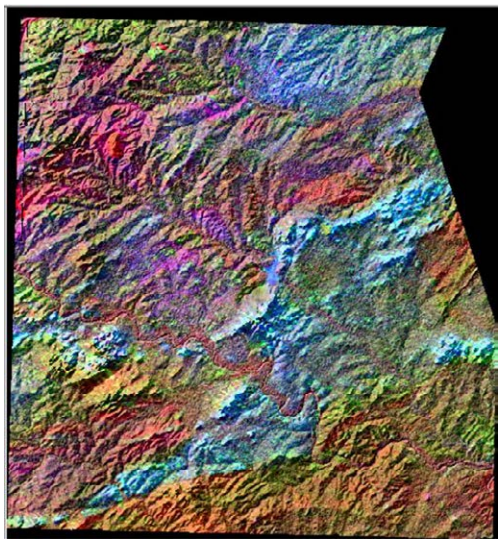

Figure 2. Composite image of U fused with shaded-relief DEM.

In addition to the PCA of single element data, we used images of element ratios reflecting contrasts in chemical compositions of major lithologies in the area. Image of Sr/Rb as CI_1 to depict variations in granitic compositions, Ga/V as CI_2 to depict variations in ultrabasic rocks, and Cr/Zr as CI_3 to depict variations in various rock types, an image useful for bedrock mapping were applied and the results is shown in Figure 3.

The fused image of element ratio images clearly distinguishes the greenstone rocks from the granitic rocks. It also shows that granitic rocks south of the greenstone rocks are different from those in the north.

3.5.2 Major oxides soil geochemical data

The same interpolation method described above for the trace elements data was applied for the major oxide data. Then, we applied PCA to produce the major oxide maps.

Among the PCs of the major element soil geochemical data, the first three PCs represent chemical

associations that reflect certain lithologies. PC1 depicts associations of MgO-MnO-Fe_2O_3 and Na_2O-K_2O reflecting ultrabasic-basic and granitic rocks, respectively. PC2 depicts associations of CaO-MgO-Na_2O-K_2O and TiO_2-Fe_2O_3-MnO reflecting granitic and ultrabasic rocks, respectively. PC3 depicts associations of CaO-TiO_2-Na_2O-Fe_2O_3 and K_2O-MgO reflecting basic and granitic rocks, respectively.

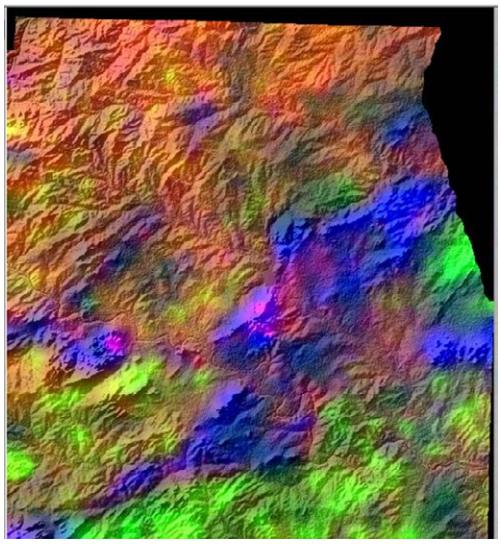

Figure 3. Composite image of Sr/Rb, Ga/V and Cr/Zr fused with shaded-relief DEM

Aside from PCA of single major oxide data, we used images of major oxide ratios reflecting contrasts in chemical compositions of major lithologies in the area. By applying the image sharpening algorithm with image of K_2O/Fe_2O_3 asCI_1, Na_2O/CaO as CI_2 and MgO/Al_2O_3 as CI_3 to depict contrasts between granitic and ultrabasic-basic rocks, an image useful for bedrock mapping is derived (Fig 4).

The fused image of major oxide ratio images clearly distinguishes the greenstone rocks from the granitic rocks. It also shows that granitic rocks south of the greenstone rocks are different from those in the north. It further shows that there are (a) variations in the greenstone unit, (b) variations in granitic rocks south of the greenstone unit, and (c) variations in granitic rocks north of the greenstone unit.

Aside from using images of major oxide ratios, we created and used images of composite major oxide ratios known as weathering indices. This is likely useful for bedrock mapping in the area because the climate of the area has probably resulted in residual weathering of rocks therein. We experimented using various weathering indices (see Price and Velbel 2003). The ones we found most useful as Vogt's index $((Al_2O_3+K_2O)/(MgO+CaO+Na_2O))$, WIP or weathering index of Parker (1970) $[100*((2Na_2O/0.35)+(MgO/0.09)+(2K_2O/0.25)+(CaO/0.9))]$, and PIA or plagioclase index of alteration $(100*[(SiO_2/TiO_2)/((SiO_2/TiO_2)+(SiO_2/Al_2O_3)+(Al_2O_3/TiO_2))]$. By applying the image sharpening algorithm with image of Vogt's index asCI_1, WIP as CI_2 and PIA as CI_3 to depict contrasts between granitic and ultrabasic-basic rocks, an image useful for bedrock mapping is derived (Fig 5).

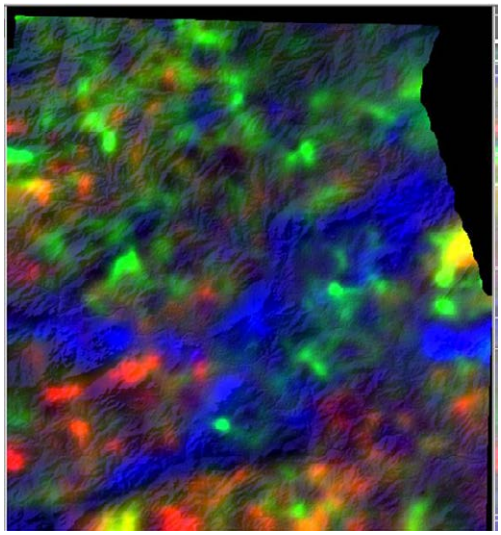

Figure 4. Composite image of K_2O/Fe_2O_3, Na_2O/CaO, and MgO/Al_2O_3 fused with shaded-relief DEM.

The fused image of images of weathering indices clearly distinguishes the greenstone rocks from the granitic rocks. It also shows that granitic rocks south of the greenstone rocks are different from those in the north. It further shows that areas north and west of the greenstone unit are likely underlain by either granitic rocks or greenstones.

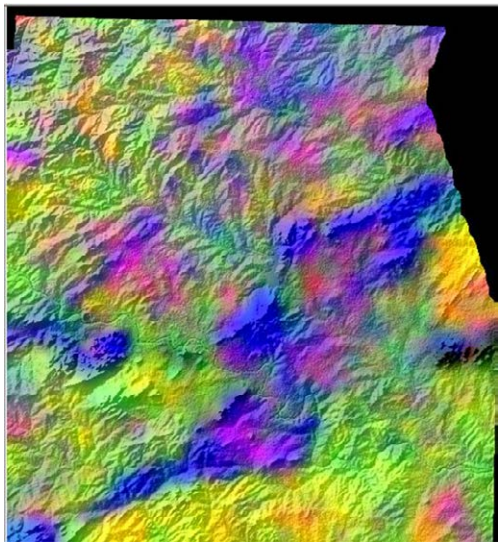

Figure 5. Colour composite image of Vogt's index, WIP, and PIA (see text for explanation) fused with shaded-relief DEM.

3.6 Landsat ETM+

First, we considered the OIFs (optimum index factors) to see which three images of Landsat ETM+ data would show the strongest contrast among features. It was found that the combination of bands 4, 5 and 7 is the most useful. Band 4 reflects areas with or without vegetation, and these areas may be defined by the underlying bedrock (e.g., greenstone terranes would be expected to non-vegetated because of the paucity in K in ultrabasic-basic rocks, whereas granitic areas would be relatively vegetated as they a more K-rich). By applying the image sharpening algorithm with image of band 4 asCI_1, band 5

as CI_2 and band 7 as CI_3 to depict contrasts between granitic and ultrabasic-basic rocks, an image useful for bedrock mapping is derived as shown in figure 6.

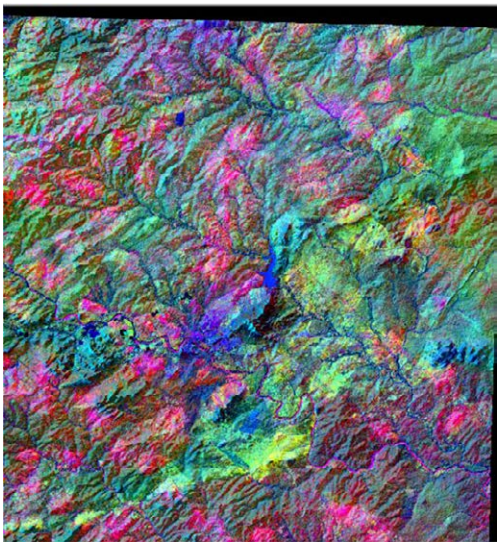

Figure 6. Colour composite image of Landsat TM bands 4, 5 and 7 fused with shaded-relief DEM.

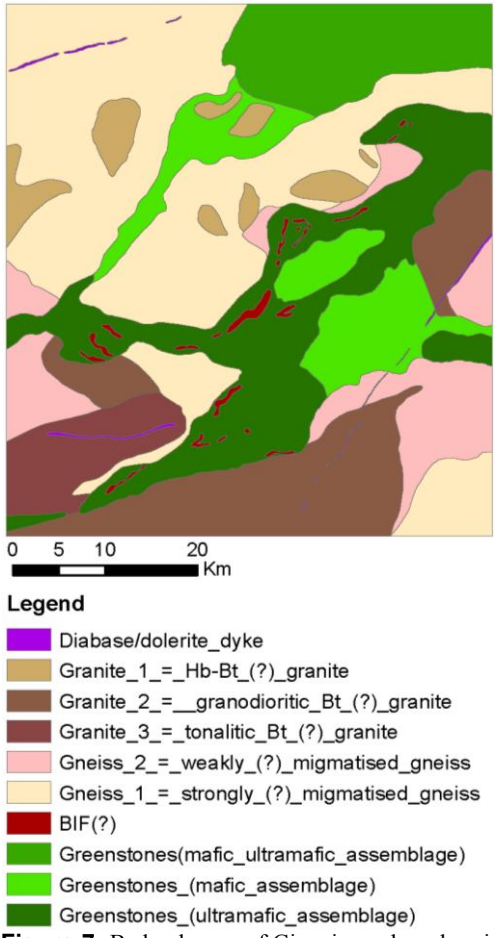

Figure 7. Bedrock map of Giyani area based on interpretation of images of fused geo-data sets.

4 Result and discussion

The interpretations were made in conjunction with existing knowledge (i.e. existing geological map) in the area. The final interpretation of bedrock geology is shown in Figure 7.The interpretive bedrock geology map is not very different from the existing 1:250,000 scale geological map. However, the former depicts presence of lithologies in various areas that are not depicted in the latter. For instance, the north eastern part of the area is likely underlain by lithologies with signatures that are similar to the mafic-ultramafic assemblage of the greenstone belt with intercalations of granitic gneisses. Clearly, the interpretive bedrock geology map suggests further follow-up in the field to check the accuracy of the interpretations.

Acknowledgements

The authors thank SGU (Meeting Point Mining Project) and CGS for funding.

References

Brandl, G. and Kröner, A. (1993). Preliminary results of single zircon studies from various Archean rocks of the north-eastern Transvaal. In: Maphalala R. and Mabuzu M. (Comp.) Abstr. 16th Int. Colloq. Afr. Geol., Mbabane, Swaziland, 54-56.

Brandl, G., Cloete, M., and Anhaeuser, C.R. (2006). Archean greenstone belts. In Johnson M.R., Anhaeuser C.R. and Thomas R.J. (Eds.), The Geology of South Africa. Geological Society of South Africa, Johannesburg/Council for Geoscience, Pretoria, 9-56.

Chavez, P., Sides, S. and Anderson, J. (1991). Comparison of three different methods to merge multiresolution and multispectral data: Landsat TM and SPOT panchromatic. Photogrammetric Engineering and Remote Sensing 57, 292-303.

Duval, J.S., (1983). Composite color images of aerial gamma-ray spectrometric data. Geophysics 48, 722-735.

Kröner A., Jaeckel P. and Brandl, G. (2000). Single zircon ages for felsic to intermediate rocks from the Pietersburg and Giyani greenstone belts and bordering granitoid orthogneisses, northern Kaapvaal Craton, South Africa. J. Afr. Earth Sci., 30: 773-793.

Lourence, E.L. (1983). Die petrografie en geochemie van gesteentes van die Sutherland-Groensteengordel Noordoos-Transvaal met spesiale verwysing na die regionale verspreiding van goud. Unpubl. MSc Thesis, RAU, Johannesburg.

McCourt, S. and van Reenen, D.D. (1992). Structural geology and tectonic setting of the Sutherland greenstone belt, Kaapvaal craton, South Africa. Precambrian Res., 55: 93-110.

Parker, A. (1970). An index of weathering for silicate rocks. Geological Magazine 107, 501-504.

Pretorius, A.I., van Reenen D.D. and Barton J.M. (1988). BIF-hosted gold mineralization at the Fumani mine, Sutherland greenstone belt, South Africa. S. Afr. J. Geol., 91: 429-438.

Price, J.R. and Velbel, M.A. (2003). Chemical weathering indices applied to weathering profiles developed on heterogeneous felsic metamorphic parent rocks. Chemical Geology 202, 397-416.

Ward, J.H.W. and Wilson, M.G.C. (1998). Gold outside the Witwatersand Basin. In: Wilson M.G.C. and Anhaeusser C.R. (Eds.), The mineral resources of South Africa. Handbook. Coun. Geosci., 16: 350-386.

Modelling target maps of future gold occurrences with combination of categorical and continuous conditionally-dependent supporting patterns

Chang-Jo Chung
SpatialModels Inc., Ottawa K1G 5K5 Canada

Andrea G. Fabbri
DISAT, University of Milano-Bicocca, 20126 Milan, Italy

Abstract. This contribution discusses procedures to obtain target maps of future events such as the likelihood of discovering new gold occurrences knowing location and spatial context of a set of genetically-related gold occurrences. A target map is generated iterating a modelling process using a subset of the known occurrences and cross-validating its prediction pattern with the distribution of the remaining subset. The target map is obtained integrating the prediction patterns from all iterations. Strategies are proposed for 37 gold occurrences in the Red Lake study area, northern Ontario, Canada: sequential elimination of 1 out of 37, and random selection of 24. In either case 37 prediction patterns are generated whose associated statistics from cross-validation provides a target pattern and associated uncertainty of class membership. Two prediction models used are: one based on a fuzzy set function and one on a logistic discriminant function. Target and uncertainty maps are based on spatial relationships between the distribution of 37 gold occurrences and that of categorical and continuous-value geophysical, geological and geochemical maps, many of which are conditionally dependent. Using rank-based statistics only marginal effects of conditional dependence appear to affect the results of the modelling.

Keywords. Target maps, cross-validation, class membership uncertainty, rank-based statistics.

1 Introduction and database

With the development of prediction modelling of spatial databases, many applications have been documented in mineral exploration. The diversity of approaches and quality of results were considered and criticized by the authors (Fabbri and Chung, 2008). This contribution discusses procedures to obtain target maps of likelihood of future discoveries of gold occurrences knowing the location and spatial context of a set of genetically-related gold occurrences.

A spatial database used for training in advanced courses (see Chung and Fabbri, 2008; Hillary *et al*., 2008, and GSC, 2000) is used here to generate target maps as results of predictive model applications. The database comes from the Red Lake study area (Figure 1A). It consists of 16 co-registered data layers of 40m pixel resolution and of size 1250 pixels by 700 lines. Within that window only 745,752 belong to the study area proper. A data layer with the distribution of 37 Au occurrences was termed direct supporting pattern (Figure 1B). The 37 occurrences that occupy 333 pixels (each covers a 3x3 pixel area) represent vein gold deposits: gold-bearing "cherty quartz with banded Fe-carbonate; "sulphide-poor veins", "sulphide-rich replacement zones", high-grade zones; strata-bound disseminations of gold in sulphide bearing tuffaceous rocks, and gold-bearing veins in granitoid intrusions. The remaining data layers, termed indirect supporting patterns, are to represent the spatial geological context as typical settings of the 37 occurrences: three thematic/categorical data layers (bedrock geology, metamorphism and alteration, with 17, 6 and 3 map units, respectively), and twelve continuous layers (4 from aeromagnetic survey data, 7 from geological data as distance functions, and 1 from geochemical samples).

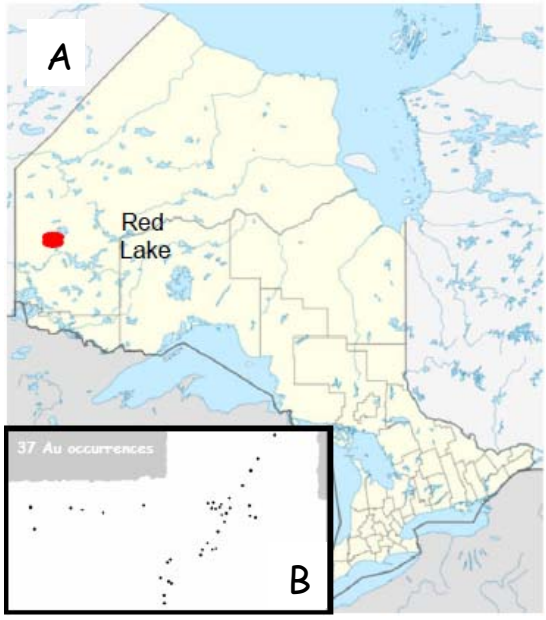

Figure 1. Location of the Red Lake study area in northern Ontario, Canada (A), and distribution of the 37 gold occurrences in the study area (B).

The applications that follow indicate methods and strategies that produce target maps from the integration of prediction maps via iterative cross-validation of prediction results. The next sections describe the modes and strategies used and discuss critical points of the results.

2 Models and strategy

Two prediction models are used to generate prediction patterns and target maps: one is based on a fuzzy set

membership functions, **fz** (Chung and Fabbri, 2001) and the other is based on a logistic discriminant function, **lg** (Chung, 2006). The models, whose performance is compared in terms of target maps, are to establish spatial relationships between the distribution of the 37 gold occurrences and those of categorical map units (**3T**) and continuous values of geophysical, geochemical and distance maps from geologic features (**12C**).

Two cross-validation strategies used for the database with 37 gold occurrences are as follows: (i) repeat predictions using sequential elimination of 1 out of the 37, to use the 36 to predict the 37th; (**37-1au**) and (ii) repeat 37 times predictions selecting 24 occurrences at random to predict the remaining 13 (**24r37x37au**). Each target map will be obtained computing the statistics from 37 prediction patterns. We use rank-based statistics to obtain the median rank as target map and the corresponding range of ranks to estimate the degree of uncertainty of class membership. A threshold of the target map can be generated using a desired area percentage of the lower range of ranks of uncertainty. In addition, the entire set of experiments is repeated using twice the thematic indirect supporting patterns to visualize the degree of disturbance introduced using such extreme conditionally-dependent patterns.

3 Results and conclusions

The results of applying the two models and the two iterative cross-validation strategies of target mapping are shown by prediction rates, target, **T**, uncertainty, **U** and combination, **C**, patterns and tables of **T** and **U** rates for the 37 gold occurrences. The histogram of prediction rates in Figure 2A shows a slight shift of 0.5% classes for the **fz_37-1au_6T12C** target map (obtained using g, a, and m twice), red columns, when compared with the **fz_37-1au_3T12C** target map, blue columns. Given the default subdivision of prediction rates into 200 equal area ranked classes, the shifts reveal only a minimal effect on the classes of the three totally conditionally-dependent data layers.

This is visualized in the 0-40% cumulative prediction-rate curves in Figure 2B. Figure 2C compares the curves from the two models, **fz** and **lg**, using the two strategies, **37-1au** and **24r37x37**. Each target prediction rate curve is the result of 37 predictions. Clearly, the **lg** results show a better performance: for instance, when considering the 10 of the study area with the highest rates, 58% and 57% of the occurrences fall within the cumulative class while the about 42% happen for the **fz** modelling. Cumulative prediction-rate curves are a useful way to compare the relative quality of modelling results.

Prediction patterns, target and uncertainty patterns can be visualized as maps, for instance, by ranking sequentially-ordered pixels values (from high to low) into 200 equal-area classes of 0.5% of the study area. Pseudo-colours are then assigned to group of classes for visual rendering.

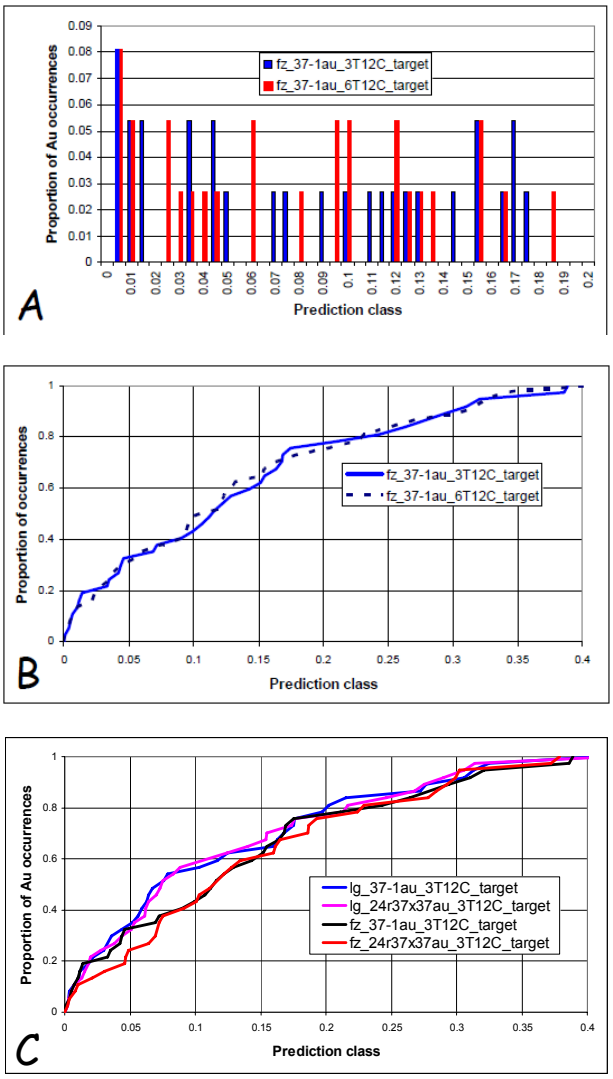

Figure 2. Prediction-rate histograms and cumulative curves from cross-validation experiments. (A), comparison of 0.5% prediction rate classes for the highest 20% of the study area. Blue indicates the rates as proportion of the occurrences in each 0.5% class for target map **fz_37-1au_3T12C**, and red for target map **fz_37-1au_6T12C**. (B), the cumulative prediction-rate curves for the maps in (A) but relative to the highest 40%. (C), prediction-rate curves for the **fz** and **lg** target maps for the two strategies.

Figures 3A-C show the target patterns of the **fz_37-1au_3T12C** cross-validation and the corresponding uncertainty and 50% combination. Figure 3D shows the target pattern for that of **fz_37-1au_6T12C**. The target patterns in Figures 3A and 3D represent the median ranks of 37 different prediction patterns, while its uncertainty pattern in Figure 3B the ranks of ranges. The 50% combination pattern in Figure 3C shows the part of the target pattern with uncertainty rates within the lowest 50% of the range. The target pattern in Figure 3D is very similar to that of Figure 3A, revealing small effect of the introduced strong conditional dependence.

As done for Figures 3-A-D, Figures 4A-C show the patterns for cross-validations **lg_24r37x37au_3T12C** and **lg_24r37x37au_6T12C**. The corresponding cumulative curves in Figure 2C show relatively better prediction-rate curves for gold occurrences. Let us observe the rates for the individual gold occurrences.

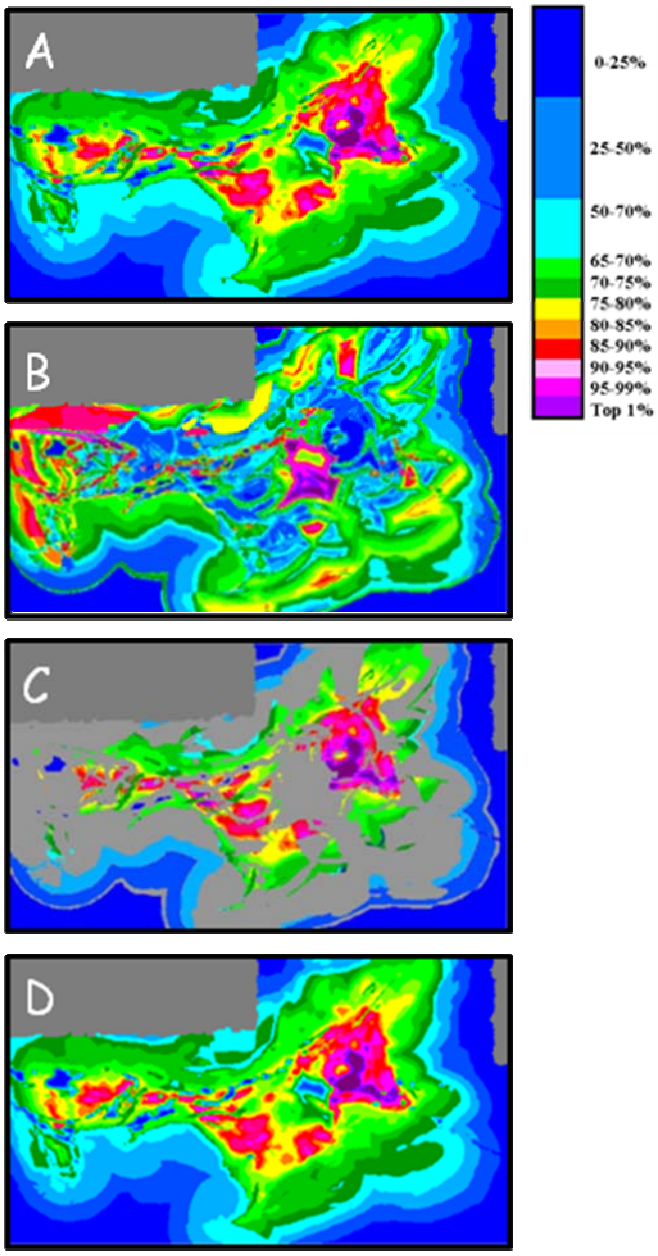

Figure 3. Target, Uncertainty and combination patterns for the Red Lake study area using a fuzzy set prediction model and the gamma operator with γ = **0.5**. (A) Target **fz_37-1au_3T12C**; (B) Uncertainty, (C) 50% Combination, and (D) Target **fz_37-1au_6T12C**, i.e., using twice geology, metamorphism and alteration.

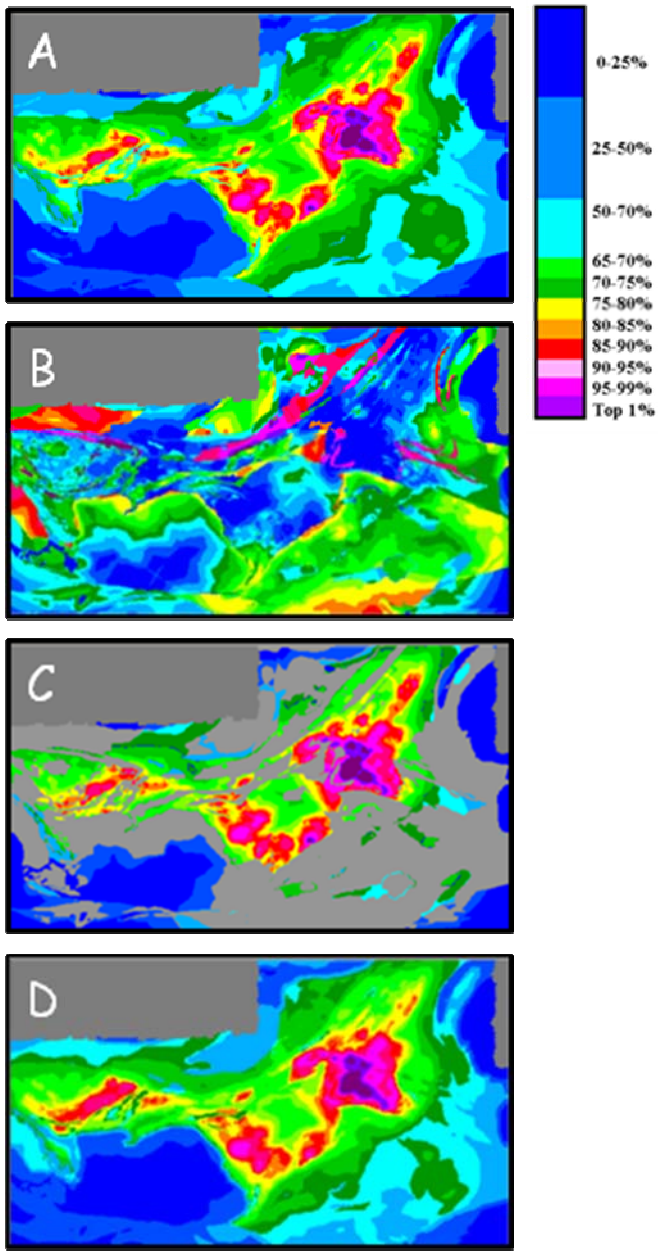

Figure 4. Target, Uncertainty and combination patterns for the Red Lake study area using a logistic discriminate function prediction model. (A) Target **lg_24r37x37au_3T12C**; (B) Uncertainty, (C) 50% Combination, and (D) Target **lg_24r37x37au_6T12C**, i.e., using twice geology, metamorphism and alteration.

The target class membership can be expressed in 1000 units overlaying their distribution of the different target and uncertainty patterns. This is done, for instance, in Table 1 for the cross-validations: **fz_37-1au_3T12C**, **fz_37-1au_6T12C**, and for **lg_24r37x37au_3T12C**. In the table T-rates above 850 represent occurrences falling within the highest 15% equal-area classes of the target pattern, while U-rates below 500 indicate occurrences within the lower 50% of the uncertainty range of ranks. The similarity between **fz_37-1au_3T12C** and **fz_37-1au_6T12C**, columns **fz-T** and **fz-T***, respectively, is evident, as well as the relatively better prediction with **lg_24r37x37au_3T12C** in column **lg-T**.

Columns **fz-T** and **fz_T*** contain 8 rates below 850 and columns **fz-U** and **fz_U*** 14 and 15 rates below 500, respectively. In comparison, columns **lg-T** and **lg-U**, contain 7 T-rates above 850 and 28 U-rates below 500. Clearly, the latter target pattern provides rates with relatively lower uncertainty.

The prediction results, prediction models and cross-validation strategies described provide an interpretation key of the relative quality of modelling a spatial database. They are to be considered as a critically useful and indispensable not only for this particular application and study area but also in general for all prediction modellings. It is an unfortunate situation, however, that in most applications to date such cross-validation

experiments are not seen in scientific geoscience literature. Because of that, the authors have contributed to the development and programming of the Spatial Target Mapping system, termed **STM** (www.spatialmodels.com), designed to provide the essential tools for generating target maps via iterative cross-validation strategies. Training initiatives have been taken (Fabbri and Chung, 2009) using different spatial databases not only for mineral exploration but also for natural hazard and risk analysis.

Acknowledgements

SpatialModels Inc., of Ottawa, Canada, has kindly provided a beta version of its new Spatial Target Mapping system **STM**. The DISAT Department of the University of Milano-Bicocca, in Milan, Italy, has partly supported this research work.

References

Chung, C. F., 2006, Using likelihood ratio functions for modeling the conditional probability of occurrence of future landslides for risk assessment: *Computers & Geosciences*, v. 32, no. 8, p. 1052–1068. doi:10.1016/j.cageo.2006.02.003.

Chung, C. F., and Fabbri, A. G., 2001, Prediction models for landslide hazard using a fuzzy set approach. In: M. Marchetti and V. Rivas (Eds.), Geomorphology and Environmental Impact Assessment. Balkema, Rotterdam, pp. 31–47.

Chung C.-J., and Fabbri A. G., 2008, Modular Course in Quantitative Methods for Mineral Exploration, Department of Earth Sciences, University of Ottawa, Canada, 16-23 February, 2008, 52 p., Unpublished manuscript.

Chung C.-J., and Fabbri A. G., 2009, Training decision-makers in hazard spatial prediction and risk assessment: ideas, tools, strategies and challenges. In, K. Duncan and C. A. Brebbia, (Eds.), Disaster Management and Human Health Risk, Southampton, WIT Press, p. 285-296.

Fabbri, A. G., and Chung C. F., 2008, On blind tests and spatial prediction models. *Natural Resources Research*, **17(2)**, pp. 107-118.

GSC, 2000. Panagapko, D. A., 2000: Preliminary release of geoscience data Red Lake greenstone belt, northwestern Ontario, *Geological Survey of Canada Open File* 3751.

Hillary B., Kerswill J., Keating P., Harris J., and Chung C.-J., 2008, Description and illustration of data used in the Red Lake case study. In, Modular Course in Quantitative Methods for Mineral Exploration, Department of Earth Sciences, University of Ottawa, Canada, 16-23 February, 2008, 28 p., Unpublished manuscript.

Table 1. Target and uncertainty rates for the 37 Au occurrences in the Red Lake study area, for cross-validations **fz_37-1au_3T12C** (**fz-T**, and **fz-U**), **fz_37-1au_6T12C** (**fz-T*** and **fz-U***), and **lg_24r37x37au_3T12C** (**lg-T**, and **lg-U**).

ID	fz-T	fz-U	fz-T*	fz-U*	lg-T	lg-U
	37-1	*37-1*	*37-1*	*37-1*	*24r37*	*24r37*
1	751	671	762	521	725	100
2	889	681	881	573	952	116
3	897	788	898	732	909	185
4	976	657	982	553	983	32
5	999	3	999	3	991	27
6	992	10	989	154	975	43
7	949	603	921	590	877	933
8	898	342	920	305	990	27
9	734	430	709	375	726	281
10	976	303	982	238	956	130
11	918	879	866	831	842	689
12	984	202	985	161	995	14
13	788	980	821	970	873	829
14	998	3	998	3	998	10
15	994	162	991	255	985	31
16	996	5	992	149	966	94
17	935	673	943	612	954	198
18	739	718	723	484	713	167
19	1000	1	1000	1	998	12
20	998	3	997	4	999	11
21	985	382	988	255	945	173
22	997	10	997	9	977	70
23	982	298	971	381	960	286
24	930	857	938	835	880	490
25	970	985	958	971	926	292
26	972	808	970	793	946	281
27	950	790	925	741	901	665
28	912	854	907	827	886	479
29	937	799	931	751	969	115
30	981	668	973	670	995	23
31	904	706	919	582	965	313
32	931	660	944	559	975	258
33	789	581	771	435	812	806
34	881	748	864	667	853	780
35	831	664	809	538	856	736
36	759	828	743	685	764	789
37	676	804	647	786	621	695

Generation of a GIS-based mineral potential map of the Neoproterozoic Gariep Belt in Namibia

Maria Lohmeyer, Hartwig E. Frimmel
Geodynamics & Geomaterials Research Division, Institute of Geography and Geology, University of Würzburg, Am Hubland, 97074 Würzburg, Germany, e-mail: maria.lohmeyer@googlemail.com

Abstract. This paper illustrates the creation of a mineral prospectivity map for SEDEX-type base metal deposits in the Nambian part of the Neoproterozoic Gariep Belt by using a Geographic Information System (GIS). Two Pb-Zn-deposits (Rosh Pinah, Skorpion) are known in the Gariep Belt and they serve as reference for testing the prospectivity map. In this study, a mineral system approach and index overlay (weighted overlay) method are used to lineate zones with high likelihood of mineral deposit occurrence. Seven GIS-based predictor maps with a pixel size of 100 x 100 m were produced on the basis of a series of prospectivity recognition criteria. By combining the predictor maps in the weighted overlay tool, a mineral potential map was created. The highest favourability was determined indeed in the area of the known Rosh Pinah deposit, thus showing that mineral prospectivity maps that are based on prior theoretical considerations can be used to lineate prospective zones.

Keywords. Gariep Belt, Rosh Pinah, GIS, mineral potential mapping

1 Introduction

In the last 20 years GIS-based mineral potential maps have become a useful tool for exploration of mineral deposits as computer technology, GIS software, data storage, remote sensing and GPS-based technologies became more and more efficient. There are two different approaches for mineral potential mapping, one being data-driven and the other knowledge-driven. Due to an increasing availability of geological, geochemical and geophysical input data, statistical, data-driven models like logistic regression (Harris et al. 2001; Agterberg & Bonham-Carter 2005), discriminant analysis (Harris et al. 2003) weights of evidence (Bonham-Carter 1994; Singer & Kouda 1999; Carranza 2004) and artificial neural networks (An et al. 1995; Singer & Kouda 1999; Brown et al. 2000) are being more and more used. The weight of the evidential maps is determined by the data itself. For this, a sufficient amount of known deposits in the target region is required. In contrast, knowledge-driven methods like Boolean overlay (Bonham-Carter 1994), mineral system approach (Wyborn et al. 1994) and index overlay (Madani 2011) depend on the knowledge and geological experience of the modeller and are therefore more subjective than the data-driven models. Their advantage is, however, that they can be used in cases for which less input data and fewer known deposits are given. Another method, fuzzy logic, can be applied in both data- and knowledge-driven approaches (Carranza & Hale 2001; Porwal et al. 2003, 2006).

The target area of this study is the Neoproterozoic Gariep Belt in southwestern Namibia. The Gariep Belt hosts two major known Pb-Zn-deposits, Rosh Pinah and Skorpion. Rosh Pinah is a sedimentary exhalative Pb-Zn sulfide deposit (Alchin & Moore 2005) whereas Skorpion is a secondary, non-sulfide supergene deposit (Borg et al. 2003). The geological background is based on several decades of mapping and research work that is summarized in Frimmel (2008).

2 Regional framework and SEDEX mineralisation of Rosh Pinah

The Gariep Belt formed during the Pan-African orogeny at around 550 Ma, when Neoproterozoic sediments and volcanic rocks where metamorphosed and deformed in a fold-thrust belt in consequence to the continental collisions giving rise to Gondwana. During that event the allochthonous, predominantly oceanic Marmora Terrane was thrust on the para-autochthonous, volcano-sedimentary Port Nolloth Zone. Preceding this orogenic event, the region was marked by continental rifting at around 750 Ma which led to the formation of a half graben (Gariep Basin proper) and further east to the Rosh Pinah Graben, which hosts the Rosh Pinah deposit, separated by the Aurus Horst.

The SEDEX-style mineralization affected predominantly shales and minor limestones that were deposited on top of a siliciclastic continental rift filling (Stinkfontein Subgroup) at a time, when the sea level dropped due to the Sturtian glaciation, evident in glaciogenic diamictite that occurs locally along the former basin margin. The eustatic sea level drop is thought to have caused the anoxic conditions in the bottom waters, required for the SEDEX mineralization (Frimmel & Jonasson 2003). Contemporaneous bimodal magmatism did not play an active role in SEDEX mineralization but may have provided the heat engine for hydrothermal convection through the underlying Stinkfontein Subgroup. That subgroup contains abundant feldspar-rich sedimentary rocks, which most likely served as predominant source at least for the Pb (Frimmel et al. 2004).

3 Methodology

Two methodological approaches were used in this work. First, through the mineral system approach, the prospectivity recognition criteria were defined. They serve as a basis of the genetic model of the mineral deposit formation of Rosh Pinah and can be derived from geological maps. In a second step we determined the score of each class and importance (weight) of each mineral-deposit-forming factor. This is the basic concept for the weighted overlay that led to the creation of the

mineral potential map.

3.1 Mineral system parameters

The following parameters, which we consider essential for SEDEX mineralization in the study area, were assessed and their classes were scored from 0 to 10 whereby 0 expresses a low influence and 10 a high one:

1. Source of base metals

The base metal source is assumed to be the arkose-rich rift-graben fill (Stinkfontein Subgroup). The feldspar-rich sediments were derived from an Eburnean (Palaeoproterozoic) magmatic arc (Richtersveld Terrane) and Pb was leached by circulating mineralizing fluids (Frimmel et al. 2004). Today's distribution of the Stinkfontein Subgroup was taken as approximation of the basin shape at 750 Ma. From the areal distribution of the various Neoproterozoic sedimentary units and their relationship to the basement, it is assumed that the thickness of the Stinkfontein Subgroup increases from the northern part of the rift graben to the south. In the northernmost parts of the Rosh Pinah rift graben, the Kaigas and Pickelhaube formations rest directly on basement, hence no Stinkfontein Subgroup sediments were deposited there. Consequently, we divided the rift in equal parts, scoring the southeastern parts with 10 and the northernmost with 0. Former basement parts where scored 4, because they are lithologically similar to the Stinkfontein arkoses and could have served as metal source as well, but were surely less permeable for the mineralizing fluids.

2. Source of anion complexes/ligands and of transport medium

As principal source of S we assume bacterially reduced marine sulfate, as indicated by S isotopes. Former evaporates are likely to have played an important role in providing the necessary salinity in the fluids to transport base metals.

The mineralizing fluids were highly saline preorogenic and of meteoric or marine origin (Frimmel & Board 2000). The Aurus Horst and other basement regions were above sea level and thus of no significance for mineralizing fluid circulation. Consequently the reconstructed former graben zones were scored with 10, and the areas of former basement with 0.

3. Fluid pathways

There are two general pathways for mineralizing fluids. The first depends on the permeability of the rock that is leached. This factor is already included in Parameter 1. The second possibility for pathways depends on basin bounding growth faults along the eastern margin of the rift graben. These normal faults may have acted as channels for mineralizing fluids in an extensional regime. During later orogeny, they were inverted to today's thrust faults. Thus we selected all thrust faults as shown on published geological maps and created a buffered layer of distance, that was reclassified in the next step. The farther away the distance to a thrust fault, the lower the class score is.

4. Source of energy for fluid convection

SEDEX-deposits need a heat source to drive hydrothermal convection. Firstly, a generally elevated geothermal gradient can be assumed in any rift setting. To take this into account, we used again our basin-horst-reconstruction with a score of 10 for the basin and 0 for the basement regions.

Secondly, the bimodal, predominantly felsic volcanism that had been active during the rifting is likely to have served as additional, more localized heat source for fluid convection (Alchin et al. 2005, Frimmel 2008). In the geological map of the Rosh Pinah Formation, Koivib/Rosh Pinah volcanic rocks and the Spitzkop member were selected and an Euclidean distance layer was created and subsequently reclassified. The farther away the distance to the volcanic units, the lower the class score is.

5. Spatial and/or chemical or physical trap

There are two possible traps of Rosh Pinah-type mineral deposition. The first one is a redox trap provided by anoxic conditions in the Rosh Pinah Graben east of the Aurus Horst. Consequently, this zone was scored with 10, all other former basins and the elevated basement regions with 0.

The second type of trap is a chemical trap provided by the presence of carbonates and led to replacement mineralization accompanied by intensive stockwork brecciation, silification and dolomitisation (Frimmel & Board 2000; Alchin & Moore 2005; Alchin et al. 2005). Consequently, limestone beds in the Rosh Pinah Formation were scored 10. Other carbonates that were deposited at more or less the same time but in different sedimentary facies (Pickelhaube Formation) were scored with 6.

6. Adequate temporal chain of the geological processes and mineral deposit preservation

Further essential parameters for the existence of mineral deposits are an adequate temporal sequence of the geological processes as well as mineral deposit preservation. They cannot be directly detected on the geological map but are already included in the factors mentioned above.

3.2 Weighted overlay

All predictor maps were created by data selection or digitization in a first step, conversion from feature to raster file and classification of the classes defined in chapter 3.1. The maps were combined in a weighted manner as follows. Following Bonham-Carter (1994) we define the score for any location as:

$$S = \frac{\sum_{i=1}^{n} S_{ij} W_i}{\sum_{i=1}^{n} W_i}$$

where S is the weighted score for an area object (pixel, polygon), W_i is the weight for the i^{th} input map, and S_{ij} is the score for the j^{th} class of the i^{th} map. The value of j is depending on the class actually occurring at the current location. We defined the values of S_{ij} in Chapter 3.1 and

the weights of the input maps (W_i) as follows.

The source of base metals as well as the source of anion complexes and fluid medium were both weighted with 15%, fluid pathways with 30%. The two mappable sources of energy were together weighted 25%, geothermal gradient with 5% and volcanism with 20%. The geothermal gradient map is more general than the spatially defined volcanism hence the evidential map "volcanism" has been weighted higher. The trap 1 (anoxic event) was weighted with 10% and trap 2 (carbonate replacement) with 5%.

4 Results

All in all seven predictor maps were created that represent the predictive model parameters. They were combined in the weighted overlay and led to a mineral prospectivity map with a pixel size of 100 x 100 m (Figure 1).

The lowest mineral potential was achieved in the basement regions and the Marmora Terrane, the highest at Rosh Pinah and in a zone 6 to 8 km north and northwest of Rosh Pinah. Relatively high potential (8 out of 10) was determined for the area south of Rosh Pinah, whereas only a medium potential was determined for the region around Skorpion (Fig. 1).

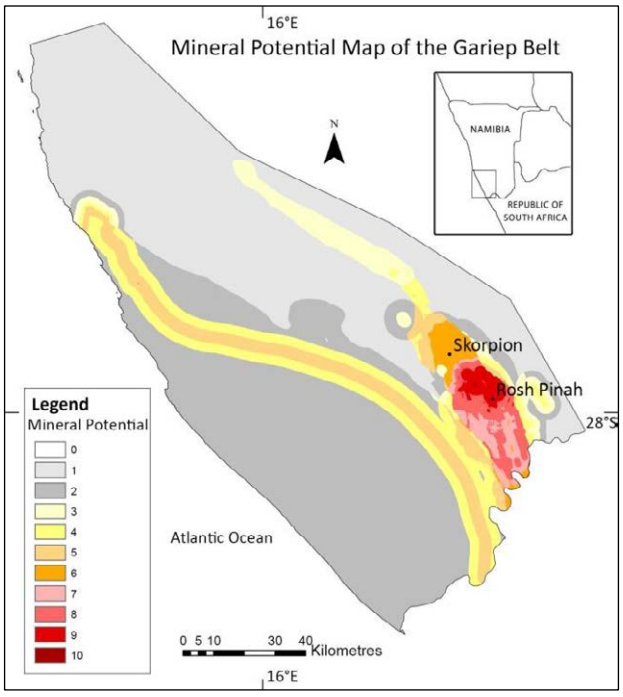

Figure 1. Evident map showing the potential for SEDEX-type base metal mineralization in the Namibian portion of the Gariep Belt.

5 Discussion and Conclusions

The perfect spatial overlap between the theoretically predicted mineral potential for SEDEX-type mineral deposits and the known Rosh Pinah ore bodies illustrates that the knowledge-driven approach can be a suitable method for exploration of this type of ore deposit indeed.

Interestingly, the region around Skorpion shows only moderate potential. It should be noted, however, that the Skorpion Zn-deposit resulted from secondary oxidation of a primary sulfide mineralization (Borg et al. 2003). It may be speculated that the Zn-enrichment to economic ore grade at that locality was achieved through the oxidation of an otherwise uneconomic primary mineralization. Consequently, a much larger area of only moderate SEDEX ore potential would be available for the presence of further, undiscovered Skorpion-type oxidized Zn deposits.

Considering scale, mineral potential maps like the one created in this study are not really useful to locate specific ore bodies but seem to be useful for exploration on a regional scale. They can help in identifying target areas of several square kilometres on which a further concerted effort, using standard geological, geochemical and geophysical mapping techniques, can be focused. Depending on the available map scale of the input maps, a smaller pixel size may be used and thus mineral potential maps may be produced also on a smaller scale.

A limitation of the mineral potential mapping approach used in this study is the two-dimensionality of the input maps and the lack of knowledge about the Neoproterozoic geology in those areas that are covered by Tertiary and Quartenary sediments. This limitation may be overcome to some extent by including drill hole data, when and if available, into the model.

All in all our study has shown that knowledge- and data-driven methods have a role to play in regional exploration and there is little doubt that their importance and popularity will increase in the coming years. This notwithstanding a solid geological knowledge based on thorough field work is required to avoid a black box analysis and thus will remain the most essential prerequisite for success in finding new ore deposits.

Acknowledgements

Some of the input maps were adapted from unpublished data provided by Ute Schreiber from the Geological Survey of Namibia, which is gratefully acknowledged. Emmanuel J. M. Carranza is thanked for reviewing this paper.

6 References

Agterberg FP, Bonham-Carter GF (2005) Measuring the performance of mineral potential maps. Natural Resources Research 14:1-17

Alchin DJ, Frimmel HE, Jacobs LE (2005) Stratigraphic setting of the metalliferous Rosh Pinah Formation and the Spitzkop and Koivib Suites in the Pan-African Gariep Belt, southwestern Namibia. South African Journal of Geology 108:19-34

Alchin DJ, Moore JM (2005) A review of the Pan-African, Neoproterozoic Rosh Pinah Zn-Pb deposit, southwestern Namibia. South African Journal of Geology 108:71-78

An P, Chung CF, Rencz, AN (1995) Digital lithology mapping from airborne geophysical and remote sensing data in the Melville Peninsula, northern Canada, using a neural network approach. Remote Sensing of Environment 53:76-84

Bonham-Carter GF (1994) Geographic Information Systems for Geoscientists. Modelling with GIS. Pergamon Press, Ontario, pp. 398

Borg G, Kärner K, Buxton M, Armstrong R, van der Merwe SW (2003) Geology of the Skorpion supergene zinc deposit, southern Namibia, Econ Geol 98:749-771

Brown WM, Gedeon TD, Groves DI, Barnes RG (2000) Artificial neural networks: a new method for mineral prospectivity mapping. Australian Journal of Earth Science 47:757-770

Carranza EJM (2004) Weights of evidence modeling of mineral potential: A case study using small number of prospects, Abra, Philippines. Natural Resources Research 13:173-187

Carranza EJM, Hale M (2001) Geologically constrained fuzzy mapping of gold mineralization potential, Baguio District, Philippines. Natural Resources Research 10: 125-136

Frimmel HE (2008) Neoproterozoic Gariep Orogen. In: Miller, R. McG. (eds.) The Geology of Namibia. Windhoek, v. 2, pp. 14-1 – 14-39

Frimmel HE, Board WS (2000) Fluid evolution in and around the Rosh Pinah massive sulphide deposit in the external Pan-African Gariep Belt, Namibia. South African Journal of Geology 103:191-206

Frimmel HE, Jonasson I (2003) The controls on Neoproterozoic base metal sulphide mineralization. In: Eliopoulos et al. (eds.): Mineral Exploration and Sustainable Development Millpress (Rotterdam), v. 2: 661-664

Frimmel HE, Jonasson IR, Mubita P (2004) An Eburnean base metal source for sediment-hosted zinc-lead deposits in Neoproterozoic units of Namibia: Lead isotopic and geochemical evidence. Mineralium Deposita 39:328-343

Harris DV, Wilkinson L, Heather K, Fumerton S, Bernier MA, Ayer J, Dahn R (2001) Application of GIS processing techniques for producing mineral prospectivity maps – a case study: Mesothermal Au in the Swayze Greenstone Belt, Ontario, Canada. Natural Resources Research 10: 91-123

Harris DV, Zurcher J, Stanley M, Marlow J, Pan G (2003) A comparative analysis of favorability mappings by weights of evidence, probabilistic neural networks, discriminant analysis, and logistic regression. Natural Resource Research 12: 241-255

Madani, AA (2011) Knowledge-driven GIS modelling technique for gold exploration, Bulgah gold mine, Saudi Arabia. The Egyptian Journal of Remote Sensing and Space Sciences 14:91-97

Porwal AK, Carranza EJM, Hale M (2003) Knowledge-driven and data fuzzy models for predictive mineral prospectivity mapping. Natural Resources Research 12: 1-25

Porwal AK, Carranza EJM, Hale M (2006) A hybrid fuzzy weights-of-evidence model for mineral potential mapping. Natural Resources Research 15:1-14

Singer DA, Kouda R (1999) A comparison of the weights-of-evidence method and probabilistic neural networks. Natural Resources Research 8: 287-298

Wyborn LAI, Heinrich CA, Jaques AL (1994) Australian Proterozoic mineral systems: essential ingredients and mappable criteria. The AusIMM Annual Conference

Using a global geodynamic model to aid mineral exploration

Graeme Nicoll, Graham Baines, James Etienne
Neftex, 97 Jubilee Avenue, Milton Park, Abingdon, Oxfordshire, OX14 4RW, UK

Abstract. The Neftex Geodynamic Earth Model is a sophisticated global plate model that currently allows reconstructions for any age between 595 Ma and present day. This internally consistent model is supported by our unique understanding of global stratigraphy and tectonics. Within this framework, we can identify (and differentiate) geodynamic features of interest including active margins, magmatic arcs, positions of major continental and oceanic plate boundaries in addition to large igneous provinces, major collisional belts, rifting and the Phanerozoic redistribution of mineral-rich Archean terranes. Reproducible workflows can test exploration concepts at the global to regional scales where input parameters can be evaluated and refined. As an example, we highlight a workflow for the global identification of Phanerozoic volcanic arc systems, which may have led to the development of shallow level copper/gold-enriched porphyritic intrusions and epithermal systems. This workflow also highlights regions of prolonged subduction and enhanced fluid flow, which have a higher potential for mineral enrichment. The results show remarkable agreement with ~85% of the known Phanerozoic porphyry copper, epithermal gold as well as volcanogenic massive sulphide deposits worldwide, providing a predictive framework and global road map for future exploration.

Keywords. Geodynamic Model, Global Mineral Dataset, Geochronology, Mineral Exploration

1 Introduction

As the number and quality of new mineral deposit discoveries continue to decline, exploration is becoming riskier and more costly as it moves deeper into the subsurface in order to discover and access mineral deposits. Whilst the tools and technology for accessing subsurface deposits are advancing, identifying the right location to explore is becoming more challenging. New tools are required that will identify subsurface or 'blind' deposits and offer a predictive model for their discovery and increase exploration efficiency.

For over 50 years, plate tectonics has underpinned concepts that explain the distribution of minerals and within this paradigm is a developing earth model that explains why minerals are found where they are, and where they are likely to be found in the future. Detailed and large scale 'earth models' have traditionally been pioneered by the oil industry. These models use data gathered from surface and subsurface surveys (geological maps, satellite images, geological interpretations, geophysics, well logs and so on) and digitally combine them to produce four dimensional models (3-D plus time).

2 A Global Geodynamic Model

Over the past three years, we have developed and delineated a global array of Geodynamic Units (GDUs) that record unique geological histories. Building upon the former plate tectonic research program of the Université de Lausanne (Switzerland), the model is undergoing constant refinement, for example with the recent addition of >2,000 oceanic crust segments, definition of intra-cratonic boundaries for crustal assembly back to 2.5 billion years and identification of zones of attenuated continental crust. The model currently allows the reconstruction of geological data to any time in the Phanerozoic and Ediacaran. The model also tracks and delineates major collisional events, subducted margins, major volcanic arc activity, large igneous intrusive events and the Phanerozoic redistribution of mineral-rich Archean terranes. As the model is global, it is possible to compare mineralising activity in one region with another, thereby providing greater insight into the processes at work. The model also allows detailed examination of magmatic and tectonic events across a region throughout geological time.

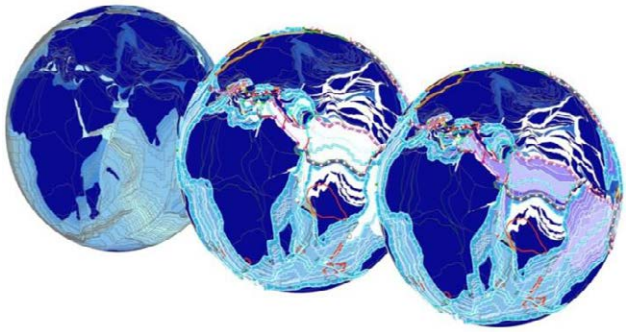

Figure 1. Reconstructions illustrating the Earth Model. ©Neftex

3 A Global Mineral Deposit Dataset

Alongside our geodynamic model, we have developed a geologically focused minerals database aimed at confronting exploration demands. So far, some 3,500 deposits (porphyry copper/gold, epithermal and orogenic gold and volcanogenic massive sulphides) are incorporated with data confirming accurate locations, precise mineralisation ages, bibliographic information and an interpretation within a global geodynamic

framework that provides greater insight into the spatial, temporal and geological contexts of known ore deposits.

Below are displayed the range of mineral deposit ages contained within the database (Fig. 2). The peaks represent the number of mineral occurrences recorded against time with specific clusters at ca. 35, 70, 350, 490, 1,800 and 2,700 Ma. The ability to geodynamically reconstruct these important Phanerozoic mineralisation periods, and in future the Precambrian, will no doubt lead to new formation models and greatly aid mineral exploration.

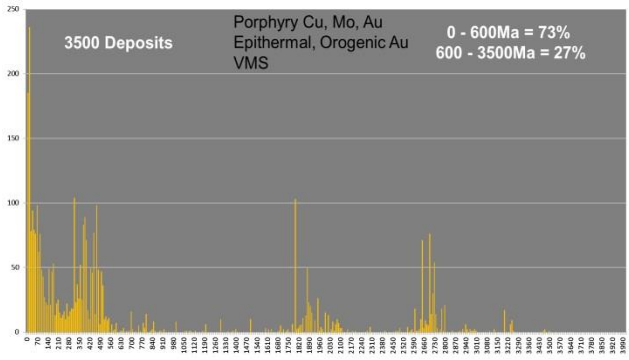

Figure 2. Histogram of the ages of mineral deposits within the Earth Model. ©Neftex

4 Using the Neftex Earth Model for Mineral Exploration

The validation of a model relies on its ability to identify known mineralisation and to predict targets defined by the established criteria. For example, an exploration model reconstructing the Upper Devonian of Eurasia (Fig. 3) shows the Siberian and Laurentian-Baltic cratons separated by the Uralian (Urals) Ocean. Regions of volcanic arc magmatism associated with subduction of the oceanic plate are shown in yellow (representing a belt 80 to 250 km inboard of the trench). This belt represents areas that have a higher chance of developing styles of subduction-related mineralisation such as porphyry copper, epithermal gold and, potentially, back-arc basin volcanogenic massive sulphides. Also highlighted are the predicted former positions of mid-oceanic ridges (double red lines) and areas where these are being subducted (solid black). These intersections potentially represent excellent targets for areas of mineral enrichment.

The Earth Model is dynamic, that is, the geology at any one location will change over time with the movement of plates. For example if all Phanerozoic volcanic arcs are mapped to their present-day locations then some of them (from different geological time periods) will overlap in areas where subduction was prolonged, or where subduction settings affected the same area of continental crust repeatedly through geological time. Such areas are likely to have been prone to significant enrichment and fluid flow, thereby enhancing the potential for large-scale mineral deposits. The results of this work, mapping out volcanic arcs, show remarkable agreement with ~85% of the known Phanerozoic porphyry copper, epithermal gold and volcanogenic massive sulphide deposits worldwide, thereby providing a predictive framework and global road map for future exploration.

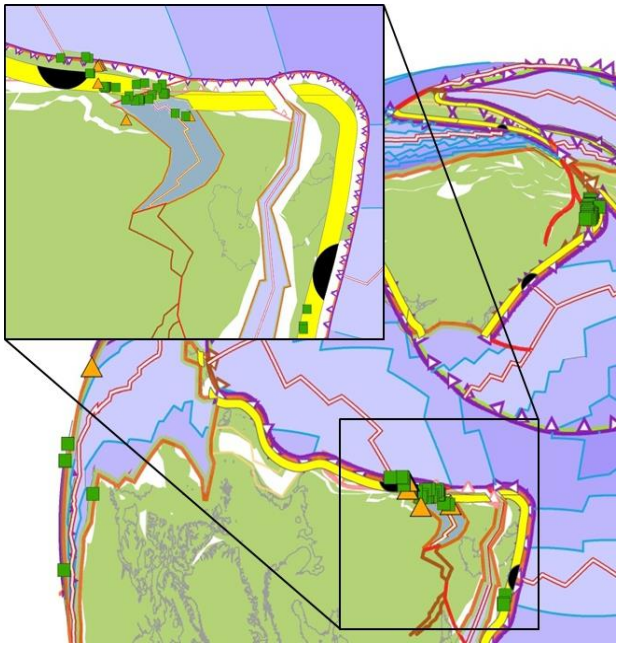

Figure 3. Upper Devonian Period of Eurasia, showing the Siberian (top right) and Laurentian-Baltic (lower left) cratons separated by the Uralian Ocean. Double red lines represents active mid-ocean spreading ridges, whereas subduction zones are shown by the purple lines with a saw tooth edge showing direction of plate motion. The yellow shapes delineate a zone, 80-250km inboard of the trench, of probable active volcanic arc magmatism. The black shapes highlight areas where mid-ocean ridges are being actively subducted. Also shown are the mineral deposits that were forming at this time period (expanded area shows some of the Ural deposits) including porphyry copper deposits (orange triangles) and VMS (green squares), highlighting a correlation to active subduction and back arc basin development. ©Neftex

Acknowledgements

For further information see www.neftex.com

The statistical distribution pattern of zinc concentrations at Belousovskoye deposit (Rudny Altai)

Petrich Katerina, Frolova Olga, Miroshnikova Anastasiya
East Kazakhstan State Technical University (EKSTU), Ust-Kamenogorsk, Kazakhstan

Abstract. The geochemical pattern of the Belousovskoye base-metal sulphide deposit was examined by sampling its largest and richest ore body #5. The samples were analyzed for copper, lead and zinc. In this paper we discuss data of zinc analyses only. The statistical distribution of elements within the deposit was analyzed using histograms that were plotted in a logarithmic scale. The distribution of metal concentrations serves as a base for the construction of reference models that will utilize a new approach for prognosis of new mineral deposits.
Previously, this approach was successfully applied for distribution analysis of Zn, Cu, Pb concentrations at the large and high-grade pyrite-polymetallic deposits of Maleyevskoe (Rudny Altai) (Los 1994), and of gold at Bolshevik (Antonov and Los 2011) and Akbakay (Rafailovich 2006) deposits.

Keywords. Rudny Altai, Belousovskoye deposit, statistical distribution, mode, average value, zinc.

1 Introduction

The detailed and complete analysis of the statistical distribution peculiarities of mineral concentrations is the requirement of the effective and qualitative deposits modelling. Statistical characteristics are the basis of the selection of method and parameters for the modelling of deposits.

The most detailed information of the statistical distribution of metals concentration is in the distribution function (normally the density function is used). In spite of the obvious deviations from the distribution of real metal concentrations, the models of normal (lognormal) principles are still widely used "by default", as it allows to calculate statistical parameters and use well-elaborated parametric criteria without problems.

2 Geological structure of the Belousovskoye deposit

The Belousovskoye sulphide-polymetallic deposit is unique in its dimensions and metal resources. It is the only sulphide-polymetallic deposit in the world, consisting of dozens of ribbon ore bodies. For these two reasons it is widely used as reference in different reviews, monographs and school-books.

The Belousovskoye deposit is situated at the south-east of the Berezovsk-Belousovskoye ore field at the junction of the north-east wing of the Irtysh anticlinorium and the Irtysh shear zone. The deposit is confined to the complex fold structure, restricted by the "Main fault" in the north-east and the "Irtysh Boundary fault" in the south-west. These faults are the branches of the trans-crustal Irtysh suture.

The ore bodies of the Belousovskoye deposit are located in intercalated tuffaceous-sedimentary Devonian strata, which are penetrated by subvolcanic bodies of rhyolitic and, more rarely, basaltic composition. These are intruded by dykes and small bodies of plagiogranite-porphyries, porphyric rhyolites and porphyrites. The oldest formations are homogeneous greenschists of the Orlovsk suite of Emsian age, developed on argillic-arenaceous and argillaceous-calcareous sediments. Their boundaries with the ore field are tectonic. Volcanogenic sediments of the Irtysh suite, terrigenous sediments of the Shipulinskaya suite and volcanogenic sediments of the Pihtovskaya suite, calcareous-argillaceous and arenaceous sediments of the lower horizons of the Belousovskaya suite, and calcareous-clayey siltstones and sandstones of the Upper-Belousovskaya sub-suite contribute to the geology of the deposit.

Sediments of the Pihtovskaya suite are trangressively overlain by calcareous and arenaceous sediments of the Bukhtarma suite, which are overlain by the coal-bearing continental formations of the Malaya Ulba suite (Fig. 1).

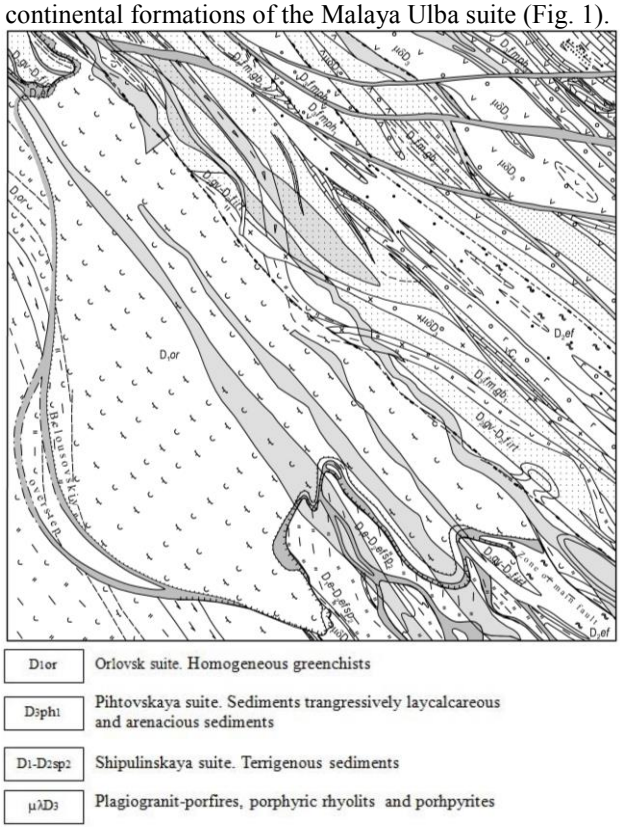

Figure 1. Geological map of the Belousovskoe deposit

Altered wall-rocks at the Belousovskoye deposit are represented by sericite and sericite-chloritic shales and micro-quartzites with pyrite and carbonate. The inner

structure of the metasomatite zones is complex with multiple pinching out and mutual transferences of one shale unit into the other.

In the structural plan the deposit is confined to a 6km long arrow-shaped tectonic block of north-western strike (about 310°), framed in the south-west by the Gluchansky thrust and in the north-east – by the Pisarevskiy-Belousovskiy fault.

The Belousovskoye deposit represents a group of long, thin, ribbon-shaped metalliferous deposits with north-west strike, situated in different stratigraphic and structural levels. The average proportion of their thickness to their width and length is 1:30:800. Within the deposit there are 10 large bodies and numerous zones of stringer-disseminated sulphide mineralization. The latter are separated into two ore branches: Belousovskaya (bodies 1, 2, 3, 7, 9, 10) and Glubochanskaya (bodies 4, 5, 6, 8). Overall, the bodies are narrow, comparatively thin, ribbon-shaped, and complicated by numerous bulges, squeezes and branches.

Ore body #5 is the largest and richest within the deposit. In the cross-section, the ore body is uniform and lensoid and can be traced for 5300m. The width of the body is 100-200m, the average thickness is about 9m but may extend to 14m thickness. The down-dip of the body is north-eastern – with angles of 10-20° at the south-eastern flank, and steep at the north-western flank. The strike of the body is north-eastern 320-325°. The ore body undulates down-dip. The features are squeezes, bulges, down-dip and rise branches at the footwall and hanging wall. The ores are mainly polymetallic massive and high-grade impregnated. The ore body is characterised by the presence of high-grade massive ribbon pyrite-polymetallic ores. The average grade in the ores is Cu - 2.6%, Pb – 2.4%, and Zn – 9.2%. In the hanging wall of the ore body copper and copper-zinc ores prevail, in the middle part dominate base-metal ores, whereas the footwall contains base-metal ore enriched in Pb. Ore body #5 contains up to 70% of all the metal resources of the deposit.

Ore mineral composition of ore body #5 includes pyrite and barite (jointly reaching up to 30-70% of the total ore mass), chalcopyrite, sphalerite, galena, more rarely fahlore, chalcosine, pyrrhotite, arsenopyrite. Rare minerals – bournonite, boulangerite, markasite, molybdenite, hessite and others.

Ore bodies are localized mostly in the sediments of the Shipulinskaya suite and appear less frequently among the sediments of the Irtysh suite where mineralization is also associated with sedimentary rocks. Ore-bearing strati are converted into sericite-quartz and chlorite-quartz slates (Fig. 2).

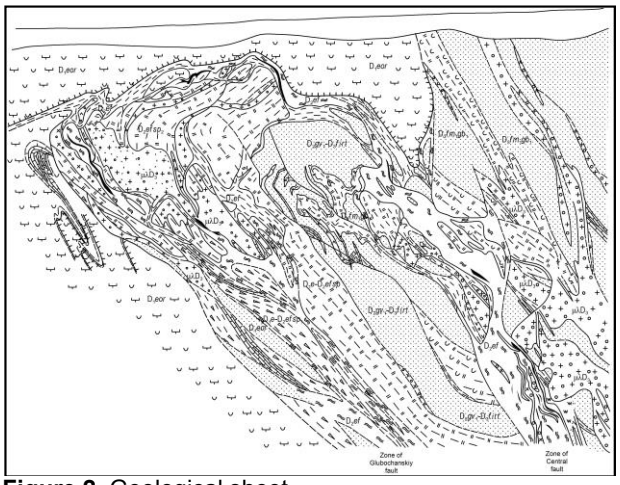

Figure 2. Geological sheet

The inner structure of the ore bodies is quite complex and is usually characterized by the following textural-morphological features: around the thin (from the first cm to one m) stock part of rich impregnated or massive ores there is an aureole of impregnated and vein-disseminated ores with gradual decrease of the level of sulphide abundance with increasing distance from the core of the body. The impregnated ores develop from both hanging wall and footwall of these ore bodies.

3 Research methods

Histograms form the basis of the structural analysis of statistical distribution of the ores. The type of the histograms depends on the scale type (standard, logarithmic) and on the assigned group interval of the examined characteristic. Mostly, studying the patterns of distribution of metal concentrations in ore deposits it is reasonable to use logarithmic scales. The influence of the group interval on the histogram type is obvious: at large intervals the features and details of the distribution patterns disappear, whereas at too small intervals the structural peculiarities are smeared by random fluctuations. During the study of the patterns of statistical distributions, the sample groups must contain not less than 150-200 samples, and the group intervals number must be 12-24 (Los 1968). This statement is explained by the fact that a larger number of samples used in the histogram construction would result in a more informative histogram. The impact of the size of grouping intervals is significant; large intervals result in a poor structure of element distribution, whereas very small intervals show that structural features erroneously change by non-representative single peaks in concentrations.

The structure of zinc distribution within the richest ore body of the deposit was studied using the compiled geological database (Fig. 3).

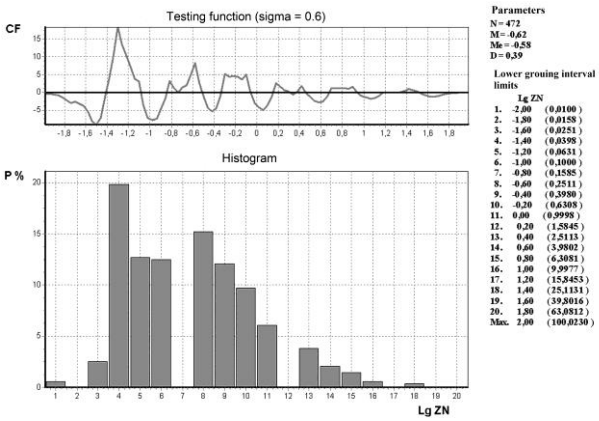

Figure 3. Parameters of level of zinc concentrations at Belousovskoye deposit; body 5.

All in all, there were processed 500 analysed samples of zinc-lead-copper sulphide ores. The histograms were built using logarithmic scale and software complex «ELAN». Table 1 contains the pre-set zinc concentration parameters at the Belousovskoye deposit, and the most stable modes of elementary components.

The research revealed that at the Belousovskoye deposit exist three characteristic robust concentration levels of zinc (natural limits of mineralization) of industrial importance: 1; 3.2; 9.5%. These values can and should be applied for outlining and calculation of the commercial zinc reserves in the ore bodies of the deposit, taking into account current and future geological-economic conditions of the region and of the country. The ores, delineated by the threshold values, were classified and calculated by the author as "sorts": poor (limit 1%), ordinary (limit 3.2%) and rich (limit 9.5%).

Table 1 Parameters of zinc concentrations level at the Belousovskoye deposit; ore body #5.

Object	Para-meters	Concentration levels					
		A	B	C	D	E	
Body #5	Mod,% lg mod	0.05 -1.3	0.25 -0.6	0.6 -0.2	1.58 0.2	6.3 0.8	15.8 1.2
	Bon,% lg bon	0.13 (-0.95)	0.4 (-0.4)	1 (0.00)	3.2 (0.5)	9.5 (1)	

Note: «mod» – modal values for elementary components of the statistical distribution of zinc (concentration levels); «bon» – "natural" limit of zinc grade values between the concentrations levels.

4 Summary

Detailed assay of the histogram pattern (the empirical analogue of frequency function of statistical distribution) of the sample group at the deposit ascertained that mostly the metal concentration distribution is polymodal. It consists of several constants, close to lognormal elementary components.

The histogram visualizes random value action. It shows the amplitude and frequency of the values. The histogram shape also bears useful information. The histogram mode corresponds to the maximum frequency.

Three morphological ore body types are allocated at the deposit. The first type contains the thickest and the richest bodies, located in the Shipulinskaya suite. They are represented by compact ribbon bodies, having the tilted yoke shape in the axial section. The bodies inside the Glubochanskaya subsuite pertain to the second type. They are characterized by asymmetrical crescent shape. The third type bodies are located in the north-east wing of the structure in the upper parts of the Glubochanskaya subsuite, where they are stowed as a system of small imbricate lodes and lenticular bodies with the shape of short ribbons. The proportion of width and length is 1:25 to 1:60 at the thickness of less than a meter to 10-15 m. Numerous apophyses and parallel lenses as well as ore bodies of complex morphology are especially common for the second type of ore bodies.

Thus, the study of the statistical distribution provides information on boundaries of ores, ore types and ore grades, and allows identification of morphological types of ore deposits. Another important practical application of the data on the patterns of statistical distribution lies in the ability to model ore objects using specifics of distribution at each level of metal concentrations. This approach was used for modeling of the gold deposit Akbakai (Kazakhstan) and showed that it is possible to obtain more accurate models and more reliable determination of the average metal content and metal resources in small blocks.

The study of statistical distribution of metals is not an absolute innovation in forecasting of new deposits and unfortunately this approach is rarely used in studies of mineral deposits of Kazakhstan as a whole, and in particular of the Rudny Altai. These studies are so far fragmental, and our goal is to use this approach more routinely in describing and predicting new mineral deposits.

References

Antonov YA, Los BL, (2011) Struktura statisticheskogo raspredeleniya kontsentratsiy zolota na mestorozhdenii "Bolshevik" (Vostochniy Kazakhstan). Geologiya I ohrana nedr 3:24-33

Los BL, (1994) Modelirovanie rudnyh mestorozhdeniy. Matematicheskie metody resheniya zadach modelirovaniya i prognozirovaniya v geologii. Almaty KazIMS. pp. 210-237

Los BL, (1968) Analiz raspredeleniya soderzhaniy osnovnyh poleznyh komponentov v rudah. Primeneniye matematicheskih metodov v geologii. Alma-Ata Nauka. pp. 239-243

Rafailovich MC (2006) Mestorozhdeniya zolota Akbakaiskogo tipa: mineralogo-geohimicheskaya zonalnost, raspredeleniye zolota, prognozo-poiskovaya model. Rudy I metally. pp. 41-53

All references are in Russian.

Bits of mathematics of potential modelling

Helmut Schaeben
Geophysics and Geoinformatics, TU Bergakademie Freiberg, Germany

Abstract. Mathematical methods of potential modelling are considered from the point of view of generalized linear models and Markov stochastic graphs. In particular, weights-of-evidence and logistic regression models are compared using stochastic graphs possessing a Markov property, where the notion of conditional independence is essential, and will be related to log-linear models. Referring to log-linear models provides a test of conditional independence. Then weights-of-evidence, logistic regression without interaction terms, and logistic regression including interaction terms can be put into a hierarchy of methods, where each former method is a special case of the consecutive latter method. Additional modelling assumptions involved in more special methods restrict their application, but may yield not surprisingly better results in terms of estimation errors.

Keywords. Weights-of-evidence, conditional independence, graphical models, logistic regression, log-linear models, artificial neural networks

1 Introduction

The ultimate goal of potential modelling or targeting is to recognize locations for which the probability of a "target" event like a specified mineralization is a relative maximum. The event must be sufficiently well understood in terms of cause and effect to collect data corresponding to spatially referenced factors ("evidences") in favour or against the event to occur. A "catalogue" of mineral deposit models has been compiled by Cox and Singer (1986). Geometallurgy and the mineral systems approach (e.g. McCuaig et al., 2010), will provide more prerequisites for practical potential modelling. Then spatially referenced "posterior" probabilities given the evidential factors can be estimated by several approaches including weights of evidence (Good, 1950), logistic regression (Hosmer and Lemeshow, 2000), artificial neural nets (Russell and Norvig, 2003), statistical learning (Hastie et al., 2001), machine learning and support vector machines (Kanevski et al., 2009), and others cf. (Porwal, 2006; Singer and Menzie, 2010; Schaeben, 2011). All methods require a training area to estimate the parameters of the model. In contrast to geostatistics, none of them considers spatially induced dependence.

2 Weights-of-Evidence

By virtue of Bayes rule for conditional probabilities the weight of a single evidential factor Z_1 is given as a ratio of some conditional probabilities, or rather as a ratio of likelihoods. This likelihood ratio is the factor by which the initial "prior" odds must be multiplied to get the final "posterior" odds (Good, 1968, p. 31). To generalize this approach for multiple evidential events Z_i, i=1,…m, the additional mathematical modelling assumption of conditional independence is required twice, once with respect to the target event T and once with respect to its complementary event. Two evidential factors Z_i, Z_j in favour of the occurrence T of a specified mineralization are conditionally independent given T, if knowledge of T renders Z_i irrelevant for predicting Z_j, and vice versa. Two factors Z_i, Z_j can simultaneously be (significantly) correlated and conditionally independent given T. The term "weights of evidence" had been coined by Pierce (1878) and used by Minsky and Selfridge (1961) and Jeffreys (1939; 1961). I.J. Good elaborated on it since the 50ies of the last century (Good, 1950; 1960; 1968; 2003) in about 33 papers (Good, 1983, p. 159). The method was introduced into geosciences since the 90ies by Agterberg, Bonham-Carter, and Cheng (e.g. Agterberg et al., 1989; Agterberg et al., 1990; Bonham-Carter and Agterberg, 1990), at some time all with the Geological Survey of Canada, and other co-authors, and further pursued in numerous successive publications by them. In practical applications the evidential factors are given in terms of presence or absence of favourable or unfavourable events, i.e., in terms of binary random variables. To consider a continuous random variable Z e.g., distance from a fault, as an evidential factor, it needs to be binarized with respect to a user defined threshold d_0, i.e., $Z_{binary} = 1$ indicating presence, if Z is less equal d_0, and $Z_{binary} = 0$ indicating absence, if Z is greater than d_0. The weights of evidence are estimated by counting the occurrences of events within the training area. All estimates come with standard errors.

Practical applications of weights-of-evidence are hampered by the mathematical modelling assumption of conditional independence which is often doubted to be satisfied by geological reasoning. Therefore, weights-of-evidence is subject to numerous attempts to develop workarounds to relax the assumption of conditional independence or to account for its partial violation (e.g. Journel, 2002; Krishnan et al., 2005; Polyakova and Journel, 2007; Krishnan, 2008; Deng, 2009), and very recently by (Daojun Zhang, Cheng and Agterberg 2012; Shengyuan Zhang and Cheng, 2012). Deng (2009) was shown to be wrong (Schaeben and Boogaart, 2011). The geoscience community appears to be somewhat reluctant to accept that logistic regression is an alternative in case the assumption of conditional independence does not apply. In fact, logistic regression yields the true joint distribution in case of linear dependencies. Moreover, logistic regression is not restricted to binary predictor

variables; thus binarization with respect to user defined thresholds is not required.

3 Logistic Regression

Logistic regression (e.g. Hosmer and Lemeshow, 2000), applies the logistic function $\Lambda(z) = 1/(1+\exp(-z))$, the graph of which is sigmoidal. The function $\Lambda(\alpha z)$ with a real constant $\alpha>0$ rapidly approximates a Heaviside function for increasingly large values of α. The logistic function is the inverse of the logit transfom which assigns to a probability the logarithm of the corresponding odds, i.e., $\text{logit}(P) = \ln(P/(1-P))$. Logistic regression generalizes ordinary linear models by using the logit transform as link function, thus establishing a relationship between the linear combination of evidential predictor variables and the logit-transformed conditional mean cf. (Nelder and Wedderburn, 1972; McCullagh and Nelder, 1989). Then the conditional probability of the target variable given the evidential predictors, which is referred to as posterior probability in weights-of-evidence, is modelled with the logistic function applied to a linear combination of the predictor variables. The model can be further generalized to include interaction terms.
In practical applications of the logistic regression model its parameters have to be estimated with respect to realizations of the target and the predictor variables within a training area. The parameters of the logistic regression model are usually estimated with the maximum likelihood method numerically realized with the Fisher scoring algorithm, a form of the Newton-Raphson algorithm, and a special case of iteratively reweighted least squares algorithm. This procedure ensures nice statistical properties of the estimates e.g., all estimates come with standard errors.

4 Artificial Neural Nets (ANN)

With respect to artificial neural nets the logistic regression model above is called a single-layer perceptron or single-layer ANN, minimization of the sum of squared residuals is referred to as training, gradient methods to solve for the model parameters are referred to as linear perceptron training rule, the step size along the negative gradient is called learning rate. Compared with logistic regression models the approach with artificial neural nets is less restrictive. The logistic function may be replaced by any sigmoidal function, the choice of the sigmoidal function may be guided by the numerical complexity to evaluate itself or functionals of it. ANN may include more involved dependencies than the logistic regression model. Thus, the model provided by ANN may be larger, more general and more flexible, requiring more data to control the additional model parameters, and applies gradient methods rather than the statistically inclined maximum likelihood method and Fisher's scoring algorithm to estimate the parameters. Usually ANN cannot provide standard estimation errors.

5 Mathematical Comparison of Methods

Graphical models (e.g. Lauritzen, 1996; Edwards, 2000; Koller and Friedman, 2009; Højsgaard, Edwards and Lauritzen, 2012), provide an appropriate approach to manage dependence or conditional independence of random variables. Thus they may be used to shed new light on the mathematical relationship of weights-of-evidence, logistic regression, and log-linear models (Schaeben, 2013). The actual clarification they provide may be summarized as follows.

If the evidential random variables are conditionally independent given the target, then
- the method of weights of evidence applies,
- logistic regression without interaction terms yields the proper complete model.

If individual evidential random variables are not conditionally independent given the target, then
- the method of weights of evidence does not apply,
- logistic regression still applies, interaction terms may be needed to yield the proper complete model.

If some evidential random variables are not binary, then
- the method of weights of evidence does not apply,
- logistic regression still applies, interaction terms may be needed, but multi-linear interaction terms may yield only approximations of the proper complete model.

6 Conclusions

Applying graphical models weights-of-evidence, logistic regression without interaction terms, and logistic regression including interaction terms can be put into a hierarchy of methods, where each former method is a special case of the consecutive latter method. Additional modelling assumptions involved in more special methods restrict their application, but yield not surprisingly better results in terms of estimation errors. In particular, if weights-of-evidence apply, then they usually yield smaller estimation errors than logistic regression due to the heavy additional modelling assumption of conditional independence. Logistic regression is more general than weights of evidence, i.e., it is unrestricted with respect to modelling assumptions (conditional independence), and type of random variables (binary). In the way defined above, logistic regression provides an optimum model for potential modelling.

Acknowledgements

Potential modelling is a contribution of the Geomathematics and Geoinformatics group at TU Bergakademie Freiberg, Germany, to the "ProMine" project funded by the European Community's Seventh Framework Programme under grant agreement no. 228559. This publication reflects only the author's view, exempting the Community from any liability.

This extended abstract is a short version of a manuscript submitted recently to Mathematical Geosciences and being reviewed now.

References

Agterberg FP, Bonham-Carter GF, Wright DF (1990) Statistical pattern integration for mineral exploration. In: Gaál G, Merriam DF (eds.) Computer Applications in Resource Estimation Prediction and Assessment for Metals and Petroleum, Pergamon Press, 1-21

Agterberg FP, Bonham-Carter GF, Wright DF, Cheng Q (1989) Weights of evidence and weighted logistic regression for mineral potential mapping. In: Davis JC, Herzfeld UC (eds.) Computers in Geology - 25 Years of Progress, Oxford University Press, 13-32

Bonham-Carter GF, Agterberg FP (1990) Application of a microcomputer based geographic information system to mineral-potential mapping. In: Hanley JT, Merriam DF (eds.) Microcomputer-based Applications in Geology - II Petroleum, Pergamon Press, 49-74

Cox DP, Singer DA, (1986) Mineral deposit models. U.S. Geological Survey Bulletin 1693

Deng M (2009) A conditional dependence adjusted weights of evidence model. Natural Resources Research 18: 249-258

Edwards D (2000) Introduction to Graphical Modelling. 2nd edn. Springer

Good IJ, (1950) Probability and the Weighing of Evidence. Griffin, London

Good IJ (1960) Weight of Evidence, Corroboration, Explanatory Power, Information and the Utility of Experiments. Journal of the Royal Statistical Society B 22: 319-331

Good IJ (1968) The Estimation Of Probabilities – An Essay on Modern Bayesian Methods. Research Monograph No. 30, The MIT Press, Cambridge, MA, USA

Good IJ (1983) Good Thinking – The Foundations of Probability and Its Applications. The University of Minnesota Press

Good IJ (2003) The accumulation of imprecise weights of evidence. http://www.sipta.org/isipta03/jack.pdf. Accessed 21 January 2013

Hastie T, Tibshirani R, Friedman J (2001) The Elements of Statistical Learning -- Data Mining, Inference, and Prediction. Springer

Højsgaard S, Edwards D, Lauritzen S (2012) Graphical Models with R. Springer

Hosmer DW, Lemeshow S (2000) Applied Logistic Regression, 2nd edn. Wiley

Jeffreys H (1939) Theory of Probability 1st ed. Clarendon Press

Jeffreys H (1961) Theory of Probability 3rd ed. Clarendon Press

Journel AG (2002) Combining knowledge from diverse sources – An alternative to traditional data independence hypotheses. Mathematical Geology 34: 573-596

Kanevski M, Pozdnoukhov A, Timonin V (2009) Machine learning for spatial environmental data – Theory, applications and software. EPFL Press

Koller D, Friedman N (2009) Probabilistic Graphical Models – Principles and Techniques. The MIT Press, Cambridge, Massachusetts

Krishnan S (2008) The τ-model for data redundancy and information combination in Earth sciences – Theory and Application. Mathematical Geology 40: 705-727

Krishnan S, Boucher A, Journel AG (2005) Evaluating information redundancy through the τ-model. In: Leuangthong O, Deutsch CV (eds.) Geostatistics Banff 2004, Springer, 1037-1046

Lauritzen S (1996) Graphical Models. Clarendon Press, Oxford

McCuaig TC, Beresford S, Hronsky J (2010) Translating the mineral systems approach into an effective exploration targeting system. Ore Geology Reviews 38: 128-138

McCullagh P, Nelder J (1989) Generalized Linear Models. 2nd edn. Chapman and Hall/CRC

Minsky M, Selfridge OG (1961) Learning in random nets. In: Cherry C (ed) Information Theory: Fourth London Symposium, Butterworths, 335-347

Nelder J, Wedderburn R (1972) Generalized Linear Models. Journal of the Royal Statistical Society Ser A 135: 370-384

Pierce CS (1878) The probability of induction. Popular Science Monthly, republished In: Newman JR (ed) (1956) The World of Mathematics 2. Simon and Schuster, New York, 1341-1354

Polyakova EI, Journel AG (2007) The ν-expression for probabilistic data integration. Mathematical Geology 39: 715-733

Porwal AK (2006) Mineral potential mapping with mathematical geological models: Dissertation, Enschede, The Netherlands

Russell S, Norvig P (2003) Artificial Intelligence – A Modern Approach, 2nd ed. Prentice Hall

Schaeben H, (2011) Comparison of Mathematical Methods of Potential Modeling. Mathematical Geosciences 44: 101-129. doi 10.1007/s11004-011-9373-2

Schaeben H (2013) John C. Griffiths Award Talk 2012 – Some Mathematics of Potential Modeling, Conditional Independence and Markov Graphs. Mathematical Geosciences, submitted

Schaeben H, van den Boogaart KG (2011) Comment on "A conditional dependence adjusted weights of evidence model" by Minfeng Deng in Natural Resources Research 18 (2009), 249-258. Natural Resources Research 20: 401-406

Singer DA, Menzie WD (2010) Quantitative Mineral Resource Assessments, an Integrated Approach. Oxford University Press

Zhang D, Cheng Q, Agterberg FP (2012) Weights of evidence method and weighted logistic regression model. Abstracts 34th International Geological Congress, 1789

Zhang S, Cheng Q (2012) A modified weights of evidence model for mineral potential mapping. Abstracts 34th International Geological Congress, 2008

S 3.1:

Volcanic-hosted base and precious metal deposits

Convenors:
Rodney Allen & Fernando Tornos

KEYNOTE SPEAKER

Hydrothermal systems related to intraoceanic arcs

Cornel E.J. de Ronde
Department of Marine Geosciences, GNS Science, Lower Hutt 5010, New Zealand

Abstract. Hydrothermal activity associated with intraoceanic arc volcanoes, including both caldera- and cone-types, is dominated by the discharge of magmatic volatiles.This hydrothermal magmatic signature, including high concentrations of S and C species gases together with high Fe contents, coupled with the shallow depths (~1800-120 m below sea level) of these volcanoes, greatly influences the chemistry of the venting fluids. This in turn afects the type of mineralization that precipitates from these fluids, and more than likely has important consequences for the biota associated with these systems. Given the high metal contents and very acidic fluids, these hydrothermal systems are also thought to be important analogues many of the porphyry copper and epithermal gold-rich deposits exploited on land today

Keywords. Intraoceanic arcs, seafloor hydrothermal systems, Kermadec arc, Mariana arc, magmatic volatiles

1 Intraoceanic arc hydrothermal systems

Volcanic arcs are the surface expression of magmatic systems that result from the subduction of mostly oceanic lithosphere at convergent plate boundaries. Arcs with a submarine component include intraoceanic arcs and island arcs that span almost 22,000 km on Earth's surface, with the vast majority located in the Pacific region (Fig. 1). Intraoceanic arcs total almost 7,000 km, thus ensuring a steady supply of dissolved gases and metals to the oceans, and the potential for the formation of polymetallic mineral deposits (de Ronde et al., 2003).

Most mineralization along intraoceanic arcs is dominated by mineral assemblages representing high-sulfidation conditions, including elemental sulfur, polymorphs of silica, alunite and lesser pyrite. This mineralizaton is typically associated with relatively low temperature (≤120°), diffuse, acidic (pH <3), metal-poor but gas-rich emissions from seafloor hydrothermal systems. Less common are focused, relatively high temperature (~300°C), metal-rich fluids where Fe-Cu-(±Au)-Zn sulfides and barite/anhydrite predominate. Both types of venting show evidence for contributions from magmatic sources. These two types of venting represent end-members of a continuum that spans magmatic-hydrothermal to water/rock dominated systems, respectively. More mature vent fields are better able to deliver and accumulate metals at the seafloor. The two intraoceanic arcs most intensively studied for their seafloor hydrothermal systems are the Kermadec and Mariana arcs.

For videos of arc seafloor hydrothermal systems, see:
http://oceanexplorer.noaa.gov/explorations/04fire/
http://oceanexplorer.noaa.gov/explorations/06fire/
http://oceanexplorer.noaa.gov/explorations/07fire/

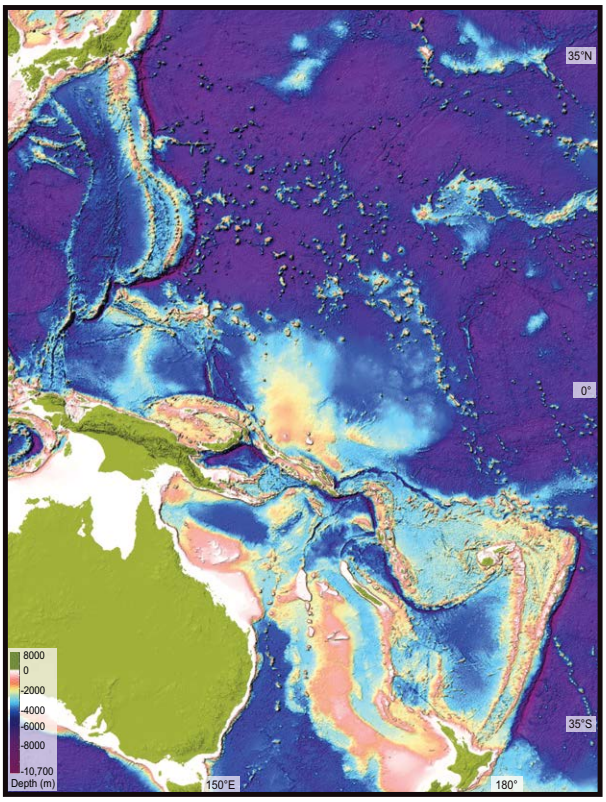

Figure 1. Map showing the western Pacific region, with the various island and intraoceanic arcs stretching from Japan in the NW to New Zealand in the SE. Map made courtesy of S. Merle (NOAA).

2 Kermadec arc

The ~1,220 km long Kermadec arc is host to ~40 large volcanoes of which 80% are hydrothermally active, making it the most active arc in the world (de Ronde et al., 2001; Fig. 2).

The March 1999 NZAPLUME (New Zealand American PLUme Mapping Expedition) cruise surveyed volcanoes of the southern 260 km of the Kermadec arc, and provided the first systematic mapping and sampling of hydrothermal plumes along a significant segment of a submerged volcanic arc (de Ronde et al., 2001). Subsequent plume mapping cruises in 2002 (NZAPLUME II) and 2004 (NZAPLUME III) surveyed the remainder of the Kermadec arc volcanoes and those of southern-most Tonga arc. Since then, cruises utilizing the submersibles *Shinkai 6500* (2004), *Pisces V* (2005), the remotely operated vehicle *Quest 6000* (2007) and the autonomous underwater vehicles *ABE* (2007) and *Sentry* (2011), together with additional surface ship surveys, have continued to explore the seafloor hydrothermal systems of the Kermadec arc. Results of this research

are given in numerous papers, but especially in the 2008 special issue of *Journal of Geophysical Research* (Embley et al., 2008) and the 2012 special issue of *Economic Geology* (de Ronde et al., 2012).

The volcanic centers of the Kermadec arc occur at systematic intervals and can be dominated either by single cones, more complex caldera volcanoes, or a combination of both (de Ronde et al. 2007; Graham et al. 2008). The size of the dominant volcanic edifice at any one center is variable, as are the depths to the volcano summits (de Ronde et al. 2001; 2007; Wright et al. 2006). The composition of the volcanic rocks can range from basaltic through rhyolitic, both between and within the different centers (Wright et al. 2006; Graham et al. 2008). Hydrothermal emissions from these arc systems are heterogeneous in their chemical composition, showing a much greater range, and elevated concentrations of Fe, S, and CO_2 especially, than those found at spreading ridges (de Ronde et al. 2001; Massoth et al. 2007).

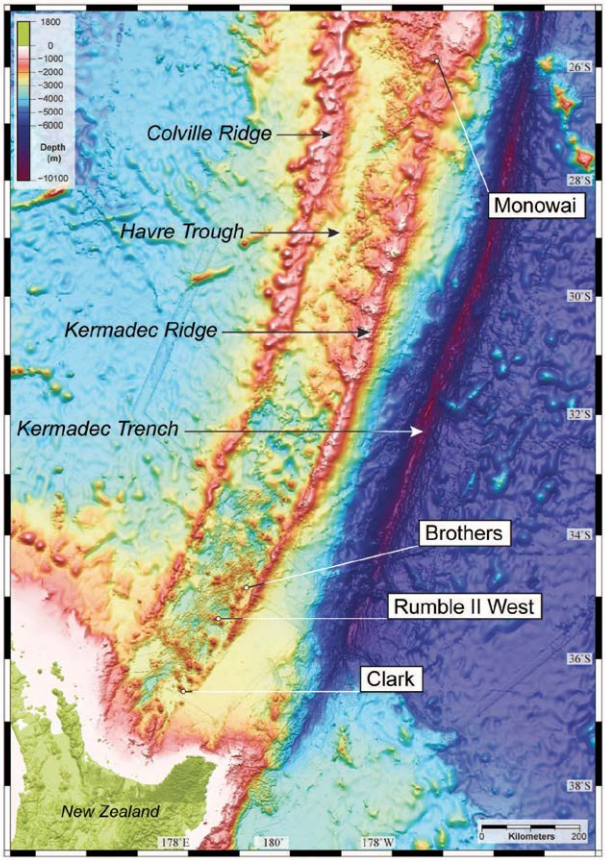

Figure 2. Map showing the location and distribution of the main tectonic features of the Kermadec arc-backarc system, NE of New Zealand and the volcanoes known to host massive sulfide mineralization (from de Ronde et al., 2012).

2.1 Case study: Brothers volcano

Brothers volcano of the Kermadec arc (Fig. 2) is host to a hydrothermal system unique among seafloor hydrothermal systems. It has two distinct vent fields, known as the NW Caldera and Cone sites, whose geology, permeability, vent fluid compositions, mineralogy and ore forming conditions are in stark contrast to each other (de Ronde et al., 2005). The NW Caldera site strikes for ~600 m in a SW-NE direction with chimneys occurring over a ~145 m depth interval, between ~1690 and 1545 m. At least 100 dead and active sulfide chimney spires up to 7 m tall occur in this field, whose ages fall broadly into three groups: < 4 years, 23 and 35 years old. Two main types of chimney predominate: Cu-rich (up to 28.5 wt.% Cu) and more commonly, Zn-rich (up to 43.8 wt.% Zn). Vent fluids here are focused, hot (≤302°C) and metal-rich, with moderate gas contents (de Ronde et al., 2011).

The Cone site comprises the Upper Cone site atop the summit of the recent (main) dacite cone, and the Lower Cone site that straddles the summit of an older, smaller, more degraded dacite cone on the NE flank of the main cone. Huge volumes of diffuse venting are seen at the Lower Cone site, in contrast to venting at both the Upper Cone and NW Caldera sites. Individual vents are marked by low relief (≤0.5 m) mounds comprised predominately of native sulfur with bacterial mats. Vent fluids are very acid (pH 1.9) and gas-rich, though metal-poor (de Ronde et al., 2011). The NW Caldera and Cone sites are considered to represent water/rock and magmatic-hydrothermal dominated end-members, respectively (Fig. 3). Proposed IODP drilling of Brothers volcano would provide an exciting opportunity to understand subseafloor volcanic architecture, hydrology, polymetallic ore deposition formation and the deep biosphere of intraoceanic arc volcanoes associated with convergent plate margins.

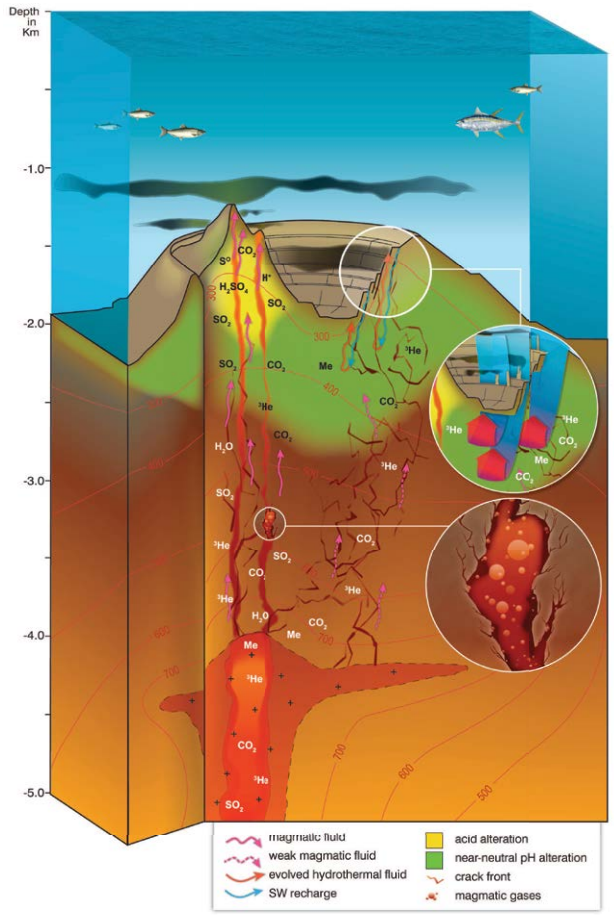

Figure 3. Cross-sectional view of Brothers (from de Ronde et al. 2011). A sill-like magma sits beneath the caldera with a dike-like volcanic pipe beneath the S-SE part of the volcano.

3 Mariana arc

Systematic exploration of Mariana arc submarine volcanoes, using the remotely operated vehicles *ROPOS* and *Jason II* in 2004 and 2006, respectively, has surveyed eleven active hydrothermal systems (Fig. 4). Eight of them are hosted by large volcanoes that have a complex history, with the majority hosted by relatively younger cones within calderas, or on the walls of the calderas themselves (Embley, et al., 2006). Two of the most active systems are associated with craters of large cones that have been constructed on top of older calderas. Almost 50% of the caldera sites are host to vent sites with temperature >100 °C; the others are low-temperature sites. Vent sites are commonly localized by faulting associated with the caldera walls. The remaining (non-caldera) sites are on young, basaltic-andesitic cones. One of these (NW-Rota-1; Fig. 4) has been erupting for the past several years (Chadwick et al., 2008). Hydrothermal activity of the Mariana arc appears to be associated with either large volcanoes with a long history of activity dominated by shallow magma chambers that produced calderas, or with cones that are currently in a state of eruption (Embley, et al., 2006).

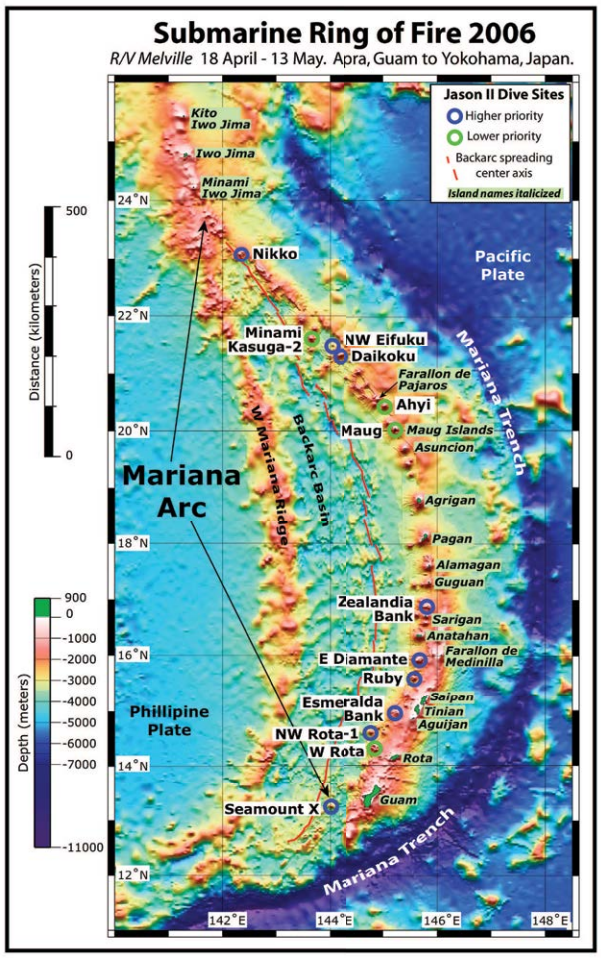

Figure 4. Bathymetric map of the Mariana arc showing the location of the volcanoes mentioned in the text. Figure from Merle et al. (2006).

Brimstone vent at NW Rota-1 provides a dramatic display of thick, bellowing, yellow plumes that contained ash and molten sulfur. This site occurs at 500 m water depth and clearly shows closely associating magmatic–hydrothermal discharge. Sulfur was the dominant hydrothermal mineral deposited around the vent and occurs as spheres in the surrounding volcaniclastic sediment, fracture fill and veins, and massive deposits. A unique hydrothermal field was found at NW Eifuku (Fig. 4) where liquid CO_2 is discharging from focused- and diffuse-flow vents at 1600 m water depth (Lupton et al. 2006). The focused-flow vents consist of small chimneys and mounds up to one meter tall composed predominantly of sulfur. Sulfur also occurs as crusts on the surface of sediment, as fracture fill and veins, and as massive deposits. Sulfides were not recovered from this site. The dominant characteristics of the hydrothermal mineralization along the Mariana arc are shallow-water systems, highly permeable rocks, gas (SO_2, H_2S, CO_2)-rich discharge, and magmatic-hydrothermal systems controlled by the depth-to-boiling-point curve. These characteristics likely result in the subsurface deposition of sulfide mineralization, except at East Diamante volcano (see below).

3.1 Case study: East Diamante volcano

The Black Forest vent field at East Diamante (Fig. 5) consists of a sulfide-sulfate chimney system formed in a depth of ~350 m. This is the only mature system discovered thus far along the Mariana arc and consists of numerous tall (up to 9 m) chimneys. The measured fluid temperature of 240° C produces boiling at the depth of the vents. Two main compositional types of sulfide chimneys have been found at East Diamante: 1) Zn-Fe-rich with sphalerite + pyrite + barite ± anhydrite as the main minerals, and 2) Cu-Fe-rich with an inner chalcopyrite zone grading to a zone composed of all or some of chalcocite + chalcopyrite + sphalerite + bornite + covellite + pyrite, together with anhydrite (Brathwaite, 2012). This mineralogy contrasts with the majority of other systems found along the Mariana arc, which are dominated by magmatic volatile discharge and high sulfidation mineralization.

Most of the Zn-Fe rich chimneys have outer zones of goethite ± hematite + opaline silica, a middle zone with sphalerite + barite + pyrite, and an inner zone of sphalerite + pyrite with minor chalcopyrite, galena and tetrahedrite-tennantite. Conductive cooling and oxidation of this fluid when it reached the exterior of the chimney likely caused deposition of opaline silica and hematite (Brathwaite, 2012).

The Cu-Fe-rich chimneys show a pronounced zoning outward from the central vent of: 1) an inner zone of semi-massive to massive chalcopyrite; 2) a middle zone composed of all or some of chalcocite + chalcopyrite + sphalerite + bornite +covellite + pyrite, with anhydrite; and 3) an outer zone of hematite + anhydrite + opaline silica. The paragenetic sequence of mineral deposition appears to broadly follow the zoning with the outer zone and middle zones being formed after the inner zone. Bornite is in turn partially replaced by covellite. Hematite and opaline silica in the outer zone likely formed late by cooling and oxidation as for the Zn-Fe-

rich chimneys (Brathwaite, 2012).

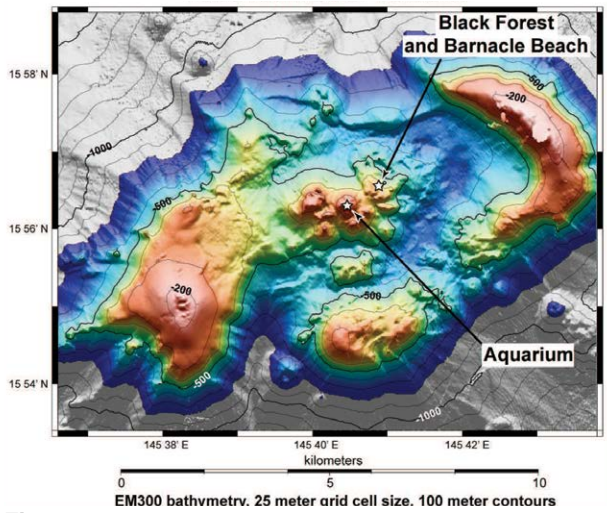

Figure 5. Bathymetric map of East Diamante volcano, Mariana arc. Coloured part of the figure represents the top of the volcano showing the partially collapsed caldera and a resurgent dome inside the caldera that is host to massive sulfide mineralization. Black Forest, Barnacle Beach and Aquarium are vent sites. Figure produced by S. Merle (NOAA).

Acknowledgements

The work presented in this paper stems from a long-standing collaboration with numerous colleagues from various institutions around the world, but especially PMEL/NOAA in the USA. Without the generosity shown by these colleagues, and others, we would never have been able to achieve what we have in our study of seafloor hydrothermal systems related to intraoceanic arcs.

References

Brathwaite B (2012) Petrographic report on samples from the East Diamante submarine volcano, Mariana arc. GNS Science internal report: 18 pp.

de Ronde CEJ, Baker ET, Massoth GJ, Lupton, JE, Wright IC, Feely RA, Greene RG (2001) Intra-oceanic subduction-related hydrothermal venting, Kermadec volcanic arc, New Zealand. Earth Planet Sci Lett 193: 359-369.

de Ronde CEJ, Massoth GJ, Baker ET, Lupton JE (2003) Submarine hydrothermal venting related to volcanic arcs, *In*, Giggenbach Memorial volume, S.F. Simmons and I.G Graham (eds.). Soc Econ Geol and Geochem Soc Special Publ 10: 91-109.

de Ronde CEJ, Hannington MD, Stoffers P, Wright IC, Ditchburn RG, Reyes AG, Baker ET, Massoth GJ, Lupton JE, Walker SL, Greene RR, Soong CWR, Ishibashi J, Lebon GT, Bray CJ, Resing JA (2005) Evolution of a submarine magmatic-hydrothermal system: Brothers volcano, southern Kermadec arc, New Zealand. Econ Geol 100: 1097-1133.

de Ronde CEJ, Baker ET, Massoth GJ, Lupton JE, Wright IC, Sparks RJ, Bannister SC, Reyners ME, Walker SL, Greene RR, Ishibashi J, Faure K, Resing JA, Lebon GT (2007) Submarine hydrothermal activity along the mid-Kermadec arc, New Zealand: Large-scale effects on venting. Geochemistry, Geophysics, Geosystems 8:Q07007.

de Ronde CEJ, Massoth GJ, Butterfield DA, Christenson BW, Ishibashi J, Ditchburn RG, Hannington MD, Brathwaite RL, Lupton JE, Kamenetsky VS, Graham IJ, Zellmer GF, Dziak RP, Embley RW, Dekov VM, Munnik F, Lahr J, Evans LJ, Takai K (2011) Submarine hydrothermal activity and gold-rich mineralization at Brothers volcano, Kermadec arc, New Zealand. Mineralium Deposita 46: 541-584. DOI 10.1007/s00126-011-0345-8.

de Ronde CEJ, Butterfield DA, Leybourne MI (2012) Introduction to the Economic Geology special issue on "Metallogenesis and Mineralization of Intraoceanic Arcs I: Kermadec arc". Econ. Geol. 107: 1521-1525.

Embley RW, and Shipboard participants (2004) Submarine Ring of Fire 2004-Mariana Arc, R/V *Thomas G. Thompson*, Cruise TN167. Cruise report: 273 pp.

Embley RW, and the Submarine Ring of Fire Investigators (2006) Geological framework for Mariana hydrothermal systems. AGU Annual General Meeting, San Francisco, 10-15 Dec, 2006.

Embley RW, de Ronde CEJ, Ishibashi J (2008) Introduction to Special Section: Active Magmatic, Tectonic and Hydrothermal Processes at Intraoceanic Arc Submarine Volcanoes. J Geophys Res 113: doi:10.1029/2007JB005871.

Chadwick WW Jr, Cashman KV, Embley, RW, Matsumoto, H, Dziak RP, de Ronde CEJ, Lau TK, Deardorff N, Merle SM (2008) Direct video and hydrophone observations of submarine explosive eruptions at NW Rota-1 volcano, Mariana arc. J Geophys Res 113: B08S10. doi:10.1029/2007JB005215.

Graham IJ, Reyes AG, Wright IC, Peckett KM, Smith IEM, Arculus RJ (2008) Structure and petrology of newly discovered volcanic centers in the northern Kermadec–southern Tofua arc, South Pacific Ocean. Journal of Geophysical Research 113:B08S02. doi: 10.1029/2007jb005453.

Lupton J, Butterfield D, Lilley, M, Evans L, Nakamura K, Chadwick W. J, Resing J, Embley, R, Olson E, Proskurowski G, Baker E, de Ronde, C, Roe K, Greene R, Lebon G, Young C (2006) Submarine venting of liquid carbon dioxide on a Mariana arc volcano. Geochem Geophys Geosyst 7. doi:1029/2005GC001152.

Massoth G, Baker E, Worthington T, Lupton J, de Ronde C, Arculus R, Walker S, Nakamura K, Ishibashi J, Stoffers P, Resing J, Greene R, Lebon G (2007) Multiple hydrothermal sources along the south Tonga arc and Valu Fa Ridge. Geochem Geophy Geosy 8:-. doi: Artn 11; Doi 10.1029/2007gc001675.

Merle S, Embley RW, Chadwick WW, and the Shipboard participants (2006) "Mariana arc submarine volcanoes", *R/V Melville* Cruise MGLN02MV, April 18 – May 13, 2006, Apra, Guam to Yokohama, Japan: 234 pp.

Wright I, Worthington T, Gamble J (2006) New multibeam mapping and geochemistry of the 30°–35° S sector, and overview, of southern Kermadec arc volcanism. J Volcanol Geoth Res 149:263-296. doi: 10.1016/j.jvolgeores.2005.03.021.

Alteration in the area of the Kristineberg VHMS deposit, Skellefte district, Sweden

Kai Bachmann, Jens Gutzmer
Department of Mineralogy, TU Bergakademie Freiberg, Brennhausgasse 14, D-09596 Freiberg, Germany

Mac Fjellerad Persson, Nils Jansson
Boliden Mineral AB, S-936 81 Boliden

Abstract. The Skellefte district in north-central Sweden is one of the most important mining districts in northern Europe. It contains over 85 pyritic Zn-Cu-Au-Ag massive sulphide deposits of which 21 deposits have been mined since 1924 and 4 are still in operation by Boliden Mineral AB. The most productive deposit, the Kristineberg mine, has been operated by Boliden since 1940 with a current annual production of 670,000 t of polymetallic ore containing 3.0 wt.-% Zn, 0.7 wt.-% Cu, 0.4 wt.-% Pb, 1.9 g/t Au and 47 g/t Ag. Alteration of the volcanic rocks around the Kristineberg deposit is very intense. The main aim of this study has been to describe the alteration intensity and to define alteration trends around the Kristineberg deposit. The success of this approach provides a new exploration tool for future exploration in the Skellefte District where alteration renders the recognition of primary volcanic facies difficult.

Keywords. Kristineberg, Skellefte district, VHMS, alteration

1 Introduction

The Skellefte district in north-central Sweden is one of the most important mining districts in Europe. The active Kristineberg as well as the abandoned Rävliden and Rävlidmyran deposits are located in the western part of the Skellefte district (Figure 1). The pyritic massive sulphide deposits occur as stratabound lenses hosted by a thick sequence of early Proterozoic felsic to intermediate metavolcanic rocks of the Skellefte Group, which is overlain by fine-grained turbiditic metasediments of the Vargfors Group (Vivallo and Willdén 1988; Weihed et al. 1992; Allen et al. 1996; Barrett et al. 2005). The deposits can be classified as VHMS deposits (Hannington et al. 2003; Barrett et al. 2005). The volcanic and syn-volcanic sedimentary and magmatic rocks have been subjected to regional deformation and greenschist facies metamorphism, and also to contact metamorphism of amphibolite facies in proximity to post-volcanic granitoids (Du Rietz 1951). Structurally, the Kristineberg area is dominated by a synform and flanking antiforms that plunge moderately to the west. Limestone and skarn-associated Zn–Pb–Cu sulphide deposits of the Rävliden horizon occur at or near the top of the volcanic sequence, close to the overlying Vargfors Group (Barrett et al. 2005). The Kristineberg sulphide ores occur deeper in this volcanic sequence, close to the Viterliden intrusive complex (VIC) (Du Rietz 1953; Edelman 1967; Grip 1978; Vivallo and Willdén 1988), but due to structural complexities and intense alteration their exact stratigraphic position is uncertain. The VIC has been dated at 1889±3 Ma and is considered to be coeval with the mineralised volcanic rocks (Skyttä et al. 2011). Allen et al. (1996) have attributed the formation of the massive sulphide deposits of the Skellefte district to extensional volcanism in a continental marginal arc setting.

Volcanic-hosted massive sulphide (VHMS) deposits show a halo of intense alteration of surrounding rocks, which is generated by metasomatic interaction between wall rock and hydrothermal fluids developed during the formation of the deposits. The present investigation aimed to test, if whole rock geochemical data can be utilized to recognize the intensity of alteration and to identify the distribution of different alteration zones. For this purpose, geochemical indicators such as the Ishikawa Alteration Index (AI) and Chlorite-Carbonate-Pyrite-Index (CCPI) as well as the Na_2O content were considered. The success of this approach provides a new exploration tool for future exploration in the Skellefte District.

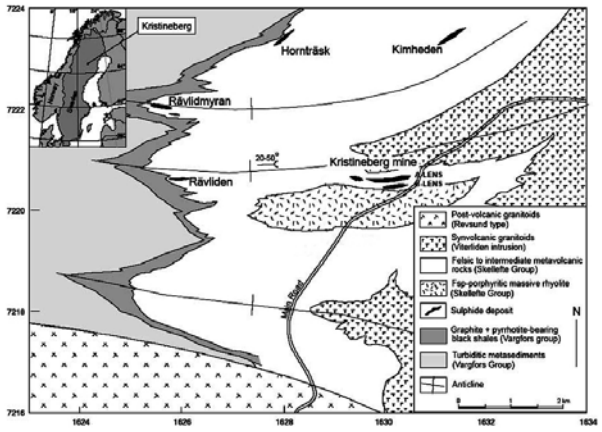

Figure 1. General geology of the Kristineberg area, Skellefte district, Sweden. Coordinates given in RT90. (Modified after Barrett et al. 2005)

2 Methodology

Available geochemical datasets were compiled into a single data base, including (1) 57 surface samples collected during the current investigation (2) 72 samples from Hannington et al. (2003) and (3) 138 surface samples collected during previous investigations. Samples cover an area of approximately 120 km^2. Due to the fact that geochemical data were supplied by different commercial laboratories and by different analytical methods, a simple error analysis has been carried out to

support the compatibility of the data.

The 57 surface samples of set (1) were collected with a rock saw from outcrops in the area and from existing drill core. The sample set (2) contains surface and drill core samples from Hannington et al. (2003). Drill core samples of set (1) and (2) were all taken from 0-50 m depth from surface. Data set (3) contains only surface samples.

All data was incorporated into the Pitney Bowes GIS-software MapInfo Professional (+ Discover) to maximize the benefit for future exploration programs.

3 Results

3.1 Relevant alteration indices

The lithogeochemical classification of Barrett et al. (2005) was applied. The suggested ranges are given in table 1.

Alteration indices used in this study are multi-component and normalised ratios of lithogeochemical composition data. They are geochemical representations of hydrothermal mineral assemblages designed to facilitate discrimination of alteration styles, quantification of alteration intensity, and alteration vectors (Gifkins et al. 2005). Alteration indices have been widely applied in research and exploration for VHMS deposits (Ishikawa et al., 1976; Large et al. 2001). In this study the Alteration Index (AI) of Ishikawa et al. (1976) and the chlorite-carbonate-pyrite index (CCPI) of Large et al. (2001) were used to determine the intensity of alteration in the Kristineberg area.

The Ishikawa Alteration Index (AI) produces a potential range from zero to one hundred, which is convenient for quantification of alteration intensity (Ishikawa et al. 1976) and is shown in the following equation:

$$\mathrm{AI} = \frac{100 \times (\mathrm{MgO} + \mathrm{K_2O})}{\mathrm{MgO} + \mathrm{K_2O} + \mathrm{CaO} + \mathrm{Na_2O}}$$

Originally it was devised as a measure of intensity of sericite and chlorite alteration associated with Kuroko-VHMS deposits. It is useful in many types of plagioclase-destructive hydrothermal alteration systems (Gifkins et al. 2005). It was developed to represent the principal components gained (MgO and K_2O) during chlorite and sericite alteration, and those lost (Na_2O and CaO) during the breakdown of plagioclase and volcanic glass (Ishikawa et al. 1976). It typically increases to maximum values in the proximal hydrothermal zones beneath massive sulphides lenses (e.g. Saeki and Date 1980). There is a strong inverse relationship between AI and Na concentrations because loss of Na, and sometimes loss of Ca, are the major chemical changes involved in the breakdown of plagioclase. Therefore, in many studies Na depletion has been used instead of AI as the principal measure of alteration intensity (Date et al. 1983).

The chlorite-carbonate-pyrite index (CCPI) was developed to also take carbonate alteration into account, which can be significant in some VHMS alteration systems. Furthermore, there is the possibility of differentiating between chlorite and sericite alteration. Variations in relative proportions of chlorite and sericite or spatial relationships between chlorite and sericite zones may be important guides to exploration in some VHMS alteration systems (Gifkins et al. 2005). The CCPI is given in the following equation:

$$\mathrm{CCPI} = \frac{100 \times (\mathrm{FeO} + \mathrm{MgO})}{\mathrm{FeO} + \mathrm{MgO} + \mathrm{Na_2O} + \mathrm{K_2O}}$$

It was developed by Large et al. (2001) to reflect the prominence of chlorite, Fe-Mg carbonates and pyrite, which are common alteration products in the proximal zone of VHMS deposits. High values of CCPI reflect high FeO and MgO contents, suggesting intense alteration to Fe- or Mg-rich minerals such as chlorite, dolomite, ankerite or siderite as well as pyrite, hematite and magnetite. However, the index is not well suited for mafic rocks with high primary FeO and MgO contents, which show usually high CCPI values above 50 even for least altered samples.

By using the x-y bivariate plots with AI on the x-axis, the CCPI provides an effective means of discriminating sericite-, chlorite- and carbonate altered zones. Furthermore, the AI-CCPI bivariate plot, termed the 'alteration box plot' by Large et al. (2001), differentiates these VHMS-related hydrothermal alteration assemblages from diagenetic albite- or albite + K-feldspar bearing assemblages. Least altered volcanic rock samples plot within a rectangle near the middle of the AI-CCPI bivariate plot. In this study the rectangle was used to assume the composition of least altered samples. This has been done, because there were not enough samples from the same stratigraphic rock units to do a proper precursor analysis.

Table 1. Ranges of ratios of the main chemical rock types at the Kristineberg deposit (Barrett et al. 2005).

	Al_2O_3/TiO_2	[a]Zr/TiO_2	[a]Zr/Al_2O_3	[a]Zr/Y	[a]Zr/Nb
Rhy A	34-42	670-820	18-22	9-13	18-23
Rhy B	28-40	500-660	15-19	7-12	18-22
Rhy X	40-52	580-720	13-16	5-9	17-21
Dac	24-31	260-380	10-14	5-10	17-21
And	21-30	160-250	7-11	4-7	17-20
Mafic	18-27	40-150	9-13	2-6	17-20

[a]Zr = original Zr in ppm x 10,000, And – Andesite, Dac – Dacite

3.2 Alteration indices

The CCPI-AI alteration box plot (Figure 2) displays all analyzed data. The abundance of high alteration index values is obvious, mainly when combining both CCPI and AI. Furthermore, there are several trends visible. The rhyolitic samples, no matter if Rhy A, B or X, which are predominant in the sample set, behave similar and can be divided in two groups. Some rhyodacites (grouped as dacites) behave similar as well. The first group (group 1)

displays mainly analyses with CCPI values from ~30 up to 55 combined with AI values ranging from around 25 to 95. The second group displays values ranging from a CCPI of 30 to 100, combined with an AI of 90 to 100.

The samples of more mafic composition scatter over a wide range of CCPI and AI values, the same goes for dacitic rocks. Noticeable is a high CCPI (70-90) combined with a low AI (10-30) of some samples. This is attributed to variations in protolith composition. Due to the fact that the rocks like, e.g. basalts have more primary Fe-rich minerals like olivine, amphiboles and pyroxene the CCPI is usually increased. This is the reason why the CCPI fits best for felsic primary rocks and is not as well suited for mafic lithologies (Gifkins et al. 2005).

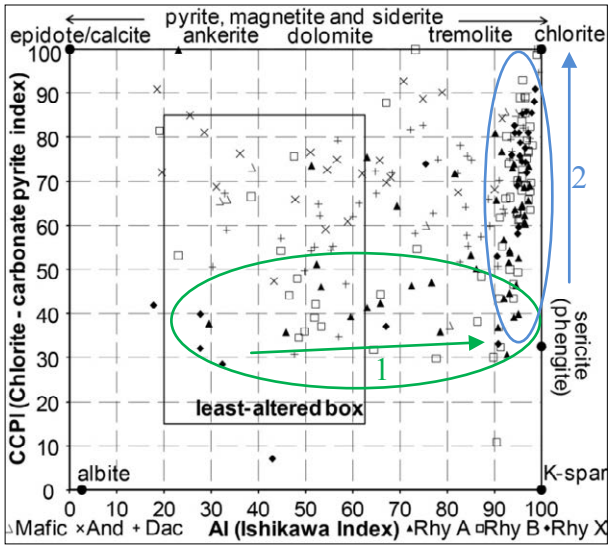

Figure 2. AI-CCPI Alteration box plot of samples from the entire dataset of the Kristineberg area. Marked is the box relating to least altered rock and two alteration trends. Trend 1 displays sericite alteration, trend 2 sericite±chlorite±pyrite alteration.

The least-altered box drawn into Figure 2 was created by Gifkins et al. (2005). In general, this box can be used to indicate which samples are least altered. By using only analyses with felsic compositions (rhyolite A, B, X) there are two trends visible. The first trend (1) corresponds to group 1 and displays a sericite-dominated alteration trend for example at the margins of the hydrothermal alteration halo in felsic volcanic rocks. The second trend (2) corresponds to group 2 and displays a footwall sericite±chlorite±pyrite alteration (Large et al. 2001).

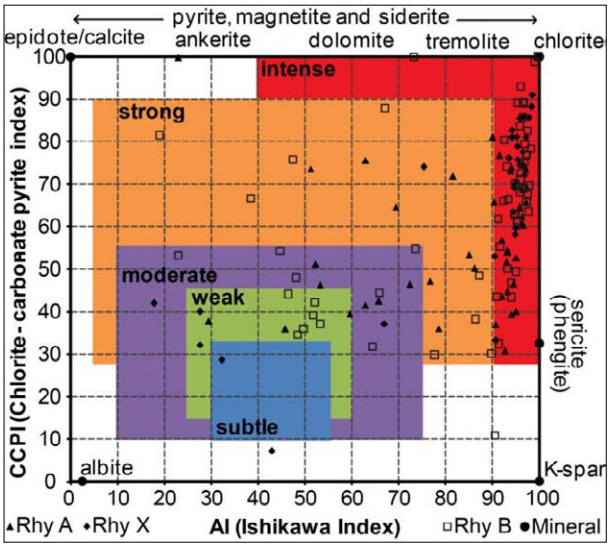

Figure 3. AI-CCPI Alteration box plot of rhyolitic samples from the study area. Displayed are the alteration boxes for subtle, weak, moderate, strong and intense alteration.

Figure 3 clarifies these results. Here, only rhyolitic samples are displayed. The alteration boxes define areas of the alteration intensity the sample have suffered. The least altered samples are weakly to moderately altered. Alteration indices increase towards sericitic alteration over strong to intense alteration. Samples corresponding to trend 2 are almost all intensely altered. Figure 4 shows the expected inverse relationship between AI and the Na_2O content due to the extreme loss of Na_2O caused by the breakdown of plagioclase during alteration. Most analyses are extremely depleted in Na_2O and corresponding with AI values between 90 and 100. Again, the plot is in agreement with the sericite-chlorite-pyrite-(K-spar) trend of Figure 2.

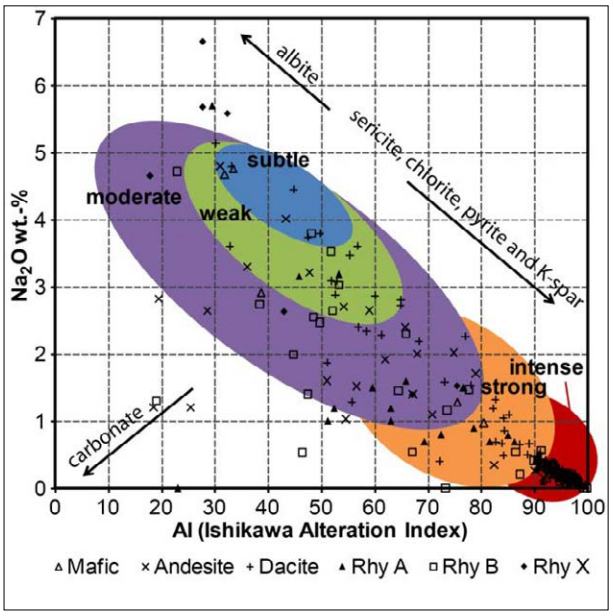

Figure 4. Na_2O-AI plot of all samples from the study area. Displayed are the areas for subtle weak, moderate, strong and intense alteration.

4 Conclusion

The description of the alteration intensity of rocks in the Kristineberg area was successfully done. Two alteration trends were observed and indicate a geochemical zoning of the area. Trend 1 represents sericite alteration while trend 2 displays sericite±chlorite±pyrite alteration. The definition of existing alteration trends provides a new tool for exploration targeting in the Kristineberg area.

Acknowledgements

We thank Boliden Mineral AB for providing the geochemical data. Funding for this project was provided by Boliden Mineral AB.

References

Allen RL, Weihed P, Svenson SA (1996) Setting of Zn–Cu–Au–Ag massive sulphide deposits in the evolution and facies architecture of a 1.9 Ga marine volcanic arc, Skellefte District, Sweden. Econ Geol 91:1099–1053.

Barrett TJ, MacLean WH, Årebäck H (2005) The Palaeoproterozoic Kristineberg VMS deposit, Skellefte district, Sweden: Part II: chemostratigraphy and alteration. Min Dep 40:368–395.

Date J, Watanabe Y, Saeki Y (1983) Zonal alteration around the Fukazawa Kuroko deposits, Akita Prefecture, northern Japan. Econ Geol Mono 5:365–386.

Du Rietz T (1951) Geology and ores of the Kristineberg Deposit, Vesterbotten, Sweden. Sveriges Geologiska Undersökning, Ser. C 524:89pp.

Du Rietz T (1953) Geology and ores of the Kristineberg deposit, Vesterbotten, Sweden. Sveriges Geol Undersökning Ser C 524 45:90pp.

Edelman N (1967) Stratigraphy and metamorphism in the Kristineberg area, northern Sweden. Sveriges Geol Undersökning Ser C 622 61:45pp

Gifkins C, Herrmann W, Large R (2005) Altered volcanic rocks: A guide to description and interpretation. Centre of Ore Dep Research Uni of Tasmania, Aus:15pp and 73pp.

Grip E (1978) Mineral deposits of Sweden. In: Bowie SH, Kvalheim A, Haslam HW (eds) Mineral Deposits of Europe 1:93–198. The Institution of Mining and Metallurgy/ The Min Soc of London, London.

Hannington MD, Kjarsgaard IM, Galley AG, Taylor B (2003) Mineral-chemical studies of metamorphosed hydrothermal alteration in the Kristineberg volcanogenic massive sulphide district, Sweden. Min Dep 38:423–442.

Ishikawa Y, Sawaguchi T, Iwaya S (1976) Delineation of prospecting targets for Kuroko deposits based on modes of volcanism of underlying dacite and alteration haloes. Mining Geol 26:105–117.

Large RR, Gemmel JB, Paulick H (2001) The Alteration box plot - a simple approach to understanding the relationship between alteration mineralogy and lithogeochemistry associated with volcanic-hosted massive sulphide deposits. Econ Geol 96:957–971.

Saeki Y, Date J (1980) Computer application to the alteration data of the footwall dacite lava at the Ezuri Kuroko deposits, Akita Prefecture. Mining Geol 30:241–250.

Skyttä P, Hermansson T, Andersson J, Weihed P (2011) New zircon data supporting models of short-lived igneous activity at 1.89 Ga in the western Skellefte District, central Fennoscandian Shield. Solid Earth 2:205–217.

Vivallo W, Willdén M (1988) Geology and geochemistry of an early Proterozoic volcanic arc sequence at Kristineberg, Skellefte district, Sweden. Geol Föreningens i Stockholm Förhandlingar 110:1–12.

Weihed P, Bergman J, Bergström U (1992) Metallogeny and tectonic evolution of the Early Proterozoic Skellefte district, northern Sweden. Precamb Res 58:143–167.

Isotope constraints on the genesis of the Arroyo Rojo VMS deposit (Tierra del Fuego, Argentina)

Biel. C., Colás, V., Subías, I.
Grupo Recursos Minerales, Dpto. Ciencias de la Tierra, Universidad de Zaragoza. c/ Pedro Cerbuna 12 (Edificio Geológicas), 50009 Zaragoza. Spain

Acevedo, R.D.
Centro Austral de Investigaciones Científicas (CADIC). Houssay, 200, V9410CAB. Ushuaia, Tierra del Fuego. República Argentina

Bilström, K.
Laboratory for Isotope Geology. Swedish Museum of Natural History. Frescativagen 40 (Box 50007). SE-104 05 Stockholm, Sweden

Abstract. The Arroyo Rojo deposit is the most important polymetallic, volcanic-hosted massive sulphide close to the town of Ushuaia in the rhyolitic belt of the Andes of the Tierra del Fuego. This deposit is hosted by a volcanic and volcanoclastic sequence, Middle Jurassic in age. This Zn-Pb-Cu deposit display a lenticular morphology developed as a stacked lenses-style, with disseminated mineralization at both the footwall and hanging-wall. The ores and host-rocks have one penetrative tectonic foliation and have been metamorphosed to greenschist facies. Associated hydrothermal alteration follows a stratabound model.
Stable isotopes geochemistry points towards the mineralizing fluids being derived from the interaction and re-equilibration with the siliciclastic portion of the host rocks, with sulphur being derived from a mixture of biogenic reduction of seawater sulphate in some restricted to closed ambient with probably magmatic influence, and heavier $\delta^{34}S_{CDT}$ values derived by leaching of H_2S from the detrital rocks. Lead and strontium isotopes indicate that the metals were leached from the sedimentary rocks. This process allowed re-equilibration and homogenization of hydrothermal fluids.

Keywords. Arroyo Rojo, stable isotopes, radiogenic isotopes, VMS, brine pool

1 Introduction

Arroyo Rojo VMS deposit is the main prospect of the Sierra de Sorondo target belonging to the Fuegian Andes (Tierra de Fuego, Argentina) and is hosted by the volcanic and volcanoclastic portion of the Lemaire Formation (Middle Jurassic in age). The Lemaire Formation is underlain by a pre-Jurassic basement and overlain by the hyaloclastic andesites belonging to the Yahgán Formation (Late Jurassic to Early Cretaceous in age) (Biel *et al*., 2010).
This polymetallic VMS mineralization displays a lenticular morphology with a stacked lens like, with disseminated mineralization at the footwall and the hanging-wall. The internal structure of the lenses is marked by massive, semimassive and laminated facies along with stringer, brecciated and minor intercalations of ore disseminations. The mineral assemblage consists of pyrite and sphalerite, with minor amounts of galena and chalcopyrite, and rare pyrrhotite, arsenopyrite, tetrahedrite and bournonite (Biel *et al*., 2010).

Ores and volcanic host-rocks were deformed and metamorphosed to prehnite-pumpellyite facies causing cataclasis in brittle sulphides, and remobilization, deformational, recrystallization and annealing textures in ductile sulphides (Biel et al., 2007). As a consequence of metamorphism and deformation, metarhyolites, mylonites and ultramylonites were developed in the host volcanoclastic sequence.

Regional seafloor alteration is partially obliterated by hydrothermal alteration, which follows a stratabound model in which Mg-chlorite and phengitic white mica typically occurs in the vicinity of the ore lenses (Biel *et al*., 2012).

The geological and mineralogical evidences point to a sulphide deposition in a brine pool at Arroyo Rojo deposit (Biel *et al*., 2010).

In this contribution, isotopic geochemistry, both stable and radiogenic is used to constraint source rocks and geologic processes responsible for mineralization.

2 Sampling and analytical methods

Ore samples were collected from outcrops and drill hole cores attending different mineralogy and textural types.

Stable isotope ratios were measured at the Servicio General de Análisis de Isótopos Estables (Universidad de Salamanca, Spain). 39 $\delta^{34}S$ determinations on all textural types of ore sulphides were made by Nd-YAG laser ablation (Fallick et al. 1992). S from underlying host rocks were recovered as Ag_2S by reaction with HCl + $CrCl_2$, using a method modified after Canfield et al. (1986) and Hall et al. (1988). Replicate analyses of reference standards gave an average reproducibility of ±0.3. Results are reported in the familiar delta per mil notation relative to CDT (Canyon Diablo Troilite).

H and O isotope analyses were carried out on chlorite hand-picked from altered wall rocks by a micro-drill. Hydrogen was extracted by induction heating (1200ºC) under vacuum of a platinum crucible containing the sample. The Pt crucible had been degassed prior to hydrogen extraction. Water produced during dehydroxylation was converted to H_2 over U at 800ºC in a multiple pass system and yield was measured by manometer employing a Toepler pump for transport of H_2. O isotope compositions were determined using the

fluorination laser technique (Sharp et al. 1990). Analytical precision of isotopic analyses is estimated at ±1‰ for δD and better than ±0.2 for $\delta^{18}O$. Values are reported relative to the SMOW (Standard Mean Ocean Water).

Radiogenic isotope analyses were carried out at the Laboratory of Isotope Geology (LIG), of the Swedish Museum of Natural History. Pb isotope compositions have been determined for 19 ore sulphides, occurring in different assemblages, 12 volcanic and detrital whole rock and 10 chlorites. Isotopic compositions of Sr of whole rocks and chlorites were also carried out. Chemical separation of Pb from sulphides involved dissolution-evaporation in HNO_3 at 100ºC. Dissolution of whole rock and chlorite samples requires about 100 mg of sample in HCl at 100º C and undissolved material was taken up in a HF/HNO_3 mixture following the Teflon bomb method of Krogh (1973) at 205 ºC. Purified Pb and Sr, was obtained using anion columns and anodic electro-deposition. Pb isotopic ratio was determined by a Micromass ISOPROBE mass spectrometer and the reproducibility of analytical method is about 0.1% (2σ). Sr isotopic ratios were measured using a Finnigan MAT261 (TIMS) mass spectrometer. The $^{87}Sr/^{86}Sr$ isotope ratios were normalized to BCR-1 standard values.

2 Isotopic geochemistry

2.1 Stable isotopes

The $\delta^{34}S_{CDT}$ values of Arroyo Rojo ore display a wide range from -27.5 ‰ to 2.6 ‰ pointing to a high variability in sources of sulphur or mechanism of deposition. Footwall and hanging-wall disseminated ores have negative $\delta^{34}S_{CDT}$ values (-21.7‰ a -2.0 ‰) and massive ores show heavier values (-12.1‰ a 2.6 ‰). Arroyo Rojo $\delta^{34}S_{CDT}$ values display a shift to heavier values with metamorphic and ore textural evolution (Figure 1).

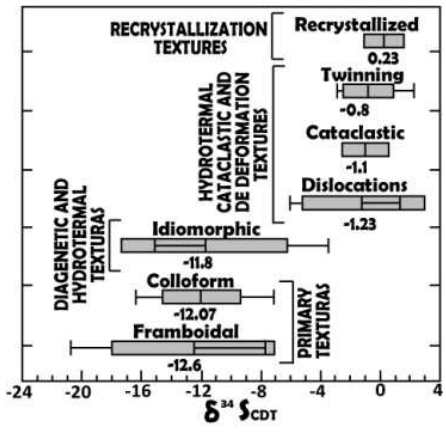

Figure 1. Mean, maximum, minimum and standard deviation of $\delta^{34}S_{CDT}$ values in different ore textures.

The wide variability of Arroyo Rojo sulphur isotopic values is consistent with a bacteriogenic reduction of sulphate. Typically, bacterial reduction of seawater sulphate results in sulphides with $\delta^{34}S$ around 40±20‰ (Ohmoto, 1986) to 35±15‰ (Boyce and Fallick, 1995) lower than the starting sulphate. Assuming that Jurassic seawater sulphate had $\delta^{34}S$ ca 17‰ (Claypool et al., 1980), its biogenic reduction could lead to sulphide with a $\delta^{34}S$ value in the range of measured sulphides. Nevertheless, from inspection of figure 2, a possible magmatic influence and/or leaching of sulphide from the detrital portion of the Lemaire Formation cannot be ruled out.

Similar sources of S have been described in other brine pool deposits as Tharsis (Tornos et al. 2008) or Feitais (Inverno et al. 2008) in the Iberian Pyrite Belt.

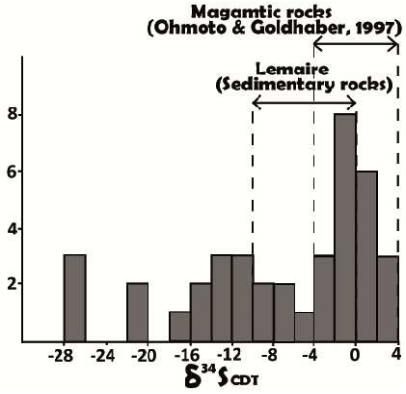

Figure 2. Distribution of Arroyo Rojo $\delta^{34}S_{CDT}$ values and range of igneous (Ohmoto and Goldhaber 1997) and sedimentary rocks of Lemaire Formation.

Temperatures of formation for pyrite-sphalerite and chalcopirite-sphalerite pairs using equations of Kajiwra and Krouse (1971), Friedman and O'Neil (1977) and Ohmoto and Rye (1979) range between 135º and 339ºC. Massive sulphides showing growing, deformation and cataclasis textures have higher equilibration temperatures (249-339ºC) than those showing deformation, recrystallization and annealing textures (135-249ºC).

Sample	Depth (m)	Ore Proximity	$\delta^{18}O_{SMOW}$	$\delta^{18}O_{SMOW}$ fluido	δD_{SMOW}
AR6-202-C1	202	Distal	11.3	11.68	-82.6
AR6-262-C1	262.5	Distal	12.3	12.68	-86.8
AR6-262-C2	262.5	Distal	12.1	12.48	-85.9
AR6-308	308	Distal	13.9	13.3	-85.6
AR2-57-C1a	57	Proximal	9.1	8.5	-66
AR2-57-C1b	57	Proximal	9.6	9	
AR2-57-C4	57	Proximal	9.8	9.2	-68.9
AR2-105-C2a	105.8	Proximal	9	7.56	-62.9
AR2-105-C2b	105.8	Proximal	9.6	8.16	
AR2-75-C1	75.3	Proximal	13.4	11.96	-68.7
AR2-75-C2	75.3	Proximal	11	9.56	-67
AR6-139-C1	139.2	Proximal	11.3	9.86	-89.7
AR6-139-C3	139.2	Proximal	13.1	11.66	-70.9
AR7-133-C2	133.4	Proximal	8.3	6.86	-54
AR7-134-C3	134.7	Semimas	9.8	8.15	-53.5
AR7-134-C2	134.7	Semimas	9	7.35	-53.9
AR3-3-C1	3	Massive	11.7	10.05	-42.4
AR7-94.8	94.8	Massive	7.7	6.05	-59.9

Table 1. O and D/H isotopic composition of Arroyo Rojo Hydrothermal alteration chlorites.

The above temperatures are in agreement with temperatures reached during metamorphic peak of Lemaire Formation corresponding to prenhite-pumpellyte facies (Biel et al., 2007).

Arroyo Rojo hydrothermal chlorites displays lighter

$\delta^{18}O_{SMOW}$ values (Table 1) within massive ore levels (7-12 ‰), intermediate values in proximal zones (8-14 ‰) and the heaviest values in distal zones (11-14%).

$\delta^{18}O$ values of the mineralizing fluids (6.05-13.3 ‰) were calculated employing Savin and Lee (1988) chlorite-water fractionation equation, assuming temperatures calculated by Cathalineau (1988) thermometer (169º to 381 ºC).

Calculated δD_{SMOW} values of hydrothermal chlorite vary from -90 ‰ in distal zones to -40 ‰ in mineralized areas. δD values of the mineralizing fluids calculated using the curve of Savin and Lee (1988) shows a wide variability (-62.7 to -15.4 ‰), unusual in VMS deposit (Table 1).

δD and $\delta^{18}O$ values of mineralized fluids are suited in the range of metamorphic water with some influence of marine, magmatic water or metasediments (Figure 3).

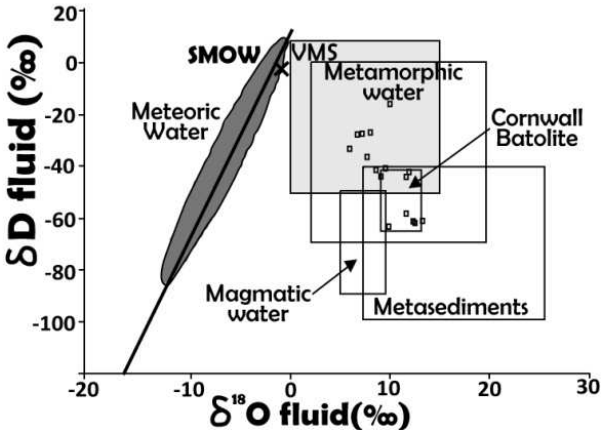

Figure 3. $\delta^{18}O_{SMOW}$ and δD_{SMOW} values of Arroyo fluids on natural waters diagram of Sheppard (1986). Main VMS deposit values range in grey.

Distal chlorites show lower isotopic signatures of H suggesting a metamorphic origin for fluids responsible for the regional hydrothermal alteration. The rest of samples are in the expected range for VMS deposit and display higher $\delta^{18}O$ values and lower δD values.

These values are consistent with a fluid that interacted and re-equilibrated with the siliciclastic rocks of the underlying Lemaire Formation and the metamorphosed basement of the Lapataia Formation. This has been described in other VMS interpreted as formed in brine pools (Tornos and Heinrich 2008; Lentz 1999).

2.1 Radiogenic isotopes

Arroyo Rojo Pb isotopic relations show a narrow scatter of $^{206/204}Pb$ (< 0.9%) pointing to a similar formation age and source of Pb. Lesser variations are observed between sulphides, sedimentary rocks and hydrothermal alteration chlorites (<0.2%) suggesting a close relationship between mineralization, hydrothermal activity and the underlying sedimentary rocks.

Lead isotope corrected ratios show a good linear array close to the "orogen" curve of Zartman and Doe (1981) except on magmatic rock values that spreads to upper crust reservoir, pointing to a main orogenic source of Pb along with some contribution from the upper crust during orogenic formation (Figure 4).

Mineralization, hydrothermal chlorite and detrital rocks of Lemaire Formation show very homogeneous Pb isotopic compositions. Mean μ (9.75-9.95) and ω (36.18-36.80) values calculating by Stacey and Kramers (1975) model point to a common source of metals. The similarity in Pb isotopic composition between sedimentary rocks, mineralization and hydrothermal alteration chlorites suggests that the former are the source of metals indicating a possible homogenization of hydrothermal fluids during the leaching of the sedimentary sequence.

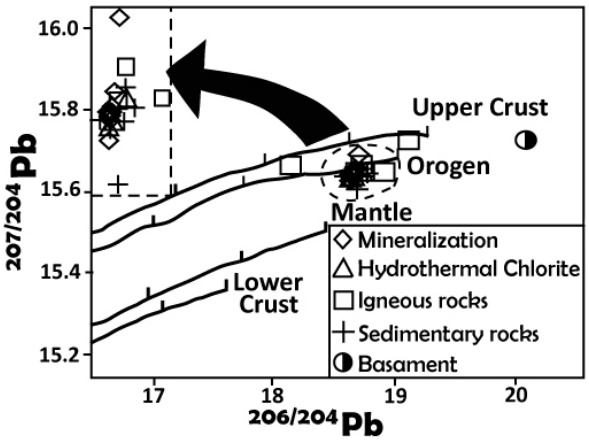

Figure 4. Lead isotope data of Arroyo Rojo deposit. Lower Crust, Mantle, Orogen and Upper crust of Zartman and Doe (1981) are shown.

$^{87}Sr/^{86}Sr$ current values vary from 0.70621 and 0.74312, showing values between 0.70621 and 0.72559 for sedimentary rock, between 0.71106 and 0.72803 for igneous rocks, and between 0.70934 and 0.74312 for hydrothermal alteration chlorites. $^{87}Sr/^{86}Sr$ value for basement is 0.71301.

$^{87}Sr/^{86}Sr$ ratios have been computed at 145 Ma (age of formation of the host Lemaire Formation, after Calderón et al. 2007) and at present for the various source rocks (volcanic, sedimentary and basement) and for hydrothermal chlorite (Figure 5).

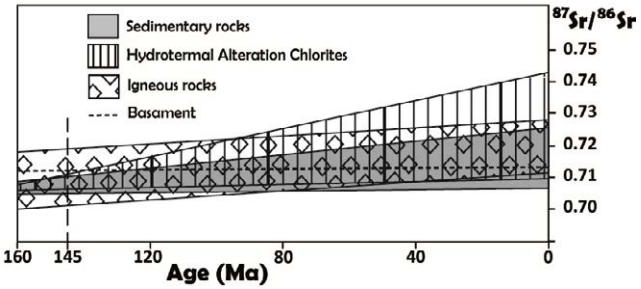

Figure 5. Current and initial (145 MA) $^{87}Sr/^{86}Sr$ value range for volcanics, sedimentary rocks, basement and hydrothermal chlorites.

At 145 Ma, Sr isotopic composition of hydrothermal chlorite overlaps that of sedimentary rocks pointing to these rocks as the more probable source of Sr in the

mineralizing fluids. This notably agrees with lead derivation.

This hypothesis is according to a hydrothermal fluids and S origin derived by leaching of the underlying sedimentary sequence, considering this portion of the Lemaire Formation as a deep aquifer as described Marcoux (1998) in the Iberian Pyrite Belt.

3 Conclusions

Based on stable and radiogenic isotopes we consider the hypothesis of a deep, highly porous aquifer in which the fluids remained for a sufficient time to become homogenized after interaction and re-equilibration with the underlying sedimentary sequence of the Lemaire Formation. In other words, fluids were retained enough time to acquire a common sedimentary "signature" for mineralization, sedimentary rocks and the hydrothermal chlorite leaching metals and S and diffuse discharging as dense brine fluids in the bottom of the seafloor through the more permeable tuffaceous volcanic rocks.

Acknowledgements

The study of the Arroyo Rojo VMS deposit is part of the project: "*The massive sulphides of Tierra del Fuego: mineral deposit modelling and geological criteria for ore exploration*", funded by Ministerio de Ciencia e Innovación (MICINN). The Spanish Ministerio de Educación y Ciencia financially supports Cecilia Biel (FPU scheme grant AP2005-0244). The stage of CB at NHM was financed through Programa Europa CAI_CONAI.

References

Biel C, Subías I, Fanlo I, Mateo E, Acevedo RD (2007) Styles, mineralogy and textures of the Arroyo Rojo polymetallic massive sulphide prospect, Tierra del Fuego (Argentina). Digging Deeper, Vol.I-II. 2007; 27:1081-1084.

Biel C, Subías I, Fanlo I, Mateo E, Acevedo RD (2010) The Arroyo Rojo volcanic-hosted massive sulphide deposit (Tierra del Fuego, southernmost Argentina): geology, mineralogy, petrography and mineral chemistry. Rev Mex Cienc Geol 27:84-96.

Biel C, Subías I, Acevedo RD, Yusta I, Velasco F (2012) Mineralogical, IR-spectral and geochemical monitoring of hydrothermal alteration in a deformed and metamorphosed Jurassic VMS deposit at Arroyo Rojo, Tierra del Fuego, Argentina. J South American Earth Sci 35:62-73.

Boyce, AJ, Fallick, AE (1995) Stable and radiogenic isotope constraints on genetic models for the Lower Carboniferous carbonate-hosted Zn+Pb+Ba deposits in Ireland. Extended Abstracts in Models for Carbonate-Hosted Base-Metal Deposits. Irish Association for Economic Geology, Dublin, pp. 49–53.

Calderón M, Herve F, Cordaní U, Massonne HJ (2007) Crust-mantle interactions and generation of silicic melts: insights from the Sarmiento Complex, southern Patagonian Andes. Rev Geol Chile: 34, 249-275.

Canfield DE, Raiswell R, Wetsrich JT, Reaves CM Berner RA (1986) The use of chromium reduction in the analysis of reduced inorganic sulfur in sediments and shales. Chem Geol 54: 149-55.

Cathelineau M (1988) Cation site occupancy in chlorites and illites as a function of temperature. Clay Miner 23: 471-485.

Claypool, G.E, Holser, WT, Kaplan, IR, Sakai, H, Zak, I (1980) The age curves of sulfur and oxygen isotopes in marine sulfate and their mutual interpretation: Chemical Geology, v. 28, p. 199-260.

Fallick AE, McConville P, Boyce AJ, Burguess R, Kelley SP (1992) Laser microprobe stable isotope measurements on geological materials: some experimental considerations (with special reference to $\delta^{34}S$ in sulphides). Chemical Geology 101:53-61.

Friedman I, O'Neil JR (1977) Compilation of stable isotope fractionation factors of geochemical interest. In: Fleischer M (ed.) Data of Geochemistry, U.S. Geological Survey Professional Paper 440-KK, Reston, VA, pp 49.

Inverno CMC, Solomon M, Barton MD, Foden J (2008) The Cu Stockwork and Massive Sulfide Ore of the Feitais Volcanic-Hosted Massive Sulfide Deposit, Aljustrel, Iberian Pyrite Belt, Portugal: A Mineralogical, Fluid Inclusion, and Isotopic Investigation. Econ Geol 103: 1, 241-267.

Hall GEM, Pelchat JC, Loop J (1988) Separation and recovery of various sulphur species in sedimentary rocks for stable sulphur isotopic determination. Chem Geol 67: 35-45.

Kajiwara Y, Krouse HR (1971). Sulfur isotope partitioning in metallic sulfide systems. Can J Earth Sci 8: 1397-1408.

Krogh TE (1973) A low contamination method for hydrothermal decomposition of zircon and extraction of U and Pb for isotopic age determination. Geochim Cosmochim Ac 37: 289-297.

Lentz DR (1999) Petrology, geochemistry and oxygen isotope interpretation of felsic volcanic and related rocks hosting the Brunswick 6 and 12 massive sulfide deposits, Brunswick Belt, Bathurst Mining Camp, New Brunswick, Canada. Econ Geol 94: 57– 86.

Marcoux, E. (1998) Lead isotope systematics of the giant massive sulphide deposits of the Iberian Pyrite Belt. Miner Deposita 33: 45-58.

Ohmoto, H (1986) Stable isotope geochemistry of ore-deposits Reviews in Mineralogy, v. 16, p. 491-559.

Ohmoto H, Goldhaber M (1997) Sulfur and carbon isotopes. In: Barnes HD (ed) Geochemistry of hydrothermal ore deposits, 3rd. Edition. New York, Wiley, pp 517-611.

Ohmoto H, Rye RO (1979) Isotopes of sufur and carbon. In: Barnes HD (ed) Geochemistry of hydrothermal ore deposits. Willey Interscience, New York, pp 509-567.

Savin S, Lee M (1988) Isotopic studies of phyllosilicates Bailey SW (ed) Hydrous Phyllosilicates (exclusive of micas). Reviews in Mineralogy 19, 189-223.

Sharp ZD (1990) A laser-based microanalytical method for the in situ determination of oxygen isotope ratios of silicates and oxides. Geochimic Cosmochim Ac 54: 1353-1357.

Sheppard SMF (1986) Characterization and isotopic variations in natural waters. In: Valley JW, Taylor HP, O´Neil JR (eds.) Stable Isotopes in high temperature geological processes. Reviews in Mineralogy, 16, 165-184.

Stacey JS, Kramers JD (1975) approximation of terrestrial lead isotope evolution by a two stage model. Earth Planet Sc Lett 26: 207-221.

Tornos F, Heinrich CA (2008) Shale basins, sulfur-deficient ore brines, and the formation of exhalative base metal deposits. Chem Geol 247: 195-207.

Tornos F, Solomon M, Conde C, Spiro BF (2008) Formation of the Tharsis Massive Sulfide Deposit, Iberian Pyrite Belt: Geological, Lithogeochemical, and Stable Isotope Evidence for Deposition in a Brine Pool. Econ Geol 103: 185 - 214.

Zartman RE, Doe BR (1981). Plumbotectonics — The Model. Tectonophysics 75: 135-162.

Geology and massive sulfide deposits in the Mofjell group in the Rödingsfjället nappe complex, Nordland, Norway

Bjerkgård, T., Marker, M., Slagstad, T., Solli, A.
Geological Survey of Norway (NGU)

Abstract. The Mofjell Group contains a number of sulfide zones and Zn-Pb-Cu deposits. New data show that the group comprises a largely bimodal volcanic-sedimentary assemblage formed in an island-arc to back-arc setting. Data on the lithologies and deposits show that the sulfide deposits belong to the bimodal-mafic or bimodal-felsic class of VMS deposits. The environment with a bimodal volcanic suite mixed with sediments is an environment which is regarded as favorable for both rich and large massive sulfide deposits.

VMS, lithogeochemistry, tectonic setting

1 Introduction

The Mofjell Group is a volcanic-sedimentary unit, occupying a c. 170 km^2 area to the east of Mo i Rana, Northern Norway. The unit contains 9 sulfide zones with c. 20 Zn-Pb-Cu sulfide deposits, which were mined or explored in the last century. The only important ore producer in the group, however, was the Mofjellet mine which produced 4.35 Mt of ore with average grades of 3.6 % Zn, 0.7 % Pb and 0.3 % Cu in the period 1928-1987 (Bjerkgård and Hallberg, 2012). Other mines and prospects have all together produced only c. 60 000 t of ore. Earlier studies in the area have classified the Mofjellet deposit as a SEDEX type deposit (e.g. see Laznicka 1981), and an intraplate (ensialic) setting for the Mofjell Group (Bjørlykke et al. 1993).

Together with the prospecting and mine developing company GEXCO, NGU has recently evaluated the potential for new economic deposits within the Mofjell Group. In this respect, it is important to know the setting of the deposits, size, metal content, if there are any metal zonations, and not least, how the deposits were formed. This presentation will provide some answers to these questions.

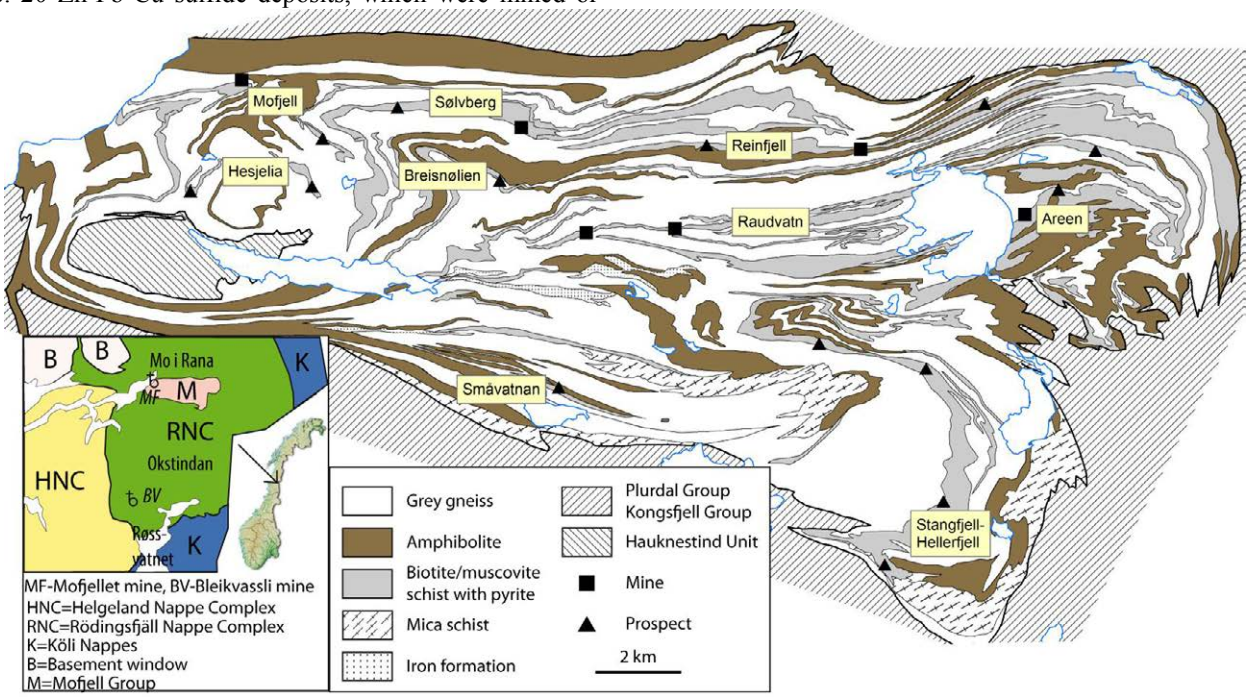

Figure 1. Simplified geology of the Mofjell Group, showing the most important ore deposits and the different ore horizons (named). The map is based on Marker, 1983 and Marker et al., 2012.

2 Geology and tectonic setting

The Mofjell Group has tectonic contacts to the sedimentary Plurdal Group in the north and the Kongsfjell Group in the south. All units are part of the Rödingsfjället Nappe Complex in the Uppermost Allochthon of the Norwegian Caledonides (Figure 1). The age of the group has not been established, but it is likely Neo-Proterozoic (590-600 Ma) on the basis of nearby geochronology data (Bjerkgård et al., 1997).

The Mofjell Group is dominated by so-called grey gneiss, which partly represents schistose, micaceous greywacke sediments and partly massive quartz-feldspathic, felsic metavolcanic/intrusive rocks. Within the gneiss are extensive layers of amphibolite and aluminous biotite and muscovite schists, as well as

minor units of metarhyolite ("keratophyre"). The amphibolites are commonly garnet-bearing, locally with pods and stripes of calc-silicate rock, and could represent deformed pillow lavas. The biotite and muscovite schists are generally rich in quartz and aluminosilicates (staurolite, kyanite) in addition to mica, as well as chlorite in the biotite schist.

The two types of mica schist form separate, generally extensive layers, but also grade into each other with changing proportions of biotite and muscovite. These schists generally contain disseminated iron sulfides (mainly pyrite) and are important in that they host the stratabound Zn-Pb-Cu sulfide mineralizations in the Mofjell Group. The most extensive zones of pyrite mineralization can be traced for several kilometers along strike. At several places the pyrite was mined, e.g. the Mos mine, which produced c. 52 000 t of pyrite in the period 1911-1920 from a total resource of c. 120 000 t.

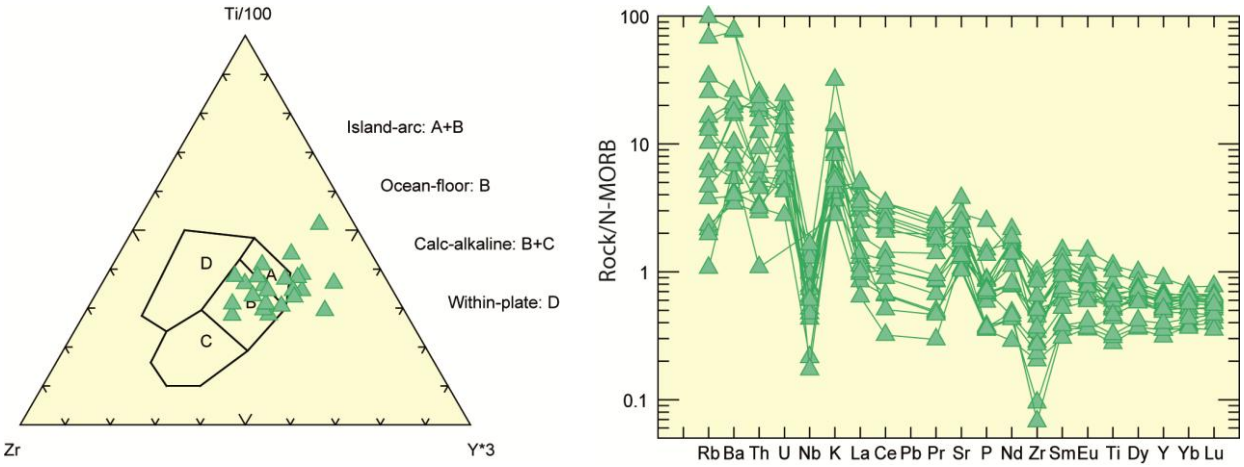

Figure 2: Amphibolites in the Mofjell Group plotted in the Ti-Zr-Y discriminant diagram (diagram by Pearce & Cann, 1973) and in an N-MORB normalized spider diagram (normalizing data from Sun & McDonough, 1989).

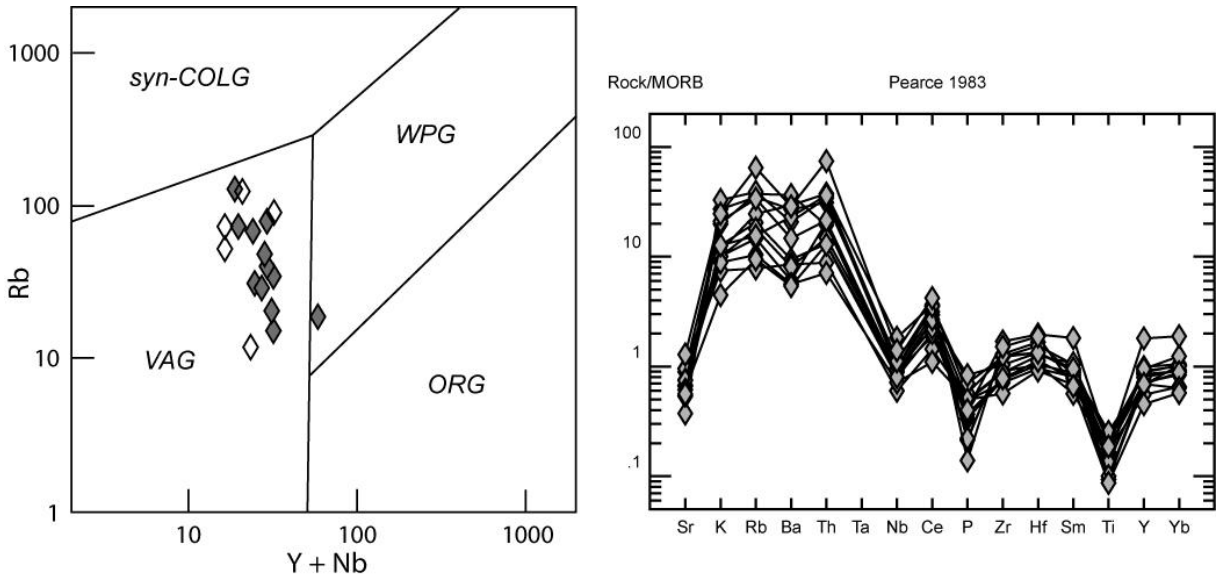

Figure 3: The composition of grey gneiss displayed in the Rb vs. Y+Nb discriminant diagram (diagram by Pearce et al., 1984) and a MORB normalized spider diagram (normalizing data from Pearce, 1983).

Analysis of the geochemical data on the amphibolites shows that they have tholeiitic compositions with a strong island-arc affinity (Figure 2). Geochemistry of the massive grey gneiss show consistent patterns, which strongly suggest an igneous (volcanic?) origin as dacites to rhyolites, formed in a volcanic arc environment (Figure 3). In conclusion, on the basis of lithological observations and geochemistry, the Mofjell Group consists of a largely bimodal volcanic-sedimentary assemblage formed in an island-arc to back-arc setting. Looking on the more regional picture, earlier work (e.g. Bjerkgård et al., 1997) strongly indicate that the part of the Rödingsfjäll Nappe Complex constituting the Kongsfjell Group to the south of Mofjellet between Røssvatnet and Mo i Rana (Figure 1), was formed in an extensional back-arc regime (based on lithological assemblages, lithogeochemistry). Thus both the Mofjell and Kongsfjell Group were formed in an arc setting, but if they were part of the same marginal regime, is difficult to say without geochronological constraints.

3 The sulfide deposits

The sulfide zones occur at different stratigraphic and structural levels within the Mofjell Group (Figure 1). Because of the strong deformation during the Caledonian events, any lithostratigraphic correlations or connections between sulfide zones have been very difficult to establish. Investigations of the geology and geochemistry of the deposits, however, reveal differences and similarities between the ore zones.

Table 1 (last page) shows the average in-situ metal contents of the main deposits in the different ore zones. The data set shows that the richer deposits are Hellerfjellet, Småvatnan and Breifonn with more than 10 % Cu+Zn+Pb but also Hesjelia and Heramb contain more than 5 %. The ones with the lowest base metal contents are the Breisnølien and Reinfjell zones, and the eastern part of the Raudvatn zone. These zones are characterized by being zones which are dominated by pyrite.

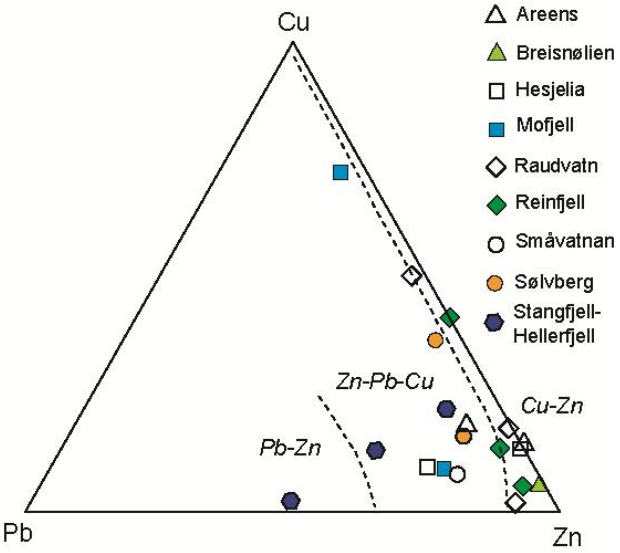

Figure 4: Ternary Pb-Cu-Zn plot showing the proportion of basemetals in the main sulfide occurrences in each ore zone. The dashed lines (from Large, 1992) distinguish between Cu-Zn, Zn-Pb-Cu and Pb-Zn type of massive sulfide deposits.

In the Cu-Zn-Pb diagram (Figure 4), the main sulfide occurrences in the different ore zones in the Mofjell Group either classify as Zn-Pb-Cu or Cu-Zn deposits. The most important occurrences which fall into the Cu-Zn class are the ones in the Raudvatn, Reinfjell and Breisnølien ore zones, which except for Heramb and Bertelberget mainly are low in base metals (Table 1). Occurrences belonging to the Mofjell, Sølvberg, Småvatnan and Hellerfjell zones plot mainly in the Zn-Pb-Cu field. In the Hesjelia ore zone, the Hammertjønna deposit plot in the Zn-Pb-Cu field and the Hesjelia deposit plot in the Cu-Zn field, indicating a lateral zonation in the zone. Similar zonations are also observed in the Mofjell and Raudvatn zones.

The geochemical data (Table 1) provides a general pattern of metal distribution in the Mofjell ore zones. The most striking is the barium-rich deposits, which are found in the western and southern part of the Mofjell Group (Mofjellet, Hesjelia, Småvatnan and Hellerfjellet). These deposits are generally rich in lead, zinc, silver and molybdenum but low in elements like cobalt, arsenic (except Småvatnan) and tin (except Hellerfjellet). The massive parts of these deposits are generally also low in gold. These similarities could point to some common sources of metals or similar physicochemical conditions during formation. It is also a possibility that these deposits originally were part of the same lithologic sequences, disrupted during the strong Caledonian deformation. This seems to be supported by the thick units of amphibolites, which are found close to all these deposits (Figure 1).

The north and eastern part of the Mofjell Group, including the Reinfjell zone, the eastern part of Raudvatn zone and Areen zone are all cobalt-rich, and partly also enriched in gold (up to several ppms in some samples) and locally bismuth. A curiosity is that zinc is partially taken up by zinc spinel (gahnite) and zincian staurolite (up to 9 % Zn in the structure).

The close association between the extensive zones of pyritiferous mica schists and the sulfide deposits (Figure 1), clearly points to a common origin. One possibility is that the schists represent distal depositions of sulfides from the hydrothermal vents. Another possibility is that the schists are parts of the alteration zones beneath and surrounding the main centers of hydrothermal activity.

The elements Al, Ti and Zr are generally regarded as some of the most immobile during hydrothermal alteration and metamorphic overprint (MacLean, 1988). They can therefore give some clues to which lithologies the deposits and zones are related to.

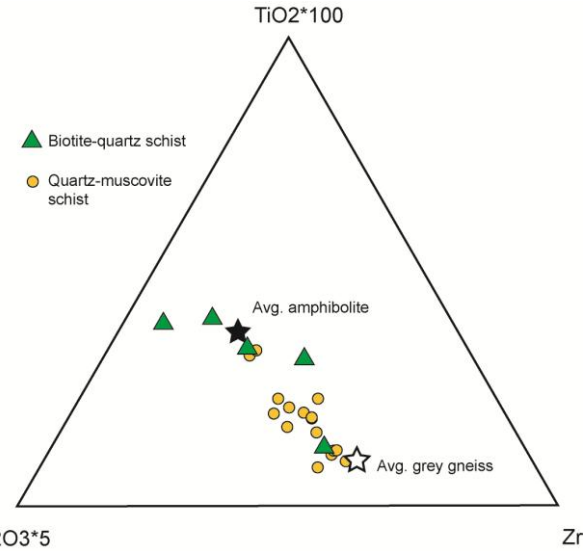

Figure 5: Ternary Al-Ti-Zr diagram for the most extensive pyritiferous muscovite and biotite zones (Raudvatn, Reinfjell), compared to the averages of the amphibolite and grey gneiss (marked by stars).

Figure 5 shows a ternary Al-Ti-Zr diagram for the most extensive, pyritiferous mica schist zones (Raudvatn East, Reinfjell). The average values for the main lithologies (amphibolite and grey gneiss) are shown for comparison. Even though the samples show a spread in the diagram, it is a tendency that the biotite-quartz schist samples group around the amphibolites, while the

quartz-muscovite schist samples distribute closer to the grey gneiss, but with an extension towards the amphibolites. Thus the muscovite schist seems to have a mixed origin, or reflect variations in the original composition, while the biotite schist seems to be mainly derived from the amphibolites. The close association of biotite schist and amphibolites units as seen in the field supports the latter.

4 Conclusions

The present investigation has shown that the Mofjell Group consists of a largely bimodal volcanic-sedimentary assemblage formed in an island-arc to back-arc setting. The collected data also show that the proportion of felsic metavolcanic rocks is much higher than earlier anticipated. The connection between the Mofjell Group and the Kongsfjell Group back-arc basin sequence to the south is so far not established.

On the basis of the data on the lithologies and deposits presented here, the sulfide deposits belong to the VMS class of massive sulfides, and fall into the bimodal-mafic or bimodal-felsic class of VMS deposits, as defined by Franklin et al. (2005).

Geochemical data also show that there are differences between the sulfide zones with respect to contents of certain elements: Some levels are strongly enriched in barium, while others are lead-, gold-, molybdenum-, nickel- or bismuth-rich. There are also metal zonations between deposits in the same level, e.g. from copper-rich to zinc-lead-rich deposits.

The environment with a bimodal volcanic suite mixed with sediments is an environment which is regarded as favorable for both rich and large massive sulfide deposits. Really large deposits have so far not been found in the area.

Table 1: Metal contents of the main sulfide deposits in the Mofjell Group (Cu, Zn, Pb in %, the other in ppm). The data set is based on a number (5-20) of representative samples from the dumps or bedrock.

Deposit	Ore zone	Ag	Au	Cu	Zn	Pb	Ni	Co	As	Sb	Bi	Mo	Ba	Sn
Areens 1-3	Areen	3.3	0.68	0.03	0.12	0.02	5	14	91	2	15	13	114	3.0
Areens 4-5	Areen	7.0	0.04	0.68	4.23	0.03	8	42	62	11	15	7	45	1.7
Breisnølien	Breisnølien	6.1	0.19	0.15	2.45	0.03	36	9	163	42	7	12	1011	4.3
Hammertjønna	Hesjelia	9.5	0.06	0.22	1.63	0.47	8	12	11	7	10	41	36630	3.5
Hesjelia	Hesjelia	13.3	0.12	0.88	5.75	0.07	11	18	40	18	15	10	30917	2.2
Mofjellet	Mofjell	20.6	0.41	0.38	3.18	0.76	22	14	27	37	7	24	80000	
Skarbekken	Mofjell	9.8	0.10	0.85	0.27	0.06	2	146	4	2	7	3	406	1.0
Bertelberget	Raudvatn	11.3	0.30	0.43	1.96	0.03	5	16	353	3	4	4	54	92.3
Heramb	Raudvatn	50.0	0.35	3.04	2.86	0.18	9	33	150	23	21	19	172	13.0
Raudsandhaugen	Raudvatn	15.6	0.12	0.03	1.99	0.17	4	21	12	4	37	11	19	1.0
Thermos	Reinfjell	7.0	0.10	0.18	1.07	0.06	4	25	17	4	11	8	76	4.6
Mos gruve	Reinfjell	5.3	0.05	0.41	0.58	0.00	3	73	80	2	3	6	2	0.5
Reinfjellet	Reinfjell	23.2	0.34	0.24	4.06	0.21	8	61	26	5	21	37	2	1.0
Småvatnan	Småvatnan	96.7	0.43	1.13	11.32	2.31	45	15	177	448	56	57	57569	5.2
Breifonn	Sølvberg	17.4	0.02	1.86	7.58	0.91	40	13	11	9	60	17	354	10.1
Sølvberget	Sølvberg	8.8	0.14	0.62	0.99	0.10	7	7	40	6	12	8	772	4.7
Stangfjellet	Stangfjellet	4.3	0.02	0.29	0.89	0.14	29	22	6	2	19	5	921	4.3
Rognhaugbekken	stangfjellet	9.13	0.06	0.15	0.71	0.34	9	33	210	5	40	14	82	28.6
Barium deposit	Stangfjellet	25.0	0.03	0.01	0.19	0.19	56	8	6	27	1	141	108467	0.7
Hellerfjellet	Stangfjellet	113.3	0.04	0.95	18.25	2.15	64	30	21	83	25	34	7875	39.0

Acknowledgements

The authors wish to thank Iain Henderson for correcting the language. Perry Kaspersen (former in GEXCO) is thanked for valuable discussions in the field, as well as for technical and logistic support.

References

Bjerkgård T, Hallberg A (2012) N028 Rana-Hemnes Zn-Pb-Cu. In: Eilu P (ed) Mineral deposits and metallogeny of Fennoscandia. Geological Survey of Finland, Special Paper 53, pp.100-102

Bjerkgård T, Larsen RB, Marker, M (1997) Regional setting of the Bleikvassli Zn-Pb deposit in Nordland, Norway. Norges geologiske undersøkelse Bulletin 433:34-35.

Bjørlykke A, Vokes FM, Birkeland A, Thorpe RI (1993) Lead isotope systematic of strata-bound sulfide deposits in the Caledonides of Norway. Economic Geology 88:397-417.

Franklin JM, Gibson HL, Jonasson IR, Galley AG (2005) Volcanogenic massive sulfide deposits. Economic Geology 100th anniversary Volume, pp. 523-560.

Large RR (1992) Australian volcanic-hosted massive sulphide deposits: features, styles and genetic models. Economic Geology 87:471-510.

Laznicka P (1981) Data on the worldwide distribution of stratiform and stratabound ore deposits. In: Wolfe KH (ed) Handbook of stratabound and stratiform ore deposits, Elsevier, Amsterdam, The Netherlands vol.9, pp. 479-576.

MacLean WH (1988) Rare earth element mobility at constant inter-REE ratios in the alteration zone at the Phelps Dodge massive sulphide deposit, Matagami, Quebec. Mineralium Deposita 23:231-238.

Marker M (1983) Caledonian and Pre-Caledonian geology of the Mofjell area, Nordland, Norway. Ph.D. thesis, Københavns Universitet. 153 p.

Marker M, Bjerkgård T, Slagstad T, Solli A (2012) Bedrock map Storakersvatnet 2027 III, M 1:50000, Geological Survey of Norway.

Pearce JA (1983) Role of the sub-continental lithosphere in magma genesis at active continental margins. In: Hawkesworth CJ, Norry MJ (eds) Continental basalts and mantle xenoliths. Shiva, Nantwich, pp.230-249.

Pearce JA, Cann JR (1973) Tectonic setting of basic volcanic rocks determined using trace element analyses. Earth Planet. Sci. Lett. 19:290-300.

Pearce JA, Harris NBW, Tindle AG (1984) Trace element discrimination diagrams for the tectonic interpretation of granitic rocks. Jour. Petr. 25:956-983.

Sun.SS, McDonough WF (1989) Chemical and isotopic systematics of oceanic basalts; implications for mantle composition and processes. In Saunders AD Norry MJ (eds.) Magmatism in the ocean basins. Geological Society Special Publications 42, pp. 313-345.

Massive Zn-Cu-Pb deposits in the Røros ore district, Norway: setting and formation

Bjerkgård, T. , Grenne, T., Sandstad, J.S.
Geological Survey of Norway (NGU)

Abstract. The Caledonian Røros Ore District is known as a copper producer; despite most of the deposits have much higher grades of Zn and Pb, than Cu. The mineralizations are hosted by sediments of two different geological formations: the Røsjø and Stugusjø formations. Bedrock mapping and lithogeochemistry show that the deposits were formed in a marginal basin environment dominated by clastic sediments. Magmatic activity related to extensional tectonics forming the basin, promoted hydrothermal activity and ore formation. Pb isotope data indicate that the differences in metal content between the deposits within the two formations may be explained by the differences in the host rock.

Caledonides, VMS, lithogeochemistry, Pb isotopes

1 Introduction

The Røros Ore District was a major copper producer in Norway in the period 1644–1977 and more than 6.5 Mt of ore was produced during the 333 years of mining. Sulfide deposits are mainly situated in two restricted areas in two different geologic formations. Individual mined deposits comprised up to 3 Mt of sulfide ore and contained on average about 2.7 % Cu and 4.2–5 % Zn (Bjerkgård et al. 1999). The zinc-rich ores were only partly exploited, and it is calculated that 250,000–300,000 t of zinc was left at the dumps during the mining operations (Bøckman 1942).

Despite the long period of mining, limited scientific work has been carried out in the Røros district. Some regional work was carried out by Sundblad et al. (2010). Data collected for a national ore database project by the Geological Survey of Norway (NGU), show that the deposits in the district generally have much higher grades of Zn and Pb than previously anticipated. These findings and interest from mining companies led to initiation of an NGU project to learn more about the known deposits and the potential for new discoveries in the Røros district. The project included detailed mapping and lithogeochemistry of the rocks and the deposits aiming at a better understanding of the metallogeny of the district.

2 Geologic setting

The Røros Ore District (Figure 1) is situated in the southeastern Trondheim Region, in the Upper Allochthon of the Scandinavian Caledonides. The ore deposits are hosted by the Aursund Group – a unit mainly comprising metagraywackes, partly calcareous, with lesser amounts of metatuffites, metabasalts and gabbroic sills and dykes, representing a marginal-basin environment, probably formed close to Baltica. It has been suggested that the unit was formed during the late closing stages of the Iapetus Ocean in the Late Ordovician/Early Silurian (Grenne et al., 1999).

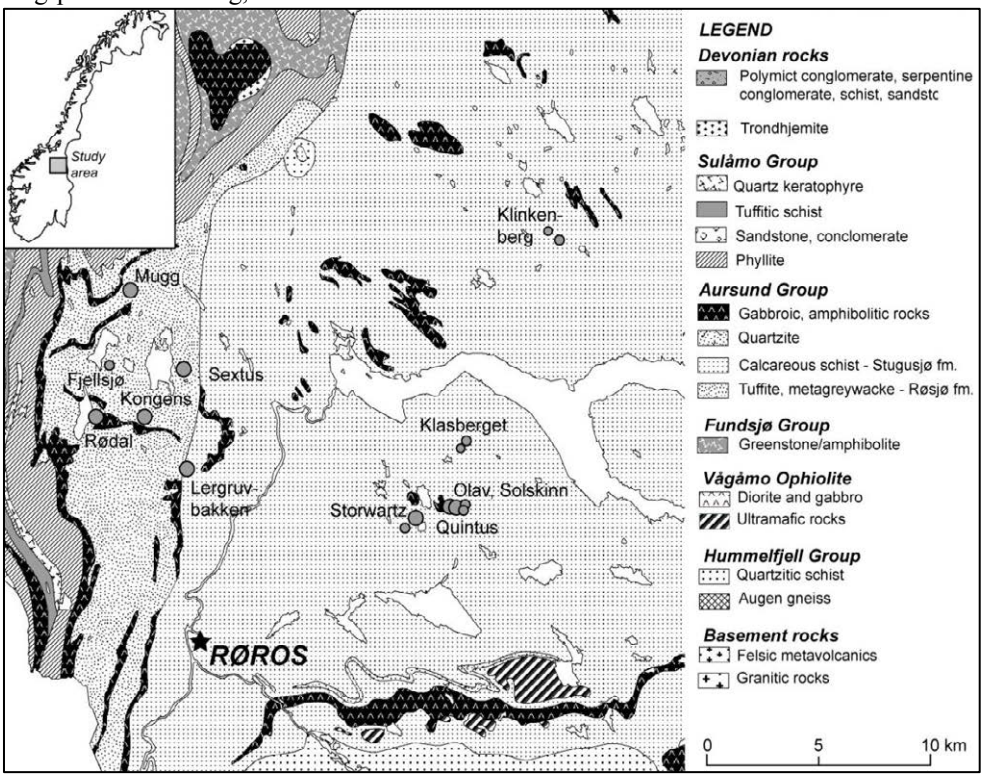

Figure 1. Geology of the the Røros Ore district (modified from Nilsen & Wolff, 1989), and including the main ore deposits (gray circles with names) in the district. The most important deposits are shown with larger circles.

The sediments of the Aursund Group are divided into two lithological units: the Røsjø and Stugusjø formations (Rui & Bakke, 1975). The Røsjø Formation is present in the western part of the district, and comprises mainly metagraywacke and quartz-biotite phyllite with thin bands of hornblende-bearing, quartz-rich tuffaceous sediment. The Nordgruve Ore Field is situated in this unit. The Stugusjø Formation covers the eastern part of the district and consists of calcareous metagraywacke, rhythmically alternating with gray carbonaceous phyllite on a meter-scale. Graded beds and cross-bedding are common. The Storwartz Ore Field and the Klinkenberg deposit are situated in this unit. Both units contain numerous gabbros, mainly as extended, sill-like intrusions, concordant with the surrounding sediments. They have lengths up to several kilometers, and are 20–50 m, rarely up to 100 m thick.

3 Lithogeochemistry

The sediments of the Stugusjø Formation are generally higher in Ca and K, but lower in Na compared to the Røsjø formation. Furthermore, the Stugusjø sediments have higher contents of Pb, V, Sc, La and Nd, whereas the Røsjø sediments are higher in Cr, Ni, Zn and Ce. These data are in agreement that the Røsjø Formation contains volcanic material, as manifested by thin tuffaceous bands.

Table 1. Chemical data of psammites in the Aursund Group compared to tectonic setting.

	Tectonic setting				Stugusjø/Røsjø		Stugusjø/setting				Røsjø/setting			
	OIA	CIA	ACM	PM	Stugusjø	Røsjø	OIA	CIA	ACM	PM	OIA	CIA	ACM	PM
Zr	96	229	179	298	193	217	2,01	0,84	***1,08***	0,65	2,26	***0,95***	1,21	0,73
V	131	89	48	31	108	92	***0,82***	1,21	2,25	3,48	0,70	***1,03***	1,92	2,97
Ce	22,5	50,5	72,7	71,9	77	80	3,42	1,52	***1,06***	1,07	3,56	1,58	***1,10***	1,11
La	8,7	24,4	33	33,5	32	26	3,68	1,31	***0,97***	0,96	2,99	***1,07***	0,79	0,78
Nd	11,4	20,8	25,4	29	24	18	2,11	1,15	***0,94***	0,83	1,58	***0,87***	0,71	0,62
Ti/Zr	56,8	19,7	15,3	6,74	23,6	20,8	0,42	***1,20***	1,54	3,50	0,37	***1,06***	1,36	3,09
Pb	6,9	15,1	24	16	23	14	3,33	1,52	***0,96***	1,44	2,03	***0,93***	0,58	0,88
Nb	2	8,5	10,7	7,9	12	12	6,00	1,41	***1,12***	1,52	6,00	1,41	***1,12***	1,52
Sc	19,5	14,8	8	6	11,9	8,6	0,61	***0,80***	1,49	1,98	0,44	0,58	***1,08***	1,43
Co	18	12	10	5	11	11	0,61	***0,92***	1,10	2,20	0,61	***0,92***	1,10	2,20
Th	2,27	11,1	18,8	16,7	9,4	8,4	4,14	***0,85***	0,50	0,56	3,70	***0,76***	0,45	0,50
La/Sc	0,55	1,82	4,55	6,25	3,58	3,7	6,51	1,97	***0,79***	0,57	6,73	2,03	***0,81***	0,59
La/Y	0,48	1,02	1,33	1,31	1,16	1,01	2,42	1,14	***0,87***	0,89	2,10	***0,99***	0,76	0,77
Ti	0,48	0,39	0,26	0,22	0,46	0,45	***0,96***	1,18	1,77	2,09	***0,94***	1,15	1,73	2,05

Data for tectonic setting from Bhatia & Crook, 1986. OIA: Oceanic Island Arc, CIA: Continental Island Arc, ACM: Active Continental Margin, PM: Passive Margin. Numbers in italics bold is best score (close to 1).

In Table 1, the psammitic rocks in the two formations are compared to data of some key elements and element ratios of graywackes from various tectonic settings (data from Bhatia and Crook, 1986). As the data show, most elements and element ratios of the two formations are comparable with a continental arc or active marginal setting (e.g. Pb, Zr, Nb, Nb/Y, La, Ce, Nd, La/Sc, Ti/Zr, Sc, V, Co); however it is impossible to distinguish between these two on the basis of the sediment data only.

The intrusive rocks are generally fine- to medium-crystalline with amphibole and plagioclase as the main phases, while chlorite, quartz and epidote are minors. A relict gabbroic texture is common in the least altered and deformed varieties. The geochemical data for the mafic rocks show that they are tholeiitic, olivine-normative gabbros (Figure 2). They show well-defined trends and plot as ocean floor (MORB) basalts. There are no differences between gabbros from the two formations regarding contents of trace elements or REE.

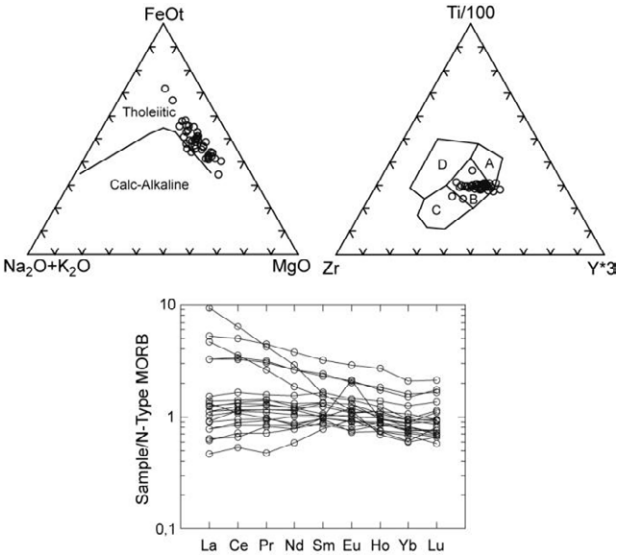

Figure 2. Classification, discrimination and spider diagrams for the mafic intrusions in the Røros District. Diagrams from Irvine & Baragar, 1971, Pearce & Cann, 1973 and N-MORB data from Sun & McDonough, 1989, respectively.

4 The sulfide deposits

The sulfide deposits occur in the sediments, and generally in close proximity to the gabbroic bodies (Figure 1). The ore bodies are generally only 1-2 meters thick, but thicker in fold hinges. The deposits are concordant with the bedding in the hosting sediments and often display a lensoid or ruler-shaped morphology, generally with long axis parallel prominent regional tectonic lineation features, mainly in the E-W direction (e.g. Kongens, Storwartz, and Mugg deposits). Discordant, stringer-type, Cu-rich mineralizations are found in the Kongens, Storwartz and Klinkenberg deposits.

The deposits in the Storwartz Ore Field have pyrrhotite as the dominating Fe-sulfide, while the deposits in the Nordgruve Ore Field and the Klinkenberg deposit contain both pyrite and pyrrhotite as major Fe-sulfides. Sphalerite, chalcopyrite and galena are generally present as major to subordinate phases. Native bismuth, dyscrasite, cubanite, hessite and arsenopyrite are accessory phases in especially the Storwartz deposits. In the Nordgruve Field these phases are rare.

Quartz and chlorite are the main gangue minerals, but locally also plagioclase (albite/andesine) is a major phase, especially in the Kongens deposit. Chlorite is generally Mg-rich, with Fe/Mg ratios between 0.25 and 0.39 (SEM data). Carbonate is subordinate and occurs in aggregates and single grains in most of the deposits.

The host rocks associated with all the main deposits in the Røros District are characterized by extensive wall rock alteration. Quartz-chlorite alteration is the dominant type, while quartz-sericite ± chlorite alteration is more restricted and most common in the Kongens and Sextus deposits.

The deposits in the Nordgruve Ore Field vary from being Cu-dominated (the Mugg deposit) to Zn-dominated (Lergruvbakken deposit). The Zn-rich deposits have very similar contents of most elements

(Figure 3a). The Cu-rich Mugg deposit has extremely low to low values of Zn, Pb, Bi, Co and As, but high contents of Cu, Mn and Au compared to the other deposits in the Nordgruve Ore Field.

In the Storwartz Ore Field, the western Zn-rich Storwartz deposits are much richer in Pb, Mn, Cd, Bi, As, Ag, Mo and Sb than the eastern Cu-rich Olav/ Solskinn deposits (Figure 3b). The latter deposits, however, are enriched in Co, Ni and Au. The Quintus deposit has contents of most elements between the two extremes. The Klinkenberg deposit is quite similar to the Zn-rich Storwartz deposits, except for an anomalously low content of Sb (Figure 3b).

Comparing the Storwartz and Nordgruve ore fields, the average values of the metals show that the Storwartz field generally have higher contents of Pb, Sb, Mo and Bi, while deposits in the Nordgruve field have higher contents of Ni and As.

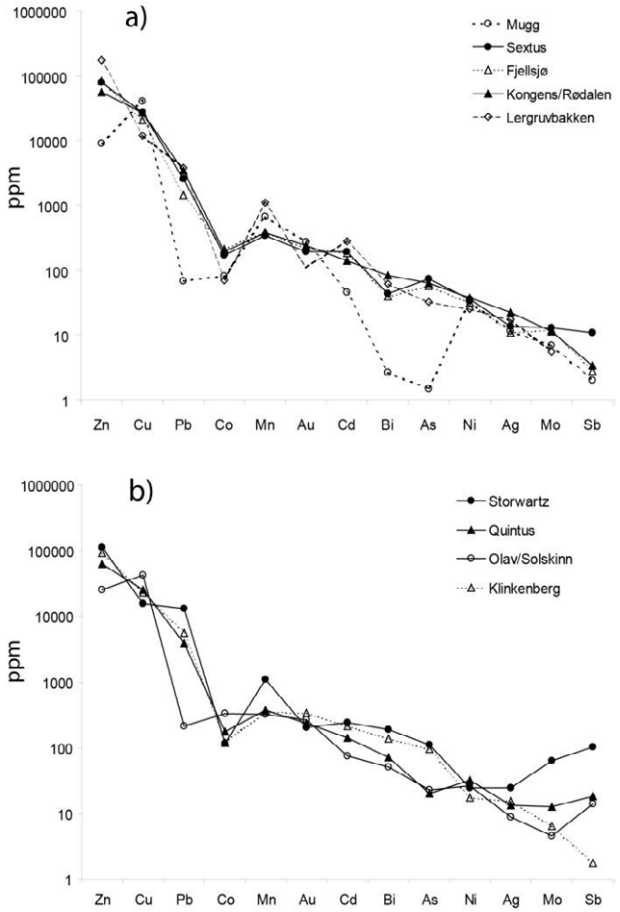

Figure 3. The metal contents in deposits of a) the Nordgruve Ore Field and b) the Storwartz Ore Field and Klinkenberg.

5 Lead isotope data

Samples for lead isotope analyses were collected of massive sulfides from several of the deposits in the Røros district. Data from the Kongens and Lergruvbakken deposits in the Nordgruve field were included from Bjørlykke et al. (1993).

The deposits in the Røros District show a rather restricted range in Pb isotope values (Figure 4). The four deposits in the Storwartz ore field have practically identical Pb isotope values with ranges of 18.215-18.220, 15.589-15.605, 38.129-38.140 for $^{206}Pb/^{204}Pb$, $^{207}Pb/^{204}Pb$ and $^{208}Pb/^{204}Pb$, respectively, and well within the uncertainty of the analyses. The three deposits from the Nordgruve ore field are distinctly less radiogenic than the Storwartz ore field, and display also a larger span in isotope values (i.e. 18.103-18.162, 15.524-15.585, 37.865-38.008, for the three isotope ratios, respectively). The Klinkenberg deposit has Pb isotope values quite similar to the most radiogenic deposit in the Nordgruve ore field (Sextus), and clearly less radiogenic than the Storwartz ore field.

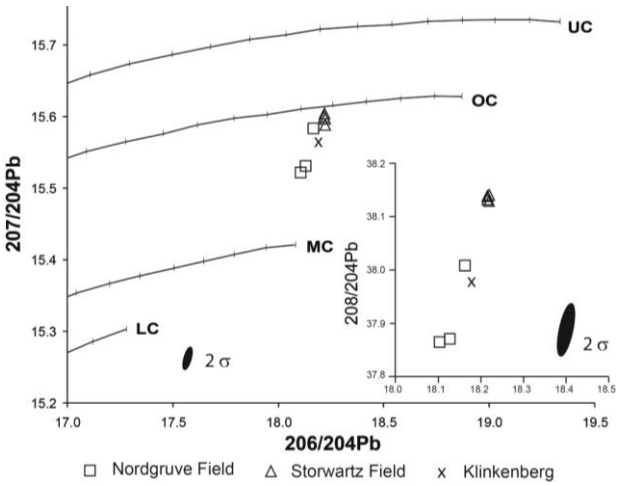

Figure 4. Lead isotope data for the Røros District ore deposits. The plumbotectonic curves from Zartman & Doe, 1981 are shown as reference.

6 Discussion

Despite the differences between the Røsjø and Stugusjø formations with respect to sedimentary structures, mineralogy and presence of subordinate lithologies, the two formations are quite similar with respect to geochemistry, and compared to sediments of different tectonic settings, similar to graywackes deposited in Continental Island Arc (CIA) or Active Continental Margin (ACM) environments (Table 1).

The geochemical data of the gabbroic intrusions show that these are tholeiites of N-MORB affinity (Figure 2), strongly suggesting an origin in a spreading regime in accordance with the interpretation of the sediment data.

This setting with minor magmatic activity of tholeiitic affinity, in an environment dominated by phyllites and metagraywacke is comparable to Besshi-type massive sulfide deposits (Slack, 1993). The tectonic setting of this type of deposits includes rifted continental margins, intracontinental rifts, back-arc basins and sediment-covered spreading ridges close to major continental masses (Slack, 1993). The ACM to CIA signature of the sediments in Røros is in agreement with such a model for the tectonic setting.

The magmatic activity during basin formation would induce hydrothermal circulation in the sediments. The spatial association between sulfide deposits and gabbroic sills suggest that the hydrothermal fluids and magma followed the same pathways through the sedimentary rocks, pathways that may have been fault zones or fracture zones, and formed during extension of the crust. This situation is analogues to the Middle

Valley at the Northern Juan de Fuca Ridge in the Eastern Pacific, where also a number of gabbroic sills are found in the sedimentary sequence above a volcanic basement, and spatially close to the major sulfide deposits, as in the Bent Hill area (Davis et al., 1992, Fouquet et al., 1998).

Comparing the sulfide deposits of the Storwartz and Nordgruve Ore fields, the major iron sulfides are pyrrhotite and pyrite, respectively. In the area around the Storwartz Ore field, the Stugusjø formation includes gray carbonaceous phyllite as a major component, providing a reducing environment, and favoring pyrrhotite as the major iron sulfide (Barton & Skinner, 1979). In contrast, the Røsjø formation contains larger amounts of metagraywacke, and much less phyllite, inferring a less reducing environment, and thereby favoring pyrite as the major iron sulfide.

There are differences regarding the contents of some key elements between the two main ore fields: The deposits in the Storwartz field as a whole generally have higher contents of Pb, Sb, Mo and Bi, while the Nordgruve field has higher contents of Ni and As. The Pb isotope values for the deposits in the Nordgruve Ore Field are distinctly lower than for the deposits in the Storwartz Ore Field (Figure 4). From this it appears that the differences in metal content between the two fields, at least partly, can be explained by lithological differences (e.g. the Røsjø Formation contains thin tuffaceous layers not found in the Stugusjø Formation).

The Klinkenberg deposit has comparable contents of a number of metals as the Nordgruve deposits, except higher contents of Bi and much lower contents of Ni. The Pb isotope values are intermediate between the values for the Storwartz and Nordgruve Fields.

Taking the Storwartz ore field as a whole, the deposits from east to west show a distinct zonation pattern in the base metals and corresponding increase and decrease in trace metal values. Together with the presence of an extensive and continuous chlorite alteration zone beneath all the deposits, this is an argument in favor of that the deposits in the Storwartz ore field originally were one deposit, with a zonation corresponding to proximal Cu-rich deposits in the east (Solskinn, Olav and Quintus), grading into more distal Zn and Pb rich deposits in the west (the two Storwartz deposits). The Pb isotope values of four of the Storwartz deposits are identical within the 2σ error, which also supports the model of one deposit (Figure 4). Taking into account the tonnages of the individual deposits and the in-situ ore grades, the proposed single deposit contained about 5 mill. tons of ore with an average grade of 3 % Cu and 9 % Zn, excluding eroded parts between the present deposits.

Acknowledgements

We wish to thank Prof. Brian L. Cousens, Carleton Univ., Canada for doing the Pb isotope analyses, while the staff at Univ. of Bristol, UK is thanked for assistance with REE analyses on ICP-MS.

References

Barton PB, Skinner BJ (1979) Sulfide mineral stabilities. In: Barnes, HL (ed) Geochemistry of hydrothermal ore deposits. Chichester, John Wiley & Sons, pp 278-403.

Bhatia MR, Crook KAW (1986) Trace element characteristics of graywackes and tectonic setting discrimination of sedimentary basins. Contributions to Mineralogy and Petrology 92:181-193.

Bjerkgård T, Sandstad JS, Sturt BA (1999) Massive sulphide deposits in the south-eastern Trondheim region Caledonides, Norway: a review. In: Stanley et al. (eds) Mineral Deposits: Processes to Processing, London, Balkema, pp 935-938.

Bjørlykke A, Vokes FM, Birkeland A, Thorpe RI (1993) Lead isotope systematics of strata-bound sulfide deposits in the Caledonides of Norway. Economic Geology 88:393-417.

Bøckman, KL (1942) Rørosviddas malmforekomster. In: Røros-bok-komiteen (ed) Rørosboka, 1. bind, Trondheim, pp 53-71 (in Norwegian).

Davis EE, Villinger H (1992) Tectonic and thermal structure of the Middle Valley sedimented rift, northern Juan de Fuca Ridge. In: Davis EE, Mottl MJ, Fisher AT (eds) Proceedings of the Ocean drilling Program, Initial Reports, 139, Ocean Drilling Program, College Station, TX, pp 9-41.

Fouquet, Y., Zierenberg, R., Miller, D. J., and Shipboard Scientific Party, 1998, Proceedings of the Ocean drilling Program, Initial Reports, Ocean Drilling Program, College Station, TX, 592 p.

Grenne T, Ihlen PM, Vokes FM (1999) Scandinavian Caledonide metallogeny in a plate tectonic perspective. Mineralium Deposita 34:422-471.

Irvine TN, Baragar WRA (1971) A guide to the chemical classification of the common volcanic rocks. Canadian Journal of Earth Sciences 26:523-548.

Nilsen O, Wolff FC (1989) Bedrock map Røros & Sveg, M 1:250 000. Geological Survey of Norway.

Pearce JA, Cann JR (1973) Tectonic setting of basic volcanic rocks determined using trace element analyses. Earth and Planetary Science Letters 11:290-300.

Rui IJ, Bakke I (1975) Stratabound sulphide mineralization in the Kjøli Area, Røros District, Norwegian Caledonides. Norsk Geologisk Tidsskrift 55:51-75.

Slack JF (1993) Descriptive and grade-tonnage models for Besshi-type massive sulphide deposits. In Kirkham RV et al. (eds), Mineral Deposit Modeling. Spec. paper 40. St. Johns, Newfoundland, Canada, Geological Association of Canada, pp 343-371.

Sun SS, McDonough WF (1989) Chemical and isotopic systematics of oceanic basalts; implications for mantle composition and processes: In Saunders AD, Norry MJ (eds) Magmatism in the ocean basins. Geological Society Special Publications, 42:313-345.

Sundblad K, Beckholmen M, Nilsen O, Andersen T (2010) Tectonostratigraphic position and depositional environment of the Røros sulphide ores, Norwegian Caledonides. Abstract 29th Nordic Geological Winter meeting, Oslo 2010, pp 192-193.

Zartman RE, Doe BR (1981) Plumbotectonics – the model. Tectonophysics 75:135-162.

Hydrothermal alteration and ore mineralogy at the Lombador massive sulphide orebody, Neves Corvo, Portugal: an on-going study

João RS Carvalho, Ana S Fernandes, Bruno B Moreira, Álvaro MM Pinto, Jorge MRS Relvas
CREMINER (LARSyS), Department of Geology, University of Lisbon, Ed. C6, Piso 4, 1749-016 Lisboa, Portugal

Nelson Pacheco, Filipa Pinto, Ricardo Fonseca
SOMINCOR, Soc. Mineira de Neves-Corvo, S.A., Mina de Neves-Corvo, 7780 Castro Verde, Portugal

Abstract. An ongoing study of the footwall hydrothermal alteration pattern and the ore mineral assemblages related to the zinc-rich stringer and massive sulphide mineralization in the Lombador orebody of the Neves Corvo deposit is here reported. Chloritization and sericitization are the main ore-related hydrothermal alteration facies recognized, but variably important silicification and carbonatization are commonly associated with either of these two main alteration facies. The sulphide mineral assemblage consists mainly of pyrite, sphalerite, galena, chalcopyrite, arsenopyrite, and minor tetrahedrite, stannite, bournonite, boulangerite, pyrrothite, complex Bi-sulphosalts, native bismuth, gold and roquesite. Preliminary EPMA data shows significant concentrations of some critical elements in different types of sulphide ores. In content in sphalerite and stannite range from 0.01 to 1.42 wt%, and 0.10 to 2.47 wt%, respectively. High In and Se contents were found in roquesite (up to 40.84 wt% In) and galena (up to 0.85 wt%), respectively. Ge concentrates in chalcopyrite (up to 0.01 wt%). Whole-rock analyses reveal significant amounts of Se in Cu-rich stringer ore samples, probably allocated to complex Bi-sulphosalts. The Lombador orebody may thus represent a promising target for critical elements. The relative abundance, spatial distribution and mineral allocation of these critical metals in the Lombador orebody, are currently under detailed investigation.

Keywords. Hydrothermal alteration, zinc-rich mineralization, Lombador orebody, Neves Corvo deposit, critical elements

1 Introduction

The Neves Corvo deposit stands out among the volcanic-hosted massive sulphide (VHMS) deposits of the Iberian Pyrite Belt (IPB), currently representing the largest base metal-mining operation in Western Europe. Since 1988 the mine has been a significant producer of copper. Recent surface drill programs looking for further development of the mine have defined over 100 Mt @ 6% zinc, turning the deposit into one of the world's largest undeveloped zinc resources.

Previous work on the massive and stringer cassiterite ores and massive sulphide copper-(tin) ores at the Corvo orebody provided answers to many metallogenic questions related with the high-temperature part of the mineralization spectrum of the Neves Corvo system (Relvas, 2000; Relvas *et al*., 2001; Relvas *et al*., 2006a; Relvas *et al*., 2006b).

In this work we report the footwall hydrothermal alteration pattern related to the zinc-rich stringer and massive sulphide mineralization in the Lombador orebody. This on-going study focuses on the recognition and characterization of the various hydrothermal alteration facies, spatial relationships, and stringer and massive sulphide ore mineral assemblages. The work is part of the first author's Ph.D. research program and is being ran under the scope of the ZHINC research contract (PTDC/CTE-GIX/114208/2009; Jorge MRS Relvas, PI), which focuses, for the first time, on the zinc-rich ores, the low-temperature end of the mineralization spectrum at the Neves Corvo deposit, and on the abundance and spatial distribution of some critical metals (In, Ge, Se and PGE's) in this unique mineralizing system.

2 Geologic Setting

The Neves Corvo deposit is located at the southeastern termination of the Rosário-Neves Corvo antiform, in the Portuguese part of the IPB, South Portuguese Zone. Six massive and stringer sulphide orebodies have already been identified in the mine perimeter: Neves, Corvo, Graça, Lombador, Zambujal, and Semblana orebodies.

The definition of the local stratigraphic sequence resulted from thorough palynostratigraphic studies (Oliveira *et al*., 1997; Oliveira *et al.*, 2004; Pereira *et al.*, 2004), coupled with underground and surface observations performed by the on-site geologists at the Neves Corvo mine. The sequence comprises the three main lithostratigraphic units previously defined at the IPB (from bottom to top): (1) the Phyllite-Quartzite Group (PQ) of late Famennian age that comprises a pre-orogenic detrital succession mostly composed by dark shale with intercalations of siltstone and quartzite, which in Neves Corvo is know to be more than 100 meters thick (base unknown); (2) the Volcano-Sedimentary Complex (VSC), of late Famennian to late Visean age, is divided into a lower, mostly autochthonous suite, and an upper allochthonous suite. It comprises a predominantly detrital sedimentary sequence (up to 600 meters-thick) of submarine sediments dominated by grey to black shale that incorporate several intercalations recording extrusive episodes of rhyolitic volcanism and the massive sulphide mineralization (Munhá *et al*., 1997;

Oliveira *et al.*, 1997; Oliveira *et al.*, 2004; Rosa *et al.*, 2008); and (3) a flysch succession (Mértola Formation) of upper Late Visean age that comprises a 3000 meters-thick synorogenic turbiditic sequence consisting of metric alternations of greywacke and dark grey shale. Major low-angle thrust faults pile up sections of the VSC and the flysch sucession over similar sections. This was the result of Hercynian thin-skinned tectonics and was followed by subsequent thrusting and folding events, accompanied by low-grade metamorphism (up to lower greenschist facies; Silva *et al.*, 1990; Silva *et al.*, 1997; Munhá, 1990).

3 Sampling and Methods

A systematic sampling campaign of the massive and stringer zinc (and In, Se, Ge and PGE)-bearing ores of the Lombador orebody was undertaken. In order to have a good representation of the different ores typologies and of the In, Se Ge and PGE's distribution within the orebody, 16 drill holes were selected, distributed over 12 cross sections that cover the south, central and north sectors of the orebody. The characterization of the footwall and hanging wall rock successions and ore types is based on detailed logging and sampling of 4112 m of core. Petrographic inspection of a suite of over three hundred thin and polished sections representing the different ore types, host rocks and alteration facies was performed. Whole-rock, EPMA, SEM/EDS, and ICP-MS analysis were made in well constrained samples. This contribution records the current stage of this on-going investigation.

4 Architecture of the Lombador Orebody

The Lombador orebody is very zinc-rich and concentrates the majority of the zinc Resources at the mine (49,9 Mt – Measured and Indicated – grading 6,44% Zn, 0.30% Cu, 1,69% Pb and 57,8 g/t Ag; and 21,1Mt of Inferred zinc Resources grading 4,51% Zn, 0.33% Cu, 0,92% Pb and 51,1g/t Ag). The orebody was discovered in 1988 following a deep drilling exploration program at the northern end of the Corvo and Neves orebodies (Pacheco and Ferreira, 1999). The orebody lies at depths ranging between 600 and 1000 m, is oriented NW-SE, and its known size is ≅1350 m long by ≅600 m wide. The ore lenses dip 20º to 40º northward, reaching a thickness of over 100 meters.

The footwall sequence hosting the Lombador orebody significantly change from the south and central sector of the orebody to its central-north sector.

In the south and central sector of Lombador, the massive sulphides directly overlay either the PQ Group sequence, or a variably thick (±0.5 to ±8 m; true thickness) volcanic unit. The PQ group comprises alternate intervals of quartzite and phyllite. This unit either grades upwards into massive sulphides, or is overlain by a volcanic package essentially dominated by coherent rhyolite. In a few positions, represented in some drill holes, the PQ phyllite grade upward into a slightly altered and mineralized dark grey to black shale (Neves Fm ?). Thin intervals (up to ±6 m) of poorly altered and mineralized dark grey to black shale seem also to occur intercalated within the volcanic sequence. However, these intercalations are most likely the result of tectonic deformation (sheared fine-grained volcaniclastic material). Shear implications are particularly intense in the central-west area of the orebody, where tectonic deformation was particularly concentrated. The volcaniclastic terms of the ore-hosting succession, when present, use to occur as thin levels (0.3 - 3.50 m).

In the northern sector of the Lombador orebody, the massive sulphides overlay a thick VSC sequence of highly altered coherent felsic volcanic rocks (up to ±20 m), and mineralized volcaniclastic (up to ±18 m) with interbedded metric thick (2 - ±20 m) dark grey to black shale layers (Neves Fm ?). Mass-flow, synsedimetary deformation and graded bedding structures are often seen in the volcaniclastic levels.

A huge stringer system consisting of variably dense and thick (±10 cm to ≥1 m) mineralized veins and veinlets underlies the Lombador massive sulphides network. This strockwork system is particularly developed in the central sector of the orebody. Both the PQ and the VSC sequences are crosscut by mineralized pyrite (±chalcopyrite) and/or pyrite-sphalerite-rich veins, and late chalcopyrite veinlets. Downwards, the mineralized vein density, thickness and sulphide contents progressively decrease.

Regarding the hanging wall succession, the massive sulphide orebody is overlaid by a thick VSC package (the upper VSC sequence). This VSC suite encompasses interbedded volcanic (up to ≈100 m) and shale (up to ≈300 m) intervals with thickness that laterally vary along the orebody. The volcanic package comprises metric-thick intercalations of clast-rotated breccias (predominant; often flattened), massive jigsaw-fit breccia, and epiclastic mass-flow sediments. Tectonically disrupted, zinc-rich mineralized lenses and/or distal stockwork mineralization can also occur within the upper VSC sequence, due to overthrust repetitions. However, in places less affected by tectonic activity, the hanging wall JC unit (discontinuous levels of jasper/chert and/or sericitic greenish-grey to grey and violet shale) can be observed in its original position, i.e. directly overlying the massive sulphides.

Regional low-angle thrust faults and late faulting events are prominent throughout the Lombador orebody. Strain has been strongly portioned into phyllosilicate-rich rocks in both footwall and hanging wall alteration zones and underlining the contacts within the massive sulphide package. Some copper- and zinc-rich ore shoots are clearly an outcome of late tectonic deformation, ascribed to tectono-metamorphic processes of remobilization, either ductile or fluid-assisted. However, local primary metal zonation features are overall preserved and still identifiable.

In the south and central-west sectors, the ore is more massive, fine-grained, recrystallized and highly variable in texture. Banded (both primary and deformational), and sheared ore intercalations are common along the ore sequence. Moreover, banded ore (both primary and deformational) with high-grade pyrite–sphalerite–

(galena) layers interbeded with pyritic layers in a carbonate(±quartz+chlorite) groundmass, graded bedding, and synsedimentary textures are increasingly more common from central-east to the northern sector of the orebody.

5 Footwall Hydrothermal Alteration Facies

The mineralogical, textural, geochemical and isotopic signatures of the Corvo orebody ore-related hydrothermal alteration system have been thoroughly described by Relvas (2000) and Relvas et al. (2001; 2006a; and 2006b). The feeder system below Corvo comprises an inner stockwork zone dominated by chlorite-donbasite-quartz-sulphide (±siderite+sericite), surrounded by a dominant k-sericite-quartz-sulphide (±chlorite+siderite) envelope, and a Na-sericite-quartz-sulphide (±siderite±chlorite) peripheral zone.

In Lombador, chloritization and sericitization are the main ore-related hydrothermal alteration facies recognized, but silicification and variably important carbonatization are often associated with either alteration facies.

In the stockwork zones underlying the massive sulphides, sericite alteration is best developed affecting the coherent volcanics in the south and central-west sectors of the orebody. In the PQ detrital facies, sericite is mostly restricted to vein-filling. Fine-grained (±10 μm) quartz is generally intimately associated with sericite, and chlorite occurs in minor variable amounts. Sericite is typically fine-grained (<10 μm), occupying intercrystalline spaces and replacing feldspars, chlorite (less frequently) and rock matrix.

Chloritization is best developed in the central and northern sector of the orebody, replacing both detritic (mainly quartz-rich siltstones/phyllites and phyllites) and volcanic facies. The altered rocks grade from moderately choritized (10-20% vol. chlorite) to almost monomineralic chlorite (over 90% vol.; chloritite). Continuous alteration halos (up to 5 cm) on both sides of mineralized veins are common features in both detrital and volcanic facies. Chlorite is typically fine-grained (<20 μm) and occurs as anhedral-euhedral crystals in aggregates, occupying intercrystalline spaces and replacing both quartz grains and rock matrix. Coarse chlorite grains (±100 μm) are also quite common. Chlorite occurs with fine-grained quartz, sericite, pyrite, and carbonates. EPMA data have shown the presence of donbasite intergrowth with chlorite.

Silicification is a common process in both footwall and hanging wall coherent volcanic facies. In the PQ detrital facies, silicification is mainly restricted to vein filling. In the stockwork zone, silicification is mostly developed in the central (near the contact with the massive sulphides) and northern sector (extends to greater depth) of the orebody. A less intense siliceous alteration is observed under the southern sector of the orebody. This type of alteration involves replacement of rock matrix by fine-grained (<10 μm) quartz with more than 60 – 70% by volume of quartz. Variable recrystallization of the quartz groundmass is conspicuous. Sericite, pyrite and variable amounts of chlorite and carbonate are commonly associated with the silicification process.

Carbonates, mainly siderite, ankerite and sideroplesite, are often present (≤10% vol.) in the upper parts of the footwall sequence of the orebody, close to the contact with the massive sulphides in both detrital and volcanic rocks. Carbonates occur in the groundmass as continuous halos (up to 1 cm) on both sides of mineralized veins, as rounded patches (up to 400 μm), and as vein-filling phases. A distinctive zone of carbonate alteration is found in the central/central-west sector of the orebody, comprising massive carbonate levels (up to 2 m) developed in the upper portions of the PQ Formation, specially in the siltstone/phyllite facies. In those domains, carbonates represent more than 90% by volume of the rock. The carbonates occur as coarse yellowish, reddish brown, to colorless aggregates (>1 mm) set in a fine-grained (±10 μm) chlorite groundmass.

6 Ore Types, Mineralogy and Critical Metals Contents

Ten different ore types can be distinguished in the Lombador orebody. These include lenticular to stratabound massive ores, which vary from Zn-rich (MZ) to Cu-rich (MC), Pb-rich (MP), Cu-Zn-rich (5C or MCZ), Zn-Pb-rich (5Z or MZP), and barren (ME) ores. Stringer/fissural ores (stockwork) can be Zn-rich (FZ), Cu-rich (FC), or barren (FE). Stockwork mineralization tectonically emplaced in a hanging wall position acquires a characteristic banded tectonic fabric and is called "rubané ore". In Lombador, the rubané ore is mainly Zn-rich (RZ).

Cu, Zn, and Pb contents in the massive sulphide ore vary along the orebody and the Zn and Zn–Pb high-grade domains are frequently intercalated (often interfingered) and followed by an upward Fe zone. Well-developed metal zonation patterns from a Cu to Zn–Pb to Fe zone in an upward and lateral sequence are recognized both in the stringer and the massive ores. However, significant thrusting, remobilization and enrichment processes along all types of ore are often present, significantly obscuring the pristine relationships. The Cu-rich ores, namely, are often "displaced" from their original position due to preferential remobilization. Cu-rich massive ore shoots occur on top of the massive sulphide package, forming "blankets" over barren or Zn- or Zn-Pb-rich massive ores. These copper zones can also occur either interbedded with zinc-rich massive sulphide ores, or forming "secondary" copper-zinc-rich domains.

The stringer sulphide mineral assemblage is mainly dominated by pyrite, chalcopyrite and sphalerite. Arsenopyrite, galena, tetrahedrite, stannite, boulangerite, bournonite, pyrrhotite and probable galenobismutite, kobelite-tintinaite and bismuthinite constitute accessory sulphide minerals. Minor amounts of bismuth, gold/electrum, rutile and cassiterite were also identified.

Pyrite is the most abundant sulphide mineral in the massive sulphide ore, representing 60 to 90% of the mineral assemblage modal volume. Sphalerite, chalcopyrite, galena, and arsenopyrite are the remaining

major sulphide minerals (≤10 % vol.). Other sulphide minerals, such as tetrahedrite, bournonite, boulangerite, pyrrothite, stannite and roquesite occur in minor quantities (<5% vol.). The most abundant gange minerals are carbonates, quartz, and phyllosilicates, and the amount of carbonate intergrown with the massive sulphide ore is increasingly higher towards the northern sector, reaching up to 40% vol. in places. Rutile, graphite and cassiterite occur in minor quantities.

Ore textures are extremely variable. Recrystallization of the massive sulphides is common along the orebody. The ore is essentially massive, banded (although with some intercalated featureless zones), and occasionally brecciated. Banded textures are particularly visible in the zinc-rich ore varieties, MZ and 5Z (and occasionally 5C). Although recrystallization, annealing and brecciation is manifest along the orebody in all types of ores, as a general rule the ore tends to be more massive and recrystallized towards the base, whereas mineral banding tends to be more common towards the top.

Typically, the banded texture consists in thin (usually ±1 mm to ±2 cm, but can reach up to 20 cm) sphalerite – pyrite or sphalerite–galena–pyrite levels, alternating with pyrite-rich levels (usually ±1 to ±20 cm, but can reach up to 50 cm). The layers rich in sphalerite (and galena) are commonly deformed and internally annealed, while pyritic levels are recrystallized, brecciated, and often boudinaged, with pyrite fractures commonly filled by galena, sphalerite, chalcopyrite, tetrahedrite, quartz and carbonates. Relics of pristine structures such as monomineralic and/or polymineralic colloform, framboidal banded structures and evidences of early growth of sphalerite and galena in dispersed nuclei within pyrite grains are still recognized.

Preliminary EPMA data have shown low contents of In and Se in chalcopyrite (up to 0.15 and 0.01 wt% respectively). In content in sphalerite range between 0.01 to 1.42 wt%. However, the major carrier of In is stannite, which contains 0.10 to 2.47 wt%. Although rare, roquesite was positively identified and analysed (up to 40.84 wt% In). Ge is mostly allocated in chalcopyrite (up to 0.01 wt%). No In, Se or Ge have been found in tetrahedrite. This sulphosalt contains up to 5.62 wt% Ag. High Se content has been found in galena (up to 0.85 wt%). Whole-rock analyses reveal significant amounts of Se in Cu-rich stringer ore samples, probably allocated to complex Bi-sulphosalts in some copper-rich fissural ore samples.

The Lombador orebody may represent a promising target for critical elements. The relative abundance, spatial distribution and mineral allocation of these critical metals in the mineralizing system of Neves Corvo and, particularly, in the Lombador orebody, are currently under detailed investigation.

Acknowledgements

This work was financially supported by the Foundation for Science and Technology (FCT-MCTES, Portugal), through project ZHINC (PTDC/CTE-GIX/114208/2009; Jorge MRS Relvas, PI). Thanks are due to SOMINCOR, SA for allowing access to the drill cores, and for logistic support. Steven Scott, Duane Smythe, George Kretschmann and Colin Bray from University of Toronto and Filipa Marques (CREMINER/LARSyS, Univ. Lisbon) are gratefully acknowledged for providing full access, formation and support in analytical data acquisition.

References

Munhá, J. (1990) Metamorphic Evolution of the South Portuguese/Pulo do Lobo Zone. In: Dallmeyer, R.D., Martinez Garcia, E. (Eds.). Pre-Mesozoic Geology of Iberia. Springer-Verlag, Berlin, pp. 363-368.

Munhá, J., Pacheco, N., Beliz, A., Relvas, J.R.S. and Hodder, R.W. (1997) Physical and Geochemical Characterization of the Neves Corvo Felsic Volcanism. Soc. Econ. Geol. Neves Corvo Field Conf. Abstr 89.

Oliveira, J.T. (1990) Straigraphy and Synsedimentary Tectonism. In: Dallmeyer R.D., Martinez Garcia E. (eds). Pre-Mesozoic Geology of Iberia. Springer-Verlag, Berlin, pp. 334-347.

Oliveira, J.T., Carvalho, P., Pereira, Z., Pacheco, N., Fernandes, J.P., Korn, D. (1997) The stratigraphy of the Neves Corvo mine region. Soc. Econ. Geol. Neves Corvo Field Conf. Abstr 86-87.

Oliveira, J.T., Pereira, Z., Carvalho, P., Pacheco, N., and Korn, D. (2004) Stratigraphy of the tectonically imbricated lithological succession of the Neves Corvo mine area, Iberian Pyrite Belt, Portugal. Mineralium Deposita, Vol. 39, pp. 422-436.

Pacheco, N., and Ferreira, A. (1999) Neves Corvo Mine. In Tornos,F., Locutura, J., Martins,L. (eds). The Iberian Pyrite Belt, Joint SGA IAGOD International Meeting, Field trip B4. ITGE-IGM, pp. 21-24.

Pereira, Z., Pacheco, N., Oliveira, J.T. (2004) A case applied palynology: dating the lithological siccession of the Neves Corvo mine, Iberian Pyrite Belt , Portuga. In: Proceedings of the XVth ICCP Stratigraphy. Wong, Th. E. (Ed.). R.D. Acadamy Arts and Sciences, pp. 345-354.

Relvas, J.M.R.S. (2000) Geology and metallogenesis at the Neves-Corvo deposit, Portugal: Unpublished Ph.D. thesis, Univ. of Lisbon, Portugal, p. 319.

Relvas, J.M.R.S., Barriga, F.J.A.S., Ferreira, A. (2006a) Hydrothermal Alteration and Mineralization in the Neves-Corvo Volcanic-Hosted Massive Sulfide Deposit, Portugal. I. Geology, Mineralogy, and Geochemistry. Economic Geology, vol. 101, pp. 753-790.

Relvas, J.M.R.S., Barriga, F.J.A.S. (2006b) Hydrothermal Alteration and Mineralization in the Neves-Corvo Volcanic-Hosted Massive Sulfide Deposit, Portugal. II. Oxygen, Hydrogen, and Carbon Isotopes. Economic Geology, Vol. 101, pp. 791-804.

Rosa, C.J.P., McPhie, J., Relvas, J.M.R.S., Pereira, Z., Oliveira, T., Pacheco, N. (2008) Facies analyses and volcanic setting of the giant Neves Corvo massive sulphide deposit, Iberian Pyrite Belt, Portugal. Mineralium Deposita, Vol. 43, No. 4, pp. 449-466.

Silva, J.B., Oliveira, J.T., and Ribeiro, A. (1990) Structural Outline. In Dallmeyer, R.D., Martinez Garcia (eds). Pre-Mesozoic geology of Iberia. Springer, Berlin, pp. 348-362.

Silva, J.B., Ribeiro, A., Fonseca, P., Oliveira, J.T., Pereira, Z., Fernandes, P., Munhá, J., Barriga, J.A.S., Relvas, J.M.R.S., Carvalho, P., Ferreira, A. Beliz, A., Noiva, P., Pacheco, N., Leitão, J.A. (1997) Tectonostratigraphic overview of the Neves Corvo Mine in the context of the Variscan Orogeny. Soc. Econ. Geol. Neves Corvo Field Conf. Abstr 88.

Mineralogy, textures and new sulphur isotope data of the Cerro de Maimón VMS deposit ores, Dominican Republic

Joan Marc Colomer, Eloi Andreu, Lisard Torró, Joaquín A. Proenza, Joan Carles Melgarejo
Dpt. Cristal·lografia, Mineralogia i Dipòsits Minerals, Universitat de Barcelona. C/ Martí i Franquès s/n 08028 Barcelona, Catalonia, Spain

Cevero Chavez, Ricardo del Carpio, Julio Espaillat
Corporación Minera Dominicana. Av. Máximo Gómez, 29B, Ed. Plaza Gazcue, local 401. Santo Domingo, Dominican Republic

John F. Lewis
Department of Earth and Environmental Sciences, George Washington University, Washington, DC 20052, USA

Abstract. Cerro de Maimón, in the central Dominican Republic, is currently the only VMS deposit under production in the Caribbean region. It is hosted in the Maimón Formation, which is part of the oldest and chemically most primitive island-arc in the Caribbean. Bottom to top, this deposit can be divided into (i) a primary sulphide zone, (ii) a supergene enrichment zone and (iii) an oxidized zone. Pyrite is the most abundant sulphide in the primary sulphide zone and often exhibits foam textures indicating re-arrangement by a dissolution/syntaxial overgrowth. Chalcopyrite, sphalerite and tennantite appear mostly as interstitial components. Ag, Au, Bi and Pb tellurides occur as minute grains. Bornite, coveline and chalcocite are the main secondary sulphide phases in the supergene enrichment zone. In the oxidized zone, goethite is the main phase and along with hematite forms cellular-boxwork, sandy-granular and massive textures. Native gold and iodargyrite (AgI) grains are detected in this zone. Newly determined $\delta^{34}S$ values in sulphide minerals range from -2.2 to 3.9‰ and are slightly lower than the values registered in similar Caribbean VMS deposits so a minor contribution of bacteriogenic sulphur is suggested.

Keywords. Cerro de Maimón, Dominican Republic, VMS, gold, copper, sulphur isotopes

1 Introduction

Since systematic exploration for mineral deposits in the Maimón Formation began in the late 1970s, several volcanogenic massive sulphide (VMS) occurrences have been discovered within this formation, in central Dominican Republic. It includes Cerro de Maimón and Loma Pesada deposits and Loma Barbuito, Río Sin, Loma la Mina and San Antonio occurrences (Nelson et al., 2011). A study of the trace element and Sr-Nd-Pb isotope geochemistry of the Maimon Fm. by Horan (1995) was followed by a summary of the structure, petrography, whole rock and oxygen isotope geochemistry of the Cerro de Maimon, Loma Pesada and Loma Barbuito VMS deposits by Lewis et al. (2000).

Cerro de Maimon copper and gold mine is located 70km northwest of Santo Domingo and 7km east of the town of Maimón (Fig. 1), in the Monseñor Nouel Province. The Cerro de Maimón open pit mine, which went into production in 2008, is 100% owned and operated by the Australian company Perilya Limited through its subsidiary Corporación Minera Dominicana.

Although Cerro de Maimón is the only VMS deposit currently under production in the Caribbeanr, few detailed studies have been made (e.g. Watkings, 1990; Astacio et al., 2000; Andreu et al., 2010). Here we present detailed mineralogical and textural data on the oxide and sulphide ores and a preliminary sulphur isotopic study in order to establish the evolution of this deposit and to constrain the nature of the mineralizing fluid.

Figure 1. Geographical location of the study area in central Dominican Republic.

2 Geological setting

The late Early Cretaceous–Eocene Circum-Caribbean island-arc system is a complex collage of crustal units which were initially formed in an intra-oceanic setting during Early Cretaceous (Pindell & Barrett, 1990). The formation of the ore deposits in the tectonic evolution of the northern Caribbean was discussed by Nelson et al. (2011).

The Maimón Formation, where the Cerro de Maimón deposit is hosted, is a NW trending belt of 9km wide and about 73km long. This Formation, together with the Amina and Los Ranchos Formations, forms part of the oldest and chemically most primitive island-arc in the Caribbean region (Lewis & Draper, 1991; Escuder-Viruete et al., 2009; Nelson et al., 2011). Lewis et al. (2000) interpreted the Maimón and Amina formations as fore-arc components and the Los Ranchos formation as the axial island arc.

The Cerro de Maimón deposit is located in the southern margin of the Maimón formation, in the Ozama shear zone and hence the rocks are strongly deformed. The deformation, metamorphism and pervasive hydrothermal alteration (specially registered in the footwall rocks) largely destroyed the original lithologies. Based on least altered lithologies, host rocks are described as mafic to intermediate submarine volcaniclastic and volcanic rocks by Lewis et al. (2000).

The massive sulphide lens is very close to the thrust-faulted contact with the Peralvillo Formation (Fig. 2), a thin belt of mafic volcanic rocks of apparent late Cretaceous age. The lens is 1000m long, about 300m wide and 15m thick on average although thicknesses up to 40m exist. The ore body can be broadly separated, from top to bottom, into (i) an oxidized zone or gossan with 1.86g/t Au, 34.5g/t Ag, 0.20% Cu and 0.02%Zn grades; (ii) a supergene enrichment zone with 0.96g/t Au, 34.9g/t Ag and up to 10% Cu grades and a Cu-Zn ratio of 3:1; and (iii) the primary mineralization with 2.54% Cu, 0.96g/t Au and 34.9g/t Ag and the Cu-Zn ratio that tends to1:1 in depth. The current proven and probable reserves are 12.35Mt of sulphide ores. (http://www.perilya.com.au/our-business/operations/ cerro-de-maimon)

3 Methodology

A total of 21 gossan rock samples were collected directly from ten mine benches (from bench 195 to bench 150) in the open pit; 42 samples of primary sulphides were picked up from 26 drill holes (DDH). They were analysed at the Serveis Científics i Tecnològics of the Universitat de Barcelona.

Mineralogical characterization was determined by the petrographic microscope, X-ray powder diffraction, SEM-EDS and EMP. XRD analyses were performed on an X'Pert PRO MPD X-ray diffractometer with a Bragg-Brentano θ/θ of 240 millimeters range. Diffractograms were processed using X'pert and Topas software. Scanning electron microscope study was done using an ESEM Quanta 200 FEI, XTE 325/D8395 electron microscope equipped with an INCA Energy 250 energy dispersive spectroscopy microanalysis system. Mineral chemistry was analyzed by electron microprobe with wavelength-dispersive spectrometry (EMPA-WDS) using an accelerating voltage of 20kV with a beam current of 5 to 20 nA and a 10-15µm spot beam diameter in a Cameca SX50 equipment

Sulphur isotopes were measured on 16 samples of pyrite, 3 of chalcopyrite and 1 of chalcocite using a Delta C Finnigan MAT Delta-S mass spectrometer with an elemental analyzer, a TC-EA. The isotope ratios were calculated using the YCEM, NBS-127, IAEA-S1, IAEA-S3, IAEA-SO5, IAEA-SO6 and internal laboratory standards. The analytical precision is within ±0.2‰ at 1σ.

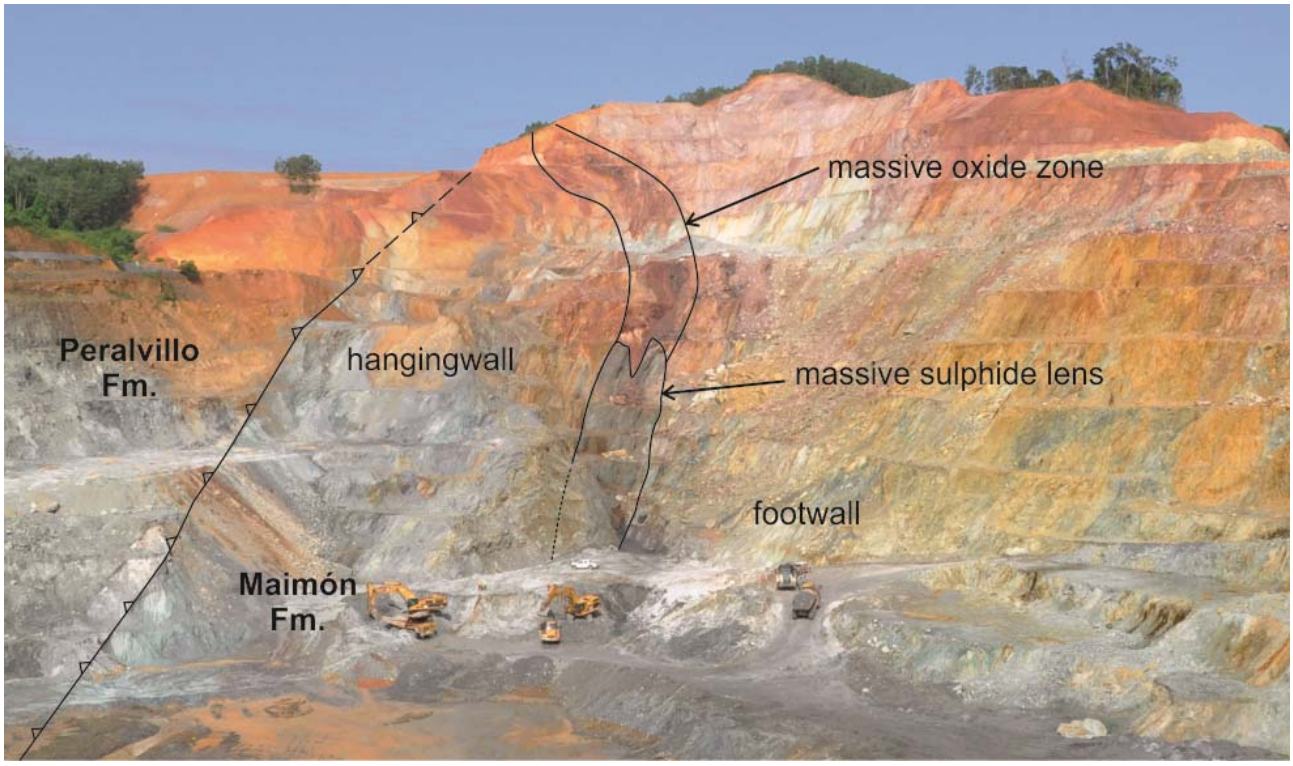

Figure 2. Photo-mapping of the Cerro de Maimón open pit in December 2012. The white all-terrain vehicle located under the massive sulphide lens is about 4.5m long.

4 Mineralogy and textures

4.1 Primary mineralization zone

Studied samples consisted of massive sulphides mainly composed of pyrite, chalcopyrite and sphalerite. Pyrite is the most abundant phase (≈80% vol.) in the deposit and presents shapes varying from rounded to euhedral or subeuhedral crystals. Pyrite grain-size ranges from 100 to 500 µm. Annealment textures are easily recognizable. Chalcopyrite (15% vol.) and sphalerite (10-12% vol.) appear mostly as interstitial components among pyrite grains and infilling pyrite fractures and voids. Chalcopyrite is the most abundant phase in the matrix of the massive sulphide body. Sphalerite often exhibits the chalcopyrite disease. Minerals of the tennantite-tetraedrite series (1-2% vol.) occur as accessory phases along with chalcopyrite and sphalerite in the matrix and more rarely as inclusions in pyrite. EMP analyses indicate that the dominant end member is tennantite. Galena (<1% vol) occurs as minute grains (1-10µm) usually as inclusions in all the sulphides or in the grain boundaries. Trace minerals include altaite (PbTe) (identified by EMPA), and Au, Ag and Bi tellurides, identified by EDS (probably hessite, krennerite and hedleyite). Tellurides seem to be late in the sequence.

Two significant gangue minerals, barite and quartz, occur among pyrite grains together within the chalcopyrite-sphalerite matrix. Quartz veinlets up to 100µm are common and appear cutting all the sulphide mineral assemblage above described above. Angular fragments of pyrite, chalcopyrite and sphalerite are included in these veins suggesting an abrupt fragmentation of the rock during the formation of these late stage gangue veinlets. Other gangue minerals include sericite, chlorite and minor calcite.

4.2 Supergene enrichment zone

A gradual evolution of copper enrichment varying from selective to pervasive replacement of the primary sulfides has been observed. A direct correlation between the grade of replacement and the porosity, up to 30-40%, is evident.

The least weathered samples are characterized by selective replacement of sphalerite by bornite and minor covellite. There is clear evidence that chalcocite replaced bornite. These supergene phases are only visible along grain margins forming thin reaction aureoles of about 5µm and filling fractures. Further stages related to weathering are characterized by covellite and chalcocite forming flamelike or featherlike replacement textures affecting both chalcopyrite and sphalerite, and progressing from fractures or voids towards the grain cores. Pyrite and tennantite are not affected at these two initial enrichment episodes. In advanced stages of replacement, chalcopyrite and sphalerite are totally replaced. Pyrite as well as tennantite is corroded along margins resulting in a semi-cariated texture. The presence of chalcanthite was detected.

4.3 Oxidized zone

The broad mineral paragenesis of the gossan of Cerro de Maimón can be described as an assemblage of a goethite-hematite-silica groundmass with abundant barite and quartz fragments. Goethite is much more abundant than hematite. Fine-grained gibbsite cemented by goethite is found as discrete layers. Malachite occurs as milimetric veins and fractures.

Three broad groups of textures have been distinguished under the microscope: (i) sandy-granular (cellular-boxwork), (ii) sandy-granular (brecciated), and (iii) massive (botryoidal-colloform). Granular samples are characterized by abundant porosity, up to 30%.

Cellular-boxwork textures consist of a limonitic sponge hosting quartz and barite fragments. Micro-breccia textures consist of angular silica and/or barite fragments cemented by oxides with colloform textures.

Botryoidal aggregates are composed of successive colloidal layers of finely crystalline goethite and minor hematite. The outer rim of the aggregates is often hematite, probably due to dehydratation (aging) of the goethitic phases. Minor manganese-rich layers have been identified.

Intermediate or mixed textures are observed. Thus, textures range from clast-supported (cemented by colloform aggregates) where the gangue minerals dominate (barite up to 90%); to massive-colloform zones where gangue only represents nucleation cores. In the same way, voids between clasts and cellular voids show different stages of infilling, from the absence of oxides in the voids to the total infilling by colloform aggregates.

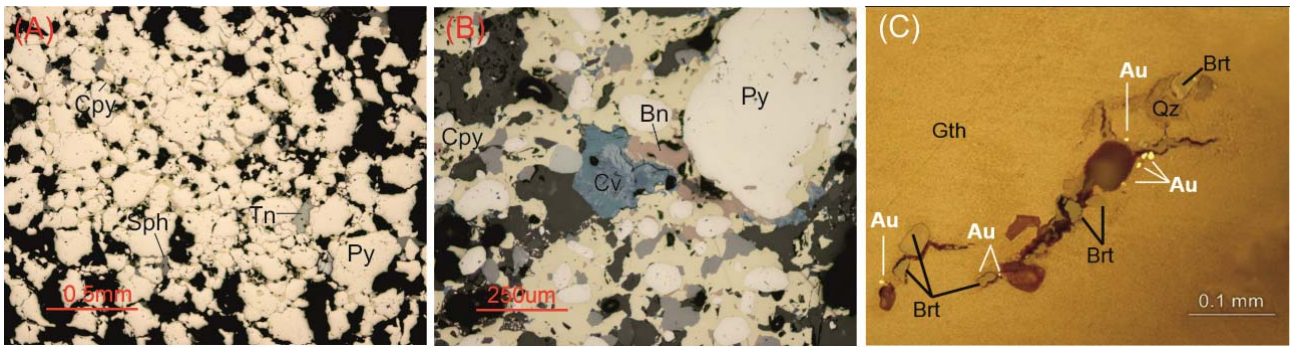

Figure 3. Micro-photographs of Cerro de Maimón samples under the petrographic microscope using reflected light. (A) Primary sulphides with pyrite showing annealment textures. (B) Primary sulphides replaced by secondary sulphides (bornite and covellite) in the supergene enrichement zone. (C) Gold grains mixed with quartz and barite in a fracture in fine goethite groundmass. Py: pyrite; Cpy: chalcopyrite; Sph: sphalerite; Tn: tennantite; Bn: bornite; Cv: covellite; Brt: barite; Gth: goethite; Qz: quartz.

Thin layers of kaolinite and of goethite-gibbsite were also found. The second are characterized by a deep yellow-mustard colour.

Au-Ag occurrences in the gossan are systematically related to botryoidal aggregates or fine goethite layers. Native gold grains are rounded and their size ranges from 2 to 10µm. They appear in voids between botryoidal layers or as intergrowth between two successive layers. Gold grains found in samples composed of a fine goethite matrix appear to be related to voids or fractures, mixed with barite grains. A remarkable concentration of gold grains is found in the kaolinite layers. Silver occurs as iodargyrite (AgI) grains ranging from 1 to 15µm in size. It is always found in voids between botryoidal aggregates adapted to the shape of the pore or as fragments mixed together with barite cemented by colloform goethite (Andreu et al., 2010).

5 Paragenetic sequence

From textural observation of mineral textures and relations, a paragenetic sequence of crystallization of the different phases has been built. Three main stages of crystallization have been considered: (1) hydrothermal alteration prior to mineralization, (2) primary mineralization and (3) oxidation and supergene enrichment (Fig. 4).

6 Sulphur isotopes

The $\delta^{34}S$ range from -2.2 to 3.9‰ with a mode of 0‰. The $\delta^{34}S$ values range from -2.2 to 3.9‰ on pyrite, from -0.7 to -0.6‰ on chalcopyrite and is of -1.2‰ on the chalcocite analysed sample.

7 Final remarks

Preservation of annealment or foam textures in pyrite of the primary sulphides zone could be attributed to surface-driven processes such as re-arrangement by a dissolution/syntaxial overgrowth rather than actually recrystallization (Barrie et al., 2010).

The $\delta^{34}S$ values on Cerro de Maimón analysed samples are slightly lower than those obtained from other Caribbean VMS deposits such as San Fernando (-0.5 ‰ and +7 ‰) and San Antonio (from 0.0 to +3.6‰), both hosted in the Los Pasos Fm. (Central Cuba), (Alfonso et al. 2007). Thus, although obtained values for the Cerro de Maimón sulphides are in good agreement with a magmatic origin of the sulphur, a minor contribution of bacteriogenic sulphur is suggested.

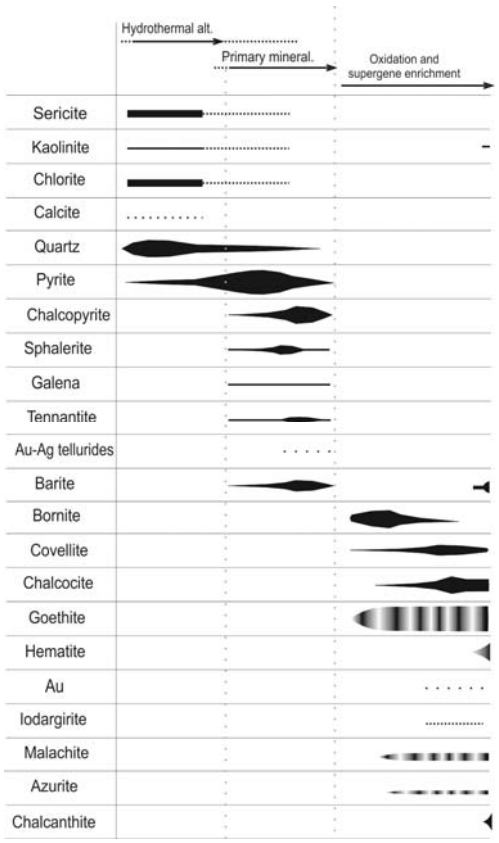

Figure 4. Paragenetic sequence of the studied mineral phases in the Cerro de Maimón deposit (adapted from Andreu, 2010).

References

Alfonso, P., Melgarejo, J.C., Proenza, J.A., Gubern, A., Gallardo, E., Cazañas, X., 2007. Mineralogy and sulfur isotopes of San Fernando VMS deposit, Central Cuba. En: Digging Deeper. Irish Association for Economic Geology, 1089-1092.

Andreu, E (2010) Textures, mineralogy and mineral chemistry of the Cerro de Maimón deposit (Dominican Republic): weathering and metallurgical implications. Unpublished Geological Engineering Thesis. Barcelona.

Andreu E, Proenza JA, Tauler E, Chavez C, Espaillat, J (2010) Gold and Iodargyrite in the Gossan of Cerro de Maimón Deposit (Central Dominican Republic). Macla, 13, 41-42.

Astacio VA, Lewis JF, Campbell A, Espaillat J (2000) Oxygen isotope and alteration geochemistry of the Cerro de Maimón deposit, Dominican Republic In Jackson T (ed) Caribbean Geology in the New Millenium, Transactions 15th Caribbean Geological Conference, Kingston, Jamaica.

Barrie CD, Boyle AP, Cook NJ, Prior DJ (2010) Pyrite deformation textures in the massive sulfide ore deposits of the Norwegian Caledonides. Tectoniphysics, 483, 269-286.

Escuder-Viruete J, Pérez-Estaún A, Weis D, Friedman R (2009) Geochemical characteristics of the Río Verde Complex, Central Hispaniola: Implications for the paleotectonic reconstruction of the Lower Cretaceous Caribbean island-arc. Lithos, 114, 168-185.

Horan SL (1995) The geochemistry and tectonic significance of the Maimón-Amina schist's Cordillera Central, Dominican Republic.unpublished M.S. thesis, University of Florida, Gainesville, 172 p.

Lewis JF, Draper G (1991) Geology ad tectonic evolution of the Northern Caribbean margin In Dengo G & Case JE (eds) The Caribeean region. Boulder, Colorado, Geological Society of America, The Geology of North America, H, 77-140.

Lewis JF, Astacio VA, Espaillat J, Jiménez J (2000) The occurrence of volcanogenic massive sulfide deposits in the Maimón Formation, Dominican Republic In Sherlock R & Logan MAV eds VMS Deposits of Latin America. Geological Association of Canada Special Publication.

Nelson CE, Proenza JA, Lewis JF, López-Kramer J (2011) The metalogenic evolution of the Greater Antilles. Geol Acta, 9, 229-264.

Pindell JK & Barrett SF (1990) Geological Evolution of the Caribbean region: A plate-tectonic Caribbean Region. Geol Soc Am, Geology of North America, H, 405-432.

Watkins J (1990) Geologic Setting of the Cerro de Maimón Deposit, Dominican Republic, Geologic report for Falconbridge Dominicana, Santo Domingo, 43pp.

Hydrothermal alteration zonation in the massive sulfide-hosting footwall sequence of Lousal, Iberian pyrite belt

Ana S.C.Fernandes, Jorge M.R.S. Relvas
CREMINER/LARSyS, Department of Geology, University of Lisbon, Ed. C6, Piso 4, 1749-016 Lisboa, Portugal

João X. Matos
LNEG - National Laboratory of Energy and Geology, Apartado 104, 7801-902 Beja, Portugal

Abstract: The secondary mineral associations present in the altered footwall rocks of the Lousal massive sulphide orebodies and its geochemical signatures were characterized in order to define the hydrothermal alteration zonation associated to the ore-forming process. Representative samples were collected in two drill holes intersecting both the massive sulphides and their footwall succession. Detailed petrography, coupled with mineral and whole-rock geochemical data have shown that the ore-related hydrothermal alteration zonation in the footwall rocks at Lousal is akin to typical IPB ore.forming systems: pervasive chloritization, sulphidization and silicification in the central stockwork (Zone 1), grading laterally into peripheral envelopes characterized by strong sericitization, pyrite-rich sulphidization and hydrothermal quartz addition. Potassium-rich metassomatism (Zone 2a) evolves laterally into more distal expressions of weak alteration characterized by partial preservation of the igneous feldspars and the progressive increase of the paragonitic molecule in the secondary phyllosilicates (Zone 2b). The recognition of this zonal pattern in alteration can be used as a criterion to reconstruct pre-tectonic geometric relationships among the massive ores and their hanging-wall and footwall host successions, ground on the interpretation of discontinuities in the alteration paths along the drill holes. This provides an additional mean to go through reconstruction of tectonically dismembered successions in the IPB, contributing to trace vectors towards mineralization in exploration campaigns in strongly deformed terrains.

Keywords: Iberian Pyrite Belt; Lousal; Hydrothermal alteration zonation

1 Introduction

The several Iberian Pyrite Belt (IPB) deposits, both in Portugal or in Spain, have been intensively exploited and have been the subject of many studies aimed at understanding and characterizing hydrothermal alteration patterns associated to their footwall rocks.

The IPB is located in the South Portuguese Zone, extending for about 250 Km, with an approximate width of 60 Km, which corresponds to an area of *ca*. 12.500 Km^2 (Carvalho *et al.,* 1999). This region corresponds to an important metallogenetic province worldwide, where polymetallic massive sulphide deposits associated to volcanic and sedimentary rocks occur. More than 80 deposits are known, representing a total accumulation of massive sulphides in excess of 1700 Mt (Leistel *et al.,* 1998; Carvalho *et al.,* 1999). In addition, hundreds of large deposits and small occurrences of manganese oxides, carbonates and silicates have been exploited in the past in this province (e.g., Carvalho *et al.,* 1999; Jorge, 2000), together with copper, lead, barium and antimony vein-type mineralization associated to late, tectonically-drove remobilization (Leistel *et al.,* 1998, Oliveira *et al.,* 2006).

Three main units constitute the IPB stratigraphic sequence: Phyllite-Quartzite Group (PQG, Upper Devonian and older), Volcano-Sedimentary Complex (VSC, Upper Devonian-Lower Carboniferous) and Baixo Alentejo Flysch Group (BAFG; Lower to Upper Carboniferous; Oliveira *et al*., 2006). The major host-rocks to ores include felsic volcanic and volcaniclastic rocks and shales with variable carbonaceous component, their relative abundance and thickness varying throughout the belt. Nevertheless, massive sulphide mineralization is clearly related with felsic volcanism, as their spatial relationship with the proximal domains of the volcanic centers along volcanic axis is quite obvious.

The Lousal massive sulphide deposit is located in NW sector of the IPB. It was exploited for pyrite, between 1900 and 1988. Nowadays, Lousal is an old mining village under a rehabilitation program (RELOUSAL, Frédéric Velge Foundation/ Municipality of Grândola; Matos e Oliveira, 2003; Relvas et al., 2012).

2 Geological setting

The Lousal mine lies on a CVS alignment locally designated as Lousal Complex. This unit is delimited to N, E and South by the Tertiary sediments of the Sado Basin, and to the West by the Mértola Formation turbiditic sediments (BAFG). It is composed of a number of ore lenses, distributed on the SW limb of an antiform (Lousal antiform) that is segmented by late faults with a N-S and NE-SW orientation (Matos and Oliveira, 2003).

The geological units represented in the Lousal mine area are, from bottom to top: *(i)* Phyllite-Quartzite Group (PQG), represented in the core of the Lousal antiform by the Corona Formation (phyllites and quartzites with intercalations of siltstones and greywacke; Upper Famennian - Upper Strunian; Pereira *et al.,* 2010); *(ii)* Volcano-Sedimentary Complex, composed by siliceous and graphitic shales, felsic volcaniclastic and coherent rocks, lavas, spilites and dolerite, jaspers and cherts (Upper Famennian- Upper Visean; Strauss, 1970; Oliveira, 1990); and *(iii)* Baixo Alentejo Flysch Group (BAFG; Mértola formation), which is locally composed by a thick sequence of shale and greywake (Upper Visean – Upper Carboniferous; Oliveira, 1983).

The Lousal VSC was strongly affected by folding, thrust faults and several families of strike-slip faults. The Corona formation is partially overthrusted on the Lousal Complex, which in turn is tectonically piled up on the Mértola formation (BAFG). The main strike-slip faults are characterized by dextral movement and N-S direction (Corona Fault). Another important fault system, with NE-SW direction, has also significant expression and partially controls the geometry of the massive sulphide lenses (Matzke, 1971; Matos e Oliveira, 2003). Regional metamorphism is low-grade and ranges from zeolite to greenschist facies (Munhá, 1990).

At Lousal the orebodies distribute over two main areas, both on the SW limb of the Lousal antiform. The orebodies are generally lenticular with variable thickness and conformably overlie altered/mineralized footwall rocks. The Lousal sulphides are hosted by a thick succession of carbonaceous shales, which contain abundant disseminated pyrite, and accessory amounts of chalcopyrite, sphalerite, galena, arsenopyrite and stannite. The alteration intensity and footwall mineralization decrease with the distance to the mineralization axis. The orebodies morphology is strongly controlled by faults that define their footwall and hanging-wall contacts. The two boreholes studied and sampled in the course of this research – LS1 and LS02 - were logged and the corresponding profiles were done and made available by Pirites Alentejanas S.A.

3 Hydrothermal alteration

The Lousal massive sulphide deposit was formed during the final stages of felsic volcanism. Ore-related hydrothermal activity produced several secondary mineral associations that are characteristic of the different zones of the hydrothermal system. These different zones were defined on the basis of textural, mineralogical and chemical characteristics of the hydrothermal products. Three alteration zones were distinguished (Zone 1, Zone 2a and Zone 2b) ground on their phyllosilicate content (*e.g.,* Barriga, 1983; Relvas, 1991). The various alteration expressions are controlled by the chemistry and physical characteristics of the mineralizing fluid (e.g., pH, redox potential, temperature, W/R ratio, composition), and also by the primary characteristics of the altered rocks (e.g., VSC *vs.* PQG)

Zone 1 corresponds to the core of the hydrothermal feeder system. This alteration zone is characterized by destructive and pervasive alteration. The hydrothermal assemblage is mainly composed by chlorite + quartz ± sericite + carbonates + sulphides. Sulphides are very abundant and occur either disseminated, or filling anastomosed veins, associated to quartz, chlorite, sericite and carbonates (Fig. 1). The sulphides are mainly pyrite, chalcopyrite, sphalerite and minor galena, arsenopyrite and stannite. This zone is characterized by intense leaching of alkalis and relative enrichment in MgO and Fe_2O_3 content. The alteration conditions are extreme and relics of the original rock are either rare or absent, leading to formation of chloritite in completely replaced domains.

Zone 2a is peripheral to zone 1 but still relatively proximal. It is also characterized by intense alteration. The alteration products are dominated by intense sericitization and sulphidization of the rock matrix, complete destabilization of feldspars and their substitution by sericite + quartz, and intense dissemination of sulphides in close dependence to mineralized veins (Fig.2). K-sericite shows significant amounts of Ba. The high content in MgO and Fe_2O_3 is due to the presence of chlorite. Carbonates are relatively abundant and occur either as a vein-filling phase, or as a secondary mineral, replacing the vitreous matrix and feldspar phenocrists. High Ba content in sericite is

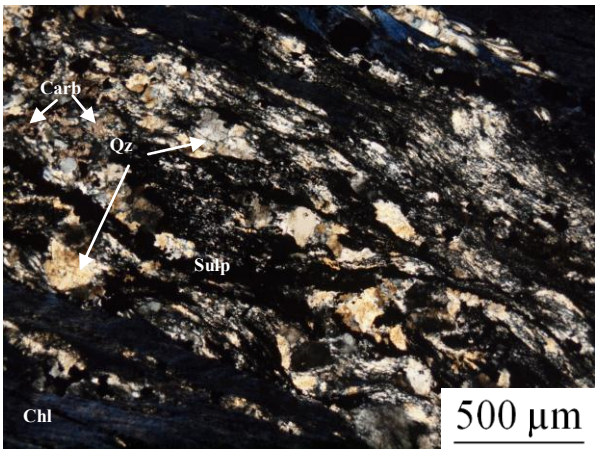

Fig. 1: Photomicrograph of an altered volcanic rock proximal to the axis of the mineralization (Zone 1) Chl-Chlorite; Carb- Carbonates; Qz-Quartz; Sulf- Sulphides

characteristic of Zone 2a. Overall, this zone is defined by intense sericitization, sulphidization and some silicification. The mineralogical assemblage is constituted by sericite + chlorite + quartz ± carbonates + sulphides. In the felsic volcanic rocks this type of alteration is texturally characterized by pervasive replacement of the matrix by a mass of sericite + quartz cut by veins filled with sericite+quartz+pyrite+minor chlorite and carbonates. Feldspar phenocrysts are often totally replaced by quartz and/or sericite. In the coarse-grained siliciclastic detrital rocks of the PQ Group, sericitization and chloritization is less pervasive as these rocks are much less reactive, and sericite and chlorite occur mostly restricted to the grain interstices, and filling veins and pressure shadows or in deformation corridors. In phillites, the alteration becomes more widespread and less controlled by veins.

In the studied footwall section of the Lousal ore-hosting sequence, hydrothermal zone 2b is the most peripheral alteration halo recognized. This zone is characterized by weaker sericite alteration, low density of hydrothermal veins, less significant sulphide dissemination and partial preservation of the igneous feldspar phenocrysts (Fig.3). The mineralogical assemblage is composed by sericite + quartz + carbonates + sulphides ± chlorite ± epidote. Whole-rock geochemical signatures are characterized by Na_2O enrichment relative to the inner alteration zones. The higher Na_2O content of the altered rocks is due both to

the larger paragonitic component of sericite and to albitization of the preserved feldspars. The dominant sulphide is pyrite, which occurs in veins and disseminated in the matrix.

Figure 4 displays a schematic reconstruction of the mineralization setting in a pre-deformation context, showing the original position of the studied samples along intersections defined by the selected drill holes (now represent as discontinuous segments), and the alteration zones identified in this study.

4 Mineral chemistry

Chlorite occurs in the central zone of stockwork as the dominant mineral (Zone 1), and as a subordinate secondary phase in the matrix or as a vein-filling mineral relatively to sericite in Zone 2a and 2b. The analyzed chlorites are mostly ripidolite, here referred as chlorite II. Chlorite IIa formed during the earliest stage of the ore-forming process, occur associated to intense and pervasive matrix alteration and is Fe-rich. Chlorite IIb is less enriched in Fe, and corresponds preferentially to vein-filling chlorite, where iron concentrates mostly in pyrite. Chlorites IIa present 0.72 <Fe/Fe+Mg < 0.88 ratios, whereas chlorites IIb has 0.56 <Fe/Fe+Mg < 0.71. The alkalis content of both generations of chlorite is extremely low, consistently with the strong alkalis acid leaching observed in the inner part of the feeder system.

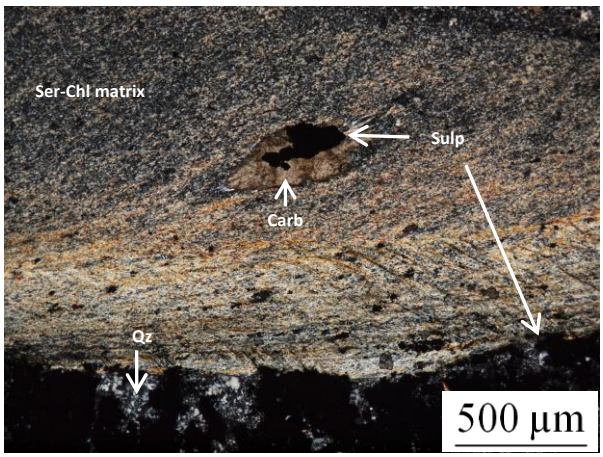

Fig. 2: Photomicrograph of a PQG sample affected by sericite-chlorite alteration and silicification associated to mineralized veins (Zone 2a). Chl- Chlorite; Ser – Sericite; Carb- Carbonates; Qz-Quartz; Sulf- Sulphides

Sericite is the dominant secondary mineral in the peripheral halos of the stockwork. Zones 2a and 2b are both dominated by sericite, but these can be distinguished on the basis of their composition: K-rich sericite in zone 2a and Na-rich sericite in zone 2b. K-sericite also occurs as a subordinate phyllosilicate in the chlorite-dominated alteration zone 1 (central stockwork). Na-sericite occurs in the distal parts of the mineralized system and is characterized by high paragonitic component, with Na/Na+K ratios ≈ 0.49.

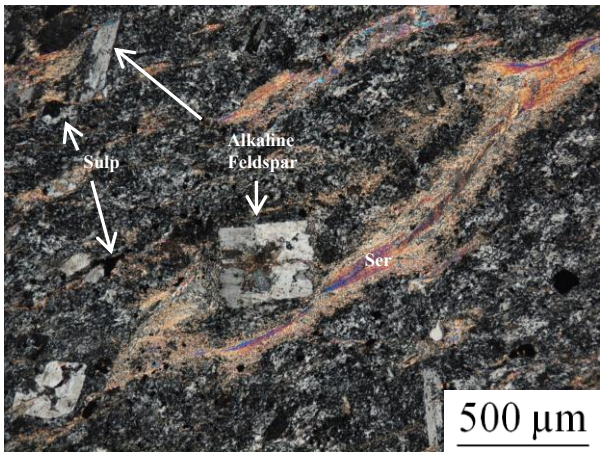

Fig. 3: Acid volcanic rock affected by sericitic alteration with original characteristics partially preserved; Ser-Sericite; Sulp- Sulphides

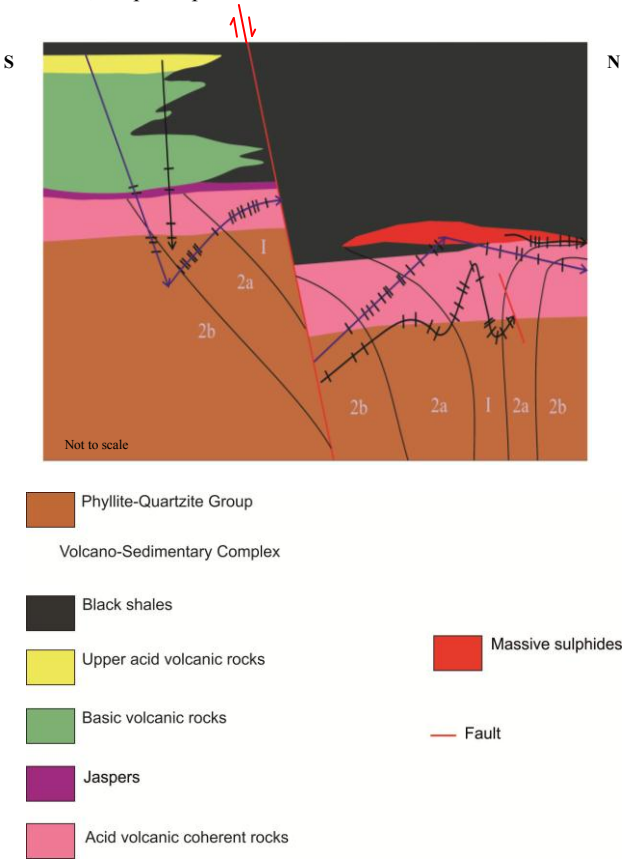

Fig 4: Schematic pre-deformational reconstruction of the massive sulfide-hosting succession at Lousal, and hydrothermal alteration zonation. Blue Line: borehole LS1; Black line: borehole LS02

The carbonates analyzed were siderite, ankerite and calcite. Siderite and ankerite are associated with mineralization, whereas calcite always occurs associated to tectono-metamorphism, being unrelated to mineralization.

Siderite generation occurred throughout the whole ore-forming process and may occur in all different alteration zones previously defined, from the core to the most distal parts of the mineralized system. Their composition evolved through time, with the later phases showing Ca-enrichment (ankerite, sideroplesite),

consistently with a decrease of temperature and an increase in the pH of the fluid during the waning stages of the ore-related hydrothermal activity.

5 Conclusions

Hydrothermal alteration patterns in the Lousal deposit are akin to typical IPB deposits. Nevertheless, the definition of its zonation is strongly obscured by structural complexity of the hosted sequence. We have defined three alteration zones that correspond to envelopes successively more distal relative to the axis of the mineralizing hydrothermal system. The hydrothermal assemblage in Zone 1 (core of the feeder system) consists of chlorite + quartz ± sericite + carbonates + sulphides. Zone 2a is peripheral to zone 1 and is characterized by K-sericite + chlorite + quartz ± carbonates + sulphides. The mineralogical assemblage in Zone 2b is composed by Na-sericite + quartz + carbonates + sulphides ± chlorite ± epidote. The recognition of this zonal pattern in alteration was used as a criterion to reconstruct the pre-tectonic geometric relationships among the massive ores and their hanging-wall and footwall host successions, ground on the interpretation of discontinuities in the alteration paths along the drill holes. This approach provides an additional mean to go through reconstruction of tectonically dismembered successions in the IPB, contributing to trace vectors towards mineralization in exploration campaigns in strongly deformed terrains.

Acknowledgements

This study is part of the MSc research program of the first author. Acknowlegdments are due to Fundação para a Ciência e Tecnologia, Portugal (FCT) for financial support through project ZHINC (PTDC/CTE-GIX/114208/2009; Jorge MRS Relvas, PI)

References

Barriga, F.J.A.S., 1983. Hydrothermal metamorphism and ore genesis at Aljustrel, Portugal, Tese de Doutoramento (não publicado), University of Western Ontario, 368 p.

Carvalho, D., Barriga, F.J.A.S., and Munhá, J., 1999. Bimodal-siliciclastic systems – the case of the Iberian Pyrite Belt, *in* Barrie, C.T. and Hannington, M.D., eds., Volcanic-associated massive Sulfide deposits: processes and examples in modern and ancient settings: Reviews in Economic Geology, v. 8, Society of Economic Geologists, Inc., p. 375-408.

Jorge, R.C.G.S.,2010. Caracterização petrográfica, geoquímica e isotópica dos reservatórios metalíferos crustais, dos processos de extracção de metais e dos fluidos hidrotermais envolvidos em sistemas mineralizantes híbridos na Faixa Piritosa Ibérica. Tese de Doutoramento (não publicado), Departamento de Geologia, Universidade de Lisboa, 272 p.

Leistel, J.M., Marcoux, E., Thiéblemond, D., Quesada, C., Sánchez, A., Almodóvar, G.R., Pascual, E., and Sáez, R., 1998. The volcanic-hosted massive sulphide deposits of the Iberian Pyrite Belt: Mineralium Deposita, v. 33, p. 2-30.

Matos, J.X., Oliveira, V. 2003. Mina do Lousal (Faixa Piritosa Ibérica) - Percurso geológico e mineiro pelas cortas e galerias da antiga mina. IGME, Pub. Museo Geominero, n°2, Espanha, pp. 117-128.

Matzke, K. 1971. Mina do Lousal. Principais Jazigos Minerais do Sul de Portugal, Livro-Guia n°4, pp. 25-32.

Munhá, J. 1990. Metamorphic evolution of the South Portuguese/Pulo do Lobo Zone, *in* Dallmeyer, R.D., and Martinez Garcia, eds., Pre-Mesozoic geology of Iberia: Berlin, Springer-Verlag, p.363-368.

Oliveira, J.T., 1983. The marine Carboniferous of South Portugal: a stratigraphic and sedimentological approach, *in* Lemos de Sousa, M.J. and Oliveira, J.T., eds., The Carboniferous of Portugal: Memórias dos Serviços Geológicos de Portugal, v. 29, p. 3-37.

Oliveira, J.T., 1990. South Portuguese Zone, *in* Dallmeyer, R.D., and Martinez Garcia, eds., Pre-Mesozoic geology of Iberia: Berlin, Springer-Verlag, p. 333-347.

Oliveira, J.T., Relvas, J.M.R.S., Pereira, Z., Matos, J.X., Rosa, C.J., Rosa, D., Munhá, J.M., Jorge, R.C.G.S., Pinto, A.M.M., 2006. O Complexo Vulcano-Sedimentar da Faixa Piritosa: estratigrafia, vulcanismo, mineralizações associadas e evolução tectono-estratigráfica no contexto da Zona Sul Portuguesa. in Dias R, Araújo A., Terrinha P, e Kulberg JC (eds.), Geologia de Portugal na Ibéria, VII Cong. Nac. Geologia, Univ. Évora, Portugal, pp. 207-244.

Pereira, Z., Matos, J.X., Fernandes, P.,Jorge, R., Oliveira, J.T., 2010. Qual a idade mais antiga da Faixa Piritosa? Nova idade Givetiano inferior para o Grupo Filito-Quartzítico (Anticlinal de S. Francisco da Serra, Faixa Piritosa). e-Terra: Revista Electrónica de Ciências da Terra, ISSN 1645-0388 ; Vol. 17, nº 13.

Relvas, J.M.R.S., 1991. Estudo Geológico e Metalogenético da Área de Gavião, Baixo Alentejo. Tese equivalente a mestrado apresentada no âmbito de Provas de Aptidão Pedagógica e Capacidade Científica (não publicado), Univ. Lisboa, 248 p

Relvas, JMRS, Pinto, AMM, Matos, JMX, 2012. Lousal, Portugal: a successful example of rehabilitation of a closed mine in the Iberian Pyrite Belt. Society for Geology Applied to Mineral Deposits; SGA News, 31: 6-16

Strauss, G.K., 1970. Sobre la geología de la provincia piritífera del Suroeste de la Península Ibérica y sus yacimientos, en especial sobre la mina de pirita de Lousal (Portugal): Memoria del Instituto Geologico y Minero de España, v. 77, p. 1-266.

The Jörn granitoid complex, Skellefte mining district, Sweden: petrography, lithogeochemistry and emplacement sequence

Manuel J. González-Roldán
CRN Consultores, Madrid, Spain

Rodney Allen
Luleå University of Technology and Boliden Mineral AB, Boliden, Sweden

Emilio Pascual, Teodosio Donaire, Manuel Toscano
Departamento de geología, Universidad de Huelva, Spain

Hans Åreback
Boliden Mineral AB, Boliden, Sweden

Abstract. On the basis of new field work and sampling, followed by petrographic and geochemical studies, we present a first interpretation of the sequence of deformation, alteration, metamorphism and magmatic emplacement for the different units constituting the Jörn Granitoid Complex, Skellefte Mining district, Sweden. Our data show that only the oldest rocks, named GI group, are significantly deformed. There rocks show, in addition, significant hydrothermal alteration and a superimposed metamorphism. In contrast the younger granitoids, named GII to GIV, are essentially unaltered and undeformed. There are significant differences between the GI and the rest of the Jörn rock groups, including contrasts in major, trace and REE elements. It is concluded that a major event separated the early intrusion of GI from that of the rest of the intrusive rocks in the area. Relative chronology of emplacement of the different units of the Jörn Complex is proposed, also including sequence of deformation, hydrothermal alteration and metamorphism.

Keywords. Jörn Granitoids, hydrothermal alteration, lithogeochemistry, Skellefte mining district, Sweden.

1 Introduction

The Skellefte Mining district is located in a Palaeo-Proterozoic domain in the Central Svecofenian Province, northern Sweden. It contains important volcanogenic massive sulphides, which were probably formed during a extensional stage within a volcanic arc, dated between 1900 and 1985 Ma (Weihed et al., 2005).

Volcanic-hosted deposits in the Skellefte Mining district have been mined since 1924. They include among others those of Boliden, Maurliden, Renström and Kristineberg, these latter still in operation.

Apart from the volcanic rocks that host the above deposits, plutonic rocks are an integral part of the long-lived igneous activity in the area. These intrusions outcrop mainly in the central and western parts of the Skellefte district and have been subdivided into syn-volcanic, dated from 1.90 to 1.87 Ga, and post-volcanic, generated after the Skellefte district volcanic activity (Allen et al., 1996).

These plutonic rocks are relevant to the genesis of ore deposits in the Skellefte area in two ways. First, they constitute a potential heat source during the stages of hydrothermal activity related to the generation of the VHMS deposits. In addition, they are related to other types of mineral deposits of economic interest, including gold mineralization like that of Algtrask, located at the southern margin of the Jorn Granitoid Complex, or porphyry copper deposits such as Tallberg, situated only 3 km west of Algtrask and hosted by propylitic and phyllic altered tonalite of the Jörn complex.

Here, we present a preliminary interpretation of a detailed survey focused on the Jörn complex, the largest of the plutonic complexes in the Skellefte area (Fig. 1). It includes the relative chronology of emplacement of the different units within the plutonic complex, as well as the sequence of deformation, hydrothermal alteration, and metamorphism. In order to suggest a tentative, more general geological interpretation, a part of the lithogeochemical data is also presented.

2 Geological setting of the Skellefte Mining District

2.1 General

Palaeo-proterozoic rocks in the Skellefte mining district mainly consist of volcanic rocks formed within an island-arc and subordinate calc-alkaline intrusions (Weihed and Eilu, 2005).

The footwall of the regional sequence comprises shallow-submarine felsic volcanic rocks of the Skellefte Group, which are overlain by sediments and lavas of the Vargfors Group. Most of the VHMS deposits are hosted by the Skellefte Group, but some of them also occur in the lower part of the Vargfors Group.

Important volumes of intrusions occur in the center of the Skellefte district, intruding both the Skellefte and the Vargfors Groups.

2.2 The Jörn Granitoid Complex (JGC)

The JGC is the largest and most important cluster of intrusions in the Skellefte mining district, contacting with rocks belonging to both the Skellefte and Vargfors Groups. The contacts with country rocks are tectonic in most cases, so that field evidence for the relative sequence of emplacement is inconclusive. Plutonic rocks in the JGC range from gabbro to granite (Fig 1).

Four main rock groups have been distinguished in the JGC, named GI to GIV (Wilson et al., 1987). GI is formed by porphyritic medium- to coarse-grained tonalites and minor trondhjemites. Rocks show moderate to intense hydrothermal alteration. Amphibole and biotite group minerals are common but usually altered to secondary minerals. Plagioclase is the most abundant feldspar, whereas alkali-feldspar is commonly related to superimposed hydrothermal alteration.

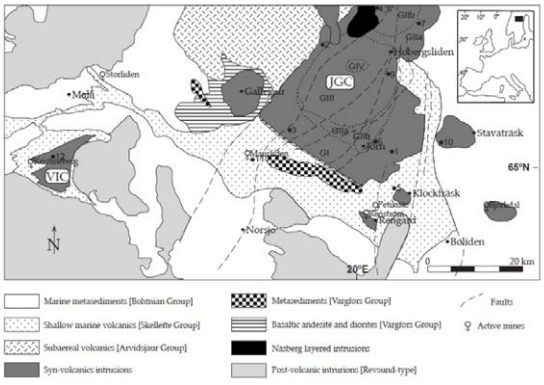

Figure 1. Regional geological map of the Skellefte mining district. Possible boundaries of the JGC phases are marked by dashed lines. Modified from Allen et al. (1996).

GII rocks can be subdivided in two subgroups: the granodiorites (GIIa) and quartz-monzodiorites (GIIb), the later containing microgranular enclaves. The main minerals are plagioclase, quartz, biotite and hornblende, along with poikilitic alkali feldspar. Some clinopyroxenes occur in the core of amphibole phenocrysts.

GIII rocks are dominant in central zones of the JGC. They are mainly coarse-grained, quartz-porphyritic monzogranites. They do not contain amphibole and the biotite content is lower than 5%.

GIV occurs within GIII as a small pluton composed by medium- to fine-grained, equigranular granodiorites.

A number of small, diorite and gabbro bodies occur within the JGC in particular at its border areas. They are commonly found at the border zones of GI and GII They are not found in the GIII and GIV facies.

Most of geochronological data previously obtained in the JGC indicates that the Skellefte Group is coeval with the GI intrusives. whereas the Vargfors and Arvidsjaur Groups show ages similar to those of the GII and GIII rocks. GI has been dated at 1885 Ma, and the GII-GIII are 10 Ma younger (Kathol and Persson, 1997; Wilson et al., 1987).

3 Sequence of emplacement of the JGC: petrographic evidence

Although field evidence is scarce, the petrography contributes to reveal a significant time gap between the GI, constituting the largest plutonic unit in the JGC, and the rest of the complex. In fact, deformation, hydrothermal alteration and metamorphism are restricted to the GI group, which suggests a significant time span between its emplacement and that of GII to GIV.

Deformation in the GI, difficult to appreciate at a mesoscopic scale, is ubiquitous at a thin-section scale. In general, the rocks are affected by a brittle-ductile deformation, reflected in the bending of the biotite crystals, as well as in orientation of the mica crystals within a groundmass of quartz subgrains. In places, deformation is concentrated in bands with intense deformation of quartz and plagioclase. Deformation is more intense in areas close to the southern contact with the volcanic rocks of the Skellefte Group, although at some places at the NW of the intrusion complex, GI also shows intense deformation.

Hydrothermal alteration involved a number of overlapping chemical processes, including albitization, epidotization/saussuritization and chloritization. It is more conspicuous at the southern margin of the GI unit, as well as in the "satellite intrusions" of GI-type within the Skellefte Group. The alteration is characterized by a pervasive replacement of the mafic minerals, biotite and hornblende to chlorite and Fe-actinolite, respectively. Calcium from plagioclases has been remobilized during the hydrothermal alteration, inducing the formation of epidote. In addition, most of the GI rocks have systematically high values of SiO_2 due to silicification.

In most instances, there is a direct relationship between the degree of deformation and alteration. Nevertheless, petrographic evidence indicates that the deformation essentially postdates the hydrothermal alteration.

According to the textural evidence, metamorphism affecting the GI clearly postdates both hydrothermal alteration and deformation. This is shown by biotite overgrowth of deformed chlorite, formed by hydrothermal alteration of igneous biotite. In other instances, decussate crystals of metamorphic biotite form pseudomorphs after igneous amphibole (Fig. 2). In places, metamorphic amphibole and quartz have also been observed.

EPMA study provides additional evidence for a metamorphic origin of biotite crystals, like those shown in figure 2, as their chemical composition is markedly different from that of igneous biotite from any of the rocks of the JGC (Fig. 3) and plots within the field of secondary biotite.

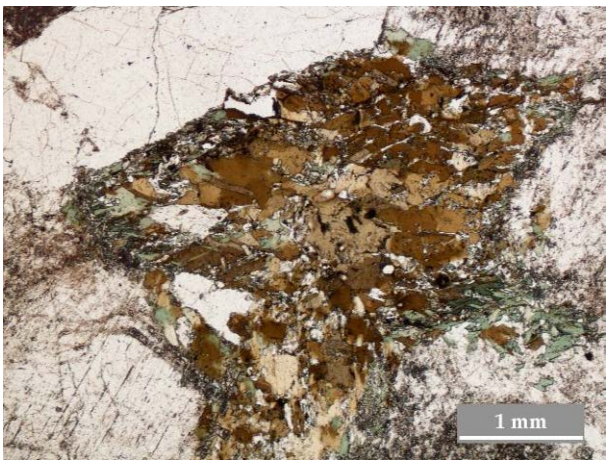

Figure 2. Growth of undeformed metamorphic biotite over an altered amphibole crystal. Note the orientation of biotite crystals along the amphibole cleavage plains.

This metamorphic stage of the GI rocks in the JGC is static, and has been interpreted as regional contact metamorphism (Spear, 1995). It develops only at its southern areas, whereas the northern part of the GI is not affected by metamorphism.

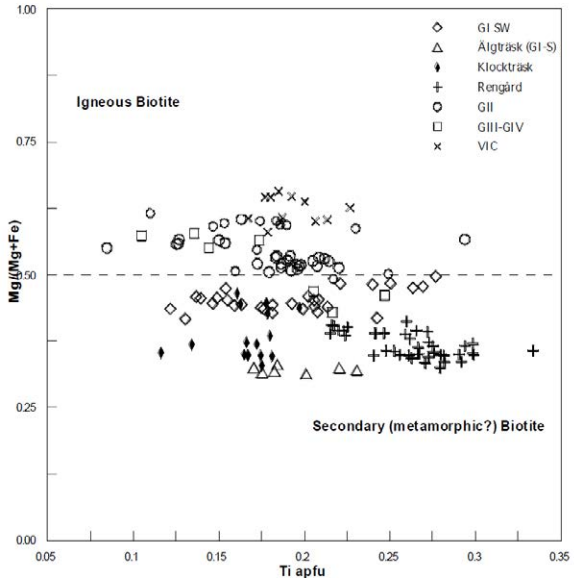

Figure 3. Contrasting composition of metamorphic biotite from GI and GII-GIV igneous biotite.

In contrast with the above description, the JGC rocks belonging to the groups GII to GIV show no deformation, hydrothermal alteration or metamorphism - a difference consistent with a younger age for these latter rocks.

4 Lithogeochemistry

Differences between GI and other facies of the JGC are apparent in terms of major and trace elements. For instance, the Al_2O_3 content in GI is lower than that in other Jörn facies at any SiO_2 percent considered. An opposite trend is shown by Fe_2O_3.

A number of chemical data of other regional igneous rocks have also been plotted in the diagrams for comparison. It is apparent that a sample from the Rengård pluton is systematically linked to those of the GI, whereas samples of the GIIa and GIIb, GIII, GIV and Stavaträsk are grouped together (Fig. 4).

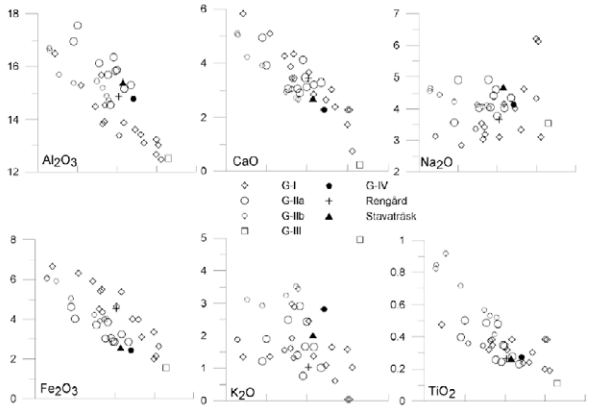

Figure 4. Chemical variation diagrams for JGC rocks and other regional plutonic rocks.

Most of the studied rocks plot within the calcalkaline field in the K_2O *vs.* SiO_2 diagram (Roberts and Clemens, 1993). In it, GI, GIIa and basic rocks related to GI show a calcalkaline trend, whereas several GI rocks are in the tholeiitic field. We interpret, however, that this is due to potassium loss during alteration processes, which exclusively affect the GI rocks.

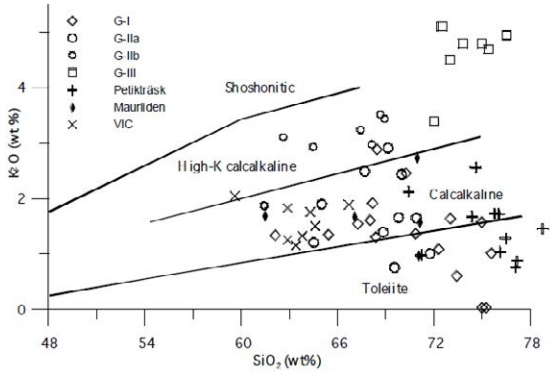

Figure 5. K2O vs. SiO2 diagram for JGC and regional related rocks.

Nevertheless, a number of geochemical features that distinguish the GI rocks from the rest of the JGC cannot be related to differential alteration. In particular, rock classification on the basis of immobile elements (e.g., Harris et al., 1986) indicates that some of these differences are best attributed to the chemical character of the magmatism, hence to the source areas of the magmas. Differences in REE diagrams corresponding to GI and GII to GIV facies are attributed to contrasts in the magma source.

We tentatively suggest that GI could be either calcalkaline or transitional from tholeiitic to calcalkaline, whereas GIIb, GIII and GIV are properly

located in the high-K2O calcalkaline field.

5 Conclusions

The Jörn Granitoid Complex has been separated into two main groups of facies: GI, GI type satellite intrusions and the related volcanic rocks compose the first group. The second group is made up by GII, GIII and GIV. The differences between those groups comprise mineralogy, textures, alteration, metamorphism and geochemical features. In fact, those geochemical differences suggest changes in the character of magmatism.

The fact that deformation, hydrothermal alteration and metamorphism are all exclusive features of GI suggest that the timing of those events is between the emplacement of GI (1888 Ma) and that of GII (1874 Ma). However, uncertainties in available age determinations do not allow us to propose an exact sequence of events.

Among the different models that can be proposed to explain these events, it could be considered that the hydrothermal alteration and late regional contact metamorphism in the Skellefte district affecting GI could be related to thermal anomalies linked, direct or indirectly, to the generation and/or emplacement of later high-K2O calcalkaline rocks represented by the GII to GIV granitoids.

Lithochemical data also suggest a variation of the chemical character of the magmatism; again, it tends to separate the samples of GI from the later JGC facies. It is important to note that GIIa is similar to GI in K2O/SiO2 but in terms of immobile elements it is grouped together with GIIb, GIII and GIV.

Acknowledgements

The authors are grateful to Boliden Mineral AB for their assistance during their work in the Skellefte area. In particular, we acknowledge the help of Sven-Åke Svenson. Helpful suggestions by Pär Weihed at LTU are also acknowledged with thanks.

References

Allen RL, Weihed P, Svenson S-A (1996) Setting of Zn-Cu-Au-Ag massive sulfide deposits in the evolution and facies architecture of a1.9 Ga marine volcanic arc, Skellefte District, Sweden. Econ Geol 91(6): 1022–1053

Harris NBW et al. (1986) Geochemical characteristics of collision zone magmatism. In: MP coward and AC Reis (Eds.) Collision tectonics Spec Publ Geol Soc, 69-81

Kathol B, Persson PO (1997) U-Pb zircon dating of the Antak granite, northeastern Västerbotten county, Sweden In: T Lundqvist (Ed.) Res Paper C830 Sveriges Geologiska Undersökning: 6-13

Roberts, MP Clemens, JD (1993). Origin of high-potassium, calc-alkaline, I-type granitoids. Geology 21(9): 825-828.

Spear FS (1995) Metamorphic phase equilibria and pressure-temperature-time paths. Mineralogical Society of America, Washington, 799 pp.

Weihed P, Eilu P (2005) Fennoscandian shield-proterozoic VMS deposits Ore Geology reviews 27(1-4): 324-325

Wilson MR et al. (1987) Jörn: an early Proterozoic intrusive complex in a volcanic-arc environment, north Sweden. Prec Research 36(3-4): 201-225

Hydrothermal imprint along the southern Central Indian ridge

K. U. Heeschen, U. Schwarz-Schampera , C. Bartsch, H. Franke, and F. Henjes-Kunst,
Federal Institute for Geosciences and Natural Resources (BGR), Hannover, Germany (Katja.heeschen@bgr.de)

J. Hansen
RWTH Aachen University, Aachen, Germany

Abstract. The southern segments of the Central Indian Ridge (S-CIR) were revisited during cruise INDEX 2011. The major emphases were to examine the bathymetry, structural geology, magnetic signatures, and the crustal development of the area as well as the petrogenesis and indicators for hydrothermal activity.

This presentation focuses on the results from mineralogical and chemical analysis of rocks and sulphides collected along the S-CIR. The rock suite predominantly consisted of normal mid ocean ridge basalts (N-MORB) with occasionally occurrence of gabbros and volcanic breccia. Enriched MORBs are rare. They have different isotopic and trace element ratios. Indications for low as well as high temperature alteration are found at several sites in the working area.

The Cu-Fe-Zn sulphide samples recovered from hydrothermal vent sites show a number of different zonal and textural attributes accompanied with large variations in major and trace element concentrations such as Zn, Co and Se.

Central Indian Ridge, hydrothermal processes, mid ocean ridge basalts, sulphide deposits

1 Introduction

The Central Indian Ridge (CIR) marks the spreading of the African and Australian plates between the Carlsberg Ridge to the North and the Rodriguez Triple Junction (RTJ) to the South. In the area of interest (21 – 25°40'S) the CIR is considered an intermediate spreading centre (Briais, 1995). The bathymetry is typically characterized by features common for slow to intermediate spreading centres including a strong segmentation of a deep central rift valley (Briais, 1995). A shallowing of the central rift valley to the north is possibly caused by a thickening of the crust that was assigned to the nearby occurrence of the Reunion Plume at roughly 19°S (Briais, 1995). This long-lived hot spot is presently forming Réunion Island (Mahoney et al., 2002 and literature therein). The geochemical imprint of this plume on the nearby mid ocean ridge through plume-ridge interactions has been a subject of several studies (e.g. Murton et al., 2005; Nauret et al., 2006).

Next to local geochemical anomalies, the DUPAL anomaly is a common feature along the CIR. It is mainly characterized by anomalous Sr, Nd and Pb isotope ratios (Hart,1994). The explanations for this large scale mantle alteration along the Indian Ocean Ridge systems include involvements of one or several of the following structures: a major mantle plume related to the breakup of Gondwana, subducted continental lithosphere and/or oceanic crust and sediments (e.g. Mahoney et al., 1992; Rekämper and Hofmann, 1997; Escrig et al., 2005; Meyzen et al., 2005, Frey et al., 2011). An impregnation of the mantle source does alter the compositions of the newly formed ocean crust and alters the isotopic signature, which often is very distinct in basalts from the Indian Basin (e.g. Hart, 1984, Rekämper and Hofmann, 1997; Meyzen et al., 2005). The authors further describe the repeated occurrences of E-MORBs with enrichments in incompatible elements compared to normal MORB.

Hydrothermal activity is a common feature along the Atlantic and Pacific Ridge systems. An increasing number of indications and actual findings of hydrothermal vent systems are being published for the the slow to intermediate spreading ridge systems of the Indian Ocean after the first large-scale expeditions in the 1980's by German research teams (e.g. Gamo et al., 2001; Gallant and Von Damm, 2006, Kuwagucci et al., 2008).

This paper presents the first geochemical and mineralogical results gained in the course of the German INDEX project. The INDEX 2011 cruise was scheduled for the reconnaissance of marine sulphide deposits along the southern Central Indian Ridge. Next to petrological and vulcanological investigations of rocks and sulphides, the campaign comprised bathymetrical, magnetic and hydrochemical studies of the areas.

2 Campaign "INDEX"

2.1 Geological Setting

The S-CIR is an intermediate to slow spreading rift system with a highly variable regional to small-scale structural pattern of seafloor spreading (Parson, 1993). The axial valley is 5 – 35 km wide and 500-1800 m deep hosting a large number of neovolcanic ridges and single cone shaped volcanoes, which are the focus of present day volcanism in the central valley or at its flanks (Fig. 1). The outline of the rift valley is usually asymmetrical with steeper slopes on the eastern part. Common structural features within the rift valley include overlapping and bending as well as updoming (Fig. 1). Spreading velocities derived from bathymetric and magnetic studies average at about 46mm/a.

2.2 Samples

Samples for the presented study originate from the cruise INDEX 2011. Sampling stations were located using multibeam bathymetry (dredge samples) and video observations (video sledge, TV-grab). Whereas the dredge allowed for the collection of a very wide variety of mafic (basalt and gabbro) to ultramafic rocks (dunite,

harzburgite), the video-guided TV-grab successfully recovered a suite of different massive sulfides. In total, five different ridge sections were targeted.

The rocks were grouped and samples were prepared for polished thin sections and a geochemical analysis of major and trace elements on bulk rock samples and individual mineral grains. Beside bulk rock samples, fresh volcanic glass was separated where present and handpicked under the binocular for geochemical and isotopic analysis.

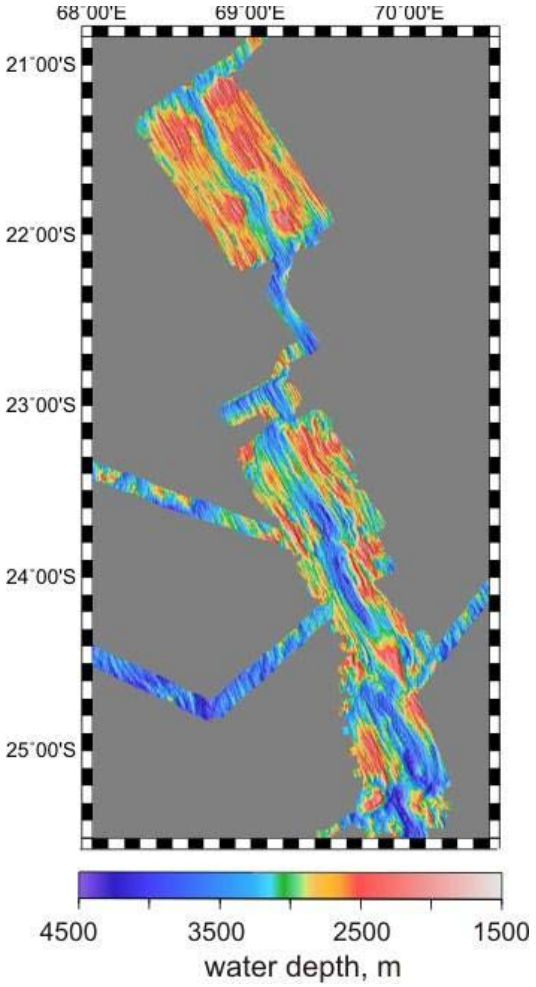

Figure 1. High resolution bathymetric map of the southern CIR from data collected during the field campaign INDEX2011.

The dm-sized sulfide samples (Fig. 2) were cut into slabs and the central slice was used for further analysis. In total 60 drill cores from the various mineralogical zones were chosen for thick sections, polished thin sections and corresponding geochemical bulk analysis.

2.3 Analytical Methods

The samples were mineralogically charcterized by microscopic and microanalytical methods. The chemical analysis included X-ray diffraction (XRF, BGR), inductively coupled plasma mass spectrometry (FUSION-ICP-MS; Actlabs), atomic absorption spectroscopy (AAS; Actlabs), and Instrumental Neutron Activation Analysis (INAA, Actlabs). The detection limit varies depending on method and concentration of the elements but was commonly within a 10% error range. The analyses were carried out on fresh samples choosen from the center of rock fragments. Using these samples the effect of chemial alteration due to submarine weathering could be minimized. The analyses focused on the differences in magma composition and indications for hydrothermal alteration. Strontium, Nd, and Pb isotope ratio were analysed on fresh volcanic glass samples in BGR laboratories using a THERMO Triton-TIMS. The analytical procedure is based on the method described by Hörnle et al. (2011).

Microanalytical analyses of single minerals on rocks and sulfides were carried out using an electron microprobe (EMP) equipped with an energy dispersive X-ray spectroscopy (EDS). Volcanic glass and sulfide samples were further analysed using Laser Ablation ICP-MS.

3 Results and Discussion

3.1 Basalt mineralogy and chemistry

The majority of rocks collected along the S-CIR during the INDEX2011 campain are pillow or less common sheet flow basalts with an aphyric to highly phyric texture. Plagioclase is the most prominent phenocryst, followed by highly variable amounts of olivine and minor clinopyroxene, often found in glomerocrysts with plagioclase. Chromium-rich spinel is present in most thin sections. Fresh volcanic glass is a common feature. On occasion, diabase and gabbros are present and locally, volcanic breccia occur as part of the rock suit.

Apart from one sampling area, the fresh MORB samples from the central and lateral rift valley of the S-CIR classify as tholeiitic basalts. On average, the Mg numbers are high (60–67), representing a rather primitive, weakly fractionated magma. There is a weak trend towards lower numbers from north to south. Due to the small fractionation, the trends of major elements with Mg# are vague. However, they indicate two major correlation patters to be present. Trace element composition, resemble the N-MORB pattern as given in Sun & McDonough (1989) with deviations towards enriched signatures and a high variability in LILE (large-ion lithophile elements) and LREE (light rare-earth elements) concentrations that exist independently of any systematic geographical trend as described further north (Murton et al., 2005; Nauret et al., 2006). Rocks from one site classify as E-MORB. Next to the enrichments in LREE, they also stand out in terms of isotopic and HREE ratios indicating a different parental magma. Whereas the DUPAL anomaly is apparent in the isotopic ratios, a local influence of the Reunion mantle plume is not.

The concentrations of transition metals commonly are in agreement with average N-MORB values (Sun & McDonough, 1989). Some exceptions can be seen in Cu and Zn, which are partly correlated with the occurrences of known hydrothermal vent sites.

3.1 Basalt alteration

While nearly all samples show different degrees of submarine weathering, alteration caused by hydrothermal fluids are restricted to a few sites which are spread across the working area. Chemically, the imprint is clearest in K and Rb enrichments, which can be ascribed to low-temperature hydrothermal alteration (< 150°C; Seyfried and Bischoff, 1979). Mineralogical studies indicate alteration to occur mainly along fractures, cleavages or interstices of the rocks. In some cases, the observed mineralogical assemblages belong to metamorphic facies up to the greenschist facies and thus indicate alteration that occur at higher temperatures.

3.2 Hydrothermal sulphide deposits

Hydrothermal vent sites are known to occur along the S-CIR from video and hydrochemical observations (e.g. Gamo et al., 2001; Gallant and Von Damm, 2006, Kuwagucci et al., 2008). Hydrothermal vents are known to be surface expressions of actively forming sulphide deposits (VMS deposits) which are currently under debate in terms of their possible size, use and metal content (e.g. Hannington et al., 2011).

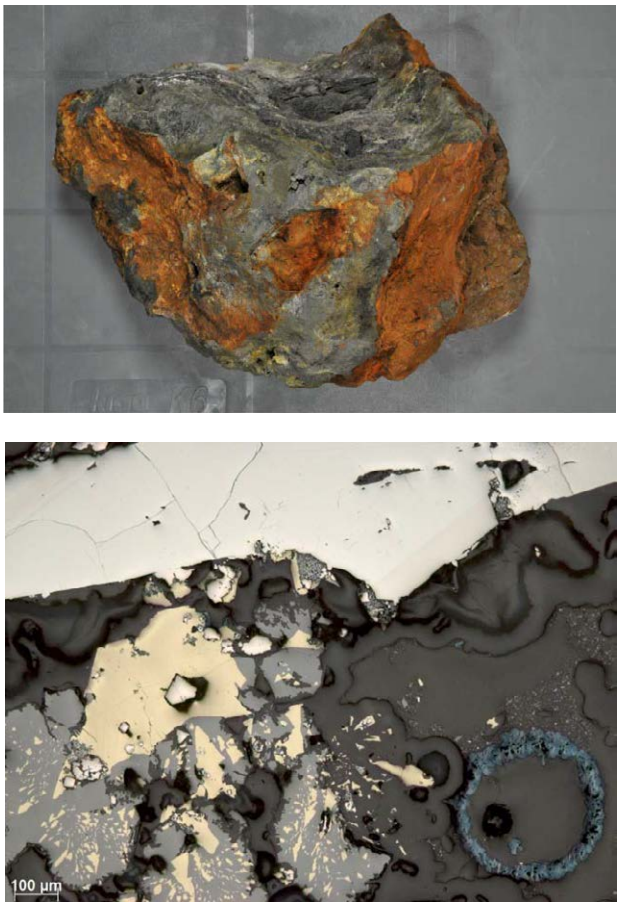

Figure 2. Photo of a recovered a strongly silicified chimney talus recovered during INDEX2011, 60 cm in length (upper panel) and a microscopic image of a chalcopyrite–pyrite–sphalerite–marcasite assemblage as found in this sulphide sample (lower panel).

The ISA database mainly lists chalcopyrite and pyrite massive sulphides to occur on the S-CIR (http://iron.isa.org.jm/images/vents-sulphides/indian_Ocean.htm; cited Feb 2013), which is in good agreement with our findings. The dominant mineral paragenesis to occur in the ore samples is chalcopyrite – pyrite – sphalerite – marcasite (Fig.2) on occasions with minor galena. Microscopic studies show a complex pattern of mineral replacements and varying depositional conditions. The iron content of ZnS is often low. Secondary Cu-minerals are common and on occasions contain significant amounts of Ag.

Significant volumetric variations of the different minerals within and between the sites occur and result in a large range of concentrations of major (Cu, Zn, Fe) and trace metals. This is particularly true for Zn and thus for Co, Cd, Ga that substitute for Zn in ZnS as can be seen in bulk rock chemistry and microscopic analysis of single grains. Element correlations vary for the different sulphide sample, including e.g. the correlation of Se with major elements or the Cu-Fe correlation that occurs in the chalcopyrite-rich samples.

4 Outlook

The INDEX 2011 expedition of BGR with R/V SONNE was the first of a number of planned research cruises along the S-CIR and the East Indian Ridge. The upcoming cruises aim at the understanding of ridge formation, the emplacement of complex structural features, the petrogenesis and the imprint on hydrothermal and biological activity close to active and inactive vent sites and fields.

Acknowledgements

Our special thanks go to the master and crew of RV SONNE and the onboard party, M. Bockrath, E. Gäbler, B. Harazim, D. Henry, A. Hofmann, F. Korte und P. Rendschmidt.

References

Briais A (1995) Structural analysis of the segmentation of the Central Indian Ridge between 20°S and 25°30′S (Rodriguez Triple Junction). Marine Geophysical Research 17: 431-467.

Escrig S, Capmas F, Dupre B, Allegre CJ (2004) Osmium isotopic constraints on the nature of the DUPAL anomaly from Indian mid-ocean-ridge basalts. Nature 431: 59-63.

Frey FA, Pringle M, Meleney P, Huang S, Piotrowski A (2011) Diverse mantle sources for Ninetyeast Ridge magmatism: Geochemical constraints from basaltic glasses. Earth and Planetary Science Letters 303: 215-224.

Gallant RM and Von Damm K L (2006). Geochemical controls on hydrothermal fluids from the Kairei and Edmond Vent Fields, 23° - 25° S, Central Indian Ridge. Geochem Geophy Geosyst, 2006, 7, doi: 10.1029/2005GC001067.

Gamo T, Chiba H, Yamanaka T, Okudaira T, Hashimoto J, Tsuchida S, Ishibashi J-i, Kataoka S, Tsunogai U, Okamura K, Sano Y, Shinjo R (2001) Chemical characteristics of newly discovered black smoker fluids and associated hydrothermal plumes at the Rodriguez Triple Junction, Central Indian Ridge. Earth and Planetary Science Letters 193: 371-379.

Hannington M, Jamieson J, Monecke T, Petersen S, Beaulieu S (2011) The abundance of seafloor massive sulfide deposits. Geology 39: 1155-1158.

Hart SR (1984) A large-scale isotope anomaly in the Southern Hemisphere mantle. Nature 309: 753-757.

Hoernle K, Hauff F, Werner R, van den Bogaard P, Gibbons AD, Conrad S, Muller RD (2011) Origin of Indian Ocean Seamount Province by shallow recycling of continental lithosphere. Nature Geosci 4: 883-887.

Kawagucci S, Okamura K, Kiyota K, Tsunogai U, Sano Y, Tamaki K, Gamo T (2008) Methane, manganese, and helium-3 in newly discovered hydrothermal plumes over the Central Indian Ridge, 18° - 20°S. Geochem. Geophys. Geosyst. 9: Q10002.

Mahoney JJ, Graham DW, Christie DM, Johnson KTM, Hall LS, Vonderhaar DL (2002) Between a Hotspot and a Cold Spot: Isotopic Variation in the Southeast Indian Ridge Asthenosphere, 86°-118°E. Journal of Petrology 43: 1155-1176.

Mahoney J, le Roex AP, Peng Z, Fisher RL, Natland JH (1992) Southwestern Limits of Indian Ocean Ridge Mantle and the Origin of Low 206Pb/204Pb Mid-Ocean Ridge Basalt: Isotope systematics of the Central Southwest Indian Ridge (17° - 50°E). J. Geophys. Res. 97: 19771-19790.

Meyzen CM, Ludden JN, Humler E, Luais B, Toplis MJ, Mével C, Storey M (2005) New insights into the origin and distribution of the DUPAL isotope anomaly in the Indian Ocean mantle from MORB of the Southwest Indian Ridge. Geochem. Geophys. Geosyst. 6: Q11K11.

Murton BJ, Tindle AG, Milton JA, Sauter D (2005) Heterogeneity in southern Central Indian Ridge MORB: Implications for ridge-hot spot interaction. Geochem. Geophys. Geosyst. 6: Q03E20.

Nauret F, Abouchami W, Galer SJG, Hofmann AW, Hémond C, Chauvel C, Dyment J (2006) Correlated trace element-Pb isotope enrichments in Indian MORB along 18-20°S, Central Indian Ridge. Earth and Planetary Science Letters 245: 137-152.

Parson LM, Patriat P, Searle RC, Briais AR (1993) Segmentation of the Central Indian Ridge between 12°12'S and the Indian Ocean Triple Junction. Marine Geophysical Research 15: 265-282.

Rehkämper M, Hofmann AW (1997) Recycled ocean crust and sediment in Indian Ocean MORB. Earth and Planetary Science Letters 147: 93-106.

Seyfried Jr WE, Bischoff JL (1979) Low temperature basalt alteration by sea water: an experimental study at 70°C and 150°C. Geochimica et Cosmochimica Acta 43: 1937-1947.

Sun SS, McDonough WF (1989) Chemical and isotopic systematic of oceanic basalts: implications for mantel composition and processes In: Saunders AD, Norry MJ (eds) Magmatism in the Ocean Basins. Blackwell Scientific Publication, London, pp 313-345.

Petrochemistry and element mobility within the upper Tyrone arc, Northern Ireland: identifying VMS-prospective stratigraphic horizons

Steven Hollis
CSIRO Earth Science and Resource Engineering, Kensington, Western Australia, 6151, Australia (steven.hollis@csiro.au)

Stephen Roberts
Ocean and Earth Science, National Oceanography Centre Southampton, University of Southampton, SO14 3ZH, UK

Richard Herrington
Department of Mineralogy, Natural History Museum, London, SW7 5BD, UK

Garth Earls
16 Mill Road, Ballygowan, Newtownards, Co. Down, Northern Ireland, BT23 6NG, UK

Mark Cooper
Geological Survey of Northern Ireland, Colby House, Stranmillis Court, Malone Lower, Belfast, BT9 5BJ, UK

Abstract. In stark contrast to the VMS rich Appalachian sector of the Grampian-Taconic orogeny, VMS deposits at first glance appear absent in the peri-Laurentian British and Irish Caledonides. The Tyrone Igneous Complex of Northern Ireland represents a ca. 484-464 Ma arc-ophiolite complex and an along strike continuation of the VMS-rich Buchans-Roberts arc system of Newfoundland. Through a combination of extensive field mapping and petrochemical analysis, stratigraphic horizons have been identified which are prospective for VMS mineralization. Each is closely associated with extensive rift related magmatism, hydrothermal alteration, synvolcanogenic faults and high-level subvolcanic intrusions. Locally intense hydrothermal alteration, characterized by Na-depletion, high Ba/Sr, Bi, Sb, CCPI, AI, etc., and variable MgO and CaO, has allowed specific target areas to be identified coincident with Pb-Zn-Cu-Ag-Au mineralization. Rift related mafic lavas occur in the hangingwall sequences of mineralization, closely associated with ironstones and/or argillaceous sedimentary rocks. In the ca. 473-469 Ma upper Tyrone arc, rift-related magmatism is dominated by OIB-like and alkali basalt overlying mineralized FII or A-type and high-Zr rhyolites. Targeted prospecting of petrochemically favourable horizons in 2011 led to the discovery of Zn-Pb-Cu-Ag-Au mineralization.

Caledonian-Appalachian, VMS, Laurentia

1 Introduction

Despite being a desirable deposit type, ancient VMS deposits remain challenging exploration targets due to their relatively small sizes, often deformed natures, and associated large-scale alteration systems. Many camps have specific stratigraphic marker horizons which are actively targeted for further mineralization along strike or down-dip, such as 'mine rhyolites' (e.g. Flin Flon), or sulphidic, waterlain tuffs, and/or chemical sedimentary units (e.g. Bathurst). Identifying fertile stratigraphic horizons, and target areas along these, remains the most effective strategy for resource-constrained greenfield exploration.

The ca. 484-464 Ma Tyrone Igneous Complex of Northern Ireland (Fig. 1a) represents a peri-Laurentian arc-ophiolite sequence accreted to the composite Laurentian margin during the Middle Ordovician (Cooper et al. 2011; Hollis et al. 2012). Close temporal, geochemical and lithological similarities with the Buchans-Robert's Arm arc system (Hollis et al. 2012) suggest the Tyrone Igneous Complex may host VMS mineralization. The Buchans-Robert's Arm arc sequence hosts the high-grade Kuroko-type Buchans deposits (16.2 Mt at 14.51% Zn, 7.56% Pb, 1.33% Cu, 126 g/t Ag and 1.37 g/t Au), as well as lesser Cyprus-type and Noranda-type mineralization (van Staal 2007). Recent advances in our understanding of how VMS deposits form and their common petrochemical associations provide an opportunity to re-examine VMS prospectivity in the complex.

2 VMS deposits in the Caledonian-Appalachian orogen

The Dunnage zone of Newfoundland, Canada, represents a tectonic collage of oceanic and ensialic arc-related terranes which formed in the Iapetus Ocean. VMS-bearing tracts of peri-Laurentian affinity (=Notre Dame subzone) are separated from those of peri-Gondwanan affinity (=Exploits subzone) by the Red Indian Line (Fig. 1b). VMS deposits are abundant in the Dunnage zone, with over 40 deposits greater than 0.1 Mt massive sulfide for an aggregate total resource of approximately 112 Mt (geological resource), and production and reserves of ~46 Mt (Piercey 2007a). In New Brunswick, Canada, 14 VMS deposits have been recognized, including the supergiant Bathurst No. 12 deposit (229.8 Mt at 7.66% Zn, 3.01% Pb, 0.46% Cu, 91 g/t Ag and 0.46 g/t Au; van Staal 2007). In South Quebéc, ~11 VMS deposits have been recognized (van Staal 2007).

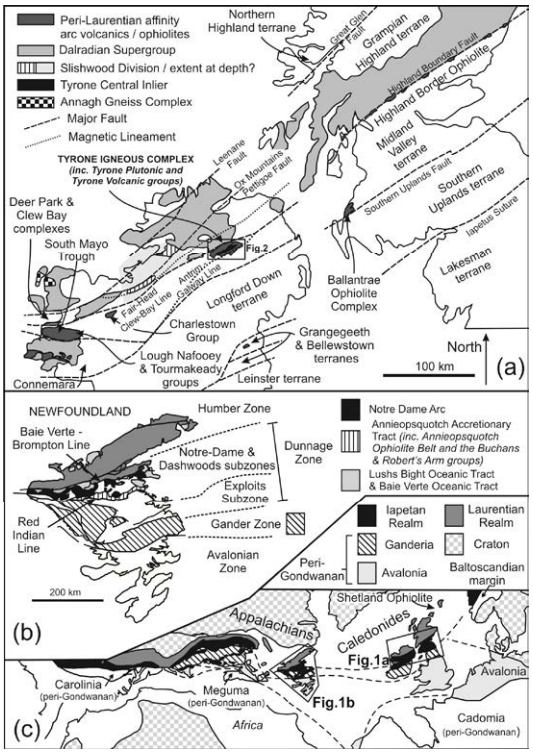

Figure 1. Fig. 1 (a) Geology of British and Irish Caledonides showing major fault lines and the position of accreted arc-ophiolite complexes. (b) Geology of Newfoundland showing the position of the Buchans-Robert's Arm arc (which hosts the Buchans VMS deposits). (c) Early Mesozoic restoration of North Atlantic region and Appalachian-Caledonian orogen (modified after Hollis et al. 2012).

The scarcity of both peri-Gondwanan and peri-Laurentian affinity VMS deposits in the British and Irish Caledondies is striking. Discovered peri-Gondwanan VMS deposits to the south of the Iapetus Suture (Fig. 1a: equivalent to the Red Indian Line) include:

- Parys Mountain, Wales (resource of 7.76 Mt at 4.86% Zn, 2.38% Pb, 1.99% Cu, 39.26 g/t Ag and 0.33 g/t Au: Anglesey Mining 2012)
- Avoca, Ireland (production from 1720-1982: ~12 Mt at 0.75 % Cu: Bayswater Uranium 2012)
- Cae Coch, NE of Snowdon, Wales (0.2 Mt of massive pyrite: Colman and Cooper 2000). This may represent the distil expression of an undiscovered base-metal deposit (also see Ball and Bland 1985).

North of the Iapetus Suture, the Vidlin VMS deposit has been recognized in the Dalradian Supergroup on the Shetland Islands (=Laurentian rift and passive margin sequences), where stratabound sulfides reach 10m in thickness and grade up to 1.19% Cu and 1.27% Zn (Colman and Cooper 2000). In the Midland Valley Terrane (equivalent to the Notre Dame Subzone) no peri-Laurentian arc-hosted VMS deposits have been recognized, except possibly the Charlestown Cu deposit of County Mayo (3 Mt at 0.6% Cu; O'Connor and Poustie 1986). Although mineralization at Charlestown was historically considered to be a porphyry Cu deposit (O'Connor and Poustie 1986), brecciation textures and alteration assemblages appear to be more consistent with a stockwork zone to a VMS deposit. Mineralization (pyrite-chalcopyrite-sphalerite-galena-barite) is confined to a central silicified zone, which is enveloped in turn by sericitic, sericitic/chloritic and chloritic zones (O'Connor and Poustie 1986).

3 Petrochemistry of the upper Tyrone arc

This paper will focus on the upper Tyrone Volcanic Group as this is the most hydrothermally altered and mineralized part of the arc. For detail on the lower Tyrone Volcanic Group see Hollis (2012; also Fig. 2). The upper Tyrone arc (ca. 473-469 Ma) comprises two formations (Greencastle and Broughderg) and is a bimodal-felsic succession. These formations are composed of (Fig. 2):

- calc-alkaline volcaniclastic rocks, with syndepositional rhyolite flows, domes and associated deposits (autobreccias);
- overlain by thick accumulations of crystal and lithic tuff, lesser arkosic sandstone, porphyritic andesite, OIB-like basalt, alkali basalt, graphitic pelite, layered chert, ironstone, and thin rhyolite flows and sills.

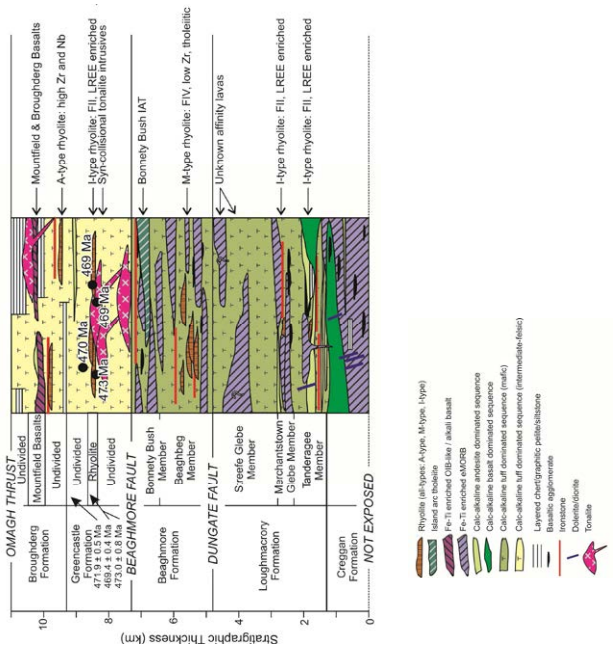

Figure 2. Petrochemical evolution of the Tyrone arc.

Basalts in the upper Tyrone Volcanic Group are borderline-alkalic to alkalic in composition, lack a dominant arc signature, and are Fe-Ti enriched (Fig. 2). These characteristics are typical of mafic rocks associated with VMS deposits in post-Archean evolved arc settings (e.g. Piercey 2007b). Felsic flows and intrusive rocks of the upper Tyrone Volcanic Group can be divided into two groups:

- I-type and FII-affinity, strongly LILE and LREE enriched calc-alkaline rhyolites with strongly –ve εNd_t values (-8.9) and low Zr contents (< 200 ppm) typical of the Greencastle Formation (Hollis et al. 2012); and

- within-plate, A-type rhyolites with high Zr (to 550 ppm), Nb (to 50 ppm) and Y (to 59 ppm) and high La_{CN} values (to ~200), recognized from historic drillcore from Broughderg.

FII-affinity (e.g. Cashel Rock) and A-type (e.g. Broughderg) rhyolites were considered the most VMS prospective types in evolved post-Archean settings by Piercey (2007b), which contain alkalic or MORB affinity mafic rocks in their hangingwall sequences. Consequently, such stratigraphic horizons in the upper Tyrone Volcanic Group are considered the most prospective for VMS mineralization herein (see Figs. 3 & 4).

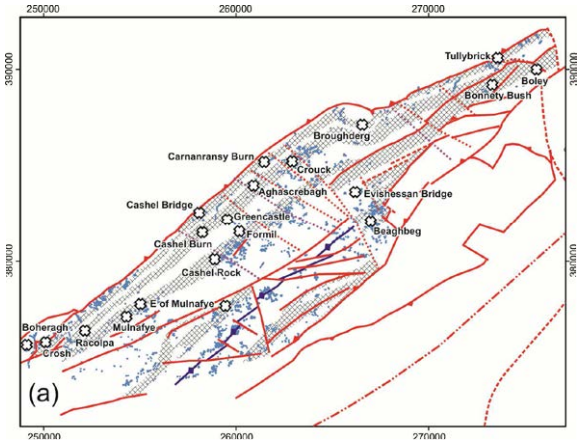

Figure 3. Petrochemically favourable horizons in the Tyrone Volcanic Group (crosshatch) and key target areas along these. Outcrop shown in blue.

4 Synvolcanogenic intrusives

Synvolcanogenic intrusions are integral to many VMS belts, often occurring in close proximity to deposits. Although these intrusions may not be the main drivers of hydrothermal circulation, they still record the presence of deeper seated heat in the region (e.g. basaltic underplating at 3-10 km depth: Piercey 2011).

Intrusions of tonalite ± diorite are spatially associated with ca. 473-469 Ma rhyolite domes and flows of the Greencastle Formation and lower Broughderg Formation, occurring in close proximity to VMS-prospective assemblages at Racolpa, Cashel Rock, Formil, Crouck, Aghascrebagh, Broughderg (drillcore) and Tullybrick (drillcore). Similar deformational histories to their host strata, a lack of contact metamorphic aureoles, field relations and U-Pb zircon geochronology (Cooper et al. 2011; Hollis et al. 2012) indicate these intrusives were high-level, composite and synvolcanogenic.

5 Hydrothermal alteration

The upper Tyrone Volcanic Group is characterized by subgreenschist to greenschist facies metamorphism, and various types and intensities of hydrothermal alteration. At Cashel Rock and Formil several distinct types of hydrothermal alteration occur in rhyolite domes and flows, which vary with distance from mineralized showings (e.g. silicification, chlorite-sericite-(pyrite), advanced argillic, sericitic). Most rocks associated with mineralization are either strongly silicified, strongly sericitized and/or strongly chloritized, with or without carbonate-alteration. Consequently, mineralized samples are characterized by higher Fe_2O_3, MgO, SiO_2, variable CaO (often depleted), low Al_2O_3 (dilution from mass gain), and significant Na_2O and Sr depletion. For example, samples of rhyolite from Cashel Rock have Na_2O contents between 0.40 and 5.43 wt%, and MgO contents between 0.11 and 14.89 wt%. Unpublished drilling results from Cashel Rock show a systematic decrease in Na (to values ~0.03 wt% Na_2O) with proximity to mineralization, with Alteration Index values increasing to 93.2. Hydrothermally altered and/or mineralized rhyolites are also characterized by elevated pathfinder elements. For example, felsic-hosted Pb-Zn-Au-Ag mineralization at Cashel Burn is associated with elevated As, Ba/Sr, Bi, Cd, Cr, Mo, Ni, Sb, Te and W (unpublished prospecting data). High Cr is clear in hand specimen by the presence of apple-green Cr-mica (fuchsite).

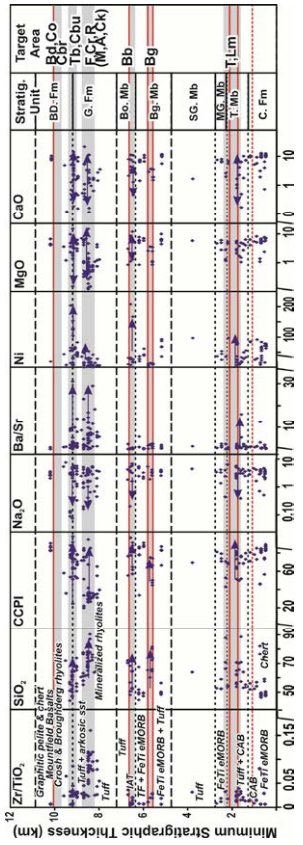

Figure 4. Whole rock geochemistry plotted against stratigraphic height for all units of the Tyrone Volcanic Group. Solid (red) lines indicate stratigraphic position of ironstones. *Stratigraphic units:* BD. Fm, Broughderg Formation; Bg. Mb, Beaghbeg Member; Bo. Mb, Bonnety Bush Member; C. Fm, Creggan Formation; G. Fm, Greencastle Formation; MG. Mb, Merchantstown Glebe Member; SG. Mb, Streefe Glebe Member; T. Mb, Tanderagee Member. *Identified target areas:* A, Aghascrebagh; Bb, Bonnety Bush; Bd, Broughderg; Bg, Beaghbeg; Cbr, Cashel Bridge; Cbu, Cashel Burn; Ck, Crouck; Co, Crosh; Cr, Cashel Rock; F, Formil; Lm, Loughmacrory; M, Murrins; R, Racolpa; T, Tanderagee; Tb, Tullybrick.

6 Mineralization

Stratigraphic horizons, and specific target areas within these, that are favourable for VMS mineralization in the upper Tyrone arc occur in the middle Greencastle Formation (e.g. Racolpa, Murrins, Cashel Rock, Formil), the uppermost Greencastle Formation (e.g. Cashel Burn, Aghascrebagh, Crouck, Tullybrick), and middle Broughderg Formation (e.g. Broughderg, Cashel Bridge, Crosh). Several of these areas, which contain high base metal and/or Au values in prospecting samples, have been partially tested by shallow drilling (e.g. Cashel Rock, Broughderg). Other areas are characterized by mineralized float with no exposure (e.g. Aghascrebagh, 4% Pb, 1.22% Zn and 5.94 g/t Au in siliceous tuff).

Grab samples can be extremely Au rich (e.g. 65.95 g/t Au: Cashel Rock), especially late quartz veins associated with intense silicification (e.g. 112.7g/t Au). The Cashel Rock Au prospect was identified through geochemical surveying, and is hosted in fine grained flow-banded rhyolite. The Au mineralized zone (e.g. 3.63m at 30.51 g/t Au) was traced for a strike length of 200 m and is open down-dip and along strike to the south (Clifford et al. 1992). Historically, the most encouraging result came from the deepest vertical hole on the most southerly section, where a > 10 m section of rhyolite that exhibited a stockwork system with extensive chloritic and silicic alteration associated with base metal mineralization was intercepted (Clifford et al. 1992). Similarly at Crosh and Racolpa, Au mineralization is hosted in silicified rhyolites and tuffs which often contain base-metal mineralization.

During 2011, targeted prospecting in the upper Tyrone Volcanic Group identified several new mineralized showings on these petrochemically favourable horizons. These include: the discovery of mineralization at Cashel Burn, and new showings around Crosh (to 2.99% Cu+Pb+Zn), Racolpa (to 2.19g/t Au), and E of Mulnafye (1.33% Cu+Pb+Zn, 0.3g/t Au), (Dalradian Resources 2011).

7 Conclusions

Through a combination of extensive field mapping and petrochemical analysis, stratigraphic horizons have been identified which are prospective for VMS mineralization in the upper Tyrone arc. Each is closely associated with:

- extensive rift related magmatism characterized by OIB-like and alkali basalt overlying FII or A-type and high-Zr rhyolites;
- hydrothermal alteration characterized by Na-depletion, high Ba/Sr, Bi, Sb, CCPI, AI and variable MgO and CaO;
- synvolcanogenic faults;
- high-level subvolcanic intrusions;
- showings of Pb-Zn-Cu-Ag±Au mineralization;
- geophysical anomalies (e.g. VLF/EM-R, magnetic, gravity; see Hollis 2012).

Targeted prospecting of petrochemically favourable units in 2011 led to the discovery of new Zn-Pb-Cu-Ag-Au mineralization.

Acknowledgements

We thank Ian Croudace for XRF analysis. Robin Taggart, Hilary Clarke, Gavin Berkenheger, Raymond Keenan and Vaughan Williams are thanked for field assistance and Dalradian Gold Ltd for access to historic drillcore and their hospitality. SPH gratefully acknowledges funding from the British Geological Survey (BGS University Funding Initiative), Dalradian Gold Ltd, Geological Survey of Northern Ireland, University of Southampton, Metallum Resources and Natural History Museum, London. Joanna Parr, Yulia Uvarova and Chris Yeats are thanked for many constructive comments.

References

Anglesey Mining (2012) http://www.angleseymining.co.uk/

Ball TK, Bland DJ (1985) The Cae Coch volcanogenic massive sulphide deposit, Trefriw, North Wales. Journal of the Geological Society, London 142: 889-898

Bayswater Uranium (2012) http://www.bayswateruranium.com/

Clifford JA, Earls G, Meldrum AH, Moore N (1992) Gold in the Sperrin Mountains, Northern Ireland: an exploration case history. In: Bowden AA, Earls G, O'Connor PG, Pyne JF (eds) The Irish Minerals Industry 1980-1990. Irish Association for Economic Geology, Dublin, pp77-87

Colman TB, Cooper DC (2000) Exploration for Metalliferous and Related Minerals in Britain: A guide. 2nd Edition. British Geological Survey, DTI Minerals Programme Publication, No. 1, pp.78

Cooper MR, Crowley QG, Hollis SP, Noble SR, Roberts S, Chew D, Earls G, Herrington R, Merriman RJ (2011) Age constraints and geochemistry of the Ordovician Tyrone Igneous Complex, Northern Ireland: implications for the Grampian orogeny. Journal of the Geological Society, London 168: 837-850

Dalradian Resources (2011). News release dated July 28, 2011. http://www.dalradian.com/investor-centre/news-releases/default.aspx

Hollis SP (2012) Evolution and mineralization of volcanic arc sequences: Tyrone Igneous Complex, Northern Ireland. Unpublished PhD thesis, University of Southampton, UK

Hollis SP, Roberts S, Cooper MR, Earls G, Herrington RJ, Condon DJ, Cooper MJ, Archibald, SM, Piercey SJ (2012) Episodic-arc ophiolite emplacement and the growth of continental margins: Late accretion in the Northern Irish sector of the Grampian-Taconic orogeny. GSA Bulletin, 124: 1702-1723

O'Connor PG, Poutsie A (1986) Geological setting of, and alteration associated with, the Charlestown mineral deposit. In Andrew CJ, Crowe RWA, Finlay S, Pennell WM, Pyne JF (eds) Geology and genesis of mineral deposits in Ireland. Irish Association for Economic Geology, pp89-101

Piercey SJ (2007a) Volcanogenic massive sulphide (VMS) deposits of the Newfoundland Appalachians: An overview of their setting, classification, grade-tonnage data, and unresolved questions. In Pereira CGP, Walsh DG (eds) Current Research. Newfoundland Department of Natural Resources, Geological Survey, Report 07-01: 169-178

Piercey SJ (2007b) An overview of the use of petrochemistry in regional exploration for volcanogenic massive sulfide (VMS) deposits. In Milkereit B (ed) Proceedings of Exploration 07: Fifth Decennial International Conference on Mineral Exploration, 223-246.

Piercey SJ (2011) The setting, style, and role of magmatism in the formation of volcanogenic massive sulfide deposits. Mineralium Deposita 46: 449-471

van Staal CR (2007) Pre-Carboniferous tectonic evolution and metallogeny of the Canadian Appalachians. In Goodfellow WD (ed) Mineral Deposits of Canada. Geological Association of Canada, Mineral Deposits Division, Special Publication 5, 793-818

VMS mineralization in the Yilgarn Craton, Western Australia: petrochemistry and recent developments

Steven Hollis, Chris Yeats, Stephen Barnes
CSIRO Earth Science and Resource Engineering, Kensington, Western Australia, 6151, Australia
(steven.hollis@csiro.au)

Stephen Wyche
Geological Survey Division, Department of Mines and Petroleum, East Perth, Western Australia, 6004, Australia

Abstract. The Archean, Yilgarn Craton of Western Australia is a world-class metallogenic province, hosting considerable resources of Au, Ni-sulfides and iron-ore. Despite close geological similarities with the VMS-rich Superior Province of Canada, there is a strong disparity in the number of discovered VMS deposits between the two cratons. Advancements in a number of key fields, such as regolith and groundwater processes, petrochemistry and lithogeochemistry, and historically high copper and zinc prices, have led to recent renewed interest in Yilgarn VMS exploration in the last decade after ~25 years of minimal investment. Several major discoveries such as Bentley, Austin, Just Desserts and Hollandaire highlight the potential of a number of greenstone belts across the Craton. VMS-prospective areas can be identified through the presence of bimodal volcanic complexes; synvolcanic faults and HFSE-enriched subvolcanic intrusions; specific petrochemical signatures of felsic and mafic volcanic rocks; hydrothermal assemblages (e.g. element mobility, hyperspectral mapping, mineral chemical vectors); and regional isotope variations indicative of rifting. The VMS prospectivity of each greenstone belt in the Yilgarn has been investigated using published geochemical data, with examples presented. Significant, recent developments in VMS exploration across the Yilgarn Craton are summarized.

Yilgarn, VMS, greenstone, petrochemistry

1 Exploration in the Yilgarn Craton

The 1963 discovery of the giant Kidd Creek Cu-Zn deposit in Canada precipitated significant VMS exploration activity in the Archean Yilgarn and Pilbara cratons of Western Australia throughout most the 1960s and 1970s (McConachy et al. 2004). The main exploration technique was gossan searching, coupled with geophysics. One substantial find in the Yilgarn Craton was made at Gossan Hill in 1971 (Golden Grove camp, Murchison Domain: Fig.1), consisting of two primary Cu and Zn resources (7.0 Mt at 3.4% Cu; 2.2 Mt at 11.3% Zn, 102g/t Ag and 1.5g/t Au) overlain by a weathered Cu-Au-Ag oxide resources (5.3 Mt at 1.5% Cu; 2.2 Mt at 86g/t Ag and 2.2g/t Au; Sharpe and Gemmell 2002). A smaller, but higher grade find was also made in 1976 at Teutonic Bore in the Eastern Goldfields Superterrane (production from 1981-1985 of 1.68 Mt at 3.5% Cu, 10.8% Zn, 140g/t Ag: Yeats 2007). Unfortunately, there were no discoveries of Kidd Creek dimensions, and the total Yilgarn resource to this day remains substantially less than similar Archean provinces of Canada. By the early 1980s, the lack of success and an increasing gold price saw a change in focus, and VMS mineralisation effectively dropped off the exploration agenda in Western Australia for the next 25 years (Yeats 2007). Few deposits were discovered in the 1980s and 1990s, except for near-mine discoveries at Golden Grove (Amity, Hougoumont and Catalpa) in 1999 and a small (0.93 Mt) Ag-Au resource at Nimbus in the Eastern Goldfields Superterrane, discovered in 1993 (McConachy et al. 2004) (Fig. 1). Perhaps unsurprisingly, there has been much discussion about whether the Yilgarn is underexplored or intrinsically impoverished in VMS mineralization (e.g. Witt et al. 1996; McConachy et al. 2004; Yeats 2007).

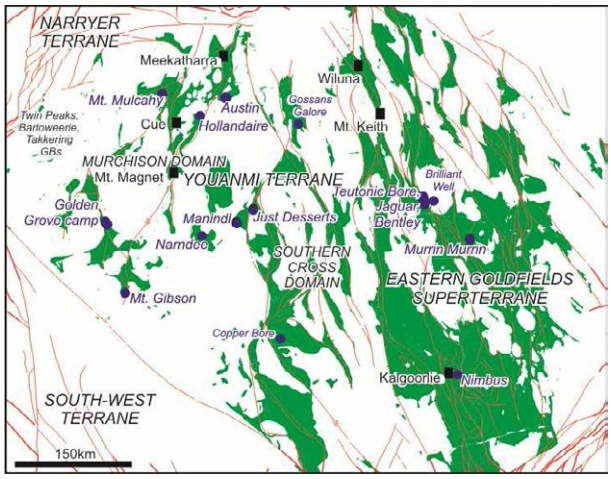

Figure 1. Tectonic division of the northern and eastern Yilgarn Craton, showing major terranes and domains, greenstone belts, and significant VMS occurrences discussed herein.

2 Recent advances in exploration

Renewed exploration activity in Yilgarn VMS exploration over the last decade has led to a number of new discoveries, including further discoveries at Golden Grove in 2000 and 2003 and new discoveries at Jaguar, Bentley, Austin, Just Desserts and Hollandaire (section 3). These successes are primarily due to advances in a number of fields, including:

- Extensive geological mapping coupled with geochemistry, U-Pb geochronology and isotope analysis across the Yilgarn Craton (section 2.1);

- An improved understanding of regolith processes and Yilgarn groundwaters;
- Advances in petrochemical (section 2.2.) and lithogeochemical exploration (e.g. mineral chemistry, hyperspectral logging and mapping);
- The correct application of geophysical techniques (e.g. Jaguar: Ellis 2004).

2.1 Geology and tectonic evolution of the Yilgarn craton

Detailed geological mapping (coupled with regional geophysical surveys), extensive geochemistry, and high-resolution U-Pb zircon geochronology, have resulted in a vastly improved understanding of the geology of the Yilgarn Craton and its potential to host VMS mineralization. Good stratigraphic control is essential for greenfields exploration, as many VMS deposits are typically clustered along well defined stratigraphic horizons associated with episodes of extension. Van Kranendonk et al. (in press) recently presented a four-fold division of the long-lived, autochthonous Murchison Domain of the Youanmi Terrane (W Yilgarn Craton: Fig. 2). In the Youanmi Terrane (Murchison & Southern Cross domains) at least three distinct episodes of rifting associated with significant VMS mineralization can be recognized:

1. Early rifting in the ca. 2960-2935 Ma Mt Gibson Group is recorded by significant VMS mineralization at Golden Grove (~40.2 Mt at 1.8% Cu, 0.9% Pb, 7.6% Zn, 103g/t Ag and 0.8g/t Au: Gawlinski 2004; plus new resources – see section 3) and Mt Gibson.
2. In the Yaloginda Formation of the ca. 2825-2805 Ma Norie Group, rifting is recorded through the presence of: (i) petrochemically prospective felsic sequences so far identified at Windimurra, Youanmi and W of Copper Hills, which are associated with base-metal occurrences; and (ii) significant VMS deposits at Manindi, Narndee, Just Desserts and Quinns (i.e. Austin deposit) whose host sequences have been dated to ca. 2818-2813 Ma (GSWA geochronology database). This period records a major geodynamic shift in the evolution of the western Yilgarn Craton with a switch from tholeiitic and komatiitic basalt (Murrouli Basalt) to sequences dominated by felsic volcanic and volcaniclastic rocks, interbedded units of ferruginous shale, chert and/or banded iron formation (Yaloginda Formation). Petrochemically unfavourable felsic rocks also exist in the Yaloginda Formation in areas devoid of base-metal mineralization (e.g. W of Lewis Au mine).
3. Dated assemblages at Hollandaire (2746 ± 4 Ma) and Mt Mulcahy (ca. 2747 Ma) imply a third episode of rifting and VMS mineralization occurred during the deposition of the largely unprospective Greensleeves Formation (of the ca. 2800-2734 Ma Polelle Group). Petrochemically prospective felsic rocks of this age have been so far been identified in the Dalgaranga greenstone belt (which hosts base-metal occurrences such as Lasoda) and NW of Cue (e.g. Emily Well occurrence).

In the Eastern Goldfields Superterrane (EGS), extension associated with ca. 2695 Ma VMS mineralization at Teutonic Bore, Jaguar and Bentley occurs along the western edge of a young T_{2DM} zone, highlighting the significance of inherited rift-related structures (Huston et al. 2005). Similar anomalies on the Nd T_{DM} map of the Yilgarn Craton also occur for other VMS-bearing greenstones belts between Mt Magnet and Meekatharra (Czarnota et al. 2010), around Golden Grove (Huston et al. 2005), and near Nimbus and Murrin Murrin in the EGS. Felsic tuff dated from Murrin Murrin has produced a similar age (2698 ± 5 Ma) to dacite from near Teutonic Bore (2692 ± 4 Ma) suggesting both domains were affected by extension at this time (GSWA geochronology database).

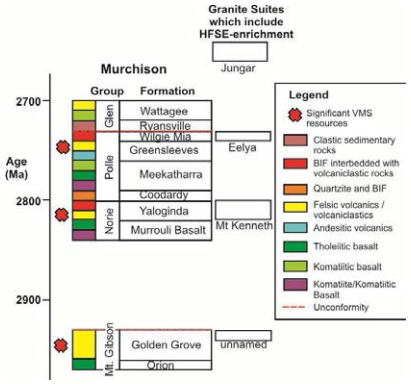

Figure 2. Stratigraphic divisions of the Murchison Domain highlighting the correlation of petrochemically favourable felsic volcanic rocks, significant VMS resources and HFSE-enriched granites. Stratigraphy from Kranendonk et al. (in press).

2.2 Petrochemically prospective terranes

Recent advances in our understanding of how VMS deposits form and their common petrochemical associations have provided an opportunity to re-examine VMS prospectivity across the Yilgarn Craton. Lesher et al. (1986) first outlined a threefold division of VMS-fertile versus barren felsic rocks from the Superior Province of Canada (FI to FIII). It was recognized that in Archean environments VMS deposits are preferentially associated with FIII and FII affinity rocks. FIII affinity felsic rocks are characterized by low Zr/Y, elevated SiO_2, HFSE (especially Zr) and REE contents (including Y and Yb), and flat chondrite-normalized REE profiles (i.e. low La/Yb; Lesher et al. 1986). These rocks are interpreted to have formed within rift sequences from high-temperature melts (T>900 °C) derived from the melting of hydrated basaltic crust at shallow to mid-crustal depths during extension (Piercey 2011). Steep chondrite-normalized REE profiles, high Zr/Y, lower REE and HFSE are typical of the petrochemically unfavourable FI suite, indicative of deeper melting and reduced crustal heat flux.

Case study: Eastern Goldfields Superterrane

In the EGS, known VMS mineralisation is scarce, and predominantly restricted to ca. 2695-2680 Ma bimodal volcanic complexes of the Gindalbie Domain of the W Kurnalpi Terrane (exceptions detailed below).

The recognition of bimodal volcanism is important as this association of high-temperature mantle melts and crustal partial melts is indicative of rift-related magmatism. The Gindalbie Domain is defined by VMS-prospective, HFSE-enriched bimodal (basalt-rhyolite) complexes (e.g. at Melita and Teutonic Bore), and largely unprospective, calc-alkaline intermediate-silicic volcanic rocks (e.g. at Spring Well and Jeedamya) (Brown et al. 2002). Felsic volcanic complexes at Melita and Teutonic Bore have elevated concentrations of SiO_2, HFSE and Y (i.e. A-type, FIII characteristics), low Zr/Y and Th/Yb, and flat to LREE-depleted REE profiles (with pronounced –ve Eu anomalies) (data of Witt et al. 1996; Brown et al. 2002; Barley et al. 2008).

HFSE-enriched (A-type) granites comprise ~5-10% by area of all granitoids of the Yilgarn Craton. In the EGS, these intrusions are mostly restricted to the Kurnalpi terrane and the NE Kalgoorlie Terrane, and show a close temporal and spatial association to geochemically similar, VMS-prospective sequences (Czarnota et al. 2010). These high-HFSE peralkaline granites occur in close proximity to VMS prospective sequences E of Teutonic Bore and near the southern and eastern margins of the Melita Complex (e.g. Hallberg 1985; Czarnota et al. 2010). In the EGS, high-HFSE granites range in age from >2720 to 2665 Ma, with a peak in activity at ca. 2680 Ma in the Kurnalpi Terrane, and ca. 2700 Ma in the Kalgoorlie Terrane (Czarnota et al. 2010). Diagnostic features of these intrusive rocks include the presence of amphibole and a combination of high FeO, MgO, TiO_2, Y and Zr (with low Rb, Pb, Sr and Al_2O_3) (Czarnota et al. 2010).

Although VMS mineralization is well known at Teutonic Bore, at Melita no significant finds have been made. Major exploration efforts in the 1970s only revealed small, sub-economic concentrations of sulphides (mostly pyrite, minor pyrrhotite, sphalerite, galena and chalcopyrite; e.g. Jungle Pool) associated with hydrothermally altered rhyolitic to andesitic host rocks (references in Witt 1994). Exploration of coeval rift-related tuffaceous and sedimentary strata between Melita and Leonora may prove to be more successful, as similar packages host mineralization at Jaguar (Ellis 2004), Golden Grove and Murrin Murrin.

VMS mineralization in the EGS has also been recognized outside the Gindalbie domain at Nimbus (Boorara domain, Kalgoorlie Terrane), Murrin Murrin (Murrin domain, Kurnalpi Terrane), and in the Agnew-Wiluna belt (Kalgoorlie Terrane), although the latter are barren and are dominated by pyrite. These occurrences, together with numerous base-metal prospects across the EGS (e.g. Yeats 2007) highlight the potential for VMS mineralization across the EGS in other, often overlooked, domains.

In the Murrin Domain, Cu has been produced from the historic Anaconda, Nangaroo and Rio Tinto mines (Hallberg 1985); with supergene and oxidized Cu ore from Anaconda (4320 t Cu) accounting for 94% of all Cu produced from the area. The Murrin Murrin VMS deposits occur in pyritic, feldspathic wacke, siltstone and shale, interpreted as distal deposits to the Welcome Well Complex to the North (Hallberg 1985). Although the Welcome Well Complex does not appear to be petrochemically prospective according to Zr, Cr and Y data of Hallberg (1985), the VMS prospectivity of the region is worthy of further study, as rocks with flat REE profiles, low Zr/Y ratios, and borderline A-type and FIII characteristics have been recognized from Murphy Well E (SE of Murrin Murrin).

In the Agnew-Wiluna belt of the Kalgoorlie Terrane, bimodal volcanism is characterized by felsic volcanic and volcaniclastic sequences emplaced coevally with large komatiitic sills. Units such as the Mount Keith Dacite host barren, pyrite-rich hydrothermal massive sulfide lenses for ~80km between Albion Downs and Perseverance (Fiorentini et al. 2012). These lenses have been suggested to play an integral role in the formation of world-class Ni-sulfide mineralization at sites such as Mt Keith (see Fiorentini et al. 2012). At Jericho and South Jericho (Albion Downs area) komatiite-hosted basal Ni-sulfides truncate a dacite-hosted Cu and Zn bearing VMS-style stringer-stockwork zone (Fiorentini et al. 2012) demonstrating at least some sulfides are associated with base-metals. Petrochemical analysis of felsic volcanics from Mt Keith and Perseverance has identified flat REE profiles, low Zr/Y ratios, and borderline A-type and FIII characteristics for some felsic rocks (although Zr contents are low). Similar felsic volcanic rocks have also been recognized at Albion Downs in the Agnew-Wiluna belt (i.e. near Jericho).

3 VMS deposits: recent developments

Significant developments have been made in Yilgarn VMS exploration since the reviews of McConachy et al. (2004) and Yeats (2007). These are summarised below.

Youanmi Terrane:

- The new Gossan Valley and Felix resource (Golden Grove) stands at: 1.5 Mt at 7.9% Zn, 10g/t Ag, 0.9g/t Au, plus 1.3 Mt at 2.3% Cu, 14g/t Ag and 0.3g/t Au (MMG unpub. report). Zn mineralization has also been intersected along strike to the southeast at Flying Hi (31m at 6.1% Zn) and Bassendean (6.6m at 5.6% Zn, 2% Pb, 86g/t Ag and 2.6g/t Au) (MMG unpub. report). Large areas of favourable stratigraphy, especially NW of Scuddles, still remain untested.
- Exploration near Youanmi has substantially upgraded the 1972 Manindi deposit, for a JORC resource of 1.354 Mt at 6.04% Zn, 0.25% Cu, 3.4g/t Ag and 0.25g/t Au (Metals Australian Ltd unpub. report).
- In September 2011 the Hollandaire VMS deposit was discovered E of Cue. As of September 2012, this deposit has a JORC resource of 2.8 Mt at 1.5% Cu, 5g/t Ag and 0.4g/t Au (Silver Lake Resources unpub. report). The supergene zone averages 390,000t at 4.7% Cu, 12g/t Ag and 0.9g/t Au.
- The Quinns Project, 55km S of Meekatharra, includes the JORC defined 1.48 Mt Austin deposit discovered in late 2008 (1.02% Cu, 1.39% Zn, 3.31g/t Ag, 0.24 g/t Au: Caravel Minerals Ltd unpub. report). VMS-style base-metal mineralization has also been intercepted along

strike at Flinders (6.0m at 3% Zn), Murchison Wonder (1.0m at 5.3% Zn, 0.2% Cu and 9g/t Ag) and Tasman (6.0m at 3% Zn, 12m at 5.5 g/t Ag, 5m at 0.4% Cu).

- The Just Desserts VMS deposit of the Youanmi greenstone belt now has an inferred and indicated resource of 1.07 Mt at 1.8% Cu and 0.8g/t Au (Empire Resources unpub. report). Significant mineralization has also been intersected at Augustus (18m at 0.5% Cu), YC14 (5m at 0.5% Cu, 1.0g/t Au), Smith Well (8m at 1.4% Cu, 0.2g/t Au) and A-zone (7m at 2.1% Cu, 0.3g/t Au).

Eastern Goldfields Superterrane:

- As of June 2012, mineral resources for the Jaguar-Bentley-Teutonic Bore operation stand at 5.06 Mt at 1.9% Cu, 7.1% Zn and 99g/t Ag; and ore reserves stand at 2.45 Mt at 1.3% Cu, 8.2% Zn and 98g/t Ag (Independence Group unpub. report). Additional lenses have been discovered by near mine drilling at depth (e.g. Comet Lens at Bentley). Exploration along strike to the NW and SE has identified numerous VMS targets including: Lagonda, Triumph, Daimler, Teutonic Bore South, and Bentley South.
- The Nimbus VMS deposit (Boorara domain, Kalgoorlie terrane), originally discovered in 1993, represents a deeply weathered high grade Ag-(Zn) resource. Several new high grade lenses have been discovered in recent years for a JORC compliant mineral resource of 2.792 Mt at 139g/t Ag-Equivalent (MacPhersons unpub. report). Additional Ag-Zn targets in the area include Gretel, Condor, Tramways and Brindabella.

4 Conclusions

VMS-prospective areas in the Yilgarn Craton can be identified through the presence of bimodal volcanic complexes, synvolcanogenic faults and HFSE-enriched subvolcanic intrusions, the petrochemistry of felsic and mafic volcanic rocks, hydrothermal assemblages and regional isotope variations indicative of rifting. At least three distinct episodes of rifting in the Youanmi Terrane are associated with VMS mineralization. Data presented herein highlight the potential for new discoveries in the Eastern Goldfields Superterrane in often overlooked greenstone belts.

Acknowledgements

This paper builds on the research of countless individuals, all of whom are gratefully acknowledged. The principal author is supported by the Exploration Incentive Scheme at the Geological Survey of Western Australia, funded from the Western Australian Government Royalties for Regions Program.

References

Barley ME, Brown SJA, Krapež B, Kositcin, N (2008) Physical volcanology and geochemistry of a Late Archaean volcanic arc: Kurnalpi and Gindalbie Terranes, Eastern Goldfields Superterrane, Western Australia. Precambrian Research 161: 53-76.

Brown SJA, Barley ME, Krapež B, Cas RAF (2002) The Late Archaean Melita Complex, Eastern Goldfields, Western Australia: shallow submarine bimodal volcanism in a rifted arc environment. Journal of Volcanology and Geothermal Research 115: 303-327.

Czarnota K, Champion DC, Goscombe B, Blewett RS, Cassidy KF, Henson PA, Groenewald PB (2010) Geodynamics of the eastern Yilgarn Craton. Precambrian Research 183: 175-202.,

Ellis P (2004) Geology and mineralisation of the Jaguar copper-zinc deposit, Western Australia. In: McConachy TF, McInnes BIA. Copper-zinc massive sulphide deposits in Western Australia. CSIRO Explores 2, pp39-46.

Fiorentini M, Beresford S, Barley M, Duuring P, Bekker A, Rosengren N, Cas R, Hronsky J (2012) District to camp controls on the genesis of komatiite-hosted nickel sulphide deposits, Agnew-Wiluna greenstone belt, Western Australia: Insights from the multiple sulfur isotopes. Economic Geology 107: 781-796.

Gawlinski S (2004) Recent exploration success at Golden Grove, Western Australia. In: McConachy TF, McInnes BIA. Copper-zinc massive sulphide deposits in Western Australia. CSIRO Explores 2, pp33-37.

Hallberg JA (1985) Geology and Mineral Deposits of the Leonora-Laverton area, Northeastern Yilgarn Block, Western Australia. Hesperian, Carlisle, W.A.

Huston DL, Champion DC, Cassidy KF (2005) Tectonic controls on the endowment of Archean cratons in VHMS deposits: evidence from Pb and Nd isotopes: In: Mao J, Bierlein FP. Mineral Deposit Research: Meeting the global challenge, pp15-18.

Lesher CM, Goodwin AM, Campbell IH, Gorton MP (1986) Trace-element geochemistry of ore-associated and barren, felsic metavolcanic rocks in the Superior province, Canada. Canadian Journal of Earth Sciences 23: 222-237.

McConachy TF, McInnes, BIA, Carr, G.R (2004) Is Western Australia intrinsically impoverished in volcanogenic massive sulphide deposits, or under explored. In: McConachy TF, McInnes BIA. Copper-zinc massive sulphide deposits in Western Australia. CSIRO Explores 2, pp15-32.

Piercey SJ (2011) The setting, style, and role of magmatism in the formation of volcanogenic massive sulfide deposits. Mineralium Deposita 46: 449-471

Sharpe R, Gemmell JB (2002) The Archean Cu-Zn magnetite-rich Gossan Hill volcanic-hosted massive sulphide deposit, Western Australia: genesis of a multistage hydrothermal system. Economic Geology 97: 517-539.

Van Kranendonk MJ, Ivanic TJ, Wingate MTD, Kirkland CL, Wyche S (In Press) Long-lived, autochthonous development of the Archean Murchison Domain, and implications for Yilgarn Craton tectonics. Precambrian Research. http://dx.doi.org/10.1016/p.jprecambres.2012.08.009

Witt WK (1994) Geology of the Melita 1: 100 000 sheet, Western Australia. Western Australia Geological Survey Explanatory Notes.

Witt WK, Morris PA, Wyche S, Nelson DR. (1996) The Gindalbie Terrane as a target for VMS-style mineralisation in the Eastern Goldfields Province of the Yilgarn Craton. Technical paper, Geological Survey of Western Australia, Annual Review 1995-1996, pp41-47.

Yeats CJ (2007) VHMS mineral systems in the Yilgarn – characteristics and exploration potential. In: Bierlein FP, Knox-Robinson CM. Proceedings of Geoconferences (WA) Inc. Kalgoorlie '07 Conference, pp65-69.

Subseafloor structure of a submarine hydrothermal system within volcaniclastic sediments: a modern analogue for 'Kuroko-type' VMS deposits

Jun-ichiro Ishibashi[1,2], Youko Miyoshi[1], Hiroyasu Inoue[1], Chris Yeats[3], Steven P. Hollis[4,3], Juan C. Corona[5], Stephen Bowden[6], Shouye Yang[7], Gordon Southam[8], Yuka Masaki[9,2], Hillary Hartnett[10], IODP Expedition 331 Scientists

[1] *Graduate School of Science, Kyushu University, Japan*
[2] *Submarine resources research project, JAMSTEC, Japan*
[3] *CSIRO Earth Science and Resource Engineering, Australia*
[4] *National Oceanography Centre, University of Southampton, UK*
[5] *Department of Geological Sciences, Binghamton University, USA*
[6] *Department of Petroleum Geology, University of Aberdeen, UK*
[7] *School of Ocean and Earth Science, Tongji University, China*
[8] *Department of Earth Science, University of Western Ontario, Canada*
[9] *School of Science, Kochi University, Japan*
[10] *School of Earth & Space Exploration, Arizona State University, USA*

Abstract. Deep drilling through an active hydrothermal field at the Iheya North Knoll in the middle Okinawa Trough during IODP Expedition 331 provided a unique opportunity to directly access the subseafloor environment. Whereas sedimentation along the slopes of the knoll was dominated by volcanic clasts of tubular pumice, intense hydrothermal alteration was recognized in the vicinity of the hydrothermal centre even at shallow depth below the seafloor. Together with extremely high temperature gradients encountered, this prevalent alteration is attributed to laterally extensive infiltration of fluid within the sediment layer. Styles of sulfide-sulfate mineralization encountered are directly comparable to those found within economically important Kuroko-type volcanogenic massive sulfide (VMS) deposits.

Keywords. Integrated Ocean Drilling Program, Okinawa Trough backarc basin, sulfide/sulphate deposits, hydrothermal alteration

1 Introduction

Up to present, about ten active hydrothermal fields have been discovered in the Okinawa Trough, considered as a rifted zone in a continental margin (Glasby and Notsu, 2003). Many of the hydrothermal fields are located on the slope of a seamount and depression structure, where the seafloor is mainly covered with sediments of volcanic origin. Fluid migration within volcanic sediment of high porosity may be a suitable environment for mineralization from the hydrothermal fluid beneath the seafloor. Seafloor drilling during the IODP (Integrated Ocean Drilling Program) Expedition 331, which was conducted at the Iheya North Knoll hydrothermal field provided a valuable opportunity to gain insights of subseafloor hydrothermal processes (Takai et al., 2011; 2012).

2 Geologic setting and drilled sites

Hydrothermal activity in the Iheya North Knoll (27° 47′50N, 126° 53′80 E; water depth: 1000 m) was located along the slope of a small knoll. Extensive surveys using deep submergence vehicle (DSV) and remotely operated vehicle (ROV) dives have revealed details regarding the location of hydrothermal activity and seafloor events, which are characterized by several hydrothermal

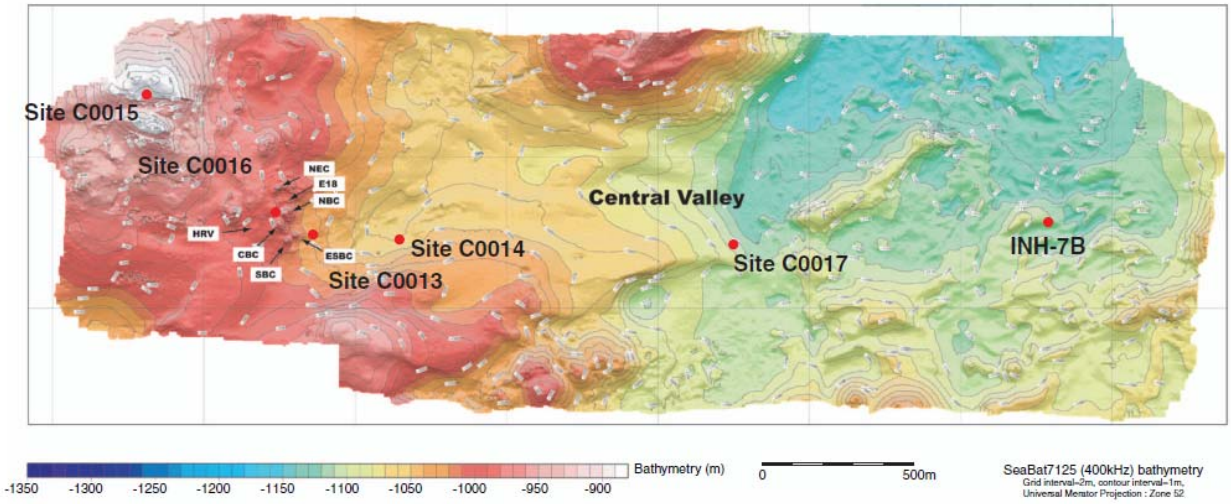

Figure 1. Map of the Iheya North hydrothermal field with the location of Sites C0013-C0017 drilled during IODP Expedition 331 (Takai et al., 2011).

mounds associated with polymetallic mineral deposits. Vigorous venting of high temperature fluid (Tmax = 311°C) was observed at the top of a large hydrothermal mound (about 30 meters high) called NBC, that is considered the activity centre. Geochemical studies on the hydrothermal fluid have revealed enrichment in volatile and organic-derived species compared with typical mid-ocean ridge hydrothermal fluids and also evidence for subseafloor phase separation (Nakagawa et al., 2005, Kawagucci et al., 2011).

Recent seismic studies of the Iheya North Knoll has demonstrated relatively disordered seismic reflectors as deep as 400-500 mbsf (meters below the seafloor) in the central valley, suggesting the presence of pumiceous volcaniclastic flow deposits below surficial hemipelagic sediments, rather than massive igneous rocks. Extensive geological studies using gravity cores have recovered a large volume of pumiceous volcaniclastic sediment, which were also reported by previous submersible studies. This kind of pumice that contains parallel tube-like vesicles is considered as formed by subaqueous eruptions at 500 to 1000 m water depth (Allen et al., 2010).

Five sites (C0013 - C0017) were drilled during the IODP Expedition 331, conducted from Sept. 1 to Oct. 4 in 2010, employing D/V Chikyu. Drill site localities along the east slope of the knoll cover the Iheya North hydrothermal field (Fig. 1). Site C0016 was located at the flank part of the active hydrothermal mound NBC. Site C0013 was drilled about 100 meters east of the mound, and Site C0014 was drilled at about 450 meters east. Site C0015 was located at the top of the knoll, and Site C0017 was located at the base of the knoll.

3 Hydrothermal alteration & mineralization

Unconsolidated sediment recovered from the Iheya North Knoll comprised three main litho-types: pumice breccias, siliciclastic sands and hemipelagic mud. At Site C0015 at the top of the knoll, volcanic clasts comprised the majority of the sediment encountered. Clasts of pumice predominated within all breccias and pelagic muds were encountered between these units. Upper portions of sediment obtained from Site C0017, located around the base of the knoll, were also dominated by volcaniclastic sediments comprising or derived from a variety of pumice types. Here also hemipelagic sediments were interbedded between pumice-deposits indicating periods free from the deposition of volcano-derived sediments.

Much of the sediment and rock we cored at Site C0013 and C0014 was intensly hydrothermally altered and mineralized (Fig.2). At site C0013, located 100 m east from the hydrothermal mound NBC, alteration was notable even at very shallow depths. Dominant alteration assemblages were represented by kaolinite and muscovite (0 - 6 mbsf), Mg-chlorite and anhydrite (6 - 24 mbsf), and quartz-Mg chlorite altered volcaniclastic breccias (24 - 45 mbsf). At Site C0014, located 450 m east from the hydrothermal mound NBC, hydrothermal alteration was broadly consistent with the alteration assemblages observed at Site C0013, although transitions in the mineralogy occurred at much greater depths. Surface sediments (0 - 10 mbsf) were comprised of hemipelagic mud and pumiceous volcaniclastics, and showed little evidence for hydrothermal alteration. The sedimentary sequence is hydrothermally altered to pale gray mottled clay (10 - 30 mbsf). Silicified volcaniclastic-breccia was encountered below 30 mbsf although cementing was intermittent and absent from some mud layers. Mg-chlorite was recognized as an important alteration phase beneath 30 mbsf, while anhydrite was found only below 57 mbsf.

A variety of hydrothermal sulfide/sulfate deposits were successfully recovered by drilling into the flank part of the active hydrothermal mound NBC at Site C0016 (Yeats et al., 2012). Blocks of massive sphalerite-(pyrite-chalcopyrite)-rich sulfides were obtained from the first core (0 - 9 mbsf). The sulfide showed clear textural evidence for formation via a combination of surface detrital and subsurface chemical processes. A snow-white, coarsely crystalline anhydrite aggregate was obtained in the second core (9 - 27 mbsf). Other core recovered included silicified rocks disseminated with veins contained pyrite. Sulfide mineralization at Sites C0013 and C0014 was characterized by occurrence of detrital grains and pyrite in the upper portions of sediment (0 - 12 mbsf at C0013 and 0 - 19 mbsf at C0014). Some sections of Core C0013 were heavily mineralized, while the sulfidic grits were relatively scarce at Site C0014. In the core at greater depths (26 - 28 mbsf at C0013 and, 109 - 113 mbsf and 127 mbsf at C0014), quartz-sulfide veins were present among silicified volcanic breccias, some of them contained chalcopyrite, sphalerite and galena.

4 Subseafloor hydrothermal flow regime

The drilling and coring operation during Expedition 331 encountered extreme thermal conditions beneath the

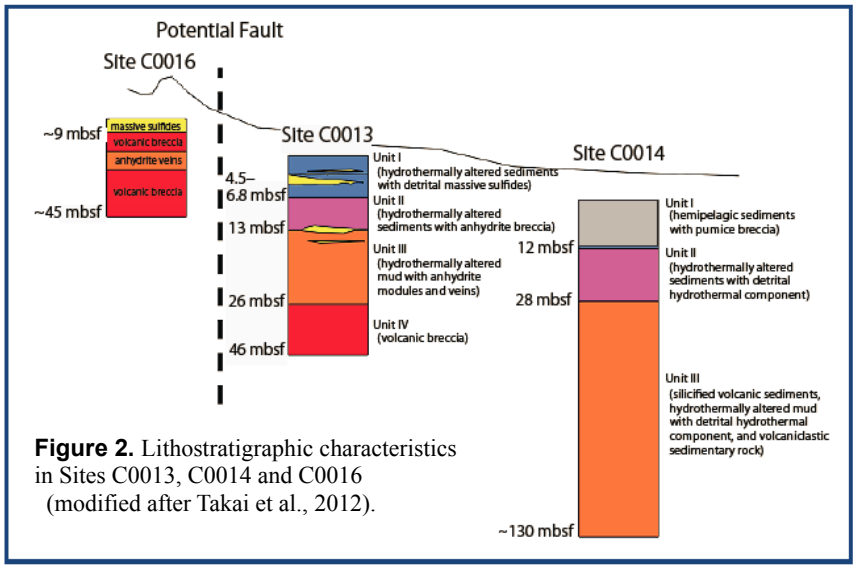

Figure 2. Lithostratigraphic characteristics in Sites C0013, C0014 and C0016 (modified after Takai et al., 2012).

Iheya North hydrothermal field. The acrylide plastic core liners melted at 12 mbsf at Site C0013. At site C0014, estimated temperature using commercial "thermoseal" strips indicated it exceeded 55°C at 16 mbsf and >210°C at 50 mbsf. Considering the hydrothermal alteration phase present, high temperature fluid intrusion and occupation within the sediment layer would be responsible for the extreme thermal conditions. Actually, vigorous fluid emanation was observed several times at Hole C0013E and Hole C0014G, strongly suggesting that the holes penetrated through the cap rock layer into the fluid reservoir.

The extensive hydrothermal fluid reservoir is interpreted to be hosted by a highly porous pumiceous volcaniclastic sediment layer. The unaltered sediment from Site C0014 showed porosity higher than 70%. The porosity drastically decreased in the layer of anhydrite formation (especially at C0013) but remained high in the layer of only chlorite alteration. Spontaneous cap rock formation caused by anhydrite precipitation among hydrothermal clays could inhibit the ascent of high temperature fluids to the seafloor. Furthermore, the interbedded nature of pelagic mud units and matrix-free pumice deposits may create a tightly layered architecture of aquifers and aquicludes. These sediment architectures should be highly conducive to lateral flow pseudo-parallel to the surface topography. Westward-dipping reflection sequences starting from the active vent field are proposed to be major pathways for hydrothermal intrusion, by previous geophysical studies (Tsuji et al., 2012). On the other hand, Site C0017 is considered to be located in a seawater recharge region, based on its significantly low temperature gradient, and on high porosity of 60-70 % in the upper portion. The hydrological regime at the Iheya North Knoll was characterized by large-scale hydrothermal alteration, deposition, and fluid migration within permeable rocks and sediments.

5 Modern analogue for Kuroko-type VMSD

It is notable that the sequence of mineral assemblages with increasing the depth was common among three sites, which suggests stratabound hydrothermal alteration and mineralization across an area of over 500 meters extent beneath the seafloor. Together with the resemblance in appearance and chemical composition of the massive sulfide block recovered from Site C0016 to kuroko ores, the styles of sulfide-sulfate mineralization revealed by the IODP drilling are directly comparable to those found within economically important Kuroko-type polymetallic volcanogenic massive sulfide deposits (Yeats et al., 2012).

As demonstrated in previous studies on typical examples in north east Japan, Kuroko-type VMS is usually composed of an upper stratiform and stratabound massive sulfide ore body (black ore) consisting of sphalerite and galena, a lower stockwork ore zone (yellow ore and/or siliceous ore) consisting of veinlets and disseminated mineralization in the footwall occasionally including chalcopyrite, together with occurrence of massive gypsum. As well as the sphalerite-rich massive sulfides found at Site C0016, the sulfidic grits in the upper portion of Sites C0013 and C0014 could correspond to "black ore". The siliceous volcanic breccias with sulfide veins found in these three sites may correspond to the "siliceous ore". Although material reminiscent of Kuroko-type "yellow ore" was not identified in the cores, the interval of thick hydrothermal alteration with abundant anhydrite may be correspond to the "gypsum ore".

One of the main accomplishments of IODP Exp.331 was locating the laterally extensive mineralization, hydrothermal alteration, and hydrothermal fluid reservoir beneath the Iheya North field. More detailed studies will shed further light on the development of this unique hydrogeological system and help to understand the formation of VMS deposits. Since the Iheya North field represents a strong modern analogue for the formation of ancient Kuroko-type deposits, studies will provide essential information on the temporal development of ore associated with hydrothermal systems related to arc-backarc settings.

Acknowledgements

We are grateful to Captain Yuji Onda, the operation superintendents Tomokazu Saruhashi and Ikuo Sawada, the crew and the onboard technical staff of R/V Chikyu. This research used samples and/or data provided by the integrated ocean Drilling Program (IODP).

References

Allen, S. R., Fiske, R. S. and Tamura, Y., 2010, Effects of water depth on pumice formation in submarine domes at Sumizu, Izu-Bonin arc, western Pacific: Geology, 38, 391-394.

Glasby, G.P., and Notsu, K., 2003, Submarine hydrothermal mineralization in the Okinawa Trough, SW of Japan: an overview: Ore Geology Reviews, 23, 299–339.

Kawagucci, S., Chiba, H., Ishibashi, J.-I., Yamanaka, T., Toki, T., Muramatsu, Y., Ueno, Y., Makabe, A., Inoue, K., Yoshida, N., Nakagawa, S., Nunoura, T., Takai, K., Takahata, N., Sano, Y., Narita, T., Teranishi, G., Obata, H. and Gamo, T., 2011, Hydrothermal fluid geochemistry at the Iheya North field in the mid-Okinawa Trough: Implication for origin of methane in subseafloor fluid circulation systems: Geochemical Journal, 45, 109-124.

Nakagawa, S., Takai, K., Inagaki, F., Chiba, H., Ishibashi, J.-I., Kataoka, S., Hirayama, H., Nunoura, T., Horikoshi, K. and Sako, Y., 2005, Variability in microbial community and venting chemistry in a sediment-hosted backarc hydrothermal system: Impacts of subseafloor phase-separation: FEMS Microbiology Ecology, 54, 141-155.

Takai, K., Mottl, M.J., Nielsen, S.H., and the Expedition 331 Scientists, 2011. Proc. IODP, 331: Tokyo (Integrated Ocean Drilling Program Management International, Inc.).

Takai, K., Mottl, M.J., Nielsen, S.H., and the Expedition 331 Scientists, 2012. IODP Expedition 331: Strong and expansive subseafloor hydrothermal activities in the Okinawa Trough. Scientific Drilling, 13, 19-27.

Tsuji, T. Takai, K., Oiwane, H., Nakamura, Y., Masaki, Y., Kumagai, H., Kinoshita, M., Yamamoto, F., Okano, T. and Kuramoto, S., 2012. Journal of Volcanology and Geothermal Research, 213-214, 41-50.

Yeats, C., Hollis, S., Corona, J. C. and Expedition 331 Shipboard Scientific Party, 2012. Actively forming Kuroko-style massive sulfide mineralisation and hydrothermal alteration at Iheya North, Okinawa Trough — key petrological results of IODP Expedition 331. Abstract, 34th International Geological Congress, Brisbane, August 5-10, 2012.

Recent advances in structural geology, lithogeochemistry and exploration for VHMS deposits, Kristineberg area, Skellefte District, Sweden

Nils F Jansson, Tobias Hermansson, Mac Fjellerad Persson, Alexandra Berglund, Annika Kruuna
Boliden Mines, Exploration Department

Pietari Skyttä
University of Helsinki

Kai Bachmann, Jens Gutzmer
TU Bergakademie Freiberg

Reia Chmielowski, Pär Weihed
Luleå University of Technology

Abstract. Kristineberg is the largest mine and VHMS deposit in the Palaeoproterozoic Skellefte District, Sweden. The deposit was discovered in 1918, and it has been mined since 1941. Besides the Kristineberg deposit, several other VHMS deposits have been mined in the Kristineberg area. Despite the long history of mining, significant advances are still being made in terms of exploration and understanding the geological framework of the ore bodies. A key to this success has been persistence in exploration and a combination of local and regional scale geological, geophysical and geochemical surveys. Holistic industry-university collaborative research projects have furthermore played an important role in bringing together geologists and geophysicists from different disciplines to tackle the large-scale geological framework. Among other things, these projects have resulted in the first structural geological 3D model of the Kristineberg area, better age constraints on the formation of the deposits, a regional alteration map as well as ongoing work to model alteration in 3D. This contribution summarizes the results of these investigations and recent exploration.

Keywords. Kristineberg, Skellefte District, VHMS, 3D modelling, Exploration

1 Introduction

Kristineberg is the largest mine in the Palaeoproterozoic Skellefte District, Northern Sweden. The deposit was discovered during an electromagnetic survey in 1918, yet production did not start until 1941. Until present, c. 27.8 Mt ore has been produced from more than 10 lenses in the VHMS deposit, on average grading 3.74 % Zn, 1.04 % Cu, 1.4 g/t Au, 39 g/t Ag and 0.24 % Pb. Successful near-mine exploration is the key to the mine's longevity, and continues to add new reserves. The current proven and probable reserve totals 4.65 Mt.

Besides the Kristineberg mine, the Kristineberg area also hosts several other, abandoned mines such as the Rävlidmyran mine (7.18 Mt mined 1950-1991), the Rävliden mine (1.56 Mt mined 1941-1988), the Kimheden mine (0.13 Mt mined 1967-1969 and 1974-1975) and the Hornträskviken mine (0.64 Mt mined 1981-1991). These mines are currently of interest for the field exploration in the area (Fig. 1).

The Kristineberg deposit is hosted by the 1.89-1.88 Ga Skellefte group metavolcanic rocks (SG). The

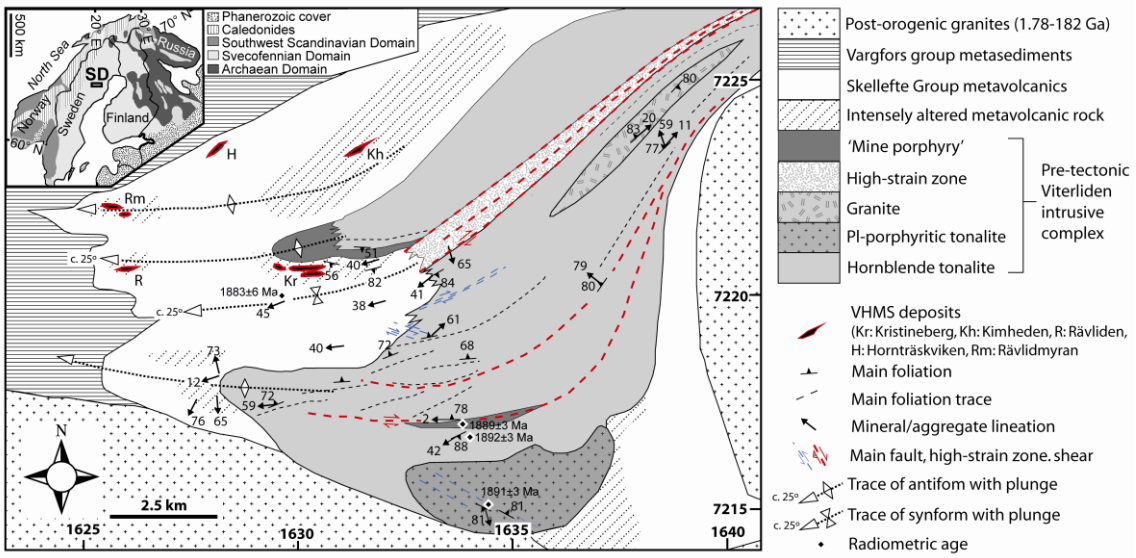

Figure 1. Regional geological map of the Kristineberg area. Inset shows the position of the Skellefte District in Fennoscandia. Modified after Årebäck et al. 2005, Barrett et al. 2005 and Skyttä et al. 2012.

volcanic rocks are towards the west overlain by the predominantly metasedimentary 1.88-1.87 Ga Vargfors group (VG). Whereas Kimheden occupies a similar stratigraphic level as Kristineberg, the other VHMS deposits occur close to the SG-VG contact (Fig. 1). The host stratigraphy is folded around gently to moderately WSW-plunging fold hinges. Axial surfaces are generally steeply-moderately S-dipping, and commonly sub-parallel to c. E-W trending high-strain zones. The ore lenses commonly have complex and variable geometries, ranging from sheet-like, moderately-steeply S-dipping lenses to more elongate, gently W plunging.

Following a review of mineral exploration in the Skellefte district carried out by Boliden in 2007, the Kristineberg area was defined as a top priority target, resulting in increased exploration activity and discoveries of new mineralization. A key to successful exploration has been the combination of local-scale exploration methodology, such as down-hole EM surveys, alteration mapping and deposit-scale lithogeochemical surveys, with regional scale geological, geochemical and geophysical surveys. The latter have in the last years been carried out as collaborations between Boliden and universities such as Luleå University of Technology (LTU), Uppsala University and TU Bergakademie Freiberg. Among other things, these projects have resulted in the first structural geological 3D model of the Kristineberg area, a regional alteration map as well as ongoing work to model alteration in 3D. This contribution summarizes the results of these investigations and recent exploration.

2 Structural geology

2.1 3D and 4D modelling of the Kristineberg area

The first regional 3D model of the Kristineberg area was developed during a recent multidisciplinary research project funded by VINNOVA (e.g. Dehghannejad et al. 2012; Skyttä et al. 2010; 2011) (Fig. 2). This was part of a larger project, aiming at developing robust 4D-models of the crustal evolution of the entire Skellefte district. The models incorporated data from field mapping, drill holes, mines, geochronology (Skyttä et al. 2011), reflection seismics (Dehghannejad et al. 2012), electromagnetics (Garcia-Juanatey 2012), locally detailed by IP and resistivity studies (Tavakoli 2012) and AMS studies (Skyttä et al. 2010).

A major outcome was the recognition of transpressional strain and coeval magmatic events across the district (Skyttä et al., 2011), indicating that the whole district was subjected to the same tectonic events at around 1.89 -1.80 Ga (Weihed et al. 2002; Skyttä et al. 2012). The new model for the regional structural evolution could explain why the NE-SW to E-W trending Kristineberg area structures deviate from the WNW-ESE structural grain of the central Skellefte district (Bauer et al. 2011). This was interpreted to reflect the localisation of the Kristineberg area at the lateral termination of a significant transpressional high-strain zone, transecting much of the central district. East of Kristineberg, the zone splays into several branches and defines zones of coaxial and non-coaxial deformation resulting in increasingly complex structure, including significant variations in the plunge of the large antiformal structure where Kristineberg is located.

Reflection seismic results in the vicinity of the Kristineberg deposit indicated that the most pronounced reflectors are sub-horizontal and occur at around 2 km depth below the surface, whereas at higher level the reflectors are less distinct and less continuous (Dehghannejad et al. 2010; 2012). The seismic data is in agreement with ore lens geometries and geological sections interpreted from drill holes, which show coincidence between seismic discontinuities and high-strain zones. The high-strain zones caused transposition of the primary strata and individual ore lense into moderately- to steeply-dipping orientations (Årebäck et al. 2005), and earlier, probably also controlled the localization of the deposits during mineralization.

Coupling between the kinematic evolution of the high-strain zones and the deposit geometries show that

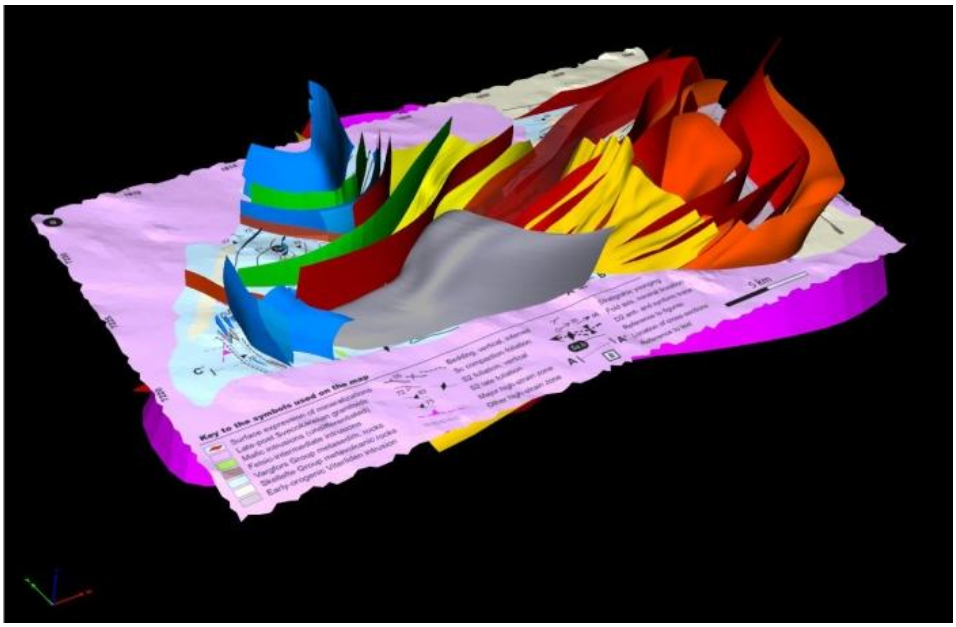

Figure 2. 3D model of the Kristineberg area. The different sheets represent modelled major stratigraphic and intrusive contacts and high-strain zones in the area, shown relative to regional surface geology map.

the most significant tectonic transposition is due to reverse movements along the S-dipping high-strain zones (Årebäck et al. 2005). However, overprinting dextral strike-slip shearing and localized sub-horizontal tectonic flow at deep crustal levels, as observed from the Viterliden intrusion stratigraphically below the ore-hosting volcanic rocks (Fig. 1), is inferred to locally have caused transposition at the ore-lens scale (Skyttä et al. 2010).

2.2 Mine-scale investigations

Pervasive overprint by strong-intense hydrothermal alteration and medium-grade metamorphism precludes the possibility of detailed stratigraphic analysis in the Kristineberg mine (Årebäck et al. 2005). Most mineralization is hosted by rocks such as sericite quartzite, andalusite quartzite, chlorite schist and sericite schist, formed by hydrothermal alteration, deformation and metamorphism of originally compositionally distinct, yet now indistinguishable volcanic rocks. The difficulty in distinguishing the various original volcanic rocks has for many years presented a major obstacle to structural analysis. By systematic drill core sampling and immobile element techniques, Barrett et al. (2005) identified several distinct rhyolitic and dacitic-intermediate precursor compositions around the mined ore lenses. These defined a distinct chemostratigraphy which could be used to differentiate between stratigraphic footwall and hanging-wall in the Kristineberg mine. Rock division based on immobile element ratios furthermore provided information on the structural framework of the ore lenses, such as the approximate concordance of the old A and B lenses to original boundaries between compositionally distinct volcanic rocks.

Recent studies have extended this approach to also include currently mined gently west-plunging lenses in the western part of the mine. The results revealed a much more complicated geological picture than inferred in previous surveys, involving significant N-vergent stacking of the altered host stratigraphy along S-dipping high-strain zones (Fig. 3). This is in agreement with the regional structural framework as described above, and provides an explanation for the complex geometry and distribution of ore lenses in the central to western parts of the Kristineberg mine.

3 Geochemistry

3.1 Kristineberg alteration map

Similar to other VHMS deposits globally, the deposits in the Kristineberg area are surrounded by hydrothermal alteration envelopes that are zoned in terms of alteration intensity, mineralogy and whole-rock composition. One approach to discover new mineralization is to study the extent and zonation of these alteration zones regionally.

Bachmann (2012) compiled all available near-surface lithogeochemical data and conducted complementary sampling in outcrops and drill holes. The aim was to obtain a regional coverage of near-surface lithogeochemical samples that could be used to extend the different chemostratigraphic units of Barrett et al. (2005) and model the variations in alteration intensity and style in the entire Kristineberg area. The data was used to construct surface alteration maps, showing variations in alteration indices such as the Ishikawa Alteration Index (AI; Ishikawa et al. 1976) and Chlorite-Carbonate-Pyrite-Index (CCPI; Large et al. 2001). Among other things, these alteration maps showed that known deposits correlate best with coincidence of high AI and CCPI values.

An ongoing research project aims at extending this approach to depth, to produce the first 3D geochemical model of a mining area in Sweden. The model will be based on lithogeochemical data from the database of Boliden and new drill core samples, and will be constrained by the existing 3D structural model. The project is a joint collaboration between the Luleå University of Technology (LTU) and Boliden. It aims at improving our understanding of the mass changes, geometry and zonation of hydrothermal alteration zones in the Kristineberg area. A benefit of 3D volumes instead of 2D sections is that prospective rock volumes can be constrained in 3D. As a result mineralization at depth can be targeted with improved accuracy.

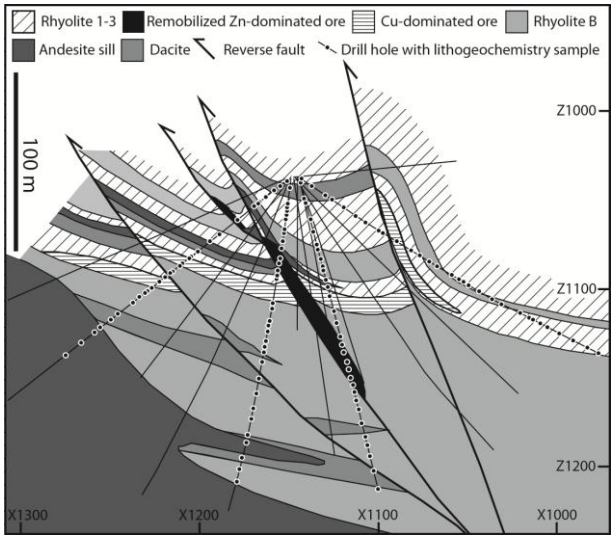

Figure 3. Cross-section along 1450Y (facing ENE) in the J zone of the Kristineberg mine, displaying interpreted chemostratigraphy and structure based on immobile element rock classification. Modified after Hermansson (2012).

3.2 Geochronology

By careful selection of samples for SIMS U-Th-Pb zircon dating, Skyttä et al. (2011) constrained the age of the Kristineberg deposit. The youngest sampled phase of the Viterliden intrusion, which contains xenoliths of hydrothermally altered volcanic rocks, was dated at 1889±3 Ma (Fig. 1). A felsic metavolcanic rock in the stratigraphic hanging-wall, inferred to be younger that the Kristineberg sulphide ore, was dated at 1883±6 Ma. These two ages were inferred to constrain a minimum age of the deposit. The 1883±6 Ma age provides a maximum age for the stratigraphically higher Rävliden,

Rävlidmyran and Hornträskviken deposits, as these are situated stratigraphically above the dated unit (Fig. 1).

4 Exploration

4.1 Near mine exploration

Recent exploration has been largely focused on the area just west of the mine, a successful strategy resulting in the discovery of several mineralized zones. One of the most important discoveries is the L-zone, which runs roughly parallel to the J-zone (Fig. 3). It was first indicated in a ground EM survey as a geophysical anomaly at depth. In 2004 a westward plunging system of massive sulphide lenses was intersected in drillholes covering a vast horizontal strike.

High-grade parts are typically chlorite schist-hosted, tectonically remobilized and rich in pyrite-sphalerite, although the zone changes character westwards and become more Cu- and Au-dominated. The geological setting of the ore lenses is consistent with that of other ore bodies in the mine, i.e. strongly altered and schistose volcanic rocks that only rarely display primary textures. Geometries vary within the zone due to folding and thrusting, but the general trend is a gentle plunge to the west in accordance with the large scale anticline-syncline structure in which the Kristineberg deposit is located.

Extensive exploration drilling has systematically followed the zone westwards and in 2006 volumes were subsequently added to mineral resources. In 2011, parts of the zone were taken into production.

4.2 Field exploration

The concept of N-vergent stacking in the Kristineberg area has been of importance during the re-appraisal of the potential for new discoveries regionally. A new structural model for the SG-VG contact has allowed more efficient targeting. The precursor to this model was first conceptualized internally by Boliden and a structural consultant (Dave Coller) supplemented by new seismic investigations during the VINNOVA project, and further refined in 3D by Skyttä et al. (2012) (Fig. 2). Successful application and continued refinement of this model has led to the recognition of new targets, which are under investigation.

5 Conclusions

After 72 years of mining, the Kristineberg area is still one of the most productive areas in the Skellefte District. A key to this success has been persistence in exploration and a combination of local and regional scale in-depth geological, geophysical and geochemical surveys. These have increased our knowledge of the structural framework and evolution of the area, the geometry of the mined sulphide lenses, the nature and zonation of hydrothermal alteration. They have furthermore led to the recognition of new prospective areas, which may help to extend the life of this mining area even further.

References

Årebäck H, Barrett TJ, Abrahamsson S, Fagerström P (2005) The Palaeoproterozoic Kristineberg VMS deposit, Skellefte District Sweden, part 1: geology. Mineral Deposita 30 351-367

Bachmann K (2012) Chemostratigraphy and alteration in the area of the Kristineberg VHMS deposit, Skellefte district, Sweden. Unpublish Dipl, Thesis. TU Bergakademie Freiberg. 29 pp.

Barrett TJ, MacLean WH, Årebäck H (2005) The Palaeoproterozoic Kristineberg VHMS deposit, Skellefte District, Sweden: Part II: chemostratrigraphy and alteration. Mineral Deposita 40:368-395

Bauer T, Skyttä P, Allen R, Weihed P (2011) Syn-extensional faulting controlling structural inversion: Insights from the Palaeoproterozoic Vargfors syncline, Skellefte mining district, Sweden. Precambrian Research 191:166-183.

Deghannejad M, Malehmir A, Juhlin C, Skyttä P (2012) 3D constraints and finite-difference modeling of massive sulphide deposits: The Kristineberg seismic lines revisited, northern Sweden. Geophysics 77: WC69–WC79

Garcia Juanatey M (2012) Seismics, 2D and 3D Inversion of Magnetotellurics: Jigsaw pieces in understanding the Skellefte Ore District. Unpublished Ph.D. thesis. Uppsala University. 46 pp.

Hermansson T (2012) Lithogeochemical characterization and structural analyses of two cross-sections in the J- and L-zones, Kristineberg mine, western Skellefte district. Boliden Mineral AB internal report 2012-30, 30 pp.

Ishikawa Y, Sawaguchi T, Iwaya S, Horiuchi M (1976) Delineation of prospecting targets for Kuroko deposits based on modes of volcanism of underlying dacite and alteration halos. Mining Geology 26:105–117.

Large RR, Gemmell JB, Paulick H (2001) The alteration box plot: A simple approach to understanding the relationship between alteration, mineralogy and lithogeochemistry associated with volcanic-hosted massive sulphide deposits. Econ Geol 96:957-971.

Skyttä P, Hermansson T, Bauer T (2009) Three Dimensional Structure of the VMS-hosting Palaeoproterozoic Kristineberg Area, Northern Sweden. Proceedings of the 10th biennial SGA meeting, Townsville, Australia, 909–911.

Skyttä P, Hermansson T, Elming S-Å, Bauer T (2010) Magnetic fabrics as constraints on the kinematic history of a pre-tectonic granitoid intrusion, Kristineberg, northern Sweden. Journal of Structural Geology 32:1125–1136.

Skyttä P, Hermansson T, Andersson J, Whitehouse M, Weihed P (2011) New zircon data supporting models of short-lived igneous activity at 1.89 Ga in the western Skellefte District, central Fennoscandian Shield. Solid Earth 2:205-217

Skyttä P, Bauer T, Hermansson T, Deghannejad M, Juhlin C, Garcia M, Hübert J, Weihed P (2012) Structural evolution of the VMS-hosting Kristineberga area, Sweden – constraints from the structural analysis and 3-D modeling. Solid Earth Discuss 4: 1281-1315.

Tavakoli S (2012) Geophysical investigation for 3D geological modelling and ore exploration in the Skellefte mining district. Unpublished Ph.D thesis. Luleå University of Technology. 33 pp.

Weihed P, Billström K, Persson P.-O, Bergman Weihed J (2002) Relationship between 1.90–1.85 Ga accretionary processes and 1.82–1.80 Ga oblique subduction at the Karelian craton margin, Fennoscandian Shield. GFF 124:163–180.

Structural investigation and 3D modelling of the Falun pyritic Zn-Pb-Cu-(Au-Ag) sulphide deposit, Bergslagen region, south-central Sweden

Tobias C. Kampmann and Pär Weihed
Department of Civil, Environmental and Natural Resources Engineering, Division of Geosciences, Luleå University of Technology, SE-971 87 Luleå, Sweden

Michael B. Stephens
Geological Survey of Sweden (SGU), Box 670, SE-751 28 Uppsala, Sweden and Department of Civil, Environmental and Natural Resources Engineering, Division of Geosciences, Luleå University of Technology, SE-971 87 Luleå, Sweden

Abstract. One of the prominent ore deposits of the Bergslagen region in south-central Sweden is located in Falun in the northern part of this mining district. A belt of 1.91-1.89 Ga metavolcanic rocks hosts both the ores and an alteration aureole of several hundreds to thousands of metres in extent at the ground surface. Analysis of the structures in the area reveals a polyphase ductile deformational history and a major, steeply plunging F_2 reclined fold. 3D modelling of the boundary surface to the pyritic Zn-Pb-Cu sulphide ore has been used to visualize the geometry of this ore body at depth, constraining its steeply plunging rod-like and NW-SE elongate shape and a geometric control by the F_2 fold structure.

Keywords. Structural geology, 3D modelling, Bergslagen, Falun, base metal sulphide deposit.

1 Introduction

The Bergslagen region in south-central Sweden (Fig. 1) hosts several thousand mineral deposits, predominantly iron oxide and base metal sulphide deposits, containing, in some cases, significant enrichments in the precious metals gold and silver. The pyritic Zn-Pb-Cu-(Au-Ag) sulphide deposit at Falun in the northern part of Bergslagen (Fig. 1) has been one of the most influential base metal producers in Sweden. Mining operation at Falun continued for about 1000 years with a total production of approximately 28-35 Mt of ore. Operation ceased during 1992.

Despite the major role of the Falun deposit in Sweden's mining history, the geology and genesis of this deposit are poorly understood. Earlier studies either have a focus on the regional context (e.g. Koark 1973; Kresten 1986; Bromley-Challenor 1988; Sundblad 1994; Allen et al. 1996; Stephens et al. 2009) or represent studies of some particular aspect of the deposit itself (e.g Koark 1962; Weijermars 1987; Gavelin 1989; Åberg & Fallick 1993). Older literature presents valuable, more detailed descriptions (e.g. Törnebohm 1893; Geijer 1917; Tegengren 1924).

This study is part of a 4-year PhD project at the Luleå University of Technology, Sweden, which aims to provide an understanding of the genesis of the Falun deposit. The main focus lies on the relationship of the ore bodies to the local structural framework, on the timing and mechanisms of ore formation, on the nature and role of hydrothermal alteration and on geometallurgical aspects. 3D modelling will aid in the visualization of the deposit thereby permitting the more detailed investigation of structures, hydrothermal alteration and ore volumes in 3D space.

In this extended abstract, some initial results of the structural investigation and the 3D modelling work are presented. The work is based on field investigations, thin-section microscopy as well as on information compiled during the active mining.

2 Regional geological setting

Bergslagen is located in the south-western part of the Svecokarelian orogen inside the Fennoscandian Shield (Fig. 1). The area consists of a supracrustal sequence of metasedimentary and felsic metavolcanic rocks, intruded by plutonic rocks. Magmatic activity, hydrothermal alteration, ductile deformation and regional metamorphism took place between 1.9 and 1.8 Ga (Stephens et al. 2009). The vast majority of the iron oxide and base metal ore deposits, including Falun, occur in the upper part of the 1.91-1.89 Ga felsic metavolcanic sequence, in close spatial affinity with carbonate rock and skarn (Allen et al 1996). Falun lies in the north-western part of a structural domain where folds with an E-W to NE-SW axial surface trace and ductile shear zones with similar strike are conspicuous (Stephens et al. 2009, Beunk and Kuipers 2012). Low-P/variable-T metamorphism prevailed (Stephens et al. 2009). The rocks formed and were affected by tectonic events along an active continental margin in a convergent plate boundary setting (Stephens et al. 2009).

3 Geology of the Falun pyritic Zn-Pb-Cu-(Au-Ag) sulphide deposit

The Falun deposit is located inside an E-W striking inlier of felsic metavolcanic rock surrounded by metamorphosed granitoid and dioritoid of slightly younger age (Kresten 1986). The mineralization is spatially associated with a complex alteration system. Ductile deformation and amphibolite-facies metamorphism overprinted the rocks in the area and also reworked the alteration mineralogies in and around the deposit. Altered rock types are represented now by

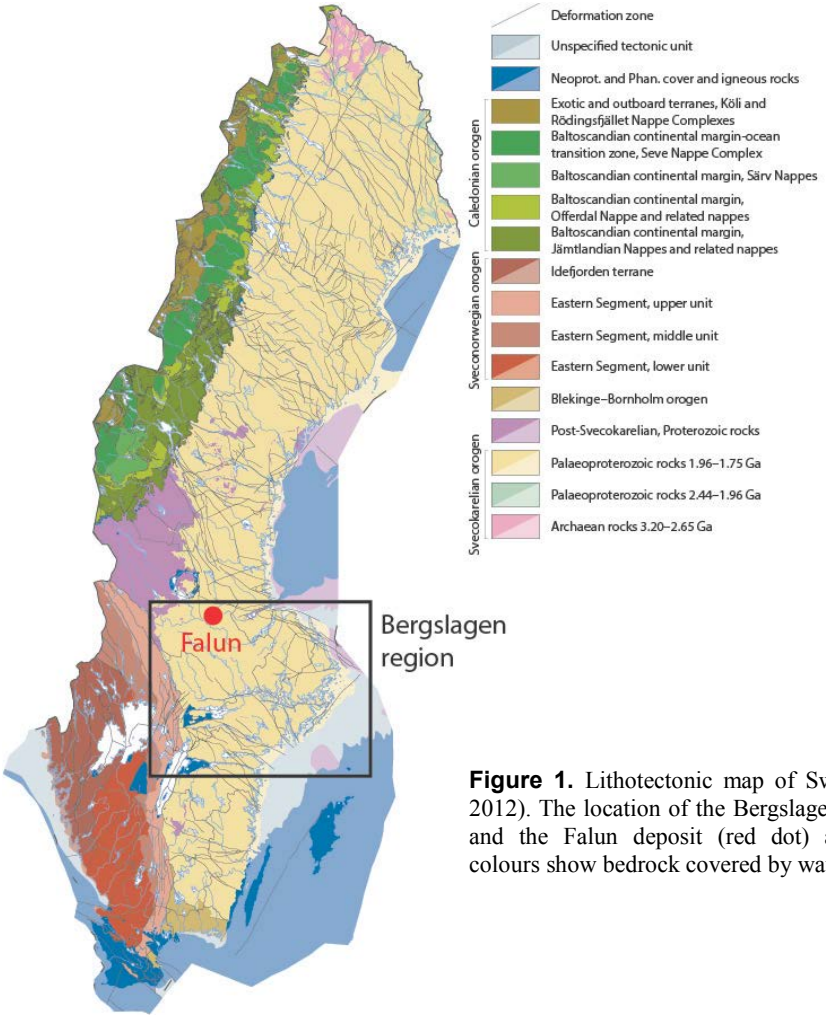

Figure 1. Lithotectonic map of Sweden (Bergman et al. 2012). The location of the Bergslagen region (black frame) and the Falun deposit (red dot) are highlighted. Paler colours show bedrock covered by water.

various types of quartzite, mica schist and skarn.

The alteration zone at Falun shows an E-W elongation and is c. 30 km^2 in areal extent at the ground surface. The main ore body is located in the central part of this alteration zone (Kresten, 1986). Zoned Mg-alteration is common, with an inner "ore-quartzite" zone characterized by the assemblage quartz-cordierite-anthophyllite-almandine-cummingtonite-(andalusite) surrounded by quartz-mica schist with cordierite-anthophyllite assemblages, representing the outer part of the zone (Koark, 1986). On a local scale in the mine, skarn horizons are common, showing assemblages of diopside-hedenbergite and tremolite.

The Falun deposit and alteration system are spatially associated with a large-scale fold structure which has been described as a steeply SSE-plunging synform (Weijermars 1987). Two main ore types can be distinguished. The pyritic Zn-Pb-Cu more massive sulphide, so-called "soft" ore is thickened and concentrated in the fold hinge, is apparently cylindrically-shaped and continues down to c. 450 m elevation below sea-level (-450 m). According to Geijer (1917), this ore type mainly replaces the carbonate rock. The Cu-Au, so-called "hard" ore is found along the limbs of the structure, both to the east and to the west of the open pit and the "soft" ore. It is hosted by quartzite, with cummingtonite as a common accessory mineral.

4 Methods

Observations of rock type and structures, both inside and up to several kilometres around the open pit, were obtained during field investigations 2012. Structural orientations were measured and both oriented and non-oriented rock samples were collected for later reference and microstructural analysis. All field observations were archived using the software BGDATA 2.0 (SGU).

The 3D modelling work has so far been based on 1:500 mine level maps from the Falun mine. The vertical distances between the mapped levels vary between 15 and 120 m. The maps were imported into the 3D modelling software GOCAD 2009.3 (Paradigm) and referenced according to their geographic (coordinate system SWEREF 99) and vertical positions. The outlines of the pyritic Zn-Pb-Cu massive sulphide ore were traced on each map level and later connected creating a surface representing the outer boundary between the sulphide body and the surrounding altered rock mass.

Geometric information on boreholes at the Falun mine was taken from a database consisting of c. 1200 boreholes drilled between 1893 and 1991. Approximately 50% of the boreholes contained sufficient information for their visualization in 3D space. These c. 600 boreholes were then modelled in GOCAD according to their start coordinates (coordinate system SWEREF 99), azimuth, inclination and length.

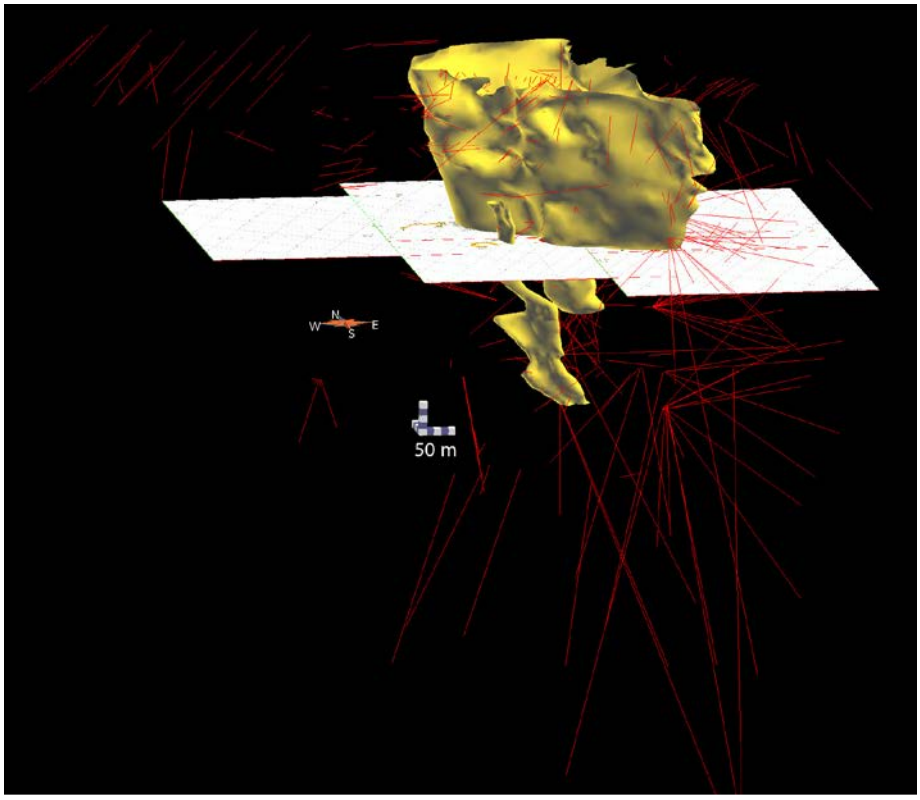

Figure 2. 3D model for the bounding surface of the pyritic Zn-Pb-Cu massive sulphide ore at Falun (yellow). Red lines represent boreholes drilled during the years 1893 to 1991 with sufficient information to permit presentation in 3D space. As an example, one layer of mine level maps at -110 m elevation is shown. The mine level maps from +120 m down to -460 m elevation have been used at this stage to model the ore body at depth. Further work is in progress. The ground surface at the open pit (top of the model) lies at +140 m elevation.

5 Results

5.1 Polyphase ductile deformation

Structural measurements indicate the presence of two distinct tectonic foliations, referred to here as S_1 and S_2. S_2 can be recognized in nearly every outcrop and is defined by oriented biotite and muscovite in the more mafic and felsic rocks, respectively. S_2 is usually steep (dip 70-90°) and strikes E-W to NE-SW, commonly with a dip to the S to SE. The foliation is generally absent or only weakly preserved in the metamorphic mineral assemblages in the strongly Mg-altered rocks. Most of the lithological contacts in the area show the same orientation as S_2. Sub-vertical phyllosilicate-rich shear zones, typically 0.5 to 1 m thick, are commonly observed along rock contacts, but also steeply cross-cut the fabric.

S_1 is characteristically deformed in sub-vertical folds with axial surfaces sub-parallel to S_2. This is most apparent in the hinge zone of a large-scale fold in the open pit where S_1 is rotated parallel to the fold geometry, whereas S_2 is penetrative and developed parallel to the NE-SW striking axial surface trace.

A SE steeply (60°) plunging stretching lineation has locally been observed in the Falun open pit. When recognizable, it is defined by oriented quartz and amphibole in the quartzitic alteration rock.

5.2 Geometry of the massive sulphide ore body using 3D modelling

The first results of the 3D modelling work are shown in Fig. 2. The pyritic Zn-Pb-Cu massive sulphide ore forms an NW-SE elongate and steeply inclined rod-like structure. It is situated in the hinge zone of the large-scale F_2 fold and follows its continuation at depth. At its base at -400 m to -200 m elevation, three spatially separated sulphide lobes are present which thin and eventually pinch out downwards at different depths. Towards the ground surface, the lobes merge and form a single body, ranging vertically from c. -160 m up to the ground surface at the top of the open pit at c. +140 m. Over these c. 300 m of vertical distance, the body thickens significantly upwards from a diameter of c. 90 m at the base to c. 270 m at the top (Fig. 2). The thin lateral continuation of the body towards the SE has not yet been modelled.

Visualization of the c. 600 boreholes shows exploration drilling at depths down to c. -850 m elevation and at the ground surface, mainly W and SE of the Falun mine. Numerous, often flat-lying to horizontal boreholes up to 100 m length penetrate the massive sulphide ore body from the surrounding rock mass or lie entirely inside this ore body.

6 Discussion

Strain-localisation in phyllosilicate-rich shear zones plays an important role in the Falun area, leaving much of the surrounding rock mass less affected by the ductile deformation.

Since many of the rock units and contacts in the Falun area, both in outcrop and on map scale (Kresten 1986), show strikes parallel to the S_2 foliation, intense D_2 transposition is inferred. The sulphide ore body at the Falun mine which is elongate in a NW-SE direction at the ground surface and steeply rod-like in shape in the vertical dimension is structurally controlled by the D_2 deformation. The large-scale fold, which hosts the ores in its hinge zone, has been previously described as a SE-dipping upright synform (Weijermars 1987). Structural data obtained in this study indicate a reclined structure with a steeply plunging stretching lineation parallel to the fold axis. This is in accordance with observations elsewhere inside the structural domain in Bergslagen where Falun is located (Stephens et al. 2009).

Folding seems to occur at different scales and with different orientations around the mine (Koark 1962). At this point in time, two possibilities could account for the observed pattern. The folding might resemble (1) parasitic folding related to the D_2 deformational event or (2) refolding of F_2 structures during a later (D_3) event. Further investigations are needed to address this matter which is crucial for our understanding of the deformational history around the Falun deposit. The origin of the observed lobes at the base of the sulphide ore body also require closer attention, bearing in mind that the quartzitic alteration rock with Cu-Au "hard" ore, east and west of the massive sulphide "soft" ore, may represent a feeder system to the latter.

7 Conclusions

Structural investigation shows two distinct foliations are present in the rocks of the Falun region. S_2 is the dominant fabric and gave rise to significant transposition of the primary stratigraphy and D_1 grain-shape fabric.

A large-scale, steeply SE-plunging, reclined F_2 fold is the dominant structural feature at the Falun mine. The presence of polyphase ductile deformation and a stretching lineation oriented parallel to the steep fold axis is consistent with earlier structural observations in the central part of the Bergslagen region.

Initial 3D visualization of the Falun pyritic Zn-Pb-Cu more massive sulphide ore ("soft" ore) shows a steeply inclined, irregular, rod-like body that is also elongate in a NW-SE direction and situated in the hinge zone of the large-scale F_2 fold. The D_2 deformation exerts significant geometric control on the ore body (see also Weijermars 1987). Several sulphide lobes at the base of the massive sulphide ore merge upwards and the rod-shaped ore body thickens significantly towards the ground surface.

Acknowledgements

SGU provides the economic support to this PhD project. Magnus Ripa, Per Nysten and Anders Hallberg (all at SGU) and Stina Danielsson (Boliden Mineral AB) are thanked for their general support and for providing key information on the old mine data from Falun. Tobias Bauer (Luleå University of Technology) is thanked for the technical assistance in the 3D modelling work.

.

References

Allen RL, Lundström I, Ripa M, Simeonov A, Christofferson H (1996) Facies Analysis of a 1.9 Ga, Continental Margin, Back-Arc, Felsic Caldera Province with Diverse Zn-Pb-Ag-(Cu-Au) Sulphide and Fe Oxide Deposits, Bergslagen Region, Sweden. Econ Geol 91:979-1008.

Åberg A, Fallick AE (1993) A fluid inclusion and light element stable isotope study of the gold-bearing quartz vein system, Falun, Sweden. Miner Depos 28:324-333.

Bergman S, Stephens MB, Andersson J, Kathol B, Bergman T (2012) Bedrock map of Sweden, scale 1:1 million. Geol Surv of Swed K 423, Uppsala, Sweden.

Beunk FF, Kuipers G (2012) The Bergslagen ore province, Sweden: Review and update of an accreted orocline, 1.9–1.8 Ga BP. Prec Res 216-219:95-119.

Bromley-Challenor MD (1988) The Falun supracrustal belt. Part 1: primary geochemical characteristics of proterozoic metavolcanics and granites. Geol en Mijnb 67:239-253.

Gavelin S (1989) Genesis of the Falun sulphide ores, central Sweden. Geol Fören i Stockh Förh 111:213-227.

Geijer P (1917) Falutraktens berggrund och malmfyndigheter. Geol Surv of Swed, Series C 275:1-316.

Koark HJ (1962) Zur Alterstellung und Entstehung der Sulfiderze vom typus Falun. Geol Rundsch 52:123-146.

Koark HJ (1973) Zur Entstehung des tektonischen Stengelbaus an präkambrischen Eisen- und Sulfiderzkörpern der zentralschwedischen Leptitserie. Miner Depos 8:19-34.

Kresten P (1986) Geochemistry and tectonic setting of metavolcanics and granitoids from the Falun area, south central Sweden. Geol Fören i Stockh Förh 107:275-285.

Stephens MB, Ripa M, Lundström I, Persson L, Bergman T, Ahl M, Wahlgren CH, Persson PO, Wickström L (2009) Synthesis of the bedrock geology in the Bergslagen region, Fennoscandian Shield, south-central Sweden. Geol Surv of Swed, Series Ba, Uppsala, Sweden.

Sundblad K (1994) A genetic reinterpretation of the Falun and Åmmeberg ore types, Bergslagen, Sweden. Miner Depos 29:170–179.

Tegengren FR (1924) Sveriges ädlare malmer och bergverk. Geol Surv of Swed, Series Ca 17, Uppsala Sweden.

Törnebohm AE (1893) Om Falu gruvas geologi. Geol Fören i Stockh Förh 15:609-690.

Weijermars R (1987) Structure, origin, history and future of Falun´s sulfide deposit, Bergslagen ore province, central Sweden. Report for Stora Kopparbergs Bergslag AB, Falun, Sweden.

Potential sulfur sources for submarine caldera associated mineralization in north-west Wales

Paul A. J. Lusty
British Geological Survey, Environmental Science Centre, Nicker Hill, Keyworth, Nottingham, NG12 5GG, UK

Craig D. Barrie
Isoprime Ltd, Isoprime House, Earl Road, Cheadle Hulme, Cheadle, SK8 6PT, UK

Adrian J. Boyce
Scottish Universities Environmental Research Centre, Rankine Avenue, East Kilbride, G75 0QF, UK

Abstract. In north-west Wales vein mineralization is hosted by the Ordovician Snowdon Volcanic Group, and older sedimentary rocks. Mineralization typically consists of narrow, steeply dipping base metal veins, stockworks, disseminated sulfides and quartz-sulfide cemented breccia zones. Sulfur isotope analyses were carried out on vein sulfides and country rocks to elucidate ore sulfur source/s. The volcanic-hosted and the majority of sedimentary rock-hosted sulfides have $\delta^{34}S$ from +9.1 to +22.3‰, with mean vein $\delta^{34}S$ of +12.2 ± 3.7‰. The Snowdon Volcanic Group is generally considered to represent a reservoir of isotopically heavy sulphur with mean $\delta^{34}S$ of +11.7‰ ± 4.5‰. The sedimentary rock diagenetic sulfides are typically heavier. These values are thus compatible with a typical volcanogenic massive sulfide system, with sulfur originating from a combination of leaching of volcanic host lithologies, and reduction of Ordovician seawater. The $\delta^{34}S$ ore sulfides from around Snowdon are comparable to those found in Ordovician age volcanogenic massive sulfide deposits globally.

Sulfides, Welsh Basin, Submarine, Caldera, VMS

1 Introduction

Calderas formed by the eruption of a sub-surface magma chamber and subsequent collapse represent very important ore-forming environments (Stix et al. 2003).

The Snowdon caldera, a Caradoc-age resurgent rhyolitic caldera developed in a shallow marine environment, in north-west Wales, hosts a well constrained, globally important record of submarine volcanic processes (Howells et al. 1986; Howells et al. 1991).

The caldera is host to numerous minor base metal veins and localised occurrences of magnetite-rich mineralization, distributed over an area of ~70 km^2 (Figure 1). Additional base metal mineralization occurs to the west of the caldera (Nantlle Valley), hosted principally by Upper Cambrian and Ordovician sedimentary rocks, proximal to a major acidic pluton.

The proposed model for the genesis of the Snowdon caldera-hosted veins invokes a sub-caldera intrusion driving convective circulation of seawater and magmatic fluids through caldera-related fractures, leaching metals from the host rocks, with mineral deposition at a late stage in the evolution of the caldera (Reedman et al. 1985). However, the link between the caldera-hosted mineralization and Caradoc magmatism is based solely on their close spatial association and a genetic and temporal relationship remains conjectural.

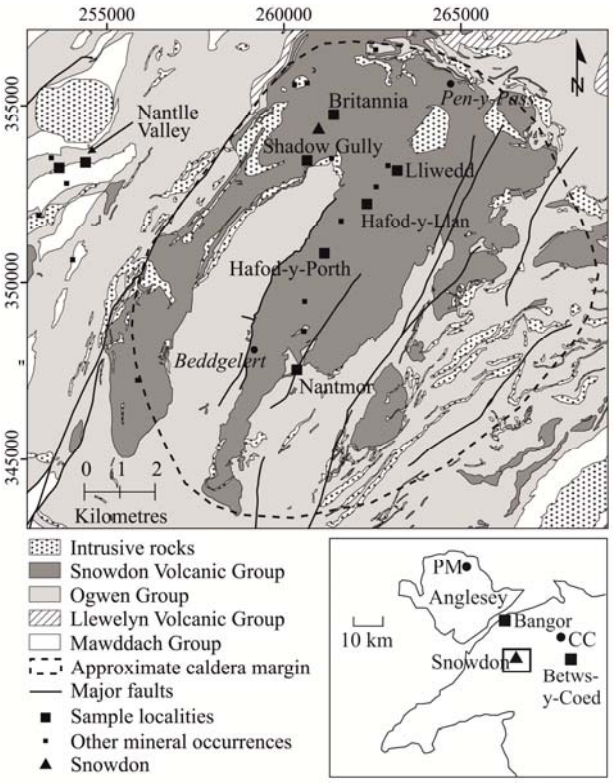

Figure 1. Inset: location of the study area in north-west Wales (black square), CC = Cae Coch, PM = Parys Mountain. Simplified geological map of the area around Snowdon, showing the extent of the caldera according to Howells et al. (1986), distribution of mineral occurrences and sample localities. BGS 1: 50 000-scale digital geological map © NERC 2013. All rights reserved.

2 Geological Setting

2.1 Tectonic Overview

The Lower Palaeozoic rocks of Wales consist of a thick sequence of principally marine sedimentary and intercalated volcanic rocks that accumulated in the Welsh Basin (Howells et al. 1991). During the Ordovician the Welsh Basin was located close to an ensialic convergent plate margin, probably active from

late Tremadoc to Caradoc times (Howells et al. 1991). Major volcanism and subsidence within the basin was focussed along relatively narrow, repeatedly-subsiding graben systems, controlled by faults splaying off deep-seated basement fractures (Kokelaar, 1992).

2.2 Local Geology

The geology around Snowdon is described in detail by Howells et al. (1991) and Howells and Smith (1997) and references therein. The Snowdon Volcanic Group (SVG) of Longvillian age (Howells et al. 1986) is the principal host to the caldera-hosted vein mineralization and represents the peak of volcanism in the Snowdon Graben (Kokelaar, 1992). In the vicinity of Snowdon, in upward succession, the SVG comprises: the Lower Rhyolitic Tuff Formation (LRTF) representing a major acidic caldera-forming phase; the overlying Bedded Pyroclastic Formation (BPF) derived from post-caldera basaltic volcanism; and the Upper Rhyolitic Tuff Formation (URTF) indicating a return to acidic volcanism (Howells et al. 1991). Intrusive and extrusive rhyolites are a conspicuous feature of the caldera. The SVG principally overlies Ordovician marine siliclastic rocks of the Ogwen Group.

North-east-striking faults were most important in the geological evolution of the Snowdon district, controlling the shape of the Snowdon Graben (Howells and Smith, 1997). The most significant structures in terms of potential controls on caldera-hosted mineralization are those related to development of the Snowdon Centre and contemporaneous volcano-tectonic structures (Figure 1).

2.3 Metallogeny and Mineralization Style

The caldera-hosted mineralization principally occurs in the SVG, although at Nantmor veins extend into sub-LRTF sedimentary rocks. The mineralization typically consists of narrow (1–30 cm wide), steeply dipping veins, which pinch and swell forming localised stockworks, quartz-sulfide cemented breccia zones and disseminated sulfides. The principal gangue mineral is quartz. Pyrite is the dominant sulfide with subordinate amounts of chalcopyrite and sphalerite, localised occurrences of pyrrhotite, galena and magnetite and sporadic native copper, hematite, marcasite, azurite and covellite (Reedman et al. 1985). Two quartz-magnetite-hematite veins occur at Shadow Gully and Cwm Tregalan at the base of the LRTF (Colman and Appleby, 1991).

Comparable base metal mineralization occurs in the Upper Cambrian (Mawddach Group) and Ordovician (Ogwen Group) sedimentary rocks to the west of the caldera. The mineralization has similar mineralogy, is structurally controlled and appears to favour more competent horizons within the sequence.

The samples used in this study are representative of the range of mineralization styles occurring within and outside the caldera and include sulfide-bearing crack-seal quartz veins, quartz-sulfide cemented breccias and zones of disseminated sulfides (Figure 2).

Reedman et al. (1985) suggested exhalation of base metal-rich fluids into an appropriate marine environment in Snowdonia could have resulted in Kuroko-style volcanogenic massive sulfide (VMS) mineralization. However, no evidence for strata-bound exhalative mineralization has been observed within the caldera. The only known VMS-style mineralization in Snowdonia is the Cae Coch deposit, located 20 km north-east of Snowdon (Bottrell and Morton, 1992). North of Snowdonia, on Anglesey, lenses of massive Zn-Pb-Cu sulfides occur at the Parys Mountain deposit (Figure 1).

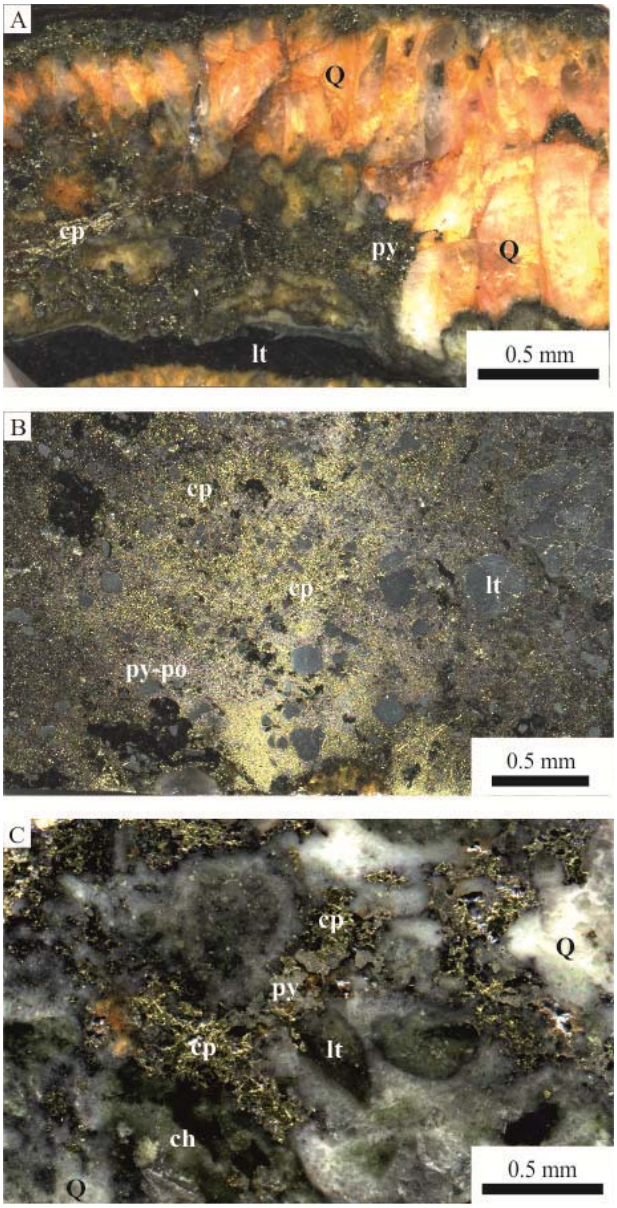

Figure 2. Examples of textures observed in the mineralization around Snowdon. A. Lliwedd (SMM137): sulfide-bearing comb quartz vein; B. Lliwedd (SMM136): sulfide (>80%) cemented breccia, dominated by pyrite, chalcopyrite, pyrrhotite; C. Nantmor (SMM16): chloritized, silicified, chalcopyrite-pyrite-bearing breccia.

3 Methodology

A selection of 75 samples was prepared from surface

exposures and mine waste tips, as polished thin sections, to supplement about 80 polished thin sections existing from previous British Geological Survey work around Snowdon. An additional 20 polished blocks were prepared for optical mineralogy and SEM study prior to isotopic analysis. A total of 19 country rock samples was collected to produce sulfide concentrates for S isotope analysis, with only seven yielding sufficient sulfide. Conventional S isotope analyses were complemented with *in-situ* laser analyses (Wagner et al. 2002) to elucidate sulfur source/s and genetic processes for the mineralization.

4 Sulfur Isotope Results

Data for vein material was collected on a range of phases: pyrite, chalcopyrite, sphalerite, galena, arsenopyrite and pyrrhotite and is summarised in Table 1. The overall mean for the vein sulfides is +12.2 ± 3.7‰.

Locality	$\delta^{34}S$ (‰) range	$\delta^{34}S$ (‰) mean
Britannia	+9.4–+12.9	+11.8
Lliwedd	+9.1–+13.3	+11.1
Hafod-y-Porth	+10.9–+22.3	+15.4
Hafod-y-Llan	+15.8–+16.3	+16.0
Nantmor	+3.6–+15.0	+10.4
Shadow Gully	+13.6–+16.1	+15.0
Nantlle Valley	+3.4–+12.9	+9.6

Table 1. Summary of the new sulfur isotope data. All values are reported in $\delta^{34}S_{V\text{-}CDT}$ (‰), n = 53.

The $\delta^{34}S$ values of the country rocks range from +7.0 to +19.0‰, with three rhyolites of the same generation ranging from +9.8 to +18.5‰. The samples from the SVG (LRTF, BPF, rhyolites) have a mean $\delta^{34}S$ value of +11.7‰ ± 4.5‰ (Figure 3).

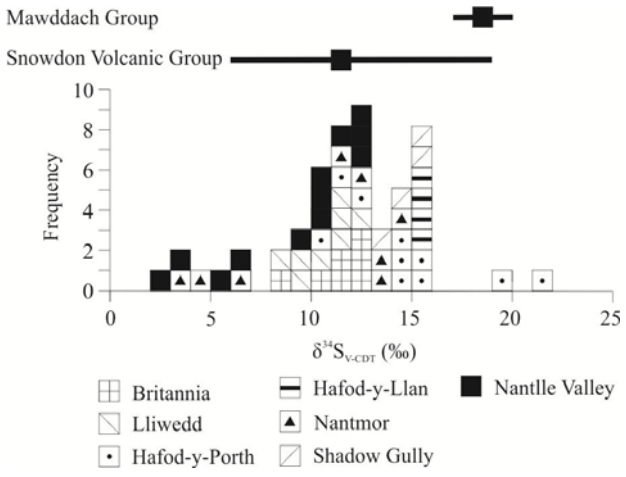

Figure 3. Summary of new sulfur isotope data separated by locality (i.e. Britannia etc), n = 53. The $\delta^{34}S$ values for the country rocks in the area are shown by range. Data presented for the Mawddach Group includes the Maentwrog Formation from Bottrell and Spiro (1988).

5 Discussion

5.1 Vein Sulfur

The volcanic-hosted quartz-sulfide mineralization (Britannia, Lliwedd, Hafod-y-Porth and Hafod-y-Llan) displays a relatively narrow range of $\delta^{34}S$ values (+9.1 to +22.3‰), with a mean of +13.4‰ ± 3.0‰. The isotopically lighter values (+10.9 to +15.8‰) from Hafod-y-Porth broadly overlap with those from Lliwedd and Britannia. The $\delta^{34}S$ values from Hafod-y-Llan are comparable to Hafod-y-Porth, and slightly heavier than those from Lliwedd and Britannia.

$\delta^{34}S$ values from the quartz-magnetite mineralization at Shadow Gully, have a narrow range of values (+13.6 to +16.1‰) and are comparable to those from the volcanic-hosted quartz-sulfide mineralization. $\delta^{34}S$ values for two of the three samples from the intra-caldera sedimentary rock-hosted mineralization at Nantmor range from +11.6 to +15.0‰, overlapping with those from the volcanic-hosted mineralization. Two of the three samples from the extra-caldera sedimentary rock-hosted mineralization of the Nantlle Valley display comparable $\delta^{34}S$ values to the volcanic-hosted quartz-sulfide veins. $\delta^{34}S$ values below +9.1‰ are not observed in the volcanic-hosted mineralization. It is also not possible to discriminate between volcanic-hosted quartz-sulfide mineralization and quartz-magnetite veins or the sedimentary rock-hosted mineralization on the basis of $\delta^{34}S$ values alone.

5.2 Sulfur Sources for the Mineralization

Potential sources of sulfur for mineralization formed in submarine volcanic environments include sulfur contained in the country rocks, both igneous and sedimentary; magmatic sulfur; and seawater dissolved sulfur (Huston, 1999).

The mean $\delta^{34}S$ value (+12.2‰) of vein sulfide falls well outside that expected for magmatic sulfur, typically –3 to +5‰ (Ohmoto, 1986), and indicates input from a source enriched in ^{34}S. Disseminated sulfide in the SVG has a similar $\delta^{34}S$ mean and range to that in the veins, which suggests this may be a likely source of sulfide sulfur in the veins. The mean $\delta^{34}S$ value of the veins is higher than that recorded for the BPF (c. +7‰), but similar to the single $\delta^{34}S$ value (+13.4‰) obtained from the LRTF. The Mawddach Group, one of the hosts to the Nantlle Valley mineralization, has heavier $\delta^{34}S$ values (+17.7 to +20.4‰) than those observed in the Nantlle Valley mineralization.

Whilst the spread of the country rock values and the limited number of samples analysed make it difficult to constrain the sulfur reservoir to a specific formation, there is little doubt that the sulfur in the veins was either derived using the same mechanism as for the disseminated sulfides, or was leached from the volcanic sequence. A large scale hydrothermal system, as is envisaged for the Snowdon caldera, is likely to have interacted with the country rocks, over several kilometres, vertically and laterally causing some degree of homogenisation of the incorporated sulfur to generate the $\delta^{34}S$ values observed.

5.3 Comparison with VMS Deposits

In some respects the mineralization around Snowdon is comparable to VMS deposits, which result from syngenetic processes in volcanically generated hydrothermal systems (Franklin et al. 2005). Whilst syngenetic sulfide ores are diagnostic of VMS deposits, epigenetic, discordant massive replacement, stockwork and quartz-sulfide vein feeder systems also characterise these deposits. In some cases, the latter dominate, as in the modern Juan de Fuca Ridge (Bjerkgard et al. 2000). Sulfur in these systems is considered to be derived from a mixture of seawater, volcanic and/or magmatic components (Huston, 1999). $\delta^{34}S$ values of sulfide minerals from VMS deposits globally range from –20 to +27‰. Average $\delta^{34}S$ for Phanerozoic VMS deposits is quite variable, with Ordovician deposits ranging from –5.0‰ to +20.7‰ (Huston, 1999). With the exception of a single analysis the $\delta^{34}S$ values for the mineralization around Snowdon fall within this range. $\delta^{34}S$ values for samples of pyrite from the Cae Coch VMS deposit range from –24 to –4‰, with most ranging from –24 to –20‰ (Bottrell and Morton, 1992). These are therefore considerably lighter than those observed in the veins around Snowdon and Ordovician VMS deposits. These are likely derived from bacteriogenic sulfate reduction. Avoca in south-east Ireland and Parys Mountain in Anglesey, North Wales are both Phanerozoic VMS deposits (Figure 1). Sulfur isotope analyses from Avoca reveal $\delta^{34}S$ values typically range from +6.8 to +12.3‰ (Williams et al. 1986). Work by Leys et al. (1990) on the Parys Mountain deposit identified a narrow range of $\delta^{34}S$ values, +8.6 to +14.1‰. It is thus possible that the Snowdon vein mineralization is related to this deposit type.

The geological setting of Snowdon mineralization is comparable to the Green Tuff region of Japan, known for its Kuroko-style VMS deposits (Sato, 1974). Epithermal base metal veins occur in the same region and formed later than the Kuroko deposits (Shikazono, 2003). Notably the epithermal veins have mineralogical and textural similarities to the Snowdon mineralization, with some copper-rich types (Shikazono, 1985).

6 Conclusion

The volcanic-hosted and the majority of sedimentary rock-hosted sulfides have $\delta^{34}S$ from +9.1 to +22.3‰, with mean vein $\delta^{34}S$ of +12.2 ± 3.7‰. The SVG is generally considered to represent a reservoir of isotopically heavy sulfur with mean $\delta^{34}S$ of +11.7‰ ± 4.5‰. Circulation of fluids through the host rocks and reduction of Ordovician seawater sulfate could generate $\delta^{34}S$ values in the range observed. With the exception of isolated samples, none of the occurrences of mineralization are isotopically distinct (79% of $\delta^{34}S$ values range from +9.0 to +16.0‰). This lack of discernible difference in $\delta^{34}S$ values from the various localities may indicate mineralization was derived from a single reservoir and that they are coeval. The $\delta^{34}S$ values of sulfide minerals from the mineralization around Snowdon are comparable to those found in Ordovician age VMS deposits globally.

Acknowledgements

PL publishes with the permission of the Executive Director, British Geological Survey (NERC). Ian Mounteney is thanked for producing the sulfide separates. Gus Gunn, Tim Colman and Rodney Allen are thanked for their reviews and comments.

References

Bjerkgard T, Cousens BL, Franklin JM (2000) The Middle Valley sulfide deposits, northern Juan de Fuca Ridge: Radiogenic isotope systematics. Econ Geol 95:1473–1488

Bottrell SH, Morton MDB (1992) A reinterpretation of the genesis of the Cae Coch pyrite deposit, North Wales. J Geol Soc London 149:581–584

Bottrell SH, Spiro B (1988) A stable isotope study of black shale-hosted gold mineralization in the Dolgellau Gold Belt, North Wales. J Geol Soc London 145:941–949

Colman TB, Appleby AK (1991) Volcanogenic quartz-magnetite-hematite veins, Snowdon, North Wales. Min Mag 55:257–262

Franklin JM, Gibson HL, Jonasson IR, Galley AG (2005) Volcanogenic Massive Sulfide Deposits. In: Hedenquist JW et al (ed) Economic Geology One Hundredth Anniversary Volume, Society of Economic Geologists, pp 523–560

Howells MF, Reedman AJ, Campbell SDG (1986) The submarine eruption and emplacement of the Lower Rhyolitic Tuff Formation (Ordovician), N Wales. J Geol Soc London 143:411–423

Howells MF, Reedman AJ, Campbell SDG (1991) Ordovician (Caradoc) marginal basin volcanism in Snowdonia (north-west Wales), London: HMSO for the British Geological Survey

Howells MF, Smith M (1997) Geology of the Country around Snowdon, Memoir of the British Geological Survey, Sheet 119

Huston DL (1999) Stable isotopes and their significance for understanding the genesis of volcanic-hosted massive sulfide deposits: a review. Rev Econ Geol 8:157–180

Kokelaar P (1992) Ordovician marine volcanic and sedimentary record of rifting and volcanotectonism: Snowdon, Wales, United Kingdom. Geol Soc Am Bull 104:1433–1455

Leys C, Caulfield JDB, Boyce AJ, Fallick AE (1990) An overview of the geology and isotope geochemistry of the Anglesey Mine, Parys Mountain, Wales. MDSG, Dublin

Ohmoto H (1986) Stable isotope geochemistry of ore deposits. Rev Mineral and Geochem 16:491–559

Reedman AJ, Colman TB, Campbell SDG, Howells MF (1985) Volcanogenic mineralization related to the Snowdon Volcanic Group (Ordovician), Gwynedd, North Wales. J Geol Soc London 142:875–888

Sato T (1974) Distribution and Geological Setting of the Kuroko Deposits. In: Ishihara S et al (ed) Geology of Kuroko Deposits, Mining Geology Special Issue 6, The Society of Mining Geologists of Japan, pp 1–18

Shikazono N (1985) Gangue minerals from Neogene vein-type deposits in Japan and an estimate of their CO_2 fugacity. Econ Geol 80:751–768

Shikazono N (2003) Geochemical and Tectonic Evolution of Arc-Backarc Hydrothermal Systems, Developments in Geochemistry 8. Elsevier

Stix J, Kennedy B, Hannington M, Gibson H, Fiske R, Mueller W, Franklin J (2003) Caldera-forming processes and origin of submarine volcanogenic massive sulfide deposits. Geol Soc Am Bull 31:375–378

Wagner T, Boyce AJ, Fallick AE (2002) Laser combustion analysis of $\delta^{34}S$ of sulfosalt minerals: Determination of the fractionation systematics and some crystal-chemical considerations. Geochim Cosmochim Ac 66:2855–2863

Williams FM, Sheppard WA, McArdle P (1986) Avoca Mine, County Wicklow: a review of geological and isotopic studies. Dublin, IAEG. In: Andrew CJ et al (ed) Geology and genesis of mineral deposits in Ireland, Dublin: IAEG, pp 49–69

Lithological controls and hydrothermal fluid characterization of the Neoproterozoic polymetallic Niblack volcanogenic massive sulfide system, Alaska, USA

Brian A. McNulty, Melissa J. Gregory
Mineral Deposit Research Unit, University of British Columbia, Vancouver, Canada

Keith Roberts
Hunter Dickinson Inc and Heatherdale Resource Ltd., Vancouver, British Columbia, Canada

Abstract. The Niblack volcanogenic massive sulfide (VMS) camp consists of multiple massive sulfide occurrences at various stratigraphic levels within a 565 ± 1.25 Ma host felsic volcaniclastic rock package. Property and deposit scale variations in the style of VMS mineralization together with metal and alteration zoning have been identified. A property scale, VMS genetic model is presented here to explain the distribution and different styles of sulfide mineralization observed. Three VMS mineralization styles occur within the host felsic stratigraphy: (1) hotter, magmatically derived, copper-rich massive sulfide seafloor accumulation at the Niblack Mine, (2) cooler, mixed seawater and magmatic fluid related copper-zinc sub-seafloor sulphide replacement at the Lookout and Trio zones and (3) un-mineralized, pyrite-rich stockwork veins located stratigraphically between the Lookout and Trio zones. Based on internal alteration and copper-zinc metal ratio zoning at Lookout, the Trio zone is interpreted to represent a distal expression of another VMS centre.

Keywords. Niblack, VMS, hydrothermal alteration, Alexander terrane

1 Introduction

The Niblack polymetallic volcanogenic massive sulfide (VMS) system is located on Prince of Wales Island in southeast Alaska, approximately 50 km southwest of Ketchikan. The property hosts a number of polymetallic VMS zones within a polydeformed felsic volcanic rock package. The Lookout and Trio zones are the primary focus of current resource delineation and contain a global indicated plus inferred resource of 9,031,000 tonnes at 0.90 wt% Cu, 1.59 g/t Au, 1.56 wt% Zn and 25.98 g/t Ag (Nowak et al. 2011).

2 Regional Geology

The southern portion of Prince of Wales Island is underlain by the Alexander Insular terrane, an exotic rock package with regionally variable character (Eberlein et al. 1983). Gehrels and Saleeby (1987) describe the formation of the Alexander terrane as the result of accretion of late Precambrian to early Paleozoic arc-type igneous and sedimentary rocks along a convergent plate margin with the North American Cordillera. The Alexander terrane is sub-divided into the Admiralty and Craig sub-terranes.

The Craig sub-terrane underlies Prince of Wales Island and is further divided into three parts by Eberlein et al. (1983): (a) the pre-Middle Ordovician dominantly volcanic Wales Group; (b) the Ordovician to Lower Silurian sedimentary dominated Descon Formation; and (c) the Lower Devonian volcanic and sedimentary Karheen Formation. The current geological interpretation is the Niblack deposits lie within the Cambrian-Neoproterozoic Wales Group based on geological mapping and U-Pb zircon geochronology (Oliver et al. 2011).

3 Niblack Property Geology

The Niblack stratigraphy consists of a bimodal mafic-felsic suite of volcanic flows, domes and volcaniclastic rocks, overlain by a younger mafic volcanosedimentary and flow cover sequence. The entire rock mass has undergone low-grade greenschist facies metamorphism. The local stratigraphy is divided into three rock packages (Fig 1): (1) The Niblack stratigraphic footwall succession, (2) the Niblack felsic succession and (3) the Niblack stratigraphic hanging wall succession.

The footwall succession consists predominantly of thick, laterally continuous dacitic flows with minor argillaceous lithic wackes and poorly bedded intermediate tuffaceous rock units. The footwall stratigraphy is topped by amygdaloidal mafic flows and at surface are in immediate contact with the Niblack felsic succession.

The Niblack felsic succession is host to all known massive and semi-massive sulfide occurrences. This rock package is comprised of rhyolitic, quartz crystal-rich tuffaceous and fragmental volcaniclastic debris flows, with lesser amounts of aphyric to moderately quartz-feldspar phyric rhyolitic flows and/or domes and related autobreccias. At the top of felsic succession there is commonly a quartz-feldspar phyric 'sill' of variable thickness. The felsic stratigraphy at Niblack has been dated at 565 ± 1.25 Ma using U-Pb zircon geochronology (Fig1, Oliver et al. 2011).

Volcanogenic massive sulfide mineralization occurs, at a minimum, at two distinct stratigraphic positions within the felsic volcanic sequence. Specifically, the Lookout zone occurs high up in the stratigraphy within coarse felsic debris flows, near the hanging wall contact and the quartz-feldspar phyric sill (Fig 1). The Trio zone

occurs deeper in the felsic stratigraphy near the footwall contact and underlies a coherent, fine-grained felsic flow/dome sequence (Fig 1).

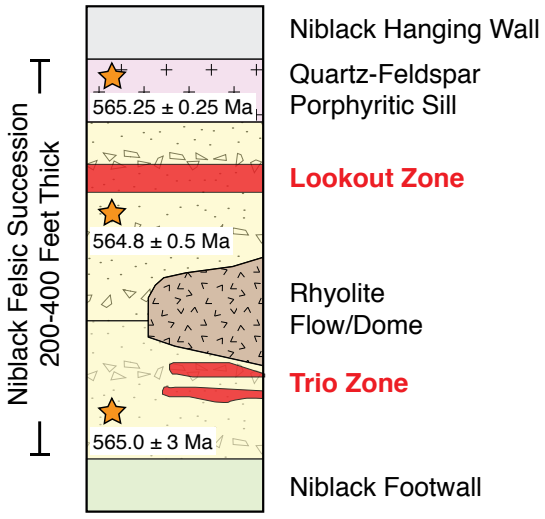

Figure 1. Generalized stratigraphic column. Stars show the sample locations for U-Pb zircon geochronology, data from Oliver et al. (2011).

The hanging wall sequence consists of moderately to strongly magnetic, reworked mafic volcanosedimentary rocks and pillowed mafic flows. The sequence varies from massive coarse-medium grained tuffaceous wackes to fine-medium grained laminated mafic siltstones. The hanging wall caps the VMS system at Niblack and mineralization found to date within this package is restricted to thin pyritic laminations within cherty siltstones, located immediately above the felsic stratigraphy (Nowak et al. 2011).

4 Style of Mineralization and Alteration

4.1 Property scale distribution

Niblack is host to at least six VMS occurrences – Lookout, Trio, Dama, Mammoth, Lindsy and the historic Niblack Mine. Distribution of these zones is controlled by fold repetition of the Niblack felsic succession. Specifically, the Lookout and Trio zones are located on the overturned, southwestern limb of a property-scale antiformal syncline. The two zones are up to 1,000 meters apart along strike. The Niblack Mine is located on the northeastern limb of the corresponding synformal anticline. An unknown amount of stratigraphy has been lost due to erosion between the two limbs and as such the original distance between the Niblack Mine and Lookout and Trio zones is unknown.

4.2 Three styles of VMS mineralization

Three styles of VMS mineralization have been identified at Niblack: (1) copper-rich vent derived seafloor mineralization, (2) copper-zinc-rich sub-seafloor sulfide replacement mineralization and (3) pyrite-rich stringer-stockwork veins. These three styles of VMS mineralization are characterized by a range in sulfide textural variations and associated alteration mineralogy.

Seafloor sulfide accumulation only occurs at the Niblack Mine and is characterized by massive chalcopyrite with lesser sphalerite and pyrite layers and brecciated vent structures composed of exhalative magnetite and jasper fragments in a chalcopyrite matrix with elevated copper to zinc ratios of 3:1. Hydrothermal chlorite is the primary phyllosilicate alteration mineral associated with both sulfide mineralization and un-mineralized exhalative massive magnetite alteration.

Sub-seafloor sulfide replacement consists of semi-massive to massive, irregular chalcopyrite + sphalerite mineralization of felsic volcaniclastic units with variable copper to zinc metal ratios of 1:1 and 1:2. Primary volcanic textures are preserved such as angular lithic fragments and volcanic quartz and feldspar crystal shards. Sulfide mineralization is associated with chlorite + sericite + silica alteration minerals. Chlorite dominant alteration and sulfide mineralization is associated with 1:1 copper-zinc ratios whereas sericite dominant alteration plus sulfide is associated with 1:2 copper-zinc ratios. Sub-seafloor sulfide replacement is observed in all VMS zones on the property except the Niblack Mine.

Deformed, recrystallized sulfide stockwork veins with illite alteration envelopes crosscut a hydrothermally altered, fine-grained rhyolite flow/dome sequence in the Trio zone. This style of mineralization is dominated by pyrite with lesser amounts of chalcopyrite. The rhyolite groundmass is intensely altered to illite + silica + pyrite.

Gold and silver are significantly elevated at the Lookout and Trio zones compared to the Niblack Mine. For example, median gold and silver concentrations from the Lookout zone range from 1-4 g/t and 20-40 g/t, respectively. Median precious metal grades at the Niblack Mine are lower and vary from 1-1.5 g/t gold and 10-20 g/t silver.

5 Chlorite Compositions

Compositional variations in chlorite were measured using microprobe analysis of samples from sub-seafloor sulfide replacement at Lookout and seafloor accumulation at the Niblack Mine. Thin section samples were selected to test two hydrothermal alteration domains in the felsic stratigraphy: (1) chlorite + magnetite ± carbonate alteration and (2) chlorite + sulfide alteration.

The results show a correlation between the composition of chlorite and base metal mineralization for each zone. Chlorite compositions from the Niblack Mine associated with sulfide mineralization are Mg-rich and have a Mg^{2+}:Fe^{3+} ratio of 0.78 and a lower ratio of 0.51 for the un-mineralized magnetite altered sample. Lookout samples are more Fe-rich with chlorite compositions from mineralized samples having an Mg^{2+}:Fe^{3+} ratio of 0.43 and a slightly lower ratio of 0.39 for the un-mineralized magnetite + carbonate altered sample.

6 Stable Isotope Characterization

Sulphur, oxygen and carbon stable isotope analyses were completed on pyrite, chalcopyrite, sphalerite, magnetite and carbonate mineral separates to characterize the

nature of the hydrothermal fluid(s) responsible for base and precious metal mineralization (Fig 2). Results for sulphur stable isotopes from each VMS zone plot in a relatively tight range between 6.6-10.5 per mil (Fig 2A). These results plot closer to a primitive signature, relative to the $\delta^{34}S$ signature for Neoproterozoic seawater from sulphate (Claypool et al. 1980). The exact source of sulphur is ambiguous based on these results. Similar results have been explained by high-temperature inorganic reduction of seawater sulphate in Kuroko VMS systems (Sangster 1968) and by leaching of igneous sulfide from footwall volcanic rocks (Shanks 2001).

The calculated fluid composition of $\delta^{18}O$ from magnetite separates for a temperature range of 200-300°C plot over a range between a magmatic and metamorphic fluid signature (Fig 2B). Samples from the Niblack Mine have a $\delta^{18}O$ fluid composition consistent with a magmatic signature; however, the results from the Mammoth, Lookout and Dama zones have fluid signatures within the metamorphic fluid signature range.

Lastly, the results of oxygen and carbon stable isotope analysis from hydrothermal carbonate separates from the Niblack Mine, Lookout and Mammoth zones plot along a trend between Neoproterozoic seawater and mantle fluid signatures (Fig 2C). Data from the Lookout zone has the largest spread of results, with the majority of samples plotting in or near the signature for seawater. Results from the Niblack Mine and Mammoth zone plot closer to mantle values.

7 Discussion

A variety of mineralization styles at different stratigraphic levels are observed in the Niblack VMS system and are interpreted to represent a large scale hydrothermal system related to multiple volcanogenic massive sulfide events within a rapidly forming felsic volcanic rock package. Variations in sulfide mineralization textures, associated non-sulfide alteration minerals and base metal ratios define three styles of VMS mineralization: (1) copper-rich, seafloor sulfide accumulation, (2) copper-zinc-rich sub-seafloor sulfide replacement and (3) un-mineralized pyrite-rich stringer-stockwork veins.

Relative ore forming fluid temperatures are estimated from variations in base metal ratios, phyllosilicate alteration mineral assemblages and chlorite compositions. The copper-rich Niblack Mine is interpreted to have formed from hydrothermal fluids that are hotter relative to the Lookout and Trio zones that are more zinc-rich. In addition to property scale VMS zoning the data also indicates local, deposit-scale zoning. The Lookout zone has internal variations in base metal ratios and phyllosilicate alteration mineralogy (Fig 3). There is a core of chlorite-sulfide alteration with 1:1 copper-zinc metal ratios and sericite-sulfide alteration with 1:2 copper-zinc ratios at the margins. The alteration and metal zoning at Lookout is interpreted to represent a transition from hotter ore forming fluids in the core to cooler fluids at the margins. The same sericite-sulfide, 1:2 copper-zinc metal ratio sub-seafloor sulfide replacement style is observed in the Trio zone, indicating it occurs in a cooler part of the hydrothermal system.

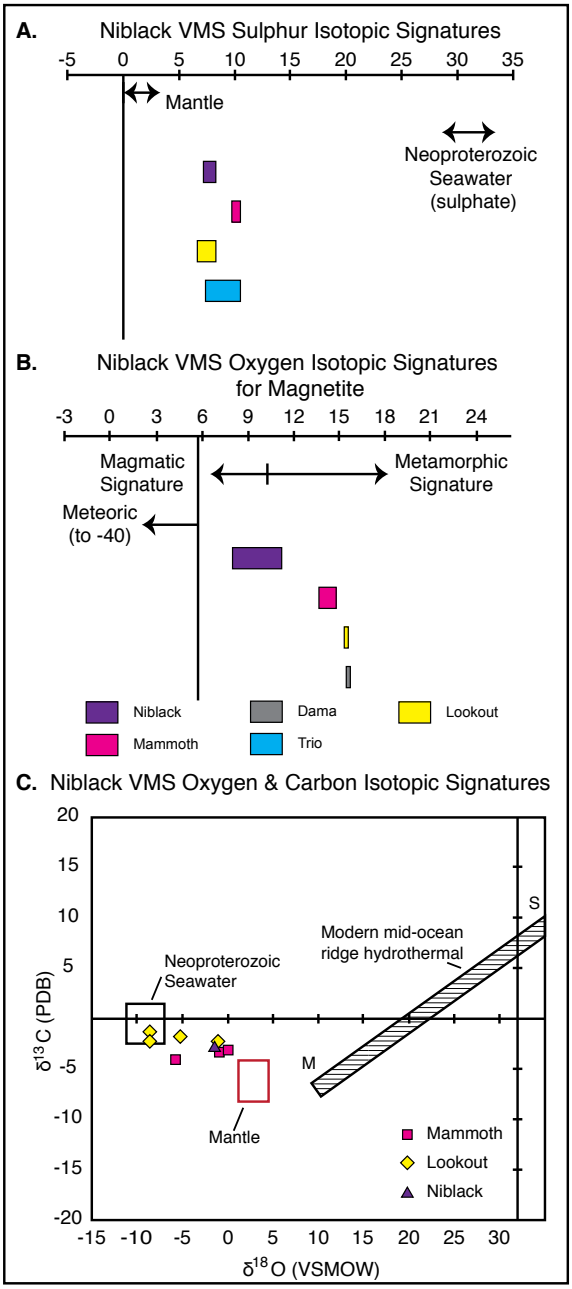

Figure 2. Summary stable isotope plots for sulphur, oxygen and carbon from Niblack VMS zones. (A) Range of $\delta^{34}S$ values for pyrite, chalcopyrite and sphalerite. (B) Calculated $\delta^{18}O$ signatures for 200-300°C fluid using the magnetite isotope fractionation equation of Zheng and Simon (1991). (C) $\delta^{18}O$ vs. $\delta^{13}C$ for carbonate separates; $\delta^{18}O$ calculated at 250°C using equation from Zheng (1999). Proterozoic seawater signature estimated from Wadleigh and Veizer (1992) and Butler et al. (1997). Data for modern mid-ocean ridge hydrothermal systems is from Stakes and O'Neil (1982).

The compositional variations in chlorite alteration associated with sulfide mineralization also supports the interpretation that hotter fluids are responsible for mineralization at the Niblack Mine (Mg-rich chlorite) and the ore forming fluids at the Lookout zone are cooler (Fe-rich chlorite). Herrmann et al. (2001) identified that Mg-rich chlorite was associated with pervasive chlorite alteration and massive sulfide mineralization at the Rosebery VMS deposit, Tasmania and a faint proximal

trend to Fe-rich chlorite farther away from the deposit. The results from the Niblack VMS system presented here are consistent with findings from Herrmann et al. (2001).

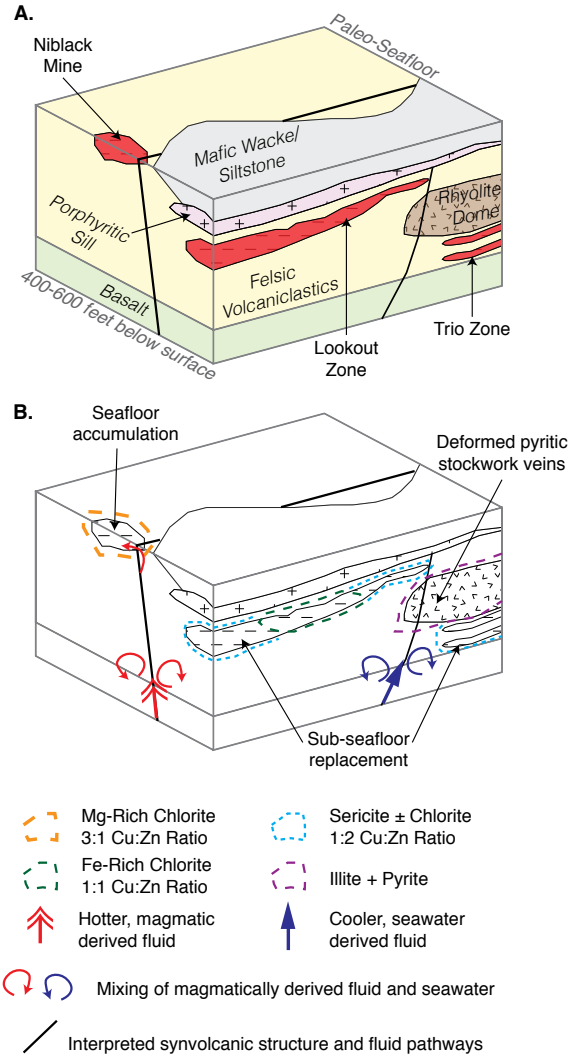

Figure 3. Schematic geology and fluid evolution model for the Niblack VMS system. Top of diagram represents the paleo-seafloor and the bottom approximately 400-600 feet below. (A) Pre-deformation, geologic model. (B) Alteration and fluid mixing model, geology same as (A).

Sulphur, oxygen and carbon stable isotope data from the Niblack VMS camp suggest two fluid sources are responsible for base and precious metal formation. In all three stable isotope datasets the Niblack Mine has the strongest isotopic affinity to a magmatically derived fluid. The Lookout and Trio zones stable isotopic signatures indicate higher degrees of mixing of magmatic and seawater fluid sources. Lastly, oxygen isotope data from magnetite separates imply there is a stronger metamorphic overprint at the Lookout, Mammoth, and Dama zones relative to the Niblack Mine.

8 Conclusion

In summary, the Niblack Mine represents a copper-rich, hotter hydrothermal VMS system formed from magmatically derived fluids and minor seawater mixing. The Lookout zone represents a cooler hydrothermal, sub-seafloor VMS system with fluid signatures suggesting greater mixing of magmatic and seawater fluid sources. The Trio zone represents the margins of a cooler hydrothermal, sub-seafloor VMS system similar to the Lookout zone, however it is positioned deeper in the host stratigraphy. Elevated precious metal grades at Trio and Lookout are consistent with cooler metal forming fluids. The proposed model is consistent with the observations of Hannington and Scott (1989) where they identified that gold-enhanced VMS deposits are associated with cooler, sphalerite-rich hydrothermal systems.

Acknowledgements

This research is funded by Heatherdale Resources Ltd and the Mineral Deposit Research Unit, University of British Columbia.

References

Butler RF, Gehrels GE, Baszard DR (1997) Paleomagnetism of Paleozoic strata of the Alexander terrane, southeastern Alaska. Geological Society of America Bulletin 109:1372-1388

Claypool GE, Holser WT, Kaplan IR, Sakai H, Zak I (1980) The age curves of sulfur and oxygen isotopes in marine sulfate and their mutual interpretation. Chemical Geology 28:199-260.

Eberlein GD, Churkin MJ, Carter C, Berg HC, Ovenshine AT (1983) Geology of the Craig Quadrangle, Alaska. US Geological Survey Open-File Report 91:1-53

Gehrels GE, Saleeby JB (1987) Geology of southern Prince of Wales Island, southeastern Alaska. Geological Society of America Bulletin 98:123-137

Hannington MD, Scott SD (1989) Sulfidation equilibria as guides to gold mineralization in volcanogenic massive sulfides; evidence from sulfide mineralogy and the composition of sphalerite. Economic Geology 84:1978-1995

Herrmann W, Blake M, Doyle M, Huston DL, Kamprad J, Merry N, Pontual S (2001) Short Wavelength Infrared (SWIR) Spectral Analysis of Hydrothermal Alteration Zones Associed with Base Metal Sulfide Deposits at Rosebery and Western Tharsis, Tasmania, and Highway-Reward, Queensland. Economic Geology 96:939-955

Nowak M, Johnson M, Van Der Heever D (2011) Mineral Resource Estimation Niblack Polymetallic Sulphide Project,

Oliver J, Roberts K, Friedman R (2011) The Niblack Mine: A Neoproterozoic, Precious Metals Enhanced, Volcanic Hosted Massive Sulphide, Prince of Wales Island, Alaska. Mining From Prospect to Feasibility, AMA Conference Abstracts 60-62

Sangster DF (1968) Relative sulfur isotope abundance of ancient seas and stratabound sulphide deposits. Proc. Geol. Assoc. Canada 19:79-86

Shanks WC III (2001) Stable isotopes in seafloor hydrothermal systems; vent fluids, hydrothermal deposits, hydrothermal alteration, and microbial processes. Stable isotope geochemistry: Reviews in Mineralogy and Geochemistry 43:469-525

Stakes DS, O'Neil JR (1982) Mineralogy and stable isotope geochemistry of hydrothermally altered oceanic rocks. Earth Planet Sci Lett 36:255-262

Wadleigh MA, Veizer J (1992) $^{18}O/^{16}O$ and $^{13}C/^{12}C$ in lower Paleozoic articulate brachiopods: Implications for the isotopic composition of seawater. Geochimica et cosmochimica Acta 56:431-443.

Zheng Y-F, Simon K (1991) Oxygen isotope fractionation in hematite and magnetite: A theoretical calculation and application to geothermometry of metamorphic iron-formations. Eur J Mineral 3:877-886

Zheng Y-F (1999) Oxygen isotope fractionation in carbonate and sulfate minerals. Geochemical Journal 33:109-126

Geochemical signature of the "zero-age chimney" formed on artificial hydrothermal vents created by IODP Exp. 331 in the Iheya North field, Okinawa Trough

Tatsuo Nozaki[1,2,3], Jun-ichiro Ishibashi[4,2], Kazuhiko Shimada[4], Yutaro Takaya[5], Yasuhiro Kato[3,2,1], Shinsuke Kawagucci[6,7,2], Takazo Shibuya[7,2] and Ken Takai[6,7,2]

[1.] JAMSTEC/IFREE, [2.] JAMSTEC/SRRP, [3.] Univ. of Tokyo, [4.] Kyushu Univ., [5.] AIST/GSJ, [6.] JAMSTEC/BIOGEOS, [7.] JAMSTEC/PEL

Keywords: seafloor hydrothermal deposit, Kuroko-type VMS deposit, zero-age chimney, Okinawa Trough

1 Introduction

From September to October 2010, the first drilling research (IODP Exp. 331) targeting the modern seafloor massive sulfide deposit in a back-arc setting which is a modern analogue of the Kuroko-type VMS deposit was conducted in the Iheya North field, Okinawa Trough. During this expedition, the massive kuroko-like sulfide ore was successively recovered and four artificial hydrothermal vents were also created (Takai et al., 2011). Semi-annual research cruises to monitor and collect chimney and hydrothermal fluid samples from these vents have been done using a remotely operating vehicle (HPD 3000), which provide us precious opportunity to investigate the petrographic and geochemical characteristics of very immature sulfide-bearing chimney formed on the artificial hydrothermal vents (hereafter called "zero-age chimney").

2 Results and Discussion

Zero-age chimneys analyzed in this study were collected from the KY11-02, NT11-16, NT12-06 and NT12-27 cruises (HPD 3000 dive No. 1247, 1317, 1355 and 1449, respectively). Now, we are doing thorough petrographic research and geochemical experiments by microscopic observation, XRD, EPMA, ICP-QMS, TIMS and MC-ICP-MS analyses. We will show some portions of these results in the present study.

Under the microscope, the zero-age chimney exhibits a porous structure whose porosity is 10 to 20% and is dominated by chalcopyrite, sphalerite/wurtzite and galena, which has a dendritic texture (Fig. 1). Inner and outer parts of dendrites are composed of chalcopyrite and sphalerite/wurtzite, respectively. Galena and minor pyrite fill spaces of these crystals. Based on the results of XRD analysis, the peak of wurtzite which hardly occur in the Kuroko-type VMS deposits on land was frequently observed. In the outermost part, spherical pyrite crystal which has a zonal structure of density and Pb-Sb-As-Ag-S minerals were also found by electron probe micro analysis. The whole-rock geochemical composition determined by ICP-QMS analyses is similar to that of high-grade kuroko ore. The Zn, Cu and Pb concentrations are 24-36, 1.9-7.2 and 0.9-7.6 wt%, respectively, together with several hundred ppm of Ag, As, Cd and Sb (Ishibashi et al., 2012). Distinct petrographic features of the zero-age chimney compared with kuroko-ore are porous and dedritic texture, abundant occurrence of wurtzite and very minor sulfate minerals. In this study, we will also present the enrichment factor of various metal elements normalized to hydrothermal fluids collected from the artificial vent.

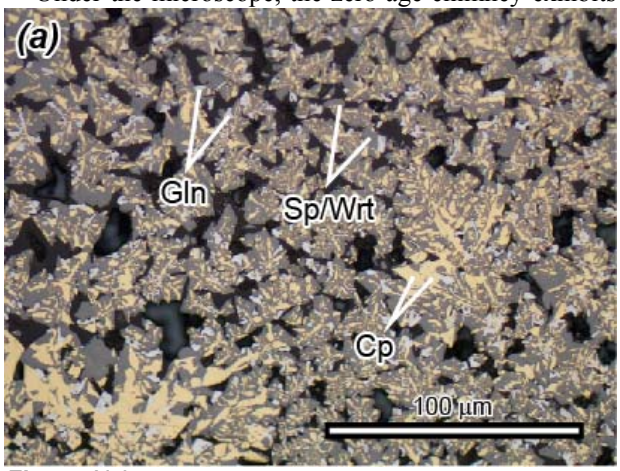

Figure 1(a). Photomicrograph of dendritic texture in the zero-age chimney. Inner and outer parts of dendrites are composed of chalcopyrite and sphalerite/wurtzite, respectively, and galena is observed between these crystals.

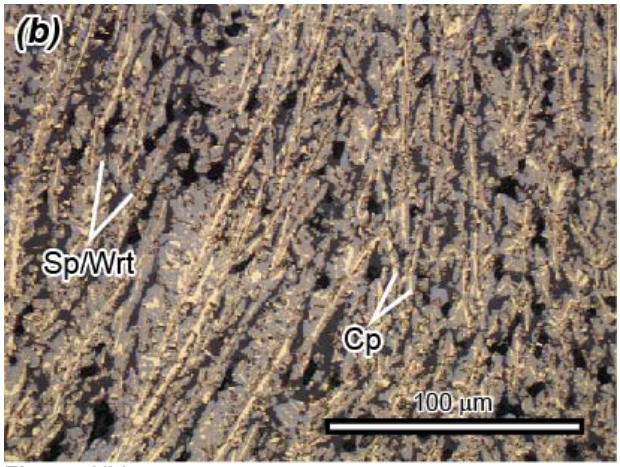

Figure 1(b). Photomicrograph showing a dendritic texture of chalcopyrite and sphalerite/wurtzite formed along with a hydrothermal path. Abbreviations: Cp = chalcopyrite, Gln = galena, Sp = sphalerite, Wrt = wurtzite.

References

Ishibashi J., Shimada K., Nozaki T., Takaya Y., Kato Y., Kawagucci S., Watsuji T., Takai K. (2012) Mineralogy and geochemistry of chimney structures built up on artificial drilled holes. Abstract of the 62th annual meeting of the Society of Resource Geology, O-08 (in Japanese).

Takai K, Mottl MJ, Nielsen SHH, the IODP Expedition 331 Scientists (2011) Deep hot biosphere. IODP Preliminary Report, 331, doi:10.2204/iodp.pr.331.2010.

Cu-Zn mineralisation at Vannareid, West Troms Basement Complex: a new Palaeoproterozoic VMS occurrence in the northern Fennoscandian Shield

V. Juhani Ojala, Harald Hansen and Hannu Ahola
Store Norske Gull AS, Postboks 613, 9171 Longyearbyen, Norway

Abstract. The Vannareid Cu-Zn occurrence is recently recognised Palaeoproterozoic base metal mineralisation within the West Troms Basement Complex (WTBC) in Troms, northern Norway. The Cu-Zn mineralisation is hosted by quatz-carbonate-chlorite veins in tonalite gneisses, mafic sills and sericite schists along a major normal fault. All rocks are deformed and metamorphosed at upper-greenschist to lower-amphibolite facies conditions. The geological setting and current exploration results suggest that the mapped part of the Cu-Zn mineralization may be a stringer zone of a volcanic hosted massive sulphide (VMS) mineralization.

Keywords. Copper, Zinc, stringer zone, volcanic hosted massive sulphide, VMS, Paleoproterozoic, Vanna, Vannareid, Norway

1 Introduction

The Vannareid Cu-Zn occurrence is within the West Troms Basement Complex (WTBC) in Troms, northern Norway (Fig. 1). WTBC is a collage of Archaean to Palaeoproterozoic crustal blocks made up of a wide range of plutonic and metamorphic rocks and intervening NW-SE trending narrow belts of metasupracrustal rocks (Bergh et al., 2007). Vannareid is currently under exploration by Store Norske Gull AS, and the first reconnaissance drilling campaign was conducted in summer 2012 to test a Zn showing along a E-W trending fault zone. The zinc showing in a road cut was originally detected at Vannareid by Kåre Kullerud in 2008. The drilling campaign, geochemical sampling, mapping, ground magnetic and IP survey revealed almost one km long Cu-Zn mineralisation along a fault zone between tonalite gneisses and supracrustal rocks.

The Cu-Zn mineralisation is hosted by quatz-carbonate-chlorite veins in tonalite gneisses, mafic sills and sericite schists. All rocks are deformed and metamorphosed at upper-greenschist to lower-amphibolite facies conditions.

2 Geological Setting

The West Troms Basement Complex comprises Archaean to Palaeoproterozoic rocks, this basement suite is separated from the structurally overlying Caledonian nappes by a combination of thrusts and Palaeozoic-Mesozoic normal faults to the east. In the Vanna island, the complex includes various tonalitic to anorthositic and migmatitic gabbroic gneisses older than 2.8 Ga overlain by Archaean and Palaeoproterozoic metasupracrustal rocks (Bergh et al. 2007). A mafic dyke swarm dated at 2403±3 Ma cut the tonalites and dioritic sill dated at 2221±3 Ma cut the supracrustal rock gives the evidence for a Paleoproterozoic depositional age.

The Vannareid Cu-Zn occurrence is located along a major normal fault cutting tonalitic gneiss and mylonitised tonalite with mafic sheets. Mylonitised tonalities are lithologically sericite schists and could be interpreted as supracrustal rocks. Northern side of the fault soil cover is thin but south of the fault overburden is over 20 m and includes beach sands and marine clays.

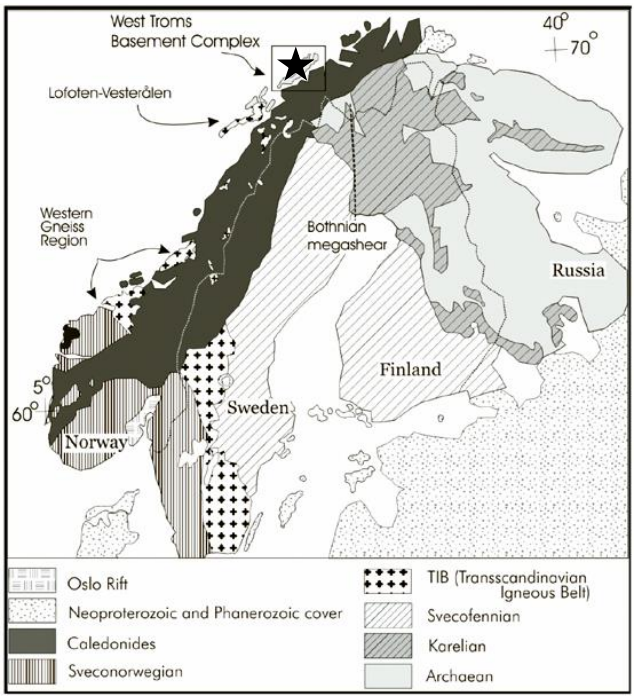

Figure 1. Location of the Vannareid Cu-Zn occurrence (star) in northern Norway (modified from Bergh et al., 2007).

3 Mineralisation and alteration

Surface expression of the mineralisation is almost one km long Cu-Zn soil anomaly. In addition, quartz-chlorite breccia and vein system with sulphide dissemination is sub-cropping in the centre of the soil geochemical anomaly. IP survey detects the disseminated sulphides north of the fault and marine clays south of the fault. Reconnaissance drilling included six drill hole with 880 m total length was drilled to test the geochemical anomaly. Drilling intersected a zone of quartz-carbonate-chlorite-sulphide alteration and veins in a package of sericite schists, mafic sills and tonalite from south to north. Under the strongest soil Cu anomaly, the drilling defined a stringer zone with the highest Cu/Zn ratio and silica-chlorite alteration and higher Zn grades related to

quartz-carbonate alteration at eastern the flank.

Further drilling to test IP and magnetic anomalies south of the fault on the interpreted hanging wall of the stringer zone has been planned for 2013

mylonitic rocks south of the stringer and fault zone are interpreted to be supracrustal rocks and not deformed tonalitic gneisses. Extensive mafic sills in and north of the stringer zone represent magmatic stage of the rifting.

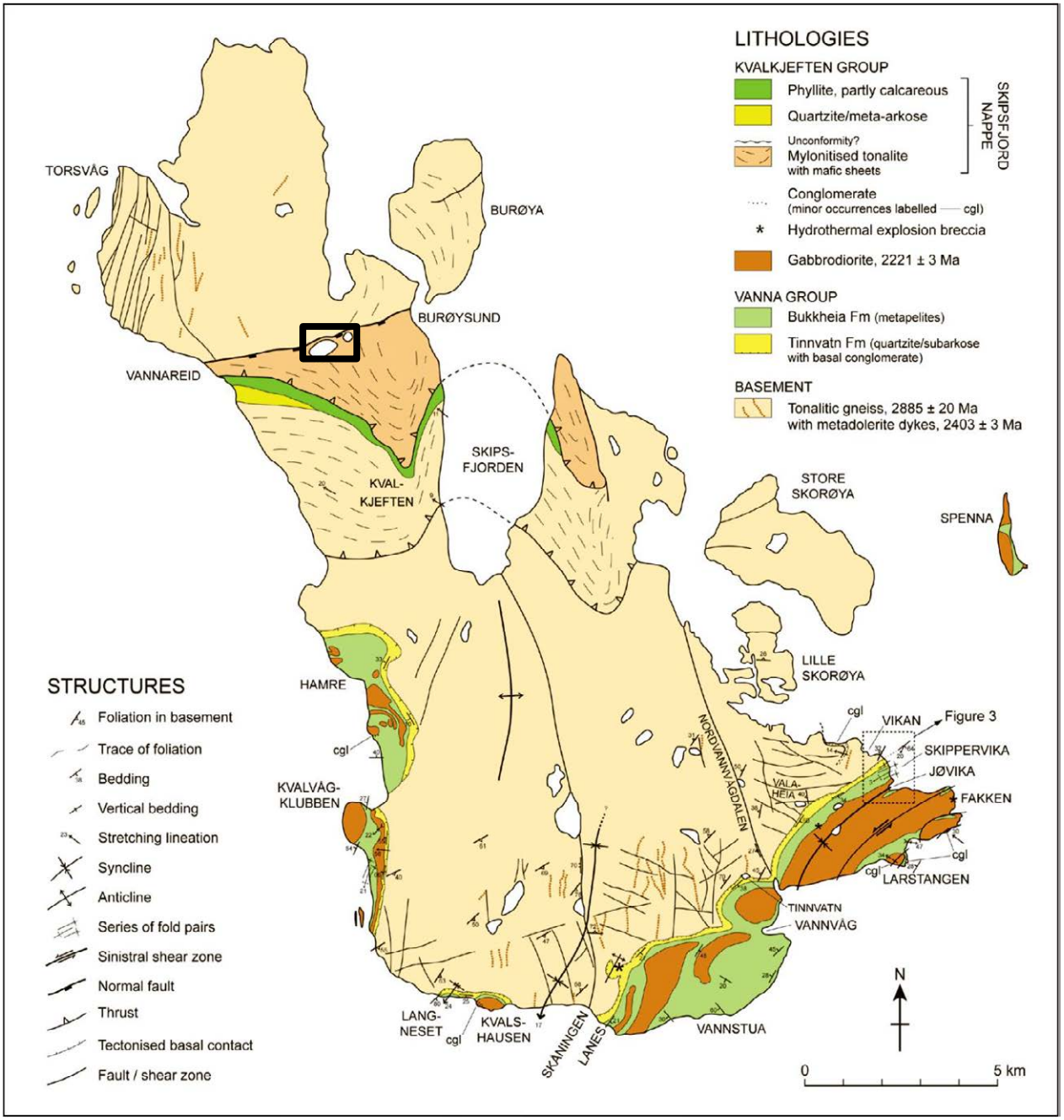

Figure 2. The location (rectangle) of the Vanna Cu-Zn mineralization on the geological map of the island of Vanna (modified from Bergh et al., 2007)

4 Conclusions

The Cu-Zn occurrence discovered at Vannareid is new style of mineralisation in the area and the exploration in the area is in the early stages. The geological setting and current exploration results suggest that the mapped part of the Cu-Zn mineralization may be a stringer zone of a volcanic hosted massive sulphide (VMS) mineralization. The stringer zone shows higher Cu grades in the core with silica-chlorite alteration and higher Zn grades related to carbonate alteration at the flanks. The Consequently, the geological framework then represents favourable geological setting for a VMS system.

Acknowledgements

We thank Store Norske Gull AS for permission to publish the work.

References

Bergh SG, Kullerud K, Corfu F, Armitage PEB, Davidsen B, Helge Johansen W, Pettersen T, Knudsen S (2007) Low grade sedimentary rocks on Vanna, North Norway: a new occurrence of a Palaeoproterozoic (2.4-2.2 Ga) cover succession in northern Fennoscandia. Norwegian Journal of Geology, vol. 87, pp. 301-318..

Occurrence of gold (electrum) in the Lousal mine, Iberian pyrite belt, Portugal

Daniel P. S. de Oliveira, Carlos J. P. Rosa, Fernanda M. G. Guimarães, João X. Matos, Zélia Pereira, Vasco C. S. Frias
Laboratório Nacional de Energia e Geologia (LNEG), Portugal

Diogo R. N. Rosa
Geological Survey of Denmark and Greenland (GEUS)

J. M. Castelo Branco
AGC- Minas de Portugal, unipessoal (Lundin Mining Corporation)

Abstract. Recent exploration drill holes in the Lousal Mine, located within the Portuguese sector of the Iberian Pyrite Belt (IPB) yielded previously unknown and significant concentrations in gold (electrum) in a section of core consisting of hydrothermally altered banded sediments with massive pyrite and cobaltite. Research indicates that the gold (electrum) is present in veinlets within the more dominant massive pyrite and cobaltite associated with native bismuth and bismuthinite and is clearly late in the paragenetic sequence occurring also with fine chalcopyrite (± covellite). The gold (electrum) grains are small, seldom reaching more than 6 µm in length and half of that in thickness. EPMA results indicate that silver concentrations in the gold grains can be as high as 26 wt%.
These results show similarities with conclusions drawn from the IPB on the Spanish side where gold is found as electrum associated with abundant to common Co and Bi minerals. The gold is associated with pyrite, cobaltite and/or chalcopyrite and hosted by sedimentary facies. This gold is interpreted to have formed at high temperature (>300 ℃) during the initial phases of massive sulfide formation. At Lousal the gold seems to occur related with hydrothermal alteration of the sulfides, and remobilized in late-stage shear zones.

Keywords: Lousal, Iberian Pyrite Belt, gold, electrum

1 Introduction

The Iberian Pyrite Belt (IPB) is a well-known Volcanic Hosted Massive Sulfide (VHMS) deposit province containing several world-class deposits. IPB deposits often contain subordinate gold values disseminated in sulfide ores and also occur locally in shear zones and even some of the high-tech metals such as Ge (Reiser et al. 2011) and In (de Oliveira et al, 2011).

The Lousal mine, is located in the Lousal-Caveira IPB NW sector (Fig. 1), an area limited by the Sado Tertiary Basin sediments to the N, E and S (Matos and Oliveira 2003; Oliveira et al. 2005).

Pyrite ore concentrates were produced at Lousal between 1900 and 1988. Presently the mine is in rehabilitation to acid mine drainage control (Silva et al. 2009). The Lousal massive sulfide deposit is located ~65 km NW of Neves Corvo.

The IPB comprises the Volcanic Sedimentary Complex (VSC) and the older Phyllite-Quartzite Group (PQ). The IPB is covered by the Baixo Alentejo Flysch sediments.

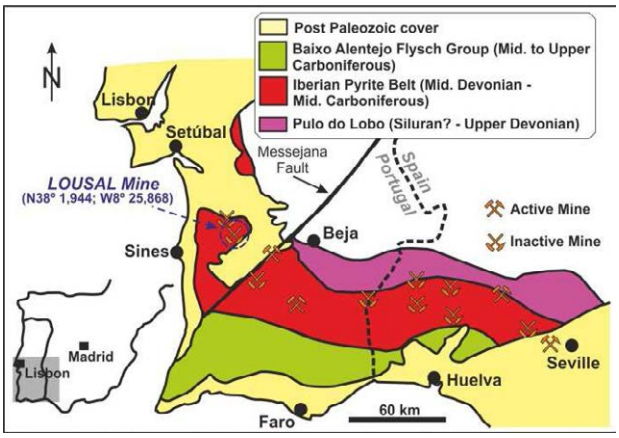

Figure 1. Location of the Lousal Mine within the geological setting of the Iberian Pyrite Belt.

At Lousal a VSC sequence is orientated N40W and compartmentalized by late Variscan N-S trending faults; the eastern sector is dominated by PQ rocks (Strauss 1970; Schermerhorn et al. 1987; Matos and Oliveira 2003; Matos and Relvas 2006). The Lousal structure consists of a narrow anticline with a nucleus formed by PQ lower Givetian age sediments and VSC units are present in both anticline limbs. PQ sediments overthrust the VSC in a SW direction (Rosa et al., 2010; Matos et al. in prep). In Lousal four separate volcanic centres could be outlined which are defined by coarse-grained porphyritic quartz-feldspar rocks with associated autoclastic breccias (Rosa et al., 2010), and due to the Variscan folding and faulting can reach thicknesses of 850 m or more (Strauss and Madel, 1974).

The Lousal VHMS deposit comprises 9 ore lenses that are lined up along one horizon extending for 1.5 km along strike (Strauss and Madel, 1974). The ore-bearing facies are predominantly fine-grained volcaniclastic units, black shales and felsic volcanic rocks. Black shales are of late Strunian age (Pereira, 2012).

This study complements a preliminary insight into the occurrence of electrum in the Lousal mine (De Oliveira et al., 2011) from samples obtained from two drill holes done in 2008 by AGC/Lundin Mining.

2 Ore geochemistry

Whole rock analytical results of selected samples in borehole LS08/01 indicate elevated concentrations of not only gold but also other elements (see Table 1, 700 m – 733,5 m borehole samples), namely copper, lead, zinc, bismuth, cobalt (and arsenic – not shown). Maximum values of ~67 g/t Au (which far exceeds those reported previously in the IPB, e.g. (Strauss and Beck, 1990) and 11 g/t Bi were obtained in one sample from drill hole LS08/01.

3 Gold in Lousal

Interesting gold values were detected throughout exploration drill holes (LS08/01 and LS08/02). However, significant concentrations were detected at approximately 700 m depth and although both holes show considerable amounts of gold, LS08/01 has considerably higher gold values (Table 1). Both holes intersected hydrothermally altered zones containing chlorite, silica and sulfide veins that locally occur as semi-massive sulfide mineralization, up to 0.5 m thick, with chalcopyrite and sphalerite as accessory minerals. The hydrothermal alteration and sulfide veins are hosted by dark grey shales and thin beds of quartzites of the PQ (late Strunian and lower Givetian age, respectively; Matos et al, 2011; Pereira et al., 2012), and by VSC dark grey shales of late Strunian age (Matos et al, 2011) and VSC (359±2 M.a. to 369±3.5 M.a.; Matos et al, *in prep.*). The hydrothermal altered intervals are delimited by thrust faults that disrupt the stratigraphy. Gold has been found to occur mostly in the hydrothermal altered zones associated with massive pyrite (close to a quartz-rich shear zone) that is replacing banded black shales, and also in the thrust zones. In hand specimen the pyrite appears as deformed rounded to subrounded grains and coalesces in places into more massive sections (Fig. 2).

Table 1. Partial results of whole rock geochemistry for selected samples from drill holes LS08/01and LS08/02. All values in ppm; number in brackets refers to the sample collection depth; Results in ppm.

	Au	Bi	Co	Cu	Pb	Sn	Zn
LOU 08/01-2(660,9)	40	79,5	628	11300	43	38	45
LOU 08/01-6(719,5)	2200	143	502	6980	147	12	841
LOU 08/01-7(732,4)	66700	11400	48400	9380	1850	44	41
LOU 08/01-8(733,5)	29400	7750	26000	3350	1230	23	189
LOU 08/01-11(835)	207	49,3	46	377	3740	122	11500
LOU 08/01-13(841,5)	14	8,5	62	285	7930	84	9030
LOU 08/01-14(720,6)	3140	469	866	4980	99	12	141
LOU 08/02(530.0)	1010	121	2860	3730	89	21	37
LOU 08/02(530.3)	578	24,3	1540	33200	88	90	75
LOU 08/02(623.6)	102	128	529	13200	202	43	4060
LOU 08/02(624.0)	143	239	795	13500	745	82	957
LOU 08/02(629.0)	30	101	554	21200	191	40	526
LOU 08/02(652.0)	179	114	1000	12000	299	8	655
LOU 08/02(669.8)	205	197	738	24500	168	54	259
LOU 08/02(670.0)	301	19,6	230	19900	139	16	400
LOU 08/02(683.7)	41	120	1080	10500	107	6	237
LOU 08/02(691.0)	1960	1990	752	1470	104000	80	36100
LOU 08/02(691.1)	2700	1130	1250	1180	117000	94	60600
LOU 08/02(694.7)	4740	1890	3210	4470	36000	103	79900
LOU 08/02(759.5)	30	155	98	19400	37	84	205

Figure 2. Hand specimen samples of gold-rich banded black shales with pyrite. The massive pyrite dominates the mineralogy at the hand specimen scale. (Borehole sample LOU 08/02 -694.7 upper photo; LOU08/01-7 lower photo).

3.1 Petrography and paragenesis

The paragenesis in the Lousal Mine, as deducted from the study of samples from drill holes LS08/01 and LS08/02, indicates it to be a 3 stage process: 1- open space growth, 2- recrystallization, substitution, annealing and 3- supergene alteration stage. Chlorite, silica and sericite hydrothermal halos are observed at Lousal (Fernandes, 2011; Relvas et al., 2012).

Petrographically, ore samples from the Lousal Mine are dominated at the handspecimen scale by pyrite and by cobaltite; the latter at the microscopic scale. Pyrite is present as homogeneous-looking masses in cases several centimetres in length and width although smaller grains rarely exceed 300 µm while large subhedral cobaltite grains are observed in independent clusters in the sedimentary gangue or adjacent massive pyrite grains and these are more often than not close to visible gold mineralization.

Pyrite and cobaltite coexist at the microscopic scale and petrographic relationships show them to be coeval. Subordinate pyrrhotite, sphalerite, galena, chalcocite are less common.

Pyrite and cobaltite minerals are cut by late-stage fractures that contain smaller irregular shaped grains of chalcopyrite, gold (electrum), native bismuth and bismuthinite (Fig. 3). The chalcopyrite is often replaced by (supergene) covellite in places.

These fractures are fine, irregular and often "radiate" from larger clusters of chalcopyrite that has grown in open space-filling regimes. The fractures are frequently offset and rarely exceed 10 µm in width (Fig. 3A).

Pale yellow gold (electrum) grains, which are late in the context of the ore paragenetic sequence are observed in fine fractures within the pyrite and cobaltite often as grains not exceeding 6 µm in length, half of that in thickness (Figs. 3A and B).

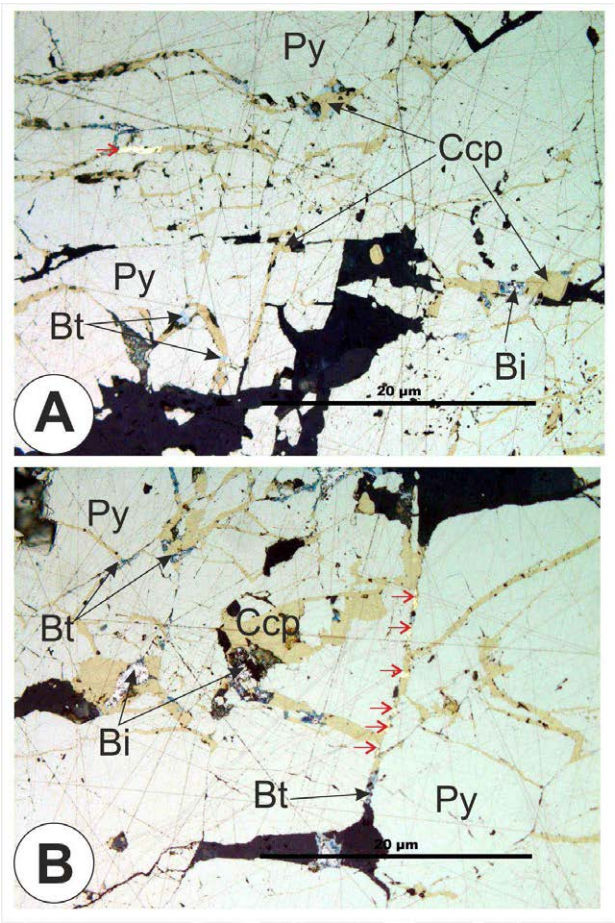

Figure 3. Photomicrographs of samples from the Lousal Mine. Py – pyrite, Ccp – chalcopyrite (with supergene covellite, vivid blue colour), Bi – native bismuth, Bt – bismuthinite, (short) Red arrows – gold (electrum). A –typical appearance of offset fractures and B- distribution of fractures from larger open space filling configuration.

3.2 EPMA characterisation

Electron-probe microanalyses (EPMA) were carried out using a fully automated JEOL JXA-8500F microprobe, equipped with one energy dispersive (EDS) and five wavelength dispersive (WDS) spectrometers. The analyses were performed with a focused electron beam of 20 kV and 20 nA incident current.

The selected analyses shown in Table 2 indicate that apart from the one sample with approximately 5 wt% Ag, most of the gold grains have a high percentage of Ag varying from 24 to 27 wt% which would classify it as auriferous electrum. Gold also contains significant amounts of Hg, Fe, and in two cases, Co as well.

Table 2. EPMA results of analysis of electrum grains in sample LS08/01-7 (732.4 m).

Element	EPMA number		
	1	2	3
Co	2.86	0.00	-
As	1.27	-	-
Ag	4.86	26.13	24.14
Hg	2.78	8.11	8.21
Au	**87.60**	**66.77**	**67.32**
Total	99.37	101.01	99.67

Ore microscopy and EPMA studies have confirmed that the gold (electrum) is genetically associated with cobaltite and native bismuth or bismuthinite (Fig. 4), an association that prevails throughout the samples studied.

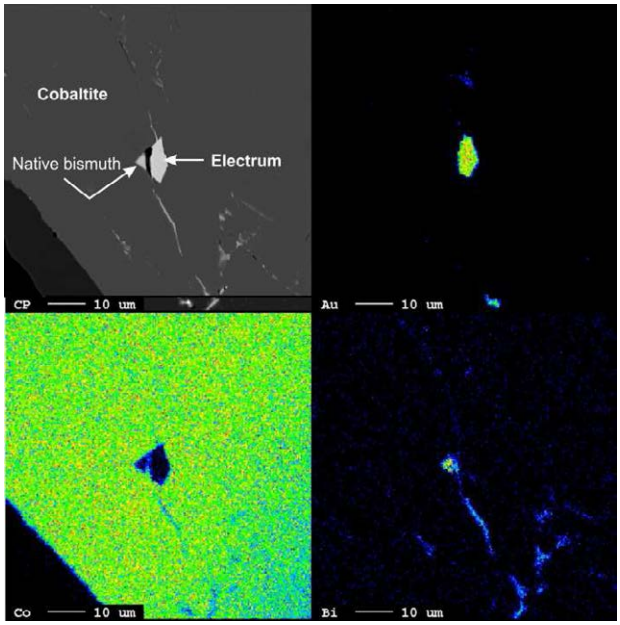

Figure 4. Element map of a region of cobaltite with late-stage fractures with native Bi and bismuthinite in association with a small grain of gold (electrum).

Additionally, the EPMA studies show that often there is also trace amounts of Te in close proximity to electrum grains and native bismuth or bismuth containing minerals.

3 Discussion

Gold (electrum) grains found in Lousal contain approximately 26 wt% Ag with Hg contents that vary from 3 to 8 wt%. One analysis detracts from this trend with only 5 wt% Ag, and therefore it will have to be further determined whether at Lousal there are two distinct gold generations although the petrographic studies coupled with the extensive EPMA do not support this theory.

There is a close association of the presence of gold with distinct zones of hydrothermal alteration characterized by chlorite, silica and ± carbonates.

EPMA results clearly indicate that the gold (electrum) occurs late in the paragenetic sequence within late-stage fractures and is closely associated with native bismuth, bismuthinite and often in close spatial association to chalcopyrite.

The Ag-rich gold is very similar to the results presented by Leistel et al (1998) in the Spanish side of the IPB. Here, two typical gold parageneses are found: 1- Gold of Co-Bi geochemical association found as electrum with abundant to common Co minerals such as cobaltite, alloclasite, glaucodot and common Bi minerals such as kobellite, tintinaite, bismuthinite and joseite associated with pyrite and/or chalcopyrite and, 2- Gold of the Zn-Ag-As geochemical association occurs in

electrum and/or auriferous arsenopyrite within a more polymetallic paragenesis (predominantly Pb-Zn).

In the first type, gold mineralization occurs associated with abundant sedimentary facies and shows that the gold association formed at high temperature (>300 °C) during the initial phases of massive sulfide formation. In the Lousal mine, preliminary analogies exist with the first type of paragenesis.

There are studies that indicate that this sort of ore mineralogy is associated with the stringer zones and the interaction zones at the base of massive sulfide mounds within the IPB and not found in the overlying massive sulfides (e.g. Marcoux et al, 1996). Rare cobalt sulphoarsenides (cobaltite) are formed at the beginning of massive sulfide genesis and in a late-stage the more common bismuth sulfides (such as bismuthinite) were deposited from last-stage Cu-bearing fluids containing Bi (+ Te and Se) and gold is undoubtedly related with this last-stage phase. However, the presence of massive sulfide mounds are absent at Lousal which would favor a tectonic explanation for the presence of late-stage gold (electrum). In this case, late deformation of the massive ore represented by localized shear zones with silica remobilization and sulfides may also explain some metal (including gold, copper and bismuth) remobilization during tectonic events. Research continues.

Acknowledgements

Research was carried out within the framework of Project INCA (Characterization of Crucial Mineral Resources for the Development of Renewable Energy Technologies: The Iberian Pyrite Belt Ores as a Source of Indium and other High-technology Elements) funded by the *Fundação para a Ciência e Tecnologia* (PTDC/CTE-GIN/67027/2006) and ATLANTERRA EU Interreg Atlantic Area Project.

References

de Oliveira DPS, Guimarães FMG, Matos JX, Rosa DRN, Rosa CJP and Castelo Branco, JM, (2011). Gold in the Lousal mine, Iberian Pyrite Belt, Portugal. *In:* Barra, F, Reich, M, Campos, E., Tornos, F (eds.), Let's Talk Ore Deposits, Proceedings 11th SGA Biennial Meeting, p. 757-759.

de Oliveira DPS, Matos JX, Rosa CJP, Rosa DRN, Figueiredo MO, Silva TP, Guimarães F, Carvalho J. Pinto A, Relvas J e Reiser F (2011) The Lagoa Salgada orebody, Iberian Pyrite Belt, Portugal. Economic Geology 106, p. 1111-1128.

Fernandes A.S. (2011) Caracterização petrográfica, mineralógica e geoquímica do padrão de alteração hidrotermal a muro das massas de sulfuretos maciços do Lousal, Faixa Piritosa Ibérica. MSc Thesis Lisbon, University, Unpub. 218p

Leistel JM, Marcoux E, Deschamps Y, Joubert M (1998) Antithetic behaviour of gold in the volcanogenic massive sulfide deposits of the Iberian Pyrite Belt. Mineralium Deposita 33, p.82–97.

Matos JX, Oliveira V (2003) Mina do Lousal (Faixa Piritosa Ibérica) - Percurso geológico e mineiro pelas cortas e galerias da antiga mina. IGME, Pub. Museo Geominero, nº2, Madrid, p. 117-128.

Matos JX, Relvas JMRS (2006) Mina do Lousal (Faixa Piritosa Ibérica). Livro Guia Excursão C.4.1, VII Congresso Nacional de Geologia, Estremoz, Univ. Évora, Portugal, pp. 23-25.

Matos JX, Pereira, Z, Rosa CJP, Oliveira, JT, Relvas JMRS (2011) Late Strunian age: a key time frame for VMS deposit exploration in the Iberian Pyrite Belt. *In:* Barra, F, Reich, M, Campos, E., Tornos, F (eds.), Let's Talk Ore Deposits, Proceedings 11th SGA Biennial Meeting, p. 790-792.

Matos JX, Rosa CJP, Pereira Z, de Oliveira D, Rosa DRN, Sofia A, Relvas JMS, Oliveira, JT (in prep.) Geology and Genesis of the Lousal Volcanic-Sediment-Hosted Massive Sulfide Deposit, Iberian Pyrite Belt, Portugal.

Marcoux E, Moëlo Y, Leistel JM (1996) Bismuth and coblat minerals as indicators os stringer zones to massive sulphide deposits, Iberian Pyrite Belt. Mineralium Deposita 31:1–26.

Oliveira JT, Pereira Z, Rosa CJ, Rosa D, Matos JX (2005) Recent advances in the study of the stratigraphy and the magmatism of the Iberian Pyrite Belt, Portugal. In: Carosi, R., Dias, R., Iacopini, D., Rosenbaum, G., (Eds.,). The southern Variscan belt, Journal of the Virtual Explorer, Electronic Edition 19/9, 1441-8142.

Pereira Z, Matos J, Rosa C, Oliveira JT (2012) Palynostratigraphic importance of the Strunian in the Iberian Pyrite Belt. Joint Meeting of the 45th Annual Meeting of American Association Stratigraphic Palynology (AASP) - The Palynological Society and Meeting of Internacional Commission of Paleozoic Microflora (Cimp), Lexington, KY, USA, Abstract Book, 42-43.

Reiser FKM, Rosa DRN, Pinto AMM, Carvalho JRS, Matos JX, Guimarães FMG, Alves LC, de Oliveira DPS (2011). Mineralogy and Geochemistry of Tin- and Germanium bearing Copper Ore from the Barrigão Remobilised Vein Deposit, Iberian Pyrite Belt, Portugal. International Geology Review, 55, nº10, p.1212-1238.

Relvas, J.M.R.S., Pinto, A.M.M.; Matos, J.X. (2012) Lousal, Portugal: a successful example of rehabilitation of a closed mine in the Iberian Pyrite Belt. Society for Geology Applied to Mineral Deposits SGA News, Nº 31, June 2012, pp. 1-16.

Rosa, C Rosa, D Matos, J and Relvas, J (2010) The volcanic-sedimentary sequence of the Lousal deposit, Iberian Pyrite Belt (Portugal). Geophysical Research Abstracts, EGU General Assembly, Vol. 12, EGU2010- 11000.

Silva, EAF, Bobos I, Matos JX, Patinha C, Reis AP and Fonseca EC (2009) Mineralogy and geochemistry of trace metals and REE in volcanic massive sulfide host rocks, stream sediments, stream waters and acid mine drainage from the Lousal mine area (Iberian Pyrite Belt, Portugal). Applied Geochemistry 24, p.383–401.

Strauss G (1970) Sobre la geologia de la provincia piritífera del SW de la Península Ibérica y de sus yacimientos, en especial sobre la mina de pirita de Lousal (Portugal). Mem. ITGE T. 77, pp.266.

Strauss, GK and Beck, JS (1990) Gold mineralisations in the SW Iberian Pyrite Belt. Mineralium Deposita, 25, p. 237-245.

Strauss GK and Madel J (1974) Geology of massive sulphide deposits in the Spanish–Portuguese Pyrite Belt. Geologische Rundschau, 63, p. 191–211.

Partial melting "fails" to deliver magma or metals to the upper crust – preservation of VHMS seafloor hydrothermal alteration patterns in central Finland

Nicholas H S Oliver
Economic Geology Research Unit, School of Earth and Environmental Sciences, James Cook University, Townsville, Australia, 4811; and Holcombe Coughlin Oliver, Consultants, Townsville, Australia

Michael D Roberts
Economic Geology Research Unit, James Cook University, Townsville, Australia; Present address – Kiska Metals, Vancouver

Pentti S Hölttä and Raimo Lahtinen
Geological Survey of Finland, FIN-02150 Espoo

Andrew G Tomkins
Monash University School of Earth Sciences

Abstract. Cordierite-anthophyllite rocks are well recognised products of the metamorphism of seafloor hydrothermal alteration associated with VHMS deposits. In the central Finland VHMS belt around Pyhäsalmi, the degree of preservation of seafloor alteration products through amphibolite-granulite facies metamorphism and anatexis is extraordinary, including stratigraphic preservation and details of mineralogical, chemical and volume changes that match former upflow and outflow zones. Deep crustal metamorphism is a good way to sequester metals by amphibolite facies melting of sulphides at relatively low temperatures, and send them to shallower environments to potentially form other ore deposits. However, sulphides here also retained broader (and most local) metal zonations reminiscent of seafloor patterns. Furthermore, partial melting of the silicate component produced peritectic (precipitated from melt) cordierites and garnets with the lowest $\delta^{18}O$ values recorded for these minerals, reflecting complete closed system metamorphism and silicate anatexis of the of chlorite-quartz rocks produced in the 'hot' (~ 300°C) upflow zones of the former VHMS deposits. Retention of the silicate melt component in their specific host rocks (at dm- to 10m-scales) and the distribution of sulphides suggest that these rocks may not have contributed to metal or magma budgets for upper crustal ore deposits.

Keywords: anatexis, seafloor alteration, sulphides, metamorphism

1 Introduction

Many Precambrian terrains contain metamorphosed mineral deposits, and many techniques have been used to recognise former deposit attributes and apply exploration models that deal with the overprinting metamorphism and deformation (e.g. Hodges and Manojlovic 1993, Allen et al. 1997). Tomkins and Mavrogenes (2003) and Tomkins et al. (2009) also proposed that the metamorphism of rocks already containing sulphide accumulations was a logical and viable mechanism for the generation of metal-rich felsic magmas during crustal partial melting (anatexis). Papers demonstrating sulphide melting in the amphibolite and granulite facies (e.g. Tomkins and Mavrogenes 2002) show the first steps required in the assembly of metal-rich melt that could be incorporated into magmas with future potential for upper crustal mineralization. In this paper, we give an example where anatexis of crustal rocks probably failed to liberate sulphides at a scale sufficient for later metal accumulation of any type. Furthermore, we show that even silicate melting failed to eradicate important signals of the details of the former VHMS alteration systems.

2 Central Finland VHMS belt

In the Proterozoic Vihanti-Pyhäsalmi metallogenic belt in central Finland (Fig. 1), numerous massive sulphide occurrences are hosted within highly deformed metavolcanic rocks and are associated with metamorphosed alteration halos composed of cordierite-orthoamphibole rocks (Ekdahl, 1993). These rocks comprise remnants of a ca. 1.92 Ga oceanic island-arc complex (Lahtinen, 1994) that forms part of a major orogenic suture zone that separates the Karelian Archean craton in the northeast from Proterozoic terrains that were accreted from the southwest (Svecofennian Domain, Fig. 1). Crustal thickening, polyphase deformation, the emplacement of synkinematic granites (1.89 – 1.88 Ga) and regional low pressure – high temperature (LPHT), amphibolite to granulite facies metamorphism (Nironen, 1997) overprinted the volcanic sequences.

Figure 1. Central Finland VHMS belt around Pyhäsalmi, the largest of the VHMS deposits. The belt formed by accretion of a former oceanic arc during 1.89 to 1.88 Ga collision during the Svecofennian Orogeny, and is dominated by amphibolite- and granulite-facies rocks and intrusions.

3 Ruostesuo

3.1 Distribution of alteration and melt

At the mined-out Ruostesuo Zn-Cu deposit (~5 Mt at 2.0 % Zn and 0.4 % Cu), 15km ESE of Pyhäsalmi, felsic metarhyolites and both Mg-rich and Fe-rich metabasalts host sulphide ore, and all can be traced around 10- to 100m-scale folds (Fig. 2). Although the orthoamphibole (oam) – cordierite (crd) –garnet (grt) - bearing mafic rocks (Fig. 3) are almost completely depleted of Ca, Na and K around the ore lodes, they grade outwards into metamorphosed primitive basalts (Mg-rich) and metamorphosed Fe-richer, evolved, tholeiites (Roberts et al. 1993), both containing abundant plagioclase and amphibole.

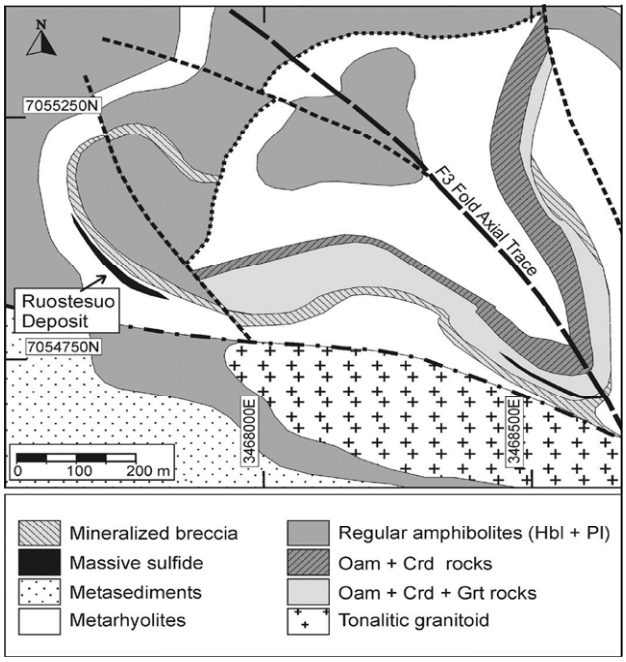

Figure 2. Ruostesuo and surrounds, modified from Roberts et al. (2003). Despite intense alteration, original volcanic stratigraphy can be recognised, as well as the change of 'normal' metabasalts to their seafloor-altered equivalents closer to the ore.

Not only are local melt products apparently retained within their original host rocks (Fig. 3), the peritectic phases produced by in situ partial melting record the original oxygen isotope signal of the seafloor alteration, corresponding to the chlorite-rich, ~ 300°C 'upflow' zones of a VHMS. Roberts et al. (2003) report $\delta^{18}O$ values amongst the lowest ever recorded for mafic rocks (whole rocks 1.0 to 3.3‰) and the constituent minerals record the same signal, but with inter-mineral values consistent with the >700°C metamorphism (cordierite 2.9 to 3.3‰, garnet 0.1 to 1.1‰).

3.2 Distribution of sulphides

Although we have little detailed information on the microscopic distribution of sulphides at Ruostesuo, Figure 2 shows the main mapped distribution of sulphides. The main ore zone in the west is situated within the northwest limb of a large refolded fold complex in metamorphosed, altered felsic volcanics, whereas the uneconomic southeastern lens is hosted in cordierite-anthophyllite mafic rocks. Ore occurs as massive to brecciated pyrite- and pyrrhotite-rich layers with base metal sulphide matrix; a stratigraphically continuous pyrrhotite-rich breccia layer can be followed around the fold complex for over 2 km (Huhtala, 1979). Different host rocks have different Cu/Zn ratios, the ore is not obviously thickened into the hinge regions of the folds, and the brecciation within the mineralized breccia appears to predate the folding. All these observations are consistent with a high degree of preservation of the original sulphide distribution relative to the alteration and the stratigraphy.

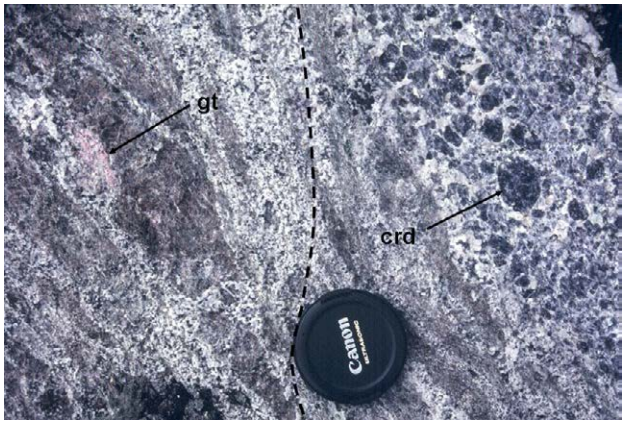

Figure 3. Within the individual units, the nature of partial melting products is internally-controlled at dm- to m-scales. The former Fe-rich tholeiites (left) contain garnet as solid (peritectic) products of melting reactions, whereas the former magnesian rocks contain gem-quality purple cordierites (right). Pale material is quartzo-feldspathic leucosome (partial melt).

4 Säviä

At the Säviä Zn-Cu prospect 60km SE of Pyhäsalmi, our detailed mapping of a key outcrop shows similar patterns to Ruostesuo, but here we have also documented the distribution of both silicate melt products and sulphides at the same scale. The main ore-bearing zones (Fig. 4) contain disseminated pyrrhotite and sphalerite in evenly foliated biotite-orthoamphibole mafic rocks; elsewhere in the outcrop thin sulphide bands parallel to bedding are found in specific competent orthoamphibole-rich layers within a orthoamphibole – garnet – cordierite – quartz mafic rock. The silicate melt component is also stratigraphy controlled similar to Ruostesuo, but here the melts have typically pooled, at cm- to dm-scales, into the necks of boudinaged layers. It appears that the distribution of sulphides is more tightly constrained by the host rock than are the silicate melts, implying minimal migration of sulphides during metamorphism, deformation and partial melting of the host rocks. This interpretation is consistent with previous work on metamorphosed ores, which suggests that sulfide melting in VHMS systems requires galena (Tomkins et al. 2007), a mineral present in only low abundances at Säviä.

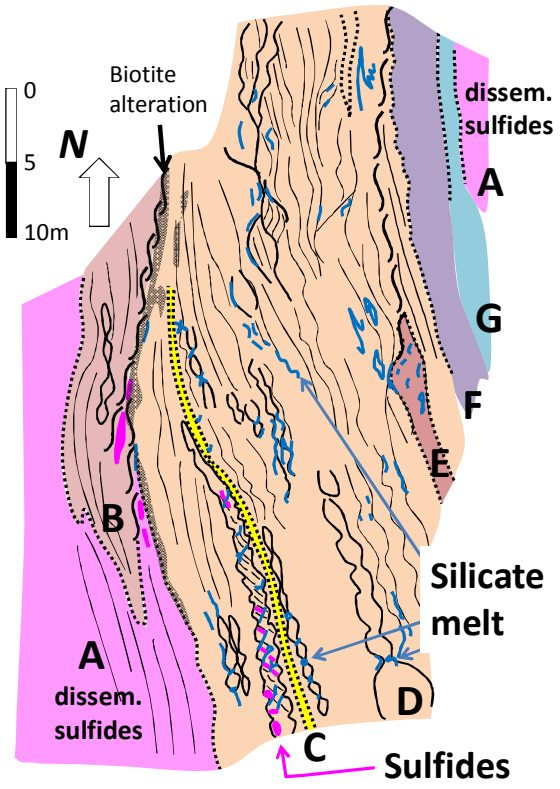

Figure 4. Our detailed map of the key outcrop at Savia Zn-Cu prospect. A is the ore zone meta-andesite, B coarse grained orthoamphibole-cordierite rock, C garnet-cordierite-rich layer within D boudinaged orthoamphibole-garnet-quartz-cordierite mafic rock, E leucosome-rich garnet-cordierite-bearing granitoid, F intermediate quartz-garnet-orthoamphibole-biotite rock and G foliated orthoamphibole-quartz-garnet rock. Note that coarse sulphides have a very specific layer-controlled distribution whereas silicate leucosomes, although predominant in unit D, appear controlled by deformation into boudin necks.

5 Kangasjärvi and Pyhäsalmi

The two largest deposits in the central part of the belt show more convincing evidence for sulphide mobility, but we are uncertain as to whether this mobility occurred in the form of a sulphide melt derived by partial melting during regional metamorphism. At Pyhäsalmi, chalcopyrite veins cut bedding containing sphalerite laminations, implying local or more distant remobilization of copper (Mäki and Luukas, 2001). At Kangasjärvi Zn-Cu-Pb deposit, sulphides occur smeared out along the S2 fabric, and within late crosscutting veins, fractures and breccias. However, it also occurs within the cores of early garnet porphyroblasts, as sulphide-matrix breccias with stratigraphic continuity similar to Ruostesuo, and irregular, locally folded biotite-garnet-sulphide seams. These latter are probably the prograde metamorphic equivalent of mineralized, chlorite- and sericite-altered fractures or faults, and may represent syn-volcanic structures that channelized hydrothermal fluids. Metamorphosed alteration zones are well preserved in the surrounding mafic and felsic meta-volcanics. Original sericite + Mg chlorite alteration (now sillimanite-cordierite-bearing) was focused beneath mineralization and may have zoned outwards or overprinted an extensive alteration halo of Fe-Mn-Mg chlorite + sericite (now with complex biotite – sillimanite – garnet – staurolite – orthoamphibole). Mafic rocks show similar assemblages to Ruostesuo, but with more preservation of plagioclase, suggesting more dispersed or possibly cooler upflow zones.

6 Geochemistry

Our whole rock geochemical database covers all the deposits and prospects covered here, and forms part of the extensive GTK geochemical database for the region. Roberts et al. (2003) used that data to identify precursor rocks and demonstrate the degree of preservation of alteration assemblages at Ruostesuo, and also at Kangasjärvi. Here we briefly try to identify the fate of the metals and sulphur in response to the early alteration and later metamorphism, deformation and anatexis.

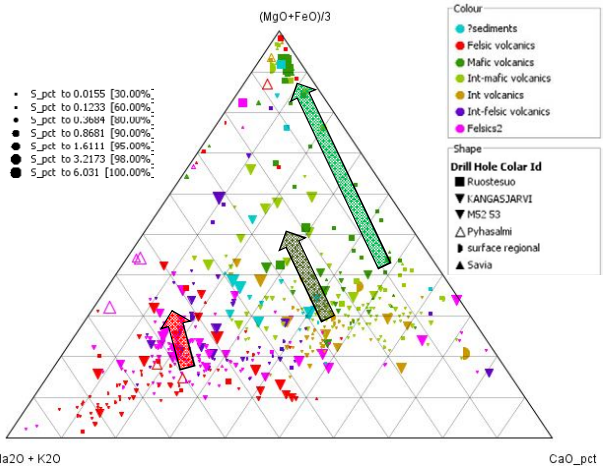

Figure 5. FeO+MgO vs CaO vs Na2O+K2O plot for rocks discussed in the text. Colours represent the different protoliths (warm colours felsic, cool colours mafic). Arrows show the trend towards enrichment in MgO+FeO caused by chloritization at the expense of feldspars in upflow zones of the former seafloor hydrothermal systems. Dot size is % sulphur.

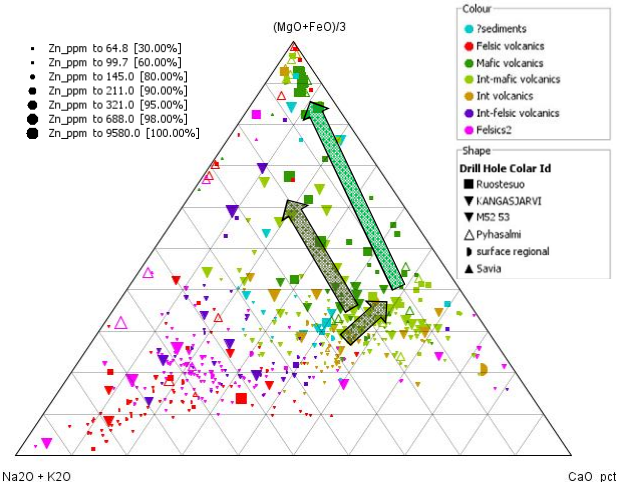

Figure 6. Symbols as for Fig. 5, but dot size is % Zn. At Kangasjärvi, there is significant sphalerite in the upflow zones in the mafic rocks, but basaltic andesites also carry Zn in rocks little-enriched in Fe + Mg. Felsic rocks have little Zn. Cu shows a similar pattern.

Using ioGAS, we separated out the different protoliths and then assessed the alteration and sulphides. Plots that show the breakdown of feldspars at the expense of chlorite and muscovite were most suitable – Figure 5 shows that the depletion in Ca + Na + K in the upflow zones was accompanied by an enrichment of sulphur. The extreme enrichment shown at Ruostesuo (right arrow) is inferred to reflect a focussed, hot (~300°C) upflow, whereas the upflow zone was more diffuse or lower temperature at Kangasjarvi (shorter two arrows).

Figures 6 and 7 show that the base metals are distributed differently to the total sulphur, reflecting lithological and/or alteration controls on the distribution of pyrrhotite-pyrite, sphalerite and galena.

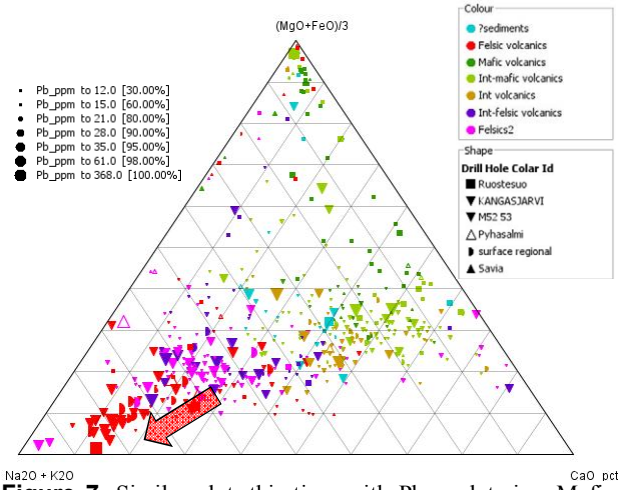

Figure 7. Similar plot, this time with Pb as dot size. Mafic rocks have little Pb; felsic rocks at Kangasjärvi show enrichment of Pb with an increase in K (former sericite alteration). Although galena facilitates amphibolite-facies sulphide melting (Tomkins et al. 2007) this does not appear to have resulted in bulk migration of sulfides away from these felsic rocks.

6 Conclusions

We document here a very unusual occurrence of the production of low $\delta^{18}O$ partial melts from anatexis of former seafloor alteration zones. However, because these melts are "frozen" close to their source, they could not have contributed to the generation of voluminous low $\delta^{18}O$ magma, such as some of those found in Iceland (e.g. Balsley and Gregory 1998). Similarly, we have demonstrated that the distribution and controls on sulphides are constrained to particular lithologies and alteration zones. Even though many rock types have undergone partial melting, it does not appear that there has been sufficient accumulation of molten sulphides to change the fairly tight controls on their spatial patterning relative to former seafloor alteration. Metamorphosed upflow zones in mafic rocks retain high initial Zn, Cu and sulphide contents relative to precursors; high Pb values are specifically found in K-altered meta-rhyolites. We regard this system as "failed" in the sense of high grade metamorphism liberating metals or magmas towards the upper crust, but "successful" in the extreme preservation of VHMS alteration signals through high grade metamorphism and anatexis.

Acknowledgements

This research was supported by the Geological Survey of Finland (GTK), the Australian Research Council, and James Cook University. We thank Ian Cartwright, Martin Fairclough, Jouni Luukas, Jukka Kousa, E. Kallio, Timo Maki, Jodie Miller, Pekka Nurmi, Kalevi Rasilainen, Mike Rubenach, Zach Sharp and Peter Ward.

References

Allen RL, Weihed P, Svenson SÅ (1997) Setting of Zn-Cu-Au-Ag massive sulfide deposits in the evolution and facies architecture of a 1.9 Ga marine volcanic arc, Skellefte district, Sweden. Econ Geol: 91, 1022 - 1053

Balsley SD, Gregory RT (1998) Low-18O silicic magmas: why are they so rare? Eth Plan Sci Lett: 162, 123 - 136

Ekdahl E (1993) Early Proterozoic Karelian and Svecofennian formations and the evolution of the Raahe-Ladoga Ore Zone, based on the Pielavesi area, central Finland. Geol Surv Finland Bull 373: 137pp

Hodges DJ, Manojlovic PM (1993) Application of litho-geochemistry to exploration for deep VMS deposits in high grade metamorphic rocks, Snow Lake, Manitoba: J Geochem Expl 48: 201 - 224

Huhtala T (1979) The geology and zinc-copper deposits of the Pyhasalmi-Pielavesi District, Finland. Econ Geol 74: 1069-1083

Lahtinen R (1994) Crustal evolution of the Svecofennian and Karelian domains during 2.1-1.79 Ga, with special emphasis on the geochemistry and origin of 1.93-1.91 Ga gneissic tonalites and associated supracrustal rocks in the Rautalampi area, central Finland. Geol Surv Finland Bull 378: 128pp

Mäki T, Luukas J (2001) Structural control of the Pyhäsalmi VMS-deposit in the Palaeoproterozoic Raahe-Ladoga Zone, central Finland, In Williams PJ (ed) *2001: A Hydrothermal Odyssey*, EGRU contribution 59

Nironen M (1997) The Svecofennian Orogen; a tectonic model. Precambrian Res 86: 21 - 44

Roberts MD, Oliver NHS, Fairclough MC, Hölttä PS, Lahtinen R (1993) Geochemical and oxygen isotope signature of seafloor alteration associated with a polydeformed and highly metamorphosed massive sulfide deposit, Ruostesuo, Central Finland. Econ Geol 98: 535-556

Tomkins AG, Grundy C (2009) Upper temperature limits of orogenic gold deposit formation: Constraints from the granulite-hosted Griffin's Find deposit, Yilgarn Craton. Econ Geol 104:669-685

Tomkins AG, Mavrogenes JA (2002) Mobilization of gold as a polymetallic melt during pelite anatexis at the Challenger gold deposit, South Australia: a metamorphosed Archean deposit. Econ Geol 97:1249–1271

Tomkins AG, Mavrogenes JA (2003) Generation of metal-rich felsic magmas during crustal anatexis. Geology 31:765-768

Tomkins AG, Pattison DRM, Frost BR (2007) On the initiation of metamorphic sulfide anatexis. J Petrology 48: 511–535.

Geology, lithogeochemistry, and sulfur isotope geochemistry of hydrothermal mudstones from the Duck Pond volcanogenic massive sulfide (VMS) deposit, Newfoundland Appalachians, Canada

Stephen J. Piercey, Graham D. Layne, Glenn Piercey
Department of Earth Sciences, Memorial University, St. John's, NL, Canada, A1B 1N3, Email: spiercey@mun.ca

Gerry Squires
Teck Resources Ltd. , Duck Pond Mine, P.O. Box 9, Millertown, NL, Canada, A0H 1V0

Terry Brace
Cornerstone Resources Inc., 26 Kyle Ave., Mount Pearl, NL, Canada, A1N 4R5

Abstract. Sulfide-rich mudstones from the Duck Pond volcanogenic massive sulfide (VMS) deposit are pyrrhotite-pyrite-rich and occur associated with pillow lavas and rhyolitic volcaniclastic rocks. They have elevated Fe_2O_3 and base and trace metal content, and have a low detrital element content, suggesting they are hydrothermal in origin. While hydrothermal, they have low Eu/Eu*, variable to high Y/Ho values, mostly low Ce/Ce*, and elevated oxyanion contents. The sulfur isotopic data ($\delta^{34}S$) from sulfides in the mudstones is predominantly negative, with the exception of euhedral pyrite, which is distinctively positive, suggesting variable contributions biogenic (diagenetic?) and hydrothermal sulfur, respectively. The collective geochemical and isotopic data from the suggest that the Duck Pond mudstones formed from low temperature discharge associated with a buoyant hydrothermal plume, where particles had significant residence time in the water column so as to scavenge oxyanions from oxygenated Cambrian seawater. They also had abundant diagenetic transformations and scavenging of diagenetic sulfur, whereas their hydrothermal sulfur contents were likely minor.

Keywords.
VMS, Lithogeochemistry, Sulfur Isotopes, Appalachians

1 Introduction

Volcanogenic massive sulfide (VMS) deposits are often spatially and temporally associated with fine-grained, Fe-rich hydrothermal mudstones. These mudstones are interpreted to represent hydrothermal discharge and vary in composition with proximity and distance from a hydrothermal vent (e.g.,German and Von Damm 2003; Peter 2003; Rudnicki 1995). In the Tally Pond group in the Newfoundland Appalachians, Canada, numerous VMS deposits and occurrences are spatially associated with hydrothermal sedimentary rocks (e.g., Lemarchant, South Moose, Boundary), including the producing Duck Pond deposit. In this contribution we provide lithostratigraphic, lithogeochemical, and in-situ sulfur isotopic data for mudstones from the Duck Pond deposit. The results are aimed at elucidating the provenance, nature of hydrothermal plume activity, seawater oxidation state, sulfur sources in the sediments and their potential applications to exploration vectoring.

2 Geological Setting

2.1 Regional to Local Deposit Setting

The Duck Pond deposit is hosted within the Tally Pond group of the Dunnage Zone of the Newfoundland Appalachians (van Staal 2007). The deposit consists of two main blocks: a mineralized block and an upper block that lie in thrust fault contact along the Duck Pond thrust fault (Fig. 1)(Squires et al. 2001). Despite thrusting and localized deformation, the stratigraphy is flat-lying and extremely well preserved. The mineralized block consists massive Cu-Zn-rich and pyritic massive sulfide that are hosted with rhyolite breccias, flows, and polygonally jointed tuff breccia, and are interpreted to have formed via subseafloor replacement (Piercey and Hinchey 2012; Squires et al. 2001). Rhyolite from the mineralized block has yielded U-Pb zircon ages of ~509 Ma (McNicoll et al. 2010).

The upper block contains a distinctive facies of flow banded rhyolite inter-bedded with pillowed and massive basalt. Sulfide-rich mudstone are interbedded with both the rhyolite and basalt (Fig. 1). All are cross-cut by the quartz-feldspar porphyry intrusions (synvolcanic?) and younger gabbroic rocks (Fig. 1). U-Pb zircon ages for rhyolitic rocks in the upper block have yielded U-Pb ages ~514-512 Ma. This suggests that the hydrothermal mudstones are hosted within a block older than the main VMS forming event in the belt.

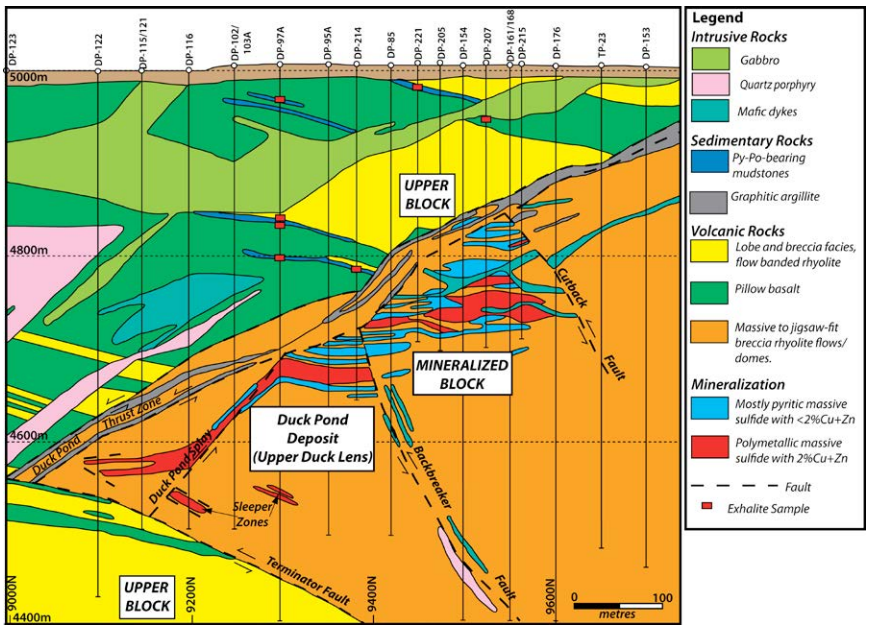

Figure 1. Long section 9600N through the Duck Pond deposit. Modified from Squires et al. (2001).

2.2 Sulfide-Rich Mudstones

Sulfide-rich mudstones in upper block are pyrrhotite-rich and found at numerous stratigraphic levels in the block (Fig. 1). The mudstones do not change texture as a function of stratigraphic position within the and occur in a variety of forms, including: 1) finely laminated pyrrhotite that is brassy in color and intergrown with black mudstone; 2) laminated to massive pyrrhotite with minor pyrite and chalcopyrite, often with rounded mudstone balls; 3) finely interlaminated pyrrhotite and black mud, with or without felsic volcanic ash layers; 4) hydrothermal mudstones with contorted hydrothermal layers (slump folds?/seismites?); 5) carbonaceous mud-rich layers with clots of pyrrhotite and intergrown with volcanic clasts (transported?); and 6) ochre-like units rich in pyrrhotite, but with a minor mm-scale surface rind of rusty weathering.

The hydrothermal mudstones occur in two main stratigraphic positions: 1) located solely within pillow lavas and forming as interflow units; and 2) located at contacts between pillow lavas and rhyolitic lavas. When hosted by pillow lavas the sulfide-rich mudstones typically occur along pillow margins, and in a single drill hole they can occur at multiple horizons between successive pillowed flows, suggesting emplacement during volcanic activity (Fig. 1). Pillow lavas proximal to the mudstones have variably pervasive epidote, quartz, and chlorite alteration with minor pyrite. At locations near rhyolite-basalt contacts, there are often felsic breccias that contain angular to subangular fragments of rhyolite that are locally flow banded, within a matrix of chlorite-sericite altered felsic ash (Fig. 1). These felsic units are often strongly sericite and quartz altered with minor chlorite alteration of the finer grained ash.

The hydrothermal mudstones consist of varying abundances of pyrrhotite with lesser pyrite, chalcopyrite, sphalerite, and arsenopyrite with varying textures and relationships. They are hosted within a matrix dominated by quartz, chlorite, Fe-oxides/hematite, organic material, calcite, dolomite, Fe-carbonate, K-feldspars, celsian, apatite, monazite, and zircon. The mineralogy and textural relationships of the ore will be reported in a subsequent paper.

3 Lithogeochemistry and Sulfur Isotopes

3.1 Essential Lithogeochemical Features

The mudstones have high Fe_2O_3 (~10-55%), S (~5-20%), and anomalous Pb (~20-100ppm), Zn (~300-3000ppm), Cu (~100-1000ppm), and Ba (10-200ppm) contents, interpreted to reflect hydrothermal input. They also have high Fe/Al and Fe-Mn-Al systematics consistent with deposition from Fe-rich metalliferous fluids. The rocks also have very significant enrichments in the P_2O_5, V, Cr, Ni, Co, As, and Hg (not shown), and it interpreted that the oxyanion enrichment was due to oxidative scavenging of elements from seawater onto Fe-oxide/oxyhydroxide particles. The mudstones also have REE-Y systematics and signatures that are identical to modern oxic seawater with high Y/Ho, negative Ce anomalies (Ce/Ce*<1), and super-chondritic Zr/Hf ratios (not shown); high Y/Ho and low Ce/Ce* also correlate with adsorbed oxyanion concentrations (Fig. 4). The mudstones also have low Eu/Eu* (i.e., ≤1; Fig. 3).

3.2 Sulfur Isotope Geochemistry

Sulfur isotope geochemistry was obtained on pyrite, pyrrhotite, and chalcopyrite in situ using thin sections and secondary ion mass spectrometry (SIMS) at Memorial University. Sulfur isotope values are broken out into textural variants including: 1) anhedral pyrite; 2) framboidal pyrite; 3) euhedral pyrite; 4) clots of chalcopyrite and pyrrhotite that are clots within the sedimentary matrix; 5) larger sheets of chalcopyrite

and pyrrhotite; and 6) cross-cutting veins, veinlets, or near vein pyrite, pyrrhotite, and chalcopyrite that represent either diagenetic remobilization of later structural remobilization.

The bulk of the sulfur isotopic data, regardless of texture exhibit negative $\delta^{34}S$ values (Fig. 5), consistent with a signficnat component of biogenic sulfur, likely obtained during diagenesis. In contrast, euhedral pyrite contains distinctly positive signatures (Fig. 5), consistent with a hydrothermal origin, likely from the thermochemical reduction of seawater sulfate (TSR).

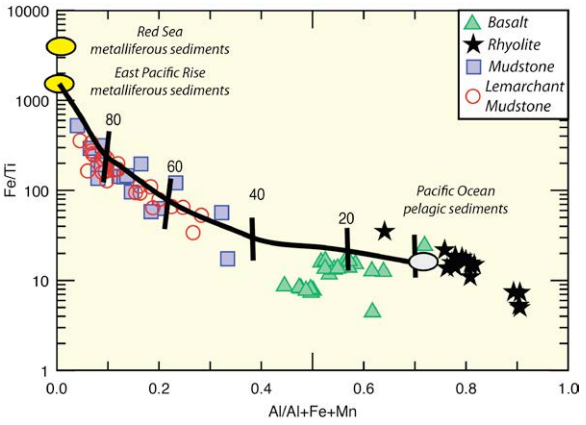

Figure 2. A) Fe/Ti-Al/Al+Fe+Mn plot for evaluating the relative contributions of hydrothermal versus detrital material within hydrothermal sedimentary rocks. From Bostrom (1973).

5 Summary

The geological and geochemical features presented herein suggest that the sulfide-rich mudstones from the Duck Pond deposit have a hydrothermal origin. However, they likely formed from low temperature (<250°C), Fe-rich hydrothermal vent fluids. The elevated Y/Ho and low Ce/Ce* values of many samples suggest that many of the samples vented into an oxic water column. Furthermore, the correlation of the latter variables with elevated oxyanion concentrations suggest that they likely formed a buoyant plume that had significant time to interact and scavenge elements from seawater. Samples with high Fe_2O_3, base and trace metal contents, low Y/Ho, higher Ce/Ce*, high Eu/Eu*, and low oxyanion values are those that likely formed closest to a hydrothermal vent source.

Sulfur isotopic data from the mudstones indicates they contain both hydrothermal and biogenic (diagenetic) sulfur. There are distinct textural associations with hydrothermal sulfur (i.e., euhedral sulfur), whereas all other phases have overlapping sulfur isotopic values (Fig. 5). The utilization of textural relationships and the relative proportions of hydrothermal versus biogenic sulfur may be useful in discriminating prospective from less prospective mudstones.

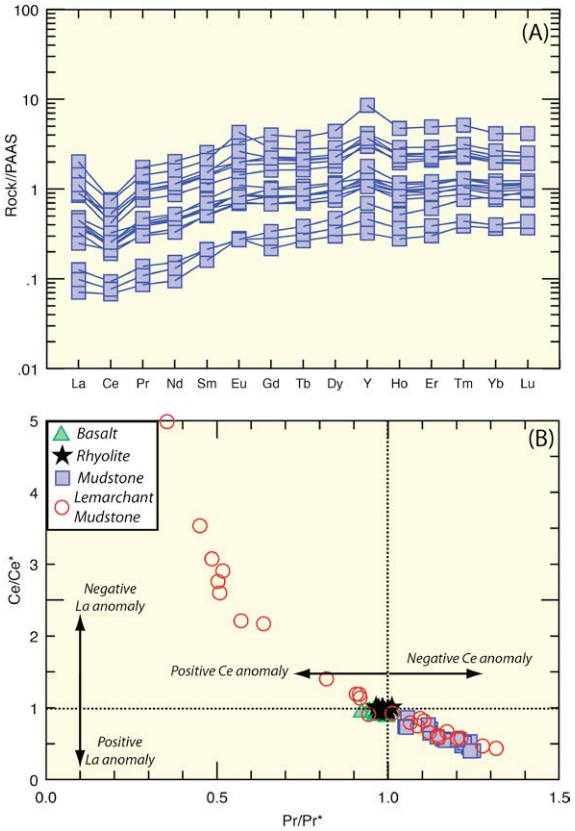

Figure 3. Rare earth element and Y (REY) systematics for Duck Pond sulphide-rich mudstones. A) Post-Archean Australian Shale normalized REY plot. B) Ce/Ce*-Pr/Pr* plot illustrating that the sulfide-rich mudstones have negative Ce and positive La anomalies (diagram from Kamber and Webb 2001).

Acknowledgements

Fieldwork for this research was funded by Aur Resources, Teck Resources, and an NSERC Discovery Grant to Piercey. Additional funding has come from the Geochemistry of Shales as Vectors to Ore Deposits: Project 08E04 funded by the Canadian Mining Industry Research Organization (CAMIRO) and an NSERC Collaborative Research and Development Grant (CRD). Piercey is also funded by the NSERC-Altius Industrial Research Chair in Mineral Deposits funded by NSERC, Altius Resources Inc. and the Research and Development Corporation of Newfoundland and Labrador. Staff at the Duck Pond mine are thanked for logistical support. Discussions with Mark Hannington, Wayne Goodellow, Tom Lane, Jan Peter, John Slack and other participants in CAMIRO Project 08E04 are acknowledged.

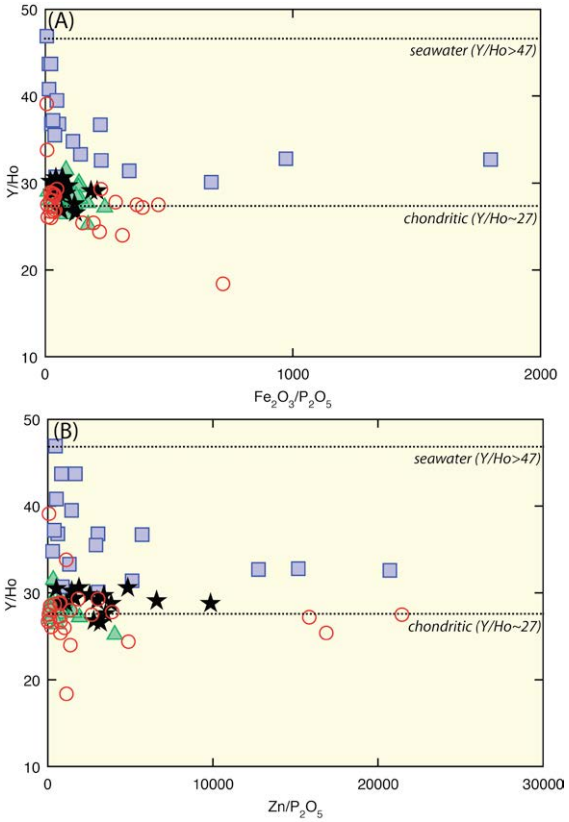

Figure 4. Y/Ho vs. Fe_2O_3/P_2O_5 (A) and Zn/P_2O_5 (B). The Y/Ho ratios become more chondritic with greater contributions from hydrothermal elements (i.e., higher Fe_2O_3, Zn), whereas they have a greater seawater signature with increasing scavenged element content (i.e., higher P_2O_5). The lower the Y/Ho ration and the higher the Fe_2O_3/P_2O_5 and Zn/P_2O_5 ratios are the more prospective the mudstone is as it likely occupies a more vent proximal location. Chondritic and seawater Y/Ho ratios from Bau (1996).

References

Bau M (1996) Controls on the fractionation of isovalent trace elements in magmatic and aqueous systems; evidence from Y/Ho, Zr/Hf, and lanthanide tetrad effect. Contributions to Mineralogy and Petrology 123(3):323-333

Boström K (1973) The origin and fate of ferromanganoan active ridge sediments. Stockholm Contributions to Geology 27:147-243

German CR, Von Damm KL (2003) Hydrothermal Processes. In: Treatise on Geochemistry. Pergamon, Oxford, pp 181-222

Kamber BS, Webb GE (2001) The geochemistry of late Archaean microbial carbonate; implications for ocean chemistry and continental erosion history. Geochimica et Cosmochimica Acta 65(15):2509-2525

McNicoll V, Squires G, Kerr A, Moore P (2010) The Duck Pond and Boundary Cu-Zn deposits, Newfoundland: new insights into the ages of host rocks and the timing of VHMS mineralization. Canadian Journal of Earth Sciences 47(12):1481-1506

Peter JM (2003) Ancient iron formations: their genesis and use in the exploration for stratiform base metal sulphide deposits, with examples from the Bathurst Mining Camp. In: Lentz DR (ed) Geochemistry of Sediments and Sedimentary Rocks: Secular Evolutionary Considerations to Mineral Deposit-Forming Environments. Geological Association of Canada, pp 145-176

Piercey SJ, Hinchey JG (2012) Volcanogenic massive sulphide (VMS) deposits of the Central Mobile Belt, Newfoundland. Geological Association of Canada–Mineralogical Association of Canada Joint Annual Meeting, Field Trip Guidebook B4. . In: Newfoundland and Labrador Department of Natural Resources, Geological Survey, p 56

Rudnicki MD (1995) Particle formation, fallout and cycling within the buoyant and non-buoyant plume above the TAG vent field. Geological Society, London, Special Publications 87(1):387-396

Squires GC, Brace TD, Hussey AM (2001) Newfoundland's polymetallic Duck Pond deposit: Earliest Iapetan VMS mineralization formed within a sub-seafloor, carbonate-rich alteration system. In: Evans DTW, Kerr A (eds) Geology and Mineral Deposits of the Northern Dunnage Zone, Newfoundland Appalachians. Geological Association of Canada/Mineralogical Association of Canada, St. John's, NL, pp 167-187

van Staal CR (2007) Pre-Carboniferous tectonic evolution and metallogeny of the Canadian Appalachians. In: Goodfellow WD (ed) Mineral Deposits of Canada: A Synthesis of Major Deposit-types, District Metallogeny, the Evolution of Geological Provinces, and Exploration Methods. Special Publication 5, Mineral Deposits Division, Geological Association of Canada, pp 793-818

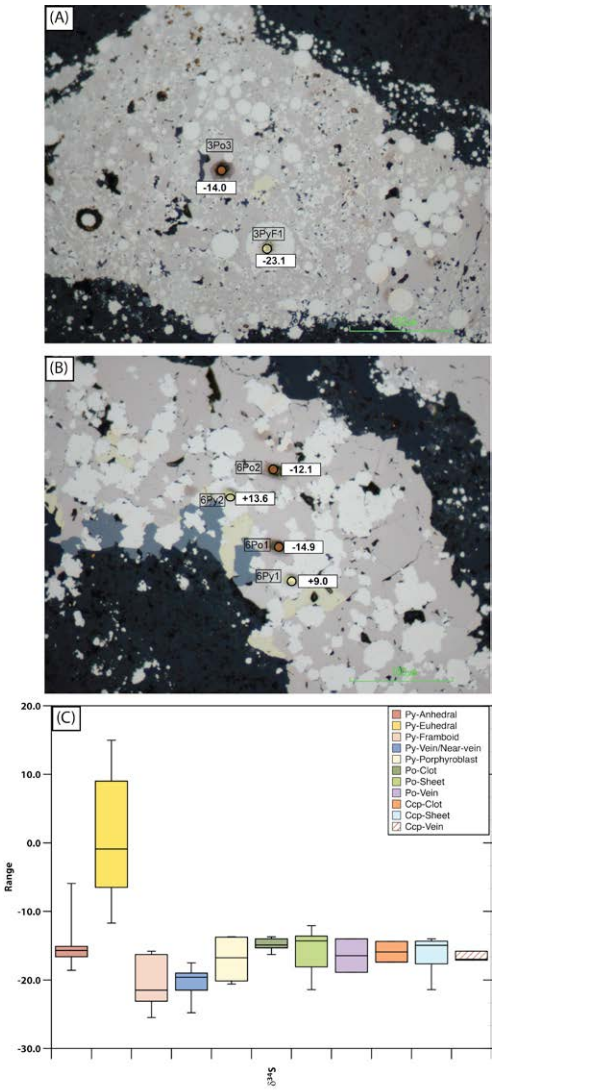

Figure 5. A) Framboidal pyrite within a sea of pyrrhotite exhibiting distinctly negative $\delta^{34}S$ values. B) Pyrrhotite sheets exhibit negative $\delta^{34}S$ values, whereas euhedral pyrite has high d34S values. C) Box and whisker plot of $\delta^{34}S$ values for various sulphide phases and textural variants in mudstones from the Duck Pond deposit.

Major volcano-sedimentary facies types of the Madneuli polymetallic deposit, Bolnisi district, Georgia: implications for the host rock depositional environment

Nino Popkhadze
A. Djanelidze Institute of Geology & I.Javakhishvili Tbilisi State University, Tbilisi, Georgia

Robert Moritz, Stefano Gialli
Earth and Environmental Sciences, University of Geneva Switzerland

Tamar Beridze, Vladimer Gugushvili, Sophio Khutsishvili
A. Djanelidze Institute of Geology, Tbilisi, Georgia

Abstract

The Madneuli polymetallic deposit is the major deposit of the Bolnisi ore district in the southeastern part of Georgia, which is in production since the 70's. The Bolnisi district is part of the Lesser Caucasus; it extends towards the west in the Eastern Pontides, Turkey. The origin of the Madneuli deposit is still controversial. Our study is based on physical volcanology and sedimentary basin analyses. Eleven principal volcanic and volcano-sedimentary facies types were identified within the Madneuli open pit based on their composition, texture, volcanic and sedimentary structures. The presence of various submarine sedimentary structures, hyaloclastite and turbiditic rocks and Radiolaria described for the first time within the host rocks of the Madneuli open pit, supports the submarine depositional setting for the volcano-sedimentary succession hosting the Madneuli deposit.

Keywords: Cretaceous, Caucasus, Volcanic lithofacies, pumice, lapilli.

1 Introduction

Despite abundant investigations, the origin of the Madneuli polymetallic deposit, hosted by Upper Cretaceous volcanic and volcano-sedimentary rocks, named Mashavera suite, of the Lesser Caucasus, is still debated. Genetic models have ranged from epigenetic scenarios (Migineishvili, 2002) relating all the ores to post-Cretaceous events (Nazarov 1966; Gogishvili et al., 1976; Tkemaladze, 1982) to those favoring a link with Upper Cretaceous volcanism (Bachaldin and Tvalchrelidze, 1963; Malinovsky et al., 1987; Gugushvili and Omiadze, 1988; Kekelia et al., 1993), including a scenario suggesting massive sulfide stratiform ore bodies of exhalative-sedimentary nature (Magalashvili, 1991). The Madneuli deposit was also interpreted as a volcanogenic massive sulfide (VMS)-epithermal transitional type of deposit (Migineishvili, 2005). The most recent investigation by Gialli (2013) was based on a detailed study of ore paragenesis and alteration combined with a stable isotope investigation and a petrologic and geochemical study of the host rocks. Gialli (2013) interpreted the Madneuli deposit as a transitional hydrothermal system with a magmatic input formed in a submarine environment.

The Cretaceous Bolnisi district of the Lesser Caucasus in Georgia lacks any detailed recent studies based on the reconstruction of volcanic and sedimentary facies architecture in contrast to other well-known volcanogenic massive sulfide ore districts in other parts of the world (McPhie and Allen 1992, Rosa et al. 2008). In this paper, we make the first attempt to describe and interpret some significant volcano-sedimentary units with an emphasis on the volcanic lithofacies recognition at the Madneuli deposit. Two different ore types are recognized in the Madneuli open pit (Gialli, 2013): a) a subvertical stockwork part occurs on the western flank of the open pit and b) a subvertical pyrite-chlorite-hematite gold-bearing vein system on the eastern flank of the open pit.

2 Regional geological setting

The Artvin-Bolnisi Unit is bordered to the North by the Adjara-Trialeti unit, which represents a Santonian-Campanian back-ark, and the Imbricated Baiburt-Karabakh unit to the South representing an Upper Cretaceous fore-arc (Figure 1). It represents the northern part of the southern Transcaucasus and the central part of the Eastern Pontides, which formed the active margin of the Eurasian continent. The Artvin-Bolnisi unit is characterized by a Hercynian basement, which consists mainly of: (1) a Late Proterozoic-Early Paleozoic basement, (2) a Neoproterozoic-Cambrian granite basement complex, (3) a Middle-Late Carboniferous microcline granite basement complex, and (4) a Late Proterozoic-Early Paleozoic Tectonic Melange Zone (Zakariadze et al.2007). In the Bolnisi region, two basement complexes are exposed, and called the Khrami and Loki salient, which are overlain by Carboniferous volcano-sedimentary rocks. Within the Artvin-Bolnisi unit, the Upper Cretaceous section is dominated by volcanic rocks consisting of calc-alkaline basalt, andesite, dacite and rhyolite (lava, and pyroclastic rocks). Their thickness reaches 3000-4000m. Volcanic rocks are of shallow marine-subaerial type. Volcanic eruptions ceased in the Late

Cenomanian, and throughout Maastrichian and Early Paleocene in the entire Transcaucasian massif (Adamia et al. 2011). The Bolnisi volcanic-tectonic depression is represented by Cretaceous, Paleogene, Pliocene and Quaternary sedimentary rocks. Three main formations are distinguished within the Albian-Upper Cretaceous volcano-sedimentary unit: 1) terrigenous-carbonate (Albian-Cenomanian), 2) volcanogenic (Turonian-Santonian) and 3) carbonate (Campanian-Maastrichtian) units. Jurassic and Cretaceous rocks consist of volcaniclastic rocks, limestone and calc-alkaline magmatic arc rocks (andesite, dacite, rhyolite, and basalt and volcaniclastic rocks intruded by granitoids). The sequence is unconformably overlain by a Maastrichtian – Paleocene turbidite sequence. A Lower Eocene formation consists of terrigenous clastic rocks. Middle Eocene volcanic rocks overlie unconformably older rocks and are conformably overlain by Upper Eocene shallow-marine clastic rocks. The youngest rocks in the region are Quarternary volcanic rocks and alluvial sedimentary rocks (Yilmaz et al.2000).

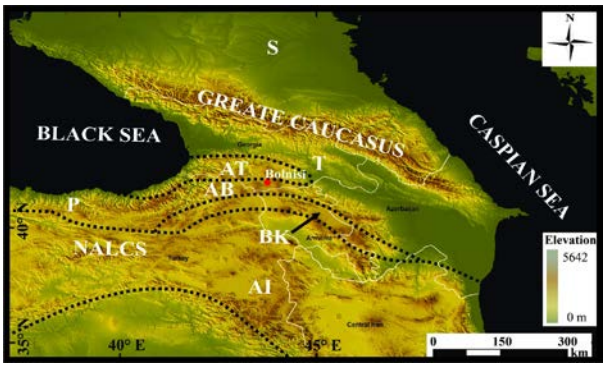

Fig. 1 Location of the Madneuli deposit in the Bolnisi region (adapted from Yilmaz et al. 2000). Abbreviations: S – Scythian Platform; GCS – Greater Caucasus Suture; T – Transcaucasus; AT – Southern Black Sea Coast-Achara-Trialeti Unit; AB – Artvin-Bolnisi Unit; P – Pontides; BK – Bayburt-Karabakh Imbricated Unit; NALCS – North Anatolian-Lesser Caucasian Suture; AI – Anatolian-Iran Platform

3 Stratigraphy

The host rock successions of the Madneuli deposit consist predominantly of rhyodacitic facies units are called Mashavera suite, and consist of lava, pyroclastic, volcano-sedimentary and sedimentary rocks of rhyodacitic composition. The Bolnisi district is a Cretaceous magmatic region, with complex, laterally and vertically variable regional stratigraphy. During mineral exploration of the region, two main stratigraphic interpretations were proposed. The first

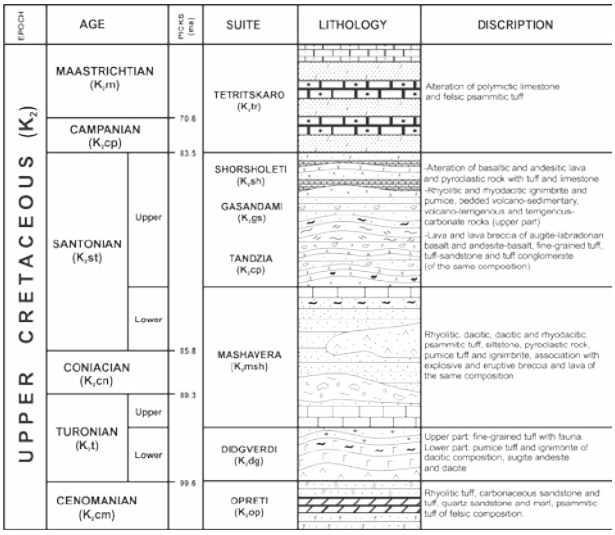

Fig. 2 Lithostratigraphic colomn of the Bolnisi ore district (according to Gambashidze 1987) and Apkhazava (1988))

one by Gambashidze et al. (1987) and Apkhazava (1988) attributes an Upper Turonian to Lower Santonian age to the Mashavera suite (Fig.2), which is underlain by the Upper Turonian Didgverdi suite and overlain by the Lower Santonian Tandzia, Gasandami and Shorsholeti suites. The second interpretation by Vashakidze et al. (1998) constrains the age of the Mashavera suite to the Upper Turonian-Coniacian, stratigraphically underlain by the Upper Turonian Didgverdi suite. A recent nanofossil study of the host rocks by Migineishvili and Gavtadze (2010) attributes a Campanian age to the Mashavera suite. Radiolaria identification from the host rocks is in progress and will allow us to solve the host rock age inconsistencies.

4 Volcanic lithofacies

Stratigraphic relationships and textural characteristics of the host rocks of the Madneuli deposit are best exposed in some key areas of the open pit (Popkhadze et al 2009). Identification and characteristics of the units are based on detailed studies of each existing mining level of the open pit. Detailed studies were undertaken to identify and characterize the facial units of each accessible level of the open pit. The different units were characterized based on variations in composition and texture. Eleven lithofacies were singled out in our study for the first time in the Madneuli deposit. Further detailed studies are in progress. Descriptions and interpretations of the eleven principal facies are summarized in Table 1.

Table 1. Summary of the main volcano-sedimentary facies of the Madneuli deposit

Lithofacies	Characteristics	Interpretation
Rhyolite pyroclastic lava-flow with flow foliation	There are shards of felsic rocks within the flow foliations. Porphyry structure with plagioclase, K-feldspar and quartz phenocryst. Groundmass is perlitic, amygdales are filled with quartz. Locally strongly silicified	Coherent facies of domes (cryptodomes) or volcanic sills
Columnar jointed ignimbrite	The shapes of columnar jointed ignimbrite are rectangular. Groundmass is typically perlitic, with a spherulitic texture of the volcanic glass, with oval-shaped quartz crystals in it. High temperature devitrification of volcanic glass	Depositional setting below a storm-wave environment
Fine-grained accretionary lapilli tuff and tuff with bioturbation	Massive or normally graded. Recrystallized volcanic glass in the groundmass. Lapilli of various sizes, oval shapes, filled with quartz. Lapilli- rim type, with a core of coarse-grained ash, surrounded by a rim of finer grained ash	Shallow water sedimentation; in part water-settled volcanic ash
Water-settled pyroclastic fall deposit	Inner flow stratification within a single layer shows fine-grained lamination, normal grading and lamination, thick units with clasts and reverse-graded at the top and fine-grained perlitic in the upper part	Resedimentation of shallow submarine pyroclastic flow; down-slope transport by high concentration turbidity current (Cas and Wright 1991)
Rhyodacitic extrusion	Massive. Evenly porphyritic groundmass micropoikilitic, locally pumiceous	Coherent facies of lavas or dome
Non-stratified rhyolitic to dacitic breccias facies	Massive, poorly sorted, clast- to matrix supported. The fragments of the rocks are slabby, irregular, blocky and oval-shaped. Locally this unit is silicified and altered	Autoclastic breccia from the margins of subaqueous lavas or cryptodomes
Hyaloclastite	Carapace rhyodacitic breccia flow. Hyaloclastite – with pillow like shapes and glass-like selvages (Popkhadze 2012). Groundmass with a perlitic structure. Fractures are defined by chlorite, and glass is replaced by quartz, feldspar, sericite and epidote	Lobe hyaloclastite facies, reflects a continuous evolution of textures and structures that formed during extrusion in response to rapid chilling and quench fragmentation of lava by water or by wet hyaloclastite formed from previous lobes (Gibson., et al, 1999)
Ignimbrite	Ignimbrite with welded structure contains lapilli and crystal shards or lapilli and matrix. Crystal shards are plagioclase, orthoclase, and quartz. Shards with cuspate and platy shapes. Some places are strongly silicified	Deposition below the wave environment
Peperite	Contact: wet sediment- hot lavas. Fluidal character	Magma - unconsolidated sediment mingling. Mingling occurred in situ at the margins of intrusions or lava within the submarine volcanic succession
Silicified bedded volcano-sedimentary facies	Alteration pelitic sedimentary rocks, sandstones and siltstones (with slide-slump unit). Sedimentary rocks with turbiditic nature (Popkhadze et al, 2009). Consists of horizons with Radiolaria.	Flow transformation into density turbidity currents. Downslope movement of sediments. Sandstones are product of channelized mass flow deposition. Subaquaeous setting
Pumice-rich ignimbrite (pyroclastic) facies	Consists of matrix-supported pumice concentration zone; low lithic clast and crystal concentration zone; stratified zone; fine-grained lithic clasts; sub-angular lapilli, locally vesicular	Deposition from pulsatory pyroclastic current (Pittari et al 2006)

5 Interpretation and Conclusions

The high proportion of volcanic glass, which is common in subaqueous lava, the presence of hyaloclastites, the abundant pumiceous ash and lapilli, the absence of subaeral lithic clasts, a relatively good hydraulic sorting, and various forms of bioturbation, which are systematically associated with wavy parallel, graded tuff are evidence for marine, locally shallow marine conditions during deposition of the Madneuli host rocks recognized in the open pit. Such a setting suggests that the immediate host rocks of the Madneuli deposit were mostly formed under subaqueous conditions, as is common for volcanogenic massive sulfide deposits, and contradicts some previous investigations suggesting mostly subaerial conditions during deposition of some of the Madneuli host rocks and ore deposit formation.

Acknowledgements

The research was supported by the Georgian National Science Grant 204 and Swiss National Science Foundation through the research grant SNF 200020-113510 and SCOPES Joint Research Projects IB7320-111046 and IZ73Z0-128324. The authors would like to thank the participants of the project and the staff of the "Madneuli Mine" for arranging access to the mine and sharing geological information.

References

Adamia Sh, Zakariadze G, Chkhotua T, Sadradze N, Tsereteli N, Chabukiani A, Gventsadze A (2011) Geology of the Caucasus: A review. Turkish journal of Earth sciences, V.20:489-544

Apkhazava M (1988) Late Cretaceous volcanism and volcanic structures of Bolnisi volcano-tectonic depression. Doctoral thesis, Caucasian Institute of mineral resources.p.1-269

Cas RAF, Wright JV (1991) Subaqueous pyroclastic flows and ignimbrites: an assessment. Bulletin of Volcanology 53: 357-380

Gambashidze R.A., Nadareishvili G.Sh (1987) Structure and stages of development of the Upper Cretaceous volcanogenic – sedimentary formation of SE Georgia. In G.A. Tvalchrelidze (Ed) Volcanism and formation of useful minerals in mobile regions of the Earth "Metsniereba", Tbilisi

Gialli S (2013) The controversial polymetallic Madneuli deposit, Bolnisi district, Georgia:hydrothermal alteration and ore mineralogy . Unpublished M.Sc. thesis, University of Geneva, p.1-143

Gibson HL, Morton RL, Hudak GJ (1999) Submarine volcanic Processes, Deposits and Environments Favorable for the Location of volcanic-associated Massive Sulfide Deposits. Reviews in Economic Geology 8:13-51

McPhie J, Allen RL (1992) Facies Architecture of mineralized submarine volcanic sequences: Cambrian Mount Read volcanics, Western Tasmania: Economic Geology 87:587-596

Migineishvili R (2002) A possible model of formation for the Madneuli copper-gold deposit. trudi GIN AN Gruzii. Nov. ser. Bip. 117:474

Migineishvili R, Gavtadze T (2010) Age of the Madneuli Cu-Au deposit,Georgia: evidence from new Nannoplankton data.Bulletin of the Georgia National Academy of Sciences,v.4,no.1:85-91

Pittari A, Cas RAF, Edgar CJ, Nichols HJ, Wolff JA, Marti J (2006) The influence of paleotopography on facies architecture and pyroclastic flow processes of a lithic-rich ignimbrite in a high gradient setting: The Abrigo Ignimbrite, Tenerife,Canary Islands. Journal of Volcanology and Geothermal Research 152:273-315

Popkhadze N (2012) First evidence of Hyaloclastites at Madneuli deposit, Bolnisi district, Georgia. Bulletin of the Georgia National academy of sciences v.6, no.3: 83-90

Popkhadze N, Beridze T, Moritz R, Gugushvili V, Khutsishvili S (2009) Facies Analysis of the Volcano-Sedimentary Host Rocks of the Cretaceous Madneuli Massive Sulphide Deposit, Bolnisi District, Georgia. Bulletin of the Georgia National academy of sciences,v.3, no.2:103- 108

Rosa CJP, McPhie J, Selvas JMRS, Pereira Z, Oliveira T, Pacheco N (2008) Facies analyses and volcanic setting of the giant Neves Corvo massive sulfide deposit, Iberian Pyrite belt, Portugal. Mineralium Deposita 43: 449-466

Zakariadze Guram S, Dilek Y., Adamia S.A, Oberhänsli R.E, Karpenko S.F, Bazylev B.A., Solov'eva N (2007) Geochemistry and geochronology of the Neoproterozoic Pan-African Transcaucasian Massif (Republic of Georgia) and implications for island arc evolution of the late Precambrian Arabian–Nubian Shield. Gondwana Research 11:92–108

Yilmaz A, Adamia Sh, Chabukiani A, Chkhotua T, Erdogan K, Tuzcu S, Karabilykoglu M (2000) Structural correlation of the southern Transcaucasus (Georgia)-Eastern Pontides (Turkey)- Tectonics and magmatism in Turkey and the surrounding area. Geological Society of London Special Publication 173:171-182.

Observation on gold-copper mineralization at Noungou, Burkina Faso

Reinhard P. Ramdohr
High River Gold Exploration Burkina, Ouagadougou, Burkina Faso

Tatiana L.Evstigneeva
IGEM RAS, Moscow

Abstract. The gold - copper occurrence at Noungou in Burkina Faso, West Africa was studied. The mineralization is confined to a NNE striking shear zone in a Birrimian greenstone belt sequence. The formation of stratiform sulfide mineralization was due to magmatic activity which was accompanied by fumaroles. Locally massive pyrite, pyrrhotite, chalcopyrite, arsenopyrite with accessory molybdenite and magnetite was formed. The sequence was subject to amphibolite facies metamorphism with isoclinal folding. In late epigenetic metamorphism quartz veins with sulfides developed. Drill cores from several holes were studied. Gold content is generally around 1 ppm. Higher concentrations of gold are found in weathered rocks and cementation zone and are defined as native gold. Copper content is occasionally above 1.000 ppm. In fresh meta-volcanic and meta-sedimentary rocks gold is not found. The “invisible” gold seems to be largely associated with the arsenopyrite occurrence. Additional study of gold (and copper) mobilization is required.

Keywords.
gold ore occurrence, stratiform sulfide mineralization, native gold, "invisible" gold

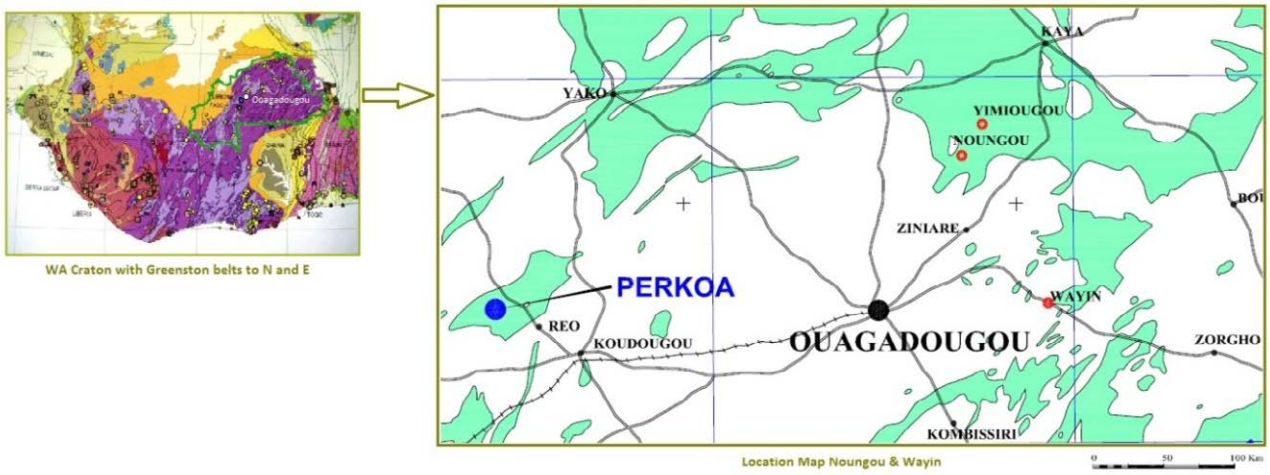

Figure 1. Geological map of Burkina Faso and the position of Noungou – Yimiougou Au (Cu)-deposit

1 Introduction

There are numerous gold occurrences and deposits in Burkina Faso. The Au (Cu) mineralization of this zone Noungou - Yimiougou was known by local diggers and by geologists BRGM for many years. The area is situated some 50 km NE of Ouagadougou (Fig.1). The terrain is generally flat with lateritic "table" hills and granite outcrops.

This area has been and still remains a target to small scale mining of various intensity depending on the gold price. Diggers track quartz veins, which often yield >5 ppm free gold mainly in the oxidation zone. Their work could be a good guide for modern prospecting. Near the water table and below the grade of the average gold content is usually less than 1 ppm Au. This is of no interest to the miners.

2 Geological setting

Apart from Pleistocene sediments, recent soils, and laterites the area is covered by deposits of Lower Proterozoic age. At approx. 2180 Ma the formation of intercontinental shallow marine sediments, of tuffs, graphitic shales and arenaceous layers took place. This sedimentation was often interrupted by acidic and basic volcanism. Magmatic activity, mainly grano-diorites and some felsic formation at the margins of the intercontinental basin caused also a lot of gases and hydrothermal fluid underwater venting. Gases rise through the black smokers, immediately condense, and form sediments. These sediments slid down the gentle submarine slope as deformed underwater mud flows. Fluids enriched in Fe,Mn,Zn,S,Si, some Cu and traces of Au were deposited in stratiform layers.

Between 2120 and 2100 Ma the magmatic – sedimentary sequence underwent greenstone phase metamorphism and three phases of deformation, which led to the formation of isoclinal structures with a NE trend. These metamorphism and folding caused mobilization of the primary mineralization. Subsequently, the circulating solutions redeposited sulfides and oxides in fractures

along the shears, combined with stockwork mineralization and cross cutting veins.

3 Mineralization

The region has been investigated by more than a hundred reverse circulation and diamond drill holes.

The samples studied are polished drill core specimens.

Methods used were optic microscopy and scanning electron microscope with energy dispersive analysis (JSM-5600LV + Link ISIS).

The dominant sulfides in veins and stockworks are pyrite, some chalcopyrite, pyrrhotite and little arsenopyrite. The massive sulfides ores are composed mainly of pyrite, and less commonly chalcopyrite (Fig. 2). Arsenopyrite, pyrrhotite, molobdenite, and chalcocite are observed rarely (Fig. 3). Arsenopyrite forms irregular grains up to 30 μm in size along with pyrite and chalcopyrite in massive ores.

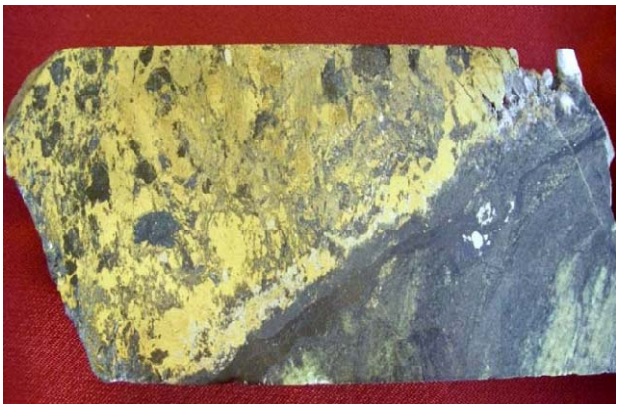

Figure 2. Breccia with massive chalcopyrite in epidote rich meta-volcanic formation. Pol. section.

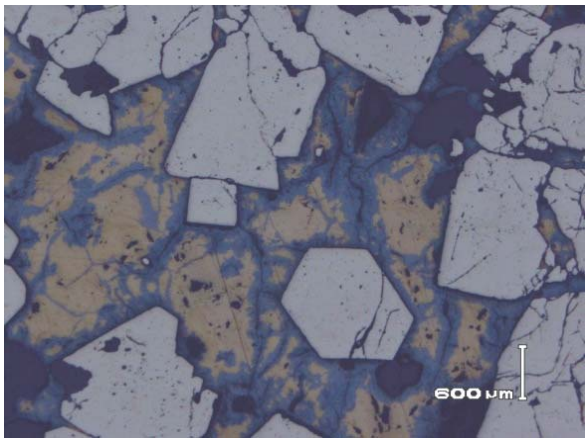

Figure 3. Pyrite-chalcopyrite-chalcocite ore from a depth of ~ 20 m, Pol. section

Titanite, ilmenite, TiO_2, fluorite, and zircon are noted among accessory minerals. They are typical for stratiform sulfide deposits. Magnetite rich layers frequently preserve the original VMS lamination.

Where the sulfides are exposed to weathering pyrite and other sulfides are destroyed, and the gold is liberated (Fig. 4). Prospectors mine this gold in gossans down to a depth of 50m (~ water level).

Gold in sulfide ores is rare. Sometimes gold occurs with silver mainly as (Au,Ag) grains of different sizes (0,n - n mm) with varying ratio Au:Ag (3:2 - up to 1: 6). Less frequent are pyrrhotite and arsenopyrite with traces of gold. The Au content in arsenopyrite can reach up to 1 Wt %,

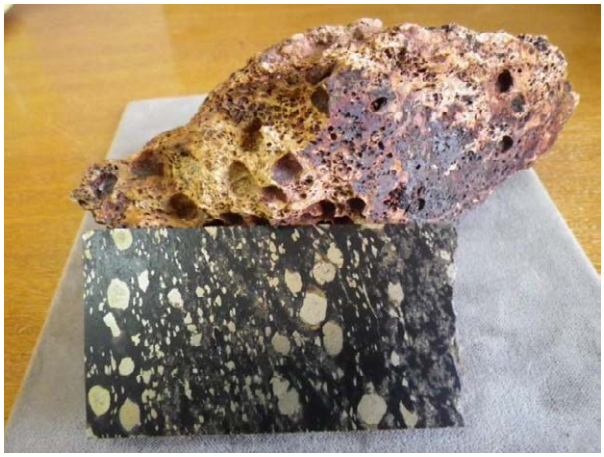

Figure 4. Lower part - magnetite rich meta-sediment containing large pyrite XX with chalcopyrite pressure shadows, pol. section. Upper part - the same rock type, but outcropping and strongly weathered, sample.

5 Discussion

Noungou mineralization is localized in sediments as VMS-type veins, stockworks and fractured formations. According to our observations, the accumulation of gold is not directly associated with copper mineralization (Fig. 5). Gold is noted in areas with both copper mineralization, and without it. However, where there is more copper, Au is always noted.

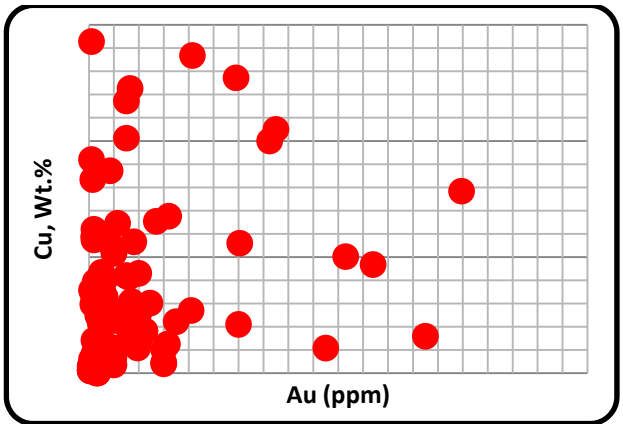

Figure 5. The diagram of Cu – Au concentrations in Noungou drill cores

The sulphide mineralization shows typical slump structures in the scale of some meters. No doubt it was the deposition with the black shales and tuffs, sometime layers of volcanic flows.

We are still searching for Au-bearing deposit of VMS type. Detailed study of geological, structural position, ore mineral composition and their associations show that the mineralization in Noungou is not a typical VMS . But

as we are finding now the type of mineralization is the same which forms VMS deposits.

4 Conclusions

A study of the mineral composition and association shows that Noungou mineralization is of igneous metamorphic origin (VMS), associated with late stockwork and vein formation. Pyrite prevails in all varieties of ores. Disseminated and massive sulfide ores are largely of pyrite – chalcopyrite composition. Magnetite, arsenopyrite, chalcocite, molybdenite and minerals of precious metals are rare. Native gold is only found in weathered rock and cementation zones but not in sulfide ores, where it is probably hidden as 'invisible' gold in arsenopyrite and pyrite. Therefore the question of the relationship between native and "invisible" gold requires additional study of the sulfide paragenesis.

Acknowledgements

This research was partly funded by the Program of fundamental researches №5 ("Nanoparticles: conditions of formation, methods of analysis, and extraction from mineral resources") of Dept.Earth.Sci. Russian Academy of Sciences.

VMS-type ore deposits and prospects in the Barberton Greenstone Belt: evidences from a 3.25 Ga epicontinental rift system

Ulrich Schwarz-Schampera
Bundesanstalt für Geowissenschaften und Rohstoffe (u.schwarz-schampera@bgr.de)

Michael Cronwright
Rock & Stock Investment Pty. Johannesburg

Andreas Wilms
Institut für Geowissenschaften, Universität Mainz

Anne Sander
Geowissenschaftliches Zentrum Göttingen

Alice Montinaro
Institut für Geologie und Paläontologie WWU Münster

Abstract. The 3.57 to 3.08 Ga Barberton greenstone belt is situated in the eastern brink of the Archean Kaapvaal Craton in the Republic of South Africa. It belongs to a group of Archean greenstone belts in the craton including the Murchison, Pietersburg and Gyiani belts, all trending subparallel to the Limpopo orogenetic belt. It is shown that intermediate to felsic volcanic units of the greenstone belts in the craton (e.g., Upper Onverwacht Group and Lower Fig Tree Group of the Barberton belt; Rubbervale Formation of the Murchison belt; Ysterberg Formation of the Pietersburg belt) are suitable exploration targets for volcanic-hosted massive sulphide deposits (Schwarz-Schampera et al., 2010). The 3.26 Ga Lower Fig Tree Group hosts several base metal sulfide prospects and iron formations delineating a zone of epicontinental rift-related hydrothermal activity. The ore prospects include the 2.9 Mt Zn-Pb-Cu-Ag Bien Venue deposit, the M`hlati zinc and iron formation exhalite prospect, and a massive iron formation at Spago. The mineralogical and geochemical characteristics of the mineralized horizons share many similarities with a number of other VMS deposits and Proterozoic to Phanerozoic iron formations above significant VHMS deposits, as well as with seafloor hydrothermal systems at modern oceanic island arcs potentially providing guidelines for further exploration.

VMS deposits, Archean, Barberton, Bien Venue, M`hlati

1 Introduction

The African subcontinent is particularly suitable for the study of early Archean granite-greenstone terranes but only few areas are as old, well-developed, preserved, exposed, and sequentially classified as the Barberton Mountain Land. Remnants of the oldest upper mantle, oceanic crust, and an overlying island arc-like rock sequence offer a unique opportunity to study early stages in the evolution of the Earth. A matter of particular interest is the existence of volcanic-hosted massive sulphide (VMS) deposits within the greenstone belts in South Africa. Even though VMS deposits occur in minor quantity compared to volcanic-hosted massive sulphide deposits in the Archean cratons of Canada (e.g. Superior province) and Australia (e.g. Pilbara craton), there are a number of VMS deposits and occurrences in the Kaapvaal craton, namely from the Barberton (Bien Venue, M'hlati) and the Murchison (e.g., Maranda J, Romotshidi, Letaba) greenstone belts (Schwarz-Schampera et al., 2010). Previous inadequate exploration concepts and strategies may be related to the limited number of VMS-type deposits in the Barberton greenstone belt. The Barberton belt, however, contains relics of volcano-sedimentary sequences, representing fragments of well-preserved ancient seafloor and continental crust. Submarine hydrothermal systems represent one of the oldest and primary ore-forming processes, depositing significant precious metal and base metals since minimum 3.6 Ga. As ore deposits may fingerprint formation processes and geological settings (Anhaeusser, 1981), the study of VMS deposits, known from many active vent sites along modern oceanic spreading centers, rift basins and island arc settings, may contribute to the understanding of Archean petrogenetic and metallogenetic processes and delineate the Archean crustal evolution.

This study aims at extensive exhalite horizons forming iron formation within the Lower Fig Tree Group of the Barberton greenstone belt (Fig. 1). Massive sulphide ores, mineralized rocks, and associated wall rocks from the Bien Venue and the M`hlati VMS deposits have been analyzed. The mineralogical, geochemical and isotopic composition has been investigated to reconstruct the processes that controlled the formation conditions and to better understand the geological evolution of the 3.45 to 3.22 Ga Fig Tree Group of the Barberton Swaziland Supergroup.

2 Bien Venue

The Bien Venue VMS deposit is hosted by the Bien Venue Formation (Kohler et al., 2003) within the sedimentary Lower Fig Tree Group (Fig. 1). The metavolcanic sequence overlies argillaceous strata of the Belvue Road Formation and is overlain by arenaceous metasediments of the Moodies Group, respectively.

Conventional U-Pb isotopic studies yield an age of 3256 ± 1 Ma (Kohler et al., 1993). Chronologically, the Bien Venue succession correlates with volcaniclastic rocks of the Auber Villiers Formation (3255 Ma) in the southern Fig Tree facies (Kröner et al., 1991).

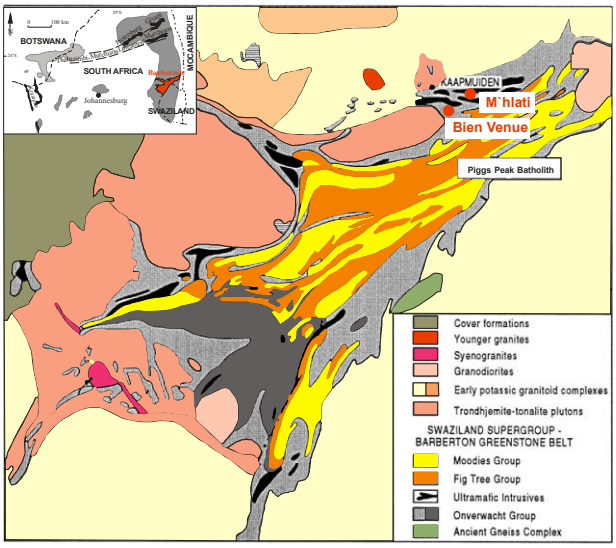

Figure 1. Generalized geological map of the lithologic units (Swaziland Supergroup) of the Barberton greenstone belt with surrounding plutons, modified after Anhaeusser et al. (1983). The location of the deposits Bien Venue and M`hlati are indicated. The inset shows the outline of the Kaapvaal Craton and the position of the Barberton greenstone belt (modified after Poujol et al., 2003).

The entire Bien Venue sequence covers an area of more than 50 km² with an estimated, total apparent thickness between 700 – 3,000 m (Kohler and Anhaeusser, 2002; Fig. 2).

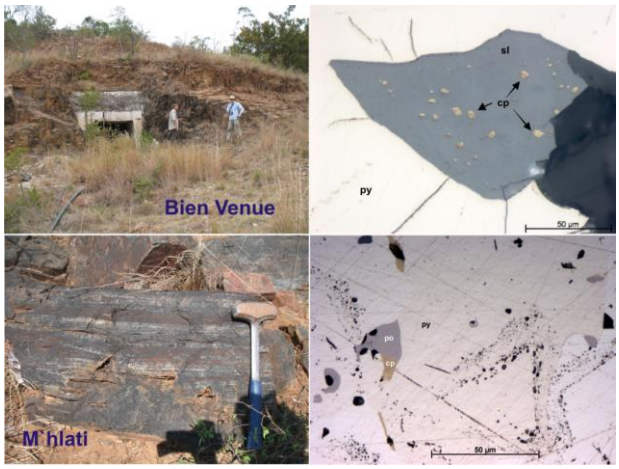

Figure 2. Location, outcrops and typical sulphide ore textures at the Bien Venue (top) and the M`hlati (bottom) VMS deposits (py=pyrite, sl=sphalerite, cp=chalcopyrite, po=pyrrhotite).

The Bien Venue deposit is associated with quartz-muscovite schists which have been derived from calc-alkaline rhyodacitic volcanic rocks. The volcanic unit is mainly composed of tuff and lapillistone, the latter includes intercalations of pyroclastic units. The massive sulphide sequence has a total thickness of about 50–70 m and is separated by an overlying distinctive marker unit, containing abundant quartz phenocrysts, the so-called quartz-eye metatuff, which has been metamorphosed to quartz-muscovite schist, but has retained some of its ancient volcanic textures.

The Bien Venue deposit is best characterized as a pyritic Zn-Ag-Au-(-Cu-Pb-Sb-As-Ba) felsic volcanic-hosted massive sulfide deposit. The mineralogical composition includes pyrite, sphalerite, chalcopyrite, tennantite-tetrahedrite-freibergite, galena, cassiterite, arsenopyrite, pyrrhotite, covellite, gersdorffite, magnetite (Fig. 3). Zinc-rich massive and disseminated sulfides show an unusual Ag-Cu-Sn enrichment including minerals like jalpaite (Ag_3CuS_2), cassiterite, freibergite ($AgSbS_4$), and canfieldite (Ag_8SnS_6; Fig. 3). The alteration assemblage includes quartz, barite, muscovite, biotite, chlorite, siderite, rutile, leucoxene, monazite, garnet, albite. The occurrence of barite is unusual for Archean VMS deposits as it suggests the presence of oxidized seawater at 3.25 Ga. The close intergrowth with pyrite and sphalerite, however, may also suggest disproportionation processes as a consequence of boiling as it has been widely described in shallow marine hydrothermal systems.

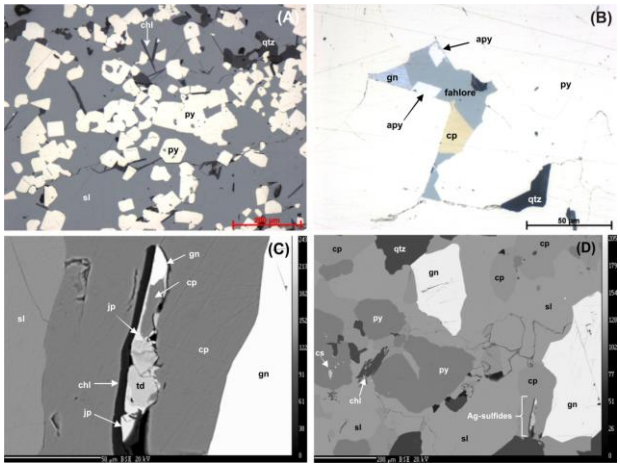

Figure 3. (A) Euhedral pyrite (py) in sphalerite (sl) matrix. Several pyrite grains contain sphalerite inclusions; (B) Massive pyrite (py) with interstices filled by intergrowth of fahlore (tetrahedrite), galena (gn), chalcopyrite (cp) and arsenopyrite (apy); (C) Mineralized veinlet composed of a complex intergrowth of galena (gn), chalcopyrite (cp), tetrahedrite (td), and jalpaite (jp) in chalcopyrite. The intergrowth is rimmed by chlorite (chl); (D) Galena (gn) associated with sphalerite (sl), pyrite (py) and chalcopyrite (cpy). Ag-rich sulfide minerals (freibergite, jalpaite) are associated with chalcopyrite (BSE image).

The massive ores and distinct mineral assemblages contain elevated As, Sb, Ag, Sn and Se concentrations; the sphalerite is generally characterized by very low Fe contents. The ores show two distinct element assemblages, i.e. (i) a polymetallic suite Zn-Sb-Pb-Cd-Ga-Ge-Sn, and (ii) a Cu-Ag-In-Se assemblage, indicating variable physicochemical formation conditions and source regions.

The sulfur isotope values of the sulphides are in the range between +0.7 to +3.5 ‰ $\delta^{34}S$. This signature is distinctly different from juvenile mantle-derived values

and strongly indicates fluid circulation within and element mobilization from a more mature crustal source. Barite shows isotope signatures between +2.9 and +7.7 ‰ $\delta^{34}S$. The precipitation process may have been influenced by boiling, associated with disproportionation and sulfur isotope fractionation.

The formation of the orebody is best explained by a moderate temperature, moderate to shallow seawater hydrothermal system with complex fluid-rock interaction and a fluid evolution which is characterized by steep physicochemical gradients.

3 M'hlati

The Mhlati iron formation and massive sulphide lens occur in the same stratigraphic interval between the metasedimentary Belvue Road Formation and the Moodies Group and is hosted by immature volcanogenic greywackes and carbonaceous shales. Synvolcanic activity in the region of deposition is evidenced by distinct lapilli layers intercalated with greywackes, shales and ferrugineous quartz horizons. M`hlati represents a base metal-rich siliceous and ferruginous exhalite horizon mainly consisting of quartz-magnetite and variable chlorite, siderite-ankerite and biotite. The chlorite and biotite are closely intergrown with the sulphide minerals. Siderite-ankerite occurs in distinct layers and disseminated in the quartz matrix. The origin as an exhalite horizon forming the possible cap and wall rock of the subsequent sulfide mineralization is suggested from the characteristic trace and rare-earth element distribution. The REE pattern shows a distinct enrichment in light rare earth elements (LREE) relative to heavy rare earth elements (HREE) with a pronounced positive europium anomaly.

The sulphide ores are partly banded and are mainly composed of pyrite, sphalerite, pyrrhotite, chalcopyrite, magnetite, with traces of pentlandite, galena, covellite and chalcocite (Fig. 4).

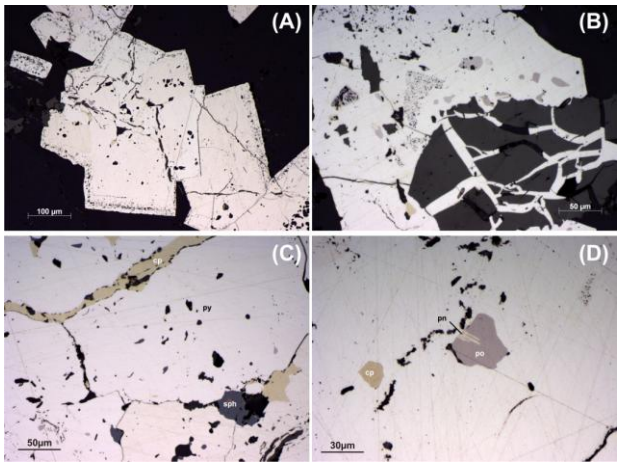

Figure 4. (A) Recrystallized pyrite (white) with distinct zonation showing rims, dominated by inclusions and impurities, likely representing relics of primary concentric growth; (B) Fractured magnetite (grey) replaced by pyrite (plane polarized reflected light, air); (C) Chalcopyrite and sphalerite along grain boundaries, in interstices and within pyrite; (D) Exsolution lamellae of pentlandite within pyrrhotite, both as inclusions in pyrite.

Pyrite predominates and hosts variable amounts of chalcopyrite, pyrrhotite, sphalerite, galena, covellite and chalcocite. Chalcopyrite and sphalerite may form larger aggregates within the quartz-magnetite matrix. Sphalerite shows low Fe contents. Pentlandite forms characteristic exsolutions in pyrrhotite. The occurrence of pentlandite in hydrothermal massive sulphide ores is rather unusual and may attest to strongly reducing conditions and (ultra)mafic source rocks.

Three element suites can be distinguished, based on statistical and solubility considerations. These include (i) elements related to the exhalative iron formation (Al-Ti-Na-K-Cr-Ba-Ga-REE, (ii) a zinc-dominated element suite of Zn-Mn-Cd-In-Sn-Co-Ni, ± As-Te-Se; and (iii) a copper-dominated assemblage of Cu-Ag-Bi-Te-Se.

Elevated Zn, Cu and Pb values indicate a distinct potential for associated sediment-hosted base metal sulfide deposits. Geochemical and mineralogical studies indicate the formation from mineralizing fluids with temperatures in excess of 250°C.

The sulfur isotope values display slightly negative $\delta^{34}S$ values between -1.2 and -0.1 ‰. This signature suggests a common juvenile source supply.

The formation of the orebody is best explained by a moderate temperature, moderate to shallow seawater hydrothermal system hosted by terrigeneous, perhaps volcaniclastic sediments. Intermittent explosive volcanic activity is evidenced by pyroclastic deposits. Formation temperatures above 250°C and the occurrence of chalcopyrite suggest a reasonable potential for larger massive sulphide orebodies at depth.

4 Summary

The 3.26 Ga Lower Fig Tree Group hosts a number of base metal sulphide prospects and iron formations, and delineates a zone of rift-related hydrothermal activity. The mineralized calc-alkaline volcaniclastic units are hosted by epicontinental sedimentary sequences. There is strong evidence for explosive volcanism at shallow water depths with the deposition of pyroclastic products. The volcanic rocks share many geochemical similarities with felsic volcanic arc magmas as evidenced by Ta-Yb, rare-earth and spider diagrams. The LREE and Eu show characteristic mobility in the seawater-dominated hydrothermal fluids and predominate over HREE. Eu enrichments in sediments indicate a strong influence of high-temperature hydrothermal fluids. The disparate behavior of Eu from neighboring REEs in hydrothermal fluids is linked to Eu(III) reduction under high-temperature (>250°C) and low-Eh conditions (Klinkhammer et al.,1983). The hydrothermal alteration trends in the wall-rocks follow the characteristic pattern of many VMS-type ore deposits and approach the ideal quartz-muscovite alteration assemblage of the immediate ore zone.

The sulphides at Bien Venue and M`hlati share a similar high-sulfidation mineralogy with a distinct trace metal enrichment. The associated sulphur isotope variation deviates from typical juvenile sources around 0‰ $\delta^{34}S$ and this is in agreement with significant variations in the barite sulphur isotope signatures. The isotope fractionation may be influenced by sulphur

disproportionation, induced by boiling processes in a rather shallow marine environment.

The composition of the wall rocks at Bien Venue and M`hlati exhibits distinct affiliation to evolved and differentiated crustal regions. The geological setting, phreatomagmatic volcanic products, carbonaceous sediments, and hydrothermal alteration as well sulphide composition all suggest formation conditions in a moderate to shallow seawater hydrothermal system. It is suggested that the Bien Venue, M'hlati and Spago sites delineate a stratigraphic horizon with products of moderate to high-temperature hydrothermal activity. The setting may be best characterized as an epicontinental immature rift system (Fig. 5). A modern equivalent may be represented in the recent offshore Taupo Volcanic Zone, New Zealand.

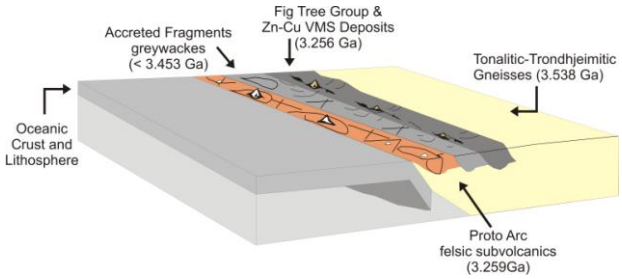

Figure 5. Sketch illustrating a proposed epicontinental immature rift system at 3.256 Ga hosting VMS-type mineralization and deposits.

References

Anhaeusser CR (1981) Barberton Excursion Guide Book: Archaean Geology of the Barberton Mountain Land. Geological Society of South Africa, p. 78.

Anhaeusser CR, Robb LJ, Viljoen MJ (1983) Notes on the provisional geological map of the Barberton Greenstone Belt and surrounding granitic terrane, eastern Transvaal and Swaziland (1:250,000 colour map). Spec. Publ. Geol. Soc. S. Afr. 9, pp. 221 – 223.

Klinkhammer GP, Elderfield H, Hudson A (1983) Rare earth elements in seawater near hydrothermal vents. Nature 305: 185–188.

Kohler EA, Anhaeusser CR, Isachsen C (1993) The Bien Venue Formation: a proposed new unit in the northeastern sector of the Barberton greenstone belt. Ext. Abstr. 16th International Colloquium on African Geology, Mbabane, Swaziland, pp. 186 - 188.

Kohler EA (2003) The geology of the Archaean granitoid-greenstone terrain in the vicinity of Three Sisters, Barberton Greenstone Belt: Geological Survey of South Africa Bulletin 133, p. 150.

Kohler EA, Anhaeusser CR (2002) Geology and geodynamic setting of Archaean silicic metavolcaniclastic rocks of the Bien Venue Formation, Fig Tree Group, northeast Barberton greenstone belt, South Africa, Precambrian Res. 116: 199 – 235.

Kröner A, Byerly GR, Lowe DR (1991) Chronology of early Archaean granitegreenstone evolution in the Barberton Mountain Land, South Africa, based on precise dating by single zircon evaporation. Earth Planet. Sci. Lett. 103: 41 – 54.

Poujol M, Robb LJ, Respaut JP, Anhaeusser CR (1996) 3.07–2.97Ga greenstone belt formation in the northeastern Kaapvaal Craton: implications for the origin of the Witwatersrand basin. Econ Geol 91:1455–1461.

Poujol M, Robb LJ, Anhaeusser CR, Gericke B (2003) A review of the geochronological constraints on the evolution of the Kaapvaal craton, South Africa. Prec. Res. 127:181–213.

Schwarz-Schampera U, Terblanche H, Oberthür T (2010) Volcanic-hosted massive sulfide deposits in the Murchison greenstone belt, South Africa. Min. Dep. 45: 113 – 145.

Polyphase secondary alteration and the formation of complex Cu and Pb-Ag-Au-rich assemblages, Las Cruces copper deposit, SW Spain

Fernando Tornos
Centro de Astrobiología (CSIC-INTA). Ctra Ajalvir km.4. 28850 Torrejon de Ardoz, Spain. f.tornos@csic.es

Francisco Velasco
Universidad del País Vasco, Dpt. Mineralogía y Petrología. Leoia, Vizcaya, Spain

Nieves G. Miguelez
Instituto Geológico y Minero. Ríos Rosas 23. 28003 Madrid, Spain

Juan Manuel Escobar
Cobre Las Cruces SAL, Guillena, Sevilla, Spain

Abstract. The Las Cruces secondary copper deposit forms a sub-horizontal blanket on dipping Paleozoic volcanogenic massive sulphides. It includes a high grade cementation zone dominated by chalcocite capped by a zone made of galena, carbonates, quartz and iron monosulphides that is rich in Au and Ag. The geology and stable isotope geochemistry indicate that the deposit underwent a polyphase secondary alteration with early sub-aerial exposure and formation of a gossan - Cu-cementation zone pair. It was followed by burial maturation controlled by microbial activity, which facilitated the replacement of the gossan by a carbonate-sulfide Pb-Ag-Au-rich assemblage.

Keywords. supergene enrichment, volcanogenic massive sulphides, geomicrobiology, Iberian Pyrite Belt, Spain

1 Introduction

The Las Cruces deposit (Seville, SW Spain) with original resources of ca. 15.6 Mt at 6.9% Cu, is one of the richest copper deposits. It is located in the eastward prolongation of the Iberian Pyrite Belt and below the Tertiary sediments of the Guadalquivir basin, a foreland shallow marine basin to the Alpine Orogen in SW Spain. The deposit is located near the NW edge of the basin and below ca. 150 m of marl (Messinian) and 3-5 m of sandstone that unconformable overlie the Palaeozoic basement. Here, the basement includes dacitic domes and shale of Late Devonian-Early Carboniferous age. The massive sulphides have an ENE-WSW trend and dip 35-45°N; they are similar to other massive sulphide deposits in the southern IPB (Tornos 2006). The primary orebody forms a stratabound lens in the contact between the dacite and the shale. The massive sulphides show replacive contacts with the dacite but also form stratiform orebodies within the shale. Underlying the massive sulphides there is a large stockwork hosted by zones of chloritic and sericitic (+ quartz) alterations. The ore assemblage includes pyrite with lesser amounts of chalcopyrite, sphalerite, galena, and tetrahedrite-tennantite and, near the shale, significant amounts of arsenopyrite.

Capping the massive sulphides along the basement-cover contact there is a large zone of secondary alteration. It shows a lower cementation zone and an upper, partially oxidized, sulphide-carbonate-rich blanket separated by a zone of sandy barren pyrite (Fig. 1). This zone is crosscut by N-S to NE-SW-trending faults of Alpine age that also affect some of the overlying Tertiary sediments.

The Las Cruces deposit was discovered in 1993 by RIOMIN Exploraciones when drilling a large gravimetric anomaly. Since 2009 it is mined in an open pit by Cobre Las Cruces, a subsidiary company of INMET Mining. There are few detailed studies on this deposit, and most of them based on incomplete information supported on drillcore logging (Blake 2008; Doyle et al. 2003; Knight 2000; Miguelez et al. 2011; Yesares et al. 2012).

Other cropping out massive sulphide deposits of the Iberian Pyrite Belt are capped by a large goethite-hematite gossan (Velasco et al. 2012) and a small cementation zone, both developed during the Alpine (Miocene?) sub-aerial exposure. Between the gossan and the cementation zone there is usually a small layer enriched in jarosite with significant Au and Ag grades.

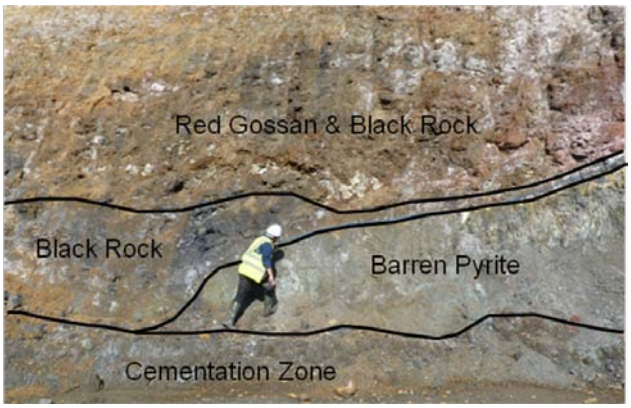

Figure 1. Relationships between the different types of secondary alteration, Las Cruces

2 The geology of the secondary zone

At Las Cruces, the secondary alteration zone covers an area of ca. 0.06 km^2 and has an average thickness of 20-30 m, with a maximum one of 40 m near the faults. The cementation zone includes chalcocite with minor

amounts of chalcopyrite, bornite, pyrite, enargite, tennantite and tetrahedrite; locally, there are deep zones of almost massive covellite (Blake 2008). Most of the mineralization occurs in joints within the primary massive sulphides. However, near the faults, the primary mineralization is almost completely replaced by fine-grained dusty chalcocite and crosscut by veins of massive chalcocite.

The cementation zone is overlain by 0-5 m of barren, coarse grained pyrite with low metal contents. Above and replacing it there is a highly heterogeneous blanket-like sub-horizontal unit, some 3-15 m in thickness, which caps the deposit. The lower zone is usually occupied by a fine-grained, massive to dusty, zone dominated by irregular proportions of calcite, galena, iron monosulphides (smythite and greigite) and barite with minor amounts of silver sulphosalts (acanthite, sternbergite and proustite-xanthoconite), electrum-gold, cinnabar and cassiterite ("Black Rock" in the miners jargon). Galena-rich veins crosscut the cementation zone but also the overlying Tertiary sediments (Videira, pers. com.). This calcite-galena rock gradually replaced another one made up of siderite with minor barite, galena, and quartz; this late one probably replaced an older gossan with hematite, goethite, cerussite, mimetite, quartz and barite. In turn, these rocks appear variably oxidized to hematite, goethite and cerussite-anglesite.

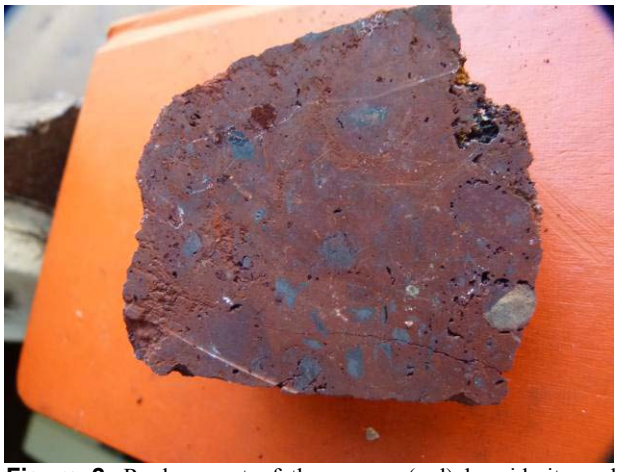

Figure 2. Replacement of the gossan (red) by siderite and galena (greyish) ("Red Rock"). Width of field: 15 cm.

Fragments of the former gossan, partially replaced by siderite and galena, are found in a sedimentary, talus or piedmont, breccia that bounds the basement-cover boundary. It is interlayered with glauconite- and quartz-rich sandstone cemented by calcite.

Finally, the cementation zone and the Black Rock are crosscut by zoned vertical veins some cm to a metre in thickness that have epithermal features. These veins are composed of low T quartz, calcite, barite and the same sulphides as in the cementation zone; they grade upwards into hydrothermal breccias locally showing bladed calcite indicative of boiling.

The basement-cover contact hosts a major regional aquifer; however, water also upflows from the fractures that crosscut the deposit. These waters are alkaline, CO_2-rich and surge at temperatures of 26-31°C.

3 Discussion: The unusual evolution of a secondary cementation zone

The zone of secondary alteration in Las Cruces deposit is different to that observed in other deposits affected by supergene alteration (Velasco et al. 2013). This replacement has been interpreted as an early submarine oxidation only slightly postdating the formation of the exhalative massive sulphides (Knight 2000) or an unusual oxidation that took place during burial below the Tertiary sediments (Blake 2008).

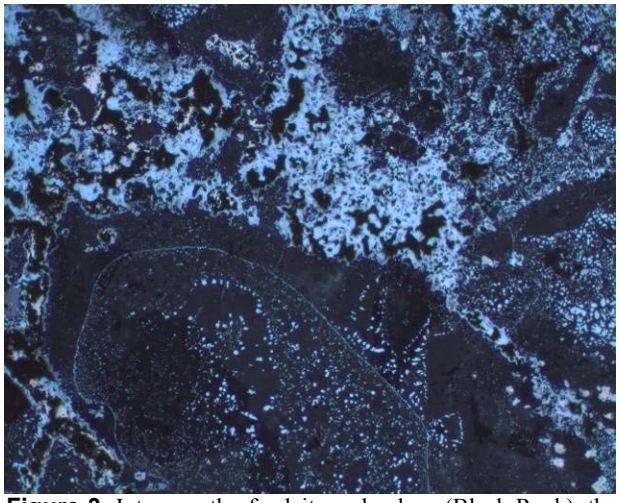

Figure 3. Intergrowth of calcite and galena (Black Rock), the later showing likely biogenic textures. Width of field: 2 mm.

However, the model seems to be more complex. The geological and geochemical data are consistent with a polyphase secondary alteration that includes, at least, four superimposed events. The **first stage** included, in a similar way to other deposits in the IPB, the erosion and sub-aerial exposure of the already formed massive sulphides during Pre-Miocene times in a tropical climate. The generation of acid waters due to the interaction with the sub-aerially exposed massive sulphides produced the typical goethite-hematite gossan enriched in Fe, Pb and Ba similar to those found nowadays in other deposits of the IPB (Tharsis, Riotinto, San Miguel). The gossan has a lower jarosite-rich layer where most of the Au and Ag are concentrated and a, probably small, cementation zone in a model similar to that described by Anderson (1982).

Later faulting and denudation related with the onset of the Tertiary extension and basin formation (**2nd stage**) likely accelerated the growth of the cementation zone – the bulk of it formed at this stage - and probably eroded part of the already formed gossan. This also changed the weathering profile, leaving a zone of barren, washed out, pyrite between the gossan and the cementation zone. K-Ar and palynological data suggest that this process took place during the Tortonian (ca. 11-6.5 Ma, (Moreno et al. 2003).

The **third stage** began with the burial of the gossan below the marl during the Messinian (6.5-5.3 Ma), something that abruptly changed the physicochemical conditions of the system. Probably, the cementation zone did not modify its size or mineralogy significantly, but conversely the gossan was almost completely

replaced by carbonates and sulphides. The evolution includes the replacement of the gossan by siderite and galena and the later replacement of the siderite by calcite accompanied by the crystallization of iron monosulphides. This process can be modelled as due to the increase in the pCO_2 and pH_2S of the system. We interpret this evolution as related to the anaerobic reduction of sulphate accompanied by the oxidation of CH_4/methane by mesophilic to thermophilic chemolithoautotrophic microbes. This process was predated by the also likely biogenic reduction of Fe^{3+} to Fe^{2+} necessary for the formation of siderite. Stable isotopes indicate that the carbon in the neoformed carbonates ($\delta^{13}C_{fluid}$, -60.4 to –27.1‰) was not in equilibrium with that of the connate waters ($\delta^{13}C$ between -9 and -6.3‰) and reflect the mixing of carbon inherited from the water with that product of the biogenic reduction of organic matter. This process is consistent with the abundance of remnants of microbes in the carbonates and sulphides – including likely fossils of bacteria and chemotaxic growths (Fig. 3). In this process, the electron donor was probably the methane released from the black shale in the basement and accumulated below the impermeable marl while the sulphate was derived from the connate waters circulating through the aquifer. Preliminary $\delta^{34}S_{galena}$ (19.8 to 25.4‰) and $\delta^{34}S_{FeS}$ (4.8-17.4‰) values are interpreted as reflecting the reduction of sulphate in a system with fluctuating conditions between open and closed.

The comparison of the $\delta^{18}O$ values of the calcite with that of the water within the aquifer suggest temperatures in the 8-32°C range (avg. 24°C), consistent the in situ measured temperatures.

The **fourth stage** includes the formation of the epithermal veins and breccias. The abundance of barite suggests mixing between the deep (reduced?) fluids and surface-derived oxidized ones. Carbon isotope signatures of the carbonate in these veins ($\delta^{13}C_{fluid}$, -40 to -25‰) indicate that biogenic reduction was active in the upper part of the system during the formation of these veins.

However, the widespread presence of high chalcocite in the cementation zone and of evidences of boiling in the veins indicate that the secondary alteration was produced by, at least intermittent, upflow of hot fluids with temperatures above 100°C. This is consistent with the high heat flow existing nowadays in the area and the existence of low enthalpy geothermal systems at depth.

The presence of secondary enargite – here stable at low temperatures and mildly acid to neutral conditions – is probably due to the high As content of the system.

4 Conclusions

Our data show that the formation of the unusually large and rich cementation zone and of the overlying sulphide-carbonate rocks of the Las Cruces deposit are the result of a polyphase (sub-)surficial alteration of Palaeozoic massive sulphides during the Cenozoic. The evolution includes the early sub-aerial exposure and oxidation of the massive sulphides during Pre-Miocene times followed by a later underground stage controlled by the evolution of a Tertiary basin. The mineral assemblages are constrained by burial synchronous with the circulation of groundwater, storage of methane and high heat flow, something that promoted extensive extremophilic microbial activity and sulphate reduction. The relative extension and distribution of the different zones was likely consequence of the composition of the former gossan, the fluid flow through the different rocks and the availability of nutrients.

Acknowledgements

This study has been funded by the ProMine project of the 7th Framework Program of the EU and the Spanish SEDI project number CGL2011-23207. We acknowledge Cobre Las Cruces and especially Gobain Obejero, Ivan Carrasco, Juan Carlos Baquero, Antonio Franco and Stephen Cooper, for granting access to the deposit and sharing their information. We also acknowledge Carmen Conde and Juan Carlos Videira their help in the realization of this work.

References

Anderson JA (1982) Characteristics of leached capping and techniques of appraisal, *in* Titkey, S.R., ed., Advances geology of porphyry copper deposits; southwestern North America: Tucson, University Arizona Press, 275-295.

Blake C (2008) The mineralogical characterisation and interpretation of a precious metal-bearing fossil gossan, las Cruces, Spain. PhD thesis, University of Cardiff.

Doyle M, Morrissey C, Sharp G (2003) The Las Cruces Orebody, Seville province, Andalucia, Spain, *in* Kelly CG, Andrew CJ, Ashton JH, Boland MB, Earls G, Fusciardi L, and Stanley G, eds., The Geology and genesis of Europe's major base metal deposits: Dublin, Irish Association for Economic Geology, 381-390.

Knight FC (2000) The mineralogy, geochemistry and genesis of the secondary sulphide mineralisation of the Las Cruces, Spain. PhD thesis, University of Cardiff.

Miguelez NG, Tornos F, Velasco F, Videira JC (2011) The Unusual Supergene Las Cruces Copper Ore Deposit, *in* Barra F, Reich M, Campos E, Tornos F eds., SGA Biennial Meeting Proceedings: Let's talk Ore Deposits: Antofagasta, 832-834.

Moreno C, Capitan MA, Doyle M, Nieto JM, Ruiz F, Saez R (2003) Edad mínima del gossan de Las Cruces: implicaciones sobre la edad del inicio de los ecosistemas extremos en la Faja Pirítica Ibérica. Geogaceta 33: 67-70.

Tornos F (2006) Environment of formation and styles of volcanogenic massive sulfides: The Iberian Pyrite Belt. Ore Geology Reviews 28: 259-307.

Velasco F, Herrero JM, Suarez S, Yusta I, Alvaro A, Tornos F (2013) Supergene Features and Evolution of the Gossans Capping the Massive Sulphide Deposits of the Iberian Pyrite Belt. Ore Geology Reviews: 53: 181-203.

Yesares L, Nieto JM, Saez R, Almodovar GR, Videira JC (2012): Geochemichal peculiarities of Las Cruces deposit (Iberian Pyrite Belt). Goldschmidt Conference.

Alteration mineral domains under Loma la Cuaba: new insights as to the origin of the mineralization in the Pueblo Viejo district

Torró, L., Proenza, J.A., Melgarejo, J.C.
Dpt. Cristal·lografia, Mineralogia i Dipòsits Minerals, Universitat de Barcelona. C/ Martí i Franquès s/n 08028 Barcelona, Catalonia, Spain

Carrasco, C.A., Domínguez, H.S.
Everton Minera Dominicana S.R.L., Av J. F. Kennedy 44D-Santo Domingo, Dominican Republic

Nelson, C.
Consulting Geologist, 2360 23rd Street, 80304 Boulder, Colorado, USA

Lewis, J.F.
Department of Earth and Environmental Sciences, George Washington University, Washington, DC 20052, USA

Abstract. The Ampliación Pueblo Viejo (APV) project is located in the central portion of Hispaniola within the world-class Pueblo Viejo gold-silver-copper district. A diamond drill program has recently been carried out at APV, close to the ore deposits and within the limits of the Pueblo Viejo alteration system. Pervasive alteration is present in all of the studied samples. Extensive advanced argillic alteration with well-developed silicification occurs in the upper 300m of drill core. The advanced argillic domain is clearly subdivided into an upper part containing kaolinite±dickite and a lower zone with pyrophyllite±diaspore. The advanced argillic domain is underlain by sericitic and propylitic domains. In the sericitic domain, sericite mainly replaces plagioclase phenocrysts. In the propylitic zone, albite replaces primary calcic-plagioclase; chlorite forms veinlets and pseudomorphically replaces primary mafic minerals; and, vein and disseminated epidote is locally abundant. Minor sodic-calcic domains are recorded at depth by anhydrite- and tourmaline-bearing assemblages. Locally, potassic domains (orthoclase plus magnetite) are observed. Higher ore metal values are systematically related to the advanced argillic domain. No or minor positive anomalies in ore metal grades are observed in the potassic, sodic-calcic, sericitic and propylitic domains.

Keywords. Dominican Republic, Pueblo Viejo, Epithermal, Alteration Minerals.

1 Introduction

Extensive exploration for metallic minerals, particularly gold and copper, is currently being carried out in the late Early Cretaceous-Late Cretaceous-Eocene belts, in Hispaniola in the Cordillera Central, Dominican Republic and the Massif du Nord in Haiti. The Hatillo area, where this project is centered, in the Median Belt in the central Dominican Republic (Bowin, 1966) has always attracted attention in the search for precious metals.

The Ampliación Pueblo Viejo (APV) project is located in the central portion of Hispaniola in the Caribbean (Fig. 1) where it abuts the world-class Pueblo Viejo gold-silver-copper deposit (Fig. 1). The origin of Pueblo Viejo, which had proven and probable reserves in 2012 of 25.3 million ounces of Au (http://www.barrick.com/operations/ north-america/pueblo-viejo/default.aspx), is a controversial topic in economic geology (Nelson et al., 2011 and references therein). Both Pueblo Viejo and the adjacent APV project are covered by an advanced argillic alteration domain, the so-called "Loma La Cuaba lithocap" (Sillitoe, 2006; Arribas et al., 2011) (Fig. 1). The limits of this advanced argillic domain were originally drawn by Bowin (1966).

A diamond drill program to depths of up to 1000m has recently been carried out by Everton Resources (TSX-V:EVR) on the southern portion of APV, close to the Pueblo Viejo ore deposits, around a magnetic high anomaly. Here we present the results of a study of the alteration minerals made on more than a hundred core samples from the APV project in order to assess their correlation with metal grades and to shed further light on the origin of Pueblo Viejo.

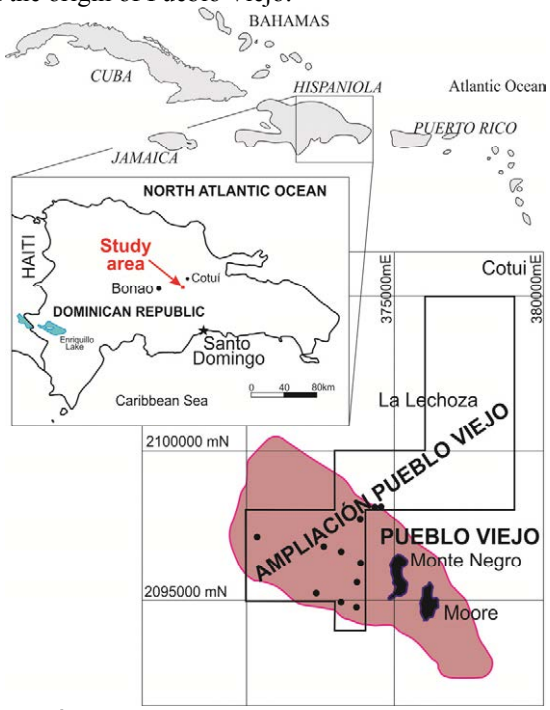

Figure 1. Location of the Pueblo Viejo district and the APV study area in the Dominican Republic showing the Loma La Cuaba lithocap (in pink), the location of the Monte Negro and Moore pits and the position of the studied DDH.

2 Geological setting

The late Early Cretaceous–Eocene Circum-Caribbean island-arc system is a complex collage of crustal units which were initially formed in an intra-oceanic setting during Early Cretaceous (Pindell & Barrett, 1990). The formation of the ore deposits in the tectonic evolution of the northern Caribbean was discussed by Nelson et al. (2011).

The geology of Hispaniola resulted largely from the oblique convergence and underthrusting of the North American Plate beneath the Circum-Caribbean island-arc. Subduction and related arc magmatism ceased in the Eocene with the collision of the arc with the Bahamas Platform. A change in the stress along the Northern Caribbean Plate Boundary Zone (NCPBZ) gave rise in the Oligocene to transform movement and strike-slip faulting parallel to the NCPBZ. This activity along the NCPBZ continues today, particularly in Hispaniola

Host rocks at APV and at the Pueblo Viejo ore deposit belong to the Early Cretaceous Los Ranchos Formation. This unit forms part of the oldest and chemically most primitive island-arc in the Caribbean region. It is composed of LREE-depleted tholeiitic island arc basalts and normal island arc tholeiites with an interval of felsic volcanism and tonalitic plutonism dated at 110-118Ma (Escuder-Viruete et al., 2007). The Los Ranchos Formation is overlain by the Hatillo Limestone, a massive micritic unit deposited under shallow-water, reef conditions during the Albian to Cenomanian (Kesler et al., 2005). The lowermost few meters of the limestone sequence display distinctive alteration and mineralization effects according to Sillitoe et al. (2006).

Lithologies recognized in the sampled cores include magmatic and rare sedimentary rocks. Sedimentary rocks are registered in the westernmost DDH as micro-conglomerates with rounded calcareous clasts and as carbonaceous sediments. Although rocks have undergone pervasive hydrothermal alteration, volcanic and hypabyssal rocks can be distinguished from textural observations. Both rock-types show a similar original mineralogy with idiomorphic plagioclase, clinopyroxene and very scarce amphibole porphyroblasts. They classify as basaltic andesite and their intrusive equivalents diorite-gabbro in the Winchester & Floyd (1977) diagram. The bulk of the samples plot within the basaltic unit field drawn by Escuder-Viruete (2006) for the Los Rancho's rocks. Hydrothermal breccias with a calcite-rich matrix containing magmatic clasts are also recognized.

3 Methodology

A hundred and thirty core samples from eleven diamond drill holes were selected for detailed alteration study at the *Serveis Científics i Tecnològics* of the *Universitat de Barcelona*. From these, a total of 65 rocks were analysed by powder XRD on an X'Pert PRO MPD X-ray diffractometer with a Bragg-Brentano θ/θ of 240 millimeters range. Diffractograms were processed using X'pert and Topas software. A hundred and eleven thin sections were prepared for mineralogical study under petrographic microscope with transmitted and reflected light and scanning electron microscope (ESEM Quanta 200 FEI, XTE 325/D8395 electron microscope equipped with an INCA Energy 250 energy dispersive spectroscopy microanalysis system). Mineral chemistry was analyzed by electron microprobe with wavelength-dispersive spectrometry (EMPA-WDS) using an accelerating voltage of 20kV with a beam current of 5 to 20 nA and a 10-15µm spot beam diameter in a Cameca SX50 equipment; standards and lines used for the analyses were: diopside (SiKα), rutile (TiKα), synthetic Al_2O_3 (AlKα) pyrite (FeKα); rhodonite (MnKα), periclase (MgKα), albite (NaKα), wollastonite (CaKα), orthoclase (KKα), sphalerite (ZnKα), fluorite (FKα).

4 Alteration Study

Pervasive alteration is present in all of the APV samples selected for study. The classification proposed by Seedorff et al. (2005) is followed here to attribute each mineral assemblage to a corresponding alteration domain.

4.1 Advanced argillic alteration

Extensive advanced argillic alteration with well-developed silicification occurs in the upper 300m of drill core from APV. It systematically correlates with the volcanic rock sequences. Silicification consists of microcrystalline quartz which appears both as vuggy silica and as a quartz-clast, hematite-cemented breccia.

This advanced argillic domain is in turn clearly subdivided in an upper part characterized by kaolinite±dickite and a lower zone with pyrophyllite± diaspore as the main alteration phases (Fig. 2B). These assemblages are classified by Seedorf (2005) as low and intermediate temperature advanced argillic alteration respectively. Locally, pyrophyllite appears wrapping kaolinite bundles and aggregates indicating a recrystallization of the second at higher temperatures (Fig. 2A). Alunite is very scarce in APV rocks and appears in both low and intermediate temperature advanced argillic assemblages.

A second advanced argillic domain is described below 300 meters depth where it cuts the sericitic and propylitic alteration zones described below. In this case, kaolinite and pyrophyllite form bundles disposed parallel to some deformed Fe-Ti oxy-hydroxides. This domain is interpreted to be related to a later low-angle thrust fault dipping SW.

4.2 Sericitic alteration

The shallow advanced argillic domain is underlain by a sericitic domain. Sericite pervasively replaces original plagioclase phenocrysts as well as forming veinlets (Fig. 2C). However, sericite is scattered throughout almost the whole alteration sequence in minor proportions. Two generations of sericite have been observed.

Sericite consists of fine grained muscovite crystals large enough to be analyzed by EMPA. Analyzed

crystals compositions have been plotted in the diagrams proposed by Dilles (2012). Although sericite composition is very constant, an incipient phengitic and illitic substitutions can be observed. Analyzed sericite grains lie in the fields proposed by Dilles (2012) as typical of advanced argillic and sericitic alteration zones.

4.3 Propylitic alteration

An extensive propylitic domain occurs beneath the sericitic alteration domain. Albite replaces primary calcic-plagioclase and chlorite forms veinlets and pseudomorphically replaces primary mafic minerals (thought to be clinopyroxenes almost exclusively). Two generations of chlorite are described. One, blue in crossed polars, appears cut by the other, which is brownish in crossed polars (Fig. 2D). Scarce tremolite replaces former mafic grains and is in turn partially replaced by chlorite. Vein and disseminated epidote occurs; epidote is also abundant in the matrix of hydrothermal breccias as well as forming reaction rims of calcite veins.

The two generations of chlorite can be also discriminated by their chemical composition and their crystallizing temperature calculated using the Kranidiotis & McLean (1987) geo-thermometer. The first generation, which is Mg-rich, is brunsvigite and formed at about 280ºC. The second, more Fe-rich, is ripidolite and formed at about 350ºC.

4.4 Sodic and sodic-calcic alteration

Minor sodic and sodic-calcic alteration domains are registered at depth in a few drill cores with anhydrite- and tourmaline-bearing assemblages (Fig. 2E). Both phases seem to have formed during late stages and replaced all the above described alteration mineral assemblages.

Analyzed tourmalines belong to the dravite and magnesio-foitite species. A concentrically zoned pattern (parallel to the growing faces) has been observed in the crystals. EMPA mappings on tourmaline sections denote a direct relation between Na and Fe-rich zones. A more detailed textural description and chemical composition of these analyzed tourmalines can be found in Torró et al. (2012).

The analyzed minerals of the epidote group in the Loma la Cuaba rocks are predominantly epidote sensu strictu with an important clinozoisite component; only one sample is clinozoisite. REE were not analyzed on epidote group minerals.

4.5 Potassic alteration

Minor potassic alteration is interspersed with the sodic and sodic-calcic alteration domains. Secondary orthoclase replaces original plagioclase crystals (Fig. 2F) and is accompanied by abundant secondary magnetite. Potassic alteration varies from incipient (orthoclase replaces plagioclase along twin lamellae) to strong (complete orthoclase replacement of plagioclase).

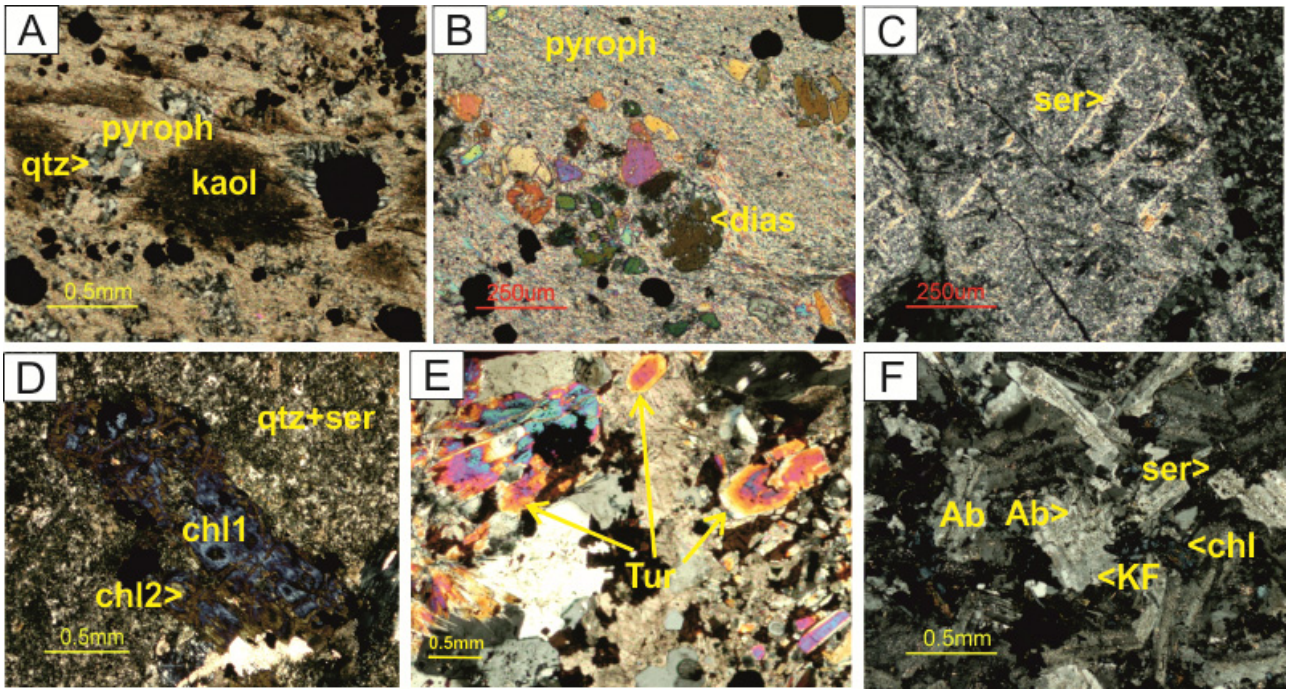

Figure 2. Microphotographs of APV altered samples under the petrographic microscope using transmitted light and crossed polars. (A) Fine grained kaolinite aggregates wrapped by pyrophyllite; note that both are replacing hydrothermal quartz. (B) Detail of the pyrophyllite and diaspore mineral assemblage. (C) Sericitized plagioclase phenocrysts that in turn is cut by thin veinlets of sericite. (D) Chlorite replacing former mafic mineral; note that two generations of chlorite occurs, the brownish replacing the blue one; the groundmass is completely silicified and sericitized. (E) Tourmaline crystal basal and longitudinal sections showing a zoning parallel to the growing faces. (F) Original plagioclase crystals partially replaced by potassic feldspar. Abbreviations: qtz: quartz; pyroph: pyrophyllite; kaol: kaolinite; dias: diaspore; ser: sericite; chl: chlorite; tur: tourmaline; ab: albite; KF: potassic feldspar.

5 Alteration-grades correlation

A comparison between ore metal grades and alteration domains has been carried out on drill logs and cross-sections. Higher grades of Au (up to 0.34g/t) and Cu (up to 0.32%) and minor Mo (0.19g/t) correlate with the advanced argillic alteration domain, especially the intermediate temperature assemblage containing pyrophyllite and diaspore. On the contrary, no or minor anomalous values are observed for ore metals values (up to 0.06g/t for Au and up to 500ppm for Cu) in the potassic and sodic-calcic domains.

6 Discussion and conclusions

All of the analyzed samples exhibit pervasive hydrothermal alteration. No completely fresh rock samples were found in any of the eleven drill holes selected for study. From the new data contributed by this study, an alteration profile for the southern part of APV has been built. The advanced argillic zone represents the continuation to the west of the alteration domain that hosts the ore deposits at Pueblo Viejo, lately referred to as a lithocap (e.g. Sillitoe et al., 2006). The distribution of the mineral assemblages in this domain for APV is equivalent to that described for Pueblo Viejo (Kesler et al., 1981) with an upper advanced argillic domain of kaolinite and dickite and a lower domain with pyrophyllite and diaspore. Alunite is very scarce in APV samples but is described as abundant in the lower part of funnel-shaped altered and mineralized zones at Pueblo Viejo (Kesler et al., 1981).

In APV drill cores, the upper advanced argillic alteration domain has a maximum thickness of 300m. It is underlain by sericitic, propylitic and, locally, potassic and sodic-calcic domains that, together, total more than 800m in thickness. The large volume of alteration registered in the region implies the existence of a buried magmatic body at depth capable of driving the hydrothermal cells that were responsible for rock alteration.

This is the first description of potassic and sodic-calcic alteration from the Pueblo Viejo district. In APV drill cores, these two assemblages overlie systematically diorites of mafic composition that are also partially or totally altered. Diorites in the Pueblo Viejo district have already been reported (Bowin, 1966; Kesler et al., 1981) and are now known to extend to the west from the new cores and mapping carried out in APV concession.

The high mobility of K, Na and Ca is a distinguishing feature of some of the sampled rocks in APV. Thus, whereas fresh Pueblo Viejo mafic rocks have only around 0.4 to 0.5% K_2O (Kesler et al., 1990), APV altered rocks have up to 4.1% K_2O according to recent analyses. This K enrichment together with trace-element discriminatory diagram plots would point to a calcalkaline trend for some of the studied rocks. Furthermore, studied tourmaline crystals in the sodic-calcic domain seem to reflect a later magmatic stage (Torró et al. 2012). The relation between the diorites registered in APV cores and the above mentioned observations is not clear at this moment. A complete study on these hypabyssal rocks is currently under way.

Higher gold, silver and copper grades are systematically related to the advanced argillic domain. This feature is equivalent to what is reported for the Pueblo Viejo ore deposits, supporting the epithermal nature of mineralization. No or minor positive anomalies in ore metals are observed in the potassic and sodic-calcic zones.

A low-angle fault zone has been interpreted on APV. Regional low-angle thrust faults were mapped by Bowin (1966) and were extended into the Los Ranchos Formation by Nelson (2000) based on mapping in the Pueblo Viejo pits.

References

Arribas A, Arribas I, Draper G, Hall C, Kesler SE, McEwan C, Muntean JL (2011) $^{40}Ar/^{39}Ar$ dating of alunite from the Pueblo Viejo Gold-Silver district, Dominican Republic. Econ Geol, 106, 1059-1070.

Bowin CO (1966) Geology of the central Dominican Republic. Geol Soc Am Mem 98, 11-84.

Dilles JH (2012) Footprints of porphyry Cu deposits: Vectors to the hydrothermal center using mineral mapping and lithogeochemistry. Final technical report. http://minerals.usgs.gov/mrerp/reports/Dilles-G10AP00052.pdf

Kesler SE, Russell N, Seaward M, Rivera J, McCurdy K, Cumming GL, Sutter JF (1981) Geology and Geochemistry of Sulfide Mineralization Underlyig the Pueblo Viejo gold-silver Oxide Deposit, Dominican Rep. Econ Geol,76,1096-1117.

Kesler SE, Russell N, Polanco J, McCurdy K, Cumming GL, (1990), Geology and geochemistry of the early Cretaceous Los Ranchos Formation, central Dominican Republic, in Mann, P., et al., eds., Geologic and tectonic development of the North America-Caribbean plate boundary in Hispaniola: Geol S Am S Paper 262, p. 187–201.

Kesler SE, Campbell IH, Allen CM (2005) Age of the Los Ranchos Formation, Dominican Republic: Timing and tectonic setting of primitive island arc volcanism in the Caribbean region. Geol Soc Am Bull, 117, 987-995.

Kranidiotis P & McLean WH (1987) Systematics of chlorite alteration at the Phelps Dodge massive sulphide deposit, Matagami, Quebec. Econ Geol, 82, 1898-1911.

Nelson CE (2000) volcanic domes and gold mineralization in the Pueblo Viejo district, Dominican Republic. Miner Deposita, 35, 511-525.

Nelson CE, Proenza JA, Lewis JF, López-Kramer J (2011) The metalogenic evolution of the Greater Antilles. Geol Acta, 9, 229-264.

Escuder-Viruete J, Díaz de Neira A, Hernaiz Huerta PP, Monthel J, García-Senz J, Joubert M, Lopera E, Ullrich T, Friedman R, Mortensen D, Pérez-Estaún A (2006) Magmatic relationships and ages of Caribbean Island arc tholeiites, boninites and related felsic rocks, Dominican Republic. Lithos, 90, 161-186.

Pindell JK & Barrett SF (1990) Geological Evolution of the Caribbean region: A plate-tectonic Caribbean Region. Geol Soc Am, Geology of North America, H, 405-432.

Seedorff E, Dilles JH, Proffett JM, Jr Einaudi MT, Zurcher L, Stavast WJA, Johnson DA, Barton MD (2005) Porphyry deposits: Characteristics and origin of hypogene features. Economic Geology 100th anniversary volume, 251-298.

Sillitoe RH, Hall DJ, Redwood SD, Waddell AH (2006) Pueblo Viejo high-sulfidation epithermal gold-silver deposit, Dominican Republic: a new model of formation beneath barren limestone cover. Econ Geol, 101, 1427-1435.

Torró L, Proenza JA, Melgarejo JC, Carrasco H, Domínguez H, Lewis JF (2012) Tourmaline composition near a diorite intrusive body under La Cuaba lithocap (Ampliación Pueblo Viejo district, Dominican Republic). Macla, 16, 196-197.

Winchester JA & Floyd PA (1977) Geochemical discrimination of different magma series and their differentiation products using immobile elements. Chem Geol, 20, 325-343.

Vascular plant materials control the formation of shale-hosted massive sulphides in the Iberian Pyrite Belt

Jesús Velasco-Acebes*, César Menor-Salván, Sara Gismera-Díez and Fernando Tornos
Centro de Astrobiología, CSIC-INTA, 28850 Torrejón de Ardoz, Madrid, Spain.
**velascoaj@cab.inta-csic.es*

Abstract. The Iberian Pyrite Belt (IPB) is one of the biggest massive sulphide concentrations in the world. The mineralization lies within a sequence called Volcano-Sedimentary Complex, and is hosted by volcanic rocks (northern zone of IPB) or shales (southern one).

We propose that sulphide formation in the southern part is due to paleogeographical changes and the onset of regional volcanism. Isotopic data of massive sulphides (-33.2 to +4.1‰) suggests that there was a second source of sulphur besides hydrothermal fluids, insomuch as the stockworks present $\delta^{34}S$ between -2.5 to +10‰.

New data of higher plant biomarkers indicate that biological crisis during D-C boundary was responsible for the input of organic matter that sulphate-reducing bacteria used to supply the necessary H_2S to the basin.

Keywords. Iberian Pyrite Belt, Tharsis, massive sulphides, biomarkers, geomicrobiology

1 Introduction. Geological setting

The Iberian Pyrite Belt (IPB) belongs to the South Portuguese Zone (SPZ) and is located in the SW of the Iberian Peninsula. It is the largest volcanogenic massive sulphide province, with more than 80 massive sulphide deposits and 1750 Mt of ore (Sáez et al. 1996; Leistel et al. 1997; Tornos, 2006).

The stratigraphy of the IPB is rather simple. The basement is not exposed and the earliest abundant rocks are shale and sandstone of Famennian age, the PQ Group (>2000 m), deposited in a stable platform. The PQ Group is conformably overlain by the Volcano-Sedimentary Complex, which was deposited in an extensional marine continental basin, likely a back arc one. It includes two groups of volcanic rocks, alkaline to tholeitic basalt, and calc-alkaline andesite to rhyolite. These rocks occur as (crypto-) domes, flows and sills and are interbedded with abundant shale and chemical sediments, chert and massive sulphides (late Devonian-early Visean). The uppermost rocks are grouped in the Culm Group, a flysch-like sequence of Serpukovian-Bashkirian age that represents the infilling of the basin during the progradation of the Variscan front.

The massive sulphide deposits of the northern and southern part of the Belt show different features. Those located in the northern IPB are invariably hosted by the apical part of felsic domes, in relationship with pumice- and glass-rich dacite to rhyolite of Early Tournaisian age. These ore deposits are interpreted as being replacive and major examples include Aguas Teñidas, La Zarza or Aljustrel. The deposits in the southern IPB are significantly younger, of Strunian age, and formed by exhalation in third order basins. This type includes deposits such as Neves Corvo, Aznalcóllar-Los Frailes, Las Cruces, Lousal, Sotiel-Migollas, Valverde or Tharsis (Tornos, 2006).

Current models suggest that the massive sulphides of the southern IPB formed at the Devonian-Carboniferous boundary in response to major paleogeographic changes and the onset of volcanism in the area (Menor-Salván et al., 2010). In brief, crustal thinning and magmatism generated large hydrothermal cells synchronous with the accelerated diagenesis and dewatering of the PQ Group. This resulted in hydrothermal venting on the seafloor and formation of anoxic conditions at the bottom of the restricted basins.

Vented fluids were metal-rich but sulphur–poor and the massive sulphides formed due to the input of large amounts of H_2S derived from the biogenic reduction of seawater sulphate (Tornos, 2006; Tornos et al., 2008).

This is consistent with the sulphur isotope values; different compilations of $\delta^{34}S$ data in the IPB show that the sulphur isotope values are more restricted and positive in the stockwork zones (-2.5 to +10‰) than in the overlying massive sulphides (-33.2 to +4.1‰). The sulphur in the stockwork zone was likely inherited from the sulphides in the PQ Group or due to the abiogenic reduction of seawater sulphate-mixed with sulphur with more negative signatures, likely the anaerobic sulphate reduction by chemolithoautotrophic microbes in an open system to sulphate. Numerical modeling and isotope geothermometry suggest that the anoxic bottoms of the basins in which the massive sulphides formed, reached a steady state at temperatures around 60-110ºC, optimal for hyperthemophilic sulphate reducers.

The electron donor for reducing such a large amount of sulphate could be the organic matter supplied by the destruction of vascular plants in subaerial forests located nearby (Menor-Salván et al., 2010). Our goal is to provide possible evidence of the importance of terrigenous organic matter input to the flourishing of microbiological activity during the formation of the giant VMS deposits of the southern IPB. However, two criteria in support of our model are lacking of increase in higher plant molecular fossils coincident with the major inorganic geochemical changes and a lack of indicators of terrigenous organic matter input to the basin.

2 Higher plant indicators and related sulphide precipitation

The Devonian-Carboniferous boundary is a very important key regarding biomass destructions. The biological crisis lead to extinction of about 21% of marine genera and a general vanishing of microfauna (McLaren and Goodfellow, 1990; Sepkoski, 1996). The

major biological crisis during DC boundary is called Hangenberg event, charactrized by geochemical, lithological and biological changes in all trophic levels, terrestrial and marine (Caplan and Bustin 1999). The paleoecological events during DC boundary could have supplied the organic matter necessary to adjust the mass balance that explain the massive sulphide formation. We considered a simple biogeochemical reaction using anaerobic fermentation of hexoses as an archetypical electron donor. Principal reactions to produce H_2S are as follows:

$$C_6H_{12}O_6 \text{ (glucose)} + SO_4^{2-} \rightarrow 2CH_3COO^- \text{ (acetate)} + H_2S + 2CO_2$$

$$CH_3COO^- \text{ (acetate)} + SO_4^{2-} + 3H^+ \rightarrow H_2S + 2CO_2 + 2H_2O$$

$$H_2S + 0.5Fe^{2+} + 0.25O_2 \rightarrow H^+ + 0.5FeS_2 \text{ (pyrite)} + 0.5H_2O$$

It is possible to combine some reactions to produce pyrite at the same time that CO_2 is released:

$$C_6H_{12}O_6 + 3SO_4^{2-} + 1.5Fe^{2+} + 3H^+ + 0.75O_2 \rightarrow 1.5FeS_2 + 6CO_2 + 7.5H_2O$$

Clearest evidence for this reaction is seen in Filón Norte of Tharsis, inside the laminated ores composed by siderite-pyrite, interpreted as biogenic mounds (Tornos et al. 2008).

If this model is not correct, we should not find evidence of higher plant and terrigenous organic matter increase coincident with the mineralization event in the vertical distribution of biomakers.

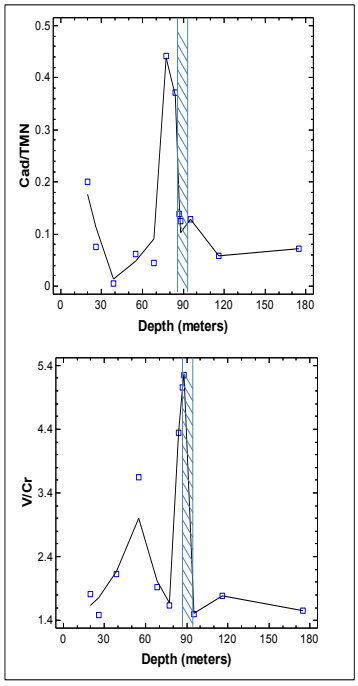

Figure 1. Cadalene/1,3,6,7-tetramethylnaphthalene ratio and V/Cr ratio versus shale depth. The marked zone correspond with pyrite orebody.

With this null hypothesis, we found in the organic extract of a shale sequence that cut the massive sulphide horizon, a strong increase in the cadalene relative concentration versus 1,3,6,7-tetramethylnaphthalene (Fig. 1), exactly coincident with the maximum increase of anoxicity (measured as V/Cr ratio) and the minimum $\delta^{34}S$ levels. 1,3,6,7-tetramethylnaphthalene has been selected because is a chemically similar to cadalene molecule and its concentration remains constant along the entire sequence. Cadalene is a higher plant biomarker and its increase suggest a rise in the input of terrigenous organic materials.

Another higher plant indicator, that suggests the contribution of gymnosperm plants, is the 2-methylretene (Bastow et al., 2001). Enhanced level of this biomarker, corrected against 9-methylphenanthrene, confirm the major input of higher plant material (Fig.2).

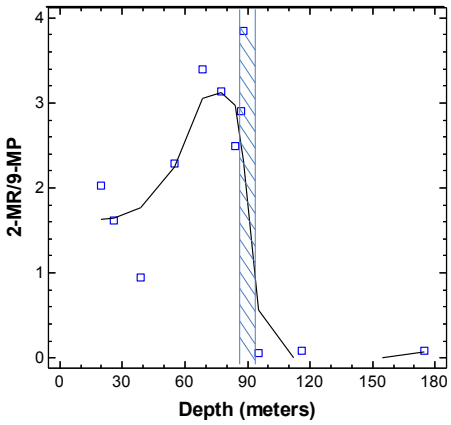

Figure 2. Vertical distribution of 2-methylretene/9-methylphenanthrene ratio versus shale depth. Marked zone represents the pyrite orebody.

Other evidences found are the enhanced levels of retene and 1-methylphenanthrene (measured as x/9-methylphenanthrene ratios). Taken together, this suite of biomarkers indicates high input of gymnosperm flora (Alexander et al. 1992). The retene/9-MP and 2-methylretene/9-MP ratios showed a linear correlation along the shale depth, confirming that both biomarkers are related and were possibly from the same biological source.

The study of the linear hydrocarbons is a proxy for the evaluation of the input of terrestrial organic matter. The terrigenous/aquatic ratio (TAR, Peters et al. 2005) evaluates the proportion of C_{27}-C_{31} n-alkanes versus lighter n-alkanes. Vertical distribution of TAR shows relative changes in the contribution of land flora versus marine input. As expected, we found a TAR increase in the interest zone, confirming the previous observation from aromatic terpene biomarkers (Fig. 3).

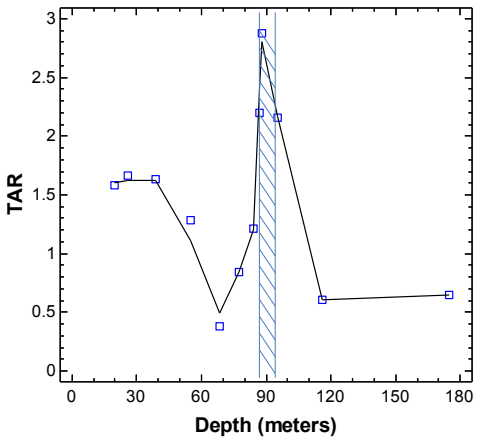

Figure 3. Vertical distribution of terrigenous/aquatic ratio versus shale depth. Marked zone corresponds with pyrite orebody.

To confirm the information of n-alkane distribution, we evaluated the hopane/sterane ratio, measured as C30 αβ-hopane/C29 sterane (Fig. 4). The increase of hopane/sterane ratio in the vertical distribution could suggest input from land or/and aerobic bacteria rich facies. An increase in hopane together with anoxicity is a strong suggestion of bacterial rich land material, consistent with the vascular plant crisis during DC boundary.

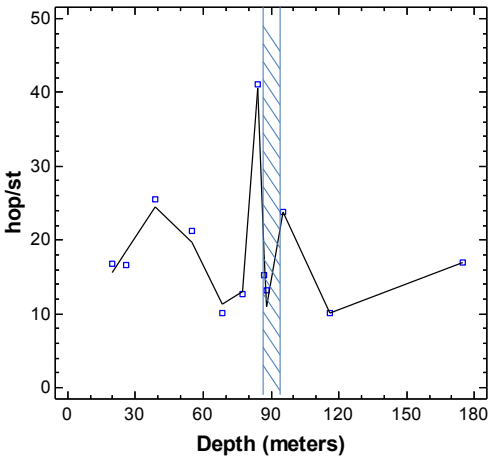

Figure 4. Vertical distribution of hopane/sterane in Tharsis shale. Marked zone represents the pyrite orebody.

It is interesting to evaluate the paleovegetation changes associated with the orebody horizon. The lower retene/cadalene ratio in the zone of interest suggests an ecological change with declining gymnosperm flora. The global dramatic increase in cadalene and abietane class biomarkers (retene and 2-methylretene), together with inverse variation in retene/cadalene ratio is suggestive of land ecosystem alteration, possibly destruction (Mizukami et al. 2013). Future work that might confirm a dramatic destructive process of the land biomass include the study of the vertical distribution of high molecular weight PAHs, a proxy of paleofires. It is possible also that the ecological change was a gradual vascular plant crisis, due to climatic changes. The declining in vascular plants could lead to an increase in erosion and incorporation of land materials to the marine basin, with concomitant increase in molecular biosignatures of land plants. Other molecular evidence in this direction is the decrease of higher plant parameters (van Aarsen et al., 2000), that indicate a decrease of abietane-class terpenoid generating gymnosperm respect to global land flora (Fig. 5).

3 Conclusions

The vertical distribution of land plant biomarkers, indicators of paleovegetation changes and indicators of terrigenous organic matter input all showed a dramatic enhancement coincident with evidences of anoxia and strongly negative $\delta^{34}S$ levels. The organic and inorganic geochemical alteration coincides with the occurrence of the shale hosted massive sulphide orebody at Tharsis.

Data suggests that the formation of the massive sulphide orebody could be related to major paleoecological changes during the Devonian-Carboniferous boundary, Hangenberg event.

We suggest that these features could be applied to the rest of the massive sulphide deposits in the southern domain of the Iberian Pyrite Belt (IPB).

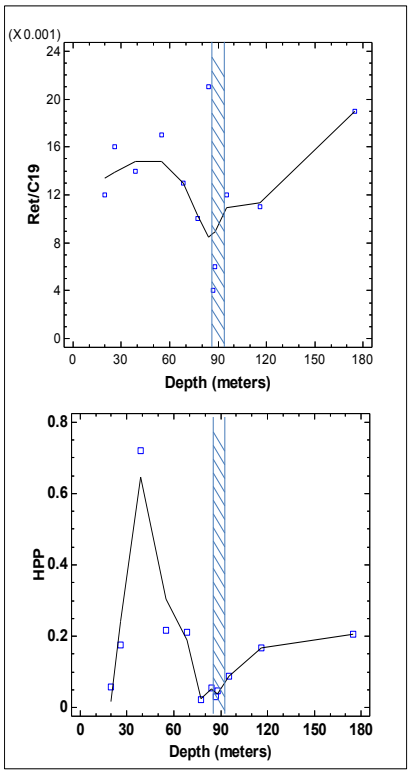

Figure 5. Vertical distribution of proxies of paleoflora changes in the Tharsis shale sequence.

Acknowledgements

Study funded by the project CGL 2011-23207.

References

Alexander R, Larcher AV, Kagi, RI, Price, PL (1992) An oil-source correlation study using age-specific plant-derived aromatic biomarkers. In Biological Markers in Sediments and Petroleum; Moldowan, Albrecht and Philp ed. Prentice-Hall, NJ, USA.

Bastow, TP, Singh, RK, van Aarsen, BKG, Kagi, RI (2001) 2-methylretene in sedimentary material: a new higher plant biomarker. Organic Geochemistry 32: 1211-1217.

Caplan ML, Bustin RM (1999) Devonian–Carboniferous Hangenberg mass extinction event, widespread organic-rich mudrock and anoxia: causes and consequences. Palaeogeography, Palaeoclimatology, Palaeoecology 148:187-207.

Leistel JM, Marcoux E, Thiéblemont D, Quesada C, Sánchez A, Almodóvar GR, Pascual E, Sáez R (1997) The volcanic-hosted massive sulphide deposits of the Iberian Pyrite Belt Review and preface to the Thematic Issue. Mineral Deposita 33:2-30.

McLaren, DJ, Goodfellow, WD, (1990) Geological and biological consequences of giant impacts. Ann. Rev. Earth Planet. Sci. 18:123–171.

Menor-Salvan C, Tornos F, Fernandez-Remolar D, Amils R (2010) Association between catastrophic paleovegetation changes during Devonian-Carboniferous boundary and the formation of giant massive sulphide deposits. Earth and Planetary Science Letters 299:398-408.

Mizukami, T, Kaiho, K, Oba, M (2013) Significant changes in land vegetation and oceanic redox across the Cretaceous/Paleogene boundary. Palaeogeography, Palaeoclimatology, Palaeoecology 369:41-47

Peters, KE, Walters, CC, Moldowan, JM (2005) The Biomarker Guide, Vol II. Second Edition. Cambridge University Press, Cambridge, UK.

Sáez R, Almodóvar GR, Pascual E (1996) Geological constraints on massive sulphide genesis in the Iberian Pyrite Belt. Ore Geology Reviews 11:429-451.

Sepkoski, JJ, (1996). Patterns of Phanerozoic extinction: a perspective from global data bases. In: Walliser, O.H. (Ed.), Global Events and Event Stratigraphy in the Phanerozoic. Springer, Berlin, pp. 35–51.

Tornos F (2006) Environment of formation and styles of volcanogenic massive sulphides: The Iberian Pyrite Belt. Ore Geology Reviews 28:259-307.

Tornos F, Conde, C. and Spiro, B. (2008) Formation of the Tharsis Massive sulphide Deposit, Iberian Pyrite Belt: Geological, Lithogeochemical, and Stable Isotope Evidence for Deposition in a Brine Pool Economic Geology 103:185-214.

van Aarssen BGK, Alexander R, Kagi RI (2000) Higher plant biomarkers reflect palaeovegetation changes during Jurassic times. Geochimica et Cosmochimica Acta 64:1417-1424.

S 3.2

Sediment-hosted deposits

Convenors:
Ross Large & Jan Pašava

KEYNOTE SPEAKER

Genetic model for the Talvivaara Ni-Cu-Zn-Co deposit and ore potential of black shale units in Finland

Loukola-Ruskeeniemi, K., Arkimaa, H., Airo, M.-L., Vuoriainen, S.
Geological Survey of Finland, P.O. Box 96, FI-02151 Espoo, Finland

Hyvönen, E.
Geological Survey of Finland, P.O. Box 77, FI-96101 Rovaniemi, Finland

Lerssi, J., Vanne, J.
Geological Survey of Finland, P.O. Box 1237, FI-70211 Kuopio, Finland

Abstract. The Talvivaara black shale deposit contains 2053 Mt of low-grade Ni-Cu-Zn-Co ore. It is currently mined with bioheapleaching technology. Characteristic features are high concentrations of organic C and S (7-8% of each). During the deposition of the organic-rich mud in a restricted rift-related sea basin the anoxic/euxinic bottom waters were enriched in Ni, Cu and Zn. The primary source of Ni is probably linked with the occurrence of ultramafic rocks. During diagenesis, both bacterial and thermochemical sulphate reductions occurred. Multiple S isotope results evidence for reactions of hydrothermal solutions (100 - 200 ^{o}C) with organic matter in some parts of the deposit. Metamorphic and tectonic deformations increased the profitability of the deposit.

The distribution of black shale units in Finland was mapped based on airborne geophysical interpretation verified by drill core studies. Nation-wide airborne surveys were carried out during 1972 - 2007. Hundreds of black shale samples were analysed for chemical composition and for petrophysical properties. High concentrations of organic C and S and thick units of black shales (> 50 m) occur especially in eastern and northern Finland, but metal concentrations as high as at Talvivaara did not occur in the studied drill cores. However, black shales occur close to many sulphide deposits and their characteristics may be used as an exploration tool.

Keywords. Black shale, sulphide deposit, genetic model, ore potential, Finland

1 Black-shale-hosted ore deposits

Sediments rich in organic C are deposited in various depositional environments. The inorganic matter may be composed mainly of clay, silt, sand, carbonate, chert, phosphate or tuff (Ketris and Yudovich 2009). Black shales also host a variety of sulphide ore deposits including gold, copper, zinc, cobalt and nickel.

Genesis of the black-shale-hosted ore deposits differ. In addition to the primary deposition of metals during sedimentation, addition of metals may have occurred during diagenesis or during tectonic or metamorphic deformation. Metamorphic and tectonic deformation can also have a major role in increasing the profitability of a syngenetic black shale deposit.

Talvivaara is at present the largest black-shale-hosted Ni-Cu-Zn-Co deposit in the world. Other Ni deposits and occurrences reported include those in South China, Yukon Territories in Canada and Czech Republic of which the 20-cm-thick Mo-Ni-PGE-rich black shale unit in China has been mined (e.g., Coveney and Chen 1991).

Black shales are associated with different types of ore deposits either as the host rock or within the host rock package. In Finland, black shales are associated with many sulphide deposits including Vihanti Zn-Cu-Pb and Outokumpu Cu-Co-Zn (Loukola-Ruskeeniemi 1999). There are many possible reasons for the relationship, for example organic matter can have a significant influence on the behaviour of mineralising fluids (e.g., Greenwood et al. 2013).

Figure 1. Metamorphosed sulphur-rich black shale from the Talvivaara Ni-Cu-Zn-Co deposit. The width of the drill core section is 3 cm and the sample length is 7 cm. The synsedimentary/syndiagenetic laminae rich in pyrite and graphite are cut by quartz-sulphide veins.

2 Talvivaara Ni-Cu-Zn-Co deposit

The Talvivaara deposit has been mined since 2008 by the Talvivaara Mining Company. It contains 2053 Mt of ore with 0.22% Ni, 0.13% Cu, 0.02% Co and 0.50% Zn. Large-scale open-pit mining and bioheapleaching technology are the main reasons for low production costs (Riekkola-Vanhanen 2010).

The original thickness of the 2.1-1.9 Ga black shale units at Talvivaara may have varied from 10 to 100 m before tectonic deformations. The maximum thickness at present is 800 m. Characteristic features are high concentrations of organic C and S with median values of 7.6% and 8.2%, respectively. Organic C is graphitic and

a variety of sulphide textures occur, representing multiphase evolution during diagenesis, tectonic deformation and medium-grade regional metamorphism (Loukola-Ruskeeniemi and Lahtinen 2013).

The main sulphides of the Talvivaara ore are pyrrhotite, pyrite, sphalerite, chalcopyrite and pentlandite. S-rich and C-rich laminae are cut by quartz-sulphide veins (Fig. 1).

The rocks at Talvivaara have undergone medium grade regional metamorphism, which has impacted on the mineralogy. The black shales contain quartz, micas, graphite and sulphides as main minerals. Tremolite-rich rocks containing graphite, sulphides and in many cases also alabandite (MnS) occur as 10-cm to 3-m thick intercalations amongst the black shales.

3 Genetic model for the Talvivaara deposit

The $\delta^{13}C$ (PDB) values of the Talvivaara black shales range from -19‰ to -30‰ indicating that the non-carbonate C has an organic origin (Loukola-Ruskeeniemi 1999). The high organic C values indicate that life was abundant and conditions were favourable for the preservation of organic C in the sediment. There are several different black shale units in the Talvivaara area (Kontinen 2012) but the mineralized black shales deposited in a restricted rift-related seawater basin 2.0 - 1.9 Ga ago.

Correlations of organic C with S, V, Mo and Ni, so strong in many black shale localities, are weak in the Talvivaara mineralized black shale unit. This is because the bottom waters were anoxic to euxinic. During the deposition of the organic-rich mud on the sea floor the anoxic/euxinic bottom waters were enriched in Ni, Cu and Zn. It is probable that the source of Ni is linked with the occurrence of ultramafic rocks in the rift zone. The Ni/Co ratio at Talvivaara is high suggesting an ultramafic rather than a mafic source.

Sulphur isotope $\delta^{34}S$ values indicate mixing of sulphur derived from different processes or fractionation by sulphate reduction in a restricted basin (Loukola-Ruskeeniemi and Heino, 1996). Similar $\delta^{34}S$ patterns to those at Talvivaara have been reported from the Sullivan Pb-Zn-Ag deposit in Canada (Taylor 2004) and from the Central African Copperbelt (Cailteux et al. 2005).

Both thermochemical and bacterial sulphate reductions were important for the generation of reduced sulphur (Young et al. 2013). Bacterial sulphate reduction occurs in low-T diagenetic environments (< 80 ^{o}C) and thermochemical sulphate reduction occurs in diagenetic environment with 100-200 ^{o}C temperature. Multiple S isotope values evidence for hydrothermal addition of S during high-T diagenesis (100 to 200 ^{o}C).

The chondrite-normalized rare earth element patterns of the Talvivaara black shales exhibit negative europium anomalies (Loukola-Ruskeeniemi and Lahtinen 2013). According to the results reported by Karakaya et al. (2012) the negative Eu anomalies indicate deposition from fluids < 200 ^{o}C confirming the conclusion drawn from the multiple S isotope results.

In addition to deposition of metals during sedimentation and diagenesis, metamorphic and tectonic deformation had a major role in increasing the profitability of the deposit.

4 Black shale units in Finland

To our knowledge, the first nation-wide black shale map in the world was published in 2000 in Finland (Arkimaa et al. 2000). We have updated the map and database during 2009-2013 with new airborne geophysical data and drill cores from new prospects. We have re-studied deep cores drilled earlier for exploration by the Geological Survey of Finland and the Outokumpu Company. The samples were selected to represent the most organic-rich parts of each of the cores. Textures, mineralogy and geochemistry were investigated. Petrophysical properties were measured from exactly the same samples as the chemical analyses to provide direct comparisons.

The database includes altogether 800 samples of which 428 were selected during 2009-2013 and the rest of the samples were selected and analysed earlier. High concentrations of organic C and S and thick (> 50 m) black shale units occur especially in eastern and northern Finland. Ni, Cu, Zn, Co and Mn concentrations as high as at Talvivaara did not occur in black shales of the studied prospects. Median values for Ni, Cu and Zn concentrations were low (Table 1). However, elevated palladium concentrations may occur in one of the prospects but unfortunately at present there is no existing technology to utilise Pd from rocks rich in organic carbon (Riekkola-Vanhanen, personal communication).

The black shale database composed of airborne geophysical, geochemical and rock physical data sets will facilitate data integration, statistical analysis and interpretation. These results integrated with magnetic structural analysis provide a tool for investigation, characterization and classification of black shale units in Finland.

Table 1. Median and maximum concentrations for total carbon, sulphur, nickel, copper and zinc of altogether 428 Palaeoproterozoic black shale samples selected from drill cores during 2009-2011 all over Finland. Study sites are shown as black dots in Fig. 2.

	Maximum	**Median value**
C %, LECO	37.40	5.99
S %, LECO	28.19	4.22
Ni %, XRF	0.56	0.03
Cu %, XRF	0.61	0.02
Zn %, XRF	1.14	0.03

The magnetic anomalies are caused by ferromagnetic, monoclinic pyrrhotite. Correlation of chemical and petrophysical characteristics of the black shale samples and airborne geophysical data indicates that increased S content is related to increased conductivity (high Re/Im ratio).

An example of a sampling locality is shown in Fig. 3.

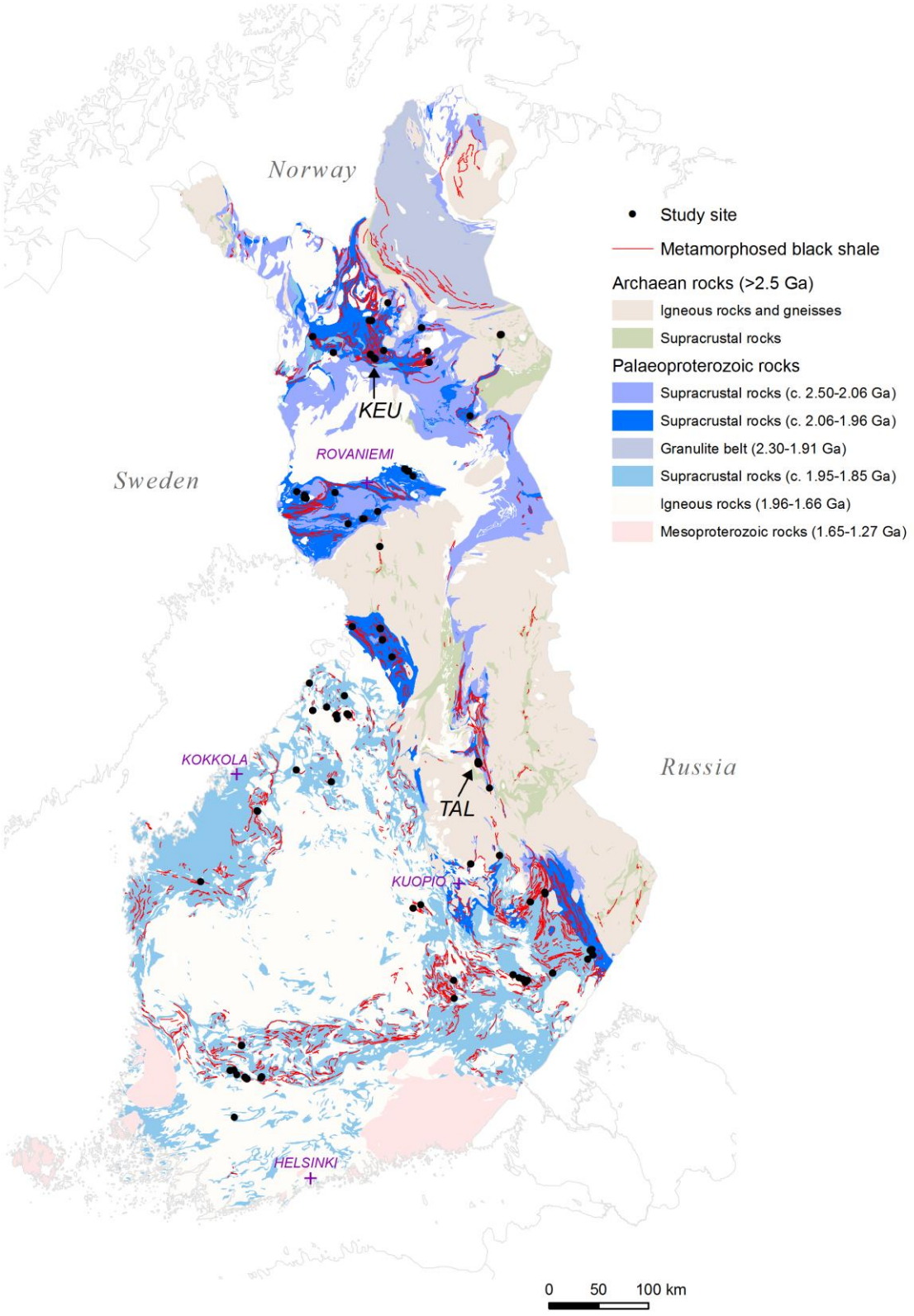

Figure 2. Sampling localities of the present project are shown as black dots on the geological map (Koistinen et al. 2001). Red lines represent Palaeoproterozoic metamorphosed black shale units based on the database of the Geological Survey of Finland (Arkimaa et al. 2000; Loukola-Ruskeeniemi et al. 2011; Hyvönen et al. 2013). TAL = Talvivaara Ni-Cu-Zn-Co deposit, KEU = Keulakkopää prospect in Finnish Lapland (Fig. 3).

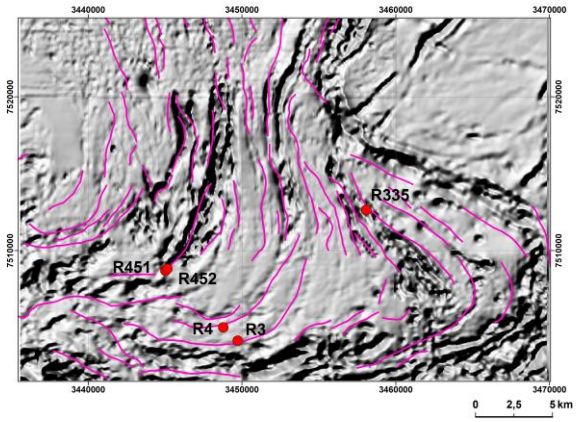

Figure 3. Aeromagnetic hill-shaded total intensity data is shown as grey tones. Black shale units are drawn with magenta. Black shale units were interpreted from aerogeophysical data and represent geophysical anomalies similar to those of known black shale units, verified from drill cores and outcrops. Drill cores re-studied for the present project are shown with red dots (map sheet 3712, 'KEU' in Fig. 2, Keulakkopää, Haurespää and Nuttio prospects). The area of the map represents 35 km x 23 km.

Black shales are easy to recognize on airborne geophysical maps because of their stratigraphy-related, coupled magnetic and conductive patterns (Airo and Loukola-Ruskeeniemi 2004).

5 Discussion and Conclusions

Even though black shales are easy to identify in airborne geophysical data, their interpretation is challenging: their geophysical properties vary from site to site and within individual lithostratigraphic units. Detailed geological mapping would be required, challenging in Finnish conditions where only 3% of the bedrock is outcropped.

The genetic models for black-shale-hosted ores have developed during past decades and followed the evolution of geological thinking. Precipitation of metals from seawater was in fashion before, then the seafloor hydrothermal vents were discovered and now the primary sedimentation model seems to be in fashion again. New methods provide tools to distinguish multiphase evolution in more detail and as more results are obtained, the overall picture will show more and more varieties in depositional environments and ore-forming processes involved.

As a conclusion of the comparative black shale study it seems likely that other black-shale-hosted ore deposits as large as Talvivaara are unlikely to exist in Finland. However, comparative black shale studies are significant for the exploration of other types of sulphide deposits, since rocks rich in organic carbon occur close to many sulphide deposits in the Fennoscandian Shield and all over the world.

Acknowledgements

We thank geologists of the Geological Survey of Finland, especially M. Iljina, T. Karinen, A. Karvinen, J. Kousa, J. Luukas, J. Nikander, M. Tiainen and T. Törmänen, who have given invaluable information of the prospects.

References

Airo M-L and Loukola-Ruskeeniemi K (2004) Characterization of sulfide deposits by airborne magnetic and gamma-ray responses in eastern Finland. Ore Geology Reviews 24:67-84.

Arkimaa H, Hyvönen E, Lerssi J, Loukola-Ruskeeniemi K and Vanne J (2000) Proterozoic black shale formations and aeromagnetic anomalies in Finland 1 : 1 000 000. Geological Survey of Finland.

Cailteux J, Kampunzu A, Lerouge C, Kaputo A, Milesi J (2005) Genesis of sediment-hosted stratiform copper-cobalt deposits, central African Copperbelt. Journal of African Earth Sciences 42: 134-158.

Coveney R and Chen N (1991) Ni-Mo-PGE-Au-rich ores in Chinese black shales and speculations on possible analogues in the United States. Mineralium Deposita 26: 83-88.

Greenwood P, Brocks J, Grice K, Schwark L, Jaraula C, Dick J, Evans K (2013) Organic geochemistry and mineralogy. 1. Characterisation of organic matter associated with metal deposits. Ore Geology Reviews 50: 1-27.

Hyvönen E, Airo M-L, Arkimaa H, Lerssi J, Loukola-Ruskeeniemi K, Vanne J, Vuoriainen S (2013) Airborne geophysical, petrophysical and geochemical characteristics of Palaeoproterozoic black shale units in Finland: applications for exploration and environmental studies. Geological Survey of Finland, Special Paper (in press)

Karakaya M, Karakaya N, Küpeli S, Yavuz F (2012) Mineralogy and geochemical behaviour of trace elements of hydrothermal alteration types in the volcanogenic massive sulfide deposits, NE Turkey. Ore Geology Reviews 48: 197-224.

Ketris M and Yudovich Y (2009) Estimations of Clarkes for carbonaceous biolithes: world averages for trace element contents in black shales and coals. International Journal of Coal Geology 78: 135-148.

Koistinen T (comp.) Stephens M (comp.), Bogatchev V (comp.), Nordgulen Ø (comp.), Wennerström M (comp.), Korhonen J (comp.) (2001) Geological map of the Fennoscandian Shield, scale 1 : 2 000 000. Espoo, Trondheim, Uppsala, Moscow, Geological Survey of Finland, Geological Survey of Norway, Geological Survey of Sweden, Ministry of Natural Resources of Russia.

Kontinen, A. 2012. F029 Talvivaara Ni-Zn-Cu. In: Eilu P (ed.) Mineral deposits and metallogeny of Fennoscandia. Geological Survey of Finland. Special Paper 53: 276-280.

Loukola-Ruskeeniemi K (1999) Origin of black shales and the serpentinite-associated Cu-Zn-Co ores at Outokumpu in Finland. Economic Geology 94: 1007-1028.

Loukola-Ruskeeniemi K and Heino T (1996) Geochemistry and genesis of the black shale –hosted Ni-Cu-Zn deposit at Talvivaara, Finland. Economic Geology 91: 80-110.

Loukola-Ruskeeniemi K and Lahtinen H (2013) Multiphase evolution in the black-shale-hosted Ni-Cu-Zn-Co deposit at Talvivaara, Finland. Ore Geology Reviews 92: 85-99.

Loukola-Ruskeeniemi K, Hyvönen E, Airo M-L, Arkimaa H, Eskelinen J, Lerssi J, Vanne J, Vuoriainen S (2011) Evaluation of the ore potential of black shale units in Finland - preliminary results of a geophysical and geochemical study. Geologi 63 (3): 68-79.

Riekkola-Vanhanen M (2010) Talvivaara Sotkamo mine – bioheapleaching of a polymetallic nickel ore in subarctic climate. Nova Biotechnologica 10-1: 7-14.

Taylor B (2004) Biogenic and thermogenic sulfate reduction in the Sullivan Pb-Zn-Ag deposit, British Columbia (Canada): Evidence from micro-isotopic analysis of carbonate and sulfide in bedded ores. Chemical Geology 204: 215-326.

Young S, Loukola-Ruskeeniemi K, Pratt L (2013) Reactions of hydrothermal solutions with organic matter in Palaeoproterozoic black shales at Talvivaara, Finland: evidence from multiple sulfur isotopes. Earth and Planetary Science Letters 367: 1-14.

Stable isotope studies of carbonate – hosted ore deposit in Cerro Minado, Huércal – Overa (Spain)

Sandra Amores, Oriol Bertran, Ferran Buireu, Miquel Febrer, Joan Carles Melgarejo
Departament de Cristal·lografia, Mineralogia i Dipòsits Minerals, Universitat de Barcelona. c/ Martí i Franquès, s/n 08028 Barcelona, Catalonia, Spain

Pedro Enrique – Gisbert
Departament de Geoquímica, Petrologia i Prospecció Geològica. Universitat de Barcelona. c/Martí i Franquès, s/n 08028 Barcelona, Catalonia, Spain

Abstract. Cerro Minado deposit is located in the eastern part of the Betic Cordilleras, near Huércal – Overa town (Almería, Spain). The mineralization is hosted in the Partaloa Unit dolostone and occurs as veinlets associated with saddle dolomite, and in disseminations. Ores are made up by sulphosalts and Ni-Co sulphides and arsenides. In order to constrain the nature of the mineralizing fluid, the C and O isotopic composition has been analysed on both the Triassic dolostone and the saddle dolomite. The $\delta^{13}C$ values in both carbonates are typical of Triassic marine carbonates (0.89 – 2.32‰). The saddle dolomite $\delta^{18}O$ values suggest hydrothermal influence. The presence of saddle dolomite implies high temperature and salinity fluid in deep burial conditions.

Keywords. Stable isotopes, Co-Ni-As sulphides, saddle dolomite, thrusting.

1 Introduction

Cerro Minado ore deposit is located near Huércal – Overa town in the Almería province (Spain) (Fig. 1). Currently abandoned, it was mined out mainly for Cu, Ag and Co during the 20th century.

Open pit mine working during the 1970s and 1980s (Gröbner and Fernández-Périz 2006) allow access to good mineralization exposures containing rare minerals. For a long time supergene specimens from this mine are well known among mineral collectors. In addition to erythrite, a large ensemble of rare sulphates, arsenates, carbonates, nitrates and halides has been described (Viñals et al. 2010). Further studies of the corresponding primary mineral assemblages have been recently published (Bertran – Oller et al. 2012).

The spatial correlation of the ore mineralization, hosted in dolostone, with the saddle dolomite and Co-bearing minerals suggest that Cerro Minado would classify as a Mississippi Valley – type (MVT) deposit.

In this paper, we focus on the study of carbon and oxygen isotopes from host dolostone and dolomite veins associated to sulphide mineralization in order to constrain the origin of the mineralizing fluid.

2 Geological Setting

Cerro Minado is located in the eastern part of the Betic Cordillera, in the Sierra de Almagro range. Three independent structural units form the Betic Cordillera: the Nevado – Filabride thrust complex, the Alpujárride complex, and the Maláguide complex. All have a Hercynian basement covered by Permo – Triassic and younger rocks (Egeler and Simons 1969). The Alpujárride complex, where the Cerro Minado deposit is

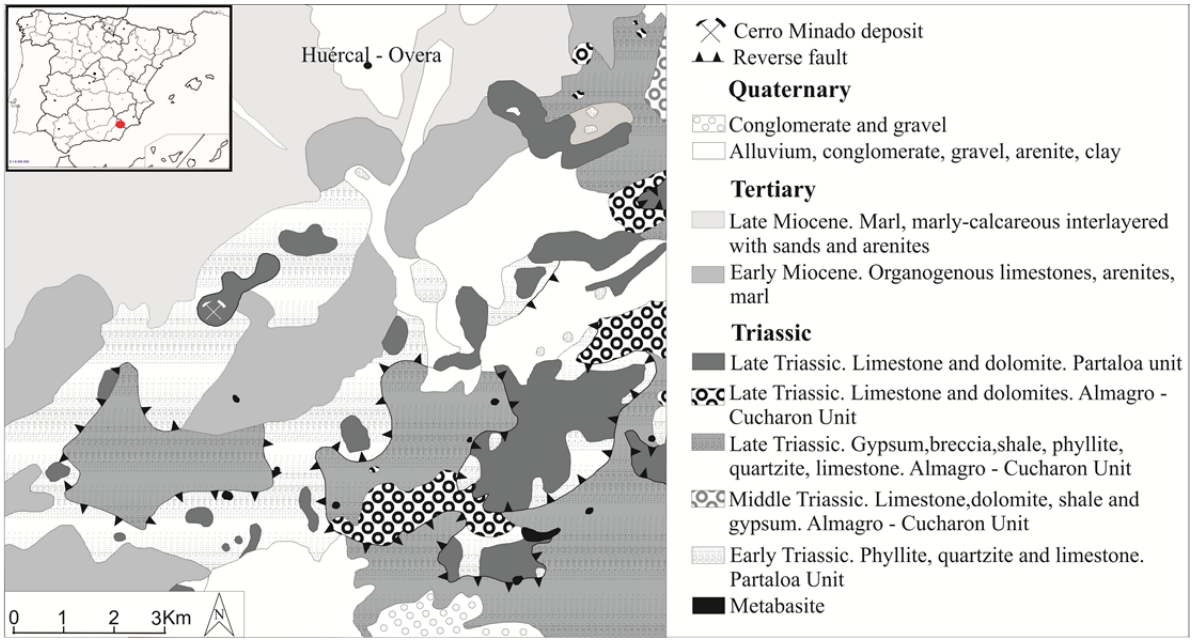

Figure 1. Geological map of Cerro Minado, modified after IGME (1980).

hosted, is the one that outcrop more extensively in the inner zones of the Betic Cordilleras.

The sulphide mineralization of Cerro Minado is hosted in the Partaloa Unit (Fig. 1) within lower Alpujárride. The Partaloa unit is composed, from the bottom to the top, of a micaschist formation, a phyllite – quartzite formation and a limestone formation (IGME 1980). The micaschist is only located in a few outcrops in the Sierra de Almagro and consists of green dark mica with quartzite and locally showing reddish meteoric alteration. Phyllite – quartzite formation is made up of interlayered quartzite-phyllite beds in the lower part and phyllite, shale and limestone in the upper zone. Some gypsum layers and metabasites can be identified. The limestone formation is characterized by yellow to grey limestone with fine phyllite sheets on the bottom and dark brownish dolostone predominance in the upper part (IGME 1980).

3 Mineralogy of sulphide veins

Mineralization is located near thrust affecting dark dolostone of the upper Partaloa Unit, which is partially silicified. The Triassic dolostone is dark owing to a high content of organic matter, and the grain size is small, less than 1 mm. Dolostone are affected by hydraulic brecciation and cemented by saddle dolomite. This cement generation consists of euhedral dolomite crystals averaging 100 μm in size (Fig. 2).

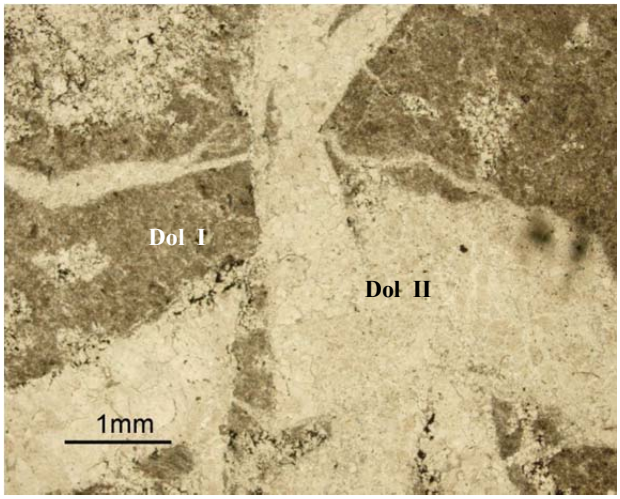

Figure 2. Detail of dolomitization in thin section. Saddle dolomite veins (Dol II) cut Triassic dolostone (Dol I). Some opaque sulphide grains are distinguished in these veinlets.

Primary ores occur extensively as disseminations of minute crystals of about 50 μm in diameter. In minor extent, they are filling discontinuous veinlets ranging from 0.1 to 2 mm in thickness, in association with saddle dolomite (Fig. 3a). They can also be concentrated in stylolitic surfaces.

The most common ore minerals are members of the cobaltite (CoAsS) – gersdorffite (NiAsS) series. These grains replace older generations of sulphides, as framboidal pyrite, pyrite nodules or pyrite – cattierite crystals, and members of the siegenite ($NiCo_2S_4$)-carrollite ($Cu(Co,Ni)_2S_4$) series (Fig. 3b).

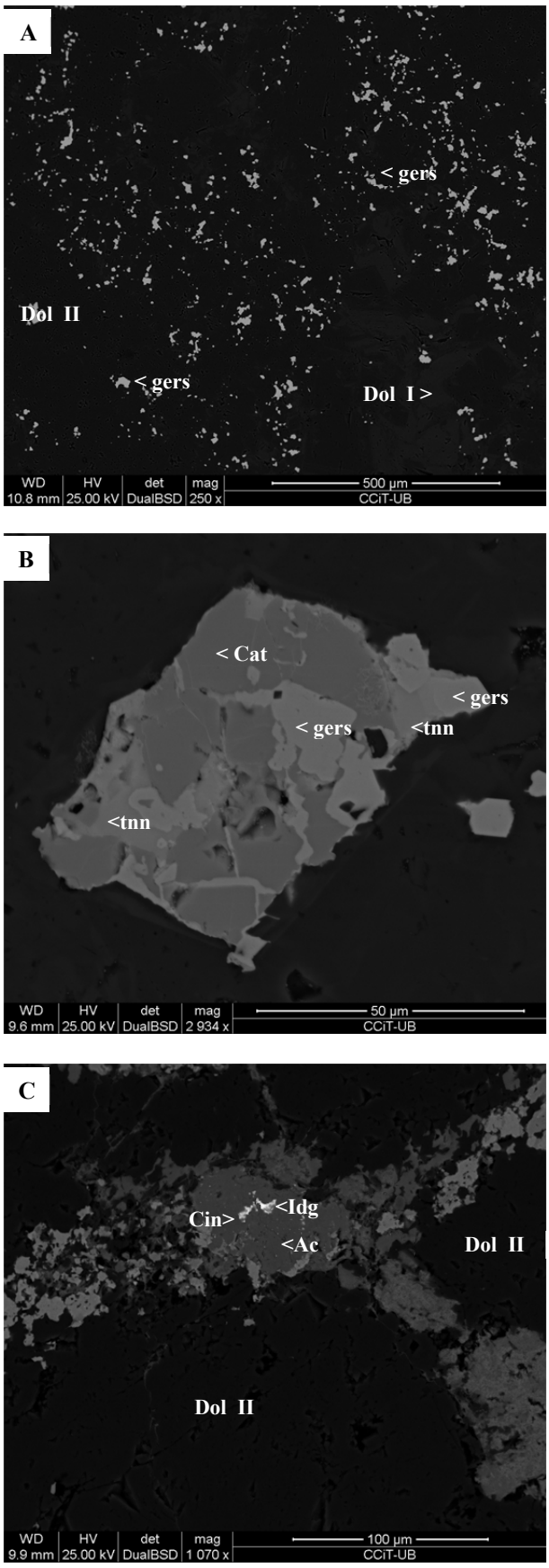

Figure 3. SEM images: a) HO-19 sample with scattered grains of gersdorffite inside dolomite; b) HO-22 with pyrite - cattierite replaced by gersdorffite veins; tennantite is substituting cattierite and gersdorffite; c) HO-8, cinnabar, iodargyrite and acanthite veins replacing Co-Ni arsenides inside saddle dolomite (dol II).

Cobaltite-gersdorffite may be accompanied by Zn-rich tennantite ($Cu_{10}(Fe,Zn)_2As_4S_{13}$). Fine late veinlets are infilled with native silver, acanthite (Ag_2S), cinnabar (HgS) and tiemannite (HgSe). Iodargyrite [(Ag,Hg)I] occur as a pseudomorphic product of replacement of tiemannite or acanthite crystals (Fig. 3c). Secondary copper minerals such as covellite, bornite and chalcocite are commonly associated with the above described mineral assemblage. These late – stage associations are interpreted as supergene.

4 C and O isotopes

A total of 9 dolomite samples including the host-rock dolostone (Dol I) and the saddle dolomite (Dol II) (Fig. 4) were selected in order to analyze their $^{13}C/^{12}C$ ratios. 50 µg of each sample from cut rock surfaces (Fig. 4) were taken using a drill. Carbon and oxygen compositions were determined using an EM mass spectrometer at the Centres Científics i Tecnològics of the University of Barcelona. The $\delta^{13}C$ is reported as relative to the PDB standard and $\delta^{18}O$ to SMOW standard. Carbon and oxygen isotope composition from carbonates of Cerro Minado (n=21, mean=1.50, σ=0.02) are given in Table 1 and Figure 5.

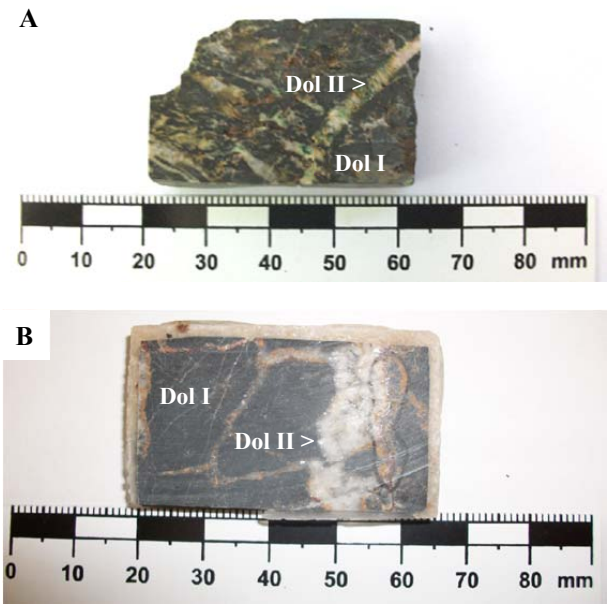

Figure 4. A) HO-25 sample with sulphide and saddle dolomite veins. B) HO-18 sample; the same as in A.

5 Discussion

$\delta^{13}C$ analyses from host rock reveal typical marine Triassic compositions. Furthermore, they display normal Triassic diagenetic oxygen isotopes values (Veizers and Hoefs 1976; Hoefs 2009).

Saddle dolomite samples have lighter $\delta^{13}C$ values than host rock although within the marine field. These data would suggest the buffering of the carbon by interaction with the carbonated host rock. On the other hand, this data would reject any influence of organic matter or organic carbon (-3 to -7‰; Spötl and Pitman 1998) in the epigenetic fluid. The $\delta^{18}O$ values are lower than those of the host rock suggesting infiltration and exchange with hydrothermal fluids (Hoefs 2009; Tritlla et al. 2001).

Saddle dolomite is an index mineral formed as a cement or replacement mineral into hydrothermal setting at relatively high temperatures (90 – 180ºC) and saline paleofluids related to deep burial diagenetic conditions. No relation exists between the oxygen isotopic composition of the saddle dolomite and the Triassic dolostone, it can be inferred that the saddle dolomite

Table 1. Carbon and oxygen isotope compositions from Cerro Minado carbonates. Dol I: Triassic dolostone; Dol II: saddle dolomite.

Sample	$\delta^{13}C$ (PDB)	$\delta^{18}O$ (SMOW)	Description
HO-10 a	0.89	22.48	Dol I
HO-10 b	1.52	23.76	Dol I
HO-10 c	1.19	23.02	Dol I
HO-12 a	1.39	20.70	Dol II
HO-12 b	1.63	20.56	Dol II
HO-12 c	2.16	25.09	Dol I
HO-13 a	1.44	21.25	Dol II
HO-13 b	2.25	25.46	Dol I
HO-14 a	1.84	24.72	Dol I
HO-18 a	1.32	19.46	Dol II
HO-18 b	1.20	19.55	Dol II
HO-18 c	2.13	25.15	Dol I
HO-20 a	1.22	21.03	Dol II
HO-20 b	1.02	21.04	Dol II
HO-22 a	0.82	18.09	Dol II
HO-22 b	1.61	21.54	Dol I
HO-23 a	1.46	19.28	Dol II
HO-23 b	1.82	20.81	Dol II
HO-23 c	2.32	25.80	Dol I
HO-25 a	1.12	21.51	Dol II
HO-25 b	1.17	22.18	Dol I

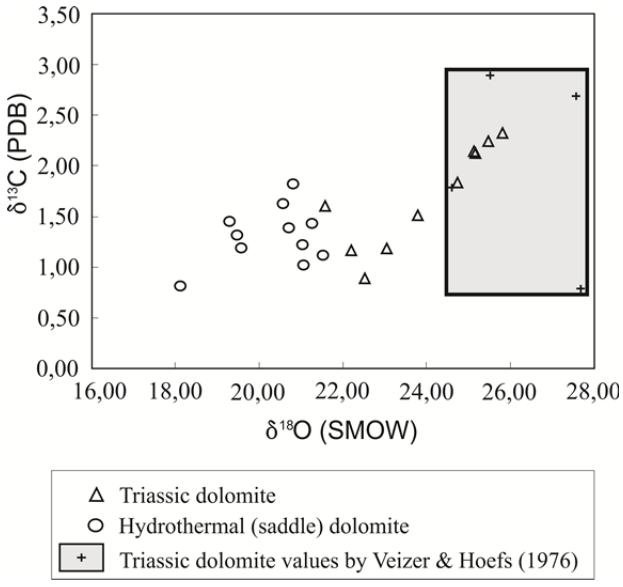

Figure 5. Plot of $\delta^{18}O$ vs. $\delta^{13}C$ values of Cerro Minado carbonates.

precipitation occurred over a similar temperature range from fluids with a similar oxygen isotopic composition (Spötl and Pitman 1998).

Because primary sulphides occur scattered within the saddle dolomite veins, we assume that both were formed in the same hydrothermal event. Hence, sulphur-bearing fluid was characterized by high temperatures and salinities linked to deep burial conditions.

Acknowledgements

This research was supported by SGR 444 project of the Generalitat de Catalunya.

References

Bertran–Oller O, Buireu–Cabello F, Febrer–Morlà M, Enrique–Gisbert P, Melgarejo JC (2012) Mineralogía del Depósito de Cuesta Alta, Cerro Minado, Huércal – Overa, Almería. Macla 16: 246–247.

Egeler CG, Simon OJ (1969) Orogenic evolution of the Betic Zone (Betic Cordilleras, Spain) with emphasis on the nappe structures. Geologie en Mijnbouw 48: 296–305.

Gröbner J, Fernández–Périz MA (2006) Los minerales de los yacimientos de Cu y Co de Molvizar y Cerro Minado en Andalucia. Mineral Up 1: 48–56.

Hoefs J (2009) Stable isotope Geochemistry. Springer Editions, 235 pp.

IGME (1980) Memoria explicativa y mapa geológico de España a escala 1:50.000. Hoja 996 (Huércal – Overa).

Spötl C, Pitman JK (1998) Saddle (baroque) dolomite in carbonates and sandstones: a reappraisal of a burial-diagenetic concept. Special Publication International Association of Sedimentology 26: 437–460.

Tritlla J, Cardellach E, Sharp ZD (2001) Origin of vein hydrothermal carbonates in Triassic limestone of the Espadán Ranges (Iberian Chain, E Spain). Chemical Geology 172: 291–305.

Veizer J, Hoefs J (1976) The nature of O^{18}/O^{16} and C^{13}/C^{12} secular trends in sedimentary carbonate rocks. Geochimica et Cosmochimica Acta 40: 1387–1395.

Vera JA (2004) Geología de España. SGE – IGME, 890 pp.

Viñals J, Favreau G, Eytier JR (2010) Bobkingite, capgaronnite, juanitaite, gerhardtite, reevesite and other rare minerals from Cerro Minado, Huércal – Overa (Almería). Mineral Up 2: 6–23.

The silver-polymetallic Mangazeyskoe deposit (Russia, Sakha-Yakutia): evidence for an involvement of magmatic and basinal fluids from fluid inclusions and stable isotopes (C, O, S)

Anikina E., Klubnikin G., Bortnikov N., Prokof'ev V, Gamyanin G.
IGEM RAS, 119017 Staromonetny 35, Moscow, (anikina@igem.ru)

Abstract. The Mangazeyskoe vein Ag-Pb-Zn deposit occurs in terrigenous rocks within the Verkhoyansk-Kolyma fold-thrust belt. Three mineralization types: gold-tungsten-bismuth (GTB), carbonate-sulfide (CS) and silver-polymetallic (SPM), comprise the ore bodies. An involvement of two compositionally and isotopically contrasting fluids: high-temperature low-salinity fluid with high $\delta^{18}O$ values and low-temperature high-salinity fluid with low $\delta^{18}O$ values, was found. A mixing of granite-derived fluid and components with external brines is assumed.

Keywords. Ag-Pb-Zn deposit, mineral associations, stable isotopes (C, O, S), fluid inclusions, mineral-forming conditions.

Introduction

Russian prospectors explored the Verkhoyansk region of Sakha-Yakutia for silver as early as the 1770-1780s. A comprehensive modern exploration efforts in the 1980s and 2010s revealed that the Verkhoyansk province contains significant silver reserves and became one of the largest silver-ore provinces in the world which contains more than 60,000t Ag (The P1+P2+P3 categories, estimation by Russia's Ministry of Natural Resources). Over the last decade, Prognoz, Kupol'noye, and Mangazeiskoye deposits were re-estimated as the world-class deposits. The indicated and inferred mineral resources at Mangazeyskoe deposit are of 6.2 Mt estimated by the Canadian Silver Bear Resources Inc. (2009).This Company estimated in 2012 that the silver resources in the Vertikalny zone and the Nizhny Endybal zone are of 30.5 Moz and at grade of 562 g/t and at 13.5 Moz at grade of 133 g/t, respectively.

These Ag-Pb-Zn deposits were considered in 60-70th of 20th century as distal zones of the intrusion-related tin mineral-forming systems. This study was carried out to prove or reject this hypothesis using data on fluid inclusions and stable isotope ratios in minerals.

1 Geological Setting

The Mangazeyskoe deposit is located in the Verkhoyansk-Kolyma fold-thrust belt. It is related to the granitoid magmatism of transverse belts (Anikina et al, 2009). The deposit occurs in the Carboniferous to Permian terrigenous rocks of the Verkhoyansk complex, which are intruded by the Endybal subvolcanic stocks and compositionally different dykes (Fig. 1). All ore zones are localized within the area of 17 km long and 4.5 km wide. The morphology of the ore zones are veins, veinlets, stockwork and the breccia zones.

Three types of mineralization such as gold-tungsten-bismuth (GTB), carbonate-sulfide (CS) and silver-polymetallic (SP) were found. They are spatially separated and confined to different structures: GTB occurs in exocontact of the Endybal stock, CS is located in faults of northwestern strike (300-350°), and SP occurs in faults with the NNW trending. They display different fabrics, mineral composition (Table 1, Fig. 2), and geochemical features.

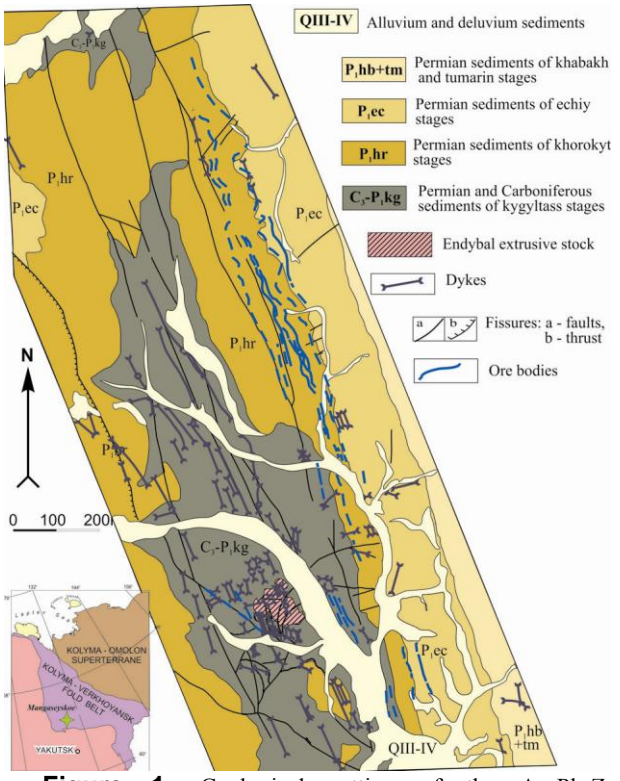

Figure 1. Geological setting of the Ag-Pb-Zn Mangazeyskoe deposit.

Table 1.

Ore types	*GTB (1)*	*CS (2)*	*SP (3)*
Texture	Massive, coarse-grained	Massive, coarse-grained, breccia-like	Fine-grained, banded, rhythmical-zoning, festoon, druse-like
Mineral composition	Quartz, arsenopyrite, pyrite, bismuthinite wolframite, molybdenite	Siderite, pyrrotite, pyrite, arsenopyrite, sphalerite, galena, tetrahedrite	Quartz, siderite, pyrite, arsenopyrite, galena, sphalerite, various sulfosalts

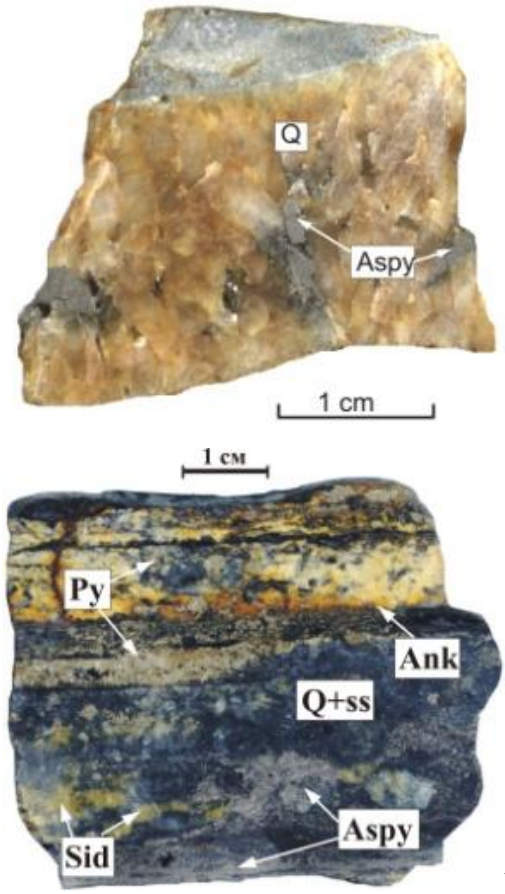

Figure 2. Ore fabrics: a – the vein of druse-like quartz (Q). Coarse-grained arsenopyrite (Aspy) fills intergrain spaces in quartz (a). b – banded fabrics due to alteration of siderite (Sid)-arsenopyrite (Aspy), quartz-sulfosalt (Q+Ss) with pyrite (Py) and ankerite (Ank)-pyrite (Py) zones.

2 Fluid inclusions

Primary, secondary and primary-secondary fluid inclusions (FI) of 25 to 2 microns in size were identified using well-known criteria (Roedder 1987). They are subdivided into three types based on phase composition at room temperature (Klubnikin et al 2011). They are: (1) H_2O-CO_2-liquid rich, (2) CO_2-vapor-rich, and (3) two-phase aqueous liquid-vapor fluid inclusions. Type 1 FI are usually syngenetic to those of type 2, as they are confined to the same growth zones of quartz. The same quartz contains secondary type 3 FI. Primary FI of type 3 are found in late quartz and sphalerite.

Type 1 FI are homogenized at 367 to 217°C (Fig. 3). Fluid salinity varies from 12.9 to 2.0 wt.% NaCl-equiv. Homogenization temperatures of type 2 FI are from 346 to 261°C. CO_2 in type 2 inclusions is homogenized at 27.2 to +29.0°C in liquid, and at 15.3 to +30.8°C in gas, i.e. CO_2 density varies from 0.67 to 0.16 g/cm^3. Type 3 FI in quartz are homogenized in liquid at temperatures from 336 to 126°C. Fluid salinity is estimated to range from 18.6 to 1.4 wt. % NaCl-equiv. Type 3 FI in sphalerite were homogenized at 222 to 179°C. Fluid salinity varies from 13.4 to 8.6 wt. % NaCl-equiv. Thus, the fluid inclusion study indicates that two compositionally contrasting fluids were involved in the ore formation: 1) the H_2O+CO_2-NaCl fluid that underwent immiscibility into liquid and vapour phases, and 2) the H_2O-NaCl fluid with varying salinity. It is of interest to note that the salinity of late fluid increases with decreasing temperature is (Fig. 3).

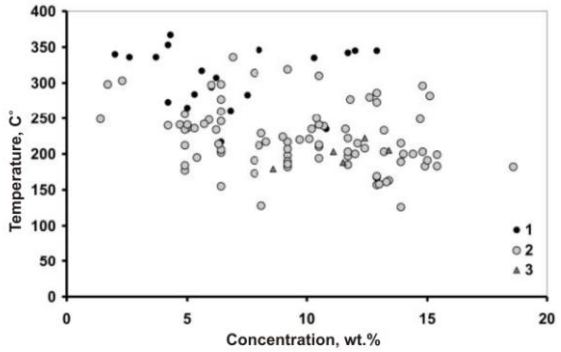

Figure 3. Temperature vs. Concentration diagram. 1 – Type 1, 2 – Type 3 in quartz and , 3 – Type 3 in sphalerite.

3 Stable isotopes

Isotope ratios of oxygen in quartz, sulfur in sulfides and carbon and oxygen in carbonates have been studied.

3.1 $\delta^{18}O$ of quartz

The $\delta^{18}O$ values measured for quartz vary from +14.8 to +21.8 ‰, in general. They are of +14.8 to +16.4 ‰ for quartz of type 1 mineralization, +16.3 to +18.5‰ for quartz of type 2, and +16.7 to +21.8 ‰ for quartz of type 3. the $\delta^{18}O_{H2O}$ values in fluids. Equations suggested by Zheng (1993) were used to calculate $\delta^{18}O_{H2O}$ values in fluids. It is assuming equilibrium between fluid and quartz. The $\delta^{18}O_{H2O}$ values of fluid that deposited quartz of the 1st type mineralization vary from +2.3 to +7.6 ‰ (T = 186-260°C), those of the second type of quartz is +8.8 ‰ (T = 290°C), and for quartz of the 3rd type range from +2.3 to +11.0 ‰ (T = 144-225°C). Variations found can be a result of temperature changes, fluid immiscibility and mixing of fluids with different oxygen isotopic composition.

3.2 $\delta^{34}S$ of sulfides

The $\delta^{34}S$ values of sulfides from all mineral zones range from -7.6 to +7.1 ‰ (Fig. 4). Those for individual minerals are -5.6 to +6.6 ‰ for arsenopyrite, -3.7 to +7.1 ‰ for pyrite, -7.6 to +2.8‰ for galena, -3.4 to +6.5 ‰ for sphalerite, and -3.3 ‰ to +6.3 ‰ for sulfosalts.

The $\delta^{34}S_{H2S}$ values of fluid are calculated using the data obtained, homogenisation temperatures and equations suggested by Li and Liu (2006). The $\delta^{34}S_{H2S}$ values of fluid that deposited pyrite of GTB is within 0±3.0‰ (T = 300°C). Sulfides from CS mineralization were formed at 320-350°C from fluid with $\delta^{34}S_{H2S}$ values ranging from -2.8 to +5.5 ‰. The $\delta^{34}S_{H2S}$ values in the fluid that deposited sulfides from SP mineralization at 186 to 320°C) vary from -2.5 to +6.3 ‰. Most of the $\delta^{34}S_{H2S}$ values lie within 0±2.0‰, inferring a contribution of magmatic sulfur. A shift of sulfur isotope ratios to a positive side is observed.

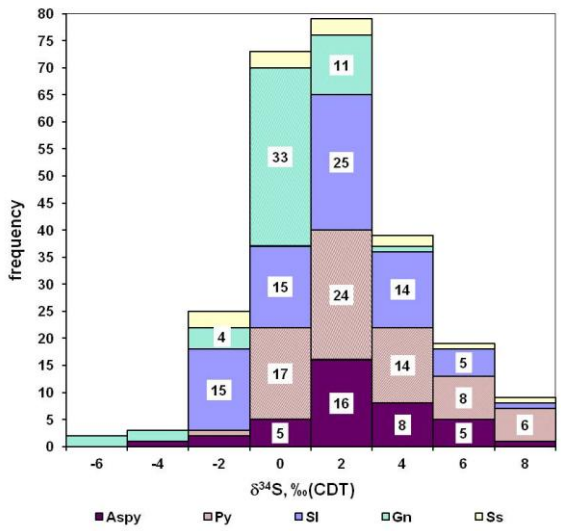

Figure 4. Sulfur isotope composition of sulfides. Aspy – arsenopyrite, Py – pyrite, Sl – sphalerite, Gn – galena, Ss – sulfosalts.

3.3 $\delta^{13}C$ and $\delta^{18}O$ of carbonates

The $\delta^{13}C$ values of carbonates range from -9.1 to -2.9‰, in general. Those for siderite-1, siderite-2, ankerite, and calcite are -7.9 to -6.9 ‰, -9.1 to -6.7 ‰; -5.4 to - 3,1 ‰;and -4.2 to -2.9 ‰, respectively.

$\delta^{18}O$ values of carbonates range from +13.5 to +18.3. Those for siderite-1, siderite-2, ankerite, and calcite are in the range from +16.2 to +17.9 ‰, +13.7 to +16.1 ‰, +15.0 to +18,3 ‰, and from +13.5 to +16.8 ‰ (63% in the range of +15 to +17 ‰), respectively. Fig. 5. shows that values are distinctly subdivided into two groups. Carbonates of two early generations (siderite-1 and siderite-2) form the first group, in which heavier $\delta^{13}C$ values are accompanied by heavier $\delta^{18}O$ values. Carbonates of late generations, ankerite and calcite fall in the second field, in which samples with different $\delta^{18}O$ values display more narrow $\delta^{13}C$ values. Such subdivision can be related to the behavior of carbon and oxygen isotopes in the process of fractionation in relation to various minerals. The temporal evolution of isotopic ratio can be other probable reason of this phenomenon.

4 Discussion

The main finding is that fluids different in the composition were involved in the formation of the deposit. They are the liquid H_2O+CO_2+NaCl fluid, the low dense CO_2-rich vapor fluid and the aqueous fluid of different salinity. The first two were formed due to immiscibility of the bicarbonate - aqueous fluid at a pressure and/or temperature drop. Variations in salinity, temperatures, and oxygen isotopic compositions indicate that at least two contrasting fluids such as the high-temperature low-salinity fluid with high $\delta^{18}O$ values and the low-temperature high-salinity fluid with low $\delta^{18}O$ values was infiltrated the system. The first fluid is assumed to be magmatic in origin, while the second one was derived due to the evolution of the meteoric or buried waters ($\delta^{18}O$ = 0 ‰). The enrichment in a heavier isotope may have resulted in fluid-rock interaction.

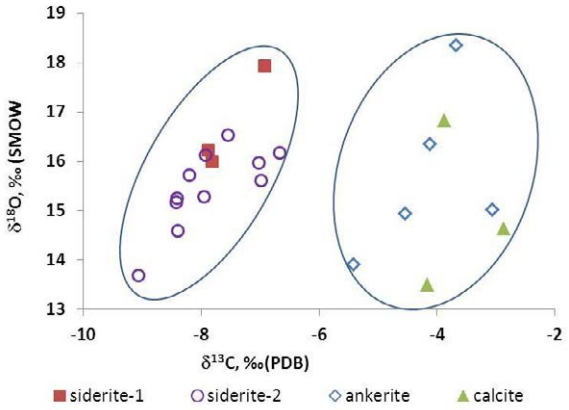

Figure 5. Ratio of carbon and oxygen isotopes in carbonates.

Data on the sulfur isotope composition suggest that sulfur derived from granitic magmas or mantle ($\delta^{34}S$ = 0 ± 4 ‰) was a major contributor during the whole mineral-forming process. Positive shift can be explained by leaching of sulfur from host terrigenous rocks. Negative shift can reflect fractionation during sequential deposition of minerals. Thus, there is an evidence for involvement of sulfur derived from granite magma and leached from marine sulfate minerals in underlying terrigenous rocks (Anikina et al 2010).

Negative $\delta^{13}C$ values and their wide range suggest that CO_2, magmatic or mantle in origin ($\delta^{13}C_{CO2} \approx -5 \pm 2$‰) (Ohmoto and Rye 1979), participated in the mineral-formation. A positive slope in O-C space can be caused by decrease of formation temperatures (Zheng 1993) or mixing of ascending brine with formation water (Schwinn et al. 2006).

The gold-tungsten-bismuth and carbonate-sulfide ores were assumed to have been formed from the high temperature moderately-low salinity fluid of magmatic origin, enriched with magmatic hydrogen sulfide, heavy oxygen isotope and light carbon isotope. This fluid could be mixed with a fluid derived of heated meteoric water in the convection cell, which resulted from the intrusion of the Endybal subvolcanic stock.

The highly concentrated low temperature fluid could be formed at participation of buried waters in the mineral-forming process. Its formation could be related to the oblique collision of the Kolyma-Omolon superterrane with the Siberian continent, which resulted in the intrusion of reverse belts of granites and the closed sea water basins due to the mountain growth. The evolution of sea water during evaporation resulted in their salinity increase. Subsequently, the basin water could also be involved in the convective cell. These processes could have led to the origin of the low temperature high salinity ore-forming fluid.

An example of the origin of such fluids can be Irish lead-zinc deposits in sedimentary strata or the Cornwall deposit, England. Fluids from these deposits were formed of sea water, which underwent the evaporitisation to varying degrees and migrated into the underlying sedimentary rocks (Muchez et al. 2005;

Wilkinson 2009; Gleeson et al. 2001).

Acknowledgements

This study was supported by the Russian Foundation for Basic Research (project no. 11-05-12017_ofi-m) and the Department of Earth Sciences, Russian Academy of Sciences (program DES-2 “Mineral Deposits: from Genetic Model to their Prediction").

References

Anikina EYu, Bortnikov NS, Gamyanin GN (2009) Mineral associations and Sulphur Isotope Cjmposition in the Mangazeyskoe Ag-Pb-Zn Deposite, Sakha, Russia. Proceedings of the 10th Biennial SGA Meeting of the Society for Geology Applied to Mineral Deposits, Townsville (Australia). 1: 198-200

Anikina EYu, Gamyanin GN, Bortnikov NS (2010) Sulfur Isotopic Composition of Sulfides at the Mangazeya Silver Deposit, Eastern Sakha-Yakutia, Russia Geology of Ore Deposits 52: 479–495.

Gleeson SA, Wilkinson JJ, Stuart FM, Banks DA (2001) The origin and evolution of base metal mineralising brines and hydrothermal fluids,South Cornwall, UK. Geochim. et Cosmochim. Acta 65: 2067–2079

Klubnikin GK, Prokof’ev VY, Anikina EY, Bortnikov NS (2011) Contrast fluids in the mineral-forming system of the Mangaseiskoe silver deposit (Republic Sakha (Yakutia). Dokl. Earth Sciences 438: 779-781

Li, Li YB, Liu JM (2006) Calculation of sulfur isotope fractionation in sulphides. Geochem. et Cosmochem. Acta 70: 1789 – 1795

Muchez P, Heijlen W, Banks D, Blundell D, Boni M, Grandia F (2005) Extensional tectonics and the timing and formation of basin-hosted deposits in Europe. Ore Geol. Rev. 241–267

Ohmoto H, Rye RO (1979) Isotope of sulfur and carbon. In Barnes, H. L. Ed. Geochemestry of Hydrothermal deposits 509-567.

Roedder E (1984) Fluid inclusions. Washington: Mineral Soc. of America

Schwinn, G., Wagner, T., Baatartsogt, B., & Markl, G. (2006) Quantification of mixing processes in ore-forming hydrothermal systems by combination of stable isotope and fluid inclusion analyses. Geoch. et Cosmochim. Acta 770: 965-982.

Wilkinson JJ (2009) A Review of Fluid Inclusion Constraints on Mineralization in the Irish Ore Field and Implications for the Genesis of Sediment-Hosted Zn-Pb Deposits. Econ. Geol. 105: 417–442

Zheng Y-F (1993) Calculation of oxygen isotope fractionation in anhydrous silicate minerals. Geochem et Cosmochem. Acta 57:1079-1091

Lead isotopes signatures of the MVT lead-zinc (±F) deposits across central-north Tunisia: evidence for the heterogeneity in uranium component of the underlying source rocks

Salah Bouhlel, Héchmi Garnit, Jalloul Béjaoui
University la Manouba Laboratoire de Biotechnologie et Valorisation des BioGéoressources (LR11 ES31); University Tunis el Manar Faculty of Sciences of Tunis Tunisia

Sheldon Skaggs
Technology Bronx Community College, CUNY 2155 University Avenue Bronx, New York 10453 USA

Abstract. About one hundred lead isotopic analyses of galena rich ores are presented to define the lead isotope signature of the Pb-Zn carbonate-hosted deposits in the north and central Tunisian region. The Pb isotopic compositions for galena in all the deposits are relatively homogeneous in each deposit. All the deposits revealed a relatively narrow range of isotopic compositions (206Pb/204Pb = 18.633 to 19.012; 207Pb/204Pb = 15.636 to 15.796; 208Pb/204Pb = 38.727 to 39.181). These compositions are typical of a crustal source for the ore lead (upper to deep crust). Lead isotope ratios of the Graben Zone-, the Triassic Salt Domes Zone- and the Nappe Zone districts indicate the dominance of non-radiogenic crustal sources. The Pb ratios of the North-South Axis district lie above the upper crust curve, indicating a significant component of a very radiogenic crustal source.

Keywords
Lead isotopes, MVT Pb-Zn deposits, Tunisia

1 Introduction

Lead isotope compositions of MVT ores have been studied by many geologists especially and a basement source for Pb is indicated for many MVT districts or deposits (Leach et al. 2005). In Tunisia numerous Miocene MVT lead-zinc deposits and occurrences are present in the foreland Atlas belt. Despite the long mining history, this proposed metallogenic model is still poorly documented. In this paper we use lead isotopes of 113 galena samples from 30 major Pb-Zn deposits of Tunisia to determine the major lead source(s) and to check possible variations of the source rock compositions from district to district, or within the same district.

2 Geological setting and ore distribution

Tunisian Pb-Zn ore deposits are located in the eastern part of the North African Atlas MVT province, which contains in its western part the Touissit-Bediane-El Abed district (Morocco-Algeria border). The Atlas Pb-Zn province belong to the Tethyan Pb-Zn belt which encompasses several large and globally significant Pb-Zn provinces running from the Mediterranean regions to China, including the Basque-Cantabrian basin (Réocin, Spain), Cevennes (France), Alpine district, Silesia-Cracow (Poland), Mehdiabad (Iran), Jiding (China) (Leach et al. 2005).

Tunisian Pb-Zn (±Ba, ±Sr, ±F) ores are hosted in Jurassic-Cretaceous platform carbonate rocks deposited on the southern passive margin of Tethys, overlying a thick Triassic evaporite sequence and Permian sediments, that are underlain by orogenic belts comprised of Paleozoic supracrustal rocks. Triassic evaporites were mobilized as fault-controlled diapirs by successive extensional and compressional loading events mainly in Albian and Eocene periods. Additional significant mineralization occurs in syn- to post collisional Miocene sediments, including calcareous sandstone, lacustrine carbonates, deposited in pull-apart basins within the thrust belt, as well as in Miocene volcanic (Rouvier et al 1985; Decrée 2008).

In term of tectonic settings and host rocks lithologies, the Tunisian Pb-Zn province is divided into four districts (Fig. 2): The Nappe Zone (NZ), the Triassic Salt Domes Zone (TSDZ)-, the Graben Zone (GZ)- and the North-South Axis (NOSA) districts (Fig. 1).

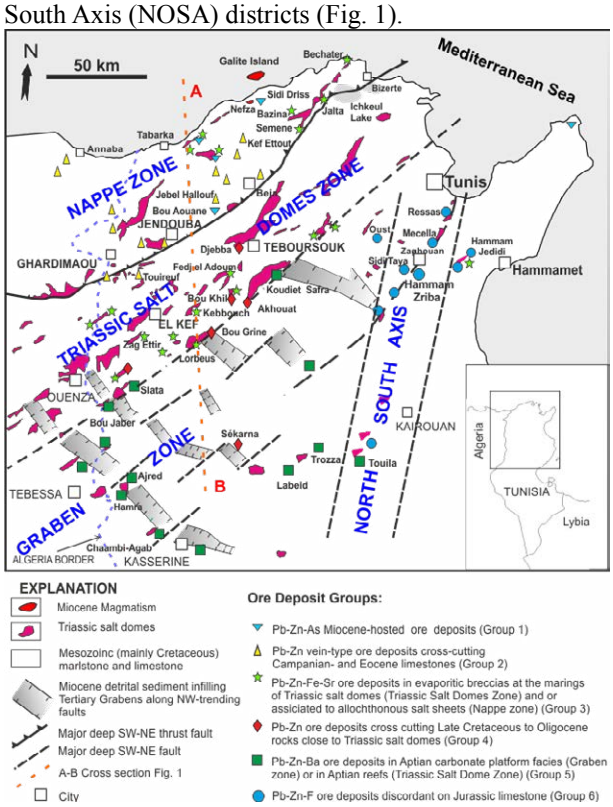

Figure 1: Map of lead-zinc-, fluorite- deposits, and structural zones of central-north Tunisia

The NZ district contains three ore deposit types : Type 1: Cap rock-type Pb-Zn-Sr hosted in Triassic breccias along thrust decollement during the Miocene orogeny (Bechater, Aïn Allegua, Besina, Semene); Type 2: Pb-Zn vein-type mineralization along faults and karstic cavites, cross-cutting Late Campanian limestone (e.g. Touireuf, Jebel Hallouf, Khanguet Kef Ettout); Type 3: Miocene stratabound Pb-Zn-As-Sb deposits, hosted in terrestrial and lacustrine sediments Late Miocene in age (Sidi Driss and Sidi Bou Aouan).

The TSDZ district encompasses three ore deposit types: *Type 1*: Cap rock-type Pb-Zn-Sr mineralization hosted in Triassic evaporite breccias lining the cortical zone of Triassic salt diapirs (e.g. Fedj el Adoum, Kebbouch, Bou Khil, Doggra, Zag Ettir); *Type 2*: Vein-type Pb-Zn concentrations cross-cutting several carbonate units ranging in age from late Albian to Eocene that form the hanging wall of Triassic salt diapirs (Koudiat Safra, El Akhouat, Bou Khil, Bou Grine, Doggra and Zag Ettir, Bou Grine, El Akhouat, Touireuf); *Type 3*: Pb-Zn ± (Ba-F) orebodies infilling hydrothermal karst cavities in Aptian reef limestone, perched on Triassic salts diapirs (Bou Jaber, Slata).

The GZ district contains numerous stratabound Pb-Zn-Ba deposits hosted in Aptian platform carbonate rocks (Ajred, Hamra, Troza, Labeid, Touila), and rarely in Cenomanian limestone or in Eocene phosphate rocks (Sekarna) (Garnit et al 2012).

The NOSA district is characterized by fluorite-dominant ore deposits ±(Ba-Sr-Pb-Zn). Mineralization forms stratabound ore bodies (replacement and open-space filling), and also forms vein-type orebodies. These ores occur in the upper parts of two Jurassic platform carbonate units: The Liassic limestone hosts the El Kohol and Oust deposits and the Tithonian limestone hosts of Hammam Zriba, Sidi Taya, Mecella and Ressas deposits.

In Tunisia, the major styles of mineralization are replacement of limestone or dolostone and open-space fillings, typical of major world MVT deposits. Ore-forming brines have salinities in the range of 10 to 20 Wt% NaCl eq. salinities and temperature in the range of 100 to 200°C. Hydrocarbons occur as oil fluid inclusions and oil seeps are abundant in most the ore-deposits. Tectonic controls and Triassic salt diapirism clearly demonstrated that the major lead-zinc mineralizing event occurred in Miocene (Sainfeld 1956; Sheppard et al 1996; Bouhlel 2005). For the genesis of the ore-deposits an orogenically-driven circulation of brines as a consequence of the tectonic collisions of the European and African plates was proposed (Fig. 2).

3 Sampling and methodology

Some 113 galena samples were collected for this study which were chosen to represent the known 30 Pb-Zn deposits. In addition, 4 to 16 samples were collected from high-grade deposits and 1 to 2 samples were collected to represent low-grade Pb-Zn deposits. Pure galena crystals fragments were prepared by careful hand picking under a binocular microscope and rinsing with doubly distilled water. We analysed 105 galena samples by Thermal Ionization Mass Spectrometry (TIMS) at the Geochronology and Isotope Geochemistry Laboratory, University of North Carolina, Chapel Hill, following the analytical procedure was described in Skaggs et al. (2012). 8 galena samples from the Fedj el Adoum mine were analyzed by Wayne Premo at the USGS (Denver).

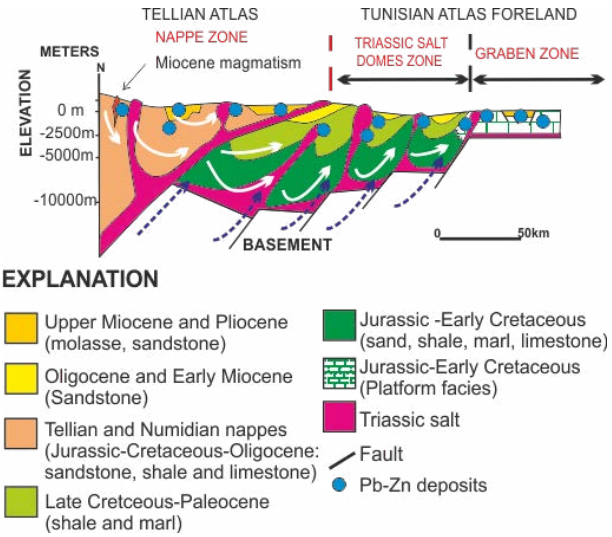

Figure 2. Cartoon showing structural units of Central North Tunisia, the distribution of ore-deposits, and potential fluid-flow from the Tellian Atlas folded belt to the Tunisia Atlasic foreland, in Late Miocene time. Thrusting, regional NE-SW and NW-SE deep faults, salt diapirs and unconformities, acted together as pathways for fluids flow (Bouhlel 2005).

4 Results and discussion

The mean of lead isotope compositions for each investigated deposit are shown in Table 1. All the original data of the 113 measured galena samples are plotted on figure 3. The ranges of isotopic compositions of the investigated deposits are:

$^{206}Pb/^{204}Pb$ = 18.633 to 19.012 (σ = 0.083)

$^{207}Pb/^{204}Pb$ = 15.636 to 15.796 (σ = 0.026)

$^{208}Pb/^{204}Pb$ = 38.727 to 39.181 (σ = 0.085).

These lead isotope compositions form a slightly elliptic field in both $^{207}Pb/^{204}Pb$ versus $^{206}Pb/^{204}Pb$ and $^{208}Pb/^{204}Pb$ versus $^{206}Pb/^{204}Pb$ plots. The majority of the analyzed galena samples plot in a field about the upper crust evolution curve in the orogenic plot (Fig. 3a) and above the orogen curve, in the orogenic plot (Fig. 3b), indicating the dominance of continental crustal sources. In the orogenic plot (Fig.3a) some of the galena samples plot clearly above the upper crust curve (i.e. high μ), indicating a large component of a very radiogenic source. Some others plot below the upper crust curve (i.e. low μ), indicating a large component of non-radiogenic sources. The Pb-Zn isotopic lead field overlaps that of the Miocene felsic rocks of the Galite Island and the Nefza region. These rocks, related to Miocene anatexis, were derived from a metalumounous basement (Belayouni et al. 2010). This feature may indicates that the ore lead and the felsic rocks were orginally from similar source rocks, and probably extracted at the same period.

Table 1 : Means of lead isotopes ratios of galena for 30 Pb-Zn deposits of Tunisia .

Deposits	$^{206}Pb/^{204}Pb$	$^{207}Pb/^{204}Pb$	$^{208}Pb/^{204}Pb$	Nb
Hamra	18.633-18.704	15.636-15.725	38.727-39.027	4
Ajred	18.662-18.717	15.644-15.667	38.751-38.813	6
Trozza	18.677-18.744	15.650-15.705	38.768-38.870	3
Touila	18.706	15.694	38.734	1
Sékarna	18.742-18.835	15.649-15.705	38.798-38.964	8
Fej El Adoum	18.717-18.804	15.639-15.706	38.796-38.878	16
Kebbouch	18.721-18.806	15.656-15.703	38.767-38.940	6
Doggra	18.707-18.731	15.660-15.665	38.755-38.812	2
Boukhil	18.774	15.670	38.829	1
Bougrine	18.710-18.770	15.660-15.702	38.800-38.970	7
K. Safra	18.828	15.690	38.928	1
Zag Ettir	18.807-18.825	15.667-15.706	38.806-38.964	2
El Akhouat	18.710-18.728	15.644-15.657	38.736-38.765	2
Bou Jaber	18.733-18.752	15.663-15.664	38.805-38.816	2
Slata	18.731-18.749	15.668-15.699	38.748-38.868	5
Sidi Driss	18.771-18.820	15.657-15.674	38.816-38.866	5
Bouaouane	18.805-18835	15.663-15.689	38.864-38.932	5
J. Hallouf	19.000-19 .002	15.681-15.681	39.900-38.910	2
Touiref	18.832-18.853	15.655-15.708	38.819-38.968	3
A. Allegua	18.704-18.874	15.645-15.665	38.887-38.904	2
Kef Ettout	18.765-18.804	15.659-15.680	38.840-38.885	3
Bazina	18.801	15.686	38.899	1
Semène	18.790	15.663	38.826	1
Bechater	18.701	15.681	38.774	1
Jalta	18.825-18.851	15.623-15.681	38.645-38.950	5
H. Zriba	18.834-18.870	15.667-15.734	38.691-39.013	6
Sidi Taya	18.959-19.003	15.695-15.767	38.846-39.099	4
Mecella	18.882-18.910	15.672-15.712	38.756-38.918	6
Ressas	18.919-19.012	15.689-15.796	38.826-39.181	4
El Kohol	18.986-18.991	15.670.15.675	38.831-38.843	2
Oust	18.953	15.679	38.930	1

The major galena samples give $^{207}Pb/^{206}Pb$ model ages from the plumbotectonic model of Zartman and Doe (1981), between 400 and 250 Ma (Fig. 3a), older than the Miocene proposed age of the ore metallognic event (Sainfeld 1956; Bouhlel 2005). This retardation which is was also observed for the Miocene felsic rocks (Decrée 2008) may be due to the contribution of a less radiogenic material with low uranium content, such as the lower crust. On the scale of the Atlas Pb-Zn province, the lead isotopes of the Tunisia Pb-Zn deposits are more radiogenic then those measured in the western part of the province (Touissit-Bediane-El Abed). Given the similar Miocene age of the mineralization in the two parts of the Atlas province, the discrimination of lead ratios between the two sub-provinces may be related to the fact that the age of the recycled sources rocks are become younger from west to east. However, the Reocin Aptian-hosted MVT district plots in the Tunisian Pb isotope field. This provides some similarity between these two MVT districts, located to either side of the passive margins of Tethys. Compared to Pb-Pb plots in Appendix 14D in Leach et al (2005), Tunisian data show much more spread, and relatively radiogenic characters, than most of the Mesozoic-Cenozoic European platform MVT ores.

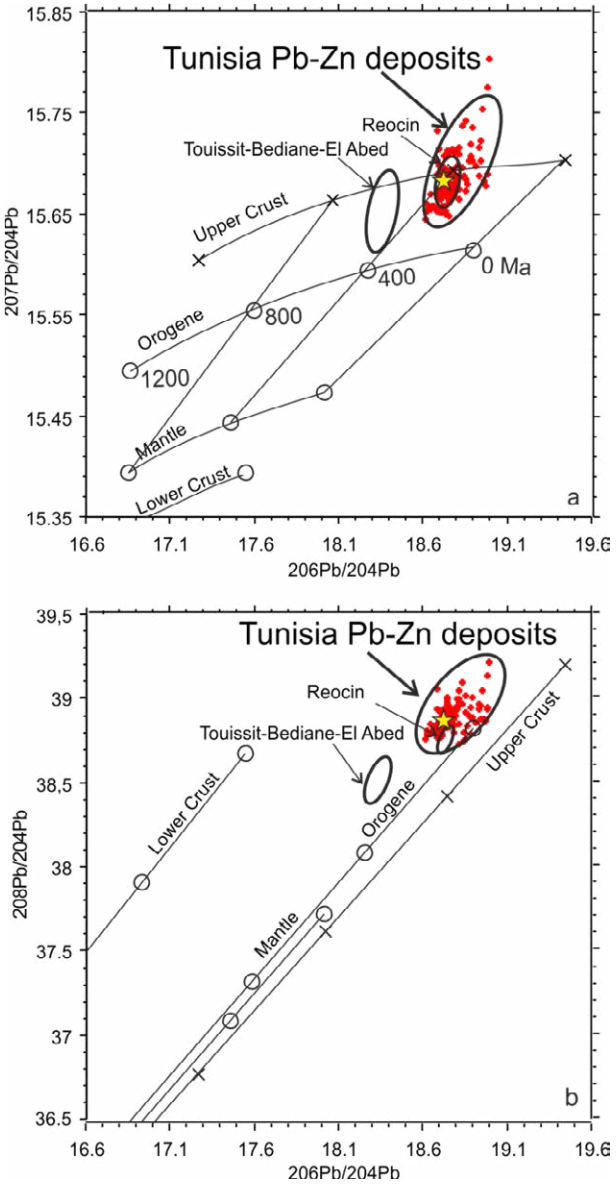

Figure 3. Plots of lead isotope compositions for 113 galenas collected in 30 Tunisian Zn-Pb deposits. Star is the lead isotopes plot of the Tunisian Miocene felsic rockss (Juteau et al 1975; Decrée 2008), Also are plotted lead for Reocin district (Spain)- and Touissit-Bediane-El Abed fields (Leach et al. 2005).The upper crust, lower crust, orogen, mantle evolution curves are from Zartman and Doe (1981)

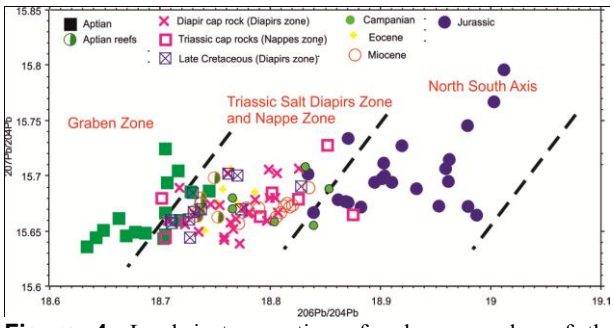

Figure 4. Lead isotope ratios of galena samples of the Tunisian Pb-Zn deposits reported in a $^{206}Pb/^{204}Pb$ versus $^{207}Pb/^{204}Pb$ diagram, highlighting the $^{206}Pb/^{204}Pb$ and $^{207}Pb/^{204}Pb$ variations according to the structural settings and hostrock ages.

On a regional scale, the Pb-Pb plot of the analyzed

galena samples provides evidence for three well-defined lead isotopes groups (Fig. 4):

Group I (16 galena samples):

$^{206}Pb/^{204}Pb$: 18.633–18.744 (mean = 18.690; σ = 0.032)
$^{207}Pb/^{204}Pb$: 15.636–15.725 (mean = 15.666; σ = 0.026)
$^{208}Pb/^{204}Pb$: 38.727–39.027 (mean = 38.802; σ = 0.076)

Group I shows the less radiogenic $^{206}Pb/^{208}Pb$ compositions of the investigated deposits. Most of the deposits of this group are located in the GZ district, and where most of the ores are hosted in the Aptian platform carbonate rocks. The relatively non-radiogenic character in the lead compositions observed in the Group I may be explained by the leaching of low radiogenic source rocks.

Group II (23 galena samples):

$^{206}Pb/^{204}Pb$: 18.834–19.012 (mean = 18.921; σ = 0.053)
$^{207}Pb/^{204}Pb$: 15.667–15.796 (mean = 15.703; σ = 0.033)
$^{208}Pb/^{204}Pb$: 38.691–39.181 (mean = 38.883; σ = 0.122)

Group II is characterized by the high $^{206}Pb/^{208}Pb$ values in the region but also in the entire Atlas Pb-Zn province. All the deposits are hosted in the Jurassic limestone and are located in the NSA district. The radiogenic signature of this Group may be explained by leaching of uranium rich rocks (red beds) or uranium-rich igneous rocks.

Group III (74 galena samples):

$^{206}Pb/^{204}Pb$: 18.701–18.874 (mean = 18.772; σ = 0.040)
$^{207}Pb/^{204}Pb$: 15.639–15.729 (mean = 15.673; σ = 0.018)
$^{208}Pb/^{204}Pb$: 38.736–39.061 (mean = 38.860; σ = 0.063)

This Group is characterized by intermediate ^{206}Pb and ^{207}Pb values that lie between Group I and Group II. However, this Group includes all the Mesozoic-hosted deposits occurring in the DZ- and NZ districts and also Miocene deposits hosted in post collision Miocene basins. Despite different ages of host rocks (Triassic, Aptian, Albian, Turonian, Campanian, Eocene, Oligocene, Miocene), and various styles of mineralization (stratabound, veins, hydrothermal karts, breccias matrix), the homogeneity in the lead isotopes ratios can be interpreted as either reflecting a homogeneous primary source of Pb isotopes, or Pb isotopes reached homogeneity by interaction between other rocks and ore fluids, which had travelled a long way during ascent.

From district to district, differences in the lead isotope ratios of the source rocks can be compared to differences in the district mineralogy. The Graben Zone is Ba rich, with less zinc; the North-South axis is Fl-Ba, with less Zn and Pb; the Triassic Salt Domes- and Nappe Zones are Zn-Pb-Sr rich with less or no Ba. This suggests that the fluids and therefore the leached source rocks were very different from district to district.

5 Conclusion

The lead isotope data of 113 galena samples from 30 Pb-Zn deposits that form, the Tunisian Atlas MVT province provide interesting insights regarding metal source (s), metallogenic processes and exploration. The lead isotopes ratios indicate crustal sources (upper to deep crust) for all the investigated Tunisian MVT deposits. The lead isotopic discriminations observed from district to district may be explained by differences in the uranium contents in the local underlying crustal rocks and/or in the deep seated recycled materials of these crustal rocks since the local host rocks do not contribute to the lead isotope compositions. Regarding the local basin scale, the Pb isotopic variations appear to be important from a genetic perspective as well as to exploration. In Tunisia, the overall crustal source for the ore lead suggests similarity with the majority of the world MVT districts and deposits, although the radiogenic character of the NOSA deposits indicates a large uranium component is best compared to the radiogenic signatures of the US Mid-continent and the Canning basin Australia MVT groups. From an economic viewpoint, the database of Pb isotopes presented here provides information on possible application of Pb isotopes to select favourable area for new exploration activities.

Acknowledgements

Support of this study by Fulbright Scholar Grant to S. Bouhlel is gratefully acknowledged. Special thanks to David Leach for enthusiastic support.

References

Belayouni H, Brunelli D, Clocchiatti R, Di Staso A, El Amrani E, Guerrera F, Kassaa S, Laridhi Ouazaa N, Martíng MM, Serrano F, Tramontana M (2010) La Galite Archipelago (Tunisia, North Africa): Stratigraphic and petrographic revision and insights for geodynamic evolution of the Maghrebian Chain: Journal of African Earth Sci. 56 15–28

Bouhlel S (2005) - Carbonate-hosted Mississippi Valley-type Pb-Zn deposits in Tunisia (Eastern Atlasic belts). Proceedings of the 8th Biennial SGA Meeting, Mineral Deposit Research, Meeting the Global Challenge China vol. 3 :19-22.

Decrée S (2008) Caractérisation géochimique et isotopique dans un système d'altération complexe du protolithe magmatique à la minéralisation fer-plomb-zinc : le cas de la mine de Sidi Driss. PhD thesis University Libre de Bruxelle pp 250.

Garnit H, Bouhlel S, Barca D, Craig AJ, Chtara C (2012) Phosphorite-hosted zinc and lead mineralization in the Sekarna deposit (Central Tunisia) Miner Deposita 47:546–562

Juteau M, Michard A, Albared F (1986) The Pb-Sr-Nd isotope geochemistry of some recent circum-Mediterranean granites. Contr Miner Petro 92:331–340

Leach DL, Sangster DF, Keller KD, Large RR, Graven G, Allen CR, Gutzmer J, Walters S (2005) Sediment-Hosted Lead-Zinc Deposits: A Global Perspective. Econ Geol 100th anniv vol: 561-607

Rouvier R, Perthuisot V, Mansouri A (1985) Pb-Zn Deposits and salt bearing diapirs in Southern Europe and North Africa. Econ Geol 80:666-687.

Sainfeld P. (1956) The lead-zinc-bearing deposits of Tunisia. Econ Geol 51:150-177

Sheppard SMF, Charef K, Bouhlel S (1996) Diapirs and Pb-Zn Mineralization: A general model based on Tunisian (N. Africa) and Gulf Coast (U.S.A.) Deposits. In: Carboanate-Hosted Lead Zinc Deposits, D.F. Sangster (Ed), Society of Economic Geologist, Special Publication n°4 : 230-243

Skaggs S, Norman N, Garrison E, Coleman D, Bouhlel S. (2012) Local mining or lead importation in the Roman province of Africa Proconsularis? Lead isotope analysis of curse tablets from Roman Carthage, Tunisia, Journal of Archaeological Science, vol 39 Issue 4 : 970-983.

Zartman RE and Doe BR (1981) Plumobotectonics – The model Tectonophysics, 75: 135-162

How did it get there? Searching for "the feeder" at the Navan Zn+Pb deposit, Ireland

Brett Davidheiser-Kroll, Adrian Boyce
Scottish Universities Environmental Research Centre, Rankine Avenue, East Kilbride, Glasgow G75 0QF, Scotland

John Ashton, Rob Blakeman, James Geraghty
Boliden Tara Mines Limited, Ireland

Abstract. Metal zoning patterns at the Navan ore body yield insight into its emplacement. Metal zoning in base metal mines has been shown to indicate feeder areas as well as fluid flow directions. By examining drill hole composite data, low Zn/Pb areas and zonations are identified. These areas show varying patterns across the mine. The north-east of the main mine has several concentrated vertical feeders. The south-west to central mine shows a large degree of horizontal flow with diffuse feeders. The south-west extension (SWEX) shows many small, scattered feeder areas. The distinct feeder patterns in different areas of the mine can be correlated with structural, textural, and stratigraphic data to infer timing and causes of ore genesis. The south-west to central main mine may have been created early in the extensional history by a slow, sub-horizontally-mobile fluid. The later un-roofing event caused by further extension is a likely culprit for the majority of the vertical trends seen within the SWEX and north-east of the main mine. Regardless of emplacement mechanism, this work shows for the first time that the SWEX has markedly different Pb-Zn zoning patterns than the main mine.

Keywords. Pb-Zn, Navan, Feeders, Ireland

1 Introduction

The Navan ore body is a giant stratabound sulfide deposit, containing >105 Mt @ 8% Zn and 2% Pb (mined+remaining resources), hosted by Lower Carboniferous limestone in the Irish Midlands (Ashton et al., in press). Navan is one of the Irish-type base-metal deposits that are noted for their complex epigenetic-replacive mineralisation styles as well as features indicative of syndiagenetic and exhalative processes (Anderson et al., 1998; Wilkinson et al,. 2003).

The timing of ore deposit formation remains controversial. Some workers favour a late, post-Arundian origin for Navan and other Irish-type deposits (e.g. Hitzman and Beaty 1996; Peace and Wallace 2000; Symons et al., 2003; Reed and Wallace 2004). A more widely held view is that onset of mineralization coincided with crustal extension and deep faulting (Tournaisian), and before the formation of a distinct large-scale erosion surface in the Chadian with mineralization continuing into the Arundian (Wilkinson et al., 2003; Leach et al., 2005; Ashton et al., in press).

There is little debate, however, that the metals were derived from a deep convecting cell of seawater-derived brines that penetrated and leached the Lower Palaeozoic basement (e.g. Everett et al., 2003). These metal-rich fluids (Fluid 1) precipitated sulfide proximal to feeder zones and can be distinguished by heavy $\delta^{34}S$ values (Anderson et al., 1998; Blakeman et al., 2002). The majority of sulphide at Navan was created by mixing Fluid 1 with a cooler seawater-derived brine containing isotopically light bacteriogenic sulfide (Fluid 2) (Anderson et al., 1998; Fallick et al., 2001).

In contrast to other Irish-type deposits (e.g. Silvermines, Taylor, 1984), to date at Navan no primary feeder zone/s have been recognised. However it is known that metal-rich fluids circulated within late Courceyan/Chadian fault arrays of varying magnitudes (Blakeman et al., 2002; Ashton et al., in press). Locating the principal feeder zone, and determining its characteristics, has obvious economic implications.

2 Geology and Structure

The stratigraphic section at Navan is dominated by a deepening marine carbonate transgression overlying an alluvial conglomerate laid unconformably on Lower Palaeozoic basement. The lower part of the sequence contains the ore-bearing Navan and 'ABL' Groups; these sediments comprise ~ 500 m of variable shallow-water limestone, micrites and minor shales, which are locally extensively dolomitised (Anderson et al., 1998; Braithwaite and Rizzi, 1997).

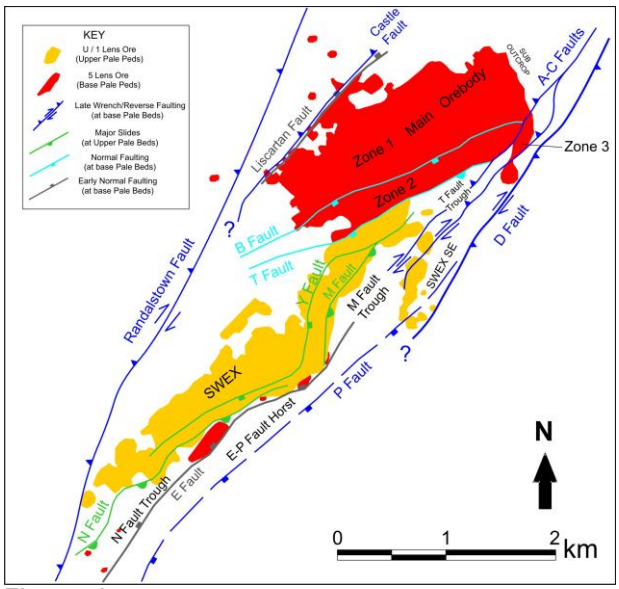

Figure 1. Simplified plan view of the Navan ore body showing the geometry of the deposit and principal structures.

This sequence was truncated to varying degrees by a number of submarine slides and an erosion surface. These slide blocks infilled a series of troughs associated with slide faults along the south-east side of the ore body (e.g. N Fault Trough, see Figure 1). This trough fill is then cut by a submarine erosion surface that is present across the ore body and incises deeper towards the

southeast. Above this surface across the mine there are polymict debris flows termed the Boulder Conglomerate. The Boulder Conglomerate marks the transition to the deep marine Upper Dark Limestone (UDL), which includes calc-turbidites and shales. The UDL is the youngest unit in the area.

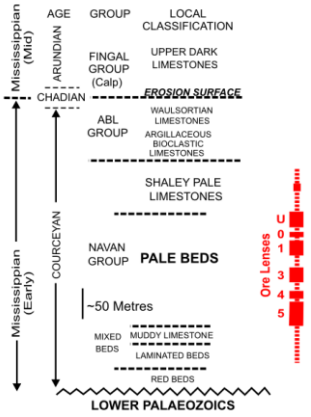

Figure 2. Stratigraphic column at Navan showing the horizons at which the mineralised lenses occur.

Within the succession there are distinct marker horizons that allow the lithological section to be divided into named lenses (Figure 2).

The oldest recognised faulting in the deposit are ENE-trending, NW-dipping normal faults (E and Liscartan, see Figure 1) that were active during the development of the 'ABL' group and into the lowermost 'UDL' (Coller et al., 2005). Within a developing relay ramp (that dipped at a shallow angle to the WSW), between the earliest faults, two listric SE-dipping, extensional faults (B and T faults with 200 m throw) became active. As extension continued, further listric faults and slide faults developed in the west (Y, M and N) again downthrowing to the southeast (Fgure 1). Later, probably Hercynian compression reactivated the main faults particularly in the northeast (A-C, D, Castle and Randalstown Faults) creating both thrusting and strike-slip movements.

3 The anatomy of ore distribution

The Navan Group has been split into 6 lenses (5, 4, 3, 2, 1 and U) separated by distinct marker horizons (Figure 2; the stratigraphically highest Conglomerate Group Ore has been omitted from this study). The deposit can be split into two main areas; the Main Orebody and the Southwestern Extension (SWEX; Figure 1). The Main Orebody is further divided into three zones based on the major faults (B and T). 1 Zone includes the area north-west of the B fault, 2 Zone between the B and T faults, and 3 Zone south of the T Fault.

The majority of mineralization in 1 Zone is hosted by the basal 5 lens (Figure 2). Other lenses within 1 Zone are overall not as strongly mineralized (< 5%) but do show enrichments closer to the B Fault.

The highest grades in 2 Zone occur within 5 lens to the NE (>20%). However, unlike 1 Zone, high grade mineralization is present within most lenses. In the upper (4 through 1) lenses mineralization is focused proximal to high grade areas in the underlying 5 lens or adjacent to the B and T faults.

Within the SWEX, mineralization is mainly focused on the 1 and U lenses. The SWEX is an irregular 2800 x 300 m NE-trending area found in the hanging wall on the western side of a normal fault (the E fault). The full lithological section is present, however, in contrast to the Main Orebody lower lenses are less well mineralized except directly abutting the E fault. The mineralization is less regular than within the Main Orebody in both grade and thickness (Ashton et al., 2003).

4 How does metal zoning help?

Metal distribution patterns have been studied by several workers (e.g. Andrew and Ashton, 1985; Ashton et al, 1986; Anderson et al., 1998; Blakeman et al., 2002; Ashton et al., 2003). We use Zn and Pb data from the basal 5 lens for the Main Orebody and 1 lens for the SWEX (Figure 3), to locate zones of fluid ingress, as well as put constraints on the migration of the main ore fluid. Drill hole assay data from >30 years production were composited into notional slices lying parallel to the stratigraphy using in-house software. These slice composites when added, enable bulk metal distributions to be examined over any part of the Pale Beds stratigraphy. In practice composited data was used to calculate bulk metal values in 10 x 10 m blocks using inverse-distance weighting and then viewed with *Leapfrog 3D*.

Zn+Pb enrichments within the Main Orebody are recognized to follow small branch faults and trend more northerly than the major faults (Blakeman et al., 2002). Multiple feeder zones have been proposed within NE 2 Zone and the north of 1 Zone based on these high Zn+Pb values and sulfur isotope values (Blakeman et al., 2002).

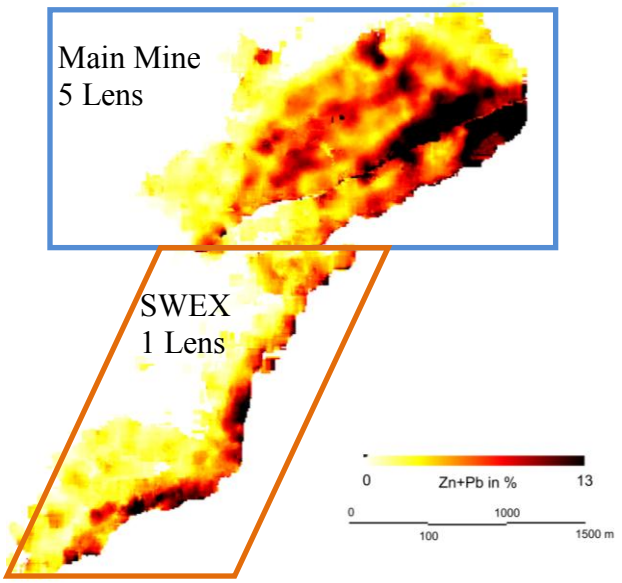

Figure 3. Zn+Pb in wt. % for the main mine 5 lens and the 1 lens in the SWEX.

The U and 1 lenses are the most widely mineralized lenses in the SWEX . The majority of the 5 lens within the SWEX is at most weakly mineralized and has not

been sampled sufficiently to create a large-scale map. However, the 4 and 5 lenses are locally mineralized to ore grade near the E fault. The areas of economically mineralized 5 lens exhibit similar Zn enrichment patterns and concentrations to the 1 lens. The eastern extent of the SWEX's mineralization generally follows the trend of the E fault and locally follows the shape of the small slides in two small half arcs (the N and M Fault Troughs; Figure 1).

4.1 Zn/Pb ratios tell a different tale

The Zn/Pb patterns differ from the metal concentration patterns for the Main Orebody (Figure 4). The Main Orebody Zn/Pb has a mean of 3.3 and shows a gradual increase in Zn to the NE with pockets of high lead in the NE 2 Zone, within the middle part of the north 1 Zone, and along the B fault. These pockets coincide with areas that have been proposed as feeders (Andrew and Ashton, 1985). A histogram of Zn/Pb from the main mine 5 lens yields a robust non-normal distribution with two populations centred around 1.5 and 4.5 (Figure 5). These populations also describe geographically distinct areas; the low Zn area is in the SW, the high Zn area in the NE

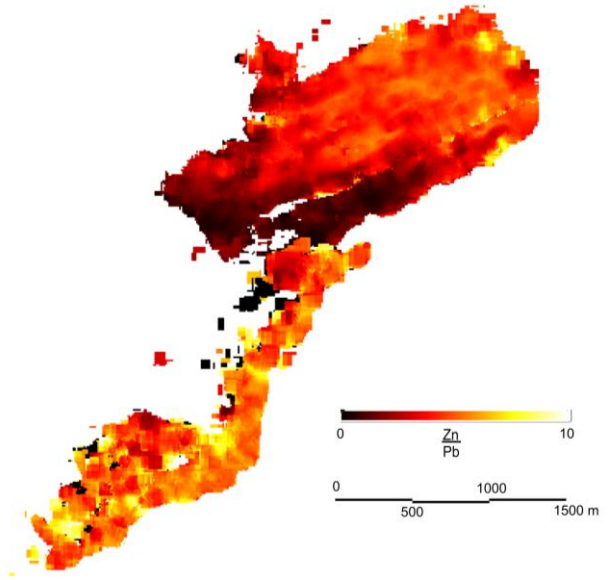

Figure 4. Zn/Pb for the main mine 5 lens and the 1 lens in the SWEX. The main mine exhibits gradients between high lead areas and lower lead areas. These gradients are absent within the SWEX. Note that the 1 Lens overlies the 5 Lens and does not match in terms of Zn/Pb.

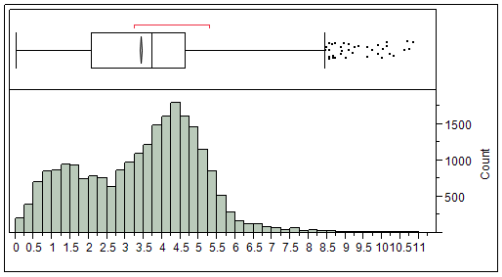

Figure 5. Histogram of all (n=22978) averaged points in the 5 lens of the Main Orebody. Note the double peak in the histogram, and that a simple average of the ratios does not convey the entire picture.

In order to identify the spatial change in Zn/Pb a filter that removed the higher values was applied. Progressively higher values were then incorporated into the figure (Figure 6). This method reveals isolated high Pb areas and the outward zoning of other areas. Low Zn/Pb ratios define feeder areas in Silvermines, Mount Isa, McArthur River and Sullivan (Large 1980, Taylor 1984), and are considered to do the same here.

Overlying lenses (4,3,2,1) yield similar patterns, however Zn/Pb distributions are typically more normally distributed and richer in Zn. When high Pb zones are present in lower lenses, the same high Pb pattern is often reflected in overlying lenses, but in a more diffuse and larger area.

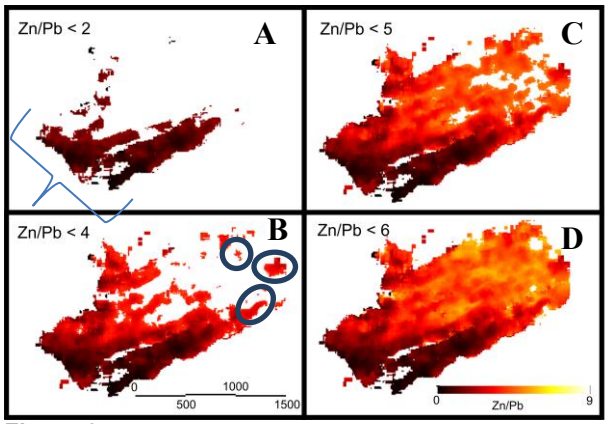

Figure 6. Four panels showing progressive increases in Zn/Pb in the Main Orebody 5 lens. The top left shows high lead areas to the south of 1 zone and the long trend of high lead along the B fault and in 2 zone. The proposed point of ingress is within the brackets. The bottom left frame shows the appearance of high lead zones in the NE (circled). The other two panels are displayed using a less stringent filter and show progressive growth to the northwest.

The SWEX has Zn/Pb with a mean of 5.0 and demonstrates a roughly normal distribution. The majority (75%) of the data have a Zn to Pb ratio between 4 and 6. The SWEX 1 Lens contains zoning on a much smaller scale (200m) than the Main Orebody, with many (~15) chaotic relatively low Zn centres. There is no apparent correlation with faulting, drilling pattern, number, or grade.

5 Can we pin the feeder down?

The Zn/Pb patterns exhibited within the Main Orebody at Navan possibly illustrates the steady progression of a hydrothermal fluid precipitating preferred metals as the thermodynamics change. This invites the proposition that a large portion of the Main Orebody was created by ingress of a buoyant fluid near the SW corner of the deposit and then moved latterly up-dip to the NE. .

The B fault and the 3 areas in the north of the Main Orebody have a low Zn/Pb that cannot be explained by a migrating fluid from the SW. This, along with textural, isotopic, and Zn/Pb evidence implies that a separate fluid with a different initial Zn/Pb ratio (as it entered the Pale Beds), is responsible for these, the most intensely mineralised areas of the mine. It is not possible to

identify the extent of the SW fluid in these areas due to the overprinting or overlap of the fluids.

The SWEX differs from the Main Orebody in its overall Zn/Pb ratio, style of mineralization, lack of horizontally contiguous ore and areas of hydrothermal sulfur isotopes. Together these imply a feeder distinct from that of the main mine. Despite subtle variations in Zn/Pb, the zoning that is present suggests that many small areas of fluid ingress were responsible for the mineralization of the SWEX. This suggests that sulphide concentrations are controlled by localized stratigraphic traps and access to bacteriogenic sulfide rather than a single dominant feeder zone.

6 Ideas gained from metal zoning

Examination of the extraordinary, quantitative metal concentration database at Navan, in 3 dimensions, is beginning to shed new light on the broad history of fluid flow responsible for this giant deposit. We are beginning to discern different styles of fluid ingress in the mine, responding to the evolution of tectonics during the Lower Carboniferous.

In the Main Orebody. spatial patterns of Zn/Pb values in the SW suggest fluids with the lowest Zn/Pb entered the Pale Beds relatively early. The low permeability of the Pale Beds suggests fluids migrated slowly, which is consistent with the developing tectonic activity at the time. They moved laterally up-dip along small existing fractures, driven by positive buoyancy. The movement of these fluids was highly controlled by the structure of the Pale Beds, local dolomites and lithological permeability variations.

A second major group of fluids with higher Zn/Pb moved upwards along the hanging wall zone of the B fault. This area contains mineralization within all major lenses; metal patterns match those from of the lower lenses. The B fault was active relatively early in the rifting sequence and it is likely that the fluids would have exploited this area while it was tectonically active.

The third major fluids created distinct small areas within the northeast 1 and 2 zones. These areas are heavily mineralized (>30%), contain many indicators of vertical flow, and have overprinted any previously existing horizontal trends. These small areas could be indicative of a drastic pressure change due to the unroofing event created by the Boulder Conglomerate.

The SWEX varies considerably from the Main Orebody and in some ways seems to be an entirely separate deposit. The metal zoning within the SWEX points to a complex of separate small feeders. The fluid flow within the Pale Beds appears to be predominantly vertical and closely tied to the Shaley Pales Trough. The existence of mineralized Pale Beds within the Trough implies that mineralization commenced prior to (or during) the creation of trough. The grand control the trough has on the total metals and zoning however creates a strong impression that the majority of the ore was emplaced after the creation of this feature. The unroofing and subsequent reduction of overpressure by the deep scouring slides is a possible mechanism for fluid focusing near the E fault.

Acknowledgements

We thank New Boliden Tara Mines Ltd for permission to publish, and for full financial support of BD-K's PhD.

References

Anderson, IK, Ashton, JH, Boyce, AJ, Fallick, AE, and Russell, MJ (1998) Ore depositional processes in the Navan Zn-Pb deposit, Ireland. Economic Geology 93:535-563.

Andrew C J and Ashton JH (1985) Regional setting, geology and metal distribution patterns of Navan orebody, Ireland. *Ireland.* Transactions of the Institution of Mining and Metallurgy, Section B: Applied earth Science 94:B66-B93.

Ashton JH, Downing DT and Finlay S (1986) The geology of the Navan Zn-Pb orebody. In Geology and genesis of mineral deposits in Ireland (ed. C. J. Andrew et al.), Irish Association for Economic Geology 243-280.

Ashton JH, Holdstock MP, Geraghty JF, O'Keeffe WG, Martinez N, Peace W and Philcox ME (2003) The Navan Orebody — discovery and geology of the SW Extension. In Europe's Major Base Metal Deposits (ed. J. H. Ashton et al.), Irish Association for Economic Geology 405–436.

Ashton JH, Blakeman RJ, Geraghty JF, Beach A, Coller D, Philcox ME, Boyce AJ, Wilkinson JJ The Giant Navan Carbonate-Hosted Zn-Pb Deposit – A Review. Irish Association for Economic Geology special publications: ZINC 2010, *in press*.

Blakeman, R, Ashton, JH, Boyce, AJ, Fallick, AE and Russell, MJ (2002) Timing of interplay between hydrothermal and surface fluids in the Navan Zn+Pb orebody, Ireland: Evidence from metal distribution trends, mineral textures and $\delta^{34}S$ analyses. Economic Geology, 97:73-91.

Braithwaite, CJR. and Rizzi, G, (1997) The geometry and petrogenesis of hydrothermal dolomites at Navan, Ireland. Sedimentology, 44:421-440.

Coller, D, Beach, A, Ashton, J, Geraghty, J, Holdstock, M, O'Keeffe W, Philcox, P and Walker, N (2005) Structural Geology and Tectonic Setting of the Navan Zn-Pb Orebody - Inversion of a Degraded Footwall-Uplift Fault Block. Presentation to Mineral Deposits Studies Group Annual Meeting, Belfast.

Everett C E, Rye D M and Ellam R M (2003) Source or sink? An assessment of the role of the Old Red Sandstone in the genesis of the Irish Zn–Pb deposits. Econ. Geol. Bull. Soc. Econ. Geol. 98: 31–50

Fallick, AE, Ashton, JH, Boyce, AJ, Ellam, RM and Russell, MJ (2001) Bacteria were responsible for the magnitude of the world-class hydrothermal base metal sulfide orebody at Navan, Ireland. Econ.Geol. 96:885-890.

Large, D E (1980) Geological parameters associated with sediment-hosted submarine exhalative Pb-Zn deposits An empirical model for mineral exploration Geol. Jahrb., ser.D , no. 40:59-129.

Leach D, Sangster D, Kelley K, Large R R, Grant Garven, C Allen, Gutzmer J, and Steve Walters (2005) Sediment-hosted lead-zinc deposits: A global perspective. *Economic Geology* 100:561-607.

Peace, WM (1999), Carbonate-hosted Zn-Pb mineralisation within the Upper Pale Beds at Navan, Ireland: Unpub. Ph.D. thesis, Univ. Melbourne, 284.

Symons DTA, Smethurst MT, Ashton JH (2002) Paleomagnetism of the Navan Zn-Pb deposit, Ireland. Econ Geol 97: 997-1012.

Taylor, S 1984. Structural and paleotopographic controls of lead-zinc mineralization in the Silvermines orebodies, Republic of Ireland. Econ. Geol: 19:529-548.

Wilkinson, JJ, Boyce, AJ, Everett, CE and Lee, MJ (2003) Timing and depth of mineralization in the Irish Zn-Pb orefield. In, Kelly J G, Andrew C J, Ashton J H, Boland MB, G. Earls, L., Fusciardi and G. Stanley (eds) EUROPE'S MAJOR BASE-METAL DEPOSITS. Irish Association for Economic Geology., Dublin, 483-497.

Stratiform fluorite deposits in the south-eastern part of the Paris basin (Morvan): paragenetic sequence, trace elements and Sr-Nd isotopes

Morgane Gigoux[1,2], Benjamin Brigaud[1], Guillaume Delpech[1], Maurice Pagel[1]
[1]Université Paris-Sud, UMR CNRS 8148 IDES, bât. 504, 91405 Orsay-France

Catherine Guerrot[2], Thierry Auge[2], Philippe Negrel[2]
[2]BRGM, 3 avenue Claude-Guillemin -BP 36009- 45060 Orléans Cedex 2 – France

Abstract: In France, stratiform fluorite deposits occurred at the base of Mesozoic sedimentary units from the Paris Basin around the Morvan massif, and reserves are estimated to about 5Mt. Detailed paragenetic sequence, fluid nature and the timing of the mineralization are still poorly constrained. In this study we examine the petrographical properties, trace elements composition and isotopic signatures of the fluorite deposits. These investigations provide insights into the parameters controlling the mineralization stages. The petrographical observations revealed a distinct growth zonation of fluorite crystals and a mineral paragenesis composed of multiple fluorite stages associated with various minerals (barite, sphalerite, galena and others). Significant variations of U, Th, Sr, Ba, and especially U/Th ratios are recorded from all fluorite stages. Concerning Rare Earth Element (REE), a bell-shaped pattern is recognized for all fluorite stages. Sr isotopic data of fluorite ($^{87}Sr/^{86}Sr$= 0.7119 to 0.7134) are incompatible with a seawater signature. Available microthermometric data and the thermal history of the basin indicate hydrothermal fluid flow. A preliminary isochron data suggest a Lower Cretaceous age for the fluorite mineralization at the Pierre-Perthuis deposits.

Keywords: stratiform fluorite deposits, paragenesis, LA-ICP-MS, REE pattern, isotopes.

1 Introduction and geological settings

Fluorite is considered as a critical raw material by the European Commission Group working on defining critical raw materials in European Union with 13 other materials (Antimony, Beryllium, Cobalt, Gallium, Germanium, Graphite, Indium, Magnesium, Niobium, Platinum Group Metals, Rare Earth, Tantalum and Tungsten) (European commission, 2010, Nowakowska, 2012). In France, stratiform fluorite deposits occur at the base of Mesozoic sedimentary units in the Paris Basin around the Morvan Massif (Fig 1). Fluorite grades are between 30-40% and CaF_2 estimated reserve is more than 5Mt within six deposits (Soulé de Lafont and Lhégu, 1980). The Morvan area is composed of sedimentary formations corresponding to the south-eastern part of the Paris Basin and plutonic and metamorphic rocks forming a horst of Hercynian basement. The fluorite deposits are hosted in sandstones/conglomerates from Late Anisien/Early Ladinian at Antully, in limestones from Hettangian/Sinemurian at Courcelles-Fremoy and in dolomite from Carnian/Norian at the Pierre-Perthuis, Pontaubert, Marigny-sur-Yonne and Egreuil deposits.

The basement is composed of granitic, gneissic or rhyolitic rocks. The origin of the stratiform fluorite deposits from the Morvan region is poorly constrained. The aim of this study is to better constrain the origin and timing of fluorite deposits with a multi-disciplinary approach including (1) field work, (2) core descriptions, (3) petrographical investigations (optical, cathodoluminescence and electron microscopy), (4) trace element analyses (REE, Y, U, Th, Sr, Mg, Ba, Rb) and (5) Sr-Nd isotopic compositions.

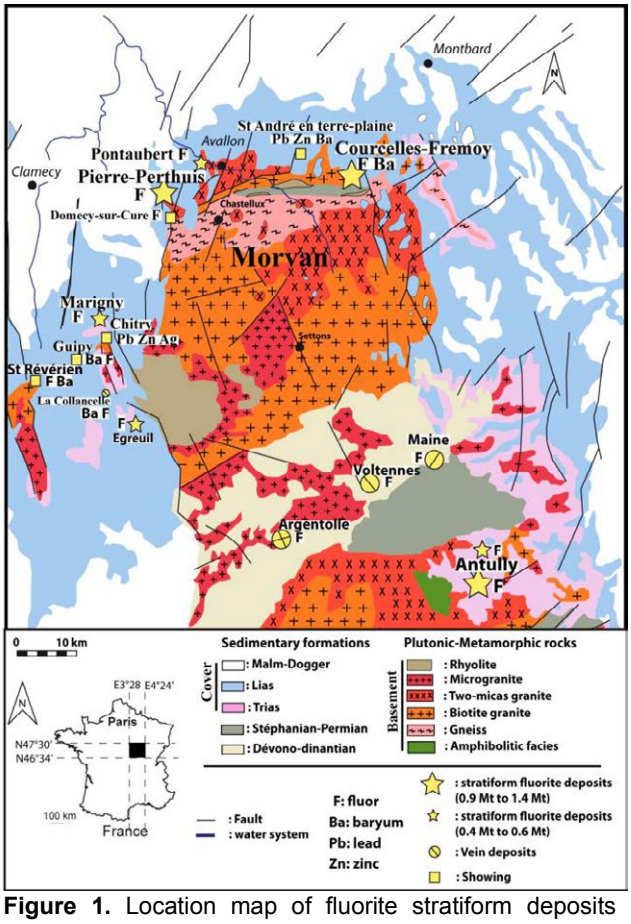

Figure 1. Location map of fluorite stratiform deposits around the Morvan Massif (modified after Soulé de Lafont and Lhégu, 1980).

2 Methods

Samples from four deposits (Pierre-Perthuis, Marigny-sur-Yonne, Antully and Courcelles-Frémoy) and three showings (Chitry, St André-en-Terre-Plaine, Guipy and Domecy-sur-Cure) were studied. Thin sections have been observed by optical, cathodoluminescence (CL) and using SEM-BSE-EDS study. Cubic fluorite crystals

have been analyzed by Laser Ablation connected with an Induced Coupled Plasma-Mass Spectrometer (LA-ICP-MS) to determine trace elements (REE, Y, Mg, Rb, Ba, Sr, Th and U). Different crystals from the same samples were also analyzed by ICP-MS. REE data were normalized to the North American Shale Composite (NASC) after Gromet et al (1984). Rb-Sr and Sm-Nd isotopic analyses have been measured by Thermal Ionization Mass Spectrometry (TIMS) from the three deposits (Pierre-Perthuis, Marigny-sur-Yonne, Antully) and one showing (Domecy-sur-Cure).

3 Results

3.1 Paragenetic sequences

The paragenetic sequence in the different samples from the four fluorite deposits and the three showings display several fluorite stages coexisting with barite, pyrite, sphalerite, galena, azurite, malachite. The mineralogical successions between the different deposits show that all the sequences began by a sulfide stage (galena, sphalerite or pyrite). In addition, the north-western deposits or showings (Pierre-Perthuis, Marigny-sur-Yonne and Chitry-les-Mines) have similar paragenetic sequences (1) sulfides (2) fluorite 1/barite (3) quartz (4) sulfides (5) fluorite 2 and 3, (6) quartz and (7) azurite/malachite. At Pierre-Perthuis, there are two galena stages, three fluorite stages (Fl1, Fl2 and Fl3), two barite stages (Brt1 and Brt2) and four quartz stages (Qz1 to Qz4). The mineral paragenesis of all deposits is composed of Fl-Brt-sulfides assemblage type. However, there are variations of mineral concentrations according to their location.

Observations under CL microscopy revealed a well-defined CL pattern of fluorite from Pierre-Perthuis composed of two distinct growth zones between Fl1 and Fl2 stages (Fig. 2A, B). Fl1 stage consists mainly of 100-250µm isolated cubic crystals in matrix, and only rarely was observed in vein. Crystals are rich in inclusions and display a dark-blue luminescent core surrounded by a rim marked by succession of 3 subzones (1) fine light blue band (2) a relatively large dark-blue band and (3) light-blue band (Fig. 2B). Fl2 stage includes large inclusion-free cubic crystals (250µm to 1cm) mainly forming geodes or veins and rarely found in carbonate matrix. The natural colour of Fl2 is white, yellow and can be marked by a fine external purple band. The Fl2 stage is characterized by a concentric zoning with blue luminescent core and bright rims composed of 3 subzones (1) light-blue band (2) large dark-blue band and (3) dark-purple band (Fig. 2A).The Fl3 stage is characterized by a fine blue band (4) (Fig. 2A).

3.2 Trace element data

The results of the fluorite crystals analyzed with LA-ICP-MS method fit well with the solution ICP-MS results (Fig. 3). Fluorite crystals from four deposits show a difference in total REE concentrations with mean value of 57 ppm at Pierre-Perthuis, 99 ppm at Marigny-sur-

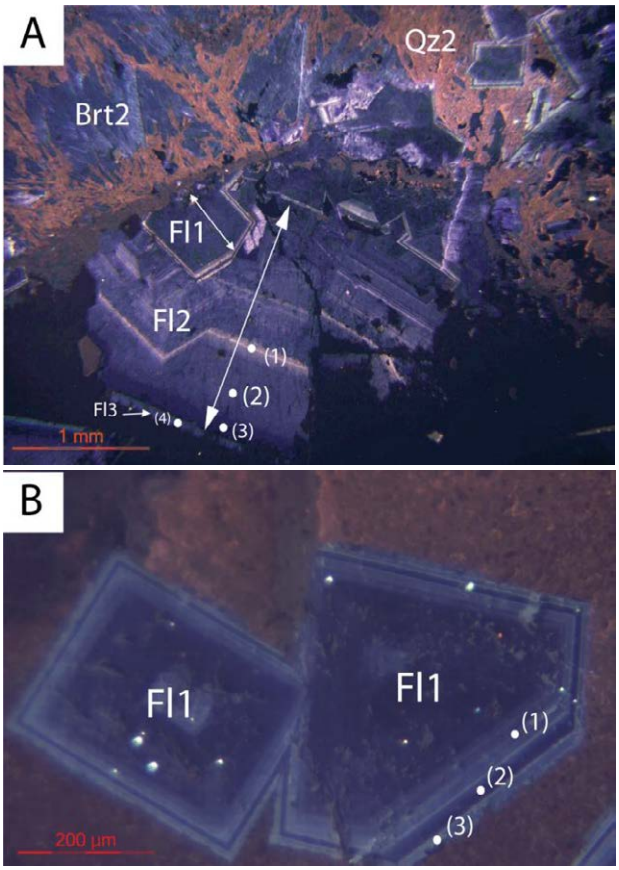

Figure 2. Cathodoluminescence microscopy image, **A**: Fl1, Fl2, Fl3 stages associated with quartz (Qz2) and barite (Brt2) stages from Pierre-Perthuis deposit; rims of Fl2: (1) light blue band (2) large dark blue band and (3) dark-purple band. (4) Fine blue band of Fl3 **B**: CL pattern of Fl1 stage from Pierre-Perthuis with a blue luminescent core and rim composed of 3 subzones (1: fine light blue band; 2: dark-blue band; 3: fine light blue band).

Yonne, 123 ppm at Domecy-sur-Cure (5km southward from Pierre-Perthuis) and 140 ppm at Antully. The distribution of normalized REE patterns displays a bell-shaped pattern in various fluorite stages (Fl1, Fl2 and Fl5) with a Mid-Rare Earth Element (MREE)-enrichment without europium (Eu) and cerium (Ce) anomalies. Significant variations of U (0.01 to 11 ppm), Th (0.01 to 12 ppm), Sr (33 to 283 ppm), Ba (0.4 to 278 ppm) and especially U/Th ratios (0.2 to 10.8) are recorded from the Fl1, Fl2 and Fl5 stages. REE patterns of fluorite can be related to the fluorite stage. In Pierre-Perthuis, for the first stage (Fl1) no variations from core to rim, and no Ce and Eu anomalies were observed. The Fl2 stage from Pierre-Perthuis displays different MREE and Heavy Rare Earth Element (HREE) content between the core (translucent white) and the rim (purple rim and yellow rim). The purple rim is enriched in Th whereas the yellow rim is enriched in U. A negative Eu anomaly is present in Fl2.

3.3 Sr-Nd isotopic data

The variations of the $^{87}Sr/^{86}Sr$ ratios range from 0.7119 to 0.7134. The $^{87}Rb/^{86}Sr$ ratios are very low (< 0.03) so whatever the "time corrected" initial $^{87}Sr/^{86}Sr$ ratios will not be very different from the measured one. For the

Pierre-Perthuis deposit, isotopic values range from 0.7119 to 0.7133 for 3 samples of Fl2. ε_{Nd} varies from -4.04 (Antully) to -6.38 (Pierre-Perthuis). Sm and Nd concentrations range from 6.29 to 10.60 ppm and from 10.84 to 20.63 ppm, respectively. The $^{147}Sm/^{144}Nd$ ratios range from 0.3083 to 0.43876.

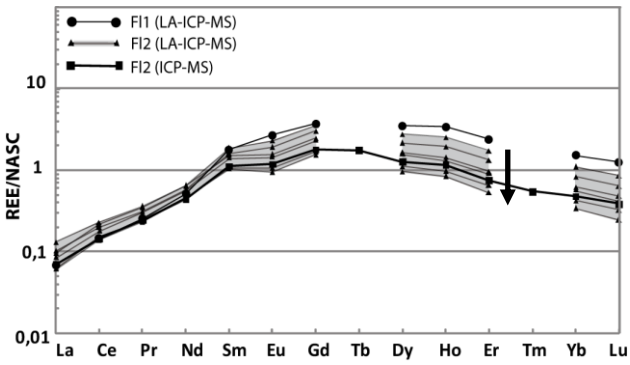

Figure 3. REE patterns for Fl1 and Fl2 stages in the Pierre-Perthuis deposit and comparison between LA-ICP-MS and ICP-MS methods for the same samples. The laser spots follow the crystal growth (the black arrow) for the Fl2 stage (LA-ICP-MS results in grey colour)

4 Discussion

4.1 Nature of mineralizing fluid

The bell-shaped REE patterns do not resemble the REE patterns of marine limestones or seawater (De Baar et al., 1985). For instance, they do not display significant anomalies in Ce and/or relative enrichment in HREE. The REE patterns in Pierre-Perthuis (Fl2) display a slight negative Eu anomaly, which could be interpreted as a geochemical fingerprint of fluid interaction inheritance from the source sedimentary or crystalline rocks. The fractionation between U and Th (U/Th>1) in fluorite crystals from most deposits could indicate an environment where redox potential (Eh) value favours a preferential transport of U over Th. On the contrary, the absence of fractionation between U and Th at Marigny-sur-Yonne suggests a lower Eh value.

The Sr isotopic data in fluorite do not display a seawater isotopic signature. However the $^{87}Sr/^{86}Sr$ ratios are similar to the$^{87}Sr/^{86}Sr$ ratios of the early diagenetic from Carnian/Norian dolomite formation (0.711; Spotl and Wright, 1992).

The reconstruction of the thermal history of the south-eastern part of the Paris Basin, and more precisely in the Pierre-Perthuis area indicates that the maximum temperature during burial reached 70°C at a depht of 1.25 km during the Late Cretaceous period (Uriarte, 1997). However the homogeneization temperatures deduced from fluid inclusions in fluorite crystals from Marigny-sur-Yonne deposit are hotter and range from 70°C to 120°C with 22 eq. wt.% NaCl (Nigon, 1988). A preliminary microthermometric study on Fl2 stage in Pierre-Perthuis also indicates warmer fluids with similar temperatures (90-120°C, 20 eq. wt. % NaCl). These higher temperatures indicate a hydrothermal fluid flow event.

4.3 Comparison with fluorite-vein deposits

Fluorite-vein deposits are known in the Morvan Hercynian basement (Voltennes, Maine and Argentolle; Joseph, 1974; Marchand et al., 1976; Valette, 1983; Jebrak, 1984 and Nigon, 1988). Some similarities exist between the last yellow-white fluorite stage (paragenesis, salinity, temperature) in Voltennes veins and yellow-white cubic fluorite stage in stratiform deposits. In fact the homogeneization temperatures range from 100 to 122°C with 16 eq. wt % NaCl which are similar with those at the Pierre-Perthuis and Marigny-sur-Yonne deposits. In terms of dating, at Voltennes, the ages determined by K-Ar dating on adularia (Fig. 4) associated to the first stage of purple/green fluorite crystallization range from 170-175 Ma (Baubron et al., 1980) to 185 ± 5Ma (Joseph et al., 1973), i.e contemporaneous to the first stage of purple fluorite. These ages correspond to a crystallization during the Early Jurassic period. The relation between stratiform deposits in Mesozoic sedimentary formation and veins in Hercynian basement will be further investigated: the adularia from Voltennes will be dated using the^{40}Ar-^{39}Ar method and the possibility of Sm-Nd dating of the purple-green fluorite will be evaluated in order to compare the timing between vein and stratiform deposits in the Morvan.

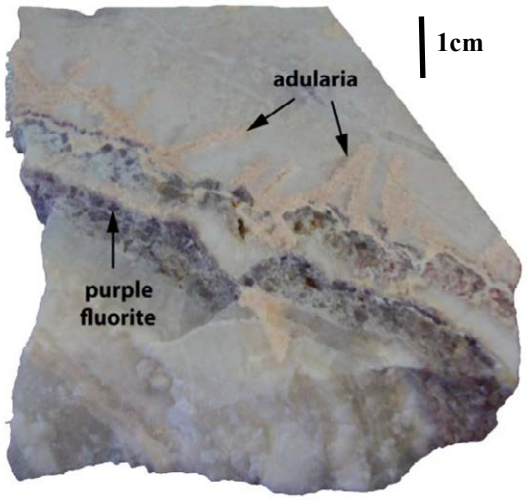

Figure 4. A sample from the Voltennes vein deposit composed of purple/green fluorite associated with adularia.

4.4 Timing of stratiform fluorite deposits

The preliminary Sm-Nd isotopic data of the Fl2 stage from Pierre-Perthuis may be interpreted as a crystallization age from the Lower Cretaceous period (Sm-Nd isochron at 135±18 Ma). In turn, these isotopic data may also reflect a mixing between fluids with different elemental and initial isotopic compositions. The analyses of new samples in the future will allow to carefully evaluate both hypotheses.

6 Conclusion

The ongoing study of stratiform fluorite deposits in the Morvan resulted in the following preliminary observations: 1) The north-western deposits or showings (Pierre-Perthuis, Marigny-sur-Yonne and Chitry-les-Mines) have similar paragenetic sequences: (1) sulfides (2) fluorite/barite (3) quartz (4) sulfides (5) fluorite, (6) quartz and (7) azurite/malachite. 2) The bell-shaped normalized REE pattern is typical for stratiform fluorite deposits in the Morvan. 3) The U/Th variation in fluorite between different deposits (Marigny-sur-Yonne and Pierre-Perthuis) suggests Eh variations in the fluid from which the fluorite crystallized the fluorite. 4) Fluid inclusions trapped in Fl2 crystals in Pierre-Perthuis and Marigny-sur-Yonne deposits revealed the presence of a warm and saline fluid (T= 90-120°C, up to 20 eq. wt % NaCl). 5) The $^{87}Sr/^{86}Sr$ ratios are different from a seawater isotopic signature but the data are consistent with the isotopic signature of the dolomitic host rocks. The timing of mineralization of the Fl2 stage at Pierre-Perthuis could indicate a Lower Cretaceous period.

Acknowledgements

This study is part of a PhD project funded by the BRGM and partially supported by INSU-CESSUR research project (Institut National des sciences de l'Univers Connaissance et Technologie du Sous-Sol pour son exploitation et Usage Durable). This paper is a contribution of the team "Relief et Basin" to the UMR-CNRS/ Université Paris-Sud 8148.

References

Baubron JC, Jébrak M, Joannès C, Lhégu J, Touray JC, Ziserman A (1980) Nouvelles datation K/Ar sur des filons à quartz et fluorine du Massif central français. C. R. Acad.Sci. Paris 290, 951-953.

De Baar HJW, Bacon MP, Brewer PG, Bruland KW (1985) Rare earth elements in Pacific and Atlantic oceans. Geochim.Cosmochim.Acta, 49, 1943-1959.

European Commission (2010) Critical raw materials for the EU.Report of the Ad-hocWorking Group on defining critical raw materials. 85p. http://ec.europa.eu/enterprise/policies/raw-materials/critical/index_en.htm

Gromet LP, Dymek RF, Haskin LA, Korotev RL (1984) The « North American composite »: Its compilation, major and trace element characteristics. Geochim.Cosmochim.Acta, 48, 2469-2482.

Jebrak M (1984) Contribution à l'histoire naturelle des filons (F,Ba) du domaine varisque français et marocain : essai de caractérisation structurale et géochimique des filons en extension et en décrochement. Thèse de doctorat en Sciences, Univ. Orléans. Doc. BRGM n°99, 510p

Joseph D, Bellon H, Derre C, Touray JC (1973) Fluorite veins dated in the 200 million year range at La Petite Verrière and Chavaniac, France.Economic geology, 68, n° 5.

Marchand L, Joseph D, Touray JC, Treuil M (1976) Critères d'analyse géochimique des gisements de fluorine basés sur l'étude de la distribution des lanthanides- application au gite de Maine (71-Cordesse, France). Mineral. Deposita, 11, 357-379.

Nigon P (1988) La fluorine stratiforme de la bordure Ouest du Morvan : Géologie, Géochimie et modélisation. Thèse de 3° cycle, Univ. Orléans, 252p.

Nowakowska M (2012) DefiningCriticalRawMaterials in the EU, InformationGapsandAvailableSolutionsec.europa.eu/enterprise/policies/rawmaterials/files/docs/eu_us_critical_raw_materials_en.pdf

Soulé de Lafont D, Lhégu J (1980) Les gisements stratiformes du Morvan (sud-est du bassin de Paris, France), 26 CGI, Paris7-17/07/1980 BRGM fascicule E2, 40 p.

Spotl C, Wright VP (1992) Groundwater dolocretes form the Upper Triassic ofthe Paris Basin, France: a case study of an arid, continental facies. Sedimentology 39, 1119-1136.

Uriarte JA (1997) Maturité thermique des sédiments de la bordure sud-est du Bassin de Paris. Terre et Environnement Genève, vol.9, 146 p.

Valette CO (1983) Karst et filons à fluorine dans le faisceau synclinal du Morvan: le gisement d'Argentolle (Saône et Loire, France). Thèse de troisième cycle, Univ. Orléans, 300p.

Developing genetic models for copper-silver mineralisation in the Kalahari Copperbelt, Botswana: mineralogy, geochemistry and structure

Gorman, A. R., Jenkin, G. R. T., Morgan, K. L.
University of Leicester, University Road, Leicester, LE1 7RH, UK

Catterall, D.
Hana Mining Ltd, Ground Floor, Fairgrounds Financial Centre, PO Box AD80AAF, Gabarone, Botswana

Abstract. The Kalahari Copperbelt stretches from central Namibia to north-western Botswana, and is relatively poorly understood. This north-east trending mineralised zone is hosted within Neoproterozoic basin metasediments and volcanics, and is both lithologically and structurally controlled. The Hana Mining Ltd. Ghanzi project, covering 2169 km^2, is located in north-west Botswana and is a potentially viable surface mineable copper-silver deposit.

This study project primarily focuses on constraining a genetic model for the formation of this sediment hosted mineralisation, and therefore a strategy for future exploration of deposits of this kind, using detailed petrological, Scanning Electron Microscope (SEM), computerised tomography (CT) and geochemical analysis. The economic sediment-hosted sulphide minerals present are bornite, chalcocite and chalcopyrite, and are hosted within various disseminated structures. Vein mineralisation is also present and is explored in detail by Morgan et al (2013).

Data gathered has been combined with the work of Morgan to facilitate the production of a large scale genetic model, and future exploration parameters, for the Ghanzi deposit. Our preliminary interpretation is that early stage mineralisation has been upgraded by metal rich, basin derived fluids during basin compression.

1 Introduction

The Kalahari Copperbelt stretches from central Namibia to north-western Botswana, and when compared to the Central African Copperbelt, is relatively poorly understood, with only an estimated 11 % explored. This north-east trending mineralised zone is hosted within Neoproterozoic basin metasediments and volcanics, and is both lithologically and structurally controlled.

The Ghanzi project, covering 2169 km^2, is located in north-west Botswana, at the north-west tip of the Central Kalahari Game Reserve, and is a potentially viable surface mineable copper-silver deposit (Hana Mining Ltd 2012).

Hana Mining Ltd. controls 100% of 5 license blocks that make up the Ghanzi property and have presented a Preliminary Economic Assessment with indicated resources of 217.516 kt copper and 10.157 Moz silver (Hana Mining Ltd 2012). Discovery Metals have recently opened the Boseto copper-silver mine on an adjacent property, producing 36 000 t of copper per annum (Discovery Metals Ltd. 2012).

In order to understand the interrelationships of mineralogy, geochemistry and structure within the deposit, detailed core logging and analysis of geochemical data has been carried out. On a smaller scale, 2–D microscopy, SEM analysis, CT scanning and other lab based techniques are being used. Detailed petrographic examination will be combined with 3–D CT scans of hand samples.

2 Geological setting

2.1 Regional geology

Crustal extension between the Congo and Zimbabwe – Kaapval cratons, commencing at 1106 Ma (Schwartz et al 1995) resulted in the formation of the bi-modal Kgwebe volcanics, which were subsequently overlain by the clastic red beds of the Kuke and Ngwako Pan formations (Modie 1996). Consequent basin evolution and transgression to a shallow marine environment facilitated the deposition of the D'Kar formation, a finer grained clastic and carbonate formation (Schwartz et al 1995), within which the majority of mineralisation is contained.

Shortly after the deposition of the Ghanzi Group– a stratigraphic section approximately 5 km thick - the closure of the rift basin occurred from 630 – 500 Ma, as a result of the Damaran Orogeny - a component of the Pan African Orogeny. This compressional event produced the Damaran belt, within which the Kalahari Copperbelt (also known as the Ghanzi-Chobe belt) is contained. The Kalahari copperbelt runs 600 km along a north-east – south-west strike from central Namibia to north-western Botswana (Figure 1).

During this period of compression, two stages of deformation took place; a primary isoclinal folding with amplitudes of 10 km and wavelengths of around 25 km (Carney 1994); and a secondary stage of folding with an oblique shear. These fold patterns outcrop as banana shaped patterns, with mineralisation concentrated in the hinge of the folds.

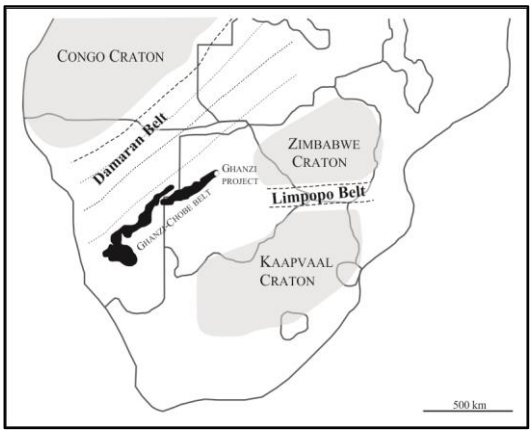

Figure 1. Map of Southern Africa showing the location of the Kalahari Copperbelt within the Damaran belt and the location of cratons. Adapted from Schwartz et al (1995).

2.2 Local geology

Sandstones, mudstones, limestones and siltstones make up the majority of stratigraphy at the Ghanzi project (Figure 2). Economic mineralisation is centred around the contact between the reduced fine grained sandstones, siltstones, marls, limestones and mudstones of the D'Kar formation, and the sandstones of the Ngwako Pan formation. Carbonate, sericite and chlorite alteration occurs as a product of diagenesis and fluid flow.

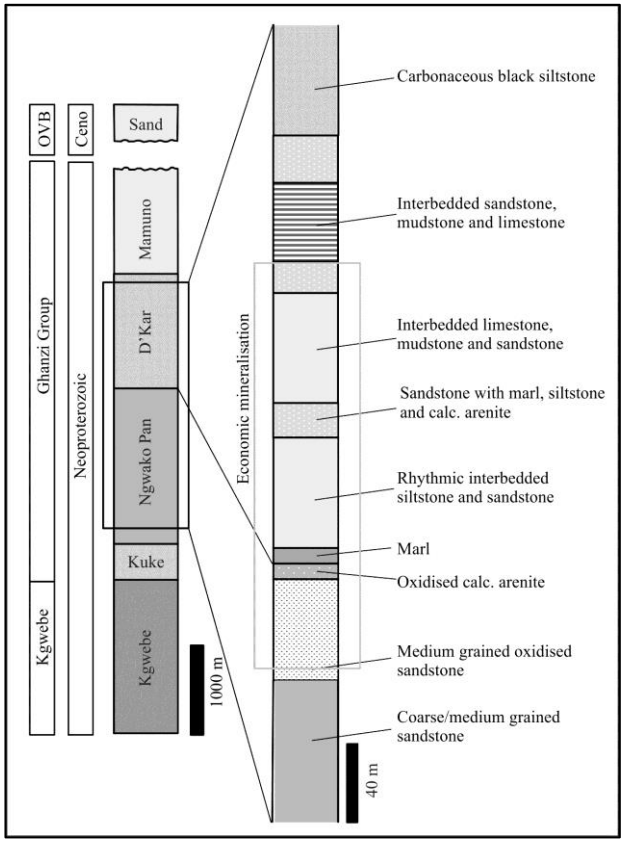

Figure 2. A generalised vertical section of the stratigraphy intersected at the Hana project. Adapted from the work of Hana Mining Ltd. geologists.

3. Petrology

3.1 Sediment-hosted mineralisation

Sediment-hosted mineralisation occurs throughout the stratigraphy, but economic mineralisation is predominantly centred around the redox and lithological boundary between the Ngwako Pan and the D'Kar formations, and the units immediately above and below this boundary. The economic sulphide minerals present are bornite, chalcocite and chalcopyrite, with minor pyrite, sphalerite, pyrrhotite, galena and covellite (in order of decreasing abundance). Mineralisation occurs in four distinct styles; microbial mat hosted, disseminated, lamination/nodule hosted, and cleavage hosted, with the latter three styles providing the bulk of economic disseminated mineralisation.

Microbial mat hosted mineralisation is hosted within sericite – carbonate rich, organic poor laminations. Rhythmic laminations bend around bornite – chalcocite mineralisation in places, suggesting an element of early mineralisation.

Disseminated sulphides occur throughout the mineralisation zone. Mineralisation is predominantly chalcocite/bornite, with blebs surrounded by calcite and carbonate sericite altered quartz.

Lamination and nodule hosted mineralisation is present predominantly in the reduced siltstone, sandstone, marl and mudstone facies of the D'Kar formation. The majority of this mineralisation is bornite chalcocite, with rosette and intergrowth textures seen. Lamination hosted mineralisation occurs preferentially in calcite and quartz rich horizons. Contrary to Sillitoe et al. (2010), evidence is seen for widespread pre-diagenetic mineralisation, although nodular mineralisation may have replaced original anhydrite nodules such as those seen in the Lufilian Arc (Haest and Muchez, 2011), although this kind of replacement is yet to be confirmed at the Ghanzi deposit.

Cleavage hosted mineralisation is again predominantly bornite-chalcocite, with minor chalcopyrite, pyrite, Sphalerite and galena. This kind of mineralisation is found at both sides of the redox boundary, and is often found in conjunction with vein hosted, nodular and lamination hosted mineralisation.

Silver occurs as both native silver, and within cupropearceite, primarily within cleavage and disseminated mineralisation.

3.2 Vein hosted mineralisation

In the complementary part of this project, Morgan (2013) is investigating the timing and sulphur signature of sediment hosted mineralisation, and its relationship to vein hosted mineralisation.

Three stages of veining have been identified: 1) Early bedding parallel to sub-parallel deformed veins, 2) Middle stage veins usually at a high angle to bedding and less deformed and 3) Late stage massive veins. Studies of both disseminated and vein hosted mineralisation imply mineralisation occurred over an extended period that potentially proceeded as well as overlapped regional deformation.

4. Preliminary genetic model

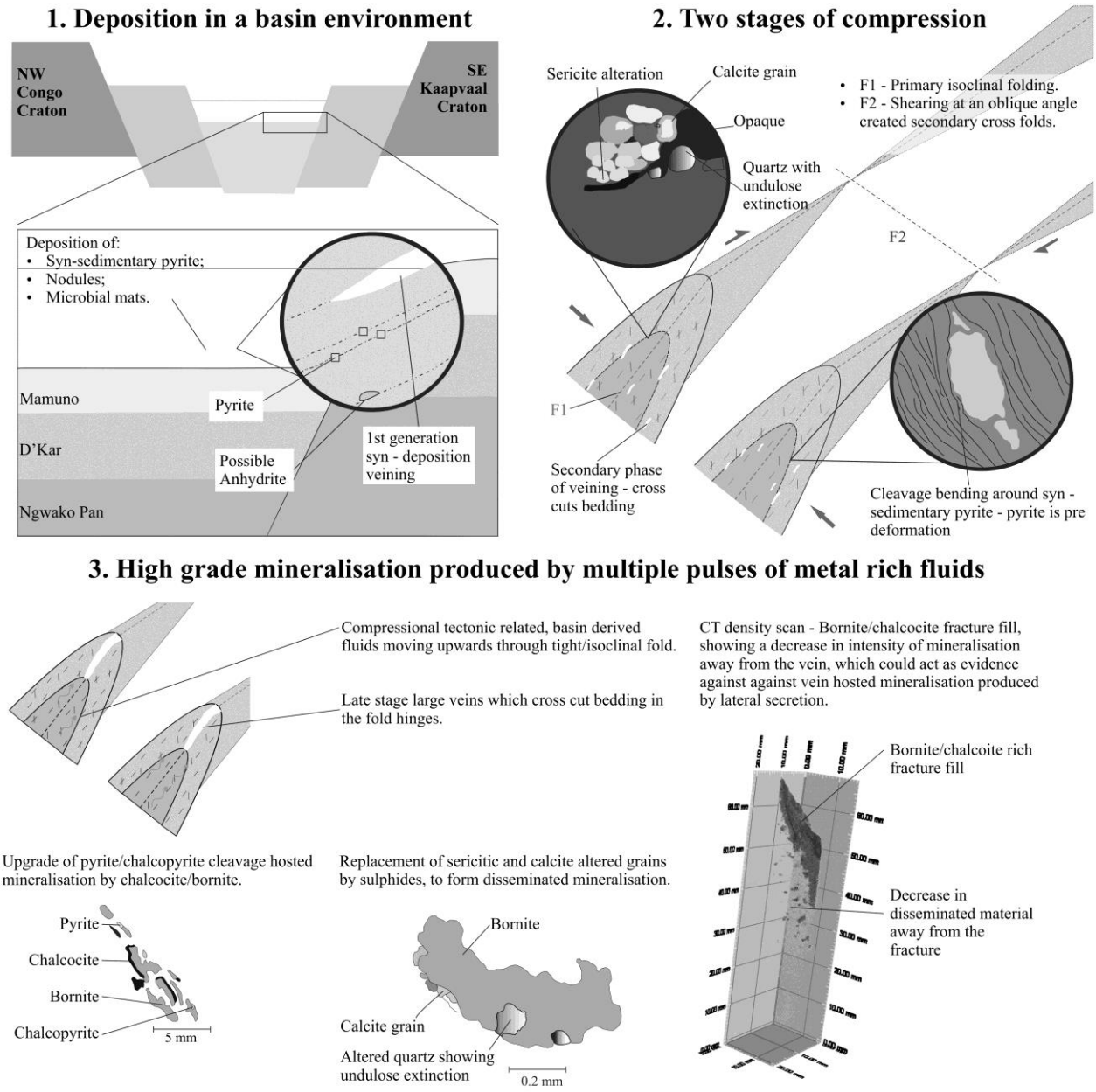

Figure 3. A preliminary genetic model for disseminated mineralisation at the Ghanzi Project. 1) Deposition of the Damaran age sedimentary sequences, including syn-sedimentary mineralisation, potential anhydrite nodule microbial mats. 2) Two stages of compression, as a result of the Damaran Orogeny. 3) Multiple pulses of metal rich fluids, produced by the compressional environment, upgraded initial mineralisation and facilitated the precipitation of further mineralisation.

5. Preliminary conclusions

Early, pre- and syn- diagenetic mineralisation occurs as isolated and microbial mat–, lamination- and nodule-hosted pyrite/chalcopyrite grains. This preliminary mineralisation was subsequently upgraded by numerous pulses of Cu-Ag enriched basinal fluids, both syn- and post- sedimentation. These fluids are thought to have been produced by compressional tectonics and basin dewatering during the Pan African Orogeny, with base metals originating from underlying volcanics.

Acknowledgements

With thanks to Hana Mining Ltd. for continued support and contribution.

References

Carney JN, Aldiss DT and Lock NP (1994) The Geology of Botswana, Geological Survey Department, Republic of Botswana: Bulletin, 37:71-83.

Discovery Metals Ltd. (2012) Annual Report 2012. Available at *http://www.discoverymetals.com/annual-reports-7.*

Haest M and Muchez P (2011) Stratiform and vein-type deposits in the Pan-African Orogen in central and southern Africa: evidence for multiphase mineralisation. Geological Belgica: 14: 23 – 44.

Hana Mining Ltd. (2012) Corporate Presentation. Available at *http://www.hanamining.com /i/pdf/Corporate-Presentation.pdf*

Modie BNJ (1996) Depositional environments of the Meso- to Neoproterozoic Ghanzi-Chobe belt northwest Botswana: Journal of African Earth Sciences: 22:255–268.

Morgan KL, Jenkin GRT, Catterall D, Boyce AJ, Gorman AR (2013) The formation of vein hosted copper-silver mineralisation in the Kalahari Copperbelt, Botswana: Preliminary results. This volume.

Muchez P, Brems D, Clara E, De Cleyn A, Lammens L, Boyce A, De Muynck D, Mukumba W, Sikazwe O, (2010) Evolution of Cu–Co mineralizing fluids at Nkana Mine, Central African Copperbelt, Zambia. Journal of African Earth Sciences: 58: 457–474.

Schwartz MO, Akanyang P, Trippler K and Ngwisanyi TH (1995) The Sediment hosted Ngwako Pan Copper Deposit, Botswana. Economic Geology: 90:118-1147.

Sillitoe RH, Perelló J and García A (2010) Sulfide-bearing veinlets throughout the stratiform mineralisation of the Central African Copperbelt: Temporal and genetic implications. Economic Geology: 105: 1361 -1368.

Tankard AJ, Jackson MPA, Eriksson KA, Hobday DK, Minter WEL (1982) Crustal Evolution of Southern Africa: 3.8 billion years of earth history, Springer-Verlag, New York, 523.

Geology, mineralogy and chemistry of some selected Pb-Zn-Cu deposits in eastern desert and Sinai Egypt

Mervat Said Hassan
Central Metallurgical R & D Institute
Box P.O.87 Helwan, Cairo, Egypt

Abstract. Lead-Zinc deposits are located in Phanerozoic sediments and crops out in seven areas in the Southern part in the Eastern Desert on the Red Sea. The Zn-poor zone of Um Gheig characterized by low ZnO and PbO content. High content of SiO_2 and Al_2O_3 reflected the abundance of quartz, clay minerals and feldspar. Meanwhile, the high Fe_2O_3 value in some samples revealed the abundance of hematite, goethite as well as jarosite minerals. Meanwhile, the ZnO content in the Zn-rich zone of Um Gheig ranged between 25 to 52% compared with 3-14.9% for PbO. The Geological Survey of Egypt estimates the reserves in Um Gheig as 1.5 million tons with an average assay of 13.8% Zn and 2.3% Pb.
Stratiform Massive Sulphides in Um Samuki, Eastern Desert represented by Cu-Pb -Zn association. Chemical analysis of primary sulphide samples showed high content of ZnO and SO_3 compared with oxidation and supergene zone. Shpalerite is abundance in the primary sulphides zone. In general zinc is predominant in the ore with subordinate amounts of copper and lead. The ore body in the Western mine assays 2.2 % Cu, 21.6 % Zn, 0.5 % Pb and 109 g/t Ag with total reserves of 200,000 tons while the Eastern mine is less in metal content where Cu possess 1.8 %, Zn 13.6 % and Pb3.4 %.
Cu-bearing granite and quartz in Wadi El Samra, Sinai characterized by high content of SiO_2, Al_2O_3, K_2O and Fe_2O_3. The abundance of these oxides attributed to quartz and mica. Meanwhile, the low S content in the oxidation and supergene zone revealed the abundance of copper carbonate compared with copper sulphides.

Keywords. Lead-Zinc –Copper, Eastern Desert, Sinai Egypt

1 Introduction

Lead-zinc-Cu mineralization in Egypt is known to occur either associated with the Precambrian basement complex or with Miocene rock units.

1.1 Precambrian basement complex

This type of ore includes Cu-Pb-Zn deposits of Um Samuiki (El Shazly and Afia 1958 and Anwar et al., 1963). Derhib deposits described by Shukri and Basta 1959, El Gorsesy 1964 and El Shazly et al., 1965. The geology of Um Samiuki area and the associated polymetallic sulphides have been studied by several authors; Garson and Shalaby (1976), Shukri and Mansor (1980), Soliman (1981), Hafez and Shalaby (1983), El Arif et al.(1985), Aly et al. (1990) and Takla et al. (1999). The deposit was exploited by the ancient Egyptians and recently in the early thirties by the "Egyptian phosphate Company" which developed two small mines namely the Western and the South-Eastern.

The ancient Egyptian was only interested in the exploitation of the oxidized parts of the deposit where malachite is the main mineral present. Geological survey exploited the lead, zinc and copper in Um Samiuki area between 1959-1961 and confirmed the occurrence of these three metals.

The Copper mineralization in Sinai were encountered at several localities, the most important of these are the Sarabit, Regeita, Wadi El Samra and Abu El Nimran (El Shazly 1969). At Sarabit, the copper minerals are found in shales intercalated with the Upper Carboniferous sandstone, while in other localities they fill fractures in pink granite, granodiorite, schists, and quartz veins of Precambrian age.

1-2 Miocene rock units

Lead-zinc mineralizations that are confined to Miocene formation occur mainly in the coastal Miocene sediments along the Red Sea between Quseir and Ras Banas. Al Aref and Amstutz (1983) classified the lead-zinc deposits along Red Sea coast into two types; 1- Lead-zinc filling type at Um Gheig and Wizer; 2-Stratiform-stratabound galena in sandstone (calcite and dolomite are absent) at Zug El-Bohar and Essel.

The aim of this study is to through some light on the polymetallic ores in Egypt although there is any production from these ores but they represent important exploration
targets.

2 Materials and Techniques

Representative samples were collected from Um Gheig, However, samples of polymetallic sulphides were collected from Um Samukui area (Eastern Desert). Copper samples were collected from Samra in Sinai. The collected samples were analyzed with standard, XRD, XRF and microscope methods.

3 Geological setting

3.1 Lead-Zinc deposits along Red Sea Coast, Eastern Desert

The most important Pb-Zn deposits occurrences of Egypt occur at few localities distributed along Red Sea coast between Quesier and Ras Banas (Figure 1).

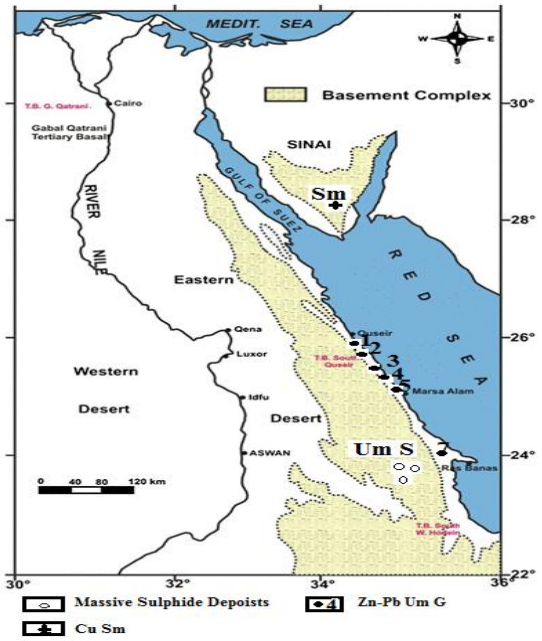

Figure 1. Geological map distribution of Lead-zinc- Copper deposits along Red Sea Coast, Sinai and Eastern Desert, Egypt.

The Um Gheig (Um G) is boarded on the west by Precambrian basement rocks, which form high hills and extend in the NW-SE direction, and is bounded on the East by the resent shoreline of the red sea. It is characteristic by drainage pattern of dentritic and sub-dentritic types. Mineralization in these localities is regulated by both structure and lithology. Both sulfide and oxidized zone are present. The Miocene sequence overlies uncomfortably the basement complex. Um Gheig is formed by the following rock types, from the top to the bottom: hard grey limestone (crustified, brecciated and silicified rocks of the caliche type) belongs to Um Gheig Formation; marly limestone, gypsum and anhydrite

3.2 Cu-Pb-Zn deposits in Um Samuiki

Um Samuiki (Um S) area is occupied by two lithotectonic units separated by a major folded thrust; these are the ophiolitic rocks and type island arc rocks. The two lithotectonic succession most probably of subaereal type. All these rocks are intruded by younger gabbro and leucogranite (Takla et al., 1999). Sulphides occur at Um Samikui (Um S) in the form of lenticular masses in the shear zones. The replacement of the sulphides in the shear zones may be almost complete, in which case massive sulphides were produced, or may be incomplete thus producing an ore which is admixture of sulphides and gangue.

3.3 Cu deposits in Wadi El Samra, Sinai

Wadi El Samra (Sm) area forms a part of the basement complex of Sinai as shown in Figure 1 (.Noor 1987 and Noor 1990). The area is dissected by three major faults, trends NE-SW, NW–SE and N-W. All wadis are covered with debris from the basement rocks surroundings and drains to the Gulf of Aqaba. This area was divided into two zones according to the rock type riches in copper mineralization:

Zone I: This zone is located in the southern flank of Wadi El-Samra and covers an area about 0.6 km^2. This area consists of metasediments, acidic metavolcanics and altered albite dissected by quartz veins and veinlets which are very rich with iron oxides (sulphide zone). The thickness of this zone is ranges from 20 cm to 90 cm, also there are acidic dykes (rhyolite porphyry).

Zone II: This zone is located in the northern flank of Wadi El-Samra and covers an area about 0.3 km^2. This area consists of metasediments and metavolcanics dissected by huge quartz and pegmatite veins rich in copper mineralization mainly malachite and azurite.

4 Results

4.1 Mineralogy

Oxidation zone of Um Gheig (Um G) characterized by distinctive colour red, Yellow and brown lithological unite which host fine grained detrital sediments (Figure 2). The following minerals were identified by XRD; clay minerals (smectite, kaolinite and illite), quartz, feldspar, carbonate (calcite and dolomite), jarosite and alunite. Lead and zinc oxides located in small amounts on the surface concentrated in the karst cavities and joints.

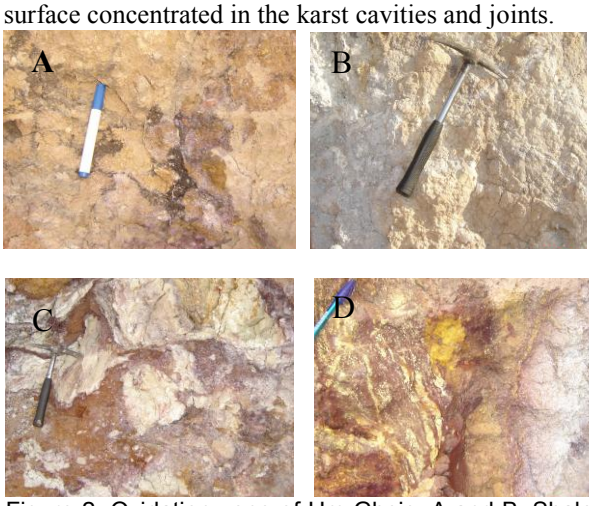

Figure 2. Oxidation zone of Um Gheig; A and B=Shale; C and D= Ferruginous rock

Zinc-lead in the poor zone found on the surface concentrated in the karst cavities and joints in the form of oxide (zincite, and lead oxide) in small amounts.

Zinc-rich or Calamine zone: Nonsulfide zinc phases are fine-grained and dominated by hemimorphite, hydrozincite and smithsonite. Lead occurs as cerussite and rare anglesite, whereas iron oxyhydroxides and oxides (mainly goethite and hematite) derived from the oxidation of pyrite are commonly present in “limonitic” boxworks and in small concretions with amorphous manganese minerals. Remnants of the primary ore mainly consist of sulfides (sphalerite, galena and pyrite/marcasite) and barite.

Primary sulphides in Um Samuiki (Um S): The primary sulphides are represented by four minerals, namely sphalerite, chalcopyrite, galena and pyrite in descending order. Sphalerite is the predominant forming the matrix of the other sulphides.

Oxidation and supergene enrichment: Bornite, covellite and dignite are the main supergene sulphides observed at Samiuki. At or near shrinkage craks, chalcopyrite may be altered to bornite, covellite or both. The chief oxidation product of sphalerite is smithsonite and hydrozincite and trace of hemimorphite However, the main oxidation product of chalcopyrite is malachite, azurite and chrysocolla.

Copper minerals encountered in Wadi El Samra (Sm) as malachite, azurite (carbonate), chrysocolla (silicate), cuprite (oxide), covellite (cupric sulphide) and chalcocite (cuprous sulphide).

4.2 Chemistry

Oxidation zone of Um Gheig: The samples from Zn-poor zone of Um Gheig (Um G) characterized by low Zn O and PbO content (Table 1). High content of SiO and Al_2O_3 reflected the abundance of quartz, clay minerals and feldspar. Meanwhile, the high Fe_2O_3 value in some samples revealed the abundance of hematite, goethite as well as jarosite minerals. The abundance of alunite mineral confirmed by K_2O and SO_3 content (Table 1)

Table 1 Chemical analysis of Um Gheig samples

Oxides	Zn-poor zone			Zn-rich zone		
SiO_2	51.3	70.9	37.2	4.9	10.8	2.2
Al_2O_3	12.9	14.0	0.74	0.88	0.54	1.01
CaO	0.5	0.25	0.18	0.33	0.33	0.44
Fe_2O_3	12.2	0.71	52.8	21.2	35.1	4.75
K_20	3.89	6.01	0.06	0.06	0.04	0.3
ZnO	1.87	2.56	1.0	45.0	25.0	52.0
NaO	1.29	1.54	1.14	4.19	1.2	1.02
PbO	2.25	2.1	2.89	3.64	14.9	6.76
SO_3	3.16	0.20	0.88	0.74	0.47	0.35
Cl	1.50	0.20	0.88	1.19	0.85	3.76
LOI	7.80	1.35	2.47	17.0	11.2	27.6

Meanwhile, the ZnO content in the Zn-rich zone ranged between 25 to 52% compared with 3-14.9% for PbO. SiO_2 content could be attributed to quartz /or hemimorphite. Fe_2O_3% represented iron minerals as goethite.

Chemical analysis of primary sulphide samples of Um Samuiki (Um S) showed high content of ZnO and SO_3 compared with oxidation and supergene zone. The result could be explained by abundance of sphalerite in the primary sulphides zone. In general zinc is predominant in the ore with subordinate amounts of copper and lead (Table 2).

Table 3 shows chemical analysis of Cu-bearing granite and quartz from Wadi El Samra (Sm). The samples characterized by high content of SiO_2, Al_2O_3, K_2O and Fe_2O_3. The abundance of these oxides attributed to quartz and mica. Meanwhile, the low S content in the oxidation and supergene zone revealed the abundance of copper carbonate compared with copper sulphides.

4.3 Petrography

Oxidation zone of Um Gheig: The Zn-rich horizon (calamine) at Um Gheig is dominated by hemimorphite, smithsonite and hydrozincite. Hemimorphite occurred in two generations; first as small concretion with dusty appearances. The second form appeared as clear

Table 2 Chemical composition of Um Samuiki samples

Oxides	Primary Sulphides				Oxidation and supergene zone				
SiO_2	13	30	17	35	32	41	3	0.9	2.2
Fe_2O_3	3.5	8	6.5	5	5	2.8	2.7	2.7	3.3
MnO	5	8	9	5	5	1	0.9	1.4	0.2
CuO	3.6	3.6	5.8	2.7	12	8	22	29	27
ZnO	45	27	12	40	26	38	30	40	42
PbO	3	4	5	3	3	3.7	٤	4	3
SO_3	35	29	25	26	6	3.4	12	12	17

Table 3 Chemical analysis of Cu-bearing samples in Wadi El Samra

Oxides				
SiO_2	54.61	54.87	42.77	45.92
Al_2O_3	15.08	11.01	10.26	9.41
Fe_2O_3	11.48	3.51	16.77	3.45
CaO	0.26	0.48	0.39	0.30
Cu	0.19	4.16	0.40	3.59
K_20	5.24	1.13	4.27	4.11
TiO_2	0.90	0.74	0.79	0.77
S	0.06	0.08	0.09	0.08
LOI	2.17	0.50	2.2	4.63

elongated crystals growing in veins and cavities (Figure .3A). Smithsonite found in different generations. Fe-rich smthsonite (early smithsonite) found as cryptocrystalline and late smithsonite occurs at the border of the small geodes, which are filled in turn by crystalline hemimorphite (Figure .3B and C). Hydrozincite in different forms includes the fibrous crystals, nodules, cryptocrystalline aggregates and botryodial (Fig.3 B). Cerussite is occurring in small quantities as Long, slender crystals of cerussite known as "jackstraw" (Figure 4D).

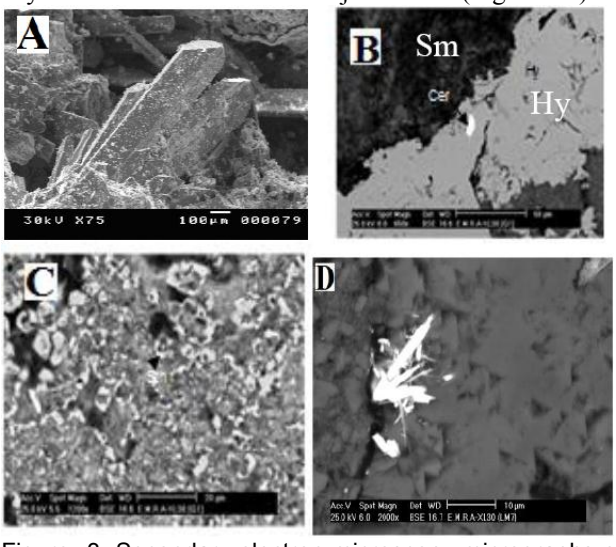

Figure 3. Secondary electron microscopy micrographs of various hemimorphite (platy crystals form of hemimorphite,with little development prisms faces; B-Backscattering image of Um Gheig calamine zone. C- BS of smithsonite as a border of geodes. D- BS of dendritic cerrussite.

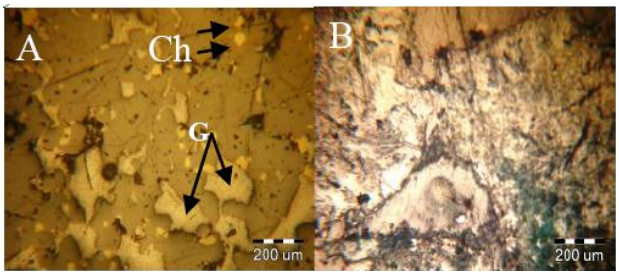

Figure 4. Polish section of Cu-Pb-Zn of Um Samuaki; chalcopyrite (yellow) found as disseminated and intergrowth or surrounding with Galena (G) and Sphalerite ; B- Langite (deep blue, right, bottom) shows tabular blades of twinned (40 um) in a mixture of hemimorphite and hydrozincite.

In Um Samuki (Um S), the sphalerite is the most important mineral. It is closely intergrown with chalcopyrite, the latter generally disseminated in the former (Figure 4A), however, the chalcopyrite may form veinlets in sphalerite. Microscopic examination shows that both minerals may enclose each other, indicating their simultaneous deposition. Galena is found as small grains either tending to be cubic or irregular dispersed in sphalerite and chalcopyrite. Langite, deginite and chalcocite are the Secondary Cu minerals formed from the oxidation of copper sulphides (Figure 4B).

In Wadi El Samra Copper deposit (Sm), secondary minerals azurite, malachite and psonjakite precipitate along foliation planes in the forms of microviens or thin bands and formed due to oxidation of sulfide minerals (Figure 5).

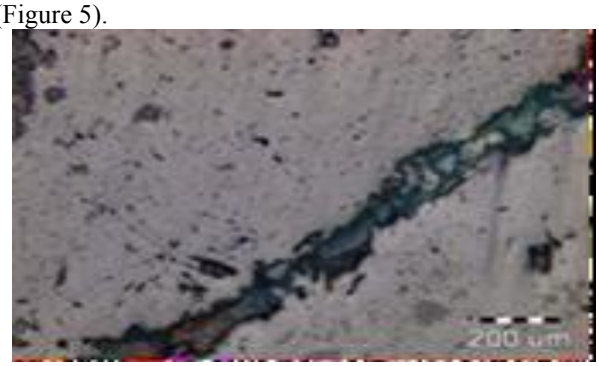

Figure 5. Polish section of Wadi El Samra Copper deposit

5 Conclusions

Although the mineral resources in Egypt are plenty, there are no mining activities in the sulphide mineralization areas except at Um Ghaig where the production is at very small scale. However, it could be multiples of the known reserves if the appropriate-ate subsurface exploration technology is used. Extrapolation of the available geological data suggests that with some additional geological efforts, clear ideas could be obtained about new mineral findings and/or extension of the existing deposits.

References

Aly SA, Fasfous BRB, Attawiya MY, El-Rahmany (1990) Contribution to the geochemistry of Um Samuki –Helgate metavolcanics, South Eastern Desert. Bull Fac Sci., Alex. Uni. 30:162-174

Anwar Y, Kotb, H (1963) Geological and mineralogical studies of the zinc-copper-lead ore of Samiuki area. Bull. Fac. Sci. Alex. Univ. 5, p. 89.

El Aref MM, Amstutz GC (1983) Lead-zinc deposits along the Red Sea coast of Egypt, new observations and genetic models on the occurrences of Um Gheig, Wizr, Essel and Zug El Bohar Monogr. Ser. on Mineral Deposits, Borntraeger Stuttgart, 21 103

El-Goresy A (1964) Neue Beobachtuxngen an der-Nickel-mognetkies-Lagerstätte Von Abu Suwayal, -Agypten. N. Jb. Miner. Abh. 102, 107.

El Shazly EM, Afia MS (1958) Geology of Um Samiuki deposits, Eastern Desert. J Geol 2: 25-42

El-Shazly EM, Farag I, Bassayuni FA (1965) Contribution to the geology and mineralization at Abu Swayal area. Part I. J. Geol. U. A. R. IX, 45.

Garson NS, Shalaby IM (1976) Precambrian Lower Paleozoic plate tectonics and metallogenesis in the Red Sea region. Spec Pap Geol Ass Canada 14: 573-596

Hafez AMA, Shalaby I M (1983) On the geochemistry Characteristics of volcanic rocks at Um Samiuki, Eastern Desert, Egypt. Egypt J Geol 27: 1-1: 73-92

Shukri MM, Basta EZ (1959) A note on the occurrence of a polysulphide deposit at Gebel Derhib, S. Eastern Desert. Egypt. J. Geol. III, 167p.

Shukri NM, Mansour MS (1980) Lithostratigraphy of Um Samiuki district, Eastern Desert, Egypt. Evaluation and mineralization of the Arabian Nubian shield. IAG Bull (Jeddah) 4:81-93. -

Solliman, FAM (1981) Geology and geochemistical studies on the mineralized area of Um Samiuki, Eastern Desert. MSc thesis Cairo Unv 92 p.

Takla MA, Sakran SHM, Awad NT, Abd El Rahim SH (1999) Geological and structural evaluation of Um Samiuki area, South Eastern Desert. Egypt. Gawa4, Int Conf of the Arab World, Cairo Egypt 168-184.

Metal sources and timing of Pb-Zn deposits associated to salt dome cap rocks in northwest Tunisia: evidence from isotope (Pb, S) geochemistry

Nejib Jemmali, Fouad Souissi
Université de Tunis El Manar, Faculté des Sciences, Département de Géologie, Tunis, Tunisia , Laboratoire des Matériaux Utiles, Institut National de Recherche et d'Analyse Physico-chimiques, 2026 Technopole de Sidi Thabet, Tunisia

Emmanuel John M. Carranza
Economic Geology Research Unit, School of Earth and Environmental Sciences, James Cook University, Townsville, Queensland, Australia

Jean-Jacques Orgeval
Bureau de Recherches Géologiques et Minières, Département Exploration, BP 36009 ,45060 - Orléans Cedex 2 - France

Abstract. The Pb-Zn ore deposits in the Oum Edeboua and Bou Grine areas (northern Tunisia) are hosted mainly by limestones in the contact zone between Triassic and Upper Cretaceous strata and by Upper Cretaceous limestones. The deposits occur as lenticular, stratiform, vein, dissemination and stockwork ore bodies consisting of sphalerite, galena, pyrite, chalcopyrite and sulfosalt (grey copper). Barite and calcite dominate the gangue. The ^{34}S of barite and celestite (12.7–15.0‰) at the Oum Edeboua (Guern Halfaya area) mine are consistent with the reduction of sulfates from Triassic evaporites within the study area ($12.8< {}^{34}S<14.0$‰). The ^{34}S values in base-metal sulfides from both study areas (2.6–9.5‰) and the presence of bacterial relics suggest involvement of bacterially-mediated sulfate reduction in the mineralizations. Pb isotope data are homogeneous with $^{206}Pb/^{204}Pb$, $^{207}Pb/^{204}Pb$ and $^{208}Pb/^{204}Pb$ ratios of 18.723–18.783, 15.667–15.685 and 38.806–38.889, respectively, which suggests a single source reservoir of Pb in the upper crust. The syn-diagenetic mineralization (F2) in the Bahloul Formation and the calculated ages from the Pb isotopic data suggest an Upper Cretaceous age for the Pb-Zn deposits in the Oum Edeboua and Bou Grine mines.

Keywords. Oum Edeboua, Bou Grine, (S, Pb) isotopes, MVT Pb-Zn deposits, Domes zone.

1 Introduction

The Domes zone (Fig. 1) is composed mainly of Mesozoic and Cenozoic sedimentary rocks that have been deformed during the Cenozoic Alpine orogeny (Jellouli et al. 2005). The entire Domes zone has undergone through multiple tectonic events from the Triassic to the Late Miocene. During the Mesozoic, from Triassic until Aptian times, the Domes zone was dominated by extensional tectonics related to the opening of the Tethys and Central Atlantic oceans. This tectonic setting generated a complex system of horsts and grabens bounded by NE-trending normal faults (Monthel et al. 1986; Orgeval et al. 1986; Bouaziz et al. 2002). The basins formed during that extensional phase were filled with thick Jurassic series mainly consisting of marine limestone and marls, followed by Lower Cretaceous series of fine-grained clastic sediments. The Upper Cretaceous series is a monotonous sequence varying from chalky limestone to marls, whereas the Cenozoic sequence consists of clay, sandstones and conglomerates that overlie unconformably the Triassic rocks (Jallouli et al. 2005). During the Upper Cretaceous to the Cenozoic, the northward movement of the African plate caused a series of compressional and extensional deformations that affected northern Tunisia, with the compressional effects reaching southern Tunisia (Bouaziz et al. 2002). The most prominent compressional event occurred during the Late Miocene, which formed the Tunisian and Tellian Atlas Mountains (Bouaziz et al. 2002). This compressional deformation caused the inversion of older normal faults, reactivated the uplift and diapirism of Triassic evaporites and created the majority of fold structures observed today (Jellouli et al. 2005).

The formation of Pb-Zn deposits in the Domes zone is akin to the classical process of formation of Mississippi Valley-type (MVT) deposits in forelands of orogens (cf. Bradley and Leach 2003). The Pb-Zn deposits in the Domes zone (Fig. 1) are distributed around NE–SW trending and evaporite-bearing Triassic outcrops. Three main mineralization types are distinguished: (i) stratabound lenticular orebodies in the contact zone (or transition zone) between Triassic and Cretaceous strata; (ii) stratabound orebodies associated to Cenomanian-Turonian strata; (iii) veins, stockworks and open-space fillings developed in the peridiapiric cover.

The present study describes geochemical analyses of ore samples in the Oum Edeboua mine, together with new sulfur and lead isotope data of ore samples from the Bou Grine deposit in conjunction with relevant data and interpretations in the literature. The objectives of the study are to derive insights into: (a) the sources of sulfur and metals, (b) the timing of mineralization and (c) the role of diapirism.

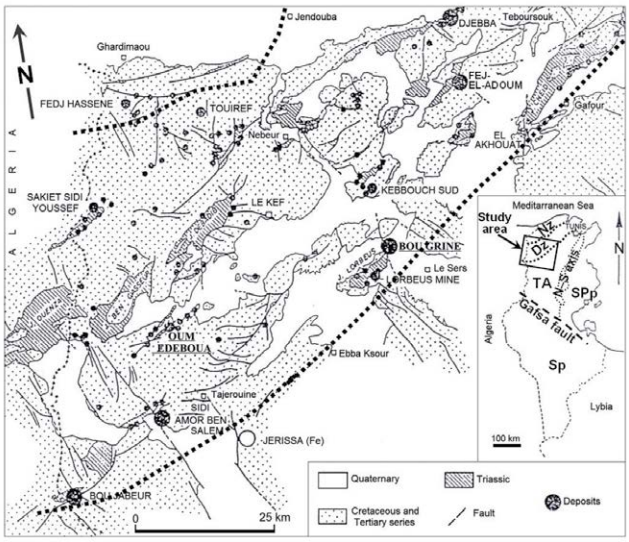

Figure 1. Map of Pb-Zn deposits and Triassic evaporite outcrops in the Domes zone, Northern Tunisia (modified from Monthel et al. 1986), indicating the locations of the Oum Edeboua and Bou Grine mines, on which this study is focused. Nz = Nappe zone. Dz = Domes zone. TA = Tunisian Atlas. N–S = North–South. SPp = Sahel–Pelagian platform. Sp = Saharan platform.

2 Geological setting and mineralization

2.1 Bou Grine Zn-Pb deposit

The Bou Grine Zn-Pb deposit is located at the northern extremity of the NE–SW trending Jebel Lorbeus evaporite dome (Fig. 1), which is one of many Triassic evaporite diapir intrusions in Lower Cretaceous to Neogene limestones, marls and shales in the Domes zone (Orgeval 1994). The Triassic evaporite diapir intrusions consist of a chaotic mass of gypsum, anhydrite, sandstone and carbonates, which were emplaced during the Jurassic and the Middle Cretaceous and continued to rise after Tertiary sedimentation. The ascent of diapiric evaporites was enhanced by major fracturing, fold and uplift movements, especially under the influence of basement faults (Rouvier et al. 1985).

At Bou Grine, five types of orebodies were distinguished (Orgeval et al. 1986) (Fig. 2). Type 1 (F1) comprises disseminations and massive lenses, breccias in the transition zone between Triassic and Cretaceous strata, with pyrite, marcasite, barite, celestite, galena and sphalerite. Type 2 (F2) consists of disseminations (high grade) in the Cenomanian–Turonian Bahloul Formation, with sphalerite, galena and pyrite. Type 3 (F3) comprises massive orebodies (very high grade Zn); with breccias that remobilized F2 mineralization in the lower part, massive ore (~30% Zn) in the central part and zinciferous clay in the upper part. Type 4 (F4) consists of some subeconomic disseminations in Cenomanian strata. Type 5 (F5) comprises some subeconomic disseminations in Turonian strata. Different generations of ore and gangue minerals are distinguished in the ore-bearing limestones and comprise a paragenetic sequence of fine-grained sphalerite impregnations within the host rocks (stage 1) and cross-cutting banded sphalerite, galena, and lesser pyrite and calcite (stage 2) (Orgeval 1994).

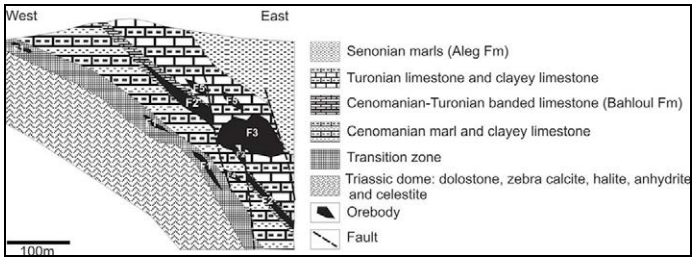

Figure 2. E–W cross-section of the Bou Grine deposit and location of ore bodies (adapted from Schmidt (2000), with geological description from Orgeval et al. (1986)).

2.2 Oum Edeboua Pb-Zn deposit

The Oum Edeboua Pb-Zn deposit, which is located in the Geurn Halfaya area, is mainly composed of (Fig. 3): (i) Triassic rocks consist of chaotic gypsiferous clays, sandstones, black dolomitic-limestones, which are overlain by large amounts of anhydrite with halite core (Hammami and Smati 1993); (ii) Lower Cretaceous rocks include the Aptian limestone and –Albian marls and limestones rocks at the core of the anticline; (iii) Upper Cretaceous is composed of Cenomanian marl-limestone alternations overlain by yellowish limestones. The Upper Cenomanian – Lower Turonian consists of laminated gray to black organic-rich limestones of the Bahloul Formation, with 3–7.5% organic C (Orgeval 1994). The Turonian includes clayey and banded limestones. The Miocene is composed of sandstones.

The Oum Edeboua orebodies are distributed around the NE–SW trending evaporite-bearing Triassic rocks and closely associated with the NE–SW and N–S trending normal faults. The deposit exhibits three styles of mineralization within the contact Triassic – Upper Cretaceous series, particularly in the Cenomanian marl-limestone alternations and in the Bahloul Formation. The first style is lenticular mineralization in the Cenomanian marl-limestone alternations consisting of abundant pyrite with marcasite, sphalerite, galena and celestite, occurring in dolostone breccias as impregnations, substitutions and replacements of the clayey-dolostone matrix. The second style is stratiform mineralization in the Bahloul Formation consisting of framboidal and cubic pyrite, disseminated sphalerite and galena. The third style comprises veins, disseminations and stockworks in breccias of Cenomanian–Turonian limestones and consisting of pyrite, galena and sphalerite.

Ore and gangue minerals consist of galena, sphalerite, pyrite, chalcopyrite, arsenopyrite, sulfosalt, marcasite, cerussite, barite, celestite, strontianite, dolomite, calcite, quartz and gypsum. The sulfosalt samples are dominated by grey copper. The homogenization temperatures of fluid inclusions trapped in celestite range from 95 to 130 ºC, with salinities between 10 and 25 wt% NaCl eq. (Kassaa 1998).

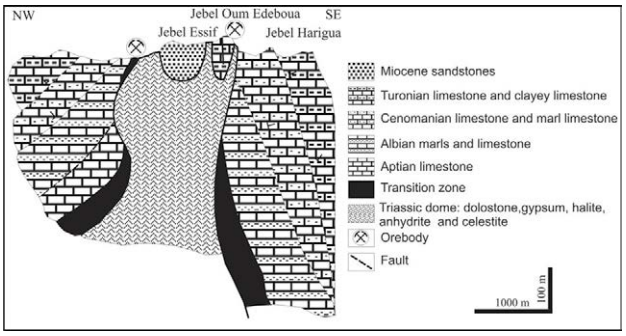

Figure 3. Schematic NW–SE cross-section of the Oum Edeboua mine (adapted from Hammami and Smati 1993).

3 Results and discussion

3.1 Sources of sulfur

Sulfur isotope compositions were determined for 3 samples of gypsum, 4 samples of anhydrite, 2 samples of celestite-barite, 10 samples of galena, and 2 samples of sphalerite. Gypsum, celestite and barite in Triassic rocks at Oum Edeboua have $\delta^{34}S$ values of 12.8–15.0‰, whereas anhydrite in Triassic evaporite (from drill core) at Tabbet Lahsan (Fedj-el-Adoum district) yielded $\delta^{34}S$ values of 14.2–15.6‰ (Fig. 4). These data are similar to typical $\delta^{34}S$ values of (a) about 15‰ obtained from regional Tunisian sulfates (Orgeval 1994; Jemmali et al. 2011a, b) and (b) 11–17‰ in Triassic marine sulfates (Claypool et al. 1980). This indicates that the Triassic evaporites are plausible sources of sulfur that can be associated with sulfate minerals in Triassic strata in the Oum Edeboua mine.

Galena in mineralized Triassic – Upper Cretaceous rocks at Oum Edeboua yielded $\delta^{34}S$ values of 3.3–9.5‰, whereas galena and sphalerite in mineralized Cenomanian–Turonian (F2) and Turonian (F3) rocks at Bou Grine yielded $\delta^{34}S$ values of 2.6–9.4‰ (Fig. 4). These ranges of sulfur isotope compositions overlap with the range of sulfur isotope compositions of F1 orebodies at Bou Grine (Orgeval 1994). This implies the same or similar source of sulfur for (a) the F1 base-metal sulfide deposits in the transition zone between Triassic and Upper Cretaceous strata in both the Oum Edeboua and Bou Grine and (b) the F2 and F3 base-metal sulfide deposits in the Bou Grine mine.

The homogenization temperatures during mineralizations at Oum Edeboua and Bou Grine (95–130 ºC (Kassaa 1998) and 75–100 ºC (Orgeval 1994), and the differences between $\delta^{34}S$ values of sulfide minerals and their possible parent sulfates are largely consistent with BSR as the mechanism for reduction of Triassic sulfates that can be associated with base-metal sulfide mineralizations at Oum Edeboua and Bou Grine. This deduction is supported further by the presence of bacterial relics in the Oum Edeboua mine (Kassaa 1998) and the Bou Grine mine (Orgeval 1994). In addition, pyrite associated with galena in the Oum Edeboua mine exhibits framboidal texture, which is characteristic of BSR-linked galena.

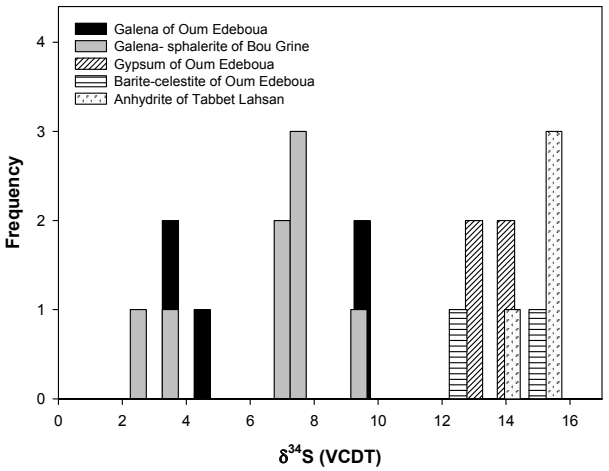

Figure 4. Distribution of $\delta^{34}S$ values of sulfides (galena + sphalerite) and sulfates (gypsum + barite + celestite + anhydrite) from the Oum Edeboua, Bou Grine and Tabbet Lahsan deposits.

3.2 Sources of metals and timing of mineralization

Galena samples from the Oum Edeboua and Bou Grine deposits yielded $^{206}Pb/^{204}Pb$, $^{207}Pb/^{204}Pb$ and $^{208}Pb/^{204}Pb$ ratios of 18.723–18.783, 15.667–15.685 and 38.806–38.889, respectively. Based on the 'plumbotectonics' model of Zartman and Doe (1981), the $^{208}Pb/^{204}Pb$–$^{206}Pb/^{204}Pb$ data for the Oum Edeboua and Bou Grine mines plot above the orogen curve, whereas the $^{207}Pb/^{204}Pb$–$^{206}Pb/^{204}Pb$ data plot close to the upper crust plot (Fig. 5). In the $^{207}Pb/^{204}Pb$–$^{206}Pb/^{204}Pb$ graph (Fig. 5), the new data from the Oum Edeboua and Bou Grine mines form a field that is closely consistent with that of Orgeval (1994) for the Bou Grine deposit lying between the upper crust and the orogene curves of Zartman and Doe (1981). This and the homogeneity of $^{208}Pb/^{204}Pb$ and $^{207}Pb/^{204}Pb$ ratios in the Oum Edeboua and Bou Grine mines (Fig. 5) imply involvement of a single source reservoir of Pb at depth (upper crust).

The timing of mineralization is constrained by: (1) the syn-diagenetic mineralization in the Bahloul Formation (Upper Cretaceous) present in the Oum Edeboua and Bou Grine mines; (2) part of the sulfur in Bou Grine comes from Cretaceous seawater sulfates (Orgeval 1994); and (3) using the Pb isotopic data to calculate and interpolate ages according to the two-stage Pb model of Stacey and Kramers (1975). From the Pb isotopic data, we obtained a median age of 82.25 Ma (or 87.71 Ma, excluding three outlier data of Bou Grine). During this Upper Cretaceous age, tectonic events resulted in NE–SW to ENE–WSW trending regional extensional structures (Bouaziz et al. 2002), which likely favored the migration of mineralizing fluids and the eventual deposition of the Guern Halfaya and Bou Grine Pb-Zn ores. The three outlier data of Bou Grine likely suggest that remobilization of the Upper Cretaceous deposits probably occurred during the Upper Eocene.

The first known phase of halokinesis has taken place during Jurassic to Middle Cretaceous (Rouvier et al. 1985). The governing mechanisms during this phase are presumably controlled by Jurassic – Lower Cretaceous normal faults inherited from Tethyan rifting (Khomsi et

al. 2009). This rifting period and the anoxic conditions resulting from the halokinesis likely created a metallogenic trap for migrating base-metal-bearing fluids (Orgeval 1994).

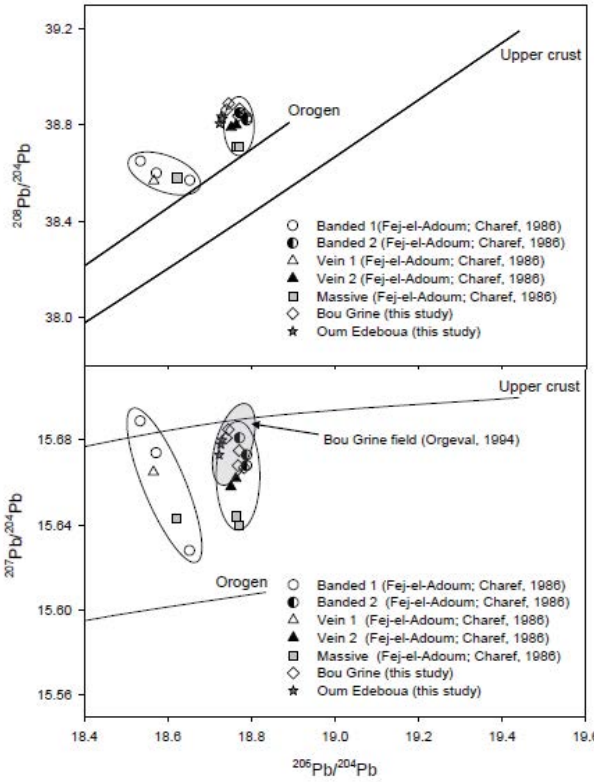

Figure 5. Plots of $^{207}Pb/^{204}Pb$ vs. $^{206}Pb/^{204}Pb$ and $^{208}Pb/^{204}Pb$ vs. $^{206}Pb/^{204}Pb$ for the Pb-Zn deposits in Oum Edeboua and Bou Grine (this study), Fedj-el-Adoum (Charef 1986) and Bou Grine (Orgeval 1994). Curves of growth trends for Pb isotope ratios are from the plumbotectonic model of Zartman and Doe (1981).

4 Conclusions

The integration of new data presented here with old literature data allow us to draw the following conclusions: 1)The observed sulfur isotope compositions of the main sulfide mineralizations at the Oum Edeboua and Bou Grine mines and the presence of bacterial relics in the Bahloul Formation indicate the contributions of bacterial reduction of sulfates in the Triassic evaporites. 2) The Pb isotope compositions of base-metal sulfides in the both mines form a homogeneous population and suggest deep-sourced metal-rich brines, which likely have been driven upward by overpressure along growth faults or margins of evaporite diapirs into the cap rock portions of these evaporite bodies. The existence of a chemical trap for mineralizing fluids located at the top of evaporite diapirs or in the contact zone between these evaporite diapirs and overlying strata could have been created by halokinesis. 3) A Cretaceous age for the mineralizations is supported by the syn-diagenetic mineralization in the Bahloul Formation and the calculated age from Pb isotopic data.

Acknowledgements

This research was funded by grants from the Tunisian Ministry of High Education and Scientific Research and from the Laboratory of Minerals Resources and Environment of the Faculty of Sciences of Tunis.

References

Bouaziz S, Barrier E, Soussi M, Turki M, Zouari H (2002) Tectonic evolution of the northern African margin in Tunisia from paleostress data and sedimentary record. Tectonophysics 357, 227-253.

Bradley DC, Leach DL (2003) Tectonic controls of Mississippi Valley-type lead–zinc mineralization in orogenic forelands. Mineralium Deposita 38, 652-667.

Charef A (1986) La nature et le rôle le des phases fluides associées à la minéralisation Pb-Zn dans les formations carbonatées et leurs conséquences métallogeniques: étude des inclusions fluides et des isotopes (H, C, O, S, Pb) des gisements des Malines (France), Jebel Hallouf-Sidi Bou Aouane et Fedj-el-Adoum (Tunisie). Thèse d'Etat, Nancy, France, 291 p.

Claypool GE, Holser WT, Kaplan IR, Sakai H, Zak I (1980) The age curves of sulfur and oxygen isotopes in marine sulfate and their mutual interpretation. Chemical Geology 28, 199-260.

Hammami M, Smati A (1993) Notes de reflexion sur les objectifs de prospection à Guern Halfaya (zone caches du flanc Est et du J. Oum Dheboua. Rapport interne, Office National des Mines, Tunis.

Jellouli C, Chikhaoui M, Braham A, Turki MM, Mickus K, Benassi R (2005) Evidence of Triassic salt domes in the Tunisian Atlas from gravity and geological data. Tectonophysics 396, 209-225.

Jemmali N, Souissi F, Villa IM, Vennemann T (2011a) Ore genesis of Pb-Zn deposits in the Nappe zone of Northern Tunisia: constraints from Pb-S-C-O isotopic systems. Ore Geology Reviews 40, 41-53.

Jemmali N, Souissi F, Vennemann T, Carranza EJM (2011b) Genesis of the Jurassic carbonate-hosted Pb-Zn deposits of Jebel Ressas (North-Eastern Tunisia): evidence from mineralogy, petrography and trace metal contents and isotope (O, C, S, Pb) geochemistry. Resource Geology 61, 367–383.

Kassaa S (1998) Pétrologie des matériaux carbonatés, sulfurés et strontianifères dans leur cadre stratigraphique, holocinétique et structural à Geurn Halfoya et au J. Boukhil (domaine des Diapirss et des Glaciers de sel Tunisie du Nord – Ouest). Thèse 3ème cycle, Fac, Sci, Tunis, 373 p.

Khomsi S, Soussi M, Mahersi C, Bédir M, Fakhfakh-Ben Jemia H, Riahim S, Bou Khalfa K (2009) New insights on the structural style of the subsurface of the Tell units in north-western Tunisia issued from seismic imaging: geodynamic implications. Comptes Rendus Geoscience 341, 347-356.

Monthel J, Lagny Ph, Orgeval JJ (1986) Inventaire des gisements et indices de la zone des Dômes de l'Atlas Tunisien et de sa bordure septentrionale. BRGM Rep 86 TUN 1127 GMX, 37 p.

Orgeval JJ (1994) Peridiapiric metal concentration: example of the Bou Grine deposit (Tunisian Atlas). In: Fontbote, L., Boni, M. (Eds.), Sediment-hosted Zn-Pb Ores. SGA Special Publication 10, Springer-Verlag, Berlin-Heidelberg, pp. 354-

Orgeval JJ, Giot D, Karoui J, Monthel J, Sahli R (1986) Le gisement de Zn-Pb de Bou Grine (Atlas tunisien). Description et historique de la drcouverte. Chronique de la Recherche Minière 485, 5-32.

Rouvier H, Perthuisot V, Mansouri A (1985) Pb–Zn deposits and salt-bearing diapirs in Southern Europe and North Africa. Economic Geology 80, 666-687.

Shmidt SC (2000) Re-activation of the Bougrine Mine, Tunisia. p. 1-9; In : Applied Geology Practice, Staffordshire University (Publisher), 2004, 700p

Stacey JS , Kramers JD (1975) Approximation of terrestrial lead isotope evolution by a two-stage model. Earth and Planetary Science Letters 26, 207-221.

Zartman RE, Doe BR (1981) Plumbotectonics—the model. Tectonophysics 75, 135-162.

Preliminary mineralogy and geochemistry of metal-rich (Mo-Ni-V-Zn) oil shale of the Carboniferous Heath Formation, Montana, USA

Karen D. Kelley, William M. Benzel
U.S. Geological Survey, Federal Center, MS 973, Denver, CO 80225, USA

Katharina Pfaff
Department of Geology and Geological Engineering, Colorado School of Mines,1516 Illinois Street, Golden, CO 80401, USA

Abstract.

Carbonaceous shales of the Cox Ranch oil shale unit in the Carboniferous Heath Formation in Montana are enriched in Ni, Mo, V, and Zn. These shales are generally thin (1.5 to 18 m thick) but laterally continuous over an area of at least 1000 km^2. Mineralogical data obtained by X-ray diffraction show that quartz, calcite, feldspar (microcline and albite), and clays are major constituents, accompanied by minor to trace amounts of pyrite, apatite, goethite, and sphalerite. Clay minerals are predominantly smectite (33-40%) and illite (1.3 to 4%), although minor kaolinite may be present. QEMSCAN analyses of the oil shale unit indicate that total porosity ranges from 4 to 18% and organic matter from 3 to 33%. New bulk geochemical data from seven drill holes show that Ni, Mo, V, and Zn contents are strongly correlated with total organic carbon (TOC), and correlations between these metals and sulphur are prominent. Low S/C ratios and low Fe contents may suggest that organically bound sulphur was an important component of the rocks. Both XRD and QEMSCAN analyses indicate that Zn is contained mainly in sphalerite. Exact metal residences for V, Ni, and Mo are unresolved, but geochemical correlations and mineralogical analyses suggest that smectite, organic matter, or pyrite (for some Ni), are all important host phases.

Keywords. Black shale, metalliferous oil shale, Mo-V-Ni-Zn enrichments, Heath Formation, Montana

1 Introduction

Black shales have been of increasing interest in recent years due to their oil and gas potential, but also because many are enriched in metals such as Co, Cr, Mo, Ni, platinum group elements (PGE), Re, U, and V. Nickel (+Cu-Zn-Co) are currently being mined from organic carbon-rich, fine-grained sedimentary rocks at the Kuusilampi and Kolmisoppi deposits (Talvivaara mine) in Finland (Jowitt and Keays 2011), following development of a bioheapleach method for extracting the metals (Mining-Technology 2012). The Alum Shale in Sweden has high contents of hydrocarbons and high concentrations of U, V, Ni, and Mo; small amounts of V were produced during World War II, and U was produced sporadically in the 1950s and 1960s (Dyni 2005). Oil shale near Julia Creek in west central Queensland, Australia, currently is being considered for development of V and Mo (Lewis et al. 2010). In the U.S., phosphatic ores in carbonaceous shales of the Phosphoria Formation contain recoverable amounts of V (McKelvey et al. 1986), which until 1999, produced approximately 2000 t of vanadium pentoxide annually from ferrophosphorus slag generated from the reduction of phosphate to elemental phosphorous (Jasinski 2004). The Gibellini project in Nevada is currently being developed to produce vanadium. The oxidized portion of the shale containing the highest V contents is the proposed ore for mining (American Vanadium 2011).

Another prospective area for V-, Mo-, and Ni-rich shales in the U.S. is the Upper Mississippian Heath Formation in central Montana (Fig. 1). In 1982, the Montana Bureau of Mines conducted exploratory drilling that included over 366 m of core. Lithologic descriptions and selected chemical analyses were reported by the Montana Bureau of Mines (Derkey et al. 1985) and the U.S. Geological Survey (Desborough et al. 1981; Desborough and Poole 1983), but questions remain about processes of metal concentration, and detailed information on the distribution and residence of the metals is lacking. This study evaluates how metal contents vary with lithological facies, and addresses the mineralogical residence of specific elements. We present here new geochemical analyses of samples from seven drill holes, supplemented by preliminary mineralogical data based on X-ray diffraction and automated mineralogy and QEMSCAN (quantitative evaluation of minerals by scanning electron microscopy) analyses in order to constrain the processes of metal enrichment.

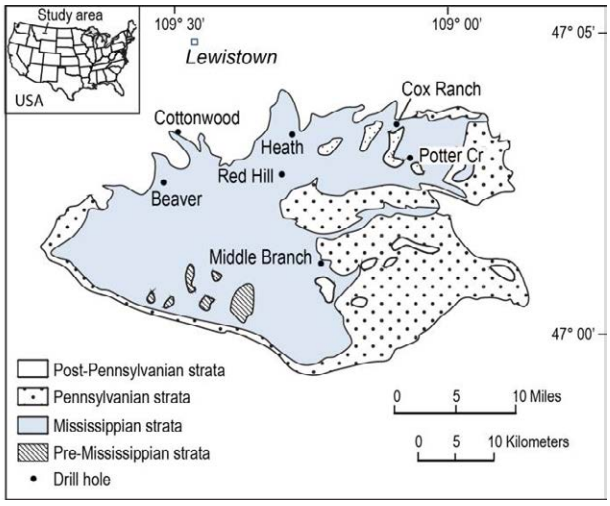

Figure 1. Map showing the distribution of Mississippian strata (including Heath Fm) in central Montana (from Derkey et al. 1985). Locations of drill holes are indicated.

2 Geology and Mineralisation

In Fergus County, Montana, the Upper Mississippian Heath Formation occurs in an east-trending belt about 40 km long by 25 km wide (Fig. 1). Strata were deposited on the cratonic platform in an east-trending marine embayment known as the Big Snowy trough. The formation reaches a maximum thickness of 120 m along the trough axis, but thins abruptly toward the northern and southern trough margins (Smith and Gilmour 1979).

The organic- and metal-rich portions occur within the Forest Grove member of the Heath Formation. From base to top, this member consists of a coal marker bed; calcareous and noncalcareous, fossiliferous dark-gray to black shales and mudstones containing a metal-rich oil shale zone termed the Cox Ranch oil shale unit; a gypsum marker bed; and limestone (Derkey et al. 1985). Claystones and siltstones are minor yet conspicuous components of the unit. The Cox Ranch oil shale unit ranges from 1.5-18 m thick and can be correlated in all 7 drill holes. Within the Cox Ranch drill hole, two additional metal- and organic-rich mudstone/shale intervals occur, one below the Cox Ranch oil shale unit and another approximately 60-65 m above the unit, but these intervals are not laterally continuous.

The Heath Formation is a thermally immature to early mature unit that has been known for decades as a metalliferous subeconomic oil-shale resource (Derkey et al. 1985; Desborough and Poole 1983) and recently has received attention as a possible tight oil resource play (McClave 2012). New advances in extracting metals from such shales (Gahan et al. 2012) make it attractive as a possible future resource for these metals.

3 Methods

Whole rock samples from 7 drill holes were collected by Barney Poole (USGS) in the early 1980s. These were reanalysed using multiple techniques. Major and trace elements were determined by (a) X-ray fluorescence and ICP-AES-MS after sodium peroxide fusion; (b) automated LECO analyser (total S); and (c) carbonate carbon (coulometric titration) subtracted from total carbon (analysed by combustion/infrared detection) to obtain total organic carbon (TOC). Standards (Ohio Shale SDO-1) were run to monitor accuracy. Select samples from the metalliferous zones (Red Hill and Cox Ranch drill holes) were analysed by XRD at the U.S. Geological Survey. Polished thin sections were studied using QEMSCAN analysis at the Colorado School of Mines, which is an automated quantitative mineralogical instrument that utilizes an electron-beam platform with four energy dispersive X-ray spectrometers to produce mineral maps from backscatter electron signals and energy dispersive spectrometer spectra.

4 Results

4.2 Mineralogy

Preliminary quantitative XRD analysis of the Cox Ranch oil shale unit (n=3) identified quartz, calcite, microcline, albite, and clays as major constituents, accompanied by minor to trace pyrite, goethite, apatite, and sphalerite. Quartz and calcite are abundant (20 to 35% and 13 to 26%, respectively). Clay minerals are predominantly smectite (33-40%) and illite (1.3 to 4%) with minor kaolinite detected in one sample.

QEMSCAN analysis of the Cox Ranch oil shale unit indicates that total porosity ranges from 4 to 18% and organic matter from 3 to 33%. Modal mineral abundances are consistent with results from XRD analyses. Mineral associations determined by high resolution scans suggest that most of the Ni and V is associated with either clays (e.g., the sample with 3% organic matter) or organic matter. Some high Ni concentrations are also associated with pyrite. Zinc resides primarily in sphalerite. In core, sphalerite is present between shale partings and in one example, forms a single ~3 mm crystal.

4.1 Geochemistry

Basic statistics for geochemical data on bulk samples of shale/mudstone are shown in Table 1. Some samples contain thin limestone interbeds and/or accumulations of fossil shells, and thus have high CaO contents. Variable Al_2O_3 and K_2O contents most likely reflect different proportions of clay minerals (illite/smectite). Concentrations of total organic carbon (TOC) display a large range with values as high as 28% (Table 1).

Table 1. Basic statistics for selected geochemical data for shales/mudstones of the Heath Formation (n = 58)

	Min	Max	Mean
SiO_2 (%)	26.3	68.2	47.9
Al_2O_3 (%)	4.9	25.7	14.6
CaO (%)	0.32	23.4	6.4
K_2O (%)	0.76	3.48	1.93
P_2O_5 (%)	0.03	1.5	0.3
TOC (%)	0.34	27.9	5.0
S (%)	0.13	4.69	1.7
Au (ppb)*	<1	7.0	2.6
Co (ppm)	4.1	80.7	17
Cr (ppm)	70	700	190
Cu (ppm)	10	163	43
Mn (%)	0.01	0.3	0.04
Mo (ppm)	<2	1,590	103
Ni (ppm)	34	509	115
Pb (ppm)	7.0	162	24
Pt (ppb)*	1.3	11.4	2.7
Pd (ppb)*	<1	10	4.7
Sb (ppm)	0.5	55	8.0
Tl (ppm)	<0.5	19	2.9
U (ppm)	2.13	67	14
V (ppm)	69	1,980	387
Y (ppm)	18	89	33
Zn (ppm)	16	5,140	598

*, Au, Pt, and Pd analysed in Cox Ranch and Red Hill drill holes only (n=32)

Downhole geochemical trends are broadly similar for all seven drill holes; the Cox Ranch hole is used for illustrative purposes (Fig. 2). All holes show extreme TOC values (>10%) associated with the Cox Ranch oil shale unit. TOC values peak in two additional stratigraphic intervals in the Cox Ranch drill hole: one is

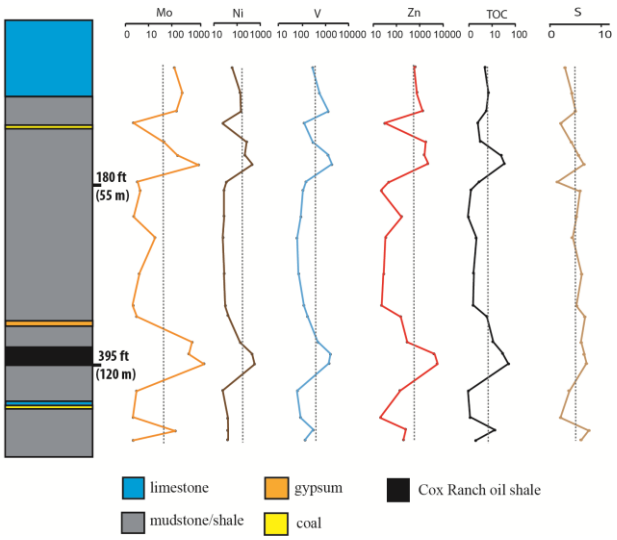

Figure 2. Lithologies of the Cox Ranch drill hole (modified from Derkey et al. 1985) showing downhole geochemistry. Mo, Ni, V, and Zn are in parts per million (ppm); TOC and S are in percent. Vertical gray dashed lines illustrate 90th percentile values.

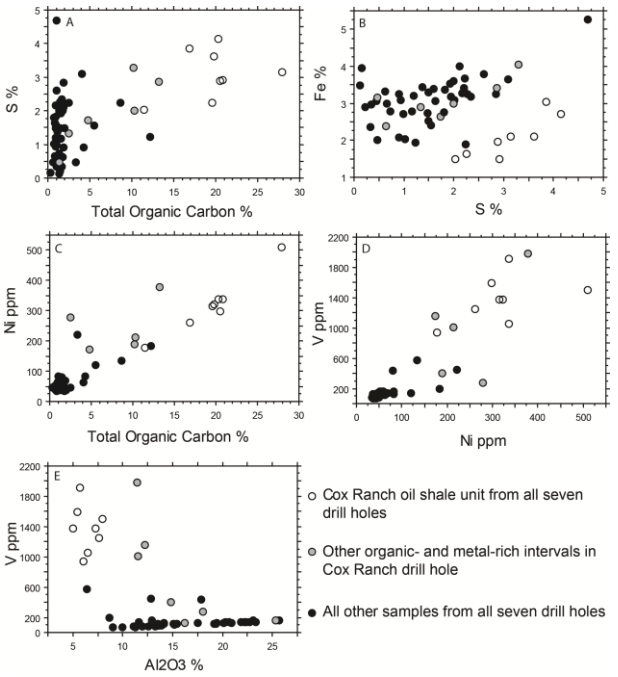

Figure 3. Bivariate plots showing element concentrations for Cox Ranch oil shale, other organic-rich intervals in the Cox Ranch drill hole, and other samples of shale/mudstone for all seven drill holes; A, Sulphur versus TOC; B, Fe versus S; C, Ni versus TOC. Similar plots for Mo, Zn, and V versus TOC are not shown; D, V versus Ni; and E, V versus Al_2O_3.

near the base (single sample) and another is approximately 60-65 m above the Cox Ranch oil shale unit (Fig. 2). In between the upper two anomalies, TOC values are generally low (<2%).

The highest concentrations of Mo (up to 1,590 ppm), Ni (509 ppm), V (1,980 ppm), and Zn (2,950 ppm) are associated with high TOC values in all three organic-rich intervals (Fig. 2). Total sulphur concentrations are also high (>2%) within these stratigraphic intervals. Metals that show the greatest range in concentration are Mo and Zn (Table 1; Fig. 2).

Bivariate plots (Fig. 3) and correlation coefficients between elements provide insights into metal associations and metal residence. Two principal trends in S/C ratios are evident. Within the Cox Ranch oil shale and other high TOC intervals, S/C ranges from 0.07 to 0.19 (Fig. 3A), whereas low TOC intervals display much higher S/C ratios of 0.1 to 3.6. This bimodal expression of S/C is reflected by two distinct Fe/S populations (Fig. 3B), suggesting preferential incorporation of S into the organic matter of the Cox Ranch oil shale. Vanadium, Ni, Mo, and Zn are all strongly correlated with organic carbon (r>0.78) (Fig. 3C). Vanadium and nickel also strongly covary, particularly in the Cox Ranch oil shale samples (Fig. 3D). P_2O_5 and Y are strongly correlated with each other (r=0.84) (not shown on Fig.), suggesting that Y resides in the apatite identified by mineralogical analysis.

A good linear relationship exists between increasing V and Al_2O_3 contents in shales/mudstones outside of the Cox Ranch oil shale unit; this contrasts with V to Al_2O_3 ratios of the Cox Ranch oil shale samples that show enrichments in vanadium (Fig. 3E).

5 Discussion

Previous hypotheses regarding the origin of unusually high concentrations of Mo, Ni, V, and Zn in black shales include (1) syngenetic, with metals sourced either from the water column (Breit and Wanty 1991; Piper 1994), hydrothermal fluids including brines (e.g., Coveney and Glascock 1989) or petroleum-rich fluids venting onto the seafloor (Emsbo et al. 2005); (2) diagenetic (Vine and Tourtelot 1970); (3) a combination of syngenetic and remobilized with metal concentrations produced during diagenesis, oxidation, and weathering (Lewis et al. 2010; Coveney et al. 1987); and (4) epigenetic meteoric fluids and/or supergene enrichment processes (Coveney et al. 1987).

Metal residences in black shale deposits are varied. Metals may occur in sulphides, as in the Kuusilampi and Kolmisoppi Ni-Cu-Zn-Co deposits in Finland (Jowitt and Keays 2011), or be concentrated in organic matter and redistributed into new phases by diagenesis (e.g., clays) and/or oxidation (goethite, metahewettite) during weathering (Lewis et al. 2010; American Vanadium 2011). Our preliminary mineralogical studies on rocks from the Heath Formation suggest that sulphides, organic matter, and clay minerals all may be important sites of metal residence. For example, most zinc is contained in sphalerite, and Fe and some Ni reside in pyrite. Specific hosts for V, Mo, and most Ni are unresolved, but element correlations and preliminary QEMSCAN analysis indicate these metals are associated mainly with organic carbon (or organically bound sulphur) and/or smectite.

Cox Ranch oil shales have low S/C ratios (<0.19) (Fig. 3A) and generally low Fe contents (mostly <3%; Fig. 3B), suggesting an iron-limited environment. Vanadium-rich carbonaceous rocks worldwide typically have low S/C ratios, and most are interpreted to have had high H_2S

concentrations in pore waters (Breit and Wanty 1991). Such iron-limited conditions promote high contents of organically-bound sulphur, because iron normally buffers H_2S activity to low values by forming iron sulphide minerals (Canfield 1989).

The association between metals and organic carbon may reflect either affinity for organic matter or favorable conditions that preserve organic matter and partition metals into the sediment (Breit and Wanty 1991). For example, clays within the organic-rich rocks could have facilitated accumulation and burial of organic matter (as suggested by Kennedy et al. 2002; 2006) that in turn favored deposition and preservation of metals.

The preliminary QEMSCAN studies suggest that some of the V and Ni are associated with clays (samples with low organic matter). Owing to the low thermal maturity of the Heath Formation (Derkey et al. 1985), smectite is the predominant clay mineral and metal host. Metal residence in clays may be variable. For example, a range of clay sites having differing binding attributes for V and Mo were determined for the Julia Creek deposit (Lewis et al. 2010). Assuming that future extraction of metals through bioleaching or other techniques will become increasingly important in the future (e.g., Gahan et al. 2012), metal residence studies are thus essential.

6 Conclusions

Our preliminary evaluation of the distribution of metals and mineralogical analyses of the Heath Formation is a first step towards better understanding the effects of geochemical processes on metal transport and accumulation. The current interest in, development of, and mining of Ni, Mo, and V from black shales worldwide suggests that such deposits will become increasingly prospective for exploration. For this to proceed, a detailed understanding of the formation of, and host mineral phases for Mo, Ni, V, and other metals is critical to facilitate metal extraction. The Heath Formation oil shale potentially has metals residing in sulphides, in association with organic carbon, and substituting in clay minerals. The presence of pyrite and sphalerite suggests sulphide residence for Zn and Fe (and minor Ni). The V and Al_2O_3 correlation suggests that V is fixed in clays for all samples except for those from the Cox Ranch oil shale unit. In this latter unit, the strong correlations between Ni and V, Ni and organic carbon, and S and organic carbon suggest metal residence in sulphide minerals or organically-bound sulfur complexes. Additional planned mineralogical studies should provide insights into precipitation mechanisms and metal distributions.

Acknowledgements

Barney Poole provided powders of drill cores from the Heath Formation for analysis, and helpful background information on the geochemical work done on the Heath Formation in the early 1980s. Comments from George Breit and Clint Scott (USGS) on an early version of the paper and review comments by John Slack and Robert Eppinger greatly improved the paper.

References

American Vanadium, Ltd. (2011) Gibellini: http://www.americanvanadium.com/gibellini-project.php

Breit GN, Wanty RB (1991) Vanadium accumulation in carbonaceous rocks: a review of geochemical controls during deposition and diagenesis. Chem Geol 91:83-91

Canfield DE (1989) Reactive iron in marine sediments. Geochim Cosmochim Acta 53:619-632.

Coveney RM Jr, Leventhal JS, Glascock MD, Hatch JR (1987) Origins of metals and organic matter in Mecca Quarry shale and stratigraphically equivalent beds across the Midwest: Econ Geol 82:915-933

Coveney, RM Jr, Glascock MD (1989) A review of the origins of metal-rich Pennsylvanian black shales, central U.S.A., with an inferred role for basanal brines. Applied Geochem 4:347-367

Derkey PD, Abercrombie FN, Vuke SM, Daniel JA (1985) Geology and oil shale resources of the Heath Formation, Fergus County, Montana. Mont Bur Mines Geol Memoir 57, 100 pp

Desborough GA, Poole FG, Green GN (1981) Metalliferous oil shales in central Montana and northeastern Nevada. US Geol Survey Open File Rep 81-121, 14 pp

Desborough GA, Poole FG (1983) Metal concentrations in some marine black shales of the United States. In Shanks WC (ed) Cameron volume on unconventional mineral deposits: New York, Soc Mining Eng, pp. 99-110

Dyni JR (2006) Geology and resources of some world oil-shale deposits. US Geol Survey Sci Inv Rep 2005-5294, 49 pp

Emsbo P, Hofstra AH, Johnson CA, Koenig A, Grauch R, Zhang X, Hu R, Su W, Pi D (2005) Lower Cambrian metallogenesis of South China: interplay between diverse basinal hydrothermal fluids and marine chemistry. In Mao J, Bierlein FP (eds) Mineral Deposit Research, Meeting the Global Challenge: Proc Eighth Biennial SGA Mtg, Beijing, China, 18–21 August 2005, pp 115-118

Gahan CS, Srichandand H, Kim D, Akcil A (2012) Biohydrometallurgy and biomineral processing technology: a review on its past, present and future. Res J Recent Sci 1(10):85-99

Jasinski SM (2004) Societal relevance, processing, and material flow of western phosphates - refreshments, fertilizer, and weed killer. In Hein JR (ed) Life cycle of the Phosphoria Formation from deposition to the post-mining environment. Handbook of Exploration and Environ Geochem 8:599-610, Elsevier

Jowitt SM, Keays RR (2011) Shale-hosted Ni-(Cu-PGE) mineralization: a global overview. Trans Applied earth sci 120:187-197

Kennedy MJ, Pevear DR, Hill RJ (2002) Mineral surface control of organic carbon in black shale. Science 295:657-660

Kennedy MJ, Droser M, Mayer LM, Pevear D, Mrofka D (2006) Late Precambrian oxygenation: inception of the clay mineral factory. Science 311:1446-1449

Lewis SE, Henderson RA, Dickens GR, Shields GA, Coxhell S (2010) The geochemistry of primary and weathered oil shale and coquina across the Julia Creek vanadium deposit (Queensland, Australia). Miner Deposita 45:599-620

McClave G (2012) Heath Formation of central Montana: a new tight oil resource play? AAPG #90156. Rocky Mountain Sec Mtg. Grand Junction, Colo, September 2012

McKelvey VE, Strobell JD, Slaughter AL (1986) The vanadiferous zone of the Phosphoria Formation in western Wyoming and southeastern Idaho: US Geol Survey Prof Paper 1465, 27 pp

Mining-Technology (2012) Talvivaara, Finland: http://www.mining-technology.com/projects/talvivaara/

Piper DZ (1994) Seawater as a source of minor elements in black shales, phosphorites and other sedimentary rocks. Chem Geol 114:95-114

Smith DL, Gilmour EH (1979) The Mississippian and Pennsylvanian (Carboniferous) Systems in the United States – Montana: US Geol Survey Prof Paper 1110-X:X1-X32

Vine JD, Tourtelot EB (1970) Geochemistry of black shale deposits – A summary report. Econ Geol 65:1469-1478

Trace elements in sedimentary pyrite through time; application to understanding temporal changes in ocean oxygenation and ore deposit cycles in marine basins

Ross R Large, Dan Gregory, Jacqueline Halpin, Leonid Danyushevsky, Elena Lounejeva, Jeff Steadman
CODES ARC Centre of Excellence, University of Tasmania, Private Bag 126, Hobart, Tasmania, Australia.

Valeriy Maslennikov
Institute of Mineralogy, Urals Branch, Russian Academy of Science

Timothy Lyons
University of California, Riverside, CA, USA

Bradley Guy
SGS South Africa, Johannesburg, South Africa

Arthur Hickman
Geological Survey of Western Australia, Perth, Western Australia

Clive Calver
Mineral Resources Tasmania, Hobart, Tasmania

Abstract. This research outlines a new and innovative method to determine variations in the trace metal content of the oceans through time, by LA-ICPMS analysis of sedimentary pyrite in black shales from early Archean to present day. The oceans are a significant source of metals that can inform us about economic accumulations in sedimentary basins; in particular of gold, iron, zinc, copper and uranium. Preliminary research shows that certain metals (e.g. Ni, Co, Cu and Au) have generally decreased in the oceans through time whereas other metals (e.g., Mo, Se and Zn) have generally increased. These changes appear to be controlled by many factors including; 1) residence times of the metals in the ocean, 2) gradual oxygenation of the Earth's atmosphere /oceans, 3) the composition of exposed crustal rocks 4) seafloor hydrothermal activity, and 5) cycles of ocean anoxia. This preliminary work also shows links between temporal curves of trace metals in the ocean and cycles of major metal accumulations of banded iron formations, sedex Zn-Pb-Ag, stratiform Cu and sediment-hosted gold (including Carlin-type) deposits. The advantages of measuring trace elements in sedimentary pyrite, rather than whole-rock shales, to develop ocean proxies are; 1) pyrite concentrates most of the elements of interest well above the whole rock value, 2) pyrite can be analysed by LA-ICPMS to very low detection levels, giving both maximum and minimum values, 3) pyrite is one mineral, rather than a mix of minerals, and thus does not require normalisation by another element, and 4) petrography and etching of pyrite, prior to analysis, provides information on metamorphic and hydrothermal effects.

Keywords. Trace elements, pyrite, oceans, atmosphere oxygenation, ore deposits

1 Introduction

Over the past five years CODES has been compiling a database on the chemistry of sedimentary pyrite in black shales through time, from the Paleoarchean to Holocene. We currently have samples from black shales in over 40 locations world wide, from both mineralised basins and barren basins. Pyrite in the shales has been analysed by LA-ICPMS for up to 25 elements, after textural screening to eliminate effects of metamorphism and hydrothermal activity. The results are very exciting and indicate a number of potential applications.

Firstly the data indicate that sedimentary pyrite is a good proxy to track changes in trace element chemistry of the oceans through time. We can tell during what periods the oceans were enriched in certain metals and periods when they were depleted in certain metals. These changes are probably related to atmosphere oxygenation, volcanic activity, supercontinent cycles and trace element residence times in the ocean, and are likely to have a major influence on evolution and extinction of marine species.

The data can also be interpreted to provide an improved curve for temporal variations in oxygenation of the atmosphere and oceans. Many workers have previously recognised the importance of oxygenation in controlling ore deposit cycles (e.g. Groves et al., 2006; Farquhar et al., 2010), especially for basin-hosted ores such as banded iron formations (Holland, 1973; Bekker et al., 2010), Manganese (Maynard, 2010), sedex Zn-Pb-Ag deposits (Lyons et al; 2006; leach et al., 2010), MVT deposits (Kesler and Reich, 2006), stratiform copper deposits (Hitzman et al., 2010), uranium deposits (Cuney, 2010) and gold deposits (Minter, 2006).

On the individual basin scale, the data may be used to predict the stratigraphic level in the basin that is most

favourable for ore deposit formation, and in many cases may provide a halo/vector tool for improved targeting. A combination using the chemistry of both sedimentary pyrite and sedimentary carbonate through the basin stratigraphy has great potential.

2 Tracking Ocean Chemistry by Using Sedimentary Pyrite

During the growth of sedimentary pyrite, both in the water column and in seafloor muds, trace elements dispersed in the seawater and sediment pore waters are adsorbed onto the active charged pyrite surface and become incorporated into the sedimentary pyrite structure. The abundance of trace elements in sedimentary pyrite is commonly in the order; As (commonly 1,000's ppm), Ni, Co, Cu, Mn (100's to 1,000's ppm), Zn, Pb, Sb (100's ppm), Mo, Se, (10's to 100's ppm), Bi, Tl, Ag, Te (1's to 10's ppm) and Au (0.001 to 2 ppm). Our work suggests that if there are more trace elements (TE) in the seawater, then more end up in the pyrite, and conversely if there are less TE in seawater, then the pyrite is depleted in TE. There are other factors that may control incorporation of TE into sedimentary pyrite, but based on our assessment so far, they appear to be second order effects compared to seawater TE concentration.

This simple relationship between sedimentary pyrite TE and seawater TE enables us to track TE in seawater through time using high quality LA-ICPMS analyses of syngenetic and diagenetic pyrite, coupled with high quality black shale dating methods. Only pyrite from below mid-greenschist facies of metamphism can be used, as at higher metamorphic grades TE are lost from pyrite (Pitcairn et al., 2007).

Our research results on the 40 well-dated pyritic black shales indicate that most trace elements vary in systematic, although different, patterns through time, with surprisingly wide variations from 2 to 5 orders of magnitude. For example Mo varies from 0.1 to 1000 ppm and Co from 1 to 5000 ppm in sedimentary pyrite.

The contrasting global curves for Ni and Mo in sedimentary pyrite are shown in Fig. 1, as examples. Each dot in Fig. 1A represents a Ni analysis and includes over 1300 analyses of sedimentary pyrite in over 40 black shale units. The 19-point moving average of the data for Ni is given in Fig.1B. A moving average is employed to smooth the trends and enhance the long term, rather than short-term variations. The pattern overall shows a decrease in Ni in pyrite, representing a decrease in the Ni content of coeval seawater through time. In more detail, Ni is very high in Archean pyrite (up to 2 wt% Ni), dropping toward the Archean-Proterozoic boundary and then remaining relatively flat around 1000 ppm Ni through the Proterozoic (but with two troughs centred on 1500 Ma and 750 Ma). In the Phanerozoic Ni is highly variable, a feature of many trace elements over this period. This variation appears to relate to supercontinent cycles, LIP events and periods of ocean anoxia. The very elevated Ni values in the Archean probably relate to predominance of nickeliferous komatiites contributing high levels of Ni to the early Archean oceans (Konhauser et al., 2009).

Molybdenum shows the reverse trend to Ni, increasing from less than 1 ppm in the early Archean, to 10 to 20 ppm through the Proterozoic, and then stepping up again to range from 10 to 1000 ppm through the Phanerozoic. Molybdenum is unusual as it forms a stable soluble molybdate $MoO_4^{=}$ complex in seawater with a very long ocean residence time. Increasing oxygenation since the Archean, has contributed to increasing Mo to the oceans (Scott et al., 2008), which has built up over time as recorded by the sedimentary pyrite. The effects of the Great oxidation Events (GOE 1 and GOE 2) are shown by the jumps in Mo at around 2500 Ma and 650 Ma (Fig. 1). As with Ni, Mo is highly variable in the Phanerozoic compared with the Precambrian.

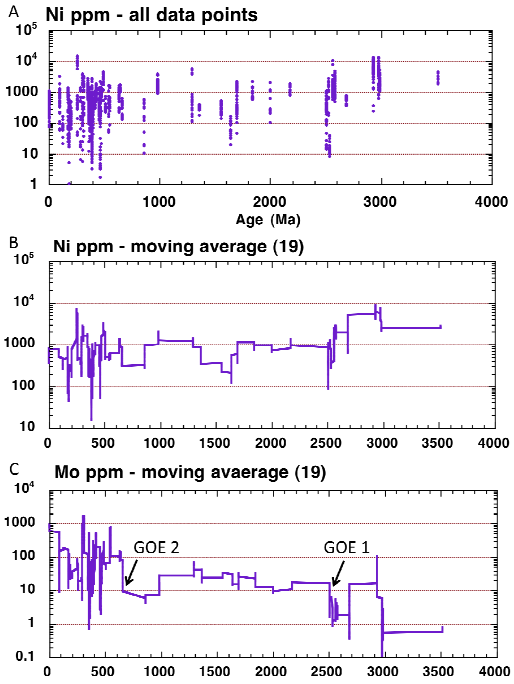

Figure 1. Variation in Ni and Mo in sedimentary pyrite from 40 globally dispersed black shales. In general terms Ni decreases and Mo increases through time.

3. Se Content of Sedimentary pyrite; a New Proxy for Ocean Oxygenation

Selenium substitutes for sulfur in pyrite and is tightly held in the structure, unlike many loosely held trace elements (e.g. Cu, Pb, Zn, Mo, Te, Ag) (Large et al., 2007; 2009). The dominant crustal source of Se is pyrite, and during oxidative continental weathering Se is released from pyrite as $SeO3^{=}$ and $SeO_4^{=}$, in a similar way that S is released as the sulfate species. Thus increased oxidative weathering leads to increased amounts of Se, S (and Mo) being released to the oceans. Se has a moderate residence time in the oceans (26,000 yrs compared to 800,000 yrs for Mo), but sufficient to cause ocean homogenisation before the Se becomes locked into sedimentary pyrite in sub-oxic to euxinic

muds on the seafloor. Thus, in a similar way to Mo, changes in Se in sedimentary pyrite, have the capacity to act as a proxy for atmosphere and ocean oxygenation. Our global curve for Se in sedimentary pyrite is shown in Fig. 2, where the positions of GOE1 and GOE2 are clearly shown by step changes in Se in sedimentary pyrite.

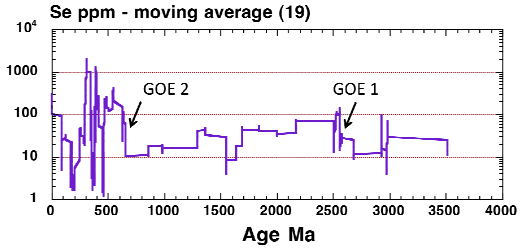

Figure 2: Se in sedimentary pyrite from 40 global black shales; 19 point moving average. GOE1 and GEO2 correspond to steps in Se. The downward trend in Se through the Proterozoic suggests a gradual decrease in atmosphere and ocean oxygenation reaching a minimum at 850-650 Ma, before rising abruptly at GEO2.

In detail the Se and Mo in pyrite proxy curves for atmosphere oxidation (Figs 1 and 2) tell a somewhat different story to that currently in the literature (e.g., Holland 1984, Canfield 1998, Scott et al., 2008).

- The rise in pyrite Se and Mo related to GOE1 is at 2550 to 2500 Ma, rather than the generally accepted 2450 to 2300 Ma
- Spikes in Se and Mo occur much earlier at 3000 to 2900 Ma, suggesting a spurt of oxygenation in the Mesoarchean. This is followed by a period of de-oxygenation (2700 to 2550 Ma) prior to GOE1.
- The Mo pyrite curve for the Proterozoic can be interpreted to indicate a gradual, but small, rise in oxygen to 1000 Ma. However the Se pyrite curve suggests a decrease in oxygen though the Proterozoic to 650 Ma. This is a critical issue to resolve.
- Both Se and Mo in pyrite show a sharp rise around 700 to 600 Ma (GOE2), followed by rapid cycles of oxygenation and de-oxygenation through the Phanerozoic.

4. Atmosphere-Ocean Oxygenation and Ore Deposit Cycles

Understanding the oxygenation of the Earths atmosphere and oceans over the past four billion years is critical to developing better models for the evolution of the atmosphere, life on Earth and ore deposit cycles.

The oxygenation of basinal hydrothermal fluids (or fluid fo_2) has a dominant control on metal transport in sedimentary basins. For example we know that, for sedimentary basins: 1) uranium is best transported in highly oxidised fluids, 2) copper is best transported by moderately oxidised fluids, 3) zinc is transported by both weakly oxidised and weakly reduced fluids, 4) iron is best transported by reduced fluids, and 5) gold is best transported by strongly reduced fluids.

Although there are a number of geological factors that promote ore deposit formation in sedimentary basins, in very simple terms we may speculate, from a geochemical perspective, that:

- the predominance of basin-hosted gold deposits in the Archean and early Proterozoic relates to a reduced atmosphere and oceans, that promoted gold transport (as the $Au(HS)_2^-$ complex) by reduced fluids circulating in reduced basin sediments. Basin-hosted gold deposits are only concentrated in the Phanerozoic during periods of ocean anoxia (Large et al., 2011).
- Banded iron formations are developed under conditions of increasing atmospheric oxygenation related to GOE1 and GOE2 (Holland, 1973). Under these conditions the soluble Fe^{2+} in the oceans converts to less soluble Fe^{3+} and precipitates Fe oxyhydroxides at continental margins to form BIF's. The spurt of oxygenation indicated by our data around 3000 Ma (Fig. 2), may explain the BIFs developed in the Pilbara and Witwatersrand basins around this time.
- VHMS deposits that form by circulation of reduced H_2S-bearing fluids, developed on the seafloor during periods of low oxygen ocean cycles throughout the Archean, Proterozoic and Phanerozoic.
- Major sedex zinc deposits formed under intermediate ocean oxygenation, but high basin salinity, during the mid Proterozoic and certain periods of the Phanerozoic (Cooke et al., 2000).
- Sediment-hosted copper deposits required periods of increased basin sediment oxygenation and salinity to promote Cu transport; rapidly followed by periods of de-oxygenation and ocean anoxia, that favoured copper sulfide precipitation during diagenetic replacement of carbonaceous shales.

5. References

Bekker A, Slack JF, Planavsky N, Krapez B, Hofmann A, Konhauser KO, Rouxel OJ (2010) Iron Formation; the sedimentary product of a complex interplay among mantle, tectonic, oceanic and biospheric processes: Economic Geology, 105:467-508

Canfield DE (1998) A new model for Proterozoic ocean chemistry: Nature, 396:450-453

Cooke DR, Bull SW, Large RR, McGoldrick PJ (2000) The importance of oxidized brines for the formation of Australian Proterozoic stratiform sediment-hosted Pb-Zn (sedex) deposits: Economic Geology 95:1-17

Cuney, M., 2010, Evolution of uranium fractionation processes through time: driving the secular variation of uranium deposit types: Economic Geology, 105, 53-570.

Farquhar, J., Wu, N., Canfield, D.E. and Oduro, H., 2010, Connections between sulfur cycle evolution, sulfure isotopes, sediments and base metal sulfide deposits: Economic Geology, 105, 509-534.

Hitzman, M.W., Selley, D. and Bull, S., 2010, Formation of sedimentary rock-hosted stratiform copper deposits through Earth history: Economic Geology, 105, 627-640.

Holland, H.D., 1973, The oceans, a possible source of iron in iron formations: Economic Geology, 68, 1169-1172.

Holland, H.D., 1984, The chemical evolution of the atmosphere and oceans: New York Princeton University Press, 582.

Kesler, S.E. and Reich, M.H., 2006, Precambrian Mississippi Valley-type deposits: Relation to changes in the composition of hydrosphere and atmosphere: Geological Society of America Memoir 198, 185-204.

Large R.R., Bull S.W. and Maslennikov, V.V., (2011) A carbonaceous sedimentary source-rock model for Carlin-type and orogenic gold deposits: Economic Geology, 106, 331-358.

Large R.R., Danyushevsky, L.D., Hollit C., Maslennikov V.V., Meffre S., Gilbert S., Bull S., Scott R., Emsbo P., Thomas H., Singh R. and Foster J., 2009, Gold and Trace Element Zonation in Pyrite using a Laser Imaging Technique; Implications for the Timing of Gold in Orogenic and Carlin-Style Sediment-Hosted Deposits: Economic Geology, 104, 635-668.

Large R.R., Maslennikov, V.V., Robert, F., Danyushevsky, L.V. and Chang, Z., 2007, Multistage sedimentary and metamorphic origin of pyrite and gold in the giant Sukhoi Log deposit, Lena gold province, Russia: Economic Geology, 102, 1233-1267.

Leach, D.L., Bradley, D.C., Huston, D.L., Pisarevsky, S.A., Taylor, R.D. and Gardoll, S.J., 2010, Sediment-hosted lead-zinc deposits in Earth history: Economic Geology, 105, 593-626.

Lyons, T.W., Gellatly, A.M., McGoldrick, P.J. and Kah, L.C., 2006, Proterozoic sedimentary Exhalative (SEDEX) deposits and links to global ocean chemistry: Geological Society of America Memoir 198, 169-184.

Maynard, J.B., 2010, The chemistry of manganese through time: a signal of increasing diversity of earth-surface environments: Economic Geology, 105, 535-552.

Minter, W.E.L., 2010, The sedimentary setting of Witwatersrand placer mineral deposits in the Archean atmosphere: Geological Society of America Memoir 198, 105-120.

Pitcairn, I. K., Teagle, D. A. H., Craw, D., Olivo, G., Kerrich, R., and Brewer.T.S, 2006, Sources of metals and fluids in orogenic gold deposits; Insights from the Otago and Alpine Schists, New Zealand: Economic Geology, 101, 1525-1546.

Scott, C., Lyons, T.W., Bekker, A., Shen, Y., Poulton, S.W., Chu, X. and Anbar, A.D., 2008, Tracing the stepwise oxygenation of the Proterozoic ocean: Nature, 452, 456-459.

A genesis model for the black shale-hosted polymetallic Ni-Mo-(PGE-Au) sulfides in south China: application of Mo isotopes

Lingang Xu, Jingwen Mao
MLR Key Laboratory of Metallogeny and Mineral Assessment, Institute of Mineral Resources, Chinese Academy of Geological Sciences, Beijing 100037, China

Bernd Lehmann
Mineral Resources, Technical University of Clausthal, 38678 Clausthal-Zellerfeld, Germany

Abstract. The Early Cambrian Niutitang Formation in South China consists of a black shale sequence with a synsedimentary organic carbon-rich polymetallic sulfide layer with extreme metal enrichment locally mined as Ni-Mo-(PGE-Au) ore. Although the mine sites of polymetallic sulfide ore are geographically several hundred kilometres apart, they have highly similar field geological features and geochemical compositions. The polymetallic sulfide ores have consistently heavy $\delta^{98/95}$Mo values of 0.94 to 1.38‰ (avg. 1.13 ±0.14‰, 1σ, n = 11), and the host black shale and phosphorite have slightly more variable $\delta^{98/95}$Mo values of 0.81‰ to 1.70‰ (n = 14). Microscopic study indicates that the sulfide ores show both nodular and laminated texture. In combination with Mo isotope and microscopic study, we conclude that metal enrichment in the polymetallic sulfide ores was caused by normal seawater chemical precipitation. Variation of $\delta^{98/95}$Mo values are due to variable paleoenvironmental conditions from suboxic to euxinic, and partly closed-system fractionation in isolated marine sedimentary basins.

Keywords. Polymetallic Ni-Mo-(PGE-Au) sulfide, Mo isotopes, Black shales, Early Cambrian, South China

1 Introduction

In South China, the transgressive Early Cambrian Niutitang Formation (and equivalent strata) black shale sequence occurs across the Yangtze Platform with variable thickness for about 1600 km-long. An unusual organic carbon-, phosphate- and sulfide-rich layer is locally distributed in the lowermost part of the black shale sequence. This sulfide-rich layer is only several centimeters thick, but it shows extreme metal enrichment with Ni + Mo reaching up to 14 wt.%, and platinum group element (PGE) + Au concentrations of about 1g/t (Lehmann et al., 2007; Xu et al., 2013). Widespread small-scale mining are active in the Hunan and Guizhou provinces in South China focusing on the extreme metal concentration of the sulfide ore layer.

Since this peculiar polymetallic sulfide ore layer has been discovered in the 1970s, many petrological, mineralogical, geochronological, paleontological, and metallogenic studies on both the sulfide ores and host black shales have been done. However, the causes for metal enrichment are still much debated. Fan et al. (1984) suggested an extraterrestrial origin, which soon was discounted based on the identification of non-chondritic PGE distribution patterns (Coveney et al., 1992). The exceptional metal grades were thereafter mostly ascribed to hydrothermal venting on the seafloor (Lott et al., 1999; Steiner et al., 2001; Jiang et al., 2006, 2007). Pašava et al. (2008) suggested multiple sources of metals related to the circulation of highly saline, low-temperature fluids that leached metals from underlying lithologies, followed by discharging into seawater and scavenging of metals via co-precipitation with sulfides and formation of metal-organic complexes. Cao et al. (2012) interpreted organic clots in sulfide ore layer as rhodophyte cystocarps and suggested biotic impact on the ore mineralization. By comparing chemical compositions of present-day seawater, the host black shales, and the polymetallic sulfide ores, Mao et al. (2002) and Lehmann et al. (2007) interpreted the metal distribution patterns as reflecting scavenging from average seawater at a very low clastic sedimentation rate. This interpretation is supported by the fact that the host black shales and the polymetallic sulfide ores have similar initial Os ratios of ~ 0.8 (Xu et al., 2011).

We investigated the localities of Dazhuliushui and Maluhe in Guizhou Province, and Sancha and Cili in Hunan Province. Based on more samples and on a broader range of localities than in previous studies, we compare Mo isotope data for the polymetallic sulfide ores and host black shales. In combination with Mo isotope and microscopic study, this paper is aimed to discuss the ore-forming processes of the polymetallic sulfide Ni-Mo-(PGE-Au) ores.

2 Geological setting

Neoproterozoic and Early Cambrian sedimentary rocks are widely exposed on the Yangtze Platform of South China. The Early Cambrian Niutitang Formation is dominated by black shale but its lower part has a variable lithology with important sedimentary phosphorite and barite units. A marker bed of polymetallic Ni-Mo-PGE-Au sulfide ore is present locally in the lowermost part with a thickness mostly of 3 to 5 cm. Xu et al. (2011) determined a Re-Os age of 521 ± 5 Ma, which is consistent with the biostratigraphic Tommotian age of about 530 Ma and with the SHRIMP U-Pb zircon age of 532.3 ± 0.7 Ma for a volcanic ash bed a few meters beneath the sulfide ore layer (Jiang et al., 2009). The black shales and phosphorite nodules/beds of the Niutitang Formation contain abundant sponges, arthropods, and other soft-bodied

fossils of wide biological diversity that mark the "Cambrian Explosion" (Steiner et al., 2001).

The Neoproterozoic-Cambrian paleogeographic reconstruction reveals a depositional zonation from a shallow shelf facies of carbonate and phosphorite rocks in the northwest to a protected and deep basinal facies of black shale and chert in the southeast (Zhu et al., 2003; Wallis, 2007). The polymetallic Ni-Mo-PGE-Au sulfide ore layer occurs in the Early Cambrian Niutitang Formation along a narrow, NE-striking belt of transitional and deep basinal facies (Figure 1).

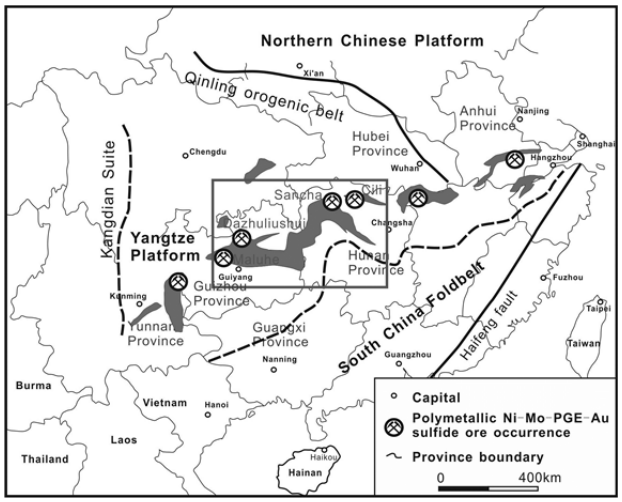

Figure 1. Sketch map showing locations of the Dazhuliushui, Maluhe, Sancha, and Cili polymetallic Ni-Mo-PGE-Au sulfide ore deposits. Black areas indicate the exposed Early Cambrian black shale sequence of the Niutitang Formation (and equivalent strata) in South China (modified from Wallis, 2007).

3 Lithology

Hand specimens of the host black shales are black, fine-grained, and massive or laminated. Framboidal and anhedral pyrite grains are common in both sulfide ores and host black shales. The Ni-Mo ore occurs within the lowermost few meters of the Niutitang Formation as both fine laminations and as a debris layer (Figure 2), consisting largely of a MoSC phase (with the approximate composition of $[(Mo,Fe,Ni)(S,As)_2C_7]$), pyrite, vaesite, bravoite, millerite, and gersdorffite, with minor arsenopyrite, chalcopyrite, covellite, sphalerite, tennantite, tiemannite, violarite, and native Au (Kao et al., 2001; Mao et al., 2002; Jiang et al., 2006). The amorphous MoSC phase (about 20 vol.%) is the Mo carrier, forming mm-sized ellipsoidal aggregates or fine laminations. Sapropel material (about 45 vol.%) occurs as a matrix, and consists of organic matter, fine-grained illite, sericite, quartz, calcite, barite, and locally abundant apatite and collophane. Pyrite (about 25 vol.%) is intergrown or rimed with the MoSC phase in oncolite-like aggregates. Pyrite is also cut by veinlets containing nickel sulfides (about 5 vol.%: millerite, gersdorffite). Sedimentary features such as fine laminations and rip-up clasts, and oncolites of pyrite and Ni-Mo sulfide, indicate an origin as a deep-water hardground supplied with organic material derived from algal mats in a wave-agitated, shallow-water environment (Kříbek et al., 2007).

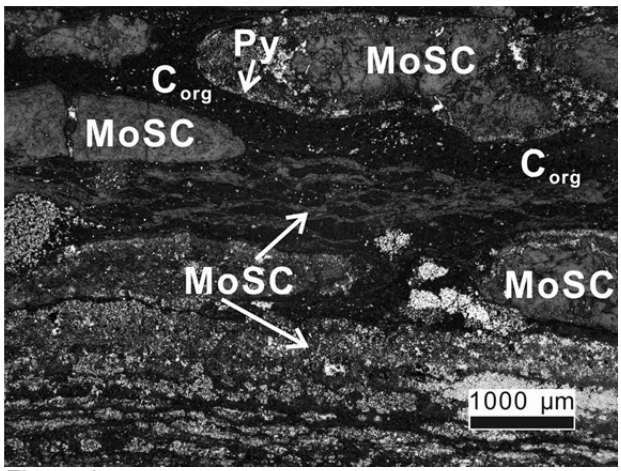

Figure 2. Photomicrograph (reflected light) of laminated and ellipsoidal MoSC phase with fine-grained pyrite rims surrounded by sapropel matrix. Re-deposited rip-up clasts in matrix of in-situ precipitated organic matter (Sancha underground mine).

4 Mo isotopes

We analyzed Mo isotope and abundance for the polymetallic Ni-Mo-PGE-Au sulfide ores, host black shales, and phosphorite from Maluhe, Dazhuliushui, and Sancha. These data are compiled with previously reported data of Lehmann et al. (2007). Mo concentrations of the polymetallic sulfide ores are extremely high, ranging from 29000 to 73000 ppm, with an average of 57800 ppm. The $\delta^{98/95}$Mo values are generally consistent, ranging from 0.94 to 1.37‰ with an average value of 1.13 ±0.14‰ (1 σ). In contrast, the host black shales and the phosphorite have relatively low Mo concentrations, ranging from 12.0 to 293 ppm (avg. 119 ppm). Their $\delta^{98/95}$Mo values are variable, from 0.48 to 1.90‰ with an average of 1.28 ±0.41‰ (1 σ), slightly heavier than that of the sulfide ores but fully overlapping their isotopic range. The heaviest $\delta^{98/95}$Mo value of black shale of 1.90‰ is greater than that of polymetallic sulfide ore with heaviest $\delta^{98/95}$Mo value of 1.37‰.

Lehmann et al. (2007) reported an average $\delta^{98/95}$Mo values of 1.06 ±0.10‰ with small scatter for five polymetallic sulfide ore samples from Huangjiawan, ~10 km southeast of the Dazhuliushui mine site, and suggested that the consistently heavy Mo was scavenged from coeval euxinic seawater. Based on the fact that some $\delta^{98/95}$Mo values of the sulfide ores are slightly lighter than those of the host black shales, Jiang et al. (2007, 2008) questioned this interpretation and proposed that the metals were not derived from euxinic seawater but instead from hydrothermal fluids. $\delta^{98/95}$Mo values versus Mo concentrations in both polymetallic sulfide ores and host black shales are presented in Figure 3. The average $\delta^{98/95}$Mo value of the polymetallic sulfide ores (1.13 ±0.14‰) is slightly lower than the average value of the host black shales (1.28 ±0.41‰), which are characterized by a larger spread of the $\delta^{98/95}$Mo values compared to the polymetallic sulfide ores.

Hydrothermal input of isotopically light Mo would have two consequences: (1) the hanging wall black shales that were influenced little or not at all by hydrothermal fluids should have heavier Mo isotope

compositions, relative to the host black shales; and (2) Mo concentrations in the polymetallic sulfide ores should be inversely correlated with $\delta^{98/95}$Mo values. However, neither trend is observed in this study. For the first case, the $\delta^{98/95}$Mo values of the host black shales scatter widely (Figure 3), and some black shale samples above the polymetallic sulfide ore layer have relatively light $\delta^{98/95}$Mo. For the second case, if the Mo in the polymetallic sulfide ores was predominantly derived from hydrothermal fluids with a low $\delta^{98/95}$Mo value, the higher the Mo content the closer the Mo isotope composition should be to that of the hydrothermal fluids, i.e., a light Mo isotope signature. However, a negative correlation between Mo concentration and $\delta^{98/95}$Mo value in polymetallic sulfide ores is not observed.

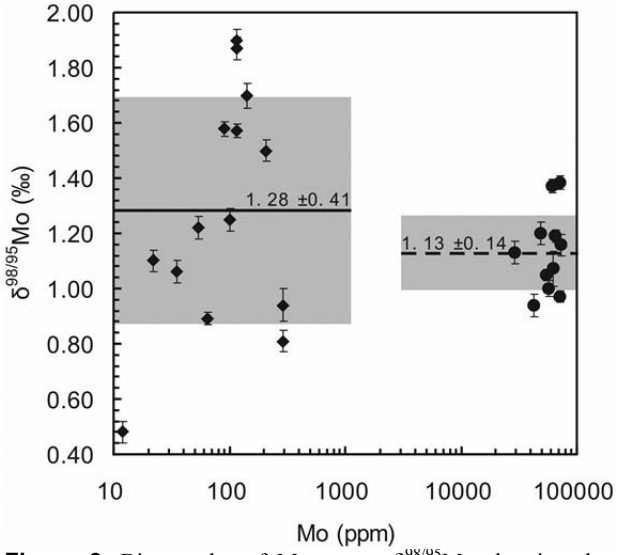

Figure 3. Binary plot of Mo versus $\delta^{98/95}$Mo showing that values for polymetallic sulfide ores and host black shales overlap within 1 sigma variation range (grey shading). Diamonds indicate black shale and solid circles indicate polymetallic sulfide ore samples. Solid and dashed black lines represent average $\delta^{98/95}$Mo value of host black shales and polymetallic sulfide ores, respectively.

Actually, an even larger scatter of values from -1.56 to 1.59‰ is observed in a stratigraphic profile across the Niutitang Formation (Xu et al., 2012). Such variations have been explained by a partly closed basin setting with periodic replenishment by oxic seawater with heavy $\delta^{98/95}$Mo values. When local basins were freely connected to the open ocean, the Mo isotopic composition would reflect the open ocean Mo signature. When the basins are restricted, Mo influx in such basins becomes dominated by continental input, and the Mo isotopic compositions of the marine sediments thus represent terrigenous material with light $\delta^{98/95}$Mo values, until replenishment by new oxic seawater with a heavy Mo isotopic signature restores the normal open-system situation.

By omitting data for two relatively high-Mo black shales reported by Lehmann et al. (2007), Jiang et al. (2008) suggested a positive correlation between Mo concentrations and $\delta^{98/95}$Mo values for the host black shales. They proposed a model in which isotopically heavier and authigenic, euxinic-sourced seawater Mo mixed with isotopically lighter Mo sourced from terrigenous materials in the black shales, and suggested that the two omitted black shales having relatively high Mo concentrations were affected by hydrothermal fluid overprint. However, it is not reasonable that hydrothermal fluids only affected the two black shales, but not others, considering that a large stratigraphic distance exists between the two omitted samples, and that Mo-low black shales occur between them. It seems more likely that the Mo isotope variation is related to variable redox conditions. The positive correlation between Mo concentration and $\delta^{98/95}$Mo value may reflect authigenic, seawater-sourced Mo and continental Mo contributions to the black shales, and changing redox conditions for the Mo-high samples.

$\delta^{98/95}$Mo values of some polymetallic sulfide ores that are isotopically slightly lighter than those of the host black shales do not conflict with the seawater scavenging model. Microscopic studies indicate that the

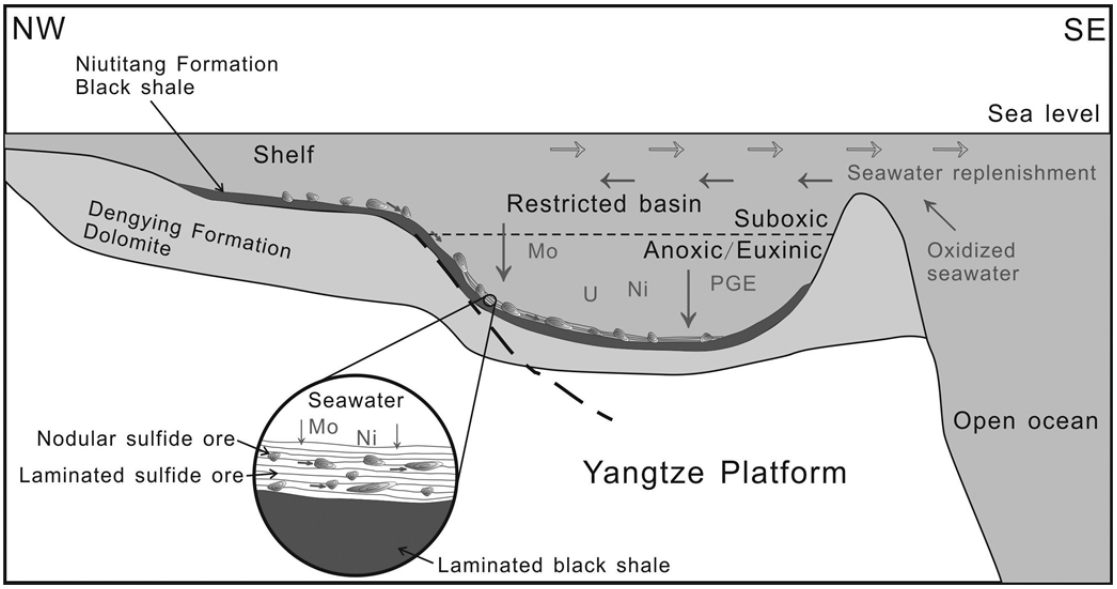

Figure 4. Two-stage model of depositional environment for the polymetallic Ni-Mo-PGE-Au sulfide ore layer with both in-situ metal precipitation from seawater and local transport and re-deposition of sulfide clasts, from wave-agitated shelf to deeper parts of the restricted anoxic/euxinic basin.

ores consist of in-situ precipitates and redeposited sulfide aggregates (rip-up clasts from hardground) (Figure 2). $\delta^{98/95}$Mo values in the polymetallic sulfide ores are therefore considered a mixture of in-situ precipitated Mo and remobilized Mo. Regardless of the causes of re-deposition (e.g. tectonic event, storm activity), it is possible that the remobilized Mo was deposited in relatively shallow waters and under intermittent suboxic conditions. $\delta^{98/95}$Mo that formed under such conditions is isotopically lighter than that formed under euxinic conditions (Anbar and Rouxel, 2007). Therefore, $\delta^{98/95}$Mo values of the polymetallic sulfide ores are best explained by a two-component mixing model of isotopically heavier in-situ precipitated Mo and lighter re-deposited Mo.

5 Conclusions

Metal enrichment in the polymetallic Ni-Mo-(PGE-Au) sulfide ore layer was likely caused by seawater scavenging at a very low clastic sedimentation rate. The Mo isotope signature supports a two-stage model for formation of the ore layer (Figure 4). Re-deposited rip-up sulfidic aggregates having relatively light and variable $\delta^{98/95}$Mo values mixed with in-situ precipitated Mo with heavy values, resulting in $\delta^{98/95}$Mo values of the polymetallic sulfide ores that are, in places, isotopically lighter than those of the host black shales.

References

Anbar AD, Rouxel O (2007) Metal stable isotopes in paleoceanography: Annual Review of Earth and Planetary Sciences 35: 717-746

Cao J, Hu K, Zhou J, Shi CH, Bian LZ, Yao SP (2012) Organic clots and their differential accumulation of Ni and Mo within early Cambrian black-shale-hosted polymetallic Ni-Mo deposits, Zunyi, South China: Journal of Asian Earth Sciences: http://dx.doi.org/10.1016/j.jseaes.2012.11.002

Coveney RM Jr, Murowchick JB, Grauch RI, Glascock MD, Denison JR (1992) Gold and platinum in shales with evidence against extraterrestrial sources of metals: Chemical Geology 99: 101-114

Fan DL, Yang RY, Huang ZX (1984) The Lower Cambrian black shales series and the iridium anomaly in south China: Developments in Geoscience, 27th International Geological Congress, Moscow, Beijing Science Press: 215-225

Jiang SY, Chen YQ, Ling HF, Yang JH, Feng HZ, Ni P (2006) Trace- and rare-earth element geochemistry and Pb-Pb dating of black shales and intercalated Ni-Mo-PGE-Au sulfide ores in Lower Cambrian strata, Yangtze Platform, South China: Mineralium Deposita 41: 453-467

Jiang SY, Ling HF, Zhao KD, Zhu MY, Yang JH, Chen YQ (2008) A discussion on Mo isotopic compositions of black shale and Ni-Mo sulfide bed in the Early Cambrian Niutitang Formation in South China: Acta Petrologica et Mineralogica 27: 341-345 (in Chincese with English abstract)

Jiang SY, Pi DH, Heubeck C, Frimmel H, Liu YP, Deng HL, Ling HF, Yang JH (2009) Early Cambrian ocean anoxia in South China: Nature 459: E5-E6

Jiang SY, Zhao KD, Li L, Ling HF, Zhu MY (2007) Highly metalliferous carbonaceous shale and Early Cambrian seawater: Comment: Geology 35: e158

Kao LS, Peacor DR, Coveney RM, Zhao GM, Dungey KE, Curtis MD, Penner-Hahn JE (2001) A C/MoS2 mixed-layer phase (MoSC) occurring in metalliferous black shales from southern China, and new data on jordisite: American Mineralogist 86: 852-861

Kříbek B, Sýkorová I, Pašava J, Machovič V, (2007) Organic geochemistry and petrology of barren and Mo-Ni-PGE mineralized marine black shales of the Lower Cambrian Niutitang Formation (South China): International Journal of Coal Geology 72: 240-256

Lehmann B, Nägler TF, Holland HD, Wille M, Mao JW, Pan JY, Ma DS, Dulski P (2007) Highly metalliferous carbonaceous shale and Early Cambrian seawater: Geology 35: 403-406

Lott DA, Coveney RM, Murowchick JB, Grauch RI (1999) Sedimentary exhalative nickel-molybdenum ores in South China: Economic Geology 94: 1051-1066

Mao JW, Lehmann B, Du AD, Zhang GD, Ma DS, Wang YT, Zeng MG, Kerrich R (2002) Re-Os dating of polymetallic Ni-Mo-PGE-Au mineralization in Lower Cambrian black shales of South China and its geologic significance: Economic Geology 97: 1051-1061

Pašava J, Kříbek B, Vymazalová A, Sýkorová I, Žák K, Orberger B (2008) Multiple sources of metals of mineralization in Lower Cambrian black shales of South China: Evidence from geochemical and petrographic study: Resource Geology 58: 25-42

Steiner M, Wallis E, Erdtmann BD, Zhao YL, Yang RD (2001) Submarine-hydrothermal exhalative ore layers in black shales from South China and associated fossils — Insights into a Lower Cambrian facies and bio-evolution: Palaeogeography, Palaeoclimatology, Palaeoecology 169: 165-191

Wallis E (2007) The climatic and environmental history of the South Chinese Yangtze platform during the Neoproterozoic and Early Cambrian: Hydrothermally active and salinity stratified epicontinental basins a key for understanding the "Cambrian explosion"? Ph.D Thesis. Berlin: 1-227 (in German with English abstract)

Xu LG, Lehmann B, Mao JW (2013) Seawater as origin of polymetallic Ni-Mo-PGE-Au mineralization in Early Cambrian black shales of South China: evidences from Mo isotope, PGE, trace element and REE geochemistry: Ore Geology Reviews 52, 66-84

Xu LG**,** Lehmann B, Mao JW, Nägler TF, Neubert N, Böttcher ME (2012b) Mo isotope and trace element patterns of Early Cambrian black shales in South China: constraints on the paleoenvironment: Chemical Geology 318-319: 45-59

Xu LG, Lehmann B, Mao JW, Qu WJ, Du AD (2011) Re-Os age of polymetallic Ni-Mo-PGE-Au mineralization in Early Cambrian black shales of South China — A reassessment: Economic Geology 106: 511-522

Zhu MY, Zhang JM, Steiner M, Yang AH, Li GX, Erdtmann BD (2003) Sinian-Cambrian stratigraphic framework for shallow- to deep-water environments of the Yangtze Platform: An integrated approach: Progress in Natural Science 13: 951-960

The Omitiomire deposit, Namibia: late tectonic copper emplacement in a Neoproterozoic (Pan-African) imbricate shear system

Ken Maiden
International Base Metals Limited, 47 Neridah Street, Chatswood, NSW 2057, Australia. kmaiden@ibml.com.au

Karl Hartmann
Craton Mining and Exploration (Pty) Ltd, PO Box 81126, Olympia, Windhoek, Namibia

Nick Steven
Rockwater Consulting Namibia, PO Box 27344, Windhoek, Namibia

Richard Armstrong
Richard Armstrong, PRISE, Australian National University, Canberra, ACT 2000, Australia

Abstract The Omitiomire deposit (> 1 million tonnes contained copper metal) is hosted by Mesoproterozoic (1115 – 1063 Ma) bimodal volcanics. These hosts were metamorphosed to amphibolite grade (7-8 kbar, 600°C) during the Damaran orogenic event at ~535 Ma. Late Damaran deformation, related to collision between the Congo and Kalahari Cratons, resulted in SE-directed nappe development and thrusting. Final (D_4) phases of transpressive deformation produced NNE-oriented folds.

Copper mineralisation occurs primarily as hypogene chalcocite, hosted by mafic schist. Interbanded felsic gneisses are barren. Stacked ore lenses define a copper-bearing system which varies from 10m to >100m in thickness. The lenses dip at a moderate angle to the east. The ore system plunges shallowly to the NNE. Drilling has shown a deposit which extends for 4,000m and remains "open" to the NNE. The orebody has a sharp hanging wall contact (probably a thrust contact) against barren felsic gneiss and a gradational lower contact into poorly-mineralised schist.

Highest copper grades occur in a retrograde mineral assemblage dominated by biotite and Cr-epidote, and focussed along an imbricate system of narrow shear zones. Chalcocite and associated epidote-sphene-magnetite overprint the shear fabric, demonstrating late tectonic emplacement of copper. Sphene ages (525 – 485 Ma) date the copper-mineralising event(s).

Keywords. Namibia, Omitiomire, copper

1 Introduction

Omitiomire is located 120 km northeast of Windhoek, the capital of Namibia. The project was acquired by Craton Mining and Exploration (Pty) Ltd ('Craton'), the Namibian-registered subsidiary of Australian-based International Base Metals Limited, in 2007. Copper mineralisation had been known in the area since the 1960s. Since Craton acquired the project, the company has drilled some 600 holes totalling over 70,000m. This drilling has resulted in a resource of 136 million tonnes at 0.53% Cu (at a cut-off grade of 0.25% Cu). Widely-spaced drill holes have identified additional potential of almost 100 million tonnes at grades of 0.53 – 0.57% Cu.

2 Geological Setting

The deposit lies in the Southern Zone of the Damara Orogen, which developed as a result of collision between the Congo Craton and the Kalahari Craton in the late Proterozoic/early Palaeozoic. The Okahandja Lineament, a regional northeast-trending feature, separates the Central Zone (high-temperature, medium-pressure metamorphism) from the Southern Zone (medium-temperature, high-pressure metamorphism) and marks the leading edge of the Congo Craton (Figure 1; Miller, 2008).

Omitiomire lies within a nappe complex, consisting of Neoproterozoic strata of the Damara Sequence and pre-Damara rocks. In particular, the deposit is within a basement dome comprising amphibolite, amphibole-biotite-plagioclase schist and felsic gneiss. The mafic rocks are interpreted as metamorphosed mafic volcanics; the felsic rocks are interpreted as meta-dacite and some tonalite sills. SHRIMP U-Pb studies on zircon cores provide Umkondo – Irumide ages of ~1115 Ma for amphibolite, ~1084 Ma for felsic gneiss and ~1063 Ma for foliated tonalite (Steven et al, 2000).

During the Damaran (Pan-African) Orogeny, D_1 and D_2 deformation, during the period 580 – 550 Ma, resulted in south- to southwest-directed nappes and thrusts. Zircon crystals have rims dated at ~550 Ma, reflecting the Damaran metamorphism. Sphene crystals also have ~1100 Ma cores and Damaran-age rims. The metamorphic peak (M2) was associated with collision at ~535 Ma, with peak P/T conditions of 600°C and 7-8 kbar. Late Damaran (D_3) deformation resulted in pronounced southeast verging structures (Miller, 2008)

Rock exposure in the region is very poor. The geology is interpreted mainly from airborne geophysical imagery supported by drill hole data. Figure 2 shows our current preferred interpretation. Following the D_3 collision (collisional peak), the orogen was 'locked up'. A change in the regional stress field produced D_4 transpression, resulting in NNE-oriented folds.

3 Deposit Geology

The Omitiomire deposit extends for ~4,000m north-south, and is up to 800m in width. It dips at a moderate angle to the east and plunges at a low angle to the north. It remains "open" to the NNE. Drilling has revealed eight lenses stacked in a staggered parallel formation above each other, but in close proximity, in effect making up a single larger body (Figure 3). Near the surface, the deposit is about 10m thick; to the east, some drill holes have intersected over 100m of copper mineralisation. The orebody has a sharp hanging wall contact (probably a thrust contact) against barren felsic gneiss and a gradational lower contact into poorly-mineralised schist. The host rocks are banded on a scale of centimetres to metres. The coarse banding may be original S_0 fabric; the fine-scale banding is interpreted as a metamorphic fabric. Recumbent Z-folds support the concept of ESE-directed tectonic transport during D_4.

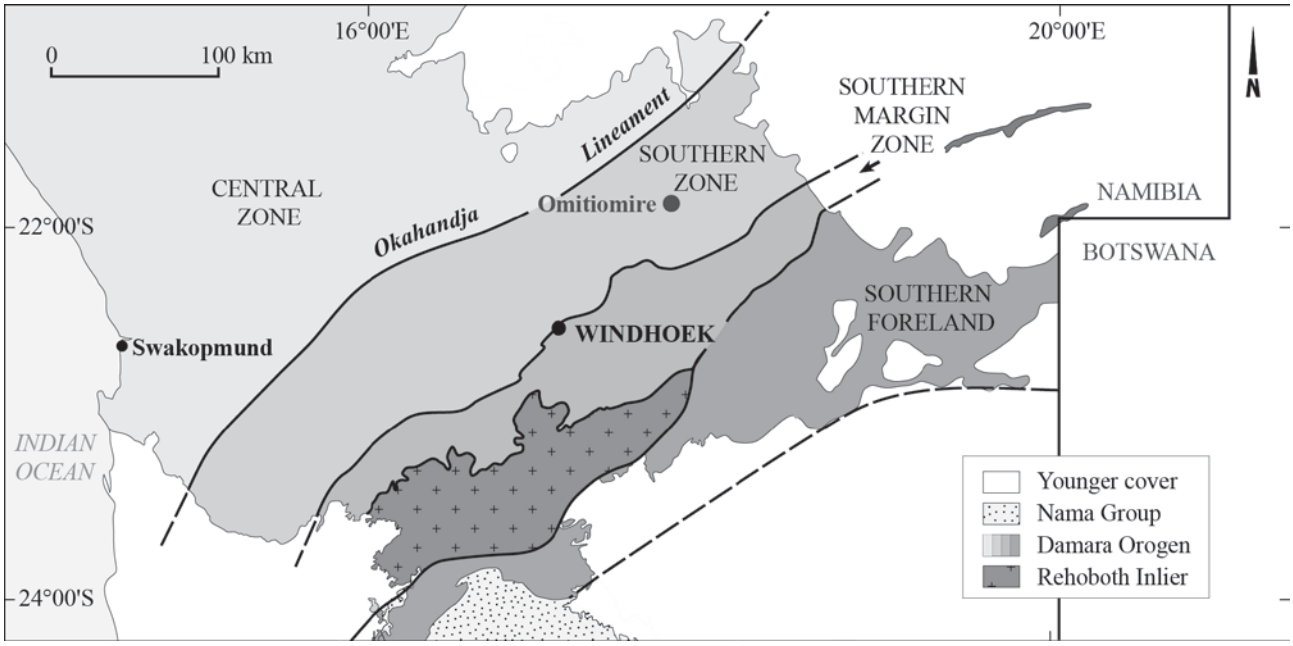

Figure 1. Regional tectonic setting of Omitiomire in central Namibia. (Modified from Miller, 2008)

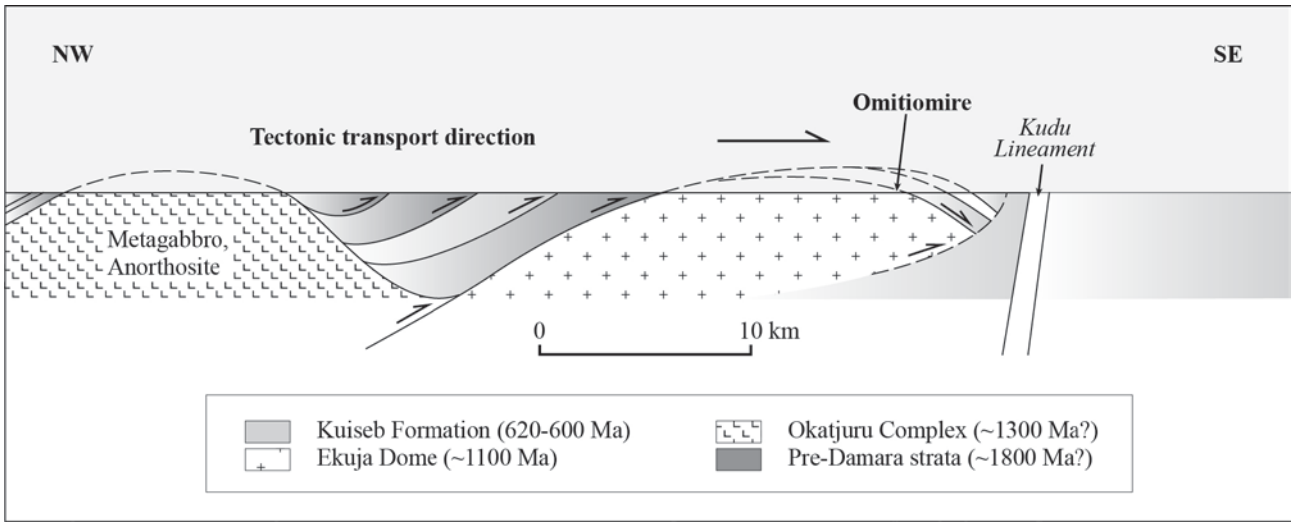

Figure 2. Interpreted cross section through the nappe complex. (based on Kasch, 1986, 1987)

Copper is hosted mainly by mafic schist and, to a lesser extent, amphibolite. Bands of felsic gneiss are barren. Approximately 90% of the sulphides are the high-pressure and high-temperature polymorph of chalcocite and digenite. About 8% is bornite and there is minor chalcopyrite. There is no iron sulphide in the deposit. Chalcocite inclusions within epidote show that chalcocite is clearly a hypogene mineral.

Highest copper concentrations are associated with a retrograde mineral assemblage dominated by biotite and Cr-epidote, with subordinate Cr- and Ti-magnetite, sphene and some fuchsite. These rocks occur in an imbricate system of narrow shear zones. Chalcocite and associated epidote-sphene-magnetite overprint the shear fabric, demonstrating late-tectonic (i.e. syn-D_4) emplacement of copper. Sphene ages (525 – 485 Ma) date a protracted, late-orogenic copper-mineralising event. D_4 transpression produced NNE–trending fold

axes and copper is concentrated within a NNE-trending corridor.

4 Discussion: Ore Genesis

The source of copper is inferred to be the voluminous subaerial copper-bearing mafic rocks in the Southern Margin Zone (Miller, 2008). Fluid inclusion studies support introduction of copper in hot, saline, oxidised, retrograde metamorphic fluids which were channelled into structural discontinuities and shear zones where they reacted with tectonised amphibolite. Copper precipitation was most likely in response to Eh-pH changes related to retrograde hornblende breakdown.

The Cr- and Ti-bearing magnetite in the Omitiomire copper ore assemblage is interpreted to have formed from retrograde breakdown of amphibolite. Retrograde biotite shows potassium mobility. In summary, Omitiomire is interpreted as a late deformational copper deposit, with copper introduced late in the Damaran orogeny (520 – 485 Ma), the result of regional retrograde fluid flow.

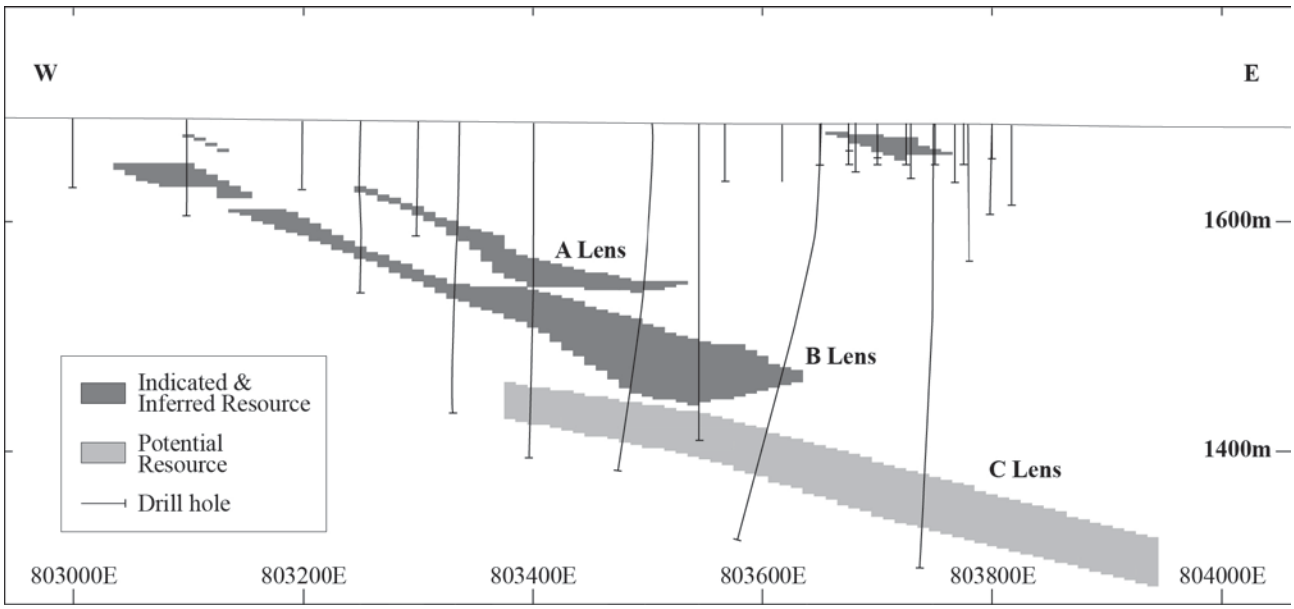

Figure 3. Drill section showing stacked ore lenses.

Acknowledgements

This paper is presented with the approval of International Base Metals Limited.

References

Kasch, KW (1986) Tectonic subdivision, lithostratigraphy and structural geology of the Upper Black Nossob River area. Communications of the Geological Society of Namibia, v 2, 117-129

Kasch, KW (1987) Metamorphism of pelites in the Upper Black Nossob River area of the Damara Orogen. Communications of the Geological Society of Namibia, v 3, 63-82

Miller RMcG (2008) The Geology of Namibia. Namibian Ministry of Mines and Energy / Geological Survey

Steven NM, Armstrong, RA, Smalley TI, Moore JM (2000) First geological description of a late Proterozoic (Kibaran) andesite-hosted chalcocite deposit at Omitiomire, Namibia. In: Cluer JK, Price JG, Struchsacker E, Hardyman RF, Morris, CL (eds) Geology and Ore Deposits 2000: The Great Basin and Beyond. Geological Society of Nevada Symposium Proceedings: 711-734

Characterising a geochemical and isotopic halo of the Navan Irish-type Zn-Pb deposit

Freya R. Marks & Julian F. Menuge
UCD School of Geological Sciences, University College Dublin, Belfield, Dublin 4, Ireland

Robert J. Blakeman
Boliden Tara Mines Ltd, Navan, Co. Meath, Ireland

Adrian J. Boyce
Scottish Universities Environmental Research Centre, East Kilbride G75 0QF, UK

Abstract: An ongoing multi-disciplinary study has revealed that the halo of the Navan orebody is characterised by epigenetic sulphides that exploit fractures and micro-faults within the carbonate host. Eight sulphide textures have been recognised ranging from coarse to fine, diffuse styles. ZnS concentration increases where bacteriogenic sulphide is present. This sulphide source is important in economic Irish-type systems and may thus assist characterisation of the halo. The average Zn:Pb of the halo is 1:1 (compared to the main orebody at 5:1), probably reflecting the overall lack of bacteriogenic sulphide. Initial cathodoluminescence work has highlighted similar early carbonate stages to those in the Navan orebody. These observations along with C, O, Zn and Fe isotope studies will improve our knowledge of the Navan halo and aid exploration within the Irish Ore Field.

Keywords: Irish-type, geochemical halo, sulphur isotopes, base metals, hydrothermal

1 Introduction

The Navan Zn-Pb Irish-type deposit, situated 40 km northwest of Dublin, is by far the biggest in the Irish Ore Field and the largest zinc producer in Europe. It is a Zn-Pb base metal deposit comprising ore minerals sphalerite and galena, with gangue minerals pyrite, marcasite, barite, calcite and dolomite. Economic mineralisation is hosted in stratabound lenses by Lower Carboniferous, Courceyan shallow-water carbonates, named the Pale Beds. It is widely accepted that it was deposited by the mixing of relatively hot metal-rich, sulphide-poor hydrothermal fluids (with +ve $\delta^{34}S$ values) and cool seawater brines enriched in bacteriogenic sulphide (-ve $\delta^{34}S$) (Anderson et al. 1998). More than 90% of the sulphide is considered to be bacteriogenic (Fallick et al. 2001). The deposit is situated on Courceyan-Chadian NE to ENE- trending extensional faults that provided pathways for the fluids to mix (Blakeman et al., 2002; Ashton et al 2010). Late compression initiated reverse movement along some of these faults including the Randalstown fault (Fig 1). (Ashton et al. 2003)

The nature of the mineralized halo around the deposit is much less well known. Lithogeochemical anomalies are another essential and inexpensive tool that is extensively used in the mining industry to find vectors to mineralized orebodies. But, this study looks at sulphide textures, geochemical data and isotope results in core samples from the halo. Can we use these parameters to determine proximity to the Navan ore? At >100Mt at 8% Zn and 2% Pb, Navan will provide a robust test of utility

2 Halo studies of Irish-type deposits

Previous lithogeochemical studies of Irish-type deposits have identified key halo elements. Early studies led by Russell (1974, 1975) looked at the Waulsortian limestone surrounding the Tynagh Irish-type deposit. He identified a manganese halo that can be identified up to 7 km distance at >1000 ppm. Clifford et al. (1988) did a similar study and confirmed the Mn halo at Tynagh. Two ideas were proposed to explain how the halo formed: (1) Distal movement of mobile elements, and/or (2) Exhaust mineralising fluid discharged at the seafloor through hydrothermal vents (Russell 1974, 1975).

Studies since the 1980s at Navan have shown a similar Mn enrichment in the country rock, as far as 2.5 km from the main orebody. Zn and As show the same trend and Fe is anomalous >4 km away (Finlay et al. 1984). Gonzalez and O'Keefe (unpublished report 2000) found Zn, Pb, Ag, Sb, baryte and dolomite enrichment and Cu depletion in host stratigraphy 200 m vertically and <4 km laterally. Walker (2005) looked at the stratigraphy above the host rocks and found Mn enrichment of >2500 ppm extending several kilometres from the orebody. Walker (2010) on a smaller scale, found that anomalous envelopes of Fe, As, Sb and Tl exist 500 m laterally and <50 m vertically.

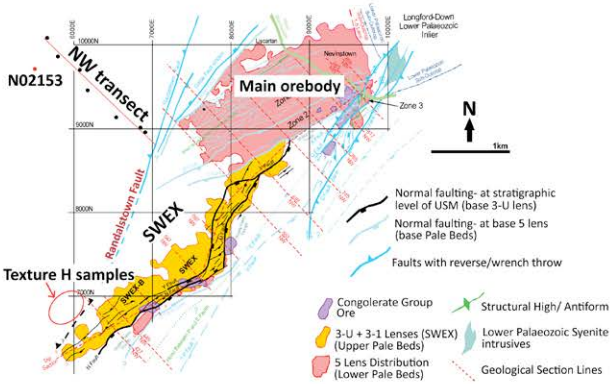

Figure 1. Map of the Navan orebody showing the geometry of the ore lenses, major structures and sample locations

Table 1. Halo mineral texture classification and interpretations. Sp = sphalerite, Ga = galena

Symbol	Mineral texture description	δ^{34}S Sp range	δ^{34}S Ga range	Interpretation
A	Coarse sulphides replacing host rock in cross-cutting diffuse vein style	+2 to +3 (n= 2)	+5 to +12 (n= 4)	Metal-rich fluids corroding host rock along "weak" zones.
B	Fine +/or coarse sulphides replacing host rock, stratabound	+7 (n= 1)	-2 to +11 (n= 2)	Metal-rich fluids selectively corroding host rock.
C	Sulphides with sharp, crosscutting contact with host rock, sometimes banded	-24 to +11 (n= 5)	-23 to +8 (n= 6)	Metal-rich fluids depositing sulphides along fractures/ faults, occasional evidence for mixing with the sulphur-bearing fluid.
D	Fine +/or coarse sulphides cross-cutting host rock in thick vein style with a large volume of insolubles. Cross-cutting lower margin and diffuse upper margin.	-23 to -21 (n= 3)	+7 to +12 (n= 3)	Near fault, dissolution by metal-bearing fluids causing insoluble material to be transported with early galena with +ve δ^{34}S values. Mixing with sulphur-bearing fluid produces fine replacive sphalerite with –ve ^{34}S values
E	Sulphides in dark matrix of jigsaw-breccia.	-16 (n= 1)	+7 to +9 (n= 2)	Away from fault (Texture D), metal-bearing fluids corrode host rock in interlinking vein network, less mixing with sulphur-bearing fluid
F	Fine sulphides replacing host rock in diffuse veinlets, often with insolubles.	-14 (n =1)	+4 to +7 (n =2)	Further away still from fault (Textures D and E) single veins of insolubles with Pb- and Zn- sulphide.
G	Coarse sulphides in carbonate veins.	+6 (n= 1)	-3 to +11 (n= 3)	Metal-bearing fluids penetrating fracture zones and precipitating calcite/dolomite with Pb- and Zn- sulphide.
H	Coarse angular sulphide, often brecciated sphalerite with calcite.	-3.9 to -1.5 (n= 5)	N/A	(i) Remobilized metal sulphide has re-crystallized and brecciated during later thrust faulting (ii) Late sphalerite, brecciated and infilled by calcite.

This study builds on this earlier work and will investigate the halo in more detail through mineral textures, isotope studies and geochemical modelling.

3 Sampling and analytical techniques

Samples of sulphide were chosen from the Pale Beds in surface drill core, west of the Randalstown Fault and the Main Orebody (Fig. 1). This area was chosen because a NW transect of 7 drill cores intersecting the halo of the deposit already existed. Where sphalerite and/or galena were present, samples were taken for analysis and textural classification. The dominant sulphide mineral per 1.5 m length of core was then noted. This could then be correlated with multi-element results of the 1.5 m sections. Samples were analysed by ICP-AES at ALS Laboratories, Loughrea, Ireland, for a suite of 46 major and trace elements.

Some samples were thin sectioned for analysis by reflected and transmitted light. Samples of texture H (see Table 1) were sampled from core from SW SWEX, in the hangingwall of the Randalstown Fault (see Fig 1).

A range of textures and geographically distributed samples were used to determine δ^{34}S values in sphalerite and galena using an *in situ* laser system (Wagner et al. 2002).

Dolomite samples for cathodoluminescence (CL) were selected from Pale Beds in drill core N02153, west of the Randelstown Fault, ~2 km from the main orebody (Fig. 1). Dolomite was identified by SEM. CL work was done using the Quanta 3D FEG DualBeam and KE centauraus at the Nano Imaging & Material Analysis Centre, UCD.

4 Results

Eight mineral textures have been identified in the halo of the Navan deposit. The textures are summarized in Table 1 along with δ^{34}S values (Fig. 2).

The textures observed are similar to those of the main deposit (see Anderson et al. 1998) but their relative frequency is different. Common textures in the halo are cross-cutting, exploiting fractures and micro-faults (Table 1 mineral textures A, F, G). This contrasts with the main orebody where massive replacive textures and banded sulphides are common. The absence of such textures in the halo is perhaps indicative of restricted sulphide availability. Complex textures in the halo (Table 1 textures C, D) appear always to have a stronger bacteriogenic sulphide component, implying greater sulphide availability. Textures associated with bacteriogenic are also usually finer grained.

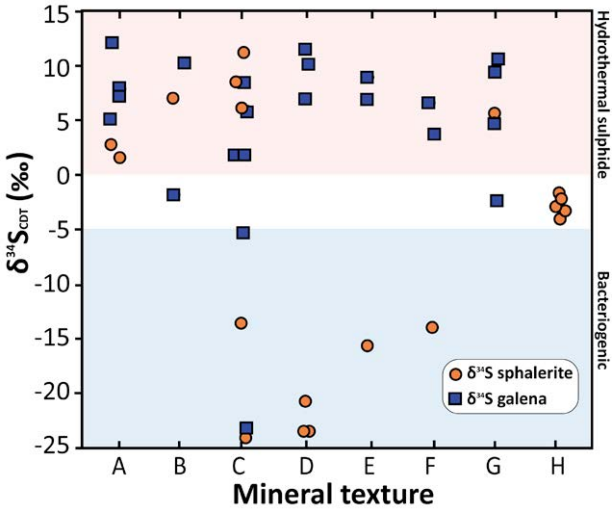

Figure 2. Graph showing δ^{34}S variation with mineral texture

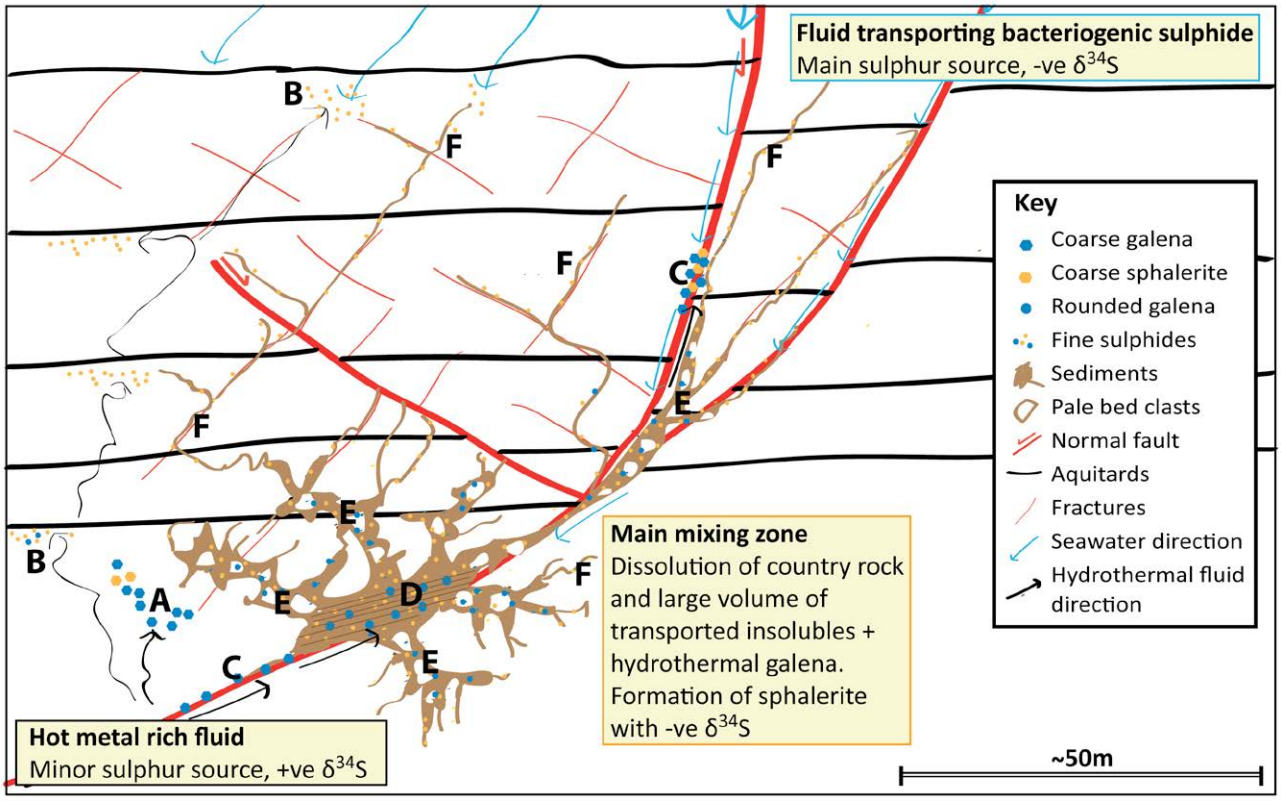

Figure 3. Schematic diagram showing formation of mineral textures A-F, NW of the main orebody.

Proposed environments of formation of the mineral textures are illustrated in Fig. 3.

Sulphur isotope values show that hydrothermal sulphur (Fig. 2, $\delta^{34}S$ = 0-13‰) is the dominant sulphur source in the halo. Near-mine samples contain more bacteriogenic sulphide, but one sample 2 km from the main deposit also contains sulphide with a bacteriogenic signature. Sphalerite dominates the negative $\delta^{34}S$ values whereas galena usually shows exclusively positive $\delta^{34}S$ values (Fig. 2). Zn:Pb in the halo are on average 1:1, compared to an average of 5:1 for the main orebody. The relative deficit of Zn may be explained by the low availability of sulphide, i.e. less bacteriogenic sulphide; areas with high Zn and Pb values and high Zn:Pb correlate with a negative $\delta^{34}S$ signature.

Previous trace element analyses on a millimetre scale in the main orebody shows that sphalerite enriched in Cd, Sb, Cu and Ag carries a hydrothermal sulphide signature, whilst sphalerite enriched in Fe and As bears a bacteriogenic sulphide signature (Gagnevin et al. 2012). In the halo whole-rock core samples Cd, Cu (correlating with +ve $\delta^{34}S$) and As (correlating with –ve $\delta^{34}S$) show the same trend as seen on a millimetre scale in the main orebody. Identification of this relationship may allow an understanding of sulphur source without analysing sulphur isotopes, which is considerably more expensive.

Four stages of dolomite growth in the halo have been identified with CL. Braithwaite and Rizzi (1997) give detailed descriptions of dolomite CL stages in the main orebody and identify three stages. Their stage 1 appears to correlate with halo stage 1. Stages can be discriminated by looking at unconformities and luminescent trends. Our halo stage 1 and their main orebody stage 1 are both replacive and show dull luminescence. Work is in progress to try to establish whether later stages can be correlated.

5 Discussion

Sulphide textures allow an insight into sulphur source without having to do $\delta^{34}S$ analysis. This is important in assessing the likelihood of proximity to an Irish-type deposit.

From the halo textures and $\delta^{34}S$ results it is possible to identify at least three stages of mineralisation. Textures A and B are almost always hydrothermal sulphide-related, whilst textures C, D, E and F are linked and related to the mixing of hydrothermal fluid and bacteriogenic sulphide-rich fluid. Textures G and H are associated with later structures and carbonate veins.

Two theories for the formation of texture H and the small $\delta^{34}S$ variation it displays (-2.64 +/- 0.95‰) are: (1) Earlier sphalerite of variable $\delta^{34}S$ has been remobilised and recrystallised, homogenising its $\delta^{34}S$; (2) Late hydrothermal mineralisation associated with fault inversion with a distinct source of sulphur not previously recognised. CL work revealed that the sphalerite is non-luminescent and appears homogeneous. Further work on texture H will include fluid inclusion studies to determine the fluid composition.

Geographical distribution of $\delta^{34}S$ shows that there are "pockets" of bacteriogenic sulphide present at distances of >2 km from the main deposit. Where the pockets exist the grade of ore increases. This supports the

hypothesis that bacteriogenic sulphide is essential for an Irish-type system to develop into an economic deposit (Fallick et al. 2001). The presence of negative $\delta^{34}S$ values in weak mineralisation strongly suggests proximity to an Irish-type deposit. The "pockets" of bacteriogenic sulphide correlate with proximity to large faults. These provide pathways for the reduced seawater brine to move down and mix with the metal-bearing fluids.

6 Outlook for C, O, Zn and Fe isotope studies

6.1 C and O isotopes

Once carbonate stages of the halo are correlated with the main deposit by CL it will be possible to compare $\delta^{13}C$ and $\delta^{18}O$ values between the main deposit and the halo. This has been applied previously to other Irish-type deposits (Hitzman and Beatty 1996).

The principle of the method relies on the inverse relationship of $\delta^{18}O$ to temperature**.** If the $\delta^{18}O$ of the water remains constant then an increased T will cause the precipitated mineral to have a lowered $\delta^{18}O$ value.

Hitzman and Beatty (1996) showed that $\delta^{18}O$ and $\delta^{13}C$ increase in value with distance from the orebody due to the reaction of hydrothermal fluids with cold country rock at the Silvermines, Tynagh, Lisheen and Keel Irish-type deposits.

$\delta\ ^{18}O$ and $\delta^{13}C$ from the main Navan orebody are respectively -6.6 to -10.4 ‰ and -0.2 to +2.5 ‰ (Braithwaite and Rizzi 1997). Samples from the halo will be compared with results from the main orebody to explore variation in ^{18}O and $\delta^{13}C$ values. Navan is a very complex deposit so correlation of ^{18}O and $\delta^{13}C$ with distance from the orebody may not be simple.

6.2 Zn and Fe isotopes

Gagnevin et al. (2012) found that in sphalerite from Navan there is a strong positive correlation of $\delta^{66}Zn$ and $\delta^{56}Fe$ values, both between samples and on a millimetre scale in banded sphalerite. $\delta^{66}Zn$ and $\delta^{56}Fe$ values become heavier in successive growth bands as $\delta^{34}S$ values becomes lighter, trending towards a more bacteriogenic sulphide source signature. This implies that early precipitated sphalerite with a hydrothermal sulphide signature acquired low $\delta^{66}Zn$ and $\delta^{56}Fe$. They conclude that kinetic fractionation is the cause of isotope variation. Rapid precipitation of sphalerite causes isotopically lighter isotopes to precipitate first.

Following Gagnevin et al. (2012), we will apply Zn and Fe isotopes on a larger scale. We hypothesise that $\delta^{66}Zn$ and $\delta^{56}Fe$ should increase outwards in the halo as the light isotopes precipitate out early, near the main faults.

Acknowledgements

This project is jointly funded by the Irish Research Council for Science, Engineering and Technology (IRCSET) and Boliden Tara Mines Ltd. We would like to thank Boliden Tara Mines Ltd for allowing access to core and data, the geology and technical staff at Tara Mines, Alison McDonald and Tom Culligan for their assistance with this project and Dr John Ashton who this project would not be possible without.

References

Anderson IK, Ashton JH, Boyce AJ, Fallick AE, & Russell MJ (1998) Ore depositional process in the Navan Zn-Pb deposit, Ireland. Economic Geology 93:535-563.

Ashton JH, Holdstock MP, Geraghty JF, O'Keeffe WG, Martinez N, Peace W, Philcox, ME (2003) The Navan Orebody - discovery and geology of the South West Extension. *In* Europe's Major Base Metal Deposits, Irish Association for Economic Geology 405-436

Ashton JH, Blakeman R, Geraghty J, Beach A, Coller, D, Philcox ME, Boyce AJ, Wilkinson JJ. (2010) The Giant Navan Carbonate-Hosted Zn-Pb Deposit – A Review. ZINC 2010 Extended Abstracts Volume, Irish Association for Economic Geology 97-102

Blakeman, RJ, Ashton JH, Boyce AJ, Fallick AE, Russell MJ (2002) Timing of interplay between hydrothermal and surface fluids in the Navan Zn+Pb orebody, Ireland: Evidence from metal distribution trends, mineral textures and $\delta^{34}S$ analyses. Economic Geology 97:73-91

Braithwaite CJR, Rizzi G (1997) The geometry and petrogenesis of hydrothermal dolomites at Navan, Ireland. Sedimentology 44:421-440

Clifford JA, Kucha H, Meldrum AH (1988) Lithogeochemistry, its applicability to base metal exploration in a carbonate environment. *In* Mineral Deposits within the European Community, Special Publication SGA, Boissonnas J and Omenetto P (eds) 6:391-405

Fallick AE, Ashton JH, Boyce AJ, Ellam RM, Russell MJ (2001) Bacteria were responsible for the magnitude of the world-class hydrothermal base metal sulfide orebody at Navan, Ireland. Economic Geology 96:885-890

Finlay S, Romer DM, Cazalet PD (1984) Lithogeochemical studies around the Navan Zn-Pb orebody Ireland. Prospecting in Areas of Glaciated Terrain, Institution of Mining and Metallurgy 35-56

Gagnevin D, Boyce AJ, Barrie CD, Menuge JF, Blakeman RJ (2012) Zn, Fe and S isotope fractionation in a large hydrothermal system. Geochimica et Cosmochimica Acta 88:183-198

Hitzman MW, Beaty DW (1996) The Irish Zn-Pb-(Ba) Orefield. *In* Carbonate-Hosted Lead-Zinc Deposits, SEG Special Publication Number 4, Sangster DF (eds) 112-143

Russell MJ (1974) Mn halo surrounding the Tynagh ore deposit, Ireland: a preliminary note. Trans. Institution of Mining and Metallurgy (Sect B: Appl. Earth Sci.) 83:B65- 66

Russell MJ (1975) Lithogeochemical environment of the Tynagh base-metal deposit, Ireland, and its bearing on ore deposition. Trans. Institution of Mining and Metallurgy (Sect B: Appl. Earth Sci.) 84:B128-133

Wagner T, Boyce AJ, Fallick AE (2002) Laser combustion analysis of $\delta^{34}S$ of sulfosalt minerals: Determination of the fractionation systematics and some crystal-chemical considerations. Geochim. Cosmochim. Acta, 66: 2855-2863

Walker M (2010) Lithogeochemical exploration surrounding the carbonate hosted Zn-Pb Navan orebody: B historic review, analysis of results and the establishment of future exploration programmes: Unpublished MSc thesis. CSM.

Walker N (2005) The distribution patterns of pathfinder elements in the Upper Dark Limestone cover sequence above the SWEX-B Mineralisation: Unpublished MSc thesis. NUIG.

Formation of vein hosted copper-silver mineralisation in the Kalahari Copperbelt, Botswana: preliminary results

Morgan, K.L., Jenkin, G.R.T., Gorman, A.R.
University of Leicester, University Road, Leicester, LE1 7RH, UK

Catterall, D.
Hana Mining Ltd, Ground Floor, Fairgrounds Financial Centre, PO Box AD80AAF, Gabarone, Botswana

Boyce, A.J.
Scottish Universities Environmental Research Centre, Rankin Avenue, East Kilbride G75 0QF, Scotland, UK

Abstract. The Kalahari Copper-belt lies within the Pan-African Damara belt extending through Namibia and Botswana. Mineralisation is generally hosted in the first 20 m above the contact between the oxidised, immature siliciclastic red-bed Ngwako Pan Formation and the overlying reduced fine grained siliciclastic and carbonate D'Kar Formation.

Early petrography carried out by the authors has revealed bornite-chalcocite-chalcopyrite mineralisation which grades into pyrite-sphalerite-galena further above the contact. Mineralisation is hosted within laminations, as nodules, in cleavages, and in associated quartz-carbonate veins; the latter being the main focus of this project.

Three stages of veining have been identified: 1) early bedding parallel to sub-parallel deformed veins, 2) middle stage veins usually at high angles to bedding and less deformed and 3) late stage massive veins. Studies of both disseminated and vein hosted mineralisation imply that mineralisation potentially preceded as well as overlapped regional deformation and resulted in multiple vein generations.

Sulphides show a large spread in $\delta^{34}S$ from -45.7‰ through to +0.4‰, with most lower than -10‰, which is characteristic of a bacteriogenic origin. Preliminary data show a tendency to increased $\delta^{34}S$ with time. Questions arise as to the timing of S input, in relation to remobilisation, and the influence of hostrock heterogeneity.

Keywords

Kalahari-Copperbelt, S isotope, Copper-silver, Ghanzi

1 Introduction

The Hana Mining Ltd. Ghanzi project is part of the Kalahari Copper-belt, which lies within the Pan-African Damara belt extending from the Atlantic coast in Namibia up through Botswana for over 1000 km (Fig. 1) (Borg and Maiden 1989, Modie 1996). The mineralisation is believed to be a sediment-hosted stratiform copper-silver deposit which has an estimated strike length of 600 km, of which only around 11% has currently been explored (Hana Mining Ltd. Corporate Presentation, 2012).

This project employs transmitted and reflected light microscopy, SEM, and sulphur isotopes, to develop a mineralisation model in this relatively understudied orefield.

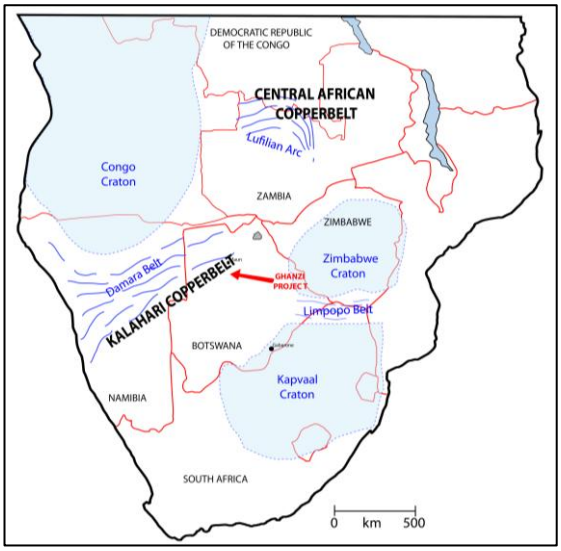

Figure 1. Map of Southern Africa showing the location of the Kalahari Copperbelt within the Damara Belt and the locations of cratons (Modified after Borg and Maiden, 1989 and Modie 1996, 2000).

2 Geological Setting

2.1 Regional Geology

Rift basins formed during a period of crustal extension and resulted in the eruption of bi-modal volcanism of the Kgwebe Formation around 1106 Ma (Schwartz et al. 1995, Modie 1996). Deposition of clastic red-beds of the Kuke and Ngwako Pan followed; these were in turn followed by a period of subsidence and basin evolution into a shallow marine environment and the deposition of finer grained siliciclastics and carbonate rocks of the D'Kar Formation (Modie 1996, 2000). The Kuke, Ngwako Pan and the D'Kar formations together make up the Ghanzi group which has an estimated thickness of around 5 km of which only a small fraction is sampled in Hana Mining drill core. The Ghanzi-Chobe belt has been regionally correlated to the Witvlei and Klein Aub basins in Namibia (Borg and Maiden 1989).

The rift basins closed during the Pan-African Orogeny between 630-500 Ma which resulted in the zone of deformation and metamorphism, the Damara belt (Miller 1983, Carney et al. 1994). In Botswana this belt is 500 km long and trends NE-SW from the Namibian border at Mamuno up to the Goha and Shinamba Hills in northern Botswana (Modie 1996).

2.2 Deposit Geology

Mineralisation is hosted in reduced facies rocks of the D'Kar formation which rests conformably above the Ngwako Pan sandstone (Fig. 2). The rocks were folded during the Damara orogeny into large-scale regional folds with amplitudes around 10 km and wavelengths of about 25 km (Litherland 1975).

The Ngwako Pan sandstone is an oxidised immature amalgamation of poorly sorted, red, brown, grey and purple bedded sandstones with compositions ranging between sublitharenite, subarkose and lithic arkose. Generally medium to medium-coarse grained it has occasional fine silt beds and coarser granule beds. The

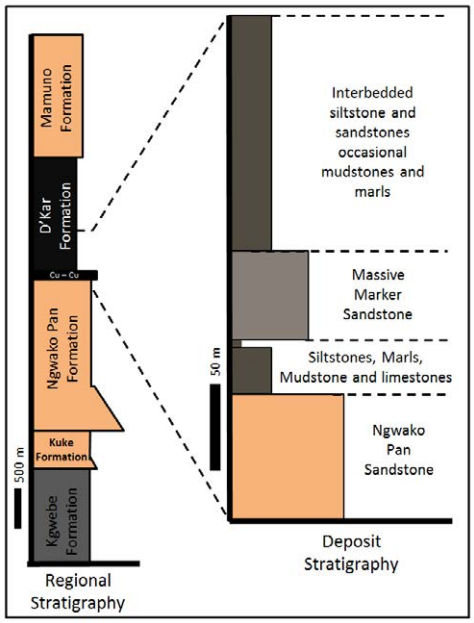

Figure 2. Stratigraphic column of the geology intersected in the Hana drill-core. Mineralisation is hosted above the Ngwako Pan sandstone within the reduced D'Kar formation.

overlying D'Kar formation consists of fine grained grey to grey-green reduced fine grained sandstones, siltstones, marls, recrystallised limestones, rhythmic siltstones, microbial laminated units and carbonaceous mudstones.

Mineralisation is dominantly hosted within the first 20m of the D'Kar formation, although minor horizons are found within the Ngwako Pan sandstone.

The region is covered in Kalahari Group sediments so that Ghanzi Group exposure is almost non-existent in the Hana Mining license areas.

3 Petrography

Mineralisation is hosted within laminations, as nodules, in cleavages, as sulphide blebs and in associated quartz-carbonate veins; a detailed study of non-vein related mineralisation has been undertaken by Gorman et al. (2013, Unpublished data) who worked in parallel with this project. The main focus of this project is the quartz-carbonate veins that are often highly mineralised and are closely associated with the disseminated mineralisation.

Hand-specimen and petrographic studies have identified three stages of veining (Figs 3, 5): 1) Early stage veins which are bedding parallel to sub-parallel and deformed, 2) Middle stage less deformed veins usually at higher angles to bedding and less deformed, and 3) Late stage massive veins.

Early veins are often mineralised with bornite and chalcocite exhibiting exsolution textures, along with chalcopyrite further above the contact. They show

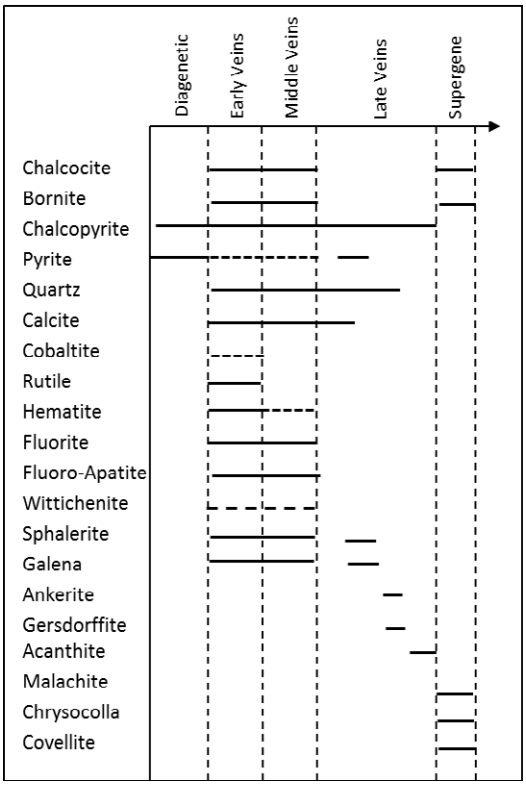

Figure 3. Paragenetic sequence of mineralisation where solid lines are observed major phases and dashed lines are observed minor phases.

evidence of being introduced before the main stage of deformation and are usually deformed to a similar degree as the bedding; they usually contain chlorite± fluorite ±hematite with occasional rutile ±ilmenite.

Middle stage veins show evidence of being introduced during deformation; cutting through already formed axial planar cleavage in finely laminated siltstones and mudstones, or cutting bedding at high angles. These vein generations also have bornite-chalcocite-chalcopyrite mineralisation in the mineralised horizon along with accessory chlorite ±fluorite ±hematite. The notable difference is the absence of hydrothermal rutile. It is over this period of veining and mineralisation that disseminated sulphides throughout the host rock were enriched from sedimentary and diagenetic pyrite to high Cu/Fe sulphides.

The late stage massive veins are large structures with apparent thicknesses of up to 4 m and are only found in the anticlinal hinge zones of the large-scale folds inferred to have formed during an intense period of regional deformation that resulted in large scale brittle fracturing. The size of these veins and their numbers makes them likely to have formed very good fluid pathways to channel and concentrate mineralisation. At least four phases of deposition have been identified in one sample: 1) subhedral to euhedral quartz-calcite, 2)

calcite-chalcopyrite-galena-sphalerite, 3) Pyrite-ankerite and 4) late stage acanthite fracture coating.

There is a general decrease in the Cu/Fe of sulphides upwards from the Ngwako Pan/D'Kar contact resulting in a zoning pattern of chalcocite- bornite- chalcopyrite with distal pyrite-galena-sphalerite.

4 Sulphur Isotopes

Twenty-two samples for S isotope analysis were drilled from primary sulphides in quartz carbonate veins or disseminated in the host rock. Values are given per mil relative to the Vienna Canon Diablo Troilite (V-CDT).

The samples show a large spread in $\delta^{34}S$ from -45.7‰ through to +0.4‰ (Fig. 4), although there is a suggestion of bimodality, but given the small populations this is speculative. Nonetheless, there is a noted absence of values between -39 and -22‰.

Figure 4A shows values for early stage disseminated sulphides, the lightest of these values represent deformed lenses of early pyrite of which some have been mobilised to bornite by the mineralising fluids.

Early stage veins (Fig. 4B) show two clusters one which can be correlated with the lightest pyrite lenses, the other is closer to the heavier disseminated pyrite. These veins show a slight overlap with intermediate stage veins (Fig. 4C). Late stage veins (Fig. 4D), drilled from 2 veins about 50 m apart show values that are -21.3±0.3‰.

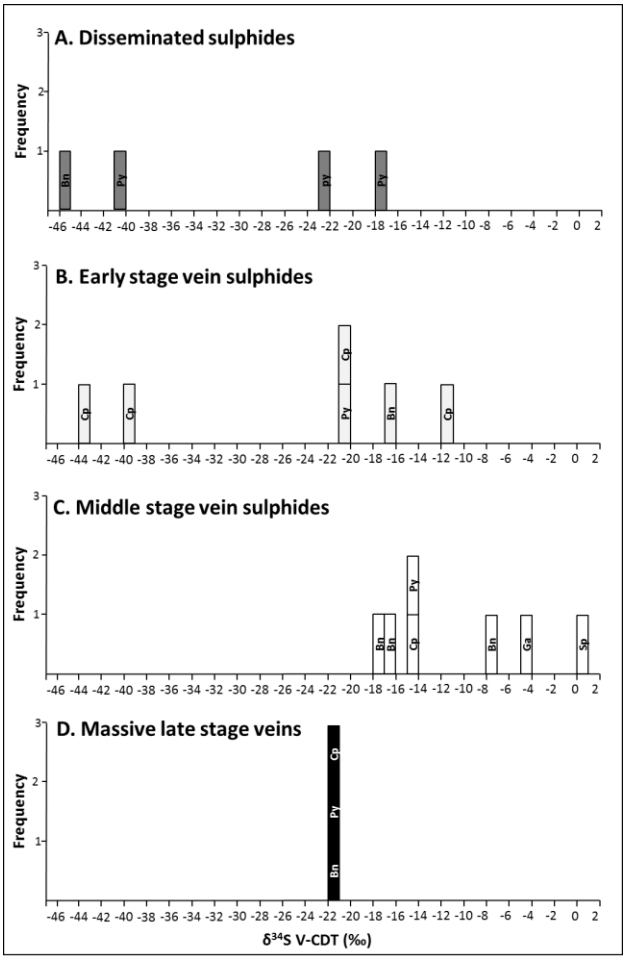

Figure 4. Frequency plots showing the distribution of sulphur isotope values in the various vein generations. Bn: Bornite, Cp: Chalcopyrite, Py: Pyrite, Sp: Sphalerite, Ga: Galena.

A magmatic source is completely discounted. Instead, a bacteriogenic origin for all sulphide is demanded, given the extent of fractionation from any potential known sulphate reservoir (e.g. a Neoproterozoic seawater value of +17.5‰ ±3‰, El Desouky et al. 2010) . The lightest values resulted from extreme fractionation of seawater sulphate by bacterial sulphate reduction; this resulted in $\Delta^{34}S_{SO4\text{-}H2S}$ values of ~55.0 to 62.5‰, comparable to the exceptionally light values seen in rocks of this age in Scotland (Parnell et al., 2010).

The low values seen in late vein developments – post deformation – retain a bacteriogenic signature, and it may be that remobilised earlier diagenetic sulphide was likely to be the source of this sulphide – a process seen in the Kupferschiefer deposits in northern Europe (Wagner et al. 2010).

These values therefore imply that the Kalahari Copperbelt is isotopically very different from what is considered normal values for the Central African Copperbelt of Zambia and DRC. In the latter, there is evidence of a new source of sulphur in later, main stages of mineralisation, with sulphide the product of thermochemical sulphate reduction (McGowan et al. 2006 and Muchez et al. 2010). There is no evidence of such a thermochemical source at the Ghanzi project.

5 Conclusion

Mineralisation occurred over a protracted period that potentially preceded as well as overlapped regional deformation and resulted in multiple vein generations. Figure 5 shows our genetic model for mineralisation at the Ghanzi project. Early stage veins are developed along bedding planes and other weakness planes in the rocks (Figure 5A), these are then subsequently deformed as deformation continues (Fig. 5B). Deformation is contained in the incompetent units of the fine-grained D'Kar, veins in the more competent Ngwako Pan are less deformed. Middle stage veins are formed later and undergo less deformation (Fig. 5C). The final stage are massive late stage veins which cross cut earlier features (Fig. 5D) and are found only in the anticlinal hinge zones of regional scale folds.

Sulphur for both disseminated mineralisation and vein hosted sulphides was likely derived from in-situ sulphur which resulted from BSR below the sediment-water interface during host rock formation in the Neoproterozoic. It is unlikely that the heavier values are the result of TSR – they are more likely due to spatial variations in BSR.

Acknowledgements

Thanks are extended to Hana Mining Ltd. who funded and provided the samples for the project, and to the geologists on site who helped with cutting and sampling.

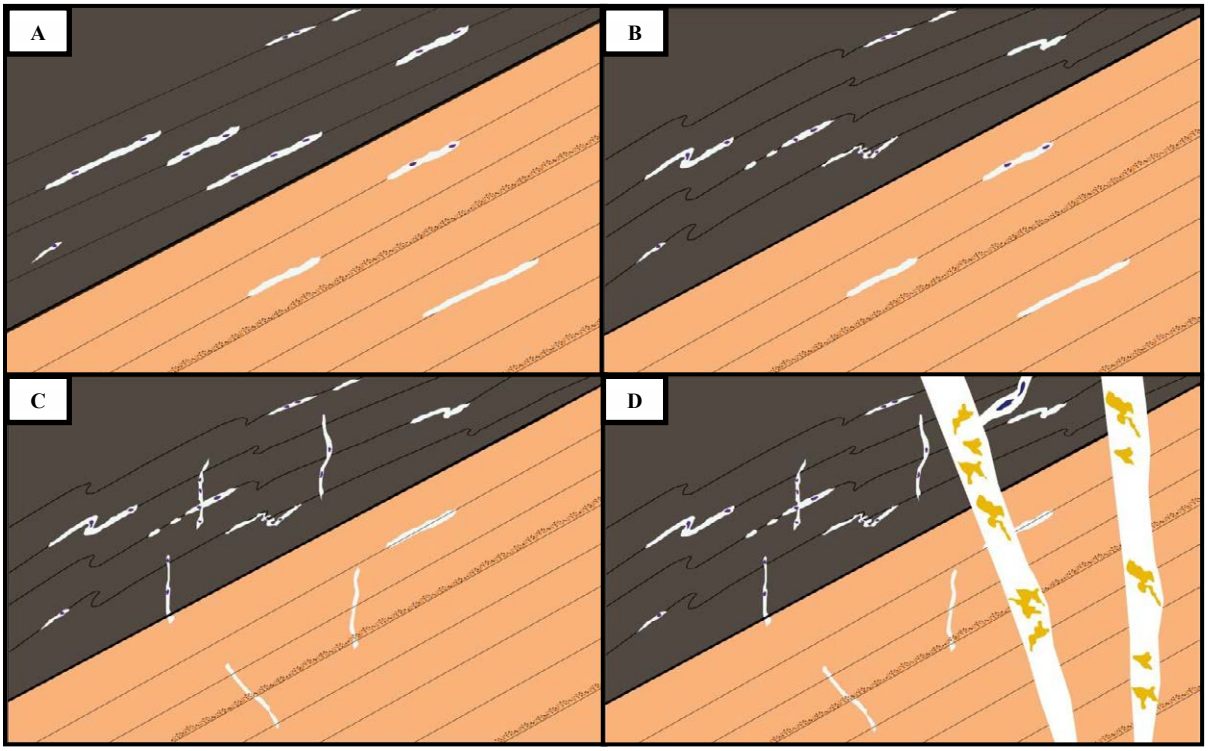

Figure 5. Genetic model for vein and disseminated mineralisation derived from a similar model proposed for Nkana Mine, Zambia by Muchez et al. (2010). A) Early stage veins are bedding parallel to sub parallel and follow planes of weakness in the rocks. B) Early veins are subsequently deformed with regional deformation. C) Middle stage veins cross cut early veins and cut bedding. They have also been observed following along already formed cleavage in some rhythmic mudstones. D) Latest stage massive cross cutting veins which form in dilation fractures in fold hinges. Stages 1, 2 and 3 may be associated with the enrichment of primary sulphides into copper rich sulphides.

References

Borg G and Maiden KJ (1989) The Middle Proterozoic Kalahari Copperbelt of Namibia and Botswana, In: Boyle RW, Brown AC, Jefferson CW, Jowett EC and Kirkham RV, (eds) Sediment-hosted Stratiform Copper Deposits: Geological Association of Canada, Special Paper 36: 525-540.

Carney JN, Aldiss, DT and Lock, NP (1994) The Geology of Botswana, Geological Survey Department, Republic of Botswana. Bulletin 37:71-83.

El Desouky HA, Muchez Ph, Boyce AJ, Schneider J, Cailteux, JLH, Dewaele S, von Quadt A (2010) Genesis of sediment-hosted stratiform copper–cobalt mineralization at Luiswishi and Kamoto, Katanga Copperbelt (Democratic Republic of Congo). Mineralium Deposita 45:735–763

Litherland M (1975) The geology of the area around Maitengwe, Sebina and Tshesebe, Northeast and Central Districts, Botswana. District Memir Geological Survey of Botswana 2:133.

McGowan RR, Roberts S, Boyce AJ, (2006) Origin of the Nchanga copper-cobalt deposits of the Zambian Copperbelt. Mineralium Deposita 40: 617-638.

Miller RM, (1983) The Pan-African Damara orogeny of South West Africa–Namibia, In: Miller RM, (eds) Evolution of the Damara orogen of South West Africa/Namibia: Geological Society of South Africa Special Publication 11:431–515.

Modie BN (1996) Depositional environments of the Meso- to Neoproterozoic Ghanzi-Chobe belt northwest Botswana: Journal of African Earth Sciences 22:255–268.

Modie BN (2000) Geology and mineralisation in the Meso- to Neoproterozoic Ghanzi Chobe Belt of northwest Botswana, Journal of African Earth Sciences 30(3): 467-474.

Muchez Ph, Brems D, Clara E, De Cleyn A, Lammens L, Boyce A, De Muynck D, Mukumba W, Sikazwe O, (2010) Evolution of Cu–Co mineralizing fluids at Nkana Mine, Central African Copperbelt, Zambia. Journal of African Earth Sciences 58: 457–474.

Parnell J, Boyce AJ, Mark DF, (2010) Early oxygenation of the terrestrial environment during the Mesoproterozoic Nature, 468: 290-293.

Schwartz MO, Akanyang P, Trippler K and Ngwisanyi TH (1995) The Sediment hosted Ngwako Pan Copper Deposit, Botswana. Economic Geology 90:118-1147.

Wagner T, Okrusch M, Weyer S, Lorenz J, Lahaye Y, Taubald H, Schmitt RT (2010) The role of the kupferschiefer in the formation of hydrothermal base metal mineralization in the Spessart ore district, Germany: insight from detailed sulphur isotope studies. Mineralium Deposita 45:217-239

Tracing seawater evaporation and evaporite dissolution in the Zambian Copperbelt: evidence from crush-leach analysis of fluid inclusions and stable isotopes

James Nowecki Stephen Roberts
Ocean and Earth Science, University of Southampton, National Oceanography Centre, Southampton, SO14 3ZH, U.K.

Sarah Gleeson
Department of Earth and Atmospheric Sciences, University of Alberta, Edmonton, AB, Canada

Adrian Boyce
Scottish Universities Environmental Research Centre, Scottish Enterprise Technology Park, East Kilbride, Glasgow, G75 QF

Abstract. Fluids in the Zambian Copperbelt have been investigated by sampling different generations of vein material from numerous deposits across the classic mining district and currently explored Western Domes region. Veins were segregated into pre kinematic, pre-syn kinematic and post kinematic groups based on their relationship to host rock fabrics. Crush-leach halogen data indicates the presence of two main fluid types, one with Cl/Br < seawater, indicative of a fluid derived from residual evaporated seawater which dominate the pre and pre-syn kinematic samples, and one with Cl/Br > seawater, characteristic of a fluid containing a component derived from dissolved evaporites which dominated the post-kinematic vein generation. Halogen data suggests fluids were ultimately derived from strong evaporation of seawater beyond the carnalite saturation point. Cation data suggests significant water-rock interaction consistent with hydrothermal alteration assemblages. $\delta^{37}Cl$ of fluid leachate is close to 0 for all samples, suggesting an ultimate seawater source of chlorine. $\delta^{18}O_{fluid}$ is variable between ~ -3 and +11, probably reflecting different amounts of water-rock equilibration and different residence times. Isotopically light $\delta^{13}C$ and δD signatures reflect oxidation of organic matter. Vein material with $\delta^{13}C$ similar to Neoproterozoic carbonates reflects buffering by host rock carbonate sequences.

Keywords.

Zambia, Copperbelt, fluids, halogens, stable isotopes

1 Sampling

Sediment-hosted stratiform copper deposits are economically important, with the Central African Copperbelt one of the largest and most well mineralised examples of a basin containing this type of deposit (Hitzman et al. 2005). These deposits are known to result from basin-scale fluid flow systems where oxidised metal-rich fluids are reduced causing sulphide precipitation (Jowett 1986; Hitzman et al. 2005).

Sampling was conducted for mineralised and barren vein quartz and carbonate samples from a suite of copper deposits from the classic Copperbelt stratigraphy Konkola, Konkola North and Nchanga, the basement in this region, Samba, and deposits and prospects from across the Domes region, Lumwana, Kansanshi, Kalumbila-Sentinel and Enterprise (Fig. 1). Vein generations were categorised by their relationship to the fabrics of the host rocks. Three main groups were identified, pre kinematic veins, pre-syn kinematic veins, and post kinematic veins (Fig. 2.). Pre kinematic veins

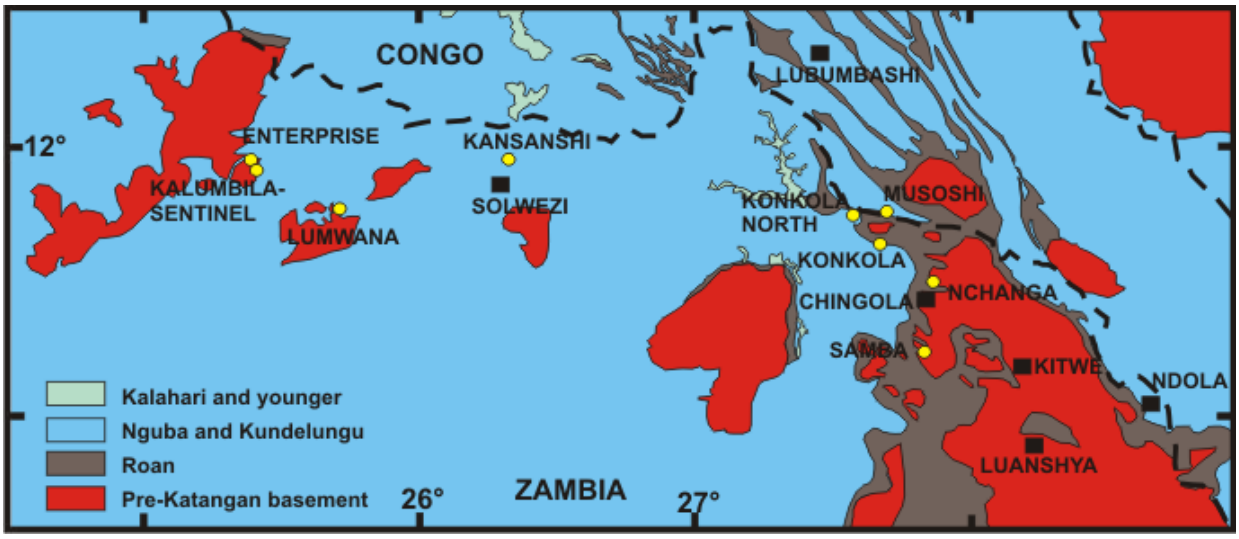

Figure 1. Map of Zambian Copperbelt and Domes Region with sampled deposits labelled.

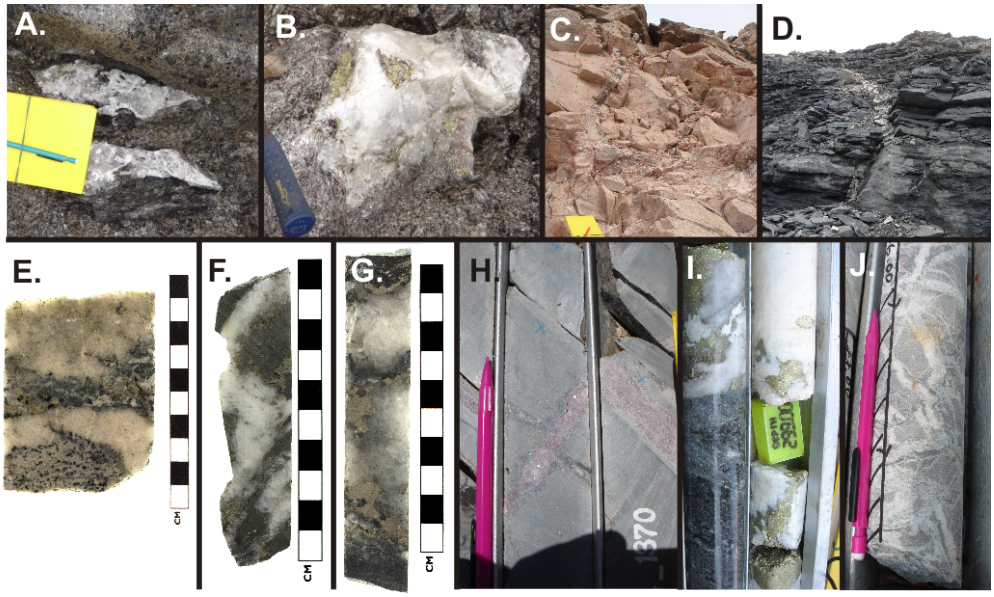

Figure 2. A) Pre kinematic vein from Lumwana. B) Pre-syn kinematic vein from Lumwana. C and D) Post kinematic veins from Lumwana. E) Pre kinematic veins from Samba. F) Pre-syn kinematic veins from Konkola. G) Pre-syn kinematic veins from Kalumbila-Sentinel. H) Pre-syn kinematic veins from Konkola North. I and J) Post kinematic veins from Kansanshi and Enterprise.

included boudinaged veins, and veins folded alongside host rock fabrics. Pre-syn kinematic veins both cut and exploited host rock fabrics such as bedding, and post kinematic veins cut all host rock fabrics such as bedding and cleavage. This categorisation allows an estimated timing of fluid migration within individual deposits and the region as a whole.

2 Crush-leach

Cl/Br ratios obtained via bulk crush leach studies of fluid inclusions indicate two main sources for the hydrothermal fluids related to these deposits. Konkola, Konkola North and Samba show Cl/Br ratios below that of seawater (Cl/Br = 658; Gleeson 2003), characteristic of a residual fluid formed by evaporation of seawater

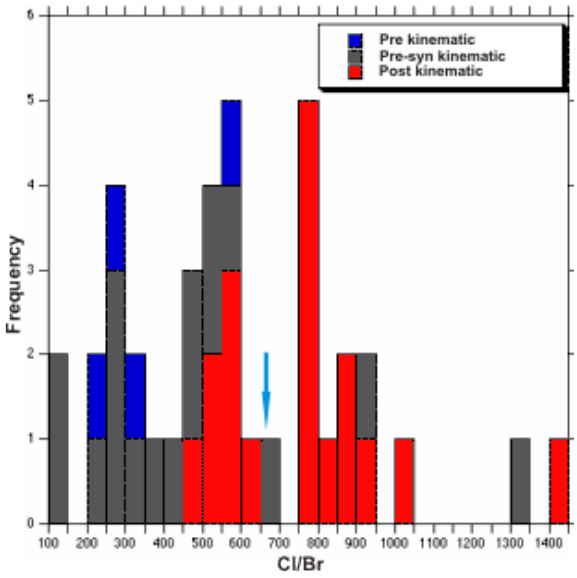

Figure 3. Chlorine-bromine ratios for veins from the different deposits studied grouped by vein textural paragenesis. Arrow indicates Cl/Br of modern seawater.

beyond the halite saturation point. Enterprise and Kalumbila-Sentinel show Cl/Br ratios above that of seawater, indicative of dissolution of halite in evaporite sequences. All veins within the ore zones at Nchanga show the seawater signature, whilst veins within the underlying granite show both the seawater signature and that of halite dissolution, suggesting multiple phases of fluid flow through the Nchanga basement. At Lumwana, pre kinematic veins show the seawater signature, whilst post kinematic veins show the halite dissolution signature indicating a change in fluid source later in the deposit history. At Kansanshi, there is a degree of mineralogical control over the two signatures, with quartz showing mostly the halite dissolution signature, and carbonate mainly showing the seawater evaporation signature. From these data, it is clear that the evaporation of seawater and the associated formation of evaporite deposits were critical in the fluid history of the basin. Though constraints on timing are limited, pre kinematic veins show a residual evaporated seawater signature, whilst the halite dissolution signature correlates with post kinematic veins (Fig. 3). This suggests a fluid event late in the basin history (post peak metamorphism) dominated by the dissolution of evaporites, whilst earlier fluid flow was controlled by the evaporation of seawater and the deposition of evaporite sequences. For these reasons, increasing Cl/Br can be used as a general proxy for passage of time in the basin history.

Reconstructing concentrations of Cl^- in the leachates using the equation of Banks et al. (2000) indicates that evaporation continued to beyond the carnalite saturation point (Fontes and Matray 1993). Cation data from leachates are indicative of water-rock interaction, particularly Na/Br, which is typically lower than expected for the seawater evaporation trajectory, reflective of the pervasive sodic alteration in the Copperbelt typified by the growth of albite and scapolite.

3 Stable isotopes

Chlorine isotope data from vein leachates are clustered around 0 ‰ (Fig. 4), indicative of a crustal Cl source. These data are all within the -1 to +1 ‰ range of seawater, evaporites and residual fluids formed after

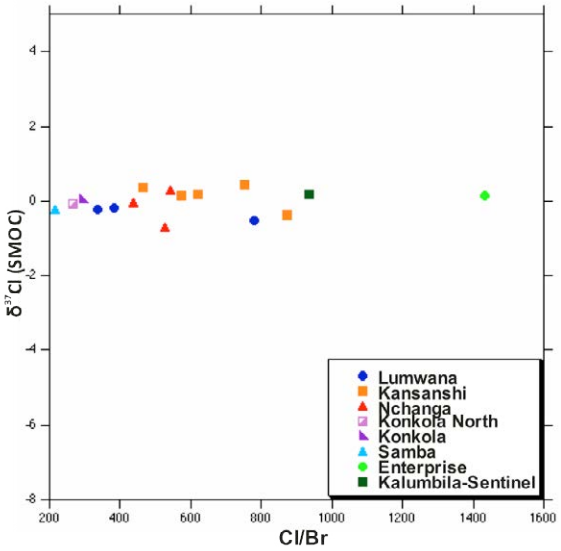

Figure 4. Stable chlorine isotope data from a subset of fluid inclusion leachates. Data fall very close to 0‰ (relative to Standard Mean Ocean Chloride) and show no variation with Cl/Br suggesting no change in isotopic source of chlorine throughout basin history.

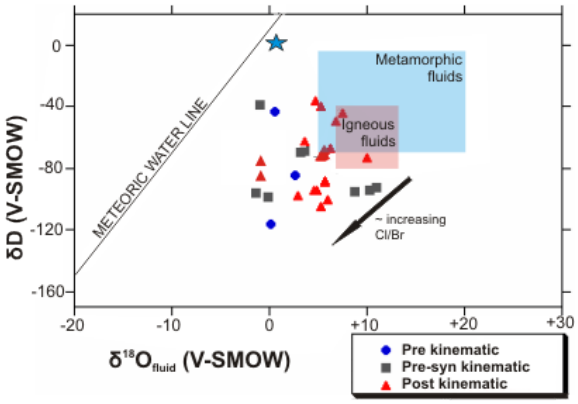

Figure 5. Isotopic compositions of Copperbelt vein samples grouped by vein textural paragenesis. (Figure after Sheppard, 1986). $\delta^{18}O_{fluid}$ calculated for each sample based on raw $\delta^{18}O$ value and average temperature of fluid inclusion assemblage for deposit using the fractionation factors of Matsuhisa et al. (1979) for quartz samples and Zheng (1999) for carbonates. Data in permil (‰) relative to V-SMOW, star represents modern seawater.

evaporite precipitation (Eastoe et al. 2007).

Oxygen isotope data from vein quartz and carbonate have is corrected for temperature using microthermometric data from fluid inclusion studies to give $\delta^{18}O_{fluid}$. Much of the data e.g. Kansanshi, Lumwana, Nchanga, Kalumbila-Sentinel, Samba, and Musoshi give values ~-3 to +6 ‰. Other data e.g. Enterprise, Konkola, and Konkola North give heavier values (~+8 to +11 ‰). These values may represent basin brines beginning to equilibrate with metasediments and metamorphic rocks (Taylor 1997; Clayton et al. 1966; McGowan 2006).

$\delta^{13}C$ of vein carbonates varies from ~-1.5 ‰ (Kalumbila-Sentinel) to -19 ‰ (Konkola; data relative to V-PDB). The Kansanshi data show very consistent $\delta^{13}C$ ~ -3 ‰ and there is good grouping in the data from Konkola and Konkola North. Isotopically light samples reflect the oxidation of organic matter and subsequent carbonate generation due to ore formation (Machel 1987; Machel et al. 1995), whereas the heavier data are similar to those of Neoproterozoic carbonate within the host sediment packages or succession reflecting isotopic buffering.

Hydrogen isotope ratios from fluid inclusions within quartz and carbonate vein material from all deposits vary greatly between -116.6 and -16.9 ‰ (V-SMOW). When combined with data for $\delta^{18}O_{fluid}$ veins from the Copperbelt plot away from the meteoric water line and seawater. The data for Nchanga show more variation in $\delta^{18}O_{fluid}$ than δD, whereas Kansanshi and Lumwana show tight grouping in $\delta^{18}O_{fluid}$ and wide variation in δD, resulting in linear trends. There is no correlation between δD and kinematic setting of veins (Fig. 5). Much of the hydrogen data from the Copperbelt shows lighter isotope ratios than expected with regards to the generally accepted palaeolatitude, suggesting a strong fractionation effect is required to produce these results. There is no correlation between sample hydrogen yield and light δD and there is no significant difference between data from carbonate and quartz samples, indicating that any influence on the results by structural hydrogen was negligible (e.g. Gleeson et al. 2008). We suggest that the light δD signatures, similar to the light $\delta^{13}C$ signatures, are a function of oxidation of organic matter. Shales and hydrocarbons show very light δD signatures, with hydrocarbons in particular typically <-100 ‰ (e.g. Savin and Epstein 1970; Burruss and Laughrey 2010) and hydrocarbons are predominantly composed of C and H, providing a plausible mechanism why δD and $\delta^{13}C$ signatures are light, whereas $\delta^{18}O_{fluid}$ is not, especially when isotopic buffering by host rocks is taken into account. There is abundant evidence for the importance of organic and shale reductants in the process of formation of sediment-hosted stratiform copper deposits, and evidence for the role of hydrocarbons is found as preserved in the form of liquid petroleum and methane in fluid inclusions (Mauk and Hieshima 1992; Greyling et al. 2005), and as metamorphosed bitumen (Heijlen et al. 2008).

There is a negative trend between $\delta^{18}O_{fluid}$ and Cl/Br. It is proposed that this trend reflects fluid residence time, with 'early' (low Cl/Br) fluids exhibiting heavier $\delta^{18}O_{fluid}$ due to longer residence times and lower water-rock ratios for isotopic equilibration.

4 Conclusion

The Zambian Copperbelt preserves a fluid system dominated by the evaporation of seawater, generation of residual saline basin brines and evaporite deposits, and the subsequent later dissolution of the evaporite sequences and incorporation into the fluid system. These saline brines were highly efficient at scavenging and transporting metals. Water-rock interaction is recorded by cation data from leachates reflective of the hydrothermal alteration assemblage present in the Copperbelt, and by variable oxygen isotope signatures of

fluids. Vein material and fluid inclusions typically show very light carbon and hydrogen isotope signatures. In the case of δD these signatures are too light to be generated by meteoric waters over the palaeogeographic history of the Copperbelt region, and we suggest that they preserve evidence for interaction with and oxidation of organic material, as has been accepted for the light $\delta^{13}C$ signatures prevalent in carbonates formed by this process.

Acknowledgements

We are extremely grateful to exploration and mining geologists at Equinox Minerals (Now Barrick) and Lumwana Mining Co., in particular to Mike Richards for provision of accommodation during fieldwork, sample acquisition and expertise. Similarly, great thanks to geologists from First Quantum Minerals and TEAL for access to samples. We also thank Philippe Muchez for very fruitful discussions on data, and the Copperbelt in general.

References

Banks DA, Giuliani G, Yardley BWD, Cheilletz A (2000) Emerald mineralisation in Columbia: fluid chemistry and the role of brine mixing. Mineralium Dep. 35: 699-713.

Burruss RC, Laughrey CD (2010) Carbon and hydrogen isotopic reversals in deep basin gas: Evidence for limits to the stability of hydrocabons. Org. Geochem. 41: 1285-1296.

Clayton RN, Friedman I, Graf DL, Mayeda TK, Meents WF, Shimp NF (1966) The origin of saline formation waters 1. Isotopic composition. J Geophys Res 71: 1197-1201.

Eastoe CJ, Peryt TM, Petrychenko OY, Geisler-Cussey D (2007) Stable chlorine isotopes in Phanerozoic evaporites. App. Geochem. 22: 575-588.

Fontes JC, Matray JM (1993) Geochemistry and origin of formation brines from the Paris basin, France: 1. Brines associated with Triassic salts. Chem. Geol. 109: 149-175.

Gleeson SA (2003) Bulk analysis of electrolytes in fluid inclusions. In Sampson et al., Fluid inclusions: analysis and interpretation, Mineralogical Association of Canada Short Course vol. 32. Chapter 9. 233-246.

Gleeson SA, Roberts S, Fallick AE, Boyce AJ (2008) A combined micro Fourier Transform Infrared and δD isotopic investigation of hydrothermal vein quartz: Implications for the interpretation of fluid inclusion δD values in hydrothermal systems. Geochim. et Cosmochim. Acta 72: 4595–4606.

Greyling LN, Robb LJ, Master S, Boiron MC, Yao Y (2005) The nature of early basinal fluids in the Zambian Copperbelt: A case study from the Chambishi deposit. J. Afr. Earth Sci. 42: 159-172.

Heijlen W, Banks DA, Muchez P, Stensgard BM, Yardley BWD (2008) The nature of mineralizing fluids of the Kipushi Zn-Cu deposit, Katanga, Democratic Republic of Congo: Quantitative fluid inclusion analysis using Laser Ablation ICP-MS and bulk crush-leach methods. Econ. Geol. 103: 1459-1482.

Hitzman M, Kirkham R, Broughton D, Thorson J, Selley D (2005) The sediment-hosted stratiform copper ore system. Econ. Geol. 100th Anniv. Vol. 609-642.

Jowett EC (1986) Genesis of Kupferschiefer Cu-Ag deposits by convective flow of Rotliegendes brines during Triassic rifting: Econ. Geol. 81: 1823-1837.

Machel HG (1987) Saddle dolomite as a by-product of chemical compaction and thermochemical sulphate reduction. Geology 15: 936–940.

Machel HG, Krouse HR, Sassen R (1995) Products and distinguishing criteria of bacterial and thermochemical sulphate reduction. Appl. Geochem. 10: 373–389.

Matsuhisa Y, Goldsmith JR, Clayton RN (1979) Oxygen isotopic fractionation in the system quartz-albite-anorthite-water. Geochim. Cosmochim. Acta 43: 1131-1140.

Mauk JL, Hieshima GB (1992) Organic matter and copper mineralization at White Pine, Michigan, U.S.A. Chem. Geol. 99: 189-211.

McGowan RR, Roberts S, Boyce AJ (2006) Origin of the Nchanga copper-cobalt deposits of the Zambian Copperbelt. Mineralium. Dep. 40: 617-638.

Savin SM, Epstein S (1970) The oxygen and hydrogen isotope geochemistry of ocean sediments and shales. Geochim. Cosmochim. Act. 84: 48-68.

Sheppard SMF (1986) Characterization and isotopic variations in natural waters. In Valley JW, Taylor HP, O'Neil JR (eds.) Reviews in Mineralogy vol. 16: Stable isotopes in high temperature geothermal processes. Mineralogical Society of America. 165-184.

Taylor HP (1997) Oxygen and hydrogen isotope relationships in hydrothermal mineral deposits. In Barnes HL (ed) Geochemistry of hydrothermal ore deposits. Wiley, New York, 229–302

Zheng Y-F (1999) Oxygen isotope fractionation in carbonate and sulphate minerals. Geochem. Journal 33: 109-126.

The principal carriers of platinum-group elements (PGE) in metal-rich black shales: new data from Mo-Ni-PGE black shales (Zunyi region, Guizhou province, south China)

Jan Pašava, Anna Vymazalová
Czech Geological Survey, Geologická 6, 152 00 Prague 5, Czech Republic

Federica Zaccarini
Montanuniversitaet Leoben, Peter.Tunner Str. 5, A-8700 Leoben, Austria

Thomas Aiglsperger
University of Barcelona, C/Marti i Franques s/n, E-08028 Barcelona, Spain

Abstract: We studied Lower Cambrian marine Mo-Ni sulfidic black shales from the Huangjiawan mine in Guizhou Province, south China in which anomalous PGE values (of up to ~1 ppm) were reported. For identification of principal PGE carriers, we used heavy mineral separates which were produced by innovative hydroseparation (HS) technique. A detailed electron microprobe study did not result in identification of discrete platinum-group minerals (PGM). The most abundant sulfides (grainy/not framboidal pyrite, millerite and gersdorffite) were analyzed for PGE and Re. Grainy pyrite contains up to 490 ppm Pt, 390 ppm Pd and 220 ppm Rh. Millerite contains up to 530 ppm Pt, 320 ppm Pd and 190 ppm Rh. Gersdorffite contains up to 410 ppm Pt, 320 ppm Pd with no Rh detected. Rhenium concentration (up to 610 ppm) was detected only in grainy pyrite. Despite anomalous PGE concentrations the Mo-Ni black shale doesn´t contain any discrete PGE phases. PGE are bound to pyrite and Ni-sulfides (millerite and gersdorffite).

Keywords. Mo-Ni-PGE black shale, hydroseparation, electron microprobe study, anomalous PGE in pyrite and Ni sulfides

1 Introduction

Anoxic sediments and metasediments have been recently recognized as important host environments for the platinum group elements (PGE) (e.g., Pašava 1993, Sawlowicz 1993). Economically significant PGE concentrations have been reported from marine, metal-rich black shales in China, Yukon (Canada) and Poland (Chen et al. 1982, Kucha 1975, Hulbert et al. 1992 and others). These ore-bearing horizons are characterized by extremely restricted vertical and sometimes larger horizontal extents. They are associated with the evolution of intracontinental rifting structures without any magmatic activity, suggesting a possible driving mechanism for mineralization processes (Pašava 1993).
The Early Cambrian marine black shales of south and southwest China host Mo-Ni-PGE-Au deposits that outcrop discontinuously throughout six provinces in a belt approximately 1600 km long (Chen et al. 1982, Fan 1983). The Mo-Ni ore contains more than 4 wt.% Mo, at least 2 wt.% Ni, up to 2 wt.% Zn, 2.5 wt.% As and 1-2 g/t of precious metals, primarily Au, Pt, Pd, and Os (Fan 1983). The deposits are important, particularly because they constitute a largely untested alternative to conventional sources of precious metals, especially PGE (Coveney and Chen 1991). Macroscopically, only pyrite can be recognized in ore samples. However, major ore minerals are vaesite, bravoite, jordisite and MoSC phase (Fan 1983, Kao et al. 2001, Orberger et al. 2007). Minor ore minerals include arsenopyrite, chalcopyrite, covellite, sphalerite, millerite, polydymite, gersdorffite, sulvanite, pentlandite, tennantite, tiemannite, violarite, and native gold (Fan 1983, Grauch et al. 1991). A highly porous matrix of the ore bed is composed of organic matter or alumosilicate-rich laminae or lenticular bodies that are intercalated with phosphate- or sulfide-rich lenses (Pašava et al. 2008). Various genetic models for the origin of these metal-rich facies were discussed by Coveney and Pašava (2005).

Despite anomalous PGE concentrations (ΣPGE ~1 ppm), no PGE discrete phases were identified to date. Using a specialized separation technique which was uniquely designed for the release and concentration of platinum-group minerals (PGM), in this work we provide a new evidence that point to a close relationship between sulfides and PGE concentrations rather than proving the existence of individual discrete PGE phases.

2 Results and discussion

2.1 Material and methods

For separation and concentration of heavy minerals fraction we used a representative sample (641 g) which was collected from fresh Mo-Ni-PGE orebody at the Huangjiawan mine area, Zunyi region, northern part of Guizhou province. The location and general geology of the sampling area is shown in Fig. 1.

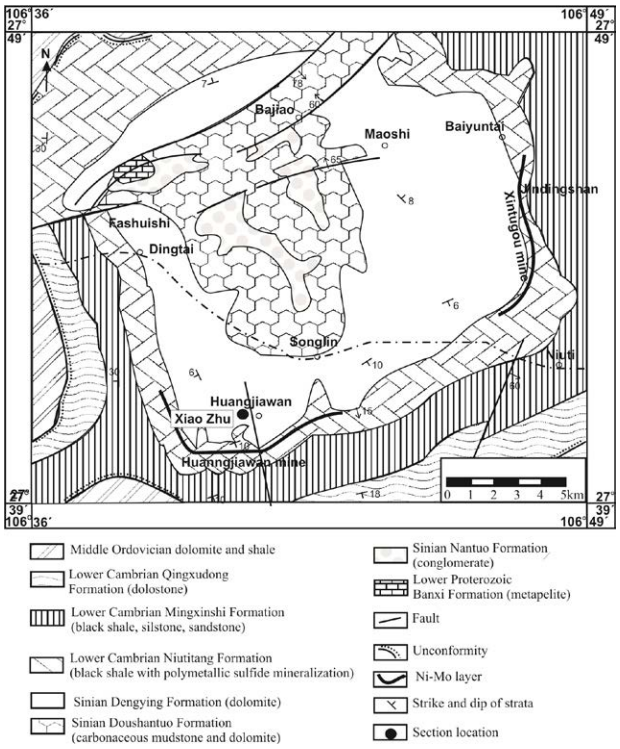

Figure 1. Simplified geology and location of Ni-Mo horizons in the Zunyi region, Guizhou Province, south China (adapted from Mao et al. 2002).

The ore sample contains 7 wt.% Mo, 2 wt.% Ni, 19 wt.% S and 13 wt.% C_{org} and C_{tot} (CO_2: 58 wt.%), 14 wt.% CaO, 1.2 wt.% As, 2000 ppm Se, 5400 ppm Zn, 450 ppm U and V, and up to 1 ppm PGE (Orberger et al. 2007).

The Mo-Ni-PGE ore was crushed down to a grain size <125 μm by means of a RETSCH vibratory disc mill (RS 100), using an agate grinding set. The resulting fine fraction was carefully wet sieved by hand through a standard screen series fallowing the methodology given by Aiglsperger et al. (2011). In continuation the finest size fraction (< 53 μm) was processed by innovative hydroseparation (HS-11) techniques (Rudashevky et al. 2001a,b ; Cabri et al. 2005; Rudashevsky and Rudashevsky 2006, 2007) at the HS laboratory Barcelona. Monolayer polished sections were produced from 0,25 g final concentrate. The polished sections were studied by scanning using the electron microscope. Pyrite (493 analyses), millerite (253 analyses) and gersdorffite (64 analyses) have been analyzed using a Jeol Superprobe JXA-8200 at the Eugen F. Stumpfl laboratory (University of Leoben, Austria) by wavelength dispersive systems (WDS) using 25 kV of accelerating voltage and 30nA of beam current. The counting times were 120 and 60 seconds for the peak and backgrounds, respectively. The beam diameter was about 1 μm. The ore minerals were analyzed using pure metals as the reference material for PGE and Re, synthetic NiS, natural pyrite, chalcopyrite, skutterudite and nickeline for Fe, Ni, Cu, Co, As and S. The X-ray lines used were: Kα for S, Fe, Cu, Ni and Co; Lα for As, Ru, Rh, Pt and Pd; Mα for Re. The following diffracting crystals were selected: PETJ for S, PETH for Ru, Rh and Re, LIF for Cu, LIFH for Ni, Fe, Co and Pt and TAP for As. The detection limits of the trace elements were calculated by the software and they are (in ppm): As = 70, S = 80, Fe = 70, Ni = 80, Co = 50, Cu = 90, Ru = 60, Rh = 50, Pd = 60, Pt = 80, Re = 110. Automatic corrections were performed for interferences involving Ru-Rh and Rh-Pd. The results are listed in Table 1.

2.2 Results

Despite of the relatively high concentration of PGE in the studied samples (ΣPGE ~1 ppm), no specific PGM have been found. However concentrations of Rh, Pt, Pd and Re detectable with the electron microprobe, have been found in grainy pyrite, millerite and gersdorffite (Table 1). Rh occurs in pyrite (up to 220 ppm) and in millerite (up to 190 ppm), but not in gersdorffite. Pt was found in all the minerals with concentration up to 490, 530 and 410 ppm in pyrite, millerite and gersdorffite, respectively. The highest concentration of Pd (430 ppm) was found in millerite, whereas pyrite and gersdorffite contain maximal 390 and 320 ppm of Pd, respectively. Re was found only in pyrite, with concentrations up to 610 ppm. Ru was always below detection limit.

Table 1. PGE and Re concentrations in sulfides from Ni-Mo sulfide black shale (Huangjiawan mine, Guizhou Province, south China).

Pyrite (n = 493)			
	Min. (ppm)	*Max. (ppm)*	*No.of analyses b.d.l.*
Rh	50	220	91
Pt	80	490	167
Pd	60	390	222
Re	110	610	112
Millerite (n = 253)			
Rh	50	190	39
Pt	80	530	94
Pd	60	430	93
Re	0	0	0
Gersdorffite (n = 64)			
Rh	0	0	0
Pt	80	410	20
Pd	60	320	40
Re	0	0	0

* Detection limits: Pd (60 ppm), Pt (80 ppm), Rh (50 ppm), Re (110 ppm), Ru (60 ppm)

2.3 Discussion

Orberger et al. (2007) reported increased Pd concentrations (up to 982 ppm) from Mo-S-C phase and increased Pt values from pyrite (up to 124 ppm, Pd = up to 66 ppm) and Ni-sulfides (up to 122 ppm Pt and Pd=up to 111 ppm) from Mo-Ni-PGE black shales of South China. We found significantly higher Pt and Pd values (up to 490 ppm Pt and 390 ppm Pd) and newly also

anomalous Rh and Re concentrations (up to 220 ppm and 610 ppm, respectively) in pyrite. Similarly, our PGE values in Ni-sulfides are significantly higher (up to 530 ppm Pt, 430 ppm Pd and 190 ppm Rh) than those reported by Orberger et al. (2007). These authors have suggested that Pd was preferentially incorporated with other biophilic elements to Mo-S-C phase and that Pt was concentrated with less biophilic elements into pyrite and Ni-sulfides. Our data suggest that not only Pt but also Pd, Rh and Re were incorporated into pyrite and besides Pt also Pd and Rh was concentrated in Ni-sulfides. We suggest that the absence of specific PGM in our Chinese samples, is related to non-existence of these phases. We are aware that PGE can also occur in the form of non-traditional PGM that were reported by many authors from various PGE occurrences. For example, oxygen-bearing compounds of Pt-Pd-Fe were described by Jedwab and Cassedanne (1998) from Minais Gerais in Brazil and Jedwab (2004) reported PGE oxides including several Ru-Ir-Pt-Ti-Cr-Fe oxide/hydroxide compounds from Ural. It is, however, very unlikely that PGE in Mo-Ni-PGE sulfide rich black shales would be associated with these phases as they originated under anoxic environment.

3 Conclusions

The special separation technique applied to Mo-Ni-PGE black shale resulted in the concentration of heavy separates consisting of grainy pyrite, millerite and gersdorffite. Subsequent detailed mineralogical study using electron microprobe resulted in the following findings:

1. Despite anomalous PGE concentrations (ΣPGE ~1 ppm) no PGM were identified through this study.
2. High concentrations of PGE were detected in grainy pyrite (up to 490 ppm Pt, 390 ppm Pd and 220 ppm Rh), millerite (up to 530 ppm Pt, 430 ppm Pd and 190 ppm Rh) and gersdorffite (up to 410 ppm Pt, 320 ppm Pd and without any Rh).
3. Newly, anomalous Re concentrations (up to 610 ppm) were detected in grainy pyrite.
4. We suggest that besides close association of Pd with organic matter (anomalous Pd concentrations found by Orberger et al. 2007 in Mo-S-C phase) Pt, Rh and also Re were incorporated into pyrite and also Ni-sulfides (millerite and gersdorffite).

Acknowledgements

This is a contribution to the INGO II – LG 10036 project (to JP) and the Czech – Austrian mobility program AKTION (project No. MEB061113). The University Centrum for Applied Geosciences (UCAG) is thanked for the access to the Eugen F. Stumpfl electron microprobe laboratory. Many thanks also go to the scientific director of the HS-11 laboratory, Prof. Joaquin A. Proenza (University of Barcelona).

References

Aiglsperger T, Proenza JA, Zaccarini F, Labrador M, Navarro-Ciurana D (2011) Looking for needles in a haystack: how to find PGM in laterites by using hydroseparation techniques. Macla 15: 23-24

Cabri LJ, Beattie M, Rudashevsky NS, Rudashevsky VN (2005a) Process mineralogy of Au, Pd and Pt ores from the Skaergaard intrusion, Greenland, using new technology. Mineral Eng 18: 887–897

Coveney R, Pašava J (2005) Origins of Au-Pt-Pd-bearing Ni-Mo-As(Zn) deposits hosted by Chinese black shales. In: Mao J, Bierlin FP (Eds) Mineral Deposits Research: Meeting the global Challenge. Proceedings of the 8th Biennial SGA Meeting, Beejing, China, Springer. Heidelberg. pp 101-102.

Coveney RM Jr., Chen N (1991) Ni-Mo-PGEAu-rich ores in Chinese black shales and speculations on possible analogues in the United States. Mineral Deposita 26: 83-88

Chen NC, Yang X, Liu D, Xiao X, Fan DL, Wang L (1982) Lower Cambrian Black argillaceous and arenaceous rock series in south China and its associated stratiform deposits. Mineral Deposita 1: 39-51 (in Chinese)

Fan D (1983) Polyelements in the Lower Cambrian black shale series in southern China. In: Augustithis SS (Ed), The Significance of Trace Metals in Solving Petrogenetic Problems and Controversies. Theophrastus Publications S.A., Athens, pp. 447-474.

Grauch RI, Murowchick JB, Coveney RM Jr., Chen N (1991) Extreme concentration of Mo, Ni, PGE and Au in anoxic marine basins, China and Canada. In: Pagel M, Leroy JL (Eds), Source, Transport and Deposition of Metals. Balkema, Rotterdam, pp. 531-534

Hulbert LJ, Gregoire CD, Paktunc D (1992) Sedimentary nickel, zinc, and platinum-group-element mineralization in Devonian black shales at the Nick property, Yukon, Canada: A new deposit type. Explor Mineral Geol 1(1): 39-62

Jedwab J (2004) 'Irite' (Hermann, 1836/1841) from the Urals. Mineral Mag 68: 369-394

Jedwab J, Cassedanne J (1998) Historical observations on oxygen-bearing compounds of platinum and palladium in Minas Gerais, Brazil. Can Mineral 36: 887-893

Kao LS, Peacor DR, Coveney RM Jr, Zhao G, Dungey KE, Curtis MD, Penner-Hahn JE (2001) A C/MoS_2 mixed-layer phase (MoSC) occurring in metalliferous black shales from southern China, and new data on jordisite. Am Mineral 86: 852-861

Kucha H (1975) Preliminary report on the occurrence of palladium minerals in the Zechstein rocks of the Fore-Sudetic monocline. Mineral Pol 6: 87-92

Mao J, Lehmann B, Du A, Zhang G, Ma D, Wand Y, Zeng M, Kerrich R (2002) Re-Os dating of polymetallic Ni-Mo-PGE-Au mineralization in Lower Cambrian Black Shales and its geologic significance. Econ Geol 47: 151-1061

Orberger B, Vymazalová A, Wagner C, Fialin M , Gallien J, Wirth R, Pašava J, Montagnac G (2007) Biogenic origin of intergrown Mo-sulphide- and carbonaceous matter in Lower Cambrian black shales (Zunyi Formation, Southern China). Chem Geol 238(3-4): 213-231

Pašava J (1993) Anoxic sediments - an important source for PGE; an overview. Ore Geol Reviews 8: 425-445

Pašava J, Kříbek B , Vymazalová A , Sýkorová I, Žák K , Orberger B (2008) Multiple sources of metals of mineralization in Lower Cambrian black shales of south China: Evidence from geochemical and petrographic study. Resource Geol 58(1): 25-42

Rudashevsky NS, Rudashevsky VN (2006) Patent of Russian Federation No 2281808, invention “Hydraulic Classifier”, Moscow, 20 August 2006.

Rudashevsky NS, Rudashevsky VN (2007) Patent of Russian Federation No 69418, industrial (useful) model, “Device for separation of solid particles”, Moscow, December 27, 2007.

Rudashevsky NS, Rudashevsky VN, Lupal SD (2001a) Patent of Russian Federation No 2165300, invention “Hydraulic

Classifier", Moscow, 20 April 2001.
Rudashevsky NS, Rudashevsky VN, Lupal SD (2001b) The method of separating granular materials and device for carrying out said method. Patent Cooperation Treaty (PCT), (16 March 2001) on the basis of Russian patent No 2165300, Moscow, 20 April 2001.
Sawlowicz Z (1993) Iridium and other platinum-group elements as geochemical markers in sedimentary environments. Paleogeography, Paleoclimatology, Paleoecology 104: 253-270

Sediment- hosted copper deposits in the Cretaceous rocks of Neuquén basin, Argentina

María JosefinaPons, Ana Laura Rainoldi, Marta Franchini,
Centro Patagónico de Estudios Metalogenéticos, CONICET-University of Comahue, 1400 Buenos Aires, 8300 Neuquén, Argentina.
josefina.pons074@gmail.com

Adolfo Giusiano
2Dirección Provincial de Hidrocarburos y Energía de la Provincia del Neuquén.

Abstract. The Tordillos and the Sapo Sur prospects are two examples of sediment-hosted Cu (V-U) deposits located in the Dorsal de Huincul and Dorso de los Chihuidos Highs, respectively. Both deposits are located near hydrocarbon fields and are hosted in the paleochannels red bed sequences of the Huincul Formation (Late Cenomanian-Early Turonian, Neuquén Group). During the eodiagenesis the precipitation of hematite gave the red coloration to the sedimentary rocks. With progressive burial precipitated pore-filling kaolinite and quartz and albite overgrowths following by calcite, barite and gypsum cements. The Cu mineralization is hosted in these pervasively bleached rocks impregnated with bitumen. The bleaching was produced by the interaction of the reducing hydrocarbons with the authigenic minerals. The synchronic oxidation of hydrocarbons locally produced carbonates precipitation.
Copper mineralization is interstitial, occludes the primary and secondary porosity of the rocks and fractures. It consists of chalcocite ($Cu_{1.8-2}S$)>chalcopyrite and bornite partially replaced by supergene minerals (chrysocolla > brochantite> malachite > azurite traces > covellite ($Cu_{1-1.014}S$) > complex oxides of Cu, Mn and Ba-copper wad > cuprite > tenorite, volborthite, and traces of U-V minerals, carnotite, franchevillite?). Hypogene sulfurs selectively replace early interstitial barite cement. This new information has enabled an interpretation of the source of sulphur and the hydrothermal fluid-flow processes that favoured the formation of these deposit.

Keywords: Cu (V-U-Ag) mineralization, hydrocarbons migration, redox reactions.

1. Introduction

Numerous (17) sediment hosted copper deposits are widely distributed along the south and central regions of the Neuquén basin, forming an important cupriferous metallogenic region. The deposits are hosted in a thick red bed sequence of the Neuquén Group (Campanian-Cenomanian, Cazau and Uliana, 1972). The sedimentary rocks represent the continentalization of the basin with the records of cyclic repetition of braided and meandering river channel facies and fine-grained alluvial plain and lacustrine deposits. These cycles were related to changes in river energy and discharge probably due to base level changes.

The Tordillos and the Sapo Sur prospects are two examples of sediment-hosted Cu (V-U) deposits located in the Dorsal de Huincul and Dorso de los Chihuidos Highs, respectively. Both deposits are located near hydrocarbon fields and are hosted in the Huincul Formation (Late Cenomanian-Early Turonian, Legarreta and Gulisano, 1989) of the Neuquén Group. The first publications about these deposits are descriptive and lack studies using modern analytical techniques (Wichmann, 1927; Fernández Aguilar, 1945; Granero Hernández and Schmid, 1956; Ramos, 1975; Lyon, 1999). Recent studies (Giusiano et al., 2006; Giusiano et al., 2008, Rainoldi et al., 2012a; Pons et al., 2009) proposed a new hypothesis that associates the cupriferous mineralization with hydrocarbons and Cu-bearing fluids migration along the main structures of the Dorsal de Huincul and Dorso de los Chihuidos Highs. In this contribution we present a summary of the alteration and mineralization present in the selected deposits. This new information has enabled an interpretation of the source of sulphur and the hydrothermal fluid-flow processes that favoured the formation of these deposits.

2 The Tordillos and Sapo Sur prospects and their relationships with tectonic features

The prospect Tordillos is located at the central-north limit of the Dorsal de Huincul structure and SW of the Sauzal Bonito anticline, near the Loma La Lata and Mangrullo hydrocarbon deposits. The Dorsal de Huincul is a structural lineament of regional scale developed at 39º S, with a E-O strike and extended along 270 km (Fig. 1). It was formed by an oblique NW-SE convergence between the North Patagonian Craton and the Neuquén basin during the lower Jurassic to early Cretaceous (Silvestro and Zubiri, 2008). The Sapo Sur prospect is located in the east flank of the Dorso de los Chihuidos High, near Sierra Chata and Parva Negra hydrocarbons deposits. This structure is a smooth north-south anticline (Fig.1) generated by tectonic inversion of the basement faults, mainly during the Miocene (Mosquera and Ramos, 2006). Both structures have been active since the Jurassic and were reactivated later during the Tertiary Andean orogeny. The associated faults acted as vertical channels connecting the reservoir fluids

(hydrocarbons + chlorides rich brines -60 to 72 gr/l chlorides-, Schiuma et al., 2002; Maretto et al., 2005) with the shallow carrier beds of the Huincul Formation. Hydrocarbons have formed since the lower Cretaceous to lower Tertiary (Legarreta, et al.,1999).

3. Stratigraphy of the Huincul Formation

The Huincul Formation represents a meandering fluvial system characterized by the development of fluvial channel and related floodplain deposits. During stable tectonic periods sediment supply was balanced with subsidence, which is represented in the sedimentary record by the development of the channels, coarse/medium-grained sandstones, and floodplain, sheet-form fine-grained mudstones and siltstones, elements. In tectonically active periods, the high sediment supply and the decrease in the space of accommodation generated the amalgamation of the channel facies and the starvation of the floodplain whose remnants are present as muddy clasts at the base of the cycles (Rainoldi et al., 2012b). This scenario favored the interconnection of more permeable and porous coarse-grained sandstones for fluid migration.

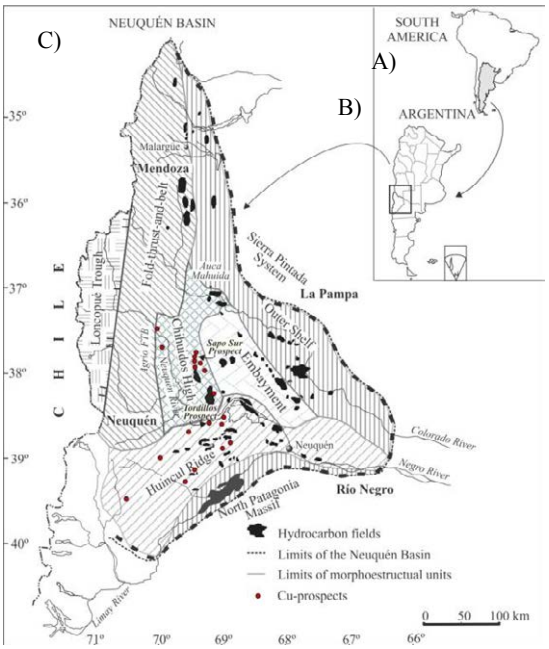

Figure 1. A-B) Location map of the Neuquén basin and C) of the Dorsal de Huincul and Dorso de los Chihuidos Highs, with the distribution of the hydrocarbons fields and copper deposits, and the position of Tordillos and Sapo Sur deposits.

3.1 Diagenesis of the Huincul Formation

The Huincul sandstones are feldspathic litharenite that consist of lithic fragments, quartz, feldspar and accessory minerals. During the eodiagenesis the precipitation of hematite gave the red coloration to the sedimentary rocks. With progressive burial precipitated pore-filling kaolinite and quartz and albite overgrowths. Late cementing minerals in the sandstones include calcite and trace amounts of barite and gypsum.

3.2. Alteration of the Huincul Formation

In the areas where the Huincul Formation hosted the Cu mineralization, the rocks are pervasively bleached and impregnated with bitumen. The bleaching was produced by the interaction of the reducing hydrocarbons with the authigenic minerals in the red sandstones, generating an increase of the porosity due to the partial dissolution of clasts and early cement minerals. In the bleached facies smectite replaces early Al-bearing minerals such as albite overgrowth and kaolinite). The oxidation of hydrocarbons locally produced late carbonates that occluded the secondary porosity.

3.3. Cu (V-U-Ag) mineralization

The mineralization in the Tordillos deposit forms an E-W trend tableland along 6 km, 0.5-07km wide and 80 to 100m thickness. It consists of a series of lenticular and discontinues bodies coincident with the coarsest facies of stacked paleochannels of the Huincul Formation (Fig. 2A, Pons et al., 2011). The mineralized bodies have Cu grade variable from 0.1-1% and present V (-100-970ppm) and U (135-190 ppm) anomalies. Several mining companies have explored this deposit (Polimet-Degerstrom, Polimet-MIM, and Orion del Sur S.A.) and estimated an average Cu grade of 0.4% (Lyon, 1999).

The mineralization in Sapo Sur is hosted in amalgamated paleochannels with a NNW-SSE trend which forms a sheet-like body 30m thick developed along 10 km x 5 km and includes a series of lenticular and discontinuous mineralized agglomerates. The Cu grades vary from 0.1 to 0.85%. V anomalies are commonly around 0.1%, and occur together with U (30-250ppm) and Ag (57-80 ppm) anomalies.

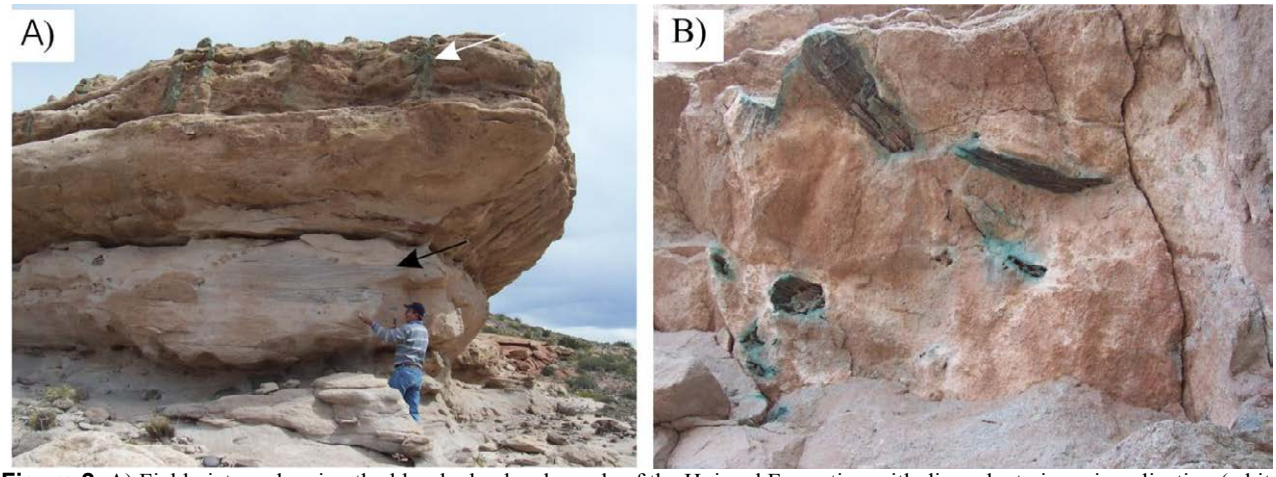

Figure 2. A) Field picture showing the bleached paleochannels of the Huincul Formation with discordant pipe mineralization (white arrow) and disseminated mineralization in contact with bitumen impregnations following the cross bedding planes (black arrows, B) Bleached sandstones host fossil trunks mineralized with malachite and chrysocolla.

The copper mineralization is always in contact with bitumen as sheet-like bodies with extensive horizontal dimensions, following stratigraphic surfaces, concordant tubes and feathers (Fig. 3A), or like discordant bubbles, cylinder pipes (Fig. 3A) and tabular shape with limited horizontal distribution. Less common are elongated bodies in the contact between the sandstone and silicified woods or carbon fragments (Fig. 3B). In some cases Cu-mineralization is rimmed by bitumen.

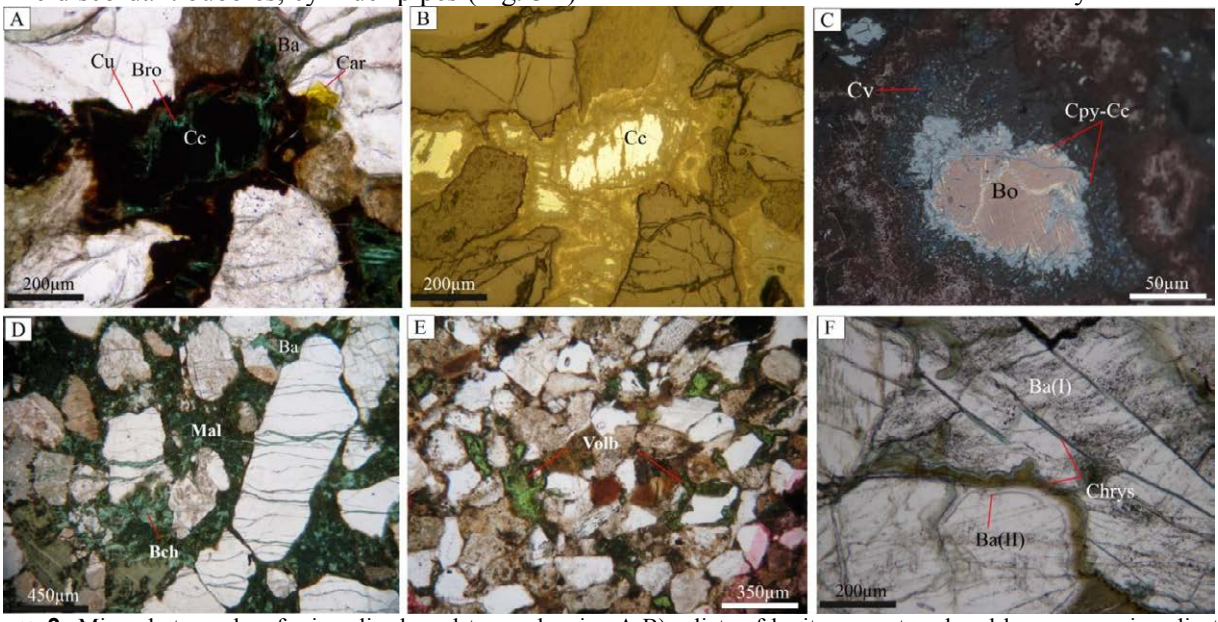

Figure 3. Microphotographs of mineralized sandstones showing A-B) relicts of barite cement replaced by copper mineralization filling the intergranular porosity; C) Texural relation between the hypogene and supergene copper sulphides. D-E) intergranular fractures and porosity filled with supergene copper minerals;and F) tabular crystal of barite (I) replaced by supergene copper minerals and anhedral barite (II). Abbs: Bro: Brochantite; Car: carnotite; Cc: Chalcocite; Chrys: Chrysocolla; Cv: Covellite; Cu: cuprite; Mal: Malachite.

A common feature of the mineralized sandstones is the major concentration of intergranular fractures in a subhorizontal and subparallel arrangement (Fig. 3) cutting the grains and diagenetic cements (quartz, carbonate, and barite).

In both deposits the highest copper grades correlate with zones enriched in hypogene copper sulfides. The vanadium anomalies are coincident with sectors of the rocks that contain the highest bitumen impregnations and abundant volborthite. Uranium anomalies are erratic and correlate with the presence of abundant supergene V-U-bearing minerals.

Copper mineralization consists of chalcocite ($Cu_{1.8-2}S$) with traces of very fine-grained chalcopyrite, and bornite partially replaced by supergene minerals (chrysocolla > brochantite> malachite > azurite traces > covellite ($Cu_{1-1.014}S$) > complex oxides of Cu, Mn and Ba-copper wad > cuprite > tenorite, volborthite, and traces of U-V minerals, carnotite, franchevillite?).

Chalcocite is the most abundant and widespread sulfide. Bornite and chalcopyrite where only observed in the western zone of the Tordillos

deposit, where Cu mineralization grades laterally and vertically to sandstones with interstitial pyrite. In thin sections, the sulfides are interstitial, occlude the primary and secondary porosity of the rocks and fractures (Fig. 3), and selectively replace early interstitial barite cement.

Bornite is replaced by flames of chalcopyrite associated with chalcocite along the cleavage planes. Chalcopyrite fills the microfractures with bitumen. Preliminary $\delta^{34}S_{CDT}$ analyses of chalcocite sulfur gave values between -7.3 and -17.7‰. These Cu sulfides are altered to supergene covellite grading outward to brochantite, and copper wad, cuprite and tenorite. The latest and more abundant supergene mineral is chrysocolla. Pyrite is replaced by iron oxides and hydroxides. Several generations of Ba-Ca sulphates cut hypogene and supergene minerals.

4. Concluding remarks

The formation of the sediment hosted copper deposits in the Neuquén Basin are the result of the combination of basin-scale features and the evolution of a fluid flow system, which includes: (I) thick red bed sequences which could act as metal source (see Brown, 2005) and as a favourable environment (oxidizing) for metal transportation, (II) the tectonic evolution and uplift of blocks in the Tertiary, that allowed the migrations of hydrocarbons and waters to the Huincul Formation, (III) chemical reactions between reducing fluids and diagenetic minerals of the sandstones that enhanced its porosity for the late sulfide precipitation, (IV) hydrocarbons as a reductant agent for Cu sulfides precipitation, (V) presence of many possible sources of S like diagenetic sulfates in the red sandstones, underlain evaporites deposits, hydrocarbons with H_2S and, (VI) the presence of chloride-rich waters capable of transport metals at basinal low-temperatures. Preliminary isotopic studies point to the bacteriogenic reduction of the sulfates as a potential mechanism for the sulfide precipitation.

Acknowledgements

This contribution forms part of a project financed by CONICET (PIP nº 6043 and PIP nº 1083), Universidad Nacional del Comahue (n° 04/I167 and 04/I002), Foncyt: Pict-prh 2008-00093, Pict-2008-1120, Acmelab-Iostipend-2009, PME-33, Universidad Nacional del Comahue.

References

Brown AC, (2005) Refinements for footwall red-bed diagenesis in the sediment hosted stratiform copper deposits model. Economic Geology 100: 765-771

Cazau L, Uliana M A (1972) El Cretácico superior continental de la Cuenca Neuquina: Buenos Aires, V Congreso Geológico Argentino (3):131-163

Giusiano A, Franchini M, Impiccini A, O`Leary S (2006) Mineralización de Cu asociada a bitumen en las areniscas cretácicas, prospecto Barda González, Neuquén, Argentina: Antofagasta, 11Congreso Geológico Chileno (2): 255-258

Giusiano A, Franchini MB, Impiccini A, Pons MJ (2008) Mineralización de Cu en sedimentitas Mesozóicas del Grupo Neuquén y hábitat de los hidrocarburos en la Dorsal de Huincul Neuquén. In: Zappetini E et al. (eds) 17° Congreso Geológico Argentino, Resumen in extenso para el Simposio de Mineralogía y Metalogenia (2): 769-770

Legarreta L, Gulisano C A (1989) Análisis estratigráfico secuencial de la Cuenca Neuquina (Triásico Superior-Terciario Inferior). In: Chebli G, Spaletti L (eds.) Cuencas Sedimentarias Argentinas. 10º Congreso Geológico Argentino San Miguel de Tucumán. Serie Correlación Geológica (6): 221-243.

Legarreta L, Laffitte S, Minniti S (1999) Cuenca Neuquina: múltiples posibilidades en la serie Jurásica-Cretácica del depocentro periándico. In: Zappetini E et al. (eds) Congreso Exploración y Desarrollo de Hidrocarburos N° 4 Mar del Plata, Actas 1:145-175

Lyon W (1999) Las areniscas cupríferas del Neuquén. In: Recursos Minerales de la República Argentina. Instituto de Geología y Recursos Minerales, SEGEMAR, Anales 35: 1149-1158

Maretto H, Carbone O, Gazzera C, Schiuma M (2002) Los Reservorios de la Formación Tordillo. In: Schiuma M et al. (eds) Rocas Reservorios de las Cuencas Productivas de la Argentina Congreso de Exploración y Desarrollo de Hidrocarburos N°5: 335-358

Pons MJ, Giusiano A, Franchini M, Impiccini A, Ríos JF, Testi A (2011) Diagénesis, alteración y mineralización de Cu en la Formación Huincul, Prospecto Tordillos, Cuenca Neuquina. In: Leanza et al. (eds) Simposio de Mineralogía, recursos minerales y rocas de aplicación XVIII Congreso Geológico Argentino Actas: 2

Pons MJ, Franchini MB, Giusiano A, Impiccini A, Godeas M (2009) Alteraciones, mineralización de Cu y Bitumen en areniscas Cretácicas del Prospecto Barda González, Neuquén, Argentina. Revista Geológica Argentina, Volume 64 (3): 321-333, ISSN: 0004-4822.

Rainoldi AL, Franchini MB, Cesaretti NN, Impiccini A, Pons M J (2012a) Alteración y decoloración de areniscas rojas, Formación Huincul (Grupo Neuquén). Evidencias de la circulación de hidrocarburos en el Dorso de los Chihuidos: Salta, XIII Reunión Argentina de Sedimentología, Actas: 183-184

Rainoldi AL, Limarino CO, Giusiano A, Bouhier E (2012b) Análisis estratigráfico de la Formación Huincul (Grupo Neuquén) en el prospecto Sapo Sur (37º47`S-69º27`O), Dorso de los Chihuidos, Neuquén: Salta, XIII Reunión Argentina de Sedimentología, Actas: 185-186

Schiuma M, Saavedra C, Malone P, Cevallos M, Rebori L, Vergani G (2002) Los reservorios del Gupo Lotena. Argentina. In: Schiuma et al. (eds) Rocas Reservorios de las Cuencas Productivas de la Argentina,Cuenca Neuquina, Grupo Lotena. 5° Congreso de Exploración y Desarrollo de Hidrocarburos: 303-334

Silvestro J, Zubiri M (2008) Convergencia oblicua: Modelo estructural alternativo para la Dorsal neuquina (39° S)-Neuquén. Revista de la Asociación Geológica Argentina 63 (1): 49-64

Genesis of the stratiform BH-t Swartberg Cu-Pb-Zn-Ag deposit, Northern Cape, South Africa

Tarryn-Kim Rudnick* and Abraham Rozendaal
Department of Earth Sciences, Stellenbosch University, South Africa
**Corresponding author. Email: tkrudnick@blackmountain.co.za*

Abstract. Swartberg is a metamorphosed Broken Hill-type Cu-Pb-Zn-Ag deposit in the north-west of South Africa. The mineralogy and stratigraphy closely resemble that of the nearby Broken Hill, Deeps and Gamsberg deposits. Swartberg is the least-studied of these and this and ongoing studies aim to complete the picture of the district by providing a clearer understanding of the deposit. It comprises two discrete, stacked stratiform orebodies, both of which are deformed by a recumbent, isoclinal F2 fold and refolded by an open F3 fold. The orebodies were deposited in a northeast-southwest trending basin, hinged to the northwest by a hydrothermal feeder fault. Both the upper orebody (UOB) and lower orebody (LOB) formed as syngenetic exhalatives, with the LOB representing an early, precursor exhalation stage to the more extensive stage that formed the UOB. The UOB displays a clear gradation from vent-source proximal chemogenic sediments in the F2 fold hinge, deposited under hotter, more reducing conditions, to distal material formed under cooler, oxidizing conditions. After deposition, the basin underwent several episodes of deformation and metamorphism to medium grades (pressure < 4.5kbar), during which the sulphides underwent limited mobilization into the F2 hinge zone.

Keywords: Swartberg, Broken Hill-type deposit, Eh-pH zonations.

1 Introduction

Swartberg is one of three known economic deposits in the Aggeneys-Gamsberg district, along with Gamsberg, in pre-feasibility stage, and Broken Hill-Deeps, with a 7 year life-of-mine (Fig.1). In light of diminishing resources at Deeps, the previously-mined Swartberg was brought back into production early in 2013.

The Swartberg deposit currently contains measured and indicated resources of 15500kt, grading at 0.67% Cu, 2.90% Pb, 0.68% Zn and 33.52g/ton Ag. However, the deposit remains open down-dip, and an intensive drilling program is underway to increase and upgrade the resource.

While much is known about the nearby deposits, only one study has focused on Swartberg (Stedman 1980). A detailed genetic model is lacking, and little is known about the relationship between the two orebodies. Thus this study aims to clarify these aspects.

2 Geological setting

All of the district's Pb-Zn-Ag±Cu deposits are stratabound and, in most cases, stratiform, and closely associated with thin banded iron formations. All exhibit similar stratigraphy, stratigraphic position, mineralogy, chemistry and metal associations. All share a common

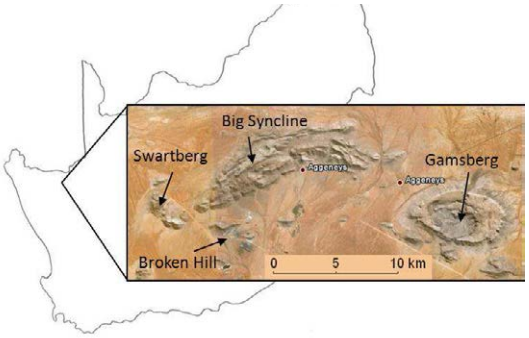

Figure 1. The base metal deposits of the Aggeneys-Gamsberg ore district (Image adapted from Google Earth).

exhalative-sedimentary genesis, followed by polyphase deformation and medium- to high grade metamorphism, and all may be classified as Broken Hill-type (BH-t) (Stedman 1980; Rozendaal 1982; Hoffmann 1993).

The deposits occur within the thin, supracrustal Aggeneys Subgroup, deposited at ca. 1120 Ma (Cornell et al. 2009), and forming part of the metasedimentary Bushmanland Group. These rocks constitute part of the western portion of the Namaqua-Natal Province, a polydeformed belt of greenschist- to granulite facies volcanic and sedimentary rocks.

3 Methodology

Polished thin sections were studied for mineralogy and textures. Quantitative mineral chemistry was carried out using a Zeiss EVO® MA15 SEM, with an Oxford Instruments® X-Max 20mm2 detector for major elements and an Oxford Instruments® Wave Dispersive X-ray Spectrometer for traces. Whole-rock chemistry was analysed by ICP-MS at Acme Analytical Laboratories Ltd. in Canada, and used in conjunction with existing Chemex Laboratories assay data, provided by Black Mountain Mine (Pty.) Ltd. (BMM). Stratigraphic and structural interpretations were made using borehole data from BMM.

4 The Swartberg deposit

The Swartberg deposit comprises a package of metalliferous to baritic chemogenic metasediments, hosted by a succession of quartzite and predominantly aluminous schist. As a result of polyphase deformation, the sequence is enveloped by basement gneiss, and displays duplication of some stratigraphic units (Fig.2). As a result, the deposit has been subdivided into two separate orebodies. The upper orebody (UOB) comprises sulphide- and magnetite-rich iron formation in the F2 hinge zone, which grades into and overlies less well

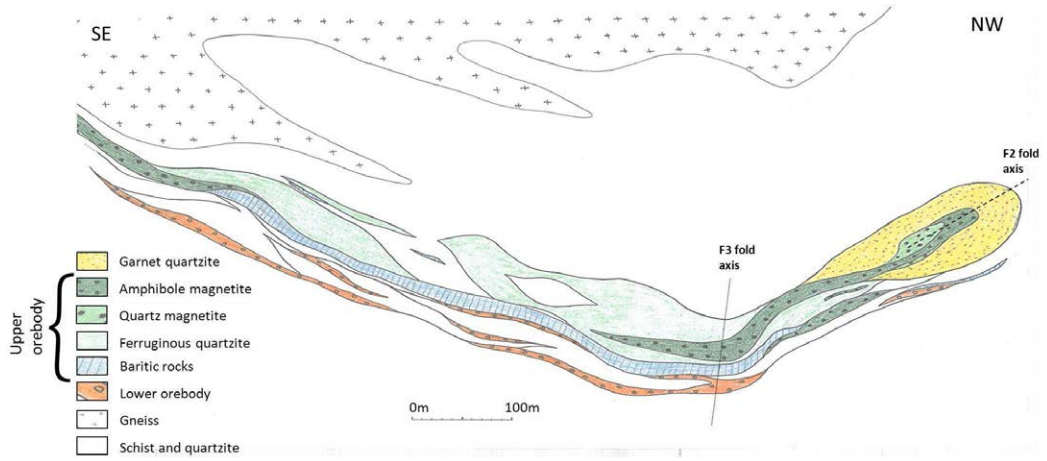

Figure 2. A representative cross-section through the Swartberg deposit, showing the structure of both orebodies.

mineralized hematite-barite and mixed siliclastic- and baritic rocks towards the flanks. The magnetite-rich part is dominated by quartz-magnetite, with increasing amphibole and pyroxenoid towards the F2 hinge zone. A prominent unit of garnet quartzite (coticule), rich in mobilised chalcopyrite, wraps around the outside of the UOB iron formation in the hinge area. The structure of the garnet quartzite around the LOB is as yet unknown.

The LOB is a fine-grained mineralized pelitic pyritic schist, with minor magnetite- and barite lithologies. It closely resembles unmineralized quartz schist, and laterally it grades into barren quartz schist or quartzite. A variable package of quartz schist, quartzite and garnet quartzite separates the LOB from the UOB, as well as lenses of the LOB. The configuration of the LOB beyond the F2 hinge zone is as yet unknown.

In a NE-SW direction, there is limited variation in the major units. In contrast, there are rapid changes in the UOB in a NW-SE direction, from the F2 hinge to the limbs. These gradations correspond to a zonation in both the chemical composition and redox state of the rocks, from more reduced magnetite-and sulphide-rich rocks in the hinge, to barren, oxidized barite-hematite rocks on the limbs.

5 Mineralogy and textures

Minerals in the UOB are generally medium- to coarse-grained and clearly recrystallised and deformed. Quartz and barite vary between polygonal granoblastic and interlobate, indicating recrystallization and annealing under raised temperatures. Up to three distinct foliations are defined, generally by mica or amphibole lathes, but also by elongated grains of hyalophane, quartz, sheaves of fibrolitic sillimanite, or clusters of garnet. Most major metamorphic minerals occur as inclusions in one another, and inclusion trails of elongated, orientated quartz and magnetite blebs occur in garnet poikiloblasts. The dominant foliation parallels the compositional banding (and concordant lithological contacts), which is regularly observed in the quartz schist, pyroxenoid- and amphibole-bearing magnetite iron formation, and the barite-magnetite/hematite rocks. The presence of cordierite indicates that metamorphism did not exceed medium grade, or pressures of ca. 4.5kbar.

Two generations of pyroxenoid have been identified: an early phase of rounded grains, and a later phase of overgrowths or rims, which display lower Fe, Ca and Mg, and higher Mn and Zn. This may indicate pyroxenoid growth during 2 separate metamorphic events, possibly the 1220-1170 Ma Kibaran and 1060-1030 Ma Namaquan events (Robb et al. 1999).

Secondary hematite is present as highly martitic magnetite, while primary hematite is less widespread, and occurs as lathes and clusters of specularite.

The sulphide minerals generally appear recrystallised, occurring as rounded to irregular blebs; as inclusions in one another and gangue minerals; as fracture-fills; interstitial to other minerals; and as fine-grained disseminations. Chalcopyrite in the garnet quartzite is mobilized, occurring as large blebs at the triple junctions between quartz crystals. Pyrite, however, may occur as euhedral cubes. Complex textures between the sulphides occur, such as pyrite-chalcopyrite intergrowths, and coronas of pyrite or pyrrhotite on chalcopyrite.

Prograde biotite, muscovite, sillimanite, barite, gahnite and sulphides may show varying degrees of retrogressive alteration. Chlorite is common, and late-stage retrogressive pyrosmalite occurs intergrown with galena. Various alteration minerals occur as rims on sulphides and magnetite. Sillimanite is commonly altered to muscovite, especially in aluminous schist adjacent to pegmatites, and gahnite may be highly retrogressed, and surrounded by an inner rim of white mica and an outer corona of secondary sphalerite.

6 Mineral chemistry

Those minerals that display solid-solution series, such as garnet, pyroxenoid and amphibole, are Fe-Mn-rich, occurring as almandine-pyrope, pyroxmangite and manganoan grunerite respectively. Although sphalerite is the dominant Zn-phase, Zn also occurs in gahnite, and is a minor constituent in pyroxenoid, amphibole, magnetite, hematite, chalcopyrite, pyrite and pyrrhotite. Biotite comprises variable proportions phlogopite (Mg), annite (Fe) and siderophyllite (Al), with up to 7.28% BaO imparting a significant ferrokinoshitalite component. The presence of Ba-rich muscovite, biotite and hyalophane indicates a Ba-halo in the footwall of the UOB, particularly surrounding the iron formation. Sphalerite is generally Fe-Mn-rich (<1.5% Mn), but later

secondary low Fe-Mn-phases occur as overgrowths. Chalcopyrite disease is common.

Silver is an important byproduct of the Swartberg deposit, and mostly occurs in solid solution with galena and chalcopyrite. Galena has an average Ag-content of 173ppm, but hosts up to 2317ppm. Bismuth and cobalt are both penalty elements and occur in galena, sphalerite and chalcopyrite. Cobalt may also occur as alloclasite. Whole rock geochemistry correlation coefficients support these mineralogical relationships.

7 Whole-rock geochemistry

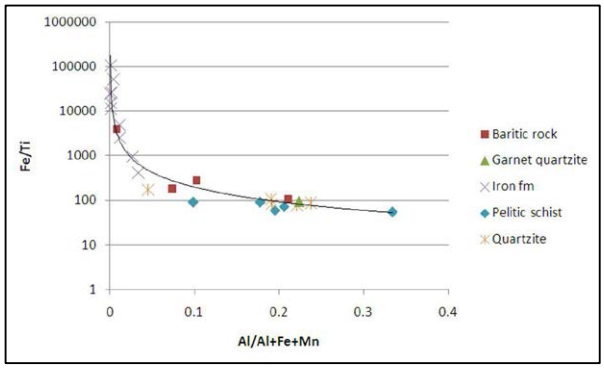

Figure 3. Fe/Ti vs Al/Al+Fe+Mn plot for the major Swartberg units. A top-left position indicates greater chemogenic component, with detrital material increasing to the right.

The iron formation has a predominantly chemogenic origin; the baritic units (which comprise varying proportions of barite, hematite, magnetite and quartz, with minor mica, garnet and sillimanite) follow a mixing trend between chemogenic and detrital material; and the pelitic schist and quartzite is predominantly detrital (Fig.3). No trend is visible for the garnet quartzite, due to limited data.

Geochemically the strongest correlations are between Zn and Cd (r=0.92), Pb and Sb (r=0.86), Ni and Co (r=0.82), V and Cr (0.79), K and Al (0.79), and Ag and Pb (0.69). These data support mineral chemistry findings that most Cd is hosted in the sphalerite crystal lattice, and that most Ag and Sb occur in galena. The strong Co-Ni correlation is explained by the partitioning of both of these elements into pyrite and pyrrhotite, as shown by their elevated concentrations in SEM analyses.

A comparison of whole-rock from Gamsberg, Deeps and Swartberg shows that Ag-Pb-Sb and Zn-Cd correlations are good throughout the Aggeneys-Gamsberg ore district. Swartberg, however, has significantly higher Ag- and Sb- to Pb ratios than Broken Hill-Deeps and Gamsberg.

8 Discussion and conclusions

8.1 Basin architecture

The sediments of the Swartberg deposit were deposited in a NE-SW trending basin, hinged to the NW by a feeder fault, as postulated by several authors (Rozendaal 1982; Lipson 1990; Hoffmann 1993; Stalder 2004). The lack of major NE-SW variation within lithological units, compared to the rapid NW-SE gradation from iron formation to barite rock over several hundred metres, implies a NE-SW elongated basin.

Also, it appears that the formational fluids at Swartberg differed from those of Broken Hill and Gamsberg: according to thermodynamic modelling, hydrothermal fluids with low pH (3.5-4), high temperatures (350˚C), and high chloride concentrations are conducive to transporting high concentrations of Ag and Sb (Pavlova et al. 2006). Following Allemann (2008, *unpub.*), this may indicate that the hydrothermal fluids that formed the Swartberg deposit, with its relatively high Ag+Sb/Pb ratio, were more acidic and chloride-rich than those forming Gamsberg or Broken Hill-Deeps, which have lower Ag- and Sb- to Pb ratios. This indicates that the fluids forming Gamsberg and Broken Hill may have had the same source, while the source of the Swartberg fluids differed, implying formation in a separate basin. The formational basin was thus narrow (hundreds of metres), elongate (several kilometres or more), and separate from those of the other deposits.

8.2 Zonations within the UOB

The gradation in the UOB from sulphide-rich, amphibole-bearing magnetite in the F2 hinge, to Pb- and Zn-rich iron formation and poorly mineralized barite-hematite rocks in the limbs, corresponds to lateral Eh-pH and temperature zonation in the basin: the hinge zone sulphide-oxide facies was deposited by dominantly reducing, high-temperature fluids proximal to the vent (Stedman 1980; Rozendaal 1982), whereas the barite-hematite facies along the limbs corresponds to deposition under cooler, more oxidizing distal conditions (Fig. 4). Comparison with the other, well-studied deposits of the district supports these ideas:

- The mineralogy of the F2 hinge zone resembles that of Broken Hill, which is considered to have formed proximal to a vent (Rozendaal 1982). Both deposits display sulphide-bearing magnetite iron formation, indicative of deposition by reduced hydrothermal fluids, and both contain Cu (although Swartberg is richer), indicating precipitation from hot fluids.
- Primary hematite and barite indicate deposition under oxidizing conditions, and at Gamsberg these have been linked to a distal chemogenic origin (Rozendaal 1982). Thus the barite- and hematite bearing portions of Swartberg (the F2 fold flanks) correspond to distal chemogenic deposition by cooler, oxidizing fluids.
- According to McClung (2006), oxygen isotope values show that the Cu-rich, Ba-poor parts of Swartberg (F2 hinge) formed at temperatures above 250˚C.

8.3 Position of the feeder fault

The F2 hinge corresponds to the region of the feeder vent, as evidenced by the zonation from proximal lithologies in the hinge zone to distal lithofacies in the limbs. It is speculated that the tensional tectonic stress regime that controlled the orientation of the growth fault and basin architecture was also responsible for the later, albeit compressional tectonic, deformation; the feeder

fault would have acted as a zone of weakness during deformation (Stedman 1980). The footwall garnet quartzite could represent the metamorphosed feeder zone (Stedman 1980; Rozendaal 1982). A similar zone of copper-pyrite-rich footwall alteration underlies several stratiform Pb-Zn orebodies, particularly close to the hydrothermal fluid feeder zone (Stedman 1980).

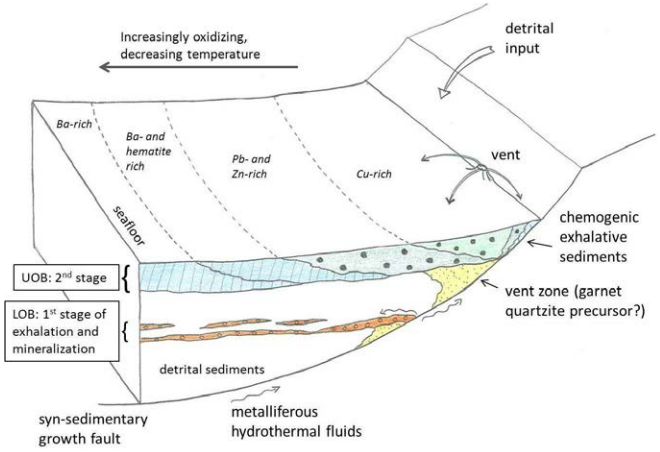

Figure 4. Schematic reconstruction of the Swartberg depositional basin, illustrating the positions of the UOB, LOB and feeder fault, and the lithological zonation of the UOB.

8.4 Mode of orebody deposition

The UOB is interpreted to be of synsedimentary exhalative origin, and formed by the direct precipitation of chemogenic lithologies mixed with limited detrital sediments on the seafloor. This is supported by:

- Several authors have interpreted finely-banded sulphides in the district as sedimentary layering (Stedman 1980; Rozendaal 1982; Lipson 1990).
- Magnetite-bearing units regularly display clear compositional banding parallel to concordant lithological contacts. Thus magnetite appears to be primary, deposited synsedimentarily with other chemogenic sediments.
- The transition from detrital metasediments (quartzite, aluminous- and quartz schist) to the chemogenic UOB lithologies is gradual, with concordant contacts.
- The ore minerals are restricted to specific lithologies, indicating synsedimentary precipitation together with the host units.

The LOB may have been deposited by an early exhalation event, prior to the more extensive exhalation of the UOB material. The two exhalation stages were separated by a period of predominantly detrital sedimentation, during which small amounts of early hydrothermal fluids were debouched onto the seafloor. These precipitated minor chemogenic material together with predominantly pelitic detrital sediments, creating the Ba-halo present in the footwall of the UOB.

8.5 Summary

The Swartberg deposit formed in a restricted basin, elongated in a NE-SW direction and hinged by a feeder fault to the NE. The LOB was formed first, by an initial pulse of hydrothermal fluids exhaled onto the seafloor from the feeder fault. This was followed by a period of predominantly pelitic detrital sedimentation, along with small amounts of early hydrothermal fluids that formed the footwall Ba-halo. Finally, a more extensive exhalation event occurred, precipitating the predominantly chemogenic lithofacies of the UOB. This package displays lateral zonations, as a result of Eh-pH and temperature variations with distance from the vent.

Like the other three deposits of the ore district, Swartberg displays lateral and vertical facies changes; evidence of multiple hydrothermal pulses; and mineralization hosted by both chemogenic and pelitic sediments. However, the restricted nature of the Swartberg basin, and the differing physico-chemical properties of the hydrothermal fluids, suggest that it formed in a sub-basin separate from the other deposits in the area, as suggested by previous authors.

Swartberg remains open down-dip, and the laterally continuous nature of the lithofacies in this direction indicates the potential for a significant increase in the resources of this deposit: could Swartberg become the "next Gamsberg"?

Acknowledgements

My sincere thanks go to the staff at BMM, for their help with sample collection, advice and ideas. I also thank the CAF staff, for their assistance with sample preparation, and for convincing the SEM to occasionally cooperate.

References

Cornell DH, Pettersson A, Whitehouse MJ, Schersten A (2009) A new chronostratigraphic paradigm for the age and tectonic history of the Mesoproterozoic Bushmanland Ore District, South Africa. Economic Geology 104: 385-404.

Hoffmann D (1993) Aspects of the geology, geochemistry and metamorphism of the lower orebody, Broken Hill deposit, Aggeneys. Dissertation, University of Cape Town.

Lipson RD (1990) Lithogeochemistry and origin of metasediments hosting the Broken Hill deposit, Aggeneys, South Africa, and implications for ore genesis. Dissertation, University of Cape Town.

McClung CR (2006) Basin analysis of the Mesoproterozoic Bushmanland Group of the Namaqua Metamorphic Province, South Africa. Dissertation, University of Johannesburg.

Pavlova G, Gushchina L, Borovikov A, Borisenko A, Palyanova G (2006) Forming conditions for Au-Sb and Ag-Sb ore according to thermodynamic modeling data. Journal of Material Science 41: 1557-1562.

Robb LJ, Armstrong RA, Waters DJ (1999) The history of granulite-facies metamorphism and crustal growth from single zircon U-Pb geochronology: Namaqualand, South Africa. Journal of Petrology 40: 1747-1770.

Rozendaal A (1982) The petrology of the Gamsberg Zinc deposit and the Bushmanland iron formations with special reference to their relationships and genesis. Dissertation, University of Stellenbosch.

Stalder M (2004) Petrology and mineral chemistry of sulphide ores and associated metalliferous rocks of the Gamsberg Zn-Pb deposit, South Africa: implications for ore genesis and mineral exploration. Dissertation, University of Stellenbosch.

Stedman DP (1980) The structural geology and metamorphic petrology of Black Mountain, Namaqualand. Dissertation, University of the Witwatersrand.

Trace and rare earth elements contents of a Sardinian sedimentary Mn-rich deposit: preliminary results

Rosa Sinisi, Paola Mameli, Giacomo Oggiano
Department of Nature and Earth Sciences, University of Sassari, Italy

Giovanni Mongelli
Department of Sciences, University of Basilicata, Italy

Abstract. Mn oxides are important scavengers of trace elements from waters. They often form deposits with high metals concentrations that sometimes have economic significance. Within a thick sedimentary deposits of northern Sardinia, Mn oxide mineralization was found as both matrix and coatings on clasts of a conglomeratic deposit, and subrounded nodules in residual clays. Lithiophorite and birnessite are the sole Mn phases that are also accompanied by variable amounts of Fe oxides and hydroxides, clay minerals, and phyllosilicates. Chemical analysis of the studied samples revealed high concentrations of most of trace metals (Co, Ni, Zn, Cu, Ba, Y, U and Pb) and all rare earth elements (REE). The latter were used to provide the first hypothesis regarding environmental conditions and chemical processes determining the precipitation of Mn oxides.

Keywords. Lithiophorite, Birnessite, Rare earth elements, Sardinia

1 Introduction

Manganese is the tenth most abundant element in the Earth's crust. In natural environments, the geochemical behaviour of Mn is mainly controlled by pH and oxidation potential (Eh). It exists as Mn^{2+}, which is soluble under reducing and acidic conditions, as well as Mn^{3+} and Mn^{4+}, which are less soluble and stabilize as Mn oxides under relatively oxidizing and alkaline conditions (Robb 2005). Hydrous Mn oxides are ubiquitous forming in a wide variety of geological environments where participate in several types of chemical reactions (Tan et al. 2006; Dixon and Skinner 1992; McKenzie 1989). The Mn oxides phases in fact are surface-active minerals with large amounts of pH-dependent surface charges, very low point of zero charge (pzc), large surface areas, and high oxidizing capacity (Post 1999).

Among natural particles, Mn oxides have long been recognized as playing an important role in controlling the chemistry of soils and sediments (Tan et al. 2005, and references therein). Owing to their high adsorption capability of trace metal from natural waters, Mn oxides accumulations often represent deposits with high economic significance. In soils and laterites, as well as in other sedimentary deposits (e.g. alluvial), Mn-bearing minerals commonly occur forming nodules, crusts, coatings on clasts, or Mn-rich horizons (Nahon et al. 1989; Neaman et al. 2008; Koschinsky and Hein 2003; Sinisi et al. 2012; Tan et al. 2006).

In northern Sardinia Mn oxides mineralizations were found into alluvial conglomeratic and residual clayey deposits of the Messinian age. In this paper the preliminary data on mineralogical and chemical composition of these Mn mineralizations are provided with the aim to decipher the environmental conditions and chemical processes occurring during Mn oxides accumulation.

2 Geology and Mn occurrences

Sardinia (western Italy) belongs to the Sardinia-Corsica microplate located in the Mediterranean Sea, and shows evidences of numerous large-scale tectonic events which lasted throughout the Phanerozoic time. Its geological evolution has been first strongly affected by the Paleozoic tectonic activity that led to the closure of Rheic Ocean and subsequent collision of the Gondwana and Laurasian continents. During Mesozoic, the whole island was tectonically stable until the lower Burdigalian when the Sardinia-Corsica plate detached from south-european edge causing the opening of the Liguro-Provencal backarc basin.

NW Sardinia, commonly named the Nurra district, consists of a structural high that represents the uplifted part of a wide, tilted block (Fig. 1).

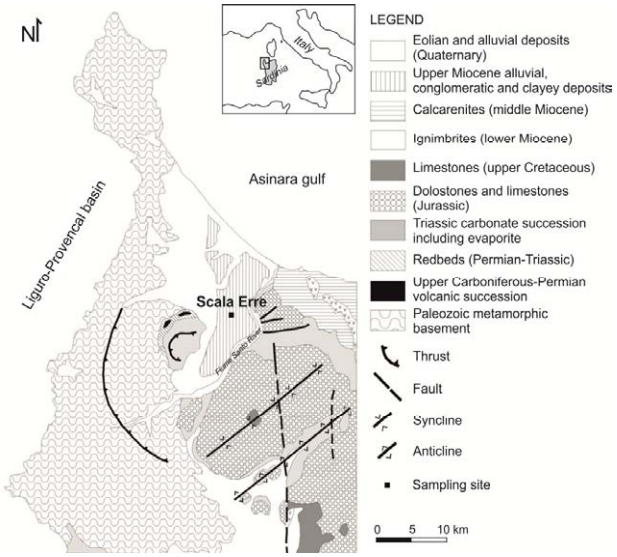

Figure 1. Geological sketch map of the Nurra district (NW Sardinia). Modified after Mongelli et al. (2012).

To the west, this structural high borders the eastern passive margin of the Liguro-Provencal backarc basin; to the east, it abuts the edge of a N–S-trending Miocene halfgraben (the Porto Torres Basin, Thomas and

Gennessaux 1986). Upper Burdigalian to Tortonian carbonate marine deposits of the Porto Torres Basin onlap the structural high, where Mesozoic and Palaeozoic sequences are exposed. The Permian and Mesozoic sequences unconformably overlie Variscan low-grade metamorphic basement and in turn are overlain by an alluvial deposit of the Messinian age (Mongelli et al. 2012 and references therein).

At the northern Nurra, where Tortonian transgression did not occurs, the Messinian continental deposits are widespread and represent the infillings of a wide depression formed between Jurassic uplands and Variscan basement after the Messinian salinity crisis. The deposits consist of an alternation of clays and conglomerates which has been interpreted as alluvial fan and braided-river plain sediment, respectively (Fig. 2, Funedda et al. 2000). However, associated to these alluvial deposits, wide outcrops of residual clays, currently under excavation, are found at the "Scala Erre" site where the sampling was carried out.

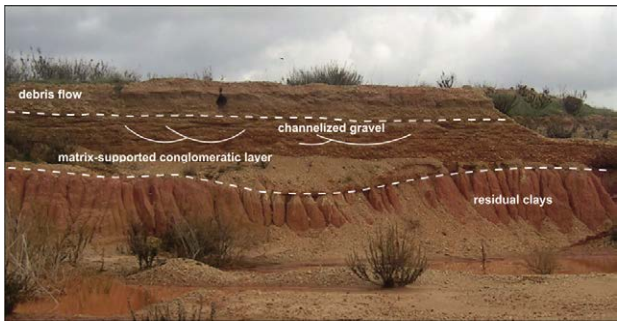

Figure 2. Messinian succession at the Scala Erre sampling site (northern Nurra).

In detail, from top to bottom, the Scala Erre succession is composed of the following: i) a debris flow layer, likely Holocenic or Pleistocenic in age, formed by clast-supported conglomerates with prevailing subrounded quartz clasts and sandy matrix; ii) a 1–3 m thick, channelized gravel horizon consisting of rounded–subrounded clasts of metamorphic quartz, quartzites, and highly weathered rhyolite within a silty–sandy matrix; iii) a 10 m-thick unit of clays and sandy clays, which show evidence of intense pedogenesis, including rhizoliths and strongly Fe-depleted zones. Locally, 1 m thick gravel layers are interbedded with the clays. The contact between the conglomeratic horizon and the clayey deposit is sharp and marked by the presence of a calcrete level, while the base of the residual clays is not exposed.

Within both conglomerate and clay deposits, hydrogenous Mn-oxyhydroxides locally occur forming the matrix of conglomerates (Fig. 3a), thin patinas covering the conglomerate clasts (Fig. 3b) and centimeter-size nodules widespread in the clays.

2 Analyses and results

Seven Mn-oxides patinas and matrix samples and three Mn-rich nodules from Scala Erre Messinian deposit have been analyzed to obtain the mineralogical and chemical composition data. X-ray diffraction (XRD), inductively coupled plasma-mass spectrometry (ICP-MS), and instrumental neutron activation analysis (INAA) were performed on all powdered, whole rock samples at Activation Laboratories (Ancaster, Canada). At present, no microscopic data are available for these mineralizations which will be subject of our future research.

2.1 Mineralogy

The main Mn phase of analysed samples is lithiophorite. Birnessite also occurs in most samples as associated Mn mineral, except for a sample where birnessite is the sole Mn mineral phase. Quartz, Fe-oxides and hydroxides (hematite and goethite), clay minerals (mainly kaolinite and scarce illite) and phyllosilicates (muscovite) complete the mineralogical association. In two samples only, feldspars are also presents with low contents.

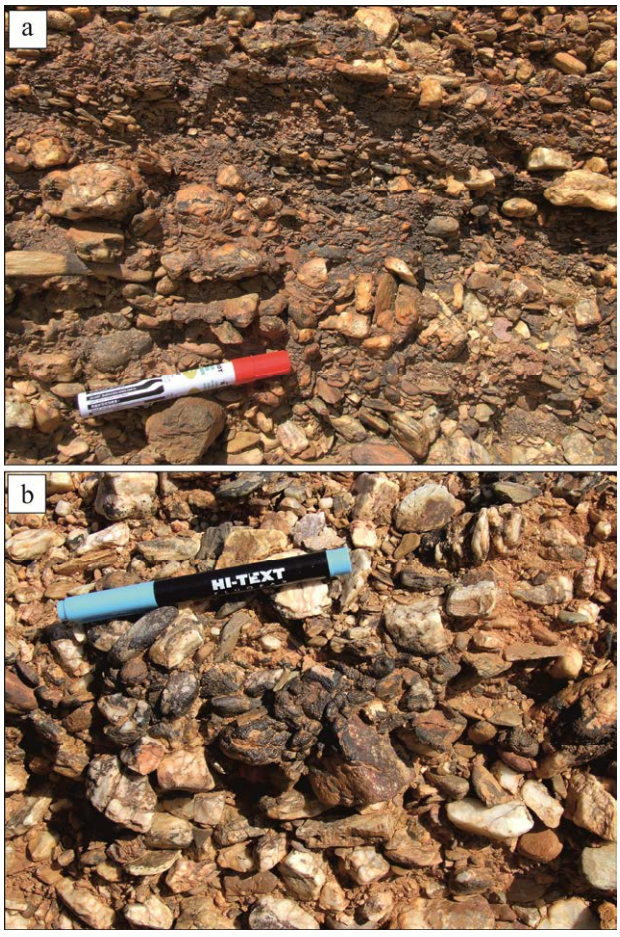

Figure 3. Mn oxides forming the matrix in a micro-conglomerate (a) and coatings on metamorphic quartz and quartzite clasts (b).

2.1 Chemistry

Normalization diagrams of major, trace and rare earth elements are shown in Fig. 4. Major elements show the same distribution patterns in all our samples. MnO contents are very high exceeding 10 to 120 times those of the GLOSS (Global Subducting Sediments; Plank and Langmuir 1998), used as reference standard. Other major

elements have concentrations constantly lower than those of the GLOSS, with the exception of Fe_2O_3, Al_2O_3, and P_2O_5 which in few sample have higher contents. Finally, large depletions are observed for alkaline and earth alkaline elements (MgO, CaO, Na_2O).

Regarding trace elements, the GLOSS-normalization patterns of both conglomerate matrix and nodules share the same elemental features. Compared to the reference standard, the analysed samples are strongly enriched in most transition metals, such as Co, Ni, Zn and Cu (the latter more enriched in the nodules), moderately enriched in Ba, Y, U and Pb (the latter strongly enriched in nodules only), and moderately depleted in the other trace elements. Among these Zr, Ta, and Cr show the lowest contents.

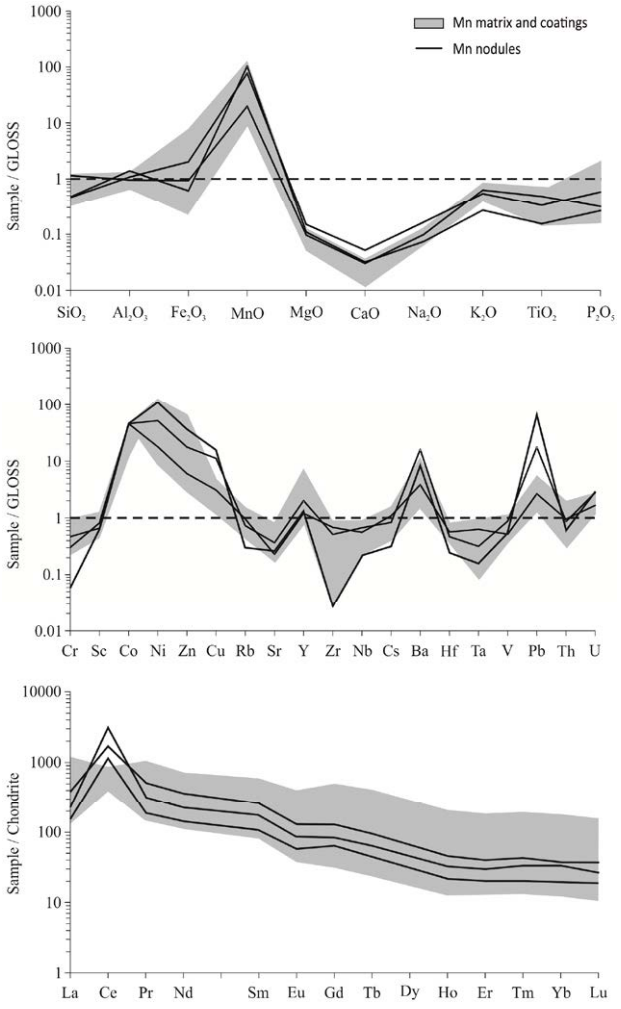

Figure 4. Major, trace and REE normalization diagrams.

The chondrite-normalized REE patterns (chondrite data are from Evensen et al. 1978) of the two types of the studied samples are comparable referring to element concentrations and distributions. However, some differences between nodules and the other Mn-rich samples are observed. Nodules are characterized by very high ΣREE values that are between 3398.5 and 1368.8 ppm; high values of LREE/HREE fractionation index ($6.82<(La/Yb)_{ch}<9.96$); and strongly positive Ce anomalies resulting in very high values of the Ce/Ce* ratio(3.90-11.75). The Mn-oxides matrix and coating are characterized by a wide range of REE contents, varying from 640.01 to 2121.60 ppm; a significant LREE/HREE fractionation with $(La/Yb)_{ch}$ values of 6.88-13.73; both positive and negative Ce anomalies expressed by values of Ce/Ce* ratio between 0.49 and 3.39.

3 Discussion and conclusions

Mn oxides are ubiquitous in rocks, soils, and sediments, and the geochemistry of Mn implies that these oxides can precipitate in a wide variety of geological settings. Lithiophorite and birnessite, the Mn-bearing minerals in the studied samples, are commonly found in soils (Koppi et al. 1996; Post 1999). These minerals are hydrous oxides of Mn and are characteristic of oxidizing environments. In lateritic sediments, their precipitation typically occur at the weathering front where the high concentration of dissolved Mn^{2+}, the alkaline pH, and high Eh values enable the formation of Mn^{4+}-bearing phases (Nahon et al. 1989). Both lithiophorite and birnessite have a layer structure consisting of edge-sharing MnO_6 octahedra sheets and interlayer spaces that commonly host water molecules and a wide range of cations (mainly trace metals, Post 1999). Due to their structure, these Mn phases readily participate in oxidation-reduction and cation-exchange reactions playing a significant role in sediment chemistry. This is consistent with trace metal enrichments of the studied samples.

On the contrary, the association between high REE contents and lithiophorite and/or birnessite is more unusual. Nevertheless, the high correlation (r=0.83) between ΣREE and MnO contents in the studied samples suggest a significant relationship between REE and Mn-bearing minerals. Therefore, as yet supposed for other Mn oxides (mainly pyrolusite, hollandite, and cryptomelane; Sinisi et al. 2012), even lithiophorite and birnessite likely exert a significant adsorption effect on REE.

The Mn oxides also play a significant role in trapping Ce and therefore generating positive Ce anomalies, commonly used to identify redox processes during weathering (Mongelli and Acquafredda, 1999; Feng 2010; Laveuf and Cornu 2009; Laveuf et al. 2012). Positive Ce anomalies occur as a result of a scavenging process including the oxidation of Ce^{3+} to Ce^{4+} (leading to the precipitation of cerianite) and the reduction of Mn^{4+} on the Mn oxides surface (Bau 1999). However, the presence of organic matter in sediments inhibits the development of negative Ce anomalies in oxidizing waters for two main reasons: (1) because Ce cannot be oxidized at the surface of Mn oxides; (2) because all of the REEs form complexes with organic molecules, meaning that Ce is not selectively removed from the solution (Davranche et al. 2005, 2008).

In the Mn-rich matrix and coatings at Scala Erre, the variation (from negative to positive) of Ce anomalies, is likely due to the presence of organic-rich and organic-poor fluids incoming during the formation of Mn phases. Therefore, the studied samples with negative to positive Ce anomalies likely formed in an environment where REE organic speciation and the formation of organic-REE complexes had an important reducing effect on

cerianite precipitation. In contrast, the Scala Erre Mn nodules, having strongly positive Ce anomalies despite their residence in lateritic clays, likely formed in an environment with little or no organic matter, where REE speciation in circulating fluids was dominated by inorganic species.

Furthermore, it is known that neutral or alkaline pH conditions may easily account for the fractionation of LREE-HREE (Henderson 1996). In non-acidic pH environment, in fact, the HREE form more soluble complexes than the LREE and thus are preferentially retained in solution. The high values of $(La/Yb)_n$ index of studied samples, therefore, might suggest that the fractionation between light and heavy REE was due to a different geochemical behaviour of REE rather than a different REE uptake capability of Mn oxides.

Acknowledgements

This research was financially supported by the Fondazione Banco di Sardegna grant.

References

Bau M (1999) Scavenging of dissolved yttrium and rare earths by precipitating iron oxyhydroxide: experimental evidence for Ce oxidation, Y Ho fractionation and lanthanide tetrad effect. Geochim Cosmochim Acta 63:67–77

Davranche M, Pourret O, Gruau G, Dia A, Le Coz-Bouhnik M (2005) Adsorption of REE(III)-humate complexes onto MnO2: experimental evidence for cerium anomaly and lanthanide tetrad effect suppression. Geochim Cosmochim Acta 69:4825–4835

Davranche M, Pourret O, Gruau G, Dia A, Jin D, Gaertner D (2008) Competitive binding of REE to humic acid and manganese oxide: impact of reaction kinetics on development of Cerium anomaly and REE adsorption. Chem Geol 247:154–170

Dixon JB, Skinner HCW (1992) Manganese minerals in surface environments. In: Skinner HCW, Fitspatrick RW (Eds) Biomineralisation Processes of Iron and Manganes-Modern and Ancient Environments. Catena 21:31–50

Evensen NM, Hamilton PJ, O'Nions RK (1978) Rare earth abundances in chondritic meteorites. Geochim Cosmochim Acta 42:1199–1212

Feng J (2010) Behaviour of rare earth elements and yttrium in ferromanganese concretions, gibbsite spots, and the surrounding terra rossa over dolomite during chemical weathering. Chem Geol 271:112–132

Funedda A, Oggiano G, Pasci S (2000) The Logudoro basin: a key area for the Tertiary tectono-sedimentary evolution of North Sardinia. Boll Soc Geol Ital 119:31–38

Henderson P (1996) The rare earth elements: introduction and review. In: Rare earth elements. Chemistry, origin and ore deposits. Jones AP, Wall F, Williams T (eds) The Mineralogical Society Series (7), 1st edn .Chapman and Hall, London, pp 1-19

Koppi AJ, Edis R, Field DJ, Geering HR, Klessa DA, Cockayne DJ (1996) Rare earth elements trend and cerium–uranium–manganese association in weathered rock from Koongarra, Northern Territory, Australia. Geochim Cosmochim Acta 60:1695–1707

Koschinsky A, Hein JR (2003) Uptake of elements from seawater by ferromanganese crusts: solid-phase associations and seawater speciation. Marine Geol 198:331–351

Laveuf C, Cornu S (2009) A review on the potentiality of rare earth elements to trace pedogenetic processes. Geoderma 154:1–12

Laveuf C, Cornu S, Guilherme LRG, Guerin A, Juillot F (2012) The impact of redox conditions on the rare earth element signature of redoximorphic features in a soil sequence developed from limestone. Geoderma 170:25–38

McKenzie RM (1989) Manganese oxides and hydroxides. In: Dixon JB, Weed SB (eds) Minerals in Soil Environments. SSSA Book Ser. 1. SSSA, Madson WI, USA. pp 439-465

Mongelli G, Acquafredda P (1999) Ferruginous concretions in a Late Cretaceous karst bauxite: Composition and conditions of formation. Chem Geol 158:315–320

Mongelli G, Mameli P, Oggiano G, Sinisi R (2012) Messinian palaeoclimate and palaeo-environment in the western Mediterranean realm: Insights from the geochemistry of continental deposits of NW Sardinia (Italy). Int Geol Rev 54:971–990

Nahon DB, Herbillon AJ, Béauvais A (1989) The epigenetic replacement of kaolinite by lithiophorite in a manganese-lateritic profile, Brazil. Geoderma 44:247–259

Neaman A, Martínez CE, Trolard F, Bourrie G (2008) Trace element associations with Fe- and Mn-oxides in soil nodules: Comparison of selective dissolution with electron probe microanalysis. Appl Geochem 23:778–782

Plank T, Langmuir CH (1998) The chemical composition of subducting sediment and its composition for the crust and mantle. Chemical Geology 145:325–394

Post JE (1999) Manganese oxide minerals: Crystal structures and economic and environmental significance. Proc Natl Acad Sci USA 96:3447–3454

Robb L (2005) Introduction of ore-forming processes. Blackwell Science Ltd, Oxford

Sinisi R, Mameli P, Mongelli G, Oggiano G (2012) Different Mn-ores in a continental arc setting: geochemical and mineralogical evidence from Tertiary deposits of Sardinia (Italy). Ore Geol Rev 47:110–125

Tan W, Liu F, Feng X, Huang Q, Li X (2005) Adsorption and redox reactions of heavy metals on Fe-Mn nodules from Chinese soils. J Coll Inter Scie 284:600–605

Tan WF, Liu F, Li YH, Hu HQ, Huang QY (2006) Elemental composition and geochemical characteristics of iron-manganese nodules in main soils of China. Pedosphere 16:72–81

Thomas B, Gennessaux M (1986) A two stage rifting in the basin of the Corsica-Sardinia strait. Marine Geol 72:225–239

REE concentrations in Mn-oxide mineralizations: a case study of a sediment hosted ore of Sardinia (western Italy)

Rosa Sinisi
Department of Nature and Earth Sciences, University of Sassari, Italy

Abstract. In north-western Sardinia (west of Italy) different types of Mn-oxide mineralizations occur as remnants of ancient, metalliferous mines. The mineralizations developed within a marine transgressive sequence where Mn phases form the matrix and/or cement of a conglomeratic level. The high-grade Mn ore consists mainly of pyrolusite and hollandite with few other Mn oxyhydroxides. Silicate phases (such as quartz, feldspar, zircon and apatite) and clay minerals represent the gangue minerals. A wide variability of element concentrations characterize the Mn ore that shows (with respect to reference standard) both enrichments and depletions of the most of trace elements. However, very high Rare Earth Elements (REE) contents occur in all samples. Factor analysis and principal components analysis (PCA) extraction method were applied to the ore samples to better identify the nature of REE enrichments. Three factors were identified and each of them suggests close relationship between REE and silicate phases, showing that Mn-oxides were not important for REE accumulation.

Keywords. Mn mineralizations, rare earth elements, geochemistry, Sardinia

1 Introduction

It is widely accepted that, regardless of the geological environment (continental, marine or hydrothermal), the occurrences of clay minerals and/or mineral phases with clay-type crystal structure (as zeolites and Mn-oxides), play a key role in the trace elements and REEs uptake processes (Koeppenkastrop and De Carlo 1992; Bau 1999; Mameli et al. 2008). The REE resources are produced mostly from ion-adsorption type REE deposits of southern China (Sanematsu et al. 2009). These are formed by weathering of granitic rocks and subsequent chemical adsorption of REE on clay minerals (principally kaolinite and halloysite; Wu et al. 1996; Murakami and Ishihara 2008).

A significant group of minerals with a high metal uptake capacity is represented by Mn oxides. Their "tunnel" structure, in fact, allows both the absorption (inside the minerals) and adsorption (outside the minerals) of cations and anions producing metal accumulations with economic and environmental significance (Post 1999).

However, the ores, mainly that forming within sedimentary environment, often have impurities due to presence of minerals unrelated to mineralization. These minerals can significantly alter the compositional features of the ores.

In north-western Sardinia (Italy, western Mediterranean), a Mn-oxide mineralization occurs and recently its origin has been discussed and identified (Sinisi et al. 2012). In this study the mineralogical and chemical compositions of the Sardinian, sediment-hosted Mn-ore are exhibit exploring the possibility that it can represent an ion-adsorption type REE mineralization.

2 Geological framework

The crystalline basement of Sardinia is a segment of the Southern European Variscan Belt that was detached from the stable European continent during the early Miocene. The Sardinian basement is made up of Carboniferous magmatic and sedimentary rocks and meta-sedimentary Cambrian to lower Carboniferous rocks, which record the increase of metamorphic grade from very low in the south-western island up to medium- and high-grade in the northern sector. These basement rocks are capped by continental upper Carboniferous–Permian sedimentary and volcanic deposits that are covered by Mesozoic–Eocene carbonatic shelf deposits (Fig. 1).

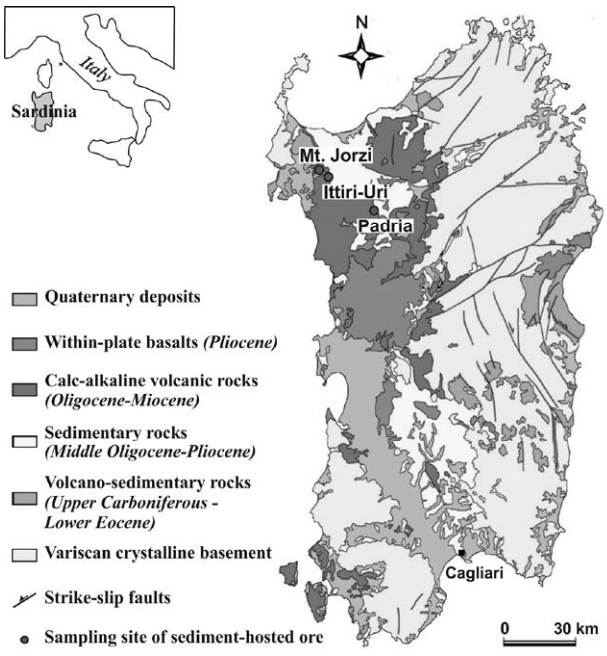

Figure 1. Geological map of Sardinia (after Sinisi et al. 2012, modified). The sampling site of sediment-hosted Mn ores are shown.

The later subduction of the Ligurian–Piedmont oceanic domain beneath the south European paleomargin gave rise to a significant calc-alkaline volcanic activity (Downes et al. 2001). From the Oligocene to middle Miocene, the volcanism produced thick volcanic and volcano-sedimentary sequences ranging in composition from basaltic to rhyolitic.

During Burdigalian time, after collision between the Europe and Adria plates, the Sardinia–Corsica block underwent back-arc spreading resulting in its counter-clockwise rotation. Afterwards, a widespread transgression phase occurred on the microcontinent and the deposition of thick carbonatic and siliciclastic sequences of upper Burdigalian–Tortonian age took place (Funedda et al. 2000).

2.1 Mineralization

In Sardinia there are different types of Mn-deposits that were assigned to sediment-hosted and volcanic-hosted Mn ore categories (Sinisi et al. 2012). In this work, only the sediment-hosted accumulations were considered. These Mn mineralizations formed in marine setting during a Miocene transgressive phase that involved wide areas of Sardinia. This ore is located in the northwest of the island (Mt. Jorzi, Ittiri-Uri and Padria localities; Fig. 1) and consists of Mn oxyhydroxides forming the matrix and/or the cement of a 1 meter-thick, clast-supported conglomerate derived from underlying calcalkaline volcanic rocks. Mn-oxides are also locally present within thin clay-rich levels separating conglomerate from hanginwall limestone of Burdigalian age.

3 Compositional features

Five samples from each sampling site were collected and studied through XRD analysis to obtain mineralogical composition, and through INAA and ICP-MS for major, trace and REE elements concentrations. Optical and SEM analyses were used to observe the microscopic texture of ores.

3.1 Mineralogy

Most of the samples shows a paragenesis dominated by pyrolusite with minor hollandite. Other Mn-oxides and hydroxides, such as todorokite and manganite, occur as accessory phases in some samples. Gangue minerals are represented by quartz, calcite, plagioclase and K-feldspar.

The XRD data also indicate trace amounts of clay minerals in the most of samples. This was also confirmed by optical and scanning electron microscope observations which showed the presence of zeolites in voids formed during Mn-oxides precipitation (Fig. 2). Few euhedral and/or subhedral crystals of apatite and zircon were also identified in Mn-oxide matrix.

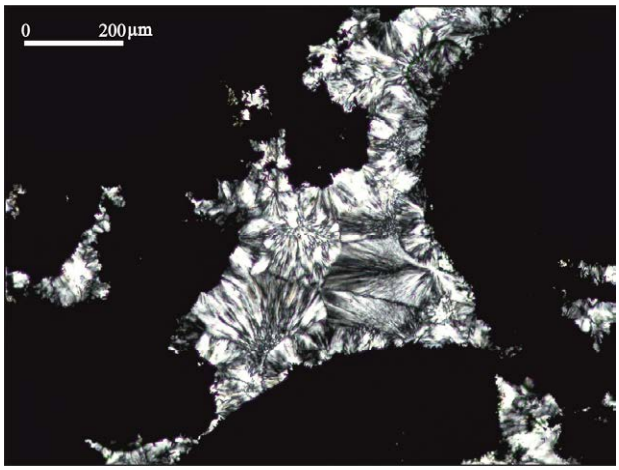

Figure 2. Zeolite (light minerals) that fills voids in Mn-oxide matrix (dark area). OM image, XN.

3.2 Chemistry

All analyzed samples have Mn contents that are commonly between 10 and 200x in excess of GLOSS (Global Subducting Sediments; Plank and Langmuir, 1998) and show a wide variability of element concentrations (Fig. 3).

The MnO content ranges from 4.2 to 77.2 wt.%. The marine Mn ores are characterized by higher CaO concentrations than that in GLOSS, and K_2O and P_2O_5 concentrations similar to or slightly lower than that of the standard. SiO_2, Al_2O_3 and Fe_2O_3 have very variable contents, similar to those of MgO, Na_2O and TiO_2, which are however constantly lower than in GLOSS.

The trace element concentrations also confirm the wide compositional variability of the ores. The samples show very complex trace element distribution patterns. Except of Cr, Sc, Zr, Nb and Ta which are depleted in all samples, the remaining trace elements of Mn ores are either enriched and/or depleted in respect to the reference standard. Among all transition metals, Co has the most variable concentrations (from 0.5 to 1000 ppm).

The chondrite-normalized REE distribution patterns (Fig. 3; chondrite composition data from Evens et al. 1978) show that Sardinian Mn-oxide mineralizations are characterized by strong enrichments of almost all REE except for Eu that has in few sample concentration slightly lower than in chondrite.

The ΣREE values range from 12.7 to 195.4 ppm and a significant fractionation between LREE (light REE) and HREE (heavy REE) was observed according to high values of $(La/Yb)_n$ ratio ranging from 2.1 to 9.2. Finally, positive to negative Ce anomalies ($0.4 < Ce/Ce^* < 1.4$) and strongly to slightly negative Eu anomalies ($0.5 < Eu/Eu^* < 0.9$) are also characteristic of the studied ore samples.

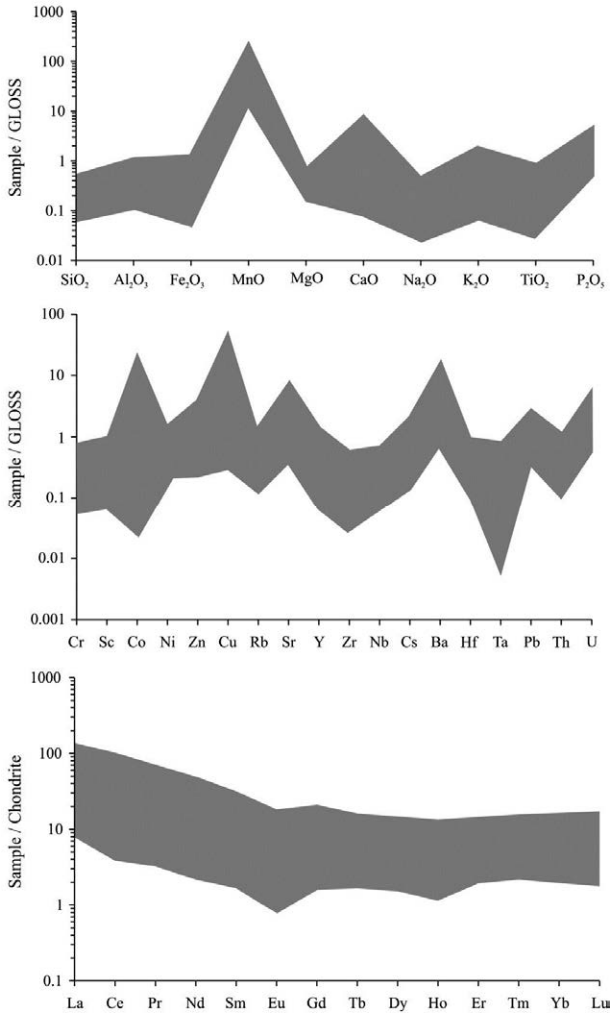

Figure 3. Major, trace and REE normalized patterns of marine Mn ores.

4 Discussion and conclusion

The REE geochemistry has been a subject of several studies not only because of its intrinsic interest but also because it provides useful information for tackling petrological and mineralogical problems (Henderson 1996), as well as paleoenvironmental reconstructions estimating the redox conditions of marine and/or continental depositional environments (Hein et al. 1997; Dia et al. 2000).

Despite the relative low solubility of REE compounds, the rare earth elements are mobile in certain geochemical systems involving aqueous media. The mobility of REE in any aqueous solution is dependent on many factors including Eh, pH, temperature, and availability of organic and/or inorganic ligands (Braun et al. 1990). However, the presence of active mineral surfaces, also strongly affect the geochemistry of REE (Laveuf et al. 2012) and, in this respect, the Mn oxides are regarded important REE scavengers in seawater (Bau and Koschinsky 2009) as well as in groundwater (Laveuf and Cornu 2009). The REE concentrations in sediments, their distribution patterns, and the presence of Ce anomalies may indicate both changes in the redox potential of the mineralizing solution and variations in the sorption properties of solid phases (El-Hasan et al. 2008 and references therein).

Sinisi et al. (2012) argue that the REE geochemistry of Sardinian Mn ores of marine origin is influenced by the presence of accessory minerals, as feldspar and carbonate, leading to a dilution effect of the LREE, MREE and HREE concentrations.

To better identify the nature of REE enrichments of these Mn ores, the factor analysis was performed on all fifteen marine samples using the StatGraphic® Centurion XVI software. To extract factors from the data sets, the Principal Components Analysis method was applied. This operation was performed on the standardized correlation matrix, thus weighting all the variables equally, and allowing to convert the principal component vectors into factors. Subsequently, the factor loadings, which represent the correlation coefficients between the variables and the factors, were considered. The factor loadings (arranged as in Table 1) form the factor matrix.

Three factors were detected for marine Mn ores. The first factor includes most of the selected variables (SiO_2, Al_2O_3, ΣREE and Ce/Ce*). This shows the strong relationship between silicate phases, ΣREE and Ce/Ce* ratio confirming the presence of rare earths, including Ce, within gangue minerals. The second factor comprises Eu/Eu* ratio and LREE/HREE fractionation index suggesting that gangue minerals (apatite and zircon that concentrate mainly LREE and HREE, respectively) affect the fractionation index values. The third factor include only MnO and confirm the free precipitation of Mn-oxides emphasizing the clear dependence of REE contents on silicate phases rather than on manganese oxides.

	Factor 1	Factor 2	Factor 3
SiO_2	0.91		
Al_2O_3	0.94		
MnO			0.89
ΣREE	0.96		
Eu/Eu*		0.87	
Ce/Ce*	0.61		
$(La/Yb)_{ch}$		0.78	

Table 1. Factor matrix for marine Mn mineralizations. Numbers are weights of the variables in the extracted factors. Variables having weight less than 0.60 are omitted.

It is obvious that the mineralizing fluid (in this case seawater, generally characterized by low REE concentrations; Robb 2005 and references therein) coupled with environmental conditions resulted in Mn precipitation not allowing any REE fractionation.

Mineralogical and geochemical studies hence are essential to understand the origin of REE also in deposits including Mn-oxide ores that may act as important sink of REE.

References

Bau M (1999) Scavenging of dissolved yttrium and rare earths by precipitating iron oxyhydroxide: experimental evidence for Ce oxidation, Y Ho fractionation and lanthanide tetrad effect. Geochim Cosmochim Acta 63:67–77

Bau M, Koschinsky A (2009) Oxidative scavenging of cerium on hydrous Fe oxide: Evidence from the distribution of rare earth elements and yttrium between Fe oxides and Mn oxides in hydrogenetic ferromanganese crusts. Geochem J 43:37–47

Braun JJ, Pagel M, Muller JP, Bilong P, Michard A, Guillet B (1990) Cerium anomalies in lateritic profiles. Geoch Cosmoch Acta 54:781–795

Dia A, Gruau G, Olivié-Lauquet G, Riou C, Molenat J, Curmi P (2000) The distribution of rare earth elements in groundwaters: assessing the role of source-rock composition, redox changes and colloidal particles. Geoch Cosmoch Acta 64:4131–4151

Downes H, Thirlwall MF, Trayhorn SC (2001) Miocene subduction-related magmatism in southern Sardinia: Sr–Nd- and oxygen isotopic evidence for mantle source enrichment. J Volcanol Geotherm Res 106:1–22

El-Hasan T, Al-Malabeh A, Komuro K (2008) Rare Earth Elements Geochemistry of the Cambrian Shallow Marine Manganese Deposit at Wadi Dana, South Jordan. Jordan Journal of Earth and Environmental Sciences 1:45–52

Evensen NM, Hamilton PJ, O'Nions RK (1978) Rare earth abundances in chondritic meteorites. Geochim Cosmochim Acta 42:1199–1212

Funedda A, Oggiano G, Pasci S (2000) The Logudoro basin: a key area for the Tertiary tectono-sedimentary evolution of North Sardinia. Boll Soc Geol Ital 119:31–38

Hein JR, Koschinsky A, Halbach P, Manheim FT, Bau M, Kang JK, Lubick N (1997) Iron and manganese oxide mineralization in the Pacific. In: Nicholson K, Hein JR, Bühn B, Dasgupta S (Eds.), Manganese Mineralization: Geochemistry and Mineralogy of Terrestrial and Marine Deposits. Geological Society of London, pp.123–138

Henderson P (1996) The rare earth elements: introduction and review. In: Rare earth elements. Chemistry, origin and ore deposits. Jones AP, Wall F, Williams T (Eds.), The Mineralogical Society Series (7), 1st edn. Chapman and Hall, London, pp. 1–19

Koeppenkastrop D, De Carlo EH (1992) Sorption of rare-earth elements from seawater onto synthetic mineral particles: An experimental approach. Chem Geol 95:251–263

Laveuf C, Cornu S (2009) A review on the potentiality of rare earth elements to trace pedogenetic processes. Geoderma 154:1–12

Laveuf C, Cornu S, Guilherme LRG, Guerin A, Juillot F (2012) The impact of redox conditions on the rare earth element signature of redoximorphic features in a soil sequence developed from limestone. Geoderma 170:25–38

Mameli P, Mongelli G, Oggiano G, Sinisi R (2008) Fe concentration in palaeosols and in clayey marine sediments: two case studies in the Variscan basement of Sardinia (Italy). Clay Minerals 43:531–547

Plank T, Langmuir CH (1998) The chemical composition of subducting sediment and its composition for the crust and mantle. Chemical Geology 145:325–394

Post JE (1999) Manganese oxide minerals: Crystal structures and economic and environmental significance. Proc Natl Acad Sci USA 96:3447–3454

Robb L (2005) Introduction of ore-forming processes. Blackwell Science Ltd, Oxford

Sanematsu K, Murakami H, Watanabe Y, Duangsurigna S, Vilayhack S (2009) Enrichment of rare earth elements (REE) in granitic rocks and their weathered crusts in central and southern Laos. Bull Geol Surv Japan 60(11/12):527–558

Sinisi R, Mameli P, Mongelli G, Oggiano G (2012) Different Mn-ores in a continental arc setting: geochemical and mineralogical evidence from Tertiary deposits of Sardinia (Italy). Ore Geol Rev 47:110–125

Wu C, Yuan Z, Bai G (1996) Rare earth deposits in China. In: Jones AP, Wall F, Williams CT (Eds.), Rare Earth Minerals: Chemistry, origin and ore deposits. The Mineralogical Society Series (7), 1st edn. Chapman & Hall, London, pp. 281–310

Aluminous alteration zones related to Stratabound Zn-Pb(-Ag-Au-Ba-F) deposits in Devonian-Carboniferous(?) metasedimentary rocks, northwestern Alaska, USA

John F. Slack
U.S. Geological Survey, National Center, MS 954, Reston, VA 20192 USA

Alison B. Till
U.S. Geological Survey, 4210 University Drive, Anchorage, AK 99508 USA

Wayne C. Shanks III
U.S. Geological Survey, Federal Center, MS 973, Denver, CO 80225 USA

Harvey E. Belkin
U.S. Geological Survey, National Center, MS 956, Reston, VA 20192 USA

Abstract. Aluminous rocks composed of muscovite+quartz+chloritoid+chlorite+ankerite±tourmaline±sulphides are spatially associated with stratabound Zn-Pb(-Ag-Au-Ba-F) lenses and deformed veins hosted by Devonian-Carboniferous(?) metasedimentary rocks on Seward Peninsula, northwestern Alaska. Bulk analyses show as much as 20.1 wt % Al_2O_3, and anomalously high Zn (to 560 ppm), Pb (to 252 ppm), and Sb (to 71 ppm) relative to unaltered clastic metasediments of the study area. The aluminous rocks are further distinguished chemically from surrounding clastic metasediments by mostly lower SiO_2/Al_2O_3 and higher $Fe_2O_3^T$/MgO ratios. Based on the lack of felsic volcanic rocks in the local Paleozoic sequence and on the absence of euhedral igneous zircons within the aluminous rocks, their protolith is interpreted to be greywacke and not rhyolite. Mass balance calculations show that the aluminous rocks are moderately enriched (10-50%) in Fe, Mn, and K, and are greatly depleted (>50%) in Ca, Na, Sr, and Ba, compared to the average composition of the surrounding clastic metasediments. Oxygen isotope values ($\delta^{18}O_{SMOW}$) for the aluminous rocks range from 13.2 to 18.2 per mil, varying inversely with Al_2O_3. These data support a model involving the alteration, at ca. 125-210°C, of permeable greywacke by seawater-derived fluids in a sediment-hosted, submarine-hydrothermal system.

Keywords. aluminous alteration, chloritoid, Zn-Pb deposits, Seward Peninsula, Alaska

1 Introduction

Aluminous rocks occur in diverse geological settings and in some areas display close spatial association with hydrothermal ores, including orogenic and epithermal gold deposits (Penczak and Mason 1999, Carrillo-Rosúa et al. 2009) and volcanogenic massive sulphide (VMS) deposits (Galley 1993). In metamorphic terranes, aluminous rocks may contain minor to abundant chloritoid, an Al-rich silicate mineral generally with Fe>Mg. The origin of such chloritoid-bearing rocks is controversial, and very different protoliths have been proposed such as sediments (Manby 1983, Gabriele et al. 2003), bauxites and laterites (Franceschelli et al. 2003, Verlaguet et al. 2011), mafic rocks (Faryad 1995), and rhyolites (Morton and Nebel 1984).

This study describes chloritoid-bearing (and locally chloritoid-rich) aluminous zones spatially related to stratabound Zn-Pb(-Ag-Au-Ba-F) lenses and deformed veins in Devonian-Carboniferous(?) metasedimentary rocks of the Nome Complex, on Seward Peninsula, northwestern Alaska. We report here geological, mineralogical, geochemical, and oxygen isotope data on these rocks and present an interpretation of their genesis.

2 Geological setting

The Nome Complex (Till et al. 2009, 2011) comprises Neoproterozoic granitic gneiss and Cambrian to Carboniferous(?) metasedimentary rocks including dolostone, calcite marble, calcareous schist, pelitic schist, graphitic quartzite, metagreywacke, and quartz-albite schist. Mafic metaigneous rocks (metabasites) occur in the Ordovician(?) part of the Nome Complex. No felsic volcanic rocks have been found within the Paleozoic strata of the study area. Ages are constrained by fossils (chiefly conodonts) and by U-Pb geochronology of igneous (granitic gneiss) and detrital zircons (Till et al. 2008, 2011). Rocks of the Nome Complex were deformed and metamorphosed to blueschist facies, and subsequently to greenschist facies, during the Jurassic-Cretaceous Brooks Range orogeny.

3 Zn-Pb-(Ag-Au-Ba-F) deposits

Stratabound Zn-Pb(-Ag-Au-Ba-F) deposits in the Nome Complex consist of two types (Slack et al. 2012): (1) lenses of disseminated to semi-massive sulphide, and (2) deformed sulphide-bearing veins.

The stratabound lenses range in length from tens of meters at the Wheeler North deposit to nearly 2 km at the Aurora Creek deposit. Thicknesses are typically 0.5 to 2 m. Both sulphide deposits are hosted by Devonian-Carboniferous(?) pelitic schist, calcareous schist, and aluminous schist. Wheeler North consists of semi-massive to massive galena and pyrite, minor sphalerite and magnetite, and sparse pyrrhotite, chalcopyrite, tetrahedrite, and Pb-Ag sulphosalts, in a gangue of quartz, fluorite, ankerite-dolomite, and minor Ba-muscovite. The small Nelson and Bluff deposits contain disseminated sphalerite, galena, and pyrite in a gangue of

quartz, muscovite, siderite, ankerite, and dolomite.

At Aurora Creek (Fig. 1), sulphide minerals occur as fillings in the matrix of brecciated dolostone, and as disseminations and semimassive lenses in calc schist and aluminous schist. Principal sulphides are sphalerite and pyrite, accompanied locally by minor pyrrhotite, with sparse galena, chalcopyrite, arsenopyrite, and electrum; the gangue is quartz, siderite, and dolomite, with minor magnetite, chlorite, chloritoid, muscovite, and fluorite, and sparse barite, hyalophane, Ba-muscovite, and local tourmaline. Sphalerite grains within schistose wall rocks are aligned in the dominant foliation. Stratiform layers 0.5-1.0 m thick, composed of microcrystalline quartz with disseminated sulphides, and of interlaminated barite and dolomite with disseminated sulphides, are interpreted as premetamorphic, exhalative chemical sediments. A distinctive lens of carbonate-clast breccia or conglomerate, with disseminated pyrite and galena in the matrix, may have formed during the development of a local growth fault.

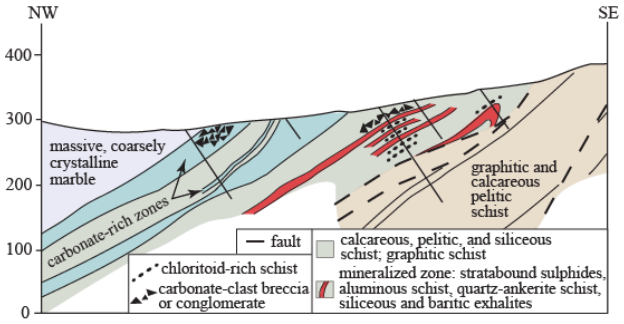

Figure 1. Schematic geological cross section of the Aurora Creek Zn-Au-Ba-F deposit showing mineralized zones and chloritoid-rich schist. Parallel inclined lines are drill holes. Vertical scale (in meters) = horizontal scale.

The deformed vein deposits are folded structures with thicknesses up to 2 m and maximum lengths of about 10 m. These veins occur in Ordovician-Devonian marble, calc schist, pelitic schist, and local aluminous schist that structurally overlie the metasedimentary sequence that hosts the stratabound sulphide lenses. At the Quarry deposit, numerous veins contain a diverse mineralogy: (1) galena with minor sphalerite, Pb- and Ag-sulphosalts, and sparse chalcopyrite, arsenopyrite, and gold in a gangue of quartz, Fe-carbonate, and sparse fluorite; (2) fluorite and barite; and (3) quartz and clots of secondary iron oxides (inferred siderite precursor). Smaller vein deposits at the Galena prospect have disseminated galena or sphalerite in quartz locally with sparse pyrite, fluorite, and celsian.

4 Aluminous alteration zones

The aluminous alteration zones occur both proximal and distal to the sulphide lenses and deformed veins. At and near these mineral deposits, aluminous rocks form stratabound units in metasedimentary wall rocks and extend along strike for as much as several kilometers. Thicknesses vary from 1cm to 3 m, forming laminae and layers interspersed with pelitic schist, calc schist, and quartzite. Mineral assemblages are muscovite+quartz+chloritoid+chlorite+ankerite+pyrite±tourmaline±barite±hyalophane±fluorite±galena±chalcopyrite±sphalerite. In hand specimen, chloritoid and tourmaline occur as 0.1-1.0 cm euhedral crystals. At the Aurora Creek deposit, chloritoid also forms disseminated grains in sphalerite-rich rock. Electron microprobe analyses indicate that the muscovite is phengitic and locally, as at Aurora Creek, contains minor Ba (up to 0.07 apfu). All chloritoid has Fe>>Mg; chloritoid in wall rocks to the Aurora Creek deposit contains minor Zn (up to 0.05 apfu).

5 Geochemistry and oxygen isotopes

Whole-rock analyses of the aluminous rocks proximal to the sulphide deposits (within ca. 300 m) show distinctive compositions including a large range in Al_2O_3 contents from 7.27 to 20.1 wt %. These rocks are distinguished from unaltered clastic metasediments of the Nome Complex by distinctive aluminous mineral assemblages (muscovite+chloritoid±tourmaline), and chemically—in most samples—by generally higher $Fe_2O_3^T$/MgO ratios and lower SiO_2/Al_2O_3 ratios (Fig. 2), and lower CaO and Na_2O contents. By comparison, the average rhyolite plots within the field for the aluminous rocks, whereas average shale and average greywacke plot at the low $Fe_2O_3^T$/MgO end of this field; average arkose has a higher SiO_2/Al_2O_3 ratio than most of the aluminous rocks. Shale-normalized rare earth element (REE) patterns are similar to those of unaltered clastic metasediments of the Nome Complex, including abundances of heavy REEs and the absence of Eu anomalies, but differ in most samples by slightly lower light REEs (La-Sm). By contrast, sulphide-rich samples from the stratabound lenses and deformed veins have lower shale-normalized REE abundances and moderate to large positive Eu anomalies (Slack et al. 2012).

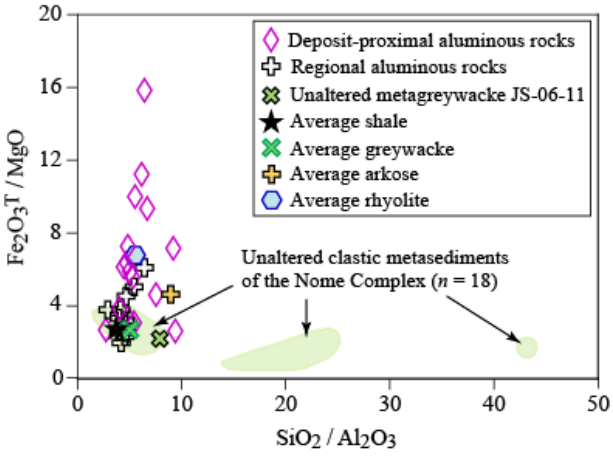

Figure 2. Bulk compositions of aluminous rocks in the Nome Complex compared to those of surrounding clastic metasediments and to average shale (Krauskopf and Bird 1995), average greywacke and arkose (Pettijohn 1963), and average rhyolite (Le Maitre 1976). Note composition of unaltered metagreywacke sample JS-06-11 from the Nome Complex.

The proximal aluminous rocks, within or near the sulphide deposits, have elevated metal contents. Relative to surrounding unaltered clastic metasediments, the

aluminous rocks have anomalously high Zn (>150 ppm; max 560 ppm), Pb (>30 ppm; max 252 ppm), Cu (>50 ppm; max 200 ppm), and Sb (>5 ppm; max 71 ppm).

Mass balance calculations, using Al as an immobile element monitor, were done in order to compare the bulk compositions of the proximal aluminous rocks with those of the unaltered clastic metasediments of the Nome Complex. Based on average compositions of each group, the aluminous rocks show major enrichment (>50 %) in Cu, Zn, Pb, Sb, and Hg, accompanied by moderate enrichment (10-50 %) in Fe, Mn, K, and Co; major depletion (>50 %) is displayed by Ca, Na, Sr, and Ba, with moderate depletion (10-50 %) in Si, Mg, P, U, V, Ni, and Tl.

Whole-rock oxygen isotope values were determined on 27 samples of aluminous rock including 15 from outcrops proximal to the sulphide deposits and 12 from distal outcrops in settings regionally within Paleozoic metasedimentary strata of the Nome Complex (Fig. 3). Values of $\delta^{18}O$ relative to the Vienna Standard Mean Ocean Water standard (VSMOW) range from 13.2 to 18.2 per mil; those for deposit-proximal samples are 14.9 to 18.2. Excluding data for one low-^{18}O sample, these values overall show a strong inverse correlation (r = -0.86) with Al_2O_3; the deposit-proximal samples (n = 15) display a similar correlation (r = -0.81).

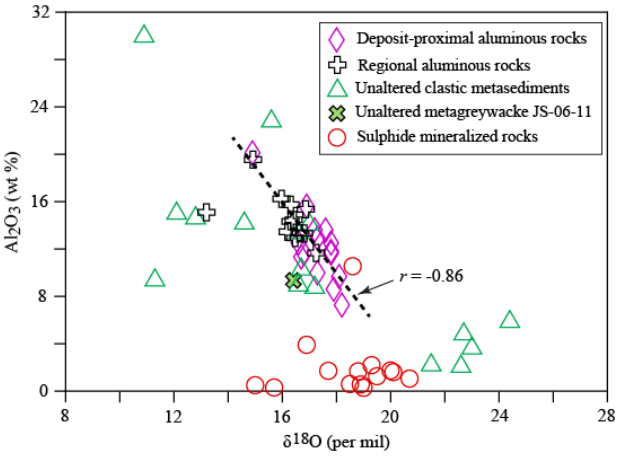

Figure 3. Whole-rock oxygen isotope values vs Al_2O_3 contents of aluminous rocks compared to those of unaltered clastic metasediments of the study area. Note the inverse $\delta^{18}O$-Al_2O_3 trend for the aluminous rocks.

6 Discussion

In order to understand the origin of the aluminous schists in the Nome Complex, the origin of the spatially associated sulphide deposits must first be evaluated. Previous workers have classified the sulphide lenses as VMS, Mississippi Valley-Type (MVT), and granite-related carbonate-replacement (CR) deposits. However, various geological, mineralogical, and isotopic data argue against each of these possibilities. First, VMS deposits are ruled out because no volcanic rocks—mafic or felsic—have been found within the metamorphic sequence that contains the sulphide lenses. Second, a MVT model is considered inapplicable because of the presence at the Aurora Creek deposit of stratiform lenses of siliceous rock and barite, neither of which is known to be related to MVT deposits. Third, sulphur isotope values for the Aurora Creek barite are 25.5 to 26.3 per mil (W.C. Shanks III and J.F. Slack, unpublished data), which are much higher than the maximum value of ca. 12 per mil known for barite in CR deposits that has been attributed to the disproportionation of magmatic SO_2 into H_2S and SO_4 (see Thompson and Beaty, 1990). Considering all of the evidence, including alignment of sphalerite grains within the dominant foliation at Aurora Creek, the stratiform sulphide lenses there and at Wheeler North are interpreted as premetamorphic, sediment-hosted deposits that formed contemporaneously with their metasedimentary host rocks. It is unclear whether these sulphide lenses formed primarily on the seafloor or in the subsurface, the latter by replacement of reactive strata such as carbonates. The mineralogically similar veins (e.g. Quarry and Galena), occurring in structurally higher rocks, are attributed to an originally deeper level of premetamorphic mineralization by compositionally similar hydrothermal fluids.

Aluminous alteration zones spatially associated with metamorphosed sulphide deposits are documented in several VMS systems. Notable is the Archean Mattabi Zn-Pb-Cu-Ag deposit, in the Sturgeon Lake district of Canada, where schist containing chloritoid+sericite+quartz+Fe-carbonate±chlorite±andalusite forms stratabound zones several tens of meters thick and up to 1800 m in length in the stratigraphic footwall of the deposit (Franklin et al. 1975, Groves 1984). Chloritoid-bearing aluminous schists also occur in other VMS deposits in this district, as both stratabound and discordant zones (Morton et al. 1996, Mumin et al. 2007). Within these VMS systems, the protolith of the aluminous rocks is interpreted to be rhyolite tuff or other types of permeable felsic volcanic rock.

The aluminous rocks in the Nome Complex represent a case in which the protolith was likely a feldspar-rich clastic sediment and not a rhyolitic volcanic rock. This hypothesis is supported by the absence of volcanic rocks in the enclosing strata and by the lack of euhedral igneous zircon grains in the aluminous rocks sampled (A.B. Till, unpublished data). A greywacke protolith is favored because it would be aluminous (abundant feldspar) and permeable, and because metagreywacke occurs within Devonian(?) rocks of the Nome Complex (Till et al. 2011). Arkose is a possible protolith but is considered unlikely because no arkose has been recognized in the Nome Complex. A shale protolith is rejected owing to low permeability; permeability is needed in order to explain the stratabound geometry of the deposit-proximal aluminous zones, facilitated in our model by stratigraphically concordant fluid flow and related hydrothermal alteration. Metamorphosed bauxites or laterites are precluded as protoliths, based on the relatively low contents of $Fe_2O_3^T$ (<10 wt %) present in the Seward Peninsula aluminous rocks, compared to $Fe_2O_3^T$ contents of >20 wt % that characterize chloritoid-bearing aluminous rocks having bauxite or laterite protoliths (Franceschelli et al. 2003). Sutton and Land (1996) invoked a different model for aluminous strata in the Ouachita Mountains, USA, involving the alteration of shales during subgreenschist-facies metamorphism by

circulating, low-temperature (125-175°C) fluids. However, such metamorphic models are discounted for the Nome Complex based on the close spatial association of the aluminous rocks with the stratabound sulphide deposits, and on other features of these deposits (e.g. siliceous and baritic layers, high $\delta^{34}S$ values of barite) that indicate formation by seawater-derived fluids prior to deformation and metamorphism.

Major depletion of Ca and Na during formation of the aluminous rocks, calculated relative to the average composition of unaltered clastic metasediments of the study area, is similar to that documented in footwall alteration zones of many VMS deposits including chloritoid-bearing aluminous zones at Mattabi (Franklin et al. 1975). The inverse correlation of $\delta^{18}O$ vs Al_2O_3 among the aluminous rocks (Fig. 3) and the inferred relation to seafloor mineralization suggest that alteration occurred by seawater-derived fluids. Assuming a $\delta^{18}O_{fluid}$ value of 3 per mil for evolved seawater, we calculate relatively low temperatures of alteration (125-210°C) based on whole-rock $\delta^{18}O$ values and the modal proportions of quartz and muscovite. The oxygen isotope temperatures are consistent with the lack of positive Eu anomalies in these rocks that implies formational temperatures of <250°C (Bau, 1991), and with oxygen isotope systematics for chloritoid-bearing aluminous alteration zones in VMS deposits of the Sturgeon Lake district in Ontario (Holk et al. 2008).

Aluminous alteration zones have been described from only a few sediment-hosted Zn-Pb deposits (e.g. Ferla and Meli 2007, Rossetti and Ferrero 2008), but may be more common than presently recognized, especially in metamorphic terranes that contain pelitic rocks.

Acknowledgements

We thank USGS colleagues J.A. Dumoulin and R.A. Ayuso for assistance in the field and helpful discussions. R. Thurston supplied the oxygen isotope data. Detailed reviews by K.J. Schulz and C. Dusel-Bacon (both USGS) are appreciated.

References

Bau M (1991) Rare-earth element mobility during hydrothermal and metamorphic fluid-rock interaction and the significance of the oxidation state of europium. Chem Geol 93:219–230

Carrillo-Rosúa J, Morales-Ruano S, Esteban-Arispe I, Hach-Alí PF (2009) Significance of phyllosilicate mineralogy and mineral chemistry in an epithermal environment: insights from the Palai-Islica Au-Cu deposit (Almería, SE Spain). Clays Clay Mins 57:1–24

Faryad SW (1995) Phase petrology and *P-T* conditions of mafic blueschists from the Meliata unit, West Carpathians, Slovakia. J Meta Geol 13:701–714

Ferla P, Meli C (2007) Petrogenesis of tourmaline rocks associated with Fe-carbonate-graphite metapelite, metabasite and strata-bound polymetallic sulphide mineralisation, Peloritani Mountains, Sicily, southern Italy. Lithos 99:266–288

Franceschelli M, Puxeddu M, Gattiglio, M (2003) Geochemistry and origin of chloritoid schist from the Alpi Apuane, Italy: evidence of a prevailing lateritic signature. Eur J Mineral 15: 575–588

Franklin JM, Kasarda J, Poulsen KH (1975) Petrology and chemistry of the alteration zone of the Mattabi massive sulfide deposit. Econ Geol 70:63–79

Gabriele P, Ballèvre M, Jaillard E, Hernandez J (2003) Garnet-chloritoid-kyanite metapelites from the Raspas Complex (SW Ecuador): a key eclogite-facies assemblage. Eur J Miner 15:977–989

Galley AG (1993) Characteristics of semi-conformable alteration zones associated with volcanogenic massive sulphide districts. J Geochem Expl 48:175–200

Groves DA (1984) Stratigraphy and alteration of the footwall volcanic rocks beneath the Archean Mattabi massive sulfide deposit, Sturgeon Lake, Ontario. MS Thesis, Univ Minnesota-Duluth, Duluth, Minnesota, 132 pp

Holk GJ, Taylor BE, Galley AG (2008) Oxygen isotope mapping of the Archean Sturgeon Lake caldera complex and VMS-related hydrothermal system, northwestern Ontario, Canada. Min Deposita 43:623–640

Krauskopf KB, Bird DK (1995) Introduction to geochemistry, Third Ed. McGraw-Hill, Inc., New York, 647 pp

Le Maitre RW (1976) The chemical variability of some common igneous rocks. J Petrol 17:589–637

Manby GM (1983) A reappraisal of chloritoid-bearing phyllites in the Forland Complex rocks of Prins Karls Forland, Spitsbergen. Mineral Mag 47:311–318

Morton RL, Nebel ML (1984) Hydrothermal alteration of felsic volcanic rocks at the Helen siderite deposit, Wawa, Ontario. Econ Geol 79:1319–1333

Morton RL, Hudak GJ, Koopman E (1996) Physical volcanology, hydrothermal alteration and massive sulphide deposits of the Sturgeon Lake caldera. Geol Assoc Canada-Miner Assoc Canada Ann Mtg, Winnipeg, MB, Field Trip Guidebook B3

Mumin AH, Scott SD, Somarin AK, Oran KS (2007) Structural controls on massive sulfide deposition and hydrothermal alteration in the South Sturgeon Lake caldera, northwestern Ontario. Expl Mining Geol 16:83–107

Penczak RS, Mason R (1999) Characteristics and origin of Archean premetamorphic hydrothermal alteration at the Campbell gold mine, northwestern Ontario, Canada. Econ Geol 94:507–528

Pettijohn FJ (1963) Chemical composition of sandstones, excluding carbonate and volcanic sands: US Geol Surv Prof Paper 440–S, 19 pp

Rossetti P, Ferrero S (2008) The Zn-Pb deposits of Casario (Ligurian Alps, NW Italy): late Paleozoic sedimentary-exhalative bodies affected by the Alpine metamorphism. Geodinam Acta 21/3:117–137

Slack JF, Till AB, Shanks WC III, Ayuso RA, Belkin HE (2012) Late Devonian-Mississippian(?) Zn-Pb-Ag-Au-Ba-F SEDEX deposits and related aluminous alteration zones in the Nome Complex, Seward Peninsula, Alaska. Geol Assoc Canada-Mineral Assoc Canada, Pgm Abst 35 (CD)

Sutton SJ, Land LS (1996) Postdepositional chemical alteration of Ouachita shales. Geol Soc Am Bull 108:978–991

Thompson TB, Beaty DW (1990) Geology and origin of ore deposits in the Leadville district, Colorado: part II. Oxygen, hydrogen, carbon, sulfur, and lead isotope data and development of a genetic model. In Beaty, DW, Landis GP, Thompson TB (eds) Carbonate-hosted sulfide deposits of the central Colorado mineral belt. Econ Geol Monogr 5:156–179

Till AB, Amato JM, Aleinikoff JN, Dumoulin JA, Bleick HA (2008) Application of detrital zircon analysis to identify protolith age, basin evolution, potential correlatives, and provenance of penetratively deformed blueschist-facies meta-sedimentary rocks, northern Alaska. In Garver JI, Montario MJ (eds) Proceedings from the 11th International Conference on Thermochronometry, Anchorage, Alaska, September, 2008, pp. 236-238

Till AB, Dumoulin JA, Ayuso RA (2009) Reconstruction of a metamorphosed Neoproterozoic to Devonian continental margin, Seward Peninsula, Alaska, and its origin. Geol. Soc. Am. Abs. Pgms. 41(7):591

Till AB, Dumoulin JA, Werdon MB, Bleick HA (2011) Bedrock geologic map of the Seward Peninsula, Alaska, and accompanying conodont data. US Geol Survey Sci Invest Map 3131, 2 sheets, scale 1:500,000, includes pamphlet 75 pp [http://pubs.usgs.gov/sim/3131/]

Exploration and mining perspective of the Kupferschiefer series in SW Poland: digging deeper?

Stanislaw Speczik
University of Warsaw, Żwirki i Wigury 93, 02-089 Warsaw, Poland

Slawomir Oszczepalski, Andrzej Chmielewski
Polish Geological Institute-National Research Institute, Rakowiecka 4, 00-975 Warsaw, Poland

Abstract. The Kupferschiefer-type ore deposits and prospects in Poland are closely associated with a redox boundary, the Rote Fäule hematitic footwall alteration. Among the designated prospects, the Ostrzeszów region, located in the eastern part of the Sudetic Foreland, represents the greatest potential. This prospect consists of eight Cu-Ag target areas with rich mineralization at the 1400-1900 m depth, with estimated hypothetical resources ranging from 0.2 to 8.1 Mt Cu and from 0.2 to 10.6 thousand t Ag grading in the range 0.9-6.2% Cu and 10-170 g/t Ag. However, there are several obstacles to resource assessment and expected mining. These include: sparse and unevenly spaced reconnaissance data (dependent on the distribution of drill holes for oil and gas), relatively great depths ranging from 1400 to 1900 m, high temperatures within an ore interval (45-65^{o}C), gas hazards, and thin ore bed (mostly <2 m thick). Since all the available archival cores were examined, future prospecting will depend on new drilling of select targets to establish their extents and potential for future development.

Keywords. Kupferschiefer, exploration, prospective areas, SW Poland

1 Introduction

The mineralization is confined to the Permian Kupferschiefer series representing the contact zone between the Rotliegend continental red beds and the Zechstein marine sediments and combines the Weissliegend sandstones, Kupferschiefer shales and carbonates of the Zechstein Limestone (Fig. 1). The ore deposits are restricted to the southern part of the Zechstein basin and closely associated with the Rote Fäule hematitic footwall alteration (Fig. 1 and 2).

In the Lubin-Sieroszowice mining district, total unexploited resources amount to 1494 Mt ore (29 Mt Cu and 88 000 t Ag) grading at 2.1% Cu and 57 g/t Ag over 3.2 m at depths of 600 to 1380 m. Within the surrounding documented reserve areas there are additional inferred and indicated resources (212 Mt ores, 4 Mt Cu and 13810 t Ag). Economically mineable reserves in the Lubin-Sieroszowice district (1252 Mt ore, 25 Mt Cu, 75000 t Ag) enable possible mine production by KGHM Polish Copper at 30 Mt of ore per year over 30–40 year period. During 45-years of copper mining, immense resources of Lubin-Sieroszowice have been gradually diminished. Currently, the degree of development of documented Cu-Ag deposits in Poland is very high and reaches 80%, implying that a sharp decline in copper production will appear in about 40 years, provided there are no new resources found at favorable depths or deeper mining does not commence. Therefore, it is strongly suggested to reevaluate adjacent reserve and prospective areas that were encountered in SW Poland. Both KGHM Polish Copper and other companies (Amarante Investments, Lumina Capital, Polmetal, Strzelecki Metals Ltd.) applied for tenders in highly prospective SW Poland.

This paper focuses on the exploration potential for the Kupferschiefer-type Cu-Ag deposits in the Ostrzeszów region, which is located in the eastern part of the Sudetic Foreland. The work deals with the distribution of the Rote Fäule zones and prospective areas in the light of the problems that can hinder the possibility of future mining operations.

2 Prospective areas

2.1 Main principles

The redox front is commonly used as a practical exploration guide (Oszczepalski and Rydzewski 1997). The largest Rote Fäule area, rimmed with the Lubin-Sieroszowice and other deposits, encompasses the western part of the Sudetic Foreland. Numerous oxidized fields are also known to occur in northern and eastern parts of this region. There is a clear genetic and spatial relationship between the distribution of the Rote Fäule-related Au-Pt-Pd mineralization and high-grade Cu-Ag bodies adjacent to the oxidized Rote Fäule areas (Fig. 2).

Vertical and large-scale lateral metal zonation is consistent with the interaction of the oxidizing fluid passing from an underlying Rotliegend aquifer, which argues in favour of an efficient metal supply and redistribution processes, during which progressive expansion of post-sedimentary oxidation took place. The crosscutting relationships, upward and lateral advancing alteration of organic matter, and variations in the stable isotope ratios, all reflect interplay of ascending fluids with the host rocks (Oszczepalski 1989, 1999; Püttmann et al. 1989; Speczik 1995; Bechtel et al. 2002; Oszczepalski et al. 2002). Centers of the most pronounced oxidation are thought to represent feeder areas, which are successively surrounded by Cu-, Pb-, Zn-, and pyrite-bearing zones (Fig. 2). Most of the base metals were removed from the oxidized rocks, whereas Au, Pt, Pd concentrated within these rocks (e.g. Oszczepalski 1999; Speczik et al. 1997, 2007; Oszczepalski et al. 2002).

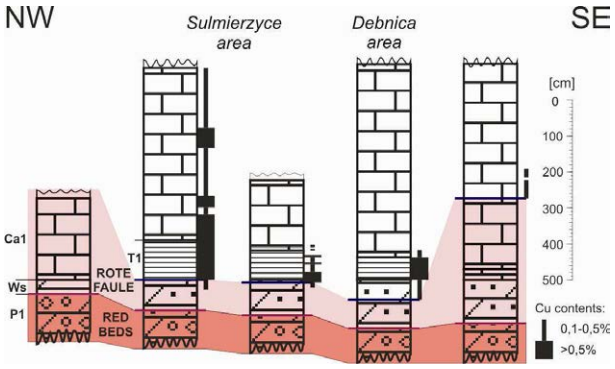

Figure 1. Correlation of the Kupferschiefer series across the Sulmierzyce and Dębnica prospective areas (Ca1 – Zechstein Limestone; T1 – Kupferschiefer; Ws – Weissliegend; P1 – Rotliegend).

2.2 Previous prospection

The Ostrzeszów region has not been explored for copper, instead being explored for oil and gas by PGNiG S.A. Due to the increased interest of KGHM Polish Copper and foreign companies in the exploration for new copper deposits, PGI-NRI conducted drill core studies for many years. The investigations tended to be concentrated in regions adjacent to the oxidized areas. Cores of 370 archival boreholes were studied outside the mining districts (Oszczepalski and Rydzewski 1997). Through subsequent research of 280 next drill holes we have gathered a substantial volume of valuable exploration data for the construction of quantitative maps. As a result, 15 prospects with total hypothetical resources amounted to c. 70 Mt Cu at depth up to 2000 m was delineated throughout the Sudetic Foreland (Oszczepalski and Speczik 2011). Those prospects indicate the potential for the discovery of large deposits. Almost all of them have been granted very recently as exploration concessions to KGHM and foreign companies, which were pursuing these concessions.

2.3 Ostrzeszów prospect

The region considered most prospective based on reconnaissance studies is the Ostrzeszów prospect (Fig. 2). It was investigated and acknowledged to have the potential for significant discoveries since the 1960's based on tens promising drill holes, oxidative alteration, high paleothermal heat flow, and geotectonic setting (Wyżykowski 1971; Oszczepalski 1989, 1999; Oszczepalski and Rydzewski 1997; Speczik et al. 1997, 2007; Blundell et al. 2003).

The prospect is located in the eastern part of the Sudetic Foreland and is approximately 15 km to the east of the Lubin-Sieroszowice Cu-Ag deposit (Fig. 2). Cores from 74 drill holes were studied previously in the Ostrzeszów region (Oszczepalski and Speczik 2011) and 62 drill holes were additionally investigated during the last two years. Present studies allowed the construction of the latest version of the prospectivity map that presents the limits of the oxidized areas, metal zones, and prospective areas in this region. Cu_{Eq} (including silver) productivity contours of 35 kg/m^2 (at cut off 0.5% Cu) define prospective areas (Fig. 2).

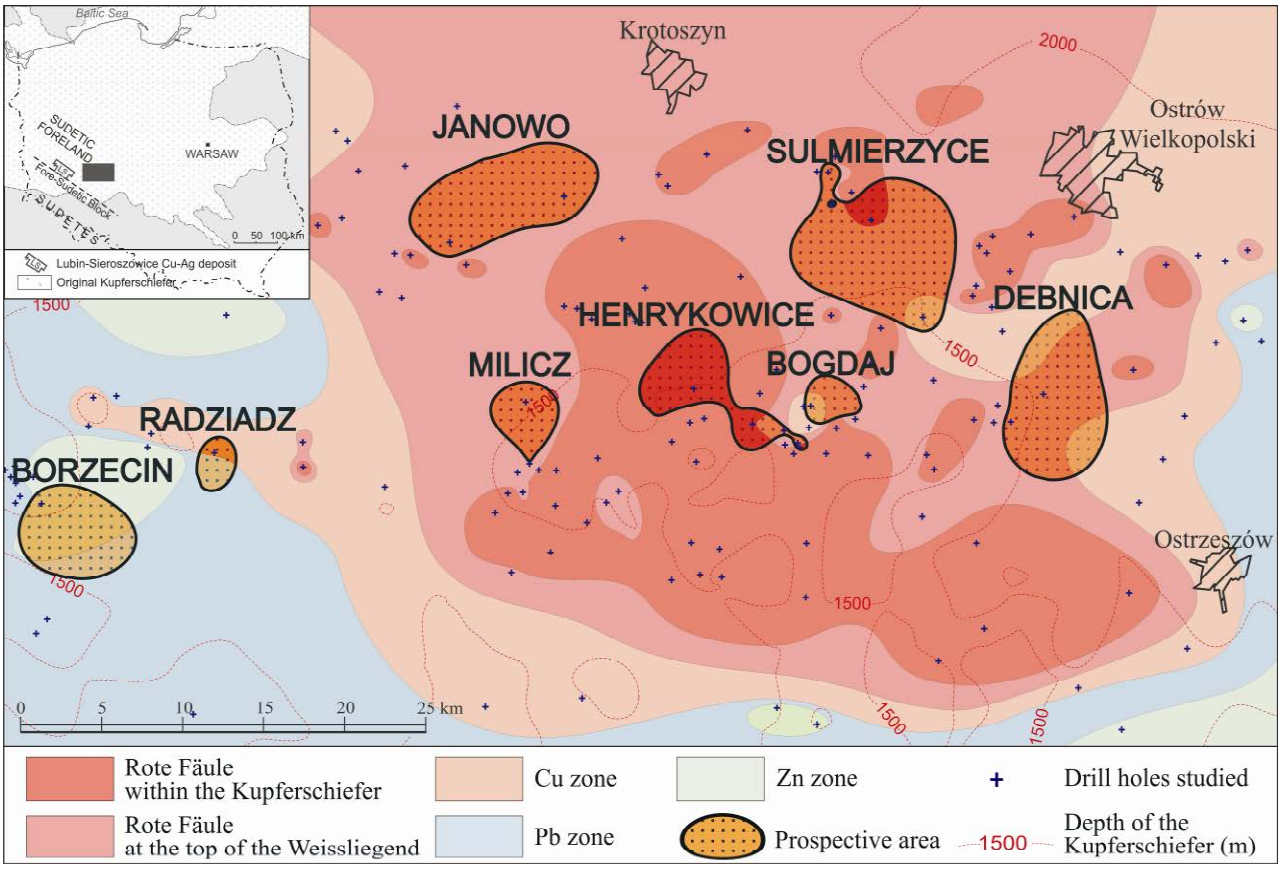

Figure 2. Cu-Ag prospectivity map for eastern part of the Sudetic Foreland (Ostrzeszów prospect) and location of the study area.

Table 1. Hypothetical copper and silver resources in the Ostrzeszów region (* – Ag not analyzed; cc – chalcocite, dg – digenite, cv – covellite, bn – bornite, ccp – chalcopyrite, tn – tennantite, gn – galena, sp – sphalerite).

Targets	Area (km^2)	Depth range (m)	Average thickness (m)	Average Cu grade (%)	Cu resources (Mt)	Ag resources (thousand t)	Main sulphides
Bogdaj	7	1400-1600	1.58	1.52	0.4	1.0	dg, cc (cv)
Borzęcin	32	1400-1600	0.51	4.91	2.0	*	ccp (sp, gn, bn)
Dębnica	50	1600-1800	0.51	6.21	3.9	10.6	cc, dg, bn (cv, gn, sp)
Henrykowice	28	1400-1700	1.08	1.73	1.3	2.4	cc, dg, cv (bn)
Janowo	51	1600-1900	1.11	1.64	2.3	5.1	cc, dg (tn)
Milicz	14	1500-1700	1.86	0.89	0.6	0.6	dg (cc, cv, bn)
Radziądz	6	1600-1800	1.65	0.93	0.2	0.2	cc, cv (bn, tn, gn, sp)
Sulmierzyce	70	1600-1900	2.13	2.18	8.1	9.7	cc, dg (cv, bn)

The Ostrzeszów prospect consists of eight Cu-Ag target areas with rich copper mineralization up to 2000 m in depth, with a number of very promising drill holes. Six targets (Sulmierzyce, Dębnica, Janowo, Henrykowice, Bogdaj and Milicz), adjacent to the recognised Rote Fäule zones, are known as having the highest potentials for copper exploration (Fig. 2; Table 1).

The highest prospectivity in the Ostrzeszów region is confined to Sulmierzyce area that covers c. 70 km^2 and contains about 8.1 Mt Cu and 9.7 thousand t Ag grading 2.1% Cu and 26 g/t Ag at depths ranging between 1600 and 1900 m (Fig. 1 and 2). It is presumed that this area is connected to the south with the Dębnica area, which contains 3.9 Mt Cu and 10.6 thousand t Ag. Janowo area, which is situated in the north-western part of the study area, amounts 2.3 Mt Cu and 5.1 thousand t Ag. Next, three areas (Milicz, Henrykowice and Bogdaj) are located (and partly overlap) at both flanks of the largest Rote Fäule zone. It seems likely that they are connected over the oxidized unit. Two other areas (Borzęcin, Radziądz) with polymetallic (Cu-Pb-Zn) mineralization are located further from the redox boundary.

2.4 Mineralization

The most characteristic feature of the Kupferschiefer mineralization in SW Poland is the zonal distribution of metal sulphides relative to the oxidized rocks. Although an ore mineral zonation pattern is observed as being complex on a mine scale (Pieczonka et al. 2007), it is clearly defined on a regional scale (Oszczepalski and Rydzewski 1997). In areas with the highest copper concentrations, chalcocite, digenite and covellite predominate over the other sulphides, whereas in areas further from the Rote Fäule, bornite, chalcopyrite, galena and sphalerite successively prevail.

In the Rote Fäule zone, there is a dominance of hematite in the form of pigment, globules and lumps of hematite crystals. Locally, remnant sulphide mineralization can be found, represented predominantly by sparse grains of chalcocite, digenite and covellite, which typically are replaced or corroded by hematite (Fig. 3A).

Highest-grade copper mineralization, which surrounds the oxidized areas, is dominated by Cu-S type sulphides (chalcocite, digenite and covellite) with minor bornite, tennantite and pyrite. Common are Cu sulphide pseudomorphs after framboidal pyrite. Cu sulphides form a large number of composites displaying mutual inter-growths (Fig. 3B).

Farther away from oxidized areas, high- and low-grade mineralization is represented by bornite-chalcopyrite assemblage (Fig. 3C), with minor digenite, chalcocite, galena, sphalerite and pyrite. The cementing of detrital grains by bornite and chalcopyrite is a common texture.

In distal areas, low-grade polymetallic ore mineralization is dominated by chalcopyrite-galena-sphalerite association (Fig. 3D), commonly accompanied by numerous pyrite and marcasite grains.

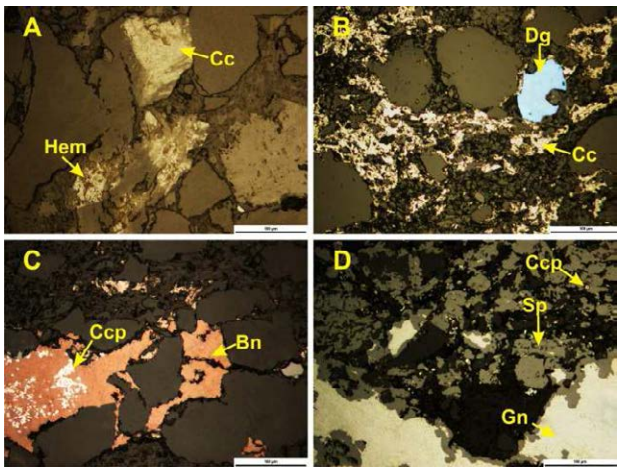

Figure 3. A. Chalcocite grain partly corroded by hematite and hematitic pseudomorphs after pre-existing chalcocite, Weissliegend sandstone, Dębnica area. **B.** Chalcocite and digenite cementing detrital grains, Weissliegend sandstone, Sulmierzyce area. **C.** Intergrowths of chalcopyrite and bornite, Weissliegend sandstone, Dębnica area. **D.** Galena and sphalerite replacing carbonates, Kupferschiefer shales, Borzęcin area (see Table 1 for other explanations).

3 The future

Gradual depletion of shallow copper reserves forces companies to investigate deeper resources. The reconnaissance studies suggest that the Ostrzeszów prospect is a large, target-rich area with potentially significant Cu-Ag mineralization. In certain prospective areas of this prospect covering approximately 260 km^2, a total of about 19 Mt of copper and 29 thousand t of silver

might be found (Table 1). Ore-grade mineralization occurs close to the redox boundary on the reduced side (Fig. 1 and 2). Richest chalcocite-digenite-covellite ore rims the Rote Fäule units grading outwards to bornite and chalcopyrite with distal galena-sphalerite assemblage (Fig. 3).

It should be noted, however, that the irregular network of examined drill holes causes an over-estimation of the tonnage, resulting in a possible overvaluation of resources present. Besides the limitations related to sparse and uneven data distribution, significant are also unfavorable geological and economic barriers for expected mining. The most important disadvantages are: deep levels, high temperature, oil and gas occurrences, and thin ore intervals.

Mining operations at moderate depths (ranging in Ostrzeszów region from 1400 to 1900 m) will require a new approach, lowering production costs. Intelligent mining solutions should be applied to meet economic trends in the world market. Progress in underground mining at depths exceeding 1250 m (a depth limit for economic viability categories in Poland in previous years) will prove this approach to be effective, profitable and technologically attainable.

The present day temperatures within the ore horizon at depth 1400-1900 m are relatively high and vary in the range 45-65^{o}C (Speczik et al. 2007). Nevertheless, modern air-conditioning systems and ventilation techniques are able to provide the appropriate conditions for mining and operating efficiency even in very hot fields. Local areas with geothermal negative anomalies, encourage the search for technologies that will allow the extraction of ores from deeper operational levels, than used currently.

One of the most important barriers is the risk of gas (hydrocarbons, nitrogen, helium) that is associated with underlying Rotliegend and overlying Zechstein rocks in many parts of prospective areas (e.g. Gast et al. 2010). Therefore it should be noted that the anticipated future mining operation in gas-containing rocks will be hard to solve from a technological and safety point of view. Highly innovative and cutting-edge solutions will need to be applied to degas ore bodies before we are able to access and mine them.

Thin ore beds, typically prevailing in the study area (generally less than 2 m thick, except for Sulmierzyce, Dębnica and Janowo, with local thickness slightly exceeding this value) and their variable thicknesses, create problems with extraction, as the mining of a thin ore layer causes barren rock to be mined along with it. However, the use of appropriately low-height machinery and modern mining technologies enable KGHM mines to mine ore bed less than two meters thick.

Since all the available cores were examined, local prospecting drilling is required to precisely determine the boundaries of targeting areas or to identify new targets. Companies having concessions are now ready to carry out a drilling program in select targets to establish their extents and potential to develop into detailed exploration.

Acknowledgements

We thank PGNiG for granting access to the cores. Partial support was provided by NFOŚiGW, Grant no. 21.6505.0501.00.9. Extended thanks are also expressed to Ostrzeszów Copper Sp. z o.o. for granting use of their new data for the entire area.

References

Bechtel A, Gratzer R, Püttmann W, Oszczepalski S (2002) Geochemical characteristics across the oxic/anoxic interface (Rote Fäule front) within the Kupferschiefer of the Lubin-Sieroszowice mining district (SW Poland). Chemical Geology 185:9-31

Blundell DJ, Karnkowski P, Alderton DHM, Oszczepalski S, Kucha H (2003) Copper mineralization of the Polish Kupferschiefer: A proposed basement fault-fracture system of fluid flow. Economic Geology 98:1487-1495

Gast R et al. (2010) Rotliegend. In: Doornenbal H and Stevenson A (eds) Petroleum Geological Atlas of the Southern Permian Basin Area, EAGE Publications b.v. (Houten), pp 101-121

Oszczepalski S (1989) Kupferschiefer in southwestern Poland - sedimentary environments, metal zoning, and ore controls. In: Boyle RW, Brown AC, Jowett EC, Kirkham RV (eds), Sediment-hosted stratiform copper deposits. Geol. Assoc. Can. Spec. Paper 36:571-600

Oszczepalski S (1999) Origin of the Kupferschiefer polymetallic mineralization in Poland. Mineralium Deposita 34:599-613.

Oszczepalski S, Nowak GJ, Bechtel A, Žák K (2002) Evidence of oxidation of the Kupferschiefer in the Lubin-Sieroszowice deposit, Poland: Implications for Cu-Ag and Au-Pt-Pd mineralization. Geological Quarterly 46:1-23

Oszczepalski S, Rydzewski A (1997) Metallogenic Atlas of the Zechstein Copper-bearing Series in Poland. Polish Geological Institute. Warsaw

Oszczepalski S, Speczik S (2011) Prospectivity analysis of the Polish Kupferschiefer – new insight. In: Barra F, Reich M, Campos E, Tornos F (eds) Let's Talk Ore Deposits, 11th SGA Biennial Meeting, Antofagasta, pp 294-296

Pieczonka J, Piestrzyński A, Lenik P, Czerw H (2007) Distribution of ore minerals in the copper deposit, Fore-Sudetic Monocline, SW Poland. Biuletyn Państwowego Instytutu Geologicznego 423:95-108

Püttmann W, Merz C, Speczik S (1989) The secondary oxidation of organic material and its influence on Kupferschiefer mineralization of southwest Poland. Applied Geochemistry 4: 151-161

Speczik S (1995) The Kupferschiefer mineralization of Central Europe: New aspects and major areas of future research. Ore Geology Reviews 9:411-426

Speczik S, Oszczepalski S, Karwasiecka M, Nowak GJ (2007) Kupferschiefer – A hunt for new reserves. In: Andrew CJ et al. (eds) Digging deeper. IAEG, Dublin, pp 237-240

Speczik S, Rydzewski A, Oszczepalski S, Piestrzyński A (1997) Exploration for Cu-Ag and Au-Pt-Pd Kupferschiefer-type deposits in SW Poland. In: Papunen H (ed) Mineral Deposits: Resources and Exploration - Where do They Meet? Balkema, Rotterdam, pp.119-122

Wyżykowski J (1971) Zechstein copper-bearing formation in Poland. Przegląd Geologiczny 19:117-122

A new sedimentary rock-hosted gold belt in eastern Serbia

J. van der Toorn, D. Davidovic, N. Hadjieva, I. Strmbanovic, I. Márton
Avala Resources doo, Bor, Serbia (TSX. V: AVZ)

M. Knaak
Domlogic Geoservice, Cologne, Germany

R. Tosdal
PicachoEx LLC, USA

B. Davis
Orefind, Fremantle, Australia

S. Hasson
Avala Resources Ltd., Longueuil, Quebec, Canada

Abstract: Avala Resources Ltd. is actively exploring a major, north-trending sedimentary rock-hosted gold mineralized belt – the Timok Gold Project – located on the western margin of the Timok Magmatic Complex in the Republic of Serbia. The Timok Gold Project comprises several targets, including Bigar Hill, Korkan and Kraku Pester. All three zones share a similarity of mineralization style, and are associated with a large hydrothermal system. Gold mineralization in the Timok Gold Project is classified as relatively low-temperature auriferous deposits that share many characteristics with Carlin-type Au deposits. To date, Avala has defined gold over a strike length in excess of 30 kilometres and has announced 2.4 million ounces in NI 43-101 compliant inferred and 0.27 million ounces indicated mineral resources. This sedimentary rock-hosted gold represents a previously unrecognized style of gold mineralization within the Timok region.

Keywords:, Timok Magmatic Complex, Cretaceous, sedimentary rock-hosted gold, Carlin-type

1 Introduction

Avala Resources Ltd. is exploring the recently discovered sedimentary rock-hosted gold (SHG) belt – the Timok Gold Project - which lies west of the well-endowed Timok Magmatic Complex (TMC), a metallogenic belt containing a range of magmatic related deposits including, high sulphidation Cu-Au and porphyry Cu-Au. These deposits have formed the basis of significant mining activity for over 100 years at the city of Bor in eastern Serbia. Exploration by Avala Resources Ltd., building upon the initial work by Dundee Precious Metals Ltd., has defined the previously unrecognized SHG prospects along the western margin of the TMC. This new deposit type for the TMC shares many characteristics with the Carlin-type gold deposits in Nevada, USA.

2 Regional Geology

The Timok Gold Project is located immediately to the west of the TMC in eastern Serbia. The TMC is part of the greater Alpine-Balkan-Carpathian-Dinaride metallogenic-geodynamic province (ABCD) (fig. 1), which in-turn is part of the Tethyan (or Alpine-Himalayan) orogenic system that extends from Western Europe to South East Asia. The orogen resulted from the convergence and collision of the Indian, Arabian, and African plates with Eurasia that initiated in the Cretaceous, and continues today. The complex arcuate geometry of the collision interface, and the presence of several micro-plates within the orogenic collage, resulted in a variety of collision products. Some segments are characterized by extensive regional metamorphism, whereas others by calc-alkaline igneous activity. The structural complexity and present-day geometry of the region reflects large-scale oroclinal bending during post-collision tectonics throughout the Tertiary including major transcurrent fault systems with an overall dextral displacement in excess of 100 km (Kräutner and Krstic, 2002).

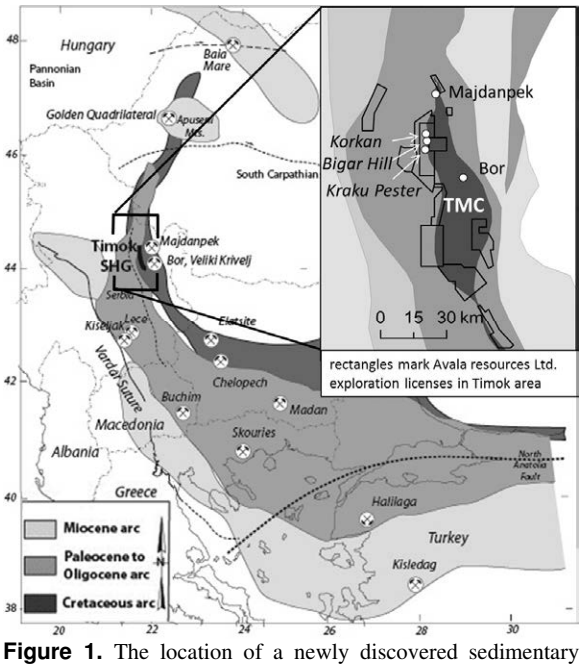

Figure 1. The location of a newly discovered sedimentary rock-hosted gold (SHG) belt within the Cretaceous arc segment of the Western Tethyan Metallogenic belt and the major ore deposits in the area.

Orogenic segmentation resulted in discontinuous distribution of mineral deposits within the ABCD province and the limited lateral extent of the various metallogenic belts along the trace of the orogen. Whereas magmatic activity is evident from the Cretaceous to the present, two overlapping, arcuate segments represent the bulk of magmatism, one located in south-western Serbia in which the majority of the intrusions and volcanic rocks are of Oligocene and Miocene age, and a second in north-eastern Serbia, where Cretaceous magmatic activity is characteristic (fig. 1). These belts and adjacent segments host significant porphyry Cu-Au deposits and related high sulphidation Cu-Au mineralization. The major deposits within these belts are Skouries, Chelopech, Bor, Veliki Krivelj and Majdanpek, as well as the many deposits in the Golden Quadrilateral of Romania.

Within the ABCD, the most economically significant segment comprises the Upper Cretaceous subduction-related magmatic rocks and mineral deposits, referred to as the Banatitic Magmatic and Metallogenic Belt (BMMB) or the Apuseni-Banat-Timok-Srednogorie Belt. This L-shaped belt extends from Romania through Serbia and into Bulgaria. The BMMB intrusive and extrusive rocks were emplaced during a 30-million-year period from ~90Ma to 60Ma and may have been the result of several different subduction zones of varying polarity. The easternmost magmatic complex in the Serbian part of the belt is the TMC.

3 Local Geology

The spatial relationships between mineralization styles in the Timok region suggest that the TMC might be composed of successively westward migrating metallogenic belts. The belts are temporally distinct events, lying from east to west, beginning with the Bor-Veliki Krivelj belt, succeeded by younger Kuruga high sulphidation belt, the Timok Diorite Porphyry belt, and the still younger SHG belt.

The project area is located at the western margin of the TMC within the SHG belt. Upper Jurassic to Upper Cretaceous calcareous rocks including limestone, marl and calcareous clastic and volcaniclastic rocks capped by TMC volcanic and derivative clastic rocks underlie most of the belt. The Late Cretaceous Potoj Cuka monzonite batholith intruded the entire sequence and developed a thermal metamorphic contact aureole. Several overprinting generations of fault systems disrupt the stratigraphy and caused structural complexity, including local reverse faulting and thrusting of stratigraphic units of the TMC area.

The SHG belt is subdivided into a western sequence of Upper Jurassic and Lower Cretaceous limestone and an eastern sequence of volcanic, volcaniclastic and diorite intrusive rocks of Cretaceous age. In the Timok Gold Project area the interface between these two sequences consists of six rock units: Jurassic to Cretaceous limestone units (JLS and KLS units), are unconformable overlain by calcareous clastic sedimentary rocks consisting of a basal grey sandstone (S1 unit) and an overlying red sandstone and conglomerate unit (S2 unit), a marl unit (Marl unit) which overlies the coarse clastic units, which in-turn is overlain by volcanic and derivative clastic rocks and intruded by sills and dykes (Andesite unit). The Jurassic and Cretaceous limestone units are highly karstified towards the upper unconformity.

4 Structural Framework

Formation of the basin hosting the TMC is a product of the Alpine Orogeny, which occurred during oblique convergence of the Indian, Arabian, and African plates with Eurasia. Convergence began in the early Cretaceous resulting in an orogenic collage that is characterized by discrete segments that have undergone a distinct geologic evolution. Major phases of mountain building associated with the Alpine Orogeny were ongoing in the Paleocene to Eocene.

The structural complexity and present-day asymmetric lozenge-shaped geometry of the TMC area resulted from oroclinal bending during post-collision tectonics throughout the Tertiary.

The TMC is generally considered to represent a basin which has an overall disjointed, elongate lozenge shape, with apparent sinistral, north-west-striking dislocations. These dislocations appear to have controlled basin opening as well as modifying the geometry of the TMC. The regional-scale north-west dislocations were second-order structures to an overall dextral, orogen-scale motion resulting from Eocene-Oligocene oroclinal bending.

The interpreted overall east-west cross-sectional geometry of the TMC is that of a synclinorium. Tertiary Alpine deformation was accommodated by several suites of fault zones that are developed across the entire TMC. Regional cross-sections confirm that the bulk of Alpine deformation was concentrated on the TMC margins whereas the central part of the magmatic complex was only affected by gentle folding and fault reactivation. Accommodation of deformation by ductile deformation is largely restricted to the eastern and western margins of TMC and was long-lived, as indicated by open folds and rotation of bedding to sub-vertical dips.

Post-mineral structures are interpreted as being active during Cenozoic transpressional deformation. These structures include pre-SHG-bearing structures that were reactivated in addition to newly-formed, post-mineral faults. Late orogen-parallel extension produced early Miocene normal faults that controlled the architecture of Miocene coal basins and numerous regional east-west trending normal faults extending into the TMC.

The sediment-hosted gold deposits Bigar Hill, Korkan and Kraku Pester are all located on north- to north-west-trending segments of the western margin of the TMC centred around the Late Cretaceous Potoj Cuka monzonite batholith. Examples of all of these structures occur at Bigar Hill and Korkan, where north- to north-east-trending strike-slip faults, reactivated north-west-trending strike-slip faults, and east-trending normal faults are developed.

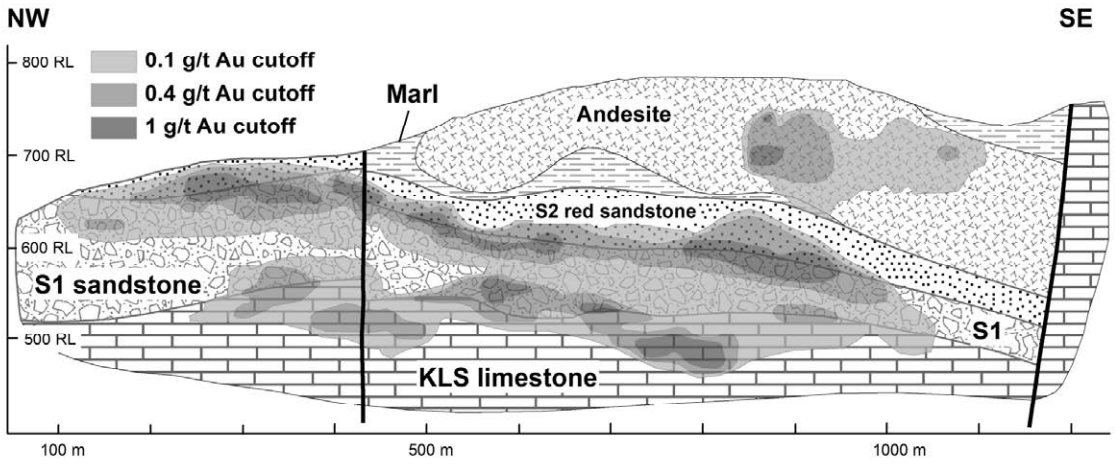

Figure 2. Schematic cross section of the Bigar Hill deposit revealing the strata bound nature of the deposit (details in text)

5 Exploration

Sediment-hosted gold mineralization, located along the western margin of the TMC, represents a previously unrecognized style of gold mineralization within the Timok region. Evidence for SHG along the western boundary of the TMC extends over a strike length of more than 30 km and is up to 8 km wide. The mineralized belt was initially identified by stream-sediment and soil geochemistry programmes conducted by Dundee Precious Metals Ltd. Avala Resources Ltd., which took over management of the Serbia-based exploration group, continues to hold the dominant land position in this newly emerging SHG province.

Detailed stream sediment sampling identified numerous gold-anomalous drainages over an area of 250 sq. km. Follow-up soil sampling defined a >30 km-long belt of strongly anomalous Au-As-Sb-Tl-Hg geochemistry largely associated with a carbonate-dominated stratigraphy. Individual soil samples returned up to 5 g/t Au and numerous rock chip samples returned greater than 1 g/t Au.

Detailed geological mapping and trench sampling has been completed over the entire +30km length of currently defined anomalous soil geochemistry. Initial exploration trenches were spaced approximately 800 meters apart within the main anomalous prospect areas of Korkan, Bigar Hill, Kraku Pester, and Umka. During 2010 infill exploration trenching was completed on the target areas; better results using a 0.4g/t Au cut-off, included 140m @ 2.67g/t Au (Korkan) and 148m @ 1.74g/t Au (Bigar Hill).

Numerous drill targets have been generated throughout the area currently defined by soil sampling and follow-up trenching.

Wide-spaced (nominal 160 m x 160 m) exploration diamond drilling has been ongoing since August, 2010. The objective of the exploration program is to determine the overall mineralized 'footprint' of the multiple target areas delineated to date. Initial drilling commenced on the Kraku Pester target area and then moved to the Korkan and Bigar Hill target areas (Avala Resources Ltd., 2013) where drilling continues.

After testing exploration targets with a detailed trenching programme Avala evaluates prospects with two to three drilling campaign stages with nominal grid spacing of 160 m × 160 m, 80 m × 80 m and 40 m × 40 m.

At present, the National Instrument 43-101 compliant combined mineral resources for Bigar Hill, Korkan and Kraku Pester have been estimated at 6.3 million tonnes grading an average of 1.31 g/t gold in the indicated resource category, and 48.7 million tonnes grading an average of 1.5 g/t gold in the inferred resource category, using a 0.6 g/t gold cut off.

6 Mineralization and Alteration

With the exception of Korkan East, there is a common character to the SHG formations regardless of the prospect. Gold is associated with pyrite based on petrographic investigation (Campbell, 2010; Pacevski, 2012). The amount of fine-grained pyrite increases from the margins toward the central and higher gold content zone in all mineralized formations.

Gold mineralization is located principally along two stratigraphic contacts within the sedimentary rock sequence, with lesser amounts present along steeply dipping fractures zones within the clastic rocks and stratigraphically higher in andesite sill (fig. 2). A lower zone is localized along the unconformable and breccia-like lower contact zone of the clastic S1 unit, against the underlying KLS limestone unit, and in isolated karst-infill zones at the upper boundary of the KLS limestone unit (dominant at the Korkan deposit). Many of these breccia-like zones are also the locus for post-mineral faulting, thus complicating the interpretation of the original mineralized rock texture.

The most continuous gold-bearing zone lies at shallow stratigraphic levels along the contact between the S1 and S2 units, forming an upper zone (dominant at the Bigar Hill deposit, fig. 2). Above this zone, gold mineralization at Bigar Hill also occurs within the andesite intrusive unit forming a sill where gold is associated with narrow zones of quartz addition.

Gold at Kraku Pester is hosted in pyritized fault breccia to cataclasite in a variably disrupted

stratigraphic sequence comprising hornfels, calc-silicate hornfels, marble, and tuffaceous rocks in the contact metamorphic aureole of the Potoj Cuka monzonite pre-ore stock. Cataclastic zones noted in the monzonite, locally host auriferous pyrite. Direct correlation of the stratigraphic sequence at Kraku Pester with those recognized regionally at Bigar Hill and Korkan is uncertain. The presence of gold and other corresponding geochemistry within the Potoj Cuka monzonite, dated at 79.9Ma (Tosdal, 2012), suggests the mineralising event is late and possibly at the end of theTMC's development.

Commonly no macroscopically visible silicate alteration minerals are evident. However, the fine grain size of the formations coupled with the common evidence for additional post-mineral brecciation precludes easy identification of silicate alteration minerals. Analysis of the geochemical characteristics of the mineralized formations using 1 m drill hole data suggests that clay minerals, presumably combinations of kaolinite, illite, and probably smectitic clays, form part of the hydrothermal alteration associated with pyrite deposition. Elevated gold is also associated with rocks containing sufficient iron, thus suggesting that the depositional mechanism was likely the sulphidation of iron present in the rocks. The recognition of auriferous concentrations in karst infill sedimentary rocks is consistent with this interpretation as iron is a common residual element during carbonate dissolution. Removal of diagenetic and detrital carbonate is associated with gold zones.

Structurally, Korkan is dominated by north-west-striking faults, which appear to be associated with mineralization, but have also dismembered mineralization and earlier structures during late reactivation. Late east-striking faults such as those found at Bigar Hill have been recorded at Korkan, but are less important in forming boundaries to the deposit and juxtaposing stratigraphy.

Unlike at Korkan, significant base metal sulphide minerals accompany gold mineralization at Korkan East. Overall, the mineralized zones in this environment have the appearance of carbonate replacement deposits.

Local repetition or imbrication of stratigraphy and mineralization are related to north- to north-east-trending faults.

The northern parts of the SHG belt are proximal to the world-class Majdanpek Cu-Au deposit. The Timok Gold Project licences and the Majdanpek deposit share similar geological settings, implying potential for skarn-type, massive sulphide, lead-zinc vein and massive replacement and porphyry Cu-Au deposits.

7 Conclusion

The dominant prospects in the clastic sedimentary rocks along the western margin of the TMC are relatively low temperature auriferous deposits that share many characteristics with Carlin-type Au deposits as outlined by Cline et al. (2005). The interpretation of the SHG prospects within the project area as Carlin-type is based upon the following criteria: (1) character of the sedimentary host, (2) the metal association (Au, As, Hg, Tl, S and Sb> base metals), (3) the fine-grained nature of the gold, high gold to silver ratio and alteration types including argillization, decarbonization and locally addition of quartz. Sulphidation reactions appear to have controlled gold deposition although the potential influence of a simple redox boundary along stratigraphic formations cannot be discounted. Fluid flow is considered to be structurally controlled along pre-ore structures. Whether the gold is sourced from the nearby porphyry systems, the Potoj Cuka monzonite or amagamtic is uncertain.

The anomalous prospect along the belt is present in Korkan East where significant gold is associated with carbonate replacement deposits composed of a variable assemblage of arsenopyrite-sphalerite-galena. The link between the replacement deposit at Korkan East and the nearby lower temperature sediment-hosted gold is unclear at this time.

Acknowledgements

The authors wish to thank Avala Resources Ltd for the permission to publish the data. We like to extend our gratitude to the geology staff at Avala Resources Ltd. who made this project work. A special thanks goes to Fred Graybeal who reviewed the abstract.

References

Avala Resources Ltd. (2013) Press Release - http://www.avalaresources.com/s/NewsReleases.asp .

Campbell G (2010) Mineralogy, Alteration and Implications for Metallurgical Response at the Kraku Pester Prospect, Serbia. Dissertation, University of Exeter Press

Cline JS, Hofstra AH, Muntean JL, Tosdal RM, Kickey KA (2005) Carlin-Type Gold Deposits in Nevada: Critical Geologic Characteristics and Viable Models. Economic Geology 100th Anniversary Volume, pp 451-484

Kräutner, HG, Krstić, B (2002) Alpine and Pre-Alpine structural units within the Southern Carpathians and the Eastern Balkanides. Proceedings of XVII. Congress of Carpathian-Balkan Geological Association Bratislava, September 1 - 4 2002, Geologica Carpathica 53, Special Issue, 7 pp.

Pacevski A (2012) Mineralization in the Korkan and Bigar Hill areas: final conclusions and discussions. Avala Resources doo internal report. 9 pp.

Tosdal, RM (2012) U-Pb SHRIMP-RG ages and trace element geochemistry of the Late Cretaceous diorite and monzonite complexes, West-Central Timok belt, Eastern Serbia. Avala Resources d.o.o. internal report. 31 pp

Structural analysis and distribution of layer-parallel veins at the Nkana stratiform Cu-Co deposit, Zambia

Koen Torremans, Philippe Muchez, Manuel Sintubin
Geodynamics and Geofluids Research Group, Department of Earth and Environmental Sciences, KU Leuven, Celestijnenlaan 200E, B-3001 Leuven, Belgium

Abstract. The Nkana ore deposit in the Central African Copperbelt is a sediment-hosted Cu-Co deposit in northern Zambia. A structural analysis of the open pit at Nkana South reveals NW-SE rending overturned, tight to isoclinal folds with a slight NE verging asymmetry. The ore occurs disseminated in the host rock and in several vein generations. A study of the distribution of pre-folding layer-parallel veins indicates negative exponential vein thickness and spacing frequency distributions. These vein-property distributions, together with microstructural observations serve as an input for numerical modelling on the formation of these layer-parallel veins.

Keywords. Central African Copperbelt, Nkana mine, layer-parallel veins, vein thickness and spacing frequency distribution, structural analysis

1 Introduction

The sediment-hosted Cu-Co deposits of the Central African Copperbelt occur in the Neoproterozoic metasediments of the Katanga Supergroup which were deposited between > 883 ± 10 Ma and < 570 Ma. This Supergroup is subdivided in the Roan, Nguba and Kundulungu Groups (Selley et al. 2005; Armstrong et al. 2005). Inversion from extensional to compressional tectonics during amalgamation of the Gondwana supercontinent led to the formation of the Neoproterozoic Pan African Lufilian Arc (Frimmel et al. 2011). At present, the Lufilian Arc is a northward convex oroclinal belt, caused by deformation of the Katanga Supergroup during the Lufilian orogeny with peak metamorphism ~ 530 Ma (John et al. 2004; Rainaud et al. 2005).

2 Nkana mine

The Nkana-Mindola mine is situated near Kitwe, Zambia and lies on the southeastern side of the Chambishi-Nkana basin (Bard and Jordaan 1963). This part of the basin is characterised by the northwest plunging Nkana Synclinorium, a series of NW-SE trending folds. The intensity of deformation varies significantly over the extent of this synclinorium with numerous tight, isoclinal folds in the SE (Nkana South) gradually becoming more open and asymmetric towards the north (Nkana Central) and ultimately showing broad warping of relatively undisturbed and steeply inclined beds at Mindola. Mining operations at Nkana South-Central are conducted from two contiguous mining sites: Nkana South and Nkana Central including an open pit at Nkana South.

The base of the Roan Group at Nkana consists of a succession of siliciclastic metasediments, mainly arkosic sandstones and conglomerates (Brems et al. 2009; Muchez et al. 2010) overlain by the Ore Shale formation. At Nkana South-Central this Ore Shale formation consists of a carbonaceous South Orebody Shale (5 – 20m) and an overlying Hangingwall Argillite (5 – 12m) with a tremolitic alteration zone of variable thickness at the base of the South Orebody Shale (Brems et al. 2009). Overlying these metapelites are the massive sandstones of the Hangingwall Quartzite formation. The sediments at Nkana show metamorphic mineral assemblages indicative of greenschist facies metamorphism.

Cu-Co mineralisation is hosted primarily by the Ore Shale formation and adjacent parts of the footwall and hanging wall formations as sulphides (Muchez et al. 2010). This mineralisation occurs disseminated as fine grains and in nodules and in several generations of veins (Brems et al. 2009; Muchez et al. 2010). The first of these veins are (sub)parallel to bedding, interpreted to have been formed during a compressive stress regime at the onset of the Lufilian Orogeny. In some cases they crosscut bedding at low angles or bifurcate (Bard and Jordaan 1963). These layer-parallel veins are subsequently folded, often showing ore and gangue mineral concentrations in saddle reefs of folded veins. This first generation of veins is crosscut by highly irregular veins. Ultimately, relatively undeformed and coarse grained massive veins crosscut all previous mineralisation phases, possibly reflecting a new fluid phase (Brems et al. 2009).

A strong link between ore forming processes and tectonic deformation is shown on a macroscopic scale by enrichment of ore in fold hinges (Brems et al. 2009). Previous studies have convincingly shown that these veins characterise major mineralisation/remobilisation stages that are linked to the geodynamic evolution (Muchez et al. 2010). Furthermore, most of the recent literature for the Central African Copperbelt indicates a metallogenetic history with multiple mineralisation and remobilisation phases related to different stages in the orogenic evolution (e.g. overview in Haest and Muchez 2011; Kampunzu et al. 2009).

This research aims to better constrain the formation mechanism and distributions of layer-parallel veins in Nkana South-Central, and to better confine the deformation styles and mechanisms during the Lufilian orogeny that ultimately influenced the nature of mineralisation. Because the layer-parallel veins are related to early mineralisation/remobilisation stages, a detailed study of formation and subsequent deformation of these veins, can lead to a better understanding of the conditions during and after mineralisation in these veins.

Our study is based on the analysis of linear vein-log transects, a detailed structural analysis, an investigation

of the vein microstructures and ultimately a comparison of inferred formation mechanisms for the layer-parallel veins with results obtained from numerical modelling experiments.

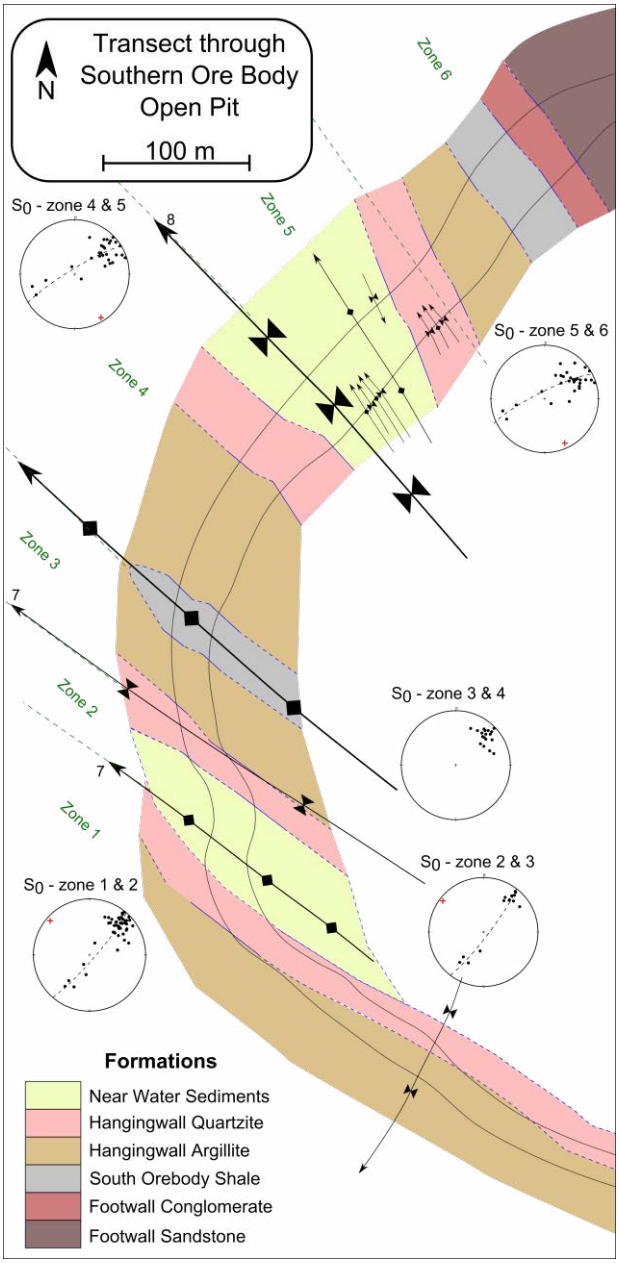

Figure 1. Geological map of the west side of the Nkana South open pit with structural features. Lower hemisphere equal-area stereoplots show poles to bedding and calculated β-girdles of these poles with corresponding L-pole (fold axis).

3 Deformation style at Nkana South

As it is difficult to fully characterise the macroscopic structural style in actively producing underground crosscuts, we conducted a detailed structural analysis at the Nkana South open pit. This open pit exploits supergene mineral deposit containing e.g. malachite, heterogenite, goethite and azurite, formed by intense lateritisation. Despite this alteration, structural features are still well preserved and measurements on two excavation levels of the west side of the open pit are shown in Figure 1. All planar features are presented in dip/dip direction and linear features in plunge/trend notation.

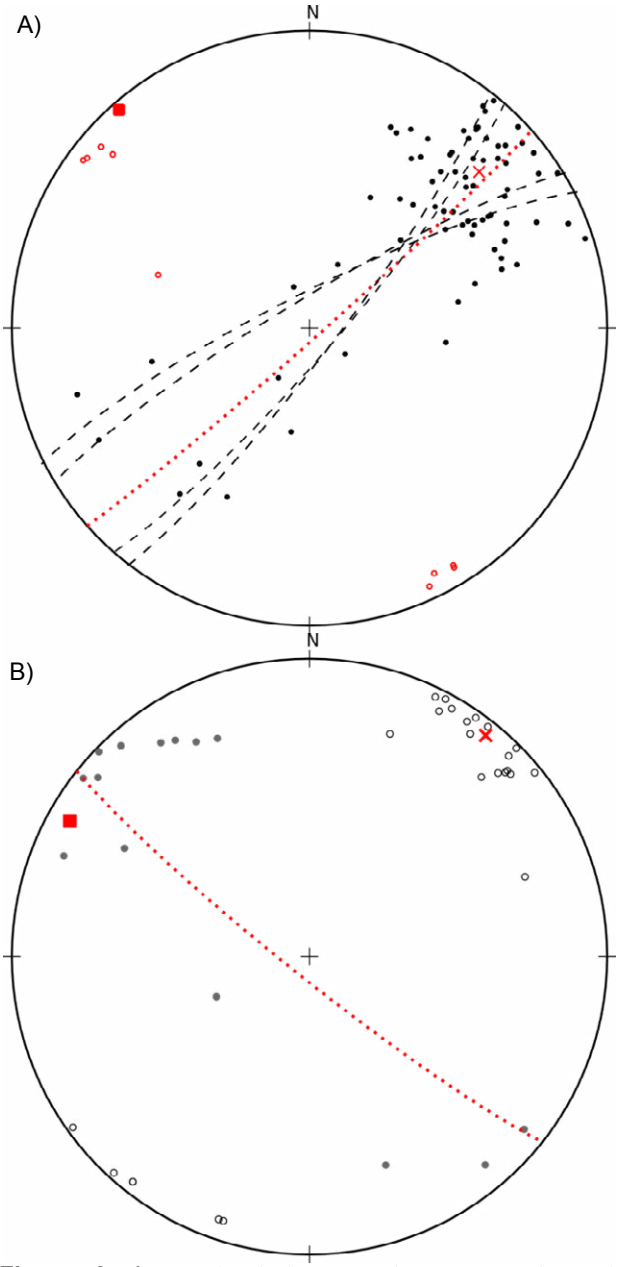

Figure 2. Lower hemisphere equal-area stereoplots of combined orientation data from the Nkana South open pit shown in Figure 1. A) Poles to bedding (dots) and mean orientation of bedding planes (cross). Best fit β-girdles of poles to bedding (black dashes) are shown for 4 major folds in hanging wall formations in the open pit, as well as L-poles to bedding (open circles) of all macro- and mesoscopic folds in the open pit. The mean β-girdle of all combined poles to bedding (red dots) yields an L-pole of 03/318 (square). B) Poles to cleavage (open circles) show slight NE vergence of axial planes as indicated by the mean cleavage plane (84/218; dotted line) and its pole to mean cleavage (cross). Orientations of bedding – cleavage intersection lineations (dots) are quite variable with the mean intersection lineation (square) slightly northwest plunging (08/299).

The architecture of the fold series is very consistent with those underground displaying NW-SE trending folds with close to isoclinal interlimb angles in overturned folds with a slight NE verging asymmetry

(Fig. 1 and Fig 2). Secondary s- and z-folds decorate the limbs of higher-order folds.

The main tectonic cleavage is not always macroscopically observable in incompetent layers, albeit pervasive in the rock. In contrast, a strong foliation is developed parallel to bedding, ultimately related to the sedimentary foliation, as also observed in thin sections. The mean cleavage plane in the open pit is 84/218, consistent with the regional SW-NE structural grain of the orogen (Fig. 2B; Porada and Berhorst 2000; Kampunzu and Cailteux 1999).

A stereographical analysis illustrates that poles to bedding of individual folds developed in the hanging wall fit a great-circle distribution fairly well, thereby demonstrating that these folds can be considered close to cylindroidal (dashed lines in Fig 2A). For the entire fold sequence, the best fit β-girdle through bedding poles yields an attitude of 87/138 with an L-pole (fold axis) oriented 03/318. The fit is reasonable as indicated by a shape parameter of 1.28 of the β-girdle with a strength of 3.95 (cf. Woodcock and Naylor 1983). The fold axis of the collective fold train (03/318) is subhorizontal, only slightly NW plunging. The L-poles of individual folds however, plunge both to the NW and SE (Fig 2B). Indeed, several folds observed in underground crosscuts are doubly plunging folds, in accordance with these observations.

In contrast, the folding style of the incompetent Ore Shale formation in zone 3 & 4 is quite different. The anticline is isoclinal with an extremely angular squeezed out fold hinge and elongate aspect ratio (Fig. 1). This exemplifies the folding style of several folds, observed in the Ore Shale in underground crosscuts in contrast to the folding style observed in footwall and hanging wall formations.

Bedding-cleavage intersection lineation varies from subhorizontal to gently NW or SE plunging with an average plunge/trend of 08/299 (Fig. 2). The attitude of the intersection lineations correspond quite well to the calculated L-poles to bedding for each of the separate zones. The average plunge/trend of the intersection lineations deviates only slightly from the orientation of the calculated fold axis of the fold train. The variability which is observed in the intersection lineation orientation can be explained by similar variability in the cleavage attitude (Fig. 2B).

5 Spacing measurements

Vein thicknesses and spacing logs often show power-law, (log) normal or negative exponential frequency distributions (Brooks Clark et al. 1995; Gillespie et al. 1999). Layer-parallel veins in the Ore Shale formation at Nkana South are very closely spaced (Fig. 3) and continue for several meters along bedding planes (i.e. extremely low aspect ratios). To better understand the mechanisms that control the formation of these veins and to quantify their distribution pattern, we conducted a vein distribution analysis.

Thirteen line transects perpendicular to the attitude of the veins were measured in underground crosscuts and on boreholes of limbs of low-amplitude folds at Nkana South-Central, representing a total of 730 veins. One such characteristic vein log for transect at 480 South decline in Nkana Central is shown in Figure 3B. Most of the crosscuts studied do show fold limbs that have suffered at least minor and mostly moderate subsequent deformation of the layer-parallel veins in the form of buckling, thrusting or boudinage. However, care was taken in selecting those line transects with straight continuous veins showing little or no apparent doubling of veins by subsequent thrusting in relatively undisturbed fold limbs. Some posterior deformation is inevitable but acceptable as we are mainly interested in the distribution characteristics of the veins in combination with observed microstructures.

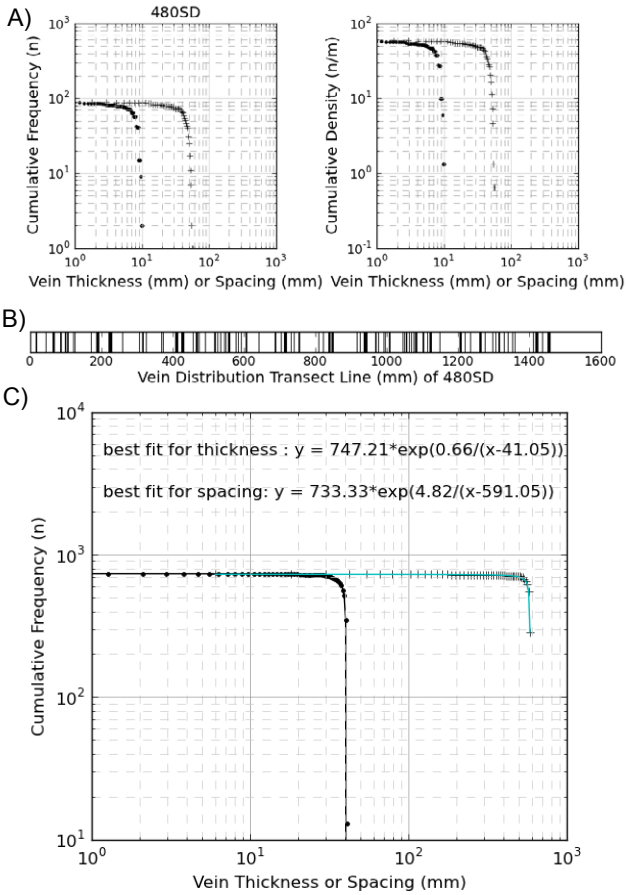

Figure 3. A) Cumulative frequency (left) and density (right) plots of vein thicknesses (dots) and vein spacing (crosses), all showing negative exponential distributions. B) Vein transect line 480SD indicating layer-parallel vein thicknesses on a vein log. Only layer-parallel veins are shown and accounted for in the vein property analysis. C) Cumulative frequency distribution of thickness (dots) and spacing (crosses) for thirteen combined vein logs (n = 730). The best-fit regression ($R^2 > 0.99$) for a negative exponential distribution is shown.

Cumulative frequency plots are shown in Figure 3 with a cut off at < 1 mm as thicknesses beneath this threshold could not be confidently measured.

Both cumulative thickness and vein-spacing frequency distributions for the transect 480SD show negative exponential distributions (Fig. 3). Curve fitting of the combined data for all vein logs using Scientific Python (SciPy) with a function y= a*exp(b/(x+c)), yields a best fit regression with a $R^2 > 0.99$ (Fig. 3C), suggesting that this distribution is a controlling factor for all transects.

Negative-exponential distributions have been previously modelled and interpreted to reflect size-independent growth of veins (Brooks Clark et al. 1995). If this is true for Nkana, veins would theoretically always form by approximately the same opening interval, independent of the size of the existing vein.

Many of the layer-parallel veins consist of elongate blocky to fibrous dolomite. These fibres are for the most part (sub)perpendicular or sometimes at a high to moderate angle to the vein wall. The fibrous crystals generally do not show crack-seal host-rock inclusion bands parallel to the vein wall but do present abundant pseudo-secondary fluid inclusion trails parallel to the growth direction of the crystals. The growth direction in the veins is indicated by solid inclusion trails often straddling or parallel to crystal boundaries which are interpreted to track the opening direction.

Multiple fine vein growth events for many of the layer-parallel veins are suggested by the presence of many closely spaced pseudo-secondary fluid inclusion planes. Future work will focus on further constraints on the microstructures and a study of the characteristics of these fluid inclusion planes to quantify and study individual growth increments and to test the hypothesis of size independent growth.

6 Numerical modelling of veins

Discrete element modelling was conducted to study possible factors governing the formation of closely spaced sets of layer-parallel veins. For this purpose, a semi-automatised procedure was developed to calibrate layered brittle-elastic numerical specimens. Consequently, these numerical rock specimens are repeatedly brought to failure and refilled with vein material after each fracture event. This methods allows to study the formation of subsequent generations of layer-parallel veins as a function of mechanical strength of rock and vein material. Different types of veins are modelled ranging from crack-seal to anastomosing veins by adjusting competence contrast and mechanical strength of the vein material. The vein distribution measurements serve as an important quantitative control for this numerical modelling.

7 Conclusion

A structural analysis of the open pit at Nkana South shows overturned tight to isoclinal folds with a slight NE verging asymmetry. Many of the pre-folding layer-parallel veins in the Ore Shale formation show evidence of multiple fine growth events. In addition, these veins are closely spaced and reveal negative exponential thickness and spacing distributions, suggesting a size independent growth mechanism. These observations provide quantitative constraints for numerical modelling of layer-parallel veins in these type of multilayer sequences.

Acknowledgements

We sincerely thank Mopani Copper Mines Plc. for access to the mine and data. Our gratitude goes to the staff of the geology departments for assistance with underground mapping and many fruitful discussions. This research project is financially supported by research grants OT/11/38 of BOF KU Leuven and G0414.08N of FWO-Vlaanderen.

References

Armstrong RA, Master S, Robb LJ (2005) Geochronology of the Nchanga Granite, and constraints on the maximum age of the Katanga Supergroup, Zambian Copperbelt. Journal of African Earth Sciences 42:32-40.

Bard P, Jordaan J (1963) Some structural features associated with the Rokhana orebodies. Stratiform Copper Deposits in Africa 2nd Part: Tectonics, Association of African Geological Surveys, Paris:179-191.

Brems D, Muchez P, Sikazwe O, Mukumba W (2009) Metallogenesis of the Nkana copper-cobalt South orebody, Zambia. Journal of African Earth Sciences 55:185.

Brooks Clark M, Brantley SL, Fisher DM (1995) Power-law vein-thickness distributions and positive feedback in vein growth. Geology 23:975-978.

Frimmel HE, Basei MS, Gaucher C (2011) Neoproterozoic geodynamic evolution of SW-Gondwana: a southern African perspective. Int J Earth Sci (Geol Rundsch) 100:323-354.

Gillespie PA, Johnston JD, Loriga MA, McCaffrey KJW, Walsh JJ, Watterson J (1999) Influence of layering on vein systematics in line samples. Geological Society, London, Special Publications 155:35-56.

Haest M, Muchez P (2011) Stratiform and vein-type deposits in the Pan-African Orogen in Central and Southern Africa: evidence for multiphase mineralisation. Geologica Belgica 14:23-44.

John T, Schenk V, Mezger K, Tembo F (2004) Timing and PT evolution of whiteschist metamorphism in the Lufilian Arc–Zambezi Belt orogen (Zambia): implications for the assembly of Gondwana. The Journal of Geology 112:71-90.

Kampunzu AB, Cailteux JLH (1999) Tectonic evolution of the Lufilian Arc (Central Africa Copper Belt) during Neoproterozoic Pan African orogenesis. Gondwana Research 2:401-421.

Kampunzu AB, Cailteux JLH, Kamona AF, Intiomale MM, Melcher F (2009) Sediment-hosted Zn–Pb–Cu deposits in the Central African Copperbelt. Ore Geology Reviews 35:263-297.

Muchez P, Brems D, Clara E, De Cleyn A, Lammens L, Boyce A, De Muynck D, Mukumba W, Sikazwe O (2010) Evolution of Cu-Co mineralizing fluids at Nkana Mine, Central African Copperbelt, Zambia. Journal of African Earth Sciences 58:457-474.

Porada H, Berhorst V (2000) Towards a new understanding of the Neoproterozoic-Early Palaeozoic Lufilian and northern Zambezi Belts in Zambia and the Democratic Republic of Congo. Journal of African Earth Sciences 30:727-771.

Rainaud C, Master S, Armstrong RA, Phillips D, Robb LJ (2005) Monazite U-Pb dating and ^{40}Ar-^{39}Ar thermochronology of metamorphic events in the Central African Copperbelt during the Pan-African Lufilian Orogeny. Journal of African Earth Sciences 42:183-199.

Selley D, Broughton D, Scott RJ, Hitzman M, Bull S, Large R, McGoldrick P, Croaker M, Pollington N (2005) A new look at the geology of the Zambian Copperbelt. Economic geology 100th anniversary volume:965-1000.

Woodcock NH, Naylor MA (1983) Randomness testing in three-dimensional orientation data. Journal of Structural Geology 5:539-548.

Geology, alteration and mineralization of the Conrad Zone, Yukon Territory – a new Carlin-type gold discovery

M.J. Tucker, C.J.R. Hart,
Mineral Deposits Research Unit, Department of Earth and Ocean Sciences, University of British Columbia

R.C. Carne
ATAC Resources Ltd.

Abstract. The Conrad Zone, east-central Yukon Territory, Canada is a newly discovered gold prospect. Gold mineralization is analogous to Carlin-type mineralization, and represents the first Carlin-type gold deposit discovered in the Yukon Territory. The regional geological framework and style of mineralization also bear similarities to the Carlin trend in Nevada. Structurally, the Conrad area is bounded to the south by the regional scale Dawson thrust and the Kathleen Lakes fault to the north. This structural setting lies at the interface between the dominantly clastic Neoproterozoic to Paleozoic rocks of Selwyn Basin and coeval carbonate rocks of Mackenzie Platform. Principal host rocks to mineralization are variably decarbonatized silty limestones. Alteration and associated processes related to mineralization include decarbonatization of host limestones with subsequent silicification and brecciation. Gold is hosted within arsenic-rich pyrite growth rims around pre-existing pyrite. Significant post-mineralization realgar, orpiment, calcite and trace stibnite are found locally as open-space minerals. Similar to Carlin-type mineralization in Nevada, this new discovery will build and refine exploration and genetic models for these systems.

Keywords. Conrad Zone, Gold, Carlin-type, Yukon

1 Introduction

The Conrad zone is a new Carlin-type gold discovery in Yukon Territory, Canada. The Nadaleen trend, which hosts the Conrad zone, lies in the eastern portion of ATAC Resources Limited's Rackla Gold Property. The Conrad zone is located in east-central Yukon Territory, 185 kilometers northeast of the town of Mayo. Significant Carlin-type mineralization discovered thus far at Conrad includes diamond drill intersections of 42.9 m of 18.44 g/t Au (ATAC Resources Ltd., 2012). The discovery of a Carlin-type deposit in the Yukon has wide ranging implications for the area given the immense size and clustered nature of Carlin deposits as recognized in Nevada (Arehart, 1996).

Numerous Carlin-type gold showings have been identified within the Nadaleen trend. An area approximately 4 km by 2.5 km contains the mineralized zones known as Conrad, Osiris, Isis, Isis East, Amon, and Sunrise. These zones occur within various carbonate packages across the trend, commonly containing realgar and orpiment with local decalcification and silicification along with trace element enrichments of Au-As-Tl-Hg. The abundance and clustered nature of these showings and deposits signifies the metallogenic potential of the Nadaleen trend.

2 Regional Geology

The Nadaleen trend lies at the interface between the Neoproterozoic to Paleozoic rocks of the Selwyn basin and MacKenzie platform (Fig. 1). Rocks of Selwyn basin in the area are dominated by slope and basin facies carbonates, clastics and siltstones with significant deep water black shales and cherts, whereas the Mackenzie platform is dominated by shallow water platformal carbonates (Abbott et al., 1986). The area is bound structurally to the south by the Dawson thrust and to the north by the Kathleen Lakes fault. The Dawson thrust is believed to be a reactivated Neoproterozoic normal fault that lies at the northernmost boundary of the Selwyn basin and is marked by an abrupt facies change to the Mackenzie platform (Mair et al., 2006). Structures in Selwyn basin are dominated by a fold and thrust belt associated with north directed Mesozoic convergence (Mair et al., 2006). Two regionally developed intrusive suites are found in the area surrounding the Nadaleen trend. The Mayo suite to the south of the Nadaleen trend consists of felsic to mafic, sub-alkalic intrusions dated between 96-90 Ma. This Mayo suite is part of the larger Tombstone suite associated with post-collisional extension in the Selwyn basin (Hart et al., 2004). The small 62.9 ± 0.5 Ma granitic Rackla pluton lies 100 km to the west of the Nadaleen trend (Theissen et al. 2011). Although these two intrusive packages exist throughout Selwyn basin, a Cretaceous granodiorite pluton of the Mayo suite ~ 50 km to the southwest is the intrusion identified closest to the Nadaleen trend.

3 Property Geology

The Nadaleen trend consists of a southward-younging sequence of sedimentary rocks that is in faulted contact with a large, argillaceous mudstone package to the north. Two different sedimentary packages can be separated in the strata to the south of the Nadaleen Fault; Conrad and Osiris. The thick package to the north of the Nadaleen fault is an argillaceous mudstone to siltstone with isolated debris flow lenses. The Conrad strata, which underlies the Osiris strata consists of silty limestones with siltstones and sandstones as well as large carbonate debris flows inter-bedded with black shales/siltstones. The Osiris strata consist of maroon and green siltstone

underlying a main limestone package. A sequence of silty limestones and siltstones, diamictites and dolomites overlie the main limestone unit. Narrow, east-west trending, mafic dykes have been identified trending parallel to the Nadaleen fault.

4 Structure

The Nadaleen trend has a complex structural history, having been affected by several generations of faults and folds. The most prominent structural feature in the trend is the Nadaleen fault which separates the Conrad and Osiris strata from the argillaceous mudstone package to the north. The Osiris strata defines two large scale antiforms that plunge steeply to the southwest. These two antiforms are separated by an east-west trending dextral strike-slip fault. The Conrad strata, on the other hand, is complexly folded. The Conrad limestone lies at the core of a doubly plunging antiform trending north-northeast. Evidence for other larger scale folds in the Conrad strata is not easily recognized, though small-scale chevron folds are observed within all siltstone and shale packages. The area is also cut by late, steeply dipping, northwest trending faults that off-set mineralization locally. North-northwest bounding structures through valleys exist on the eastern and western extents of the area, separating the Conrad and Osiris strata from different sequences.

5 Alteration and Mineralization

The primary style of alteration associated with mineralization is decarbonatization of host limestones. Large amounts of carbonate are removed from the host limestone creating large amounts of insoluble residue, consisting primarily of detrital materials from within the host carbonate. In hand specimen, this is manifested as a very fine grained, sooty, black material, which is commonly found within early stylolites. The majority of this material is very fine grained brown to black residue with detrital quartz and pyrite. The composition of the black residuum is a combination of fine silt and carbonaceous material.

Pyrite can be abundant in mineralized zones. Pre-ore stage pyrite is concentrated within these zones as residuum from decarbonatization. Small pyrite crystals, occurring as very small framboids, euhedral crystals or anhedral grains/masses. Pyrite content within mineralized zones can be abundant. The large increase in the amount of pyrite provides a suitable nucleus for later trace-element and gold rich pyrite. Secondary growth around early crystals of pyrite is commonly visible. This secondary growth can be arsenic and trace element enriched. Arsenian pyrite forms as secondary growths around early pyrite crystals. The secondary arsenian pyrite is very small, commonly only 1-5 microns in size; and locally forms anhedral buds or euhedral growths around pre-existing pyrite crystals. Despite a significant abundance, pyrite is not readily visible in hand specimens, probably because of its dark, sooty colour. Where observed petrographically, the highest abundance of pyrite is spatially associated with areas of increased illite content.

Cryptic carbonate alteration is associated with mineralization in the host limestone. This alteration is characterized by significant depletions of $\delta^{13}C$ and $\delta^{18}O$ in carbonate compared to background values. These depletions are often found outside visible alteration and trace element halos indicating their value as a vectoring and exploration tool.

The Conrad zone contains no visible gold, although other minerals that can be recognized in hand specimen can be key indicators of gold enrichment. Realgar and orpiment are spatial indicators of gold mineralization. In silicified and brecciated mineralized zones these arsenian sulphides are commonly observed disseminated within pore spaces or filling interstices. Massive realgar, orpiment and fluorite are commonly observed, but rarely contain significant gold. Massive realgar can be associated with peripheral rhombohedral calcite veins up to 3m thick. Rare, narrow stibnite veins and veinlets are also present locally. Although not always directly associated with gold, stibnite veins, with realgar, orpiment and fluorite, serve as important indicators of possible gold mineralization.

4 Discussion

Gold mineralization within the Conrad zone is intimately associated with decarbonatization of host limestone and subsequent silicification. It is associated with a variety of minerals including realgar, orpiment, quartz, illite, fluorite and calcite. Very fine grained arsenic-rich pyrite typifies areas of gold mineralization. Texturally, zones of gold mineralization appear as black breccias or replacement/dissolution zones, typically occurring with abundant visible realgar.

Host rock permeability is the controlling factor on the distribution alteration and mineralized zones. The core of mineralization appears to define a large antiformal structure within the Conrad limestone; however, a combination of factors controls the permeability of the rock. Apart from primary fluid conduits such as fault and shear zones, features controlling permeability are stylolites, veinlets, fold hinges and faults. Three generations of stylolites are present within the Conrad limestone. Up to four generations of calcite veins and veinlets are also present within the host limestone. Small scale folds are readily observed throughout the Conrad limestone package, many of which have faults and fractures propagating through fold hinges. These features create preferential fluid pathways for mineralizing fluids. The network of porosity created by the stylolites, vein sets, fold hinges and isolated shears and faults control the distribution and intensity of mineralization and alteration.

5 Conclusions

The Conrad zone is located in on the northern margin of the Selwyn basin proximal to the Dawson thrust, a major structure at the interface of Selwyn basin and MacKenzie platform. Proximity to a major structure may be analogous to the Roberts Mountain thrust in the Carlin-trend where the majority of giant deposits lie

within 100 km of the thrust (Cline et al., 2005). Geology of the Conrad zone is dominated by slope facies carbonates and clastic rocks with gold preferentially hosted within secondary arsenian pyrite in the carbonate rocks. Mineralization consists of decarbonatization, silicification, and subsequent gold deposition; realgar, orpiment, calcite and fluorite are commonly observed as post mineralization open space minerals. A trace metal suite of As-Tl-Hg-Sb is found at the Conrad zone, this is consistent with the trace element enrichments found in the Carlin trend in Nevada (Muntean *et al.,* 2011). The regional tectonic setting and local features at Conrad are similar to sediment hosted gold deposits found in the Carlin trend of Nevada in that gold is hosted in silty carbonates and intimately associated with arsenian pyrite growth rims around early pyrite. Based on detailed core logging, surface mapping and laboratory work on both host rocks and mineralized zones we suggest the Conrad zone is a Carlin-type gold deposit

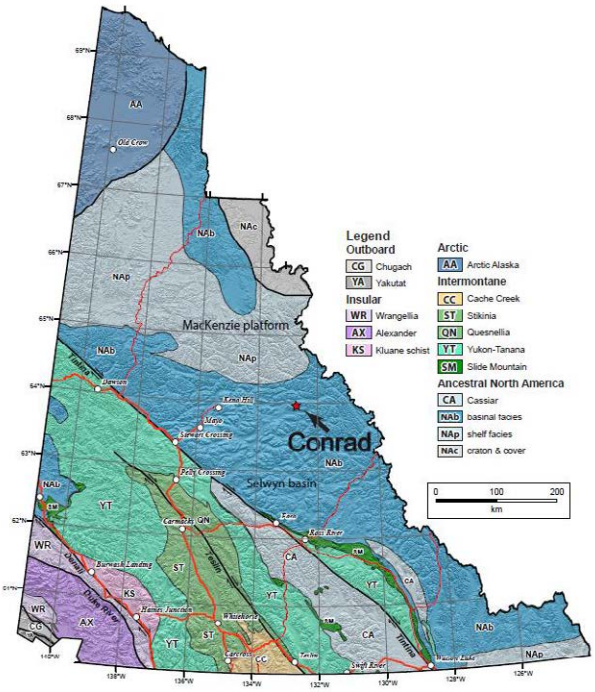

Figure 1. Terrane map of the Yukon Territory; The Conrad zone lies on the northern margin of Selwin basin.

Acknowledgements

The authors would like the thank Rob Carne of ATAC Resources Ltd. for financial and logistical support of this project. Special thanks to Joan Carne and Julia Lane for their helpful geologic discussions and continued help and support through the duration of this project.

References

Abbott, J.G., Gordey, S. P., and Tempelman-Kluit, D.J., (1986) Setting of stratiform, sediment-hosted lead-zinc deposits in the Yukon and northeastern British Columbia. In: Mineral deposits of the northern Cordillera, J.A Morin (ed.), Canadian Institute of Mining and Metallurgy, Special vol. 37, p. 1-18.

Arehart, G.B., (1996) Characteristics and origin of sediment-hosted disseminated gold deposits: a review. Ore Geology Reviews, vol. 11, p. 383-403.

ATAC Resources Ltd., 2012a. ATAC Resources Ltd. Intersects 42.93 m of 18.44 g/t Gold at its Rackla Gold Project – Yukon. August 21, 2012. Retrieved from http://www.atacresources.com/s/NewsReleases.asp.Web. August 21, 2012.

Cline, J. S., Hofstra, A., Muntean, J.L., Tosdal, R.M., and Hickey, K.A., 2005. Carlin-Type Gold Deposits in Nevada: Critical Geologic Characteristics and Viable Models. Economic Geology 100th Anniversary Volume, p. 451-484.

Hart, J.R., Mair, J.L., Goldfarb, J.R., and Groves, I.G., 2004. Source and redox controls on metallogenic variations in intrusion-related ore systems, Tombstone-Tungsten Belt, Yukon Territory, Canada. Transactions of the Royal Society of Edinburgh: Earth Sciences, vol. 95, p. 339-356.

Mair, J.L., Hart, C.J.R., and Stephens, J.R., (2006) Deformation history of the northwestern Selwyn Basin, Yukon, Canada: Implications for orogeny evolution and mid-Cretaceous magmatism. Geological Society of America Bulletin, vol. 118, p. 304-323.

Muntean, J.L., Cline, J.S., Simon, A.C., and Longo, A.A., (2011) Magmatic-hydrothermal origins of Nevada's Carlin-type gold deposits. Nature, vol. 4, p. 122-127.

Thiessen, E.J., Gleeson, S.A., Dufrane, S.A., Carne, R.C., and Dumala, M., 2011. Upper age constraint and paragenesis of the Tiger zone, Rau property, central Yukon. In: Yukon Exploration and Geology 2011, K.E. MacFarlane and P.J. Sack (eds.), Yukon Geological Survey, p. 151-164.

Sr and Nd isotope ratio data of the Nkana and Kipushi deposits and of basement to the Central African Copperbelt

Van Wilderode, J., Muchez, Ph.
KU Leuven, Department of Earth and Environmental Sciences, Celestijnenlaan 200 E, 3001 Leuven, Belgium

Elburg, M.A.
University of KwaZulu-Natal, School of Geological Sciences, Westville Campus Private Bag X54001, 4000 Durban South-Africa

Vanhaecke, F.
UGent, Department of Analytical Chemistry, Krijgslaan 281-S12, 9000 Ghent, Belgium

Abstract. The Central African Copperbelt lies at the border of Zambia and the Democratic Republic of Congo (DRC). To examine the metal source of the Cu-ore deposits, Sr and Nd isotope ratios from basement rocks are compared with those of gangue carbonates occurring adjacent to ore minerals. Isotope ratio data is presented for the Domes Region, the Kibara Belt and the Irumide Belt, which form the basement to the Copperbelt. The deposits of Nkana (Zambia) and Kipushi (DRC) are taken as case studies. The first stratiform mineralisation phase at Nkana took place under influence of a fluid that likely interacted with felsic rocks of the Domes Region. A second mineralisation phase formed Co- and Ni-sulphides largely absent in the first phase, arguing for a new metal input originating from rocks of mafic affinity. However, isotopic signatures of gangue carbonates resemble those of the first phase, suggesting a buffering role of the siliciclastic host rocks. Gangue dolomites of the vein-type Kipushi deposit have high εNd-values, falling outside the range of any basement unit displayed here. Their isotopic composition corresponds best with an unknown source rock of mafic nature, although fluid inclusion data points towards interaction of the fluid with felsic rocks too.

Keywords. Domes Region, Kibara Belt, Irumide Belt, Nkana, Kipushi, Sr & Nd isotope ratios

1 Introduction

The Central African Copperbelt is located within the Lufilian Arc, running along the borders of Zambia and the Democratic Republic of Congo (DRC; Fig. 1). Carbonates and siliciclastics of the Neoproterozoic Katanga Supergroup host world-class ore deposits and were deformed during the Pan-African Lufilian orogeny. Sediment-hosted stratiform Cu-Co mineralisations include the deposits of Luiswishi, Nkana and Tenke-Fungurume. Vein-type mineralisations like the Kipushi Cu-Zn deposit represent a second major mineralisation mode. Different metallogenic models have been invoked to explain the formation of the Copperbelt ores. Recently, consensus is growing towards a multiphase mineralisation process (e.g. Cailteux et al. 2005; Selley et al. 2005; Dewaele et al. 2006; El Desouky et al. 2010; Haest and Muchez 2011). It includes two main phases of stratiform Cu-Co mineralisation, the first diagenetic in origin (~816 Ma) and a second syn-orogenic (~530 Ma). Vein-type mineralisation occurred syn- to post-orogenic, as for example the Kipushi deposit at 450 Ma (Schneider et al. 2007).

The rocks directly underneath the Katanga Supergroup are not well characterised. The basement is outcropping in the southern Domes Region (Zambia). The latter is interpreted as part of the Bangweulu Metacraton (De Waele et al. 2006b). Other major tectonic units bordering the Lufilian Arc are the Kibara Belt in the northwest and the Irumide Belt in the east (Fig. 1). Radiogenic Sr and Nd isotope ratios of basement rocks are compared with the isotope ratios of gangue carbonates occurring adjacent to ore minerals. This enables an assessment of the interaction of the mineralising fluids with basement rocks and the possible metal origin. Regarding the basement, results are presented for rocks of the Kibara Belt and the Domes Region. Published data for the Irumide Belt (De Waele et al. 2006b) is also shown. The Nkana (Zambia) and Kipushi (DRC) deposits serve as case-studies of stratiform Cu-Co and vein-type Cu-Zn mineralisations.

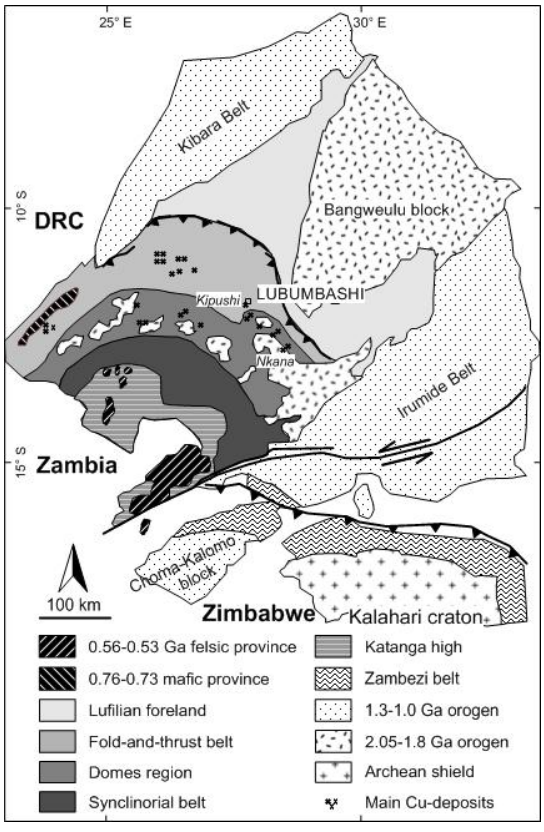

Figure 1. The Lufilian orogen with the Central African Copperbelt (after Kampunzu and Cailteux 1999).

2 Geology

2.1 The basement

The Kibara Supergroup is subdivided into five stratigraphic units, of which the oldest Kiaora Group predates an important phase of deformation and granitoid intrusion at ca. 1.4 Ga (Kokonyangi et al. 2006). The peak of the Kibaran orogeny affected the whole supergroup, which was subsequently intruded by tin granites and pegmatites around 1.0-0.95 Ga (Kokonyangi et al. 2004, 2006).

The Domes Region consists of outcropping basement rocks. Based on age data, the domes are considered a continuation of the Bangweulu Block, which lies to the north-east of the Copperbelt (De Waele et al. 2006b).

The Irumide Belt contains extensive quartzite-metapellite successions which are collectively known as the Muva Supergroup. Four different magmatic phases were recognised within the Muva Supergroup, using petrographic and age data (De Waele et al. 2006a, 2006b). The Irumide Belt is considered to be a partly reworked south-eastern margin of the Bangweulu Block (De Waele et al. 2006b).

2.2 The Nkana and Kipushi deposits

The Cu-Co deposit at Nkana formed through at least three mineralisation and/or remobilisation phases, characterised by folded layer-parallel veins, irregular veins crosscutting the folds, and unfolded massive veins (Muchez et al. 2010). The first two veining phases took place during early to peak Lufilian orogenesis, between 583 ± 24 Ma and ~530 Ma, while the massive veining occurred late in the orogeny at 525.7 ± 3.4 Ma (Barra et al. 2004). Chalcopyrite, bornite, chalcosite and carrolite are the main ore minerals.

The Kipushi vein-type Cu-Zn deposit formed after the Lufilian orogeny at 450.5 ± 3.4 Ma (Schneider et al. 2007). The mineralisation occurs along the Kipushi fault, which crosscuts the stratigraphic sequence and borders a breccia in the core of a large anticline. Chalcopyrite, sphalerite and galena are the most important sulphides.

Besides the mineralisation mode and metal content, the Nkana and Kipushi deposits also differ in the type of host rocks. The Nkana deposit is situated in a mainly siliciclastic stratigraphic sequence, whereas the host rocks of the Kipushi mineralisation are predominantly dolomites.

3 Methodology

Forty-one Sr and Nd isotope ratio determinations have been carried out for rocks of the Kibara Belt and the Domes Region, including siliciclastic (meta)sedimentary and (mostly felsic) igneous rocks. Gangue carbonates of seven Nkana and seven Kipushi samples have been investigated. Sr was isolated according to the procedure of De Muynck et al. (2009) and Nd was isolated following the methods of Pin et al. (1994) and Ganio et al. (2012). The isotope ratios were measured at the Department of Analytical Chemistry of UGhent on a Thermo Scientific Neptune multi-collector inductively coupled plasma mass-spectrometer.

4 Results

Present-day $^{87}Sr/^{86}Sr$ ratios for the Kibara Belt samples vary between 0.71920 and 1.51541. For the Domes Region, this is between 0.72312 and 1.27363. Due to high $^{87}Rb/^{86}Sr$ ratios, age corrections can be very large. Present-day $^{143}Nd/^{144}Nd$ ratios vary from 0.51121 to 0.51216 and from 0.51118 to 0.51206 for the Kibara Belt and the Domes Region, respectively. These data are recalculated to the relevant ages of mineralisation, e.g. 583 Ma, 525.7 Ma and 450.5 Ma, and shown in Figures 2-4. Nd isotope ratios are plotted in ε-notation.

At 583 Ma, the early orogenic mineralisation phase at Nkana shows $^{87}Sr/^{86}Sr$ ratios between 0.71613 and 0.74086. At 525.7 Ma, the massive veining phase at Nkana had $^{87}Sr/^{86}Sr$ ratios between 0.71927 and 0.72934. εNd for both phases and ages varies between -14.8 and -12.3 and between -16.2 and -15.8, respectively. The Kipushi gangue carbonates have $^{87}Sr/^{86}Sr$ ratios between 0.71116 and 0.71332 and εNd values from -5.4 to -0.87, at 450.5 Ma.

5 Discussion

At 583 Ma, the gangue carbonates of the early orogenic Nkana mineralisation plot close to some of the felsic rocks of the Domes Region (Fig. 2). The Kibara Belt samples have mostly much more radiogenic Sr signatures, while the Irumide Belt rocks have more negative εNd values. Some intermediate and mafic basement rocks lie close to Nkana carbonates but trend to lower Sr isotopes and more positive εNd values. This might indicate that the mineralising fluid interacted with and derived metals from felsic basement in the Domes Region. However, at this stage of research it cannot be excluded that the "felsic" signature resulted from rock buffering by the local siliciclastic strata near the Nkana deposit.

The late orogenic mineralisation phase (525.7 Ma) at Nkana plot close to the early phase at that time, but with somewhat more negative εNd values (Fig. 3). This association could indicate remobilisation of the early mineralisation. However, the host rocks adjacent to the massive veins are not depleted but enriched in metals (Brems et al. 2009). Furthermore, the massive veins contain carrolite, pentlandite and molybdenite. These Co- and Ni-sulphides are rare to absent in the early phase, suggesting renewed input of metals. Co and Ni are typically associated with mafic rocks, which are generally characterised by more positive εNd values. Hence a shift towards more negative εNd values relative to the early phase is unexpected and may be the result of additional interaction with felsic basement or host rocks.

Gangue dolomites of the Kipushi deposit show low radiogenic Sr isotopic signatures and high εNd values at 450.5 Ma (Fig 4). Such isotopic compositions do not

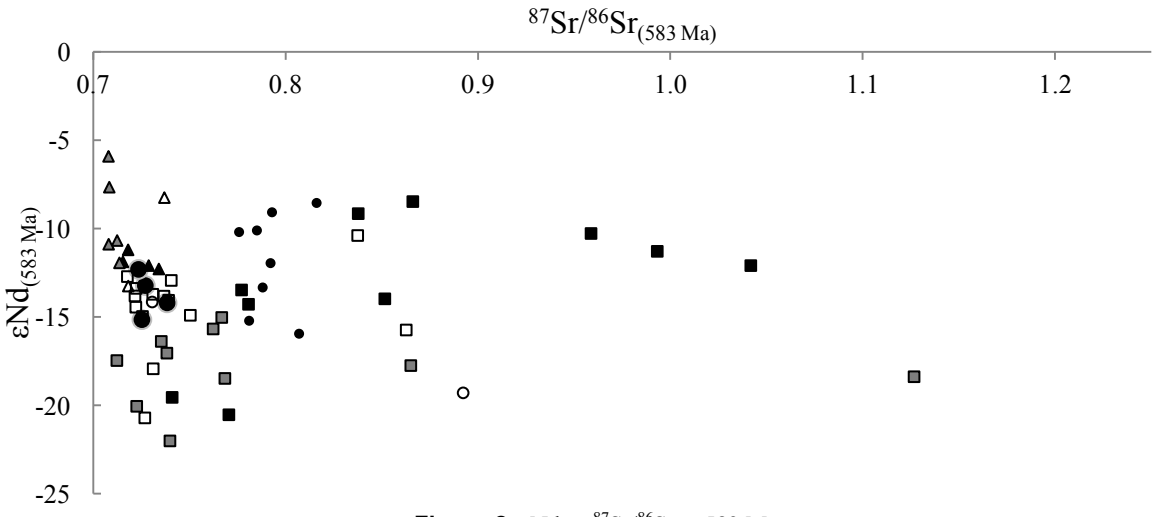

Figure 2. εNd vs $^{87}Sr/^{86}Sr$ at 583 Ma.

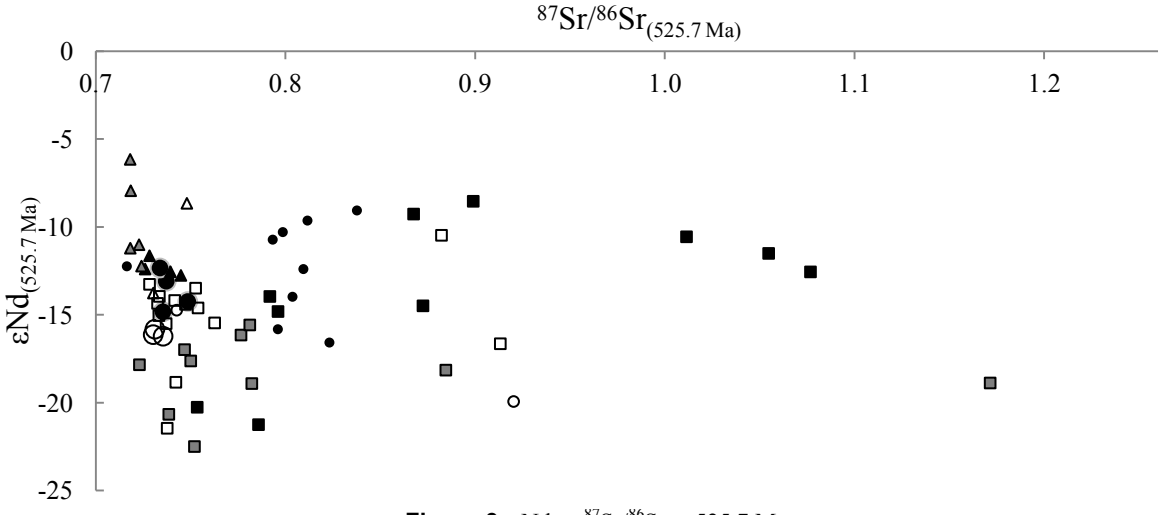

Figure 3. εNd vs $^{87}Sr/^{86}Sr$ at 525.7 Ma.

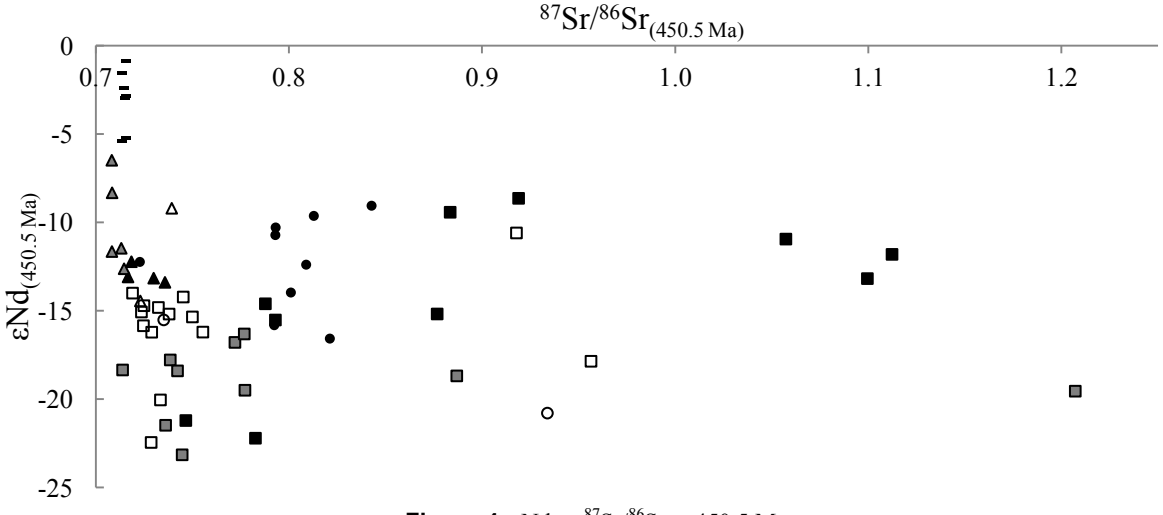

Figure 4. εNd vs $^{87}Sr/^{86}Sr$ at 450.5 Ma.

Legend

Kipushi – Veins
Nkana – Massive veins
Nkana – Early orogenic veins
Kibara Belt – (Meta)sedimentary rocks
Kibara Belt – Felsic magmatics
Kibara Belt – Intermediate & mafic magmatics
Domes Region – Lufubu Schist
Domes Region – Felsic magmatics
Domes Region – Intermediate & mafic magmatics
Irumide Belt – Felsic magmatics
Irumide Belt – Mafic magmatics

match with analysed rocks of the Domes Region, Kibara Belt or Irumide Belt, and correspond best with rocks of mafic origin. Gabbroic bodies recognised in the vicinity of the ore deposit (De Magnée and François 1988), might have played a role in the metallogenesis. However, a felsic metal source rock was proposed based on the chemical composition of fluid inclusions (Heijlen et al. 2008). Consequently, the metal source may involve different rock types.

6 Conclusion

The earliest Cu-Co mineralisation phase at Nkana occurred at 583 Ma. The mineralising fluid likely interacted with and derived metals from felsic rocks belonging to the Domes Region. Similar isotopic signatures for the second mineralisation phase at 525.7 Ma could indicate the same source rock or remobilisation of the first phase. However, a change in ore metal content suggests a renewed metal input from a different source. The isotopic signatures may be obscured by interaction of the mineralising fluid with felsic basement or siliciclastic host rocks. None of the rocks analysed belonging to the Domes Region, Kibara Belt or Irumide Belt, have isotopic compositions similar to the gangue dolomites of the Kipushi deposit. Their high εNd values indicate interaction with mafic rocks of unknown origin. However, taking into account fluid inclusion analyses, the mineralising fluids at Kipushi may have interacted with different rock types.

Acknowledgements

The Royal Museum for Central Africa (RMCA, Tervuren) is thanked for permission to study the collection of L. Cahen. Lumwana Mining Company and African Minerals are acknowledged for providing samples from the Mwombezhi Dome and the Nzilo basement anticline (Kibara Belt), respectively. This research is financially supported by Agentschap voor Innovatie door Wetenschap en Technologie (IWT, Vlaanderen), research Grant ZKC2784-00-W01, and Fonds Wetenschappelijk Onderzoek (FWO, Vlaanderen), research Grants G.0585.06, G.0414.08 and G.A078.11N.

References

Barra F, Broughton D, Ruiz J, Hitzman M (2004) Multi-stage mineralization in the Zambian Copperbelt based on Re-Os constraints. Geol. Soc. Am. Abstracts with Programs, 36(5):516

Brems D, Muchez Ph, Sikazwe O, Mukumba W (2009) Metallogenesis of the Nkana copper-cobalt South Orebody, Zambia. J. Afr. Earth Sc., 55(3-4):185-196

Cailteux JLH, Kampunzu AB, Lerouge C, Kaputo AK, Milesi JP (2005) Genesis of sediment-hosted stratiform copper-cobalt deposits, Central African Copperbelt. J. Afr. Earth Sc., 42(1-5):134-158

De Magnée I and François A (1988) The origin of the Kipushi (Cu, Zn, Pb) deposits in direct relation with a Proterozoic salt diapir. copperbelt of Central Africa, Shaba, Republic of Zaïre. In: Friedrich GH and Herzig PM (eds) Base metal sulfide deposits, Berlin Heidelberg, Springer-Verlag, 74-93

De Muynck D, Huelga-Suarez G, Van Heghe L, Degryse P, Vanhaecke F (2009) Systematic evaluation of a strontium-specific extraction chromatographic resin for obtaining a purified Sr fraction with quantitative recovery from complex and Ca-rich matrices. J. Anal. Atom. Spectr., 24:1498-1510

De Waele B, Kampunzu AB, Mapani BSE, Tembo F (2006a) The Mesoproterozoic Irumide Belt of Zambia. J. Afr. Earth Sc. 46(1-2):36-70

De Waele B, Liègeois J-P, Nemchin AA, Tembo F (2006b) Isotopic and geochemical evidence of Proterozoic episodic crustal reworking within the Irumide Belt of south-central Africa, the southern metacratonic boundary of an Archaean Bangweulu Craton. Precambr. Res. 148(3-4):225-256

Dewaele S, Muchez Ph, Vets J, Fernandez-Alonzo M, Tack L (2006) Multiphase origin of the Cu-Co ore deposits in the western part of the Lufilian fold-and-thrust belt, Katanga (Democratic Republic of Congo). J. Afr. Earth Sc. 46(5):455-469

El Desouky HA, Muchez Ph, Boyce AJ, Schneider J, Cailteux JLH, Dewaele S, von Quadt A (2010) Genesis of sediment-hosted stratiform copper-cobalt mineralization at Luiswishi and Kamoto, Katanga Copperbelt (Democratic Republic of Congo) Miner. Deposita, 45(8):735-763

Ganio M, Latruwe K, Brems D, Muchez Ph, Vanhaecke F, Degryse P. (2012) The Sr–Nd isolation procedure for subsequent isotopic analysis using multi-collector ICP-mass spectrometry in the context of provenance studies on archaeological glass. J. Anal. Atom. Spectr. 27:1335-1341

Haest M, Muchez Ph (2011) Stratiform and vein-type deposits in the pan-African orogen in Central and Southern Africa: evidence for muliphase mineralisation. Geol. Belgica 14(1-2):23-44

Heijlen W, Banks DA, Muchez Ph, Stensgard BM, Yardley BWD (2008) The nature of mineralizing fluids of the Kipushi Zn-Cu deposit, Katanga, Democratic Republic of Congo: quantitative fluid inclusion analysis using laser ablation ICP-MS and bulk crush-leach methods. Econ. Geol. 103(7):1459-1482

Kampunzu AB., Cailteux J. (1999) Tectonic evolution of the Lufilian arc (Central Africa Copper belt) during Neoproterozoic Pan African orogenesis. Gondwana Res. 2(3):401 – 421

Kokonyangi JW, Armstrong R, Kampunzu AB, Yoshida M, Okudaira T (2004) U-Pb zircon geochronology and petrology of granitoids from Mitwaba (Katanga, Congo): implications for the evolution of the Mesoproterozoic Kibaran belt. Precambr. Res. 132(1-2):79-106

Kokonyangi JW, Kampunzu AB, Armstrong R, Yoshida M, Okudaira T, Arima M, Ngulube DA (2006) The Mesoproterozoic Kibaride Belt (Katanga, SE D.R. Congo). J. Afr. Earth Sc. 46(1-2):1-35

Muchez Ph, Brems D, Clara E, De Cleyn A, Lammens L, Boyce A, De Muynck D, Mukumba W, Sikazwe O (2010) Evolution of Cu-Co mineralizing fluids at Nkana mine, Central African Copperbelt, Zambia. J. Afr. Earth Sc., 58(3):457-474

Pin C, Briot D, Bassin C, Poitrasson F (1994) Concomitant separation of strontium and samarium-neodymium for isotopic analysis in silicate samples, based on specific extraction chromatography. Anal. Chim. Acta 298:209-217

Schneider J, Melcher F, Brauns M (2007) Concordant ages for the giant Kipushi base metal deposit (DR Congo) from direct Rb-Sr and Re-Os dating of sulfides. Miner. Deposita, 42:791-797

Selley D, Broughton D, Scott R, Hitzman M, Bull S, Large R, McGoldrick P, Croaker M, Pollington N, Barra F (2005) A new look at the geology of the Zambian Copperbelt. Econ. Geol. 100th Anniversary Volume:965-1000

S 3.4

Magmatic and hydrothermal hypogene and supergene iron ores

Convenors:
Steffen Hagemann, Paul Duuring & Thomas Angerer

Mt. Whaleback: chemical constraints on the genesis of the largest hematite ore body in the Hamersley Province, Australia

Thomas Angerer, Steffen G. Hagemann,
Centre for Exploration Targeting, University of Western Australia, Crawley WA 6009, Australia

Adrian Boyce
NERC Isotope Community Support Facility, University of Glasgow, Rankine Avenue, East Kilbride, Glasgow G75 0QF, Scotland

Henning Reichardt
BHP Billiton Iron Ore, Level 29, 125 St Georges Terrace, Perth WA 6000, Australia

Abstract. New whole-rock, microchemical and stable isotope data from Mt. Whaleback, Australia's largest high-grade iron ore body, demonstrate at least two generations of microplaty hematite: (1) a Cu-Zn-Ni-Co rich phase that is related to the Central Fault (~2.2 Ga Ophthalmian orogeny), and (2) a second Cu-Zn-Ni-Co poor hematite that is hosted by the Whaleback Fault (~1.7 Ga Capricorn orogeny). In both faults, O isotopic values of hematite are the most negative, pointing towards a high fluid-rock ratio in these structures. The Hashimoto and Mt. Helen deposits in the Ophthalmian Range are also Cu-Zn-Ni-Co poor, suggesting that multi-stage hematite mineralisation is of regional significance.

A single supergene-metamorphic ore formation as proposed by Morris (1985) and Morris and Fletcher (1987) seems unlikely, considering the strong mineralogical and chemical evidences for the multi-stage hematite formation associated with (heated) meteoric fluid flow and spatially related to diachronous ore-controlling structures.

Keywords: banded iron formation, high-grade iron ore, geochemistry, Laser ablation ICPMS, Oxygen isotopes.

1 Introduction

The genesis of Paleoproterozoic martite-microplaty (M-mplH) ore in the Ophthalmian Range of the Hamersley Province, Western Australia (e.g., Mt. Whaleback, Tom Price) remains a matter of debate. The two current model classes are the supergene-metamorphic (Morris 1985; Morris and Fletcher 1987) and the hypogene-hydrothermal models (Barley et al. 1999; Powell et al. 1999; Taylor et al. 2001; Thorne et al. 2004). The present genetic models were mainly developed based on studies of deposits in the central Hamersley Province, i.e., Mt. Tom Price and Paraburdoo. The strongly deformed eastern part of the province is comparably less well studied, despite hosting a wealth of resources in M-mplH and hematite-martite-goethite deposits including the largest (more than 1.8 Gt Fe), structurally most complex, and deepest-seated of all, Mt. Whaleback deposit (Powell et al. 1999; Webb et al. 2004).

The present contribution is a new approach to unravelling the origin of hematite and martite in Mt. Whaleback and other occurrences in the South Ophthalmian Range, namely the Hashimoto deposit and the Mt. Helen prospect. In this study we apply whole-rock geochemistry, mineral chemistry (Laser ablation ICPMS, element mapping by field emission SEM), and stable isotopic chemistry. The aims are to identify the various types of hematite within deposits, link them to controlling structures and model their genesis and related fluid-rock interaction.

2 The hematite controversy

2.1 Supergene-metamorphic genetic model

Until early 2000, the widely accepted uniformitarian CSIRO model, proposed martite-goethite formation driven by giant electrochemical cells in Paleoproterozoic (~2.0 Ga) deep supergene environments. This ore was considered to be the direct precursors of all M-mplH ore that formed by metamorphic dehydration of goethite at temperatures of just 80-100 °C. The model predicts an upward direction to ore formation, accommodating the genesis of ore bodies concealed beneath BIF, such as Mt. Whaleback.

The structural control of mineralisation in the supergene-metamorphic model is considered to be restricted to the post-Ophthalmian martite-goethite formation, because later burial metamorphic dehydration is not a function of localised fluid flow. Late Ophthalmian faults, i.e., the Central East-Footwall Faults at Mt. Whaleback, are proposed to be major conduits for cold supergene fluids.

2.2 Supergene-modified hypogene model

Since the late 1990s, delineation of pervasive carbonate alteration zones in BIF located proximal to M-mplH ore, and advances in fluid characterisation, have led to development of hydrothermal models for the Hamersley Province (and also worldwide). The most elaborate models are from the Mt. Tom Price and Paraburdoo deposits, which exhibit, at least locally in unweathered zones, complex hydrothermal alteration in BIF that surrounds high-grade M-mplH ore. A three-stage sequence is proposed (Taylor et al. 2001): (1) early siderite-phosphorous alteration by infiltration of basinal brines, derived from the stratigraphically lower

Wittenoom dolomite, (2) heated meteoric water infiltration with mplH-ankerite mineralisation, and (3) supergene modification and final leaching of carbonate and phosphorous.

Alternative models propose fluid flow in a Ophthalmian synorogenic compressional setting with mixing of basinal brines and meteoric water (Powell et al. 1999), or early chert removal by downward flow of heated fluids derived from inferred evaporites high up in the stratigraphic sequence (Evans et al. 2012).

Structures controlling proposed hypogene fluids are either predominantly compressional faults (Powell et al. 1999) or exclusively extensional faults (Taylor et al. 2001), which may have been rotated at a later stage. At Mt. Whaleback, the Central Fault and secondary parallel faults are proposed to be the major controlling fault system.

2.3 Escaping the model stalemate with a new analytical approach

The two genetic models for hematite formation in the giant hematite deposits in the Hamersley Province are contrasting: hematite mineralisation is proposed as a metamorphic dehydration product after goethite, but also as a hydrothermal replacement product after quartz, silicates, and hydrothermal carbonate. Hematite should therefore retain specific habits and growth patterns, and also isotopic and (trace) chemical signatures, related not only to a specific mineralising fluid, but also to the precursor phases. Whole-rock geochemistry in altered BIF and ore is expected to be influenced by hydrothermal fluids, allowing the identification of specific mineralising fluids.

Several diamond cores that intersect the Dales Gorge Member BIF and related ore in proximity to the Central Fault and Whaleback Fault were sampled. In addition, M-mplH ore from selected deposits throughout the Ophthalmian Range were sampled for comparison (Hashimoto and Mt. Helen are presented here). Hashimoto M-mplH ore is from the lower Dales Gorge, in close proximity to the Mt. McRae Shale Member that is here highly brecciated and carbonate-rich. Based on logging and petrographically constrained styles of alteration and ore formation processes, chemical data (whole rock and hematite crystals) are presented in the following subsections.

3 Results

3.1 Petrography

The most common ore type at Mt. Whaleback is a high-grade (>65 wt% Fe) laminated M-mplH ore in the Dales Gorge Member BIF, with mm to cm thick bands of hard martite (oxidised BIF magnetite) intercalated with microporous mplH bands. Aluminum-rich "shaly BIF" bands are mineralised when located within an ore zone, showing mplH replacing red Al-silicates- and clay-rich shale zones. Shale macrobands (dm to m thick lithologies) are typically only oxidised and ferruginized but lack significant mplH mineralisation.

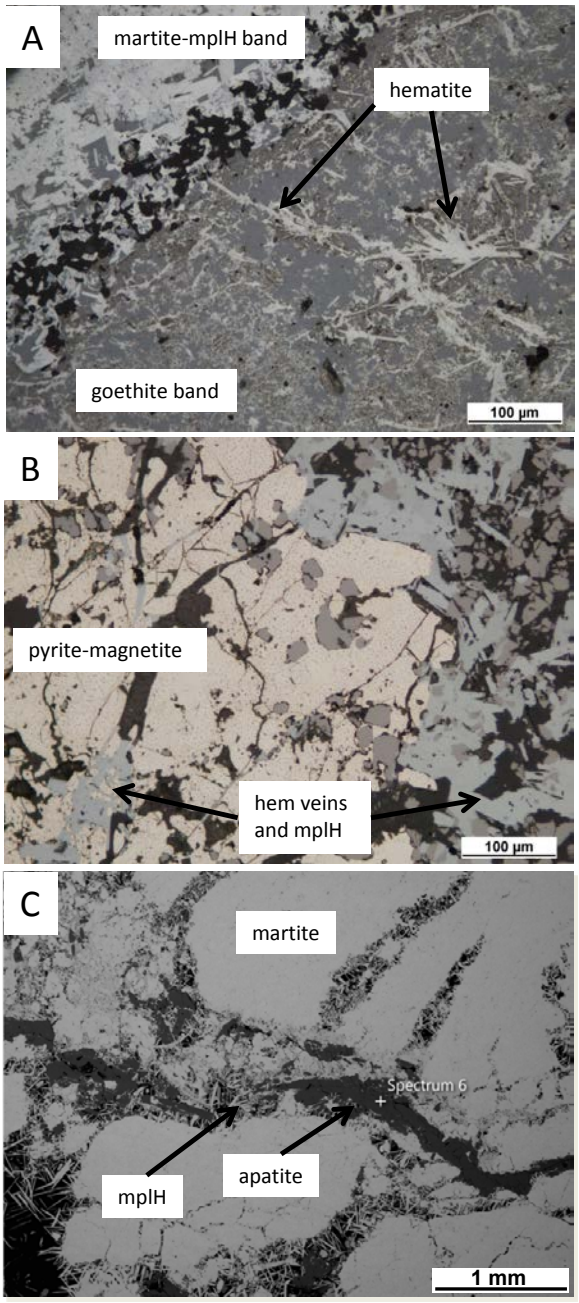

Figure 1. Microphotographs: A) hematite after deep goethite zone (sample WHB1113-208); B) pyrite-mplH after magnetite assemblage in Whaleback Fault (WHB1113-353.2); and C) SEM micrograph showing apatite-mplH veins in Central Fault shaly ore (D373-238).

Various complex mplH assemblages are observed in drill cores intersecting Central and Whaleback Faults distal to intermediate to ore: BIF of the "Colonial Chert" unit below high-grade ore and oxidised Dales Gorge BIF exhibits at 208m relative depth deep-seated goethite alteration with crosscutting hematite veinlets and overprinting mplH (Figure 1A).

Apatite-mplH veins in phosphorous-rich shaly ore are observed proximal to Central Fault, mplH after magnetite and pyrite, and in Fe-dolomite veins are a feature in Whaleback Fault. These structurally controlled hydrothermal assemblages support hypogene hydrothermal models.

3.2 Whole-rock geochemistry

The variations of major elements with the transition from BIF to high-grade M-mplH ore are typical for iron ore formation: an increase of Fe, P, LOI, a decrease of Si, Mg, Ca, and variable changes in Al, Ti, Mn, depending on initial silicate content. Trace element analyses reveal anomalous enrichment in Cu (27 to 50 ppm, compared to <10 ppm in other samples) and locally Mo (>1 ppm), As (20 to 85 ppm), Au (90 ppb) in M-mplH ore and mplH-altered BIF in the vicinity of Central Fault. Similarly, local occurrences of M-mplH ore in Hashimoto deposit have high Cu values (27 to 38 ppm). These signatures are both observed in "shaly" and "non-shaly" BIF and ore, and thus are inferred to be linked to hydrothermal fluid flow. Furthermore, ΣREE is up to 10x higher in high-Cu samples, compared to other BIF and ore samples with comparable Fe and Al contents.

3.3 Elemental mapping of oxides

Element mapping of oxides by SEM serves two purposes, firstly the influence of inclusions and compositional heterogeneity and their impact on laser ablation data can be assessed, and secondly microtextural observations between oxides generations can be made.

Common inclusions in BIF are quartz, silicates, and carbonates, leading to partially overestimated Si, Ca, Mn, and Mg concentrations. However, most other consistently detected elements (Ti, Zn, Ni, V, Cr, Co, Cu, Ga, Pb, W, Sn, Mo) are not correlated with these diluting elements, and therefore not significantly affected by inclusions.

The mplH is compositionally complex with Si-rich cores and growth zones with weak Al oscillation. The mplH in contact with goethite exhibits micrometre-thin Al- and Si-rich diffusion rims.

3.4 Laser ablation ICPMS oxides chemistry

Metamorphic BIF-Magnetite (from Bruno's Band, i.e., upper Mt. Sylvia Member) has generally low trace element concentrations (value ranges for Si: 1000-10000; Ca, Al, Mg, Mn: 100-1000 ppm; Ti: 10-100 ppm; Zn, Ni: 1-10 ppm; V, Cr, Co, Cu, Ga, Pb, W, Sn, Mo: 0.1-10 ppm). This is the combined result of primary oxide precipitation from low temperature seawater and a very low metamorphic overprint (Nadoll et al. in press). The Ti/V ratio of >10 is typical for magnetite from Paleoproterozoic basinal BIF (Nadoll et al. in press).

Martite in oxidised BIF and M-mplH ore show on average lower Si, Mg, Ti, Sn, and higher V, As, Pb, Zn, Cu, Co, Ni than magnetite in unaltered BIF.

Microchemistry reveals variable and internally consistent mplH types: Central Fault-related mplH (abundant and ore-forming) is enriched in Cu-Zn-Ni-Co compared with Whaleback Fault-related mplH (minor and not ore-forming) (Figure 2). Hematite from the Hashimoto deposit, Mt. Helen prospect, Mt. Tom Price, Channar, and Prairie Downs (mplH-bearing martite-goethite deposits), have distinct chemical patterns. In the case of Hashimoto, Mt. Helen, and Channar deposits,

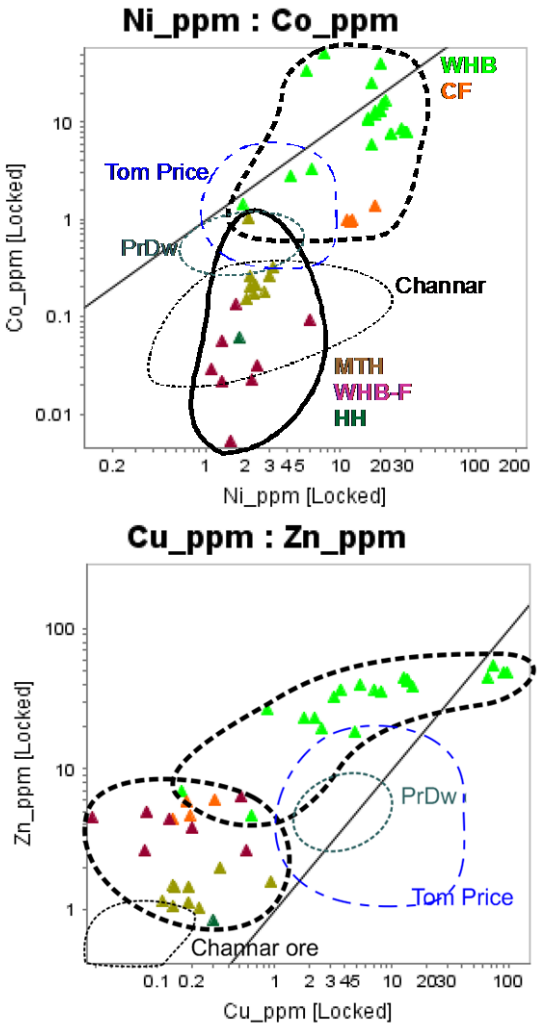

Figure 2. Microchemical Zn, Cu, Ni, and Co data for mplH from Mt. Whaleback in proximity to and in Central Fault (WHB and CF, respectively), and Whaleback Fault (WHB-F) and selected other deposits in the Ophthalmian Range (MTH: Mt. Helen; HH: Hashimoto, PrDw: Prairie Downs, Channar and Mt.Tom Price).

low Cu, Zn, Ni, and Co concentrations are in the same magnitude as the Whaleback Fault mplH type.

The variation of base metal concentrations in mplH is yet not fully understood. One possibility is that it is directly related to the fluid chemistry, i.e, hotter and/or more saline fluids controlled by Central Fault were base metal-rich. Alternatively, in the Whaleback Fault, abundant pyrite precipitation (Figure 1b) led to a base metals depletion of the mineralising fluid prior to mplH mineralisation. In the latter case sulphur activity was higher, probably related to interaction with reduced shales below the Brockman Formation, and facilitated pyrite precipitation in the fault.

3.5 Oxygen isotopes in hematite

New stable oxygen isotope data from hematite support results obtained by Powell et al. (1999): Negative $\delta^{18}O$ values (-0.6 to -12.8) in mplH and martite in ore suggests a strong meteoric water influence during ore formation. Samples from Central Fault and Whaleback Fault show

most negative isotope values within the Mt. Whaleback sample set (-9.6 to -12.1 and -17.4, respectively), which is interpreted to be the result of a high fluid-rock interaction compared to zones away from the fault. This supports the importance of the Central and Whaleback Faults as mineralising structures. MplH from ore in Hashimoto proximity to brecciated, carbonate-rich, upper Mt. McRae shale have values as low as -12.8, which suggests that mineralising fluids may have used the faulted shale-BIF contact zone as a pathway.

4 Evidences for hypogene genesis of iron ore

Fluid inclusion studies of quartz-hematite assemblages by Powell et al. (1999) show epigenetic homogenization temperatures of very low to high salinity around 270-420 °C. Negative $\delta^{18}O$ in mplH and martite indicate oxide growth in equilibrium with predominantly meteoric water. High fluid-rock interaction in the Central and Whaleback Faults suggests the importance of controlling structures for mineralisation. These data are generally compatible to findings in controlling structures at Mt. Tom Price and Paraburdoo (Thorne et al. 2009), and may also be valid in other mplH deposits in the Eastern Hamersley Province, such as Hashimoto.

Apatite-mplH veins proximal to Central Fault, and mplH after magnetite and pyrite and mplH-Fe-dolomite veins in Whaleback Fault are hydrothermal assemblages that support structurally controlled hypogene models. Further indications for hypogene genesis of M-mplH ore in proximal to intermediated distance to Central Fault are the high REE-Cu-Mo-As-Au anomalies in M-mplH ore and associated altered BIF. That these metal anomalies are linked to ore formation is supported by hematite chemistry, which shows elevated Cu, Ni, Co, Zn, and Pb values in proximity to Central Fault, when compared to hematite from zones away from the fault. The Al- and Si-rich diffusion patterns in mplH at the contact with surrounding goethite give evidence for goethite growth in the ore matrix subsequent to mplH formation. Despite these evidences against the supergene-metamorphic model, deep-seated goethite zones with crosscutting hematite veinlets and overprinting mplH are observed at the microscale. In the absence of absolute ages of oxides the nature of this goethite-hematite assemblage remains unsolved.

Distinct microchemical groups of mplH in high-grade ore and altered BIF point towards hematite mineralisation under variable fluid-rock conditions: Cu-Zn-Ni-Co-rich group in proximity to Central Fault and Cu-Zn-Ni-Co-poor group in Whaleback Fault and also in Hashimoto and Mt. Helen. Because Central (~2.2 Ga) and Whaleback (1.8-1.7 Ga) Faults are diachronous (Powell et al. 1999), an at least two-phase M-mplH ore genesis can be concluded. This is in agreement to protracted M-mplH ore formation at Mt. Tom Price, which has been constrained by multiple U-Pb ages of xenotime associated with mplH that correspond with the major Paleoproterozoic tectonic events recorded in the southern Pilbara Craton (Rasmussen et al. 2007).

5 Conclusion

Variable mineralogical and chemical patterns in dependence to diachronous structures suggest at least two phases of mplH genesis at Mt. Whaleback and in smaller Ophthalmian deposits. Multiple stages of hematite formation are likely and solely a supergene-metamorphic formation can be excluded. Microchemistry of hematite (LA-ICPMS and elemental maps) can be used as tracers for fluid-rock interaction during hematite ore genesis, and is therefore a valid tool for deposit characterisation.

Acknowledgements

This study is part of a project on ore genesis carried out by CET in collaboration with BHP Billiton Iron Ore. The financial and logistic support from BHP Billiton is highly appreciated.

References

Barley ME, Pickard AL, Hagemann SG, Folkert SL (1999) Hydrothermal origin for the 2 billion year old Mount Tom Price giant iron ore deposit, Hamersley Province, Western Australia. Mineralium Deposita 34 (8):784-789

Evans KA, McCuaig TC, Leach D, Angerer T, Hagemann SG (2012) Banded iron formation to iron ore: A record of the evolution of Earth environments? Geology. doi:10.1130/G33244.1

Morris RC (1985) Genesis of iron ore in banded iron-formation by supergene and supergene-metamorphic processes; a conceptual model. In: Wolf KH (ed) Handbook of Strata-bound and Stratiform Ore Deposits, vol 13. Elsevier Science Publications, Amsterdam, pp 73-235

Morris RC, Fletcher AB (1987) Increased solubility of quartz following ferrous-ferric iron reactions. Nature (288):250-252

Nadoll P, Angerer T, Mauk JL, French D, Walshe JL, Koenig A (in press) The Chemistry of Hydrothermal Magnetite - a Review. Ore Geology Reviews

Powell CM, Oliver NHS, Li Z-X, Martin DM, Ronaszeki J (1999) Synorogenic hydrothermal origin for giant Hamersley iron oxide ore bodies. Geology 27 (2):175-178. doi:10.1130/0091-7613(1999)027<0175:shofgh>2.3.co;2

Rasmussen B, Fletcher IR, Muhling JR, Thorne WS, Broadbent GC (2007) Prolonged history of episodic fluid flow in giant hematite ore bodies: Evidence from in situ U-Pb geochronology of hydrothermal xenotime. Earth and Planetary Science Letters 258 (1-2):249-259

Taylor D, Dalstra HJ, Harding AE, Broadbent GC, Barley ME (2001) Genesis of high-grade hematite orebodies of the Hamersley province, Western Australia. Economic Geology and the Bulletin of the Society of Economic Geologists 96 (4):837-873

Thorne W, Hagemann S, Vennemann T, Oliver N (2009) Oxygen Isotope Compositions of Iron Oxides from High-Grade BIF-Hosted Iron Ore Deposits of the Central Hamersley Province, Western Australia: Constraints on the Evolution of Hydrothermal Fluids. Economic Geology 104 (7):1019-1035. doi:10.2113/gsecongeo.104.7.1019

Thorne WS, Hagemann SG, Barley M (2004) Petrographic and geochemical evidence for hydrothermal evolution of the North Deposit, Mt Tom Price, Western Australia. Mineralium Deposita 39 (7):766-783. doi:10.1007/s00126-004-0444-x

Webb AD, Dickens GR, Oliver NHS (2004) Carbonate alteration of the Upper Mount McRae Shale beneath the martite-microplaty hematite ore deposit at Mount Whaleback, Western Australia. Mineralium Deposita 39 (5):632-645. doi:10.1007/s00126-004-0434-z

Diversity in iron ore deposits in Western Australia

Paul Duuring, Thomas Angerer, Steffen Hagemann
Centre for Exploration Targeting, The University of Western Australia, Crawley, Western Australia 6009

Abstract. Iron ore deposits hosted by Banded Iron Formation (BIF) in the Weld Range greenstone belt record five main iron ore types: (1) 'Residual' ore formed as a result of two generations of hypogene alteration of BIF. The first alteration phase replaced silica-rich bands with carbonates; the second phase involved the removal of carbonate gangue minerals and the concentration of residual Fe oxide-rich bands in the BIF via volume reduction. The product is a high-grade, high-tonnage Fe orebody, with minor contaminants. (2) Magnetite-bearing shear and fault zones cut BIF along lithological contacts and produce narrow, high-grade magnetite-rich ore zones with high levels of contaminants (e.g. SiO_2, Al_2O_3). (3) Specular hematite ± quartz-bearing shear and fault zones cut residual orebodies and magnetite-bearing structures. (4) Goethite-hematite supergene ore zones are controlled by brittle faults that cut BIF. (5) Detrital deposits comprise transported BIF fragments and are intensely goethite-hematite supergene-altered. Similar iron ore types and their relative timing relationships are expressed by other BIF-hosted iron ore deposits located throughout the Murchison Domain of the Yilgarn Craton (e.g. Windarling and Koolyanobbing). A "mineral systems" approach to understanding controls on iron ore formation will lead to a more predictive exploration strategy for targeting iron orebodies.

Keywords. Iron ore, Yilgarn, Weld Range

1 Introduction

Our concept of how iron ore deposits formed in Western Australia is greatly influenced by what we've learned about the giant deposits hosted by Banded Iron Formations (BIF) in the Hamersley Province. This is a logical outcome since most iron ore exported from Western Australia during the last decade has originated from this well-endowed area of the state. In fact, from a total of 422 Mt of iron ore shipped in 2010, about 95 percent was sourced from the Hamersley Province (www.dmp.wa.gov.au).

However, the rise in iron ore demand during the past decade has led to a broadening of the exploration workspace to include significant parts of the Yilgarn and Pilbara cratons. Early exploration success in these areas include the resource delineation of the Mt Webber and McPhee Creek goethite-hematite deposits in the Pilbara, and similar ore types at Koolyanobbing, Windarling, and Madoonga in the Midwest region of the Yilgarn. At face value, these defined resources of near-surface, goethite-hematite ore appear to reinforce the Hamersley exploration paradigm, which focuses on the discovery of ores that require minimal metallurgical processing and are shipped directly to market.

An important consequence of recent exploration ventures in the Yilgarn is the recognition that magnetite (-martite) and coarse-grained hematite ores potentially add significant value to the profitability of an iron ore deposit. Although these iron ore types usually demand more energy for metallurgical processing compared with softer goethite-hematite-rich direct shipping ores, they add an important vertical extension to shallower ore zones and thereby increase the overall size of ore deposits. In these deposits, the goethite-hematite (supergene) ore zones are located in the modern regolith zone and locally replace existing magnetite and coarse-grained hematite (hypogene) ore zones. The coincidence of multiple styles of iron ore in these "hybrid" (or, so-called "supergene-modified hypogene") deposits results in a larger ore body, but significant heterogeneity in terms of Fe grades and contamination elements, such as phosphorus, silica, and aluminium.

2 BIF-hosted Iron Ore Deposits of the Yilgarn Craton: Iron Ore Types

Recent deposit- to camp-scale studies by the Iron Research Group at the Centre for Exploration Targeting have examined the physical, chemical, and genetic relationships between different styles of high-grade (>55 wt% Fe) iron ore hosted by BIF in as geographically diverse locations as the Murchison Domain (e.g. Weld Range, Duuring and Hagemann 2012a; Duuring and Hagemann 2012b), Southern Cross Domain (Koolyanobbing and Windarling, Angerer and Hagemann 2010; Angerer et al. submitted; Angerer et al. 2012), and the Narryer Terrane (Jack Hills, Maskell et al. submitted) of the Yilgarn Craton. Surprisingly, these greenstone belt-hosted deposits record a strikingly similar sequence of hypogene hydrothermal fluid alteration events that are temporally followed by supergene alteration; all of which result in the upgrade of iron concentrations in BIF (Figs. 1 & 2):

(1) The earliest recognized hydrothermal alteration event recorded by most deposits is the replacement of silica-rich bands in BIF by hypogene carbonate-magnetite. These early carbonate replacement minerals are in turn removed by a later hydrothermal fluid that concentrates the primary magnetite-rich bands, resulting in a residual magnetite(-martite) ore.

(2) Magnetite-talc-rich shear zones are also present in BIF, commonly along the limbs of isoclinal folds, or at a shallow angle to bands. The mineralized shear zones are most likely a product of district-wide deformation, during which hypogene magnetite precipitated from Fe-Mg-rich hydrothermal fluids that flowed through the shear zones. Magnesium may be sourced from dissolved carbonate-rich rocks, or from surrounding altered mafic country rocks.

(3) The subsequent reactivation of earlier magnetite-rich shear zones, potentially at shallower crustal levels,

resulted in the overprinting of magnetite-rich ore zones by oxidized hypogene fluids to produce coarse-grained hematite-quartz (-carbonate) veins with surrounding hematite-rich hydrothermal alteration zones in BIF.

(4) More recently (?Mesozoic to today), uplift of these hypogene-altered rocks resulted in their modification by near-surface, cold, oxidized supergene fluids and the formation of goethite-hematite-rich ore zones, as well as the local formation of supergene-modified, goethite-hematite-rich detrital ores.

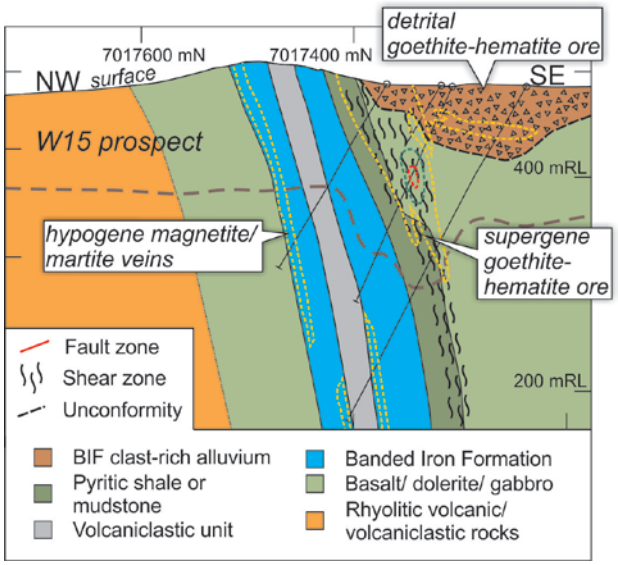

Figure 1. Representative cross section through the Madoonga deposit in the Weld Range greenstone belt demonstrates the spatial relationships between the near-surface, supergene goethite-hematite ore and deeper hypogene magnetite (-martite) ores. Note the presence of the hypogene iron ores beneath the weathering front (from Duuring and Hagemann 2011).

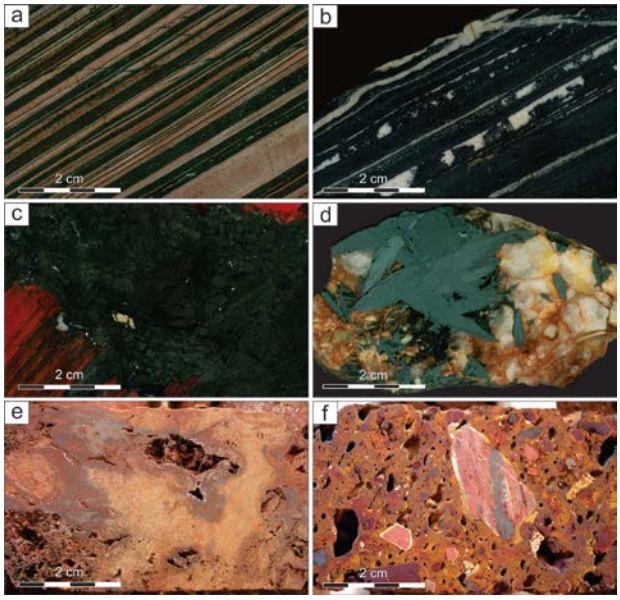

Figure 2. Hand specimen examples of BIF and iron ore types from the Weld Range: (a) fresh, unmineralized BIF; (b) hypogene magnetite (-martite) rich ore in BIF, showing the replacement of primary silica-rich bands by carbonate, followed by its partial dissolution, and the concentration of the primary magnetite-rich bands; (c) a magnetite±talc vein cuts and brecciates existing jaspilite wallrock; (d) coarse-grained crystalline hematite is intergrown with quartz in a vein that cuts BIF; (e) supergene-modified, goethite-hematite-rich BIF; and (f) supergene-modified, goethite-hematite-rich detrital ore (modified after Duuring and Hagemann 2011).

As mentioned above, the greenstone belt-hosted deposits in the Yilgarn Craton are markedly smaller than the giant iron ore deposits of the Hamersley Province and similar deposits in Brazil and Africa. Reasons for this may be due to the narrower starting thickness of the BIF, its steep attitude in the greenstone belt, or its tectonic dismemberment by faults and shear zones. In addition, the crucial hypogene and supergene processes required for Fe upgrade may have been less pervasive or intense compared with the processes responsible for the giant deposits. If size matters when it comes to assessing the economic importance of an ore deposit, then how significant are the greenstone belt-hosted deposits for our understanding of ore formation processes and exploration strategies in areas outside of the Yilgarn Craton?

The greenstone belt-hosted iron deposits offer important insights into ore formation processes in that they commonly preserve the step-wise, hypogene and supergene alteration of BIF that lead towards the formation of an iron ore deposit. In comparison, the giant deposits of the Hamersley Province and Carajas Mineral Province of Brazil often display one or two main ore types (e.g. goethite-hematite ore and microplaty hematite) that are so widespread and intensively developed that they obliterate earlier textural and mineralogical relationships. A consequence of these relationships is the ongoing lively debate regarding the genesis of hematite ores in these deposits.

A key outcome from the study of greenstone belt-hosted deposits in the Yilgarn is the observation that there are many ways to form an iron ore deposit in BIF, involving several possible hypogene and supergene processes. As a general rule of thumb, the more complex the genesis the larger the deposits tend to be. Consequently, exploration strategies need to recognize the possible existence of multiple iron ore types in a district, rank each ore type in terms of its economic value (measured in terms of size, iron grades, and the presence of contaminant elements), and develop detection methods that target diagnostic physical and chemical properties of the iron ore type of interest.

3 Exploration Strategies for Iron Ore

Historically, first-pass exploration for iron ore in many districts has centred mainly on the detection of ore bodies rather than the prediction of their location. Conventional detection methods include the acquisition and interpretation of aerial photographs and geophysical data sets in GIS environments, combined with field visits, geochemical sampling and ground-based geophysical surveys, followed by the testing of targets by drilling. A recent addition to the arsenal of detection tools includes the integration of spectral imaging techniques (e.g. ASTER, HyMap, HyLogger, ASD data

sets) for the detection of iron oxide ore minerals and their associated hydrothermal alteration mineral assemblages. Recognition that some iron ore deposits may be a product of structurally-controlled, hydrothermal fluid movement through BIF and nearby country rocks has led to the expansion of the detectable footprint for these deposits. For example, at the Weld Range high-grade iron ore bodies that constitute the Beebyn deposit are surrounded by an outer halo of carbonate alteration expressed in BIF and in mafic igneous country rocks. This alteration halo increases the detectable footprint of the ore deposit by a factor of two in this example (Duuring and Hagemann 2012a; Duuring et al. 2012).

In more mature exploration districts, the opportunity now exists to develop a more predictive exploration strategy that targets: (1) near-surface supergene hematite-goethite ore, (2) deeper extensions of hypogene magnetite-rich ore, and (3) the detection of "blind" supergene and hypogene ore bodies beneath surface transported cover and/or unmineralized BIF. The predictive strategy hinges on the application of a mineral systems approach (McCuaig et al. 2010; Wyborn et al. 1994) to understanding the controls on iron ore formation. Such an approach has been successfully applied during the past decade to hydrothermal (Au), magmatic (Ni), and hydrothermal-magmatic (Au-Cu-Mo) systems. Such an holistic approach for the study of BIF-hosted iron ore systems would include understanding the source of hydrothermal fluids and metals, the structural framework for the fluid plumbing system that controls permeability, as well as the down-stream portion of the hydrothermal system that describes how "spent" ore fluids migrate away from the site of ore deposition.

The mineral systems model for supergene-modified hypogene deposits in the Yilgarn Craton is presently incomplete in that the source of hydrothermal fluids and the T-P-X conditions of the fluid during ore formation are only poorly constrained. For example, what role if any do felsic igneous intrusions have in contributing fluids and driving them through BIF to initiate widespread carbonate alteration followed by magnetite mineralization? Can hypogene magnetite-rich ore bodies hosted by BIF be an expression of VMS-style hydrothermal systems? Are hypogene iron ore bodies the result of orogenic deformation events affecting a greenstone belt?

Attempts at developing a more predictive approach to iron ore exploration are presently being made by the Iron Research Group at the CET through the ongoing and recent initiation of several CET-university, industry, and GSWA-funded projects, which include camp-scale studies in the: (1) Hamersley Province, (2) Yilgarn Craton, (3) Pilbara Craton, and (4) the Iron Quadrangle and Carajas Mineral Province of Brazil. The eventual synthesis of outcomes from these projects will benefit our understanding of iron ore formation processes, and translate to the better detection and prediction of iron ore bodies.

Acknowledgements

Paul Duuring acknowledges the financial support of the Government of Western Australia through the Department of Mines and Petroleum's Exploration Incentive Scheme.

References

Angerer T, Hagemann SG (2010) The BIF-hosted high-grade iron ore deposits in the Archean Koolyanobbing greenstone belt, Western Australia: Structural control on synorogenic- and weathering-related magnetite-, hematite-, and goethite-rich iron ore. Economic Geology 105:917-945.

Angerer T, Hagemann SG, Danyushevsky LV (2012) Geochemical evolution of the Banded Iron Formation-hosted high-grade iron ore system in the Koolyanobbing greenstone belt, Western Australia. Economic Geology 107:599-644.

Angerer T, Hagemann SG, Danyushevsky L (submitted) High-grade iron ore at Windarling, Yilgarn craton: a product of syn-orogenic deformation, hydrothermal alteration, and supergene modification in an Archean BIF-basalt lithostratigraphy. Miner Deposita.

Duuring P, Hagemann SG (2011) Contrasting styles of high-grade iron mineralisation at Weld Range, Western Australia Iron Ore 2011. The Australasian Institute of Mining and Metallurgy, Perth, pp 87-92.

Duuring P, Hagemann SG (2012a) Leaching of silica bands and concentration of magnetite in Archean BIF by hypogene fluids: Beebyn Fe ore deposit, Yilgarn Craton, Western Australia. Miner Deposita. doi: 10.1007/s00126-012-0428-1.

Duuring P, Hagemann SG (2012b) Genesis of superimposed hypogene and supergene Fe orebodies in BIF at the Madoonga deposit, Yilgarn Craton, Western Australia. Miner Deposita. doi: 10.1007/s00126-012-0429-0.

Duuring P, Hagemann SG, Novikova J, Cudahy T, Laukamp C (2012) Targeting iron ore in Banded Iron Formation using ASTER data: Weld Range greenstone belt, Yilgarn Craton, Western Australia. Economic Geology 107:585-597.

Maskell A, Duuring P, Hagemann SG (submitted) Hydrothermal alteration events controlling magnetite-rich iron ore at the Matthew Ridge prospect, Jack Hills greenstone belt, Yilgarn Craton. Aust J Earth Sci.

McCuaig TC, Beresford S, Hronsky J (2010) Translating the mineral systems approach into an effective exploration targeting system. Ore Geology Reviews 38:128-138. doi: DOI: 10.1016/j.oregeorev.2010.05.008.

Wyborn LAI, Heinrich CA, Jaques AL (1994) Australian Proterozoic Mineral Systems - Essential Ingredients and Mappable Criteria. Australas I Min Met 94:109-115.

Multiple dissolution-reprecipitation processes of iron oxides in the Chengchao iron skarn deposit: implications for ore genesis and elemental analysis of magnetite

Hao Hu, Jian-Wei Li
Faculty of Earth Resources, China University of Geosciences (Wuhan), Wuhan 430074, China

David Lentz
Department of Earth Sciences, University of New Brunswick, 2 Bailey Drive, Fredericton, NB, E3B 5A3 Canada

Abstract. Magnetite is one of the most common accessory minerals in magmatic and metamorphic environments and forms in a variety of hydrothermal deposits. Textural and compositional analysis of magnetite from the Chengchao Fe skarn deposit, China is carried out to better understand the genesis of the deposit and shed lights on the analytical protocols for hydrothermal magnetite. We analyzed magnetite from the ore-related granitic intrusion and three types of ores related to this intrusion. BSE images reveal that magnetite from the skarn and massive ores were all reequilibrated with late hydrothermal fluids, forming secondary magnetite grains. These textural relationships, however, are mostly obscured under optical microscope. These textures are interpreted to have formed by dissolution-reprecipitation processes (DRP).

Primary magnetite grains from the endoskarn and massive ores contain high SiO_2, Al_2O_3, and low MgO, whereas equivalents from the exoskarn have high MgO and low SiO_2 and Al_2O_3. Compared to the precursor mineral, the secondary magnetite is significantly depleted in most trace elements. In contrast, iron has considerably increased in the secondary magnetite grains. It is concluded that dissolution-reprecipitation processes is an important mechanism in effectively removing impurity elements to form high-grade, high-quality iron ores in hydrothermal environments. Results from this study also highlight the importance of textural characterization using BSE imaging before compositional analysis of magnetite.

Keywords. Magnetite; dissolution-reprecipitation; skarn deposits; ore genesis; Chengchao

1 Introduction

Magnetite and hematite are common oxide minerals in igneous, metamorphic and sedimentary rocks. They also widely occur in a variety of iron ores, including BIF, Kiruna-type, magmatic Fe-Ti oxide, and skarn (Nadoll et al. 2012; Dupuis and Beaudoin 2011), and in other types of hydrothermal deposits such as IOCG and porphyry Cu-Au systems (Liang et al. 2009; Williams et al. 2005), among others. Magnetite commonly hosts a range of trace elements, such as Al, Ti, V, Si, Ca, and Mg (Dupuis and Beaudoin 2011; Nadoll et al. 2012). Types and concentrations of the elements are largely dependent on the magnetite-forming parameters, such as temperature, fO_2, fS_2, silica activity, and melt/fluid composition (Nadoll et al. 2012 and references therein). There is an increasing interest in using trace elements from magnetite as a provenance and genesis indicator of this mineral and associated ore deposits (Dupuis and Beaudoin 2011; Dare et al. 2012; Nadoll et al. 2012). We present detailed petrographic and compositional data for magnetite from the Chengchao Fe skarn deposit to illustrate how magnetite was re-equilibrated with late stage fluids, leading to textural and chemical alteration. The results are used to provide constraints on the genesis of magnetite and the Chengchao deposit. The findings from this study also highlight the utilization of textural examination prior to *in situ* compositional analysis of magnetite aiming to provide insights into the genesis and evolution of magnetite-bearing deposits.

2 Geological Setting

The Chengchao Fe skarn deposit is located in the northern portion of the Daye Fe-Cu ore district, western Middle-Lower Yangtze River Metallogenic Belt (MLYMB) along the northern margin of the Yangtze Craton, which contains more than 200 deposits and has been one of the most important Fe-Cu-Au producers in China in the last three decades. The Daye district is well known for its endowment with numerous Fe, Fe-Cu-(Au), and Cu-Mo-(W) skarn deposits (Zhai et al. 1996; Pan and Dong 1999; Li et al. 2008). Mineralization associated with these deposits is mostly located in the contact zones between marine carbonates of the Lower Triassic Daye Formation and Early Cretaceous (143-127 Ma) intermediate to acidic intrusions (Shu et al. 1992; Li et al. 2008; Li et al. 2010; Xie et al. 2011). The Chengchao deposit represents the largest Fe skarn in Daye, with a proven reserve of 280 Mt Fe at an average of 44 wt% Fe (up to 61 wt%) (Xie et al. 2011). Mineralization at Chengchao is related to a granite and diorite stocks that intruded the Daye Formation, which comprises evaporite-bearing dolomitic limestones, limestones and dolomite.

3 Samples and analytical methods

Four samples were collected for this specific study. Sample CC01-125 is granite collected from a drill hole at a ~800 m depth. The granite consists of K-feldspar, plagioclase, quartz, biotite and hornblende, with

accessory apatite, zircon, titanite and magnetite. The other three samples are all from the major ore body III. Sample CC05 was collected from the serpentine-bearing exoskarn, which comprises massive magnetite (>80 vol. %) and subordinate pyrite, chalcopyrite, serpentine, and calcite. Sample CC102 is a mineralized endoskarn in close proximity of the diorite, and consists of diopside, actinolite, and magnetite with minor albite, titanite, and pyrite. Sample CC28 is a massive magnetite vein intrudes marbles of the Daye Formation, with additional (<20 vol%) calcite, and accessory pyrite and hematite. All samples were prepared for standard petrographic polished sections that were initially examined using optical microscopy to characterize the mineralogical and textural relationships, with an emphasis on the occurrence, morphology, and texture of magnetite. The thin sections were then carbon-coated for scanning electron microscopy (SEM) and electron microprobe analysis (EMPA).

The morphology and textures of magnetite were investigated using FEI Quanta200 environmental scanning electron microscope equipped with an energy dispersive spectrometer at the State Key Laboratory of Geological Process and Mineral Resources of the China University of Geosciences, Wuhan. Electron probe microanalyses were performed with a JXA-8230 Superprobe at the Center for Material Research and Analysis, Wuhan University of Technology. Standards and unknowns were analyzed with 1 μm beam diameter at an accelerating voltage 20 kV and a beam current of 20 nA. Integration time for peak of Al, Si and Mg are 30 seconds, and the remaining elements are 20 seconds. The following standards were used: Fe_3O_4 (Fe), $Mg_3Al_2Si_3O_{12}$ (Mg, Al and Si), (Mn, Ca)SiO_3 (Ca and Mn), $(ZnMn)_2SiO_4$ (Zn), TiO_2 (Ti), $FeCr_2O_4$ (Cr), vanadium metal (V), cobalt metal (Co) and Ni_2Si (Ni). Oxygen was calculated from cation stoichiometry, and the chemical formula was normalized to 32 O atoms.

4 Results

4.1. Petrography and texture of magnetite

Magnetite in the granite (sample CC01-125) comprises euhedral to subhedral grains ranging in size from 100~200 μm. They are commonly enclosed in or marginal to K-feldspar, biotite, and hornblende. BSE imaging did not reveal any oscillatory and other secondary texture. Under SEM, two distinct generations of magnetite, hereafter termed as primary or secondary, have been recognized in samples CC05, CC102, and CC28. The primary magnetite grains are enhedral to anhedral from 100 to 500 μm, whereas the secondary ones are characterized by irregular domains in the primary magnetite (Fig. 1).

4.2. Chemical composition of magnetite

The accessory primary magnetite from the granite have high contents of TiO_2 (0.02-1.27 wt.%) and V_2O_3 (0.32-0.48 wt.%), with minor ZnO (0.02-0.19 wt.%) and CoO (0.15-0.19 wt.%). SiO_2, Al_2O_3, MnO, and MgO are below or near the detection limit.

Primary magnetite in the exoskarn (sample CC05) contains high MgO (2.76-3.07 wt.%)., Al_2O_3 (0.54-1.05 wt.%), and MnO (0.30-0.47 wt.%). These elements, however, are significantly lower in the secondary magnetite, which are 0.07-0.71 wt.% (MgO), 0.05-0.48 wt.% (Al_2O_3), and 0.10~0.34 wt.% (MnO). There is no difference in ZnO and CoO between the primary (0.09-0.21 wt.% ZnO and 0.14-0.22 wt.% CoO) and secondary magnetite (0.06-0.23wt.% ZnO; 0.14-0.22% CoO).

Primary magnetite in the endoskarn sample is enriched in SiO_2 (1.03~1.88 wt.%), Al_2O_3 (1.04~2.83 wt.%), and CaO (0.10~0.88 wt.%), relative to the secondary magnetite (0.14~0.80 wt.% SiO_2; 0.21~0.40 wt.% Al_2O_3, and<0.1 wt.% CaO). MgO and TiO_2 are also relatively high in the primary magnetite, which are 0.28~0.68 wt.% and 0.14~0.25 wt.%, respectively. The values for MgO and TiO_2 are <0.08 wt.% and <0.05 wt.% in the secondary magnetite.

Primary magnetite in the vein-type ore (sample CC28) is characterized by high concentration of SiO_2 (0.92~3.21 wt.%), Al_2O_3 (0.51-2.18 wt.%), CaO (0.69-1.64 wt.%), low contents of MgO (0.15-0.49 wt.%), ZnO (0.08-0.24 wt.%) and CoO (0.10~0.18 wt.%). In sharp contrast, the secondary magnetite contains no MgO and very low CaO (<0.11 wt.%, with exception for two analyses that have 0.01 wt.% MgO). No obvious changes for ZnO (0.07-0.21 wt.%) and CoO (0.13~0.19 wt.%) are observed between the primary and secondary magnetite. Primary oscillatory growth zones with light contrast have moderate SiO_2 (0.92 wt.%), Al_2O_3 (0.51 wt.%) and MgO (0.15 wt.%; point CC28-5; Fig. 1e); whereas growth bands with dark contrast have relatively high MgO (1.56 wt.%), Al_2O_3 (1.03 wt.%) and MgO (0.27 wt.%) (e.g. point CC28-6; Fig. 1e).

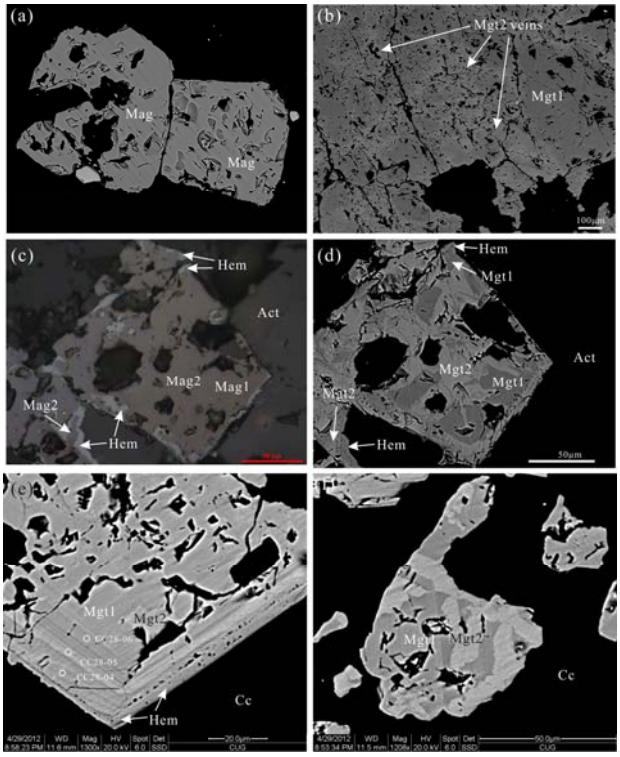

Figure 1. SEM-backscattered electron (SEM-BSE) images of typical magnetite grains from the Chengchao deposit; (a)

BSE image in granite sample CC01-125 showing magnetite that is homogenous and not altered by secondary magnetite; (b) The primary magnetite (Mgt1) are cut by secondary magnetite veinlets that are commonly porous and in sharp contact with primary magnetite. Fine chalcopyrite and pyrite grains occur as inclusions in the Mag2; (c) Reflected-light photomicrograph showing magnetite altered by hematite; however, the two generations of magnetite cannot be easily distinguished (sample CC102); (d) SEM-BSE image of the same magnetite grain in (c) that displays two generations of magnetite. The dark gray domains are the primary magnetite, while the light gray domains are the secondary magnetite. The Mag1 and Mag2 are locally altered by hematite; (e) and (f) primary magnetite with weak to intense oscillatory zoning replaced by secondary homogeneous magnetite rims (SEM-BSE images).

Four types of magnetite can be readily distinguished on the basis of their texture, occurrence, and composition of major and trace elements: (1) Type 1: magmatic magnetite in granite (CC125); primary magnetite (Mag1) in the ore can be divided into two types of magnetite: (2) Type 2: Si-enriched magnetite (sample CC102 and sample CC28) and (3) Type 3: Mg-enriched magnetite (CC05) and (4) Type 4 magnetite in secondary pure magnetite (Mag2) in sample CC01-125, CC102 and CC28.

5. Discussion

5.1. Iron oxide mineral dissolution-reprecipitation and a potential enrichment mechanism for hydrothermal iron deposits.

Magnetite from the skarn and vein-type ores of the Chengchao deposit have several striking textural features: (1) primary magnetite is mostly replaced by late stage minerals along fractures and/or grain margins, (2) secondary magnetite are generally in sharp contact with the primary phase, and (3) secondary magnetite grains are commonly characterized by abundant porosity. These features are interpreted to result from dissolution-reprecipitation process (DRP; Putnis, 2009; Putnis and John, 2010) during the mineralization of the Chengchao deposit. The textural data presented here suggest that DRP may have been much more important in the formation of hydrothermal magnetite and associated deposits than previously thought, similar to the scenario of U-Th-bearing accessory minerals in a wide range of formational environments (Geisler et al., 2007; Kusiak et al., 2009; Putnis, 2009; Harlov et al., 2011)

The dissolution-and-precipitation process of magnetite can be illustrated in Figure 2. Primary magnetite (Mag1; type 2 and type 3) occurs as euhedral to subhedral grains and some of them have oscillatory zoning formed during fluid-wall rock interaction in the retrograde stage; magnetite in this generation is characterized by high concentrations of impurity elements. The secondary magnetite formed by replacing the primary magnetite along the factures or rims within the same grain. Replacement reactions result from an interface coupling between the dissolution of the impure primary magnetite and precipitation of the secondary magnetite at the site of dissolution. Silicon, Al, Ca, and Mg were effectively removed as a result of this reaction, whereas iron contents are increased from 67.5 to 71 wt.% (Fig. 3). It is therefore concluded that the dissolution-reprecipitation process has played an important role in the formation of high-grade and high-quality iron ores in the Chengchao deposit.

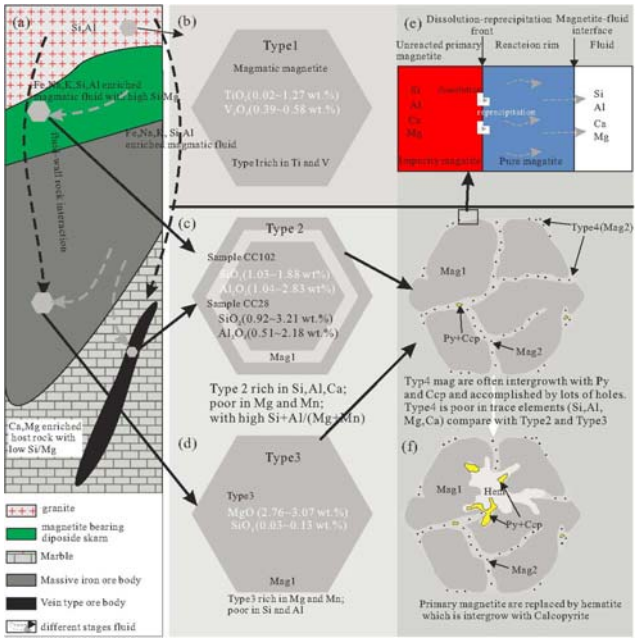

Figure 2. Schematic illustration of multistage history of iron oxide minerals formation observed in Chengchao Fe deposit.

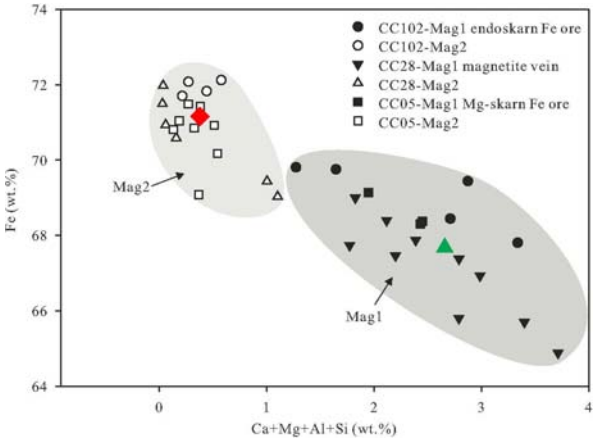

Figure 3. Fe vs Ca+Mg+Al+Si contents of magnetite of different generations from the Chengchao deposit. Note red diamond and green triangle represent the average value of primary magnetite and secondary magnetite, respectively.

5.2. Implications for *in situ* micro-analysis of magnetite

Magnetite formed in different environments commonly has distinct trace element compositions (Dupuis and Beaudoin, 2011; Nadoll et al., 2012). Thus, the chemical composition of the mineral may potentially be used as an indicator for its origin (Dupuis and Beaudoin, 2011; Dare et al., 2012a; Nadoll et al., 2012). Results from this study, nevertheless, suggest that magnetite is more susceptible to subsequent hydrothermal replacement or alteration to form secondary magnetite than previously

thought. The dissolution and reprecipitation process could lead to intergrowth of multiple generations of magnetite in a single grain that have distinctly different composition. In this case, chemistry of bulk magnetite composition represents an average of multiple generations. To better understand the genesis and evolution of magnetite and related ore deposits, it is imperative to precisely determine the composition of distinct domains of single crystals recording multiple hydrothermal events. Dupuis and Beaudoin (2011) used trace element data of magnetite, obtained by electron microprobe analysis, to distinguish different types of ore deposits using the Ni/(Cr+Mn) vs. Ti+V and Ca+Al+Mn diagram. Replacement between hematite and magnetite, as well as zoning in magnetite, is common in iron deposits and has been discussed in the diagram (Dupuis and Beaudoin, 2011). It seems that different types of ore deposits can be well distinguished using those discrimination diagrams. However, it is more unlikely to ascertain whether the magnetite was formed in a single stage or generated by multiple dissolution and precipitation processes without the textural characterization (Dupuis and Beaudoin, 2011; Dare et al., 2012a; Nadoll et al., 2012). This suggests that the geological significance of the compositional data reported by those authors needs to be reconsidered. In this study, Ti+V and Ca+Al+Mn contents of magnetite are significantly decreased from primary phases to secondary domains in the same grains, strengthening the need for high spatial-resolution *in situ* analysis for distinct generations of the mineral. If being altered by the DRP, magnetite from magmatic V-Ti iron oxide deposits, porphyry systems, Kiruna-type iron and IOCG deposits, as well as BIF, could potentially be plotted in the fields of skarn deposits. In this regard, trace element data of magnetite for each type of deposits should be revisited before applying to those discrimination diagrams. Detailed SEM-BSE imaging of magnetite should be carried out to determine whether the grains have been affected by subsequent hydrothermal alteration, so that reliable trace-element compositions of primary or secondary domains can be obtained. Only if an integration of textural and compositional data enable a better understanding in the origin and evolution of iron deposits formed in a range of environments.

Conclusions

(1) Primary magnetite from the four samples of magnetite-rich skarn show the enrichment in iron relative to Ca, Mg, Al and Si during the formation of secondary magnetite.
(2) Dissolution-reprecipitation reactions are very important mechanisms in forming high-grade and high-quality ores in hypogene environments.
(3) BSE imaging of magnetite should be carried out to determine if the grains have survived hydrothermal alteration to provide reliable trace element composition for primary or secondary domains to better constrain ore-forming processes and the origin of ore deposits.

Acknowledgements

Ms. Su-Xin Zhang and Ms. Meijun Yang are thanked for their expert assistance during the SEM and EMPA analysis, respectively. Research work is jointly supported by the National Basic Research Program of China (2012CB416802) and Special Fund for Basic Scientific Research of Central Colleges, China University of Geosciences (Wuhan) (Grant No. CUG120102). DL is supported by a NSERC Discovery grant.

References

Dare SAS, Barnes SJ, Beaudoin G (2012) Variation in trace element content of magnetite crystallized from a fractionating sulfide liquid, Sudbury, Canada: Implications for provenance discrimination. Geochim Cosmochim Ac 88:27-50.

Dupuis C, Beaudoin G (2011) Discriminant diagrams for iron oxide trace element fingerprinting of mineral deposit types. Miner Deposita 46: 319-335.

Geisler T, Schaltegger U, Tomaschek F (2007) Re-equilibration of zircon in aqueous fluids and melts. Elements 3: 43-50.

Harlov DE, Wirth R, Hetherington CJ (2011) Fluid-mediated partial alteration in monazite: the role of coupled dissolution-reprecipitation in element redistribution and mass transfer. Contrib Mineral Petr 162:329-348.

Kusiak MA, Dunkley DJ, S Aby E, Martin H, Budzyń B (2009) Sensitive high-resolution ion microprobe analysis of zircon reequilibrated by late magmatic fluids in a hybridized pluton. Geology 37: 1063.

Li JW, Deng XD, Zhou MF, Lin YS, Zhao XF, Guo JL (2010) Laser ablation ICP-MS titanite U-Th-Pb dating of hydrothermal ore deposits: A case study of the Tonglushan Cu-Fe-Au skarn deposit, SE Hubei Province, China. Chem Geol 270: 56-67.

Li JW, Zhao XF, Zhou MF, Vasconcelos P, Ma CQ, Deng XD, de Souza ZS, Zhao YX, Wu G (2008) Origin of the Tongshankou porphyry−skarn Cu−Mo deposit, eastern Yangtze craton, Eastern China: geochronological, geochemical, and Sr−Nd−Hf isotopic constraints. Miner Deposita 43: 315-336.

Liang HY, Sun W, Su WC, Zartman RE (2009) Porphyry copper-gold mineralization at Yulong, China, promoted by decreasing redox potential during magnetite alteration. Economic Geology 104: 587-596.

Nadoll P, Mauk JL, Hayes TS, Koenig AE, Box SE (2012) Geochemistry of magnetite from hydrothermal ore deposits and Host Rocks of the Mesoproterozoic Belt Supergroup, United States. Economic Geology 107: 1275-1292.

Pan Y, Dong P (1999) The Lower Changjiang (Yangzi/Yangtze River) metallogenic belt, east central China: intrusion-and wall rock-hosted Cu-Fe-Au, Mo, Zn, Pb, Ag deposits. Ore Geol Rev 15: 177-242.

Putnis A, John T (2010) Replacement processes in the Earth's crust. Elements 6: 159.

Williams PJ, Barton MD, Johnson DA, Fontboté L, De Haller A, Mark G, Oliver NHS, Marschik R (2005) Iron oxide copper-gold deposits: Geology, space-time distribution, and possible modes of origin. Economic Geology: 371-405.

Xie G, Mao J, Zhao H, Duan C, Yao L (2011) Zircon U−Pb and phlogopite ^{40}Ar–^{39}Ar age of the Chengchao and Jinshandian skarn Fe deposits, southeast Hubei Province, Middle−Lower Yangtze River Valley metallogenic belt, China. Miner Deposita 47: 633-652.

Zhai YS, Xiong Y, Yao S, Lin X (1996) Metallogeny of copper and iron deposits in the Eastern Yangtse Craton, east-central China. Ore Geol Rev 11: 229-248.

REE-enrichment in hydrothermal carbonates from the Cauê BIF, Quadrilátero Ferrífero, Brazil

Tatiana A. Fernandes Lima, Carlos A. Rosière
Instituto de Geociências, Universidade Federal de Minas Gerais, 31270-901, Belo Horizonte, MG, Brazil

Francisco Javier Rios
Centro de Desenvolvimento da Tecnologia Nuclear, CDTN / CNEN, PO Box 941, Belo Horizonte, MG, Brazil

Sandra Andrade, Renato Moraes
Instituto de Geociências, Universidade de São Paulo, 05508-080, São Paulo, SP, Brazil

Abstract. Three generations of carbonates were characterized in the Cauê Iron Formation Quadrilátero Ferrífero, Brazil: an early dolomite, micro-sparitic named Cb1; Cb2 in either as fracture-filling veins or as disseminated crystal aggregates in the fine-grained matrix; and Cb3 the youngest generation also related to late-stage-veins. Different hydrothermal carbonates were discriminated according to microstructural and petrographic features and the REE content determined by ICPMS and LA-ICPMS. The analytical results indicate the following mineral-chemical changes from the older to the younger generation: (a) a general REE enrichment; (b) distinctive fractionation between HREE and LREE, (c) decrease in the Hf/Zr ratio, (d) minor decrease in the Y/Ho ratio; and (e) increasing Pr/Pr* by variable Ce/Ce* values. These variations are preliminary interpreted as the result of fluid mixing during hydrothermal alteration and Fe-mineralization.

Keywords: Rare Earth Element, Carbonates, BIF, Quadrilátero Ferrífero

1 Introduction

Carbonates have received considerable attention by having participated in the hydrothermal systems associated with the formation of high-grade Fe orebodies. ICPMS and LA-ICPMS geochemical studies of trace elements including REE in carbonates from the Cauê itabirite - BIFs of the Quadrilátero Ferrífero (QF) mining district are expected to provide important new information regarding supergene alteration associated with Fe-mineralization. Although carbonates do not constantly appear in all high-grade BIF-hosted iron orebodies of the QF, it is a remarkable fact that below the water table relicts of carbonates have been consistently observed, suggesting a close association with Fe-enrichment. In this study, we investigate the formation conditions of several sequentially crystallised generations of carbonates from hydrothermal veins and how they influenced Fe mineralization.

2 Geological Setting

In the QF (Fig. 1) located in central Minas Gerais (20°15'S and 43°30'W), southern Brazil (Almeida 1977; Dorr 1969; Herz 1978) the Paleoproterozoic metamorphic Cauê banded iron formation covers a wide range of textural and mineralogical facies that reflects metamorphic reactions, deformation and hydrothermal alteration superimposed and defining a variety of different lithofacies. These were already distinguished by Dorr (1969), namely quartz-itabirite, amphibole itabirite and dolomitic itabirite.

This BIF-unit hosts giant supergene-modified hypogene high-grade iron orebodies which are, commonly, associated with dolomitic itabirites (Spier et al. 2003; Suckau et al. 2005) and hydrothermal carbonate alteration under strong structural control. These characteristics are particularly clear in the western structural domain (Rosière et al. 2001). A direct association of Fe-mineralization and the presence of carbonates in BIFs has been already established for the Águas Claras deposit (Spier et al. 2003) and also indicated in other orebodies such as in Mutuca, Conceição and, recently, in the Casa de Pedra deposits (see Rosière et al. 2008 and references therein).

Several samples were collected from different open pits and drill cores from numerous deposits across the Quadrilátero Ferrífero. They are currently analyzed as a part of an on-going investigation. In the present work, however, we have focused our attention to the Esperança deposit, at the northwestern border of the QF, where the iron orebody is comprised primarily by a small, several tens of meter thick, hard high-grade vein that cuts across partially hydrothermally altered and Fe-mineralized carbonate-rich BIFs. Centimeter thick fibrous gash vein system with carbonate, quartz and specularite are hosted by the dolomitic itabirite and record consecutive periods of mineral precipitation during the alteration and mineralization history of the orebody.

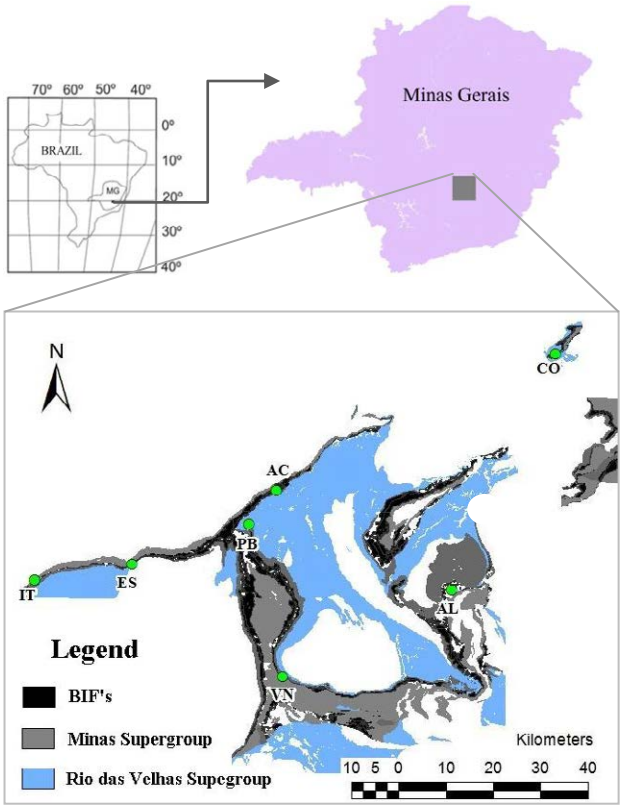

Figure 1. Geologic map of the Quadrilátero Ferrífero; highlighted letters indicate iron ore deposits studied: IT = Itatiaiuçu, ES = Esperança, PB = Pau Branco, VN = Viga Norte, AC = Águas Claras, AL = Alegria, CO = Conceição (modified after Dorr 1969; Rosière and Rios 2004).

3 Carbonates from Dolomitic Itabirites

Petrographic analyses of the textural features, combined with microprobe data of dolomitic itabirites allowed the definition of three generations of carbonates (Fig. 2) (see also Ferreira-Santos and Rosière 2004) that are redefined in this study:

a) Cb1, mainly dolomite (80% - $(Ca_{0,5}Mg_{0,5})CO_3$), micro-sparitic, comprised by fine anhedral crystals with or without iron oxide inclusions, distributed along the BIF layers alternating with the iron oxide bands (mainly martite-magnetite) (Fig. 2A);

b) Cb2 occurs as aggregates of sparitic subhedral ferroan dolomite ($(Ca_{0,5}Mg_{0,4}Fe_{0,1})CO_3$) crystals or cm – to mm veins fillings (Fig. 2B);

c) Cb3 occurs as dolomite and calcite in younger veins than Cb2 and Cb1 and usually associated with minor quartz and specularite (Fig. 2C).

A zoned sigmoidal-shaped gash vein from the Esperança deposit was selected for detailed analyses mainly due to the relationship of its carbonate crystals (Cb3) with a younger fracture and presence of quartz and specularite. The asymmetrical and displaced vein show typical zoning and the carbonate is intergrown with hematite. Dolomite (Cb3a) and hematite fibres (specularite) display syntaxial growth from one wall of the vein. In the centre of the vein, fibrous and subhedral crystals of specularite, quartz and ferroan dolomite (Cb3b) are observed. At the other side of the wall, antitaxial, euhedral, sparritic white calcite and minor dolomite (Cb3c), both in sharp contact with the host rock are recorded.

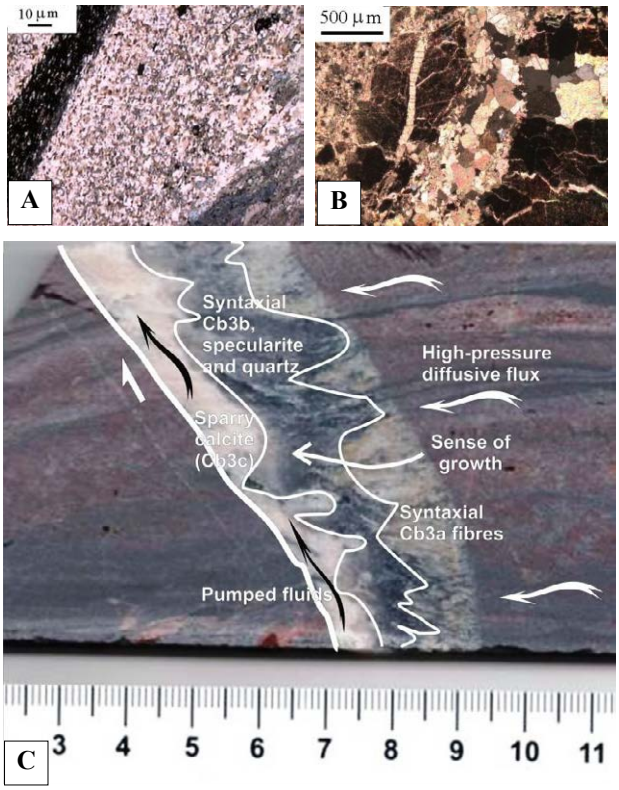

Figure 2. Main features of the analysed carbonate types: **A.** fine-grained Cb1 aggregates defining the BIF-layers – sample PZ69.90m_A; **B.** coarse-grained iron-rich Cb2 dolomite crystals cut by Cb2 veins, sample PZ75.55m from the Águas Claras deposit (A and B): photomicrographs, transmitted light, X polarisers; **C.** polished rock slab with Cb3 vein in sigmoidal shaped tension gash, comprising Cb3a dolomite fibres on the vein wall, Cb3b ferroan dolomite with specularite and quartz, and Cb3c sparry calcite; sample ES02_F024_249,2m from the Esperança deposit.

4 REE of the Carbonates

Carbonate chemistry of the different carbonate generations was determined in:

a) Hand-picked aggregates from 24 fresh samples of dolomitic itabirite from drill cores by ICPMS using the ACME Analytical Laboratories.

b) Single crystal analyses with electron microprobe in 18 samples of seven deposits in the QF: IT = Itatiaiuçu, ES = Esperança, PB = Pau Branco, VN = Viga Norte, AC = Águas Claras, AL = Alegria, CO = Conceição (Fig. 1) and LA-ICPMS mineral analysis of three samples from the Esperança deposit using the Geochemical Laboratory of IGC/USP.

Major Elements: EMPA analyses have shown a wide variation in the contents of Ca (2 to 54%), Mg (1 to 52%), Fe (1 to 49%) and Mn (<5%) that, together with the textural features, assisted to define the carbonate generations. Besides the compositional variation all

carbonates show a positive correlation in the cation substitution between Mn, Fe and Mg-Fe.

REE: The ICPMS analyses were performed on:

a) hand-picked crystals separated based on the textural features (Fig. 3A).
b) *in situ LA*-measurements on the gash vein with the carbonates interpreted to be part of the Cb3-type (Figs. 2C and 5).

The general trend of the REE spidergrams (PAAS normalized) from the different carbonate generations is not very distinct from the available results of whole rock analyses from dolomitic itabirite (see Spier et al. 2007). There is a consistent light to heavy REE enrichment pattern (average Pr/Yb_N = 0.25; range 0.08–0.58) and a positive Eu anomaly which is more pronounced in Cb3 samples followed by Cb1 and Cb2 (average Eu/Eu^*_N = 2.01; 1.53 and 1.28, respectively). A negative, but not prominent Ce anomaly is also present in all types. Seventy-six percent of the samples present a true negative Ce anomaly with the measured values scattered to some extent (average Ce/Ce^*_N = 0.88; range 0.61–1.13) but with a wide variation in the Pr/Pr* ratios (Fig. 3B). The Y anomaly is always positive (average Y/Y^*_N = 1.75; range 0.96–2.25). Very distinctive, however, is the enrichment in LREE for Cb2, whereas Cb3 carbonates show a clear fractionation in the HREE (Fig. 3A).

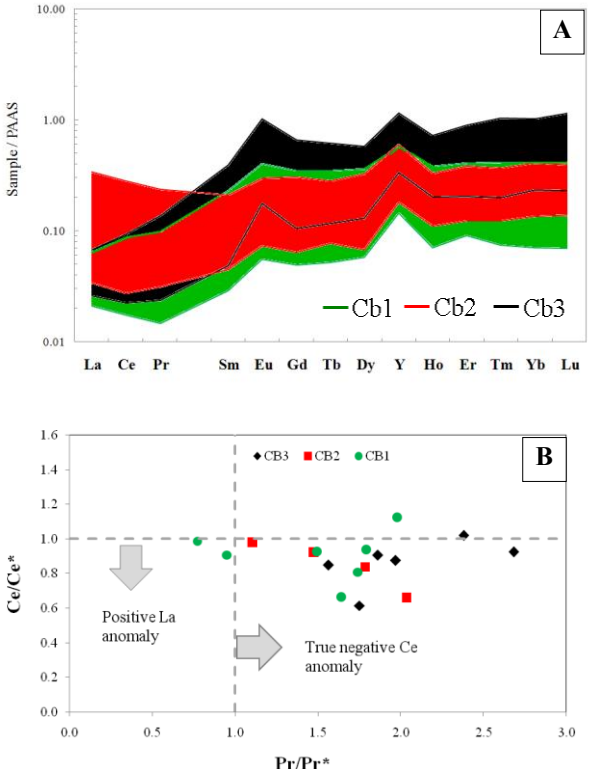

Figure 3. A. PAAS-normalized REE spidergrams with REE-data for each carbonate generation. **B.** Binary plot of Ce/Ce* vs. Pr/Pr* (normalized after PAAS) used to identify the La and Ce anomaly.

The Y/Ho ratios vary from an average 42.9 (Cb3) to 43.1 (Cb2) and 44.8 (Cb1) and fall mainly in the field of marine-sedimentary carbonates, indicating a seawater signature inherited from BIFs and dolostones which progressively changes with the evolution of the hydrothermal alteration (Fig. 4A).

This variation is particularly clear in the Y/Ho versus Zr/Hf diagram (Fig. 4B). Analyzed values range from close to the seawater field to the hydrothermal fluorite domain.

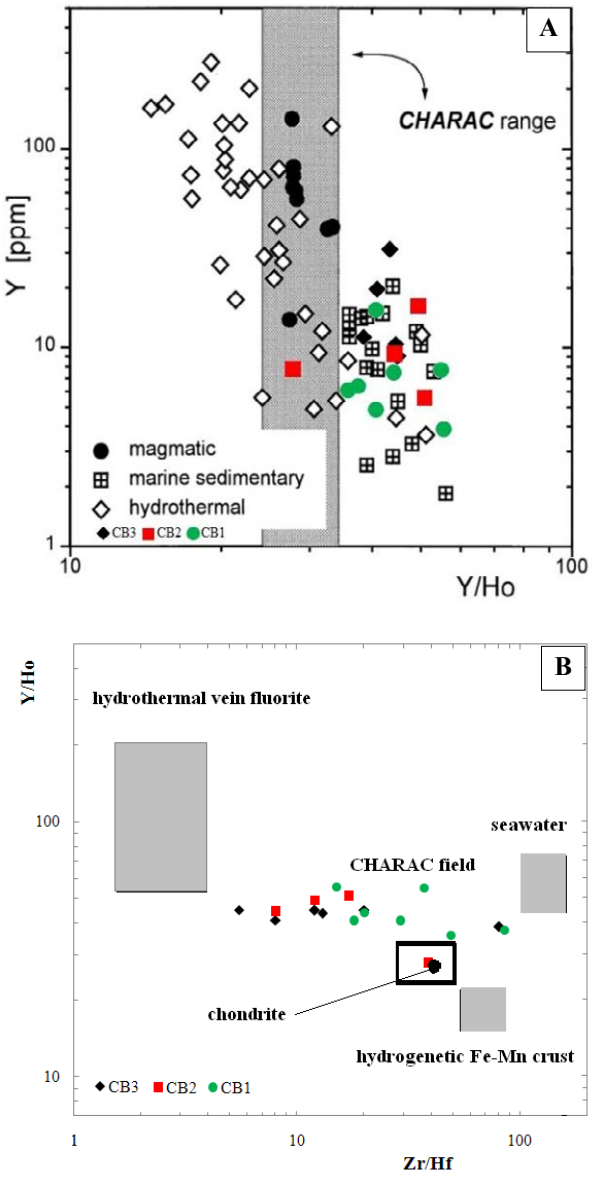

Figure 4. A. Binary plot of Y *vs* Y/Ho ratio for Cb1, Cb2 and Cb3 carbonates with typical values for magmatic, marine sedimentary and hydrothermal carbonates according to Bau (1996). The *CHARAC (CHA*rge and *RA*dius *C*ontrolled) field is defined by the crosshatched area. **B.** Binary plot Y/Ho *vs* Zr/Hf ratios for Cb1, Cb2, Cb3 carbonates (from Bau 1996).

The carbonates Cb3a, Cb3b and Cb3c (Fig. 2C) show a progressive fractioning from light to heavy REE pattern, remarkably for Cb3c (average Pr/Yb_N = 0.04). Furthermore there are positive Eu and Y anomalies in Cb3a, Cb3b and Cb3c samples (Eu/Eu^*_N = 2.12, 2.35, 2.12 and Y/Y^*_N = 1.63, 1.92, 1.59; Fig. 5).

The Cb3 carbonates present progressive REE-enrichment (ΣREE+Y = 29.5ppm) when compared to the host rock - dolomitic itabirite (17.1ppm) and to the microsparritic carbonate Cb1 (17.3ppm).

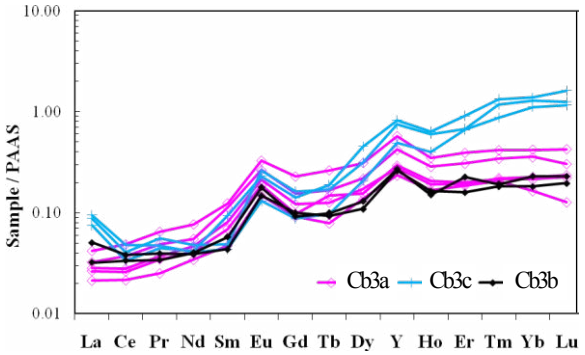

Figure 5. PAAS-normalized REE spidergrams for carbonates: Cb3a, Cb3b, Cb3c from the Esperança deposit.

5 Concluding Remarks

During the Transamazonic orogeny (Rosière et al. 2013) hydrothermal fluids percolated into the BIF-associated dolomitic rocks from the Itabira Group/QF producing CO_2-rich fluids and precipitated carbonate generations Cb2 and Cb3 with high concentrations of REE and enhancement of the positive Y and Eu anomalies. The sequence of precipitation in the veins indicated that, after formation of dolomite fibres, the fluids became progressively Fe saturated under oxidic conditions, with precipitation of hematite as specularite fibers and quartz. The remaining fluid, depleted in Mg and Fe but relatively enriched in HREE, was probably pumped during seismic activity into open vugs that were subsequently sealed by precipitation of calcite (crack-seal mechanism).

The variability of the REE composition in the carbonate generations associated with the hydrothermal alteration of the itabirite-BIFs from the Quadrilátero Ferrífero probably indicate a mixture of very distinctive fluids of different origins. The physico-chemical characteristics of these fluids will be subject of further studies.

Acknowledgements

TAFL is thankful to the CNPq for the scholarship at UFMG. The authors also acknowledge the Ferrous Resources Brazil particularly Dr. H. P. Meireles, for providing full access to geological information and samples. Financial support and infrastructure for this study was provided by CNEN/CDTN; FAPEMIG (CAG PPM00666-11); CNPq (307546/2011-0) and CNPq-Vale Project (12/2009).

References

Almeida FFM (1977) O Craton de São Francisco: Rev. Bras. Geoc., 7:349 – 364.

Bau M (1996) Controls on the fractionation of isovalent trace elements in magmatic and aqueous systems: evidence from Y/Ho, Zr/Hf, and lanthanide tetrad effect. Contrib Mineral Petrol 123: 323–333.

Dorr JVN II (1969) Physiographic, stratigraphic and structural development of the Quadrilátero Ferrífero, Minas Gerais: U. S. Geological Survey Professional Paper 641-A, 110p.

Ferreira-Santos NB, Rosière CA (2004) Generations of carbonates in the dolomitic itabirites of the Cauê Formation, Quadrilátero Ferrífero. In: Proceedings of the 32nd Internat. Gelogical Congress, Resumos. IGC, Florença.

Herz N (1978) Metamorphic rocks of the Quadrilátero Ferrífero, Minas Gerais, Brazil. U.S.Geological Survey Professional. 641C, 78 p.

McLennan SB (1989) Rare earth elements in sedimentary rocks. Influence of provenance and sedimentary processes. In: Lipin, B.R., McKay, G.A. (Eds.), Geochemistry and Mineralogy of the Rare Earth Elements. Mineral Soc. Am, Washington, pp. 169–200.

Planavsky N, Bekker A, Rouxel OJ, Kamber B, Hofmann A, Knudsen A, Lyons TW (2010) Rare earth element and yttrium compositions of Archean and Paleoproterozoic Fe formations revisited: New perspectives on the significance and mechanisms of deposition. Geochimica et Cosmochimica Acta 74(22): 6387-6405.

Rollinson HR (1993) Using geochemical data: evaluation, presentation, interpretation. Harlow: Longman, pp133-150.

Rosière CA, Sanglard J, Sabadini R, Hensler AS, Hagemann SG, Santos JOS, McNaughton N, Fletcher IR (2013) Iron mineralization in the Quadrilátero Ferrífero: Structural Control, Age and Mineral-Chemical Changes. In: 12th SGA Biennial Meeting, Uppsala: this volume.

Rosière et al (2008) The Itabirites of the Quadrilátero Ferrífero and Related High Grade Iron Ore Deposits: An Overview. SEG Reviews. 15, chapter 9.

Rosière CA, Rios FJ (2005) Specularitic Iron Ores and Shear Zones in the Quadrilátero Ferrífero District. Iron Ore Conference, Fremantle, WA, 19-21.

Rosière CA, Rios FJ (2004) The origin of hematite in high-grade iron ores based on infrared microscopyand Fluid inclusion studies: the example of the Conceição Mine, Quadrilátero Ferrífero, Brazil. Econ. Geol. 99: 611-624.

Rosière CA, Siemes H, Quade H, Brokmeier HG, Jansen EM (2001) Microstructures, textures and deformation mechanisms in hematite. Journal of Structural Geology, 23: 1429-1440.

Spier CA, Oliveira SMB, Sial AN, Rios FJ (2007) Geochemistry and genesis of the banded iron formations of the Cauê Formation, Quadrilátero Ferrífero, Minas Gerais, Brazil. Precambrian Research 152: 170-206.

Spier CA, Oliveira SMB, Rosière CA (2003) Geology and geochemistry of the Águas Claras and Pico Iron Mines, Quadrilátero Ferrífero, Minas Gerais, Brazil. Mineralium Deposita 38: 751–774.

Suckau VE, Suita MTF, Zapparolli AC, Spier CA, Ribeiro DT (2005) Transitional pyroclastic, volcanic-exhalative rocks to iron ores in the Cauê Formation, Tamanduá and Capitão do Mato Mines: An overview of metallogenetic and tectonic aspects. In: Simpósio do Cráton de São Francisco, III, Companhia Bahiana de Pesquisa Mineral/Universidade Federal da Bahia/Sociedade Brasileira de Geologia, Salvador, Anais, p. 343–346.

Regolith geochemistry of the Mbalam iron ore, southeast Cameroon – an emerging iron ore province

Nforba Melvin Tamnta
Department of Earth Science, University of Yaoundé I, BP Yaoundé, Cameroon, nforbamel@gmail.com

Suh Emmanuel Cheo
Economic Geology Unit, Department of Geology, University of Buea, PO Box 63 Buea, Cameroon

Kamgang Veronique Kabeyene Beyala
Higher Teacher's Training College, University of Yaounde 1, P.O. Box 8127, Yaounde, Cameroon.

Abstract.
Mbalam is a major emerging iron ore district in Cameroon within the Congo craton. This region within the equatorial Africa is dominated by regolith terrain with deep weathering. This study seeks to establish the geochemical signature of the mineralised system in the weathered itabirite at Mbalam, Southeastern Cameroon. The vast majority of the regolith dominated terrains in equatorial Africa have accommodated little to no exploration activities or research. The lack of research or little exploration activities form the bases of this work. The regolith over the Mbalam itabirite, consists of relict, erosion and depositional units. Itabirite rock fabric is preserved in the relict regolith, the erosion unit is marked by erosion of the carapace cap regolith, with the depositional unit dominated by canga (loose fragments of hematite and/or itabirite cemented by goethite) or loose scree. Fe concentration (Table 1) increases from average of 46.18 wt% in the depositional soil material to as much as 69.08 wt% in the relict regolith regime with variation due to supergene weathering. Fe is the least mobile of the major elements, and the Fe oxides become significant phases and control the distributions of many elements. Absorption of P by iron oxides or oxyhydroxides appears to be the major mechanism of P retention in the different regolith environment. Au dispersion in the weathering profile occurs by two possible mechanisms (mechanical and hydromorphic) and it distribution is sporadic. Zr maintains a positive correlation with Al and Ti indicating extensive chemical weathering in the source area (Mbalam itabirite) and resulting in a relative concentration of those residual elements in the weathered material. The weathered material show relatively high ΣREE.

Keywords: Mbalam, Cameroon, Regolith, itabirite, Geochemistry

1 Introduction -Mbalam Iron ore deposit

Banded Iron Formation is the most important source of iron ore today. It occurs on all continents and it iron content can be significant if not essential for its economic value. Geochemistry is an essential component in most modern integrated mineral exploration programs. It has taken on an increasingly significant role in recent years. The greenstone belts of the Congo craton, Central West Africa host numerous Archaean gold, nickel/manganese/Cobalt (all being explored as a single project close to the study area: www.geovic.net) and iron ore deposits. These deposits are typically found in complex geological structures associated with crustal scale shear zones. In this respect they have structural similarities with many other commercial mineral deposits or areas where similar deposits are found (Milesi et al., 2006; Oliveira et al., 2006). The Mbalam iron ore district is host to over 4.8Bt of iron ore (www.sundanceresources.com.au). The main ore is hematite while the protolith is itabirite. It is located on the northwest edge of the Congo Craton, where it is overthrusted by rocks of the Pan African (late Proterozoic) Central African Fold Belt (Toteu et al. 1994, Toteu et al. 2006). Previous studies in this area have focused on the tectonic evolution of the area (Toteu et al., 2006, Ngako et al., 2008, Milesi et al., 2006), with no attention to the economic potential. This study therefore seeks to highlight the economic potential of this area and the subregion.

Global interest in iron deposits has reached new levels. This is partly due to the high demand for steel in the emerging economies of Asia. In the last five years before 2008, the demand for high-grade iron ore derived from banded iron formation increased. This was motivated by the high demand from Chinese steel mills needing large volumes of iron ore. Meeting this increasing demand is steadily becoming difficult and new research in locating more iron ore deposits especially in Africa has become a critical part of this effort. The use of regolith geochemistry will play an increasingly important role in mineral exploration in this region.

The Mbalam study area (Fig. 1) lies between longitude $02^0$13'21.4"N and latitude $13^0$48'57.6"E, in the equatorial forest belt characterised by humid equatorial climate. Geologically, the itabirite of the Mbalam region form part of the Mbalam Series, an Archean greenstone belt composed of chlorite sericite or amphibolite schists, pyroxene-bearing amphibolites and serpentinites which have been dated at 2850 Ma (Milesi et al., 2006). Lateritic Co-Ni-Mn mineralization is developed on the serpentinised peridotites located about 1000km due north of the study area (www.geovic.net).

2 Mbalam Regolith Geochemistry

The Mbalam regolith/soil developed over the itabirite is made up of three major regimes: relict regime dominated by hematite, goethite, kaolinite and gibbsite. The relict regime shows strong leaching with preservation of primary texture or relict lamination. Results from chemical analysis shows that quartz which is an essential component of the Mbalam itabirite (Fig. 2) weathers very fast and only appears as disseminated minor components in the relict regime (mostly at plateau highs). The erosional regime on the Mbalam slopes

typically shows a vermicular to massive and/or friable biscuit-like texture rich in hematite, goethite and kaolinite (Fig.3). The depositional portions are dominated canga or loose scree with patches of silcrete.

The different regimes have similar contents of trace elements and are enriched in Y, Zr, Nb, Hf, Ta, Th and U compared to the Mbalam itabirite. These elements are associated with heavy minerals, such as zircon, which is resistant to weathering. The regolith shows Sc, Cu, and V contents similar to, or even above, abundances for Upper Crust. However, they are depleted in Zn, Ni, Cr, Co, Rb, Sr as well as in Cs and Ba contents (Table 1 & Fig 4a-c). Generally those elements are associated with clay minerals, and their low values could be attributed to low values in parent itabirite and the high quartz content. This also shows that the Mbalam regolith regimes are rich in clay (kaolinite and gibbsite) minerals.

The Mbalam profile shows enrichment in REE (Table 1 & Fig. 5) when compared with the itabirite protolith rock. This can equally be interpreted as largely due to the residual enrichment of immobile minerals zircon, phosphates, titanate and apatite. The enrichment in these elements (Table 1) implies that they easily mobilized from the bottom of the profile. Their enrichment results from their remobilization and upward transportation after dissolution of the primary bearing minerals and the downward leaching of the upper mineralized horizons by the descending epigenetic solutions or supergene modification.

3 Conclusion and Recommendations

The investigation of the regolith material indicates that there has been significant leaching of metals and distribution of remaining geochemical signatures into Fe oxides. Hematite and goethite are the major host to major elements.

Exploration in Central Africa has entered its mature phase and future discoveries of large deposits at greater depths will depend on focussed exploration programs where there is little or no exposure of Archaean geology. Consequently the traditional prospecting will have to be complimented with smart, effective and efficient exploration techniques. The use of regolith geochemistry will play an increasingly important role in mineral exploration. However these techniques need to be in turn complimented by other applicable techniques.

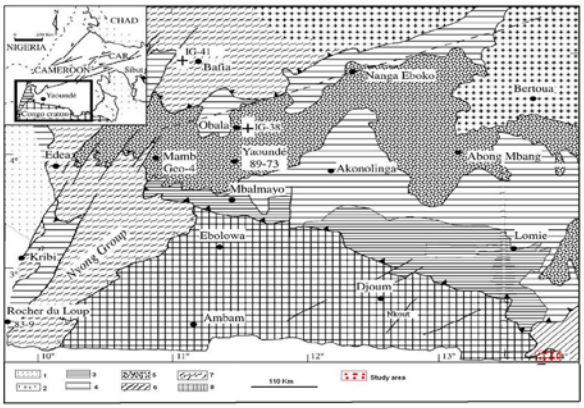

Figure 1: Geological Sketch map of the southern Cameroon (modified from Toteu et al. 2006) showing the study area. (1) Coastal Cenozoic basin, (2) Pan-African granitoids; Yaounde Group with (3) Low-grade schists, (4) medium-grade schists, (5) high-grade gneisses and granulites, (6) schisto-doleritic complex, (7) high-grade Paleoproterozoic or assumed gneisses (Nyong and Bafia Group), (8) Archaean Congo craton. Insert: Location of the studied area in the central African fold belt (white).

Table1: Average major, trace and REE composition of itabirite (MB=6), Relict (MR=12, Erosion (ME=12) and Deposition (MD=12) soil samples from Mbalam regolith.

	DL	MB	MR	ME	MD
Major & minor oxides (wt %)					
SiO_2	0.01	37.40	8.32	11.60	36.79
TiO_2	0.01	0.03	0.22	0.51	0.35
Al_2O_3	0.01	1.08	6.84	18.48	9.68
Fe_2O_3	0.04	60.36	69.08	57.39	46.18
MnO	0.01	0.02	0.01	0.01	0.09
MgO	0.01	0.04	0.01	0.01	0.04
CaO	0.01	0.02	0.02	0.01	0.02
Na_2O	0.01	0.01	0.02	0.01	0.03
K_2O	0.01	0.10	0.08	0.02	0.28
P_2O_5	0.01	0.09	0.20	0.26	0.13
Cr_2O_3	0.00	0.04	0.03	0.03	0.04
LOI	-5.10	0.73	5.07	11.53	6.23
TOT/C	0.02	0.01	0.16	0.15	0.13
TOT/S	0.02	0.01	0.02	0.03	0.02
Rare earth elements (ppm)					
La	0.10	2.88	18.66	35.19	11.69
Ce	0.10	4.65	35.75	68.26	35.59
Pr	0.02	0.64	4.23	7.88	2.68
Nd	0.30	2.62	16.66	30.23	10.68
Sm	0.05	0.69	3.11	5.22	1.97
Eu	0.02	0.44	0.92	1.18	0.59
Gd	0.05	1.04	2.97	4.29	1.80
Tb	0.01	0.19	0.48	0.63	0.30
Dy	0.05	1.25	2.52	3.17	1.66
Ho	0.02	0.29	0.48	0.56	0.32
Y	0.10	10.87	13.62	14.73	8.98
Er	0.03	0.91	1.30	1.45	0.92
Tm	0.01	0.16	0.19	0.23	0.15
Yb	0.05	0.89	1.20	1.55	0.98
Lu	0.01	0.15	0.18	0.24	0.16
Trace elements (ppm or ppb)					
Ag	0.10	0.13	0.24	0.63	0.19
As	0.50	0.73	5.75	7.20	3.88
Au	1.00	2.83	1.58	0.83	1.57
Ba	1.00	154.17	73.42	69.83	216.58
Be	1.00	1.08	1.21	0.50	0.71
Bi	0.10	0.05	0.22	0.31	0.23
Cd	0.10	0.05	0.05	0.05	0.05
Co	0.20	1.75	1.95	1.73	5.08
Cs	0.10	0.21	0.30	0.12	0.42
Cu	0.10	4.13	10.13	13.37	37.78
Ga	0.50	1.59	8.07	18.53	12.28
Hf	0.10	0.21	2.41	7.00	2.68
Hg	0.01	0.01	0.09	0.17	0.04
Mo	0.10	0.30	1.72	2.44	1.55
Nb	0.10	0.45	5.10	12.57	4.58
Ni	0.10	3.75	5.86	3.66	10.72
Pb	0.10	0.58	6.22	7.55	12.32
Pd	0.50	0.25	0.72	1.48	0.76
Pt	0.10	0.23	1.75	1.10	2.79
Rb	0.10	2.03	2.57	0.89	6.78
Sb	0.10	0.05	0.33	0.43	0.17
Sc	1.00	1.42	11.08	15.67	18.33
Se	0.50	0.29	0.30	0.53	0.45
Sn	1.00	0.50	0.96	2.21	0.88
Sr	0.50	31.75	29.24	39.00	12.48
Ta	0.10	0.05	0.31	0.88	0.29
Th	0.20	0.28	5.09	13.42	4.58
Tl	0.10	0.05	0.05	0.05	0.05

	DL	MB	MR	ME	MD
U	0.10	0.36	2.38	2.79	1.66
V	8.00	13.33	116.50	193.25	211.25
W	0.50	1.48	2.68	6.58	1.77
Zn	1.00	2.00	7.08	7.92	20.50
Zr	0.10	7.28	92.36	249.46	99.12

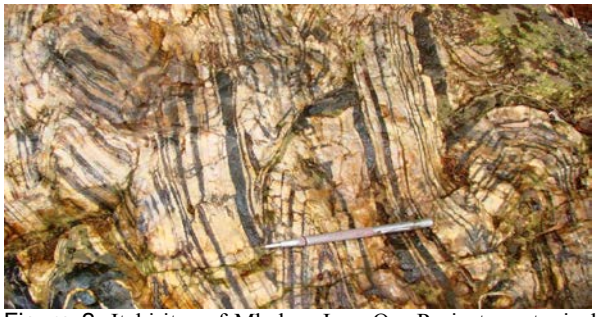

Figure 2: Itabirites of Mbalam Iron Ore Project are typically gray-brown to dark grey in colour, show pronounced bands and or laminations of iron oxides and silica, and have been tightly folded with subvertical plunge of the fold axis.

Figure 3: High grade enriched soft laminated (biscuity) supergene ore (Direct shipment Ore -DSO) at Mbalam. DSOs are limited or related to a very well defined plateau with deep soil and areas of laterite development.

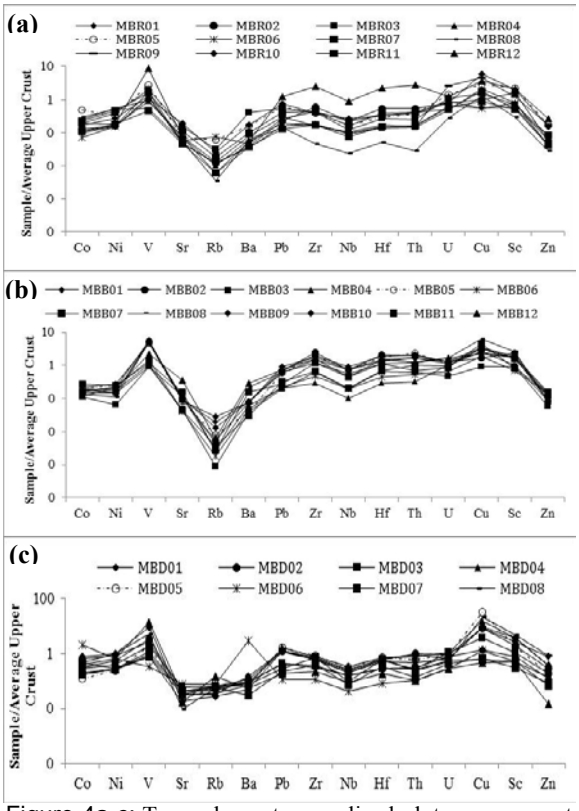

Figure 4a-c: Trace element normalized plots or representative samples from the different regolith soil regimes (a-Relict, b-Erosion & c-Deposition) relative to Average Upper Crust (Taylor & McLennan, 1995)

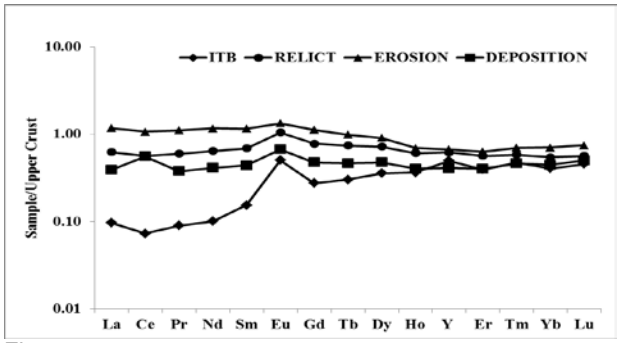

Figure 5: Rare earth element plots of regolith samples normalized to Upper Crust after Taylor and McLennan (1984).

Acknowledgements

This presentation is part of PhD thesis on regolith geochemistry applied to mineral exploration at the University of Yaoundé I by NMT. This work is part of a collaborative work between the University of Yaounde I and the Univeristy of Buea under the frame work of research on "The Precambrian mineral belt of Cameroon". The presentation benefited from reviews by Thomas Angerer.

Selected References

Horbe A. M. C. and da Costa, M.L (2005) Lateritic crusts and related soils in the eastern Brazilian Amazonia. Geoderma 126: 225-239.

Lerouge C., Cocherie A., Toteu S.F., Penaye J., Milesi J.P., Tchameni R., Nsifa E.N., Mark Fanning C., and Deloule E. (2006) Shrimp U-Pb zircon age evidence for Paleoproterozoic sedimentation and 2.05 Ga syntectonic plutonism in the Nyong Group, South-Western Cameroon: consequences for the Eburnean – Transamazonian belt of NE Brazil and Central Africa. Journal of African Earth Sciences **44**: 413 – 427.

Milesi, J.P., Toteu, S.F., Deschamps, Y et al (2006) An overview of the geology and major ore deposits of Central Africa: Explanatory note for the 1:4,000,000 map "Geology and major ore deposits of Central Africa". Journal of African Earth Sciences, **44**:571-595.

Nesbitt, H.W., and Young, G.M., (1996) Petrogenesis of sediments in the absence of chemical weathering: effects of abrasion and sorting on bulk composition and mineralogy. Sedimentology 43:341-358.

Nyakairu, G.W.A. and Koeberl, C., (2001) Mineralogical and chemical composition and distribution of rare earth elements in clay-rich sediments from central Uganda. Geochemical Journal 35: 13-28.

Oliveira, E.P., Toteu S.F., Arau´jo, M. N.C., Carvalho, M.J., Nascimento, R.S., Bueno, J.F., McNaughton, N., Basilici, G. (2006): Geologic correlation between the Neoproterozoic Sergipano belt (NE Brazil) and the Yaounde´ belt (Cameroon, Africa). Journal African Earth sciences, 44: 470-478.

Taylor, S.R. and McLennan, S.H. (1985) The Continental Crust: Its composition and evolution. Blackwell, Oxford.

Tsaléfac M., (2007) Climate. In Atlas of Cameroon (eds. N. Houstin and C. Seignobos), Les Éditions Jeune Afrique, Paris

Toteu S.F., Fouateu R.Y., Penaye J., Tchakounte J., Mouangue A.C.S., Van Schmus W.R., Deloule E., and Stendal H. (2006) U-Pb dating of plutonic rocks involved in the nappe tectonic in southern Cameroon: consequence for the Pan African orogenic evolution of the central African fold belt. Journal of African Earth Sciences **44**:479 – 493.

www.sundanceresources.com.au

www.geovic.net

REE+Y chemistry of iron oxides from BIFs and hosted Fe high-grade ores from the Esperança deposit, Quadrilátero Ferrífero, Brazil – first results

Lucilia Aparecida Ramos de Oliveira, Carlos Alberto Rosière
Instituto de Geociências, Universidade Federal de Minas Gerais (UFMG), Presidente Antonio Carlos Av. 6627, Belo Horizonte, Brazil

Francisco Javier Rios
Centro de Desenvolvimento da Tecnologia Nuclear (CDTN/CNEN), Presidente Antonio Carlos Av. 6627, Belo Horizonte, Brazil

Sandra Andrade, Renato de Moraes
Instituto de Geociências, Universidade de São Paulo, R. do Lago 562, São Paulo, Brazil

Abstract. High-grade iron ore REE-Y patterns from the Esperança deposit, northwest Quadrilátero Ferrífero, indicate that polycyclic processes probably took place during iron enrichment. At least two different types of hard iron ore are found: the first is a compact rock with a breccia fabric and it is likely to have originated from hydrothermal enrichment of dolomitic itabirite, whereas the second has an affinity to quartz itabirite. Long-lasting percolation of hydrothermal fluids and shifting in the redox conditions have depleted the REE-Y content of the hematite from the older to the younger generation (martite → microplaty hematite → specularite).

Keywords. Iron ore, Geochemistry, LA-ICP-MS, Yttrium-Rare Earth Elements.

1 Introduction

The genesis of high-grade iron ore-bodies has been extensively discussed worldwide and different processes are considered to be responsible for the iron enrichment (eg. Dorr 1964, 1965, 1969; Guild 1953, 1957; Eichler 1968; Morris 1980; Hagemann et al. 1999; Powell et al. 1999; Taylor et al. 2001; Rosière and Rios 2004; Hagemann et al. 2005).

In most of the large iron deposits, however, the Fe enrichment seems to be a polyphasic and multistage process involving hydrothermal leaching of gangue minerals (Taylor et al. 2001; Hagemann et al. 2005) and Fe remobilization, forming several Fe-oxide generations that record these different mineralization stages as documented by Rosière and Rios (2004).

The purpose of this work is to contribute to the understanding of the geochemical during mineralization in the Esperança deposit, western Quadrilátero Ferrífero district (QF) and expand the geochemical database published by earlier authors (eg. Klein and Ladeira 2000; Spier et al. 2003, 2007, 2008). New analytical results are presented for rare earth elements and Y (REE-Y) from whole-rock (ICP-ES and ICP-MS) and mineral (LA-ICP-MS) analyses from two different textural types of high-grade iron ore: one is massive and cross-cut by a fibrous tension gash vein, whereas the other contains a partially brecciated rock.

2 Geological Setting of the Quadrilátero Ferrífero

The QF district is located in the central part of Minas Gerais, southeastern Brazil (Fig. 1) where the itabirites of the Cauê banded iron formation (BIF) from the Minas Supergroup host high-grade iron orebodies. Itabirite and orebodies are comprised of older magnetite/martite aggregates and younger granoblastic, microplaty and specular hematite crystals that show a wide variation of fabrics such as massive, compact banded and brecciated.

The Minas Supergroup units were affected by two main orogenic events: the Transamazonian (2.1 - 2.0 Ga) and the Pan-African/Brasiliano (0.8 to 0.6 Ga), that allow the QF to be separated into two main structural domains: a western low-strain domain and an eastern high-strain domain (Rosière et al. 2001).

3 Esperança Deposit

The Esperança deposit is located in the northwest of the QF, in the western branch of the Serra do Curral Ridge (Fig. 1). In this middle-sized deposit, high-grade iron ore occurs as a massive body embedded in dolomitic itabirite (DI). Quartz itabirite (QI) also occurs in the deposit but not in direct contact with the ore.

The regional structure is controlled by NE-SW trending folds and related thrusts, which formed during the first tectonic event. A second group of NNW-SSE trending folds partially overlap the NE-SW trending folds (Sanglard et al. 2011). According to these authors the structural arrangement led to the development of open spaces and strain gradients that allowed the circulation of fluids responsible for the hydrothermal alteration and mineralization of the BIF.

The relatively small size of the orebody allows distinguishing a carbonate hydrothermal alteration zone that is characterized by the presence of several veins comprised of carbonate, quartz and iron oxide, minor amounts of silicates such as chlorite, amphiboles, stipnomelane and rare sulfides. Massive Fe-oxide veins also crosscut from the itabirite layer into the upper stratigraphic sequence.

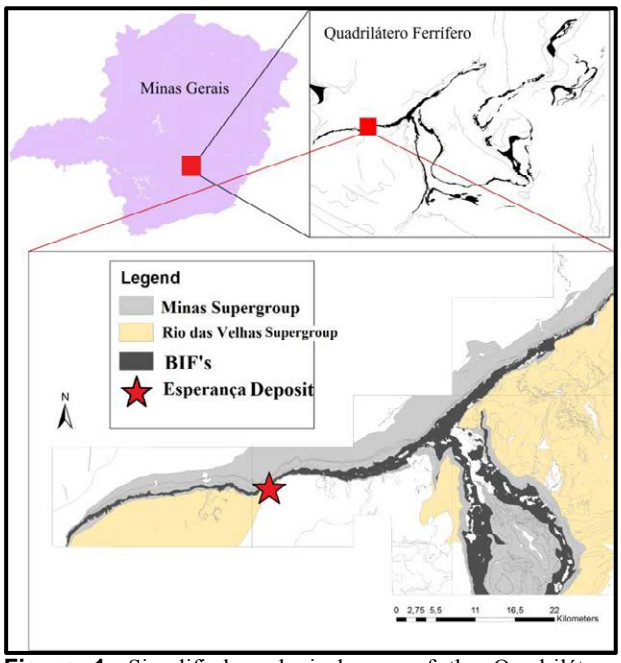

Figure 1. Simplified geological map of the Quadrilátero Ferrífero highlighting the location of Esperança deposit.

4 Whole Rock Geochemistry

Four fresh samples of quartz itabirite (QI), dolomitic itabirite (DI) and high grade hard iron ore (HIO1 and HIO2) were analyzed (Figs. 2, 3 and 4).

4.1 Quartz and dolomitic BIF (itabirite)

The QI is a fine-grained folded and banded rock, comprised of quartz and iron oxide (martite/magnetite) layers with lesser carbonate and amphibole as accessory minerals. Several mm and cm-thin quartz and talc veins also cut the folded iron oxide bands (Figs. 2A and 2B).

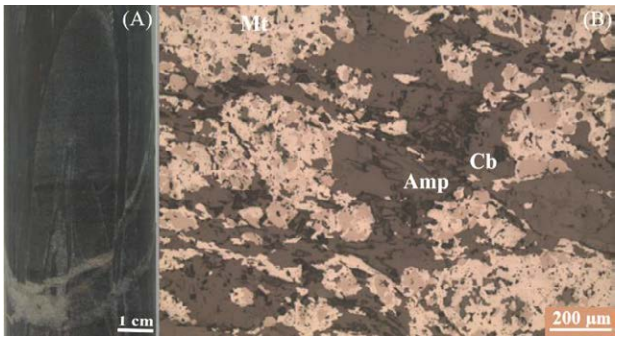

Figure 2. Quartz itabirite. (A) Hand specimen. (B) Elongated aggregates of martite (Mt), amphibole (Amp) and carbonate (Cb) with oriented platy hematite crystals. Photomicrograph, partially polarized, reflected light.

The DI is also fine-grained and banded, with alternating gray to red (mainly dolomite) and dark (martite/kenomagnetite) layers. Accessory minerals are quartz, amphibole and chlorite. A discordant vein with carbonate (calcite-dolomite), quartz and specularite cut the banding. Specularite is fibrous and crystallizes syntaxially perpendicular to the vein wall, whereas the rock layers seem to continue into the vein (Figs. 3A and 3B).

The whole rock major oxide elements chemistry of DI and QI are similar to those reported by Spier et al. (2007). The QI contains 68.19% SiO_2, 22.75% Fe_2O_3, 2.46% CaO and 2.84% MgO. The Al_2O_3, Na_2O, K_2O, P_2O_5, TiO_2, MnO and Cr_2O_3 content are all lower than 0.5%. The DI contents are 16.49% CaO, 10.94% MgO, 42.04% Fe_2O_3, 2.31% SiO_2, 0.69% Al_2O_3 and 0.62% MnO. The Na_2O, K_2O, P_2O_5, TiO_2, and Cr_2O_3 contents are lower than 0.5%.

Both rock types show REE-Y patterns very similar to those found in other Proterozoic BIFs worldwide, with ratios $(La/Sm)_{CN}$ and $(Eu/Sm)_{SN}$ higher than 1, and ratio $(Sm/Yb)_{SN}$ lower than 1; whereas QI is more depleted than the dolomitic rock exhibiting lower ΣREE (Fig. 5). They are all depleted in light REE relative to heavy REE (Pr/Yb > 1) and have prominent positive Y and Eu anomalies (Bau and Dulski 1996).

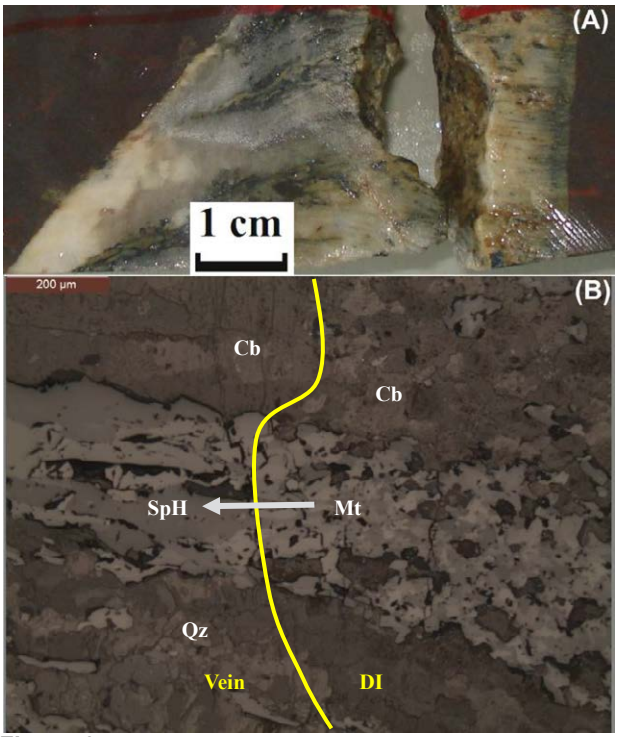

Figure 3. Dolomitic itabirite (DI) cut by a syntaxial fibrous vein. (A) Hand specimen vein, (B) Fibrous carbonate, and hematite crystals show syntaxial growth in continuity with the wall rock. Yellow line indicates the edge of the vein. Mt – martite; Cb – carbonate; SpH – specularite; Qz – quartz. Photomicrograph, partially polarized, reflected light.

4.2 High grade hard iron ore

The analyzed high grade hard iron ore (HIO) samples have a very simple mineralogical composition and are mainly comprised of hematite/martite. Both samples are extremely iron rich (99.64% Fe_2O_3 for HIO1 and 98.45% Fe_2O_3 for HIO2) with very low contents of SiO_2, CaO, MgO, Al_2O_3, Na_2O, K_2O, P_2O_5, TiO_2, MnO and Cr_2O_3 (< 0.5%). The textural features and REE-Y signatures of both samples however are very distinctive and may indicate different host rocks (Figs. 4 and 5).

Sample HIO1 is compact with a brecciated fabric comprised by fine-grained aggregates of hematite/martite (~90 vol%) and relicts of kenomagnetite (Figs. 4A and 4B). Fine microplaty

hematite occurs in the interstices of martite aggregates. Elongated coarse platy hematite crystals (specularite) fill micro-fractures.

Sample HIO2 is massive, homogeneously fine grained and comprised of kenomagnetite and martite. It is cut by a tension gash vein filled with syntaxially grown fibrous specularite and quartz (Figs. 4C and 4D).

Both samples, HIO1 and HIO2, contain slightly higher ΣREE than the hard high-grade ores from the Águas Claras deposit (Spier et al. 2008) with a light to heavy REE depletion. Sample HIO1 has a positive Y and Eu anomalies, whereas HIO2 has Eu/Eu* ~ 1 and a distinguishable negative Nd anomaly (Fig. 5A).

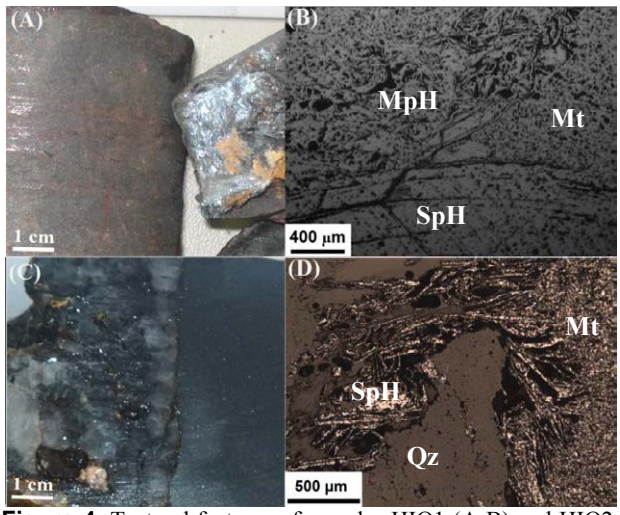

Figure 4. Textural features of samples HIO1 (A-B) and HIO2 (C-D). B and D: Photomicrographs, partially polarized reflected light. Mt – martite; MpH – microplaty hematite; SpH – specularite; Qz – quartz.

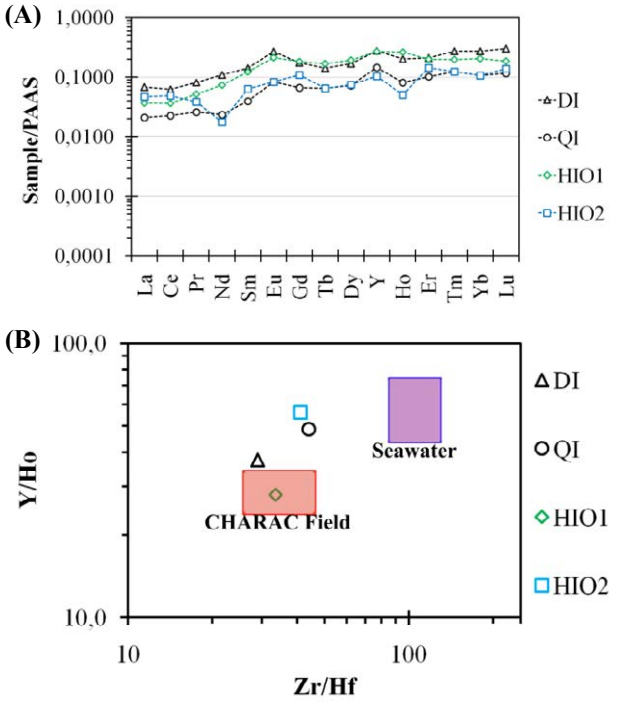

Figure 5. (A) REE-Y spidergrams based on whole-rock ICP-MS data from samples quartz itabirite (QI), dolomitic itabirite (DI) and hard iron ore (HIO1 and HIO2), PAAS normalized according to MacLennan (1989). (B) Y/Ho vs Zr/Hf diagram (Bau 1996) CHARAC: Charge-and-Radius-Controlled Field.

5. Trace element chemistry of the iron oxide species (LA-ICPMS)

The average values of ΣREE were very low for all analyzed iron oxides from DI, HIO1 and HIO2. They show a general LREE/HREE depletion, similar to that observed in whole rock analyses (Fig. 6A). The REE content of martite grains is higher than the younger hematite generations (microplaty and specularite).

Nearly all crystals have a positive Eu anomaly with the exception of martite grains from sample HIO2 where Eu/Eu* ~1.00. In contrast, a positive Y anomaly is observed only in the iron oxides from DI. The calculated values for Ce anomaly vary widely in the plot $(Ce/Ce^*)_{SN}$ vs $(Pr/Pr^*)_{SN}$ (Fig 6B): microplaty hematite from HIO1 and specularite from HIO2 show distinctive positive Ce anomalies, different from the iron oxide from the DI that fall in the field of true negative values.

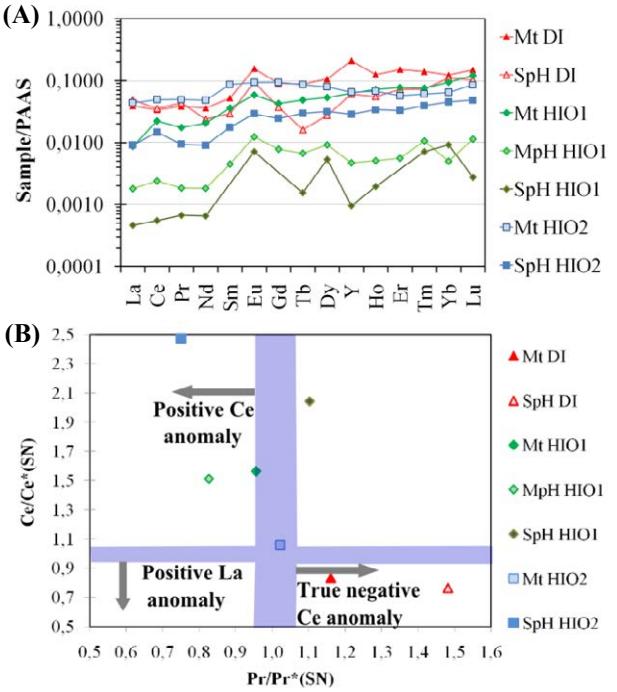

Figure 6. (A) Y-REE spidergrams based on LA-ICPMS data from the different iron oxide generations, PAAS normalized according to MacLennan (1989). (B) $(Ce/Ce^*)_{SN}$ vs $(Pr/Pr^*)_{SN}$ (Bau and Dulsky 1996).

6 Concluding remarks

In the Esperança deposit high-grade iron ores are hosted mainly by DI and to a lesser extent by QI. Whole rock REE-Y patterns for both rocks are very similar to those published by Spier et al. (2007). The sample HIO1 sample shows REE-Y pattern similar to the dolomitic itabirite-hosted iron ore of the Águas Claras deposit (Spier et al. 2008). Nevertheless, the sample HIO2 sample shows a slightly different whole rock REE-Y pattern, similar to the QI, except for the negative Nd anomaly and a relative enrichment of LREE (Fig. 5A).

The Y/Ho vs Zr/Hf diagram (Fig. 5B) indicates a fractionation of the Y/Ho system with values that vary from near-chondritic (CHARAC - Charge-and-Radius-Controlled Field) for the DI and the HIO1 samples to

hyper-chondritic for the QI and the HIO2 samples, whereas the range for the Zr/Hf ratios is much narrower, falling between the values of the CHARAC-field.

As a preliminary result it is evident that the younger iron oxides generations are depleted in REE-Y when compared to martite. This depletion is interpreted to be the result of long-lasting percolation of hydrothermal fluids. Nevertheless, a heterogeneous behavior is also evident for different groups of REE during hydrothermal alteration and BIF Fe enrichment. Although the general REE whole rock patterns and the relative content of immobile elements such as Y, Ho, Hf and Zr have undergone little variation during the mineralization, LREE and redox-sensitive elements such as Ce may show very distinctive changes. These changes reflect a hydrothermal system by abrupt changes in the redox conditions, probably due to fluid mixing during the precipitation of each iron oxide generation.

Acknowledgements

The financial support and infrastructure for this PhD study have been provided by UFMG, CNEN/CDTN, FAPEMIG, CNPq (projects CAG PPM00666-11 and 307546/2011-0), ETH-Zurich and FCS-Switzerland.
The authors thank the Ferrous Resources for providing full access to geological information.
Whole rock analyses were accomplished by the ACME Analytical Laboratories and mineral-chemistry analyses were accomplished at the ICP-AES/MS Lab from the Universidade de Sao Paulo, Brazil.

References

Bau M, Dulski P (1996) Distribution of yttrium and rare-earth elements in the Penge and Kuruman iron-formations, Transvaal Supergroup, South Africa. Precambrian Res 79:37-55.

Bau M (1996) Controls on the fractionation of isovalent trace elements in magmatic and aqueous systems: evidence from Y/Ho, Zr/Hf, and lanthanide tetrad effect. Contrib Mineral Petrol 123:323-333.

Dorr JVN (1964) Supergene Iron Ores of Minas Gerais, Brasil. Econ Geol 59:1203-1239.

Dorr JVN (1965) Nature and Origin of the High Grade Hematite Ores of Minas Gerais, Brazil. Econ Geol 60(1):1-46.

Dorr JVN (1969) Physiographic, Stratigraphic and Structural Development of the Quadrilátero Ferrífero, Minas Gerais. U S Geol Surv Prof Pap 641-A 110p.

Eichler JO (1968) Enriquecimento Residual e Supergênico dos Itabiritos Através do Intemperismo. Geol I:29-40.

Guild P W (1953) Iron deposits of the Congonhas District, Minas Gerais, Brazil. Econ Geol 48:639 – 676.

Guild P W (1957) Geology and Mineral Resources of the Congonhas District, Minas Gerais, Brazil. U S Geological Surv Prof Pap 290 90p.

Hagemann SG, Barley ME, Folkert SL, Yardley BW, Banks DA (1999) A Hydrothermal Origin for the Giant Tom Price Iron Ore Deposit. In: Hughes FE (ed) Mineral Deposits, Process to Processing. Balkema, pp 41-44.

Hagemann SG, Rosière C A, Lobato LM, Baars FJ, Zucchetti M, Figueiredo e Silva RC, Thorne W (2005) Controversy in Genetic Models for High-Grade BIF-related Fe Deposits: Unifying or Discrete Model(s)? Iron Ore 2005, The Australasian Institute of Mining and Metallurgy, Publication Series No 8/2005, Perth, Austrália, pp 67-71.

Klein C, Ladeira EA (2000) Geochemistry and Petrology of Some Proterozoic Banded Iron-Formations of the Quadrilátero Ferrífero, Minas Gerais, Brazil. Econ Geol 95:405-428.

McLennan SB (1989) Rare earth elements in sedimentary rocks. Influence of provenance and sedimentary processes. In: Lipin BR, McKay GA (eds) Geochemistry and mineralogy of the rare earth elements. Mineralogical Society of America, Washington, pp 169–200.

Morris RCA (1980) Textural and Mineralogical Study of the Relationship of Iron Ore to Banded Iron Formation in the Hamersley Iron Province of Western Australia. Econ Geol 75:184–209.

Powell McAC, Oliver N, Li ZX, Martin McBD, Ronaszeki J (1999) Synorogenic Hydrothermal Origin for Giant Hamersley Iron Oxide Ore Bodies. Geol 27(2):175-178.

Rosière CA, Siemes H, Quade H, Brokmeier HG, Jansen E (2001) Microstructures, textures and deformation mechanisms in hematite. Journal of Structural Geology 23(8):1429-1440.

Rosière C A, Rios F J (2004) The Origin of Hematite in High Grade Iron Ores Based on Infrared Microscopy and Fluid Inclusion Studies: The Example of the Conceição Mine, Quadrilátero Ferrífero, Brazil. Econ Geol 99:611-624.

Sanglard J, Rosière CA, Suckau VE, Amaral U, Meireles H (2011) The structure of the western Serra do Curral Range, QuadriláteroFerrífero and the tectonic control of the high-grade Fe-orebodies. In: 11th SGA Biennial Meeting, Antofagasta, pp 879-881.

Spier CA, Oliveira SMB, Rosière CA (2003) Geology and geochemistry of the Águas Claras and Pico iron mines, Quadrilátero Ferrífero, Minas Gerais, Brazil. Miner Depos 38:751–774.

Spier CA, Oliveira SMB, Sial AN, Rios FJ (2007) Geochemistry and genesis of the banded iron formations of the Cauê Formation, Quadrilátero Ferrífero, Minas Gerais, Brazil. Precambrian Res 152:170–206.

Spier CA, Oliveira SMB, Rosière CA, Ardisson JD (2008) Mineralogy and trace-element geochemistry of the high-grade iron ores of the Águas Claras Mine and comparison with the Capão Xavier and Tamanduá iron ore deposits, Quadrilátero Ferrífero, Brazil. Miner Depos 43:229-254.

Taylor D, Dalstra HJ, Harding AE, Broadbent GC, Barley ME (2001) Genesis of High-Grade Hematite Orebodies of the Hamersley Province, Western Australia. Econ Geol 96:837-873.

Iron mineralization in the Quadrilátero Ferrífero: structural control, age and mineral-chemical changes

C. A. Rosière, J. Sanglard, R. Sabadini
Instituto de Geociências, Universidade Federal de Minas Gerais (UFMG), Presidente Antonio Carlos Av. 6627, Belo Horizonte, Brazil

A.-S. Hensler, S.G. Hagemann, J. O. S. Santos
Centre for Exploration Targeting, University of Western Australia, Crawley, WA 6009

N. McNaughton, I. R. Fletcher
Curtin University of Technology, Bentley, WA 6102

Abstract. The high-grade iron ore deposits of the Quadrilátero Ferrífero, Brazil are controlled by the hinge zones of regional NE-SW and NW-SE-trending folds, and associated with blind faults and shear zones developed during the Transamazonian collage (2.034 Ga U-Pb SHRIMP). Mineralization was accompanied by large volume of hydrothermal fluids of still uncertain origin. During the oxidization of magnetite to martite and the formation of new hematite grains, meteoric fluids played an important role resulting in the depletion of ^{18}O in hematite. Specularite associated with late stage shear zones comprise schistose orebodies, formed under higher fluid ratios and with an increased participation of isotopically heavier water, possibly derived from granites of the MIneiro Belt. Fluids were transported via seismic pumping along the tectonic discontinuities leading to enriched ^{18}O in hematite.

Keywords. Structural control, iron mineralization, U-Pb SHRIMP age data, Quadrilátero Ferrífero.

1 Introduction

In most of the large iron deposits, Fe enrichment appears to be a polyphasic process involving leaching of gangue minerals (Taylor et al. 2001; Hagemann et al. 2005) and Fe remobilization, forming several Fe-oxide generations associated with coeval tectonic structures that record different metallogenetic/tectonic stages as documented by Rosière & Rios (2004).

In the Quadrilátero Ferrífero tectonic structures such as blind faults and related folds played an active role controlling the location of the orebodies, their mineralogy and texture and also their microchemical characteristics. In this paper we combine new structural and textural data, geochronological analyses and mineral chemistry in order to present a radical re-interpretation of the Fe-mineralization and its relation with the regional tectonic history.

2 Quadrilátero Ferrífero

The BIF-bearing succession of the Minas Supergroup is located in the southern Sao Francisco Craton covering a large area of the Quadrilátero Ferrífero mining district in Brazil although the outer limits of the basin to the east have presently not been defined due to the overprinting of the Neoproterozoic Brasiliano orogeny (Fig. 1). The lithological record of the 3,700 m thick lower sequence of the Minas Supergroup (Caraça, BIF-bearing Itabira and Piracicaba Groups) has tentatively been interpreted to reflect deposition in either an intracratonic basin (Chemale Jr. et al. 1994) or a passive margin basin (Alkmim and Marshak, 1998).

The Cauê iron formation conformably overlies black metapelites and grades upwards to carbonates of the Gandarela Formation comprising the Itabira Group. The Cauê iron formation contains a single prominent BIF layer, ca. 250 to 300 m thick, which is the host to all high-grade iron ore deposits. The age of deposition of the Itabira Group was constrained by Babinski et al. (1995), who dated stromatolitic carbonate rocks of the Gandarela Formation at 2419 +/- 19 Ma (Pb-Pb isochron data). Based on this upper limit, and considering the U-Pb ages on detrital zircons of the Moeda Fm (Caraça Group), these authors suggested that the deposition of the BIF of the Cauê Formation occurred between 2520 and 2420 Ma, 300 myrs before the Transamazonian collage.

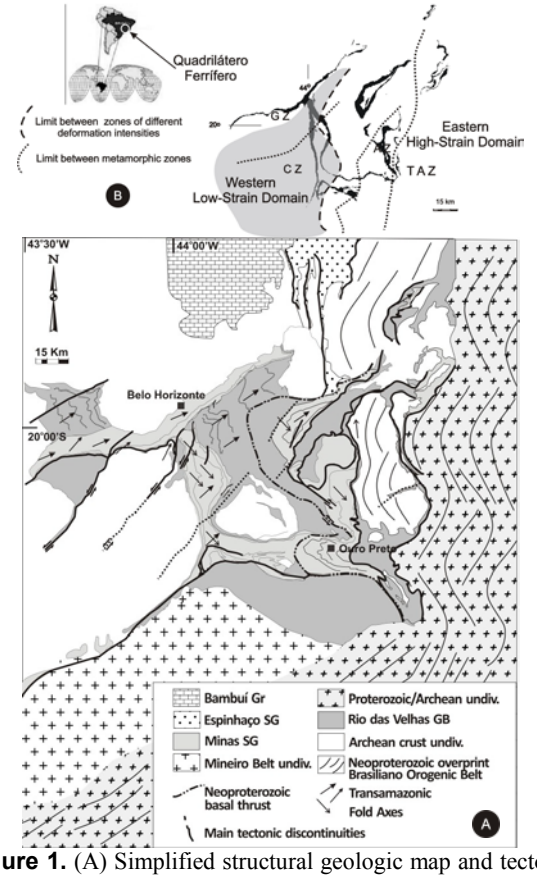

Figure 1. (A) Simplified structural geologic map and tectonic setting of the Quadrilátero Ferrífero and surroundings. (mod. after Dorr, 1969, Teixeira et al, 2000, Ávila et al, 2011). (B) Location of metamorphic and structural domains in the Quadrilatero Ferrifero. Metamorphic zones after Pires (1995): AZ = Actinolite zone, CZ = Cummingtonite zone, GZ = Grunerite zone, TAZ = Tremolite-antophyllite zone. Banded iron formation of the Itabira group is shown in black.

3 Tectonic Setting and Structural Geology

The structural geometry of the Archean Rio das Velhas greenstone belt and the surrounding granite-gneissic bodies have strongly influenced the structural *dome and basin* and large-scale B1–B2 fold interference pattern of the overlying metassedimentary rocks of the Minas Supergroup. Large domal Archean gneissic basement highs appear as "traced" from below, penetrating the overlying supracrustal units and enclosed by wide megasynclines.

The regional cross-fold tectonic pattern of the Minas Supergroup developed during the Transamazonic event and is better observed in the western domain (Rosiere et al. 2008), where the younger structures related to the Brasiliano orogeny (500 Ma) are not conspicuously imprinted. The NE-SW-trending structures (Serra do Curral, Bom Sucesso and Gandarela Synclines) represent the main paleoproterozoic tectonic features; superposed by the approximately NW-SE trending Moeda megasyncline that envelope the gneissic basement domes. The regional tectonic features are associated with flexural and flexural-slip folds (Hippertt et al. 2001) and thrust faults in outcrop up to 100m-scale. In the Serra do Curral Range NE-SW trending folds build Type 3 (Ramsay, 1967) co-axial (Sanglard et al., 2011), and nearly co-axial, oblique interference patterns (Vieira Neri, 2012), whereas metric dome and basin structures are also found at the Gandarela and Moeda synclines. Nevertheless, many structures are disharmonic and have been interpreted in the past as the product of multi-phase fold events (Ladeira and Viveiros 1985).

The Archean granitic bodies have not been affected by folding and acted as rigid bodies, which were locally sheared and uplifted by oblique fault zones with the development of a steep foliation at the contact zone between the gneisses and the supracrustal units (Fig.2). In the eastern domain internal deformation was more intense and most of the primary features of the Minas Supergroup units are thoroughly obliterated, with the flattening of early developed folds and the development of a continuous to anastomosing foliation.

The understanding of the mechanism responsible for the uplift of the rigid granite-gneiss domes giving rise to the tilting of the strata has been subject to controversial interpretations from different authors: Chemale Jr et al. (1994) have interpreted the structures as relic core complex developed during the rift stage. Hippertt and Davis (2000) argued for the Transmazonic compression as the cause of the uplift and Alkmim and Marshak, (1998) postulated a tectonic collapse at the end of the orogeny. This difficulty is partially due to the fact that during the Brasiliano orogeny, major thrusts (e.g., Cambotas-Fundão thrust system - see Chemale Jr. et al, 1994) modified the older megasynclines (e.g., Itabira and João Monlevade synclinoria, and the Santa Rita Syncline). They were probably reactivated, rotated or deformed, bringing foliations of distinct ages and morphologies into parallel arrangement, whereas the gneissic domes were sheared (Chemale Jr. et al., 1994). Splays from the Cambotas–Fundão thrust system have juxtaposed tectonic slices comprised of the Archean (Rio das Velhas Supergroup), Paleoproterozoic (Minas Supergroup), the Mesoproterozoic (Cambotas Formation) and units of undefined age at the eastern border of the Quadrilátero Ferrífero.

4 High-Grade Iron Ore Types

High-grade ores of the QF (typically ≥ 64 wt % Fe), as in other BIF-areas worldwide, are the product of residual concentration of Fe by gangue mineral leaching via combined hypogene and supergene fluids with only subordinated Fe-remobilization (Rosière and Rios, 2004; Spier et al., 2008). The orebodies are usually hard, composed of magnetite/martite, granular and platy hematite and are enclosed by soft, friable, high-grade ore or BIF due to the supergene leaching of residual gangue minerals such as quartz or dolomite. Hard hematite/martite ore may be massive or banded to schistose. Schistose orebodies comprised of elongated platy hematite crystals (specularite) overprint the hematite/martite fabric.

4.1 Structural control of the high-grade orebodies

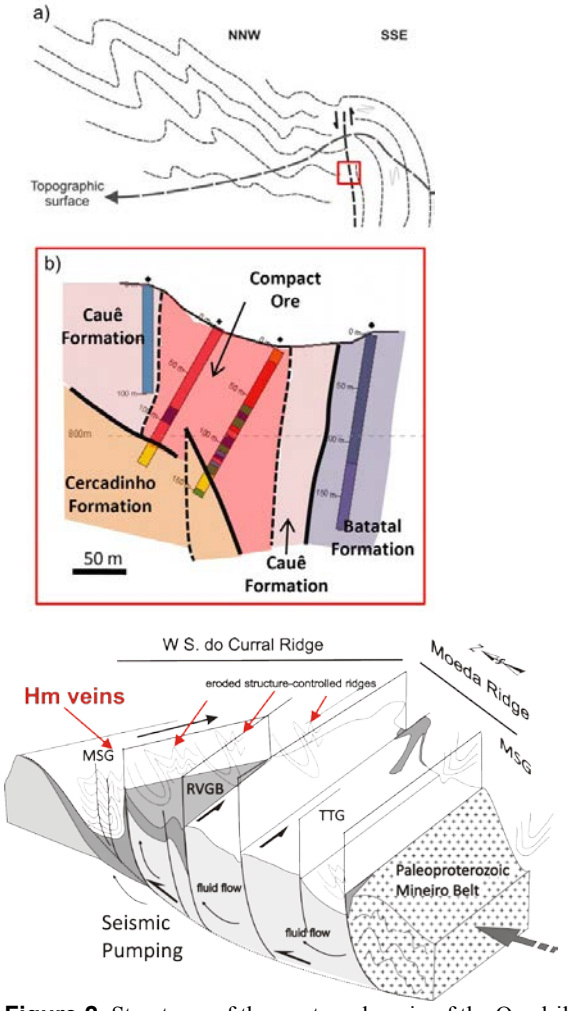

Figure 2. Structures of the western domain of the Quadrilátero Ferrífero. (a and b) schematic representation of the structure of the W Serra do Curral Ridge, (c) Schematic block diagram of the structures of the western domain of the Quadrilátero Ferrífero, with tectonic control of the fluid flux and the position of high-grade iron orebodies. MSG: Minas Supergroup; RVGB: Rio das Velhas Greenstone Belt; TTG: tonalite-trondhjemite-granodiorite terrane.

Hypogene high-grade iron orebodies are controlled by the hinge zone of large folds or by thrusts and strike-slip shear zones commonly parallel to the axial planes of tight folds. The enrichment of iron, in most of the large deposits, develops as a polyphase process, with the formation of several Fe-oxide generations, which record distinct stages of the deformation history.

The structural control of the orebodies is particularly clear in the western structural domain. Here, magnetite-martite middle-sized (~100Mt) orebodies along the western branch of the Serra do Curral Range are controlled by NE-SW trending nearly coaxially superimposed folds in the tip zone of related blind thrusts, overprinted by NNW-SSE trending folds. On the eastern limb of the NW-SE trending Moeda Syncline several large hematite bodies (reserves up to ~ 250Mt with 68wt%Fe) concentrate on second order folds of the regional structure that may locally interfere with each other. One of the largest and richest ore concentrations of the Quadrilátero Ferrífero is located along the Mutuca fault. In the deposits located at the limbs of the Moeda syncline several schistose orebodies are observed, which are genetically related to the massive ore. That is particularly visible in the Pau Branco deposit at the western flank of the Moeda syncline where schistose ore comprised mainly of platy hematite crystals (specularite) represents the lower stratigraphic limit of the high-grade body at the contact with mineralized phyllite of the underlying Batatal Formation. In the eastern domain specularitic ore dominates with large orebodies concentrated in shear zones related to thrust planes (see Rosiere et al. 2008 and references therein).

Further to the west of the QF district, on the other hand, the orebodies become progressively smaller especially in the extreme western branch of the Serra do Curral Ridge where large iron orebodies are conspicuously replaced by magnetite-martite-hematite veins, which crosscut in the upper stratigraphic sequence.

4.2 Characteristics and age of iron oxide veins

The presence of Fe-oxide veins in the upper stratigraphic levels of some deposits attests an upward mobilization of Fe along extensional fractures, which are commonly developed in outer fold hinge zones and fault tips. The same mineralogical and textural features that have been earlier documented by Rosière and Rios (2004) for the large ore bodies are also visible in the hematite veins. The earliest stage of ore formation is recorded by the growth of submillimetric, euhedral to subhedral magnetite blasts that undergo oxidation (martite). Oxidation was likely coeval with the precipitation of hematite in the matrix as grainy to platy crystals that are flamy intergrown with monazite. Geochronological studies in monazite (U-Pb SHRIMP) from these veins (Fig. 3) indicate that they formed at about 2.05 Ga which corresponds to the paroxysm of the Paleoproterozoic Transamazonian orogenic cycle (2.26-2.00 Ga) (Almeida et al., 1981)

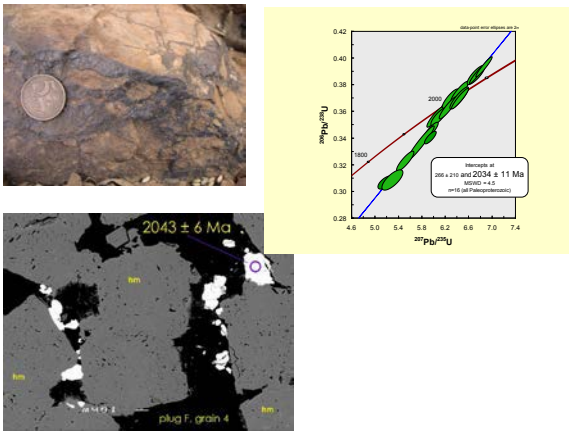

Figure 3. Monazite-bearing martite/hematite vein: (a) vein in the outcrop crosscutting quartzite of Piracicaba Group. (b) SEM-image of the vein with hematite and monazite. Circle represents analyzed spot with age. (c) U-Pb concordia plot and calculated age using the conventional intercept method.

5 Structural control, age and chemical changes in ore-forming hematite species

The age of the high-grade iron ore vein is coincident with the generation of a gigantic volume of granitic bodies and juvenile crustal accretion during the end of the Rhyacian time in the adjoining magmatic arc of the Mineiro Belt (Teixeira and Figueiredo, 1991). Magmatism likely produced a large volume of fluids that circulated during the development of the Transamazonian collage event.

Alternatively, the association of the mineralization with superposed folds and thrusts of different orientations and the wide textural variation in a single ore body indicate that the latter formed during long periods of tectonic activity**.** The structures developed during the Transamazonian orogeny in the QF are associated with regional variations in the deformation processes (buckling to shearing), burial regimens (shallow to deep), tectonic environments (thin- to thick-skinned) and transport vector (SE to NW frontal fold and thrust to SW to NE transpressive scape and uplift) and the high-grade orebodies have formed during a single orogeny of Palaeoproterozoic age and not in two distinct mountain building events (Transamazonian vs Brasiliano) as previously interpreted by Rosière and Rios (2004).

Oxygen isotope analyses of the iron oxide species developed during the distinct tectonic stages of the mineralization (buckling to shearing) reveals significant changes in the O-isotope signature and remarkable consequences in the interpretation of ore evolution in relation to deformation.

Firstly a depletion in ^{18}O from BIF-hosted hematite ($\delta^{18}O$ = 7.0‰, Hoefs et al., 1982) to high-grade iron ore forming martite ($\delta^{18}O$ = -2.5‰,σ = 1.7, n=16) (Fig. 4). Across the paragenetic sequence of the ore-forming hematite species, however, a shift towards more positive ratios is recorded from the older (martite/granoblastic hematite) to the younger iron oxide (platy hematite/specularite).

The shift in oxygen isotopes indicates a considerable

change in the conditions of the fluid and in the fluid /rock ratio during the mineralization. During a first stage typical thin-skinned tectonics with the detachment of the sediments over the Archean basement developed. Modified metamorphic fluids (Rosière and Rios, 2004) percolated along the BIF layer. These fluids subsequently mixed with meteoric waters with the preferential formation of high-grade iron ore bodies in fold hinges, which nucleated at the upper edge of blind faults. During a second stage increased mechanical resistance of the folded BIF layers caused deformation mainly by shearing with intensive fluid flow derived from the near Mineiro Belt along regional scale shear planes. Shearing was probably related to seismic pumping and resulted in higher fluid-rock ratio at the iron ore site and the formation of specularite by syntectonic solution-precipitation processes. This process has probably repeated itself recurrently at the same ore site resulting in the present variation of textural and chemical characteristics of the orebodies.

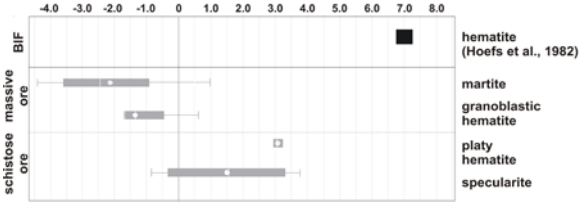

Figure 4. Bar-diagram with O-isotope values for the different iron oxide generations of the high-grade ore from the Quadrilátero Ferrífero.

Acknowledgements

The authors thank the USIMINAS Mineração, particularly the chief-geologist Viktor Suckau and to the Ferrous Resources do Brasil SA for the most generous all-round support. The results are from a cooperation project between the UFMG and the UWA financially supported by the CNPq/Conselho Nacional de Desenvolvimento Científico e Tecnológico (Pr. 472602/2009-8.). The Society of Economic Geologists Foundation, Inc., provided financial help through a Graduate Student Fellowship 2010 and the Hugh E. Mc Kinstry Student Research Grant 2011. Oxygen isotope analysis at University of Wisconsin-Madison was funded by NSF (EAR-0838058 to JW Valley).

References

Alkmim FF, Marshak S (1998) Tranzamazonian Orogeny in the southern São Francisco Craton region, Minas Gerais, Brazil: evidence of Paleoproterozoic collision and colapse in the Quadrilátero Ferrífero. Precambrian Research 90: 29–58.

Almeida FFM, Hasui Y, Brito Neves BB, Fuck RA. (1981) Brazilian structural provinces: an introduction. Earth Sci Reviews 17: 1-29.

Ávila CA, Teixeira W, Cordani UG, Moura CAV, Pereira RM (2010) Rhyacian (2.23–2.20 Ga) juvenile accretion in the southern São Francisco craton, Brazil: Geochemical and isotopic evidence from the Serrinha magmatic suite, Mineiro belt. Journal of South American Earth Sciences 29: 464–482.

Babinski M, Chemale F, Jr., Van Schmus WR (1995) The Pb/Pb age of Minas Supergroup carbonate rocks, Quadrilatero Ferrifero, Brazil, and its implications to the correlation with ElFs from South Africa and Australia. Precambrian Research 72: 235-245.

Chemale F, Jr., Rosiere CA, Endo I, (1994) The tectonic evolution of the Quadrilritero Fernfero, Minas Gerais, Brazil: Precambrian Research 65: 25-54.

Dorr II JVN (1969) Physiographic, stratigraphic and structural development of the Quadrilátero Ferrífero, Minas Gerais, Brazil. U.S. Geological Survey Professional Paper 641-A: 1–110.

Hagemann SG, Rosière C A, Lobato LM, Baars FJ, Zucchetti M, Figueiredo e Silva RC, Thorne W (2005) Controversy in Genetic Models for High-Grade BIF-related Fe Deposits: Unifying or Discrete Model(s)? Iron Ore 2005, The Australasian Institute of Mining and Metallurgy, Publication Series No 8/2005, Perth, Austrália: 67-71.

Hippertt J, Davis, B, 2000, Dome emplacement and formation of kilometer-scale synclines in a granite-greenstone terrain (Quadrilatero Ferrifero, southeastern Braz(l): Precambrian Research 102: 99-12.1

Hippertt, J, Lana C, Takeshita T (2001) Deformation partitioning during folding of handed iron formation. Journal of Structural Geology 23: 819-834.

Hoefs J, Müller G., Schuster AK (1982) Polymetamorphic relations in iron ores from the Iron Quadrangle, Brazil: The correlation of oxygen isotope variations with deformation history. Contributions to Mineralogy and Petrology. 79: 241-251.

Ladeira EA, Viveiros JFM (1984) Hipótese sobre a estruturação do Quadrilátero Ferrífero com base nos dados disponíveis. SBG/Núcleo Minas Gerais, Belo Horizonte, Bol. 4: 18 p.

Pires, FRM (1995) Textural and mineralogical variations during metamorphism of the Proterozoic Habira Iron Formation in the Quadrilátero Ferrifero, Minas Gerais, Brazil. Anais Academia Brasileira de Ciencias 67: 77-105.

Ramsay, JG (1962) Interference patterns produced by the superposition of folds of similar types. Journal of Geology 70: 466-481.

Rosière CA, Rios, FJ (2004) The origin of hematite in high-grade iron ores based on infrared microscopy and fluid inclusion studies: the example of the Conceição Mine, Quadrilátero Ferrífero, Brazil. Economic Geology and the Bulletin of the Society of Economic Geologists 99: 611-624.

Sanglard J, Rosière CA, Suckau VE, Amaral U, Meireles H (2011) The structure of the western Serra do Curral Range, QuadriláteroFerrífero and the tectonic control of the high-grade Fe-orebodies. In: 11th SGA Biennial Meeting, Antofagasta: 879-881.

Spier CA, Oliveira SMB, Sial AN, Rios FJ (2007) Geochemistry and genesis of the banded iron formations of the Cauê Formation, Quadrilátero Ferrífero, Minas Gerais, Brazil. Precambrian Research 152: 170-206.

Spier CA., Oliveira, SMB, Rosiere, CA, Ardisson, JD (2008) Mineralogy and trace-element geochemistry of the high-grade iron ores of the Aguas Claras mine and comparison with the Capao Xavier and Tamandua iron deposits, Quadrilatero Ferrffero: Mineralium Deposita, 43: 2.2.9-254.

Taylor, D, Dalstra, HJ, Harding, AE, Broadbent, GC, Barley, ME, (2001) Genesis of high-grade hematite orebodies of the Hamersley province, Western Australia. Economic Geology and the Bulletin of the Society of Economic Geologists: 96: 837-873.

Teixeira W, Figueiredo MCH, (1991) An outline of Early Proterozoic crustal evolution in the São Francisco craton, Brazil: a review. Precambrian Research 53: 1–22.

Teixeira W, Sabaté P, Barbosa J, Noce CM, Carneiro MA, (2000) Archean and Paleoproterozoic Evolution of the São Francisco Craton, Brazil. In: Cordani UG., Milani EJ, Thomaz Filho A, Campos, DA (Eds.). Tectonic Evolution of South America. Rio de Janeiro, 31 IGC: 101–137.

Vieira Neri, MEN (2012) O Supergrupo Minas na Serra de Bom Sucesso, extremo SW do Quadrilátero Ferrífero-MG: Petrografia, Geoquímica e Isótopos de U-Pb. Unpubl. MSc thesis, Inst. de Geociências, UFMG: 156p.

Mass independent and mass dependent sulfur isotopes of hydrothermally altered jaspilite and mafic wallrocks, Serra Norte iron ore deposits, Carajás mineral province, Brazil

Rosaline Cristina Figueiredo e Silva, Lydia Lobato
Universidade Federal de Minas Gerais, CPMTC-IGC-UFMG, 31270-901, Belo Horizonte, MG, Brazil

Steffen Hagemann
University of Western Australia, School of Earth and Environment, Centre of Exploration Targeting, M006, Crawley WA 6009, Australia

John Cliff
University of Western Australia, Centre for Microscopy Characterisation and Analysis, Australia and Australian Research Council Centre of Excellence for Core to Crust Fluid Systems (CCFS), M010, Crawley WA 6009

Abstract. The Carajás iron ore deposits located in the southern part of the state of Pará in Brazil are hosted by the Neoarchean metavolcano-sedimentary sequence of the Grão Pará Group, Itacaiúnas Supergroup. The protoliths to high-grade iron ore in the Serra Norte deposits are jaspilites, which are surrounded by basalts. The major Serra Norte N1, N4E, N4W, N5E, and N5S iron ore deposits of the Carajás mineral province are distributed along, and structurally controlled by, the northern flank of the Carajás fold. High-grade iron mineralization (>64% Fe) is made up of hard and soft ores. The basal contact of high-grade iron ore is defined by a hydrothermally altered basaltic rock mainly composed of chlorite and microplaty hematite. Varying degrees of hydrothermal alteration have affected jaspilites to form iron ores. Sulfides are associated with a distal alteration zone, characterized by vein-breccias containing chalcopyrite, pyrite, carbonate, magnetite and/or quartz. Mass dependent $\delta^{34}S$ compositions of chalcopyrite and pyrite from veins in hydrothermally altered jaspilite and mafic wallrocks have revealed a range of values suggesting a magmatic source for the early stage/distal hydrothermal alteration zone. On the other hand, mass independent $\Delta^{33}S$ slightly positive (> +0.05 per mil) and slightly negative (<–0.05 per mil) values suggest a non-magmatic source, sedimentary affinity for sulfur, probably incorporated from the crust (Farquhar et al. 2002).

Keywords. Mass independent sulfur isotopes; hydrothermal alteration; iron ore; Carajás

1 Introduction

The Serra Norte jaspilite-hosted iron ore deposits are located in the Carajás mineral province (CMP), part of the Archean Grão Pará Group. They were discovered in 1967 and have produced about 80 million metric tons (Mt) of iron ore annually. The deposits represent one of the largest high grade (>64 wt % Fe) BIF iron ore deposits and resources in the world. Four main open pits N4E, N4W, N5E and N5W have produced about 1.2 billion tons of high-grade iron ore with further resources of 5 billion tons. Ore types at the Serra Norte deposits include soft and hard ores; the former are interpreted to be supergene in origin, whereas the latter consists of banded, massive and/or brecciated hypogene ores, and is mainly located along the contact with the surrounding hydrothermally altered basalts.

In order to better constrain and understand the hydrothermal processes that led to the upgrade of jaspilite to form hard, high-grade iron ores in the Serra Norte deposits, we have investigated the composition of mass independent $\Delta^{33}S$ and mass dependent $\delta^{34}S$ of chalcopyrite and pyrite from different vein-breccia types located in the distal hydrothermal alteration zone. The results of these methods, paired with detailed mineralogy and paragenetic studies (Figueiredo e Silva et al. 2008), help to support the dual magmatic-meteoric hydrothermal model proposed by Figueiredo e Silva et al. (2008) responsible for the transformation of jaspilite to high-grade iron ore.

2 Methods

In situ sulfur 3-isotope ratios ($\delta^{34}S$ and $\delta^{33}S$) were determined in eight polished sections using a Cameca secondary ion mass spectrometer-SIMS 1280 multi-collector ion microprobe located at the Centre for Microscopy, Characterisation and Analysis (CMCA), University of Western Australia. Rock fragments were cut from slabs and mounted with in-house standards SON-3 ($\delta^{33}S$ = 0.83 ± 0.03‰ VCDT, and $\delta^{34}S$ 1.61 ± 0.08 VCDT) for S isotopes. Mass independent fractionation (MIF) of ^{33}S was calculated as $\Delta^{33}S=\delta^{33}S-1000[(1+\delta^{34}S/1000)^{0.515}-1]$. Error bars are propagated according to standard methods and contain components of internal and external precision, the uncertainty of the standard relative to VCDT as well as additional uncertainty from calibrating chalcopyrite from pyrite. We consider here a sample to have a MIF if the average $\Delta^{33}S$ ± 95% CI falls outside the analytical uncertainty of $\Delta^{33}S=0$ ±0.054‰.

3 Hydrothermal Alteration

In the altered jaspilites (Fig. 1), two vein-breccia types characterize the distal alteration zone, which represents an early alteration/mineralization stage: V1a - quartz ± sulfide breccia and V1b - carbonate ± sulfide ± quartz

breccia-veins. The intermediate alteration zone is represented by the following vein types: V2a - quartz ± hematite bedding discordant veins; V2b – quartz-hematite bedding discordant vertical veins with characteristic vug textures; V3 - hematite ± quartz veins crosscut and/or parallel to the jaspilite beds. The proximal alteration zone is characterized by V4 – carbonate ± quartz breccias with disseminated Fe-particles in the carbonate, and V5 - quartz ± microplaty hematite breccia, both are located in high-grade ore.

In the altered mafic wallrock (Fig. 1), the distal alteration zone is represented by amygdale 1, which is filled with quartz ± carbonate ± chlorite, fractures filled quartz ± carbonate ± sulfides, and quartz breccia with quartz ± chlorite and sulfides in the matrix. The intermediate alteration zone contains: amygdale 2 filled with quartz ± hematite ± chlorite, fractures filled with hematite and quartz, and hematite-quartz breccias.

At the Serra Norte hematite iron deposits, a systematic relationship exists between sulfides, such as pyrite and chalcopyrite, and hydrothermal iron oxides, quartz and carbonate (Zucchetti, 2007; Figueiredo e Silva et al. 2008). Sulfides are characterized by chalcopyrite and pyrite, mainly distributed along veins and breccias (Fig. 2) in distal alteration zone. In V1b carbonate ± sulfide ± quartz vein-breccia that formed synchronously with the early iron mineralization stage in the distal alteration zone of altered jaspilites, pyrite crystals occur in equilibrium with magnetite and calcite (Fig. 2A), and locally overgrow magnetite (Fig. 2B). Chalcopyrite crystals are commonly associated with kutnahorite in V1b vein-breccia from distal alteration zone of altered jaspilites (Figs. 2C, D). Pyrite and chalcopyrite crystals are mostly associated with calcite and/or quartz in vein-breccias from distal alteration zones of hydrothermally altered mafic wallrock (Figs. 2E, F).

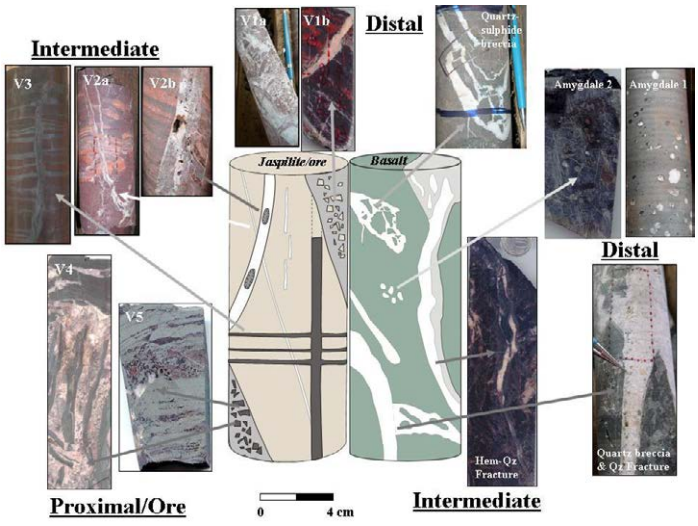

Figure 1. Schematic diagram illustrating the different vein and breccia types in altered jaspilites and mafic wallrocks (Zucchetti, 2007) observed in diamond core and open pit. Also shown are photographs of core samples.

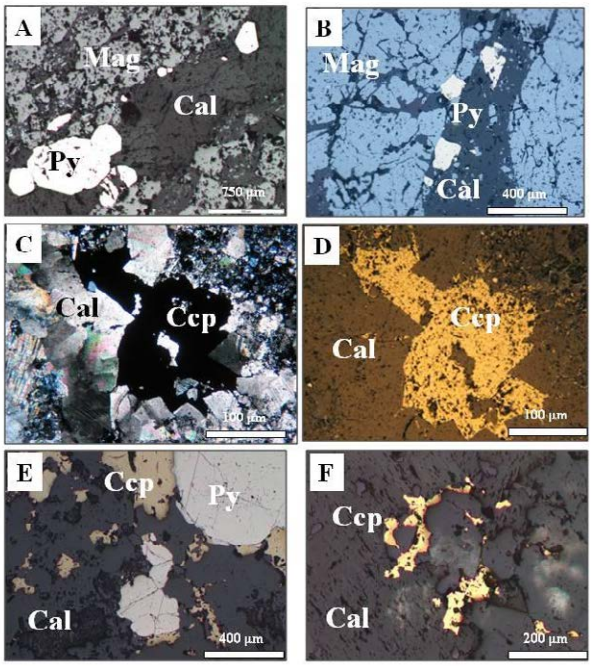

Figure 2. Photomicrographs showing the mode of occurrence of: A, B. Pyrite crystals associated with magnetite (in equilibrium and/or overgrowing) and calcite in V1b vein-breccias from a distal alteration zone (early-stage) of altered jaspilites (reflected light 25X, 50X). C, D. Chalcopyrite (Ccp) crystals associated with kutnahorite in V1b vein-breccias from a distal alteration zone of altered jaspilites (transmitted and reflected light 20X). E. Pyrite and chalcopyrite associated with calcite in a vein-breccia from a distal alteration zone of hydrothermally altered mafic wallrock (reflected light 50X). F. Chalcopyrite crystals from a distal alteration zone of hydrothermally altered mafic wallrock (reflected light 100X).

4 Results

A range of in situ ionprobe sulfur isotope analyses were obtained from hydrothermal pyrite and chalcopyrite crystals in: (i) textural equilibrium with magnetite, in V1b discordant veins (Fig. 1) located in the distal alteration zone, i.e., early hydrothermal stage of jaspilite; (ii) equilibrium with quartz in hydrothermal veins, mainly fracture fillings (Fig. 1) in the distal alteration zone of hydrothermally altered basalts. Sulfides from amygdales 1 (Fig. 1) filled with quartz ± carbonate ± chlorite (Zucchetti, 2007; Figueiredo e Silva et al., 2008) were also analysed. Ionprobe analyses were preferred because the sulfide (pyrite, chalcopyrite) grain size is too small (< 1 mm diameter) for separation of pure pyrite and chalcopyrite by conventional hand drilling. In addition, this technique allowed the selection of grains that were not affected by other sulfide inclusions.

Results of mass independent $\Delta^{33}S$ and mass dependent $\delta^{34}S$ analyses are shown in Figure 3. Mass independent sulfur displays non-zero $\Delta^{33}S$ values varying from -0.5 to 0.5‰ (Fig. 3). Negative values were obtained in sulfides in mafic wallrocks, whereas positive values are from veins in hydrothermally altered jaspilites.

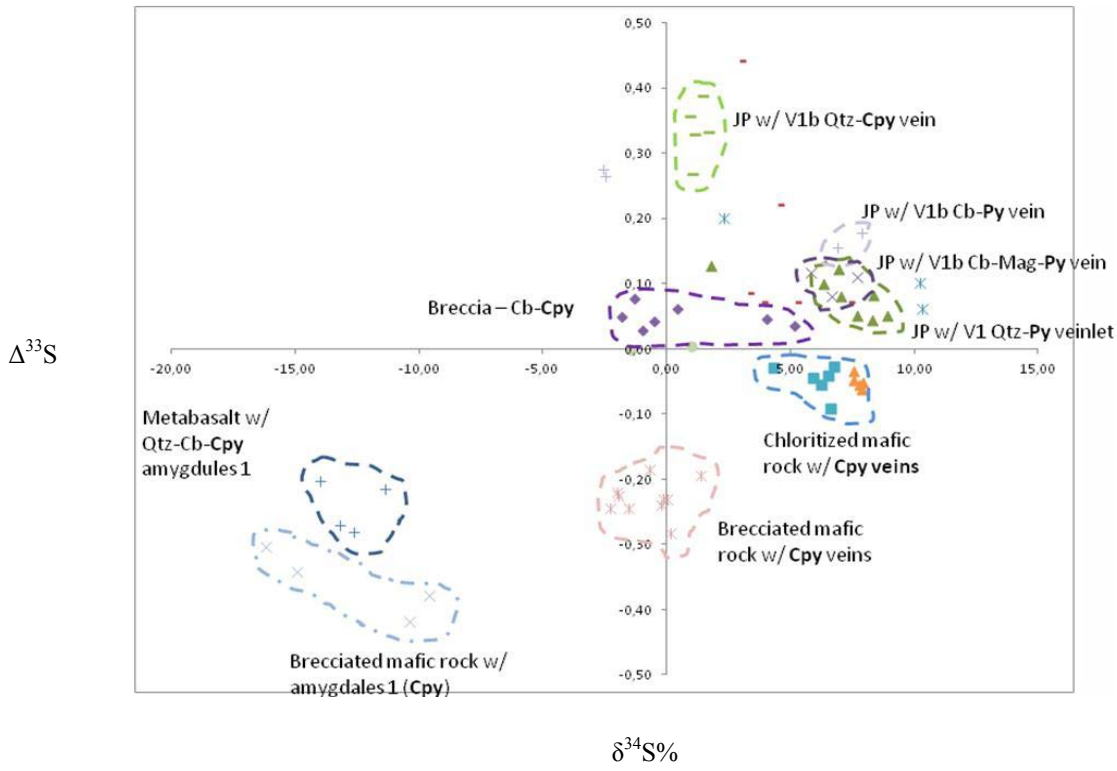

Figure 3. Mass independent $\Delta^{33}S$ versus mass dependent $\delta^{34}S$ values of sulfides from different vein and breccias types in altered jaspilites and mafic wallrocks.

Mass dependent $\delta^{34}S$ show different ranges of values (Fig. 3). Chalcopyrite and pyrite (n=8) from amygdales 1 in least altered metamafic wallrocks show the most negative $\delta^{34}S$ values, from –16.19 to –9.59‰ (Fig. 3). On the other hand, chalcopyrite and pyrite inclusions (n=10) from brecciated hydrothermally altered mafic wallrock show $\delta^{34}S$ values from –2.28 to 1.37‰.

Sulfides in vein-breccias of the distal hydrothermally altered jaspilite show the following ranges: i) chalcopyrite crystals (n=8) from Qtz-Cpy V1 veins display a range of $\delta^{34}S$ values between –1.0 and 5.0‰; ii) pyrite crystals (n=14) from carbonate-magnetite-rich V1b veins display $\delta^{34}S$ values from 5.82 to 7.88 ‰; and pyrite crystals from another sample in the same vein type display a wide range from 2.54 to 7.35 ‰ with 3 outliers (12.56; 12.59; 18.40‰); iii) pyrite crystals (n=7) from V1b Qtz veins display a range of $\delta^{34}S$ values from 6.32 to 8.90 ‰; iv) chalcopyrite crystals (n=4) from V1b Qtz-veins have a narrow range of $\delta^{34}S$ values between 0.94 and 1.70‰.

Chloritised mafic rocks contain chalcopyrite crystals near the contact with altered jaspilite, and both are crosscut by intermediate alteration zone V2b veins. These crystals (n=11) show $\delta^{34}S$ values from 4.33 to 7.90‰. Two chalcopyrite crystals from V3 Hem-Qtz veins show $\delta^{34}S$ values of –1.46 and 1.01‰.

Figure 4 shows results previously obtained by laser ablation coupled to ICP-MS analyses in sulfides related to the Serra Norte iron deposits in comparison with Cu-Au deposits in Carajás. The results show two different populations of ^{34}S values: (i) high $\delta^{34}S$ values from +7.4 to +10.8‰, which are measured for pyrites in V1 veins from the early stage of alteration (Fig. 1), with the exception of two data points having $\delta^{34}S$ values of 2.5 and 3.0‰; and (ii) low $\delta^{34}S$ values from –5 to 5‰, obtained for pyrite and chalcopyrite from the intermediate alteration zone of hydrothermally altered basalts (Fig. 4). The majority of the data points of the latter population are between –2.5 to 2.5‰, but several analyses display a shift of up to 2.5‰ towards higher $\delta^{34}S$ values (Fig. 4).

5 Discussion and Conclusions

The presence of slightly positive $\Delta^{33}S$ values suggest a sedimentary affinity for sulfur, probably incorporated from the crust (Farquhar et al. 2002). Values of mass independent $\Delta^{33}S$ higher than 0.05‰, and lower than –0.05‰ in sulfides from V1 veins (Fig. 3) further suggest that the early hydrothermal fluid responsible for the iron mineralization at the Serra Norte iron deposits may have interacted with metasedimentary sequences during its ascending path.

Chalcopyrite from brecciated, mafic wallrocks and jaspilites, associated with V1 carbonate veins, show $\delta^{34}S$ values around 0‰, indicating a magmatic origin of sulfur for the early hydrothermal stage. Sulfides from amygdales in the least altered metabasalt show the most negative $\delta^{34}S$ values (down to -16.19‰), indicating sulfate reduction related sea-floor alteration. According to Gemmel et al. (2004), organically reduced seawater sulfate in marine sediments has been considered an

important source of isotopically light sulfur in some sea-floor hydrothermal systems (Shanks et al. 1995 in Gemmel et al. 2004).

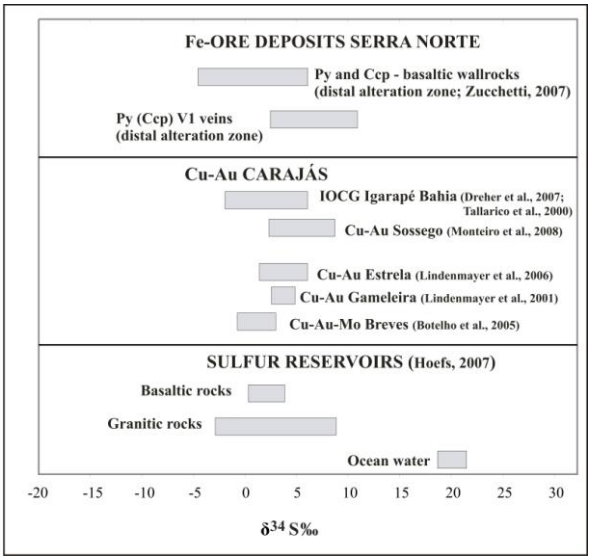

Figure 4. Range of sulfur isotope values of pyrite and chalcopyrite from the Serra Norte iron deposits hydrothermal vein-breccias located in the distal alteration zone of altered jaspilites and vein-breccia of hydrothermally altered basaltic wallrocks (data from Zucchetti 2007); Archean Cu-Au deposits of Gameleira (Lindenmayer et al. 2001), Igarapé Bahia (Tallarico et al. 2000; Dreher et al, 2008), Sossego (Monteiro et al, 2008a), Estrela (Botelho et al. 2005), Breves (Lindenmayer et al. 2005). Also shown are sulfur isotope reservoirs of basaltic, granitic rocks and ocean water (Hoefs 2007).

Therefore, at temperatures between 200° and 300°C organically reduced seawater sulfate cannot be considered to be a significant source of sulfur in sulfide minerals; this is the same range of trapping temperatures for the Carajás iron ore deposits (Figueiredo e Silva et al. 2008). Alternatively, Gemmel et al. (2004) suggest that the evolution of isotopically light sulfur, directly from magmatic volatiles, and/or boiling, are also required to explain light sulfur values, and these could have been the case for similar $\delta^{34}S$ values in mafic wallrock amygdales/veins in the Serra Norte, Carajás iron deposits.

The $\delta^{34}S$ values obtained in sulfides from other Carajás ore deposits include those of the Archean Igarapé Bahia IOCG deposit, from –1.1 to 5.6‰ (chalcopyrite), with an outlier at –10.8‰ (Dreher et al., 2008; Fig. 4). The authors suggested that most of the sulfur is magmatic or was leached from magmatic rocks. The same origin is indicated by sulfur isotopic values for chalcopyrite and pyrite of 0.1 to 4.1‰ for the Paleoproterozoic Cu (Mo-Au-Sn) Estrela deposit (Lindenmayer et al., 2005; Fig. 4). Data from the Archean Sossego IOCG deposit (Fig. 4; Monteiro et al., 2008) are similar to those for the iron deposits reported here, and are interpreted to record a combination of hot, deep-seated hydrothermal fluids from volcanic and intrusive rocks, and externally derived, modified meteoric water.

Acknowledgements

We wish to thank Vale for providing logistical, technical and finantial support. Thanks are also due to UFMG, FAPEMIG and CET for financial assistance, and Australian Microscopy & Microanalysis Research Facility at the CMCA at the University of Western Australia.

References

Botelho NF, Moura MA, Teixeira LM, Olivo GR, Cunha LM, Santana MU (2005) Caracterização geológica e metalogenética do depósito de Cu (Au, W, Mo, Sn) Breves, Carajás. In: Marini OJ, Queiroz ET de & Ramos BW (eds), Caracterização de depósitos minerais em distritos mineiros da Amazônia. DNPM/CT-Mineral/FINEP/ADIMB, Brasília, pp 340-389.

Dreher, AM, Xavier RP, Taylor BE, and Martini SL (2008) New geologic, fluid inclusion and stable isotope studies on the controversial Igarapé Bahia Cu-Au deposit, Carajás Province, Brazil. Mineralium Deposita, 43: 161-184

Farquhar J, Wing BA, McKeegan KD, Harris JW, Cartigny P, and Thiemens MH (2002) Mass-independent sulfur of inclusions in diamond and sulfur recycling on early Earth: Science 298: 2369–2372.

Figueiredo e Silva RC, Lobato LM, Rosière CA, Hagemann S, Zucchetti M, Baars FJ, Morais R, and Andrade I (2008) Hydrothermal origin for the jaspilite-hosted, giant Serra Norte iron ore deposits in the CMP, Para State, Brazil. In: Hagemann, SG, Rosière, CA, Gutzmer, J, and Beukes, NJ (eds.) BIF-Related High-Grade Iron Mineralization. Reviews in Economic Geology 15: 255-290

Gemmel, JB, Sharpe, R, Jonasson, IR, Herzig, PM. 2004. Sulfur Isotope Evidence for Magmatic Contributions to Submarine and Subaerial Gold Mineralization: Conical Seamount and the Ladolam Gold Deposit, Papua New Guinea. Economic Geology, Vol. 99, pp. 1711–1725.

Hoefs J (2007) Stable isotope geochemistry, (5th ed). Springer-Verlag, New York, USA, 244 p.

Lindenmayer ZG, Fleck A, Gomes CH, Santos ABZ, Caron R, Paula FC, Laux JH, Pimentel MM, and Sardinha AS (2005) Caracterização geológica do Alvo Estrela (Cu-Au), Serra dos Carajás, Pará. 2005, in Marini, O.J., Queiroz, E.T., and Ramos B.W. (eds), Caracterização de depósitos minerais em distritos mineiros da Amazônia. DNPM/CT-Mineral/FINEP/ADIMB, Brasília, p. 157-226.

Monteiro LVS, Xavier RP, Carvalho ER, Hitzman MW, Johnson CA, Souza Filho CR, and Torres II (2008) Spatial and temporal zoning of hydrothermal alteration and mineralization in the Sossego iron oxidecopper-gold deposit, Carajás Mineral Province, Brazil: Paragenesis and stable isotope constraints. Mineralium Deposita, 43:129-159

Tallarico FHB, Figueiredo BR, Groves DI, Kositcin N, McNaughton NJ, Fletcher IR, and Rego JL (2005) Geology and SHRIMP U-Pb geochronology of the Igarapé Bahia deposit, Carajás copper-gold belt, Brazil: An Archean (2.57 Ga) example of iron-oxide Cu-Au-(U-REE) mineralization. Economic Geology, 100: 7-28

Zucchetti M (2007) Rochas máficas do Supergrupo Grão Pará e sua relação com a mineralização de ferro dos depósitos N4 e N5, Carajás, (PA): Unpublished Ph.D. thesis, Belo Horizonte, Brazil, Universidade Federal de Minas Gerais, Departamento de Geologia, pp 125

Stable isotope analyses of fluid inclusions: constraints for the formation of high-grade Fe ore, Krivoy Rog, Ukraine

Marta Sośnicka
AGH University of Science and Technology, Faculty of Geology, Geophysics and Environmental Protection, Department of Economic and Mining Geology, al. A. Mickiewicza 30, 30-059 Krakow, Poland

Volker Lüders
Helmholtz Centre Potsdam GFZ, German Research Centre for Geosciences, Telegrafenberg, D-14473 Potsdam, Germany

Abstract. This paper presents carbon stable isotopic compositions of CO_2 in fluid inclusions trapped in quartz, hosted by rocks of the Krivoy Rog banded iron formation (BIF). The fluid inclusion data are compared with published carbon isotopic compositions of carbon-bearing surrounding rocks. The study aims to provide the understanding of the processes that led to the formation of high-grade Fe ores. Fluid inclusions preserved in quartz from different stratigraphic units contain gas mixtures of $CO_2 \pm N_2 \pm CH_4$. The $\delta^{13}C$ values of CO_2, which is the dominant gas species in inclusions, range between -2.7 and -11.7‰. Methane and nitrogen were detected in trace amounts. The results show that negative $\delta^{13}C$ values of inclusion gases in quartz from ore and schist horizons may be correlated with magmatic or metamorphic carbon sources. The carbon isotopic compositions of gaseous fluid inclusions in quartz from the thrust zone area are more variable compared to those in quartz from areas which were not affected by thrusting.

Keywords. iron ore, banded iron formation, BIF, fluid inclusions, carbon isotopes, Krivoy Rog

1 Introduction

The aim of the study is to identify the sources of carbonic-rich fluids that were involved in the formation of the Krivoy Rog iron ore deposit. Multiple hydrothermal events have affected the Krivoy Rog deposit causing, for example, upgrading of magnetite iron quartzites (31-38% Fe) to high-grade massive magnetite ores containing 52-56% Fe (Belevtsev 1991). Previously, solely carbonate rocks from the Krivoy Rog basin have been investigated for carbon isotopic compositions. This study presents carbon isotopic compositions from CO_2-rich fluid inclusions in quartz veins from the low-grade and high-grade ore zones.

2 Regional geology

The evolution of the Krivoy Rog Belt began in the Neoarchaean by early rifting and the formation of greenstone belts, reflected currently by the metavolcano-sedimentary complex association (Konska Series) (Bobrov et al. 2002). At that time the Archaean plagiogranite (trondhjemite)-amphibolite protocrust was divided into two megablocks (terranes): Kirovograd and Middle Dniprean (Bobrov et al. 2002).

In the Early Proterozoic, deposition of the metaterrigenous-ferruginous complex (Krivoy Rog Series) took place. The rift basin was initially filled with ocean floor weathering products and clastic material of the metaconglomerate-schist, and metaconglomerate-sandstone-schist rock associations (Novokrivorozhska and Skelevatska Suites, respectively) (Paranko 1993). This cycle lasted until more stable conditions favoured the deposition of the banded iron formation (jaspilite-silicate-schist rock association - Saksaganska Suite) (Bobrov et al. 2002). The Krivoy Rog BIF comprises seven suites of alternating schist and ore horizons. During the deposition of BIF, an increased volcanic activity caused the formation of flows of extremely viscous ultramafic material within the BIF rocks, represented by discrete layers of metakomatiite rock association which have been metamorphosed to talc-carbonate schists (Paranko and Mikhnitskaya 1991). The closure of the rift basin was accompanied by several tectonic events including ductile (multiple folding) and brittle deformation (formation of faults and thrusts), metamorphism and metasomatism. This stage is also associated with the development of the main intrusive bodies surrounding the basin, for instance the Saksagan plagiogranite (Belevtsev 1991). During the late episodes of basin evolution (2.0-1.8 Ga) low-grade and high-grade iron ore deposits of the metamorphosed genetic type were formed (Bobrov et al. 2002). All iron ore deposits in the study area are confined lithologically to the Krivoy Rog BIF. Low-grade iron ores occur in the southern and northern parts of the Krivoy Rog structure, whereas the occurrences of high-grade iron deposits are restricted to the 5^{th} and 6^{th} iron ore horizons of the Saksaganskiy tectonic block, located in the central part of Krivoy Rog Belt. The Archaean and Paleoproterozoic complexes are dipping westward and form a monoclinal structure (Bobrov et al. 2002).

In the Mesoproterozoic a new paleobasin developed and lagoon-like sediments were deposited (Paranko and Mikhnitskaya 1991). They are represented by carbonate-graphite schists of the carbonate-carbonaceous-metaterrigenous complex (Gdantsivska Suite), which unconformably overlie the Krivoy Rog BIF. After deposition the complex was subsequently intruded by mafic dikes (Bobrov et al. 2002).

The evolution of the Krivoy Rog Belt ended in the Neoproterozoic with the deposition of the metaterrigenous complex (Gleyuvatska Suite)

unconformably overlaying the Gdantsivska Suite. This stage was accompanied by the orogenic activity that led to vertical fault systems (Bobrov et al. 2002).

3 Genetic concepts

The low-grade iron ores (jaspilites) and iron-rich quartzites are believed to be the precursors for the unoxidized high-grade iron ores that were the parental rocks for the oxidized high-grade Fe ores (Belevtsev et al. 1991). Massive high-grade iron ores are associated with folds and flexures (Belevtsev et al. 1991) and their formation is considered to be a result of the multiple epigenetic processes. The high-grade martite ores (65-70% Fe) were formed by supergene processes due to the deep oxidation of the high-grade massive magnetite ores (Belevtsev et al. 1991). The formation mechanisms of the high-grade massive magnetite ores, containing 52-56% Fe, are poorly understood. They were assumed to result from the adjacent schist horizons replacement during Mg-Fe metasomatism (Belevtsev et al. 1991). Currently, the origin of the high-grade unoxidized ores is attributed to metamorphogenic processes associated with volume reduction caused by metasomatic silica removal (metasomatic contraction), excluding any additional Fe input (Belevtsev et al. 1991). According to Belevtsev et al. (1991), these ores are of residual hydrothermal-metamorphic type. They occur solely in the footwall of the thrust zones controlled by talc-carbonate rocks that acted as barriers for the metasomatising fluids (Paranko 1993). The thrust formation is believed to be the result of the same compressional processes that were involved in the hypogene metasomatic contraction and pervasive fluid percolation, confined by the talc barriers. However, these fluids played a key role in the formation of the high-grade massive magnetite Fe ores (Khudur 2006; Paranko 1993). The source of the compressional stress is still under debate. There are two major hypotheses, one of which claims that the stress was induced by the partial subduction (Reshetnyak 1993), whereas the second model invokes compression with reactivation of the adjacent Saksagan plagiogranite intrusion (Khudur 2006; Paranko 1993). Investigation of the fluids from various types of iron ores may help to trace their potential sources and to improve the understanding of the genetic model.

4 Research area

Sampling was carried out within the jaspilite-silicate-schist rock association of the metaterrigenous-ferruginous complex (Saksaganska Suite). This complex extends longitudinally at the entire length of the Krivoy Rog Belt.

Rock material was collected in the southern and the central parts of the Krivoy Rog structure. Selection of the area was dictated by the distribution of various types of iron ores. The sample suite comprises quartz from the magnetite-silicate ores as well as from the schist horizons. Samples of quartz veins hosted by the low-grade iron ores come from the Yugok open pit in the Skelevatskie-Magnetitove deposit (4^{th} ore horizon), exploiting ore in the southern region. Quartz from schist bands was collected from the 4^{th} schist horizon at the natural surface outcrop (MOPR), located in the vicinity of the Skelevatskie-Magnetitove deposit. Samples associated with the high-grade ore region were collected within the Saksaganskiy tectonic block, in the Frunze underground mine at the depth of 1135 meters. Due to the lack of veins crosscutting the high-grade massive magnetite ores in the mine, the quartz bands and crosscutting quartz veins of the $3/4^{th}$ graphite-chlorite-biotite schist horizon were included. Veins hosted by magnetite-silicate iron-rich quartzites (1^{st} ore horizon) were collected at the same depth. Orientation of the veins is parallel to the iron-rich quartzites dipping direction. Samples of quartz veins, crosscutting the iron quartzites, which are located in the main thrust zone, were collected from a highly silicified area in natural outcrop at the Balka Severnaya Chervonaya area situated in the northern part of the Saksaganskiy tectonic block.

5 Methodology

Stable isotope analyses were performed at the Helmholtz Centre Potsdam GFZ. The analytical setup for determinations of stable carbon isotopes of gases in quartz-hosted fluid inclusions comprises a sample crusher connected to a GC column and an isotopic ratio mass spectrometer (IRMS). During analyses the isotopic compositions of N_2, CH_4 and CO_2 gas mixtures are measured simultaneously. After the liberation of gases from fluid inclusions by crushing, the gases are separated from each other and analysed by the isotopic ratio mass spectrometry (Lüders et al. 2012).

6 Results

Analyses of gases preserved in fluid inclusions revealed the presence of two types of carbon: oxidized carbon included in carbon dioxide and also traces of reduced carbon from methane. Several samples released negligible amounts of nitrogen. The CO_2 was present in measureable amounts in fluid inclusions in all of the samples. Methane was completely absent in fluid inclusions from low- and high-grade iron ore zones, however traces of N_2 were detected. The presence of CH_4 and N_2, besides CO_2, is characteristic for all fluid inclusions measured in quartz from the schist horizons. Samples from the thrust zone show various compositions including lack of the CH_4 and N_2 or presence of both gases.

All measured samples show negative $\delta^{13}C$ values. The variation of measured $\delta^{13}C$ values is presented in Fig. 1. The $\delta^{13}C$ values of fluid inclusions in syngenetic quartz layers within schist horizons range between -11,7 and -8,1‰ and they are similar for all sample sites. The $\delta^{13}C$ values of CO_2 of fluid inclusions in quartz from veins crosscutting schists range between -8,2 and -8,0‰ and are mostly less negative when compared to the

values obtained for the syngenetic quartz bands from schists (-11,7; -10,4 and -8,1‰). Fluid inclusions in quartz from veins intersecting low-grade Fe ores show $\delta^{13}C$ values in the range between -2,7 to -5,4‰ and are less negative compared to the values for the iron-rich quartzites (-5,9; -6,2‰). The values from the low-grade ores and rich-iron quartzites are less negative than fluid inclusion data from quartz veins from the thrust zone (Fig. 1).

The CO_2 of fluid inclusions, trapped in quartz and associated with schist horizons, shows different isotopic compositions compared to CO_2 of fluid inclusions in quartz related to the low-grade and high-grade iron quartzite horizons. It exhibits more negative $\delta^{13}C$ values of fluid inclusion gases. This relationship is clearly illustrated in Figure 1 and points to the transitional isotopic compositions obtained for the thrust zone area.

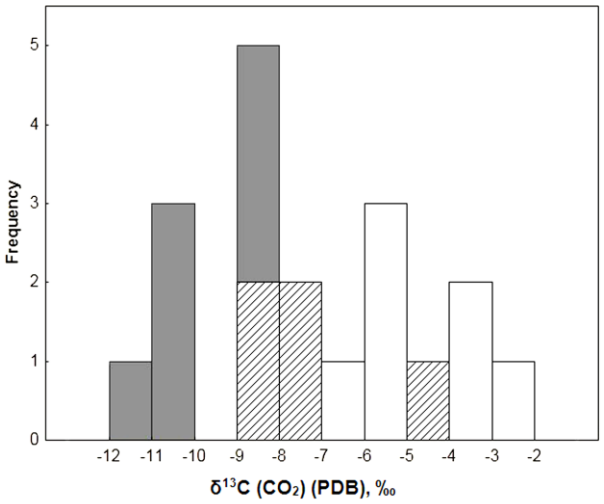

Figure 1. Stable carbon isotopic composition of CO_2 in quartz hosted fluid inclusions from low-grade Fe ores and iron-rich quartzites (white), schist horizons (grey) and tectonic zone (hatched), Krivoy Rog BIF.

7 Discussion

The interpretation of fluid inclusion isotope data requires the constraint of the isotopic compositions of the carbon-bearing minerals within the surrounding rocks of the Krivoy Rog BIF. Several studies of stable carbon isotopic compositions of carbonates and graphite related to the Krivoy Rog BIF have been performed by Kalinichenko (1992), Belevtsev et al. (1983), Perry and Ahmad (1981), and Lazarenko et al. (1977). Figure 2 illustrates a compilation of overall isotopic compositions of carbonates and graphite present in the Krivoy Rog rocks (schists, gneisses, BIF) and the carbon isotopic composition of CO_2 in fluid inclusions. The histogram is characterized by bimodal distribution. The mode with more negative $\delta^{13}C$ values is related to organic carbon, whereas the less negative values were measured in carbonate minerals (siderite, calcite and dolomite). The range of $\delta^{13}C$ values of carbonates overlaps with the range of the $\delta^{13}C$ values of fluid inclusion carbon from CO_2-rich fluid inclusions.

Fluid inclusions in quartz from veins intersecting the iron ore horizons show carbon isotopic compositions in the range between -2,7 and -6,2‰ (Fig. 1). Therefore, a supply of carbon derived from magmatic-hydrothermal activity cannot be excluded.

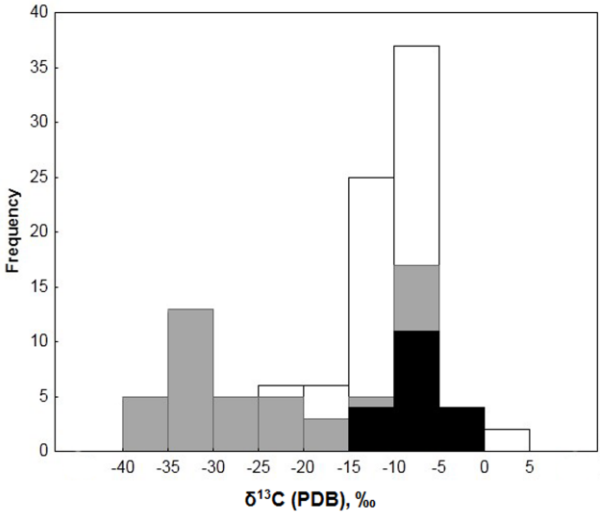

Figure 2. Carbon isotope data of carbonates and graphite from Krivoy Rog rocks (data compiled from the literature: Kalinichenko 1992; Belevtsev et al. 1983; Perry and Ahmad 1981; Lazarenko et al. 1977) (graphite – shaded, carbonate C – white) compared to present isotopic study of the gaseous fluid inclusions (black).

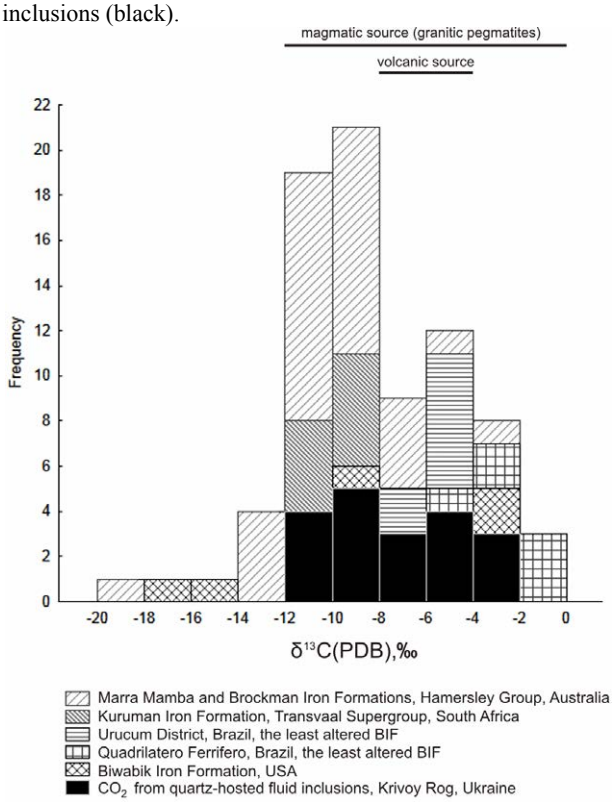

Figure 3. Stable carbon isotopic data compilation of carbonates from Proterozoic BIFs worldwide (compiled from the literature: Steinhöfel et al. 2010; Klein and Ladeira 2004; Klein and Ladeira 2000; Baur et al. 1985; Perry et al. 1973) compared with the isotopic data from fluid inclusions in quartz from Krivoy Rog.

A compilation of the $\delta^{13}C$ signatures of carbonates (Fig. 3) confirms that the range of carbon isotope data from gaseous fluid inclusions in quartz from Krivoy Rog overlies the range for other Proterozoic BIFs worldwide. The $\delta^{13}C$ values of the Krivoy Rog carbon-

bearing minerals are consistent with the data for other Proterozoic BIFs.

The study indicates the relationship between the $\delta^{13}C$ values of CO_2 of fluid inclusion gases in quartz and their host lithology. Fluids percolating the iron ore horizons show less negative $\delta^{13}C$ values when compared with quartz-hosted inclusions from schist horizons. The same relationship may be concluded from isotopic compositions of carbonates from schist and iron ore horizons from the Yugok open-pit in the Krivoy Rog deposit (Perry and Ahmad 1981). The variation in isotopic values suggests multiple fluid sources. The $\delta^{13}C$ values of CO_2 of fluid inclusions in quartz from the thrust zone fall between the $\delta^{13}C$ values of CO_2 in inclusions hosted by quartz, associated with schists and iron ores (Fig. 1). This area was probably affected by more extensive mixing of fluids containing carbon derived from distinct sources. The $\delta^{13}C$ values of quartz-hosted, carbonic-rich fluid inclusions from the iron-rich quartzites are slightly less negative compared to the $\delta^{13}C$ values from the fluid inclusions present in the quartz veins from the thrust zone.

Fluid inclusion carbon isotope data correlate well with the isotopic data for carbonates from the Krivoy Rog BIF, therefore these rocks may be considered as one of the carbon sources. The carbon isotopic signatures around -6‰ may also indicate an additional magmatic source of carbon in the fluids.

8 Conclusions

The results of stable carbon isotope analyses of CO_2 in quartz-hosted fluid inclusions from BIF in the Krivoy Rog Belt are equivocal. Fluid inclusions contain vapour phases consisting of one or more gas components (mixtures of CO_2-N_2-CH_4). Traces of methane and nitrogen, as well as very negative $\delta^{13}C$ (CO_2) that were measured in fluid inclusions in quartz related to schist rocks from different horizons, suggest water-rock interaction (WRI) between quartz-forming fluids and organic matter in Precambrian sedimentary rocks and/or C_{org}-rich metamorphic rocks.

This study shows the intricate character of the fluid systems of the Krivoy Rog BIF and iron ore and indicates several possible fluid sources for the upgrade to iron ores. The isotope data of CO_2 from fluid inclusions in quartz from the thrust zone (Saksaganskiy tectonic block), associated with the high-grade massive magnetite and martite ores, shows inconsistent and variable isotopic compositions compared to fluid inclusions in quartz from low-grade iron ore, iron-rich quartzites and schist horizons. It is assumed that in the area of thrusting fluid mixing took place where additional carbon was supplied from other sources which may include decomposed carbonate rocks or magmatic-hydrothermal fluids from the adjacent igneous bodies. Therefore, the influence of the Saksagan igneous body on the origin of the high-grade Fe ores cannot be excluded.

Acknowledgements

A special thank you from MS goes to Prof. Igor Paranko for guidance, advice during sample collection and discussions during the geological practice in Krivoy Rog.

References

Baur ME, Hayes JM, Studley SA, Walter MR (1985) Millimeter-scale variations of stable isotope abundances in carbonates from Banded Iron-Formations in the Hamersley Group of Western Australia. Econ Geol 80:270-282.

Belevtsev YaN, Belevtsev RYa, Siroshtan RI (1983) The Krivoy Rog Basin, Chapter 5, In Trendall AF, Morris RC (ed) Developments in Precambrian Geology, Iron-Formation Facts and Problems v. 6, p. 211–249.

Belevtsev YaN et al (1991) Precambrian banded iron formations of the European part of the USSR. Genesis of iron-ores, Naukova Dumka Press, Kiev, IGCP UNESCO Project, No 247 (in Russian)

Bobrov OB et al (2002) Main types of rock complexes and mineral deposits in the Ukrainian Shield, Geological Excursion Guidebook, International Symposium organized by Ukrainian State Geological Survey, Ukrainian State Geological Research Institute, Ukrainian National Academy of Sciences, European Program "Ore Deposits Geodynamics" (GEODE), Kyiv, Ukraine, September 13-26, 2002, Ukrainian State Geological Survey, Kiev

Faure G, Mensing TM (2005) Isotopes: Principles and Applications, 3rd Edition, Hoboken, New Jersey, USA, Published by John Wiley&Sons, Inc.

Kalinichenko OA (1992) Geologo-geochimicheskiye osobennosti stroyenia i formirovania glubinnych zon okislenia Krivorozhskovo Basena w svyazi z otsenkoy ich rudonosnosti na glubinu. PhD Dissertation, Dniepropetrovsk, Ukraine, Dniepropetrovsky Gorny Institut Imenia Artema. (in Russian)

Khudur D (2006) Geologiya Saksaganskogo nadviga Krivorozhskoy Struktury i yego rol v formirovanii zalezhey bogatykh zheleznykh rud, PhD Dissertation, Dniepropetrovsk, Ukraine, Ministerstvo Obrazovaniya i Nauki Ukrainy Natsionalny Gorny Universitet (in Russian)

Klein C, Ladeira EA (2000) Geochemistry and Petrology of some Proterozoic Banded Iron-Formations of the Quadrilatero Ferrifero, Minas Gerais, Brazil. Econ Geol 95:405-428.

Klein C, Ladeira EA (2004) Geochemistry and mineralogy of neoproterozoic banded iron-formations and some selected, siliceous manganese formations from the Urucum District, Mato Grossa Do Sul, Brazil. Econ Geol 99:1233-1244.

Lazarenko EK et al (1977) Mineralogy of the Krivoy Rog Basin, Kiev, Naukova Dumka, 544 p. (in Russian)

Lüders V, Plessen B, Primo R (2012) Stable carbon isotopic ratios of CH_4-CO_2-bearing fluid inclusions in fracture-fill mineralization from the Lower Saxony Basin (Germany) – A tool for tracing gas sources and maturity. Mar Petrol Geol 30:174-183.

Paranko I (1993) Nyektorye osobennocti geologicheskogo razvitija Krivorozhskoy struktury. Geol Zhurn. 4:112-133

Paranko I, Mikhnitskaya TP (1991) Etapy geologicheskogo razvitiya i stratigrafiya Krivorozhskoy Struktury. Preprint 91-10, 1-51 Akademia Nauk Ukrainy Institut Geologicheskikh Nauk, Kiev (in Russian)

Perry EC, Ahmad SN (1981) Oxygen and carbon isotope geochemistry of the Krivoy Rog iron formation Ukrainian SSR. Lithos 14:83-92.

Perry EC, Jr Tan FC, Morey GB (1973) Geology and stable isotope geochemistry of the Biwabik Iron Formation, northern Minnesota. Econ Geol 68:1110-1125.

Reshetnyak VV (1993) Glubinnoye geologicheskoye stroyenie Krivorozhskogo zhelezorudnogo basseyna i perspektivy yego rudonosnosti. PhD Dissertation, Kiev (in Russian)

Steinhöfel G et al (2010) Deciphering formation processes of banded iron formations from the Transvaal and the Hamersley successions by combined Si and Fe isotope analysis using UV femtosecond laser ablation. Geochim Cosmochim Ac 74:2677-2696.

Mineralogical characterization and different types of iron oxides of iron ores from the Serra do Sapo, Minas Gerais – Brazil

Amanda A Pires e Souza, Rosaline C Figueiredo e Silva, Carlos A Rosière
Universidade Federal de Minas Gerais, CPMTC-IGC-UFMG, 31270-901, Belo Horizonte, MG, Brazil

Geraldo Dias Sarquis, Fernando Prudêncio Morais, Henrique D Gatti Turrer
Anglo American, Projeto Minas-Rio, 35860-000, Conceição do Mato Dentro, MG, Brazil

Abstract. The Serra do Sapo is located at the east side of the southern portion of Serra do Espinhaço, near Conceição do Mato Dentro, Minas Gerais, Brazil. In the area several supergene low- to medium-grade banded iron formation-BIF-hosted hematite/martite iron orebodies occur interlayered with quartzites. Three ore types can be classified with variable grade according to the degree of weathering and compactness: hard (31 wt % Fe), semi-friable (33 wt % Fe) and friable or soft (39 wt % Fe) itabirite. They are all comprised mainly by quartz and hematite and locally some kenomagnetite relics. Hematite crystals were classified after their textural and morphological characteristics as: microplaty, anhedral, platy, and martite (pseudomorphic after magnetite).
BIFs in the Serra do Sapo are metamorphic and intensely sheared with transposition and obliteration of the primary features in most of the outcrops. Fresh BIF consists of hard itabirite with quartz and oriented platy hematite bands (specularite). Friable (soft) itabirite is the final weathering product although very few hydroxides are present. Soft itabirite occurs both in the upper and the lower saprolite zone together with remnants of hard itabirite. Semi-hard ore represent an intermediate type of partially weathered BIF. Quartz and platy hematite veins, common in all lithotypes, are parallel or discordant to banding.

Keywords: Iron ore; Itabirite; Serra do Espinhaço; Serra do Sapo

1 Introduction

The Serra do Sapo is located in the Serra do Espinhaço Range and extends for over 12-km a N-S trend (Fig. 1). The Espinhaco Range is divided in two domains near the 17°00'S parallel: the northern and the southern ranges (Knauer 2007).

The eastern border of the southern Espinhaço encompasses the main occurrences of iron formation (Knauer 2007) comprised by the Itapanhoacanga and Serra da Serpentine Groups. The Serra da Serpentina Group (Almeida Abreu and Renger 2002; Grossi Sad et al. 1990; Knauer and Grossi 1995) outcrop in the homonymous range and consists of quartz-schists, quartzites, phyllites and the Serra do Sapo iron formation (SSIF). The BIF unit is in average 120m thick, although locally thicknesses of up to 350 m are recorded (Rolim and Rosière 2011).

Low-grade supergene iron ores (up to 39 wt % Fe) have been intensively explored by Anglo American Corporation along the Serra do Sapo, and production is estimated to begin in 2014. The potential resources so far estimated are of about 8 billion tons of iron ore (Rolim & Rosière, 2011).

For the present study we have analysed the different minable iron ore types and characterized the iron oxide components with the ultimate purpose of establishing an industrial/geometallurgical classification based on the micro-chemical and micro-structural features.

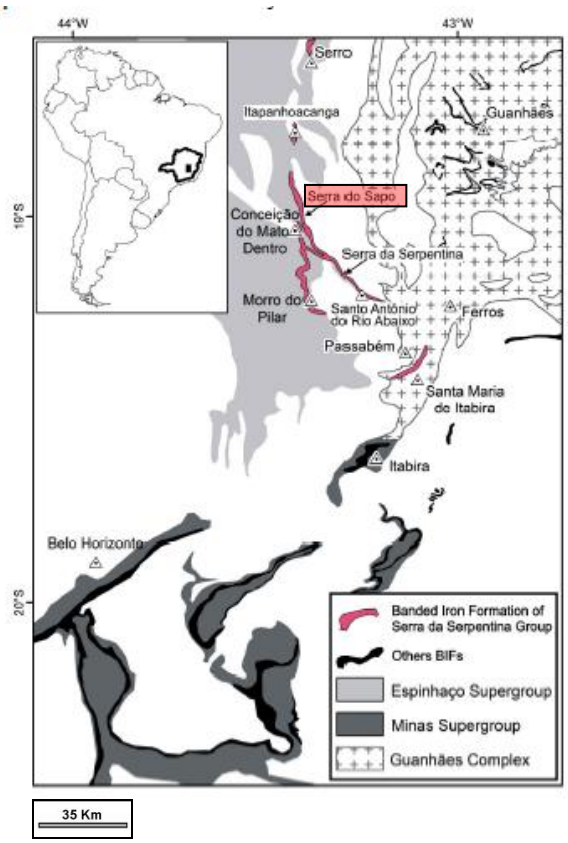

Figure 1. Regional geological map showing the location of the BIFs in the Serra da Serpentina Group, and distribution of other BIF-bearing sequences in southeast Brazil, including Serra do Sapo (Rolim and Rosière 2011; based on Grossi-Sad et al. 1997; Pedrosa-Soares et al. 1994).

2 The Serra do Sapo Iron Formation

The BIFs from the Serra da Serpentina Group are comprised of metamorphic quartz-itabirite, similar to the Cauê Formation from the Quadrilátero Ferrífero District SW of the Espinhaço Range.

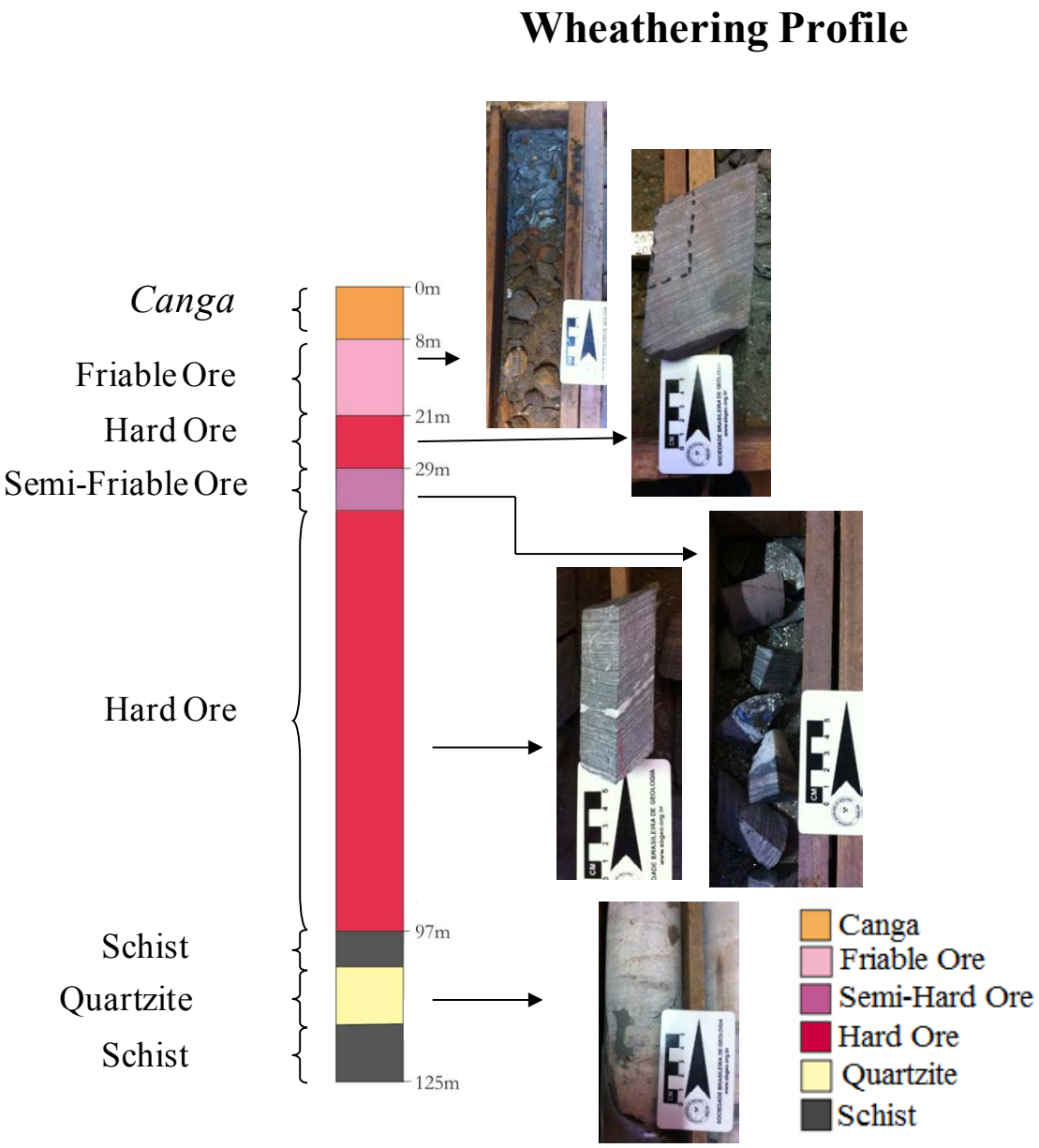

Figure 2: Schematic log of a drill holes in the Serra do Sapo showing different iron ore types related to weathering profile from Serra do Sapo deposit.

The Serra do Sapo iron formation presents similar mineralogical and chemical characteristics in the entire area of the range. Petrographic and SEM analyses allowed the discrimination of the following iron oxide phases: (i) Magnetite; (ii) Martite (Mt); iii) Microplaty hematite (MpHem) in most localities occurs banded (Figs. 3A, B), but is locally observed as disseminated crystals; (iv) Microgranular hematite (MgHem); (v) Anhedral hematite (AHem) generally occurs as oriented rounded clusters of various sizes. Large (0.005mm and 0.42mm) platy hematite crystals may occur oriented along the bands, or may occur as late-stage veins.

Preliminary results show that microplaty and anhedral hematite crystallized at the expense of martite crystals (Fig. 3G).

Microgranular hematite appears to be the product of progressive martitization (Figs. 3E and F). Secondary martite crystals may overgrow MpHem (Fig. 3H), indicating a late stage phase of martite formation.

Quartz veins with variable thickness (cm to m) are common, usually oriented parallel to the schistosity and may contain hematite lamellae (Figs. 2 and 3D). Discordant veins and veinlets are observed as well. A continuous foliation (schistosity) defined by oriented hematite plates transposes and obliterates entirely the primary bands which are only rarely observed as relics.

3 Ore Types

Petrographical and mineralogical studies were accomplished in 45 hand samples and 20 polished thin sections from six drill cores. Three different supergene

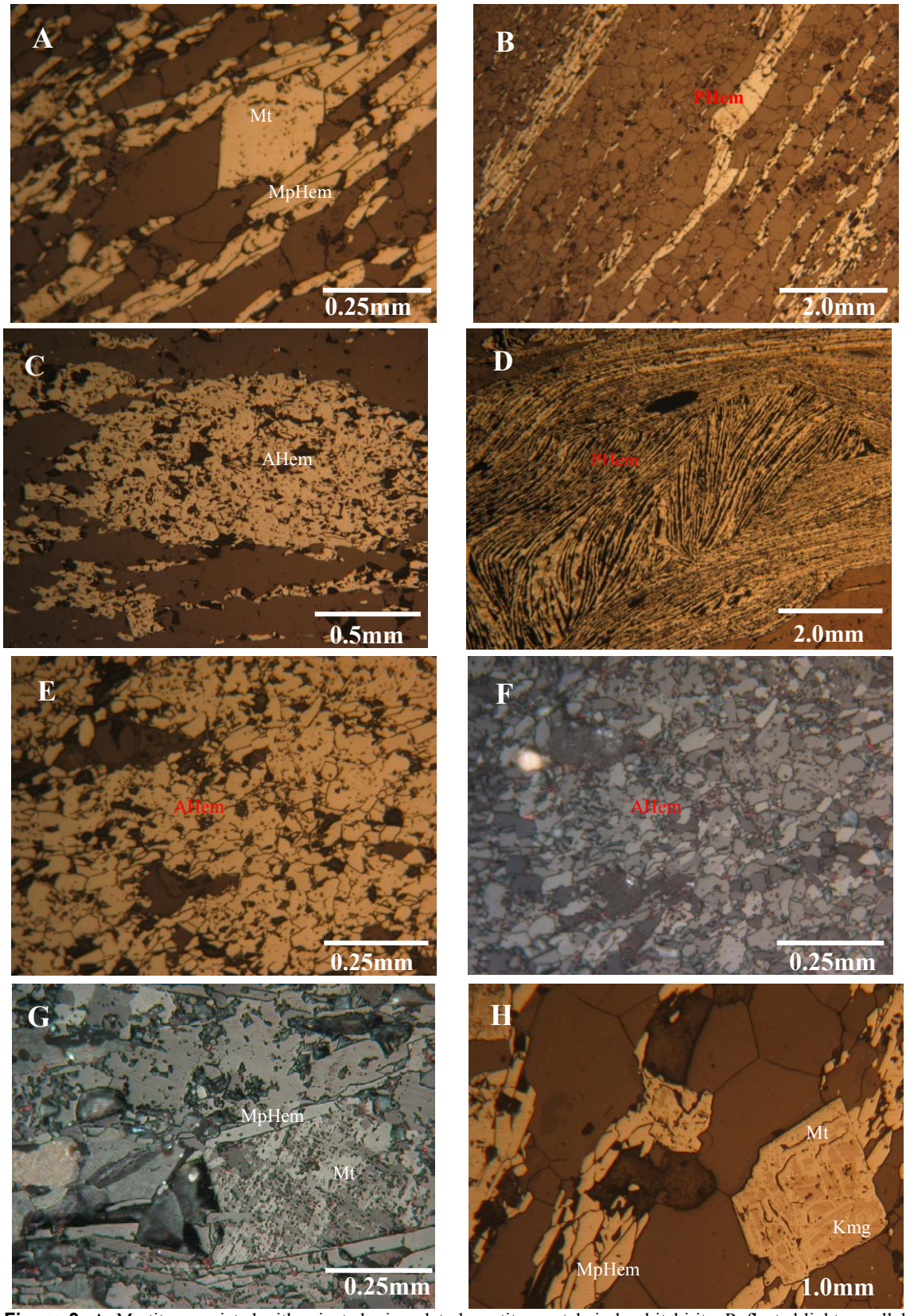

Figure 3: A. Martite associated with oriented microplaty hematite crystals in hard itabirite. Reflected light, parallel nicols (200X); **B.** Irregular banding, pronounced by an alternation of quartz and hematite bands in hard itabirite. Reflected light, parallel nicols (25X); **C.** Agglomerates of anhedral hematite in hard itabirite. Reflected light, parallel nicols (100X); **D.** Large platy hematite crystals along veins in hard itabirite. Reflected light, parallel nicols (25X). **E and F.** Hematite agglomerates in friable itabirite. Reflected light, parallel and crossed nicols (200X); **G.** Microplaty hematite crystals on martite grain boundaries. Martite shows typical trellis texture. Reflected light, parallel nicols (200X); **H.** Euhedral martite crystal with kenomagnetite relicts in semi-friable itabirite. Reflected light, parallel nicols (50X).

iron ore types were classified based on the physical characteristics such as toughness and friability, and also on microstructural/textural features: Hard, friable and semi-friable ores (Fig. 2).

Hard ore represents the fresh, unweathered itabirite mostly with a pervasive schistosity (Fig. 3B) and tectonic banding comprised of quartz, and dark grey metallic hematite. Hard itabirite contains 31 wt % Fe, and microplaty hematite dominates with subordinate martite and anhedral hematite (Figs. 3A-C). Small amounts of sericite-rich layers may be present. Intervals of magnetic itabirites are common, with rare magnetite crystals observed in hand sample.

Friable ores comprise gray fragments to powdery ore with a metallic luster (Fig. 2), the Fe content may reach 39 wt % Fe. Hematite crystals are fine-grained (0.03mm to 0.15mm), anhedral/subhedral (Figs. 3E, F) crystals. Quartz grains are fine- to medium-grained (0.01mm to 0.25mm). Sericite is locally present that gives a silky luster to the rock.

Semi-friable ore is an intermediate stage between hard and friable ore. It contains 33 wt % Fe, hematite crystals are platy very fine- to medium-grained (0.005mm to 1.2mm), and associated with martite containing kenomagnetite relics (Fig. 3H).

4 Preliminary Conclusions

In the Serra do Sapo deposit, BIFs are metamorphic and intensely sheared with transposition and obliteration of the primary features in most of the outcrops. Low-grade iron ores (31 to 39 wt % Fe) are represented by hard, friable and semi-friable itabirites. Hard itabirite consists in the fresh BIF with quartz and oriented (micro) platy hematite bands (specularite). Friable (soft) itabirite is the final weathering product although very few hydroxides are present. Soft itabirite occurs both in the upper and the lower saprolite zone together with rests of itabirites. Semi-hard ore represents an intermediate type of partially weathered BIF. Iron oxide phases are represented by: (i) Magnetite; (ii) Martite (Mt); iii) Microplaty hematite (MpHem); (iv) Microgranular hematite (MgHem), and; (v) Anhedral hematite (AHem). Large platy hematite crystals are common in late-stage quartz veins.

Acknowledgements

This research is a partial result of the AAPS M.Sc. thesis at the UFMG, which is fully financed by Anglo American. We wish to thank the company for providing logistical and technical support.

References

Almeida-Abreu PA, Renger FE (2002) Serra do Espinhaço Meridional: um orógeno de colisão do Mesoproterozóico: Revista Brasileira de Geociências 32: 1-14

Grossi-Sad JH, Mourão MAA, Guimarães MLV, Knauer LG (1997) Geologia da Folha Conceição do Mato Dentro. In: Grossi-Sad JH, Lobato LM, Pedrosa-Soares AC, Soares-Filho BS (eds.) Projeto Espinhaço em CD-ROM (textos, mapas e anexos). COMIG, Belo Horizonte, pp. 2533-2693

Knauer LG (2007) O Supergrupo Espinhaço em Minas Gerais: considerações sobre sua estratigrafia e seu arranjo estrutural. Geonomos 15(1): 81-90

Knauer LG and Grossi-Sad JH (1995) Geologia da Folha Serro (SE-23-Z-BIV). In: Grossi-Sad JH, Lobato LM, Pedrosa-Soares AC, Soares-Filho BS (eds.) 1997. Projeto Espinhaço em CD-ROM (textos, mapas e anexos). Belo Horizonte. COMIG

Pires e Souza, AA (2012) Caracterização Mineralógica de Minério de Ferro da Serra do Sapo, MG: Aplicação da técnica MLA. Estudos Supervisionados, UFMG, Belo Horizonte, 50 p

Pedrosa-Soares AC, Dardenne MA, Hasui Y, Castro FDC, Carvalho MVA (1994) Nota Explicativa dos Mapas Geológico, Metalogenético e de Ocorrências Minerais do Estado de Minas Gerais, Escala 1:1.000.000. SEME/COMIG, Belo Horizonte, 231 p

Renger FE, Noce CM, Romano AW, Machado N (1994) Evolução sedimentar do Supergrupo Minas: 500 Ma. de registro geológico no Quadrilátero Ferrífero, Minas Gerais, Brasil. Geonomos 2(1): 1-11

Rolim VK and Rosière CA (2011) The Conceição do Mato Dentro Iron Formation Province in southeastern Brazil. Biennial Meeting of the Society for Geology Applied to Mineral Deposits 11th. Proceedings, SGA, Antofagasta, Chile, p. 927-929

Geological characteristic and age of the Tuomoerte Fe-(Mn) deposit Altay Mountains, Xinjiang, China

Fuquan Yang, Feng Liu, Xinxia Geng
Institute of Mineral Resources, Chinese Academy of Geological Sciences, 26 Baiwanzhuang Road, Beijing 100037, P.R. China

Fengmei Chai
College of Geology and mining Engineering, Xinjiang University, Urumqi, 830049, P.R. China

Abstract. The Tuomoerte Fe-(Mn) deposit occurs in metavolcanic- sedimentary sequence of the upper Kangbutiebao Formation from the Upper Silurian to Lower Devonian. Three periods of mineralization can be distinguished: volcano- sedimentation, magmatic - hydrothermal, and regional metamorphism. The majority of the Fe-Mn metallogenic activity occurred during the volcano-sedimentation period. The zircon U-Pb age by SHRIMP and LA–MC–ICP–MS of the meta-rhyolite of the Kangbutiebao Fm is (406.7±4.3) Ma, and the age of biotite granite porphyry dyke, which intruded to Fe orebody, is (401.6±0.6) Ma, respectively. The zircon U–Pb ages indicate that the Fe–Mn mineralization period during the volcano–sedimentation and magmatic-hydrothermal periods coincides with early Devonian timing (401–407 Ma).

Keywords. Iron deposits, geological characteristics, zircon U-Pb dating, Tuomoerte, Altay

1 Introduction

The Altay Mountains are located in the southwestern part of the Central Asian orogenic system (or collage). While the southern margin of the Altay (which lies within the Xinjiang Autonomous Region) is one of China's major nonferrous and rare–metal metallogenic belts, the region also contains important Fe deposits. More than 100 Fe deposits (occurrences) have been discovered throughout the Altay Mountains. The Tuomoerte Fe–(Mn) deposit is the largest deposit in the volcano-sedimentary Kelan Basin, located about 12 km from Altay City. This paper is the first to describe the metallogenic setting and geological characteristics of the Tuomoerte Fe– (Mn) deposit and reports the U–Pb ages for meta-rhyolite and biotite granite porphyry dyke, which intruded the Fe orebody, that provide important time constraints on the genetic relation between Tuomoerte Fe– (Me) deposit and Kangbutiebao Formation Volcanic rocks.

2 Regional Geology

Within Xinjiang, the Altay is divided into Northern, Central, and Southern provinces. The Southern Altay is composed mainly of volcano–sedimentary rocks of the Upper Silurian–Lower Devonian Kangbutiebao Formation and the Middle–Upper Devonian Altaizhen Formation, with subordinate Carboniferous volcano–sedimentary units, as well as Middle–Upper Silurian schist, gneiss, and leptynite. Devonian marine volcano–sedimentary rocks occur mainly in four NW–SE–trending fault–bounded volcano–sedimentary basins (in order from northwest to southeast): the Ashele, Chonghu'er, Kelan, and Maizi basins. These basins also host Cu, Pb, Zn, and Fe deposits.

The Kelan basin is located between the Bazhai fault and the Kezijiaer fault. The main exposed strata from base to top include the Upper–Middle Silurian Kulumuti Group locally distributed along the margin of the basin, the Upper Silurian–Lower Devonian Kangbutiebao Fm. and the Middle –Upper Devonian Alaty Fm. All the Fe deposits (e.g. the Abagong Fe deposit, Tuomoerte Fe deposit, Qiaxia Fe–Cu deposit) are hosted in the various lithologic units of the Kangbutiebao Fm. The Kangbutiebao Fm. is a suite of low– grade metamorphosed volcanic– clastic rocks, composed of meta–volcanic agglomerate, meta–volcanic breccias, metatuff, felsite, metarhyolite, metatuffite, quartz schist, amphibolite, hornblende granulite, leucoleptite, meta–sandstone and marble. It is divided into two parts from base to top. The lower part consists of metasilicic pyroclastic rocks and lavas intercalated with meta–mafic volcanic rocks and meta– sedimentary rocks. The upper part comprises meta– silicic lavas intercalated with metapyroclastic rocks and marble. SHRIMP and LA–MC–ICP–MS analyses of zircons from metarhyolites of the Kangbutiebao Fm. in the Kelan Basin yield weighted mean $^{206}Pb/^{238}U$ ages of 388.9± 3.2 Ma to 412.6±3.5 Ma, which can be interpreted as the eruption age of the Kangbutiebao silicic volcanic rocks in the Kelan Basin (Chai et al., 2009; Dan et al., 2009; Geng et al., 2012). The Middle–Upper Devonian Altaizhen Fm. consists of slate, greywacke, schist, and phyllite. Pillow basalts are mainly located at the top of the Altaizhen Fm. All the Devonian rocks were folded and metamorphosed to greenschist facies during the Hercynian Orogeny.

Faults in the Kelan Basin are mainly NW–trending and are present as boundaries between terranes and between different stratigraphic units. The Keyingong and Hongdun faults divide the Silurian and Devonian strata, whereas the Abagong and Altay faults separate the Kangbutiebao and Altaizhen Fm.

3 Deposit geology

The Tuomoerte Fe–(Mn) deposit occurs in the middle–upper sections of the Second Member of the upper Kangbutiebao Formation (Fig. 1) and is composed of marble, meta–calcareous sandstone, meta–calcareous siltstone, chlorite quartz schist, meta–rhyolitic tuff, meta–tuffaceous sandstone, meta–rhyolite, and meta–

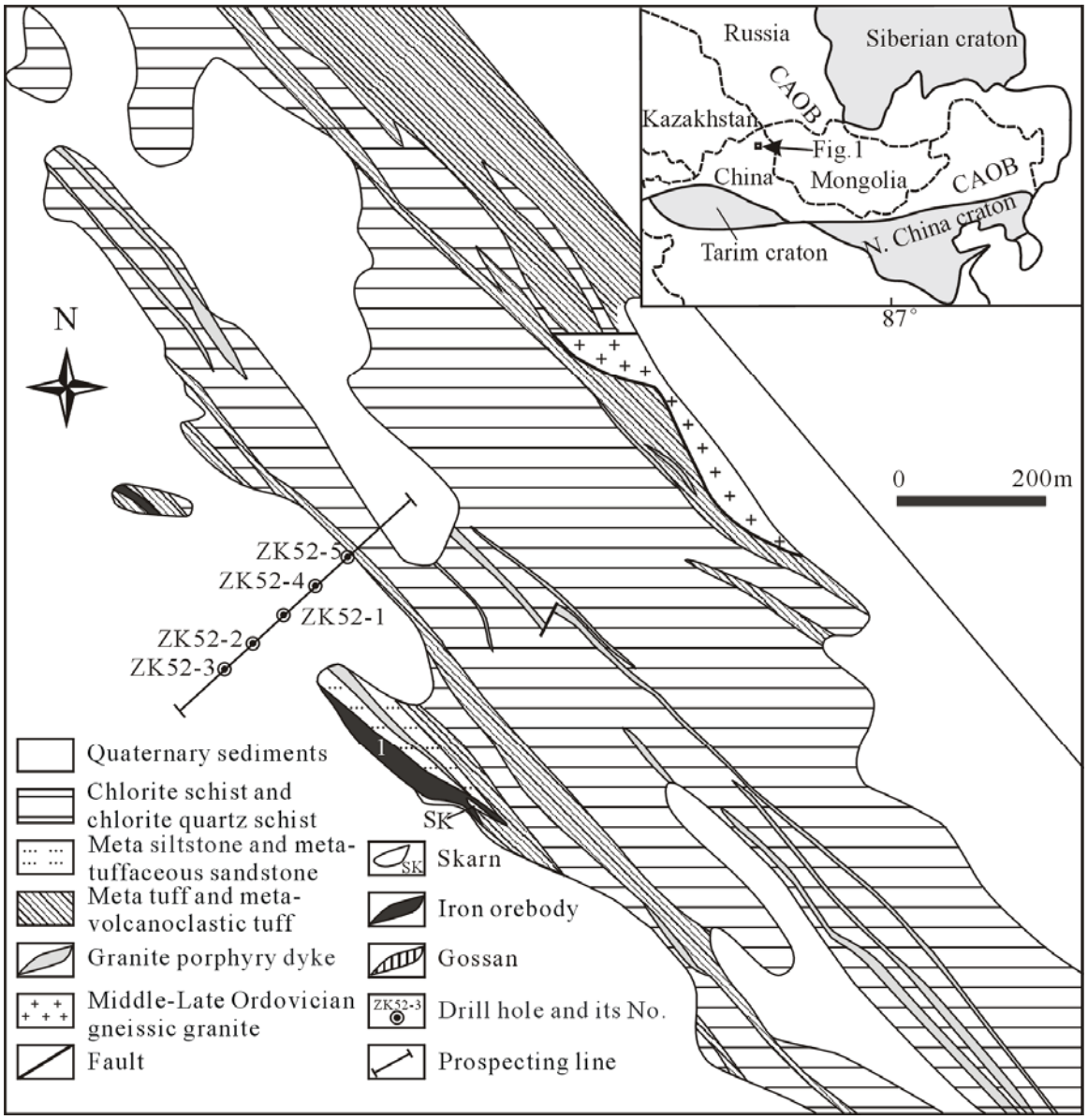

Fig. 1 Simplified geological map of the Tuomoerte Fe deposit (after Huang et al., 2008)

volcanic breccia. The host rocks contain chlorite schist, meta–tuffaceous sandstone, meta–volcanic breccia tuff, meta–tuff, meta–calcareous siltstone, and marble.

The Tuomoerte Fe metallogenic belt extends over 1500 m in length and is subdivided into three distinct sub-parallel ore bodies, two of which are not exposed at the surface. The orebodies are stratiform, showing branching and merging along both strike and dip. The orebodies are 350–650 m in length, 8.8–15.0 m in average thickness, and extend to a depth of 615 m. The Fe ores types are mainly dense disseminated and massive, with minor banded ores.

The ores are characterized by disseminated, massive, banded, brecciated, veinlet, and network structures (Fig. 2). Metallic minerals in the ores are mainly magnetite, maghemite, pyrite, chalcopyrite, pyrrhotite, and pyrolusite; nonmetallic minerals are dominantly calcite, quartz, biotite, sericite, garnet, actinolite, and epidote. The Fe grades of the ores vary from 22.31 wt.% to 46.36 wt.%. The average Mn concentrations in the deposit are 4.45 wt.% to 7.64 wt.%. Locally (e.g., along prospecting line 48), Cu mineralization occur with an average grade of Cu of 0.21 wt.%–1.03 wt.%.

Wall–rock alteration of the Tuomoerte Fe–(Mn) deposit is dominated by quartz, sericite, chlorite, garnet, actinolite, and tremolite. Three periods of mineralization can be distinguished on the basis of field evidence and petrographic analyses: volcano–sedimentation, magmatic –hydrothermal, and regional metamorphism. The volcano –sedimentation period was the main stage of Fe–Mn mineralization in the Tuomoerte deposit. During the magmatic–hydrothermal period, a biotite granite porphyry dike intruded the Fe ore bodies, resulting in the formation of veins of pyrite and magnetite (mainly networks of veinlets and other disseminated forms with some quartz veinlets and epidote). Magnetite– bearing skarns occur in areas of limestone wall rock. Similarly, chalcopyrite–bearing quartz veins and chalcopyrite occur in areas of siltstone and limestone. The ores in the regional metamorphism period experienced greenschist facies metamorphism, was characterized by deformation of the ore bodies and wall rocks.

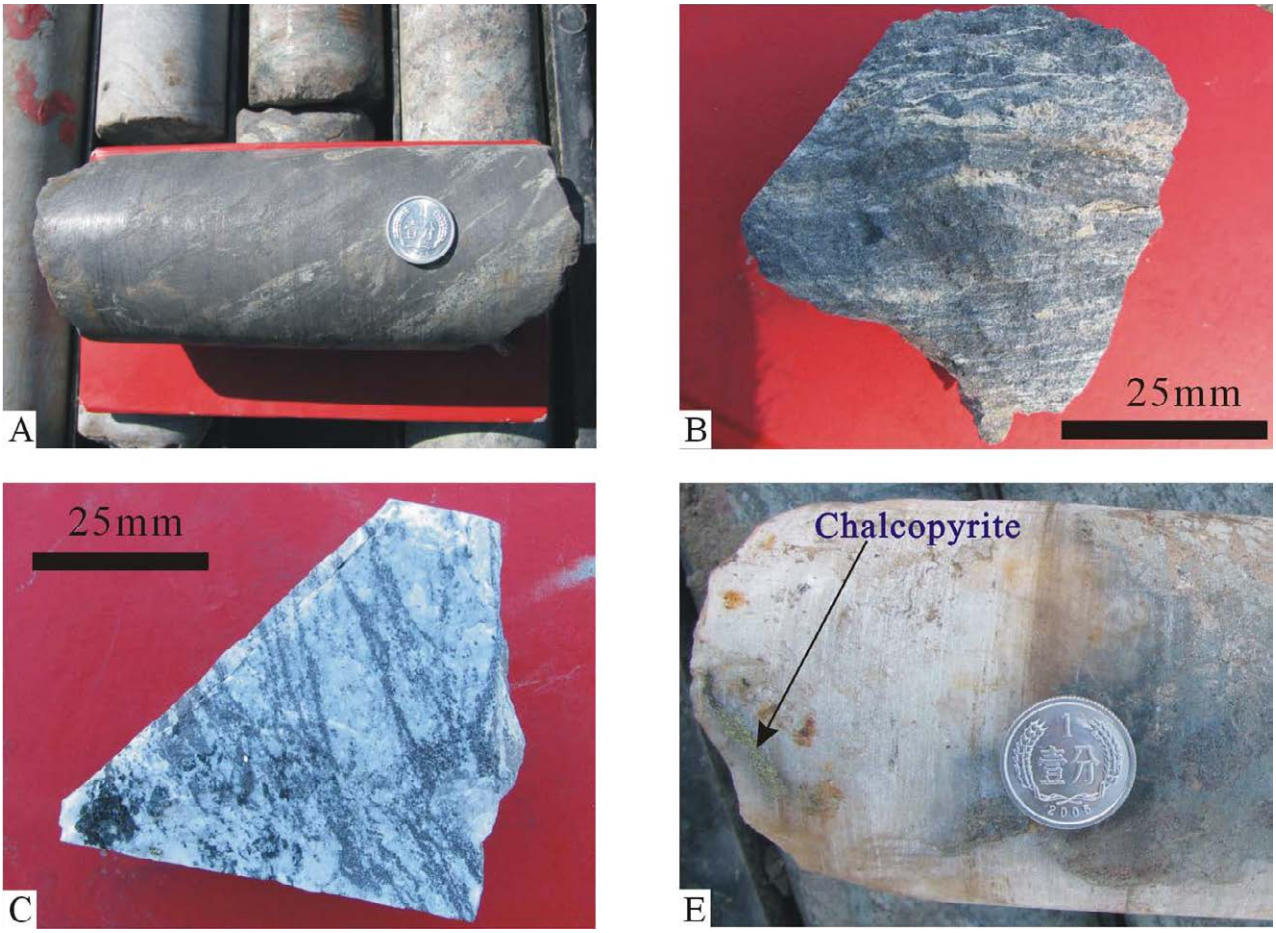

Fig. 2 Characteristics of wall rock alteration and ores in the Tuomoerte Fe-(Mn) deposit

A- Massive magnetite ore; B- Banded magnetite ore; C- Magnetite occur veinlet- stockwork in biotite granite porphyry; D- Chalcopyrite quartz vein

4 Geohronology

The meta–rhyolite samples (TM 51) for SHRIMP zircon U–Pb dating was collected from Third Member of the upper Kangbutiebao Fm. The biotite granite porphyry samples (ZK52–5–25) for LA–MC–ICP–MS zircon U–Pb dating was collected from biotite granite porphyry dyke, which intruded to Fe orebody.

Fifteen analyses were conducted on 15 zircons from the metarhyolite sample. There is a wide range of U concentrations, from 69 to 1099 ppm. Th concentrations range from 24 to 424 ppm. Th/U ratios are 0.18 and 1.26. In addition, the overgrowths have higher U concentrations and lower Th/U ratios (0.18) compared with the grains without cores. Common Pb concentrations have large spreads, from 0.39 to 5.27%, mostly >1%. Except for one analysis, fourteen analyses form a coherent group with a weighted mean $^{206}Pb/^{238}U$ age of 406.7± 4.3 Ma (MSWD=1.6) and a cluster of concordant data points (Fig. 3). This age is interpreted to represent the extrusive and crystallized age of the rhyolite in the Kelan basin. In addition, the remaining one from spot 7.1 yields a $^{206}Pb/^{238}U$ age of 455.2 Ma, which is similar to the age of Abagong gneissic granite in the area (Liu et al., 2008). It can be interpreted as an inherited age of captured zircon from granites during the ascent en route to the surface.

Twenty analyses were conducted on 20 zircons from the biotite granite porphyry sample. There is a wide range of U concentrations, from 300 to 4356 ppm. Th concentrations range from 96 to 4150 ppm. Th/U ratios are 0.32 and 1.63. The twenty spots gave consistent $^{206}Pb/^{238}U$ ages (397.1– 403.6 Ma) and they plot in groups on the LA–MC–ICP–MS U–Pb concordia diagram (Fig. 3). The weighted average $^{206}Pb/^{238}U$ age and concordia age of the 20 zircon grains are 400.9±1.3 Ma (MSDW=0.12) and 401.6±0.6 Ma (MSWD=3.9), respectively, which represents the age of crystallisation of the biotite granite porphyry.

5 Discussion and Conclusion

The Tuomoerte Fe-(Mn) deposit occurs in the middle–upper sections of the Second Member of the upper Kangbutiebao Formation. Orebodies are concordant with the bedding of the strata, the ores are characterized by disseminated, massive and banded structures. The principal mineralization forming element groups of the deposit is Fe–Mn. The $\delta^{34}S$ values of pyrite from the volcano–sedimentation period ranged from 6.2‰ to 13.1‰ and -20‰, indicating that the sulfur was mainly derived from the volcanic rocks, with some minor contributions from the bacteria–reduced sulphate in the seawater (our unpublished data). These characteristics show that the Tuomoerte Fe–(Mn) deposit is volcano–

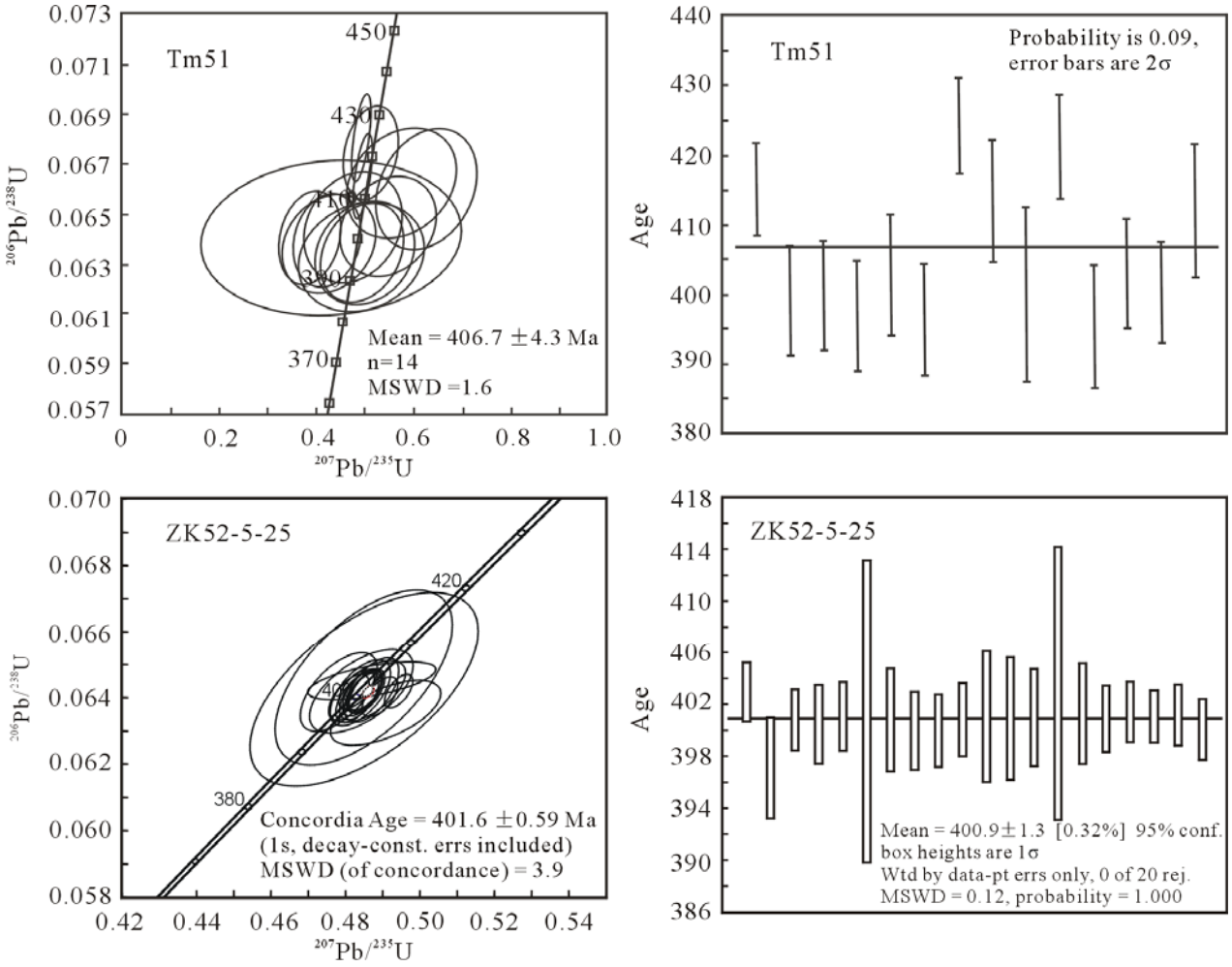

Fig. 3 Zircon SHRIMP (Tm 51) and LA–MC–ICP–MS (ZK52-5-25) U–Pb ages of the metarhyolite and biotite granite porphyry

sedimentation type deposit, and mineralization age of the Fe and Mn accord with the age of volcanic rocks wall rock of orebody. Our obtained zircon U–Pb age of 406.7±4.3 Ma for the meta–rhyolite from Third Member of the upper Kangbutiebao Fm. provide the maximum formation age of mineralisation.

The weighted average $^{206}Pb/^{238}U$ age and concordia age of the 20 zircon grains from biotite granite porphyry are 400.9±1.3 Ma and 401.6±0.6 Ma, respectively, indicating that the dyke is of Early Devonian age. Biotite granite porphyry dyke which crosscuts the Fe orebody is younger than Fe mineralization, so it minimum formation age of the iron orebody as early as 401 Ma. Chalcopyrite and magnetite mineralization occur disseminated and veinlets in biotite granite porphyry dyke with some mineralization also occurring in its nearby country rocks.

In summary, age of volcanic sedimentary period and magmatic hydrothermal period in Tuomoerte Fe–(Mn) deposit are very close together, 401– 407 Ma (Early Devonian). Tuomoerte Fe–(Mn) deposit is the product of Early Devonian volcanic eruptions and magma intrusion activities.

Acknowledgements

This research was jointly supported by the National Key Technologies R&D Program (2011BAB06B03-02), the Special Research Funding for the Public Benefits Sponsored by MLR Program (201211073).

References

Chai, FM, Mao JW, Dong LH, Yang FQ, Liu F, Geng X, Zhang ZX (2009) SHRIMP zircon geochronology of the metarhyolites from the Kangbutiebao Formation in the Kelang basin at the southern margin of the Altay, Xinjiang and its implications. Gondwana Research, 16:198 -200

Geng XX, Yang FQ, Chai FM, Liu M, Guo XJ, Guo ZL, Liu F, Zhang ZX (2012) LA-ICP-MS U-Pb dating of volcanic rocks from Dadonggou ore district on southern margin of Altay in Xinjiang and its geological implications. Mineral Deposits 31:1119-1131 (in Chinese with English abstract)

Huang CK (2008) Geological exploration report of Tuomoerte iron deposit in Altay City, Xinjiang. 1–60 pp (in Chinese) (unpubl.)

Liu F, Li YH, Mao JW, Yang FQ, Chai FM, Geng XX, Yang ZX (2008) The SHRIMP U–Pb ages of Abagong granites in the Altaid Orogen and its geologic implication. Acta Geoscientica Sinica 29:795-804(in Chinese with English abstract)

Shan Q, Zeng QS, Luo Y, Yang WB, Zhang H, Qiu YZ, Yu XY (2011) SHRIMP U-Pb ages and petrology studies on the potassic and podic rhyolites in Altai, North Xinjiang. Acta Petrologica Sinica 27:3653-3665 (in Chinese with English abstract)

Mineralization, alteration, and ore fluid source for iron deposits in Western Tianshan, NW China

Zuoheng Zhang, Wei Hong, Zongsheng Jiang, Shigang Duan
MLR Key Laboratory Metallogeny and Mineral Assessment, Institute of Mineral Resources, CAGS, Beijing 100037, China

Zhihua Wang
School of Earth Sciences and Resources, China University of Geosciences, Beijing, 100083, China

Fengming Li
The Bureau of Geology and Mineral Resources Development of Xinjiang, Urumqi, Xinjiang, 830000, China

Fupin Shi
No.3 Unit of the Bureau of Geology and Mineral Resources Development of Xinjiang, Korla 841000, China

Abstract. Several magnetite iron deposits that are mainly hosted in Carboniferous volcanic rocks have been discovered in Western Tianshan of NW China in recent years. Three iron ore types could be preliminarily recognized as volcanic-sedimentary type, magmatic-hydrothermal type and skarn type. A range of wallrock alteration styles are mostly categorized as Na or K-calc mineral assemblages, commonly represented as pyroxene, albite, K-feldspar, epidote, actinolite, and garnet. Oxygen and sulfur isotopes indicate the ore-fluid source might consist of early magmatic derived fluids followed by hydrothermal fluids during a late stage.

Keywords. Iron mineralization, stable isotope, Western Tianshan

1 Introduction

Since 2004, iron exploration has made a notable advance in Western Tianshan Mountains, NW China, due to discoveries of several iron deposits with estimated reserves of more than 2,000 million tonnes (Zhang et al., 2011). These ore bodies are hosted in Carboniferous volcanic rocks, in association with regional or local faults, and are thus usually arranged along strike of one another. Based on field work and experimental data obtained during the last three years, this paper introduces the main mineralized characteristics, and briefly elucidates possible source fluids for the ore, and initially discusses ore formation processes for these deposits.

2 Regional background

The Western Tianshan is located along the southwest margin of the Central Asia Orogenic Belt (CAOB), which is the largest Phanerozoic accretionary orogeny in the world (Windley et al., 2007). It can traditionally be divided into three sections: North Tianshan, Central Tianshan and South Tianshan, all of which can be separated by major suture zones and regional-scale strike-slip faults. Within the confines of the northern tectonic nappe and southern fault zone, this triangular area is regarded as a fan-shaped orogenic zone that overthrusted towards the northern and southern margins, respectively. It is believed that two collisional-accretionary activities subducted successively southward and northward in the Early Palaeozoic (Allen at al., 1992), ceased in the Late Carboniferous and thus this orogen belonged to a late Paleozoic accretionary zone (Gao et al., 1998). During this period, a large volume of Carboniferous volcanic rocks erupted and formed, coinciding with tectonic transformation. Carboniferous Dahalajunshan Formation volcanic rock formed widely in these areas. The interpreted sedimentary-tectonic environment for the volcanic rock is contentious. Different interpretations include, 1) a large igneous province related to a mantle plume (Xia et al., 2004), 2) active continental arc (Wang et al., 2007; Zhu et al., 2009) and 3) back-arc extensional environment related to an active continental margin (Qian et al., 2006).

3 Deposit geology

3.1 Mineralization types

Apart from epithermal gold deposits and skarn-porphyry Cu-Mo deposits in Western Tianshan, most exploration efforts have been directed towards iron ore in recent years. These Fe deposits mainly occur in Carboniferous volcanics, particularly in the Dahalajunshan Formation, which comprises andesite, trachyte, trachyte andesite, basaltic andesite, basalt, and andesitic volcaniclastics. Furthermore, they are concentrated linearly in the Awulale Mountain, situated in the Yili-middle Tianshan suture, indicating that Fe mineralization might be fault-controlled. There are three chief iron ore types:

(1) volcanic-sedimentary type; mainly distributed along the eastern and western edges of Awulale Mountain, and usually containing manganese (example as Shikebutai, Motuosala, and Jiamantai). Ore minerals include hematite, magnetite, and minor rhodochrosite or hausmannite, whereas gangue minerals include jasper, barite, sericite, chlorite, quarts and calcite. Besides volcanic rocks, andesite-dacite tuff and sandstone, siltstone or conglomerate are exposed in ore districts. Orebodies form as layers, lenses and lenticular bodies that are often integrated with wallrock. Banded hematite is interlayered with jasper (Fig. 1a), suggesting sedimentary deposition during ore formation.

(2) magmatic-hydrothermal iron deposits (e.g. Zhibo, Nixintage) are believed to be exposed near or around Carboniferous craters, although no paleo-volcanic centres have been identified owing to rough terranes (more than 4 km altitude), intense deformation, and

intermittent geological mapping. This ore type is interpreted to have been formed during a magmatic-hydrothermal event related to eruptions of the Dahalajunshan Formation volcanic rocks. Some features of these ores are comparable to volcanic iron deposits in the Lower Yangtze River of eastern China (Mao et al., 2011) and Kiruna ores in Sweden and Chile (Nyström and Henriquez, 1994). Magnetite is the leading ore mineral with minor pyrite and chalcopyrite, whilst K-feldspar, actinolite, pyroxene, chlorite, and epidote are common gangue minerals. Ore bodies with more than 45% Fe are directly in contact with volcanic wallrock without alteration or minor orthoclase-epidote assemblages. Moreover, vesicular, dendritic and platy magnetites (Fig. 1b) formed at Zhibo deposit, similar to textual features reported in Kiruna-type deposits, which were interpreted as rapid-growth from ore magmas (Nyström and Henriquez, 1994). Thus, they can possibly be interpreted as additional evidence for magmatic melt being involved with iron mineralization. An obvious difference is that this type of deposit contains very minor apatite.

(3) iron skarn deposits are exemplified by the Beizhan, Dunde, Chagangnuoer and Kuolasayi deposits, which contain skarn assemblages including garnet, diopside, actinolite, and locally wollastonite, scapolite, as well as retrograde stage minerals, such as chlorite, epidote, quarts, calcite or sericite. Ore minerals are mostly magnetite, and minor pyrite, chalcopyrite, whereas pyrrhotite, sphalerite and galena are enriched locally (e.g., Dunde). However, there is no direct evidence for iron mineralization that is genetically related to intrusions. An interesting phenomenon is that lenticular carbonate crops out as an interlayer between volcanic strata, and proximal to the main orebodies. In these cases, garnet and diopside could be found to be extensively intergrown with magnetite (Fig. 1c). These features indicate that iron mineralization probably resulted from the metasomatism between volcanic and carbonate-rich rocks.

3.2 Wall rock alteration

Four main hydrothermal alteration mineral assemblages are recognized in wall rock in the Western Tianshan. 1) pyroxene-albite alteration is present in the early stages of magmatic-hydrothermal deposits, with minor anhedral magnetite filled in interstitial areas among these minerals; 2) garnet-pyroxene (-wollastonite-scapolite) veins developed widely in ore districts with carbonate-rich and volcanic rocks. Electron microprobe analyses reveal that the end composition of garnet and pyroxene are andradite, grossularite and diopside, hedenbergite, respectively, similar to typical iron skarn deposits. Commonly, magnetite grew outside of euhedral-subhedral garnet and pyroxene, which indicates magnetite formed later than these prograde products; 3) K-feldspar-actinolite-epidote-chlorite alteration is commonly developed during the middle stages of magmatic-hydrothermal and skarn deposits. From wall rock central to iron ore, K-feldspar, actinolite and epidote-chlorite could be identified, in particular in the term of K-feldspar-epidote banded layer or cemented with brecciaed magnetite. K-feldspar occurs as a xenomorphic granular crystal form, possibly altered from albite or diopside. At this stage, magnetite deposited as massive breccias; 4) sulfide-quartz-calcite alteration may be regarded as the latest stage of mineralization. Sulfides include pyrite, chalcopyrite and pyrrhotite or sphalerite, usually occurring as anhedral and coarse particles. Moreover, quartz-calcite veins are widely present and cut early minerals and rocks along fissures. Volcanic-sedimentary Fe deposits developed weak chlorite-sericite-quartz-calcite alteration.

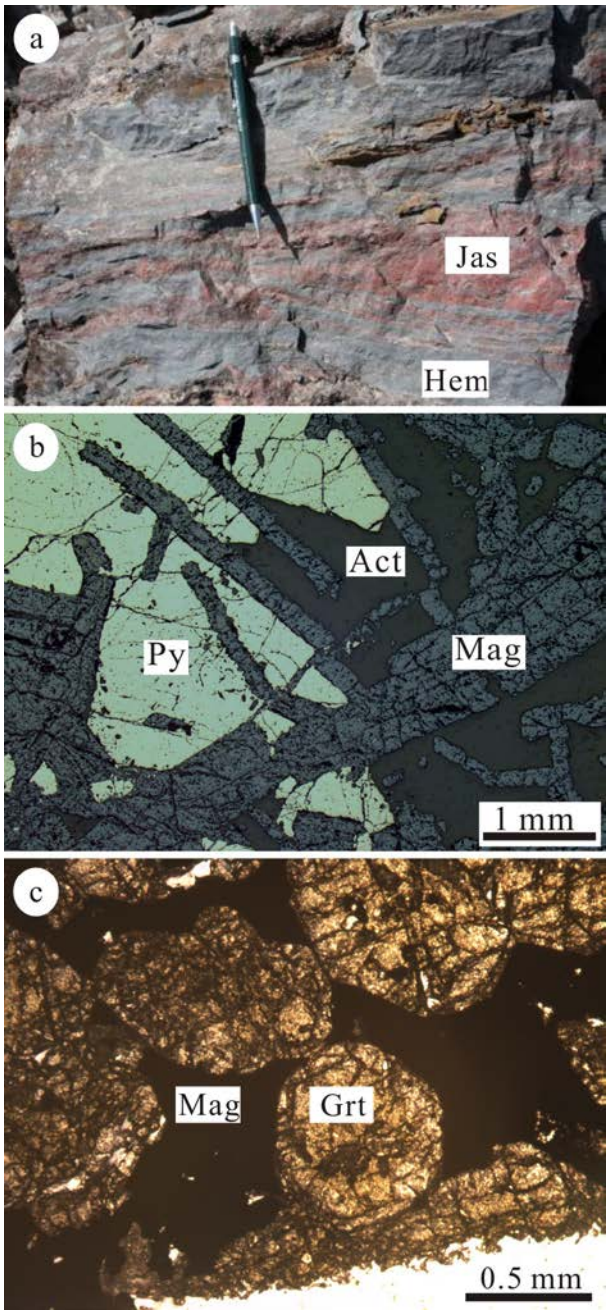

Figure 1. (a) Banded ore with hematite (Hem) interlayered with jasper (Jas) at the Shikebutai deposit; (b) Platy magnetite (Mag) at Zhibo deposit, under reflected light; (c) Anhedral magnetite (Mag) is intergrown with euhedral garnet (Grt) at the Chagangnuoer deposit, under transmitted light.

4 Stable isotopic features

Samples chosen from several typical deposits have been measured for oxygen and sulfur isotopes.

4.1 Oxygen isotopes

$\delta^{18}O_{V\text{-}SMOW}$ values for magnetite from Chagangnuoer ore (iron skarn) vary between 0.5-3.5‰, $\delta^{18}O_{V\text{-}SMOW}$ values for magnetite from the Dunde deposit (iron skarn) range from 7.1-8.1‰, whereas $\delta^{18}O_{V\text{-}SMOW}$ values for magnetite from the Zhibo deposit (magmatic-hydrothermal type) vary from 3.5-9.8‰. Oxygen isotopes for igneous magnetite are confined to 1-4‰, thus the magnetite deposits with $\delta^{18}O$ values exceeding this range probably have a different origin, or have been recrystallized and altered subsequent to its formation (Taylor, 1967). $\delta^{18}O_{V\text{-}SMOW}$ values for magnetite selected from early stages are close to 1-4‰, indicating that magmatic derived fluids may have been involved in early mineralization; whereas those analysed magnetites from later stages deviate from this range, suggests the influence of later hydrothermal fluids. More specifically, lower $\delta^{18}O$ values (0.5-1‰) might result from the strong alteration between wall rock and ore-forming fluids (Nyström et al, 2008; Hoefs, 2009) in iron skarn deposits, whereas mineral recrystallization effects (Nyström et al, 2008) might also contributed to these anomalously higher $\delta^{18}O$ values (7.1-9.8‰) for coarse magnetites from both iron skarn and magmatic-hydrothermal deposits.

4.2 Sulfur isotopes

$\delta^{34}S_{CDT}$ values for pyrite associated with Chagangnuoer ore (iron skarn) are 0.8-13.1‰, $\delta^{34}S_{CDT}$ values for sulfides at the Dunde deposit (iron skarn) vary from 3.8-8.0‰, whereas $\delta^{34}S_{CDT}$ values for pyrite from the Zhibo deposit (magmatic-hydrothermal type) range between 0.3-1.2‰. Most of these sulfur isotopic components are concentrated around 0‰, representing a presumed magmatic mantle source (e.g., Ni-Cu deposits, Ripley and Li 2003; Hoefs, 2009), especially in the magmatic-hydrothermal type of iron ore (e.g., the Zhibo deposit). But certain minor sedimentary sulfur (-40‰ to -50‰ , Hoefs, 2009) or oceanic sulfur (around 20‰, Hoefs, 2009) might contaminate the composition of ore-forming fluid during the later mineralized stage, exemplified from iron skarn deposits whose $\delta^{34}S$ values are greater than 10‰.

5 Summary

(1) Iron deposits in Western Tianshan can initially be divided into three types including volcanic-sedimentary type, magmatic-hydrothermal type and iron skarn type.
(2) These Fe ores display characteristic wall rock alteration mineral assemblages that can be summarized as sodic-calc and potassic alteration, expressed by pyroxene, albite, K-feldspar, epidote, actinolite, and garnet.
(3) Oxygen and sulfur isotopes indicate that magmatic derived fluids might have been involved during early mineralization, whereas hydrothermal fluids had a leading role during the later stages.

Acknowledgements

The study was jointly supported by National Key Basic Research and Development Program (No.2012CB416803), National Science and Technology Support Program (NO.2011BAB06B02) and Geological Survey Projects (No.1212010010220).

References

Allen M.B., Windley B.F., Zhang Chi.(1992).Palaeozoic collisional tectonics and magmatism of the Chinese Tien Shan, central Asian. Tectonophysics, 220:89-115.

Gao J, Li M S, Xiao X C, Tang Y Q, He G Q.(1998) Paleozoic tectonic evolution of the Tianshan Orgen northern China. Tectonophysics, 287: 213-231.

Hoefs J. (2009). Stable isotope geochemistry. 6th edition. Berlin: Spring Verlag, 1-285.

Mao J W, Xie G Q, Duan C, Pirajno F, Ishiyama D and Chen Y C. (2011). A tectono-genetic model for porphyry–skarn–stratabound Cu–Au–Mo–Fe and magnetite–apatite deposits along the Middle–Lower Yangtze River Valley, Eastern China. Ore Geology Reviews, 43 (1): 294-314.

Nyström J O and Henriquez F.(1994) Magmatic features of iron ores of the Kiruna type in Chile and Sweden; ore textures and magnetite geochemistry. Economic Geology, 89(4): 830-839

Nyström J O, Billström K, Henríquez F, Fallick A E and Naslaud H R. (2008). Oxygen isotope composition of magnetite in iron ores of the Kiruna type in Chile and Sweden. GFF, 130(4): 177-188.

Qian Q, Gao J, Xiong X M, Long L L and Huang D Z (2006) Petrogenesis and tectonic setting of Carboniferous volcanic rocks from north Zhaosu, western Tianshan Mountains: constrains from petrology and geochemistry. Acta Petrologica Sinica, 22(5): 1307-1323 (in Chinese with English abstract)

Ripley EM, Li C (2003) Sulfur isotope exchange and metal enrichment in the formation of magmatic Cu-Ni-(PGE)-deposits. Econ Geol 98: 635–641.

Taylor. H.P. Jr. (1967). Oxygen isotope studies of hydrothermal mineral deposits. In: Barnes HL (ed.): Geochemistry of hydrothermal ore deposits. New York: John Wiley & Sons, 109-142.

Wang B., Shu L.S., Cluzel D., Faure M., Charvet J.(2007). Geochemical constrains on Carboniferous volcanic rocks of the Yili Block (Xinjiang, NW China): Implication for the tectonic evolution of Western Tianshan. Journal of Asian Earth Sciences, 29: 148-159.

Windley B F, Alexeiev D, Xiao W, Kröner A and Badarch G. (2007). Tectonic models for accretion of the Central Asian Orogenic Belt. Journal of the Geological Society, 164 (1): 31-47.

Xia L Q, Xu X Y, Xia Z C, Li X M, Ma Z P, Wang L S. (2004) Petrogenesis of Carboniferous rift-related volcanic rocks in the Tianshan, Northwestern China. Geological Society of America Bulletin, 116: 419-433.

Zhang Z H, Hong W, Li F M, Wang Z H, Liu M. (2011).Geological characteristics of iron ore deposits in the western Tianshan Mountain, NW China. 11th SGA Biennial Meeting Let's Talk Ore Deposits, 26–29th September 2011 Antofagasta, Chile: 782-84.

Zhu Y F, Guo X, Song B, Zhang L F and Gu L B (2009) Petrology, Sr-Nd-Hf isotopic geochemistry and zircon chronology of the Late Palaeozoic volcanic rocks in the southwestern Tianshan Mountains, Xinjiang, NW China. Journal of the Geological Society, 166 (6): 1085-1099.

S 3.5:

Porphyry systems and epithermal deposits

SPONSORED BY SEG

Convenors:
Jeffrey Hedenquist & Ferenc Molnár

KEYNOTE SPEAKER

Role of porphyry copper models in exploration and discovery

Richard H. Sillitoe
27 West Hill Park, Highgate Village, London N6 6ND, England

Abstract. A variety of regional and deposit-scale geological features are routinely employed in porphyry copper exploration at the area selection, prospect appraisal and detailed exploration stages; well-founded genetic explanations are available for many of them. These features and the resulting geological model underpin proper interpretation of geochemical and geophysical anomalies. A majority of porphyry copper discoveries worldwide during the past decade or so have been particularly dependent on mineralogical vectors based on informed (re)logging of drill core and cuttings, followed by deep drill testing of the resulting predictive models. Nonetheless, conventional geochemical and prospect-scale geophysical surveys also made significant contributions.

Keywords. Porphyry copper model, alteration zoning, copper exploration, discovery

1 Introduction

Porphyry copper deposits are centred on small, originally subvertical porphyry intrusions in hydrothermal systems that have vertical extents of at least 4 km. They contain approximately 80 % of the world's copper resources and, as a consequence, have for many years been a prime exploration objective for the major, mid-tier and junior sectors. The geological model for porphyry copper deposits has developed progressively over the past half century and, arguably, is now more robust than that for any other major ore deposit type. When applied to exploration, the model successfully integrates empirical features with most elements of porphyry copper genesis (Thompson 1993) as well as providing a template for interpretation of geochemical and geophysical responses.

This summary highlights basic features of the porphyry copper model that can be employed at the area selection, prospect appraisal and detailed exploration stages preparatory to considering methods that were critical to the most recent major discoveries. Current versions of the porphyry copper model are summarised elsewhere (Seedorff et al. 2005; Sillitoe 2010).

2 Area selection criteria

Porphyry copper deposits form at convergent plate margins in both Cordilleran and island arc (including back arc and post-collisional) settings in which they are related to low- to high-K calc-alkaline and, far less commonly, alkaline magmatism (Sillitoe 1972; Richards 2009). Magmatic arcs constructed during contractional tectonism are deficient in volcanic rocks, and tend to host most of the largest and highest-grade deposits (Sillitoe 1998). Arcs characterised by chemically reduced crustal profiles (e.g. Japan; Sato 2012), crustal extension resulting in compositionally bimodal (basalt-rhyolite) magmatism (Sillitoe 1999) or widespread ash-flow caldera development (Sillitoe 1980) are not prospective. Arcs older than mid-Mesozoic also tend to be less prospective because of the greater likelihood that any porphyry copper deposits have already been eroded (Sawkins 1972).

Porphyry copper deposits form in spatially and temporally restricted belts and corresponding epochs, some of which are more productive than others (e.g. central Andes; Sillitoe 1988). Therefore isotopic dating of prospects offers a valid means of preliminarily assessing their potential. Porphyry copper deposits also tend to occur in groups, forming either apparently random clusters or well-defined alignments. This fact emphasises the importance of brownfields exploration in the vicinity of known deposits, where the largest and highest-grade orebody is not necessarily the first to be discovered; for example, Hugo Dummett in the Oyu Tolgoi district of Mongolia was the fourth (Kirwin et al. 2003).

Development of high grades in many hypogene porphyry copper deposits appears to be influenced by host-rock permeability and/or chemical composition (Sillitoe 2010). Massive carbonate sequences inhibit dissipation of the mineralizing fluid, thereby enhancing internal copper precipitation. Proximal copper skarns are commonly higher in grade than the contiguous porphyry and form in carbonate wall rocks where permeability is adequate. Ferrous iron-rich host rocks reduce the mineralizing fluid, causing highly effective copper precipitation beyond the porphyry intrusions.

3. Prospect appraisal criteria

Porphyry copper exploration in exposed areas commonly focuses on prominent colour anomalies produced by the limonite and associated kaolinite that result from supergene oxidation of pyrite, much of it located either above or around the main copper concentrations. However, deposits that are relatively deeply eroded and dominated by potassic alteration may lack appreciable peripheral pyrite and, hence, give rise to far more subtle visual anomalies.

During early exploration stages, alteration zones related to porphyry copper deposits need to be distinguished from those of different origins, such as IOCG, VMS or epithermal deposits. The most distinctive criterion is undoubtedly the presence of A-, B- and D-type stockwork or, less commonly, sheeted veinlets (Gustafson and Hunt 1975), all of which withstand the

effects of weathering. Although the quartz-dominated, A- and B-type veinlets formed along with potassic alteration, they may be inherited by any overprinted alteration type, including chlorite-sericite, sericitic and advanced argillic. At the scale of individual prospects, veinlet intensity is an effective vector to ore (Titley et al. 1986).

Surface recognition of alteration zoning is also a good method of determining vectors towards ore in porphyry copper systems (Jerome 1966; Nielsen 1968; Lowell and Guilbert 1970). Centrally positioned potassic and overlying and/or overprinted chlorite-sericite or sericitic alteration can constitute ore, although the first two of these are unstable in the supergene environment where they may be at least partially masked by kaolinisation. Although the propylitic haloes that encircle the other alteration types tend to be highly pyritic, their outermost parts contain only traces of pyrite, which when transformed to supergene jarosite at and near surface can be tricky to detect. Where exploration is conducted in areas of post-mineral cover, such subtle distal features may be the only direct indication of porphyry copper prospects, although petrographic, mineral chemistry and isotopic studies could prove helpful (Baker et al. 2012; Djouka-Fonkwé et al. 2012). Widespread sodic-calcic alteration suggests that the roots of a system may be exposed and any orebody is either eroded or, as in parts of southwestern North America (Seedorff et al. 2008), located at some considerable distance because of the effects of extension-induced tilting and structural dismemberment.

Many visually and topographically prominent and, commonly, areally extensive alteration zones defined by advanced argillic assemblages constitute the shallow portions of porphyry copper systems (Sillitoe 1975; Wallace 1979); they may host high-sulphidation epithermal gold ± silver orebodies of either lode or disseminated types (Sillitoe 1983; Hedenquist et al. 1998). Since most advanced argillic lithocaps are erosional remnants, exploration should commence around their peripheries, in case the porphyry copper centre(s) have already been exhumed, before they are tested at depth internally (Sillitoe 1995). Lithocap mineralogy, particularly higher-temperature silicate species (e.g. pyrophyllite, andalusite) and alunite compositions, indicate proximity to the heat and fluid sources associated with the underlying porphyry intrusions (Watanabe and Hedenquist 2001; Chang et al. 2011). Intermediate-sulphidation epithermal gold ± silver orebodies can form on the margins of lithocaps, where they tend to be overshadowed by the more conspicuous advanced argillic alteration (Sillitoe and Hedenquist 2003).

The hydrothermal breccias common in porphyry copper deposits need to be carefully distinguished. Magmatic-hydrothermal breccias that contained appreciable open space at the time of sulphide introduction may have enhanced copper tenors, whereas matrix-supported, phreatomagmatic breccias filling kilometre-scale diatreme vents are commonly barren, and may even destroy pre-existing ore (Sillitoe 1985). Mineralized clasts in diatreme breccias may provide direct evidence for underlying porphyry copper and associated mineralization.

The alteration-mineralization zoning of porphyry copper systems is reflected in their soil and rock-chip geochemical responses. Maximum copper values, accompanied by molybdenum and/or gold, define potential ore zones and are surrounded by propylitic haloes containing zinc, lead, silver (± gold) and manganese (Jerome 1966). In contrast, gold-rich deposits are typified by annular molybdenum haloes that overlap external parts of the copper-gold cores (Sillitoe 1979). Leached capping developed in the supergene environment over relatively pyritic systems may be almost devoid of copper, leaving molybdenum ± gold to denote the position of the underlying chalcocite enrichment blanket (e.g. Escondida, Chile; Lowell 1991). However, polished-section study of residual sulphide minerals encapsulated in quartz veinlets can throw light on former copper contents (Hunt et al. 1983).

4. Detailed exploration criteria

Copper and any accompanying molybdenum and/or gold mineralization in porphyry copper deposits is normally heterogeneously distributed as a result of a combination of factors, including relative intrusion age and sulphide zoning. This heterogeneity needs to be appreciated promptly and defined precisely for resource estimation purposes.

The porphyry copper stocks or dykes that are the foci of porphyry copper deposits are typically composite, comprising early, inter-mineral and late-mineral phases (Gustafson and Hunt 1975; Sillitoe 2000; Proffett 2003). Inter-mineral porphyries cut the already-mineralized early porphyry phases and, consequently, are lower in grade. By the same token, the late-mineral phases are subeconomic and, commonly, barren. The porphyry phases may intrude sequentially along the same vertical axis or be more randomly emplaced.

Porphyry copper deposits are characterised both upwards and outwards by sulphide zoning, particularly increases in pyrite/chalcopyrite ratios, which can provide a useful vector at the drilling stage (Lowell and Guilbert 1970). Within some internal, low sulphidation-state potassic zones, bornite/chalcopyrite ratios increase downwards, whereas pyrite-rich, high sulphidation-state assemblages, containing bornite, chalcocite, covellite and/or enargite, characterise the shallower sericitic and advanced argillic environment where elevated arsenic contents can increase upwards and be metallurgically troublesome. Where sericitic and/or advanced argillic alteration overprint mineralized quartz veinlet stockworks, the resulting high-sulphidation sulphide assemblages may have higher copper contents (hypogene enrichment).

This sulphide zoning, which can result in total sulphide contents that range from 2-3 vol. % in the cores of deposits to 10-20 vol. % in their outer (sericitic and inner propylitic) and upper (sericitic and advanced argillic) parts, is a critical factor for interpretation of induced-polarisation chargeability responses. The addition of up to 10 vol. % of magnetite during potassic alteration in gold-rich porphyry copper deposits (Sillitoe

1979) can give rise to readily detectable magnetic anomalies, particularly where magnetite-deficient host rocks are present. Properly interpreted induced-polarisation and magnetic anomalies can assist with the efficient drill-out of porphyry copper prospects.

5. Recent discovery methodology

Discoveries of major porphyry copper deposits are rare and noteworthy events. During the last decade or so, there were nine such discoveries worldwide (Table 1): three resulting from greenfields and six from brownfields exploration programmes, and three partially exposed and six entirely concealed beneath post-mineral cover.

Table 1. Recent major porphyry copper discoveries

Deposit, country	Discovery method	Reference
Toki cluster (four deposits), Chile	Top-of-bedrock geochemistry in RC drill holes; instigated by re-examination of pre-existing drill cuttings	Rivera and Pardo (2004)
Pebble East, Alaska, U.S.A.	Step-out drilling based on mineralogical and grade vectors	Rebagliati and Lang (2009)
Pampa Escondida, Chile	Deeper drilling of previously known mineralization based on mineralogical vectors in pre-existing drill core	Hervé et al. (2012)
Esperanza, Chile	Deeper drilling using mineralogical vectors; influenced by magnetic anomaly	Perelló et al. (2004)
Caracoles (Encuentro), Chile	Drilling previously known prospect based on mineralogical vectors in pre-existing RC cuttings; influenced by IP results	Perelló et al. (2010)
Boyongan, Mindanao, Philippines	Follow-up of drainage geochemical survey; mineralogical vectors in core from initial drill holes	Waters (2002)
Los Sulfatos, Chile	Deeper drilling of old prospect; mineralogical vectors in core from initial drill holes	Irarrazaval et al. (2010)
Tujuh Bukit, Java, Indonesia	Drilling beneath lithocap; based on drill-core observation of mineralized porphyry clast in breccia	Snow (2013)
Hugo Dummett, Oyu Tolgoi, Mongolia	Deep drilling of IP chargeability anomaly	Kirwin et al. (2003)

Mineralogical vectors based on alteration and/or sulphide mineralization observed in pre-existing drill core or cuttings were influential in eight of the discoveries (Table 1). In five of these, previous explorers failed to make the key observations that led to eventual discovery, thereby emphasising the critical importance of involving geologists familiar with the porphyry copper model and able to effectively log drill core and, perhaps even more importantly, reverse-circulation cuttings. At Esperanza and Pampa Escondida, the exploration models correctly predicted the existence of downward increases in bornite/chalcopyrite ratios and, hence, copper (and gold) contents (Perelló et al. 2010; Hervé et al. 2012). In the case of Los Sulfatos, it was recognised that pyritic magmatic-hydrothermal breccia could (and does) become chalcopyrite- and then bornite-rich with increased depth (Irarrazaval et al. 2010). At Tujuh Bukit, recognition of a single mineralized porphyry clast in hydrothermal breccia led to deeper drilling and successful discovery of its porphyry copper-gold source (Snow 2013).

Geochemistry was a key ingredient in discovery of the Toki cluster in the Chuquicamata district, where reverse-circulation grid drilling carried out to detect top-of-bedrock geochemical anomalism resulted in direct detection of three of the four deposits (Rivera and Pardo 2004). A drainage geochemical survey resulted in recognition of the well-mineralized boulders that eventually led to discovery of the concealed Boyongan deposit (Waters 2002). Persistent drill testing of two markedly different chargeability anomalies generated by independent induced-polarisation surveys resulted in the deep Hugo Dummett discovery in a brownfields setting at Oyu Tolgoi (Kirwin et al. 2003). Geophysical results, integrated with the geological models, played a role in the Esperanza and Caracoles (Encuentro) discoveries in the Centinela district (Perelló et al. 2004, 2010; Table 1), but failed to assist at Pebble East, Pampa Escondida, Boyongan and Tujuh Bukit.

Therefore detailed geological appraisal or reappraisal of drill core or cuttings has been the premier tool used in recent porphyry copper discoveries, with significant contributions also being made by conventional drainage or rock-chip geochemistry and prospect-scale magnetic or induced-polarisation geophysical surveys. In recent years, there has also been a markedly greater appetite for both more and deeper drill testing of many porphyry copper prospects: a tendency that contributed importantly to the discoveries listed in Table 1. Moreover, it is worth noting that regional geophysical surveys, partial- or selective-extraction geochemical sampling of post-mineral cover, satellite imagery analysis, structural (including lineament) studies and computer modelling played no role in these recent porphyry copper discoveries.

Acknowledgements

Jeff Hedenquist and Ferenc Molnár are thanked for the invitation to contribute this presentation, and Jeff Hedenquist and Pepe Perelló for reviewing the manuscript.

References

Baker MJ, Cooke DR, Hollings PN, Wilkinson JJ, Wilkinson C (2012) Epidote trace element geochemistry as an exploration tool: El Teniente porphyry Cu-Mo deposit case study. In: 15th Congreso Peruano de Geología & SEG 2012 Conference, Lima, 2012, Oral Abstracts, Pendrive

Chang Z, Hedenquist JW, White NC, Cooke DR, Roach M, Deyell CL, Garcia Jr J, Gemmell JB, McKnight S, Cuison AL (2011) Exploration tools for linked porphyry and epithermal deposits: Example from the Mankayan intrusion-centered Cu-Au district, Luzon, Philippines. Econ Geol 106:1365–1398

Djouka-Fonkwé ML, Kyser K, Clark AH, Urqueta E, Oates CJ, Ihlenfeld C (2012) Recognizing propylitic alteration associated with porphyry Cu-Mo deposits in lower greenschist facies metamorphic terrain of the Collahuasi district, northern Chile–Implications of petrographic and carbon isotope relationships. Econ Geol 107:1457–1478

Gustafson LB, Hunt JP (1975) The porphyry copper deposit at El Salvador, Chile. Econ Geol 70:857-912

Hedenquist JW, Arribas Jr A, Reynolds TJ (1998) Evolution of an intrusion-centered hydrothermal system: Far Southeast-Lepanto porphyry and epithermal Cu-Au deposits, Philippines. Econ Geol 93:373–404

Hervé M, Sillitoe RH, Wong C, Fernández P, Crignola F, Ipinza M, Urzúa F (2012) Geologic overview of the Escondida porphyry copper district, northern Chile. Soc Econ Geol Spec Publ 16:55–78

Hunt JP, Bratt JA, Marquardt JC (1983) Quebrada Blanca, Chile: An enriched porphyry copper deposit. Min Eng 35:636–644

Irarrazaval V, Sillitoe RH, Wilson AJ, Toro JC, Robles W, Lyall GD (2010) Discovery history of a giant, high-grade, hypogene porphyry copper-molybdenum deposit at Los Sulfatos, Los Bronces-Río Blanco district, central Chile. Soc Econ Geol Spec Publ 15:253–269

Jerome SE (1966) Some features pertinent in exploration of porphyry copper deposits. In: Titley SR, Hicks CL (eds) Geology of the porphyry copper deposits, southwestern North America. University of Arizona Press, Tucson, pp 75–85

Kirwin DJ, Foster CN, Garamjav D (2003) The discovery history of the Oyu Tolgoi porphyry copper-gold deposits, South Gobi, Mongolia. In: Proc NewGenGold 2003 Conference, Perth, 2003. Australian Mineral Foundation, Adelaide, pp 130–146

Lowell JD (1991) The discovery of the La Escondida orebody. Econ Geol Monogr 8:300–313

Lowell JD, Guilbert JM (1970) Lateral and vertical alteration-mineralization zoning in porphyry ore deposits. Econ Geol 65:373–408

Nielsen RL (1968) Hypogene texture and mineral zoning in a copper-bearing granodiorite stock, Santa Rita, New Mexico. Econ Geol 63:37–50

Perelló J, Brockway H, Martini R (2004) Discovery and geology of the Esperanza porphyry copper-gold deposit, Antofagasta Region, northern Chile. Soc Econ Geol Spec Publ 11:167-186

Perelló J, Muhr R, Mora R, Martínez E, Brockway H, Swaneck T, Artal J, Mpodozis C, Münchmeyer C, Clifford J, Acuña E, Valenzuela D, Argandoña R (2010) Wealth creation through exploration in a mature terrain: The case history of the Centinela district, northern Chile porphyry copper belt. Soc Econ Geol Spec Publ 15:229–252

Proffett JM (2003) Geology of the Bajo de la Alumbrera porphyry copper-gold deposit, Argentina. Econ Geol 98:1535–1574

Rebagliati M, Lang J (2009) The Pebble porphyry copper-gold-molybdenum discovery, Alaska, USA. In: Proc NewGenGold Conference 2009–Case histories of discovery, Perth, 2009. Paydirt Media Pty Ltd, West Perth, pp 121–132

Richards JP (2009) Postsubduction porphyry Cu-Au and epithermal Au deposits: Products of remelting of subduction-modified lithosphere. Geology 37:247–250

Rivera SL, Pardo R (2004) Discovery and geology of the Toki porphyry copper deposit, Chuquicamata district, northern Chile. Soc Econ Geol Spec Publ 11:199–211

Sato K (2012) Sedimentary crust and metallogeny of granitoid affinity: Implications from the geotectonic histories of the circum-Japan Sea region. Res Geol 62:329–351

Sawkins FJ (1972) Sulfide ore deposits in relation to plate tectonics. J Geol 80:377–397

Seedorff E, Dilles JH, Proffett Jr JM, Einaudi MT, Zurcher L, Stavast WJA, Johnson DA, Barton MD (2005) Porphyry deposits: Characteristics and origin of hypogene features. In: Hedenquist JW, Thompson JFH, Goldfarb RJ, Richards JP (eds) Economic Geology 100th Anniversary Volume, pp 251–298

Seedorff E, Barton MD, Stavast WJA, Maher DJ (2008) Root zones of porphyry systems: Extending the porphyry model to depth. Econ Geol 103:939–956

Sillitoe RH (1972) A plate tectonic model for the origin of porphyry copper deposits. Econ Geol 67:184–197

Sillitoe RH (1975) Lead-silver, manganese, and native sulfur mineralization within a stratovolcano, El Queva, northwest Argentina. Econ Geol 70:1190–1201

Sillitoe RH (1979) Some thoughts on gold-rich porphyry copper deposits. Mineral Deposita 14:161–174

Sillitoe RH (1980) Cauldron subsidence as a possible inhibitor of porphyry copper formation. Min Geol Spec Issue 8:85–93

Sillitoe RH (1983) Enargite-bearing massive sulfide deposits high in porphyry copper systems. Econ Geol 78:348–352

Sillitoe RH (1985) Ore-related breccias in volcanoplutonic arcs. Econ Geol 80:1467–1514

Sillitoe RH (1988) Epochs of intrusion-related copper mineralization in the Andes. J South Am Earth Sci 1:89–108

Sillitoe RH (1995) Exploration of porphyry copper lithocaps. In: Proc Australas Inst Mining Metall Pacific Rim Congress, Auckland, 1995, pp 527–532

Sillitoe RH (1998) Major regional factors favouring large size, high hypogene grade, elevated gold content and supergene oxidation and enrichment of porphyry copper deposits. In: Porter TM (ed) Porphyry and hydrothermal copper and gold deposits: A global perspective. Australian Mineral Foundation, Adelaide, pp 21–34

Sillitoe RH (1999) VMS and porphyry copper deposits: products of discrete tectono-magmatic settings. In: Stanley CJ et al. (eds) Mineral deposits: Processes to processing. Proc 5th Biennial SGA Meeting and 10th Quadrennial IAGOD Symposium, London, 1999, vol 1, pp 7–10

Sillitoe RH (2000) Gold-rich porphyry deposits: Descriptive and genetic models and their role in exploration and discovery. Rev Econ Geol 13:315–345

Sillitoe RH (2010) Porphyry copper systems. Econ Geol 105:3–41

Sillitoe RH, Hedenquist JW (2003) Linkages between volcanotectonic settings, ore-fluid compositions, and epithermal precious metal deposits. Soc Econ Geol Spec Publ 10:315–343

Snow G (2013) The giant Tujuh Bukit porphyry discovery: Persistence, geology, process, corporate commitment and luck. In: Prospectors and Developers Association of Canada International Convention, Trade Show and Investors Exchange, Toronto, 2013, Technical Sessions Abstracts, www.pdac.ca

Thompson JFH (1993) Application of deposit models to exploration. Geol Assoc Can Spec Pap 40:51–67

Titley SR, Thompson RC, Haynes FM, Manske SL, Robison LC, White JL (1986) Evolution of fractures and alteration in the Sierrita-Esperanza hydrothermal system, Pima County, Arizona. Econ Geol 81:343–370

Wallace AB (1979) Possible signatures of buried porphyry-copper deposits in middle and late Tertiary volcanic rocks of western Nevada. Nevada Bur Mines Geol Rep 33:69–76

Watanabe Y, Hedenquist JW (2001) Mineralogic and stable isotope zonation at the surface over the El Salvador porphyry copper deposit, Chile. Econ Geol 96:1775–1797

Waters P (2002) Discovery of the Boyongan Cu-Au porphyry deposit, Surigao gold district, NE Mindanao. In: Prospectors and Developers Association of Canada Annual Convention, Toronto, 2002, Technical Programme and Core Shack Abstracts, pp 25

Geology, geochemistry and genesis of Mastra Au-Ag deposit in NE Turkey

Neslihan Aslan
Dept. of Geological Engineering, Karadeniz Technical University, Trabzon 61080, Turkey

Miğraç Akçay*
Dept. of Geological Engineering, Karadeniz Technical University, Trabzon 61080, Turkey

Abstract. An active Au-Ag producing mine, Mastra gold deposit occurs in a fault zone dipping 65-80° towards 20-40° in andesitic volcanics and volcanoclastics of Eocene age. Hydrothermal alteration is represented mainly by propilitic alteration, argillic alteration and silicification. The main ore minerals are pyrite, chalcopyrite, galena, sphalerite, tetrahedrite, silver and gold with minor secondary digenite, covellite, chalcocite, hematite and limonite. Quartz, barite, adularia, calcite, cerussite, gypsum, sericite and clay minerals are the gangue minerals. Quartz veins display massive, comb, crustiform, coquade and brecciated textures, typical for epithermal conditions. Homogenisation temperatures measured in quartz and barite are in the ranges of 113 to 331°C and 150 to 390 °C, respectively. Sulphur isotope values obtained from pyrite, chalcopyrite, galena and sphalerite range from -6,2‰ to -1,7‰. Oxygen isotope values from quartz in mineralised veins and hydrogen isotope values from fluid inclusions in these quartz vary from +8,1‰ to +12,4‰ and from -56,2 to -96,4‰, respectively. The sulphur and oxygen isotope thermometries yielded temperatures in the ranges of 145-400°C and 310-405 °C, respectively for the ore formation. These results, coupled with mineralogical and textural data, indicate that the Mastra deposit is a low sulphidation type epithermal system.

Keywords. Mastra, Epithermal, Gold, Fluid inclusions, Sulphur isotopes, Oxygen isotopes, Hydrogen isotopes

1 INTRODUCTION

The Eastern Black Sea Orogenic Belt (EBSOB) hosts various types of economic mineral deposits including massive sulphide, porphyry copper, skarn and epithermal vein type ore deposits (Akçay and Gündüz, 2004; Eyüboğlu et al., 2011). There is no doubt that these deposits have been formed in an island arc setting. However, there is no consensus on the geodynamic evolution of the region, especially on the polarity of subduction. Some authors claim that the EBSOB is the consequence of southward subduction of an oceanic lithosphere situated in the north of the belt during the Mesozoic-Cenozoic (Bektaş, et al., 1999). In contrast, others favour a northward subduction model for the late Mesozoic-Cenozoic geodynamic evolution of the belt (Karslı et al., 2007). Recent studies by Eyüboğlu et al. (2011 and 2012) on magmatic rocks, however, support the former view. They indicate that the early Cenozoic magmas vary in composition, with some having adakite-like affinities, and have been generated by slab window-related processes in a south-dipping subduction zone beneath EBSOB magmatic arc. They also suggest that epithermal gold deposits in the region are related to non-adakitic Lutetian magmatism consisting of basaltic-andesitic volcanic rocks and associated pyroclastic rocks (Alibaba Formation), well-exposed in the north of the Gümüşhane-Bayburt-İspir line (Eyüboğlu et al., 2011).

Discovered in 1989 by the MTA (Mineral Research and Exploration Institute of Turkey), the Mastra gold deposit is one of these deposits and is situated near the Demirkaynak village, 22 km's to the northwest of Gümüşhane in the southern zone of the EBSOB. Koza Gold Company purchased the ownership of the deposit, explored and developed the mine and started the gold extraction in 2005. It is still an active mine producing Au-Ag both in an open pit and underground. The total reserve is calculated as 1.427.000 tons with average grades of 12,13g/t for Au and 5,5 g/t for Ag corresponding to 556.000 ounces Au and 252.000 ounces Ag.

The second significant gold mine brought into operation in Turkey, the Mastra deposit has not been investigated in detail. The work by Tüysüz et al. (1995) is far from explaining the geology of the deposit. The current work puts forward a portion of a master thesis (Aslan, 2011; unpublished master thesis) that has shed light on many aspects of the mine and the region, and reports the data on fluid inclusion and stable isotope analyses.

2 Geology and Hydrothermal Alteration

The Mastra gold deposit is hosted by altered basaltic-andesitic rocks of the Eocene Alibaba Formation. The deposit occurs within quartz veins in a fault zone dipping 65-80° towards 20-40°. The veins are about 2,5 km's long and a few cm's to 5 m's wide. Native Au, Ag, pyrite, chalcopyrite, sphalerite, sulphosalts and galena are the main ore minerals with minor amounts of secondary digenite, covellite, chalcosite, hematite and limonite. Quartz, barite, adularia, calcite, cerussite, gypsum, sericite, and clay minerals are the gangue minerals.

Quartz is by far the most abundant of the gangue minerals and the main constituent of the veins. Due mainly to the conditions of mineral precipitation, various types of crystallisation, growth and replacement textures are present in the quartz veins. Among such textural features are massive, comb, crustiform, coquade, brecciated, breccia-fill, mosaic, flamboyant, ghost-sphere, saccaroidal, and lattice bladed textures, indication of epithermal conditions (Fig. 1).

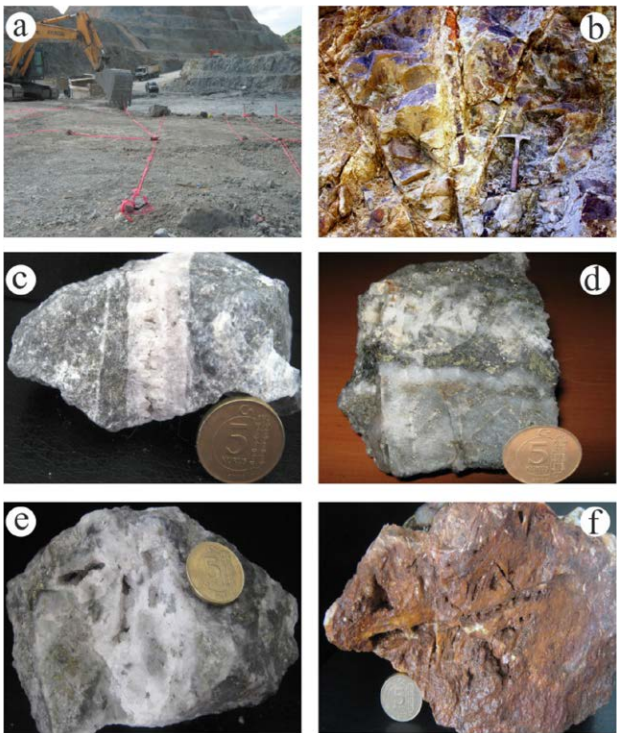

Figure 1. Pictures showing a) the high grade ore zone in the open pit, b) the quartz vein along fault zone, c-f) comb-, banded-, vuggy-, and lattice bladed quartz textures observed in quartz veins at Mastra, respectively.

Hydrothermal alteration varies depending on the distance from quartz veins. Propilitic alteration is widespread in outer zones, which grades into an argillic alteration zone, and finally into silicification near the quartz veins (Fig. 2). Using inter-element correlations, Zr was calculated to be immobile during hydrothermal fluid-rock interaction. Mass-change calculations based on the method of Mclean and Kranidiotis (1987) showed significant changes in mass and volume as a result of hydrothermal alteration. The outer section of the propilitic alteration zone, represented by chlorite-clay minerals±carbonates is characterised by mass and volumetric changes of about 30g/100g. Towards the argillic zone, the change goes up to 42g/100g. The argillic zone displays a volumetric change (25 g/100g) similar to the outer propilitic zone. The highest change (4157 g/100g) was estimated in the silicified zone, the center of the alteration halo. Silica, Al, Fe, Mg and K are the elements with the highest net gains in the outer propilitic zone, Fe, Mg, Ca and K in the inner propilitic zone, Si, Al and K in the argillic zone, and Si, Al, Fe and K in the silicified zone. Argillic alteration is very intense at the surface around the quartz veins, and changes in composition. The outer alteration halo is characterised by smectite-kaolinite and illite, whereas the inner zones by illite with minor kaolinite and smectite, based on microscopic examination and XRD studies of clay fractions of altered rocks. Variation in crystallinity of these clay minerals was not studied.

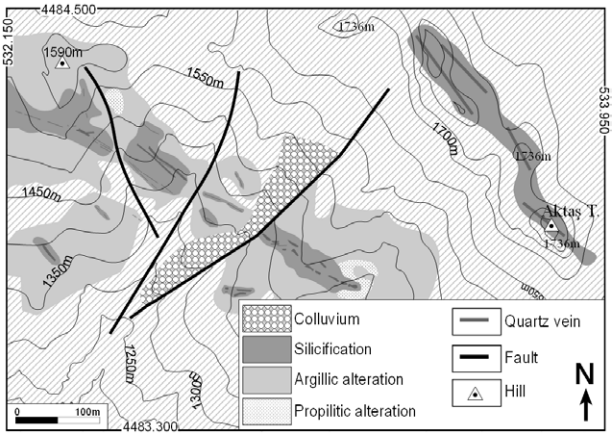

Figure 2. Alteration map of Mastra gold deposit

3 Geochemistry

3.1. Fluid Inclusion

Fluid inclusion studies were performed on quartz and barite from the Mastra ore veins. Primary and secondary fluid inclusions were observed in both minerals. The primary fluid inclusions occur as mono-phase and two-phase inclusions. Two-phase primary fluid inclusions are divided into liquid-rich and gas-rich subtypes. Liquid-rich inclusions are dominant, but gas and liquid rich inclusions of comparable degrees of fill are also found in some sections suggesting boiling conditions (Drummond and Ohmoto, 1985). Monophase inclusions are also of two contrasting compositions supporting boiling.

Homogenization temperatures range from 113 to about 400 ^{o}C with three distinctive populations reflecting different stages of mineral formation. The first population has temperatures ranging from 113 to 230 ^{o}C, the second population from 190 to 290 ^{o}C and the third population from 270 to 331 ^{o}C. The temperatures obtained from barite range between 150 to 390 ^{o}C. These relatively high temperatures for barite are in line with measurements in barite from Hazinemağara deposit nearby (Akçay et al., 2010). The eutectic melting temperatures span a wide range (-31 to -15,4 ^{o}C), suggesting complex and variable compositions, which is yet to be determined. The final ice melting temperatures obtained from quartz and barite are similar and vary between -0,2 and -6,8 ^{o}C, corresponding to salinities up to 10 wt.% NaCl eq. It could be generalised that, both for barite and quartz, higher salinity values were obtained from inclusions with higher homogenisation temperatures (Fig. 3).

3.2. Stable Isotope Geochemistry

δ^{34}S isotope values of pyrite, galena, chalcopyrite and sphalerite from Mastra deposit range from -6.2‰ to -1.7‰. These values are similar to those of granitic rocks and indicate that the origin of sulphur is predominantly

magmatic (Ohmoto and Rye, 1979). Pyrite-galena and sphalerite-galena pairs determined to be in equilibrium indicate formation temperatures of 350±25 °C, and 145±15 °C and 245-400±25 °C, respectively, consistent with the temperatures obtained from the fluid inclusions. The hydrogen and oxygen isotope values of quartz and clay minerals from the Mastra deposit are in the ranges of -56,2‰ to -96,4‰ and +8,1‰ to +12,4‰, respectively. Quartz and illite, formed as a result of hydrothermal alteration, are determined to be in isotopic equilibrium. Formation temperatures for this alteration are calculated to be in the range of 310 – 405 °C (348,5 °C on average) based on geothermometric calculations on quartz-illite pairs using fractionation equations of Matsuhisa et al. (1979) and Friedman and O'Neil (1977). These temperatures, in turn, correspond to oxygen isotope values of +4,5‰ and +10,2‰ for hydrothermal solutions in equilibrium with quartz and illite.

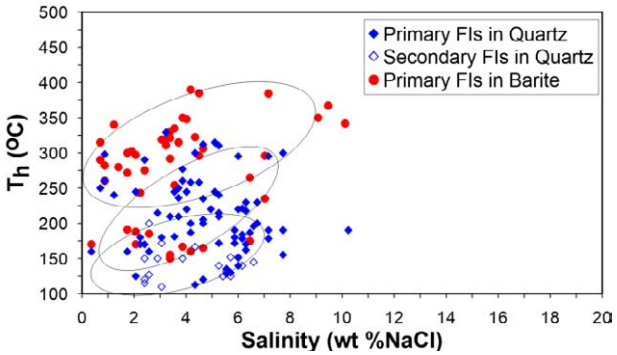

Figure 3. Salinity vs Th diagram for fluid inclusions in quartz and barite from the Mastra deposit.

The diagram created using δD values of water in clay minerals and FI's in quartz, and $\delta^{18}O$ values calculated for the solution in equilibrium with quartz and clay minerals suggest that the hydrothermal solutions are dominantly of magmatic origin (Fig. 4). The very slight shift towards meteoric water line could also be considered as evidence showing the interaction of meteoric waters with magmatic rocks under low fluid/rock ratios.

4 Discussion and Conclusions

The region near Gümüşhane is favourable for vein type barite, Cu-Pb-Zn-Au-Ag, and manganese deposits. All of these deposits are structurally controlled and hosted by basic to acidic volcanics. The presence of these numerous, usually small-scale mineralised systems attracted the attention to the region, and boosted exploration campaigns, which have already paid back by new discoveries. The Mastra deposit was the first major discovery, and enhanced the hopes that new deposits could be found in the region. The fact that the EBSOB is a fossil island arc producing a number of various pulses of magmatic activities and that there are numerous sites of vein formations with widespread hydrothermal alteration zones supports this view.

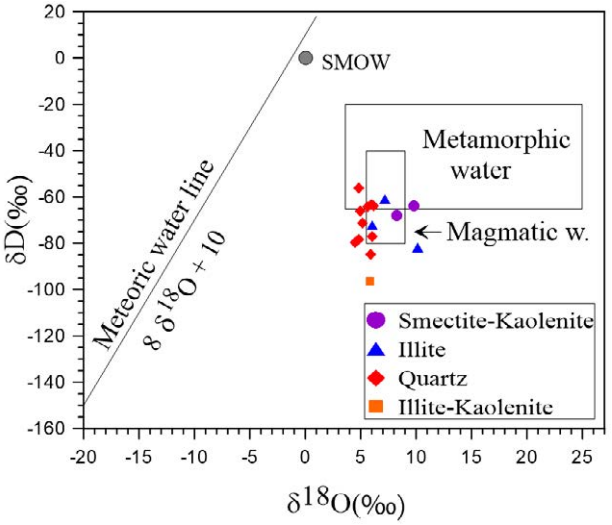

Figure 4. δD‰ versus δ18O‰ diagram showing the distributions of oxygen isotope values in clay minerals and quartz and hydrogen isotope values from clay minerals and fluid inclusions in quartz (after Taylor, 1974 and Ohmoto, 1986).

The main magmatic activity starts in Cretaceous and goes into Eocene with some stops. Those which are most favourable for ore formations are Eocene in age, though Cretaceous ones also include some mineral enrichment of mainly manganese and barite. Gold and silver are more dominant in Eocene rocks.

Quartz veins at Mastra occur in a fault zone within the Alibaba Formation, which is the continuation of a major NW-SE fault zone. Fluid inclusion results and stable isotopic data indicate that the hydrothermal fluids responsible for the formation of Mastra deposit are dominantly magmatic in origin, as reflected by the distribution of δD and $\delta^{18}O$ values in line with magmatic water field (Fig. 4). However, the values show a slight shift towards the meteoric water line. This could be interpreted as an evidence of contribution of meteoric water. The isotopic signature of such waters may have been modified as a result of interaction with magmatic rocks under low fluid/rock ratios. This in turn suggests that a magmatic activity is needed as a driving source for quartz vein formation at Mastra and other similar deposits in the region. The Dölek and Sariçiçek plutons are the youngest magmatic rocks in the Gümüşhane region and have a wide contact aureole with andesitic rocks of the Alibaba Formation. These plutons were dated at 42–44 Ma using K–Ar method based on biotite separates by Karsli et al. (2007). However, considering the distance, it is very likely that the Dölek Pluton and the hydrothermal activity associated with it resulted in the mineralisation at Mastra.

The vein formation at Mastra took occurred over a broad range of temperatures (145 to 400 °C) as determined based on microthermometric and geothermometric calculations. This temperature range is compatible with epithermal conditions. $\delta^{34}S$ isotope values of sulphides from the Mastra deposits are near 0 per mil, indicating magmatic origin for sulphur (White and Hedenquist, 1995). This is further supported by the oxygen and hydrogen isotope data obtained from quartz, illite, smectite and kaolinite. The calculated hydrogen

isotope composition and measured oxygen isotope compositions are in line with magmatic fluids. The presence of a minor shift towards meteoric water line suggests also contribution of meteoric waters, the isotopic signature of which was modified due to their interaction with magmatic country rocks. This is in accordance with fluid inclusion data showing a transition from relatively high temperature-moderately saline fluids to low temperature-low salinity fluids (Fig. 2). Minerals early in the paragenesis, such as barite are more magmatic than those formed at later stages. Studies by Akçay et al. (2010) and Turan (2012; unpublished master thesis) on barite-containing mineralised systems nearby reflected similar temperatures but higher salinities, which were used as a fingerprint of magmatic fluid.

The mineral assemblage of the studied quartz veins includes quartz, calcite, adularia and gold, which is characteristic for epithermal conditions. The sulphide content of the veins is low and represented mainly by pyrite, chalcopyrite, galena, sphalerite and tetrahedrite, indication that the system is of low sulphidation type (White and Hedenquist, 1995). Epithermal conditions are also supported by textural evidence from the quartz veins. Massive, comb, crustiform and brecciated textures are widespread. Especially, the presence quartz pseudomorphs after bladed calcite (Fig. 1) and adularia indicate the presence of boiling (Drummond and Ohmoto, 1986). Additional evidence for boiling comes from the presence of contemporaneous gas and liquid rich fluid inclusions with similar homogenisation temperatures. So, it is highly likely that precipitation of gold took place due to boiling of hydrothermal fluids, which also caused intensive brecciation.

Felsic intrusives with adakite-like geochemical signatures are known to be potential hosts for gold-copper mineralization worldwide (Castillo, 2006; Wang et al. 2006). Recent studies in the region concentrate on the geochemical affinity of the magmatic rocks with an attempt to be able to identify whether or not a connection can be made between mineral enrichment and geochemical affinity. Volcanic rocks hosting the quartz veins at Mastra and nearby do not show adakitic affinity. In addition, as determined by Eyüboğlu et al. (2011), adakitic activities prevailed during late Paleocene-early Eocene (58 to 47 Ma), prior to the emplacement of volcanic rocks hosting the Mastra deposit, and their products do not contain any gold-copper mineralisation in the Gümüşhane region. Therefore, zones affected by middle to late Eocene magmatic activities are likely to have a potential for new exploration activities near Gümüşhane.

Acknowledgements

This study was supported by the Karadeniz Technical University Research Fund (2008.112.005.4). We would like to thank Koza Gold Company for their support during the field sessions.

References

Akçay M, Gündüz Ö (2004) Porphyry Cu-Au mineralisation associated with a multi-phase intrusion and related replacement fronts in limestones in an island arc setting near the Gümüşhane Village (Artvin) in the Eastern Black Sea Province (Turkey), Chem. der Erde, 64:359-383.

Akçay M, Gündüz Ö, Yaşar R, Gümrük O (2010) Hazinemağara ve Kırkpavli (Gümüşhane) polimetalik Pb-Zb-Cu-Au-Ag madenleri: Kökensel bir yaklaşım. KTÜ Jeoloji Bölümü 45. Yıl Sempozyumu, 63-65,Trabzon

Bektas O, Şen C, Atıcı Y, Köprübaşı N (1999) Migration of the Upper Cretaceous subduction-related volcanism toward the back-arc basin of the Eastern Pontide Magmatic Arc (NE Turkey). Geol. J. 34:95-106.

Castillo PR (2006) An overview of adakite petrogenesis. Chin.Sci. Bull. 51:257-268

Drummond SE, Ohmoto H (1985) Chemical evolution and mineral deposition in boiling hydrothermal systems. Econ. Geol, 80:126–147.

Eyüboğlu Y, Santosh M, Chung SL (2011) Petrochemistry and U-Pb ages of adakitic intrusions from the Pulur Massif (Eastern Pontides, NE Turkey): Implications for slab roll-back and ridge subduction associated with Cenozoic convergent tectonics in Eastern Medit. J. of Geol. 119: 394-417.

Eyüboğlu Y, Santosh M, Dudas FO, Akaryalı E, Chung SL, Akdag K, Bektas O (2012) The nature of transition from adakitic to non-adakitic magmatism in a slab-window setting: a synthesis from the Eastern Pontides, NE Turkey. Geosci.Fronti. http://dx.doi.org/10.1016/j.gsf.2012.10.001.

Friedman I and O'Neil JR (1977) Compilation of stable isotope fractionation factors of geochemical. In: Fleisher M (ed.) Data of geochemistry, 6th edn. ch, kk, US. Geol. Surv. Prof, pp 440.

Karsli O, Chen B, Aydın F, Sen C (2007) Geochemical and Sr-Nd-Pb isotopic compositions of the Eocene Dölek and Sarıçiçek Plutons, Eastern Turkey: implications for magma interaction in the genesis of high-K calc-alkaline granitoids in a post-collision extensional setting. Lithos 98: 67-96.

Mclean WH and Kranidiotis P (1987) Immobile elements as monitors of mass transfer in hydrothermal alteration: Phelps Dodge massive sulphide deposit, Mataami, Quebec. Econ. Geol. 82: 951-962.

Matsuisha Y, Goldsmith JR and Clayton RN (1979) Oxygen isotopic fractionation in the System Quartz-Albite-Anorthite-Water. Geochim. Cosmochim., Acta. 43: 1131-1140.

Ohmoto H, Rye RO (1979) Isotopes of sulfur and carbon. In: Barnes HL (Edn.) Geochemistry of hydrothermal ore deposits, 2nd ed. Wiley and Inc, New York, pp 509-567.

Ohmoto H (1986) Stable isotope geochemistry of ore deposits. In: Valley JW, Taylor HP, O'Nein JR (Ed) Stable isotopes in High Temperature Geological Processes. Rev. in Min. vol. 16: 491-560.

Taylor HP (1974) The application of oxygen and hydrogen isotope studies to problems of hydrothermal alteration and ore deposition. Econ. Geol. 69: 843-883.

Tüysüz N, Sadıklar MB, Er M, ve Yılmaz Z (1995) An epithermal gold-silver deposit in the Pontide Island are Mastra-Gümüşhane (NE-Turkey). Econ. Geol. 90: 1301-1309

White N C and Hedenquist JW (1995) Epithermal gold deposits: styles, characteristics and exploration. Published in SEG Newsletter. 23, 1: 9-13.

Wang Q, Derek A W, Xu JF, Zahao Z H, Jian P, Xiong XL, Bao ZW, Li CF and Bai Z H (2006) Petrogenesis of Cretaceous adakitic and shoshonitic igneous rocks in the Luzong area, Anhui Province (eastern China): implications for geodynamics and Cu-Au mineralization. Litos 89:424-446

The Boorhaman intrusive complex, Victoria, Australia: geology, geochemistry and potential for porphyry-style mineralisation

Michael J. Baker, David R. Cooke, Katherine L. Webb
ARC Centre of Excellence in Ore Deposit Research, University of Tasmania, Private Bag 126, Hobart, Tasmania, Australia 7001

Abstract. The Boorhaman Intrusive Complex of north-central Victoria, Australia, comprises a series of Devonian felsic intrusive and associated volcanic rocks with high-K calc-alkaline affinities. The intrusive rocks are predominantly medium-grained plagioclase-rich quartz monzonite to quartz monzodiorite. The volcanic rocks are a sequence of coherent andesite to dacite lavas and syn-eruptive feldspar-rich volcanic mass-flow deposits. Sulfur isotope values decrease from +5.8‰ to +2.1‰ towards a biotite-quartz monzonite intrusion at depth, potentially due to fluid-rock interaction during propylitic alteration.
Three stages of hydrothermal activity are recognised at Boorhaman, with propylitic alteration being the dominant alteration assemblage in all rock types. A transitional stage of potassic alteration is represented by pyrite-magnetite-tourmaline-albite veins, with vein frequency highest in a biotite-quartz monzonite intrusion. Late-stage phyllic alteration overprints potassic and propylitic alteration, comprising sericite-quartz alteration with quartz-carbonate-zeolite-pyrite veinlets. Mineralisation consists of minor disseminated and late-stage pyrite veinlets, with minor chalcopyrite and bornite clots. The hydrothermal and geochemical characteristics of the Boorhaman Intrusive Complex suggest that it is prospective for porphyry-style mineralisation.

Keywords. Geochemistry, Porphyry Cu, Propylitic alteration

1 Introduction

The Boorhaman Intrusive Complex (BIC) comprises an early Devonian sequence of andesite to dacite lavas, along with felsic quartz monzonite to monzodiorite intrusive rocks that together form the basement of the Ovens Graben in the central Lachlan Fold Belt (LFB) of north-central Victoria, Australia (Fig. 1). The area incorporating the BIC has been a target for recent porphyry-style mineral exploration by Highlake Resources Pty Ltd, based on a series of eight broadly coincident magnetic and gravity anomalies.

The LFB is situated in the central part of the Tasman Fold Belt of eastern Australia (Fig. 1). It is ~1500 km long and stretches from eastern Tasmania, through Victoria and into northern New South Wales. The LFB is bounded to the west by the Kanmantoo Fold Belt, north by the Thomson Fold Belt and east by the New England Fold Belt. The LFB predominantly comprises deep marine turbidites, shallow marine to sub-aerial sediments, extensive igneous suites and volcano-intrusive complexes (Hough et al., 2007). Outcropping rocks range from Cambrian to Carboniferous in age and are partially covered by Palaeozoic to Mesozoic-Cenozoic sediments of the Great Australian and Murray basins (Walshe et al., 1995). The LFB is interpreted to have developed by the eastward progression and accretion of deformed sedimentary rocks and volcanic arcs in an oceanic setting behind a long-lived subduction zone, most likely a back-arc setting (Bierlein et al., 2002; Gray and Foster, 2004).

The igneous rocks of the BIC bear a strong resemblance to porphyritic alkalic igneous rocks associated with porphyry-style mineralisation in the North Parkes district in central New South Wales (Wolfe, 1994). Consequently, this study is aimed at identifying whether or not the BIC is prospective for porphyry-style mineralisation.

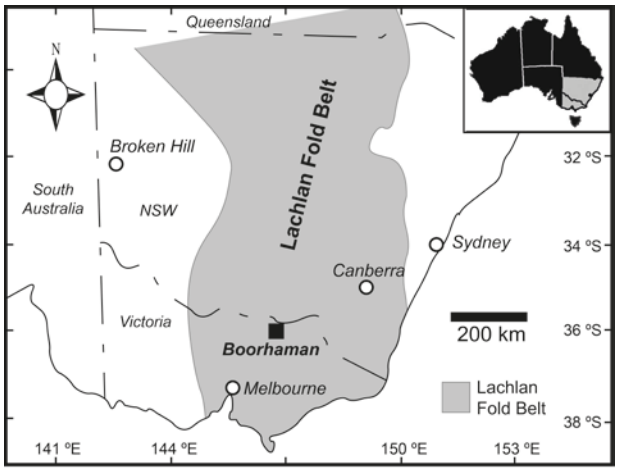

Figure 1. Location of the Boorhaman Intrusive Complex within the Lachlan Fold Belt of southeastern Australia (modified from Cooke et al., 2007)

2 Boorhaman Intrusive Complex

The BIC is an early Devonian sequence of extrusive andesitic to dacitic, and felsic quartz monzonite to monzodiorite intrusions that form the basement rocks of the Ovens Graben, in the central Lachlan Fold Belt of north-central Victoria. The BIC was intercepted by five drillholes drilled by Highlake Resources between 2007 and 2009.

Permian glacial tillite unconformably overlies and completely covers the BIC. The thickness of the cover sequence varies between 63 to 234 metres. The tillite is comprised of laminated mudstone, siltstone and sandstone, sub-rounded to well-rounded lithic conglomerate and gravels of felsic and sedimentary origin. The cover sequence is a part of the Permian

Boorhaman Conglomerate.

2.1 Volcanic rocks

The BIC volcanics consist of a sequence of coherent and clastic volcanic rocks. The sequence includes a biotite-plagioclase-phyric dacite that has been identified from two drillholes. The facies is porphyritic in texture, with intervals varying in thickness from 40 to 110 m. Within each sequence the dacite varies from massive to weakly or moderately flow banded. The dacite is characterised by phenocrysts of strongly zoned, moderately sericitized euhedral plagioclase, euhedral biotite that is partially to totally chloritized, and sparse microphenocrysts of quartz. The dacite contains numerous angular lithic clasts of quartz wacke, mudstone and rare feldspathic igneous fragments that range from a few millimetres up to 4 cm across.

A strongly altered, dark grey-green, feldspar-phyric andesite was also identified in one drillhole over a 20 m interval. The exact thickness of the andesite is unclear, as biotite-plagioclase-phyric dacite lavas occur both above and below. The facies is porphyritic and shows no obvious flow features, as observed in the dacite. The andesite is characterised by phenocrysts of zoned plagioclase that are partly to entirely replaced by sericite, abundant hematite and rare, partially altered clinopyroxene. The phenocrysts are set in a fine-grained quartz-feldspar-sericite groundmass, with abundant biotite laths partially altered to chlorite. A defining feature of the andesite is the lack of prominent igneous biotite, with the majority of biotite grains occurring in the groundmass.

2.2 Intrusive rocks

Each intrusive phase of the BIC is characterised by the presence of well-zoned plagioclase, either as phenocrysts or crystal fragments. Alkali feldspars typically occur as fine-grained anhedral crystals intergrown with anhedral quartz. Secondary quartz occurs as coarse anhedral grains in discrete veinlets. Biotite occurs in two forms: large, euhedral tabular crystals that are interpreted to be igneous in origin, and smaller blocky or shreddy grains interpreted to be of hydrothermal origin. The intrusive igneous rock types represent a range of compositions from granodiorite to monzodiorite that are potentially related via crystal fractionation.

Quartz monzodiorite (QMD) has been identified in one drillhole, occurring as a fine-grained, pale grey-green to dark green holocrystalline equigranular rock. Composition varies from quartz-monzodiorite to quartz-monzonite. However, QMD is the dominant composition. The monzodiorite comprises euhedral plagioclase, chlorite-altered hornblende, unaltered to chlorite-altered biotite, minor magnetite and interstitial anhedral alkali feldspar and quartz. Dark green-grey mafic minerals typically occur together as aggregates less than 2 mm in width, along with accessory sphene, zircon and sulfides. Numerous fracture veins and veinlets cut the QMD. They appear to be hydrothermal in origin as they contain variable amounts of calcite, chlorite and epidote. Aplite veinlets also cut the QMD, with their abundance and thickness increasing with depth, where observed cross-cutting dykes up to 1.5 m thickness are found.

Biotite-quartz monzonite (BQM) is encountered in drillholes throughout the district and is volumetrically the most common intrusive rock encountered. The BQM is commonly medium- to coarse-grained, dark red to dark green-grey and equigranular to porphyritic in texture. Notably, at higher levels the BQM is strongly hematite altered and has a definitive dark brick-red colour. The BQM is composed of euhedral plagioclase, biotite, chlorite-altered hornblende and anhedral alkali feldspar intergrown with quartz. Accessory minerals include magnetite, augite, apatite and zircon.

A volumetrically minor plagioclase-phyric dacite porphyry intrusion has also been identified. It has been identified over two intervals, with both having sharp upper and lower contacts with the BQM. The porphyry is phenocryst-poor, comprising plagioclase and minor biotite and hornblende phenocrysts set in an aphanitic to micropoikilitic, sericite-altered quartz-feldspar-rich groundmass. Large (> 3 mm) plagioclase phenocrysts are characteristic of the intrusion. The plagioclase phenocrysts and megacrysts are strongly altered to a pale green-yellow illite.

2.3 Hydrothermal alteration and mineralisation

Hydrothermal alteration of the BIC is weakly to moderately developed, with igneous textures mostly preserved. Plagioclase is commonly albitised or sericite-altered, K-feldspar grains are generally affected by fine-grained clay alteration and minor hematite dusting, clinopyroxene is partially replaced by amphibole and biotite crystals are selectively replaced by chlorite. The hydrothermal mineral assemblages commonly observed are consistent with moderate to weak potassic and propylitic alteration assemblages that have been overprinted by late-stage phyllic alteration (Sillitoe, 2010).

Higher temperature potassic alteration is represented in the BIC by rare veinlets of actinolite-tourmaline-magnetite-(biotite). Vein halos display alteration of primary pyroxenes and hornblende to hydrothermal amphibole and biotite.

Propylitic alteration has been observed in all rock types of the BIC. Selectively pervasive hematite dusting of feldspars and selectively pervasive chlorite, epidote, carbonate and sericite replacement of primary minerals are associated with this style of alteration. It is also characterised by the presence of occasional chlorite-epidote ± albite ± carbonate ± pyrite veins and veinlets in the intrusions. However, epidote veinlets are a characteristic feature of the propylitic alteration at Boorhaman and are abundant in all rock types. The epidote veins typically have diffuse margins and are enclosed by a halo of pink albite. Epidote alteration also occurs as a selective replacement of amphibole and plagioclase, imparting a dull green appearance to altered rocks. Chlorite alteration occurs as weak to moderate alteration of groundmass material, replacing primary ferro-magnesium minerals including biotite and hornblende.

Pyrite, chalcopyrite, arsenopyrite, bornite and galena are found throughout the BIC and are likely to have formed during the later stages of hydrothermal activity in the district. The most abundant sulfide is pyrite, while other sulfide occurrences are infrequent and rare. Narrow late-stage quartz and quartz-carbonate veins are common and are associated with sulfides. Pyrite and minor chalcopyrite occur as disseminated grains (<3% by volume), within all rock types, with their abundance increasing in the BQM. Arsenopyrite was only observed in thin section in a sample of the QMD within fracture-located veinlets and as rare disseminated sulfide (< 0.1 mm). It was also observed occurring with chalcopyrite in altered mafic crystal sites. Rare trace amounts of galena and bornite are also intergrown with clots of chalcopyrite.

3 Geochronology and Geochemistry

Five samples of the main intrusive phases of the BIC were collected for U-Pb zircon LA-ICPMS dating. The analyses were performed at the CODES ICP-MS facility at the University of Tasmania. Samples selected for analysis included two samples of the BQM, one sample of the QMD, one plagioclase-phyric dacite porphyry and one plagioclase-phyric andesite (Table 1).

Rock Type	ID	Mineral	Method	Age (Ma)
Plagioclase-phyric dacite porphyry	KW015	zircon	U-Pb	405.8 ± 3.8
Andesite	KW016	zircon	U-Pb	405.8 ± 5.8
Quartz monzodiorite (QMD)	KW017	zircon	U-Pb	404.7 ± 2.7
Biotite-quartz monzodiorite (BQM)	KW018	zircon	U-Pb	399.3 ± 2.9
Biotite-quartz monzodiorite (BQM)	KW013	zircon	U-Pb	399.2 ± 2.8

Table 1. Zircon U-Pb ages for samples of the Boorhaman Intrusive Complex analysed in this study

The QMD intrusion was dated to 404.7 ± 2.7 Ma, while the BQM intrusion yielded an age of 399.2 ± 2.9 Ma. These dates suggest that intrusive activity in the BIC commenced with the more primitive QMD. As magma fractionation continued, the more evolved BQM was emplaced. The oldest ages were obtained from the plagioclase-phyric dacite porphyry and andesite with ages of 405.8 ± 3.8 and 405.8 ± 5.8 Ma, respectively. Contact relationships between the BQM, dacite porphyry and andesite are sharp with minimal to no evidence of chilled margins, as would be expected if the latter rocks were dykes.

The intrusive and volcanic rocks of the BIC are classified as high-K calc-alkaline to shoshonitic rocks, based on their position on the K_2O vs. SiO_2 discrimination diagram (Fig. 2). The intrusions define a fractionation trend from less-fractionated biotite monzodiorite and QMD to more fractionated BQM and biotite-plagioclase-phyric dacite. Data from the volcanic rocks of the BIC overlap with those of the intrusive rocks, suggesting the volcanics are related to and sourced from the local intrusive complex. In contrast, some andesite xenoliths and plagioclase-phyric dacite porphyry and plagioclase-hornblende-phyric dacite porphyry dykes do not plot along the same fractionation trend, suggesting that a different magma was the source of these rocks.

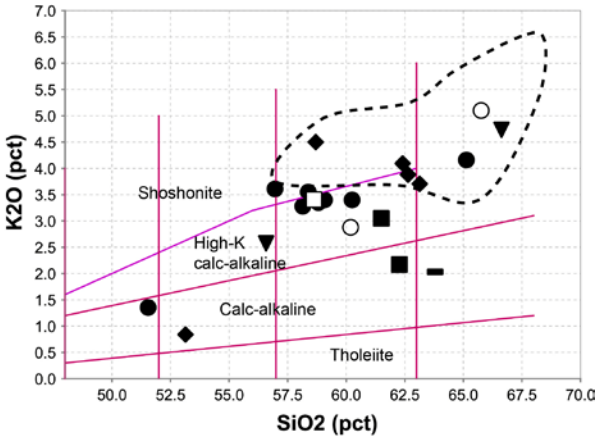

Figure 2. SiO_2 versus K_2O diagram for samples of the BIC (after Peccerillo and Taylor, 1976). Diamonds: BQM; open square: QMD; black circles: biotite monzodiorite; black squares: plagioclase dacite porphyry; open circle: plagioclase-hornblende dacite porphyry; dashes: andesite; triangles: biotite-plagioclase-phyric dacite; brown dashes: plagioclase-phyric andesite; black star: crystal-rich fiamme breccia. Dashed line field shows compositional range of biotite-quartz monzonite samples from the Endeavour 48 Cu-Au porphyry deposit, North Parkes (Wolfe, 1994) used for comparison

4 Sulfur Isotope Chemistry

Distinctive sulfur isotope zonation patterns have been identified within the Cadia and North Parkes districts through the work of Radclyffe (1995), Harper (2000), Lickfold (2002), Wilson (2003) and Wilson et al. (2007), enabling $\delta^{34}S$ data to be used as an effective spatial exploration tool towards Cadia-style porphyry Cu-Au mineralisation. This study aims to determine whether the BIC displays sulfur isotope zonation patterns similar to that of the Cadia district.

The $\delta^{34}S$ values of pyrite in the BIC range from +1.0 to +5.8‰, with a mean of 3.5‰. However, the majority of values fall between +2 and +4‰. The $\delta^{34}S$ values from the BQM range from +2.1 to +4.8‰, with a mean of +3.4‰. Vertical zoning in $\delta^{34}S$ values within the BQM is evident, with values decreasing with depth. Two $\delta^{34}S$ values from the biotite monzodiorite are +4.3 and +5.7‰. Consequently, there is insufficient data to observe any vertical zonation in its $\delta^{34}S$ values.

The $\delta^{34}S$ values from the biotite-plagioclase phyric dacite range between +1.7 and +5.8‰. The $\delta^{34}S$ values are sporadic and show no clear vertical zonation. Three samples from a crystal- and lithic-rich volcanic breccia have $\delta^{34}S$ values between +3.4 and +4.4‰, with a mean of +3.8‰.

5 Conclusions

The study carried out by Ohmoto and Rye (1979) determined that sulfides in igneous rocks typically have an average $\delta^{34}S$ close to 0‰. In magmatic-hydrothermal ore deposits, the source fluid, temperature and interaction with surrounding country rocks can be interpreted to account for $\delta^{34}S$ values near 0‰. Previous

studies by Harper (2000), Lickfold (2002), Wilson (2003) and Wilson et al. (2007) on $\delta^{34}S$ values around known porphyry mineralisation sites in eastern Australia have concluded that low $\delta^{34}S$ values (-4‰) are characteristic of the deposit core, consistent with sulfide precipitation from an oxidised magmatic fluid. As the alteration halo moves away from the deposit core and into the propylitic zone, the $\delta^{34}S$ values approach 0‰. Rollinson (1993) indicated that magmatic sulfur in island arc settings may deviate to positive values, varying from -0.2 up to 20‰, which appears to be the case at Boorhaman and contrasts with $\delta^{34}S$ values from Cadia and North Parkes (Wolfe, 1994; Wilson et al., 2007). However, previous studies have identified positive $\delta^{34}S$ values in association with porphyry-style mineralisation in northern Philippines (Cooke et al., 2011), suggesting that the similar values obtained in this study do not exclude the presence of porphyry-style mineralisation in the Boorhaman district.

A possible explanation for the positive $\delta^{34}S$ values seen at Boorhaman may involve fluid-rock interaction during propylitic alteration, where oxidised fluids migrate into and react with the reduced volcanic host rocks, resulting in a decrease in isotopic fractionation. Despite this, the isotopic zonation patterns at Boorhaman are comparable to the values found on the periphery of the Cadia porphyry copper-gold system (Harper, 2000; Lickfold, 2002; Wilson et al., 2007), suggesting that the Boorhaman district may be prospective for porphyry-style mineralisation.

Despite the limited amount of geological data currently available, a number of key results have been obtained by this study. Together, the petrological, geochemical, and sulphur isotope characteristics of the intrusive and volcanic rocks of the BIC all suggest that the area is prospective for porphyry-style mineralisation and should help serve as a tool for future exploration in the district.

Acknowledgements

This work formed part of the B.Sc. Honours thesis of KLW at the University of Tasmania. We would like to acknowledge the logistical and in-kind support provided by Highlake Resources, in particular Greg Ebsworth and Anthony Gray, for making this work possible. Staff at the University of Tasmania, including Katie McGoldrick, Al Cuison, Phil Robinson, Ian Little, Sebastien Meffre, Keith Harris, Christine Cook, Karsten Goemann, Sandrin Feig, Marcel Guillong and Zhaoshan Chang are also thanked for assisting with various aspects of the analytical work that formed part of this study.

References

Bierlein FP, Gray DR Foster DA (2002) Metallogenic relationships to tectonic evolution - the Lachlan Orogen, Australia: Earth and Planetary Science Letters 202: 1-13.

Cooke DR, Wilson AJ, House MJ, Wolfe RC, Walshe JL, Lickfold V, Crawford AJ (2007) Alkalic porphyry Au-Cu and associated mineral deposits of the Ordovician to Early Silurian Macquarie Arc, New South Wales: Australian Journal of Earth Sciences 54: 445-463.

Cooke DR, Deyell CL, Waters PJ, Gonzales RI, Zaw K (2011) Evidence for magmatic-hydrothermal fluids and ore-forming processes in epithermal and porphyry deposits of the Baguio District, Philippines: Economic Geology 106: 1399-1424.

Gray DR, Foster DA (2004) Tectonic evolution of the Lachlan Orogen, southeast Australia: historical review, data synthesis and modern perspectives: Australian Journal of Earth Sciences 51: 773-817.

Harper BL (2000) Hydrothermal alteration at the Ridgeway porphyry gold-copper deposit, NSW: B.Sc. Honours thesis, University of Tasmania, Hobart, p130.

Hough MA, Bierlein FP, Wilde AR (2007) A review of the metallogeny and tectonics of the Lachlan Orogen: Mineralium Deposita 42: 435-448.

Lickfold V (2002) Intrusive history and volatile evolution of the Endeavour porphyry Cu-Au deposits, Goonumbla district, NSW, Australia: Ph.D. thesis, University of Tasmania, Hobart: p245.

Ohmoto H, Rye RO (1979) Isotopes of sulfur and carbon. In: Barnes HL (ed.) Geochemistry of hydrothermal ore deposits: Wiley Interscience, New York: 509-567.

Radclyffe D (1995) Regional scale propylitic alteration in the Goonumbla Mineral Field, Parkes, NSW: B.Sc. Honours thesis, University of Tasmania, Hobart, p118.

Rollinson H (1993) Using geochemical data: evaluation, presentation, interpretation: Longman, London: p352.

Sillitoe RH (2010) Porphyry copper systems: Economic Geology 105: 3-41.

Walshe JL, Heithersay PS, Morrison GW (1995) Toward an understanding of the metallogeny of the Tasman fold belt system: Economic Geology 90: 1382-1401.

Wilson AJ (2003) The geology, genesis and exploration context of the Cadia gold-copper porphyry deposits, New South Wales, Australia: Ph.D. thesis, University of Tasmania, Hobart, p335.

Wilson AJ, Cooke DR, Harper BJ, Deyell CL (2007) Sulfur isotopic zonation in the Cadia district, southeastern Australia: exploration significance and implications for the genesis of alkali porphyry gold-copper deposits: Mineralium Deposita 42: 465-487.

Wolfe RC (1994) The geology, paragenesis and alteration geochemistry of the Endeavour 48 Cu-Au porphyry, Goonumbla NSW: B.Sc. Honours thesis, University of Tasmania, Hobart, p102.

Porphyry-epithermal system of the Baimka Cu-Au trend, Western Chukchi Peninsula, Russia

Ivan A. Baksheev, Yurii N. Nikolaev, Vsevolod Yu. Prokof'ev, Ekaterina V. Nagornaya, Yuliya N. Sidorina, Lyubov' I. Maruschenko, Ildar A. Kal'ko
Geology Department, Moscow State University, Russia

Andrey A. Chitalin
Regional Mining Company LLC, Russia

Abstract. The Cu-Au porphyry-epithermal system of the Baimka trend comprising Peschanka, the largest porphyry copper deposit in Russia, is related to the Early Cretaceous Egdykgich Complex (U/Pb zircon age 138-141 Ma) of monzonitic rocks. Four types of hydrothermal alteration have been recognized in the Baimka properties: potassic (Rb/Sr age 136-140 Ma), propylitic, quartz-sericite, and an insignificant amount of advanced argillic. The ore mineralization is divided into three types: (1) porphyry type, (2) IS epithermal, and (3) HS epithermal. The Re-Os age of molybdenite from the porphyry-type mineralization is around ~140 Ma. The economic gold-bearing IS mineralization is abundant only at the southern flank of the Nakhodka ore field. The gold-bearing HS mineralization is sporadic and not economic, due to the comparatively deep erosion level. The inclusions of chloride brines homogenized at 290-580°C, gas-dominated homogenized at 400-540°C, and aqueous solution homogenized at 120-420°C were found in vein quartz. The sulfur isotopic composition of sulfide minerals ranging from -6.4 to +4.8‰ indicates a magmatic sulfur source.

Keywords. Porphyry Epithermal Alteration Ore Fluid Inclusions Age Chukchi Peninsula Russia

1 Introduction

The Baimka Cu-Au trend is located 200 km south of Bilibino, on the Chukchi Peninsula. This trend consists of four ore fields: Yuryakh, Peschanka (total reserves ~6 Mt Cu), Nakhodka (~3 Mt Cu) and Burgakhchan. These ore fields were discovered between the late 1960s to the early 1970s and were explored from 1972-1986. In 2009, prospecting and exploration were renewed. Most data of the porphyry deposits located in the Baimka trend were published between 1980-1990 (e.g. Kaminski 1989; Migachev et al. 1995). This paper summarizes novel geological, mineralogical, fluid inclusion, and isotopic data of the first three fields (Fig. 1), which were obtained over the last three years.

2 Brief geology

The Baimka trend is a part of the Oloi metallogenic zone, where the Cu-Mo-Au-porphyry system was formed in a continental arc environment. This trend comprises Upper Jurassic and Lower Cretaceous stratified volcanic and terrigenous sequences intruded by igneous rocks of various composition and age. The Late Jurassic gabbro is the most ancient. Then, large bodies of porphyry diorite of the Late Jurassic-Early Cretaceous age (?) were emplaced. The Cu-Mo-Au-porphyry system is related to the Early Cretaceous Egdykgich Complex.

In the northern Baimka trend, the Egdykgich rocks

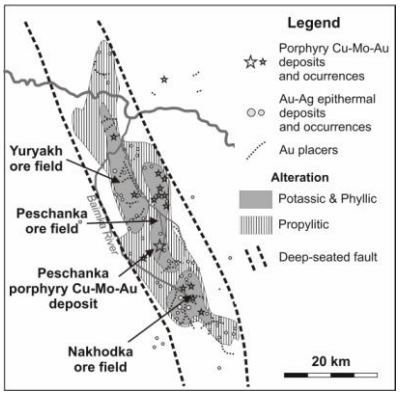

Figure 1. Location of deposits and prospects of the Baimka trend.

compose large bodies intruding in both earlier gabbro and volcano-sedimentary sequences. Three intrusive phases were identified: (1) monzodiorite, (2) syenite and (3) porphyry monzodiorite and porphyry quartz monzodiorite. Monzodiorite is the most abundant in the central Baimka trend (Peschanka deposit); syenite is widespread in the northern part (Yuryakh ore field) and forms small bodies at the southern Peschanka deposit; and the third-phase rocks were found in both the central and southern (Nakhodka ore field) parts. The third-phase bodies, to which Cu-Mo porphyry mineralization is related, are stocks and large dikes. The Upper Jurassic sequences and Late Jurassic and Early Cretaceous intrusion are overlain in places by the sediments of the Early Cretaceous Ainakhkurgen Formation. The Late Cretaceous basaltic and andesitic dikes are the youngest in the trend, with the exception of Quaternary alluvium.

Structural features of the Baimka trend indicate that it is a regional-scale dextral strike-slip fault zone formed under latitudinal horizontal extension and meridional compression. Echelon-like meridional extension zones within the Baimka Fault Zone control localization of the Early Cretaceous plutons, porphyry dikes and stocks, metasomatic rocks, mineralized stockworks and zones. Taken together, they make up a porphyry system. The latest NW-SE trending dextral strike-slip faults and conjugated SW-NE-trending sinistral strike-slip faults transect the porphyry deposits.

3 Hydrothermal alteration

Like other porphyry copper deposits, four major types of

altered wall rocks were identified at the Baimka properties: (1) quartz-biotite-potassium feldspar (potassic alteration), (2) propylite, (3) quartz-sericite (phyllic alteration), and (4) argillic. In addition, zones of quartz-potassium feldspar alteration were found at the deep level of Nakhodka and Peschanka. Potassic alteration is predominant at the Peschanka deposit and prospects of the Yuryakh field. Fe-rich and Fe-poor types of hydrothermal biotite were distinguished in the potassic alteration (Fig. 2). In the case of Fe-poor biotite, altered rock contains chalcopyrite and bornite, which are cogenetic with mica. Owing to high activity of H_2S, Fe is proportioned into sulfide minerals, rather than biotite. In the case of Fe-rich biotite, potassic-altered rock does not contain sulfide minerals, and the increase of Fe content in biotite is probably caused by the decreasing temperature of mineral deposition.

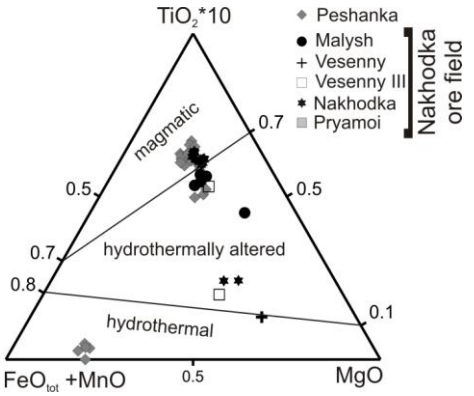

Figure 2. A FeO_{tot}+MnO-TiO_2•10-MgO ternary for dark mica (Nachit et al., 1985, 2005) of magmatic rocks and potassic alteration of the Peschanka deposit and Nakhodka ore field

Propylite alteration occurring in all locations forms an outer zone of hydrothermal alteration and replaces intrusive, volcanic, and volcano-sedimentary rocks. This metasomatic rock is composed of epidote, magnesiohornblende, actinolite, tourmaline, clinochlore, potassic feldspar, albite, and quartz. At the Peschanka deposit, clinochlore is characterized outward by a decrease of ^{IV}Al content. Propylitic tourmaline is an intermediate member of the oxy-dravite--povondraite series; it is distinguished by the $Fe^{3+} \rightarrow$ Al isomorphic substitution that is typical of propylitic tourmaline from porphyry systems (Baksheev et al. 2012).

An abundance of phyllic alteration increases from the Yuryakh to Nakhodka ore field, indicating shallower erosion levels of the ore fields. In the Nakhodka field, phengite and Na-bearing muscovite occur at the upper and lower levels of phyllic bodies, respectively, whereas at the Peschanka deposit, only muscovite develops in phyllic alteration (Fig. 3). This finding testifies to the shallower erosion level of the Nakhodka field.

Argillic alteration is sporadic in the Nakhodka ore field and is absent at Peschanka and Yuryakh. In the Nakhodka ore field, argillic alteration occurs in 2-3m thick zones. On the surface, argillic rocks are highly weathered and transformed to clay with varied sulfate minerals. The drill core study established that fresh argillic rock is composed of relict albite and sericite, illite, dickite, rare Fe-poor clinochlore, quartz, and tourmaline. Argillic alteration is cut by veinlets with

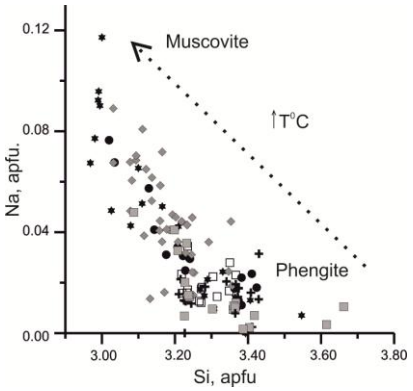

Figure 3. A Na versus Si plot for white micas of the Baimka. See Fig. 2 for legend.

rhodochrosite and Mn-rich dolomite. In contrast to dolomite from quartz-sericite rock, where the proportion of the kutnahorite end-member does not exceed 10%, dolomite from argillic rock contains up to 45% of this end-member (Fig. 4). In this value, it is close to dolomite from volcanic-related gold deposits (Generalov 1990; Spiridonov 1991).

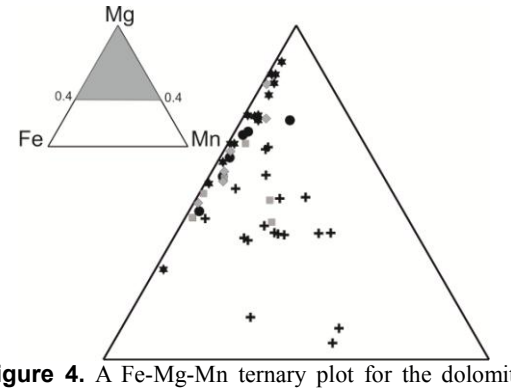

Figure 4. A Fe-Mg-Mn ternary plot for the dolomite group minerals of the Baimka trend. See Fig. 2 for legend.

Tourmaline is classified as an intermediate member of the dravite--magnesio-foitite series.

4 Ore mineralization

Orebodies are isometric or slightly elongated on NW-trending stockworks of quartz veinlets hosted in quartz-sericite rocks; in the case of epithermal mineralization, ore veinlets are hosted by argillic alteration or cut silicified zones. In addition, explosion-hydrothemal breccias, which are an important carrier of the Cu-Mo mineralization, are abundant in the Peschanka and Nakhodka ore fields. The zone of secondary enrichment is weakly developed.

4.1 Porphyry Cu-Mo stage

The porphyry Cu-Mo mineralization is spatially related to the potassic and phyllic alteration zones and consists of bornite, chalcopyrite, molybdenite, pyrite and rare Ti-free magnetite. The average grade of Cu and Mo at Peshanka and Nakhodka is 0.53% and 140 g/t and 0.34% and 54 g/t, respectively. Bornite occurs as grains with or without the exsolution of chalcopyrite lamellas.

Chalcopyrite replaces bornite. Molybdenite is present in thin veinlets, small pockets and clusters of fine flakes. According to the ICP-MS study, the content of Re in molybdenite from the Peschanka and Nakhodka ore fields is 1259-2673 and 21-1308 ppm, respectively.

4.2 Epithermal stage

Epithermal mineralization is divided into two types: (1) high sulfidation (HS) and (2) intermediate sulfidation (IS). The economic IS-type mineralization only occurs at the southern flank of the Nakhodka ore field, (the Vesenny and Praymoi prospects) with the average grade as follows: 2.9 g/t Au, 56 g/t Ag, 0.9% Pb+Zn, and 0.15% Cu. The ore consists of As-rich pyrite (up to 10 wt% As), sphalerite, galena, chalcopyrite, Zn-rich tennantite-tetrahedrite (replacing sphalerite and chalcopyrite), native gold, and hessite; petzite, stützite, pearceite, and acanthite are rare. Low fineness gold (756-857) and electrum (657-743) enclosing and filling fractures in pyrite, galena, and tennantite-tetrahedrite are intimately intergrown with hessite and petzite.

The Vesenny prospect is vertically zoned (Fig. 5). Epithermal mineralization occurs in the upper part. At a depth of 150-200 m below the surface, it cuts Cu-Mo stockwork and gradually damps down to 400 m. Gold grade decreases downward, whereas copper grade increases downward. At the upper levels, the tennantite-tetrahedrite group minerals are the major carrier of Cu, whereas chalcopyrite is the major carrier of Cu in the deep levels.In addition, this prospect is characterized by subtle lateral zoning in the chemical composition of

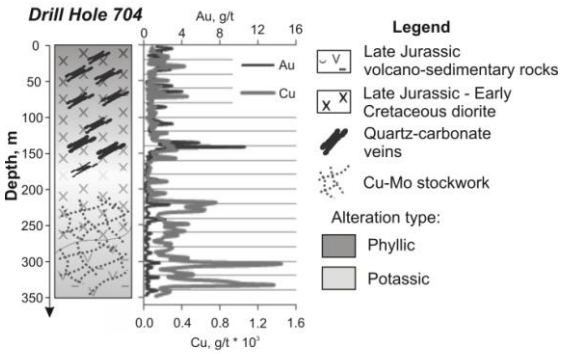

Figure 5. Variation of copper and gold grade along drill hole 704, Vesenny prospect, Nakhodka ore field.

tennantite-tetrahedrite: an increase of Ag content outward from hundredths to 4 wt%.

Due to significant erosion, the HS mineralization related to argillic alteration is sporadic in the Baimka trend. The ore minerals are As-rich pyrite, enargite, digenite, chalcopyrite, Zn-poor tennantite, Se and Te minerals (altaite; clausthalite; kurilite; native tellurium; and phases Ag-Te-Se, Pb-Ag-Bi-Te-Se, and Bi-Te-Se), and high fineness native gold (>900).

5 Fluid inclusions

The petrography and microthermometry of fluid inclusions from vein quartz of porphyry-type ore indicates three types of inclusions: (1) chloride brines with gas bubble and one or a few daughter crystals (halite, sylvite, chalcopyrite, and magnetite) homogenized at 290-580°C via vapour phase disappearance or halite dissolution, fluid salinity 37-58 wt% NaCl equiv.; (2) gas-dominated homogenized at 400-540°C into vapour phase; and (3) aqueous solution with gas bubble homogenized at 120-420°C into liquid phase, fluid salinity 0.4-19.7 wt% NaCl equiv. (Fig. 6). The inclusions of only the third type were found in vein quartz and sphalerite of the epithermal stage. The first and the second inclusion types are related to the formation of potassic alteration; the inclusions of the third type are related to the formation of the phyllic alteration (T_{hom} 240-420°C) and epithermal mineralization (T_{hom} 120-275°C).

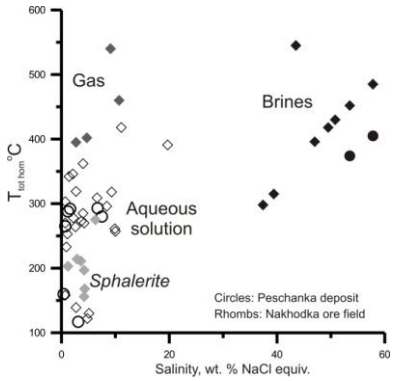

Figure 6. A temperature of total homogenization versus salinity plot for fluid inclusions from quartz and sphalerite of deposits and prospects in the Baimka trend.

6 Age of intrusive rocks, hydrothermal alteration, and ore mineralization

According to Moll-Stalcup et al. (1995), the U/Pb age of zircon from monzodiorite of the Peschanka deposit is 142Ma. We have dated zircon with the LA ICPMS technique from magmatic rocks in the Nakhodka ore field. These rocks are hydrothermally altered monzodiorite, quartz monzodiorite porphyry, granodiorite porphyry, diorite and quartz diorite porphyries. The statistical processing of 318 point analyses of zircon gave a U/Pb age of 139.6±0.3 Ma (Fig. 7).

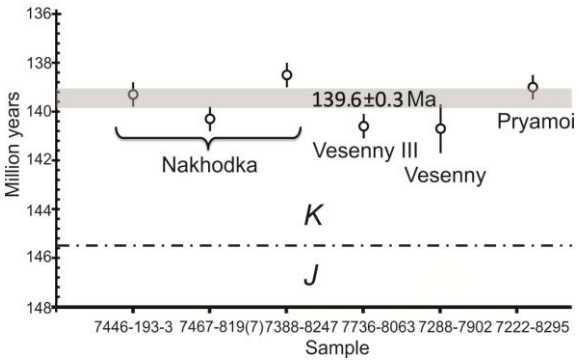

Figure 7. U/Pb ages of zircon from magmatic rocks of the Nakhodka ore field. Grey stripe denotes confidence interval for the common age taken from 318 point analyses.

At the Peschanka deposit and Kust occurrence

belonging to the Peschanka ore field, we have dated quartz-biotite-potassium feldspar metasomatic rock using the Rb/Sr method. The age is about 136 and 140Ma, respectively (Fig. 8).

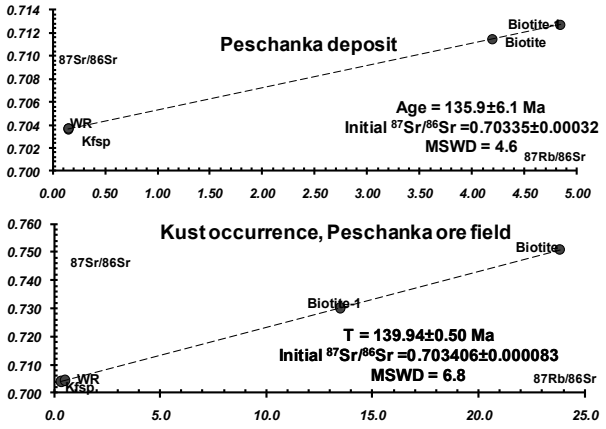

Figure 8. Rb/Sr ages of quartz-biotite-potassium feldspar rock of the Peschanka deposit and Kust occurrence.

The Re/Os ages of molybdenite from the Peschanka deposit and Malysh prospect located in the Nakhodka ore field are similar - 144.3±3.4 and 138±11 Ma, respectively. These ages are essentially the same as those for intrusive and metasomatic rocks.

7 Sulfur isotopes

Sulfur isotope analyses were obtained from four samples of chalcopyrite, one sample of bornite, four samples of pyrite, four samples of sphalerite and one sample of galena. Of those samples, twelve were associated with epithermal mineralisation and two were collected from porphyry mineralisation. The sulfur isotopic composition of epithermal minerals ranges from -6.4 to +4.8‰; porphyry minerals have the $\delta^{34}S$ value ranging from -5.2 to -3.8‰. All but one value are within the 0±5‰ range expected for sulfur from a magmatic source (Ohmoto and Goldhaber 1997). The ranges of epithermal and porphyry minerals overlap, suggesting a common magmatic component to the ore-forming fluid of both types of mineralization.

The sulfur isotopic composition of sulfide minerals from deposits and prospects of the Baimka trend ranging from -6.4 to +4.8‰ is typical of porphyry copper deposits worldwide (Fig. 9).

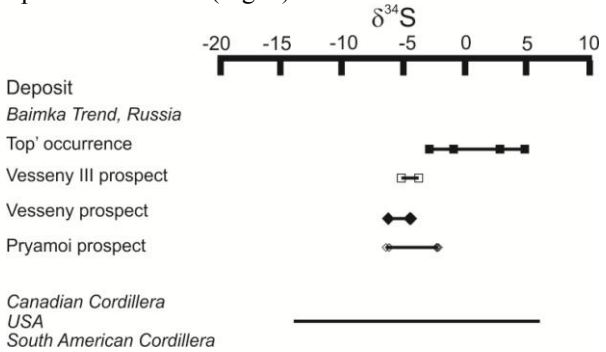

Figure 9. Sulfur isotopic composition of sulfides from porphyry copper deposits and prospects of the Baimka trend, and from North and South America. Data of the North and South American deposits were taken from Wilson et al. (2007).

Conclusions

The porphyry-epithermal system of the Baimka trend comprising the Peschanka deposit, the largest porphyry copper deposit in Russia, is related to the monzonitic rocks of the Early Cretaceous Egdykgich Complex. Quartz-biotite-potassium feldspar, propylitic, quartz-sericite and argillic rocks were identified in the deposits and prospects. Ore mineralization was formed during the porphyry and epithermal stages from magmatic fluids.

Acknowledgements

This study was supported by the Russian Foundation for Basic Research (project nos. 11-05-00571, 12-05-31067) and the Baimka Mining Company LLC.

References

Baksheev IA, Prokof'ev VYu, Zaraisky G.P., Chitalin AF, Yapaskurt VO, Nikolaev YN, Tikhomirov PL, Nagornaya EV, Rogacheva LI, Gorelikova NV, Kononov OV (2012) Tourmaline as a prospecting guide for the porphyry-style deposits. Eur J Mineral 24: 957-979.

Generalov ME (1990) Carbonates of gold deposit and formation conditions of carbonate-bearing assemblages. Geol Bull MSU no 2: 88-94 (in Russian).

Kaminski VG (1989) A geologic exploration model for porphyry copper deposits of the Baimka zone. Internat Geol Rev 31: 1240-1250.

Migachev IF, Girfanov MM, and Shishakov VB (1995) Copper porphyry Peschanka deposit. Rudy i Metally no. 3: 48-58 (in Russian).

Moll-Stalcup EJ, Krogh TE, Kamo S, Lane LS, Cecile MP (1995) Geochemistry and U/Pb geochronology of arc-related magmatic rocks, Northeastern Russia. GSA, Abstracts with programs. P 65

Nachit H, Razafimahefa N, Stussi J.M, Carron JP (1985) Composition chimique des biotites et typologie magmatique des granitoides. C. R. Hebd. Acad. Sci 301: 813–818.

Nachit H, Ibhi AB, Abia El-H, El Hassan, Abia Ben Ohoud M (2005) Discrimination between primary magmatic biotites, reequilibrated biotites, and neoformed biotites. C. R. Geosci. 337, 1415–1420.

Ohmoto H, Goldhaber MB (1997) Sulfur and carbon isotopes. In: Barnes HL (ed) Geochemistry of hydrothermal ore deposits, 3rd edn. John Wiley and Sons, New York, pp 517–612.

Spiridonov EM (1991) Listvenite and zodite. Geol Ore Dep 33 (2): 38-48 (in Russian).

Wilson AJ, Cooke DR, Harper BJ, Deyell CL (2007). Sulfur isotopic zonation in the Cadia district, southeastern Australia: exploration significance and implications for the genesis of alkalic porphyry gold-copper deposits. Miner Deposita 42: 465-487.

Tectonomagmatic aspects of intrusive hosted Cu-Au-Mo deposits in the Skellefte District, northern Sweden

Therese Bejgarn
Nordic Rock Tech Centre AB, c/o Luleå University of Technology, SE-971 87 Luleå, Sweden

Pär Weihed
Luleå University of Technology Department of Civil, Mining and Natural Resources Engineering, Luleå University of Technology, SE-971 87 Luleå, Sweden

Juhani Nylander & Hans Årebäck
Boliden Mineral AB, SE-936 81, Sweden

Ulf Söderlund
Department of Earth and Ecosystem Sciences, Lund University, SE-223 62 Lund, Sweden

Richard Ernst
Department of Earth Sciences, Carleton University, Ottawa, Ontario, Canada K1S 5B6

Abstract. The Älgträsk gold deposit and several low grade base metal deposits, e.g. the Tallberg porphyry deposit, are hosted by the Jörn intrusive complex in the northern part of the Skellefte District, northern Sweden. The intrusive complex was emplaced at 1.89-1.86 Ga in a continental margin volcanic arc setting, and the oldest 1.89 Ga phase is coeval with volcanic rocks within the Skellefte Group, a complex volcano-sedimentary succession hosting numerous VMS deposits. The intrusive hosted deposits are associated with 1.88 Ga quartz-feldspar porphyritic intrusive rocks, which formed from 1.89 Ga recycled crust. Hence, it is interpreted that the intrusive hosted deposits formed when the arc was under transpression-compression, 10 Myr after the spatially related VMS deposits, which formed when the arc was under extension.

Keywords. Intrusive hosted, Cu-Au-Mo, Skellefte District, U-Pb dating

1 Introduction

After almost 90 years of exploration in the Skellefte District, northern Sweden, more than 85 VMS deposits have been discovered, of which four currently are in production. During the last 30 years, several intrusion hosted deposits have been discovered in the northern part of the district. Boulders with massive pyrite in silicified rock were discovered by Boliden Mineral AB in the Tallberg-Älgträsk area (Fig. 1) in the 1940's, an area covered with about 10 m of glacial till. However, the origins of the boulders were never confirmed and the area was down-prioritised. After the discovery of the Aitik deposit in the 1960's, new possibilities were seen in low-grade, large tonnage base metal deposits, which tentatively led to soil sampling and geophysical investigations in the Tallberg-Älgträsk area. During the 1970's the Tallberg area was the main target for geophysical and geological investigations up until the 1980's when the Älgträsk deposit was discovered by till sampling. Since then, the Tallberg-Älgträsk area has been the target for multiple drilling campaigns, and the geological information is today covering an approx. 25 km^2 large area. A historical mineral resource estimation based on around 40 loosely spaced drill cores and additional rock chip samples in the mid 1980's indicates 44 Mt with an average of 0.27% Cu at a cut-off grade of 0.20% Cu, although assays of Au, Mo, and Zn were too sparse to give any definite grades of these elements

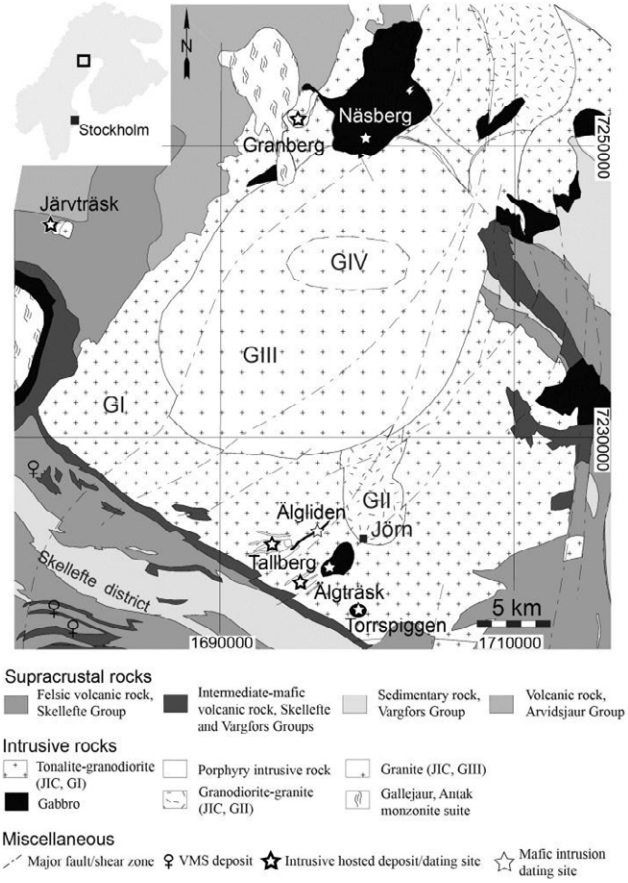

Figure 1. Geological map of the Jörn Intrusive Complex and central part of the Skellefte district with major VMS deposits and intrusive hosted mineralization indicated (Modified from Wilson et al. 1987). Inset: Outline of the Fennoscandian shield with the Skellefte district indicated

(Weihed, 1992). No recent estimates exist, but re-analysed old material as well as around 240 new drill cores (approx. 50 000 m) and additional rock chip samples as well as geophysical measurements have been made. In the Älgträsk area, around 400 drill cores (approx. 80 000 m), with additional rock chip samples have been sampled from the deposit, and it is estimated that the Älgträsk deposit comprises an indicated resource of 3 Mt @ 2.6 g/t Au (New Boliden, 2013). These intrusion hosted deposits have previously been interpreted as coeval with the 1.89 Ga VMS deposits in the Skellefte district (Billström & Weihed, 1996; Mercier-Langevin et al., 2012). However, recent zircon and baddeleyite dating by Bejgarn et al. (2012) shows that the VMS deposits are c. 10 Myr older than the intrusion hosted deposits.

2 Regional geology

The syn-volcanic to early orogenic the Jörn intrusive complex (JIC) ranges from gabbro to granite in composition (Fig. 1) and shows a calc-alkaline, I-type signature. It intruded a continental margin or island arc volcano-sedimentary succession at 1.89-1.86 Ga (Wilson et al. 1987; Gonzalés Roldán, 2010). The oldest, 1.89 Ga, phase is spatially, temporally and possibly genetically linked to the oldest volcanic units in the area, which in turn host over 80 volcanogenic massive sulphide deposits of varying sizes (Wilson et al., 1987; Allen et al., 1996; Billström & Weihed, 1996; Gonzalés Roldán, 2010). At 1.88 Ga, the JIC was intruded by quartz-feldspar porphyritic (QFP) dykes and related hydrothermal activity formed porphyry style Cu±Mo±Au deposits at Järvträsk, Granberg and Tallberg, and also the Älgträsk Au deposit (Bejgarn et al., 2012). When peak metamorphic conditions were reached at 1.87 Ga (e.g. Skyttä et al., 2012) the JIC likely acted as a rigid body, partly shielding the deposits from deformation. However, reactivation of the structures controlling the emplacement of QFP dykes and mineralisation resulted in several generations of overprinting ductile–brittle deformation partitioned into pre-existing structurally weakened zones, such as propylitic and phyllic alteration zones related to ore deposition (Bejgarn, 2012).

2.1 Porphyry deposits

The Tallberg porphyry Cu-Au-Mo deposit located 3 km northwest of the Älgträsk deposit (Fig. 1) is associated with a QFP intrusion and associated numerous QFP dykes (Weihed, 1992). A QFP dyke at Tallberg have been dated by U-Pb in zircon at 1876±5 Ma (core), 1890±7 Ma (rim), while the JIC tonalitic host unit is dated at 1886±3 Ma, as shown in Figure 2 (Bejgarn et al., 2012). The northern part of the Tallberg deposit is characterised by multiple generations of quartz vein stockwork hosted and disseminated pyrite, chalcopyrite, molybdenite and magnetite (Weihed, 1992). The northern part of the deposit is cross-cut by the Älgliden mafic-ultramafic intrusion (Fig. 1), which in turn hosts a Cu-Au-Ni deposit (Bejgarn, 2012). The southern part of the Tallberg deposit hosts similar style mineralisation as the northern part, although with a less dense quartz vein stockwork, here overprinted by subvertical NE–SW chloritic, sericitic and silicic alteration zones with disseminated pyrite and chalcopyrite. These alteration zones are mainly situated at the contacts of the QFP dykes (Fig. 1) and in places carry gold-copper mineralisation. The Järvträsk and Granberg deposits share characteristics with the Tallberg deposit, although gold bearing sericitic alteration-zones are rare, or are yet to be discovered.

2.2 The Älgträsk deposit

The Älgträsk Au deposit is structurally controlled and characterised by NE–SW striking, steeply dipping zones of intense phyllic-silicic alteration enveloped by pervasive distal propylitic alteration. The mineralisation occurs both as dissemination and in veins, dominated by pyrite, locally enriched in chalcopyrite, sphalerite, arsenopyrite, Te-minerals and gold. The deposit is mainly hosted by a 1.89 Ga granodiorite and cross cut 1.88 Ga QFP dykes (Fig. 2) similar to the ones associated with porphyry style mineralisation in other parts of the JIC. Gold is positively correlated with SiO_2, K_2O, Ag, Te, Bi, Fe, Cu, Zn, Mo and As, coupled with feldspar destructive alteration and Sr depletion (Bejgarn et al., 2011). Several stages of mineralisation occur at Älgträsk, but it has been suggested that these formed during one prolonged hydrothermal event, where gold was associated with both early and late stages of pyrite

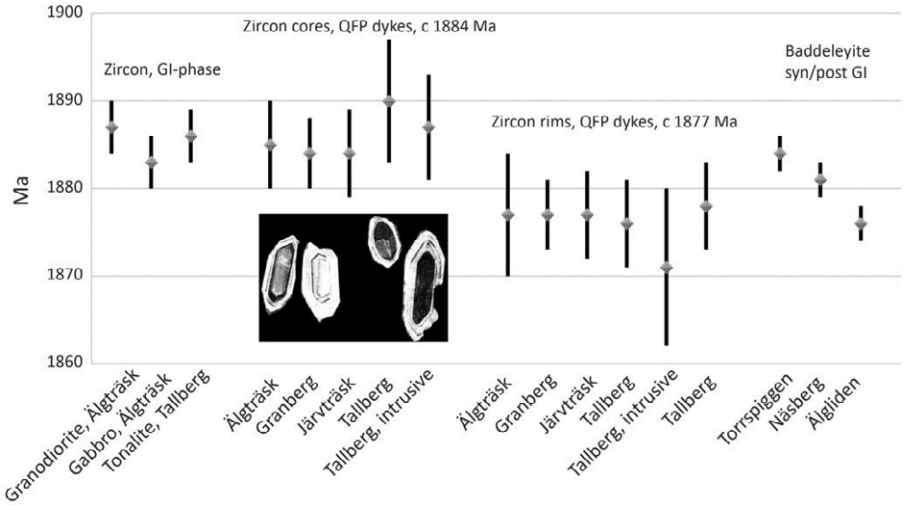

Figure 2. U-Pb zircon SIMS ages from intrusive rocks in the Jörn Igneous Complex. Inset: Approx. 100-200 µm long zircons from a quartz feldspar porphyry dyke in Tallberg with the typical oscillatory overgrowth on a sub-rounded core (after Bejgarn et al., 2012).

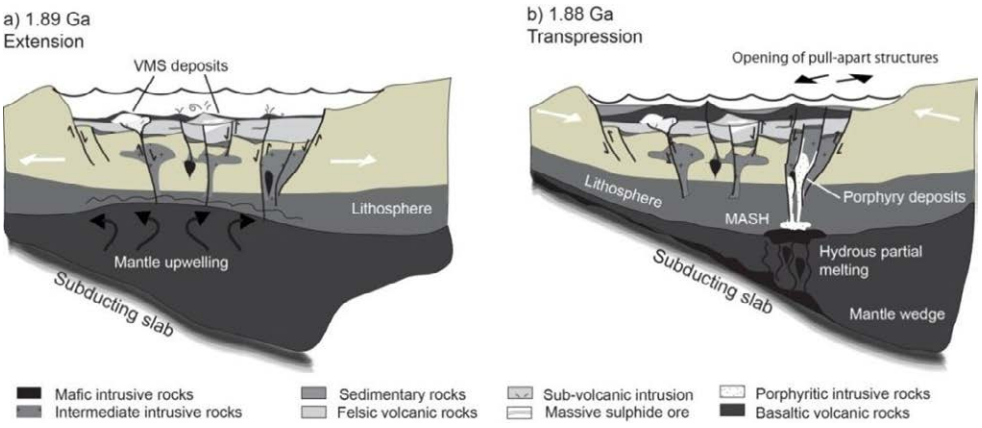

Figure 3. Schematic cross-sections illustrating the tectonic evolution of the Skellefte District (after Allen et al., 2002; Richards, 2009; Bejgarn et al., 2012).

precipitation (Bejgarn, 2012). Fluid inclusion data and trace element zonation in pyrite indicate that mineralisation in the Tallberg deposit formed from two hydrothermal fluids, one similar to the fluids associated with gold from the Älgträsk deposit (Bejgarn, 2012). Bejgarn (2012) proposed that the Älgträsk deposit represents a telescoping, later phase of the hydrothermal system forming the Tallberg deposit, or alternatively Tallberg represents a similar, but deeper section, of a porphyry system.

3 Geochronology and crustal evolution

Rounded cores overgrown by an oscillatory zoned rim (Fig. 2) is a common texture in zircons from QFP dykes associated with mineralisation in the intrusive-hosted deposits in the Järvträsk, Granberg, Tallberg and Älgträsk areas (Bejgarn et al., 2012). While the rim age is interpreted as the age of intrusion at 1.88 Ga, the 1.89 Ga cores are interpreted as the age of the remelted protolith, which is similar to the age of the oldest JIC units and the volcanic rocks of the Skellefte Group (Bejgarn et al., 2012). Mafic rocks spatially related to the intrusive hosted deposits yield U-Pb TIMS baddeleyite ages of 1.88 Ga, which is similar to the intrusive age of the QFP dykes (Fig. 3). However, the 3 km long, 100 m wide, NE–SW striking mafic dyke at Älgliden, dated at 1876±1 Ma, crosscuts porphyry style mineralisation at Tallberg and, is therefore younger than the porphyry style mineralisation (Bejgarn et al., 2012). The spatial and temporal relationship with coeval mafic–ultramafic intrusions, evidence for magma mingling/mixing and porphyry style mineralisation in both the southern and northern part of the JIC suggest that the formation of porphyry style mineralisation may have been triggered by the upwelling of mafic magma and partial melting at the base of the crust (Bejgarn et al., 2012). This is further supported by inherited 1.89–1.88 Ga zircon cores in zircons from the QFP dykes, indicating recycling of Palaeoproterozoic crust. Geochemically similar and coeval QFP dykes are also associated with mineralisation in the Granberg and Järvträsk areas, indicating that this event was not limited to the southern part of the JIC (Fig. 1).

4 Tectonomagmatic implications

The U-Pb geochronology of zircon and baddeleyite from the Älgliden dyke, QFP dykes and the JIC units indicates a c. 10 Myr age difference between the spatially related VMS and intrusion related deposits in the Skellefte district. This also tentatively corresponds to the tectonic transition of the volcanic arc (Fig. 3) from extension during formation of the VMS deposits, basin inversion (described by Bauer et al., 2012) and exhumation of the arc during compression or transpression during the formation of the intrusive hosted Au-Cu and porphyry Cu-Au deposits at 1.88 Ga (Bejgarn et al., 2012).

Acknowledgements

The authors would like to acknowledge M Whitehouse and L Ilyinsky at the Nordsim laboratory and K Billström at the Swedish Natural History Museum in Stockholm, Sweden, for thoughtful discussions during interpretations of dating results. The reviewer is also thanked for the comments on this extended abstract.

References

Allen RL, Weihed P, Svenson SA (1996) Setting of Zn–Cu–Au–Ag massive sulfide deposits in the evolution and facies architecture of a 1.9 Ga marine volcanic arc, Skellefte district, Sweden. Economic Geology 91: 1022–1053.

Billström K, Weihed P (1996) Age and Provenance of Host Rocks and Ores in the Paleoproterozoic Skellefte District, northern Sweden: Economic Geology 91: 1054-1072.

Bejgarn T, Årebäck H, Weihed P, Nylander J (2011) Geology, petrology and alteration geochemistry of the Palaeoproterozoic intrusive hosted Älgträsk Au deposit, Northern Sweden. In: Sial AN, Bettencourt JS, De Campos CP, Ferreira VP (eds) Granite-Related Ore Deposits. Geological Society, London, Special Publications 350: 105–132.

Bejgarn T (2012) The Älgträsk intrusion-related Au (Cu, Zn) deposit, Skellefte district, northern Sweden: Relationships between ore forming events in the Palaeoproterozoic Jörn intrusive complex. PhD thesis, Luleå University of Technology, Sweden. ISBN978-91-7439-467-2.

Bejgarn T, Söderlund U, Weihed P, Årebäck H, Ernst RE (2012) Palaeoproterozoic porphyry Cu-Au, intrusion-hosted Au and ultramafic Cu-Ni deposits in the Fennoscandian Shield: Temporal constraints using U-Pb geochronology. Lithos 19 pp (in press)

González Roldán MJ (2010) Mineralogy, Petrology and Geochemistry of syn-volcanic intrusions in the Skellefte mining district, Northern Sweden. PhD thesis. University of Huelva, Spain.

Mercier-Langevin, P, McNicoll V, Allen RL, Blight JHS, Dubé B (2012) The Boliden gold-rich volcanogenic massive sulfide deposit, Skellefte district, Sweden: new U-Pb age constraints and implications at deposit and district scale. Mineralium Deposita 20pp.

New Boliden 2013. New Boliden Annual report 2012. http://www.boliden.com/Press/Publications/

Richards JP (2009) Postsubduction porphyry Cu-Au and epithermal Au deposits: Products of remelting of subduction–modified lithosphere. Geology 97: 247–250.

Skyttä, P., Bauer, T.E., Tavakoli, S., Hermansson, T., Andersson, J., Weihed, P., 2012. Pre-1.87 Ga development of crustal domains overprinted by 1.87 Ga transpression in the Palaeoproterozoic Skellefte district, Sweden. Precambrian Research 206-207: 109-136. . http://dx.doi.org/10.1016/j.precamres.2012.02.022,

Weihed P (1992) Geology and genesis of the Early Proterozoic Tallberg porphyry–type deposit, Skellefte district, northern Sweden. PhD thesis, University of Gothenburg, Sweden.

Wilson MR, Sehlstedt S, Claesson L–Å, Smellie JAT, Aftalion M, Hamilton PJ, Fallick AJ (1987) Jörn: an early Proterozoic intrusive complex in a volcanic–arc environment, north Sweden. Precambrian Research 36: 201–225.

Mineralogy of the medieval Ag-Au ores in Banská Belá, Treiboltz, Rabenstein, and Kopanice in the Banská Štiavnica epithermal ore district (Slovakia)

Khulan Berkh, Juraj Majzlan
Institute of Geosciences, Friedrich-Schiller University, Carl-Zeiss Promenade 10, D-07745 Jena, Germany

František Bakos
EMED Slovakia

Martin Chovan, Jaroslav Kozák
Department of Mineralogy and Petrology, Comenius University, Mlynska dolina G, SK-842 15 Bratislava, Slovakia

Abstract. Medieval mining sites at Banská Belá, Kopanice, Treiboltz and Rabenstein in the Banská Štiavnica ore district (Slovakia) are epithermal Ag-Au occurrences.
From bulk chemical analysis, local Au grades are > 20 g/t and the Ag > 650 g/t. In Banská Belá, the Ag minerals include acanthite, polybasite-pearceite, pyrargyrite, stephanite, rare proustite and freibergite and occur mostly as inclusions in pyrite. In Kopanice, the main Ag mineral is acanthite and the only base metal sulfide is pyrite. Both minerals are often rimmed by an unnamed AgFe(Ni) or AgSe(Te) sulfide. At Treiboltz, the dominant Ag carriers are hessite and benleonardite, both associated with galena. In Rabenstein, pyrargyrite and freibergite are the main Ag minerals. Silver bearing gold and uytenbogaardtite are present in all sites except for Treiboltz. The Au-Ag minerals appear always to be younger than the base-metal sulfides although the precipitation of these two groups of minerals predicts partial time overlap. We assume that some of them were formed by processes of secondary enrichment (weathering and oxidation).

Keywords. epithermal gold-silver occurrence, mineralogy

1 Introduction

The precious and base metal ore district of Banská Štiavnica is one of the largest camps in the Carpathian arc and has been an important source of precious and base metals since the Middle Ages (Bakos and Chovan, 2004). The historical total production during the past 400 years was approximately 80 t of Au, 4,000 t of Ag, 8,000 t of Cu, 55,000 t of Pb, and 70,000 t of Zn (Lexa et al., 1999).

It is a paradox that the precious metal (Ag-Au) mineralization which sustained the mining activities over centuries has received less attention during the past decades than the other types of mineralization. This lack of knowledge can be partially explained by the fact that the precious-metal mineralization has been exhausted in the mid-20th century and was never systematically studied.

The aim of this work is to investigate the mineral assemblages at the four Medieval mining sites. The results of this study can provide not only a scientific overview of the epithermal gold and silver deposits in the studied region, but also reveal the potential to develop these areas for a future economic use as a result of the rising gold and silver prices.

2 Geological setting

The Banská Štiavnica ore district is located in the central zone of a large Miocene andesite stratovolcano, with an area of almost 2500 km^2, within the Central Slovak volcanic field. The volcano is manifested today as a huge caldera with a radius of 10 km hosting a late stage resurgent horst. The structure is intruded by an extensive subvolcanic complex (Konečný et al., 1995).

The volcanic field comprises mostly rocks of andesitic composition with minor proportions of rhyolites and basalts. Most of the volcanic rocks are chemically similar to medium- to high-K andesites of continental margins or evolved island arcs involving older continental crust. The intrusive rocks are granodiorite to monzonite (Lexa et al., 1999).

Neogene volcanism of the Central Slovakia Volcanic field was related closely in space and time to back-arc extension processes, giving rise to horsts and grabens. This structural setting led to the evolution of a long-lasting hydrothermal system and formation of various mineralization types, ranging from intrusion-related magnetite skarn, base-metal stockwork, and metasomatic base metal to epithermal Au-Ag-base metal (Lexa et al., 1999).

The extensive epithermal system of the ore district contains 120 veins over an area of almost 100 km^2 and is temporally and spatially linked to the post-caldera resurgent horst. The spatial extent of epithermal veins corresponds approximately to the extent of the bell-shaped granodioritic subvolcanic intrusive complex (Lexa et al., 1999).

3 Results

Our study focused specifically on the historic mining sites and was carried out by investigations on polished sections from drill core samples, heavy mineral concentrates, and chemical analysis. Banská Belá and Rabenstein are described together because of their

similarities, including Au-Ag mineralogy. The localities Kopanice and Treiboltz are described separately.

3.1 Ore mineralogy

Banská Belá and Rabenstein

The ore minerals in Banská Belá occur in veinlets or they are disseminated in a strongly altered and weathered andesite. The ore body at Rabenstein consists of a massive quartz vein in strongly altered granodioritic rocks.

The base-metal sulfide association in Banská Belá is dominated by pyrite (up to 10 wt.% As), arsenopyrite, and marcasite. Minor phases are chalcopyrite, sphalerite, galena and very rare pyrrhotite. In contrast, pyrite in Rabenstein is almost devoid of As with an average As content of 0.1 wt.% (Majzlan, 2009). Arsenopyrite is missing there, whereas galena and sphalerite are the most abundant base metal sulfides.

The precious metal ores comprise silver-rich sulfides and sulfosalts, such as acanthite (Ag_2S), polybasite-pearceite [$(Ag,Cu)_{16}(As,Sb)_2S_{11}$], pyrargyrite ($Ag_3SbS_3$), stephanite ($Ag_5SbS_4$), rare proustite ($Ag_3AsS_3$) and freibergite ($(Ag,Cu,Fe)_{12}(Sb,As)_4S_{13}$). Polybasite-pearceite is the most common Ag-mineral in Banská Belá and form mostly inclusions in pyrite, whereas pyrargyrite and freibergite are the main Ag-mineral in Rabenstein and occur as intergrowths with galena and chalcopyrite. All As-Sb-minerals contain more antimony than arsenic. The Sb/(Sb+As) ratios range generally from 0.67 to 0.98.

Gold occurs as silver bearing gold and uytenbogaardtite (Ag_3AuS_2). Silver bearing gold with the Au/(Au+Ag) ratios from 0.34 to 0.47, occurs principally as inclusions in pyrite, quartz and sometimes in acanthite or chalcopyrite. Uytenbogaardtite is always associated with acanthite (Fig. 1a).

Precious metals are clearly restricted to relatively shallow depths but the base-metal mineralization extends to the deeper portions of the mineralized structures. They seem to be spatially separated.

Kopanice

The ore minerals in Kopanice occur in banded veins up to 1 m thick in a strongly altered and weathered quartz diorite.

The ore mineralogy in Kopanice is relatively simple but the amount of Au- and Ag-minerals is greater than in the other sites. Pyrite is the only base metal sulfide. The most abundant Ag mineral is acanthite. Pyrite and acanthite are often corroded by unnamed Ag-Fe and Ag-Fe-Ni sulfides (Fig. 1b and c), which show ochreous brown or bluish grey color with a moderate reflectance in reflected light microscope. No pleochroism, no internal reflection and none to slight anisotropy were observed.

Other unnamed Ag-Se and Ag-Se-Te sulfides are also found at Kopanice. In reflected light, they are creamy grey to bluish grey with a moderate reflectance. They have weak anisotropy, no pleochroism, and no internal reflections. They occur separately or replace pyrite and may be intergrown with silver bearing gold.

Native silver is rare; it forms up to 15 μm large irregular grains and occurs separately or replaces acanthite (Fig. 1b).

Silver bearing gold occurs commonly and forms separate grains up to 50 μm in diameter or inclusions up to 10 μm large in pyrite and acanthite. Intergrowths with Ag-Fe sulfide (Fig. 1c) and Ag-Se-Te sulfide are frequently found. Therefore, it appears that silver bearing gold is younger than pyrite and acanthite. The Au/(Au+Ag) ratios range from 0.43 to 0.72 and are higher than in Banská Belá and Rabenstein. The Au concentration within a single grain varies strongly, with Au/(Au+Ag) ratios changing abruptly from 0.47 and 0.66 over a distance of a few micrometers. Such grains show patchy zonation. Uytenbogaardtite is a very rare mineral in Kopanice and seems to postdate silver bearing gold because it occurs as rims on silver bearing gold grains.

Treiboltz

The ore minerals occur in hydrothermal breccias with up to 3 cm large angular rock fragments. The porphyric texture is distinguishable despite intense silicification, but the mineralogical nature of the phenocrysts cannot be discerned anymore.

Galena is the major base-metal sulfide in this site. Furthermore pyrite, sphalerite and chalcopyrite are present.

The principal Ag carrier is hessite (Ag_2Te) which forms inclusions in galena. Other Ag mineral is benleonardite $Ag_8(Sb,As)Te_2S_3$. In contrast to hessite, benleonardite appears to have grown on the pre-existing galena crystals (Fig. 1d), together with hessite, and not as inclusions in galena. Freibergite, polybasite-pearceite and acanthite are infrequently found. Moreover grains of tellurosulfides, tentatively identified as chenguodaite ($Ag_9FeTe_2S_4$) and cervelleite (Ag_4TeS), are rarely observed.

3.2 Chemical composition of the ores and its relationship to the mineralogy

Results of multi-element analyses for selected samples are shown in Figure 2. The correlation between Au and Ag content in the investigated sites is documented in Figure 2a. Increased Au contents above average of 0.25 ppm are mostly accompanied by increased Ag contents above average of 10.45 ppm in Banská Belá. In comparison to Banská Belá, the Au and Ag contents at Rabenstein and Kopanice are more than an order of magnitute higher with averages of 4.36 ppm Au, 199.32 ppm Ag (Rabenstein) and 3.47 ppm Au, 121.52 ppm Ag (Kopanice). The average Au:Ag ratio is 1:63.

An interesting feature of the results of chemical analyses is that the samples with high Au content tend to have lower Ag/Au values (Fig. 2b). That may indicate a supergene enrichment of Au (weathering and oxidation?).

Specific features of the mineralogy at the Rabenstein locality display a strong positive correlation between Cd and Zn due to the composition of Cd in sphalerite (Fig.

2c). It was also reported in Majzlan (2009) that sphalerite from the Rabenstein occurrence contains an average concentration of 0.42 wt.% Cd. In comparison to that the analyses from Kopanice show low contents of Cd and Zn because sphalerite was not found there but its existence is possible because the elements correlate with each other also positively (Fig. 2c).

A further match of the chemical analyses and ore microscopy is apparent in Figure 2d. The As and Sb contents are elevated. The average As and Sb contents of 152 ppm As and 57 ppm Sb in Rabenstein are much higher than in Kopanice, in which they are only 7 ppm (As) and 1 ppm (Sb). The reason for that is that As and Sb carrier minerals like pyrargyrite, freibergite and polybasite-pearceite form abundant large grains at Rabenstein. In comparison to that these minerals are missing in Kopanice. However, the As and Sb values show no linear correlation in both localities.

4 Discussion and conclusion

The investigated localities have very different mineralogy. The differences were expected to some extent because the four localities belong to different zones as defined by Gargulák et al. (2010). Treiboltz and Rabenstein belong to the Ag-Au (Pb-Zn) zone, Banská Belá and Kopanice belong to the Au-Ag zone. Here, interestingly, we see distinct similarities between the mineralogy of Banská Belá and Rabenstein.

Based on our results, we can clearly distinguish three stages of ore mineral deposition, partially in agreement with previous studies (Koděra 1960, 1969, Onačila et al. 1993).

The first stage is dominated by pyrite and base-metal sulfides, if the latter are present. Pyrite is almost invariably the oldest mineral and may be present in several generations. In our samples from Kopanice, this stage is developed very weakly. Slight deviations can be seen only in the presence of arsenopyrite and pyrrhotite in Banská Belá. Arsenopyrite is missing at the other studied site. Some of pyrite crystals show As zonation which indicates variations in the composition of the ore-forming fluids.

The second stage is represented by the primary minerals of precious metals with a great variability observed at different sites. The main Au carrier is silver bearing gold, the Ag minerals are represented by a number of Ag sulfides and sulfosalts. Onačila et al. (1993) described some minerals which were not found in our study and vice versa. The results are divergent especially for the Hlavná vein in Kopanice, where Onačila et al. (1993) reported silver bearing gold, acanthite, polybasite, pyrargyrite, and freibergite in the samples collected from the Móder adit which were not accessible to us. They also collected samples from Banište where our samples come from. They concluded that the mineralization is "not macroscopically visible, represented by tiny silver bearing gold and acanthite grains". It appears that the mineralization of the Hlavná vein, sampled at the level of the Móder adit, represents the slightly deeper portions of the vein system with first- and second-stage minerals. The uppermost portions belong more likely to the third stage.

Geochemically and mineralogically anomalous is the second stage at Treiboltz where the main Ag carriers are tellurides instead of sulfides. Hessite was also described from the Ján Benedikty vein (Onačila et al. 1993). Hessite and petzite occur in the deep gold-mineralization spatially associated with the Svätozár structure (unpublished data). Therefore, tellurium appears not to be an exceptional or unusual component of the ore veins in this region. The distribution and enrichment patterns of this element in the Hodruša ore field, however, are far from understood.

The third stage is the enrichment in the cementation zone. This stage is distinguished not only by its mineralogy and geochemistry, in terms of enrichment with respect to Ag and Au, but also with the textures of the minerals. Most typical are replacement textures where acanthite encases and ravens pyrite or galena. Acanthite also forms pseudomorphs after pyrite. Encasement and replacement of pyrite is seen also for the Ag-Fe and Ag-Fe-Ni sulfides found at Kopanice. In all cases, these minerals are fine-grained and porous. Uytenbogaardtite appears also as a typical late replacement product of silver bearing gold. The unusual enrichment of Ni in the sulfides at Kopanice is controlled locally, likely by the nearby body of forsterite skarn.

Acknowledgements

We thank M. Abratis (Jena) for help with the electron microprobe analyses. This study was financially supported by the *Deutsche Forschungsgemeinschaft*, grant no. MA 3927/11-1.

References

Bakos F, Chovan M (2004) Zlato na Slovensku. Sprievodca zlatou históriou, tažbou a náleziskami na našom území. Slovenský skauting, Bratislava, p 298

Gargulák M, Lexa J, Koděra P (2010) Evaluation of the performed geological exploration of the raw material potential in the Banská Štiavnica - Hodruša ore field. Unpublished Report. State Geological Institute of Dionýz Štúr, Bratislava (in Slovak)

Koděra M (1960) Paragenetic and geochemical research of the Všechsvätých vein in Hodruša. Acta geol. Geogr. Univ. Comen. 4:69-105 (in Slovak)

Koděra M (1969) To the question about the relationship between the Banská Štiavnica and the Hodruša ore fields. Mineralia Slovaca 3-4:247-250

Konečný V, Lexa J, Hojstričová V (1995) The Central Slovakia Neogene Volcanic Field. Acta Volcanol. 7(2):63-78

Lexa J, Štohl J, Konečný V (1999) The Banská Štiavnica ore district: relationship between metallogenetic processes and the geological evolution of a stratovolcano. Miner Deposita 34:639-654

Majzlan J (2009) Ore mineralization at the Rabenstein occurrence near Banská Hodruša, Slovakia. Mineralia Slovaca 41:45-54

Onačila D, Rojkovičová Ľ, Žáková E, Repčok I, Eliáš K, Ferenčíkov R, Harčová E, Hašková A, Kovárová A, Rúčka I, Kalinaj M (1993) Metallogenetic model and raw material resources of the central zone of the Banská Štiavnica stratovolcano. Unpublished report. Geological Institute of Dionýz Štúr, Bratislava (in Slovak)

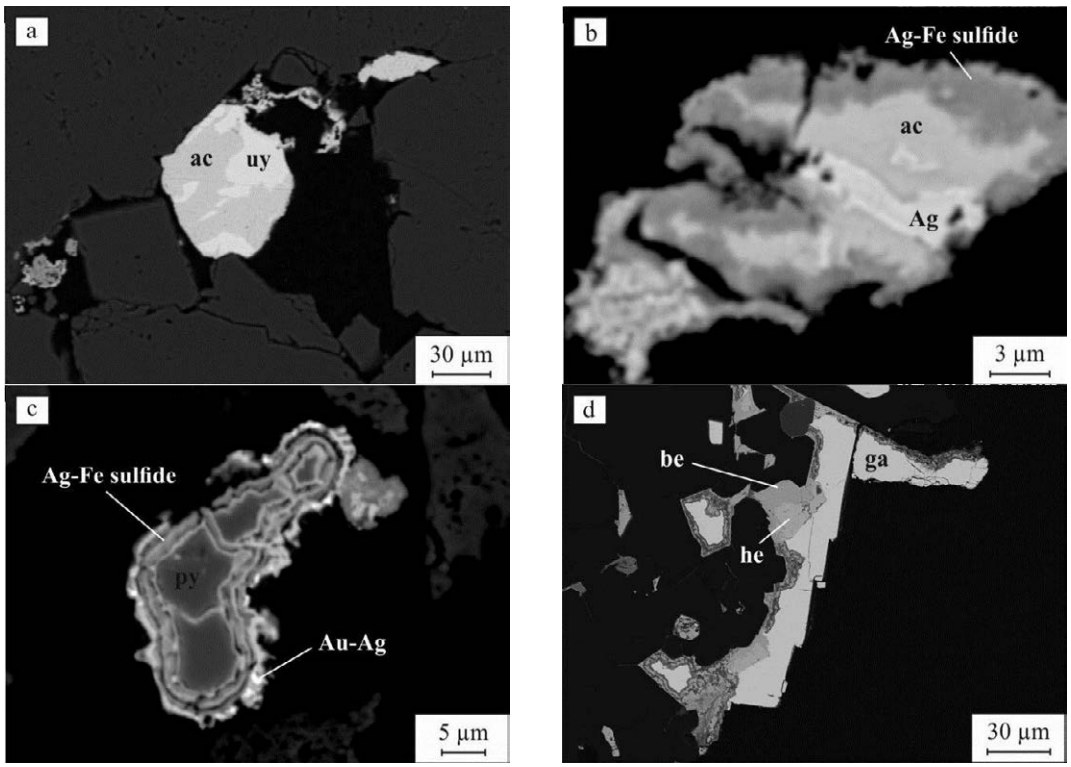

Figure 1. Back-scattered electron images: **a** uytenbogaardtite intergrown with acanthite in Banská Belá. **b** acanthite grain with an Ag inclusion replaced by Ag-Fe sulfide from outside in Kopanice. **c** pyrite grains surrounded by multiple layers of Ag-Fe sulfide with silver bearing gold inclusions in Kopanice. **d** benleonardite together with hessite grown on a pre-existing galena crystal in Treiboltz.

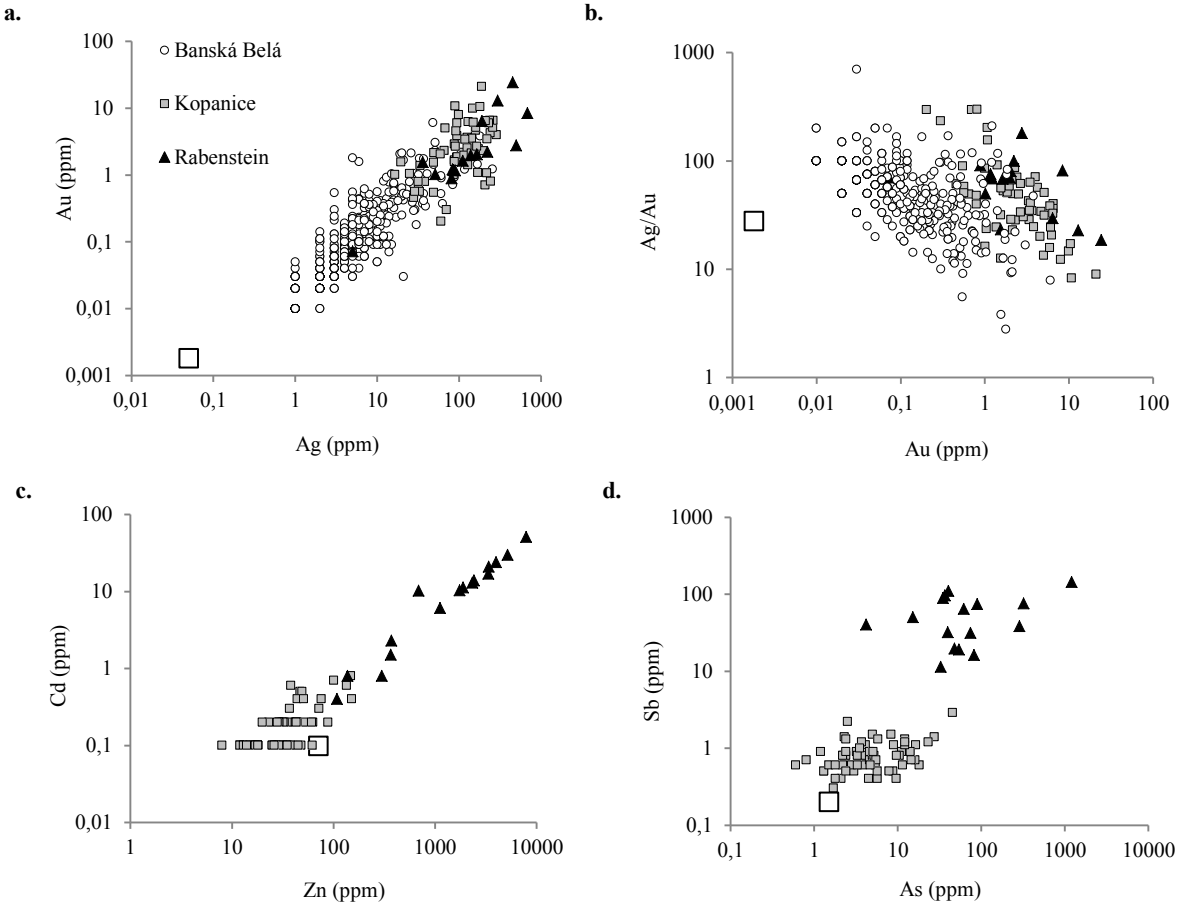

Figure 2. Variation diagrams for pairs of elements: **a** correlation between Au and Ag content in Banská Belá, Rabenstein and Kopanice (due to the logarithmic scale zero values in Banská Belá are not shown). **b** negative correlation between Au content and Ag/Au ratio, indicating a supergene enrichment of Au. **c** Cd and Zn correlations due to composition of Cd in sphalerite in Rabenstein and Kopanice. **d** higher Sb and As values in Rabenstein than in Kopanice due to the large amount of pyrargyrite and freibergite.

The Vysokogorskoye tin-porphyry deposit, Primorye, Russia: fluid inclusion evidence for contribution of magmatic and nonmagmatic fluids

Bortnikov N.S., bns@igem.ru, Gorelikova N.V., Balashov F.V.
Institute of Geology of Ore Deposits, Petrography, Mineralogy and Geochemistry, Russian Academy of Sciences, (IGEM RAS) Moscow, Russia

Kryazhev S.G.
Central Research Institute Of Geological Prospecting for Base and Precious Metals (TsNIGRI), Moscow, Russia)

Gonevchuk V.G.
Far East Geological Institute, Far East Division of Russian Academy of Sciences

Ryabchenko V.M.
Krasnoyarsk Geological Survey

Abstract. The Vysokogorskoe tin deposit is spatially and temporally related to the granite magmatism. The important ore bodies are dyke-like mineralised fluid-magmatic breccia. A fluid inclusion study revealed a coexistence of the hypersaline aqueous fluid and the vapor-rich fluid assuming the exsolving of the boiling fluid at the crystalization of granodiorite-porphyry. The boiling fluid infiltrated the granite-porphyry dikes and breccias. The metal-bearing magmatic fluid was mixed with the nonmagmatic (meteoric) fluid during the breccia formation.

Keywords. Tin porphyry deposit, granite-porphyry, fluid-magmatic breccia, fluid inclusions.

1 Introduction

Most typically, tin deposits are related to postmagmatic proceses of granite magmatism (Lehmann, 1990). Tin is belived to be derived directly from a highly fractionated S-type granitic melt due to a partition into an exsolved fluid. The leaching of tin-bearing magmatic minerals by later fluids may be another process involved in formation of tin deposits. Primary magmatic fluids or evolved meteoric waters, basinal brines, and metamorphic fluids, may be involved in the formation of tin deposits (Walshe *et al.*, 1996, Bortnikov et al., 2005). Thus, the origin of tin-bearing ore-forming fluids is controversial.

This paper reports results of a study of fluid inclusions in fluid-magmatic breccias and granite-porphyries at the Vysokogorskoe tin-porphyry deposit, which can provide a further understanding on origin of ore forming fluids. This deposit is one of largest deposits in Primorye, Russia. Total production of tin to the end of 1990 has been about 50 000 tons. It's proved reserves and resources are estimated more than 50 000 tons.

2. Regional Geology

The Vysokogorskoe tin deposit is located within the Sikhote Alin' accretionary fold system. This system was formed from the Cretaceous to the Paleogene due to repeated alternation of suprasubduction (Andean) and transform (Californian) continental margin environments (Khanchuk, 2000). That results in the formation of multiphase magmatic plutons and multistage tin and tungsten deposits.

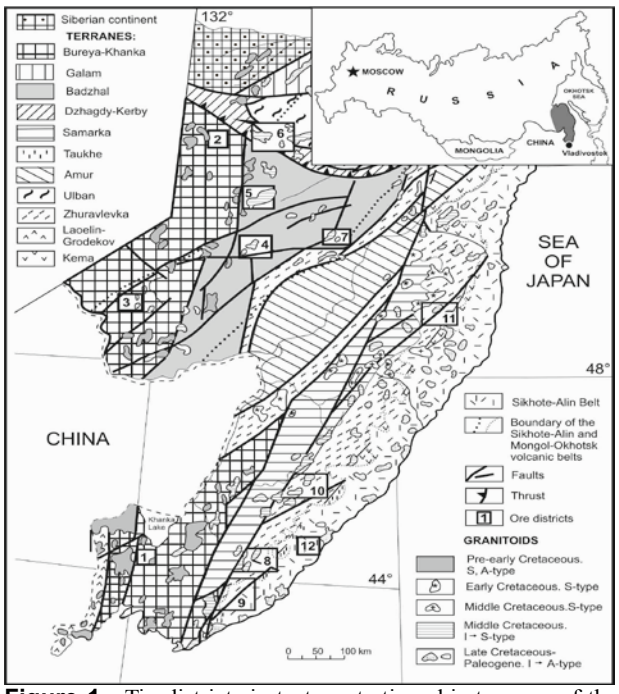

Figure 1. Tin districts in tectonostratigraphic terranes of the Russian Far East (Khancuk, 2000).
8 - Kavalerovo region (Vysokogorskoe deposit)

3. Local Geology

The deposit is located in a strongly fractured latitudinal zone within a narrow EW-trending tectonic "window" composed of Triassic, Jurassic, and Cretaceous terrigenous–carbonate sequence among flows of Upper Cretaceous acid volcanic rocks. Sedimentary sequence forms a flexure fold due to change its strike from NE to SW. The deposit area consists of sandstones with the siltstone and chert layers. It was intruded by pre- and intra-ore magmatic rocks. The pre-ore granodiorite-porphyry comprises a stock. Numerous intra-mineralization dykes of granite-porphyries, quartz porhyries, dacite-porphyries, and diabase porphyrites occur as well.

3.1 Granodiorite-Porphyries and Granite-Porphyries

Granodiorite-porphyies of the 1st megastage and injected granite-porphyries of the 2nd megastage are recognised at the deposit. Granodiorite-porphyries of the 1st megastage form a large stock at the deep (Fig. 1) and small bodies at the surface. They consist of phenocrysts of feldspar (№ 20-25), potassium feldspar, biotite, and quartz. The groundmass consists of feldspar, and quartz. Accessory minerals are zircon, apatite, rutile, and tourmaline. Granite-porphyries, which postdates the granodiorite-porphyries, occur at depth as elongated dikes. They consist of phenocrysts of potassium feldspars, intratelluric quartz phenocrysts and a fine-graded groundmass of feldspar-quartz composition. A characteristic accessory mineral is fluorite.

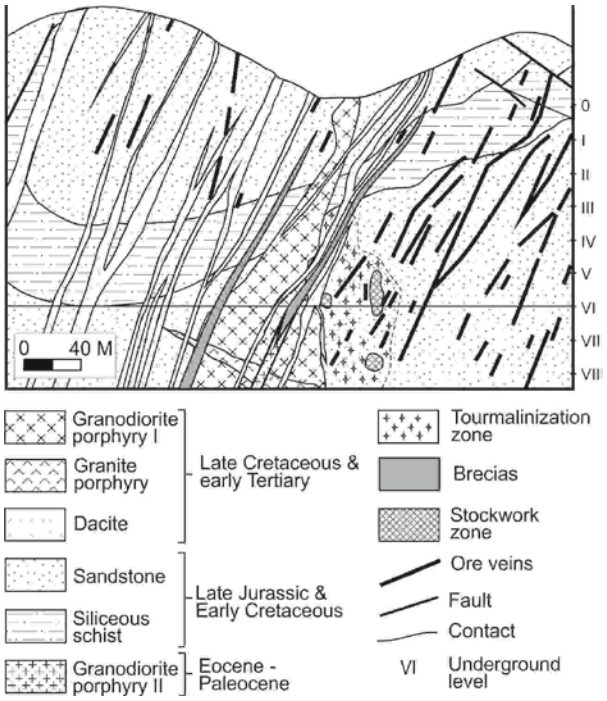

Figure 2. Geological chematic map of the Vysokogorskoe deposit (Kosenko, Ryabchenko, 1975).

3.2. Ore Bodies and Mineralization Styles

About 100 veins, stockworks, and mineralized breccias comprise Vysokogorskoe tin-porphyry deposit. Three mineral-forming events (megastages) that result in formation three types of mineralization, which different in age and spatially juxtaposed on each other.

The earliest mineralization stage consists of the quartz-tourmaline metasomatites, which have replaced sandstones and siltstones. They are related to the emplacement of granodiorites found in the centre of the deposit. The quartz–tourmaline bodies form linear bodies filling a series of contiguous fractures with total thickness up to 100 m, every vein of which is 0.5-15 m thickness. Their minimal age is constrained by injection of dacite and rhyolite dikes.

The second mineralization stage consists of rare-metal–molibdenum greisen metasomatites and molybdenite-bearing quartz veinlets in exocontact of the dike-like granite porphyry–rhyolite body.

The latest mineralization event resulted in the formation of economically important tin ore bodies. They consist of veins and mineralized breccia zones, which are localized in the Silinka fracture zone of ~1 km thick. The vein series is replaced by mineralized breccias at a depth of ~500 m. Tin ore bodies were formed in three three stages. Cassiterite-quartz-tourmaline and cassiterite-quartz-chlorite metasomatites formed in breccias and stockwork zones during the first stage. The quartz–sulfide mineralization with pyrrhotite, pyrite, sphalerite, chalcopyrite, and galena was next in the paragenetical sequence. The quartz–fluorite–carbonate aggregates were deposited at the final stage.

3.3 Fluid-Magmatic Breccias

Fluid-magmatic breccias are located in en echelon shear fractures. The dike-like breccia bodies extend from 100 m up to 1000 meters in S-E direction with a width of few cm to 6 m. Their vertical extent is of several hundreds of meters. Whereas the dike-like breccia bodies intrude the granodiorite-porphyries of the first megastage, the granite-porphyries of the second megastage filled fractures in a breccia. Their injections do not cement fragments in breccias. The granite-porphyries form fragments of an irregular shape in breccias. This assumes that its injection occurred latter in ductile fluidizated breccia. Breccias are mainly matrix-supported mono- to heterolithologic rocks and consist of angular and rounded fragments (Fig. 3 and 4).

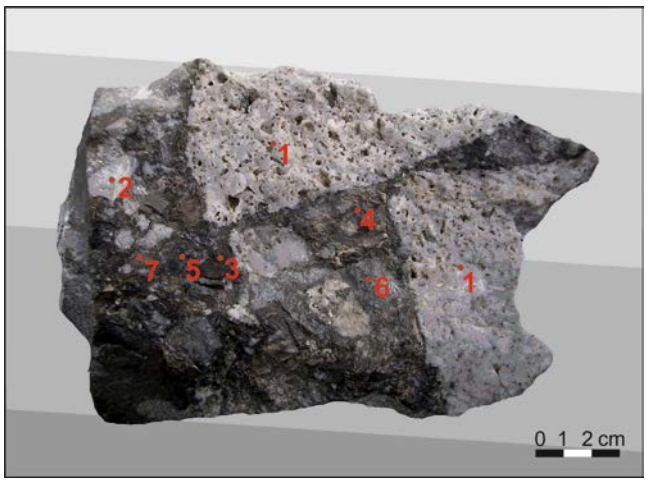

Figure 3. Fluid-magmatic breccia from the zone Ryabininskaya, V horizon. Legend: 1 - granite-porphyry; 2 – quartz-molibdenum vein; 3 – shist; 4 – sand; 5 – tourmalinites; 6 – quartzite; 7 - flint; 8 – quartz-tourmaline-carbonate cement.

The volume proportion of fragments varies between 40% and 70%. Monolithologic breccia consists of hydrothermally altered granite fragments in rock flour matrix.

Heterolithologic breccias are composed of intermixed fragments of granite-porphyries, tourmalinized and sericitized sandstones, siltstones, cherts, quartzits, and quartz-molybdenite aggregates in milled rock matrix and hydrothermal aggregates. These fragments were

removed from various depths. Breccias consists of fragments of silicified rocks cemented by comb quartz and radial schorl–dravite tourmaline in association with

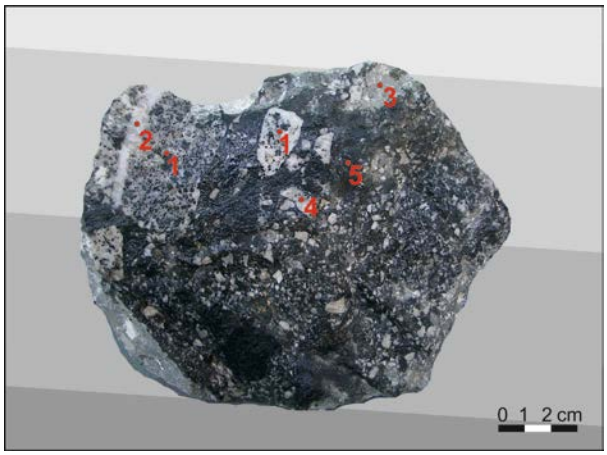

Figure 4. Fluid-magmatic breccia from the zone Glavnaya, V horizon. Legend: 1 – granite-porphyry; 2 – quartz-molibdenum vein; 3 – cherts; 4 – quartzite; 5 - quartz-tourmaline cement.

fine-grained cassiterite. Cassiterite veinlets and lenses crosscut fragments. The coexistence of the fragments of different rocks transported from deeper levels is evidence for the turbulent mixing of fragments within a fluidized system.

4. Fluid Inclusions

4.1 Granodiorite-Porphyries 1st

Abundant fluid inclusions were observed in quartz phenocrysts from granodiorite-porphyries. Three types of fluid inclusions were identified at room temperature (Fig. 2): polyphase brine-melt (type «a»), vapor-rich two- or three phase (type «b»), and three-phase (type «c»). Type «a» fluid inclusions form isolated clusters within phenocrysts, that infer their primary origin. All these inclusions contain a vapor bubble, aqueous liquid, and three isotropic daughter solid phases: sylvite (KCl), halite (NaCl), and an unindentified phase F_1 and an anisotropic phase F_2. Heating runs showed that bubbles disappeared at 255–355°C, phase F_1 dissolved at 375 to 420°C. Phase F_2 did not dissolve up to 650°C, while this phase observed in all inclusions of this type. No stretching of fluid inclusions during heating was recognised. Sylvite and halite dissolved at 215 to 255°C, and 450 to 550°C, respectively. These suggest the brine salinity of 53.3–66.5wt% NaCl-equiv., Na/K of 2.7–1.3 and trapping temperature T≥550°C.
Types "b" and "c" of inclusions are respectively vapour and brine inclusions trapped simultaneously along healed fractures.

Type «b» fluid inclusions predominate in quartz phenocrysts. They consist of H_2O-vapor bubbles occupied 65 up to 95% of vacuoles, and aqueous solutions containing dissolved alkali chlorides. Fluid salinity ranges from 19 wt. % NaCl-equev. up to salt saturation concentration as halite crystals were observed at a room temperature. Rare inclusions contain phase F_2 and an unidentified opaque mineral.

Type «c» fluid inclusions contains aqueous liquid, the vapor and solid phases (halite, opaque mineral, and anisotropic phase F_2). Vapor bubbles homogenised at 275°C. Halite dissolved at 370 to 400°C.
A variable vapor/liquid ratio in vacuoles of type «b» fluid inclusions and simultaneous trapping of vapor and brine fluid inclusions suggests a "boiling" of the fluid exsolved at the crystallization of granodiorite-porphyry.

The coexistence of salt and ore mineral crystals in inclusions indicates that brines released were capable to bear metals suggesting that magma was their source.

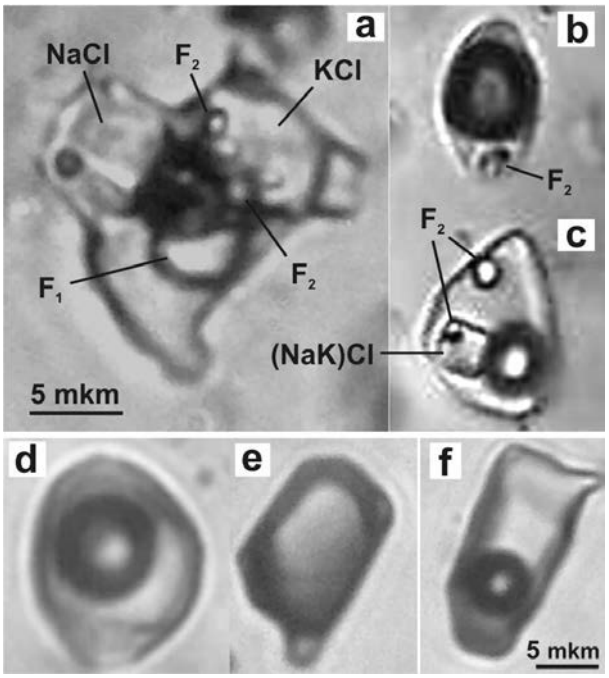

Figure 2. Fluid inclusions in quartz from granite-porphyry. a–c: first stage, d–f: second stage. See text for details.

4.2 Granite-Porphyries 2nd

Three types of fluid inclusions in quartz from granite-porphyries: secondary vapor-liquid (type «d») and vapor-rich (type «e»), and secondary vapor-liquid (type «f»).
Type «d» fluid inclusions are located in short cracks at quartz grain edges which do not cut boundaries. Fluid inclusions are isometric or «negative crystal» in shape. They are two-phase ones filled with liquid and vapor bubbles. The degree of filling is 70%.

Type «f» fluid inclusions are confined to long cracks, which cross grains of quartz. They are interpreted as secondary. They are flattened or tubular in shape. These two-phase inclusions contain liquid and a bubble. The degree of filling is 80-90%.
Type «e» fluid inclusions are rare vapor-rich inclusions, which are intimately and spatially associated with type «d» fluid inclusions.

The homogenization of type «d» and type «f» from fluid inclusions into a liquid phase occurred at 380 to 430°C and at 225 to 280°C, respectively. First-melting temperature of –31 to –28°C infers that both type inclusions contained dissolved NaCl. Fluid salinity estimated from measured ice melting temperatures of

–8.8 to –3.4°C varies from 12.6 to 5.6 wt.% NaCl-equiv., in general. Salinity of the fluid in type «f» inclusions is of 7.9 to 5.0 wt.% NaCl-equiv. It is obvious that salinity fluid trapped in inclusions decreases when their homogenization temperature falls (Fig. 3). A coexistence of type «d» and «e» fluid inclusions assumes that the aqueous fluid was close to the line of two-phase equilibrium. These suggest the fluid entrapment temperature of 400°C and pressure of 200–300 bar (see Fig. 3).

4.3 Fluid-Magmatic Breccias

Rare primary two-phase vapor-liquid fluid inclusions were observed in carbonate from the breccia matrix. They were homogenized at 340 to 350°C. Fluid salinity is estimated to be equal to 8.9 wt.% NaCl-equiv..

Secondary two-phase vapor-liquid fluid inclusions similar to those of type «f» were found in quartz fragments from breccias. Their homogenization occurred at 270 to 280°C. Fluid salinity estimated is of 6.5 wt.% NaCl-equiv.

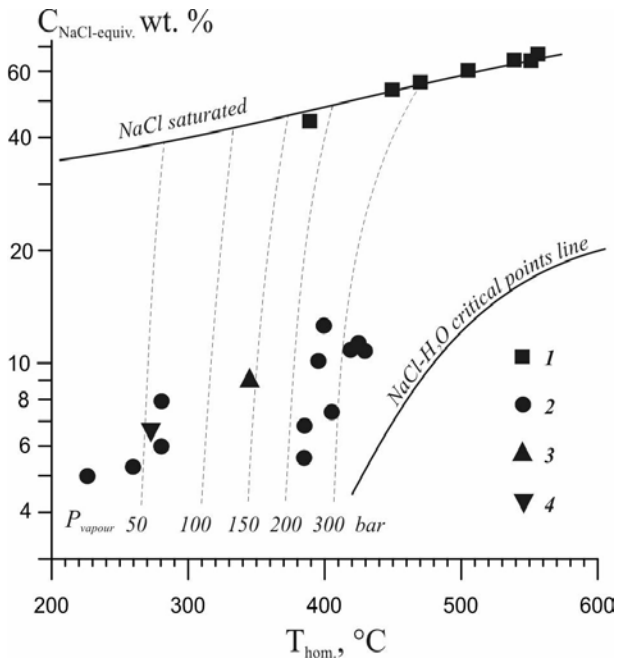

Figure 3. The relationship between salinity of the solutions and homogenization temperatures of fluid inclusions in minerals of the granite-porphyries of the I and II stages and fluid-magmatic breccias. $C_{NaCl\text{-}equiv.}$ salinity estimated by a final ice melting temperature or halite dissolution temperature (Bodnar and Vityk 1995), wt. %. The isolines on the diagram are plotted after Roedder E. (1984). An every point corresponds to a group of syngenetic inclusions (from 5 up to 35 separate inclusions) with identical microtermometric characteristics. Standard deviation error bars are not exceed the symbol size. The total number of inclusions is equal to 243.
Legend: 1 – quartz from granodiorite-porphyries 1st, 2 – quartz from granite-porphyries 2nd, 3 – carbonated cement of breccia, 4 – quartz from fluid-magmatic breccias.

4 Conclusions

The Vysykogorskoye mineralized breccia dikes are spatially and temporally associated with the emplacement of two phases of granites: they formed later granodiorite-porphyries 1st and contemporarily with injected granite-porphyries. The fluid inclusion study indicates that at the high-temperature (≥550°C) hypersaline metal-rich fluid exsolved from magma at the crystalization of granodiorte-porphyries 1st and suggests the "boiling" of the exsolved fluid. The secondary fluid inclusions in the quartz phenocrysts of the granite-porphyries also provide evidence for the infiltration these rocks of hydrothermal fluid.

Exsolution of aqueous fluid phase is considered to be resulted from the second boiling reaction H_2O-saturated melt (Burnham, 1985). The processes of second boiling and subsequent decompression are the main source of energy for breccia formation. The escape of a boron-rich magmatic hydrothermal fluid from the apical portions of one or more bodies of crystallizing granite-porphyries may result in the formation of breccia dykes. Mixing of magmatic brines with a more dilute fluid possibly meteoric in origin yielded the trends in temperature-salinity space observed in the granite-porphyries. Therefore, the ore-forming fluids involved in the formation of the Vysokogorskoe deposit are of both magmatic and nonmagmatic origin. Ore deposition is related to the initiation of retrograde boiling in an epizonal magma chamber, as it suggested for the porphyry environments (Sillitoe et al., 1975, Seedorff et al. (2005)

Acknowledgements

This study was supported by the Russian Foundation for Basic Research (project no. 11-05-00942-a) and Department of Earth Sciences of Russian Academy of Sciences (Program for Basic Researches No 2).

References

Bodnar RJ, Vityk MO (1995) Interpretation of microthermometric data for H2O–NaCl fluid inclusions. In: De Vivo B, Frezzotti ML (eds) Fluid inclusions in minerals, methods and applications. Virginia Polytechnic Institute and State University, pp 117–130

Bortnikov N.S. et al. Geochemistry of the Mineral-Forming Fluids in Some Tin-Bearing Hydrothermal Systems of Sikhote Alin, the Russian Far East. Geology of Ore Deposits, 2005, Vol. 47, No. 6, pp. 488–516

Burnham C.W. Energy Release in Subvolcanic Environments: Implications for Breccia Formation, 1985, v. 80, pp.1515-1522

Khanchuk A.I. Paleogeodynamic analysis of ore deposit formation in the Russian Far East. Vladivostok. Dal'nauka. 2000, pp.5-34

Lehmann, B., 1990, Metallogeny of tin: Lecture Notes in Earth Sciences, v. 32, Berlin,Springer-Verlag, 211 p.

Roedder E (1984) Fluid inclusions in minerals. Mineral Soc Am Rev Mineral 12

Seedorff E, et al. (2005) Porphyry deposits: characteristics and origin of hypogene features. Econ Geol 100th Ann vol: 251–298

Sillitoe RH, Halls C, Grant JN (1975) Porphyry tin deposits in Bolivia. Econ Geol 66: 215–225

Walshe J.L. et al. The Interplay of Groundwater and Magmatic Fluids in the Formation of the Cassiterite–Sulfide Deposits of Western Tasmania," Ore Geol. Rev", 1996, Vol. 10, p. 367

Hydrothermal alteration, SWIR-mineral mapping, vein distribution and age of the Haquira East porphyry Cu-Mo deposit

Federico Cernuschi, John H. Dilles
College of Earth, Ocean and Atmospheric Sciences, Oregon State University, Corvallis, Oregon, USA
cernuscf@geo.oregonstate.edu

Robert Creaser
Department of Earth and Atmospheric Sciences, University of Alberta, Edmonton, Alberta, Canada

Abstract. The Haquira East porphyry Cu-Mo deposit has Re/Os and $^{40}Ar/^{39}Ar$ ages of ~33.8 to 33.2 Ma. The ores are hosted in the Haquira granodiorite porphyry stock that intruded a compressionally deformed sequence of Mesozoic quartzite, meta-siltstone, and minor marble in the Andahuaylas-Yauri porphyry belt of southern Perú. New core logging observations, geochemical data, cross-sections, petrography and SWIR-scan images of hydrothermally altered samples document the vein sequence and alteration mineralogy. From oldest to youngest, the sequence consists of aplite dikes, barren quartz-K-feldspar veins, biotite micro-breccias/veins, actinolite veins with plagioclase halos and epidote veins, EDM-type dark and pale micaceous halos with bornite-chalcopyrite, A quartz veins with bornite-chalcopyrite, quartz-molybdenite veins, B quartz-bornite-chalcopyrite veins, D pyrite-quartz veins with sericitic halos, and smectite-chlorite-kaolinite ± pyrite halos. The distribution of both Cu-sulfide and Mo-bearing veins forms an inverted cup-shaped volume or shell above a core zone of high density aplite and barren quartz-K-feldspar veins. The copper shell forms a continuous high-grade ore zone in the Haquira stock, but is low grade where it projects into the relatively non-reactive quartzites, likely as a result of a limited supply of iron to enable copper-iron sulphide precipitation. In contrast, molybdenite mineralization forms a roughly symmetric shell overlapping both stock and quartzite with an axis of symmetry located along the southwest contact of the Haquira stock.

Keywords: Cu-Mo porphyry, Haquira-East, SWIR, CoreScan, hydrothermal alteration, isotopic ages

1 Introduction

Haquira East is a well-defined and relatively high-grade porphyry Cu-Mo deposit hosted in a porphyry stock intruded in a compressionally deformed sequence of Mesozoic quartzite, meta-siltstone and minor limestone. Haquira-East is part of the Eocene-Oligocene (ca. 43-31 Ma) Andahuaylas-Yauri porphyry belt of southern Perú (Perello *et al*., 2003).

Intrusions can be divided into four groups based on cross-cutting age relationships (see Cernuschi *et al.,* 2012): 1) early Lahuani quartz monzodiorite to granodiorite sills and dikes that intrude the sedimentary wall-rocks and that are moderately deformed together with these wall rocks, 2) the porphyritic Haquira granodiorite stock (Hp stock), 3) narrow sub-vertical Haquira porphyry dikes (Hp dikes) that are similar in composition to and cross-cut the Hp stock, and 4) the late Pararani quartz monzodiorite to granodiorite porphyry dikes (Pp dikes) that cut the previous intrusions and the Cu-Mo mineralization.

We present new core logging observations, Re/Os (University of Alberta), $^{40}Ar/^{39}Ar$ ages (Oregon State University), geochemical data, cross-sections, and SWIR (Short Wave Infrared) images of hydrothermally altered samples, and use these to relate the hydrothermal alteration and vein distribution to the emplacement of the igneous intrusions and Cu-Mo ore formation.

2 Hydrothermal system and mineralization

2.1 Ages

Re/Os ages of molybdenite in three samples of banded quartz-molybdenite veins yield ages of 33.86±0.14 Ma, 33.75±0.14 Ma, and 33.93±0.03 Ma (error =2 s.d.), and are similar to U/Pb zircon ages from the Haquira stock and porphyries (Philip Gans, *person. commun.,* 2011). A $^{40}Ar/^{39}Ar$ analysis of muscovite from a D vein selvage yielded a weighted mean plateau age of 33.18±0.21 Ma. These isotopic data suggest a short period (~33.9-33.8 Ma) of porphyry intrusions and high temperature Mo mineralization followed by cooling through the Ar-closure temperature (~325-350°C) by 33.2 Ma.

2.2 Hydrothermal veins

Veins and mineralization were first described by the Antares exploration team, summarized by Einaudi (2008), and modified by Cernuschi *et al.* (2012).Veins follow a sequence, from oldest to youngest, of: 1) aplite dikes, 2) barren quartz-K-feldspar veins, 3) biotite micro-breccias/veins, 4) actinolite veins with plagioclase halos and epidote veins, 5) dark and pale micaceous (EDM, PGS) halos, 6) A quartz veins with bornite-chalcopyrite, 7) banded quartz-molybdenite veins, 8) B quartz-bornite-chalcopyrite veins, 9) D pyrite-quartz veins with sericitic halos, and 10) smectite-chlorite-kaolinite ± pyrite halos.

In the center of the Haquira granodiorite stock barren veins (1 to 3) are cut off by narrow Hp porphyry dikes, which are in turn cut by a second set of high temperature veins (1 to 2), yielding reverse-age relations. All veins

are interpreted to be magmatic hydrothermal in origin, except type 4 veins that have sodic-calcic alteration selvages that are interpreted as produced by non-magmatic fluids elsewhere (Dilles and Einaudi, 1992). The highest copper grade zone is associated with hydrothermal biotite alteration and vein sets 5, 6 and 8, and is underlain by a low-grade core that has biotite alteration and abundant type 2 veins.

2.3 SWIR data

The hydrothermal vein and alteration halo mineralogy have been examined using a short wave infrared (SWIR) mapping of thin section billets to produce images (Figure 1). Identification of hydrothermal minerals from SWIR spectra relies on matching empirically identified absorption produced by stretching and bending energies of metal–OH or other chemical bonds (see Thompson *et al.,* 1999). The HCI-2 spectrometer available with CoreScan™ uses a 0.5x0.5mm analytical spot (at 4 nm spectral resolution) in contrast to other SWIR systems such as PIMA and ASD that use a ~1 to 2.5 cm diameter spot (Zhaoshan and Yang 2012). By scanning a flat rock surface, a SWIR spectrum can be obtained for each spot on the surface. Software is used to identify a mineral on the basis of the strongest SWIR absorption, and a color-coded raster image of the minerals is produced (Figure 1). Because of the small spot size and spectral resolution, this type of SWIR-imaging can texturally identify the sites where hydrothermal biotite has replaced hornblende (Figure 1A,D,G). Some conclusions about the sequence of hydrothermal events can be drawn with the aid of these images based on the stability temperature/pH ranges of the identified minerals (see Seedorff *et al.* 2005 for all T°C/pH references cited below).

Pale green to white argillic alteration in some cases forms outer halos surrounding older alteration mineral assemblages such as sericitic haloes on D veins and EDM-PGS haloes. These argillic zones are composed of mixtures of smectite-kaolinite-chlorite, and by definition constitute intermediate argillic alteration (Figure 1B,E,H and C,F,I). Smectite and kaolinite are formed at lower temperatures (<100 °C) and higher pH than the muscovite present in the inner D vein halos (550 ~ 300°C). Therefore, the lower temperature of the outer haloes is consistent with formation of this intermediate argillic event by re-opening of older and higher temperature EDM and D veins.

The inner biotite-rich zone of the imaged EDM halo (Figure 1C,F,I) was likely related to a slightly earlier and higher temperature event (>500°C, near-neutral pH) than the outer sericite-chlorite±biotite halo (550~300°C and lower pH).

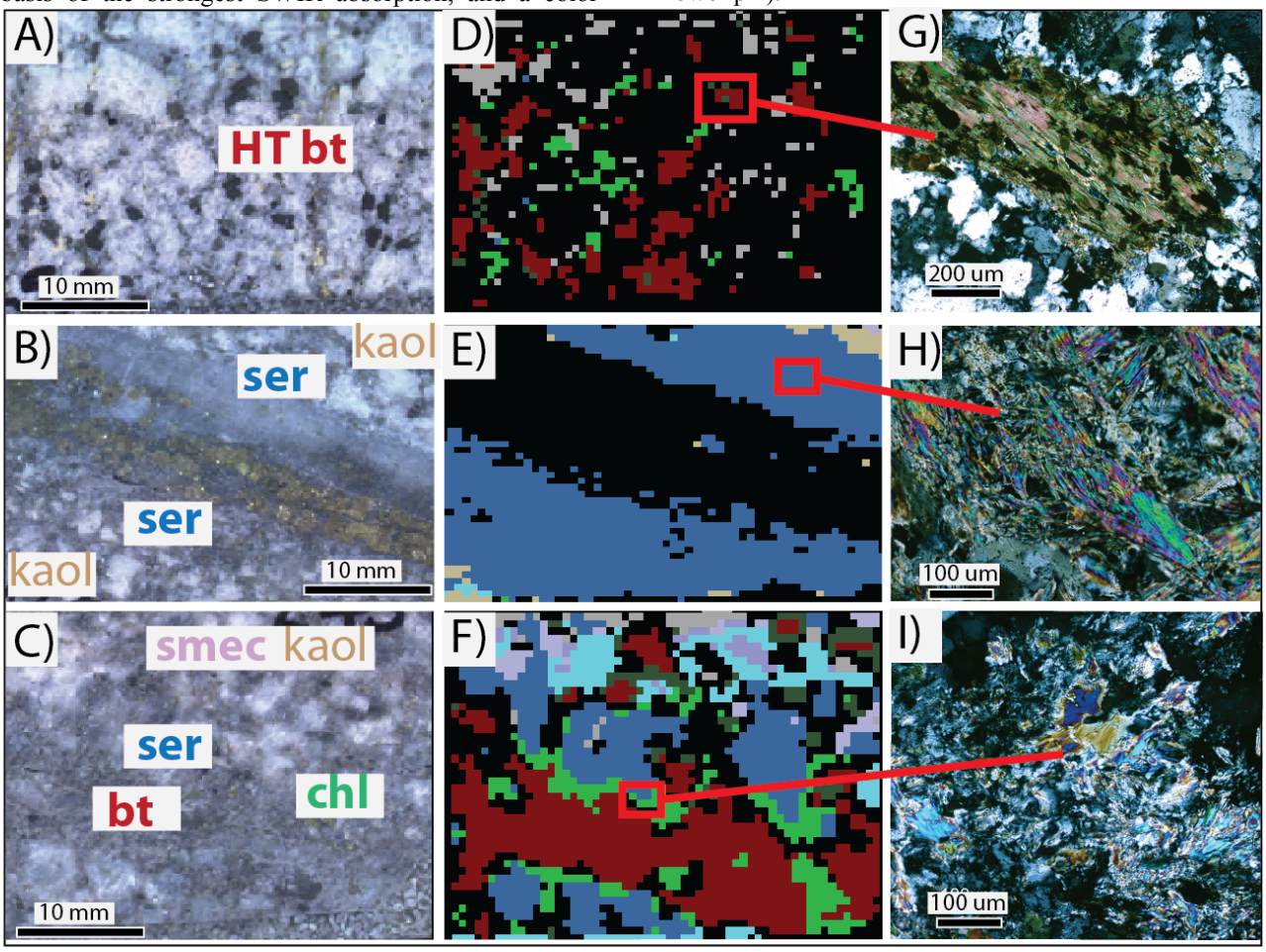

Figure 1. Selected hydrothermal veins and halos in porphyry samples. **A,B,C:** Thin section photos, indicating minerals identified by SWIR-mapping and color-coded according to images **D,E,F:** mineral map images from CoreScan™ of the same billets. **G,H,I:** thin sections photos (transmitted light and crossed polars) of the same samples. **Upper row (A,D,G):** FC-HAQ-225a (AHAD108-112m), **Middle row (B,E,H):** FC-HAQ-127 (AHAD106-618m) and **Lower row (C,F,I):** FC-HAQ-243 (AHAD98A-267m).

2.2 Hydrothermal flow and Cu-Mo ores

Mapping the vein type distribution and density provides valuable information about the distribution of the fluid flow zones and the flux of fluid through the porphyry system.

The high density of barren quartz-K-feldspar veins is coincident with low grades of Cu and Mo in the core of the deposit, near the southwest contact of the Haquira stock with the wall-rock (Figure 3). The density of these veins decreases upward and outward symmetrically around a central vertical axis. We infer the center of the fluid flow as roughly coincident with this contact. The aplite vein density distribution is similar to the barren quartz vein distribution and defines the same center, but it also identifies a second and weaker center to the northeast.

The zones of most abundant Cu-sulfide bearing veins (EDM, A and B veins) lie above and to the northeast of the zone of abundant barren quartz-K-feldspar and aplite veins. EDM veins are restricted to the Hp stock and do not occur in quartzite. Some B veins extend to the southwest and northeast into the quartzite, but in general, the B vein density is much lower in the quartzite than in the Hp stock (Figure 3A). The banded quartz-molybdenite veins form an inverted-cup shape distribution that lies above and outside of the central high-density zone of both barren quartz-K-feldspar and aplite veins, and slightly above and outside the zone of most abundant Cu-bearing veins. In contrast to the B veins, the density of quartz-molybdenite veins is similar and high in both the stock and the quartzites (Figure 3B). The Hp stock is strongly mineralized with copper in steeply dipping northwest trending zones parallel to the elongation of the stock, but in the relatively non-reactive quartzite, copper grades are low. In contrast, molybdenum mineralization forms a roughly symmetrically shell outlined by the quartz-molybdenite veins that overlap both stock and quartzite with an axis of symmetry located along the southwest contact of the Haquira stock. The molybdenum and copper grade zones overlap with a tendency for molybdenum to be above and outboard of copper. Because of the compositional contrast between the meta-sedimentary wall-rock and the Hp stock wall-rock, the Fe-Cu sulfides tend to precipitate principally in the more reactive intrusive rocks. Alteration of mafic minerals in the intrusive rocks by the acidic and Cu-rich hydrothermal fluids releases Fe and enables the precipitation of Fe-Cu sulfides. The sedimentary wall-rock, which are mainly quartzites, are poor in Fe-bearing minerals. Therefore, wall-rock reactions do not liberate much Fe to solution, and Fe-Cu sulfides precipitation is suppressed. This phenomenon produces only a "half" Cu-ore shell in the Hp stock that disappears abruptly in the contact with the quartzites (Figure 2, 3A). However, molybdenite precipitation reactions are not governed by the wall-rock protolith composition, and a more continuous inverted-cup shaped Mo-ore shell is observed (Figure 2, 3B). Despite this, a permeability contrast between the sedimentary wall-rock and the stock can be inferred based on the slightly lower density and more discontinuous zones of banded quartz-molybdenite veins in the sedimentary rocks compared to the Hp stock. This observation is supported by the lower Mo grade distribution in quartzite compared to the Hp stock: when the Mo-shell is modelled with a higher grade (>250 ppm compared to 125 ppm, Figure 3B), the southwest limb of the Mo-shell almost disappears.

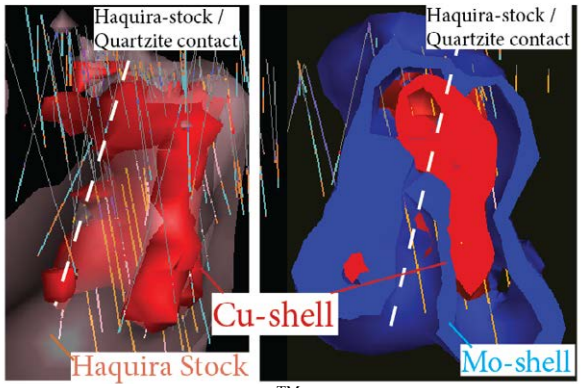

Figure 2. 3D Leapfrog™ model of Haquira stock porphyries (brown), Cu-ore shell (red) and Mo-ore shell (blue) showing the abrupt discontinuity of the Cu-shell in the porphyry stock-quartzite contact. **Left:** oblique view looking north/northeast. Quartzite contact is projected towards the viewer. **Right:** looking northwest, similar view to 2D sections shown in figure below.

Acknowledgements

We greatly appreciate and thank Quantum LTD for fully funding this PhD research. CoreScan™ (in particular Neil Goodey and Ronell Carey) scanned and processed hundreds of thin section billets. LeapFrog™ provided an academic license of its software. Morgan Salisbury and Nansen Olson reviewed this abstract.

References

Cernuschi F, Einaudi, M T, Dilles, J H, Heather K B, Barr N C (2012) Hydrothermal Veins, Porphyry Geochemistry and Mineralization Zonation of the Haquira-East Porphyry Cu-Mo Deposit, Perú. SEG Conference 2012, Lima, Perú.

Dilles J H, Einaudi M T (1992) Wall-rock Alteration and Hydrothermal Flow Paths about the Ann-Mason Porphyry Copper Deposit, Nevada. A 6 km Vertical Reconstruction. Economic Geology (87): 1963-2001.

Einaudi M T (2008) Distribution of Vein Types, Alteration, Sulfides, and Metal Grades. Haquira Porphyry Cu-Mo-Au Deposit, Departamento De Apurímac, Perú. Unpub. Report for Antares Minerals Inc. *(September):* 47.

Perello J, Carlotto V, Zarate A, Ramos P, Posso H, Neyra C, Caballero A, Fuster N, Muhr R (2003) Porphyry-Style Alteration and Mineralization of the Middle Eocene to Early Oligocene Andahuaylas-Yauri Belt, Cuzco Region, Peru. Economic Geology 98 (8): 1575.

Seedorff E, Dilles J H, Proffett J M Jr, Einaudi M T, Zurcher L, Stavast W J A, Johnson D A, Barton M D (2005) Porphyry Deposits: Characteristics and Origin of Hypogene Features. Economic Geology 100th Anniversary Volume 29: 251–298.

Thompson A J B, Hauff P, Robitaille J A. (1999) Alteration Mapping in Exploration; Application of Short-wave Infrared (SWIR) Spectroscopy. SEG Newsletter 39: 16–27.

Zhaoshan C, Yang Z (2012) Evaluation of Inter-instrument Variations Among Short Wavelength Infrared (SWIR) Devices. Economic Geology 107: 1479 – 1488.

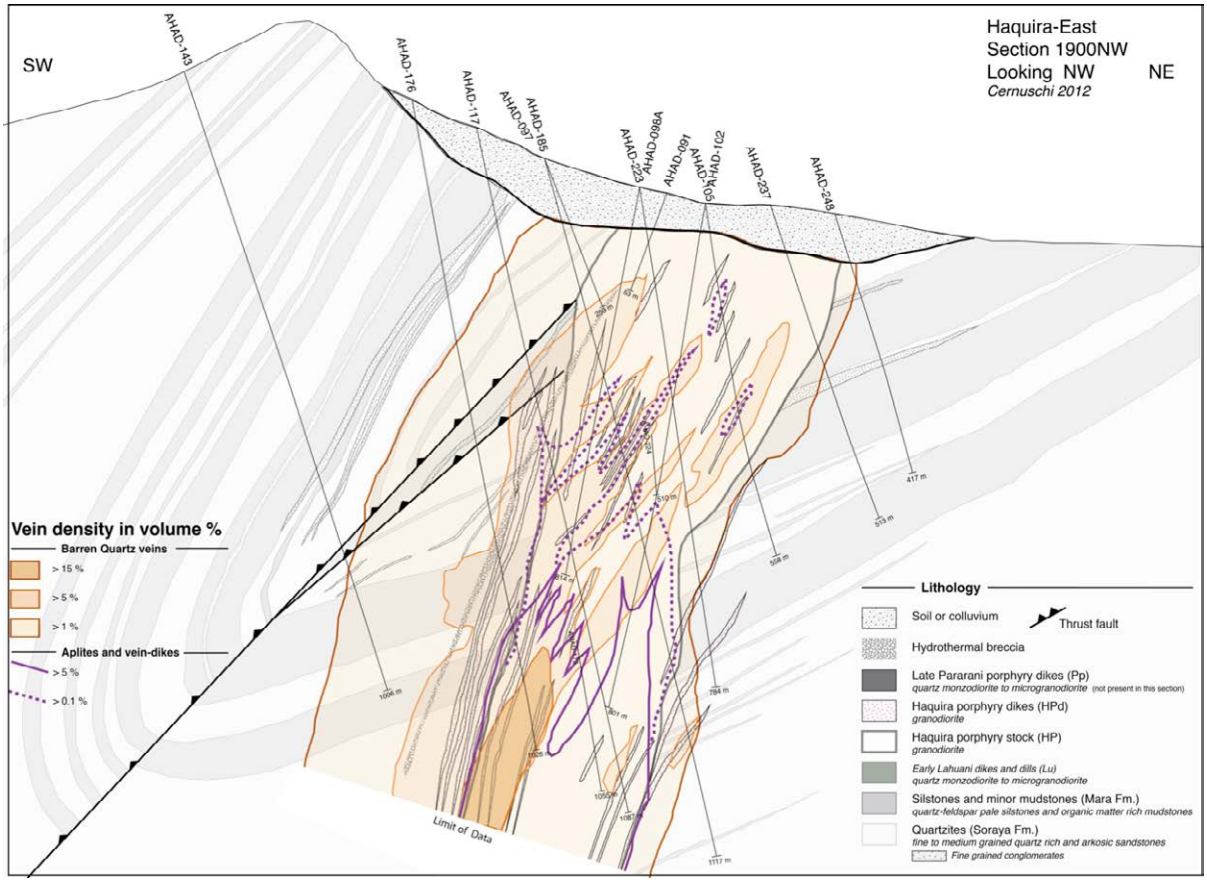

Figure 2. Cross-section 1900NW showing barren-quartz vein and aplite distribution and density with relation to the porphyry dike swarm and lithological boundaries.

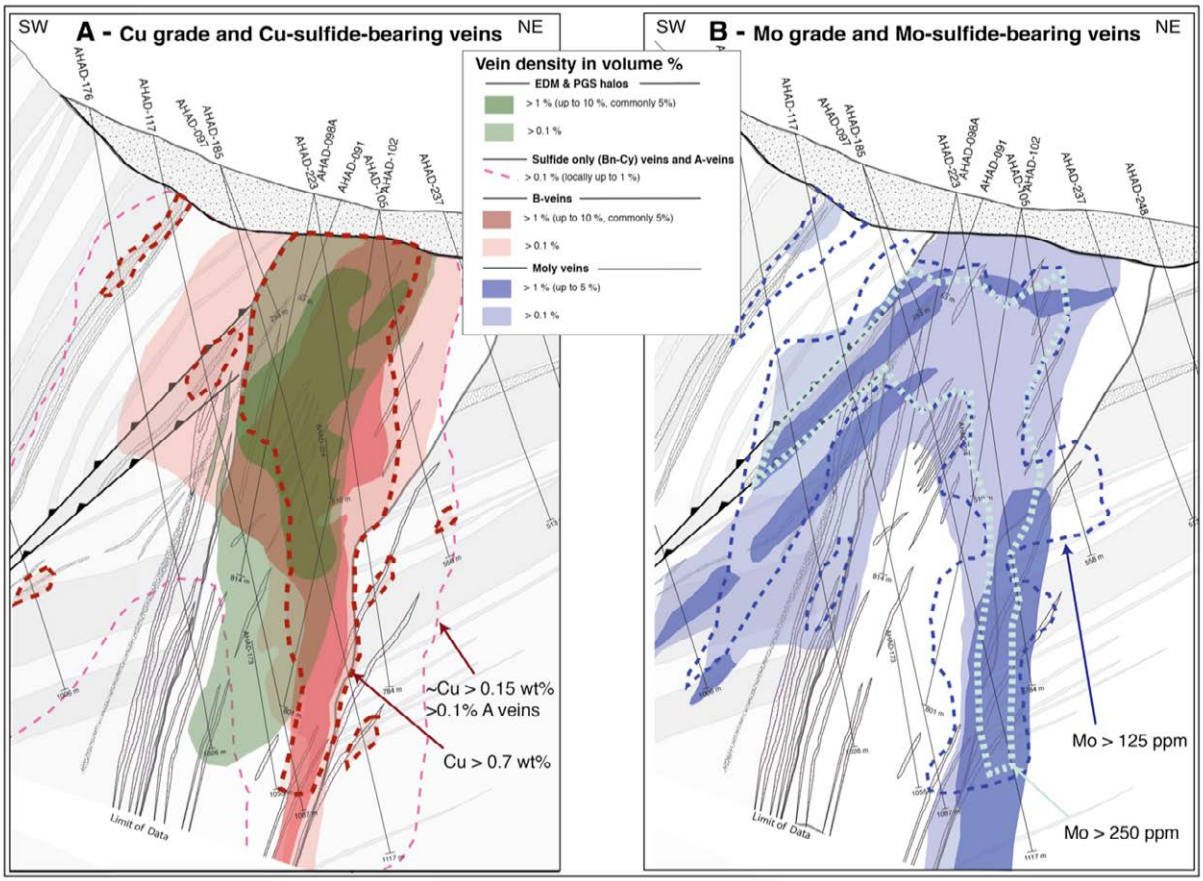

Figure 3. Cross-section 1900NW **A:** Sulfide bearing A veins, B veins, and EDM/PGS halos distribution and density with relation to the high grade copper, the porphyry dike swarm, and lithological boundaries. **B:** Molybdenite bearing veins distribution and density with relation to the high molybdenum grade, the porphyry dike swarm, and lithological boundaries.

A mineralogical and fluid inclusion study of the Patricia Zn-Pb-Ag deposit (Paguanta, NE Chile)

Darío Chinchilla[12], **Andrea Rodríguez**[1], **Rubén Piña**[1], **Lorena Ortega**[1], **Rosario Lunar**[12]
[1]*Departamento de Cristalografía y Mineralogía, Facultad de Ciencias Geológicas, Universidad Complutense de Madrid, Spain*
[2]*Instituto de Geociencias (CSIC, UCM), Facultad de Ciencias Geológicas, Universidad Complutense de Madrid, Spain*

Cecilio Quesada
Instituto Geológico y Minero de España (IGME), Madrid, Spain

Antonio Valverde
Herencia Resources Plc. Compañia Minera Paguanta, Santiago de Chile, Chile

Abstract. The Patricia Zn-Pb-Ag ore deposit is located within the Paguanta mining project, situated at the northern end of the Andean Oligocene Porphyry Copper Belt of Chile. The sulfide mineralization occurs as W-E oriented veins hosted in volcanic rocks, mainly andesite (pyroclastic, ash and lavas), of Upper Cretaceous to Middle Tertiary age. The ore mineralogy comprises pyrite, sphalerite (5.5 -10.89 wt % Fe), arsenopyrite, galena, chalcopyrite and Ag-bearing sulfosalts. These Ag-bearing sulfosalts are typically phases of the series freibergite - argentotennantite, polybasite and stephanite and minor argentite, pyrargirite and diaphorite. All these phases are commonly associated with chalcopyrite, galena, sphalerite and pyrite and, to a lesser extent, quartz. Alteration minerals are dominated by chlorite, illite and kaolinite. The primary fluid inclusions indicate fluids with moderate salinity (11 - 17.8 wt % eq. NaCl) and temperatures between 180 °C and 200 °C. This study suggests that the Patricia deposit represents an example of epithermal mineralization of intermediate sulfidation state.

Keywords Ag-bearing sulfosalts, Zn-Pb-Ag epithermal deposit, fluid inclusions, Patricia, Paguanta

1 Introduction

The Patricia Zn-Pb-Ag ore deposit represents economic mineralization (4.53 Mt with average grades of 3.7 % Zn, 1.3 % Pb, 83 g/t Ag and 0.2 g/t Au, www.herenciaresources.com) discovered by Herencia Resources Plc in 2006 during exploration over mine workings dating back to the nineteenth century. The ore mineralization forms part of the Paguanta mining project that also includes other two prospects called, La Rosa and Doris. The Paguanta project is located in the Tarapacá region ~ 150 km NE from Iquique and ~ 30 km from Colchane on the border with Bolivia (Fig. 1). It is located at the boundary between the Precordillera and Western Cordillera of the Andes (UTM coordinates - (WGS84): 19K 494 300 E - 7809300 S). Geologically, the project is at the northern end of the Andean Oligocene Porphyry Belt of Chile that hosts 9 of the 16 largest porphyry Cu-Mo deposits associated with the Circum-Pacific Belt (Teniente, La Escondida, Chuquicamata, El Salvador) (Camus and Dilles, 2001; Behn et al., 2001). The porphyry belt is structurally controlled by the N-S-oriented Domeyko fault system characterized by sinistral transpressive kinematics and

Figure 1. Schematic map showing the position of Paguanta in the Oligocene Porphyry Copper belt of Chile. Modified from Camus (2003).

important extensional areas (pull-apart basins) (Maksaev et al., 2007). The Paguanta project consists of three main prospects:

- Patricia: located at the south part of the project and constitutes the most explored and economically interesting resource. It is a hydrothermal Zn-Pb-Ag sulfide mineralization infilling veins with E-W orientation.
- La Rosa: comprises a 3 km2 area located to NNW of Patricia with intense argilic alteration in a pull apart basin. It hosts disseminations and veinlets of Cu-oxides, pyrite and Fe oxy-hydroxides.
- Doris: this prospect located NNE of Patricia is characterized by the presence of fractures filled with secondary copper minerals (*i.e.*, chrysocolla and atacamite).

In this contribution, we present a preliminary mineralogical study of the Patricia Zn-Pb-Ag ore

deposit, including the first fluid inclusion data.

2 The Patricia Zn–Pb–Ag ore deposit

The lithologies forming the surroundings in Patricia area comprise sequences of intermediate and acidic volcanic rocks, mainly andesites (pyroclastics, ash and lavas) of Upper Cretaceous to Middle Tertiary age (Sillitoe, 1991). These rocks are unconformably overlain by ignimbrites of Miocene to Quaternary age (Bouzari and Clark, 2002). Regionally, the bedrock is formed by volcanic and sedimentary rocks of Paleozoic to Mesozoic age with strong folding and fracturing (Camus and Dilles, 2001).

The ore deposit comprises four main vein systems, generally oriented E-W to ENE-WSW, and called from N to S: Campamento, Central, Carlos and Catedral. The term vein refers to an area with intense mineralization, in the form of well-developed stockwork structures (Fig. 2). These veins range in thickness between 1 and 100m at Catedral and between 1 and 15 m at Campamento, Central and Carlos. They typically thin out towards both east and west from a thicker central zone where the old workings are located. Ongoing exploration has recently identified other new veins to the south of the above, which may eventually lead to enlarge the Patricia total resources.

Figure 2. Typical well-developed stockwork (Catedral vein system at Patricia area).

The veins are hosted by volcanic and volcaniclastic andesitic breccias with variable-sized clasts. These rocks show regional propylitic (chlorite) alteration superimposed by illite and kaolinite alteration in the mineralized area making difficult recognizing the original rock texture. Silicification and disseminations of arsenopyrite and pyrite in the host rocks are locally present. The ore minerals in the veins comprise in order of abundance, pyrite, sphalerite (5.5 - 10.89 wt % Fe, 9.8-19 % mol FeS and 0.52 wt % Cd), galena, arsenopyrite, chalcopyrite and Ag-bearing sulfosalts. The veins show a zoned and banded internal structure with pyrite at the edges and sphalerite in the center (Fig. 3). The Ag occurs mostly as Ag-Cu-Sb sulfosalts, in order of abundance: series freibergite - argentotennantite ($(Ag, Cu)_{10}(Fe, Zn)_2Sb_4S_{13}$) – ($(Ag, Cu)_{10}(Fe, Zn)_2As_4S_{13}$), polybasite ($(Ag, Cu)_{16}(Sb, As)_2S_{11}$) and stephanite ($Ag_5SbS_4$) (Fig. 4). Other minor Ag phases such as argentite (Ag_2S), pyrargirite (Ag_3SbS_3), and diaphorite ($Pb_2Ag_3Sb_3S_8$) were also identified. These Ag phases are typically associated with the base-metal sulfides. Freibergite occurs filling voids within sphalerite, chalcopyrite and at the contact between sphalerite and galena (Fig. 4 and 5).

Figure 3. Photograph of drillcore showing a zoned mineralized veinlet cross-cutting the andesitic host rock.

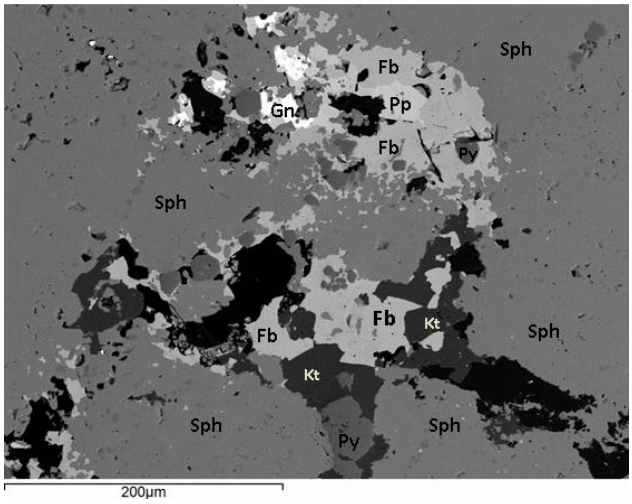

Figure 4. Representative back-scattered electron microprobe image of Ag-bearing sulfosalts. Freibergite (Fb), polybasite (Pp), galena (Gn) and pyrite (Py) filling voids between crystals of sphalerite (Sph). Kutnohorite (Kt) also occurs.

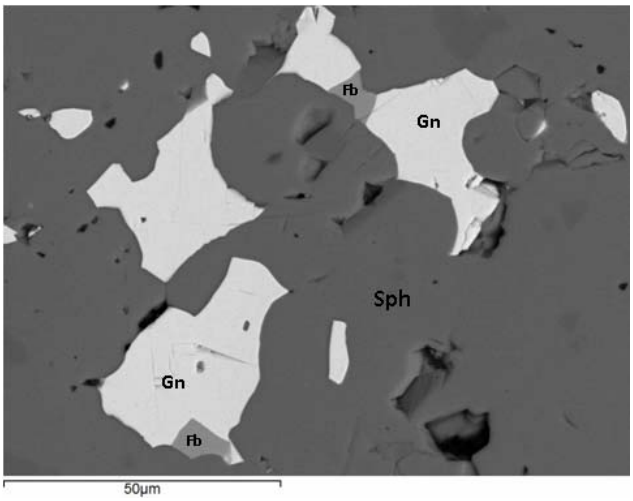

Figure 5. Representative back-scattered electron microprobe image of Ag-bearing sulfosalts. Freibergite (Fb), galena (Gn) and sphalerite (Sph).

Polybasite, stephanite, pyrargirite and argentite are mostly in close association with freibergite. In the case of diaphorite, it commonly occurs filling voids between galena crystals or as inclusions within galena. Some minor Ag-bearing sulfosalts are also identified between

pyrite crystals. The gangue minerals consist of quartz and carbonates identified by XRD as kutnahorite (Ca (Mn, Mg, Fe) $(CO_3)_2$).

4 Fluid Inclusions

The fluid inclusions study was carried out on samples from a mineralized vein formed by microcrystalline quartz which surrounds a nodule of sulfides grading to zoned prismatic quartz crystals with sizes ranging from 200 μm to 2 mm. The studied primary inclusions are two phase and are distributed from the center to the edges in the growth faces of prismatic quartz. The selected inclusions represent the fluid circulating through fractures when the mineralization precipitated.

During the cooling process, ice + hydrohalite nucleation is observed between -40 °C to -46 °C. Hydrohalite phase was confirmed by performing four cooling-heating cycles between -25 °C and -20 °C. The melting temperature obtained for the hydrohalite was -21.3 °C, which corresponds approximately to the eutectic temperature of NaCl-H2O system. The ice melting temperature is between -3.4 °C and -14 °C, with a modal value of -13 °C, indicating salinity values between 11% and 17.8% eq. by weight of NaCl. The homogeneization temperature ranges between 140 °C and 240 °C. However, 44% of fluid inclusions became homogenized between 180 °C and 200 °C.

5 Concluding remarks

The alteration halo around mineralized veins is characterized by illite and kaolinite, minerals typically formed by fluids with a pH below 6 (very slightly acidic to slightly acidic). This halo is superimposed upon the regional propylithic alteration whose pH is almost neutral. The presence of carbonates in veins that cut the previous alterations indicates that conditions varied at the end of the process towards neutral-alkaline pH.

The ore paragenesis has a polymetallic character, with pyrite, sphalerite and galena as major sulfides. Silver occurs forming own minerals (freibergite, argento-tennantite, polybasite, stephanite), not having identified argentiferous galena. The phases of ~ 25% Ag, corresponding to the series freibergite – argentotennantite, are the most common in the deposit while the Ag-rich phases (~ 70%), correspoding to polybasite, stephanite and pyrargyrite, are less abundant, appearing only in areas with high percentage of argentiferous minerals.

The fluid inclusion data indicate that the mineralizing fluid had salinity between 11% and 17.8% eq. by weight of NaCl and a minimum temperature of circulation between 180 °C and 200 °C. Regarding the composition of the fluid, the average salinity for mineralizing fluids of Au-Ag and Pb-Zn-Ag ore deposits is commonly lower than 5 % eq. NaCl and from 10 to 20 % eq. NaCl, respectively (Simmons et al., 2005; Hedenquist and Lowenstern, 1994). Accordingly, the results obtained in this study are typical of Ag polymetallic deposits. Higher salinity of fluids in Pb-Zn-Ag deposits favors metals to be transported as chlorine complexes while in the Au-Ag deposits these precious metals are transported as sulfide complexes (Hedenquist and Lowenstern, 1994). The sphalerite would precipitate following the reaction:

$$ZnCl^{+}_{(aq)} + HS^{-}_{(aq)} \rightarrow ZnS_{(s)} + H^{+}_{(aq)} + Cl^{-}_{(aq)}$$

According to Barton et al. (1977), the substitution of Fe by Zn in the sphalerite is common, resulting in extensive solid solutions whose composition is indicative of the sulfur fugacity of the system. Sphalerite ores commonly contain up to 24% moles of Fe, although there have been reports of up to 56% molar of FeS replacing ZnS (Pattrick et al. 1998). The sphalerite crystals analyzed in Patricia exhibit FeS molar contents between 9.8% and 19%, so that the composition would be in the normal range of Fe-Zn replacement. According to the log aS_2 *vs*. log aO_2 plot (Barton et al., 1977), the sphalerite would precipitate from a fluid with values of log aS_2 ranging from -12 to -12.8 and values of log aO_2 lower than -36.

All these results suggest that the Patricia Pb-Zn-Ag ore deposit probably represents an example of epithermal mineralization of intermediate sulfidation state, with periods of lower sulfidation state during sphalerite deposition (Simmons et al., 2005; Hedenquist and Lowenstern, 1994).

Acknowledgements

The authors are very grateful to Herencia Resources Plc. and its staffs for invaluable help and support during field work and sampling at Paguanta. This research was funded by the Spanish research project CGL-2010-17668.

References

Behn G, Camus F, Carrasco P (2001) Aeromagnetic Signature of Porphyry Copper Systems in Northern Chile and Its Geologic Implications. Economic Geology 96:239–248

Barton PB, Bethke PM, Roedder E (1977) Environment of ore deposition in the Creed mining district, San Juan Mountains, Colorado, Part III, Progress towards interpretation of chemistry if the ore-forming fluid for the OH vein. Economic Geology 72:1-24

Bouzari F, Clark AH (2002) Ore body of the Cerro Colorado Porphyry Copper Deposit, I Region, Northern Chile. Economic Geology 97:1701–1740

Camus F (2003) Geología de los sistemas porfíricos en los Andes de Chile. Servicio Nacional de Geología y Minería, Santiago de Chile, pp 267

Camus F, Dilles JH (2001) A Special Issue Devoted to Porphyry Copper Deposits of Northern Chile. Preface Economic Geology 96:233–238

Hedenquist JW, Lowenstern JB (1994) The role of magmas in the formation of hydrothermal ore deposits. Nature 370:519-527

Maksaev V, Townley B, Palacios C, Camus F (2007) Metallic ore deposits. In: Moreno T, Gibbons W. (ed) The Geology of Chile. The Geological Society. London, pp 179-199

Pattrick RAD, Mosselmans JFW, Charnock JM (1998) An X-ray absorption study of doped sphalerites. European Journal of Mineralogy 10:239−249

Sillitoe RH (1991) Gold metallogeny of Chile; an introduction. Economic Geology. 86:1187-1205

Simmons S, White N, John DA (2005) Geological characteristics of epithermal precious and base metal deposits. In: Hedenquist JW, Thompson JFH, Goldfarb RJ, Richards JP (ed) One hundredth anniversary volume, 1905-2005. Economic Geology:485-522

Paleoproterozoic gold-rich intrusion-hosted deposit in the Alta Floresta gold province, Amazon Craton (Brazil): the example of the X1 deposit

Rafael Rodrigues de Assis; Roberto Perez Xavier; Rosana Mara Rodrigues, Verônica Godinho Trevisan, Giseli Silva Ramos, Antônio João Paes de Barros
Departamento de Geologia e Recursos Naturais, Universidade Estadual de Campinas, Campinas, Brasil; Instituto Nacional de Ciência e Tecnologia de Geociências da Amazônia (GEOCIAM).

Antônio João Paes de Barros
Companhia Matogrossense de Mineração, Cuiabá, Brasil.

Abstract. The Alta Floresta Gold Province, which is located in the southern portion of the Amazon Craton, represents a tectonic unit composed primarily of plutono-volcanic sequences generated in a continental arc during the Paleoproterozoic. Particularly, in the easternmost segment of this province, the plutonic and volcanic rocks host to more than one hundred gold ore deposits and occurrences along a NW-SW striking belt (Peru – Trairão belt). Within this context lies the X1 deposit, an Au±Cu-type mineralization hosted by oxidised I-type, calc-alkaline granodiorite and sub-volcanic tonalite. The ore consists of pyrite ± molybdenite ± chalcopyrite ± rutile ± hematite that occur in zones of strong pervasive muscovite + quartz alteration. Fluid inclusion assemblages from ore zones revel that CO_2-rich fluid of lower salinity (≤ 8.9 eq. wt% NaCl) and higher temperature (251 < T < 334 °C) coexist with two-phase aqueous fluids of varying salinity (2.1 to 26 eq. wt% NaCl) and lower temperature (126 < T < 268.4°C), suggesting that the deposit may have resulted from immiscibility processes with CO_2 degassing and mixing process between magmatic(?) and surface-derived fluids (meteoric? basinal?), or even both. Therefore, the X1 deposit represents a magmatic-hydrothermal system, similar to the Au-porphyry deposits, however, at a greater depth.

Keywords: Alta Floresta Gold Province, gold mineralizations, intrusion-hosted gold deposit.

1. Introduction

The Alta Floresta Gold Province (AFGP), in the southern portion of the Amazon Craton, consists primarily of plutono-volcanic sequences generated in continental arc settings during the Paleoproterozoic. The AFGP lies within the limits of two geochronological provinces: Ventuari – Tapajós (1.95-1.8 Ga) and Rio Negro – Juruena (1.8-1.55 Ga) (Tassinari & Macambira 1999).

It is estimated that from 1980 to 1999 the AFGP may have produced approximately 160 t Au (Paes de Barros 2007). This production came from a significant number of alluvial and small size (<5 t), and high grade primary gold deposits along a NW-SW striking belt (Peru – Trairão belt) in the eastern segment of this province. Within this belt, primary gold ores are confined to veins, stockworks and disseminations mostly in I-type, calc-alkaline to sub-alkaline, medium to high K, meta- to peraluminous, magnesium to slightly ferrous granitic rocks and, more subordinately in volcanic sequences.

In this work, we characterize the litogeochemistry of host rocks as well as wall-rock alteration and fluid inclusions constrains of the X1 deposit. Additionally, we argue that the X1 Au±Cu deposit may be similar to gold-rich, copper-poor porphyry deposits.

2. Host rocks

The deposit lies in the Intrusive Matupá suite, dated at 1.872 ±12 Ma (Moura 1998). This area is composed by hornblende monzogranite, biotite-hornblende monzonite and hornblende monzodiorite. However, the host rocks of the deposit consist of two different lithotypes:

(1) Medium to coarse-grained, equigranular to porphyritic biotite granodiorite (Fig. 1A), with 1.5 to 3 cm large phenocrysts of quartz and plagioclase, and rare mafic volcanic enclaves. It consists of quartz (45-58%), plagioclase (43-55%), K-feldspar (2-10%), besides biotite (< 3%) with apatite, zircon and magnetite accessories.

(2) quartz-feldspar porphyry of tonalite composition (Fig. 1B). It contains 5-10% phenocrysts of bipyramidal quartz and plagioclase in an afanitic to very-fine-grained matrix. The rock comprises quartz (60-75%), plagioclase (15-30%) and K-feldspar (1-8%), besides apatite, zircon and rutile accessories. Mafic minerals are absent.

Quartz-feldspar porphyry enclaves with angular shapes and dimensions ranging from 3 to 8 cm are often recognized in the porphyritic biotite granodiorite. However, 7-15 cm large, angular shaped granodiorite enclaves enclosed in quartz-feldspar porphyry are also found (Fig. 1C). Although the temporal relationships between these two lithotypes have not been yet defined by geochronology, the geological relationships suggest to a single magmatic system with multiple intrusions.

3. Lithogeochemistry

According to Ramos (2011), the biotite granodiorite displays a narrow major, minor and trace elements range; for exemple the SiO_2 contend of the rock is between 72.5 to 73.6 wt.%. This rock is also characterized by high K_2O/TiO_2 rations, (23 to 37.3), intermediate MgO/TiO_2 ratios (2.2 to 2.7), Al_2O_3 content from 14.4 to 15.1 wt.%, as well as low Fe_2O_3 (0,8-1.1 wt.%) and CaO (1,1-1,7 wt.%) contents. It also exhibits

high Ba (983-1.206 ppm) and Sr (383.5-498.38 ppm), but low Cs (0,9-1 ppm), Ni (0.8-1.2 ppm), Nb (6.9-9.2 ppm), V (10-15 ppm), Hf (1,9-2.7 ppm), Th (5.3-7.1 ppm), Zr (61.3-85.7 ppm), Rb (100.3-126.2 ppm) and REE (∑REE= 57-82.4 ppm) contents. The high silica contents reflect an evolved felsic magma with high acidity and differentiation. In additional, small (insignificant) scattering of the geochemical data is typical of weakly fractionated granitic series. REE patterns are enriched in light REE with $(La/Lu)_n$ between 10.1 and 18.5, suggesting weak to moderate igneous fractionation. Additionally, a moderate negative Eu anomaly ($0.64 < Eu/Eu^* < 0.86$), indicates plagioclase fractionation or its retention in the source. According the diagrams of tectonic-magmatic affinities, the biotite granodiorite represents a calck-alkaline, sub-alkaline, medium to high-K, peraluminous and ferrous felsic magmatism (Figs. 2A-B). The high contents in Nb and Ta, but low in Y and Yb are typical of volcanic-arc setting (Fig. 2C).

The bioite granodiorite shows K/Rb ratios that range from 240.5 to 270.3, whereas the Rb/Sr ratios are from 0.2 to 0.32. According to Blevin (2004) these ratios are typical for moderately evolved granites with low igneous fractionation index. Additionally, this granite is illmenite-free, with low amounts of magnetite that allow us to classify it into the magnetite-series. The oxidation parameter (Blevin 2004) of the biotite granodiorite lies especially in the strongly oxidized field, with ΔOx values from 0.13 to 0.48 ($0.8 < Fe_2O_3 < 1.8$; $0.45 < FeO < 2.1$; $1.2 < FeO^* < 3.1$).

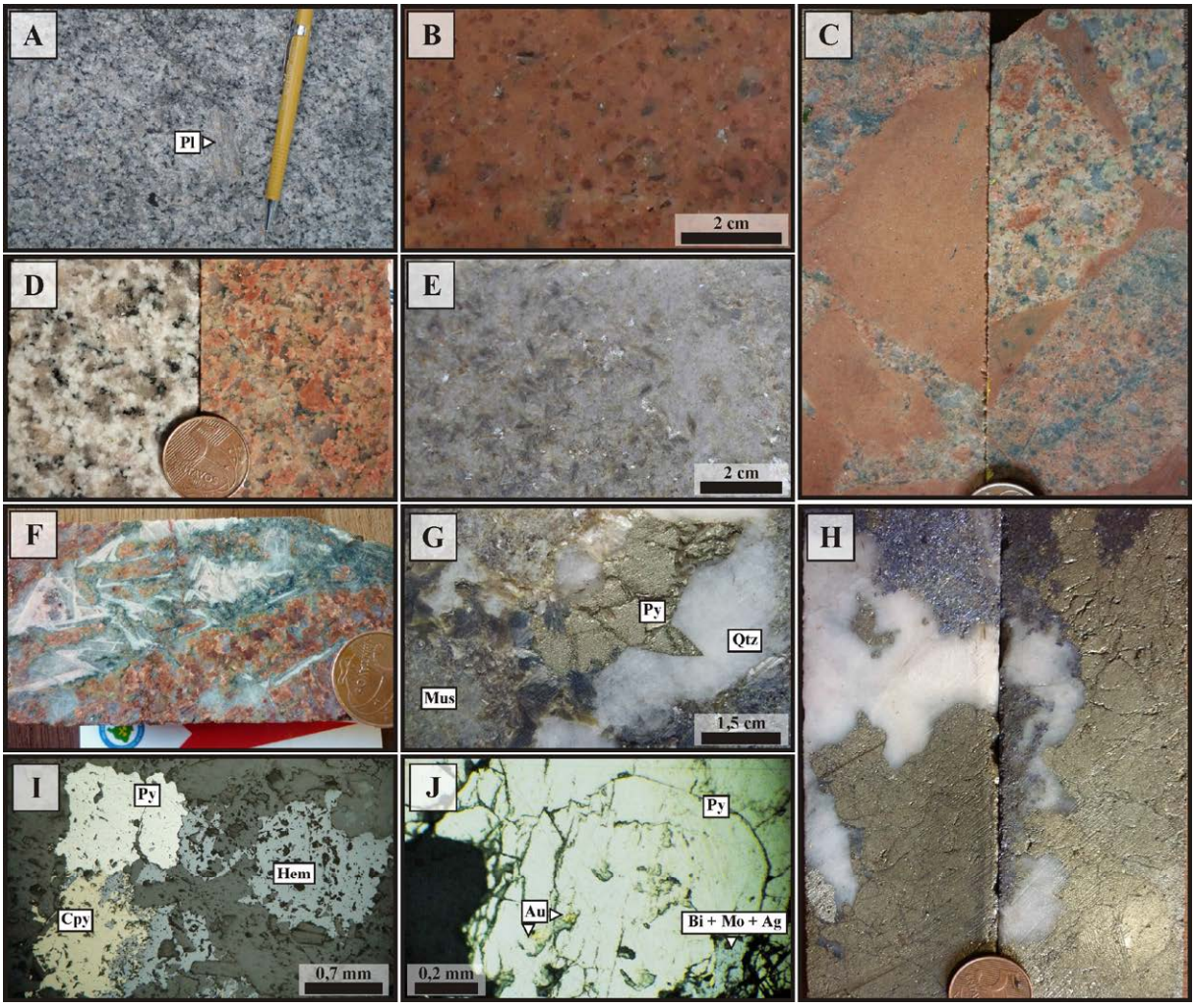

Fig. 1. (A) Porphyritic biotite granodiorite with sub-euhedral plagioclase phenocrystal; (B) Quartz-feldspar porphyry with bipyramidal quartz phenocrystals; (C) Quartz-feldspar porphyry enclaves within granodiorite (*left side*) and granodiorite enclaves in the sub-volcanic granite (*right side*); (D) The strongly pervasive potassic alteration is responsible for the reddish color of the granodiorite; (E) Muscovite + quartz alteration zone (phyllic alteration); (F) Bladed calcite is usually related to the propylitic alteration; (G) Vein and pods filled by milky-quartz within coarse-grained muscovite + quartz + massive pyrite alteration; (H) Massive pyrite and molybdenite in a muscovite + quartz alteration is the major ore-style; (I) Pyrite + sphalerite + hematite paragenesis; (J) Gold occurs as small inclusions in pyrite, together with Bi-Te-Mo-Ag-rich phases.

4. Hydrothermal alteration and ore zones

Both the biotite granodiorite and the quartz-feldspar porphyry host the X1 deposit. These rocks have variably been affected by the following hydrothermal alterations: (1) potassic alteration with orthoclase ± hematite; (2) phyllic alteration zone with muscovite + quartz + pyrite; (3) propylitic; (4) chloritic; and (5) carbonate alterations (Rodrigues 2011).

The potassic alteration is pervasive, it has a broad spatial distribution, is responsible for the reddish colors of the lithotype (Fig. 1D), and is usually placed around the mineralized zones, but in more distal sectors. The potassic alteration is partially to completely replaced by the muscovite + quartz + pyrite association (phyllic alteration; Fig. 1E), in 1 to 30 meters thick zones, usually in the core of the hosts or as alteration halos around quartz-veins, in both cases, as shapeless masses, with no structural controls. Veinlets and/or pods of coarse-grained muscovite are often found within this alteration. The propylitic alteration is characterized by chlorite + epidote + calcite ± apatite ± rutile ± hematite ± pyrite mineral assemblage that shows restrict and distal dispersion around the ore zones, whereas late calcite-rich veinlets and pervasive carbonate alteration are commons and overprint the earlier hydrothermal stages. In additional, bladed calcite can also be found (Fig. 1F), but in minor amounts. Taken collectively, the hydrothermal patterns normally occur as irregular patches, with only scarce exceptions exemplified by veins and/or veinlets styles, normally as stockworks.

The gold mineralization at the X1 deposit is manly disseminated within the phyllic alteration zones, with no structural control, and subordinately in late quartz-rich veins (Figs. 1G-H). The ore consists of pyrite ± molybdenite ± chalcopyrite ± rutile ± hematite (Fig. 1I), with gold grade ranging from 0.5 to 10 g/t. Unoriented quartz veins as stockwork ore usually exhibit a centimetric to metric phyllic alteration halo, have the same sulfide mineral assemblages, but lower gold contends (<0.2 ppm). Within quartz + muscovite alteration the ore texture is mainly disseminated and represented by fine to coarse-grained pyrite aggregates with up to 5 cm large and euhedral to sub-euhedral shapes, or even as massive ore. Within this zone, chalcopyrite and molybdenite occupy the pyrite, quartz and muscovite interstices, or occur as small inclusions in pyrite. In the veins, however, the ore is massive and dominantly composed by medium to coarse-grained pyrite, sometimes in fractured or brecciated zones. Chalcopyrite and molybdenite can also fill some veinlets/veins mostly constituted by pyrite and milky white to translucent quartz. Gold (Ag = 20-30 wt.%) occurs as small inclusions (~20 µm) in pyrite together with tsumoite (BiTe) and hessite (Ag_2Te), galena, monazite, sphalerite, apatite and molybdenite (Fig. 1J). According to Rodrigues (2011), the whole rock ore-geochemistry indicates a strong positive correlation between Au, Ag and Bi, but lesser with the Pb and Cu.

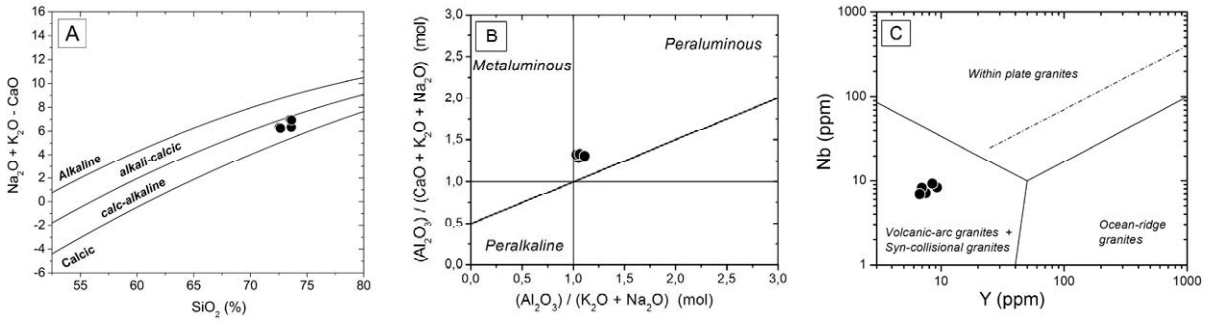

Fig. 2. Petrogenetic diagrams for X1 biotite granodiorite: (A) Modified alkali-lime index; (B) Aluminum saturation index; (C) Nb-Y discrimination diagram.

5. Fluid inclusions

Fluid inclusion assemblages (FIA) in quartz from phyllic alteration zones and quartz + sulfide veins reveal the coexistence between two different types of fluids:

(1) Primary and more abundant aqueous two-phase inclusions with wide salinity (2.1-26.1 wt.% eq. NaCl) and homogenization temperatures ranging from 126.5°C to 268.4°C, that homogenizes into the liquid phase. These inclusions exhibit morphologies ranging from rounded to sub-angular, small sizes (8-20 µm) and a heterogeneous vapor-phase filling degree (5-95 wt.%), and;

(2) Primary H_2O-CO_2 (0.35-0.77 g/cm^3) inclusions of low salinity (6.1-8.9 wt.% eq. NaCl) and higher homogenization temperatures (251.6-334.6°C) into the liquid phase. These inclusions show sizes from 8 to 20 µm, sub-rounded to sub-angular shapes and preferentially occur along planar arrays. Moreover, these fluids are represented by fluid inclusions with heterogeneity in the vapor-phase filling degree (10-95 wt.%).

According to the descriptions provided above, there is an aqueous two-phase fluids and aqueous-carbonic FIA that have been trapped from a heterogeneous fluid. The minimum temperature and pressure conditions of entrapment for the ore fluids are, respectively, between 126.4-334.8 °C and 1.02-4.9 kbars, which correspond to a depth of approximately 3.7 to 12.6 km. Taken together, these data are suggestive of early fluid released from a felsic melt with high CO_2-conted that will initially be CO_2-rich (CO_2 is ten times less soluble than H_2O in melts; Blank et al. 1993). Consequently, under lower

pressures, later fluids had exsolved and became progressively more saline and H_2O-rich.

6. Conclusions

The close spatial relationship with granitic plutons suggests that the X1 deposit may be genetically linked to a magmatic-hydrothermal system. Furthermore, the volcanic arc setting attributed to the host intrusions as the types and distribution of the hydrothermal alteration open the possibility to envisage genetic processes similar to those related to porphyry systems to explain the formation of the Au mineralization, however, deeper than the 3-5km usually assigned for porphyry systems, as observed by the fluid inclusions data (depth ranging from 3.9 to 12.6 km). Taken collectively, all data suggest that the ore precipitation might have taken place by fluid immiscibility and/or mixing processes between magmatic (high temperature CO_2-rich fluids) and surface-derived fluids (meteoric? basinal?; high salinity aqueous fluid), or even both, in a deep magmatic-hydrothermal system.

In additional, the hydrothermal alteration types show oscillations in the $a\mathrm{Na}^+$, $a\mathrm{K}^+$, $a\mathrm{H}^+$ and $a\mathrm{Ca}^{2+}$ which are suggestive of multiple pulses of hydrothermal fluids due to magma degassing, exemplified by blanded calcite, CO_2-rich fluids, carbonate alteration and coarse-grained muscovite from the phyllic alteration. Taken collectively, the observed fluid evolution at the X1 deposit may be result of entirely hydrothermal processes of boiling/immiscibility with cooling (fluid mixing), which resulted in a low density and salinity CO_2-rich fluid and more saline H_2O-rich liquid.

In this context, during the cooling history of the host rocks emplaced above a larger magma chamber, the magma-crystallization front retracts to progressively greater depths and temperatures (~9km and 251-334°C), leading to fluid exsolution at higher P (CO_2-rich fluids), leading to potassic alteration. Due to cooling of the ascending fluid through the 126-268°C, the potassic alteration is replaced by muscovite + quartz alteration at lower P (~3km) and pH. The involvement of external fluids (e.g. meteoric) may promote further cooling of the ascending solutions to enhance the K-mica zone (muscovite from phyllic alteration) and, perhaps gold precipitation. In this scenario, if two-phase fluid separation/boiling (vapour + brine) took place and sulphur lost during flashing of the vapour phase, precipitation of iron and iron-copper sulphides would have been inhibited, resulting in deposition of magnetite/hematite. Since gold and iron do not need sulfur to precipitate, whereas copper does, this loss of sulfur may be the primary cause of the high gold and low copper contents at the X1 gold deposit.

In addition, it is known that the CO_2 solubility increases with pressure and alkalinity of the magma (Lowenstern 2001). Thus, as the biotite granodiorite exhibits affinity to the medium to high-K and calc-alkaline magmas, it is suggested that the oscillations at the crustal level might have been decisive in CO_2 degassing from the magma chamber, further than geochemical controls, because it is observed at the X1 deposit immiscibility process between low temperature and high to low salinity aqueous fluids, but high temperature and low salinity CO_2-rich fluids. Therefore, exsolved magmatic fluids in deep crust (> 8km) usually exhibit high CO_2/H_2O ratio when compared to exsolved systems near the surface (Lowenstern 2001), as noted to X1 deposit, with depths ranging from 3.7 to 12.6 km. The gradual emplacement to shallower crustal levels of the host granite of the X1 mineralization might have contributed to the CO_2 solubility, releasing it to the hydrothermal system.

Despite containing some features also encountered in intrusion-related gold deposit class (Thompson et al. 2004), such as the correlation of Au with Bi and Te, the oxidized nature of the granitic host rocks, the widespread nature of the alteration type and the conspicuous occurrence of hematite in the gold ore seem not to be consistent with this gold mineral system.

All this features, therefore, are consistent with the model similar to those related to deep zones of porphyry gold-rich systems.

Acknowledgements

We thank METAMAT to the logistic support provided during the field trips, as well to the Rio Novo Mineração Ltda company. Research funded by CNPq/MCT (Grant 475152/03-4) and the Instituto Nacional de Ciência e Tecnologia da Amazônia (GEOCIAM).

References

Blank JG. Stolper EM. Carroll MT (1993) Solubities of carbon dioxide in rhyolite melt at 850 °C and 750 bars. Earth and Planet Science Letters 119:27-36.

Blevin, PL (2004) Redox and Compositional Parameters for Interpreting the Granitoid Metallogeny of Eastern Australia: Implications for Gold-rich Ore Systems. Resource Geology 54(3):241–252.

Paes de Barros AJ (2007) Granitos da região de Peixoto de Azevedo – Novo Mundo e mineralizações auríferas relacionadas – Província Aurífera Alta Floresta (MT). PhD thesis, Universidade Estadual de Campinas, Campinas, Brazil, 171p.

Lowenstern JB (2001) Carbon dioxide in magmas and implications for hydrothermal systems, Mineralium Deposita 36(6):490-502.

Moura MA. (1998) O Maciço Granítico Matupá e o Depósito de Ouro Serrinha (MT): Petrologia, Alteração Hidrotermal e Metalogenia. PhD thesis, Instituto de Geociências, Universidade de Brasília, Brasília, Brazil, 238p.

Ramos GS. (2011) Características geoquímicas de plutons graníticos auríferos e estéreis da Província Aurífera de Alta Floresta (MT). Monograph on geology, Instituto de Geociências, Universidade Estadual de Campinas; Campinas, Brazil, 84p.

Rodrigues RM (2012) Caracterização geológica e metalogenética do Depósito X1 – Província Aurífera de Alta Floresta, Região de Matupá (MT). Instituto de Geociências; Dissertation 70p.

Tassinari CCG, Macambira MJB (1997) Geochronological Provinces of the Amazonian Craton. Episodes 22(3):174-182.

Thompson JFH, Sillitoe RH, Baker T, Lang JR, Mortensen JK (1999) Intrusion-related gold deposits associated with tungsten-tin provinces: Mineralium Deposita, 34:323-334.

Gold and trace-element content in epithermal sulfides from the Agua Rica deposit, Catamarca, Argentina

Marta Franchini
Centro Patagónico de Estudios Metalogenéticos, CONICET, Departamento de Geología y Petróleo, Facultad de ngeniería, Universidad Nacional del Comahue, Neuquén, Argentina

David R. Lentz, Yan Luo,
Dept. of Earth Sciences, University of New Brunswick, Fredericton, NB E3B 5A3 Canada

Laura Maydagán
Centro Patagónico de Estudios Metalogenéticos, CONICET, Departamento de Geología y Petróleo, Facultad de Ingeniería, Universidad Nacional del Comahue, Neuquén, Argentina

Abstract. Agua Rica is a world class Cu-Au-Mo deposit located in Catamarca, Argentina. In this deposit, the polymetallic epithermal alteration-mineralization stages are superimposed upon older porphyry Cu-Mo mineral assemblages.

Laser ablation inductively coupled plasma-mass spectrometry (LA ICP-MS) analysis of sulfides at Agua Rica revealed "invisible" Au content in pyrite and marcasite in the upper levels of the hydrothermal matrix-supported hydrothermal breccia. The ore pyrite occurs as either very fine, irregularly shaped grains in late veinlets, or in colloform rims on earlier gold-free and Co-Mo rich pyrite cores. In the pyrite rims Ag, Pb, Bi, Cu, and Zn have a behavior comparable with that of Au; As does not correlate with Au. The very fine-grained pyrite crystals from the veinlet have the highest Au content (up to 12.9 ppm) of all analysed pyrite crystals. It is possible that these greigite-like precipitation stages reflects rapid boiling events in an open space filled with hydrothermal solutions supplied by continued fluid pathways generated by brecciation. The study has also demonstrated the presence of Au and other trace elements in other sulfides and enargite at Agua Rica.

Laser spot analysis in combination with the element-distribution images show the heterogeneous distribution of the trace elements in pyrite, their associations, and the presence and distribution of nuggets.

Keywords: high sulfidation, colloform pyrite, marcasite, Invisible gold, trace metals

1 Introduction

Agua Rica is a world class Cu-Au-Mo deposit located in Catamarca (27º26'S-66º16'O), Argentina. In this deposit, the polymetallic epithermal alteration-mineralization stages are superimposed upon older porphyry Cu-Mo mineral assemblages. Sulfides of iron, copper, molybdenum, arsenic, zinc, lead, and tin, as well as related bismuth-bearing sulfosalts were precipitated during the high-sulfidation epithermal stages. High Au and Ag grades (up to 5.6 g/t Au and 325 g/t Ag) occur in brecciated and fractured sectors of the deposit with advanced argillic alteration and mineralization. However, native gold (electrum) has rarely been observed (one thin section) as 2 micron grains in cracks in quartz (Franchini et al. 2011).

In this study we present the results of the *in situ* laser ablation inductively coupled plasma-mass spectrometry (LA ICP-MS) analysis of sulfides in zones at Agua Rica with high sulfidation epithermal mineralization that revealed "invisible" Au content in colloform pyrite and marcasite from zones of the deposit enriched in Au. This pyrite exhibits pervasive growth zoning and as such can provide a better record of the later Au-rich fluid-flow event in the high sulfidation environment and Au precipitation. Covellite, enargite, sphalerite, and galena contain traces of Au and are also enriched in other trace elements.

2 Geology of the deposit

The Agua Rica deposit is localized in the Sierra del Aconquija, one of the uplift blocks of the Sierras Pampeanas basement, 200 km east of the Cordillera de los Andes. The oldest rocks in the region are Precambrian to Early Paleozoic schistose and massive metasedimentary rocks (Koukharsky and Mirré 1976). These metamorphic rocks were folded and intruded by Paleozoic granitic plutons and pegmatites (422.7 ± 6.1 and 438.4 ± 6.3 Ma, K-Ar muscovite ages; Capillitas-Belén granite suite; Caelles et al. 1971; Koukharsky and Mirré 1976). During the Miocene, a series of porphyritic stocks intruded the country rocks (Navarro 1986; Sasso and Clark 1998; Perelló et al. 1998). Landtwing et al. (2002) identified and described in detail various breccia types in the Agua Rica district. Several small porphyritic bodies have been mapped at the margin of the deposit. The porphyries and breccias were emplaced along the SE-striking Quebrada Minas lineament. East-west striking, south-dipping normal faults were active both syn- and post-mineralization. The Quebrada Seca fault offsets leached material, and epithermal fluids moved along the same structure (Landtwing et al. 2002).

Agua Rica has an estimated resource total 797 Mt of 0.49 % Cu, 0.23 g/t Au, 0.03 % Mo, and 3.62 g/t Ag (Yamana Gold 2006, Feasibility Study Update; wwcw.yamana.com). Koukharsky and Mirré (1976), Navarro (1986), Sasso and Clark (1998), Perelló et al. (1998), BHP (1999), and Landtwing et al. (2002) document a complex history of overprinting stages of subvolcanic intrusions, mineralization, brecciation, and erosion at Agua Rica. Recent studies of the hydrothermal alteration and mineralization stages along the east-west 6969400 N main section provide additional information of the episodic superposition of multiple igneous and related hydrothermal breccia events, and the spatial distribution and composition of phyllosilicate minerals (Franchini et al. 2011, 2012).

3 Methodology

Trace-element analyses in sulphide (118 points) were performed at the LA ICP-MS laboratory of the Department of Earth Sciences, the University of New Brunswick, Canada (McFarlane and Luo 2012). The LA ICP-MS system was using a Resonetics M-50 193nm excimer laser system connected, via Nylon tubing, to an Agilent 7700x quadrupole ICP-MS equipped with dual external rotary pumps. Sulfide samples were ablated using 64 µm craters and a 5 Hz repetition with the laser energy at the energy density (fluence) regulated at ~1.5 J/cm^2. The ICP-MS was operated at 1450W and a torch depth of 5.0 mm. Pyrite (and marcasite) samples were calibrated against sulfide standard reference material Mass-1 with internal standardization using Fe. BCR-2G or GSE-1 glass was used as a quality control standard. All data were reduced offline using Iolite v2.2 (Paton et al. 2011) under Wavemetrics IgorPro v6.22.

4 Results

4.1 Pyrite-Marcasite

Pyrite is the most abundant sulfide in this deposit. Two main groups of pyrite are recognized, based on its origin: early crystals related to the porphyry stage and pyrite related to the epithermal stage. Within the epithermal stage, various pyrite generations are distinguished based on differences in texture and in composition.

Analysed pyrite crystals belong to zones of the matrix-supported heterolithic hydrothermal breccia enriched in Au (AR82-146, 147, and 96m depth). In the crystals of the breccia matrix, pyrite cores are corroded and rimmed by at least two generations of pyrite. These pyrite bands are irregular and could have recrystallized from colloform pyrite. Locally, they form micro-geodes up to 60 µm in diameter with pyrite crystals protruding into vugs. In many cases individual, subhedral crystals exhibit numerous vugs filled with late pyrite bands. Pyrite also occurs as a very fine-grained, sub-rounded crystals intergrown with fine-grained marcasite + sphalerite + alunite, emplectite, aikinite cementing the breccia clasts, replacing the matrix, and filling veinlets that cut the breccia and vugs.

Spot analyses conducted on both the crystal core and the bands show that the later are enriched in Au (up to 5.3 ppm), Cu (up to 4160 ppm), Pb (up to 3300 ppm), Zn (up to 902 ppm), Bi (up to 208 ppm), Ag (up to 148.1 ppm), and minor Mn, Sn, and Te compared to early pyrite. Interestingly, the late pyrite bands average 3.1 ppm Au, 62.7 ppm Ag, 80 ppm Bi, 2064 ppm Pb, and 1420 ppm Cu. Au shows a clear positive correlation with Cu, Pb, Ag, Bi, and Zn. There is no correlation between Au and Co, Mo, Ni, and Ge. However, the element association are more readily determined in the LA ICP-MS trace element maps (AR82-146m, Fig. 1). These images indicate that distinctive zones enriched in V, Sn, Cu, and Sb form micro- to nano-scale inclusions of possible colusite. Porosity of pyrite and its intimate spatial association with the inclusions of sulfosalts are documented on both the micro- and nano-scale. The maps also show a Co- and less Mo-rich core, a thin middle band enriched in As, and a rim more homogeneously enriched in Au, Ag, Cu, Zn, and Bi.

The very fine-grained pyrite crystals from a veinlet that cut the breccia has the highest Au content (up to 12.9 ppm) of all analysed pyrite crystals in this study that correlates with its enrichment in Ag, Pb, Bi, Mo, Cu, Zn, Mn, Sb, Sn, and V compared to the average early, subhedral crystals from the matrix and clasts of the breccia.

The shallowest analysed pyrite crystals are from a similar heterolithic hydrothermal breccia sample (AR82-96 m) that contains later sphalerite and marcasite. Spot analyses conducted on a pyrite clast, fragments of pyrite in the matrix and later, fine-grained marcasite cement, show that the later is enriched in Au, Ag, Bi, Cu, Zn, Sn, Sb, Mo, and Cd compared to the pyrite clasts and fragments of the matrix, and has the highest Zn (up to 21500 ppm) and Ag (926 ppm) contents of all sulfides.

4.2 Covellite-Enargite

The covellite in the epithermal stage occurs with pyrite ± enargite ± molybdenite ± kuramite and advanced argillic alteration assemblages as hydrothermal cement in the clast-supported

heterolithic hydrothermal breccia (AR82-359 and 265m depth) and replacing early chalcopyrite in quartz veinlets (A18-85m and AR69-276m). Covellite crystals are euhedral, hexagonal sheets or prismatic, and locally reach up to 1cm in diameter. Twelve spots in different covellite crystals were analysed. The results of this group show that covellite contains up to 3.9 ppm Au and Zn (up to 610 ppm). Crystals from the veinlets also contain As (up to 236 ppm), Ag (up to 47 ppm), and Sn (up to 129 ppm).

Enargite is the most abundant sulfosalt in the deposit and it is widespread in the central heterolithic and jigsaw clast-supported breccias and in veinlets cutting earlier alteration types. Enargite compositions vary from the typical enargite chemical formula with low Sb substitution for As (0-0.52 wt% Sb), Sn-V enargite (0.87 wt% V-0.45 wt% Sn), and colusite with V (2.95-3.13 wt% V) and Sn (4.61-6.60 wt% Sn) lithophile element substitution (Franchini et al. 2011). Six enargite crystals associated with covellite in the jig-saw breccia (AR82-359m) and in a veinlet (AR69-182m) were analysed by LA ICP-MS. The results show that they belong to the typical enargite with low Sb substitution for As (2120 to 3830 ppm Sb) and they contain Sn (2630 to 6830 ppm), but very low V (up to 1.56 ppm). An enargite crystal from the breccia has Au (2.33 ppm) and Te (1474 ppm) and an enargite crystal from the vein is enriched in Zn (1180 ppm).

4.3 Sphalerite-Galena

Sphalerite occurs at shallow levels as cement in the matrix-supported hydrothermal breccia, with late colloform pyrite bands, emplectite, aikinite, and marcasite. At deeper levels, and surrounding the core of deposit centered in the Seca Norte hydrothermal breccias, sphalerite + galena with alunite fill veins that cut early advanced argillic and porphyry alteration-mineralization stages. Sphalerite is the most abundant sulfide in these later veins (up to 2 cm thick), whereas it is generally colour zoned and include euhedral crystals of galena.

As previous preliminary microprobe data reported in Franchini et al. (2011), the LA ICP-MS analysis of sphalerite from the later veins (AR135-257m and AR57-372m) at Agua Rica contain very low Fe (5.5 to 470 ppm Fe). The crystals are enriched in Au (up to 9.44 ppm), Cd (up to 7320 ppm), and Cu (up to 1923 ppm). Galena from a vein (AR57-372) is enriched in Ag (up 1210 ppm) and Bi (up to 1718 ppm); two grains contain more than 1 ppm Au (1.1 and 2.5 ppm).

4 Concluding remarks

Gold is commonly associated with sulfides and sulfosalts in epithermal deposits (Griffin et al. 1991; Pačevski et al. 2008, 2012). For example, in the high-sulfidation epithermal Pascua Au–Ag–Cu deposit, the "invisible" gold in pyrite accounts for approximately 50% of the ore reserves of the deposit (274 Mt; Chouinard et al. 2005). Entrapment of Au and trace metals in the epithermal environment has been associated with abrupt changes in ore-forming conditions (e.g. Pačevski et al. 2008, 2012) and rapid co-precipitation of metal-bearing sulfides associated with unknown lattice substitutions (see McClenaghan et al. 2009) possibly by chemisorption (see Fleet and Mumin 1997).

The LA ICP-MS output traces from each laser spot analysis presented in this study confirms the presence of Au and trace elements in pyrite, marcasite, covellite, enargite, galena, and sphalerite at Agua Rica.

Early pyrite deposited during the porphyry stage is commonly depleted in chalcophile trace elements. In contrast, pyrite crystals from the later epithermal high-sulfidation stages are texturally complex, compositionally heterogeneous, and enriched in trace elements.

The gold–rich zones of the deposit correlate with invisible gold- and trace elements-enriched pyrite and marcasite. The matrix-supported breccia with rock flower and minor hydrothermal cement that host the analysed pyrite and marcasite, is a product of a high degree of mixing and milling of fragments, which indicates the highest zone of energy released of the examined breccias. These processes may have been repeated several times during the protracted magmatic hydrothermal activity at Agua Rica.

The ore pyrite occurs as either very fine, irregularly shaped grains in late veinlets, or rims on earlier, gold-free pyrite. Based on textural and mineral chemistry data, the Co-Mo-bearing cores depleted in trace elements represent relict pyrite fragments from the early porphyry stage. These fragments were cemented by successive collomorphic pyrite bands enriched in Au with Cu, Pb, Ag, Bi, and Zn, with the intermediate band the most enriched. It is possible that these greigite-like precipitation stages reflects rapid boiling events in an open space filled with hydrothermal solutions supplied by continued fluid pathways generated by brecciation. Fluids were already depleted in Cu and As (this breccia zone does not contain covellite or enargite like in deeper zones were the hydrothermal breccia becomes clast-supported) and probably had lower temperatures, but still high sulfur and /or low

pH to precipitated alunite (Stoffregen 1987) and late marcasite (Murowchick and Barnes 1986). The role of fluid mixing in this low temperature - open system is not excluded.

Based on the element map images (Fig. 1), As does not correlate with Au. Instead, Ag, Pb, Bi, Cu, and Zn have an elemental association comparable with that of Au. Such elements -part of the melting point chalcophile group (Frost et al. 2002)- are constituents of bismuth sulfosalts and tellurides, minerals that carry invisible Au (Ciobanu et al. 2009). This breccia sector contains emplectite and aikinie, but they were not analysed by LAICP-MS.

Our study has also demonstrated the presence of Au and other trace elements in sulfides and enargite at Agua Rica that are the subject of our present research. Of these sulfides, it is noteworthy the gold-rich sphalerite from the latest veinlets points to a still high sulfur and (or) oxygen activity in the hydrothermal fluids as is indicated by the absence or very low Fe content in the sphalerite.

Acknowledgements

This work forms part of a project financed by Consejo Nacional de Investigaciones Científicas y Técnicas Argentino (CONICET PIP n° 1083), and Facultad de Ingeniería de la Universidad Nacional del Comahue (PIP N° 04/I167). D. Lentz is supported by a NSERC Discovery grant.

References

BHP (1999) The Agua Rica porphyry Cu-Mo-Au deposit, Catamarca. Geol and Min Resource Update, Internal report, 420 p

Caelles JC, Clark AH, Farrar E, McBride SL, Quirt S (1971) Potassium-argon ages of porphyry copper deposits and associated rocks in the Farallón Negro-Capillitas district, Catamarca, Argentina. Econ Geol 66: 961–964

Chouinard A, Paquette J, Williams Jones AE (2005) Crystallographic controls on trace-element incorporation in auriferous pyrite from the Pascua epithermal high-sulfdation deposit, Chile-Argentina. Can Mineral 43: 951–963

Ciobanu CL, Cook NJ, Pring A, Brugger J, Danushevsky L, Shimizu M (2009) Invisible gold in bismuth chalcogenides. Geochim Cosmochim Acta 73: 1970 –1999

Fleet, M, Mumin, H (1997) Gold-bearing arsenian pyrite and marcasite and arsenopyrite from Carlin Trend gold deposits and laboratory synthesis. Am Min 82: 182-193

Franchini MB, Impiccini A, Lentz D, Ríos FJ, O´Leary S, Pons J, Schalamuk IA (2011) Porphyry to Epithermal Transition in the Agua Rica Polymetallic Deposit, Catamarca, Argentina: An intergrated petrologic analysis of ore and alteration parageneses. Ore Geol Rev 41: 49–74

Franchini MB, Impiccini A, Beaufort D, Patrier P, Anderson C, Pons J, (2012) Mineral assemblages and distribution of phyllosilicates composition along the main section of the Agua Rica deposit, Catamarca, Argentina. Implications for future mine developments. Appl Clay Sci 67-68: 61–71

Frost BR, Mavrogenes JA, Tomkins AG (2002) Partial melting of sulfide ore during medium- and high-grade metamorphism. Can Mineral: 40, 1–118

Griffin WL, Ashley PM, Ryan SG, Sie SH, Suter GF (1991) Pyrite geochemistry in the North Arm epithermal Ag-Au deposit, Queensland, Australia. A proton microprobe study. Can Mineral 29: 185–19

Koukharsky M, Mirré JC (1976) Mi Vida prospect: a porphyry copper-type deposit in northwestern Argentina. Econ Geol 71: 849–863

Landtwing M, Dillenbeck E, Leake M, Heinrich C (2002) Evolution of the breccia-hosted porphyry-Cu-Mo-Au deposit at Agua Rica, Argentina: Progressive unroofing of a magmatic-hydrothermal system. Econ Geol 97: 1273–1292

McClenaghan, S, Lentz, DR, Martin, J and Diegor, J (2009) Gold in the Brunswick No. 12 volcanogenic massive sulfide deposit, Bathurst Mining Camp, Canada: Evidence from bulk-ore analysis and laser-ablation ICP-MS data on sulfide phases. Mineral Deposita 44: 523-557

McFarlane C, Luo Y (2012) U-Pb geochronology using 193 nm excimer LA-ICP-MS optimized for in situ accessory mineral dating in thin section. Geoscience Canada 39: 158–172

Murowchick JB Barnes HL (1986) Marcasite precipitation from hydrothermal solutions. Geochim Cosmochim Acta 50: 2615–2629

Navarro H (1986) Geología general y económica del pórfido de cobre-molibdeno "Mi Vida", Andalgalá, Catamarca. Revista del Instituto de Geología, Universidad Nacional de Jujuy 6: 127–154

Pačevski A, Libowitzky E, Živković P, Dimitrijević R, Cvetković LJ (2008) Copper-bearing pyrite from the Čoka Marin polymetallic deposit, Serbia: Mineral inclusions or true solid-solution?. Can Mineral 46: 249–261

Pačevski A, Moritz R, Kouzmanov K, Marquardt K, Živković P, Cvetković L (2012) Texture and composition of Pb-bearing pyrite from the c oka marin polymetallic deposit, Serbia controlled by nanoscale inclusions. Canadian Mineral 50: 1–2

Perelló J, Rojas N, Devaux C, Fava L, Etchart E, Harman P (1998) Discovery of the Agua Rica porphyry Cu-Mo-Au deposit, Catamarca Province, northwestern Argentina, Part II: Geology, In: Porter TM (ed). Porphyry and hydrothermal copper and gold deposits, a global perspective: Glenside, South Australia, Austral Mineral Foundation, Symposium, Perth, Western Australia, pp.117–132

Sasso AM, Clark AH (1998) Magmatic, hydrothermal and tectonic evolution and implications for Cu-Au metallogeny in the Andean back-arc. Soc Econ Geol (SEG) Newsletter 34, 1: 8-17

Stoffregen RE (1987) Genesis of acid-sulfate alteration and Au-Cu-Ag mineralization at Summitville, Colorado. Econ Geol 82: 1575–1591

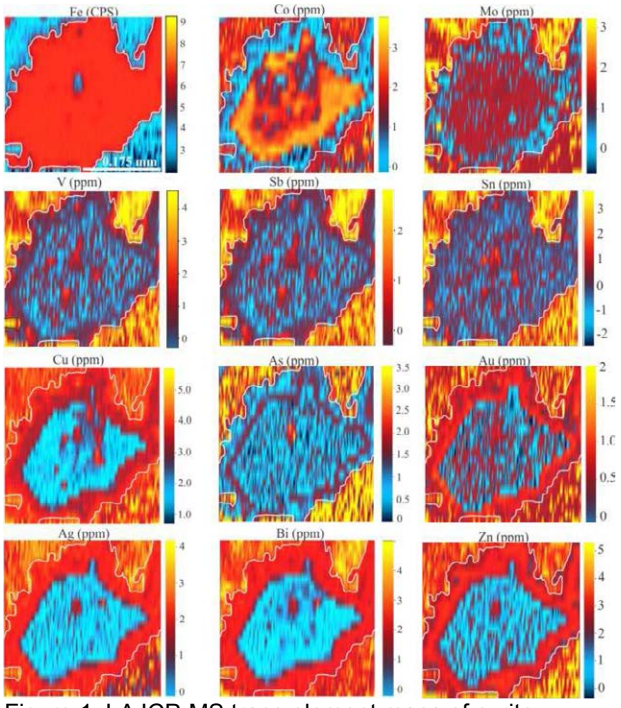

Figure 1. LA ICP-MS trace element maps of pyrite

Ore-forming fluid of Yulekenhalasu Cu-Mo deposit on the northern margin of Junggar basin, Xinjiang

Xin-xia Geng, Fu-quan Yang, Feng Liu, Qiang Li
MLR Key Laboratory of Metallogeny and Mineral Assessment,Institute of Mineral Resources, Chinese Academy of Geological Sciences, Beijing, 100037

Feng-mei Chai
Xinjiang Research Center for Mineral Resources, Xinjiang Institute of Ecology and Geography Chinese Academy of Sciences, Urumqi, 830011

Zhi-xin Zhang
Xingjiang Key Laboratory for Geodynamic processes and Metallogenic Prognosis of the Central Asian Orogenic Belt, Xinjiang University, Urumqi, 830046

Wen-juan Gao
Institute of Prospecting Technology Research of the Hebei Bureau of Geology, Sanhe City, 065201

Abstract The medium-sized Yulekenhalasu porphyry copper–molybdenum deposit is an important deposit in the Kalaxianger porphyry copper belt, located on the northern edge of the Junggar area of Xinjiang Province, China. Here, we present new data for quartz-hosted fluid inclusions from the main stage of mineralization of the deposit, and for calcite-hosted inclusions from the carbonate alteration stage of the deposit. Various types of quartz-hosted fluid inclusions are present in the deposit, and these yield homogenization temperatures of 140–340°C, with an average of 234°C, salinities of 3.06–14.97 wt.% NaCl equivalent (7.65 wt.% average), and densities of 0.61–1.01 g/cm^3. These fluid inclusions contain gaseous H_2O, CO_2, N_2, and CH_4, and they contain liquids with significant amounts of Na^+ cations and smaller amounts of Ca^{2+}, K^+, and Mg^{2+}, in addition to anions dominated by SO_4^{2-}, with minor Cl^- and F^-. Calcite-hosted inclusions are less variable, and have lower homogenization temperatures (161°C–298°C), lower salinities (4.65–7.17 wt.% NaCl equivalent), and lower densities (0.78–0.95 g/cm^3). The formation of the deposit involved a deeply sourced H_2O–NaCl–CO_2–CH_4–(N_2) mineralizing fluid, suggesting that this copper mineralization was associated with a porphyry copper-type system. In comparison, the ore-forming fluid within the carbonate stage of alteration was dominantly meteoric water.

Keywords: Fluid inclusions · porphyry · copper–molybdenum deposit · Yulekenhalasu · Xinjiang

1 Introduction

The Kalaxianger porphyry copper belt is the westward extension of the southern Mongolian porphyry copper deposit zone, and is located within the central Asian mineral belt (Rui et al., 1984; Zhang et al., 2003; Nie et al., 2004; Wu et al., 2008; Yang et al., 2010). This belt hosts a number of copper–(molybdenum) deposits, including the Kalaxianger and Xileketehalasu copper deposits, and the Xilekuduke and Yulekenhalasu copper–molybdenum deposits. Previous research on the Yulekenhalasu copper–molybdenum deposit has focused on the geology and geochronology of the deposit, and the potential for mineral exploration in this area (Zhao et al., 2009; Liu et al., 2010; Xue et al., 2010; Yang et al., 2012). Here, we provide new insights into the fluids that formed the Yulekenhalasu copper deposit by presenting temperature and compositional data for quartz- and calcite-hosted fluid inclusions, providing an important basis for future research into the controls on and processes involved in the formation of this deposit.

2 Geological background

The Yulekenhalasu copper–molybdenum deposit is located at the junction of the NW–SE striking Kalaxianger fault zone and the E–W striking Ertix–Mayinebo fault zone, the latter forming the boundary between the Siberia and Kazakhstan–Junggar plates. The area around the deposit is dominated by sediments of the Middle Devonian Beitashan and Lower Carboniferous Jiangbasitao formations (Fig. 1). Intrusive rocks in the Yulekenhalasu area include irregular quartz diorite stocks that intruded into the Beitashan Formation in the south and east of the study area, irregular porphyritic biotite–quartz monzonite stocks that intruded into the Beitashan Formation in the south and north–west of the study area, and porphyritic biotite–quartz intrusions within the Yulekenhalasu area that intruded into the Lower Carboniferous Jiangbasitao Formation. The study area also hosts a number of gabbro, quartz syenite, porphyritic granite, and quartz monzonite porphyry dykes.

The Yulekenhalasu copper–molybdenum deposit is hosted by porphyritic diorite and porphyritic biotite–quartz monzonite intrusions, and volcanic and volcaniclastic rocks of the Beitashan Formation. Two mineralization zones have been delineated, and are here termed zones I and II. Mineralization zone I is located in the central–eastern section of the mining area, and is ~800 m long and 20–120 m wide, whereas mineralization zone II is located in the northwest of the mining area, and is 350 m long and 10–100 m wide.

The deposit contains disseminated, crumb-textured and porphyritic ores that have xenomorphic granular textures and allotriomorphic granular and filling structures. The main ore types are pyrite–copper pyrite and molybdenite-bearing copper ores.

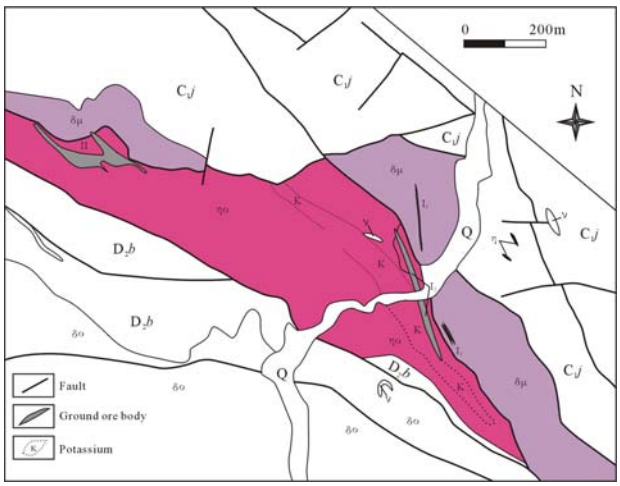

Figure 1. Geological map of the Yulekenhalasu Cu-Mo deposit, Xinjing (Modified after No. 4 Geological Party, Xinjiang Bureau of Geology and Mineral Exploration and Development, 2009)

Q- Quaternary; C_1j- Lower Carboniferous Carbonaceous shale, tuffaceous sandstone, tuff of the Jiangbasitao Formation; D_2b- Middle Devonian augitophyre, tuffaceous sandstone, tuff of the Beitashan Formation; δμ- diorite-porphyrite; ηο- Porphyritic biotite quartz monzonite; δο- Quartz diorite; ν- Gabbro; η- Monzonite

The rocks that host mineralization within the deposit are strongly altered, more kinds of lithology and the alteration within the study area is zoned from the central porphyritic diorite, through K-feldspar, biotite, silica–sericite zones to an outer propylitic alteration zone.

The Yulekenhalasu copper–molybdenum deposit formed in two separate stages: a porphyry stage and a shear deformation stage, and the majority of mineralization formed during the porphyry stage.

3 Sample Tests and Results

Samples were collected from drillcores ZK0805 and ZK0806 during this study; all 12 samples are ore-bearing quartz veins, and include quartz veins in altered tuffs, pyrite-bearing calcite–quartz veins, and biotite-bearing calcite veins.

Native fluid inclusions within quartz and calcite have a generally planar distribution and have sub-oval, flat–round, spindle, triangular, and irregular shapes. The long axes of the inclusions range between 2 and 20 μm in length.

A total of 121 quartz-hosted fluid inclusions from the main mineralization stage were classified into five types: pure gas, fluid, gas, three-phase liquid CO_2-bearing, and two-phase CO_2-bearing inclusions. Homogenization temperatures for the 84 fluid inclusions vary from 111°C to 381°C, with peaks at 150°C, 230°C, and 310°C (Fig. 2), and with freezing temperatures that vary from –11.0°C to –1.8°C. These inclusions have salinities ($NaCl_{eq}$) of 3.06–14.97 wt.%, with a peak at 6.5 wt.% (Fig. 3), and have densities of 0.61–1.01 g/cm^3, as calculated using the *T–W–ρ* characteristics of the NaCl–H_2O system (Bodnar, 1983; Fig. 4).

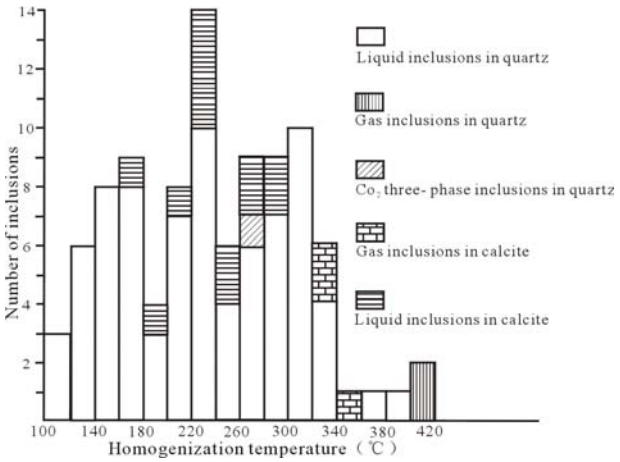

Figure 2. The histograms of homogenization temperature of fluid inclusions in the Yulekenhalasu Cu-Mo deposit

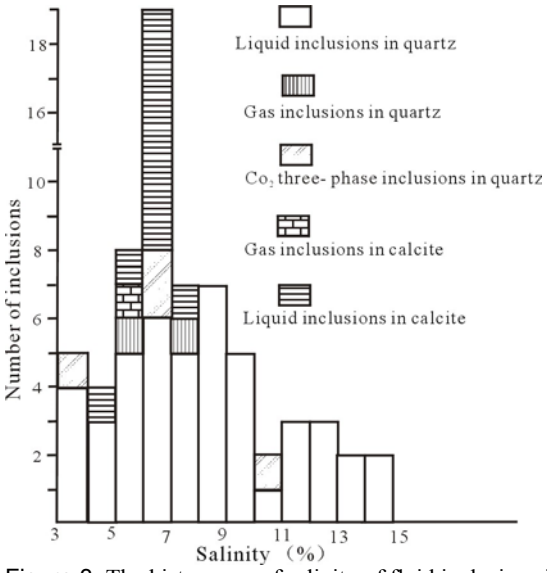

Figure 3. The histograms of salinity of fluid inclusions in the Yulekenhalasu Cu-Mo deposit

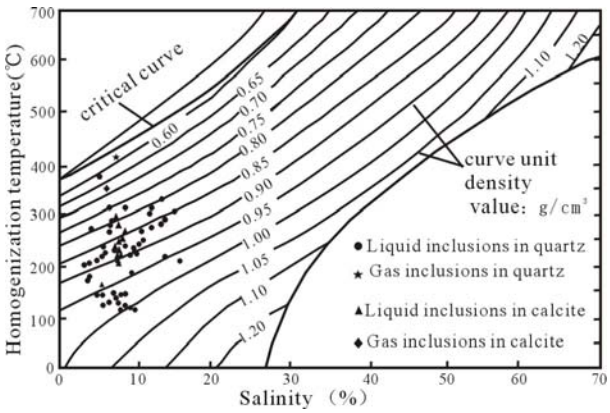

Figure 4. Diagram of homogenization T-W-ρof NaCl-H_2O in the Yulekenhalasu Cu-Mo deposit (follow Bodnar, 1983)

Analysis of six gas inclusions yielded only two reasonable homogenization temperatures, at 419°C and 410°C (Fig. 2). These gas inclusions have a freezing temperature of –4.6°C, a salinity ($NaCl_{eq}$) of 7.31 wt.% (Fig. 3), and a density of 0.58 g/cm^3 (Fig. 4). The 16 three-phase liquid CO_2-bearing inclusions have initial CO_2 melting temperatures of –62.4°C to –61.9°C, lower

than the three-phase point of CO_2 (– 56.6°C), indicating that these inclusions contain gaseous CO_2 or N_2 (Burruss, 1981). These inclusions also have homogenization temperatures of 13.8°C–13.1°C (Fig. 2) and salinities ($NaCl_{eq}$) of 3.89–10.19 wt.% (Fig. 3). The 15 two-phase CO_2-bearing inclusions analyzed during this study have initial melting temperatures of –62.2°C to –61.0°C, consistent with three-phase liquid CO_2-bearing inclusions, indicating that these inclusions also contain CO_2, CH_4, or N_2 within the liquid part of the inclusion. These inclusions have overall homogenization temperatures of –14.0°C to 27.0°C.

Seventeen calcite-hosted fluid inclusions that formed during the carbonate stage of mineralization have homogenization temperatures of 161°C–298°C (Fig. 2), freezing temperatures of –4.5°C to –2.8°C, and salinities ($NaCl_{eq}$) of 4.65–7.17 wt.% (Fig. 3). These inclusions have densities of 0.78–0.95 g/cm^3 (Fig. 3). The three calcite-hosted gas inclusions analyzed during this study have homogenization temperatures of 327°C, 332°C, and 355°C, a freezing temperature of – 3.1°C, a salinity ($NaCl_{eq}$) of 5.11 wt.%, and a density is 0.73 g/cm^3.

Seven quartz-hosted inclusions contain gaseous H_2O (25.35–79.10 wt.%) and CO_2 (12.69–73.24 wt.%), with minor N_2, CH_4, and C_2H_6, and trace Ar and H_2S, and have liquid contents that contain Na^+ (0.48–8.10 μg/g), Ca^{2+}, K^+, and Mg^{2+} cations, and SO_4^{2-} (1.09–20.2 μg/g), Cl^- (0.081–1.68 μg/g), and F^- (0.018–0.9576 μg/g) cations.

4 Discussion

Thermometric analysis of quartz-hosted fluid inclusions indicates a variation in the temperature of mineralization from high to low, as shown by the range of homogenization temperatures (140°C–340°C) and salinities (3.06–14.97 wt.%). The presence of quartz-hosted H_2O–NaCl and H_2O–NaCl–CO_2 inclusions indicates that the mineralizing fluids were part of the H_2O–NaCl–CO_2–CH_4–(N_2) system. The gas–fluid ratios of the H_2O–NaCl inclusions analyzed here are highly variable, leading to the formation of pure gas inclusions, despite these inclusions having relatively invariant homogenization temperatures. This, together with the co-existence of H_2O–NaCl and H_2O–NaCl–CO_2 inclusions, suggests that these fluids underwent boiling. The ratios of Na^+ to K^+ in quartz-hosted liquid inclusions analyzed during this study are >>1, whereas magmatic fluids generally have Na^+/K^+ ratios of <1 (Roedder, 1972). The anions within the fluid inclusions are dominantly SO_4^{2-}, with minor Cl^- and F^-, indicating that the mineralizing fluids that formed the Yulekenhalasu copper deposit belong to the H_2O–NaCl– CO_2–CH_4– (N_2) system. The fact that these inclusions contain more SO_4^{2-} than Cl^- indicates that metals within these fluids are present as sulfide complexes rather than chloride complexes, as also suggested by the presence of copper sulfide mineralization associated with the porphyritic diorite.

The formation of the Yulekenhalasu copper–molybdenum deposit was associated with oxidizing O_2 and CO_2, and reducing CH_4, C_2H_6, H_2S, and N_2 gases, suggesting that the deposit formed in an oxidizing environment.

The main stage of mineralization was associated with a Na^+-rich, and CO_2- and CH_4-bearing fluid. The fact that the fluid inclusions within the deposit are small, combined with the rarity of gas inclusions and the abundance of CO_2-bearing inclusions, suggests that the fluids that formed the deposit were generated at a significant depth (Grapner, 2001).

The last phase of deposit formation is represented by the carbonate stage of mineralization. This stage saw the formation of significant amounts of carbonate and minor quartz, pyrite, and chalcopyrite, and is characterized by low temperatures (161°C–298°C), low salinity (4.65–7.17 wt.% $NaCl_{eq}$), and low-density (0.78–0.95 g/cm^3) H_2O–NaCl type fluids, indicating derivation from meteoric water.

5 Conclusions

(1) Five types of quartz-hosted fluid inclusions were formed during the main stage of mineralization within the Yulekenhalasu copper–molybdenum deposit: pure gas, gas, fluid, three-phase CO_2-bearing, and two-phase CO_2-bearing inclusions. The latter three are the dominant types of inclusions that formed during this stage of deposit formation. Calcite-hosted fluid inclusions that formed during the carbonate stage of mineralization are less variable in terms of carbonate alteration stage and are dominated by inclusions with minor gas inclusions.

(2) The main stage of mineralization occurred at temperatures of 140°C–340°C, and involved fluids with salinities of 3.1–15.0 wt.% $NaCl_{eq}$. These fluids were associated with gaseous H_2O, CO_2, N_2, CH_4, and C_2H_6. They also contain Na^+, Ca^{2+}, K^+, and Mg^{2+} cations, and SO_4^{2-}, Cl^-, and F^- anions, and represent H_2O–NaCl–CO_2–CH_4– (N_2) system fluids.

Acknowledgements

This work was granted by the National Natural Science Foundation of China Program (40972069) and the Project of China Geological Survey (12120113093600).

References

Bodnar R J. 1983. A method of calculateing fluid inclusion volumes based on vapor bubble diameters and PVTX properties of inclusion fluids. Econ. Geol., 78: 535-542

Burruss R C. 1981. Analysis of phase equilibria in C-O-H-S fluid inclusions. Mineralogical Association of Canada. 6: 39-74.

Grapner T, Kempe U, Spooner E T C, et al. 2001. Microthermometric, laster Roman spectroscopic and volatile-ion chromatographic analysis of hydrothermal fluids in the Paleozoic Muruntau Au-bearing quartz vein ore field, Uzbekistan. Economic Geology, 96: 1-23.

Liu G R, Dong L H, Xue C J, Li X R, Zhang L W, Wei G Z, He L X, Zhao Z H, Qin J H, Zhang Z X. 2010. Geological Characteristics And Exploration Direction Of The Yulekenhalasu Copper Deposit, Xinjiang. Xinjiang Geology, 28(4): 377-384 (in Chinese with English abstract).

Nie F J, Jiang S H, Zhang Y, Liu Y, Hu P. 2004. Geological Features and Origin of Porphyry Copper Deposits in China-Mongolia Border Region and Its Neighboring Areas. Mineral

Deposits, 23(2): 176-198 (in Chinese with English abstract).
Roedder E. 1972 In Physics and Chemistry of the Earth (Vols. 13-14). Oxford: Pergamas Press , 9- 35
Rui Z Y, Huang C K, Qi M, et al. 1984. Porphyry copper-molybdenum deposit in China. Bei jing: Geological Publishing House, 1-350 (in Chinese with English abstract).
Wu G G, Dong L H, Xue C J, Feng J, et al. 2008. Major porphyritic copper deposit belts in the northern Xinjiang Region. Bei jing: Geological Publishing House, 1-345 (in Chinese with English abstract).
Xue C J, Zhao Z F, Wu G G, Dong L H, Feng J, Zhang Z C, Zhou G, Chi G X, Gao J G. 2010. The multiperiodic superimposed porphyry copper mineralization in Central Asian Tectonic Region:A case study of geology,geochemistry and chronology of Halasu copper deposit,Southeastern Altai,China. Earth Science Frontiers, 17(2): 53-82 (in Chinese with English abstract).
Yang F Q, Yan S H, Liu G R, Zhou G, Zhang Z X, Liu F, Geng X X, Guo C L. 2010. Geological characteristics and metallogenesis of porphyry copper deposits in Junggar,Xinjiang. Mineral Deposits, 29(6): 956-971 (in Chinese with English abstract).
Yang F Q, Zhang Z X, Liu G R, Qu W J, Zhang L W, Wei G Z, Liu F, Chai F M. 2012. Geochronology of Yulekenhalasu porphyry copper deposit in northtern Junggar area,Xinjiang,China. Aacta Petrological Sinica, 28(07): 2029-2042 (in Chinese with English abstract).
Zhang Y, Nie F J, Jiang S H. 2003. Discovery of the Ouyu Tolgoi copper-gold deposit in the Sino-Mongoliaborder region and its significance for mineral exploration. Regional Geology of China, 22(9): 708-713 (in Chinese with English abstract).
Zhao Z F, Xue C J, Zhang L W, Wen C S, Zhou G, Liu G R. 2009. U-Pb dating of zircons from acid intrusions in Yulekenhalasu copper deposit of Qinghe,Xinjiang,and its geological significance. Mineral Deposits, 28(4): 425-433 (in Chinese with English abstract).

Understanding controls on gold mobility in large hydrothermal systems: an example from the Pebble porphyry Cu-Au-Mo deposit, Alaska

Melissa J. Gregory
Mineral Deposit Research Unit, Department of Earth, Ocean and Atmospheric Sciences, University of British Columbia, Vancouver, Canada

Abstract. The gold distribution in porphyry deposits can be highly variable due to the changing physiochemical conditions associated with multiple hydrothermal alteration events that commonly overprint each other. Geochemical modelling of mineralogical data from the Pebble porphyry Cu-Au-Mo deposit, Alaska, provides insights into the controls on variations in gold distribution. During potassic alteration at Pebble, gold and silver are transported as bisulfide complexes in the vapor phase and have low solubility, resulting in both metals being deposited together as electrum inclusions in chalcopyrite. During illite alteration, gold and silver are also transported as bisulfide complexes but gold solubility is higher compared with silver solubility. Gold solubility is highest during weak illite alteration of K-feldspar and lower during intense illite alteration. As a result, gold is locally remobilized during illite alteration, being redeposited as pure gold inclusions in pyrite. During advanced argillic alteration, the acidic conditions enhance the separation of gold and silver which partition to the vapor and brine, respectively, and both metals have relatively low solubilities. As a result pure gold inclusions are deposited with the dominant sulfide minerals in the alteration assemblage. Overall, these results show that the pH of the alteration mineral assemblage controls the degree to which gold is transported or deposited by low salinity fluid phases in porphyry deposits.

Keywords. Porphyry, gold, Pebble, hydrothermal alteration, modelling

1 Introduction

The gold distribution in porphyry deposits can be highly variable as a consequence of dynamic hydrothermal processes that result in changing physiochemical conditions during deposit formation (e.g., Gregory et al. 2013). Porphyry deposits contain numerous styles of hydrothermal alteration and mineralization, each with its own unique gold associations. A porphyry Cu-Au deposit may have gold associated with bornite or chalcopyrite in its high temperature potassic core, whereas gold can be associated with pyrite in more peripheral, lower temperature clay alteration zones (e.g., Granisle and Bell porphyry deposits, British Columbia, Cuddy and Kesler 1982; La Fortuna porphyry and epithermal deposits, Chile; Perrello et al. 1996; Pebble porphyry deposit, Alaska, Gregory et al. 2013). Geochemical modelling of quantitative mineralogical data, including measured gold mineral data, in porphyry systems can help identify the key controls on these variations. Such data exists for the Pebble porphyry Cu-Au-Mo deposit in Alaska (Gregory et al. 2013).

2 Gold and Silver Mobility in the Pebble Porphyry Cu-Au-Mo Deposit, Alaska

2.1 Geology of the Pebble deposit

The Pebble porphyry Cu-Au-Mo deposit in Alaska is one of the world's largest porphyry deposits and has the largest gold resource of all known deposits discovered to date with over 107 million ounces (Sebag 2012). The deposit is related to 90 Ma granodiorite porphyry intrusions and is dominated by chalcopyrite-pyrite-rich mineralization hosted by a variety of hydrothermal alteration assemblages including sodic-potassic, potassic and quartz-sericite-pyrite. Low temperature illite and kaolinite overprint these higher temperature assemblages and is subsequently overprinted by a higher temperature advanced argillic assemblage (Lang et al. 2013). Detailed gold characterisation studies have documented the composition of gold minerals and their distribution throughout the deposit (Gregory et al. 2013), and this data together with recent fluid inclusion data (Gregory, unpublished data) are combined to model the controls on variations in the gold distribution.

2.2 Physiochemical modelling of gold and silver mobility at Pebble

The copper, gold and silver that are deposited in porphyry deposits are transported in magmatic-hydrothermal fluids that are exsolved from crystallizing magmas at depth (e.g., Audetat et al. 2008). Typically, a high temperature (>500°C) single phase parental fluid will ascend to shallower levels and undergo phase separation, condensing a small volume of highly saline brine from an expanding vapor phase (Henley and McNabb 1978; Williams-Jones and Heinrich 2005). During phase separation, copper partitions into both the brine and vapor phase (Lerchbaumer and Audetat 2012; Seo and Heinrich in press), however gold is strongly partitioned into the vapor phase (Pokrovski et al. 2008). Silver can partition into either the vapor or brine depending on the physiochemical conditions during phase separation (Pokrovski et al. 2008).

Copper sulfide precipitation occurs from the co-existing brine and vapor (Lerchbaumer and Audetat 2012), as the fluids cool to near 400°C where copper becomes saturated and SO_2 disproportionates to form the H_2S required for sulfide formation (Burnham 1979). Gold and silver may precipitate with chalcopyrite or

bornite even if these metals are not saturated in the hydrothermal fluids (Gammons and Williams-Jones 1997; Simon et al. 2000; Kesler et al. 2002).

Physiochemical modelling of hydrothermal mineral assemblages at Pebble together with gold and silver solubility demonstrates the key controls on gold mineral distribution (Fig. 1). The gold distribution in potassic alteration assemblages at Pebble is dominated by electrum inclusions in chalcopyrite (Gregory et al. 2013). The potassic alteration is characterized by an assemblage of K-feldspar-quartz-biotite-chalcopyrite-pyrite (Lang et al. 2013), and the interpretation here is that the silicate minerals were deposited during reactions between wallrock and hypersaline brine with an average composition of 33.8 wt% NaCl and 17.8 wt% KCl at 350°C (Gregory, unpublished data). This assemblage is stable at pH values of 5 to 6 and log fO_2 of -31.7 to -27.5 (Fig. 1A). Gold and silver are transported as bisulfide complexes in the vapor phase under these conditions (Pokrovski et al. 2008) and would have low solubility during potassic alteration (Fig. 1A). This is consistent with the deposition of gold and silver together as electrum.

Following potassic alteration and the deposition of metals, the brine and vapor phases would continue to migrate upwards and outwards from the core of the hydrothermal system and ultimately interact with meteoric groundwater. The low-temperature illite overprint on potassic alteration at Pebble occurred through wallrock reaction of an acidic, low salinity fluid with a mixed magmatic-meteoric signature (Gregory, unpublished data). Condensation and mixing of H_2S-rich magmatic vapor and meteoric water would result in a fluid of this composition (e.g. Gammons and Williams-Jones 1997) and during cooling this fluid would flow back into the mineralized zone and result in the illite alteration overprint, a process also documented at Bajo de la Alumbrera (Ulrich et al. 2001; Harris et al. 2005).

Illite alteration at Pebble is accompanied by a change in gold association with an increasing amount of pure gold inclusions occurring in pyrite at the expense of electrum inclusions in chalcopyrite (Gregory et al. 2013). A 2.5 wt% NaCl fluid at 250°C is related to illite alteration resulting in a K-feldspar-illite-pyrite-chalcopyrite mineral assemblage (Gregory, unpublished data).

Physiochemical modelling of illite alteration suggests that as the fluid interacted with the potassic alteration assemblage the pH would be buffered at near neutral conditions by the conversion of K-feldspar to illite (Fig. 1B). In the sulfur-rich fluid responsible for illite

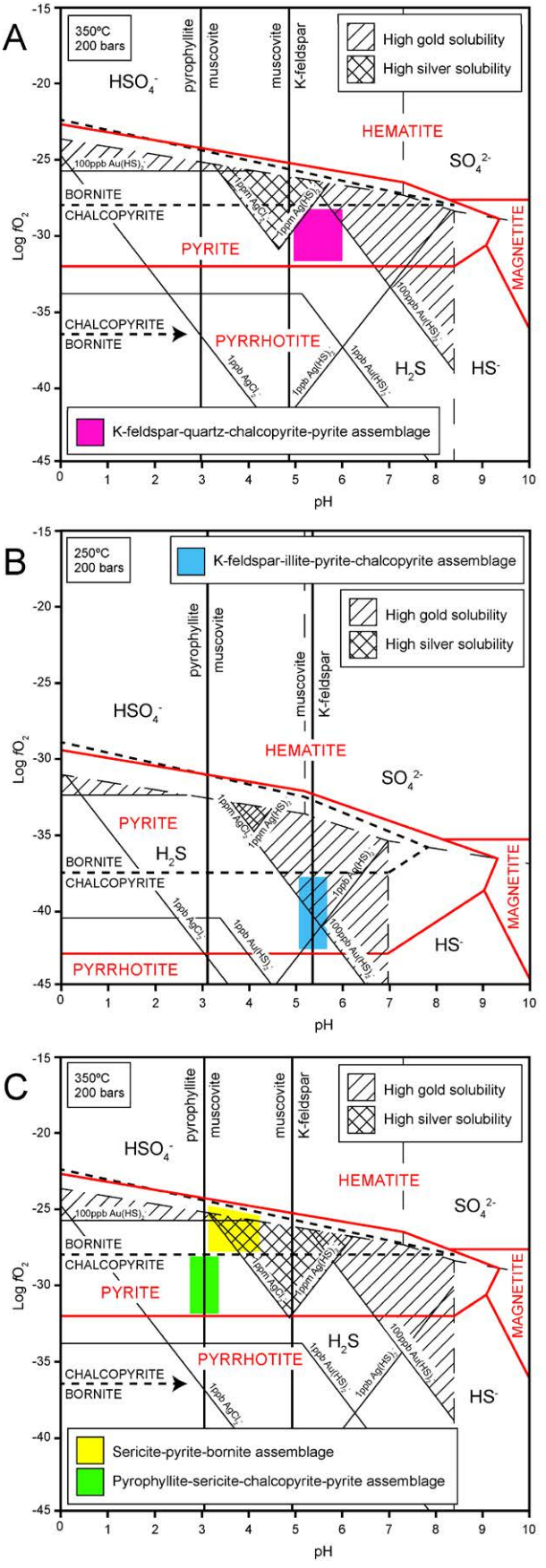

Figure 1. Log fO_2-pH diagram showing mineral stability fields and metal solubility contours. Phase boundaries and predominance fields for aqueous species calculated using SUPCRT92 (Johnson et al. 1992). Gold and silver solubility contours calculated using data from Stefansson and Seward (2004), and Gammons and Williams-Jones (1995), respectively. All diagrams calculated at 200 bars with aS = 0.1. Activities of Na and K are based on fluid inclusion data from the Pebble deposit (Gregory, unpublished data) and calculated with HCh modelling software (Shvarov and Bastrakov 1999) using the extended Debye-Huckel equation of Helgeson et al. (1981). Metal solubility contours calculated only in H_2S field where relevant mineral assemblages are stable. A. Potassic alteration at Pebble at 350°C. Activities: Na 0.106, K 0.053. B. Illite alteration at Pebble at 250°C. Activities: Na 0.127, K 0.035. C. Advanced argillic alteration at Pebble at 350°C. Activities: Na 0.156, K 0.045.

alteration gold is soluble as a bisulfide complex, however, the level of solubility is controlled by the pH. As a result, gold is highly soluble in more neutral K-feldspar-rich assemblages and has lower solubility in more acidic illite-rich assemblages (Fig. 1B). This means gold can be locally remobilised as illite alteration progresses from weak to intense. Silver is not soluble under these conditions (Fig. 1B), resulting in the separation of the two metals during low-temperature illite alteration. Iron released into solution from the replacement of biotite by illite will react with H_2S in the fluid to form pyrite, thereby decreasing the H_2S activity of the fluid which also reduces gold solubility (Gammons and Williams-Jones 1997). The result at Pebble is pyrite-hosted pure gold inclusions associated with low-temperature illite alteration.

The advanced argillic alteration at Pebble was also the product of a magmatic fluid that underwent phase separation. This alteration is characterized by a quartz-sericite-bornite-pyrite assemblage with pure gold inclusions in pyrite, around a core of quartz-pyrophyllite-sericite-chalcopyrite-pyrite alteration with pure gold inclusions in chalcopyrite (Gregory et al. 2013; Lang et al. 2013). The silicate mineralogy formed during interaction of older potassically-altered wallrocks with hydrothermal brines with an average composition of 35.5 wt% NaCl and 9.0 wt% KCl (assuming a K/Na ratio of 0.2) at 350°C (Gregory, unpublished data). Physiochemical modelling indicates these assemblages are stable at pH values of 3 to 4. Gold was most likely transported as a bisulfide complex in the vapor phase under these conditions, however, silver was more likely partitioned into the brine and transported as a chloride complex (Pokrovski et al. 2008) (Fig. 1C).

Under conditions where sericite and pyrophyllite are stable (Fig. 1C), gold solubility is low and silver solubility is moderate to high. Together with the different metal complexing behaviour, these solubility characteristics result in the precipitation of pure gold inclusions in chalcopyrite in pyrophyllite-rich assemblages and in pyrite in sericite-rich assemblages. Simple cooling of a fluid in equilibrium with sericite will cross into the pyrophyllite stability field between 300 and 350ºC explaining the transition from one mineral assemblage to the other (Lang and Gregory in press).

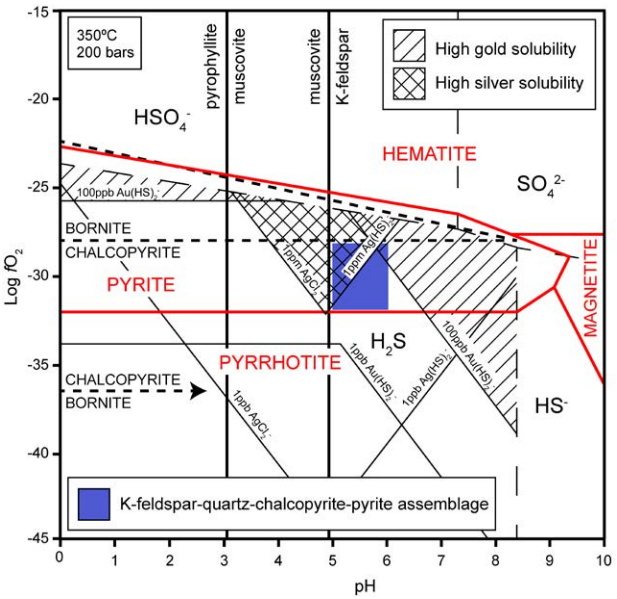

Figure 2. Log fO_2-pH diagram showing mineral stability fields and metal solubility contours. Data, assumptions and sources as for Figure 1. Diagram calculated for typical potassic alteration at 350°C. Activities: Na 0.156 and K 0.045 based on a 42 wt% NaCl equivalent fluid with a K/Na ratio of 0.2.

3 Application to Other Porphyry Deposits

In the Pebble porphyry Cu-Au-Mo deposit dominantly hypersaline brines are associated with potassic alteration and mineralization, however, in many other porphyry deposits, simple brines with lower salinity are associated with potassic alteration (e.g., 45 wt% NaCl equivalent at Bingham Canyon (Landtwing et al. 2010)). Physiochemical modelling suggest that this difference in fluid composition may have a large influence on the gold distribution associated with potassic-types of alteration.

For example, a simple brine associated with a K-feldspar-quartz-chalcopyrite-pyrite assemblage will occur over a range in pH values from 5 to 6 (Fig. 2). Gold and silver will be transported as bisulfide complexes in the vapor phase under these conditions (Pokrovski et al. 2008), however, gold solubility is low but silver solubility is very high compared with the conditions at Pebble (compare Fig. 1A with Fig. 2). As a result much less silver may be deposited with potassic alteration in this environment and could result in pure gold inclusions in chalcopyrite rather than electrum.

Variations in the potassic alteration mineral assemblages such as the presence of magnetite and bornite suggest varying temperature, pH and fO_2 conditions at the time of alteration. Geochemical modelling (not shown here) suggests gold solubility is very low at the higher temperatures where magnetite and bornite are stable with K-feldspar. This is consistent with the common association between high gold grades and magnetite-rich alteration assemblages (Sillitoe 2000).

4 Implications and Future Work

The physiochemical modelling presented here indicates that the temperature and hydrothermal brine salinity are closely related to variations in the hydrothermal alteration mineral assemblage. The alteration mineral assemblage determines the pH conditions under which gold and silver transport are taking place. These are the overriding controls on the distribution and composition of gold minerals despite the fact that gold, and commonly silver, are transported in a different fluid phase to the one responsible for the alteration mineralogy.

Future work will aim to document and model the gold mineralogy and mineral associations in other porphyry Cu-Au±Mo deposits. This will lead to an improved understanding of the key controls on gold mobility between different hydrothermal alteration assemblages, and also between different mineral assemblages that are

grouped within the one alteration type.

Acknowledgements

This research is funded by the Pebble Limited Partnership and Hunter Dickinson. A.E. Williams-Jones is thanked for calculating activity data for geochemical modelling.

References

Audétat A, Pettke T, Heinrich CA, Bodnar RJ (2008) The Composition of Magmatic-Hydrothermal Fluids in Barren and Mineralized Intrusions. Econ Geol 103: 877–908

Burnham CW (1979) Magmas and hydrothermal fluids. In: Barnes HL (ed) Geochemistry of hydrothermal ore deposits, 2nd edition. John Wiley & Sons, New York, pp 71-136

Cuddy AS, Kesler SE (1982) Gold in the Granisle and Bell Copper porphyry copper deposits, British Columbia. In: Levinson AA (ed) Precious metals in the northern Cordillera, Association of Exploration Geochemists, Spec. Publ. no.10, Nepean, Ontario, pp 139–156

Gammons CH, Williams-Jones AE (1997) Chemical mobility of gold in the porphyry-epithermal environment. Econ Geol 92: 45– 59

Gammons CH, Williams-Jones AE (1995) Hydrothermal geochemistry of electrum: Thermodynamic constraints. Econ Geol 90: 420-432

Gregory MJ, Lang JR, Gilbert S, Hoal KO (2013) Geometallurgy of the Pebble Porphyry Copper-Gold-Molybdenum Deposit, Alaska: Implications for Gold Distribution and Paragenesis. Econ Geol 108: 437-462

Harris AC, Golding SD, White NC (2005) Bajo de la Alumbrera Copper-Gold Deposit: Stable Isotope Evidence for a Porphyry-Related Hydrothermal System Dominated by Magmatic Aqueous Fluids. Econ Geol 100: 863-886

Helgeson HC, Kirkham DH, Flowers GC (1981) Theoretical prediction of the thermodynamic behavior of aqueous electrolytes by high pressures and temperatures: IV. Calculation of activity coefficients, osmotic coefficients, and apparent molal and standard and relative partial molal properties to 600°C and 5kb. Am J Sci 281: 1249-1516

Henley RW, McNabb A (1978) Magmatic vapor plumes and groundwater interaction in porphyry copper emplacement. Econ Geol 73: 1-20

Johnson JW, Oelker EH, Helgeson HC (1992) SUPCRT92: A software package for calculating the standard molal thermodynamic properties of minerals, gases, aqueous species, and reactions from 1 to 5000 bar and 0°C to 1000°C. Comp Geosci 18: 899-947

Kesler SE, Chryssoulis SL, Simon G (2002) Gold in porphyry copper deposits: its abundance and fate. Ore Geol Rev 21: 103–124

Landtwing MR, Furrer C, Redmond PB, Pettke T, Guillong M, Heinrich CA (2010) The Bingham Canyon Porphyry Cu-Mo-Au Deposit. III. Zoned Copper-Gold Ore Deposition by Magmatic Vapor Expansion. Econ Geol 105:91-118

Lang JR, Gregory MJ, Rebagliati CM, Payne JG, Oliver JL, Roberts K (2013) Geology and Magmatic-Hydrothermal Evolution of the Giant Pebble Porphyry Copper-Gold-Molybdenum Deposit, Southwest Alaska, USA. Econ Geol 108:437-462

Lang JR, Gregory MJ (in press) Magmatic-Hydrothermal-Structural Evolution of the Giant Pebble Porphyry Cu-Au-Mo Deposit with Implications for Exploration in Southwest Alaska, USA. In: Hedenquist JW, Harris M, Camus F (eds) Geology and Genesis of Major Copper Deposits and Districts of the World: A Tribute to Richard Sillitoe. Econ Geol Spec Pub 16

Lerchbaumer L, Audetat A (2012) High Cu concentrations in vapor-type fluid inclusions: An artifact? Geochim Cosmochim Acta 88: 255-274

Perrello J, Urzua F, Cabello J, Ortiz F (1996) Clustered, gold bearing Oligocene porphyry copper and associated epithermal mineralization at La Fortuna, Vallenar region, northern Chile. In: Camus F, Sillitoe RH, Petersen R (eds.) Andean Copper Deposits: New Discoveries, Mineralization, Styles and Metallogeny. Econ Geol Spec Pub 5: 81–90

Pokrovski GS, Borisova AY, Harrichoury J (2008) The effect of sulfur on vapor-liquid fractionation of metals in hydrothermal systems. Earth Planet Sci Let 266: 345-362

Sebag R (2012) Global Gold Mines & Deposits 2012 Ranking: Natural Resource Holdings. pp 1–29

Seo JH, Heinrich CA (in press) Selective copper diffusion into quartz-hosted vapor inclusions: evidence from other host minerals, driving forces, and consequences for Cu-Au ore formation. Geochim Cosmochim Acta

Shvarov YV, Bastrakov EN (1999) HCh: a software package for geochemical equilibrium modelling. User's Guide. AGSO Record 1999/25

Sillitoe RH (2000) Gold-rich porphyry copper deposits: descriptive and genetic models and their role in exploration and discovery. In: Hagemann SG, Brown PE (eds) Gold in 2000. Rev Econ Geol 13: 315– 344

Simon G, Kesler SE, Essene EJ, Chryssoulis SL (2000) Gold in porphyry copper deposits: experimental determination of the distribution of gold in the Cu-Fe-S-Au system at 400 to 700C. Econ Geol 94: 259–270

Stefánsson A, Seward TM (2004) Gold(I) complexing in aqueous sulphide solutions to 500°C at 500 bar. Geochim Cosmochim Acta 68: 4121–4143

Ulrich T, Gunther D, Heinrich CA (2002) The Evolution of a Porphyry Cu-Au Deposit, Based on LA-ICP-MS Analysis of Fluid Inclusions: Bajo de la Alumbrera, Argentina. Econ Geol 96: 1743-1774

Williams-Jones AE, Heinrich CA (2005) Vapor Transport of Metals and the Formation of Magmatic-Hydrothermal Ore Deposits. Econ Geol 100: 1287-1312

Mineral chemistry of biotite and chlorite from the Karakartal (Kemaliye, Erzincan) porphyry Au-Cu deposit: a geothermometric approach on mineral paragenesis and succession

Oğuzhan Gümrük
Department of Geology, Karadeniz Technical University, Turkey, 61080

Miğraç Akçay
Department of Geology, Karadeniz Technical University, Turkey, 61080

Neslihan Aslan
Department of Geology, Karadeniz Technical University, Turkey, 61080

Abstract. The Karakartal deposit, is located in the eastern part of central Anatolia, is related to multi-phase porphyritic intrusive rocks intruding Jurassic-Cretaceous Munzur limestones and Early Eocene Subaşı formation. The deposit is characterized by a central potassic alteration zone that grades into propilitic alteration towards the outer zones. The central zone is generally overprinted by a chlorite-sericite alteration. Veins identified within the potassic alteration zone include Type 1 (quartz+magnetite+ chalcopyrite)-, Type 2 (quartz + chalcopyrite)- and Type 3 (K'feldspar +quartz+ pyrite+chalcopyrite +molybdenite) veins. In addition to these, Type 4 (chlorite+quartz+chalcopyrite +pyrite) veins occur in chlorite-sericite alteration zone. Both primary and secondary biotites have similar and re-equilibrated compositions and yield formation temperatures of 485-840 ^{o}C according to Ti^{+4} contents. Chlorites are mainly pynochlorite and ripidolite in composition, and are calculated to have formed at 216-432 ^{o}C based on the Fe# and Al^{+4} contents. Fluid inclusion homogenization temperatures obtained from the chlorite-sericite-, potassic- and early potassic alteration-related quartz veins are 200-330, 340-635 and 750-850 ^{o}C respectively and have salinities up to well over 80 wt% NaCl equivalent.

Keywords: Turkey, Erzincan, Karakartal, Kabataş, porphyry Au-Cu, biotite geothermometry, chlorite geothermometry, fluid inclusions, microthermometry

1 Introduction

The Karakartal deposit is located in a metallogenic zone extending from Sivas to İliç and Tunceli provinces of east central Anatolia, 15 km south-south east of İliç, near the Kabataş village. The deposit has typical properties of porphyry systems with respect to alteration types, mineralisation style, ore resource and grade, tectonic setting, and igneous rock features. It is genetically related to middle-late Eocene multiphase porphyritic intrusive rocks, cutting through the Jurassic-Cretaceous Munzur limestones and Early Eocene clastic and volcanic rocks (REF), and contains a resource of 17.8 mt with Au and Cu grades of 0,3 g/t and 0,22% respectively (www.alacergold.com).

The deposit has recently been discovered following the major discovery at Çöpler, the second largest Au deposit in Turkey, and therefore was not previously studied in detail. This study is part of a broad research covering all granitic stocks in the region as well as the mineral occurrences associated with them, and aims to discuss thermal evolution of mineral succession on the basis of mineral chemistry and microthermometry of fluid inclusions.

2 Geology and hydrothermal alteration

The Karakartal ore deposit is hosted mainly by middle-late Eocene multiphase porphyritic intrusive rocks with granodioritic composition, and, to lesser extent, by hornfelsed clastic and volcanic rocks intruded by these porphyry phases. When in porphyries, the ore is mainly in the form of cross-cutting veinlets and disseminations to a lesser extent. In hornfelsed zones, however, bands, lenses and veinlets are dominant with minor occurrences of disseminations. The deposit has well developed hydrothermal alteration zones represented by potassic-, phyllic-, propylitic-, and chlorite-sericite alteration, that can be observed at depth, but not on the surface due to weathering. The central zone of alteration halo is characterised by potassic alteration that grades outwards into phyllic- and into propylitic alteration. Near the surface till a depth of about 200 m, the potassic alteration is overprinted by a chlorite-sericite alteration assemblage.

The potassic alteration zone contains three disctint types of mineralised veinlets named here as Type 1, Type 2 and Type 3 veinlets. These veinlets are composed of quartz + magnetite + chalcopyrite ± biotite, quartz+ chalcopyrite ± biotite, and K'feldspar + quartz + pyrite + chalcopyrite, respectively. In addition to these, Type 4 veinlets occur in association with chlorite-sericite alteration and made up of chlorite +quartz +chalcopyrite + pyrite. Besides these ore-bearing veins, the deposit also contains veinlets of varying compositions. Among them, are pre-mineralisation biotite and post-mineralisation anhydrite veinlets in potassic alteration zones, anhydrite veins in phyllic alteration zones, and ubiquitous calcite veinlets cutting through all other veins, as well as rare quartz+molibdenite and quartz+specular hematite veins. The anhydrite veinlets

are absent till depths of several hundred meters beneath the current surface. Quartz+molibdenite and quartz+specular hematite veins occur near the hornfelsed zones and have no cross-cutting relationship with other veins, and are probably related either to a different phase of intrusion or to the formation of a skarn.

3 Mineral Chemistry

3.1 Plagioclase

Plagioclases in both minerilasation-related and barren porphyrytic intrusives are zoned and andesine-labrador (An:40-55) in composition. In samples of potassic alteration, in which plagioclases with a composition of albite-oligoclase are also present, plagioclase is transformed into orthoclase with an increase in K. In chlorite-sericite alteration zones, however, they are partly altered to sericite.

3.2 Biotite

Magmatic and hydrothermal biotites from the Karakartal deposit can easily be distinguished from each other by means of petrographic studies. Magmatic biotites have large and euhedral grains, whereas hydrothermal biotites have relatively small and euhedral to unhedral shapes. There is only a slight chemical difference between magmatic and secondary biotites with respect to Mg#. Ti contents of these biotites, however, show a significant variation, with decreasing values towards secondary biotites. The Mg/(Fe+Mg) and Al^{iv} values of biotites indicate flogopite-eastonite composition, based on the International Mineralogical Associations mica classification scheme (Rieder et al., 1988). These chemical features are in line with biotites from the phyllic and potasic alteration zones of the Sarcheshmeh- (Boomeri et al., 2010) and Miduk porphyry Cu deposits (Boomeri et al., 2009), respectively (Fig. 1). The ternary diagram of Nachit et al., (1985) show that the biotites have re-equilibrated compositions, and displays a characteristic trend with decreasing TiO_2 contents in biotites in strongly potassic samples to those in potassic and to those in chlorite-sericite alteration (Fig. 2).

Various attempts have been made to formulate geothermometres based on composition of biotites from porphyry Cu deposits Beane (1974) and from metamorphic environments (Henry et al., 2005 and references therein). Geothermometric calculations for the Karakartal biotites based on these methods give formation temperatures of 350 to 500 ^{o}C, and 485-840 ^{o}C, respectively. As shown above, biotites in the studied deposit is found within pre-mineralisation veinlets, which indicates rather high temperatures for their formation. This is also supported by the observations that magnetites cut veinlets with secondary biotites. In addition, fluid inclusion microthermometry on vein quartz contemporaneous with and postdating biotite-containing veins show homogenisation temperatures in the range of 360 to 850 ^{o}C (Akçay et al., 2012). These results are not compatible with the results calculated based on the geothermometre of Beane (1974), but agrees well with that of Henry et al., (2005), despite the fact that their geothermometre was developed for metamorphic conditions up to pressures of 4-6 kb. This is in line with the fact that Ti contents of both metamorphic- and hydrothermal biotites are temperature dependant (Le Bel, 1979) and that no code has been developed yet to quantify this relationship. So, the results (485-840 ^{o}C) obtained from the latter geothermometre will be used from now on to account for the formation of secondary biotites in the Karakartal deposit, even though the pressure conditions are not comparable.

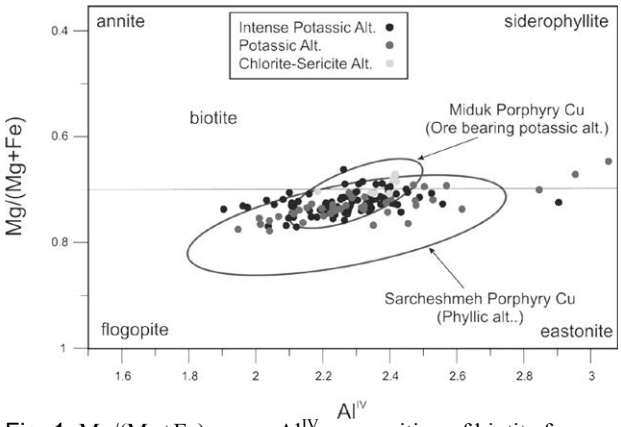

Fig. 1. Mg/(Mg+Fe) versus Al^{IV} composition of biotite from Karakartal.

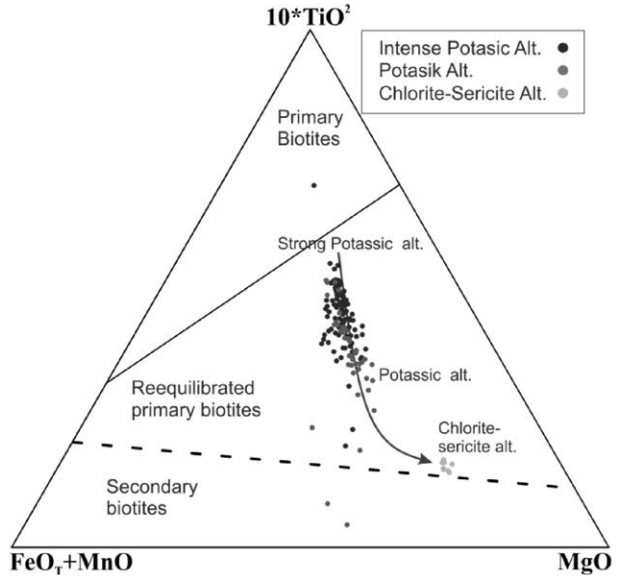

Figure 2. Ternary diagram by Nachit et al. (1985) denoting the changes in studied biotite during hydrothermal alteration.

3.3 Chlorite

Chlorites formed by alteration of magmatic and secondary biotites have compositions of pynochlorite and ripidolite based on both Fe# vs Si and Fe^{+2}+Fe^{+3} vs Si diagram of Hey (1954; Fig. 3). There are various equations to calculate formation temperatures based on Al^{IV} content of chlorite (Cathelineau, 1988) and Al^{IV} content and Fe# (Kranidiotis and McLean, 1987; Jowett, 1991). The method by Kranidiotis and McLean produced highly contrasting results (<120-195^{o}C) for the chlorite

formation compared to other two equations, not in line with fluid inclusion data from vein quartz associated with chlorite-sericite alteration zone. The remaining two methods, however, yielded similar results (216-432 ^{o}C), and are in accordance with FI data.

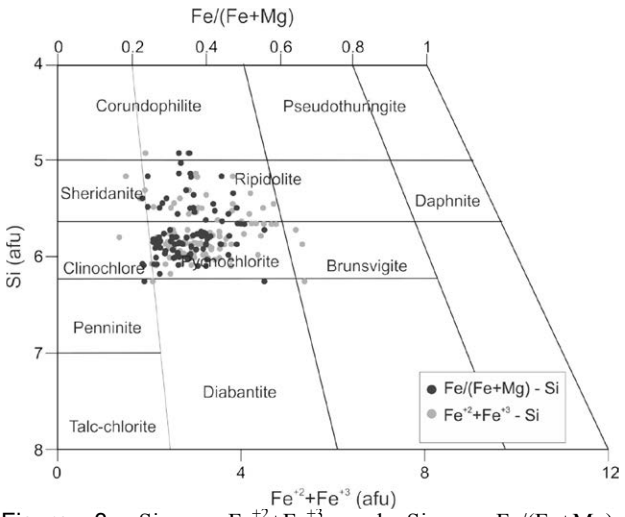

Figure 3. Si vs Fe^{+2}+Fe^{+3} and Si vs Fe/(Fe+Mg) discrimination diagram of chlorites (Hey, 1954).

3.4 Magnetite

Microscopic, BSE and Raman studies show that the potassic alteration-related magnetite is transformed to exsolution-free hematite and to magnetite with rutile and/or ilmenite exsolutions (Fig. 4). Rutile is also present as disseminations cutting through chalcopyrite in potassic alteration-related magnetite-free samples (Phyllic alteration (?); Fig. 5).

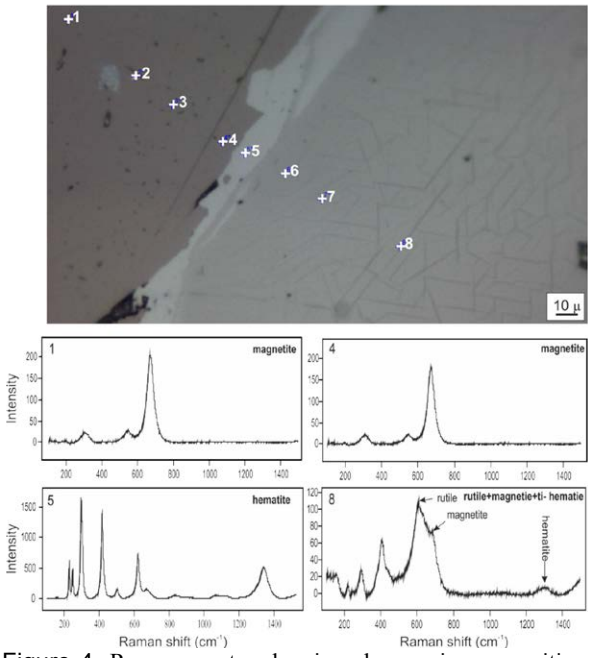

Figure 4. Raman spectra showing changes in composition of magnetite in potassic alteration.

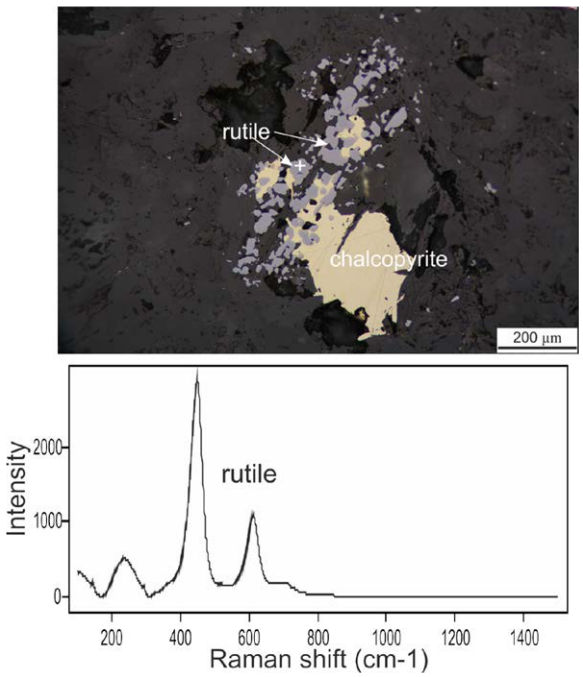

Figure 5. Raman spectrum of rutile cross-cutting chalcopyrite in the outer parts of the pottasic zone.
z

5 Fluid Inclusions microthermometry

Fluid inclusions found in quartz veins in different hydrothermal alteration zones have very complex compositions. Varying in size from <5 to 35 micron, the inclusions are grouped as single phase, two-phase, and multi-phase inclusions. The two-phase inclusions are enriched in $CaCl_2$+$FeCl_2$+NaCl+KCl, have salinities of 15-25 wt% NaCl eq. and homogenise at 200-350^{o}C. Multi-phase inclusions contain salt crystals, and/or Fe-oxide and sulphides, sulphates and silicates, have rather low liquid- and variable gas contents. Some inclusions contain only halite, some halite and sylvite, some Ca- and Fe-salts in addition to others, supported by eutectic temperatures as low as -55^{o}C. The homogenisation of gas in these inclusions takes place at 300-873^{o}C. Salt phases homogenise at 125-425^{o}C and 400-680^{o}C, and opaque phases (Fe oxides and sulphides) at 850-1050^{o}C, resulting in salinity values of up to 80 wt % NaCl eq. (Akçay et al., 2012). These temperatures are compatible with results from biotite and chlorite geothermometry (Fig. 6; see above).

6 Discussion and conclusions

As a result of microscopic and geotermometric studies the mineral deposition at the Karakartal ore deposit can be divided into five different phases (Fig. 7). Formation of the deposit was initiated at temperatures over 700 ^{o}C with the occurrence of albitisation at the expense of plagioclase (Fig. 7) as shown by albitised plagioclase predating biotites of K-silicate alteration. This change is directly related to the introduction of NaCl-over-saturated fluids with salinities well over 80% to the environment. Cooling of fluids resulted in

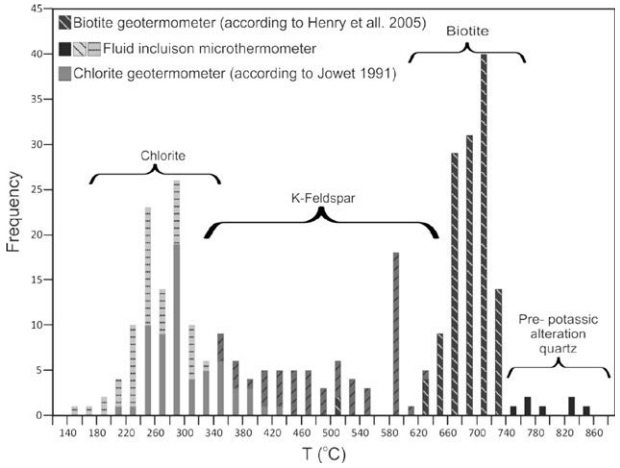

Figure 6. Histogram showing microthermometric data from biotite and chlorite geothermometer and fluid inclusion microthermometer.

hydrothermal stage of mineralisation starting with the formation of biotites below 800 °C, as supported by bitotite geothermometry. Results obtained from the potassic alteration-related fluid inclusions indicate that the formation of mineralised veins took place at 700 to 400 °C. With decreasing temperatures below 400 °C and salinities of hydrothermal solution less than 20 wt% NaCl eq., formation of the chlorite-sericite alteration commenced at the shallower parts of the deposit. Magnetite to hematite transition also occur at this stage as a result of high oxidized properties of solutions. Copper mineralization and Type 4 veins are present where the magnetite hematite transition is widely observed in the Karakartal deposit, due probably to this transition as emphasized by Su et all (2012).

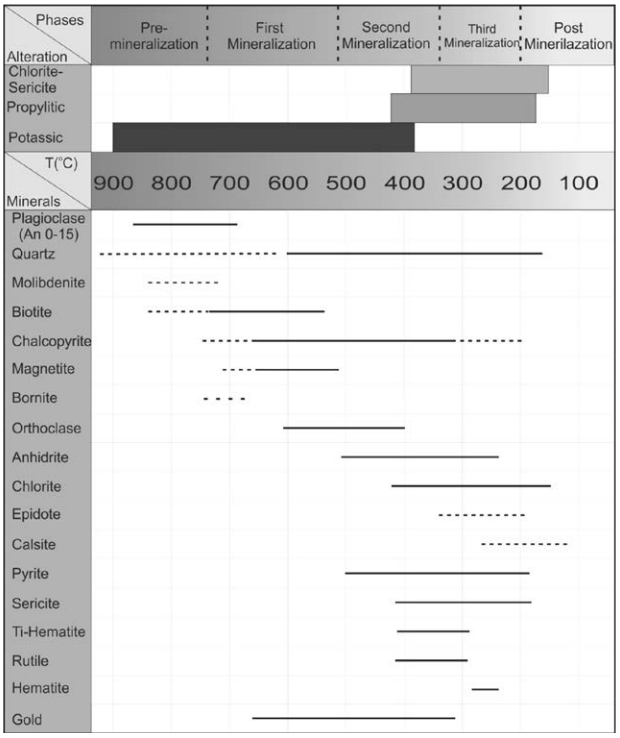

Figure 7. Mineral paragenesis and succession table of the Karakartal porphyry Au-Cu deposit.

Formation of Ti minerals both in and outside the potassic alteration zone is directly related to the biotite-chlorite transition, which releases Ti into solution. This Ti was used to form Ti-bearing phases such as rutile and / ilmenite within Fe minerals. Microthermometric data obtained from these veins and chlorite geothermometry show that chlorite-sericite alteration occurs at 400 to 180 °C. On the other hand anhydrite veins are present at the deeper parts of the deposit, but not where potassic alteration is overprinted by the chlorite-sericite alteration at shallower depths.

Acknowledgements

This study is supported by a fund from the Turkish Science Foundation (Project Number 110Y308) and from Karadeniz Technical University Research Funds (Project number 1070). The authors thank Alacer Gold Company for the logistical support provided in the field.

References

Akcay M., Gümrük O, Aslan N, (2012) Ultra-High temperature K-silicate alteration in porphyry systems: Examples from the Çöpler (İliç) and Karakartal (Kemaliye) deposits in eastern Turkey, IESCA,İzmir, 347.

Beane ER, (1974) Biotite stability in the porphyry copper environment, Econ. Geol., 69:241-256.

Boomeri M, Nakashima K, Lentz DR, (2009) The Miduk Porphyry Cu Deposit, Kerman,Iran: a geochemical analysis of the potassic zone including halogen element systematics related to Cu mineralization processes. J. Geochem. Exp., 103: 17–29.

Boomeri M, Nakashima K, Lentz DR, (2010) The Sarcheshmeh porphyry copper deposit, Kerman, Iran: A mineralogical analysis of the igneous rocks and alteration zones including halogen element systematic related to Cu mineralization processes. Ore. Geol. Review. 38:367-381

Cathelineau M, (1988) Cation site occupancy in chlorites and illites as a function of temperature, Clay Min. 23:71-485.

Henry DJ, Guidotti CV, Thomson JA, (2005) The Ti-saturation surface for low-to-medium pressure metapelitic biotite: Implications for Geothermometry and Ti-substitution Mechanisms. American Mineralogist, 90, 316-328.

Hey MH, (1984), A new review of chlorites: Min. Mag., 30: 277-292

Jowett EC, (1991), Fitting iron and magnesium into the hydrothermal chlorite geothermometer: GAC/MAC/SEG Joint Annual Meeting (Toronto), Program with Abstracts, 16, A62

Kranidiotis P, MacLean WH, (1987) Systematics of chlorite Alteration at the Phelps Dodge massive sulfides deposit, Matagami, Quebec, Econ. Geol. 82:1898-1911.

Nachit H, Razafimahefa N, Stussi JM, Carron JP, (1985), Composition chimique des biotites et typologie magmatique des granitoides. Comtes Rendus Hebdomadaires de l'Académie des Sciences 301, 813–818.

Rieder M, Cavazzini GD, Yakonov YS, Frank-Kamenetskii VA, Gottardi G, Guoggenheim S, Koval PV, Müller G, Neiva AMR, Radoslovich EW, Robert JL, Sassi FP, Takeda H, Weiss, Z. Wones DR, (1998), Nomenclature of the micas, Canadian Mineralogist, 36:905–912.

Sun W-d, Liang H-y, Ling M-x, Zhan M-z, Ding X., Zhang H., Yang X-y, Li Yl, Ireland T, Wei Q-r, Fan W-m, (2012) The link between reduced porphyry copper deposits and oxidized magmas, Geochim. Cosmchim. Acta, 103:263-275.

Ore-forming conditions of the Tertiary Kadjaran Mo-Cu-porphyry deposit, Lesser Caucasus, Armenia: evidence from fluid inclusions

Samvel Hovakimyan
Institute of Geological Sciences of National Academy of Sciences of Republic of Armenia
E-mail: samvel.hovak@gmail.com

Robert Moritz
Earth and Environmental Sciences, University of Geneva, Switzerland
E-mail: Robert.Moritz@unige.ch

Rodrig Tayan, Rafael Melkonyan, Marianna Harutyunyan
Institute of Geological Sciences of National Academy of Sciences of Republic of Armenia
E-mail: tayan@geology.am

Abstract. This paper investigates the evolution of hydrothermal fluids of variable salinity, temperature and pressure in the world-class Kadjaran Mo - Cu- porphyry deposit, based on a detailed petrographic and microthermometric study of fluid inclusions.

Five types of fluid inclusions were distinguished according to their nature, bubble size, and daughter mineral content.

Microthermometric studies were carried out according to major mineralization stages including: quartz-molybdenite, quartz-molybdenite-chalcopyrite, quartz-chalcopyrite.

Molybdenite precipitation during the quartz-molybdenite mineralization stage occurred during a boiling stage, with total homogenization temperatures of fluid inclusions ranging between 360° and 425°C. The main copper deposition at Kadjaran is associated to the chalcopyrite stage. It consists of small veins and veinlets. Copper sulfides were also precipitated mainly from high temperature and high-salinity fluids, but lower, in comparison to fluids associated with molybdenite precipitation. An intermediate quartz- molybdenite-chalcopyrite stage was mainly formed from low salinity and low temperature fluids compared with the two other stages.

Keywords. Mo-Cu-porphyry; fluid inclusion; Kadjaran; Lesser Caucasus

1 Introduction

The Tertiary evolution of the Lesser Caucasus is dominated by collisional and postcollisional tectonics and magmatism. The most important Tertiary mineral district is the Zangezur block (Meghri composite pluton) in southern Armenia (Fig.1), which consists of Eocene to Miocene magmatic suites and ore forming events, and hosts major Mo-Cu-porphyries, including the world-class Kadjaran deposit (2244 Mt reserves, 0.18% Cu, 0.021% Mo and 0.02 g/t Au) and subsidiary precious and base metal prospects (Karamyan 1978; Melkonyan et al. 2008; Moritz et at. 2012).

On-going, Re-Os molybdenite dating from different Mo-Cu porphyry deposits of the ore region indicates discrete ore forming events at 40-44 Ma (Agarak, Aygedzor, Dastakert deposits), 31 Ma (Kaler) and 26 Ma (Kadjaran). These dates essentially overlap with magmatic events (Moritz et at. 2012). This study aims at illustrating the hydrothermal history and quantifying some of the characteristics of the fluids that formed the giant Kadjaran deposit.

2 Geological And Structural Setting Of The Kadjaran Deposit

The deposit is hosted by a monzonite intrusion belonging to the Meghri composite pluton. The western part of the deposit is limited by the Tashtun fault, which traces the contact between the host- monzonite and a porphyritic granite. The dykes of the deposit consist mainly of granodiorite-porphyry. These dikes are east-west oriented, and are interpreted to be genetically related to porphyry granitoids of Lower Miocene age (22 Ma).

The deposit is structurally controlled by a steeply-dipping (65-85^0) orthogonal system of east-west, north-south- and north-east-oriented (45-65^0) fractures.

The major ore-containing faults of the deposit host a stockwork mineralization, with veins ranging in thickness from a few mm up to 5 cm. They can be traced up to a few tens of meters. They are predominantly shallow-dipping (25-40^0), rarely up to 60^0, they form parallel to sub-parallel oriented systems of veins, with a thickness reaching a few tens of meters. Crosscutting and displacement relationships of the mineralized fractures and detailed studies of the age relationship between different paragenetic mineral associations were the criteria for distinction of ten stages of mineralization at the Kadjaran deposit (Karamyan & Faramazyan 1960). The economic paragenetic stages are: quartz - molybdenite, quartz – molybdenite -chalcopyrite, and quartz-chalcopyrite.

3 Ore Types And Orebody Geometries

At the Kadjaran deposit, the ore-enriched areas occur along sub-parallel zones of the east-west-oriented fractures. In particular, they are located in areas where they crosscut steeply-dipping (70-85^0) east-west- and north-east-oriented fractures. The dykes have played an important structural control on the location of mineralization. The economic ores are located within the

hanging wall, on the eastern side of the north-west-oriented (320-340^0) Tashtun fault. Copper-molybdenum ore stockwork is recognized along a more than 3.5 km-long and about 2 km-wide corridor. Along the footwall of the fault, the porphyry granite is devoid of mineralization and pronounced alteration.

4 Fluid Inclusion Petrography

Quartz from the different mineralization stages contains a large variety of fluid inclusions, which can be classified into five families according to their nature, bubble size, and daughter mineral content: vapor-rich (VR), aqueous-carbonic (Ac), brine (B_1), polyphase brine (B_2) and liquid-rich (LR) inclusions (Fig. 2).

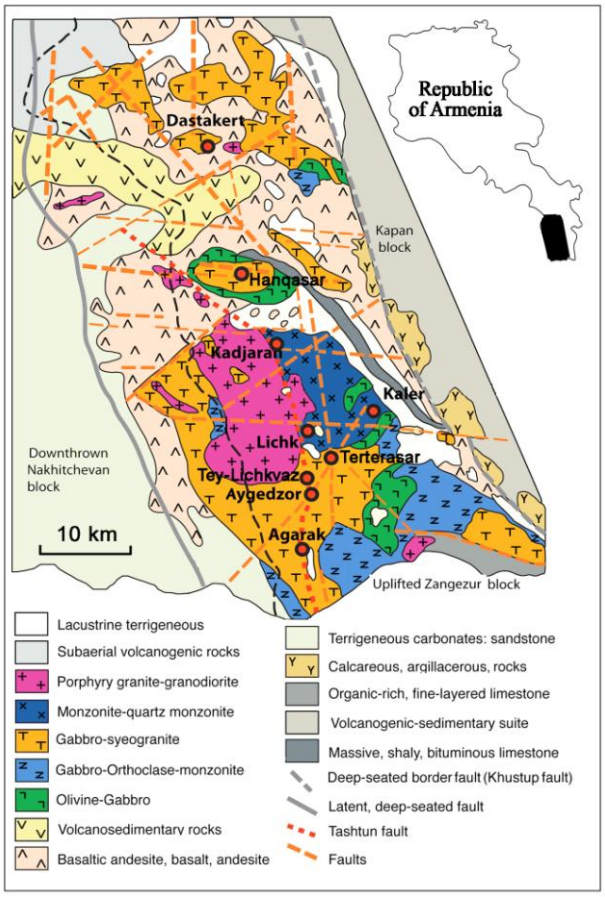

Figure 1. Geological map of the Zangezour ore region [Karamyan 1978; Moritz et al. 2012].

The size of fluid inclusions ranges from 2 μm up to 100 μm. In some cases they can be larger. Generally, they have a negative crystal or irregular shape, tubular and spherical shapes are also present.

Vapor-rich (VR; Fig. 2C) fluid inclusions contain a large vapor bubble at room temperature (80–90 vol %). They contain a thin crescent-shaped meniscus with a liquid phase. These inclusions have isometric, rarely irregular shapes, as well as negative crystal shapes. Their size can be up to 10 μm.

Aqueous-carbonic (Ac, Fig.2A) fluid inclusions are complex inclusions with three phases at room temperature, containing aqueous liquid, carbonic liquid and carbonic vapor phases. Relatively large inclusions (up to 20 μm) have irregular shapes. The smaller inclusions (less than 7 μm) are characterized by isometric and negative crystal shapes. The inclusions are dominated by high concentrations of CO_2 and the vapor/liquid ratio is 1 (Pashkov 1975).

Brine (B_1, Fig.2C) fluid inclusions contain an aqueous liquid, a vapor bubble and a halite crystal at room temperature. The bubble fills ~20 to 30 vol % of the inclusion.

Polyphase brine (B_2, Fig. 2B) fluid inclusions contain daughter crystals and a bubble. The volume of the vapor phase is about 10-20 vol %. Daughter crystals are halite, sylvite and hematite. They rarely also contain biotite, tourmaline, magnetite and feldspar (Madanyan 1980), and are interpreted as accidentally trapped minerals. Halite is present in almost all the inclusions of this type and occupies 2-7 vol %. Sylvite does not occur in all the inclusions and the volume is less than 8 vol %. The relative volume of these phases in the inclusions varies widely.

Liquid-rich (LR, Fig. 2D) fluid inclusions contain a vapor bubble, which fills 20-30 vol % of the inclusions. The size of the oval and elongated inclusions does not exceed 20 μm, the inclusion of irregular shape may reach 100 μm in diameter. The liquid phase constitutes between 80 and 100 % of the inclusion.

5 Fluid Inclusion Microthermometry

Petrography and fluid inclusion microthermometry were carried out at the University of Geneva, Switzerland. We have compared our new data set to the ones of previous studies by Madanyan (1980) and Pashkov (1975). Measurements were made using a Linkam THM-600 combined heating and freezing stage with a temperature range of −196°C to 600°C, mounted on a Leica DM LB petrographic microscope.

The density and pressure of entrapment were calculated using the sowatflinc_inclusion computer program of Driesner and Heinrich (2007) (www.geopetro.ethz.ch/people/td/sowat).

Determinations were carried out for liquid-rich and brine inclusions. Computation of pressure estimates of the liquid-rich fluid inclusions were performed by the values of salinity in wt % NaCl equiv. and the values of total homogenization temperature. For brine inclusions, we used the values of homogenization temperatures of vapor phase and the total homogenization temperature of inclusions. In our case, it was the homogenization temperature of halite disappearance, because all brine inclusions homogenize by halite dissolution.

Microthermometric studies of the Kadjaran deposit were carried on ten thick sections from the economic paragenetic stages: quartz-molybdenite, quartz-molybdenite-chalcopyrite, and quartz-chalcopyrite, sampled from outcrops of the open pit.

The primary inclusions of different stages are distinguished by the shape and by the type of homogenization, the contents of various daughter minerals and the salinity. The salinity in the inclusions of each mineralization stage are different, the salinity decreases with decreasing temperature.

Microthermometry revealed that total homogenization of all brine inclusions occurs by halite dissolution. The salinity of brine (B_1) inclusions in

quartz - molybdenite vein was determined by dissolution of halite between 356° ± 8° and 422° ± 10°C, corresponding to about 42.6 to 50.7 wt % NaCl equiv. Th of vapor bubbles lie between 278 ± 4°C and 327 ± 5°C (Fig. 3). They have been trapped at pressures of 1.2 and 1.5 kbars (120 and 150 MPa). These high pressures were also calculated by Madanyan (1980).

Total homogenization of this type of inclusions in quartz- molybdenite- chalcopyrite veins occurs by halite dissolution between 295° ± 4° and 299° ± 3°C temperatures. Salinities lie between 37.6 and 37.9 wt % NaCl equiv. Vapor bubble disappearance occurs at 236 ± 2°C and 219± 4°C. The pressures of entrapment were 1-1.4kbars (100-140 MPa). It should be noted that these inclusions are primary and within one fluid inclusion assemblage they have a similar homogenization temperature. This indicates that they were not reequilibrated with respect to different pressure conditions after their entrapment.

Brine inclusions in quartz- chalcopyrite vein homogenize by halite disappearance between 361° ± 4°C and 385° ± 3°C. Salinities lie between 43.4 and 45.9 wt % NaCl equiv. Vapor bubble disappearance occurs at 300^0C. The pressures of entrapment were 0.9-1.2 kbars (90-120MPa).

In many cases, brine inclusions (B_1) coexist with VR inclusions in boiling assemblages (Fig. 2E).

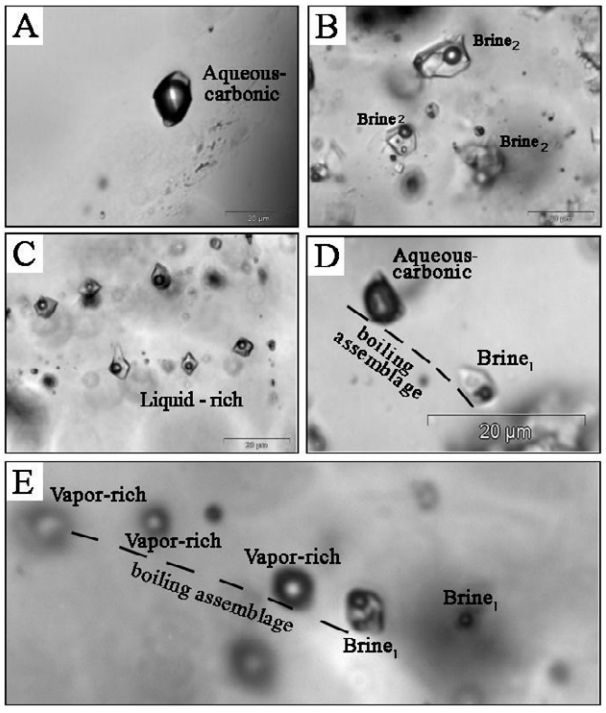

Figure 2. Different fluid inclusion types from the Kadjaran molybdenum-copper porphyry deposit: A- Aqueous-carbonic fluid inclusions; B- Polyphase brine inclusions; C- Secondary liquid-rich inclusions; D- Brine inclusion coexisting with Ac in boiling assemblages; E- Brine inclusions coexisting with VR in boiling assemblages.

Microthermometry of Vapor-Rich inclusions in quartz - molybdenite veins revealed ice-melting temperatures between -4.0° and -3.7°C, and total homogenization temperatures lie between 369° ± 1° and 420° ± 4ºC. Salinities fall between 6.0 and 6.5 wt % NaCl equiv.

Ice-melting temperatures of VR inclusions in quartz-molybdenite-chalcopyrite veins are between -3.2° and -2.8°C. Total homogenization temperatures lie between 264° ± 3° and 287 ± 4ºC. Salinities fall between 4.7 and 5.3 wt % NaCl equiv.

Microthermometry of Ac inclusions in quartz - molybdenite vein showed CO_2-melting temperatures between –58.5° and -56.9°C. The final clathrate melting temperature between 7.3º and 8.3ºC. Homogenization temperature of CO_2 could not be measured reliably, because of difficulties in observing phase boundaries. The total homogenization was to the vapor phase between 398° ± 10° and 427° ± 8ºC. The clathrate melting temperatures yield salinities from 3.3 to 5.2 wt % NaCl equiv.

Microthermometry of Ac inclusions in quartz - molybdenite - chalcopyrite veins showed CO_2-melting temperatures between –57.3° and -56.8°C. The final clathrate melting temperature between 7.2º and 7.7ºC. Homogenization temperatures of CO_2 could not be measured reliably. The total homogenization to the vapor phase was between 298° ± 3° and 323° ± 5ºC. In quartz-chalcopyrite veins total homogenization temperatures lie between 345° ± 4°C and 386° ± 6ºC. The clathrate melting temperatures yield salinities from 4.4 to 5.3 wt % NaCl equiv. In some sections of the quartz- molybdenite mineralization stage, brine inclusions coexist with Ac inclusions in boiling assemblages (Fig. 2D).

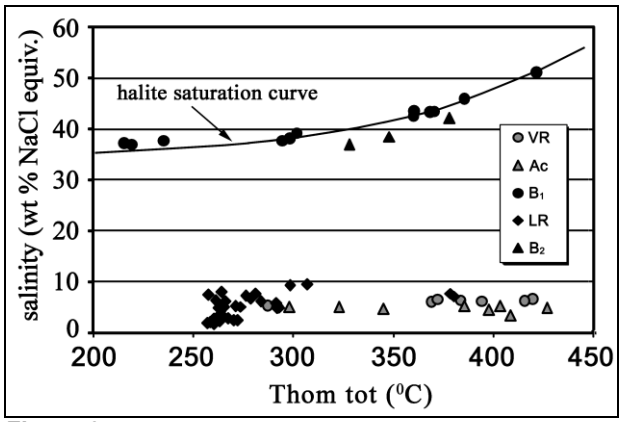

Figure 3. Summary plot of the microthermometric data of all fluid inclusion types at the Kadjaran deposit.

Liquid-rich (LR) fluid inclusion assemblages are the dominant inclusion type in the deposit. Petrographic observations of the sections of the economic mineralization stages, including quartz-molybdenite, quartz-molybdenite-chalcopyrite and quartz-chalcopyrite, indicate that the majority of the liquid-rich inclusions are secondary inclusions. They overprint the earlier stages as secondary trails. Final melting of ice of LR inclusions in quartz-chalcopyrite veins is between –1.4° and –2.0°C, corresponding to salinities of 2.41 to 3.39 wt % NaCl equiv. Total homogenization is between 296° ± 3° and 315 ± 5ºC. They have been trapped at pressures between 80 and 104 bars.

Ice-melting temperatures of LR inclusions in quartz - molybdenite - chalcopyrite vein fall between -1.0° and -1.7°C. Total homogenization temperatures lie between 257° ± 3° and 272 ± 4ºC. Salinities lie between 1.8 and

2.9 wt % NaCl equiv. The pressure of entrapment ranges between 46-55 bars.

Microthermometric data of this study for brine inclusions (ThL-V and Tmhalite), which were obtained following the methodology of Goldstein and Reynolds (1994) and data of previous studies were plotted on the diagram developed by Becker et al. (2008) (Fig. 4).

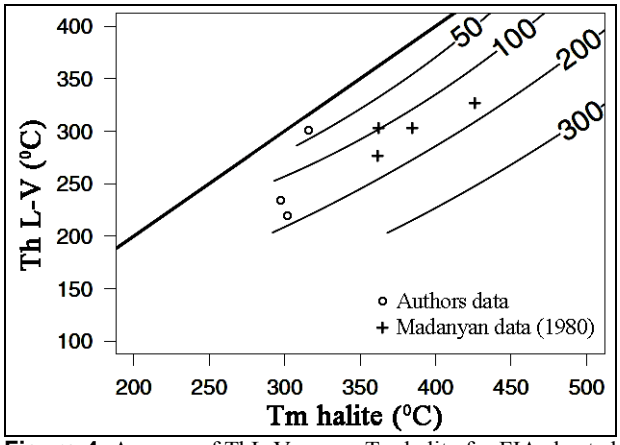

Figure 4. Average of ThL-V versus Tm halite for FIAs hosted in quartz from the Kadjaran molybdenum-copper - porphyry deposit. The plot displays the 50, 100, 200, and 300 MPa isobars as determined using synthetic fluid inclusions (Becker et al., 2008). The heavy diagonal line is the projection of the vapor-saturated halite solubility curve in ThL-V versus Tmhalite space (Th L-V = Tm halite).

The pressures obtained in our study are in agreement with the maximum pressure of 1.6 kbars (160 MPa) estimated by Madanyan (1980) for the Kadjaran deposit.

6 Discussion and conclusions

Detailed fluid inclusion petrography and microthermometry of the major and economic quartz-molybdenite, quartz- molybdenite- chalcopyrite, and quartz- chalcopyrite mineralization stages, revealed some characteristics of ore-forming fluids at Kadjaran.

Molybdenite precipitation within quartz-molybdenite mineralization stage were from high-salinity and initially from boiling fluids with the total homogenization temperatures between 360° and 425°C.

The main copper deposition at Kadjaran is associated to the chalcopyrite stage. It consists of small veins and veinlets. Copper sulfides were also precipitated mainly from high -salinity and high temperature fluids, but lower comparing with molybdenite precipitation.

The quartz- molybdenite- chalcopyrite stage formed in-between the two other mineralization stages mainly from lower salinity and lower temperature fluids in comparison with the two other stages.

The calculated pressures based on the fluid inclusion data are high at Kadjaran, higher than the ones reported in most porphyry systems. This discrepancy is still not fully understood. One explanation is that the high pressures obtained in our study may be related to overpressurized systems such as the ones reported by Erwood et al. (1979) at the Naica deposit, Mexico, or Rusk et al. (2008) at Butte, Montana, U.S.A.

Based on petrographic observations of the sections of economic mineralization stages quartz-molybdenite, quartz-molybdenite-chalcopyrite and quartz-chalcopyrite the majority of the liquid-rich inclusions are secondary inclusions. They were trapped at lower pressures and temperatures and overprint the earlier stages as secondary trails.

Acknowledgements

The authors would like to thank Cristina Tomé. She very much helped the first author during identification of fluid inclusions types and their petrographic and microthermometric studies. We gratefully thank Johannes Mederer for numerous assistances and useful discussions during all the time of studies at the University of Geneva.

This study was financially supported by the National Academy of Sciences of Republic of Armenia, the SCOPES Joint Research Projects Grant IB 7320-111046 and the Swiss National Science Foundation project 200020-121510.

References

Becker S P, Fall A, and Bodnar R J (2008) Synthetic Fluid Inclusions. XVII.1 PVTX Properties of High Salinity H_2O-NaCl Solutions (>30 wt % NaCl): Application to Fluid Inclusions that Homogenize by Halite Disappearance from Porphyry Copper and Other Hydrothermal Ore Deposits. Economic Geology, v. 103, pp. 539–554.

Driesner T & Heinrich CA (2007) The system H_2O-NaCl. I. Correlations for molar volume, enthalpy, and isobaric heat capacity from 0 to 1000 degrees C, 1 to 5000 bar, and 0 to 1 X-NaCl. Geochim. Cosmochim. Acta71, 4880-4901.

Erwood R J, Kesler S E and Cloke P L (1979) Compositionally distinct, saline hydrothermal solutions, Naica mine, Chihuahua, Mexico: Economic Geology, v. 74, p. 95–108.

Goldstein R H and Reynolds T J (1994) Systematics of fluid inclusions in diagenetic minerals: Society for Sedimentary Geology Short Course 31, p. 199.

Karamyan K A (1978) Geology, structure and condition of formation copper-molybdenum deposits of Zangezour ore region. Yerevan; Publishing House of the Academy of Sciences Armenian SSR, 179 p. (in Russian).

Karamyan K & Faramazyan A (1960) The mineraliztion stages of the Kadjaran copper-molybdenum deposit. The Izvestia of Academy of Sciences Armenian SSR., the series of geology and geography, № 3-4, p.65-88. (in Russian).

Madanyan O (1980) Conditions of formation of copper-molybdenum deposits Zangezur ore district according to the fluid inclusions. Summary report on the works of 1975-1980. Geological Sciences of Armenian SSR. Yerevan. 148 pp. (in Russian).

Melkonyan R, Ghukasyan R, Tayan R, Harutyunyan M (2008) Geo-chronometry of the Meghri pluton monzonites (Armenia) – results and consequences. Proceedings of the National Academy of Sciences of the Republic of Armenia, Earth Sciences., №2, p.3-10. (in Russian with English abstract).

Moritz R, Selby D, Ovtcharova M, Mederer J, Melkonyan R, Hovakimyan S, Tayan R, Popkhadze N, Gugushvili V, & Ramazanov V (2012) Diversity of geodynamic settings during Cu, Au and Mo ore formation in the Lesser Caucasus: New age constraints. 1st European Mineralogical Conference, 2-6 September 2012, Frankfurt, Germany, abstract volume.

Pashkov Y (1975) Physico-chemical features of ore-formation of Kadjaran copper-molybdenum deposit (according to the fluid inclusions study). Author's abstract of PhD thesis. M., 23 p. (in Russian).

Rusk B G, Reed M H and Dilles J H (2008) Fluid inclusion evidence for magmatic-hydrothermal fluid evolution in the porphyry copper-molybdenum deposit at Butte, Montana: Economic Geology, v. 103, p. 307–334.

Gold occurrence, mineral textures and ore fluid properties at the Viper (Sappes) epithermal Au–Ag–Cu orebody, Thrace, Greece

SP Kilias, M Paktsevanoglou, M Giampouras, A Stavropoulou, D Apeiranthiti, I Mitsis
National and Kapodistrian University of Athens, Fac. Geology and Geoenvironment, 157 84, Athens, Greece

J Naden, SJ Kemp, TJ Shepherd
British Geological Survey, Keyworth, Nottingham, NG12 5GG UK

T Koutles
Thrace Minerals S.A. 74, Papadima Str., PC 69300, Sappes, Rodopi, Greece

C Michael
IGME, Regional Branch of Eastern Macedonia and Thrace, Brokoumi 30, Xanthi 671 00, Greece

C Christidis
National and Kapodistrian University of Athens, Fac. Geology and Geoenvironment, 157 84, Athens, Greece

Abstract. Optical and electron microscopy studies coupled with Laser ablation analyses of pyrite and enargite of the Viper orebody at the Sappes gold prospect in Thrace, north-east Greece show that it has a number of characteristics in common with high sulfidation (HS) epithermal mineralisation. These include hypogene dickite, vuggy quartz and pyrite+enargite as the dominant sulfides. However, it also exhibits features such as (i) mineralization is flat-lying rather than an upwardly flaring vertical pipe-like structure more typical of HS mineralisation; (ii) high grade (>30 g/t) sections of drill core have a sericite-quartz pattern of alteration, spatially associated with advanced argillic+vuggy silica+silicification, and, iii) areas of colloform–banded and chalcedonic quartz can also be correlated with high-grade intersections, and, (iv) iv) sub-micron to micron-sized inclusions or chemically held gold within, pyrite and enargite.

Fluid inclusion data of decreasing salinity (1 to 6 wt% NaCl equiv.) and homogenization temperature (140 to 270ºC) indicate fluid mixing. It is suggested that the distribution of high-grade gold zones in the Viper orebody is the combined result of advanced argillic alteration, multi-stage hydrothermal brecciation and vuggy silica development, as well as ore-forming fluid chemistry changes, which are reflected by sericite and colloform banded quartz precipitation.

Keywords. Pyrite, enargite, gold, high-sulfidation, epithermal, fluid inclusion, Greece

Figure 1. Geological map showing the location of the Sappes gold prospect.

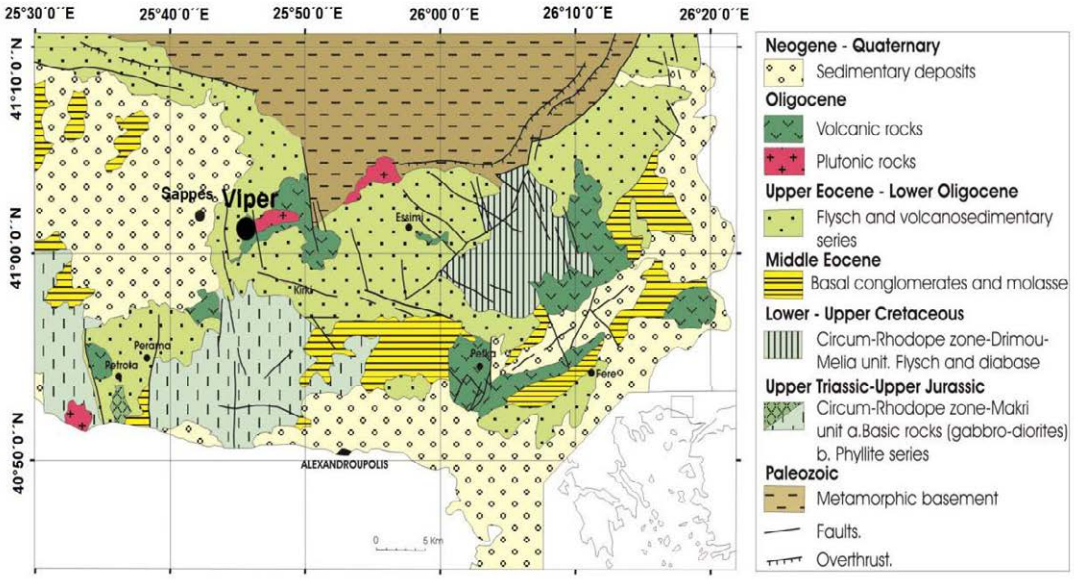

1 Introduction

The Viper orebody at the Sappes gold prospect in Thrace–north-east Greece (Fig. 1), is a high-grade Au–Ag–Cu deposit (280 kt @ 19.5 g/t Au; 9 g/t Ag; 0.4 % Cu—Glory Resources, 2012). The economic mineralization forms a northwesterly-trending, elongate "blind", flat-lying ~ 60 m thick orebody, and has estimated dimensions of 550 by 1310 m, at a depth of approximately 200–240 m below the current surface. Hydrothermal ore occurs as multi-stage silicified hydrothermal breccias, and disseminations in stockwork quartz veinlets and vug-fillings, within altered calc-alkaline to high–K Miocene andesitic–dacitic volcanic rocks. The host volcanics were extruded in a small volcano-sedimentary basin developed at the contact between the Rhodope metamorphic core complex and the Circum-Rhodope belt (Voudouris 2006, and references therein). It is classified as a high-sulfidation (HS) epithermal deposit (Arribas 1995; Cooke and Simmons 2000; Hedenquist et al. 2000) with an oxidation overprint.

2 Alteration and Mineralization

In terms of alteration, optical microscopy study and PIMA and XRD analyses of drill core identify at least 3 stages of hydrothermal alteration: (1) Pre-ore stage with advanced argillic (AAA I) and vuggy silica(VS) alteration that dominates the top of the preserved hydrothermal system above the Viper ore body. The AAA I alteration assemblage is quartz, pyrite, diaspore and pyrophyllite, that grades upwards to alunite±dickite, kaolinite, fine-grained pyrite and microcrystalline quartz; (2) Ore-stage IIa includes the apparent superposition of one event of gold associated advanced argillic+vuggy silica alteration+silicification (AAA II) and one event of argillic alteration+silicification (AAS), which are strongly correlated with hydrothermal breccias and veinlets. The AAA event is pervasive and is characterized by assemblages of dickite, pyrite, enargite, lesser alunite and Ca–Sr–Pb bearing aluminum-phosphate-sulphate (APS) minerals, in vugs. APS minerals, woodhouseite, svanbergite and hinsdalite overgrow tabular to bladed alunite. Dickite occurs as fine-grained masses. AAS alteration is characterized by sericite, colloform-banded quartz and pyrite without alunite, and it is interpreted to reflect an increase in mineralizing fluid pH, possibly a result of a reduction in magmatic-hydrothermal fluid flux and/or an incursion of meteoric water (Chouinard et al. 2005). At the microscopic scale a variety of complex Pb–Bi–Cu sulfosalts, tellurides and selenides are intimately associated with gold. Based on optical microscopy, SEM-EDS and Laser ablation ICP-MS studies, there are at least three major modes of occurrence for micron-sized gold at Viper (Fig. 3) that in decreasing order of abundance include: (i) readily liberated and discrete free native gold/electrum grains, intergrown with metallic minerals, quartz and APS minerals; (ii) discrete free native gold grains either enclosed in sulfides (i.e. pyrite, enargite, goldfieldite), in random position, or along growth zones in pyrite; and (iii) sub-micron to micron-sized inclusions or chemically held gold within, pyrite and enargite.

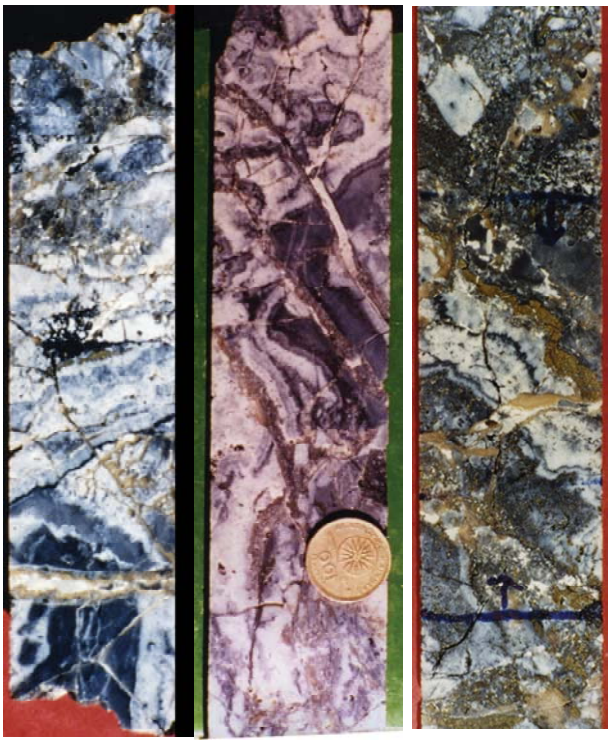

Figure 2. Drill core from a high-grade ore zone showing repeated silicification and alteration events

Enargite constitutes the most important and widespread Cu-ore mineral, comprising more than 30 per cent of the total sulfide content. Enargite is commonly intergrown with its polytype luzonite and with variable amounts of mainly pyrite, Pb–Bi–Cu sulfosalts, tellurides and selenides, gold, quartz, alunite, kaolinite/dickite. Elongate prismatic crystals are common and found in druse-like cavities in breccias and veinlets. The bulk of Au–Ag–Cu mineralization is invariably associated with AAA assemblages. Silica textures associated with high-grade gold ore include colloform-banded plumose quartz, colloform-banded jigsaw quartz, ghost-sphere and moss-textured quartz, and to a lesser extend feathery/flamboyant textured quartz and spider quartz–veinlets and are indicative of rapid deposition (Moncada et al. 2012) The textures that are most closely associated with elevated concentrations of Au are colloform-banded, plumose and jigsaw quartz, , and vuggy quartz; and, (3) Post-ore stage III includes advanced argillic alteration (AAA III) with alunite, quartz, dickite and pyrite containing veins, veinlets and cavity fillings that crosscut all previous alteration stages, and a final vuggy silica infilling by late amethystine quartz and barite.

3 Fluid Inclusion Microthermometry

Preliminary microthermometric measurements (Fig. 4) of primary aqueous liquid-rich fluid inclusions in auriferous plumose and jigsaw quartz from breccias and veinlets in high-grade (>11–63.4 g/t) intersections have decreasing salinties from 6 to 1 wt% NaCl eq. and Th

from 270 to 140ºC, indicating fluid mixing and cooling (Fig. 4). They coexist with low-density vapor-phase inclusions, suggesting low-pressure

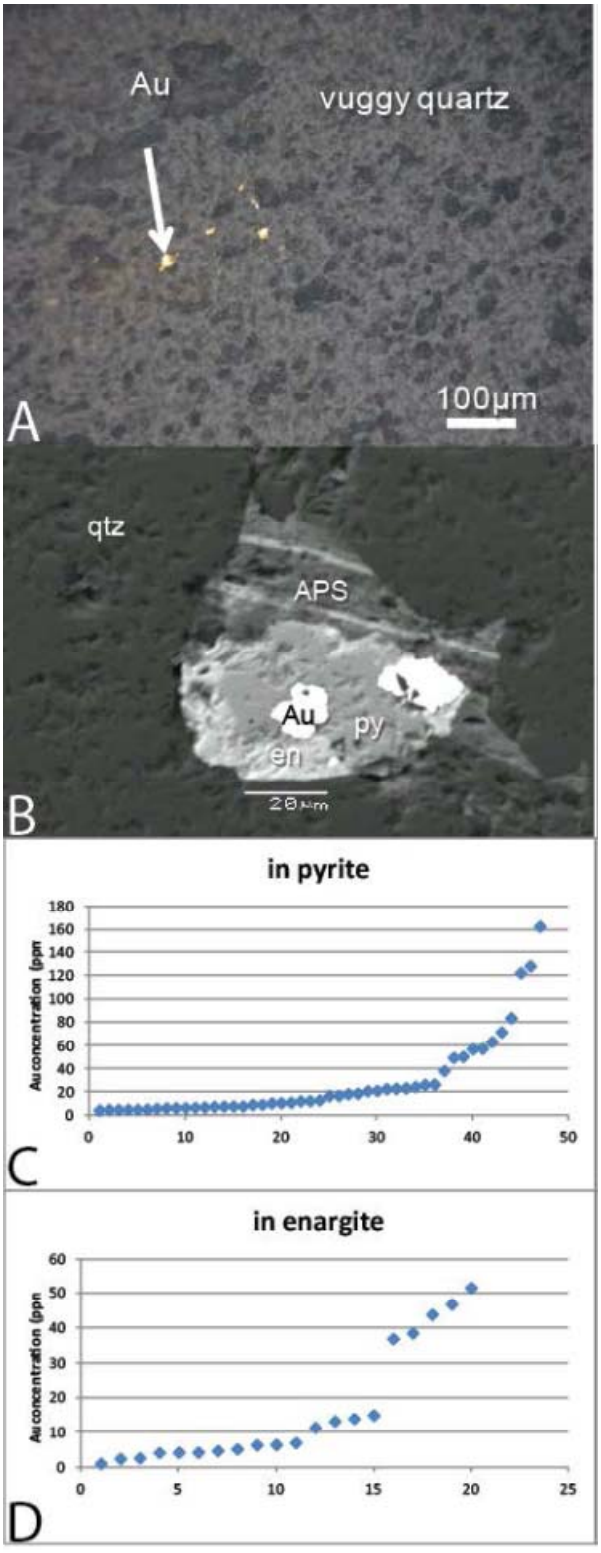

Figure 3. Different types of gold occurrence A: free gold; B: discrete free native gold/electrum grains enclosed in a microassemblage of pyrite, enargite and an alumina-phosphate sulfate (APS) mineral; C and D: Concentration of gold in sulfides and sulfosalts determined by laser ablation ICP-MS.

conditions. Precipitation of pyrite and enargite in response to rapid cooling of the system evidenced by colloform-banded quartz textures may have been the main control on deposition of pyrite- and enargite-hosted gold.

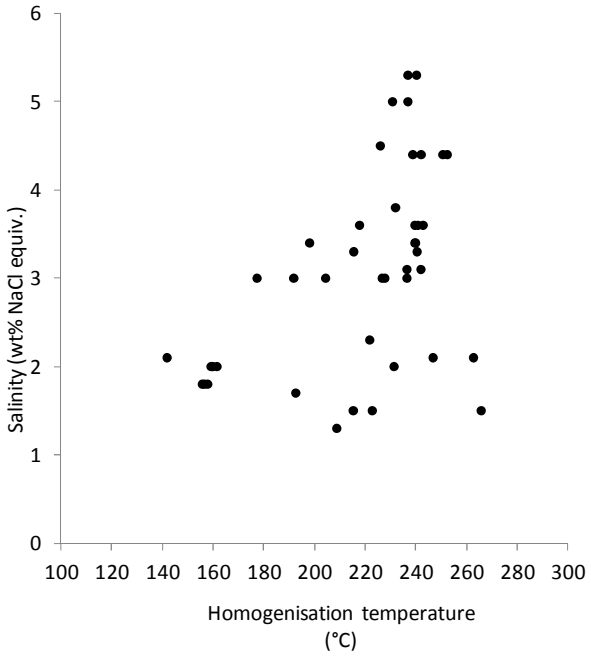

Figure 4. - Positive correlation of decreasing fluid inclusion homogenisation temperature and salinity indicating rapid cooling and fluid mixing

4 Discussion and Conclusions

Although similar in many respects to classic high-sulfidation epithermal deposits, the Viper deposit it has some atypical features: (i) drilling shows that the mineralization is flat-lying rather than an upwardly flaring vertical pipe-like structure more typical of HS mineralisation; (ii) Pima and mineralogical analyses show that high grade (>30g/t) sections of drill core have also a sericitic pattern of alteration, associated with advanced argillic+vuggy silica alteration+silicification. (iii) some sections of drill core show significant development of colloform–banded and chalcedonic quartz, that can be correlated with high-grade (>30 g/t) intersections, and (iv) sub-micron to micron-sized inclusions or chemically held gold within pyrite and enargite, as indicated b laser ablation analyses (Fig. 3c,d).

An important feature of the Viper deposit is the apparent changes in fluid chemistry, reflected by sericite and colloform-banded quartz, coupled by Cu–As-rich growth zones in pyrite(unpublished data)Gold and associated metals are interpreted to have been transported and deposited by magmatic fluids. In general, the distribution of the gold grade seems to be controlled by secondary porosity caused by multi-stage hydrothermal brecciation and widespread void-development as well as chemical changes of the mineralizing fluids.

Acknowledgements

This work was in part funded by a Marie Curie Experienced Researcher Fellowship to JN (HPMF-CT-2000-00762). Funding by the Special Account for Research Grants of the National and Kapodistrian University of Athens to SPK is thankfully acknowledged. JN publishes with permission of the Executive Director, British Geological Survey (NERC).

References

Arribas, A. Jr (1995) Characteristics of high-sulfidation epithermal deposits and their relation to magmatic fluid. In: Thompson JFH (ed) Magmas, Fluids, and Ore Deposits. Min Assoc Canada Short Course 23: 419–454

Chouinard A, Williams-Jones A. E., Leonardson, R. W., Hodgson, C. J., Silva, P., Téllez, C., Vega, Rojas, F. (2005). Geology and genesis of the multistage high-sulfidation epithermal Pascua Au-Ag-Cu deposit, Chile and Argentina. Economic Geology, 100:463-490.

Christofides G, Pecskay, Z, Eleftheriadis G, Soldatos T, Koroneos A, (2004) The Tertiary Evros volcanic rocks (Thrace, northeastern Greece): Petrology and K/Ar geochronology. Geologica Carpathica, 55: 397–409

Cooke, D.R., and Simmons, S.F., (2000) Characteristics and genesis of epithermal gold deposits: Reviews in Economic Geology, 13:241-244.

Glory Resources (2012) website http://www.gloryresources.com.au; accessed Nov 2012

Hedenquist JW, Arribas AR, Gonzalez-Urien E (2000) Exploration for epithermal gold deposits. Rev Econ Geol 13: 245–277

Moncada, D., Mutchler, S., Nieto, A., Reynolds, T.J., Rimstid, J.D., Bodnar, R.J. (2012) Mineral and fluid inclusion petrography of the epithermal Ag–Au deposits at Guanajuato, Mexico: Application to exploration. Journal of Geochemical Exploration, 114:20-35

Voudouris P, A comparative mineralogical study of Te-rich magmatic-hydrothermal systems in northeastern Greece. Mineralogy and Petrology, 87: 241-275.

Application of CL-imaging and mineral geothermometry on the porphyry gold deposit Biely vrch, Slovakia

Peter Koděra
Department of Geology of Mineral Deposits, Faculty of Natural Sciences, Comenius University, Mlynská dolina, 842 15 Bratislava, Slovakia, kodera@fns.uniba.sk

Jaroslav Lexa
Geological Institute, Slovak Academy of Sciences, Dúbravská cesta 9, 840 05 Bratislava, Slovakia

Patrik Konečný
State Geological Institute of D. Štúr, Mlynská dol. 1, 817 04 Bratislava, Slovakia

Abstract. Recently developed mineral geothermometers, especially their combination for proper calibration, have been used to evaluate the pressure-temperature (P-T) path that magma and fluids followed during formation of the Biely vrch Au-porphyry deposit. CL imaging enabled to visualize complicated relationships in porphyry quartz stockworks combined with TitaniQ geothermometer calibrated for the local conditions. Other geothermometers included plagioclase-amphibole thermobarometry, two-feldspars thermometry, Fe-Ti oxides thermometry and Zr-in-rutile thermometry. Early evolution of magma took place at 720–700 °C in the depth of ~22 km. Emplacement of fluid-saturated magma to the present position took place at ~725 °C, in low pressure environment of shallow depth (~500 m). Early quartz veinlets started to form, but majority of the A-type veinlets precipitated in range 580–650°C. Subsequent cooling resulted in progressively decreasing amount of precipitating quartz, with the minimum in range from 460 to 380°C, corresponding to retrograde solubility of quartz. Large proportion of vein quartz has precipitated below 380°C, after fluid decompression due to change from lithostatic to hydrostatic pressure conditions when most porphyry ore bodies are precipitated.

Keywords. cathodoluminiscence, geothermometers, TitaniQ, porphyry gold

1 Introduction

Quantitative evaluation of the pressure-temperature (P-T) paths that magmas and fluids follow during and after their emplacement is essential information to model evolution of any porphyry-type ore deposit. Most usually applied technique is fluid inclusion microthermometry, however, in cases where measureable fluid inclusions are rare, mineral geothermometers and geobarometers have to be applied. Various mineral geothermometers enable to calculate temperatures or pressures from precise WDS microanalyses of quartz, rutile, Fe-Ti oxides, amphibole and/or feldspars. Due to the abundance of vein quartz, porphyry systems can be well studied by the recently developed Ti in quartz geothermometer (TitaniQ; Thomas et al. 2010), especially in combination with SEM–cathodoluminescence (CL), since Ti concentration in quartz is a function of CL intensity as well as temperature (Rusk et al. 2008). However, due to problems of proper calibration of this geothermometer, a combination of several independent geothermometers is the best approach.

2 Biely Vrch Deposit

The Biely Vrch deposit is located in the central zone of the Javorie andesite stratovolcano, situated in the NE part of the Central Slovakian Volcanic Field on the inner side of the Carpathian arc. The central zone of this stratovolcanic structure hosts several small deposits and occurrences of Au-porphyry mineralization (Hanes et al. 2010), but just the locality Biely vrch represents an economic accumulation of ore. The deposit is centered on a diorite to andesite porphyry stock 300x400 m in size, emplaced into andesitic volcanic host rocks.

Parental diorite porphyry intrusion contains 40 to 50 % phenocrysts of amphibole, biotite, plagioclase and quartz. Rare quartz phenocrysts are strongly resorbed. Groundmass is microhypidiomorphic, composed of plagioclase, quartz, sporadic K-feldspar, mafic minerals and accessory apatite, magnetite, ilmenite. In shallower level primary minerals are obscured by alteration. Relics of groundmass are finer grained, and locally host quartz "eyes" up to 1 mm in diameter. Prior to its emplacement, magma was composed of roughly 50 % phenocrysts in highly differentiated K_2O-rich melt of rhyolitic composition as indicated by analyses of melt inclusions in amphibole phenocrysts.

The porphyry stock and surrounding andesite are affected by extensive hydrothermal alteration (Koděra et al. 2010). Intermediate argillic alteration dominates, and variably overprints earlier high-temperature K-silicate and Ca-Na silicate alteration at deeper levels of the system. Propylitic alteration affects the outer zone of the system. Ledges of advanced argillic alteration represent the youngest stage of alteration. Hydrothermal veinlets. include earliest biotite-magnetite veinlets associated with and several generations of quartz veinlets including A-type and later banded quartz with banding resulting from high content of vapour-rich fluid inclusions and tiny magnetite and ilmenite grains. Rare veinlets of sulphides (mostly pyrite, chalcopyrite) are related to intermediate argillic alteration (Koděra et al. 2010).

Mineralization extends from surface to a depth of at least 740 m. Stockwork of quartz veinlets marks the area of economic Au mineralization that has a very low Cu/Au ratio (0.018 wt% Cu/ppm Au; Hanes et al. 2010). Small gold grains of high fineness occur next to quartz veinlets in altered rock with clays, chlorite and K-feldspar, sometimes attached to sulphides or Fe-Ti oxides (Koděra et al. 2010).

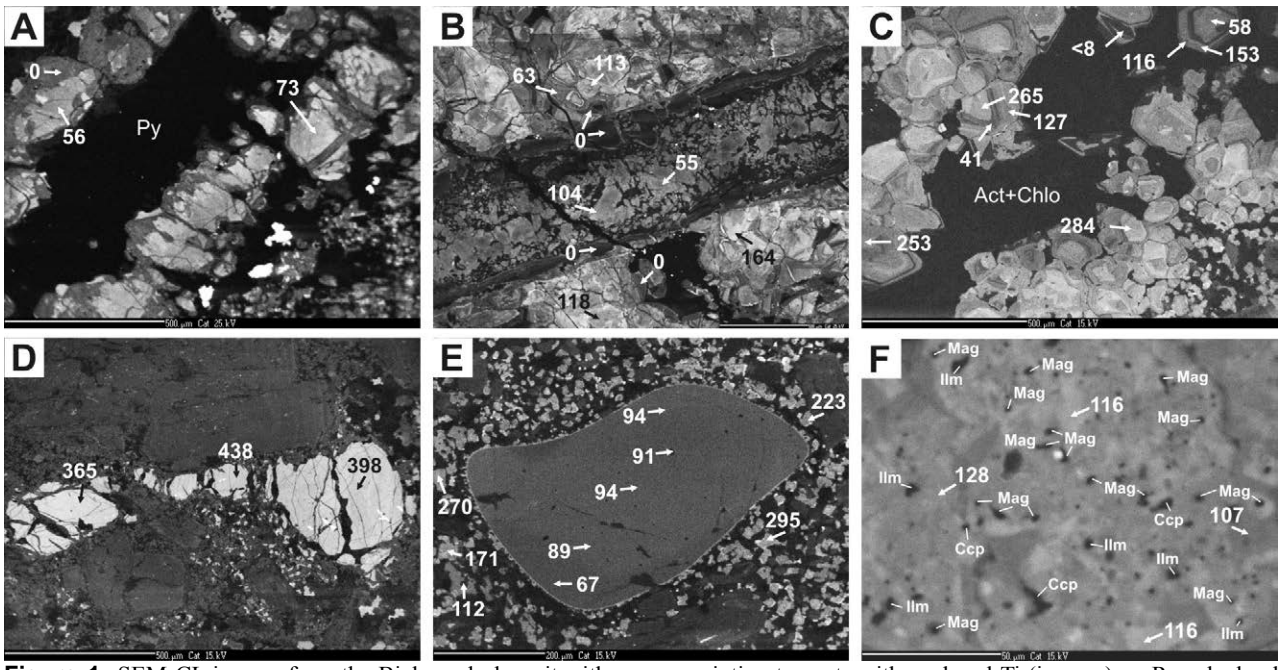

Figure 1. SEM-CL images from the Biely vrch deposit with arrows pointing to spots with analysed Ti (in ppm): a. Resorbed pale early quartz grains, with late quartz associated with pyrite (Py); b. Dark banded quartz crosscutting A-type vein with different cycles of vein filling; c. Early A-type vein in deep fresh porphyry with actionolite– chlorite filling; d. Quartz eye in shallow porphyry; e. Resorbed quartz phenocryst in groundmass; f. A-type quartz with inclusions of Fe-Ti minerals used for Fe-Ti geothermometry.

The volcanological reconstruction of the Javorie stratovolcano indicates that the intrusion was emplaced in a depth of about 500 m below the paleosurface. (Konečný et al. 1998). Shallow emplacement is also suggested by dominant vapour-rich fluid inclusions, locally accompanied by Fe-rich hydrous salt melts, probably resulting from magmatic fluid immiscibility of fluids at very low pressure (Koděra et al. 2011).

3 Cathodoluminiscence imaging

CL study showed that quartz in earliest A-veinlets has the strongest luminescence, while the latest banded veinlets showed the weakest luminescence (Fig. 1). Most of the A-veins contained both early and late quartz with strong and weak CL response, respectively, as well as various transitional phases, overgrown or crosscutting in a complicated manner in several cycles (Figs. 1 a-c). Resorbtion of early quartz grains with strong luminescence has been also often observed (Fig. 1a). Quartz eyes hosted by porphyry groundmass showed very strong luminescence (Fig. 1d). This was in contrast to relatively low luminescence of resorbed quartz phenocrysts (Fig. 1d). Finegrained quartz in groundmass showed tile-like texture with brighter cores and darker margins, indicating partial subsolidus recrystallisation and overgrowth by hydrothermal quartz (Fig. 1d).

4 Thermobarometry

For application of selected thermobarometers WDS microanalyses of silicates and Fe-Ti oxides were carried out on the instrument CAMECA SX-100 at standard conditions. Precise analyses of Ti and Zr for the application of TitaniQ and Zr in rutile geothermometers were measured at current 180 nA simultaneously on two spectrometers in 5 cycles, each lasting 1 minute, resulting in detection limits ~8 ppm Ti and ~35 ppm Zr.

Plagioclase-amphibole thermobarometry (Holland and Blundy 1994; Anderson and Smith 1995) was applied on 18 pairs of minerals at phenocrysts contacts or plagioclase inclusions in amphibole. The thermobarometer produced temperature range 733–660°C (mean 703°C, σ 19.6°C) and pressure in the range 7.5–4.4 kb (mean 5.8 kb, σ 0.72 kb).

Two-feldspar thermometry (Putirka 2008 - average of two equations and global regression) applied on 7 plagioclase-K-feldspar pairs in groundmass provided temperature range 749–617°C. Nine feldspar pairs in intergranular spaces of a deep A-type quartz vein (with recrystallised melt inclusions and actinolite, chlorite, epidote and magnetite in central part of the vein) produced temperature range 720–475°C.

Fe-Ti oxides geothermometry also enables to calculate oxygen fugacity and activity of TiO_2 (Ghiorso and Evans 2008). It was applied on 14 pairs of magnetite and ilmenite inclusions in amphibole phenocrysts, 40 pairs representing aggregates in groundmass and 61 pairs in vein quartz, but most of the analyses were affected by partial alteration of ilmenite to leucoxene. Inclusions in amphibole provided a single reasonable result 718°C, $\log fO_2(NNO) = 0.80$ and $aTiO_2 = 0.74$. In groundmass 14 pairs unaffected by alteration yielded broad ranges of temperature 399–702°C and $aTiO_2$ 1.0–0.50. A linear regression provided the relationship $aTiO_2 = 1.16 - 0.0007*T°C$. Isolated 17 magnetite and 12 ilmenite inclusions in vein quartz (DVE-1/100.5 m; Fig. 1f) enabled calculation of 61 Fe-Ti oxide pairs (by combination in 4 classes based on Ti content in magnetite and Fe content in ilmenite), resulting in temperature range 736–526°C and $aTiO_2$ range 0.79–0.58. A linear regression provided the relationship $aTiO_2$

= 1.06 - 0.0006*T °C. As other geothermometers applied on the same area of vein quartz provided much smaller interval of temperatures 612–591°C (see below), the large interval of Fe-Ti oxide temperatures is most probably a result of a fast disequilibrium precipitation. More useful is the temperature and activity calculated from a pair of mean magnetite and mean ilmenite compositions (599°C; 0.69 $aTiO_2$).

Zr-in-rutile thermometry (Tomkins et al. 2007) was used on 19 grains of rutile, representing aggregates in altered groundmass in 6 samples, and on 4 grains enclosed in vein quartz in 2 samples. Rutile in altered rock provided temperatures from 612 down to <480°C (Zr detection limit). Rutile in veins yielded 580–611°C.

Ti-in-quartz (TitaniQ) is the most widely used geothermometer in this study. There are two recent calibrations of this geothermometer. While the calibration of Thomas et al. (2010) reflects a relatively fast growth rate leading to higher Ti concentrations, the calibration of Huang and Audétat (2012) reflects a relatively slow growth rate leading to lower Ti concentrations. Therefore, the later calibration provides a considerably higher temperature for a given Ti concentration. Furthermore, the geothermometer requires information on $aTiO_2$ during quartz growth which is often difficult to constrain. The effect of lowering $aTiO_2$ shifts the geothermometer curves towards higher temperatures, thus approaching curves of Thomas et al. (2010) at lower $aTiO_2$ to curves of Huang and Audétat (2012) at higher $aTiO_2$ (Fig. 2). In other words, the effect of slower growth rate is similar as the effect of decreasing activity. In order to create appropriate calibration curves for our system, we have tried to fix the temperature with other geothermometers by lowering of $aTiO_2$ in the relevant formula of Thomas et al. (2010) to obtain desired temperature. The correction factor for slower growth rate -0.145 $aTiO_2$ was calculated by fitting the mean temperature of vein quartz in the sample DVE-1/100.5 m with the mean temperature of included Fe-Ti oxides (599 ºC).

As the activity of TiO_2 is likely to change with changing temperature, gradient of changing $aTiO_2$ had to be incorporated in the calibration to calculate correct calibration curve. Ghiorso et al. (2013) have concluded that genetically related groups of Fe-Ti oxide pairs show negative activity–temperature trends. As discussed above, our Fe-Ti oxide pairs show such trends and provided equations related to groundmass hosted pairs and vein hosted pairs. TiO_2 activities predicted by these equations were used with the formula of Thomas et al. (2010) via 4-step iteration. Application of the calibrated curves also includes correction for the real depth of the analyzed samples (lithostatic pressure corresponding to present depth + 500 m of estimated eroded overburden). A different calibration had to be applied to quartz eyes showing extremely high Ti content. Ti enrichment can be explained here by an increase of $aTiO_2$ of parental residual melt due to preferential partitioning of Ti in the melt after fluid exsolution (Vasyukova et al. 2013). The $aTiO_2$ was set here to obtain temperature of magma crystallization determined above.

The calibrated TitaniQ geothermometer was applied to samples of vein quartz, quartz eyes, quartz in groundmass and quartz phenocrysts, with results plotted in Figure 3. Vein quartz was examined by 154 analyses applied on 20 samples from different depths. Ti content in nearly all analysed quartz was well corresponding to intensity of cathodoluminiscence. A few exceptions were most likely related to tiny inclusions of Ti-bearing minerals. Analyses of Ti provided a broad continuous range of values from 0 to 326 ppm, corresponding to temperatures from 744 to < 380°C (detection limit of Ti). Frequency histogram (Fig. 3) shows irregular distribution of values with peaks in ranges 700–740°C indicating temperature of magma solidification, 580–650°C related to major temperature range for precipitation of A-type veinlets and a strong peak at <380°C, corresponding to precipitation of banded veinlets. Systematically highest Ti content in quartz veinlets was measured in early veinlet hosted by relatively fresh porphyry from depth of 751 m corresponding to temperatures up to 728°C.

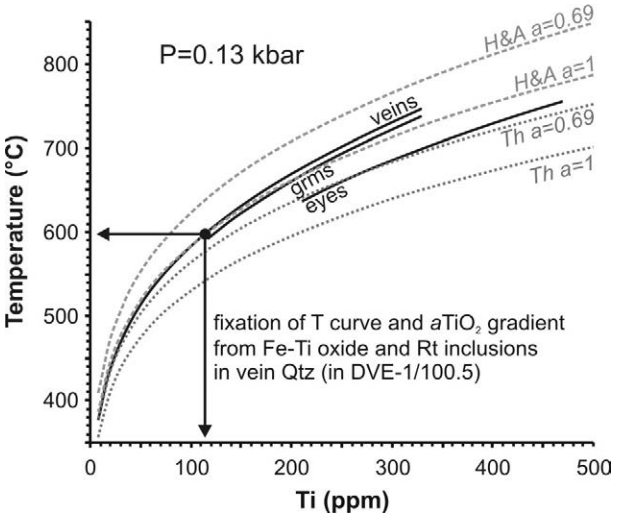

Figure 2. Calibration curves of the TitaniQ geothermometer for quartz veins, quartz eyes and quartz in groundmass (grms) in this study, calculated at 0.13 kbar. Also shown are curves calculated from Thomas et al. (2010) and Huang and Audétat (2012) for two different TiO_2 activities (1 and 0.69). See text for details for methods of calculation of calibration curves.

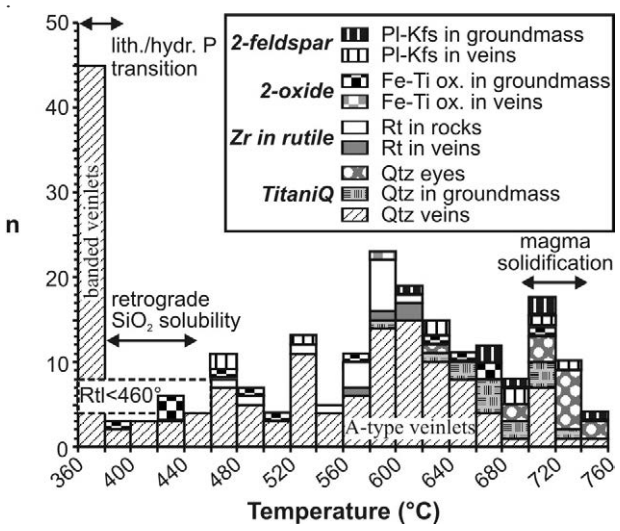

Figure 3. Frequency histogram of temperatures obtained from different geothermometers in this study (except phenocrysts).

Groundmass quartz grains were examined by 14 analyses in two deep samples, providing temperature range 725–592°C. Quartz "eyes" were examined by 15 analyses in two shallow samples, providing temperature range 753–636°C with the mean temperature 725 °C.

Partially resorbed quartz phenocrysts provided 65 to 95 ppm Ti. Two ranges of temperatures 646–685°C and 812–862°C were calculated using calibrations of Thompson et al. (2010) and Huang and Audétat (2012), respectively, at $aTiO_2$ 0.74 (from Fe-Ti oxides thermometry) and at 5.8 kbar (from plagioclase-amphibole barometry). This indicates that to obtain real temperatures, some correction for growth rate has to be applied.

5 Discussion and conclusions

Application of different geothermometers enabled reconstruction of P-T evolution from magmatic to late hydrothermal stages in the studied Au-porphyry system. Data from Fe-Ti oxide geothermometry (718 °C) and plagioclase-amphibole thermobarometry (703±20°C; 5.8±0.72 kb) from phenocrysts of the porphyry intrusion correspond to depth of ~22 km. Thick reaction rims of amphiboles and biotite and resorbtion of quartz phenocrysts confirm the high-pressure evolution of magma before the intrusion emplacement. Relationship among pressure, temperature and water content of haplogranite melts (Holtz et al. 2001) implies water content of magma around 7 %. Such melt would reach saturation by fluids in the depth of 3–4 km. As indicated by maximum crystallization temperatures of groundmass and veins, emplacement of fluid-saturated magma occurred at ~725°C, in shallow depth (~500 m). Lower temperatures obtained from groundmass indicate subsolidus re-equilibration.

Early hydrothermal fluids started to form veinlets already at temperatures of final magma solidification, supported by the presence of silicate melt inclusions hosted in grains with highest determined temperatures. However, majority of A-type veinlets have formed at lower temperatures (580–650°C) at ductile conditions, probably after the exsolving fluids were able to accumulate and focus into dynamic fluid plumes, that probably occurred in several cycles (Weiss et al. 2012). High temperatures of A-type veinlets correspond to the presence of salt melt inclusions that show anomalously high homogenization temperatures (>850°C; Koděra et al. 2011) probably related to post-entrapment modification due to ά- to β-quartz that occurs at 573°C.

Subsequent cooling resulted in progressively decreasing amount of precipitating quartz, with the minimum in range from 460 to 380°C. This interval coincides with retrograde solubility of quartz during isobaric cooling from ~450 to 350°C at <0.3 kb (Fournier 1985). Large proportion of vein quartz has precipitated below 380°C, including all veinlets with banded structure. These bands are commonly botryoidal, suggesting that the quartz has crystallized due to a quick oversaturation of SiO_2 after fluid decompression at 350-400°C, where brittle-ductile transition starts and corresponds to change from lithostatic to hydrostatic pressure conditions (Cathles 1993). In the interval 425 to 320°C bulk of metals in porphyry ore bodies precipitate (Richards 2011), including golg in porphyry gold deposits (Muntean and Einaudi 2001).

Acknowledgements

This study was supported by the Slovak Research and Development Agency, contract No. 0537-10.

References

Anderson JL, Smith DR (1995) The effect of temperature and oxygen fugacity on Al-in-hornblende barometry. Am Mineral 80: 549-559.

Cathles LM (1993) A capless 350°C flow zone model to explain megaplumes, salinity variations, and high-temperature veins in ridge axis hydrothermal systems. Econ Geol 88: 1977-1988.

Fournier RO (1985) The behavior of silica in hydrothermal solutions. In: Berger BR, Bethke PM (eds) Geology and geochemistry of epithermal systems. Rev Econ Geol Vol. 2. Society of Economic Geologists, Littleton, pp 45–61

Ghiorso MS, Evans, BW (2008) Thermodynamics of rhombohedral oxide solid solutions and a revision of the Fe-Ti two-oxide geothermometer and oxygen-barometer. American J of Science 308: 957-1039.

Ghiorso MS, Gualda GAR (2013) A method for estimating the activity of titania in magmatic liquids from the compositions of coexisting rhombohedral and cubic iron–titanium oxides. Contrib Mineral Petrol 165: 73-81.

Hanes R, Bakos F, Fuchs P, Žitňan P, Konečný V (2010) Exploration results of Au porphyry mineralizations in the Javorie Stratovolcano. Mineralia Slovaca 42: 15-32

Holland T, Blundy J (1994) Non-ideal interactions in calcic amphiboles and their bearing on amphibole-plagioclase thermometry. Contrib Mineral Petrol 116: 433-47.

Holtz F, Johannes W, Tamic N, Behrens H (2001) Maximum and minimum water contents of granitic melts generated in the crust: a reevaluation and implications. Lithos 56: 1-14.

Koděra P, Lexa J, Biroň A (2010) Gold mineralization and associated alteration zones of the Biely Vrch Au-porphyry deposit, Slovakia. Mineralia Slovaca 42: 33-56.

Koděra P, Heinrich CA, Wälle M, Fallick AE (2011) Au mineralisation at Biely Vrch deposit (W Carpathians, Slovakia): example of a very shallow porphyry system. In: Barra F, Reich M, Campos E, Tornos F (eds) Let's Talk Ore Deposits. Proc 11th SGA Meeting, Antofagasta, 417-419.

Konečný V et al. (1998) Explanatory text to geological map of Javorie 1 : 50 000. Geological Survey of the Slovak Republic, Bratislava (in Slovak with English summary).

Muntean JL, Einaudi MT (2001) Porphyry-epithermal transition: Maricunga belt, northern Chile. Econ Geol 96: 743-772.

Putirka KD (2008) Thermometers and barometers for volcanic systems. In Putirka KD, Tepley-III FJ (eds) Minerals, Inclusions and volcanic processes. Review in Mineralogy and Geochemistry 9: 61-120.

Rusk BG, Lowers HA, Reed MH (2008) Trace elements in hydrothermal quartz: Relationships to cathodoluminescent textures and insights into vein formation. Geology 36: 547-550.

Thomas JB, Watson EB, Spear FS, Shemella PT, Nayak SK, Lanzirotti A (2010) TitaniQ under pressure: the effect of pressure and temperature on the solubility of Ti in quartz. Contrib Mineral Petrol 160: 743-759.

Tomkins HS, Powell R, Ellis DJ (2007) The pressure dependence of the zirconium-rutile thermometer. J. Metamorphic Geol 25: 703-713.

Vasyukova OV, Goemann K, Kamenetsky VS, MacRae CM, Wilson NC (2013) Cathodoluminescence properties of quartz eyes from porphyry-type deposits: Implications for the origin of quartz. Am. Mineralogist 98: 98-109.

Weiss P, Driesner T, Heinrich CA (2012) Porphyry-copper ore shells form at stable pressure-temperature fronts within dynamic fluid plumes. Science 338: 1613-1616.

Metal zoning and precipitation mechanisms in porphyry systems

Kalin Kouzmanov
Earth and Environmental Sciences, University of Geneva, 13 rue des Maraîchers, CH-1205 Geneva, Switzerland

Gleb S. Pokrovski
Géosciences Environnement Toulouse, GET, University of Toulouse, CNRS-IRD-OMP, 14 av. E. Belin, F-31400 Toulouse, France

Abstract. A great majority of porphyry districts around the world show a regular pattern of zonal metal distribution – both vertically and laterally. Metal zonation commonly consists of a Cu±Mo±Au core ringed by successive Cu-Zn, Zn-Pb-Ag, Pb-Ag (±Mn), and As-Sb-Hg±Au zones. If a high-sulfidation epithermal system is developed above the porphyry center, a vertical Cu±Au±Ag zone may be present in the central upflow conduits.

Comparing metal content in natural fluid inclusions from porphyry and associated skarn and epithermal deposits with thermodynamic predictions provides useful constraints on the mechanisms and processes controlling metal transport and deposition in porphyry systems. Results show that decompression and cooling of a magmatic fluid, accompanied by boiling and water-rock interaction, are likely to be the major causes of zonal metal deposition in magmatic-hydrothermal systems. Large-scale fluid mixing is a relatively uncommon phenomenon during metal precipitation and is not expected to be a major cause of ore formation in the porphyry environment.

Keywords: porphyry systems, fluids, metal zoning, solubility, precipitation

1 Introduction

Porphyry deposits are composite magmatic-hydrothermal systems that involve large volumes (10 to >100 km^3) of altered rocks resulting from extensive circulation of hydrothermal, dominantly magmatic in origin, fluids at shallow crustal levels (Seedorff et al. 2005, Sillitoe 2010). No matter their age, tectonic setting, and size, porphyry systems around the world share common alteration and mineralization styles with broadly similar spatial distribution patterns (Meyer and Hemley 1967, Lowell and Gilbert 1970, Rose 1970). Broad-scale alteration zoning comprises sodic-calcic, potassic, chlorite-sericite, sericitic, and advanced argillic assemblages, from the base upward and outward to propylitic alteration and is commonly associated with ore-body to district-scale metal zoning (Fig. 1).

In this contribution we discuss different processes controlling mineral solubility, metal transport and deposition, and zonal distribution of metals in magmatic-hydrothermal systems.

2 Metal zoning in porphyry systems

A characteristic feature of many porphyry systems is the regular pattern of zonal metal distribution – both vertically, from deep levels proximal to the composite porphyry stocks to near-surface epithermal environment, and laterally, from centrally located potassic alteration to marginal propylitic zones (Fig. 1).

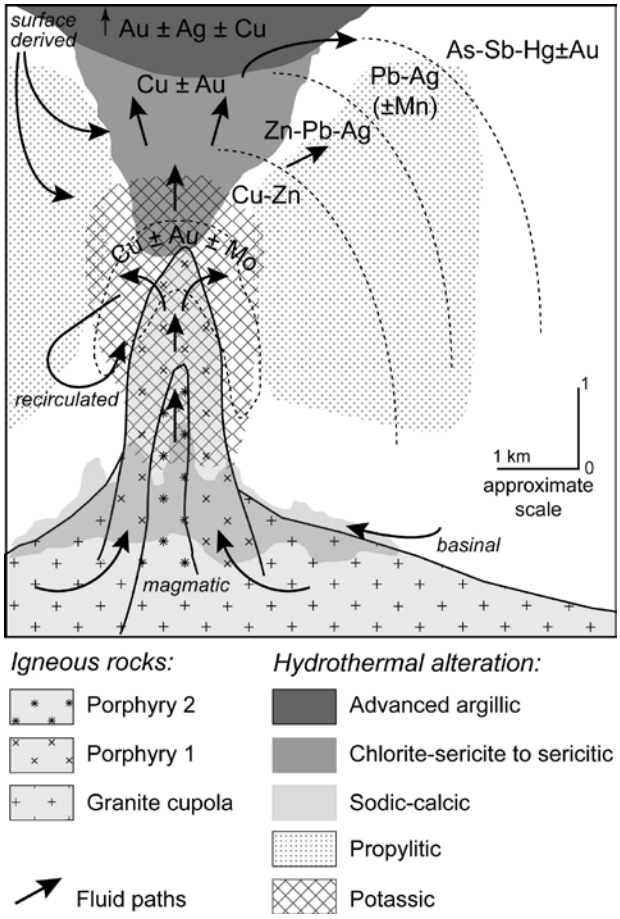

Figure 1. Generalized scheme of metal zoning, alteration pattern and fluid paths in a porphyry-centered system. Ore shell of Cu±Au±Mo is centered on the porphyry stock and extends to the wall rocks. Outward base-metal zoning, commonly observed in porphyry-centered districts, includes in order of increasing distance from the porphyry: Cu-Zn, Zn-Pb-Ag, Pb-Ag (±Mn), and As-Sb-Hg-Au zones. Modified from Kouzmanov and Pokrovski (2012), based on Seedorff et al. (2005, 2008) and Sillitoe (2010).

In porphyry-centered districts like Butte, Bingham Canyon, Mineral Park, Tintic (USA), Morococha (Peru), the Cu±Mo±Au association characterizes the central, deep parts of the systems, forming an ore shell in the upper parts of the potassic alteration zones. Vertical Cu±Au±Ag zones may be present in the upflow conduits

above the centers of the systems, as high-sulfidation Cu-Au-Ag lodes and high-sulfidation disseminated epithermal Au-Ag deposits. However, due to erosion, these zones are commonly absent in porphyry-centered districts; in such cases, a Cu±Mo±Au core ringed by successive Cu-Zn, Zn-Pb-Ag, Pb-Ag (±Mn), and As-Sb-Au-Hg zones is observed. Metal zoning both upward and outward from the core is a primary function of mineral solubility, transport, and depositional mechanisms of base and precious metals, controlled by intensive parameters of the fluids as discussed below.

3 Major processes leading to metal precipitation in porphyry systems

During their evolution in porphyry systems, magmatic-hydrothermal fluids undergo five major processes that cause metal distribution and deposition: decompression, phase separation, cooling, fluid-rock interaction, and mixing with external waters. These processes are interconnected and one may overprint or act in parallel with another in various parts of the systems. As a result, variations of fluid parameters, such as temperature, pressure, salinity, pH, and H_2S content, affect solubility of the main base- and precious metal minerals resulting in ore formation in both, porphyry and epithermal environments. The effect of these parameters on the different ore-mineral solubility may be qualitatively evaluated using the available thermodynamic data for the major ore minerals and metal aqueous species (Fig. 2). These predictions, when combined with the fluid compositions inferred from natural fluid inclusions allow a first-order estimation of metal behavior and fractionation during the evolution of the magmatic ore-bearing fluid, as discussed below.

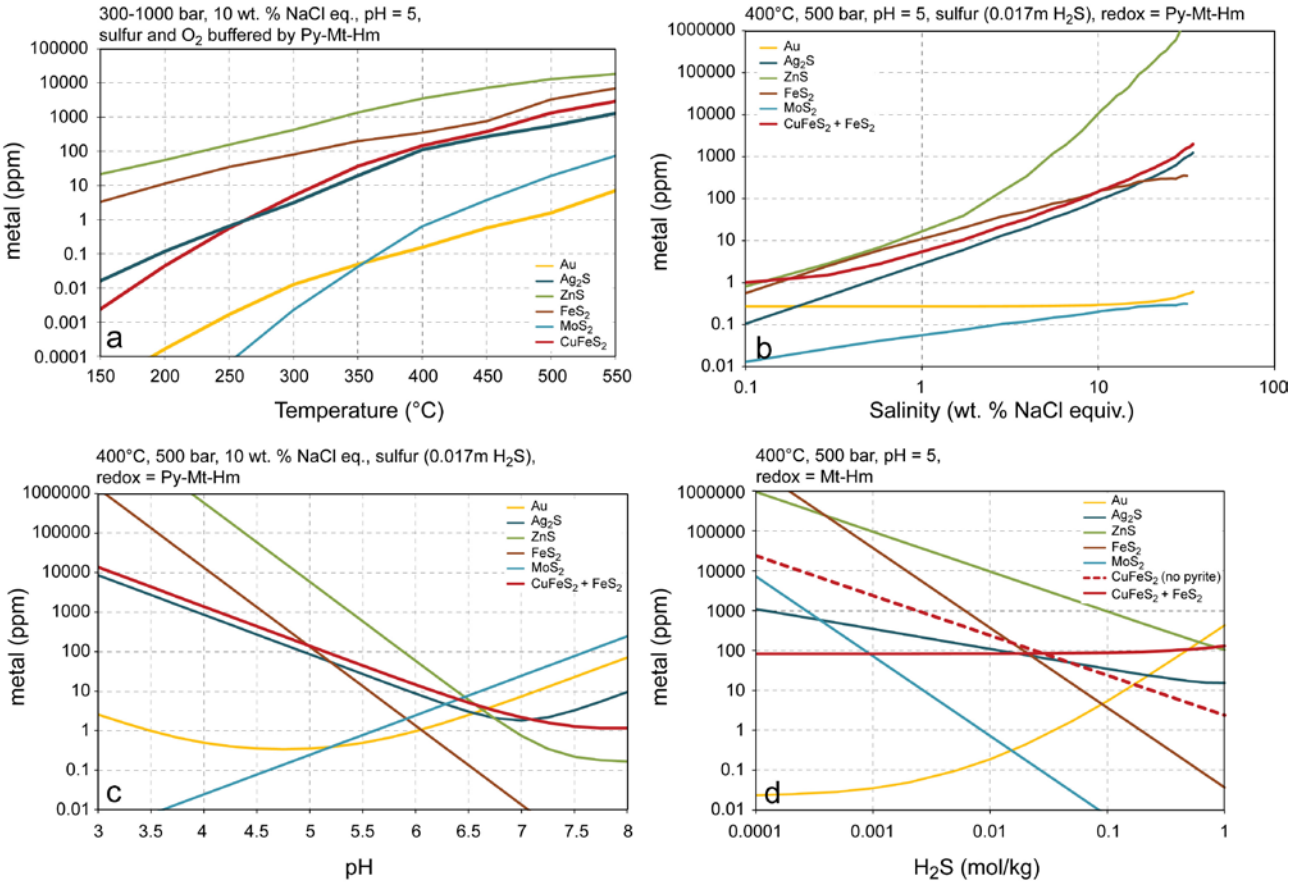

Figure 2. Solubility of chalcopyrite, pyrite, sphalerite, molybdenite, argentite, and native gold as a function of temperature (a), salinity (b), pH (c) and H_2S concentration (d) of hydrothermal fluids under conditions relevant to porphyry Cu (-Mo-Au) formation. Calculations are preformed with using HCh computer code (Shvarov 2008). Thermodynamic properties of the minerals are taken from SUPCRT (Johnson et al. 1992) and sources of the stability constants of metal complexes are summarized in Kouzmanov and Pokrovski (2012). *Abbreviations:* Hm – hematite, Mt – magnetite, Py – pyrite.

3.1 Decompression and phase separation

On their ascent toward the surface magmatic-hydrothermal fluids undergo pressure decrease, resulting in phase separation and temperature decline. Quantifying the effect of fluid decompression on solubilities of sulfide minerals is difficult because of lack of experimental data. In contrast, the available data clearly demonstrate that decompression strongly affects quartz solubility whose changes induce either precipitation or dissolution (depending on T and P). This has an impact on vein formation and fluid flow by changing host rock permeability in the porphyry environment.

Phase separation is recorded in various parts of magmatic-hydrothermal systems by co-existing liquid- and vapor-rich fluid inclusions. In the deep porphyry

environment, phase separation leads to condensation of a minor amount of hypersaline liquid from the dominant low-salinity vapor phase. Metal distribution during this process is controlled by vapor-liquid partitioning coefficients, which depend on the vapor and liquid densities, S and Cl content, and metal chemical speciation in both phases. As evidenced by *in situ* analyses of metals in individual fluid inclusions from porphyry systems, Fe, Mn, Zn, Pb, and Ag, which form chloride complexes in both phases, are largely enriched in the saline chloride liquid, whereas Au, which forms hydrogen sulfide complexes, is systematically enriched in the vapor phase (Fig. 3). Sulfur is likely to play an important role in the distribution of Cu and Au between liquid and vapor phases, particularly considering the fact that the mass of the S-enriched vapor produced during magmatic fluid separation largely exceeds that of the hypersaline liquid. Metalloids, like As and Sb, and Mo show, on average, similar concentrations in the liquid and vapor phase, consistent with the volatile properties of their oxy-hydroxide species as revealed by laboratory experiments in model systems. Copper contents exhibit the largest variation relative to the other metals, with vapor-liquid distribution coefficients from 0.01 to 100, which is likely to be caused by post-entrapment modifications due to Cu diffusion exchange between the inclusion and the surrounding external fluid as recent experiments suggest (Lerchbaumer and Audétat 2012).

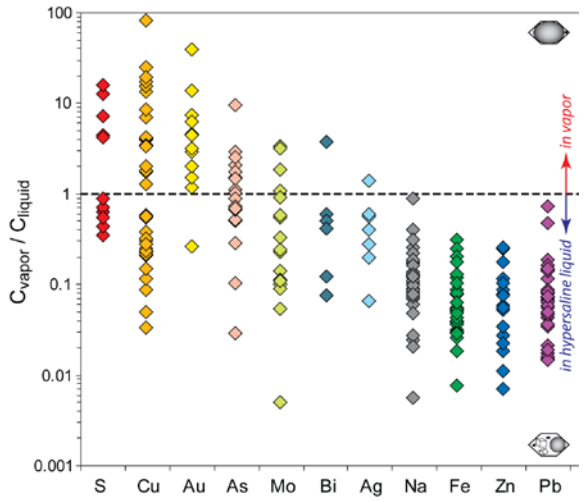

Figure 3. Sulfur and metal concentration ratios (equivalent to vapor-liquid distribution coefficient) measured in coexisting vapor and hypersaline liquid inclusions from "boiling assemblages" in quartz from porphyry and related deposits (modified from Kouzmanov and Pokrovski 2012).

In the epithermal environment, at relatively low T and P, most metalloids and metals, including Au and Cu, have partitioning coefficients many orders of magnitude in favor of the dense liquid phase. Phase separation occurring by boiling of the dominant aqueous liquid phase, results in the removal of H_2S and CO_2 from the fluid causing breakdown of Au hydrogen-sulfide complexes and gold precipitation. In addition, boiling leads to a pH increase of the liquid phase due to the loss of CO_2; this, in turn, may lead to precipitation of base metal and Ag sulfides.

3.2 Cooling

Temperature is likely the most direct factor that influences mineral solubility and, thus, metal transport and precipitation (Fig. 2a). A number of case studies demonstrate that cooling of a magmatic-hydrothermal fluid over a small temperature interval between ~450° and 300°C is the main cause of Cu±Au±Mo deposition in the deep central parts of porphyry systems (Ulrich et al. 2001, Rusk et al. 2004, Landtwing et al. 2005), while Cu-Zn-Pb-Ag-Mn precipitate in an increasing proportion in a distal position in porphyry-related polymetallic veins characterized by lower temperatures, commonly <350°C (Catchpole et al. 2011).

Cooling of a magmatic fluid is also accompanied by large changes in sulfur speciation, which in turn affect H_2S concentration and acidity, according to the reaction:

$$4\ SO_2 + 4\ H_2O = H_2S + 3\ HSO_4^- + 3\ H^+$$

This reaction does not lead to significant redox changes since it is independent of oxygen fugacity, whereas it is strongly pH-dependent, and its extent will depend on the degree of fluid interaction with surrounding silicate rocks. Disproportionation of SO_2 has an important impact on metal transport, because an increase of H_2S content and acidity of the fluids will affect mineral solubility in different ways for different metals (Fig. 2c, d). This SO_2 breakdown is likely to control the fractionation of Au from Cu and other base metals during fluid evolution on ascent and the transport of Au to the low-temperature and pressure epithermal environment. Further fluid neutralization by interaction with host rocks in intermediate to lower-temperature environments is a key factor for base-metal deposition.

3.3 Fluid-rock interaction

In porphyry settings, fluid-rock interaction is expressed as alteration and mineral zonation centered on the fluid source and propagating into the surrounding rocks, generated by changes of pH, redox state and sulfide content (Fig. 1). The stronger the neutralizing capacity of the rock, the more efficient will be the metal precipitation (Fig. 2c). A particularly good example is the skarn environment with its commonly observed metal zonation from proximal Cu±Au to distal Zn-Pb zones, resulting from a combination of temperature decrease and neutralization of the fluid by the carbonate wall rocks.

3.4 Fluid mixing

In porphyry deposits there is little evidence for incursion of external waters into the deep porphyry orebody, either before or during Cu and Au precipitation. It is widely accepted, based on stable isotope and fluid inclusion studies that fluids, which cause potassic alteration cores and large sericitic alteration overprints, have a dominantly magmatic fluid component. As emphasized by Seedorff et al. (2008), field evidence and hydrological modeling suggest that dense brines such as saline formation waters or re-circulated magmatic hypersaline liquid (Fig. 1) may access the deep, central, and peripheral high-temperature parts of the hydrothermal

systems, causing deep sodic-calcic alteration during heating. However, the influence of such potential fluid mixing on Cu and Au precipitation in porphyry orebodies has not been properly evaluated.

4 Thermodynamic predictions versus metal concentrations in natural fluid inclusions

The thermodynamic predictions shown in Figure 2 may also be directly compared with the recently compiled large dataset on metal, salt and sulfur concentrations measured in different types of fluid inclusions from porphyry systems owing to recent advances in *in situ* microanalytical techniques (LA-ICP-MS, PIXE, SR-XRF). When the major parameters of fluids, such as temperature, pressure, Cl and S content, acidity, and redox potential, are constrained to the typical range of porphyry systems, based on recorded fluid inclusion temperatures, pressures, and salt content, and observed alteration mineral patterns, calculations of mineral solubilities generally reproduce well the Cu, Ag, Fe, Zn, and Pb concentrations measured in the different types of fluid inclusions typically found in the porphyry and epithermal environments of magmatic-hydrothermal systems (Kouzmanov and Pokrovski 2012). In contrast, thermodynamic predictions for Au in epithermal fluids, and, Mo in both epithermal and porphyry fluids underestimate by up to several orders of magnitude their contents compared to natural compositions. This discrepancy points to gaps in existing speciation models of both metals and S, likely due to neglecting some important species (Kouzmanov and Pokrovski 2012).

5 Summary and conclusions

Thermodynamic modeling supported by large dataset of natural fluid inclusion compositions from a variety of porphyry and associated epithermal deposits shows that cooling of a magmatic fluid, accompanied by phase separation and water-rock interaction, are likely to be the major causes of most metal deposition in porphyry systems.

Decompression on ascent, leading to phase separation and cooling of the pristine magmatic-hydrothermal fluid in the central upflow zone results in the formation of Cu ± Au ± Mo ore shells, centered on the porphyry stock above the cupola of the underlying parental magma chamber. Further cooling (<350°C) causes SO_2 disproportionation and acidification of the magmatic fluid, inducing changes in S speciation directly affecting the fractionation of Au from Cu and the transport of Au to the low-temperature and pressure epithermal environment. Efficient fluid neutralization through water-rock interaction is a major driving force for Zn, Pb, Ag, and, in part, Au deposition in more distal portions of porphyry systems. Thus the resulting outward base-metal zoning consists of Cu-Zn, Zn-Pb-Ag, Pb-Ag (Mn), and As-Sb-Hg-Au zones, in order of increasing distance from the porphyry center reflecting progressive cooling of the ore-forming fluids, neutralization and possibly mixing with meteoric waters in the periphery of the system, corresponding to the shallow epithermal environment. Fluid immiscibility is a major process that may occur at different levels in magmatic-hydrothermal systems and strongly affects the behavior of S and Au versus other metals by contrasting fractionation between the resulting vapor and liquid phases. Large-scale mixing with meteoric and sedimentary-basin fluids is a relatively uncommon phenomenon in the deep high temperature and pressure porphyry environment and is not expected to be a major cause of porphyry Cu ore body formation.

Acknowledgements

This work was supported by the Swiss National Science Foundation (grant 20021-127123 to KK) and l'Agence Nationale de la Recherche (grant SOUMET-ANR 2011 Blanc SIMI 5-6/009-01 to GSP).

References

Catchpole H, Kouzmanov K, Fontboté L, Guillong M, Heinrich CA (2011) Fluid evolution in zoned Cordilleran polymetallic veins - Insights from microthermometry and LA-ICP-MS of fluid inclusions. Chemical Geology 281: 293-304

Johnson JW, Oelkers EH, Helgeson HC (1992) SUPCRT92: A software package for calculating the standard molal thermodynamic properties of minerals, gases, aqueous species, and reactions from 1 to 5000 bar and 0 to 1000°C. Computers & Geosciences 18: 899-947.

Kouzmanov K, Pokrovski GS (2012) Hydrothermal controls on metal distribution in porphyry Cu (-Mo-Au) systems. In: Hedenquist JW, Harris M, Camus F (eds) Geology and genesis of major copper deposits and districts of the world: A tribute to Richard H. Sillitoe. SEG Special Publication 16: 573-618.

Landtwing MR, Pettke T, Halter WE, Heinrich CA, Redmond PB, Einaudi MT, Kunze K (2005) Copper deposition during quartz dissolution by cooling magmatic-hydrothermal fluids: The Bingham porphyry. Earth and Planetary Science Letters 235: 229–243.

Lerchbaumer L, Audétat A (2012) High Cu concentrations in vapor-type fluid inclusions: An artifact? Geochimica et Cosmochimica Acta 88: 255-274.

Lowell JD, Guilbert JM (1970) Lateral and vertical alteration-mineralization zoning in porphyry ore deposits. Economic Geology 65: 373–408.

Meyer C, Hemley JJ (1967) Wall rock alteration. In: Barnes HL (ed) Geochemistry of hydrothermal ore deposits, New York, Holt, Rinehart and Winston: 166–235.

Rose AW (1970) Zonal relations of wallrock alteration and sulfide distribution at porphyry copper deposits. Economic Geology 65: 920-936.

Rusk B, Reed MH, Dilles JH, Klemm L (2004) Compositions of magmatic-hydrothermal fluids determined by LA-ICPMS of fluid inclusions from the porphyry copper-molybdenum deposit at Butte, Montana. Chemical Geology 210: 173–199.

Seedorff E, Dilles JH, Proffett JM, Jr, Einaudi MT, Zurcher L, Stavast WJA, Johnson DA and Barton MD (2005) Porphyry deposits: Characteristics and origin of hypogene features. Economic Geology 100th Anniversary Volume: 251–298.

Seedorff E, Barton MD, Stavast WJA and Maher DJ (2008) Root zones of porphyry systems: Extending the porphyry model to depth. Economic Geology 103: 939–956.

Shvarov YS (2008) HCh: New potentialities for the thermodynamic simulation of geochemical systems offered by Windows. Geochemistry International 46: 834-839.

Sillitoe RH (2010) Porphyry copper systems. Economic Geology 105: 3–41.

Ulrich T, Günther D, Heinrich CA (2001) Evolution of a porphyry Cu-Au deposit, based on LA-ICP-MS analysis of fluid inclusions, Bajo de la Alumbrera, Argentina. Economic Geology 96: 1743-1774.

Geological and geochemical features of the Cerro Maricunga project in the Maricunga gold belt, northern Chile

S. Lohmeier, B. Lehmann
Mineral Resources, Technische Universität Clausthal, 38678 Clausthal-Zellerfeld, Germany

A. Schneider
Atacama Pacific Gold Corporation, Santiago de Chile, Chile

Abstract. The Cerro Maricunga gold deposit is located in a porphyry-breccia system within the partially eroded mid-Miocene Ojo de Maricunga stratovolcano in the High Andes of northern Chile. The host rock is of andesitic composition and is affected by argillic alteration, veinlet-controlled silicification and a late-stage chlorite and diopside-hedenbergite overprint. The andesitic rocks have a steep and spoon-shaped REE pattern and adakitic affinity. The hydrothermal gold mineralization is controlled by banded quartz veinlets with amorphous silica precursors and locally restricted disseminated mineralization. The hydrothermal paragenetic sequence consists of abundant magnetite, and minor pyrite, chalcopyrite, bornite, chalcocite and sphalerite. Native gold and silver flakes are rare and of supergene origin. Gold is easily leachable and probably occurs as nanoparticles in the silica veinlets

Keywords. Maricunga belt, Cerro Maricunga project, gold, Chile

1 Introduction

The Cerro Maricunga gold project (Atacama Pacific Gold; Fig.1, 2) is situated in the central part of the Maricunga gold belt, about 20 km south of the La Coipa mine. The Maricunga belt is a metallogenic unit with several gold, silver and copper deposits of porphyry and epithermal style. The aggregated geologic resource was estimated at approximately 40 Moz Au (Muntean et al. 2001) mostly from the established mines such as La Coipa, Marte-Lobo, Refugio-Maricunga and La Pepa. The current measured and indicated gold resource of the Cerro Maricunga deposit is 2.7 Moz (164 Mt @ 0.51 g/t Au, at a 0.3 g/t Au cut-off plus inferred resources of 121 Mt @ 0.47 g/t Au) based on more than 80,000 meters of drilling since 2010. Metallurgical testing indicates gold recoveries of about 80 %.

2 Maricunga gold belt

The Maricunga belt is situated in the southern part of the Central Volcanic Zone (CVZ), just inboard of the modern volcanic arc, close to the northern end of the zone of flat-slab subduction in central Chile. The basement comprises mid-Paleozoic clastic sedimentary sequences intruded by late-Paleozoic granitic rocks. Mesozoic continental andesitic lavas and siliciclastic units plus carbonate sediments form the lower unit of the cover sequence, followed by Cenozoic intrusive and volcanic calc-alkaline rocks and rhyolitic and dacitic ignimbrite blankets, which evolved until 5 Ma ago when the magmatic activity in the belt ceased (Vila et al. 1991, Mpodozis et al. 1995, Mahlburg Kay 2002). The modern landscape is characterized by Cenozoic volcanoes, including subvolcanic stocks and widespread breccias, and NNE striking inverted mid- to late-Cretaceous and Miocene faults generated by compressional tectonics (Muntean et al. 2001). The ore deposits in the Maricunga belt are of a transitional porphyry to epithermal style reflected by intrusion-hosted porphyry-type gold deposits and volcanic-hosted epithermal gold deposits of high sulfidation style and acide sulfate alteration. Their age is 13-14 Ma and 20-24 Ma (Sillitoe et al. 1991).

3 Cerro Maricunga project

The Cerro Maricunga deposit is situated within the partially eroded mid-Miocene Ojo de Maricunga stratovolcano. Preliminary petrographic and geochemical data define the Cerro Maricunga porphyry-breccia system as andesite with wide-spread argillic alteration, veinlet-controlled silicification and a late-stage metasomatic overprint with chloritization and formation of diopside-hedenbergite. The andesitic rocks have a steep and spoon-shaped REE pattern indicating a source with amphibole and garnet stable, e.g. thick continental crust. Proterozoic lower continental crust with variable mantle input is seen as the (main) magma source, as suggested by initial εNd data between -3 and -4. Multielement patterns with slight negative anomalies for Nb, P and Ti demonstrate a subduction-related component. Remarkable features are high Sr, low Y and HREE, and low HFSEs that identify these rocks as of adakitic affinity. The hydrothermal mineralization is controlled by banded veinlets with amorphous silica precursors and locally restricted disseminated mineralization. Banded quartz veinlets are characterized by a wide spectrum of boiling features (jigsaw, feathery, flamboyant, plumose, colloform and crustiform; Fig. 3a,b), very abundant vapor-rich fluid inclusions and a vast amount of μm-sized magnetite crystals and minor sulfides. The hydrothermal paragenetic sequence starts with abundant variably martitized magnetite intergrown with ilmenite. Abundant hydrothermal magnetite occurs as fine grained crystals in banded quartz veinlets (Fig. 3c). Sulfides are relatively rare and consist of fine-grained pyrite, chalcopyrite, bornite, chalcocite and sphalerite. The dominant ore assemblage comprises

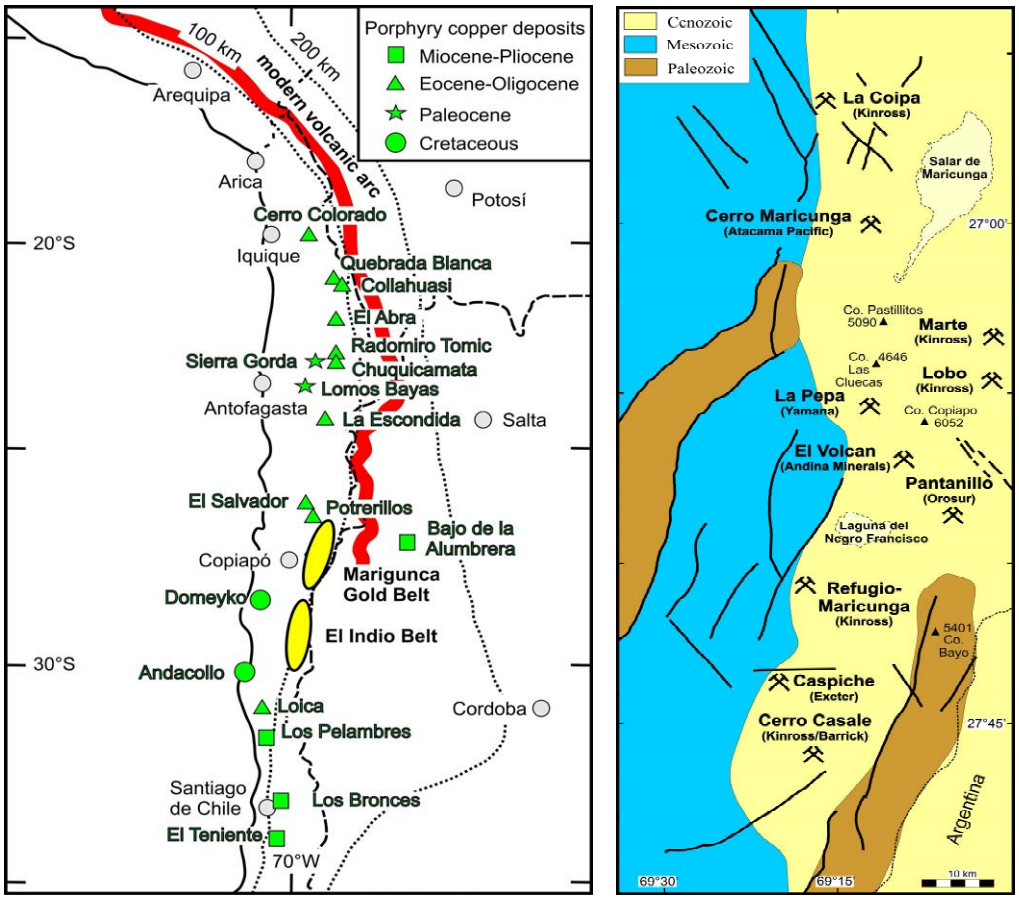

Figure 1. The Cerro Maricunga project is located in the central part of the Maricunga gold belt in the High Andes of northern Chile. The Maricunga belt lies in the southern part of the CVZ, immediately in the south of the modern volcanic arc. The figure on the right shows established mining areas and exploration projects in the central part of the belt (map modified after Mpodozis et al. 1995).

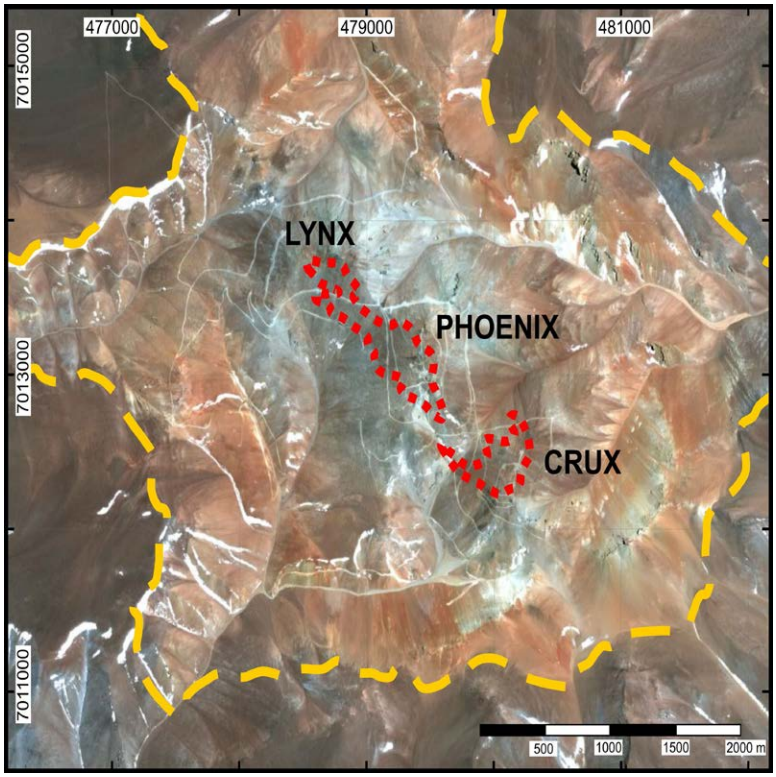

Figure 2. The satellite image shows the currently identified zones of mineralization (Lynx, Phoenix and Crux zone) of the Cerro Maricunga project. The dotted lines mark the 0.3 g/t Au cut-off. The dashed line surrounds the zone of argillic alteration in the interior part of the partially eroded Ojo de Maricunga stratovolcano. The outer zone within this halo is characterized by pyrite alteration (reddish).

bornite, chalcopyrite, chalcocite and very minor accessory sphalerite. Replacement of bornite by chalcopyrite is common, as well as replacement of chalcopyrite by covellite. Occasionally, poriferous and hypidiomorphic pyrite crystals occur, but they cannot be assigned to a specific stage. Native silver, gold, acanthite, alloclasite and Ag-bearing sulfosalts are rare. They occur as very small grains in the µm-range on quartz-grain boundaries and vugs, and are probably of supergene origin (Fig. 3d). Given the scarcity of detectable gold flakes and the low content of gold in sulfides (e.g. ± 0.05 ppm in pyrite, Fig. 4b, 4d), the banded quartz veinlets seem to have a large component of "invisible" gold that is assumed to occur as gold nanoparticles in the silica component. This assumption is confirmed by gold values of ± 0.3 ppm in banded quartz veinlets measured by LA-ICPMS (Fig. 3a, c), but the system has no As enrichment.

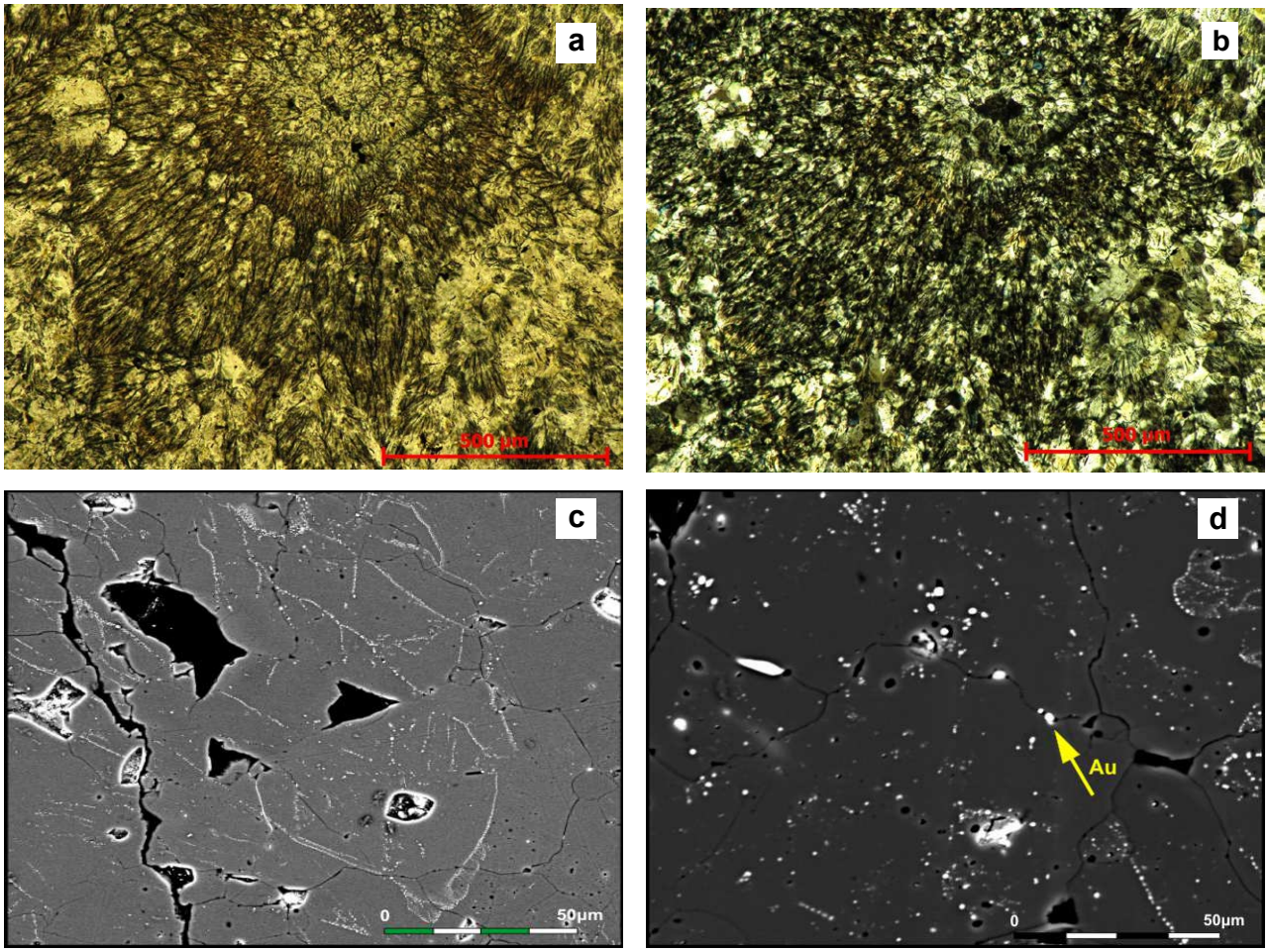

Figure 3. Boiling textures in banded quartz veinlets. a) Feathery boiling textures of quartz; dark color is due to a vast amount of vapor fluid inclusions and tiny magnetite crystals. Plane transmitted light. b) Same as (a) but with crossed nichols. c) Scanning electron microscope (SEM) image of boiling features in a banded quartz veinlet marked by tiny magnetite and accessory pyrite crystals. d) Backscatter electron microscope (REM) image of boiling features in a banded quartz veinlet marked by tiny magnetite crystals. One gold grain of likely supergene origin is marked by an arrow. The large bright spot is from polishing (lead).

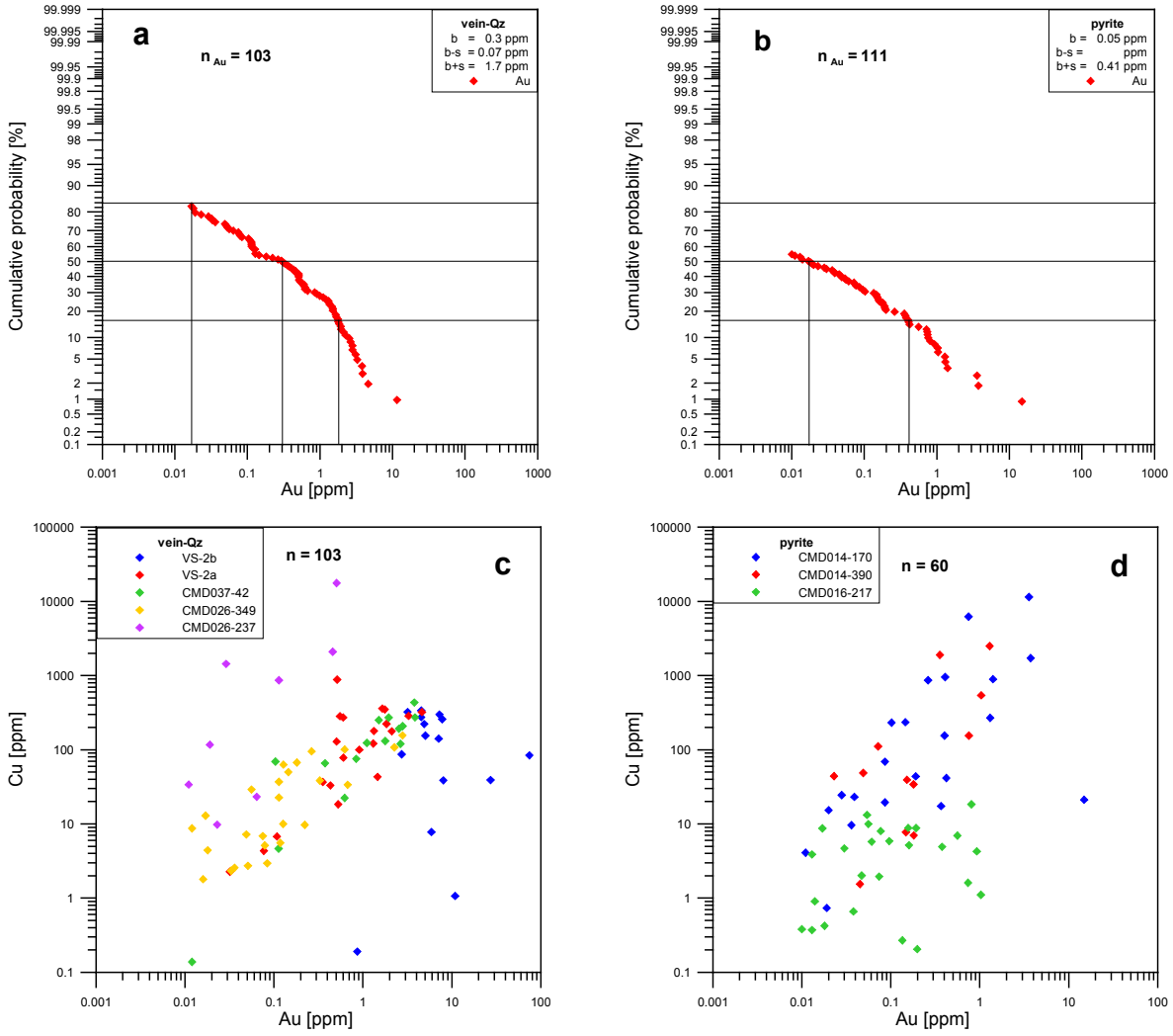

Figure 4. Probability plot of Au contents in vein-quartz (a) and in pyrite (b) established by LA-ICPMS. Correlation plot of Au vs Cu in vein-quartz (c) and in pyrite (d) showing linear trends, established by LA-ICPMS.

References

1. Mahlburg Kay S, Mpodozis C, Ramos VA, Munizaga F (1991) Magma source variations for mid-late Tertiary magmatic rocks associated with a shallowing subduction zone and a thickening crust in the Central Andeas (28°-33°S). Geol Soc Am Spec Paper 265.

2. Mahlburg Kay S, Mpodozis (2002) Magmatism as a probe to the Neogene shallowing of the Nazca plate beneath the modern Chilean flat-slab. J South Am Earth Sci 15: 39-57.

3. Mpodozis C, Cornejo P, Kay SM, Tittler A (1995) La Franja de Maricunga: síntesis de la evolución del Frente Volcánico Oligoceno-Mioceno de la zona sur de los Andes Centrales. Revista Geológica de Chile 21: 273-323

4. Muntean JL, Einaudi, MT (2001) Porphyry-epithermal transition: Maricunga belt, northern Chile. Econ Geol 96: 743-772.

5. Sillitoe RH, McKee EH, Vila T (1991) Reconnaissance K-Ar geochronology of the Maricunga gold-silver belt, northern Chile. Econ Geol 86: 1261-1270

6. Vila T, Sillitoe RH (1991) Gold-rich porphyry systems in the Maricunga belt, northern Chile. Econ Geol 86: 1238-1260.

Geology, geochemistry and petrogenesis of the Twin Bonanza intrusion-related gold deposit: implications for a post-collisional lithospheric mantle source for the Granites-Tanami gold province, North Australian Craton

Ben Li, Leon Bagas, T. Campbell McCuaig
Centre for Exploration Targeting, ARC Centre of Excellence for Core to Crust Fluid Systems, The University of Western Australia, 35 Stirling Highway, Crawley WA 6009, Australia

Abstract. The multi-phase Buccaneer Porphyry (BP) hosts the Twin Bonanza intrusion-related gold deposit (IRGD) in the Palaeoproterozoic Granites-Tanami Orogen. The mineralization is in an early porphyritic quartz monzonite and a late porphyritic quartz monzonite pipe containing mafic microgranular enclaves (MMEs). The roof of the late porphyritic quartz monzonite pipe is characterized by abundant quartz stockworks with comb and crustiform textures cemented breccia of quartz monzonite fragments. Most of the gold is distributed in thick low-grade disseminated sulfidic ore body with mild alteration, in high-grade disseminated sulfidic ore with strong sericite-silica alteration in shear zones containing abundant fine-grained euhedral arsenopyrite, and in quartz veins with or without comb texture. SHRIMP U-Pb zircon dating yielded three indistinguishable weighted average ages for the early porphyritic quartz monzonite (1793.5 ± 6.9 Ma), MMEs (1793.4 ± 8.8 Ma), and the late porphyritic quartz monzonite pipe (1794.7 ± 9.8 Ma). Major element, trace element and Sr-Nd isotope geochemistry data suggest that the porphyritic quartz monzonite at the Twin Bonanza IRGD evolved from the magma forming the MMEs. The source of the magma is metasomatised subduction-related lithospheric mantle. Convective removal of the thickened lithospheric mantle root triggered partial melting of the lithospheric mantle material in a post-collisional tectonic setting during ca. 1795 Ma. The metasomatised lithospheric mantle could also be the source of the gold-bearing hydrothermal fluids for the Twin Bonanza IRGD.

Keywords: Granites-Tanami Orogen, intrusion-related gold deposit (IRGD), quartz monzonite porphyry, mafic microgranular enclaves (MMEs), post-collisional magmatism

1 Introduction

The poorly exposed Palaeoproterozoic Granites–Tanami Orogen (GTO) is part of the North Australian Craton. The orogen straddles the state border between Western Australia and the Northern Territory, and is situated between the Halls Creek Orogen to the northwest and the Arunta Orogen to the southeast. The importance of GTO is that it contains several large gold deposits that highlight the considerable exploration potential for undiscovered mineral occurrences in the region (e.g. Wygralak et al. 2004; Huston et al. 2007; Bagas et al. 2009, 2013). Several economically important gold deposits and prospects are present, such as Callie, The Granites, Tanami, Coyote, Twin Bonanza, and Old Pirate, which have a combined reserve of over 400 tonnes of gold (Huston, et al. 2007). The Twin Bonanza gold deposit is apparently unique for being the only intrusion-related gold deposit (IRGD) discovered in the Granites-Tanami gold province. The total inferred resource for the deposit is 127.9 tonnes at a grade of 0.65 g/t Au for 2.67 Moz Au. However, the geology, petrogenesis and geodynamic setting of the Twin Bonanza IRGD remain poorly understood. This study reports on the geology, geochemistry and geochronology characteristics of the deposit with the aim of defining the genesis of the host-rocks and possible source for the gold-rich hydrothermal system forming IRGDs in the GTO.

2 Geology, geochemistry and geochronology of the Twin Bonanza IRGD

2.1 Regional Geology

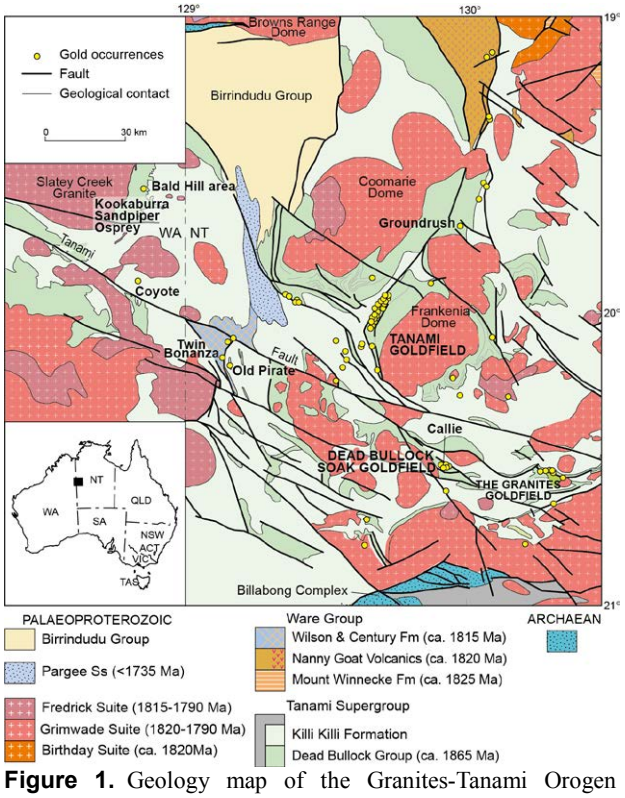

Figure 1. Geology map of the Granites-Tanami Orogen showing the locations of gold deposits (after Bagas et al. 2013).

The GTO includes Palaeoproterozoic greenschist-facies sedimentary rocks and rare volcanic rocks that are tightly to isoclinally folded, and granitic rocks (Fig. 1). The

Buccaneer Porphyry (BP) is located between the Trans-Tanami and Mongrel faults and intrudes sedimentary rocks assigned to the ca. 1825 Ma Ware Group. A north-trending thrust linking the Trans-Tanami and Mongrel fault is inferred to be present immediately to the west of the BP.

The BP is a multi-phase body composed of syenogranite, monzogranite and two main phases of porphyritic quartz monzonite. The younger (late) quartz monzonite forms a pipe intruding the early quartz monzonite in the southern part of the BP. Both the early and late quartz monzonites contain abundant and scattered mafic microgranular enclaves.

2.2 Rocks types and petrography

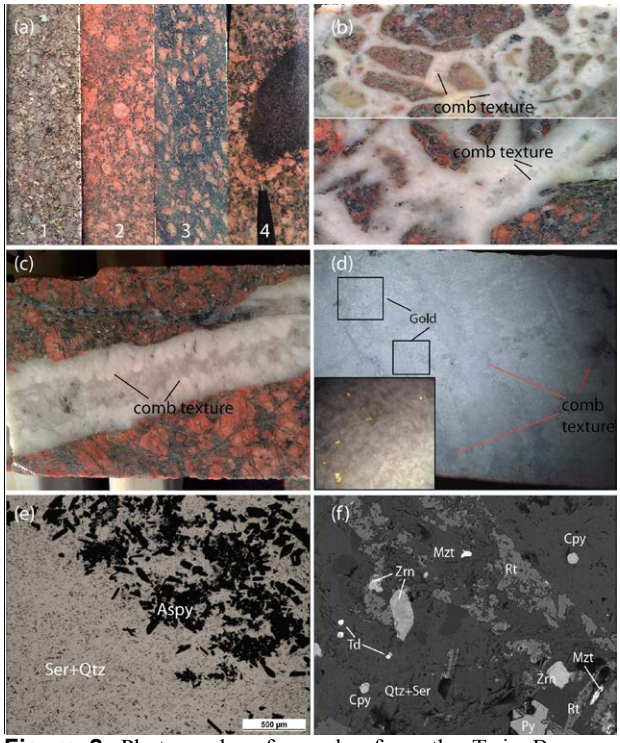

Figure 2. Photographs of samples from the Twin Bonanza IRGD: (a), 1: Ca-rich quartz monzonite end member; 2: K-rich quartz monzonite end member; 3: Late quartz monzonite porphyry pipe; 4: Mafic microgranular enclave; (b) Type 1 quartz vein with comb texture and brecciated host rock; (c) Type 2 quartz vein with comb texture; (d) visible gold in Type 2 quartz vein; (e) high-grade disseminated ore with sericite-silica alteration and abundant fine-grained euhedral arsenopyrite; and (f) BSE image of high-grade disseminated ore. Ser = sericite, Qtz = quartz, Aspy = arsenopyrite; cpy = chalcopyrite, py = pyrite, Td = tetrahedrite, Mzt = monazite, Zrn = zircon, Rt = rutile.

The two quartz monzonite bodies in the BP have porphyritic and phaneritic textures. The early quartz monzonite includes high-Ca and high-K end members. The high-Ca end member has a relatively higher proportion of plagioclase and a lower proportion of K-feldspar (Photograph 1 in Fig. 2a). The high-K end member has a higher proportion of K-feldspar and a lower proportion of plagioclase (Photograph 2 in Fig. 2a). The K-feldspar phenocrysts are pale grey (high-Ca end member) to pink (high-K end member) subhedral-anhedral granular grains with axis ratios of ~1:1 to 1:2. Biotite and amphibole are less than 2% in of these units.

The late porphyritic quartz monzonite pipe contains a higher proportion of euhedral K-feldspar, amphibole and biotite, and a lower proportion of euhedral plagioclase than the early quartz monzonite phase. The K-feldspar phenocrysts in the pipe are pink with higher axis ratios of ~1:3. A distinctive feature of this quartz monzonite is the vertical igneous foliation of the K-feldspar and plagioclase with no evidence for structural deformation (Photograph 3 in Fig. 2a). Another characteristic feature is the abundant quartz stockworks with comb and crustiform textures cementing in-situ breccia of the quartz-monzonite in the roof zone of the pipe (Fig. 2b).

Mafic microgranular enclaves (MMEs) are widespread in the early and late porphyritic quartz monzonite. The MMEs are commonly 50–200 mm in diameter, have sharp contacts with the quartz monzonite, and are rounded, ovoid or irregular in shape (Photograph 4 in Fig. 2a). The MMEs are gabbroic to dioritic in composition, dark coloured, and subhedral to anhedral in textures. Amphibole is abundant and chloritic alteration is present in plagioclase, amphibole, biotite and pyroxene. The matrix displays a quenching texture with acicular apatite and hornblende, and laths of plagioclase. Some apatite is present as inclusion in plagioclase and quartz grains.

2.3 Veins

Quartz veins are the dominant vein type at the Twin Bonanza IRGD and can be divided into three types. Type 1 veins are quartz stockworks with comb and crustiform textures. These veins are located at the roof of the late porphyritic quartz monzonite pipe, where host rock (quartz monzonite) breccia is cemented by quartz (Fig. 2b) and quartz cavities are present in the veins. Type 2 veins also have comb layers, although no host rock breccia is present between the veins (Fig. 2c). The Type 2 veins developed from the Type 1 quartz stockworks and are located at the top of the Type 1 quartz stockworks. The Type 3 veins are homogeneous, sheeted quartz veins located above and around Type 2 veins. Type 3 veins are more common than any other types of veins in the deposit, range in width from 50 mm to ~200 mm, and fill extensional fractures in the host rocks. K-feldspar and more sulfides such as pyrite, arsenopyrite, minor chalcopyrite and cinnabar are present in Type 3 veins.

K-feldspar-quartz veins, quartz-calcite, and rare quartz-fluorite and quartz-calcite-chlorite veins are also present at the Twin Bonanza IRGD. The K-feldspar-quartz (pegmatite) veins range from 20 mm to >1 m. K-feldspar is the dominated mineral with minor quartz. K-feldspar contains comb texture in thin veins and as quartz fills along crystal edges. Rare sulfides such as pyrite and chalcopyrite are present in the K-feldspar-quartz veins. Quartz-calcite veins commonly form crustiform quartz bands with centres filled with anhedral calcite, but also form mixture of anhedral quartz and calcite. Quartz-fluorite veins are located at the top of the Type 3 veins,

and quartz-calcite-chlorite veins are usually associated with strong sericite-chlorite-silica alteration and sulfidation. In places, 10-20 mm thick chlorite-rich veins are present, which sharply cross-cut the early quartz monzonite and Type 3 veins without obvious alteration halos.

2.4 Ore types

Twin Bonanza contains three types of mineralisation: 1) visible gold with rare sulfide associations in the upper parts of Type 1 veins, Type 2 veins, and the lower parts of Type 3 veins (with grade of ≤88.6 g/t Au, Fig. 2d); 2) disseminated ore at the top of the combined vein system with grades of <2 g/t Au, and over a constant thickness of ~100 m. The second style of mineralization is associated with weak to moderate potash-silica-sericite-calcite-chlorite alteration hosting disseminated and veined pyrite-chalcopyrite-arsenopyrite(-bismuthinite-tennantite-tetrahedrite-molybdenite-stibnite-cinnabar); and 3) high-grade ore with densely disseminated sulfides in strongly sheared zone. The third type of ore is hosted by sheared quartz monzonite and is characterized by very strong sericite-silica alteration with abundant disseminated and fine-grained euhedral arsenopyrite and pyrite- chalcopyrite- rutile-monazite-tetrahedrite association with grades up to 12.5 g/t Au (Figs 2e, 2f)

2.5 Geochronology

U-Pb SHRIMP dating was conducted on zircons separated from the early porphyritic quartz monzonite, MMEs and the late porphyritic quartz monzonite pipe. The weighted average ages for the three samples are 1793.5 ± 6.9 Ma (early porphyritic quartz monzonite, n=18), 1793.4 ± 8.8 Ma (MMEs, n=12), and 1794.7 ± 9.8 Ma (late porphyritic quartz monzonite pipe, n=12). These ages are well defined and statistically indistinguishable from each other, suggesting that these three units were emplaced as magma during a short period in time. The age of ca. 1795 Ma is interpreted as crystallisation age for the MMEs and the two quartz monzonite phases.

2.6 Geochemical characteristics

Geochemical data suggests that the early quartz monzonite is shoshonitic and metaluminous to peraluminous, the late quartz monzonite is shoshonitic and peraluminous, and the MMEs are high-K calc-alkaline to shoshonitic and metaluminous to peraluminous. On Harker diagrams (not shown here), the MgO, TiO_2, Fe_2O_3, CaO and P_2O_5 contents for the the MMEs and quartz monzonites define tight and negative correlations with SiO_2, the Cr and Ni concentrations have positive correlations with MgO and negative correlations with SiO_2, and Al_2O_3, K_2O, Na_2O show positive correlations with SiO_2. These features are suggestive of crystallisation fractionation during magma evolution.

Mg# for most of the MMEs and quartz monzonites range between 40 and 60. These values are higher than the field for garnet amphibolite and eclogite melts and experimental fields for partial dehydration melting of metaigneous, pelitic and metagreywacke sources, but are close to the fields expects for peridotite melts, high-magnesium andesites, and metasomatized lithospheric mantle-derived mafic dykes in the GTO (Li et al. 2013). Therefore, the MMEs and quartz monzonites are probably derived from a mantle source (Fig. 3).

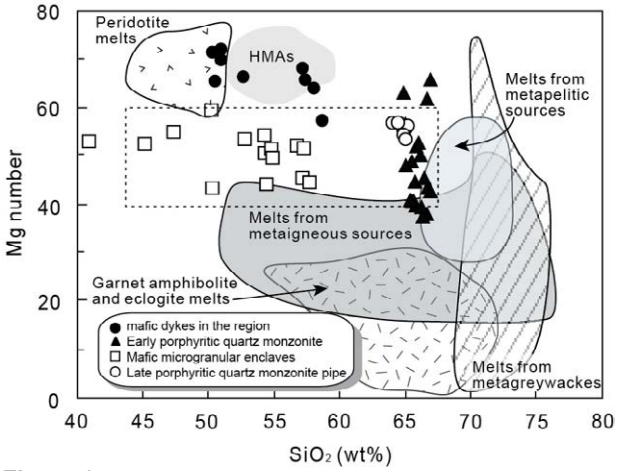

Figure 3. Plot of SiO_2 vs Mg#.

Chondrite-normalized REE patterns for the quartz monzonites are more enriched in LREE than the MMEs, while both are much more enriched than the lithospheric mantle-derived mafic dykes and lower continental crust. The primitive mantle-normalised trace element patterns for the quartz monzonites and MMEs show enrichment of LILE (Rb, Ba, Th, U, K, LREE) and depletion of HFSE (Nb, Ta, Zr Hf, Ti, etc.), which are similar to features for the mafic dykes. The values of εNd(t) for the MMEs and quartz monzonites range from -1.1 to -2.6, which are close to those for the mafic dykes (0.3 to -4.5). On the $(^{87}Sr/^{88}Sr)_i$ vs εNd(t) diagram, the MMEs and quartz monzonites plot close to the fields for EM I and other IRGDs in the world. In addition, the R1-R2 diagram in Fig. 4 indicates that the quartz monzonites had a late-orogenic (post-collisional) tectonic setting during their emplacement (Fig. 4).

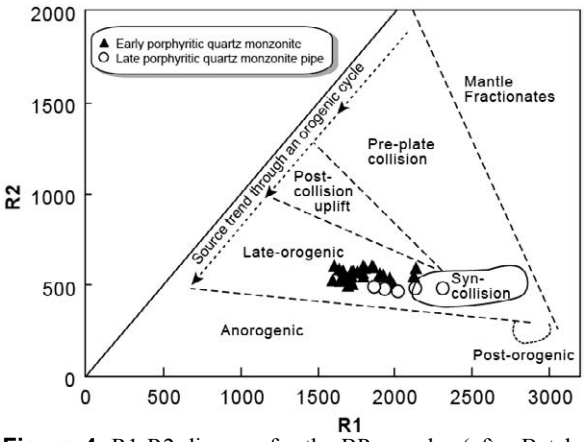

Figure 4. R1-R2 diagram for the BP samples (after Batchelor and Bowden (1985).

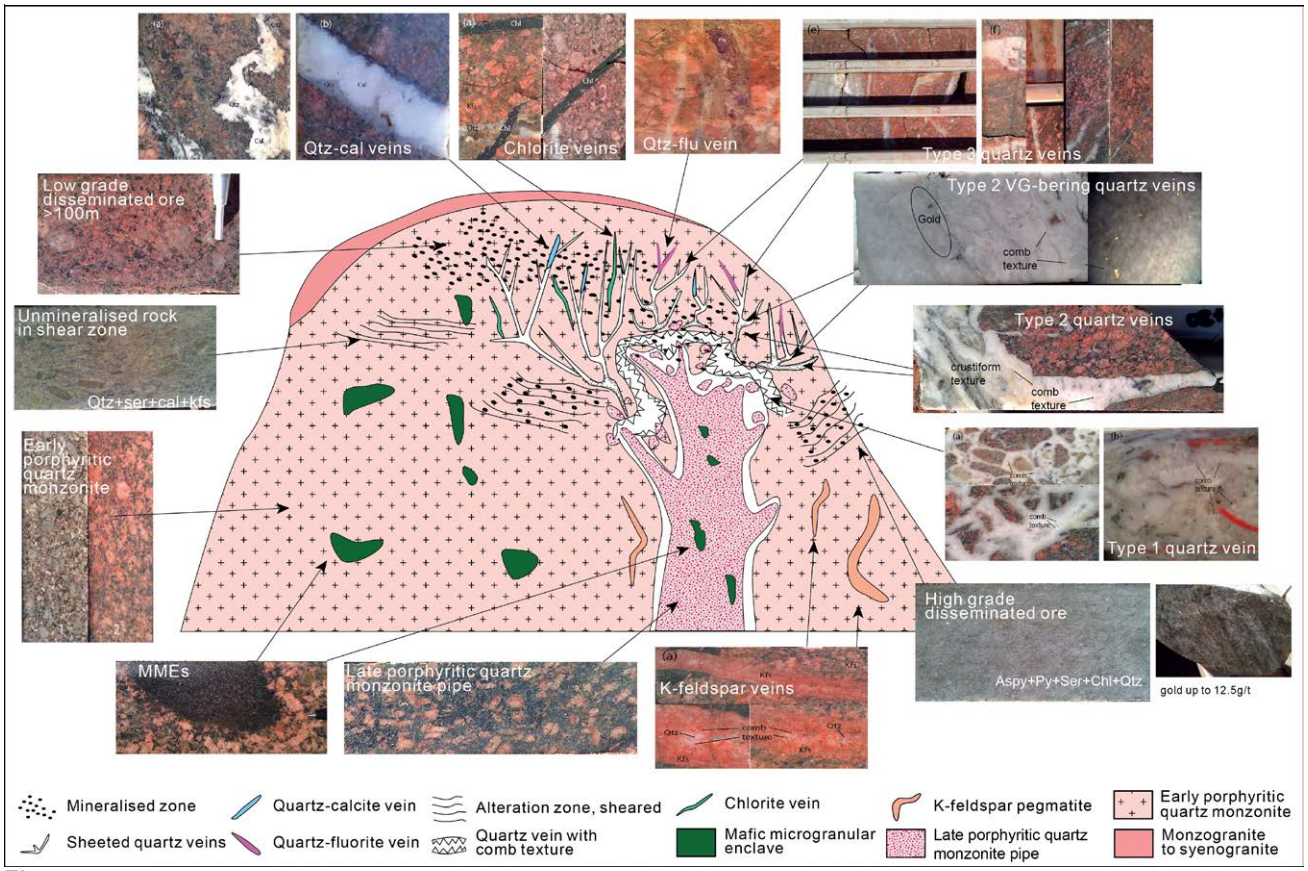

Figure 5. Proposed scheme for the Twin Bonanza gold deposit.

3 Petrogenesis and tectonic setting

The early and late porphyritic quartz monzonite and MMEs formed in a late orogenic (post-collisional) tectonic setting at ca. 1795 Ma in the GTO. This event was coeval with the widespread emplacement of mafic dykes, convective removal of a thickened lithospheric mantle root, hot asthenospheric mantle upwelling, and lithosphere extension (Li et al. 2013). Partial melting of subduction-modified hydrous lithospheric mantle was induced by heat and decompression generated the source magma (Li et al. 2013). The MMEs at the deposit may represent the mafic to intermediate component of a replenished magma chamber that survived mixing with evolved magma. Crystallisation fractionation of the mafic to intermediate magma with minor crustal assimilation generated the magma for the early and late porphyritic quartz monzonite. The presence of quartz veins with comb and crustiform textures and brecciated host rock fragments in the roof zone of the late porphyritic quartz monzonite pipe suggest that gold-bearing fluid was generated during its emplacement. The source of gold could be the metasomatized lithospheric mantle (which is the focus of further studies).

Acknowledgements

We gratefully acknowledge AMIRA International and the industry sponsors, including AusAid and the ARC Linkage Project LP110100667 for their support of the WAXI project (P934A).

References

Bagas L, Anderson JAC, Bierlein FP (2009) Palaeoproterozoic evolution of the Killi Killi Formation and orogenic gold mineralization in the Granites-Tanami Orogen, Western Australia. Ore Geol Rev 35: 47–67.

Bagas L, Boucher R, Li B., Miller J., Hill P, Depauw G, Pascoe J, Eggers B (2013) Paleoproterozoic stratigraphy and gold mineralisation in the Granites-Tanami Orogen, North Australian Craton. Aus. J Earth Sciences (in press).

Batchelor RA, Bowden P (1985) Petrologic interpretation of granitoids rocks series using multicatonic parameters. Chem Geol 48: 43-55.

Huston DL, Vandenberg LC, Wygralak A, Mernagh T, Bagas L, Crispe A, Lam-beck L, Cross A, Fraser G, Williams N, Worden K, Meixner A, Goleby B, Jones L, Lyons P, Maidment D (2007) Lode gold mineralization in the Tanami region, northern Australia. Miner Deposita 42: 175–204.

Li B, Bagas L, Gallardo LA, Said N, Diwu C, McCuaig TC (2013) Back-arc and post-collisional volcanism in the Palaeoproterozoic Granites-Tanami Orogen, Australia. Precam Res 224: 570-587.

Wygralak AS, Mernagh TP, Huston DL, Ahmad M (2004) Gold mineral system of the Tanami Region. In: Northern Territory Geological Survey Report: 18.

Geochemical analysis of the Pingüino vein system, Patagonia, Argentina – implications in exploration

Luciano López, Diego M. Guido, Sebastián M. Jovic, Gerardo N. Páez, Remigio Ruiz, Conrado Permuy Vidal
Instituto de Recursos Minerales (INREMI), Universidad Nacional de La Plata. Calle 64 s/n, (1900) La Plata, Argentina. Consejo Nacional de Investigaciones Científicas y Técnicas (CONICET) Buenos Aires, Argentina

Abstract. Geochemical data from 19 of the 70 veins of the Pingüino project were analysed. Pingüino vein system is characterized by two vein types: early polymetallic rich veins, and late quartz rich veins. Determinations of average vein metal values and spatial distribution of In, Au, Ag; Pb, Zn, Cu; As, Cd and Mn were performed in order to conform groups with similar geochemical behaviour. Individual elements distribution shows a main metals source point on top of the interpreted Kasia dioritic intrusion, with other secondary metal sources at KAL, TR, LUN, FAN, MN, KAR and ISL veins areas/intrusives. According to Ag/Au ratio and indium content three trends were identified; T1 (high In and low Ag/Au) is related to Lower Jurassic diorites and sulphide-rich veins. T2 (low to highest Au/Ag and low In values) is related to Middle Jurassic andesitic porphyries and Ag-rich quartz-rich veins. T3 gather veins with intermediate In and Ag/Au values, reflecting the mixing between the two main type of veins. These trends have a clear geographic association with Kasia intrusion and show a zonation pattern. The geochemical distribution and relationship of metal sources with intrusions should be considered in future Deseado Massif exploration.

Keywords: Metal zoning, Ag/Au ratio, polymetallic veins.

1 Introduction

The Pingüino deposit is located in the central portion of the Deseado Massif (Fig. 1). The area is characterized by a sedimentary sequence of Middle to Upper Triassic age (El Tranquilo Group) composed by sandstones with volcanic clasts, mudstones and black shales with coal. Intrusion of dioritic bodies, intermediate sills and dikes of the La Leona Formation was assigned to Lower Jurassic age (Jovic 2010). The Lower Jurassic Roca Blanca Formation is composed of epiclastic and pyroclastic fine sandstones with conglomerate and tuffitic rocks, volcanic sandstones and some tuffaceous levels and minor ignimbrite deposits. In the northwestern sector, the sequence is intruded by andesitic subvolcanic bodies, assigned to the Middle Jurassic Cerro León Formation.

Pingüino vein district contains more than 70 veins (Fig 1). This deposit is characterized by two vein types related to different magmatic events; (a) polymetallic sulphide-rich veins related to Lower Jurassic (194 Ma) diorites of the La Leona Formation, and (b) Ag-Au quartz veins related to Cerro León Formation Middle Jurassic (168 Ma) andesitic porphyries. The quartz veins cross-cut the polymetallic veins, providing further evidence of overlapping of the two different mineralization events (Jovic et al. 2011).

The polymetallic mineralization presents banded and massive textures in sulphide veins and vein breccias up to 13 m width, and with important Zn, Ag, Pb, Au, In, Cu, Sn, W and Bi anomalies (Jovic et al. 2011). Veins are poorly exposed and develop Fe-rich gossans. Jovic et al. (2011) defined two main mesoscopic pulses of polymetallic mineralization: First pulse (PS_1) composed of mainly pyrite, arsenopyrite and chalcopyrite, with late cassiterite cross-cutting these minerals, ferrokësterite replacing cassiterite and replaced by stannite. Complex Sb-rich sulphosalts of Ag-Pb-Cu-Fe are present in this pulse (Jovic et al. 2005, Crespi 2006), and Ivonne vein is the best example of this pulse. Second pulse (PS_2) is characterized by a Zn, Pb, Ag, In, Cd and Sb paragenesis that represents the infill of a breccia with PS_1 clasts. Galena and black sphalerite are the main minerals of the pulse, with minor sulphosalts of Ag-Pb. This pulse is best characterized in Marta Centro vein (Jovic et al. 2010).

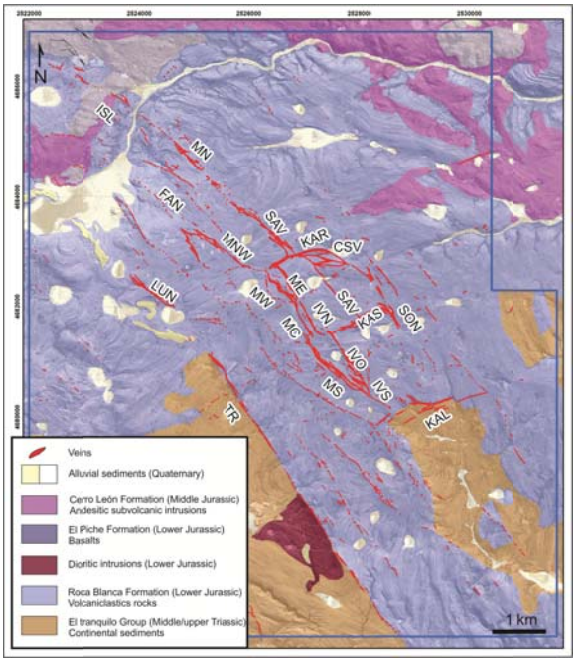

Figure 1. Geological and mineralization map of the Pingüino claim.

Quartz-rich structures are veins and vein-breccias with up to 20 m width, composed by quartz, carbonates and clays with colloform/crustiform banding, comb, cockade and lattice bladed textures. These veins have higher Ag-Au values in comparison with rich-sulphide veins (Jovic et al. 2011). Three quartz pulses were identified in these veins (Jovic 2010; Jovic et al. 2010): First pulse (Q_1) is composed by grey sacharoid-masive quartz with pyrite, chalcopyrite, sphalerite, galena, Ag-

Pb sulphosalts and native silver. The second pulse (Q_2) is characterized by colloform/crustiform banded quartz-carbonate with minor fluorite. Third pulse (Q_3) is represented by white coarse comb textured quartz in veins, veinlets and minor breccias.

The majority of the veins present complex relationships involving the sulphide-rich and quartz rich pulses. The late quartz-rich veins used the same fractures occupied by the previous sulphide-rich veins, therefore most of Pingüino veins exhibit a superimposed paragenesis; "pure" sulphide veins (e.g. Ivonne) and pure Quartz-rich vein (e.g. Marta Sur and Marta Norte) are less frequent. Dominant sulphide-veins considered in this contribution are Marta Centro (MC), Ivonne (IVO), Ivonne Sur (IVS), Ivonne Norte (IVN), Savary (SAV), Kasia (KAS), Karina (KAR) and Sonia (SON), tending to be hosted in NNW direction (N330° azimut) faults, while dominant quartz-veins rich are Marta Noroeste (MNW), Marta Norte (MN), Marta Este (ME), Tranquilo (TR) and Marta Sur (MS), that are mainly hosted in NW direction (N300° azimut) faults.

The aim of this study is to define the geochemical characteristics of each vein, in order to group them according to similar geochemical behavior. Also, it is pretended to make some interpretation about the characteristics of the hydrothermal fluids and to elaborate a hypothesis of the fluid paths. This information could be important for the metallurgy of the several Pingüino veins.

2 Methodology

Statistical analyses of the geochemistry data of veins were performed. Samples from 422 DDH, 225 RC drill holes and 551 trenches were considered and more than 50,000 ICP analyses were used. Only the samples corresponding to veins were selected for further analysis. To perform this selection, each sample was identified with VM (vein mineralization), DM (disseminated mineralization or stockwork halo) and HR (host rock) according to geological logs and cross section interpretation. The studied elements were Au, Ag, In, Cu, Pb, Zn, As, Cd and Mn. Several ratios were analysed, but two (Ag/Au and As/In) were defined as the best for this study. The interception lengths of the VM and VM + DM were calculated from every drill hole or trench.

Analyzed veins were MC, ME, TR, MN, KAS, MNW, IVO, MS, SON, IVS, SAV, IVN, KAR, Colita de Savary (CSV), Kalia (KAL), Isla (ISL), Marta Oeste (MW), Luna (LUN), and Fantasma (FAN). Some of them are conformed by one single vein, but others present several splays (in the hanging or the footwall), but to perform this study, only the main vein was used.

From each vein, media, standard deviation and maximum values were calculated. For further analysis, VM+DM (i.e. vein and halo mineralization) data was used to have a higher number of samples for statistical purpose. This is even more important in those veins with few drills and/or trenches.

3 Geochemical Analysis

3.1 In–Au–Ag

Indium values are very variable in Pingüino project veins. The vein with the maximum media values is MC. Other veins with high In values are, in order of In content: IVN, SAV, IVO, IVS and KAS Distribution of In content in plan view shows a restricted area with high concentrations near MC vein, that elongates to the SSE in the 330° direction to KAL vein.

Gold shows the maximum average value in MNW vein; veins with high Au values are: IVN, SAV, IVO, ME and ISL. In plan view Au values are concentrated in the IVN-SAV veins area, and extend to the NW (N300°) direction to FAN vein. An isolated increase of Au mean value was registered in ISL vein.

Silver exhibits the maximum average value in MNW and ME. Veins with high Ag values are MN, TR, SAV, LUN, CVS FAN and KAL. In plan view, Ag values elongate to NNW and NW directions, and also extends to the WSW to TR vein.

3.2 Cu-Pb-Zn:

Highest Cu average values are located at IVN, TR and IVO veins. In plan view copper shows a wide distribution with a WSW elongated shape related to TR and LUN veins.

The highest Pb average values are in SAV vein, and also is concentrated in MC, ME, KAL, KAS and CSV. Plan view shows a wide distribution of Pb values with a center in SAV, MC and ME and a general extend NW to MN, LUN and KAL.

The vein with the maximum media Zn values is MC, but other veins with high Zn values are IVS, SAV and KAS. Distribution in plan view is reduced in area concentrated in MC and with a trend to SSE to KAL vein and to the WSW to TR vein.

3.3 As-Cd-Mn:

Arsenic has the highest average value in IVN vein, and elevated values were registered in IVS, IVO, SAV and ME. High arsenic values are centered in IVO with a NW-SE trend, and also extends to the WSW to LUN vein.

MC is the vein with the highest average Cd value, followed by SAV, ME, KAS and IVS. In a plan view Cd distribution is similar to Zn.

The highest Mn average values are in ISL, KAL, TR, and MC veins. The Mn distribution is opposite to previous showing the lower values in the central sector of the project.

3.4 Ag/Au ratio

The Pingüino project Ag/Au ratio, considering the 19 veins studied, has an average value of 883. This ratio is elevated compared with others epithermal deposits of the Deseado Massif (Fernández et al. 2008). But, this ratio is highly variable when considering the different vein types. While the dominant sulphide-rich veins (MC, IVO, IVS, IVN, SAV, KAS, KAR and SON) shows an average Ag/Au ratio of 307; the dominant quartz-rich veins (MNW, MN, ME, TR, MS), presents a higher

average ratio of 1334. The last value can be only compared in the Deseado Massif with the high Ag/Au ratio of the silver-rich Martha mine (Fernández et al. 2008).

The spatial distribution of the Ag/Ag ratios exhibits a zonation at Pingüino, with relative low Ag/Au ratios in the central area (IVO vein has Ag/Au=48), that rises up to 200 involving IVS, MC, SAV, MW, ME, KAR, CSV and ISL veins, and increases outwards to the rest of the veins, up to 3,889 in the TR vein (Fig. 2).

The Ag/Au ratio is a very effective indicator of geochemical environment and spatial position of gold and silver in hydrothermal ores (e.g. epithermal, porphyries) (Cole 1986; Einaudi 1994). This ratio was even used to distinguish a gold zone from a silver zone in the epithermal deposits Tuscorara (Nevada, Castor et al. 2003). However metal zoning and distribution of Au/Ag exhibits different patterns from core to outside in different deposits (e.g. low sulphidation epithermal deposits and porphyries).

A similar zonation pattern of Ag/Au of Pingüino veins was described in Tayoltita mine silver-gold epithermal vein deposit, Mexico. It shows a zonal pattern characterized by a central core of low Ag/Au ratios and higher salinities about which develop increasingly higher ratios and diluted salinities (Clarke and Tiltley, 1988).

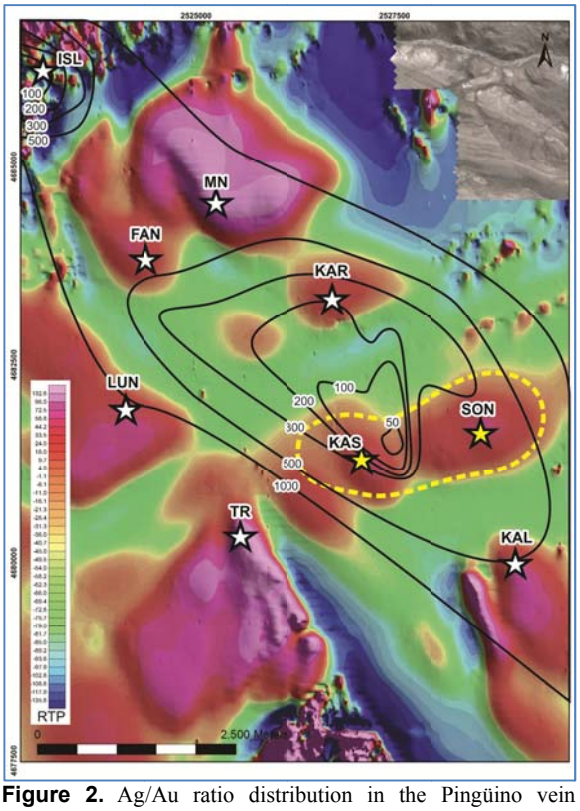

Figure 2. Ag/Au ratio distribution in the Pingüino vein system. Lower ratios are close to Kasia intrusive and extends to NW-SE. Base map is showing ground magnetics RTP evidencing the mafic intrusions (violet anomalies) of La Leona or Cerro León Formations at Pingüino project. White stars represent possible intrusion-related sources for metals (KAL, TR, LUN, FAN, MN, KAR and ISL), dashed yellow polygon is the interpreted location of the Kasia intrusion at depth, with two yellow stars at the possible source points (SON and IVO).

When average Ag/Au ratios are plotted versus In, three clear trends can be recognized (Fig 3) for the Pingüino project veins. Trend 1 (violet arrow), exhibits high In contents (18 to 36 ppm) but a low Ag/Au ratio (~50 to 200), and comprises IVO, SAV, IVN and MC veins. Trend 2 (pink arrow), shows a wide dispersion in the Au/Ag ratio, but In values are low, usually below 1 ppm. This trend is constituted by the following veins ordered with increasing Ag/Au ratio (from ~100 to 4,000): ISL, KAR, CSV, FAN, MS, MNW, MS, KAL, LUN, MN and TR. Trend 3 (orange arrow) gather veins with intermediate In (2 to 15 ppm) and Ag/Au (200 to 1,000) values, involving ME, MN, SON, KAS and IVS. The cluster conformed by ME, KAR and CSV since they are very close to Trend 2 and Trend 3, are difficult to associate to any of these trends.

The three trends have a clear geographic association in plan view (Fig. 4), where the center is occupied with Trend 1, surrounded by Trend 3, and then by Trend 2 group of veins.

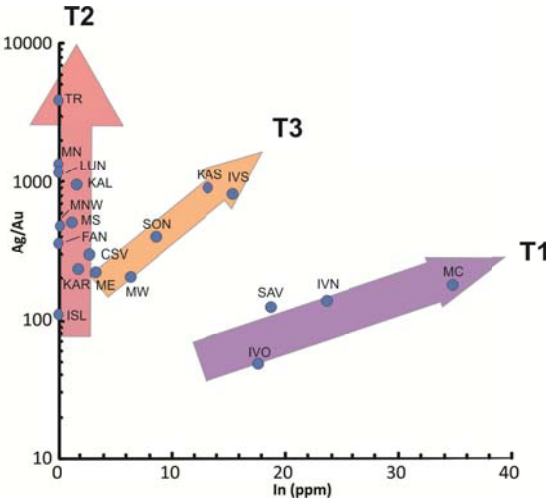

Figure 3. Binary diagram of averaged Ag/Au ratio vs. In values for the Pingüino project veins. Colored arrows represent three Trends, T1, T2 and T3.

Concluding remarks

Plan view of individual elements distribution show a main metals source point centered in the IVO and SON veins, and above the interpreted dioritic Kasia intrusion (Peñalva et al. 2008), with other secondary metal sources at KAL, TR, LUN, FAN, MN, KAR and ISL veins (see stars plotted at Fig. 2). The Au/Ag ratio also shows minimum values concentrated at the Kasia intrusion area.

Metals distribution at the Pigüino vein system show an important zonation and a good spatial correlation with geophysically (ground magnetics) interpreted intrusions at depth.

Kasia mafic intrusion is the most important metal source for the vein district, but also the related to or below the KAL, TR, LUN, FAN, MN, KAR and ISL veins represent a secondary or local metal source for the system.

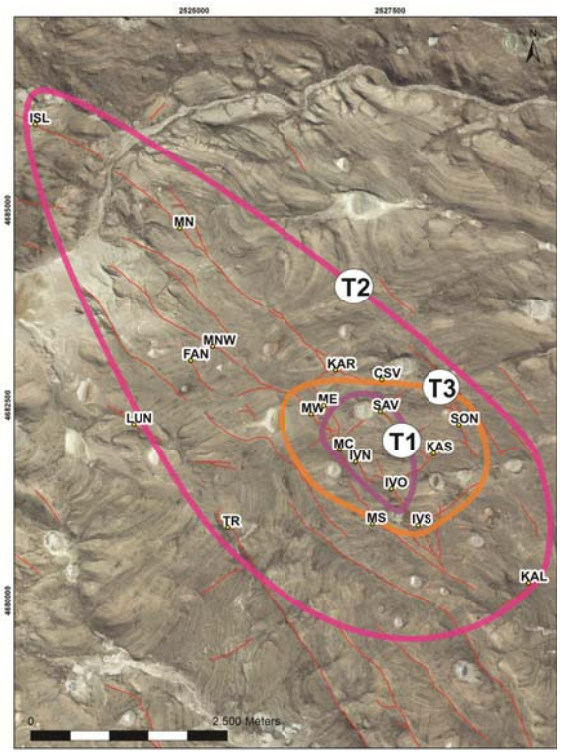

Figure 4. Veins grouped according to Ag/Au vs In. The center occupied with Trend 1, is surrounded by Trend 3, and then by Trend 2.

The three trends defined at Pingüino (Fig. 3 and 4) represent the different veins types. Trend 1 is represented by the dominant sulphide-rich veins (related to Lower Jurassic diorites), surrounded by Trend 2 dominant quartz-rich veins (related to Middle Jurassic andesitic porphyries), with Trend 3 being an intermediate zone that could reflect the mixing between the two main type of veins.

The quartz-rich veins shows very high Ag/Au ratio, compared with other deposits in the Deseado Massif, only comparable with the Ag-rich Martha mine.

The metals distribution and the relationship of possible metal sources with outcropping and/or not-outcropping intrusions should be considered as an important tool for further exploration programs at Pingüino, and other projects in the Deseado Massif.

References

Castor, S., Boden, D., Henry, C., Cline, J., 2003. The tuscarora Au-Ag district: eocene volcanic-hosted epithermal deposits in the Carlin gold region, Nevada. Economic Geology 98, 339–366.

Clarke, M., Titley, S., 1988. Hydrothermal evolution in the formation of silver-gold veins in the Tayoltita Mine, San Dimas District. Economic Geology 1830–1840.

Cole, D. R., & Drummond, S. E., 1986. The effect of transport and boiling on Ag/Au ratios in hydrothermal solutions: a preliminary assessment and possible implications for the formation of epithermal precious-metal ore deposits. Journal of Geochemical Exploration, 25(1-2), 45–79.

Eunadi M.T., 1994. Ag/Au Ratios in time and space in the Bingham Mining District, Utah: Implications for genesis and exploration. Society of Economic Geologists International exchange lecture. Stanford University Stanford, California, U.S.A.

Fernández, R., Blesa, A., Echeveste, H., Myketiuk, K., Andrada De Palomera, P., Tessone, M., 2008. Los depósitos de oro y plata vinculados al magmatismo Jurásico de la Patagonia Argentina. Revista de la Asociación Geológica Argentina 63, 665 – 681.

Jovic, S.M., 2010. Geología y metalogénesis de las mineralizaciones polimetálicas del área El Tranquilo (Cerro León), sector central del Macizo del Deseado, Provincia de Santa Cruz. (1ra ed.) Editorial de la Universidad de La Plata (EDULP), La Plata, Argentina.

Jovic, S.M., Guido, D.M., Schalamuk, I.B., Ríos, F.J., Tassinari, C.C.G., Recio, C., 2010. Pingüino. In-bearing polymetallic vein deposit, Deseado Massif, Patagonia, Argentina: characteristics of mineralization and ore-forming fluids. Mineralium Deposita 45, 735-763.

Jovic, S., Guido, D., Melgarejo, J., 2011. The indium-bearing minerals of the Pingüino polymetallic vein system, Deseado Massif, Patagonia, Argentina. The Canadian Mineralogist 49, 931–946.

Peñalva GA, Jovic SM, Chernicoff CJ, Guido, DM, Schalamuk IB, 2008. Cuerpos intrusivos asociados a las mineralizaciones polimetálicas del depósito Cerro León, área del anticlinal El Tranquilo, Santa Cruz: Evidencias Geofísicas. Rev Asoc Geol Argentina 63 (1): 14-23.

Intrusion-alteration-mineralization relationships from the porphyry Cu-Au deposit at Kiseljak, Serbia

I. Márton*, D. Dragić, B. Djordjević & P. Fox
Dunav Resources doo, Tulare, Serbia (TSX. V: DNV)
** Current affiliation: Avala Resources doo, Bor, Serbia*

R. M. Tosdal
PicachoEx LLC, USA

J. van der Toorn
Avala Resources doo, Bor, Serbia (TSX. V: AVZ)

S. Hasson
Dunav Resources Ltd, Longueuil, Quebec, Canada

Abstract. The Tulare ore field (Lece Magmatic Complex, southern Serbia) hosts porphyry Cu-Au and epithermal Au-Ag-Pb-Zn-Cu vein deposits centred on dioritic subvolcanic intrusions of Oligocene age. The most explored prospect within the Tulare ore field is the Kiseljak porphyry Cu-Au deposit, where recent exploration by Dunav Resources Ltd. has outlined a NI 43-101 compliant inferred resource of 300 Mt grading an average of 0.27% copper and 0.26g/t gold. This study presents new field relationships, petrology, mineralogy and geochemical data acquired during the recent resource drilling campaign. These results define the geochemical, spatial and temporal evolution of the intrusive and alteration processes and the scale of the porphyry mineralization system at Kiseljak.

Keywords. Serbo-Macedonian-Rhodope province, Lece Magmatic Complex, Oligocene, Kiseljak porphyry Cu-Au

1 Regional Geology

The Kiseljak porphyry Cu-Au deposit is located in the southwestern part of the Lece Magmatic Complex (LMC) in southern Serbia. The LMC is part of the Serbo-Macedonian-Rhodope province of the Tethyan Metallogenic Belt (Fig. 1). Beginning in the Cretaceous, the region has been a part of the convergent margin of the Eurasian plate, experiencing a series of Late Cretaceous to Miocene subduction and collision events interspersed with syn- and post-orogenic extension.

The basement to the Eocene-Oligocene magmatic rocks in southern Serbia is formed by the Serbo-Macedonian Massif, which is a NW-SE-oriented tectonic block situated between the Carpatho-Balkanides in the east and the Vardar Suture Zone in the west (Schmid et al., 2008). The currently northwest-trending Serbo-Macedonian-Rhodope province is characterized by mostly Pb-Zn-Ag-Cu-Sb deposits consisting of Pb-Zn replacement, fracture-controlled Sb-vein, porphyry Cu±Au±Mo, and stratiform volcano-sedimentary deposits extending across several geotectonic units from Hungary through Serbia and Macedonia to southern Bulgaria, northern Greece and western Turkey where it connects to the Anatolian metallogenic province. The porphyry Cu-Au systems are well known in northern Greece and Macedonia where the world class Skouries porphyry Cu-Au deposit (Frei, 1995; Kroll et al., 2002) or the operating Buchim mine (Serafimovski et al., 2010) share many similarities with the Kiseljak porphyry deposit.

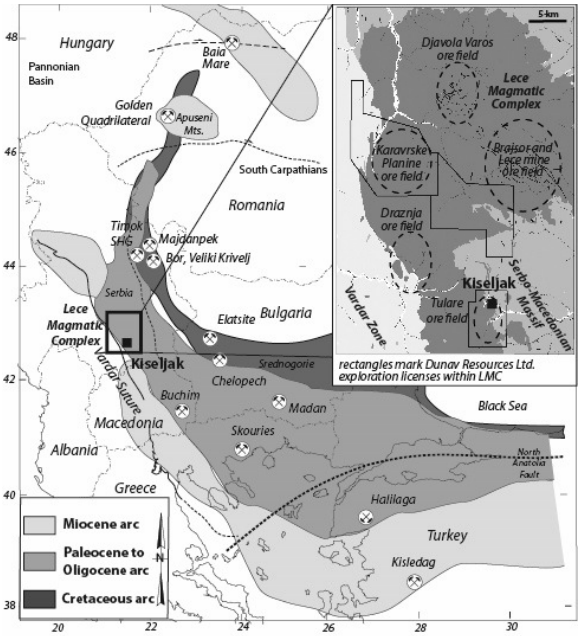

Figure 1. The location of the Paleocene-Oligocene Serbo-Macedonian-Rhodope segment of the Western Tethyan Metallogenic belt and the major ore deposits in the area.

The Lece Magmatic Compex (LMC) is a northerly elongate, 45 km long and 25 km wide belt of predominantly andesitic volcanic rocks intruded by diorite porphyries. The LMC is made up by Eocene to Oligocene volcanic-sedimentary and sub-volcanic dioritic intrusions. These units overlie and intrude the metamorphic Serbo-Macedonian Massif basement along the Vardar suture zone (Karamata and Krstic, 1996; Schmid et al., 2008). The volcanic rocks include lavas, pyroclastic breccias and lapilli tuffs with andesitic to dacitic composition. Volcanic vents, and three ring structures interpreted to be caldera margins, have been proposed initially (Gajtan, Djavolja Varos and Tulare calderas; Pešut, 1976), but now the field is considered to consist of numerous smaller calderas and volcanic vents (Serafimovski, 1990). The igneous and basement rocks in the LMC are locally hydrothermally altered and host metal concentrations in seven distinguished ore fields (Fig. 1): I) Lece ore field, II) Brajsor ore field, III)

Djavolja Varos ore field, IV) Kravarske Planine ore field, V) Tulare ore field, VI) Sijarinska Banja ore field (~20 km east of Tulare) and VII) Draznja ore field.

The Lece ore deposit, that has become an operating Pb-Zn-Au mine in recent times is underlain by numerous small magmatic centres localized along faults. Hydrothermal activity formed complex, several kilometres long silicified zones and localized hydrothermal breccias with both NW-SE and ESE-WNW trends, known as the "quartzose-brecciated Suta–Resovaca and Jezerina zones", which are the main host of the base-metal veins (Stajević, 2004).

The Tulare ore field is an area of approximately 25 km² in the southeastern part of LMC. Geophysical data suggest a larger pluton at depth and several hydrothermal systems presently outcropping at different levels of erosion (Kiseljak, Yellow Creek and Calovica Vis South porphyry Cu-Au and the Gubavce-Bakrenjaca epithermal Au-Ag-Pb-Zn-Cu mineralization; Dunav Resources Ltd. Press Release, 2013). The most explored prospect within the Tulare ore field is the Kiseljak porphyry Cu-Au deposit, which occupies the northern part of the project.

2 Stratigraphy, Intrusive Types and Timing of Porphyry Mineralization

Major rock units at the Kiseljak prospect, from oldest to youngest, are (Figs. 2 and 3): 1) Precambrian and Early Palaeozoic metamorphic basement rocks; 2) Tertiary volcanic and sedimentary rocks; 3) Early Oligocene diorite stocks and 4) Quaternary alluvium and colluvium deposits.

The metamorphic basement outcropping in the northern and eastern part of the Kiseljak prospect consists of biotite-plagioclase-quartz±hornbelende ±garnet gneiss, two-mica schist, and intercalated amphibolite. The quartzo-feldspathic and micaceous rocks contain abundant metamorphic quartz veins. The metamorphic rocks, especially the Fe-rich varieties, are hydrothermally altered and mineralized where intruded by dioritic rocks.

The Tertiary volcanic and sedimentary rocks unconformably overlie the metamorphic basement rocks. The supracrustal rocks dominate the southern part of the Kiseljak prospect where lapilli tuffs, pyroclastic breccias and lava flows are present. South of Kiseljak, at the Yellow Creek prospect, these rocks exceed 400 meters in thickness and dip shallowly toward the southeast.

At Kiseljak, dioritic stocks and dikes intruded both the metamorphic basement and Tertiary volcanic and sedimentary rocks. Three intrusive phases are distinguished based on cross cutting relationships within the porphyry Cu hydrothermal system. These are: (1) main or early porphyry, (2) intra-mineral porphyry and (3) post-mineral porphyry. The dioritic porphyry stocks cannot be separated petrographically and they are uniformly characterized with porphyritic texture consisting of fine-grained mafic rich feldspathic matrix and plagioclase-amphibole-biotite phenocrysts. Locally, fine-grained and equigranular varieties are present. The separation of intrusions into the three broad units is based on alteration characteristics, textural variations, xenolith content and intrusive contacts such as chilled contacts or truncated veins (Fig. 4). The main intrusive stock is elongated in outcrop along a 020° direction, and underlies most of the Kiseljak prospect. Drill holes along the eastern and northern margin of the intrusion demonstrate complex dikes extending from the main intrusive into the metamorphic basement. The intra-mineral intrusive suite intrudes the central part of the main intrusive stock and is exposed in the central and eastern part of the prospect. The post-mineral intrusions are narrow dykes (from to 1 to 5m) and are exposed only in the northern part of the Kiseljak prospect.

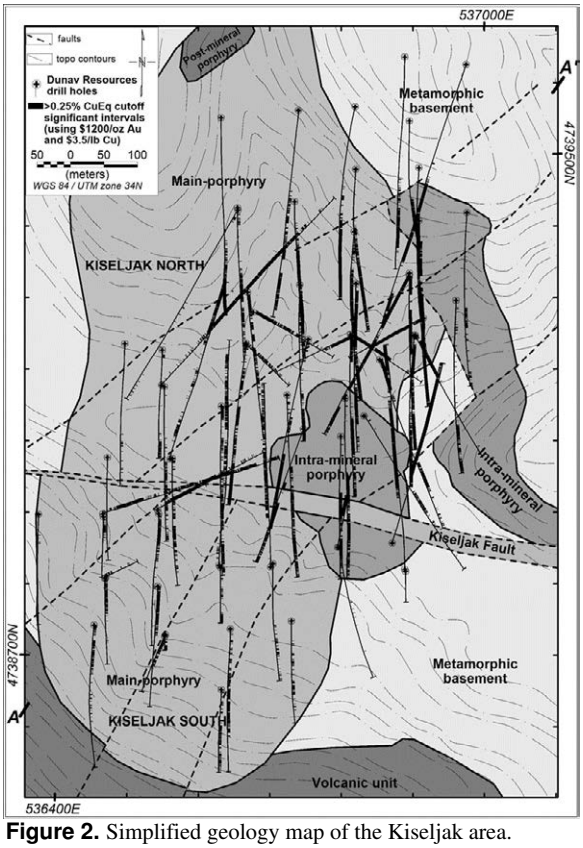

Figure 2. Simplified geology map of the Kiseljak area.

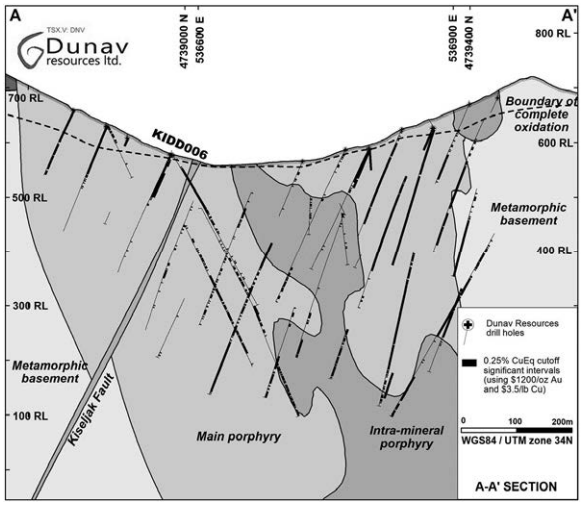

Figure 3. Representative SW-NE (A-A') cross-section (looking west) through the Kiseljak area (for location see Fig. 1).

Zircons from four diorite porphyry samples collected at Kiseljak were dated using the Sensitive High-Resolution Ion Microprobe – Reverse Geometry co-operated by the U.S. Geological Survey and Stanford University (Tosdal, 2012). The following U-Pb SHRIMP-RG ages are

calculated from the weighted mean $^{207}Pb_{corrected}$ $^{206}Pb/^{238}U$ ages of spot analyses on individual crystals:

- a sample from the early-porphyry shows an age of 33.0±0.3 Ma;
- two samples from intra-mineral porphyry show ages of 32.8±0.4 Ma and 33.0±0.3 Ma
- the late post-mineral porphyry suggest a distinctive younger age of 31.8 ± 0.3 Ma, different from the mineralized porphyry.

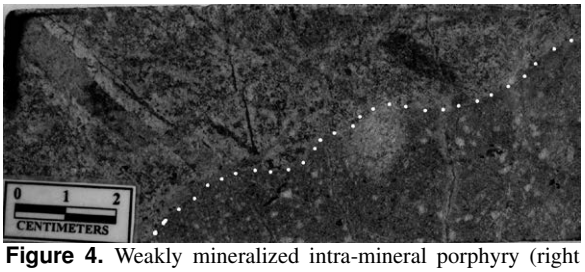

Figure 4. Weakly mineralized intra-mineral porphyry (right part of the image) intrudes potassic altered and well mineralized porphyry (left part of the image). Note that early-formed quartz-magnetite-k-feldspar-chalcopyrite veins are truncated by the intra-mineral porphyry, but later pyrite-chalcopyrite veinlets crosscut the intrusive contact.

The main post-mineral fault is the Kiseljak fault, which divides the prospect, strikes WNW and dips steeply southward. This fault zone has been intersected by several northward oriented drill holes. Based on drilling intersections and geological reconstructions it has an apparent normal displacement in cross section and dextral separation in plan view (Figs. 2 and 3). Kiseljak South (hanging wall) is displaced from Kiseljak North (footwall) by several tens of meters. The porphyry Cu-Au system appears inclined 20-25° to SSW based upon vein orientations and regional stratigraphic dips in the supracrustal rocks. Several northeast striking normal faults cut Kiseljak North and South. No significant displacement was observed along these faults.

3 Hydrothermal Alteration and Porphyry Veinlet Relationship

The Kiseljak alteration system covers an area of more than 2.5 x 1.5 km, affecting all rock types that occur within the prospect, and displays a characteristic alteration and vein pattern typical for porphyry Cu-Au deposits. Based on cross cutting relationships, a series of veinlets and associated alteration assemblages are distinguished (Fig. 5):

M-type veins are characteristic of the early main porphyry intrusion and are represented by sheeted or stockwork magnetite-quartz-K-feldspar-chalcopyrite-bornite veins, and correlate with high-grade ore zones.

Early A-type veins are the most important ore constituents. They form sheeted or stockwork arrays of quartz-chalcopyrite±magnetite assemblages within the potassic zones. Chalcocite has been recognized in some of these veins but it is unclear whether the high-sulphidation state mineral is hypogene or a supergene overprint. Distinct pale purple quartz-molybdenite-pyrite veins (A3-type) are present in the phyllic-altered assemblage.These late quartz veins contain very low Au-Cu grades and elevated but sub-economic Mo grades.

B-type pyrite-dominated stockwork veins form a broad halo around the potassic core where they constitute a phyllic alteration zone. A sericite-pyrite-quartz assemblage characterizes felsic host rocks, whereas a chlorite-pyrite assemblage characterizes mafic host rocks. A propylitic alteration assemblage of chlorite-carbonate-sericite-hematite lies outside the phyllic-altered zone or overprint the earlier alteration assemblages.

A porphyry-stage hydrothermal breccia formed at the transition between the high-grade quartz-chalcopyrite-pyrite-magnetite stage and barren quartz-pyrite-molybdenite stage. The breccia is related spatially to the occurrence of intra-mineral porphyry. At depths of below 0mRL chalcopyrite veins and chalcopyrite-bearing aplite and micropegmatite cut the porphyry host rock that also contains quartz and quartz-magnetite UST textures. Identification of UST textures in the deeper parts of the deposit suggests the possibility that the cupola zone of the underlying pluton may have been intersected.

Intermediate argillic alteration is widespread but not strongly developed, and overprints early potassic alteration where the porphyry system collapsed and meteoric fluids entered the system. The assemblage is characterized by hematite replacement of the early magnetite and by the formation of greenish smectite and illite assemblages in the plagioclase and mafic minerals.

Late calcite and gypsum veins cut the porphyry hydrothermal system. These veins are commonly associated with late-stage mineralized pyrite-galena-sphalerite assemblages.

4 Cu, Au and Mo Grade Distribution

At Kiseljak North, the highest grade Cu and Au ore is localized along the intrusive contact of the main intrusive and the basement. Dominantly easterly striking and steeply dipping (70±10° northward) sheeted and stockwork veins host the Cu and Au bearing minerals. The grade of mineralized rock gradually decreases toward east and west from the central area. The lateral changes in grade are asymmetric as it diminishes faster toward the basement on the east. At Kiseljak South and at the western margin of Kiseljak North, the ore is hosted by dominantly north-striking sheeted veins.

Globally the Au (ppm)/Cu (%) ratio is around 1 within in the hypogene sulphide ore. Locally within the deposit, the Au/Cu ratio may range between 0.5-2.5 depending upon the dominant hydrothermal alteration. The Au/Cu ratio decreases and the Mo content increases toward the low temperature alteration zones or with depth (Fig. 6).

Intra-mineral intrusions are characterized by abrupt changes in Au and Cu grade at the contact with pre-mineral rocks. The grade varies from barren above ~250mRL to high grade in the deeper parts. The mineralization remains open below the systematically explored depth of 150mRl as most drill holes stop in moderate to high Cu and Au grades (Fig. 3). Post-mineral dykes are barren.

Weathering affected the top 5 (in the valley) to 15 (on the hills) m of the ore body (Fig. 3). Cu is almost completely leached from this zone. The base of the complete oxidation zone generally includes a 1-2m thick zone of secondary Cu enrichment.

INTRUSIVE EVENTS	VEIN TYPES		MINERAL PARAGENESIS	STYLE/TEXTURE	ALTERATION HALO
PO1 main porphyry (33.0±0.3 Ma)	KI_M1	porphyry stage	MT>>KF>AC	discontinous, discrete	POTASSIC (±CALCIC) ALTERATION
	KI_M2		MT>>QZ>KF>CPY>CC>BN>AY	massive (w. halo), sheeted, stockwork, pegmatoid	
PO2 + PO3 intra-mineral porphyry (32.6±0.3 – 33.0±0.3 Ma)	KI_A1		QZ>>CPY-PY-CC-MT	stockwork and sheeted, massive or symmetric w. sulfide in centre	POTASSIC, INTERMEDIATE ARGILLIC AND PHYLLIC ALTERATION
	KI_A2		QZ>>MT-AC		
	KI_A3		QZ>>PY-MO-CPY		
	KI_B1		PY>>CPY>>CC>MT	stockwork, massive (w. halo), granular sulfide	PHYLLIC AND PROPYLITIC ALTERATION
	KI_B2		PY>>CH-SE		
PO4 post-mineral porphyry (31.8±0.3 Ma)	KI_B3		PY>>MO>CPY		
	KI_E1	epithermal stage	CA-CY-CH-RH-SP-GA	discrete, massive, coarse crystallin	CARBONATE, SILICA AND ARGILLIC ALTERATION
	KI_E2		GY-CY		
	KI_E3		AY		
	KI_E4		QZ-CY-GY		
			SI-LI-HM-GO-CY-MA-CS	massive, crustiform	WEATHERING

Figure 5. Summary table with the different vein types, their mineral composition and associated alteration halo observed at Kiseljak. Abbreviations: Ac - actinolite, Amp - amphibole, Ay - anhydrite, Bi - biotite, Bn - bornite, Cc - chalcocite, Ca- carbonate, Ch - chlorite, Cpy - chalcopyrite, Cy - clay, Hm - hematite, Ga - galena, Go - goethite, Gy - gypsum, Kf - K-feldspar, Ma - malachite Mo - molybdenite, Mt - magnetite, Py - pyrite, Qz - quartz, Rh - rhodochrosite, Se - sericite, Si - silica, Sp – sphalerite.

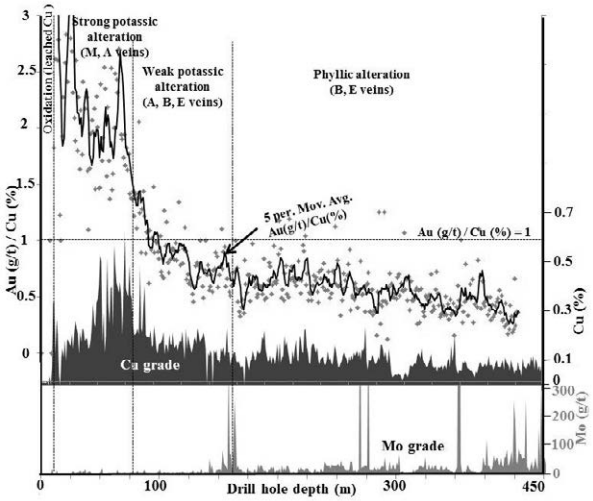

Figure 6. Au(ppm)/Cu(%) ratio, Cu and Mo grade distribution along KIDD006 drill hole.

5 Conclusions

The zircons from the Kiseljak porphyry systems indicate the diorite porphyry complex formed over a short time frame, from about 33 to 31 Ma. Based on cross cutting relationships and alteration zonation we define three main porphyry stages and related hypogene ore assemblages within the Kiseljak area:

a) The main-mineral assemblage includes the basement, and the early-porphyry intrusive. Within this assemblage the high-temperature silicate and oxide alteration minerals form the Au-Cu mineralized core of the deposit with a metal budget characterized by Au(ppm)/Cu(%) >1. Lower temperature alteration mineral assemblages overprint the mineralized rocks and show Au(ppm)/Cu(%) <1. At Kiseljak North, the highest grade Cu and Au is localized along the intrusive contact of the main intrusive and the basement and is hosted by easterly striking stockwork veins. At Kiseljak South and at the western margin of Kiseljak North, the ore is hosted by dominantly north-striking sheeted veins.

b) The intra-mineral assemblage includes the intra-mineral porphyry intrusives and is characterized by abrupt changes in Au and Cu grade at the contact with main-mineral rocks. The grade varies from barren above ~250m RL to high grade in the deeper parts. We interpret that the grade within the intra-mineral assemblage is associated with a second (telescoping) porphyry mineralization, which is open toward depth and suggests the potential for significant vertical extent to the mineralized system.

c) Post-mineral assemblage includes only few barren post-mineral dykes at Kiseljak North.

Acknowledgements

The authors wish to thank Dunav Resources Ltd. for the permission to publish the data. We would like to extend our gratitude to the geology staff at both Avala Resources Ltd. and Dunav Resources Ltd. who have contributed to making this project work. We are grateful to Mat Knaak, Fred Graybeal and Yordan Genchev who reviewed the abstract.

References

Dunav Resources Ltd. (2013) Press Release on January 09, 2013 - http://www.dunavresources.com/s/NewsReleases.asp .

Frei R (1995) Evolution of mineralizing fluid in the porphyry copper system of the Skouries deposit, Northeast Chalkidiki (Greece): evidence from combined Pb-Sr and stable isotope data. Economic Geology 90:746-762.

Karamata S, Krstic B (1996) Terranes of Serbia and neighbouring areas. In Karamata S, Knezevic-Djordjevic V & Krstic B (ed) Terranes of Serbia, University of Belgrade, pp 25-40.

Kroll T, Muller D, Seifert T, Herzig PM, Schneider A (2002) Petrology and geochemistry of the shoshonite-hosted Skouries porphyry Cu-Au deposits, Chalkidiki, Greece. Mineralium Deposita 37:137-144.

Pešut D (1976) Geology, tectonics and metallogeny of Lece massif. Rasprave Zavoda za geoloska i geofizicka istrazivanja 14:1–59 (in Serbian with English summary).

Schmid SM, Bernoulli D, Fügenschuh B, Matenco L, Schefer S, Schuster R, Tischler M, Ustaszewski K (2008) The Alpine-Carpathian-Dinaridic orogenic system: correlation and evolution of tectonic units. Swiss J of Geosci 101:139–183.

Serafimovski T (1990) Metallogeny of the Lece-Chalkidiki Zone, Doctoral dissertation, University of Stip.

Serafimovski T, Stefanova V, Volkov AV (2010) Dwarf copper-gold porphyry deposits of Buchim-Damjan Borov Dol ore district, Republica of Macedonia (FYROM), Geology of Ore Deposits 52:179-195.

Stajević B (2004) Geochemical haloes of gold in the Lece ore field (southern Serbia). Annales Geologiques de la Peninsule Balkanique 65:93-99.

Tosdal RM (2012) U-Pb SHRIMP-RG ages and trace element geochemistry of the Kiseljak and Yellow Creek porphyry Cu-Au prospects, Southern Serbia. Dunav Resources doo internal report. 21 pp.

Reopening and retrograde dissolution in the early quartz veins of the Altar porphyry Cu-(Au-Mo) deposit (Argentina)

Laura Maydagán, Marta Franchini
CONICET; b Departamento de Geología y Petróleo, Facultad de Ingeniería, Universidad Nacional del Comahue, Buenos Aires 1400, 8300 Neuquén, Argentina

Francisco Javier Ríos
Centro de Desenvolvimento da Tecnologia Nuclear, CNEN, Universidade Federal Minas Gerais, Belo Horizonte, Brazil

David Richard Lentz
Department of Earth Sciences, University of New Brunswick, Fredericton, New Brunswick, E3B 5A3, Canada

Abstract. Cathodoluminescence (CL) images and fluid inclusion analysis in the early quartz veins of the Altar (31° 29' S, 70° 28' W) porphyry Cu-(Mo-Au) (Argentina) have yielded preliminary results on the characteristics of the hydrothermal fluids of the Altar system.
Early type 2 veins show a complex growth history that revealed the existence of three generations of quartz: bright luminescence quartz (Ql), moderate luminescence quartz with euhedral growth zoning (Qmz), and reddish and low luminescence quartz (Qr); and textures that indicate processes of reopening, dissolution, and corrosion. Primary and pseudo-secondary fluid inclusion assemblages hosted in Qmz and Qr quartz generations suggest two episodes of unmixing (boiling) of the hydrothermal fluids. The last episode of fluid unmixing occurred between 350° and 370 °C and ~150 bars and correlated with the dissolution of the Qmz quartz, followed by the precipitation of Qr quartz. The youngest quartz generation (Qr) precipitated with chalcopyrite ± pyrite ± Au (capillary thin type 2b veinlets) that, together with disseminated mineralization in the potassic alteration, constitute the first pulse of Cu-Au-bearing fluids.

Keywords: Cathodoluminescence, dissolution, quartz, fluid inclusions, porphyry

1 Introduction

Altar porphyry Cu-(Au-Mo) deposit with epithermal Au-(Ag-Cu) veins (802 MT, 0.42% Cu and 0.059 g/t Au, cut-off 0.30% Cu equivalent; Peregrine Metals 2010) is located in the Andean Main Cordillera of San Juan Province (31° 29' S, 70° 28' W; Argentina), in the southern portion of the flat-slab segment (28-33°S), 25 km north of the world-class porphyry Cu-Mo deposits of Los Pelambres and El Pachón.

Igneous rocks in the area have been grouped into the Early Miocene lower volcanic complex that are composed of intercalations of lava flows and thin volcaniclastic units that grade upwards to a thick massive tuff and the Middle-late Miocene upper subvolcanic suite that consists of a series of porphyritic stocks and dikes and magmatic and hydrothermal breccias (Maydagán et al. 2011).

The mineralization at Altar is hosted in a complex stockwork with different generations of veinlets and disseminations, formed from several hydrothermal pulses and resultant repeated fracturing events. Based on the ore mineralogy and alteration envelopes according the classification of Gustafson and Hunt (1975), these veins can be grouped into EB (type 1), A (types 2a) and 2b chalcopyrite ± pyrite ± Au), B (type 3 quartz ± molybdenite), retrograde chlorite veinlets (type 4), D (types 5 and 6: tennantite (chalcopyrite, bornite) ± quartz ± pyrite ± gold ± tetrahedrite and enargite + pyrite, and E (types 7 and 8 of quartz ± sphalerite ± galena ± pyrite) veins and veinlets.

Porphyry-style quartz-sulfide stockwork has been explained by hydraulic fracturing caused by saturation of volatiles in the magmatic chamber (and) or by expansion of the exsolved hydrothermal fluids that decompress from lithostatic to hydrostatic conditions (e.g., Burnham 1979; Hedenquist and Lowenstern 1994; Bodnar 1995; Candela and Piccoli 1995). Recent studies revealed that porphyry veins are commonly multi-generational (e.g., Rusk and Reed 2002; Müller et al. 2003; Rusk et al. 2006, 2008).

Cathodoluminescence (CL) textures in quartz can be used to distinguish among multiple generations of quartz precipitated at different times in the veins, and to relate this quartz and the fluid inclusions it contains to specific fluid-flow events (Rusk and Reed 2002). This contribution presents a combined study of cathodoluminescence (CL) and fluid inclusions of the Altar early quartz type 2 veins in order to analyse fluid characteristics during vein formation and relationship with ore precipitation.

2 Materials and methods

Three samples representative of the early type 2 quartz veins were selected for CL imaging in specific areas, each accompanied by back scattered electrons (BSE) images and secondary electron (SE) at the University of New Brunswick, Canada.

Microthermometric analyses of fluid inclusion assemblages (FIAs) in quartz were carried out with a Linkam FTIR600 stage at the Centro de Desenvolvimento da Tecnologia Nuclear, Belo Horizonte, Brazil. The volatile components of selected fluid inclusions were analysed using Raman

microspectroscopy at the Departamento de Engenharia, Universidade Federal de Minas Gerais, Belo Horizonte, Brazil. Salinity, CO_2 content and density of inclusions with CO_2 were calculated using the program MacFLINCOR. Salinities of inclusions containing halite and sylvite temperatures were determined using the triangular phase diagram KCl-NaCl-H_2O (Roedder 1984). Salinities (wt % NaCl equiv) of inclusion with halite crystals were estimated from halite dissolution temperatures (Bodnar and Vityk 1994). Thermometric data associations in boiling fluid inclusions were compared to the surfaces of two phase stability NaCl-H_2O system (isobars of Driesner and Heinrich 2007) to determine trapping pressures and estimating absolute trapping depth (Shepherd 1985). True pressures are probably higher than indicated by the NaCl-H_2O model system because of the presence of minor CO_2 indicated by Raman analyses (Table 1).

3 Results

Early veins associated with the first stage of Cu-Au mineralization are characterized by an assemblage of quartz, anhydrite, feldspar, chalcopyrite, pyrite, and bornite. We have identified two subtypes: one subtype in which quartz is the most abundant mineral (2a) and a subtype in which chalcopyrite is dominant (2b).

Subtype 2a (quartz ± feldspar ± anhydrite, pyrite ± chalcopyrite ± bornite) veins are the most abundant and forms a stockwork of veins and veinlets. They have wavy (irregular) to straight walls and thicknesses ranging from ~1 mm to 4 cm. Anhedral quartz grains (0.1 to 0.8 mm) with crenulated edges occupy 90% of the vein. Subtype 2b (chalcopyrite ± quartz ± feldspar ± biotite ± anhydrite ± pyrite) are thin (<3 mm) veins and cut the subtype 2a veins. Traces of Au (0.5 ppm) were detected in chalcopyrite and pyrite crystals disseminated in the potassic alteration, whereas free gold was not recognized.

In the CL images of a 2a vein cut by chalcopyrite microveinlets (subtype 2b veins) is possible to recognize relicts of a bright luminescence quartz (Ql) surrounded by a moderate luminescence quartz with euhedral growth zoning (Qmz) and a youngest quartz generation of reddish and low luminescence quartz (Qr) (Fig. 1). Qr quartz accompanies the chalcopyrite in the irregular subtype 2b microveinlets that cut a 2a vein and shows irregular diffuse contacts toward the previous quartz cutting the growth zones of Qmz quartz. These textures indicate that the sulfides in these early veins are associated with the youngest quartz generation (Qr) that precipitated in vugs left by the dissolution of the previous quartz generations (Ql and Qmz) of the 2a vein.

The petrography of fluid inclusions and subsequent analysis were made on primary and pseudo-secondary fluid inclusions assemblages following the criteria of Goldstein and Reynolds (1994). Ql, Qmz, and Qr quartz generations contain four main types of fluid inclusions assemblages: intermediate-density, vapor-rich, liquid-rich, and saline inclusions (Fig. 2). Primary origin for the fluid inclusion assemblages was evidenced by the ocurrence of the inclusions along growth zones of the quartz crystals. They present variable sizes (10-30µm) and regular shapes (Fig. 2).

Primary intermediate-density fluid inclusions were only recognized in the Ql quartz from subtype 2a veins. The intermediate density inclusions have comparable proportions of liquid and bubble and contain minor CO_2 as indicated by melting events close to -56.6 °C and Raman analysis. Homogenization temperatures of CO_2 to a liquid between 22 and 24 °C and clathrate melting between 6.5 and 8.0 °C indicate CO_2 densities between 0.25 and 0.74 g/cm^3 and salinities of 3 to 6 % (Table 1). They did not reach total homogenization at 550 °C (Table 1).

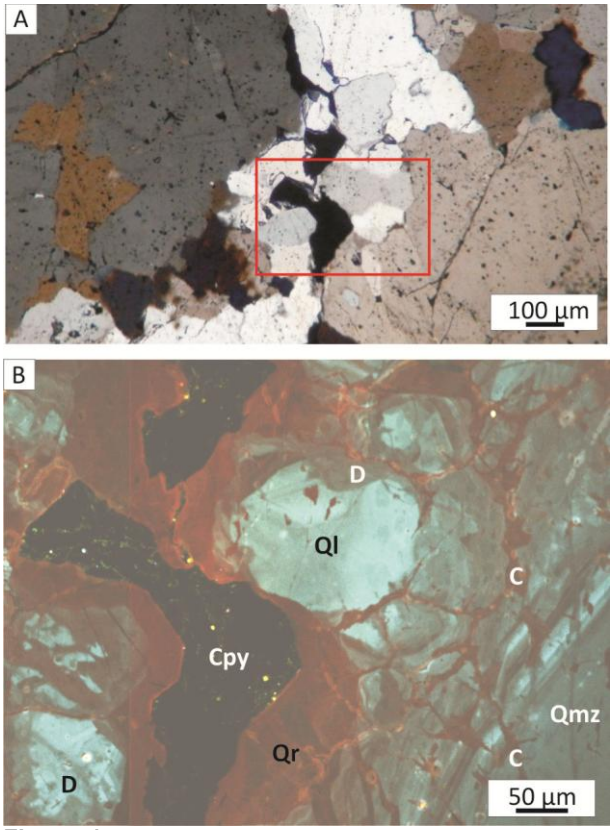

Figure 1. (A) Cross polarized transmitted light image of a subtype 2a vein cut by a subtype 2b vein, (B) Scanning electron microscope–cathodoluminescence (SEM-CL) image of the same area shows that three generations of quartz are present. Qr reddish quartz accompanies the chalcopyrite of the subtype 2b vein that precipitated in vugs left by the dissolution of the previous quartz generations (Ql and Qmz) of the 2a vein. Transmitted light image shows that the generations of quartz observed with SEM-CL are optically continuous. Quartz textures include (D) dissolution of CL-bright quartz followed by growth CL-gray quartz and (C) cobweb and splatter texture (e.g. Rusk and Reed 2002).

Liquid-rich inclusions were not clearly defined as primary inclusions. They contain minor CO_2 as indicated by melting events close to -56°C and confirmed by Raman analysis. Clathrate melting between 6.0 and 8.2 ° C indicate salinities of 3 to 7 % (Table 1) and homogenization temperatures of CO_2 to liquid phase of 22° and 26 °C indicate CO_2 densities of ~0.19 g/cm3. Total homogenization to a liquid (ThL) were registered at temperatures between 425 and 540 °C.

In Qmz and Qr quartz generations primary and

pseudosecondary saline fluid inclusions coexist with vapor-rich fluid inclusions (Table 1; Fig. 2). The vapor-rich inclusions (also contain minor CO_2 identified by Raman microspectroscopy. Homogenization temperatures of CO_2 to a liquid phase between 20° and 26 °C and clathrate melting between 6° and 8 °C, were used to calculate salinities of 3 to 7 % (Table 1). They homogenized to a vapor (ThV) at temperatures of 420 to 480 °C.

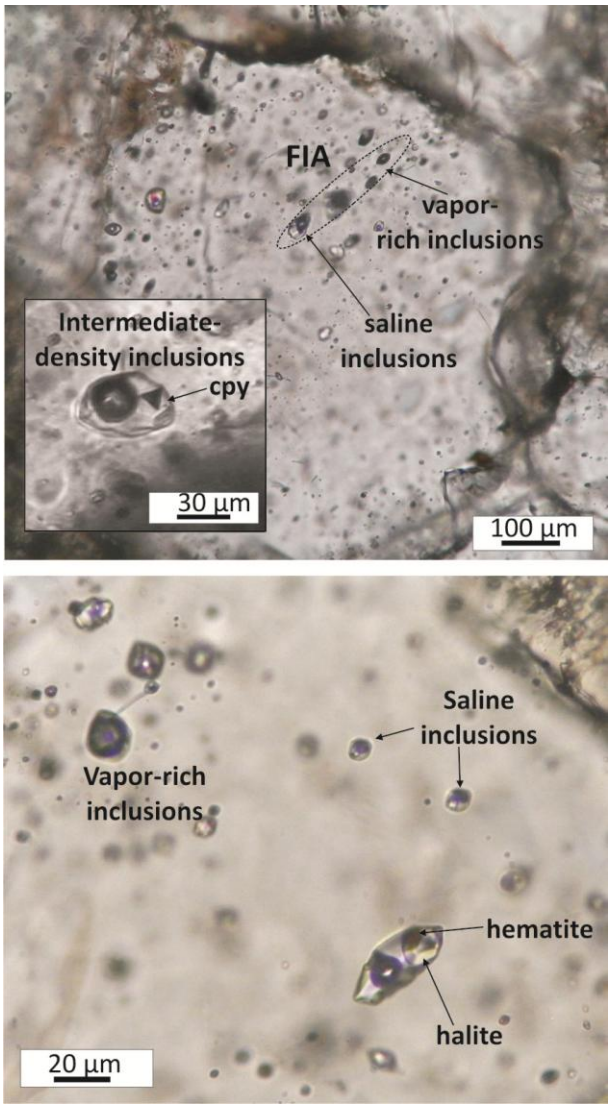

Figure 2. Examples of several fluid inclusion assemblages analysed in the type 2a vein.

The saline inclusions are classified into three phase saline inclusions with a daughter crystal of halite and multisolid inclusions containing halite, sylvite, reddish hematite, anhydrite, and chalcopyrite daughter crystals. Three-phase inclusions homogenized to a liquid between 339° and 405°C and by halite dissolution between 289° and 469°C. These inclusions reflect variable salinities between 30 and 36 wt % NaCl equiv for the first group and between 32 and 56 wt % NaCl equiv for the second group (Table 1).

Multisolid inclusions homogenized to a liquid between 242° and 540°C, most between 350° and 390°C, and by halite dissolution between 260° and 454°C. These inclusions also have variable salinities between 32 and 42 wt % NaCl equiv for the first group and between 36 and 70 wt % NaCl equiv for the second group (Table 1).

4 Discussion

The SEM-CL images of the type 2 veins studied show a complex growth history revealed by the existence of three different generations of quartz and textures indicating reopening, dissolution and corrosion of quartz (e.g. Rusk and Reed 2002). In a system of this nature, it is difficult to obtain data representative of the compositions and temperatures at which the fluids were originally trapped, without any subsequent modification.

Table 1. Fluid Inclusions assemblages of subtype 2a Altar veins

Quartz	Ql	Ql	Qmz/Qr	Qmz/Qr	Qmz/Qr
FI type	ID	L-rich	V-rich	three-phase	mulisolid
Salinity	3.9-6.5	3.2 - 7.3	3.0 - 7.0	30.5 - 48.5	32 - 70
Th (°C)	>550	425 - 540	390 - 480	340 - 410	300 - 550
Mode		L	V	L-hal diss.	L-hal diss.
Unmixing			X	X	X
Raman	CO_2	CO_2	CO_2	n.a	n.a
Pressure (bars)	500-650 (min)	500-700 (min)	150-350 (real)		150-350 (real)

Table 1. ID: Intermediate density fluid inclusions; L-rich: Liquid-rich inclusions; V-rich: Vapor-rich inclusions; L: liquid phase; V: vapor phase; n.a: not analized; Th: temperature of homogenization; hal diss: halite dissolution; (min): minimum trapping pressure; (real): real trapping pressure.

The intermediate-density fluid inclusions recognized in the Ql quartz homogenized at very high temperatures (425 to > 550 ° C); saline fluid inclusions with these homogenization temperatures were not recognized. This fluid may represent the first aqueous fluid exsolved from the magma at lithostatic pressures of >450 to 650 bars, temperatures of 425°-540°C and > 550 °C and low salinities of 3-7 wt % NaCl equiv. This fluid contained CO_2 and may have been responsible for altering the host rocks to form the potassic alteration and precipitated the bright luminescence quartz (Ql) of the 2a veins.

In Qmz quartz, the presence of primary coexisting saline fluid inclusions and vapor-rich fluid inclusions (along growth zones) that homogenized at similar temperatures (420° to 450°C), suggests that immiscibility of the magmatic–derived fluid (Henley and McNabb 1978; Roedder, 1984, 1992) occurred at vapor pressures of ~300 bars. These parameters correspond to a depth of ~3 km under hydrostatic pressures or ~1 km under lithostatic pressures (Shepherd 1985).

Another episode of fluid unmixing occurred between 350° and 370 °C and ~150 bars, consistent with the complex history of growth of these veins. The episodes of fluid immiscibility at these temperature and pressure conditions could produce retrograde dissolution and reprecipitation of quartz (e.g., Kennedy 1950; Fournier 1985).

The last episode of fluid unmixing in these veins (350 - 370 °C and ~150 bars) may correlate with the dissolution of the Qmz quartz, followed by the precipitation of the Qr quartz. Qr quartz precipitated with chalcopyrite ± pyrite ± Au (capillary thin type 2b

veinlets) that, together with disseminated mineralization in the potassic alteration, constitute the first pulse of Cu-Au-bearing fluids.

The textures of dissolution and corrosion of the quartz veins analysed indicate that the hydrothermal system was dominated by vapor-phase fluid (e.g., Landwing et al. 2010). S volatile agents (H_2S and possibly SO_2) have been proposed to be responsible for enhanced Cu and Au partitioning into the vapor phase (e.g., Heinrich et al. 1999; William-Jones and Heinrich, 2005; Nagaseki and Hayashi, 2008; Pokrovski, 2008) in contrast to other metals. Recent experiments have shown that Cu concentration in vapor-rich fluid inclusions can be modified by post-entrapment diffusional exchange through the host quartz (e.g Zajacz et al. 2009; Lerchbauer and Audétat 2012). However, significant transport of Cu and particularly Au in S-rich vapor-like fluids remains an important natural process compared to Fe, Zn, Pb that are invariably enriched in Cl-rich brines (e.g., Seo and Heinrich, in press). Pressure fluctuations of the hydrothermal fluids may have favoured the rapid decrease of the solubility of the metal complexes (e.g., William-Jones et al., 2002) that produced the first pulse of Altar Cu-Au mineralization.

Acknowledgements

This contribution forms part of a project financed by CONICET (PIP nº 6043 and PIP nº 1083), Universidad Nacional del Comahue (n° 04/I167 and 04/I002) and a Student Research Grant awarded by the Society of Economic Geologists. We also thank the support of FAPEMIG and CNPq (Brazil) research grants FAPEMIG CAG-PPM00666-11 and CNPq 307546/2011-0. David Lentz is supported by a Natural Sciences and Engineering Research Council Discovery research grant. We thank Dr. Douglas Hall (UNB) for the Chroma SEM-CL imaging.

References

Bodnar RJ (1995) Fluid-inclusion evidence for magmatic source for metals in porphyry copper deposits. In: Thompson JFH (ed) Magmas, fluids, and ore deposits. Mineralogical Association of Canada, Short Course Series vol. 23. Mineralogical Association of Canada, Ottawa, pp 139–152

Bodnar JR, Vityk MO (1994) Interpretation of microthermometric data for H2O-NaCl fluid inclusions. In De Vivo B and Frezzotti ML (ed) Fluid Inclusions in minerals: Methods and applications. Blacksburg VA, Virginia Technical Institute, pp 117−130

Burnham CW (1979) Magmas and hydrothermal fluids. In Barnes, HL (ed) Geochemistry of hydrothermal ore deposits. New York, Wiley and Sons, pp 71–136

Candela PA, Piccoli PM (1995) Model ore-metal partitioning from melts into vapor and vapor/brine mixtures. In: Thompson JFH (ed) Magmas, fluids, and ore deposits. Mineralogical Association of Canada, Short Course Series Vol. 23. Mineralogical Association of Canada, Ottawa, pp 101–127

Driesner T, Heinrich CA (2007) The system H2O-NaCl. Part I: Correlation formulae for phase relations in temperature-pressure-composition space from 0° to 1000°C, 0 to 5000 bars, and 0 to 1 X-NaCl. Geochim Cosmochim Acta 71: 4880−4901

Fournier RO (1985) The behavior of silica in hydrothermal solutions. In: Berger BR, Bethke PM (eds) Geology and geochemistry of epithermal systems. Rev Econ Geol Vol. 2. Society of Economic Geologists, Littleton, pp 45–61

Goldstein RH, Reynolds TJ (1994) Systematics of Fluid Inclusions in Diagenetic Minerals, SEPM Short Course 31. Society of Sedimentary Geology, 199 p.

Gustafson LB, Hunt JP (1975) The porphyry copper deposit al El Salvador, Chile. Econ Geol 70: 857–912

Hedenquist JW, Lowenstern JB (1994) The role of magmas in the formation of hydrothermal ore deposits. Nature 370:519–527

Heinrich CA, Gunther D, Audetat A, Ulrich T, Frischknecht R, (1999) Metal fractionation between magmatic brine and vapor, determined by microanalysis of fluid inclusions. Geology 27: 755–758

Henley RW, McNabb, A (1978) Magmatic vapor plumes and groundwater interaction in porphyry copper emplacement. Econ Geol 73: 1–20

Kennedy GC (1950) A portion of the system silica-water. Econ Geol 45: 629−653

Landtwing M, Furrer C, Redmond P, Pettke T, Guillong M, Heinrich C (2010) The Bingham Canyon Porphyry Cu-Mo-Au Deposit. III. Zoned Copper-Gold Ore Deposition by Magmatic Vapor Expansion. Econ Geol 105: 91–118

Lerchbaumer L, Audétat A (2012) High Cu concentrations in vapor-type fluid inclusions: An artifact? Geochim et Cosmochim Acta 88: 255–274.

Maydagán L, Franchini M, Chiaradia M, Pons J, Impiccini A, Toohey J, Rey R (2011) Petrology of the Miocene Igneous Rocks in the Altar Region, Main Cordillera of San Juan, Argentina. A Geodynamic Model within the context of the Andean Flat-Slab Segment and Metallogenesis. J S Am Earth Sci 32: 30–48

Müller A, Armstrong R, Herrington R, Seltmann R (2003) Characterization of quartz textures in porphyry copper ore deposits by scanning electron microscope–cathodoluminescence (SEM-CL). Mongol Geo 21: 32–35

Nagaseki H, Hayashi KI (2008) Experimental study of the behavior of copper and zinc in a boiling hydrothermal system. Geology 36: 27−30

Peregrine Metals Ltd (2010) Altar Project San Juan Province Argentina Project, Province, NI 43-101 Technical Report

Pokrovski GS, Borisova AY, Harrichoury JC (2008) The effect of sulfur on vapor-liquid fractionation of metals in hydrothermal systems: Earth Planet Sci Let 266: 345−362

Roedder E (1984) Fluid inclusions. Rev Min 12, 644 p

Roedder E (1992) Fluid Inclusion evidence for fluid immicibility during magmatic differentiation. Geochim et Cosmochim Acta 56:5–20

Rusk BG, Reed M (2002) Scanning electron microscope–cathodoluminescence analysis of quartz reveals complex growth histories in veins from the Butte porphyry copper deposit, Montana. Geology 30:727–730

Rusk BG, Reed MH, Dilles JH, Kent AJR (2006) Intensity of quartz cathodoluminescence and trace element content in quartz from the porphyry copper deposit at Butte, Montana. Am Mineral 91:1300–1312

Rusk BG, Reed MH, Dilles JH (2008) Fluid inclusion evidence for magmatic–hydrothermal fluid evolution in the porphyry copper–molybdenum deposit at Butte, Montana. Econ Geol 103: 307–334

Seo JH, Heinrich CA (2013) Selective copper diffusion into quartz-hosted vapour inclusions: evidence from other host minerals, driving forces, and consequences for Cu-Au ore formation. Geochim et Cosmochim Acta, in press

Shepherd TJ, Rankin AH, Alderton DHM (1985) A practical guide to fluid inclusion studies. Blackie and Son, New York.

Williams-Jones AE, Migdisov AA, Archibald SM, Xiao ZF (2002) Vapor-transport of ore metals. Geochemical Society Special Publication 7: 279–305

Williams-Jones AE, Heinrich CA (2005) Vapor transport of metals and the formation of magmatic-hydrothermal ore deposits. Econ Geol 100: 1287–1312

Zajacz Z, Hanley JJ, Heinrich CA, Halter, WE, Guillong M (2009) Diffusive reequilibration of quartz hosted silicate melt and fluid inclusions: Are all metal concentrations unmodified? Geochim et Cosmochim Acta 73: 3013–3027

Aitik – a Palaeoproterozoic porphyry copper deposit in northern Sweden

Nordin R.
Exploration Department, Boliden Mineral AB, Kontorsvägen 1, 936 81 BOLIDEN, Sweden

Karlsson P. & Lawther A.
Exploration Department, Boliden Mineral AB, Sakajärvi 1, 982 92 GÄLLIVARE, Sweden

Joslin G. & Höglund S.
Aitik Mine, Boliden Mineral AB, Sakajärvi 1, 982 92 GÄLLIVARE, Sweden

Wanhainen C.
Division of Geosciences, Luleå University of Technology, SE 971 87 LULEÅ, Sweden

Abstract. The Palaeoproterozoic Aitik porphyry Cu-Au-Ag-(Mo) deposit is situated in northern Sweden. It is a strongly deformed, metamorphosed and altered deposit, elongated in a northwest-southeast direction. The deposit is hosted within 1.9 Ga metamorphosed intrusive and volcano-sedimentary rocks. The Nautanen regional deformation zone is present to the east of the deposit. The ore body is 5 km long, known down to 800 m depth and it dips c. 45-60° west. The local mine stratigraphy is divided into three parts, the footwall complex, the main ore zone and the hanging wall. The footwall complex consists of multiphase quartz-monzodiorite intrusions, which intrudes into feldspar-amphibole-biotite gneisses. Adjacent to the contact with the footwall complex, the intrusion display biotite and K-feldspar alteration. The main ore zone consists of biotite gneisses, biotite schists and quartz-muscovite schists, containing 2-7 % pyrite, chalcopyrite and pyrrhotite. Trace molybdenite occurs associated with quartz veins, as well as within quartz veins. The overlying hanging wall rocks are banded hornblende-feldspar-biotite gneisses. A thrust separates the main ore zone and the hanging wall unit. The preferred genetic model is a metamorphosed and deformed porphyry Cu-Au-Ag deposit. Since mining started 1968 a total of 595 Mt has been mined. Ore reserves in the beginning of 2013 were 702 Mt.

Keywords. Aitik, Sweden, Porphyry Copper Deposit, Paleoproterozoic

1 Introduction and Exploration History

The Aitik deposit is situated some 15 km east of the town of Gällivare, Norrbotten, northern Sweden. Large scale mining has taken place in the Gällivare area since the late 1800's, when the iron ore mining in Malmberget started. Between 1902-1907 small scale mining at Nautanen (Cu-Au), some 15 km north of Aitik, took place.

Successful exploration work by Boliden in 1930's discovered the large and low grade Cu-mineralization at Aitik. Instrumental in the discovery was boulder hunting. A decision to develop the deposit as a conventional open pit mine, with a floatation plant, was taken in 1966. The production at Aitik commenced in 1968, at a rate of 2 Mt of ore per year. Since 1968 a series of production expansions has increased the annual production to 36 Mt. The Cu-(Au)-concentrates are railed to the Rönnskär smelter near Skellefteå.

Since 1968 some 595 Mt of ore has been mined with an average grade of 0.35 % Cu, 0.19 ppm Au and 3.5 ppm Ag. Ore reserves at the start of 2013 were 702 Mt grading 0.25 % Cu, 0.14 ppm Au and 1.6 ppm Ag. Measured and indicated mineral resources are 2354 Mt (New Boliden, Q4-2012 report) at 0.18 % Cu, 0.10 ppm Au and 0.9 ppm Ag. This brings the pre mining tonnage to 3651 Mt.

Boliden has started a scoping study looking into the possibility of raising annual production to 45 Mt of ore.

2 Geology and Mineralization

2.1 Regional Geology

The Aitik deposit is hosted within a 1.9 Ga old sequence of highly metamorphosed, hydrothermally altered and deformed volcanic, sedimentary and intrusive rocks. Subduction of oceanic crust around 1.9 Ga (Svecofennian event), took place ca. 200 km south of Aitik in the Skellefte district, north of the Archaean-Proterozoic paleoboundary of the Fennsocandian shield margin (Öhlander et al. 1999). The Svecofennian arc magmatism is present as calcalkaline to andesitic volcanic rocks and as the comagmatic Haparanda intrusive suite (Witschard 1984; Bergman et al. 2001). At 1.81-1.78 Ga extensive S-type magmatism (lina-type) dominates the region. These anatectic melts gave rise to an abundance of granitic rocks and pegmatites in Norrbotten (Skiöld et al. 1988).

To the east of Aitik the Nautanen Deformation Zone (NDZ) is present. NDZ is a major NNW-SSE crustal structure that can be traced throughout the entire Aitik field from Lake Ladoga to north of Gällivare (Bergman et al. 2001).

2.2 Local Geology of the Aitik Cu-Au-Ag deposit

The local geology at the Aitik mine is divided into three main parts, the footwall complex, the main ore zone and the hanging wall. The footwall complex, a multiphase intrusion complex, ranging in composition from monzodiorites to diorites, is hosting low-grade porphyry

style mineralization (Wanhainen et al. 2006). The footwall complex occurs as a km-sized plug-like large intrusion, but also as small sills or dikes, some 5-20 m thick. North of the main intrusive body a swarm of elongate dykes intrude roughly parallel to the NDZ. The surrounding host rocks to these intrusives are (feldspar)-amphibole-biotite and biotite gneisses. The main sulphides present are pyrite, chalcopyrite and pyrrhotite. Trace bornite and molybdenite is present. Sulphide-bearing quartz veins, sulphide stingers and dissemination is present throughout the footwall complex. Hornblende veins with an albitic halo and sulphide mineralization is also a common feature. The total sulphide content is normally between 1-3 %. In the upper part of the intrusion potassic alteration is present as K-feldspar and biotite.

Adjacent to the contact between the dioritic porphyries and the main ore zone, a transitional zone of intensely banded and mottled K-feldspar-biotite-hornblende-garnet alteration is often present. The main ore zone at Aitik consists of strongly deformed and foliated muscovite-(sericite) schist, biotite schist and biotite gneisses, normally with 2-7 % sulphides. The contact between muscovite and biotite schist is gradational, with muscovite schist preferably occurring at the upper contact to the hornblende banded gneisses of the hanging wall. Garnet porphyroblasts are present in minor amounts throughout the entire ore zone, but occur more frequently towards the footwall side, where the biotite gneiss is present.

Multiple veins consisting of quartz, barite, epidote, hornblende and k-feldspar occur in the main ore zone. The most abundant sulphide is pyrite, followed by chalcopyrite. Pyrite occur most frequently at the contact to the hanging wall, and chalcopyrite becomes more abundant towards the footwall contact. Pyrrhotite occurs throughout the entire ore zone. Molybdenite is present in and along edges of quartz veins, particularly in the northern part of the open pit. 1-2 % magnetite occurs as dissemination within the muscovite and biotite schists. Gold occurs as native, amalgam and electrum, often associated with K-rich silicate phases, or chalcopyrite (Sammelin et al. 2011). Gold gives an important economic contribution.

The hornblende banded gneiss in the hanging wall is thrusted over underlying muscovite schists. The hanging wall contact is sharp, and display C-S shear fabric, indicating either a thrust or a slide contact. The hornblende banded gneiss is medium grained, greenish grey and exhibits a fine banding. It is un-mineralized, and occur stratigraphically above the overlying main ore zone over a strike length in excess of 5 km. The thickness of the unit have been proven by drilling to be more than 400 m. Locally the hornblende banded gneiss exhibits garnet porphyroblasts and silicification.

Pegmatites of the Lina type occur throughout the entire stratigraphy. They are steeply dipping and emplaced during the folding and shearing of the volcanic units. Texturally they are very coarse grained and reddish to pink in colour. Mineralogically they are composed of K-feldspar, plagioclase, quartz, and euhedral tourmaline, with minor stilbite and chabazite (Wanhainen and Martinsson 2003). Local folding of the steeply dipping Lina pegmatites can be observed in the open pit (Wanhainen et al. 2012). Thickness of pegmatites can be in excess of 40 m..

The ore zone at Aitik is 5000 m long and up to 450 m wide. It strikes roughly N-S, and it is gently folded around the intrusive footwall complex. The hanging wall contact dips at 45° to the west and on the footwall side the dip is roughly 55° to the west, giving the ore zone a funnel shaped geometry. The Ore contact towards the hanging wall is sharp, which is in contrast to the footwall where it is gradational. Drilling has encountered mineralization down to 600 m level in the southern part of the open pit, and down to 800 m in the north. The mineralization remains open at depth. Figure 1 shows a general geological map of the Aitik mine area, with a sketch outline of the main open pit and the Salmijärvi open pit in the south.

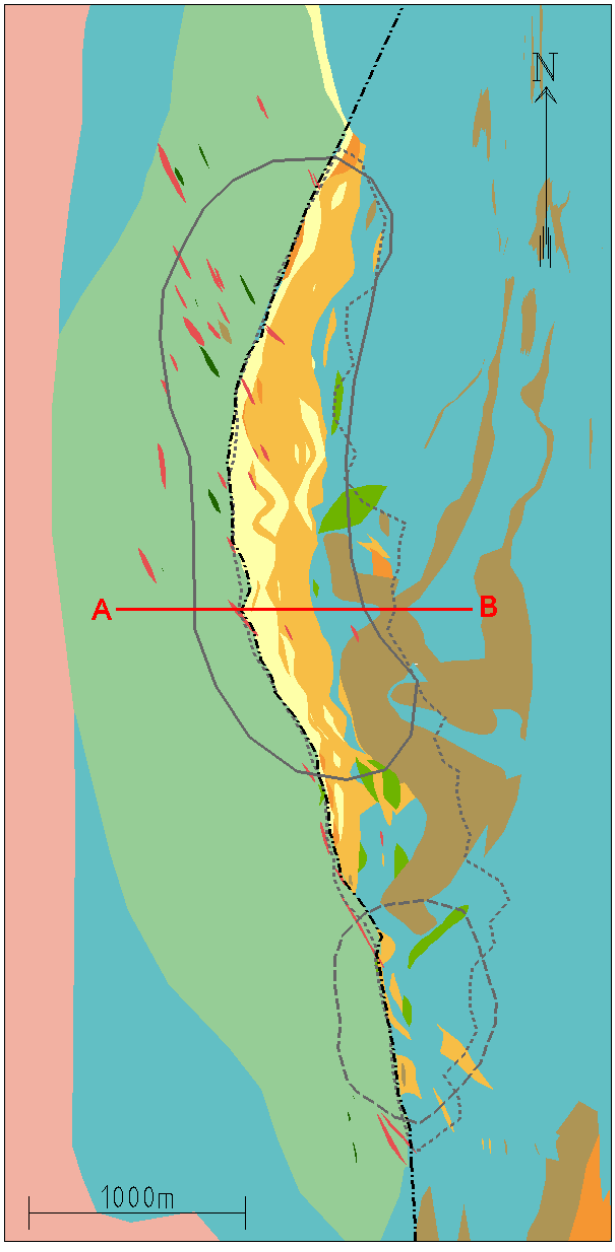

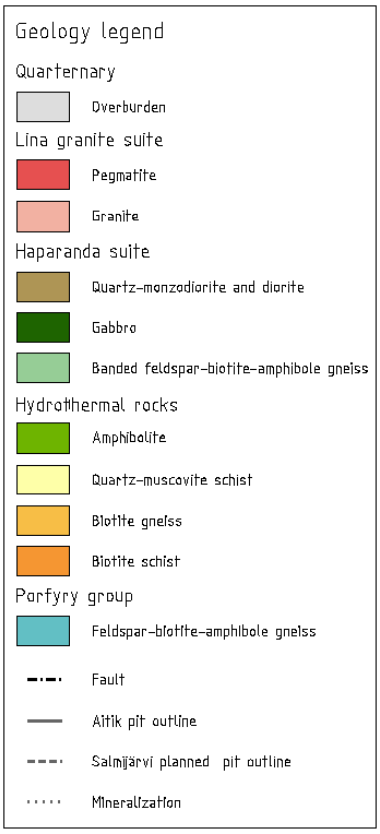

Figure 1. Geological map and legend of the Aitik mine area, showing the main rock types and the open pit outlines, of the Aitik main open pit (the northern pit), and the Salmijärvi open pit (the southern pit).

3 Genesis of the Aitik deposit

The presence of several 1.9 Ga old co-magmatic phases of quartz-monzodiorite and diorite with porphyritic and medium grained texture displaying classical sulphide-quartz-vein stockwork in the apex of the intrusion and a pyrite-chalcopyrite dissemination with associated potassic alteration, is strongly reminiscent of younger porphyry copper deposits (Lowell and Guilbert 1970). Later deformation, partly associated with the NDZ, strongly affected the rocks in the area and elongated the Aitik deposit in a NNW-SSE direction. Metamorphism at amphibolite facies, and the associated deformation, caused the development of schists, the gneissic textures, and the growth of garnet porphyroblasts. Fluid inclusions from chalcopyrite-pyrite quartz stockwork mineralization at Aitik yields high salinity values (30-38 eq.wt.% NaCl, 300° C and pressures of nearly 3 kbar), which together with the high pressures supports the genetic model of a highly metamorphosed and deformed porphyry copper deposit, associated with the intrusion of 1.9 Ga quartz monzodiorites (Monro 1988; Wanhainen et al. 2012). Sillitoe (2012) describes similar salinity values for modern system, and Roedder (1984) describes salinity values ranging from 35 up 70 % when coexisting hypersaline liquid and vapour is present in modern systems.

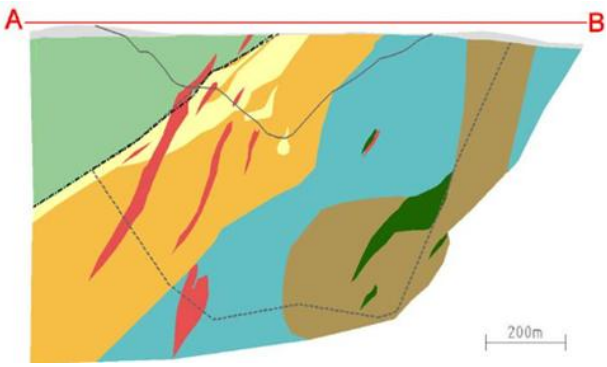

Figure 2. A Geological profile in Aitik looking north. The A (west) – B (east) profile shows the main rock types (for legend see figure 1) and the open pit outline of the Aitik main open pit at around 5000 Y.

A later event of overprinting IOCG-style character is also present within the Aitik area (Wanhainen et al. 2012). It manifests itself through locally abundant albite, scapolite and amphibole assemblages. Magnetite enrichment is locally found within amphibole-K-feldspar-epidote veins associated with scapolite alteration. Fluid inclusions associated with this event display high salinity (>30 eq.wt.% NaCl) and ferropyrosmalite ($(Fe, Mn)_8Si_6O_{15}(OH,Cl)_{10}$) and hematite as solid phases. Ferropyrosmalite has been identified as an alteration mineral after pyroxene in high-salinity brines in several IOCG deposits in the Cloncurry district in Australia (Williams et al. 2003).

This IOCG-style event has been dated to around 1.8 Ga (Wanhainen et al. 2005), and represents a late hydrothermal event overprinting the pre-existing porphyry copper mineralization displaying temperatures of 200-500° C and ~1 kbar.

Acknowledgements

The authors would like to thank New Boliden for the permission to publish these results.

References

Bergman S, Kubler L, Martinsson O (2001) Description of regional geological and geophysical maps of northern Norrbotten county. SGU Ba 56: 5-100

New Boliden (2013) press release Q4-2012, www.boliden.com.

Lowell JD, Guilbert JM (1970) Lateral and vertical alteration-mineralization zoning in porphyry ore deposits. Econ Geol 65: 373-408

Monro D (1988) The geology and genesis of the Aitik copper gold deposit, Arctic Sweden. Unpublished Ph.D. thesis, Univ of Wales, College of Cardiff, UK, 386p.

Öhlander B, Mellqvist C, Skiöld T (1999) Sm-Nd isotope evidence of a collisional event in the Precambrian of northern Sweden. In: Mengel F (ed.). Precambrian orogenic processes. Special Issue. Precam Res 93: 105-117

Roedder E. (1984), Fluid inclusions: Reviews in Mineralogy, v. 12, 644 p.

Sammelin M, Wanhainen C, Martinsson O (2011) Gold mineralogy at the Aitik Cu-Au-Ag deposit, Gällivare area, northern Sweden. GFF133 (1-2): 19-30

Sillitoe R. H. (2012) Porphyry Copper Systems. Econ. Geol. v.

105, pp. 3-41.
Skiöld T, Öhlander B, Vocke Jr RD, Hamilton PJ (1988) Chemistry of Proterozoic orogenic processes at a continental margin in northern Sweden. Chem Geol 69: 193-207
Wanhainen C, Martinsson O (2003) Evidence of remobilisation within the Palaeoproterozoic Aitik Cu-Au-Ag deposit, northern Sweden: A sulphur isotope study. In: Eliopolous et al. (eds.). Proceedings of the 7th Biennial SGA Conference, Mineral Exploration and Sustainable Development, Athens, Greece, 24-28 August 2003, pp. 1119-1122
Wanhainen C, Billström K, Stein H, Martinsson O, Nordin R (2005) 160 Ma of magmatic/hydrothermal and metamorphic activity in the Gällivare area: Re-Os dating of molybdenite and U-Pb dating of titanite from the Aitik Cu-Au-Ag deposit, northern Sweden. Miner Deposita 40: 435-447
Wanhainen C, Billström K, Martinsson O (2006) Age, petrology and geochemistry of the porphyritic Aitik intrusion and its relation to the disseminated Aitik Cu-Au-Ag deposit, northern Sweden. GFF 128: 273-286
Wanhainen C, Broman C, Martinsson O, Magnor B (2012) Modification of a Palaeoproterozoic porphyry system in northern Sweden; integration of structural, geochemical, petrographic, and fluid inclusion data from the Aitik Cu-Au-Ag deposit. Ore Geol Rev 48: 306-331
Williams P, Guoyi D, Pollard P, Broman C, Martinsson O, Wanhainen C, Mark G, Ryan C Mernaght T (2003): The nature of iron oxide-copper-gold ore fluids: fluid inclusion evidencefrom Norrbotten (Sweden) and the Cloncurry district (Australia): Proceedings of the seventh biennal SGA meeting, Athens, Greece, 24-28 August 2003, Extended Abstract, pp. 1127-1130.
Witschard F (1984) The geological and tectonic evolution of the Precambrian of northern Sweden - a case for basement reactivation? Prec Res 23: 273-315

District-scale fluid evolution in the Main Stage veins at Butte, Montana

Melissa Ortelli, Kalin Kouzmanov
Earth and Environmental Sciences, University of Geneva, 13 Rue des Maraîchers, CH1205 - Geneva, Switzerland

John H. Dilles
Geosciences, Oregon State University, Wilkinson Hall 104, Corvallis, OR 97331-5506, USA

Brian G. Rusk
Dept of Geology, Western Washington University, Bellingham, WA, 98225, USA

Abstract. To constrain the fluid evolution in the polymetallic Main Stage (MS) veins at Butte, USA, we present microthermometric measurements of fluid inclusions assemblages (FIAs) in co-genetic ore and gangue minerals through the different mineralization stages. Early quartz-hosted FIAs indicate the highest homogenization temperatures (T_h, between 290° and 320 °C) with salinity similar to the intermediate density FI of the pre-Main Stage (4 to 6 wt. % NaCl equiv). During the Cu-rich mineralization stage, a drop in salinity to 2 wt.% NaCl equiv. at temperature ~280°C, precedes locally developed phase separation, witnessed by coexisting vapor-rich and liquid-rich FI with similar T_h but with higher salinity (2.5 to 7 wt.% NaCl equiv.). Primary FIAs in sphalerite and rhodochrosite from the late mineralization stage indicate fluid temperature (T_h~210°C) and salinity (1.7 to 4 wt.% NaCl equiv.) decrease through time, towards the periphery of the district. This study suggests that mixing of a high-temperature fluid with salinity similar to fluids from the pre-Main Stage quartz-pyrite veins with cooler and lower salinity fluids (potentially of meteoric origin) combined with local boiling processes are responsible of the ore precipitation in the MS veins.

Keywords: fluid inclusions, enargite, sphalerite, epithermal polymetallic veins, Butte

1 Introduction

In the early 20th century, the studies of Reno Sales and Charles Meyer of the Butte ore district, Montana, USA, brought the new concept of "district scale metal zonation", and highlighted the role of sulfur fugacity in hydrothermal fluids as a key factor controlling ore precipitation and associated wall-rock alteration. (Sales 1913, Sales and Meyer 1949, Meyer et al. 1968). Today, the Butte Main Stage veins are considered as a typical example of a porphyry-centered polymetallic mineralization (Einaudi et al. 2003). According to Rusk et al. (2008b), formation of the polymetallic Main Stage veins at Butte results from fluids that formed porphyry-related pyrite-quartz veins, subsequently cooled, decompressed and mixed with circulating meteoric fluids under hydrostatic pressure regime. A fluid inclusion study in quartz from Main Stage veins, revealed CO_2-bearing (0.2 to 1 mol%) liquid-rich fluid inclusions that homogenize to liquid at temperatures between 250° and 300°C, with salinities ranging from 1 to 4 wt% NaCl equiv. (Rusk et al. 2008b).

In this study, we report new microthermometry data on fluid inclusions in ore minerals (enargite, sphalerite) and associated gangue minerals (quartz and rhodochrosite) through the paragenetic sequence of the Main Stage mineralization in the Butte district, Montana.

2 The Butte "Main Stage" mineralization

2.1 District scale metal zonation and sampling strategy

The ore mineralization at Butte is hosted by the Boulder batholith, quartz-monzonitic in composition and follows an E-W-striking swarm of porphyry dikes (Meyer et al. 1968). A first event of Cu-Mo porphyry-type mineralization ("pre-Main Stage", pMS; Meyer et al. 1968, Rusk et al. 2008a) centered onto the Anaconda and Pittsmont domes (Fig. 1), is crosscut by late Cordilleran base-metal lodes ("Main Stage", MS) characterized by strong mineral zoning. Sales (1913) defined three main metal and mineralization zones: (1) a central Cu-rich, (2) an intermediate Cu-Zn (Ag) and (3) a peripheral Zn-Pb-Ag-$MnCO_3$ zone (Fig. 1).

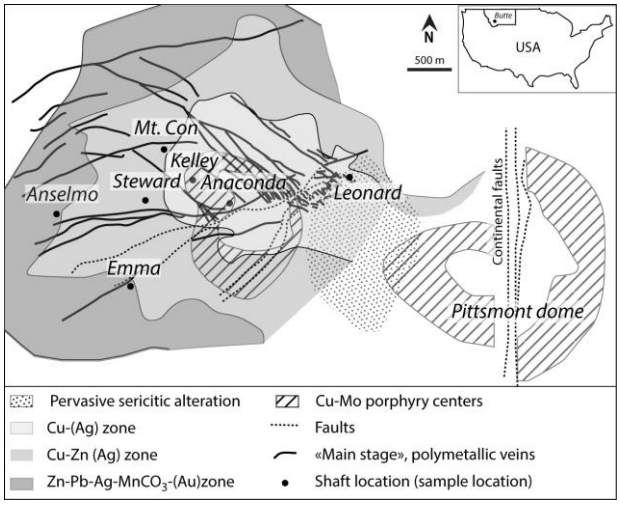

Figure 1. Simplified map of the Butte district (compiled from Meyer et al. 1968 and Rusk et al. 2008a) showing the Cu-Mo porphyry domes, the district metal zonation associated with the Main Stage veins, and the shaft or mine corresponding to the location of samples selected for this study.

Mineralization zones defined by Sales (1913) highlight the most abundant ore mineral associations through the district. In this study, we propose a simplified paragenetic sequence (Fig. 2), according to our textural

observations and cross-cutting relationships described by Weed (1912) and Meyer et al. (1968). Pre-Main Stage quartz-pyrite veins associated with grey sericite alteration (Rusk et al. 2008a) are commonly reopened during the early MS and re-filled by widespread quartz-pyrite veins (Stage 1, Fig. 2). A second stage marked by the deposition of Cu-rich mineral assemblages within the early quartz-pyrite veins regroups first the precipitation of enargite (Stage 2a), which is gradually replaced by a high-sulfidation mineral assemblage (covellite-chalcocite-digenite) in the central zone, or by sulfosalts or sphalerite in the intermediate Cu-Zn(Ag) zone (Stage 2b). Late sphalerite and rhodochrosite, abundant in the peripheral zone but present through the district, fill the open space, occasionally containing brecciated enargite, pyrite or sulfosalts.

Fluid inclusion samples were selected from different locations (Fig. 1) following the orientation of the main Anaconda vein (roughly corresponding to an E-W cross-section of the district), and from different levels, to investigate the vertical and lateral variations of intensive parameters and chemistry of mineralizing fluids on a district scale.

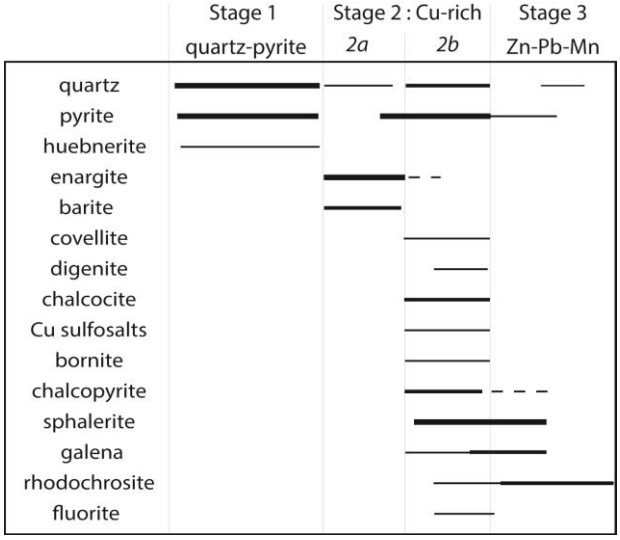

Figure 2. Simplified paragenetic sequence of the Butte Main Stage mineralization. Thick bars indicate higher abundances and dashed bars lesser abundances.

2.2 Trace elements in sphalerite

Sphalerite contains numerous primary fluid inclusions and is abundant in two mineralization stages. We have analyzed therefore sphalerite from the Leonard, Steward, Anselmo and Emma mines by electron microprobe (EMP) and have determined three generations of sphalerite according to their trace element composition.

The first generation of sphalerite is associated with galena and contains less than 100 ppm Cu, whereas the second generation associated with enargite and Cu-sulfosalts is enriched in Cu and Cd (up to 1.63 wt.% and 1.31 wt. %, respectively) and depleted in Fe (Fig. 3a). The late sphalerite, associated with rhodochrosite, reveals strong growth zoning with growth bands showing variable concentration of Cu, Fe and Cd below 0.35, 0.2 and 0.35 wt. %, respectively. Concentration of Mn in the sphalerite from the intermediate to peripheral zones in the district (Fig. 1) varies from 300 to 10,000 ppm (maximum content at the Steward mine), whereas sphalerite from the central zone contain <300 ppm.

Electron microprobe analyses were performed on the sample surface above single primary fluid inclusions measured by microthermometry. There is a strong positive correlation between homogenization temperature and Cd content of sphalerite hosting the FIAs (Fig. 3b). Laser ablation ICP-MS analyses will be performed to investigate the potential use of Cd concentration in sphalerite as a geothermometer.

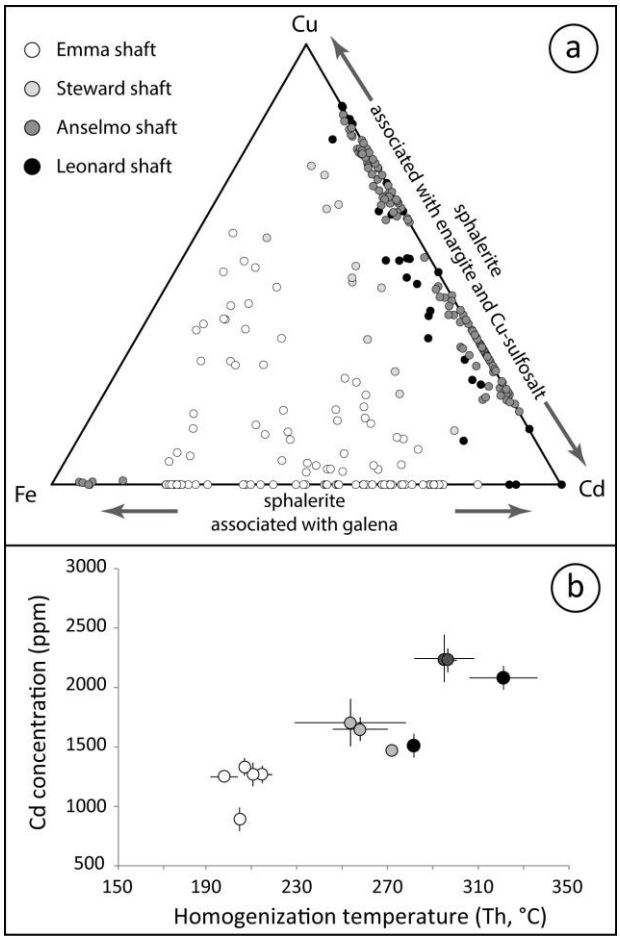

Figure 3. a) Ternary diagram showing the trace element ratio (mol %) between Cu-Cd-Fe in the sphalerite from the different mines. b) Homogenization temperature of fluid inclusion assemblages (FIAs) versus Cd concentration of the associated host sphalerite.

3 Fluid inclusion study

Pre-Main Stage primary fluid inclusion assemblages in quartz (PFIAs in pMS, Fig. 4) have been identified in samples from the deepest part of Leonard and Kelley mines as intermediate-density fluid inclusions related to the quartz-pyrite-grey sericite veins (Rusk et al. 2008a) with homogenization temperatures (T_h) between 360° and 380°C and salinity between 3 and 6 wt.% NaCl equiv. The FIAs hosted in the early quartz of the MS mineralization (stage 1, Figs. 2 and 4) have T_h between 290° and 320°C with salinity ranging from 4 to 6 wt. % NaCl equiv., and are similar to some primary FIAs in sphalerite. FIAs in quartz and enargite (stage 2a), have

similar T_h but lower salinity ~1.5 wt.% NaCl equiv. FIAs in quartz related to covellite and bornite (stage 2b) contain various fluid inclusion types. Vapor-rich fluid inclusions, locally associated with liquid-rich fluid inclusions which contain unidentified solids, indicate a heterogeneous fluid entrapment at ~280°C with a salinity ranging from 3 to 7 wt.% NaCl equiv. Primary FIAs hosted in sphalerite and secondary FIAs hosted in enargite have similar T_h but a lower salinity of 3 and 4 wt.% NaCl equiv., respectively. Secondary fluid inclusion assemblages (SFIAs) in quartz and sphalerite from stage 2b (Fig. 4) indicate a decrease of temperature and salinities down to 200°C and 2 wt.% NaCl equiv. and are similar to primary FIAs in late sphalerite and rhodochrosite. Finally, late sphalerite and rhodochrosite (stage 3) contain primary fluid inclusions with T_h ~210°C and salinity slightly higher in the sphalerite-hosted fluid inclusions than in the rhodochrosite-hosted ones (Fig. 4).

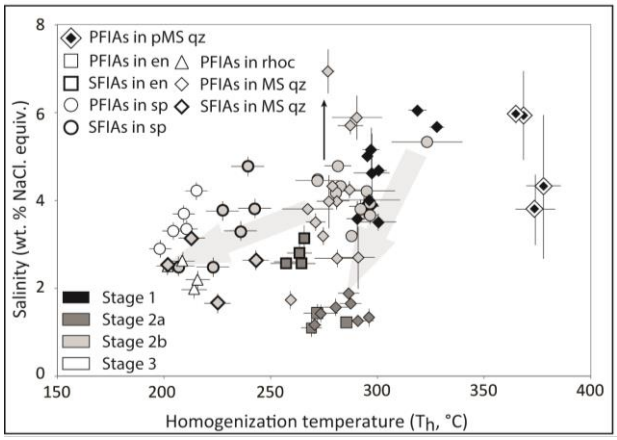

Figure 4. Microthermometric data from fluid inclusions hosted in quartz (diamonds), enargite (squares), sphalerite (circles) and rhodochrosite (triangles). Each point represents a FIA with error bars corresponding to 1σ standard deviation within the assemblage. Different stages correspond to the subdivision of the paragenetic sequence (see Fig. 2). Light gray arrows represent possible mixing paths, whereas the small black arrow represents the increased salinity due to boiling. Abbreviations: PFIAs – primary and pseudo-secondary fluid inclusion assemblage, SFIAs – secondary fluid inclusion assemblages, pMS – pre-Main Stage, en – enargite, sp – sphalerite, rhoc – rhodochrosite, qz – quartz.

4 Discussion

Primary fluid inclusion assemblages from the earliest quartz-pyrite veins of the Main Stage have T_h of 300-330°C and salinities similar to those of the intermediate-density fluid inclusions of the pre-Main Stage mineralization (B60, according to Rusk et al., 2008a): thus they can be considered as a lower-temperature analogue of the magmatic fluids responsible for the pMS mineralization at Butte. A drop of the fluid salinity from the first to the second stage by ~5 wt.% NaCl equiv., may be attributed to mixing of the pristine magmatic fluid with cooler and dilute fluid (meteoric water). Local heterogeneous fluid entrapment or boiling witnessed by coexisting vapor and liquid-rich fluid inclusions, is common during the late Cu-rich mineralization stage (2b) and provide a minimum pressure estimation around 80 bars, corresponding roughly to a minimum depth of 1 km under hot-hydrostatic conditions. The CO_2 content of the FIAs will be estimated by Raman microspectroscopy to better constrain the formation depth of the MS veins. Primary FIAs in sphalerite and rhodochrosite from the peripheral zone (Emma mine, Fig. 1), have the lowest measured temperature (T_h ~ 210 °C) through the district.

Trace element content of sphalerite (Cu-Fe-Cd-Mn) from the Butte MS veins varies through time on a district scale. Sphalerite replacing enargite or other Cu-sulfosalts reveals marked Cu and Cd zonation (central part, Fig. 1), with low Fe content, whereas the sphalerite associated with galena and rhodochrosite have clear zonation in Fe and Cd. Furthermore, the potential use of Cd concentration in sphalerite as a geothermometer is indicated by the strong positive correlation between T_h of the fluid inclusions and the Cd content of the host sphalerite.

5 Conclusion

The temperature of homogenization and salinity range of the FIAs in ore and gangue minerals from MS veins, between 200° and 350°C and between 1 and 5 wt. % NaCl equiv., is similar to the results of Rusk et al. (2008b). However, local boiling process during the Cu-rich mineralization stage, indicate a shallower emplacement depth of the Butte Main Stage veins than the Cu-Mo porphyry mineralization (5 to 9 km, Rusk et al. 2008a). This fluid inclusion study brings new data concerning the fluid evolution through the Main Stage polymetallic mineralization at Butte and indicates that mixing of a high-temperature and intermediate-salinity fluid (most probably magmatic in origin) with cooler and low-salinity fluid, combined with local boiling, result in ore mineral precipitation. Hydrogen and oxygen isotope studies of MS veins alteration and gangue minerals (micas and clay, Sheppard and Taylor 1974) and barite (Field et al. 2005), indicate meteoric water influx into the system, whereas sulfur isotope evolution remains poorly understood with sulfate–sulfide isotopic disequilibrium (Field et al. 2005). To further document the processes of mixing and boiling and determine the variation of CO_2 and metal concentrations in the mineralizing fluid, Raman microspectroscopy and laser ablation ICP-MS analyses on the studied fluid inclusion assemblages are currently in progress.

Acknowledgement

This study was supported by the Swiss National Science Foundation (grant 20021-127123).

References

Einaudi MT, Hedenquist JW, Inan E (2003) Sulfidation state of fluids in active and extinct hydrothermal systems: Transitions from porphyry to epithermal environments: Soc. of Econ Geol Spec Publ 10 : 285–314.

Field CW, Zhang L, Dilles JH, Rye RO and Reed MH (2005) Sulfur and oxygen isotopic record in sulfate and sulfide minerals of early, deep, pre-Main Stage porphyry Cu-Mo and late, shallow Main Stage base-metal mineral deposits, Butte

district, Montana: Chem Geol 215 : 61-93.
Meyer C, Shea E, Goddard C (1968) Ore deposits at Butte, Montana. In: Ridge JD (ed) Ore deposits of the United States 1933–1967: New York, American Institute of Mining, Metallurgical, and Petroleum Engineers 2:1363–1416.
Rusk BG, Reed M, Dilles JH (2008a) Fluid inclusion evidence for magmatic–hydrothermal fluid evolution in the porphyry copper–molybdenum deposit, Butte, Montana. Econ Geol 103:307–334.
Rusk BG, Miller BJ, Reed M (2008b) Fluid-inclusion evidence for the formation of Main Stage polymetallic base-metal veins, Butte, Montana, USA. Iin Spenser JE, and Titley SR (eds.), Circum-Pacific tectonics, Geologic Evolution, and Ore Deposits: Tucson, Arizona Geological Society, Digest 22 :573-581.
Sales RH (1913) Ore deposits at Butte, Montana. Transactions of the American Institute of Mining Engineers 46: 3-109.
Sheppard SMF, Taylor HP (1974) Hydrogen and oxygen isotope evidence for the origins of water in the Boulder Batholith and Butte ore deposits, Montana. Econ. Geol. 69: 926– 946.
Weed WH (1912) Geology and ore deposits of the Butte district, Montana: United States Geological Survey Professional Paper 74.

Supergene ore modifications of epithermal silver mineralization at Martha Mine, Deseado Massif, Argentina

Gerardo N. Páez, Remigio Ruiz, Conrado Permuy Vidal, Luciano López, Diego M. Guido, Sebastián M. Jovic
Consejo Nacional de Investigaciones Científicas y Técnicas (CONICET).
Instituto de Recursos Minerales (INREMI). Facultad de Ciencias Naturales y Museo.
Universidad Nacional de La Plata, Paseo del Bosque s/n, B1900FWA, La Plata, Argentina.

Abstract. The Martha underground silver mine is located in the southwestern portion of the Deseado Massif, Santa Cruz province, Argentina. Martha is an intermediate sulphidation epithermal deposit with a complex mineralogy dominated by Ag-As-Sb sulphosalts and Cu-Pb-Zn sulphides. The deposit is characterized by a structurally controlled vein system characterized by a complex history of fracturing and cementation, arranged in nine paragenetic stages that can be grouped into four episodes. Metal ratio vs. depth profile show a shallow 20 m thick oxidation zone dominated by mean Ag/Au ratio of about 800:1. This upper zone is composed an association of kaolinite, plumbogummite, limonites, jarosite, cerussite, chlorargyrite/embolite, native silver, malachite and azurite. Below the oxidized zone, a 30 m thick enrichment zone can be recognized by a sharp increase in the Ag/Au ratio (up to 20,000:1). This zone is composed by a mineral assemblage dominated mainly by argentite/acanthite, pyrargirite, native silver, chalcocite, digenite, covelite, and minor bornite and spionkopite. Below the enrichment zone, the primary hypogene zone is characterized by a progressive reduction in the Ag/Au ratio to values of about 1000:1. These changes are the first mention of a supergene enrichment blanket in the Deseado Massif; this possibility must be considered during exploration, as high grade ore-shoots may be concealed below a lower grade oxidized horizon at surface.

Keywords. Silver enrichment, Epithermal deposit, Jurassic, Deseado Massif, Patagonia.

1. Introduction

Supergene ore modifications, such as oxidation and secondary enrichment, can be a main factor in building up an economic-grade mineral deposit. This is especially true in terms of porphyry systems (e.g. Sillitoe and McKee, 1996; Hartley and Rice, 2005), but can also be an important ore forming process contributing to high grade ore shoots in epithermal deposits (e.g. Gröpper et al., 1991; Milési et al., 1999, Greffié et al., 2002; Chauvet et al., 2006).

The Deseado Massif (Fig. 1) is a 60 000 km^2 geological region located in the southern part of Extra-Andean Patagonia in the central portion of Santa Cruz province. For the past 15 years, this region has produced more than 3 million oz of gold and over 40 million oz of silver from four operational mines (Cerro Vanguardia, Martha, Manantial Espejo and San José; Fig. 1). This gold and silver producing district also has a great potential for expanding its known resources, as there are currently more than 50 prospects undergoing different stages of exploration.

In this work we address the role of supergene ore mobilization in an epithermal environment from the Deseado Massif, analysing the consequences on mineralogy and grade distribution in one of richest silver deposits in Patagonia, with significant implications for future exploration activities in the Deseado Massif and other epithermal districts.

2. Geologial setting

During the Middle to Upper Jurassic (177.8 to 150.6 Ma; Pankhurst et al. 2000), a volcanic mega-event occurred in Patagonia giving rise to the Chon Aike Large Igneous Province (Pankhurst et al., 1998; Pankhurst et al., 2000). In the Deseado Massif, this event is represented by a volcanic suite that was named the Bahía Laura Volcanic Complex (BLVC; Fig. 1) by Guido (2004). Pyroclastic rocks predominate within the BLVC, with subordinate amounts of intercalated lavas of andesitic to rhyolithic composition, and with a calcalkaline, peraluminous and high potassium signature (Pankhurst et al., 1998; Guido, 2004). Intricate stratigraphic relationships characterise this complex, with multiple intercalations of different rock facies (Echeveste et al., 2001; Lopez, 2006; Ruiz, 2012; Wallier, 2009).

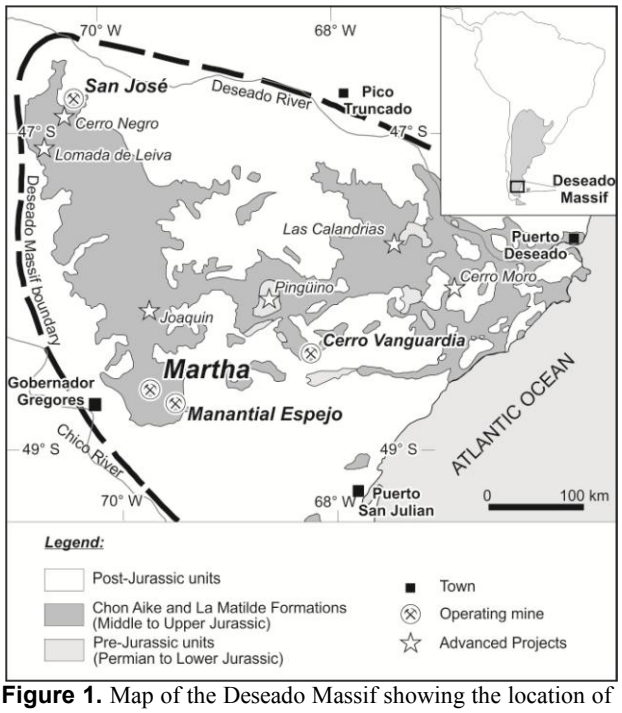

Figure 1. Map of the Deseado Massif showing the location of the study area and other localities mentioned in the text.

The BLVC contains numerous gold and silver epithermal deposits, leading Schalamuk et al. (1999) to define the Deseado Massif as an Au–Ag metallogenic province. The majority of the Au-Ag occurrences are low sulphidation (LS) style (Guido and Schalamuk, 2003; Echavarría et al., 2005; Fernández et al., 2008), but in the past few years intermediate sulphidation and polymetallic deposits also have been reported (Gonzalez Guillot et al., 2004; Guido et al., 2005; Jovic et al., 2010; Páez, 2012). Associated with the epithermal veins, widespread hot spring deposits are present (Guido and Campbell, 2011).

3. Martha Mine epithermal deposit

The Martha underground silver mine is located in the southwestern portion of the Deseado Massif (Fig. 1). The mine is operated by Coeur d'Alene Mines Corporation and has been under production since 2001. It has produced more than 21 million oz of silver (more than 50% of the Deseado Massif's total silver production) and over 28,000 oz of gold, with an average grade of about 3,500 g/t Ag and almost 5 g/t Au (Páez, 2012).

This deposit is characterized by a structurally controlled vein system hosted in Jurassic acid rocks of the BLVC that are locally represented by thick ash flow tuffs with thin intercalations of epiclastic sediments derived from a pyroclastic source (Páez et al. 2010). Mineralized veins can be subdivided into two groups (Páez et al. 2011): master structures that trend N120 (Martha and R4 veins), and tensional structures that trend E-W and coalesce into the master structures (Catalina, Francisca and Belén veins). High grade mineralization (up to 20% Ag eq.) has been encountered in both systems (Páez, 2012).

3.1. Vein paragenesis

Martha is an intermediate sulphidation epithermal deposit with a complex mineralogy dominated by Ag-As-Sb sulphosalts and Cu-Pb-Zn sulphides (Gonzalez Guillot et al., 2004; Gonzalez Guillot et al., 2008; Márquez-Zavalía et al., 2008; Páez, 2012). Veins are characterized by a high Ag/Au ratio of about 800:1 (Páez, 2012).

Mineralized structures at Martha are characterized by a complicated history of fracturing and cementation (Páez et al. 2011), arranged in nine paragenetic stages that can be grouped into four episodes (Páez, 2012). The first episode (E1) is characterized by a barren quartz-adularia vein network with no associated sulphides and is poorly represented within the deposit (Páez, 2012).

The second episode (E2) comprises four stages with a progressively decreasing sulphide content, ranging from a massive sulphide stage to an almost sulphide free stage (Páez, 2012). This episode is responsible for part of the high grade ore and is composed of silver and base metal bearing sulphides and sulphosalts, mostly pyrite, sphalerite, chalcopyrite, galena, silver bearing tetrahedrite (freibergite), native silver, electrum, pyrargirite, miargyrite, polybasite and minor arsenopyrite. Gangue minerals with this episode are adularia and minor quartz with associated illite. This episode has typically a breccia texture; however some crustiform banding may be present locally.

The third episode (E3) is composed of two barren stages characterized by massive adularia and minor quartz (Páez, 2012). This episode is typically massive to brecciated in texture and widespread among all vein structures, in most cases building up to the 95% of the veins.

Finally, the fourth and last episode (E4) is characterized by two late stages that partially remobilized the previously deposited metals, mostly due to re-brecciation followed by partial dissolution and re-precipitation (Páez, 2012). This episode is composed by discontinuous chalcedonic breccias with highly variable sulphide content and a system of thin (1-5 mm) sulphosalt veins that can locally build up a dense network. Ore minerals are composed mostly by pyrargirite, miargirite and native silver with minor chalcopyrite. This episode has a widespread distribution among Martha and R4 veins, but is less important or even absent among the E-W trending veins (Páez, 2012).

4. Supergene ore modifications

The shallowest portions of the Martha Mine vein system was affected by a series of changes that can be related to supergene alteration and secondary enrichment.

4.1. Geochemical changes

To analyze the effects of the supergene alteration on the metal distribution in the mineralized structures, a geochemical database of 3,226 geochemical assays were used in order to analyze the vertical distribution of metal ratios and Au, Ag, Cu, Pb and Zn contents.

The metal ratio (Ag/Au) vs. depth profile shows a shallow 20 m thick oxidation zone (Fig. 2) dominated by a maximum Ag/Au value of about 2,000:1 (with a mean value of 800:1); this shallow portion of the deposit is also characterized by higher Pb contents along with lower Cu and Zn grades, respect to the primary zone.

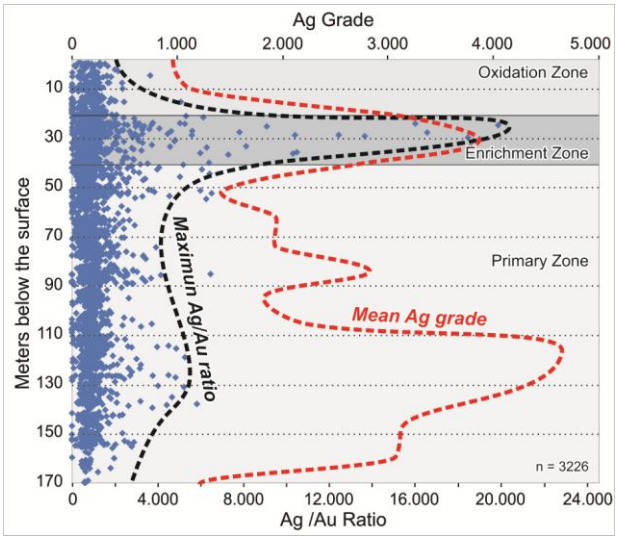

Figure 2. Vertical extent of the oxidation, enrichment and primary zones of Martha Mine as indicated by the changes in the Ag/Au ratio.

Below the oxidized zone, a 20-30 m thick enrichment zone can be recognized by a sharp increase in the maximum value of the Ag/Au ratio (up to 20,000:1, Fig. 2); this change is followed by an increase in Cu and Zn grades, and a progressive reduction in Pb contents.

Downwards, the primary hypogene zone (Fig. 2) is defined by a progressive reduction in the Ag/Au ratio to values as high as 4,500:1 (with a mean of 1,000:1), Cu and Zn values are also lower but they remain higher than in the oxidized zone; finally, Pb values reach the lowest values in the profile.

4.2. Mineralogical changes in the vein paragenesis

Geochemical changes are accompanied by a series of mineralogical modifications in the upper parts of the vein system (Páez, 2012). The newly formed minerals usually overprint the original textures, obscuring the paragenetic scheme discussed earlier.

The ore mineral association of the oxidized zone is characterized by native silver (*Ag°*), limonites ($FeO(OH)\cdot nH_2O$), jarosite ($KFe_3(SO_4)_2(OH)_6$), plumbojarosite ($PbFe_6(SO_4)_4(OH)_{12}$), chlorargyrite-embolite ($Ag(Br,Cl)$), boleite ($KPb_{26}Ag_9Cu_{24}Cl_{62}(OH)_{48}$), cerussite ($PbCO_3$), malachite ($Cu_2(CO_3)(OH)_2$) and azurite ($Cu_3(CO_3)_2(OH)_2$). This assemblage is recognized usually as thin veinlets and/or as cavity infill (Fig. 3a).

The enrichment zone is typically composed of argentite/acanthite (Ag_2S), pyrargyrite (Ag_3SbS_3), native silver (*Ag°*), chalcocite (Cu_2S), digenite (Cu_9S_5), covellite (CuS), and minor bornite (Cu_5FeS_4) and spionkopite ($Cu_{1.4}S$). These minerals can be identified partially replacing the primary sulphides (Fig. 3b), forming thin veinlets, or also as small cavity infill.

Finally, the enrichment zone grades downward into the primary mineral association, composed of Ag-As-Sb sulphosalts and Cu-Pb-Zn sulphides (Páez, 2012).

4.3. Mineralogical changes in the host rocks.

During hydrothermal circulation, the pyroclastic host rocks were altered to a narrow halo of adularia + illite ± smectite around the veins (Baluz et al., 2010; Páez, 2012).

This assemblage was overprinted by a supergene weathering, which produced an association of low crystallinity kaolinite + jarosite ± plumbogummite ($PbAl_3(PO_4)_2(OH)_5\bullet H_2O$) defining a advanced argillic alteration zone (Cedillo Frey et al., 2009; Páez, 2012) that is related to the descent of post hydrothermal acidic meteoric waters (Scott, 1990; Tzvetanova, 2003; Páez, 2012).

5. Concluding remarks

During extensive weathering of mineralized bodies, significant amounts of silver and copper may be dissolved from oxidizing zones and may be redeposited as supergene sulphides and sulphosalts at deeper levels dominated by reduced conditions (Boyle, 1968; Mann, 1984; Sillitoe and McKee, 1996; Greffié et al., 2002).

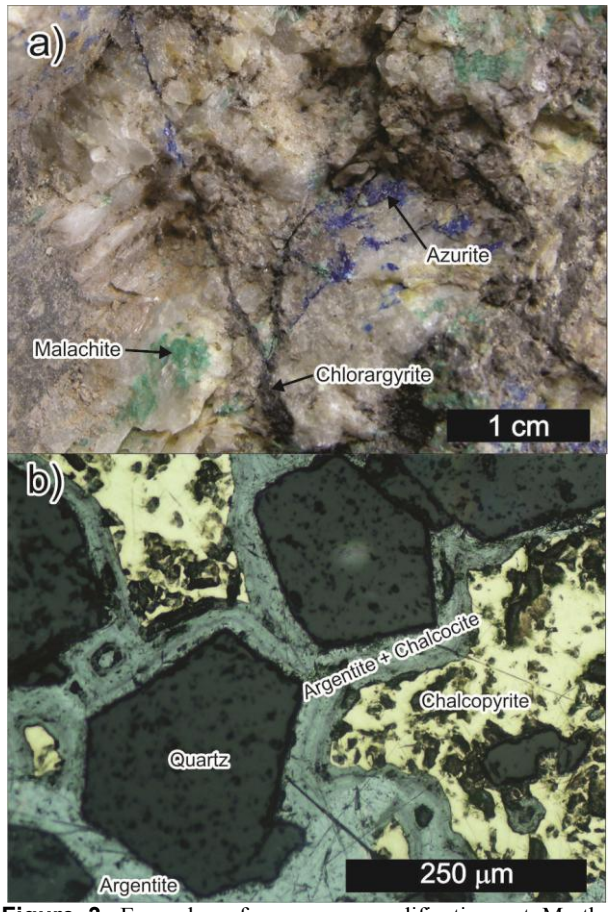

Figure 3. Examples of supergene modifications at Martha Mine. (a) Veinlets in the oxidation zone. (b) Replacement patches in the enrichment zone.

At Martha Mine, the vertical changes in geochemistry and in the mineralogy allow the definition of a 40-50 m thick zone with evidences for dissolution and re-precipitation of silver and copper minerals.

The presence of Fe and Pb sulfates, Cu and Pb carbonates and Ag, Cu and Pb chlorides in the mineralized structures, along with jarosite, kaolinite and alunite group minerals in the host rocks, suggests that acidic and oxidizing conditions prevailed in the upper 20 m of the Martha deposit, leading to the mobilization of certain metals (especially copper and silver) and the consequent destruction of most sulphides (Scott, 1990; Sillitoe and McKee, 1996; Hartley and Rice, 2005).

Below this supergene zone, the presence of Cu and Ag sulphides and sulfosalts with replacement textures over primary ore minerals, indicate a 20-30 m thick zone where reduced conditions prevailed, leading to the re-precipitation of ore metals (mostly copper and silver) from descending waters (Sillitoe and McKee, 1996; Greffié et al., 2002; Hartley and Rice, 2005).

These changes are the first mention of a supergene enrichment blanket in an epithermal vein system from the Deseado Massif; and should be taken into consideration during exploration, as high grade portions of a silver deposit may be concealed below a lower grade oxidized horizon at surface as exemplified in Fig. 2.

Acknowledgements

This work is part of a PhD thesis carried out at the Universidad Nacional de La Plata (UNLP) with the support of Coeur d'Alene Mines and a Hugh E. McKinstry Student Research Award from the Society of Economic Geologists. The authors wish to thank Alfredo Cruzat, Claudio Romo and the Martha Mine staff for their help, discussions and access to data.

References

Bauluz B, Cedillo A, Subias, I, Páez GN, Ruiz R, Guido DM (2010) Hydrothermal clays at the Futuro Vein, Martha Mine silver epithermal deposit, Deseado Massif, Patagonia, Argentina. Trilateral Meeting on Clays (2010TMC), Abstracts. Spain.

Boyle RW (1968) The geochemistry of silver and its deposits. Geological Survey of Canada, volume 160, 264 p.

Cedillo Frey A, Páez GN, Ruiz R, Bauluz Lázaro B, Subías Pérez I (2009) Mineralogía de la alteración hidrotermal en el yacimiento epitermal Mina Martha, Macizo del Deseado, Argentina. Revista de la Sociedad Española de Mineralogía (Macla) 11: 57-58.

Chauvet A, Bailly L, André AS, Monié P, Cassard D, Tajada FL, Vargas JR, Tuduri J, Llosa Tajada F, Rosas Vargas J (2006) Internal vein texture and vein evolution of the epithermal Shila-Paula district, southern Peru. Mineralium Deposita 41, 387–410.

Echavarría LE, Schalamuk IB, Etcheverry RO (2005) Geologic and tectonic setting of Deseado Massif epithermal deposits, Argentina, based on El Dorado-Monserrat. Journal of South American Earth Sciences 19: 415-432.

Echeveste H, Fernández R, Bellieni G, Tessone M, Llambias E, Schalamuk IB, Piccirillo E, Demin A (2001) Relaciones entre las Formaciones Bajo Pobre y Chon Aike (Jurásico medio a superior) en el área de Estancia El Fénix-Cerro Huemul, zona centro-occidental del Macizo del Deseado, provincia de Santa Cruz. Revista de la Asociación Geológica Argentina 56 (4): 548-558.

Fernández RR, Blesa A, Moreira P, Echeveste H, Mykietiuk K, Andrada de Palomera P, Tessone M (2008) Los depósitos de oro y plata vinculados al magmatismo jurásico de la Patagonia: revisión y perspectivas para la exploración. Revista de la Asociación Geológica Argentina 63 (4): 665-681.

Gonzalez Guillot M, De Barrio R, Ganem F (2004) Mina Martha, un yacimiento epitermal argentífero en el Macizo del Deseado, provincia de Santa Cruz. VII Congreso de Mineralogía y Metalogenia, Actas: 119-204.

Gonzalez Guillot M, Biel Soria C, Fanlo Gonzalez I, Subías Perez I, Mateo Gonzalez E (2008) Cobres grises y sulfosales de plata del yacimiento epitermal de Mina Martha, Macizo del Deseado, Santa Cruz (Argentina). Revista de la Sociedad Española de Mineralogía (Macla) 8: 127-128.

Greffié C, Bailly L, Milési JP (2002) Supergene Alteration of Primary Ore Assemblages from Low-Sulfidation Au-Ag Epithermal Deposits at Pongkor, Indonesia, and Nazareño, Perú Economic Geology 97: 561-571.

Gröpper H, Calvo M, Crespo H, Bisso CR, Cuadra WA, Dunkerley PM, Aguirre E (1991) The epithermal gold-silver deposit of Choquelimpie, northern Chile. Economic Geology 86: 1206–1221.

Guido DM, and Schalamuk IB (2003) Genesis and exploration potential of epithermal deposits from the Deseado Massif, Argentinean Patagonia. In: Eliopoulos et al. (editors). Mineral Exploration and Sustainable Development. Balkema-Rotterdam, Vol I: 493-496.

Guido DM (2004) Subdivisión litofacial e interpretación del volcanismo jurásico (Grupo Bahía Laura) en el este del Macizo del Deseado, provincia de Santa Cruz. Revista de la Asociación Geológica Argentina 59 (4): 727-742.

Guido DM, Campbell KA (2011) Jurassic hot spring deposits of the Deseado Massif (Patagonia, Argentina): Characteristics and controls on regional distribution. Journal of Volcanology and Geothermal Research 203, 35–47.

Hartley AJ, Rice CM (2005) Controls on supergene enrichment of porphyry copper deposits in the Central Andes: A review and discussion. Mineralium Deposita 40: 515–525.

Jovic SM, Guido DM, Schalamuk IB, Ríos FJ, Tassinari CCG, Recio C (2010) Pingüino In-bearing polymetallic vein deposit, Deseado Massif, Patagonia, Argentina: characteristics of mineralization and ore-forming fluids. Mineralium Deposita 45: 735-763.

López R (2006) Estudio Geológico-Metalogenético del area oriental al curso medio del Río Pinturas, sector noroeste del Macizo del Deseado, provincia de Santa Cruz, Argentina. Universidad Nacional de La Plata, Argentina. Unpublished PhD Thesis.

Mann AW (1984) Mobility of gold and silver in lateritic weathering profiles: Some observations from Western Australia. Economic Geology 79: 38–49.

Márquez-Zavalía MF, Bindi L, Márquez M, Menchetti S (2008) Se-bearing polybasite-Tac from the Martha Mine, Macizo del Deseado, Santa Cruz, Argentina. Mineralogy and Petrology 94 (1): 145 - 150.

Milési JP, Marcoux E, Sitorus T, Simandjuntak M, Leroy J, Bailly L (1999) Pongkor (west Java, Indonesia): a Pliocene supergene-enriched epithermal Au-Ag- Mn) deposit. Mineralium Deposita 34: 131–149.

Páez GN, Ruiz R, Guido DM, Jovic SM, Schalamuk IB (2010) Estratigrafía volcánica del yacimiento argentífero Mina Martha, Macizo del Deseado, Provincia de Santa Cruz. Revista de la Asociación Geológica Argentina 6: 77–90.

Páez GN, Ruiz R, Guido DM, Jovic SM, Schalamuk IB (2011) Structurally controlled fluid flow: High-grade silver ore-shoots at Martha epithermal mine, Deseado Massif, Argentina. Journal of Structural Geology 33: 985–999.

Páez, GN (2012) Génesis del yacimiento de metales preciosos Mina Martha, sector sudoccidental del Macizo del Deseado, provincia de Santa Cruz. Universidad Nacional de La Plata, Argentina. Unpublished PhD Thesis.

Pankhurst R, Leat P, Sruoga P, Rapela C, Marquez M, Storey B, Riley T (1998) The Chon Aike province of Patagonia and related rocks in West Antarctica: a silicic large igneous province. Journal of Volcanology and Geothermal Research 81: 113-136.

Pankhurst R, Riley T, Fanning C, Kelley S (2000) Episodic silicic volcanism in Patagonia and the Antarctic Peninsula: chronology of magmatism associated with the break-up of Gondwana. Journal of Petrology 41 (5): 605-625.

Ruiz R. (2012) Geología y Mineralizaciones del sector sudoccidental del Macizo del Deseado, Santa Cruz. Universidad Nacional de La Plata, Argentina. Unpublished PhD Thesis.

Schalamuk IB, de Barrio R, Zubia M, Genini A, Echeveste H (1999) Provincia Auroargentífera del Deseado, Santa Cruz. In: Recursos Minerales de la República Argentina (Ed. E. Zappettini), Instituto de Geología y Recursos Minerales SEGEMAR, Anales 35: 1177-1188.

Scott KM (1990) Origin of alunite- and jarosite-group minerals in the Mt. Leyshon epithermal gold deposit, northeast Queensland, Australia. American Mineralogist 75: 1176–1181.

Tzvetanova Y (2003) Lead Phosphate Minerals from Brussevtzi Deposit (Eastern Rhodopes, Bulgaria) - SEM, IR and DTA Studies. Comptes Rendus de l'Academie Bulgare des Sciences 56, 55.

Wallier S (2009) The geology and evolution of the Manantial Espejo epithermal silver (+gold) deposit, Deseado Massif, Argentina. University of British Columbia, Canada. Unpublished PhD Thesis.

Gold-telluride mineralization in the Chukchi Peninsula: mineralogy, geochemistry and fluid inclusions

Vsevolod Yu. Prokofiev
Institute of Geology of Ore Deposits, Petrography, Mineralogy, and Geochemistry, Russian Academy of Sciences, Russia

Yuriy N. Nikolaev, Andrey V. Apletalin, Ivan A. Baksheev, Eugeniy A. Vlasov, Ildar A. Kal'ko
Geology Department, Moscow State University, Russia

Abstract. The ores of the Sentyabr'sky prospect the first economic occurrence of the Au--Te mineralization in the Chukchi Peninsula have been studied. Gold occurs as native form and telluride compound petzite intergrown with hessite. Petzite and hessite are the major ore minerals of the Au-Te ores. Altaite and coloradoite, have been also identified. Fluid inclusion data from sphalerite and quartz indicate different composition of fluid and parameters of the Au-Te ore deposition at the Sentyabr'sky prospect (360-155ºC, 570-80 bar, 8.1-0.7 wt.% eq. NaCl) from the typical of Chukotka the low-sulphidation type epithermal Au-Ag mineralization, which forms neighbor deposits Kupol and Dvoinoi (257-155ºC, 50-25 bar, 3.9-0.5 wt.% NaCl equiv.). The differences are caused by the multistage ore-forming process in the Ilirnei ore district resulted from long-active porphyry-epithermal system. The Au-Te mineralization is related to alkaline magmatism. According to mineralogical and geochemical features, the Sentyabr'sky ores are referred to the middle level of the porphyry-epithermal system and deep levels of the prospect are prospective.

Keywords. Gold-telluride deposits, Native gold, Petzite, Hessite, Fluid inclusions, Chukchi Peninsula.

1 Introduction

Epithermal gold deposits, where substantial gold is chemically bonded to tellurium, rather than native form are frequently referred to the special Au-Te type (Lindgren, 1933; Head *et al*., 1987). Owing to high grade of gold in the ores, such deposits are of heightened interest. According to Sillitoe (1997), about 20% of large gold deposits in the volcanic belts of the circum-Pacific region belong to the Au-Te type.

In the Northeastern Russia, the Au-Te epithermal deposits are known only from the Cenozoic volcanic belts of the Kamchatka Peninsula (Ozernovskoe and Aga). Deposits of this type were not identified in the Cretaceous Okhotsk-Chukchi volcanic belt (OCVB) until recently, while the largest low-sulphidation type epithermal Au-Ag deposit (Kupol and Dvoinoi). Therefore, the Au-Te mineralization found at the estimated Sentyabr'sky prospect, Ilirnei ore district is important for economic prospects of the district. The Kinross Gold Corporation operates the Dvoinoi and Kupol deposits located 10 km east and 80 km south of Sentyabr'sky, respectively.

2 Geological setting

The Sentyabr'sky prospect is located in the Ilirnei ore district on the Upper Rauchua and Ilirneiveem.

The Vodorazdel'nyi gold cluster comprising the

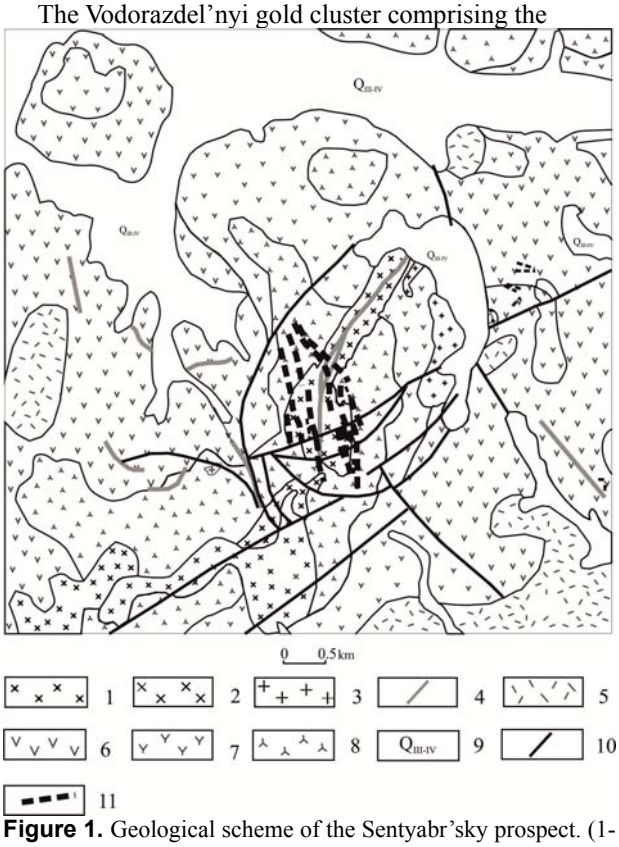

Figure 1. Geological scheme of the Sentyabr'sky prospect. (1--4) Intrusive rocks of the Late Cretaceous Ilirney Complex: (1) quartz monzonite, (2) granodiorite, (3) porphyry granite, (4) dykes of porphyry granosyenite; (5) rhyolite subvolcanic bodies of the Tytyl'veem Complex; (6--8) Tytyl'veem Formation: (6) lower subformation, andesite and basaltic andesite, (7) middle subformation, rhyolite, dacite, and their tuff, (8) upper subformation, andesite, its clastic lava and tuff; (9) Quaternary; (10) faults; (11) quartz veins and zones of quartz veinlets.

Dvoinoi deposit and Sentyabr'sky prospect is spatially related to the volcano-tectonic structures of the Central Chukchi Zone of OCVB. The Sentyabr'sky prospect is located in the intrusive dome structure of the same name superimposed on the Ilirnei collapsed volcanic structure (caldera). The geological scheme of the prospect is shown in Fig 1. The area comprises the Early Cretaceous volcanic rocks of the Tytyl'veem Formation (K_1tt). In the central part, volcanic sequence is intruded by quartz monzonite ($q\mu_1K_2il$) and granodiorite ($\gamma\delta K_2il$) referred to the Late Cretaceous Ilirnei Complex of subalkaline granites. Volcanic rocks are also intruded by numerous dykes of the Ilirnei syenite (ξ_2K_2il) and porphyry granite ($\gamma\pi K_2il$), and rhyolite bodies of the Early Cretaceous

Tytyl'veem Complex ($\lambda K_1 t$).

Wall-rock alteration is propylitic, silicific, sericitic, and argillic. Hydrothermally altered rocks occur as isometric or extended alteration zones 0.5 to 5.0 sq. km.

The mineralization is controlled by steep north-west and near-meridional striking faults. The orebodies at the prospect are veins, and veinlet and vein zones, which cut the Ilirnei quartz monzonite, andesite and basaltic andesite of the intermediate subformation of the Tytyl'veem Formation. The veins are composed of quartz (80-90%), sericite, adularia and chlorite. Few ore minerals were found, with their content reaching 20% in quartz-sulfide veins.

3 Mineralogy of gold ores

Two economic ore types are recognized at the Sentyabr'sky prospect: (1) Au-Ag-As impregnation, veinlet, and vein and (2) Au-Ag-Te vein. The following concentrations (ppm) were determined in the first type: 2.1-9.5 Au, 16-3588 Ag, 3713-49571 As, 176-13961 Sb, 57-28183 Cu, 193-14321 Zn, 5-558 Cd, 6-2207 Bi, 4-1203 Sn, and up to 278 W. The content of Au is well correlated with that of As and not with Te. The following grades were measured in the second-type ores, ppm: 2.3-5459 Au, 50-10165 Ag, 30-3000 Te, 553-129752 Pb, 165-20071 Cu, 99-19344 Zn, 3-4137 Hg, up to 689 Se, 1-348 Cd, 26-516 As, 7-32 Sb, up to 50 Bi. The gold grade is well correlated with that of tellurium and not with arsenic.

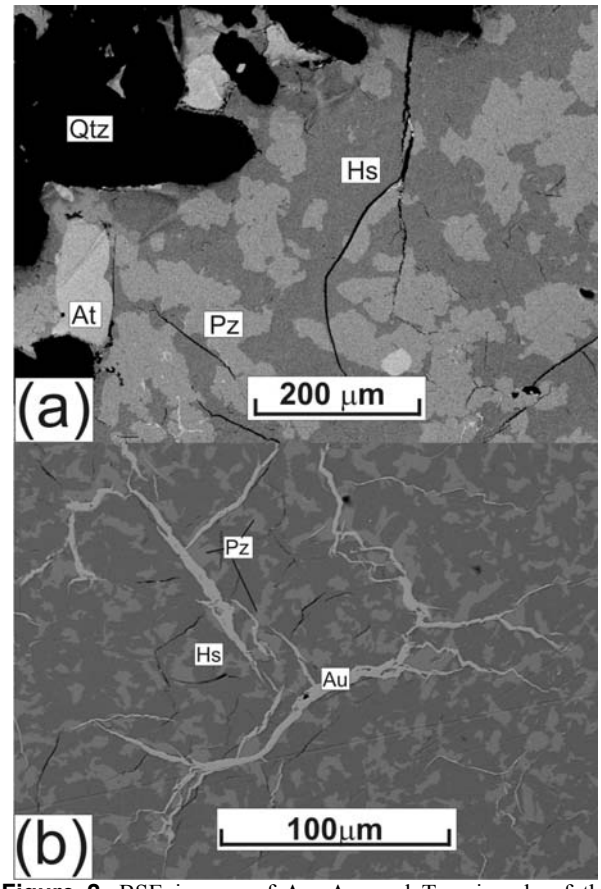

Figure 2. BSE images of Au, Ag, and Te minerals of the Sentyabr'sky ores: (a) petzite-hessite aggregate with altaite, (b) veinlets of native gold cutting petzite-hessite aggregate.

Three major successive mineral assemblages were identified in the ores of the Sentyabr'sky prospect (from early to late): pyrite-arsenopyrite, base-metal, and gold--silver-telluride.

The minerals of the gold-silver-telluride assemblage that is dominated by petzite, hessite, altaite, and coloradoite overgrow or replace minerals of the base-metal assemblage. Gangue minerals are quartz, ankerite, Fe-rich dolomite, calcite, muscovite-phengite, and chamosite.

Petzite and native gold are the major ore minerals. The former occurs as isometric or weakly elongated segregations up to 100 μm in size intimately intergrown with the latter (Fig. 2a). In these clusters, the proportion of petzite reaches 20-50%.

Native gold was found in aggregates of telluride minerals. Numerous thin branched micro veinlets in the hessite-petzite aggregate are the most widespread form of native gold (Fig. 2b). The gold fineness is 832-853, only Hg (up to 1.2 wt. %) was found as trace element.

4 Fluid inclusions

4.1 Petrography

At room temperature, the fluid inclusions from quartz and sphalerite of the Sentyabr'sky prospect are divided into two types in phase composition (Fig. 3): (1) gas-dominated with occasional CO_2 upon freezing and (2) two phase fluid inclusions, which are both primary and secondary. The second- and first-type inclusions are frequently syngenetic indication boiling of their parent fluid.

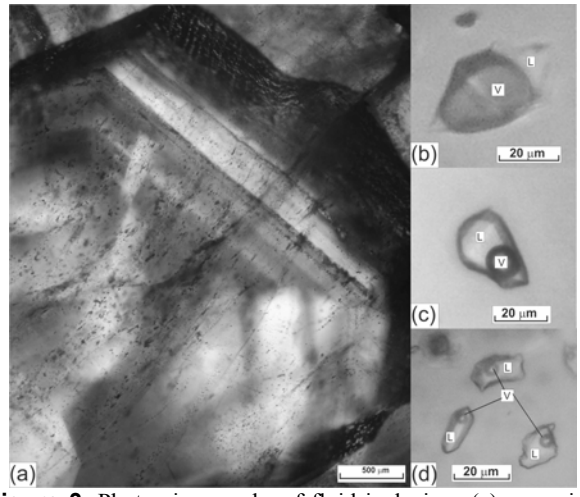

Figure 3. Photomicrographs of fluid inclusions (a) occurring along growth zones, (b) the first type, and (c, d) second type. (L) – aqueous solution, (V) – gas.

4.2 Methods

Fluid inclusions have been studied in double polished plates, first optically, then with a THMSG-600 'Linkam' freezing/heating stage equipped with Olympus-80 objective at IGEM RAS, Moscow, Russia. Precision at low temperature (cooling) was about 0.1°C and about 1°C at high temperature (heating). Salinity was estimated from final ice melting temperature (T_m). A pressure was determined using the syngenetic gas-dominated and

aqueous saline inclusions trapped during fluid boiling.

Bulk inclusion analysis was carried by gas chromatography, ion chromatography, and ICP-MS was carried out according to the techniques reported by Kryazhev et al. (2006) at TsNIGRI, Yu.V. Vasyuta analyst. The analyzed samples were 0.5-g aliquots of milled quartz (0.25- to 0.5-mm sieved fraction).

4.3 Results of microthermometry and bulk analysis

The primary and pseudosecondary two-phase inclusions of the second type from quartz and sphalerite homogenize into liquid at 360-213°C and contain aqueous solution with salinity 8.1-0.9 wt.% NaCl equiv. The density of the fluid is 0.58-0.90 g/cm^3.

The primary gas-dominated inclusions of the first type syngenetic to the second-type aqueous inclusions and occasionally containing CO_2 (density 0.32-0.23 g/cm^3) homogenize into gas at +23.6 to +29.3°C. The melting temperature of CO_2 ranges from -57.7 to -59.5°C that indicates the impurity (up to 7 mole %) of gasses boiled at low temperature (CH_4, N_2). The homogenization temperature 295°C is identical to that of the second-type syngenetic primary inclusions. The pressure during fluid immiscibility was 250 bar.

According to bulk analysis, in the fluids, the major cations are Na, K, and Ca, while Mg is minor. Significant concentration of Cl^-, HCO_3^-, CO_2, CH_4, As, and B was established. In addition, Fe, Mn, Sb, Sr, Li, REE, P, Cd, Cs, Ba, Ni, Rb, Mo, Cu, Bi, Cr, Ag, Ge, Co, U, V, Sn, Ti, Ga, Tl, Pb, and Th were detected in the fluids.

5 Discussion

Geological structure, metasomatic rocks, and ore mineralogy indicate that the Sentyabr'sky prospect is related to the porphyry-epithermal system (Hedenquist, Lowenstern, 1994; Hedenquist *et al.*, 2000; Simmons *et al.*, 2005). The ore mineralogy corresponds to the IS type of Silitoe and Hedenquist (2003).

The assemblage of Te minerals (altaite, hessite, coloradoite, petzite) identified in the Sentyabr'sky ores is typical of many Au-Te epithermal deposits. However, various Au tellurides are characteristic of the ores from these deposits, whereas only one Au telluride petzite was found in the ores of the Sentyabr'sky prospect. At the same time, according to computation, 40-70% of Au of the Au-Ag-Te ores at the Sentyabr'sky prospect are present as petzite. It is probable new type of the Au-Te mineralization transitional from shallow- to deep-seated ores.

According to fluid inclusion data, the Sentyabr'sky ores started to precipitate at higher temperature (about 300°C) than low-sulphide Au-Ag mineralization of the Dvoinoi deposit (257°C, after Prokofiev et al., 2012), Figure 4. Based on mean gradient of hydrostatic pressure (100 bar/km), the Sentyabr'sky ores can be formed at the depth about 1 km.

The salinity of mineralizing fluids of the Sentyabr'sky prospect and Dvoinoi deposit is dramatically different. A similar picture is seen at the Au-Ag and Au-Te epithermal deposits (Simmons *et al.*, 2005). The composition of solution from fluid inclusions is also different not only in the major constituents, but wider array micro elements and higher concentration of these elements in fluid responsible for the formation of the Sentyabr'sky prospect. The values used as geochemical indicators, which are Na/K, CO_2/CH_4, CO_2/HCO_3, Cl/Br, K/Rb and Cl/As, are also appreciably different (Table).

Table. Average chemical ratio of the solutions of fluid inclusions in quartz from the ore at the Sentyabr'sky prospect and Dvoinoi deposit

Component	Sentyabr'sky	Dvoinoi
Na/K	3.1	1.5
CO_2/CH_4	214.4	57.6
CO_2/HCO_3	279.3	7.0
Cl/B	4.1	1.2
K/Rb	424.3	333.3
Cl/As	3.85	0.275

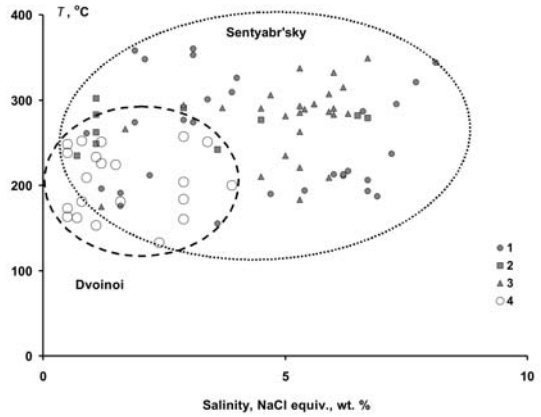

Figure 4. A temperature of total homogenization *versus* salinity plot for fluid inclusions from quartz and sphalerite of deposits Sentyabr'sky (1-3) and Dvoinoi (4). Data for different mineral associations: 1 – pyrite-arsenopyrite, 2 – base-metal, 3 – gold-silver-telluride, 4 – low-sulphide Au-Ag.

The Au-Ag-Te mineralization of the Sentyabr'sky prospect and low-sulfide Au-Ag mineralization of the Dvoinoi deposit are resulted from different hydrothermal fluids, which are related to the different phase of magmatic activity. The Sentyabr'sky prospect was formed as a part of multistage porphyry-epithermal system with different types of mineralization and the transition of epithermal to porphyry mineralization with depth is suggested. According to classification of Silitoe (2010), the Sentyabr'sky prospect may be referred to the subepithermal type.

On a Ag/Au versus Se/Te diagram for Au-Ag deposits in the Northeastern Russia and Kamchatka Peninsula, the Sentyabr'sky ores are plotted in the field of the gold deposits with tellurium minerals (Fig. 5). The separation of Au-Ag ores by the Se/Te value in the field reflects predominant volcanic-related origin of Au-Se deposits, whereas Au-Te deposits are spatially (and probably genetically) related to the deeper magmatic chambers (Nikolaev, Apletalin, 1998).

Low As and Sb and elevated Pb and Zn are characteristic of Au-Te ores. The Au-Te properties fall into two separate groups on the diagram shown in

Figure 5: (1) Au-Te deposits of Kamchatka (Aga and Ozernovskoe) with varied gold tellurides and (2) the Sentyabr'sky prospect and Au-Ag-Te and Te-bearing deposits of OCVB with predominant petzite. The principal geochemical difference between these groups is the higher Ag/Au value and grade of Pb and Zn in the latter.

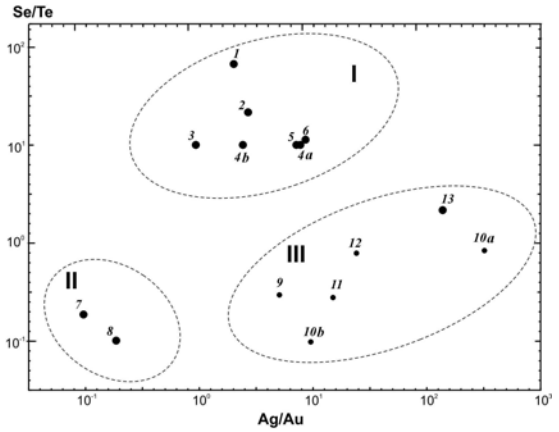

Figure 5. A Au/Ag versus Se/Te plot for Au-Ag deposits and prospects. I–III – fields of various ore types: (I) selenide and Se_bearing, (II) telluride (sylvanite–calaverite), (III) telluride (petzite–hessite).
(1-8, 13) Deposits: (1) Klen, (2) Dvoinoi, (3) Asacha, (4) Ametistovoe ((a) low-sulfide Au-Ag ores, (b) sulfide Au-Ag ores), (5) Kupol, (6) Rodnikovoe 7 – Ozernovskoe, (8) Aga, (13) Arykevaam. (9-12) Prospects: (9) Televeem, (10) Sentyabr'sky ((a) Au-Ag-As ores, (b) Au-Ag-Te ores), (11) Vesenny, (12) Pryamoi.

The ores of the Vesenny deposit located in the margin of the Nakhodka porphyry copper system, Western Chukchi Peninsula and according to the recent study referred to the IS type (Nikolaev et al., 2011) are closest in composition to the Sentyabr'sky ores. According to mineralogical data, the major Ag mineral in the Vesenny ores is hessite that is intimately associated with native gold; insignificant petzite and native Te were identified. The native gold-hessite assemblage was found in epithermal ores of the Pryamoi and Malysh prospects in the Nakhodka ore field.

Goryachev et al. (2010) published new data of widespread development of Au- and Ag-Te mineralization at both known and recently discovered Au-Ag prospects in the Anadyr segment of OCVB, which confirm that the belt is poor studied and discovery of this type economic deposits is probable.

In the Au-Ag-Te ores of the OCVB deposits, the Se/Te value increases with the Ag/Au value (Fig. 5). It is caused by decreasing content of petzite and other Au tellurides, which are displaced by hessite with increasing content of Pb, Zn, and Cu sulfides. Tellurium minerals are enclosed in the sulfides, especially galena; increasing concentration of Se determines increasing Se/Te value.

The found evolution trend of relationships between elements corresponds to vertical zoning: Te-bearing deposits with the high Ag/Au value (Vesenny, Pryamoi) are related to the intrusive porphyry bodies. The Au-Ag-Te deposits are located in volcanic edifices below which the blind porphyry intrusions are probable.

It is known that the deposits with Te minerals are genetically related to alcalic magmatism (Richards, 1995; Jensen and Barton, 2000). Therefore, the spatial relation of the Sentyabr'sky prospect to the enriched in K-specialized magmatic rocks of the Ilirney Complex is naturally determined. The composition of metasomatic tourmalines from the Sentyabr'sky deposit is similar to that of tourmalines from the Darasun deposit (Baksheev *et al.*, 2011) that is also related to K-rich porphyry granodiorite. The areas of the potassium specialized intermediate and acidic alkali magmatism are suggested to be the most prospective to fined Au-Te mineralization in the Chukchi Peninsula.

Acknowledgements

This work was carried out within the framework of the Russian Foundation for Basic Research (project no. 12-05-01083).

References

Baksheev IA, Prokofiev VYu, Yapaskurt VO, Vigasina MF, Zorina LD, Solov'ev VN (2011) Ferric-iron-rich tourmaline from the Darasun gold deposit, Transbaikalia, Russia. Can Mineral 49: 263-276.

Goryachev NA, Volkov AV, Sidorov AA, Gamyanin GN, Savva NE, Okrugin VM (2010) The epithermal Au-Ag mineralization in volcanic belts of northeast Asia. Lithosphere (3): 36–50 (in Russian).

Heald P, Foley NK, Hayba DO (1987) Comparative anatomy of volcanic-hosted epithermal deposits: acid-sulfate and adularia-sericite types. Econ Geol 82 (1): 1–26.

Hedenquist JW, Arribas AJr and Gonzales-Urien E (2000) Exploration for epithermal gold deposits. Gold in 2000. Rev Econ Geol 13: 245–277.

Hedenquist JW, Lowenstern JB (1994) The role of magmas in the formation of hydrothermal ore deposits. Nature 370: 519–527.

Jensen EP, Barton MD (2000) Gold deposits related to alkaline magmatism. Gold in 2000. Rev Econ Geol 13: 279−314.

Kryazhev SG, Prokofiev VYu, Vasyuta YuV (2006) The application of ICP-MS technique to determine composition of mineralizing fluids. Geol Bull MSU (4): 30–36 (in Russian).

Lindgren W (1933) Mineral deposits. 4th ed. McGraw-Hill. N.Y.

Nikolaev YuN, Apletalin AV (1998) Geochemical prospecting of gold deposit in Kamchatka. In: Geohemical and geophysical methods in prospecting of mineral deposits. OME, Alexandrov. P. 59–71 (in Russian).

Prokof'ev VYu, Volkov AV, Sidorov AA, Savva NE, Kolova EE, Uyutnov KV, Byankin MA (2012) Geochemical Peculiarities of Ore_Forming Fluid of the Kupol Au–Ag Epithermal Deposit (Northeastern Russia). Doklady Earth Sciences 447 (2): 1310–1313.

Richards JP (1995) Alkalic-type epithermal gold deposits – a review. In: Magmas, fluid and ore deposits. Short course ser. mineralogical association of Canada 23: 367–400.

Sillitoe RH (1997) Characteristics and controls of the largest porphyry copper-gold and epithermal gold deposits in the circum-Pacific region. Austral J. Earth Science 44: 373–387.

Sillitoe RH (2010) Porphyry copper systems. Econ Geol 105: 3–41.

Sillitoe RH, Hedenquist JW (2003) Linkages between volcanotectonic settings, ore-fluid compositions, and epithermal precious metal deposits. Soc. Econ Geol Special Publ 10: 315–343.

Simmons SF, White NC, John DA (2005) Geological characteristics of epithermal precious and base metal deposits Econ Geol 100th Anniversary Volume: 485–522.

Quantitative assessment of porphyry copper resources in Finland

Kalevi Rasilainen, Pasi Eilu, Niilo Kärkkäinen, Mikko Nironen, Markku Tiainen
Geological Survey of Finland, 02150 Espoo, Finland

Jukka Kousa, Kaj Västi
Geological Survey of Finland, 70211 Kuopio, Finland

Laura Lauri, Tero Niiranen
Geological Survey of Finland, 96101 Rovaniemi, Finland

Abstract. The copper, molybdenum, silver and gold resources in undiscovered porphyry copper deposits in the Finnish bedrock were estimated down to 1 km depth using the 3-part quantitative assessment method. A grade-tonnage model was constructed based on data from 27 well-known Precambrian porphyry copper deposits. Ten permissive tracts for porphyry deposits were delineated and the number of undiscovered deposits in each tract was estimated. The mean estimate of the number of undiscovered porphyry copper deposits across the permissive tracts is 11. The median estimate of the resources contained in the undiscovered deposits is 2.1 Mt of copper, 100,000 t of molybdenum, 1000 t of silver and 170 t of gold.

Keywords: Porphyry copper deposits, resources, evaluation, Finland.

1 Introduction

Porphyry copper deposits constitute the world's largest source and resource of copper and a major source of molybdenum, gold and silver (John et al. 2010). No copper has been produced from this deposit type in Finland, but the existence of several porphyry deposit in the Fennoscandian shield indicate potential for porphyry-type mineralisation also in Finland. We describe here the results of an assessment of copper, molybdenum, silver and gold resources in porphyry-type copper±molybdenum±gold deposits in Finland. The assessment is part of an ongoing series of assessments started by Geological Survey of Finland (GTK) in 2008 to estimate the undiscovered resources of several metals in the Finnish bedrock.

The GTK assessments estimate the total amount of metals in undiscovered deposits down to one kilometre depth using the three-part quantitative assessment method of the US Geological Survey (Singer 1993; Singer and Menzie 2010). The process consists of (1) evaluation and selection or construction of a descriptive model and a grade-tonnage model for each deposit type being assessed, (2) delineation of areas permitted by the geology for the deposit types (permissive tracts), and (3) estimation of the number of undiscovered deposits of each deposit type within the permissive tracts. The estimated numbers of deposits and the grade and tonnage distributions are used in Monte Carlo simulation to model the total undiscovered metal endowment.

2 Porphyry copper deposits in Finland

Mikkola (1963) was perhaps the first to suggest similarities between Phanerozoic porphyry copper deposits in North and South America and certain Precambrian granitoid-related sulphide occurrences in central Finland. Further studies of these occurrences commenced only at the end of the 1970s (Gaál and Isohanni 1979; Gaál et al. 1981; Nurmi 1984; Nurmi et al. 1984) but due to the rather poor results from initial exploration, efforts were soon directed to other deposit types. Interest in porphyry copper deposits has recently been rekindled in Finland with the discovery of new targets, especially the Kedonojankulma prospect in Southern Finland (Tiainen et al. 2012). The existence of several porphyry copper deposits within the Fennoscandian shield (FODD 2011), including the world-class Aitik deposit in Sweden (Monro 1988; Drake 1992; Wanhainen et al. 2012), suggest the potential for this deposit type also in Finland.

Porphyry copper deposits generally form in the upper crust (less than 5–10 km depth) in tectonically unstable convergent plate margins, which makes them prone to erosion. Although porphyry copper systems were generated worldwide since the Archean, more than 90% of the known deposits are Meso-Cenozoic (John et al. 2010; Sillitoe 2010). Hence, it is not surprising that in the Precambrian bedrock of Finland, only few porphyry deposits and occurrences are known. These are mostly situated along the margins of the large granitoid area in central Finland (Fig. 1).

The characteristic features of the Finnish occurrences have been summarised and compared with Phanerozoic porphyry deposits by Nurmi et al. (1984) and Nurmi (1984). The following brief summary is based on their work. Mineralisation (molybdenum-copper, molybdenum, copper, copper-gold, copper-tungsten) is associated with late-stage felsic and usually porphyritic phases of synorogenic 1900–1850 Ma granitoid batholiths, stocks and plutonic complexes showing I-type characteristics. Molybdenite and chalcopyrite are the most important sulphide minerals. Other major ore minerals include magnetite, arsenopyrite, pyrrhotite and scheelite. Mineralisation has a structural control and occurs mostly as stockworks or quartz or tourmaline breccias with minor dissemination of sulphide minerals. Significant wall-rock alteration is generally restricted to the immediate vicinity of the mineralized fractures and

includes propylitisation, silicification, sericitisation and potassic alteration. Both mineralisation and wall-rock alteration show zoned patterns in some occurrences.

The known Finnish occurrences differ from Phanerozoic porphyry deposits principally in their smaller size, the weakness of wall-rock alteration and the absence of a pyritic halo (Nurmi et al. 1984). In Finland, the best known and most thoroughly explored example of porphyry-type mineralisation is the Kopsa deposit, which has a resource of 25 Mt containing 0.18 % copper and 0.57 g/t gold (Gaál 1978).

3 Data used and the assessment process

Primary sources of information for Finland used in the assessment include geological maps and map data bases, geochemical and geophysical survey data, reports on known deposits, and exploration reports. Data for deposit models was gathered from databases of Singer et al. (2005), Sinclair (2007), FODD (2011) and Geoscience Australia (2012).

Preliminary permissive tracts were defined by the assessment team members who had personal working experience in the areas under study. The tracts were finalised after a review by other team members.

A grade-tonnage model was constructed using data from the above mentioned databases. Only data that were estimated to represent the whole deposit with no missing information for tonnage and copper grade were accepted. The combined data set contains 27 Precambrian and 462 Phanerozoic deposits. Non-parametric statistical tests indicated that Precambrian deposits have significantly lower average tonnage and copper values, as well as marginally higher molybdenum and gold grades compared to Phanerozoic deposits. For this reason, the grade-tonnage model for the assessment of Finnish porphyry copper deposits was constructed using only data from Precambrian deposits. The final model is based on 27 deposits, only one of which is in Finland (Kopsa).

The Precambrian porphyry copper deposits in the model can be classified into three subtypes based on gold and copper grades (Cox and Singer 1992): copper-gold (Au/Mo≥30, N=12), copper-molybdenum (Au/Mo≤3, N=8) and copper (3<Au/Mo<30, N=7), where Au is gold grade in grams per metric ton and Mo is molybdenum grade in weight percent. Based on statistical tests, these subtypes do not differ in tonnage or copper grade. The subtypes are expected to differ in molybdenum and gold grades (Singer et al. 2005) but due to the small number of samples in the Precambrian data set and the difficulty to select the correct subtype for each individual permissive tract, no Precambrian grade-tonnage sub-models were constructed.

The number of undiscovered porphyry copper deposits was estimated for each permissive tract in an assessment workshop by GTK experts. Each expert independently estimated the number of undiscovered deposits within each permissive tract at the 90%, 50%, and 10% certainty levels. These figures were then discussed in order to reach a consensus estimate for each tract. For tracts where consensus was not reached,

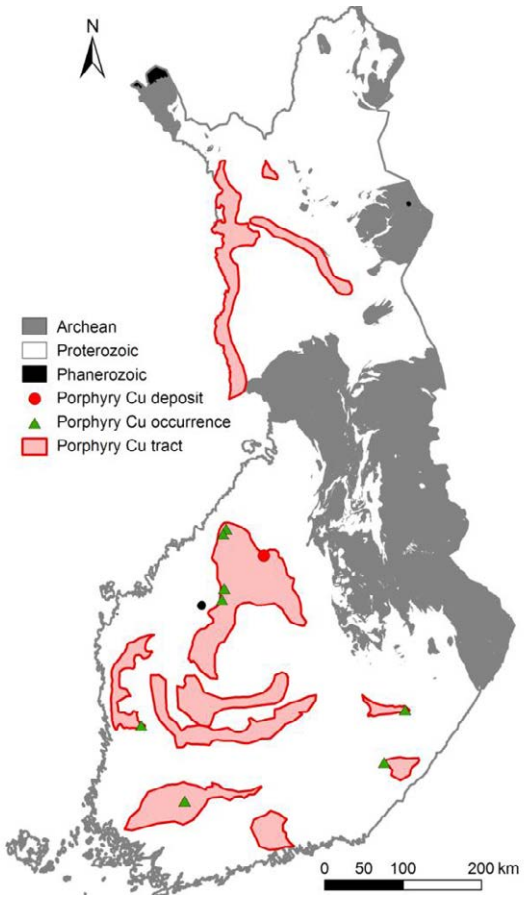

Figure 1. Permissive tracts for porphyry copper deposits in Finland.

arithmetic means of the experts' estimates at each probability level were used as the final estimates.

The amounts of undiscovered metals were calculated by Monte Carlo simulation using the estimated numbers of undiscovered deposits and the grade-tonnage model as input. The calculations were performed using the Eminers software (Root et al. 1992; Duval 2004).

4 Results and discussion

Altogether, 10 permissive tracts were delineated for porphyry copper deposits in Finland (Fig. 1). The total area of the tracts is 38,200 km^2, which is 11% of the land area of Finland. The tracts contain all the known porphyry copper occurrences and the Kopsa deposit, and within their boundaries, geology permits the existence of other, yet undiscovered, porphyry-type deposits. The sum of the mean estimates of the number of undiscovered porphyry copper deposits across all the permissive tracts is 11, and the undiscovered deposits are estimated to contain at 50% probability at least 2.4 Mt of copper (Table 1). Of the 10 permissive tracts, five are estimated to contain no undiscovered resources at the 50% probability level. The assessment results indicate that 98% of the copper, 100% of the molybdenum and about 90% of the silver and gold that are estimated to be in porphyry-type deposits within the topmost one kilometre of the Finnish bedrock occur in poorly known or undiscovered deposits.

It must be noted that these assessment results do not in any way imply the potential for discovery of any of the estimated undiscovered resources. The probabilities associated with the resource estimates are probabilities of existence, not of discovery. Further, due to the nature of the method, a part of the estimated undiscovered resource is in deposits that would not be economically viable to exploit for various technical or socio-economic reasons.

Table 1. Known and estimated tonnages of metals and ore in porphyry copper deposits in Finland. The known resources consist only of the Kopsa deposit.

	Known resources (t)	Median estimate (t)	Mean estimate (t)	Probability of mean or greater
Cu	45,000	2,400,000	9,300,000	0.25
Mo	-	100,000	460,000	0.21
Au	14	170	1,100	0.20
Ag	100	1,000	12,000	0.14
Ore	25,000,000	830,000,000	3,600,000,000	0.29

t metric tons, - data not available
The numbers have been rounded to two significant digits

Acknowledgements

Several geologists at the northern, eastern and southern regional offices of the GTK gave their time and expertise to the assessment. Sari Grönholm, Jouni Luukas and Ferenc Molnár are thanked for their contribution to the assessment meeting.

References

Cox DP, Singer DA (1992) Distribution of gold in porphyry copper deposits. In: DeYoung JH, Hammerstrom JM (eds) Contributions to commodity research. U.S. Geol Surv Bull 1877:C1–C14

Drake B (1992) Aitik copper mine. Geology 2:19–23

Duval JS (2004) Version 2.0 of EMINERS – Economic Mineral Resource Simulator. U.S. Geol Surv Open-File Rep 2004-1344

FODD (2011) Fennoscandian Ore Deposit Database. Geological Survey of Finland (GTK), Geological Survey of Norway (NGU), Geological Survey of Russia (VSEGEI), Geological Survey of Sweden (SGU), SC Mineral. Online database, available at: http://en.gtk.fi/ExplorationFinland/fodd. Last accessed 17 Sep 2012

Gaál G (1978) Raportti Haapajärven Kopsan ja Vehkan tutkimuksista vuosina 1939–1978. Outokumpu Oy report 20.3.1978, 55 p (in Finnish)

Gaál G, Isohanni M (1979) Characteristics of igneous intrusions and various wall rocks in some Precambrian porphyry copper-molybdenum deposits in Pohjanmaa, Finland. Econ Geol 74:1198–1210

Gaál G, Front K, Aro K (1981) Geochemical exploration of a Precambrian batholith, source of a Cu-W mineralization of the tourmaline breccia type in southern Finland. J Geochem Explor 15:683–698

Geoscience Australia (2012) Australian Mines Atlas. Online database, available at: http://www.australianminesatlas.gov.au. Last accessed 24 September 2012

John DA, Ayuso RA, Barton MD, Blakely RJ, Bodnar RJ, Dilles JH, Gray F, Graybeal FT, Mars JC, McPhee DK, Seal RR, Taylor RD, Vikre PG (2010) Porphyry copper deposit model, chap. B of Mineral deposit models for resource assessment. U.S. Geol Surv Sci Invest Rep 2010-5070-B, 169 p

Mikkola A (1963) Porfyyri-kuparimalmeista. Geologi 15:5–6 (in Finnish)

Monro D (1988) The geology and genesis of the Aitik copper–gold deposit, Arctic Sweden. Ph.D. Thesis, University of Wales, College of Cardiff

Nurmi PA (1984) Applications of lithogeochemistry in the search for Proterozoic porphyry-type molybdenum, copper and gold deposits, southern Finland. Geol Surv Finland Bull 329, 40 p

Nurmi PA, Front K, Lampio E, Nironen M (1984) Etelä-Suomen svekokarjalaiset porfyyrityyppiset molybdeeni- ja kupariesiintymät, niiden granitoidi-isäntäkivet ja litogeokemiallinen etsintä. Summary: Svecokarelian porphyry-type molybdenum and copper occurrences in southern Finland: their granitoid host rocks and lithogeochemical exploration. Geol Surv Finland Rep Invest 67, 88 p

Root DH, Menzie WD, Scott WA (1992) Computer Monte Carlo simulation in quantitative resource estimation. Nat Resources Res 1:125–138

Sillitoe RH (2010) Porphyry Copper Systems. Econ Geol 105:3–41

Sinclair WD (2007) Porphyry deposits. In: Goodfellow WD (ed) Mineral Deposits of Canada: A Synthesis of Major Deposit-Types, District Metallogeny, the Evolution of Geological Provinces, and Exploration Methods. Geol Assoc Canada, Miner Dep Div Spec Publ 5:223–243, Appendix 2

Singer DA (1993) Basic concepts in three-part quantitative assessments of undiscovered mineral resources. Nonrenewable Resources 2:69–81

Singer DA, Berger VI, Moring BC (2005) Porphyry Copper Deposits of theWorld: Database, Map, and Gradeand Tonnage Models. U.S. Geol Surv Open-File Rep 2005-1060, 9 p

Singer DA, Menzie WD (2010) Quantitative mineral resource assessments: An integrated approach. Oxford University Press, New York, 219 p

Tiainen M, Kärkkäinen N, Koistinen E, Lohva J, Sipilä P, Huhta P (2012) Discovery of the Kedonojankulma Cu-Au occurrence, hosted by a Svecofennian porphyritic granitoid in Southern Finland. Geol Surv Finland, Spec Paper 52:73–90

Wanhainen C, Broman C, Martinsson O, Magnor B (2012) Modification of a Palaeoproterozoic porphyry-like system: Integration of structural, geochemical, petrographic, and fluid inclusion data from the Aitik Cu–Au–Ag deposit, northern Sweden. Ore Geol Rev 48:306–331

Early mineralization at Cerro de Pasco (central Peru) revisited

Bertrand Rottier, Vincent Casanova, Lluís Fontboté and Kalin Kouzmanov
Earth and Environmental Sciences, University of Geneva, rue des Maraîchers 13, CH-1205 Geneva, Switzerland

Hugo Alvarez
Volcan Compania Minera S.A.A., Avenue Gregorio Escobedo 710, Lima, Peru

Ronner Bendezú
Terra Pristina S.A.C., Calle Bilbao 295, San Isidro, Peru

Abstract. The large Cerro de Pasco Cordilleran base metal deposit in central Peru is located on the eastern margin of a Middle Miocene diatreme-dome complex. A striking characteristic is the presence of a N-S trending massive funnel-shape pyrite-quartz replacement ore body that contains pyrrhotite pipes grading outwards to lead-zinc replacement bodies, along the eastern contact of the diatreme-dome complex. Earlier workers interpreted the pyrrhotite pipes as postdating the pyrite-quartz body. This study, that has been possible through access to new mining areas and drill cores, allows an alternative interpretation. The new data strongly suggest that the pyrrhotite pipes and their associated lead-zinc replacement bodies predated the formation of the pyrite-quartz body.

Keywords. polymetallic, base metals, pyrrhotite, pyrite, Cerro de Pasco

1 Introduction

Cerro de Pasco, central Peru, is a large Cordilleran base metal deposit located on the eastern margin of a diatreme-dome complex (15.36 ± 0.03 Ma, Baumgartner et al., 2009) which is part of the Miocene metallogenic belt of central and northern Peru. Previous studies (Lacy 1949, Ward 1961, Einaudi 1968, 1977, Baumgartner 2007, Baumgartner et al., 2008) defined two main mineralization stages. According to this interpretation, during the first stage, a N-S trending funnel shape, ~1.5 km in length, 250 m wide and more than 550 m deep massive body consisting mainly of pyrite and quartz was formed. It includes a number of pyrrhotite pipes that grade outwards into massive Fe-rich sphalerite and galena replacement bodies. The inner parts of the pipes contain minor amounts of arsenopyrite and Fe-rich sphalerite as well as traces of chalcopyrite, galena and stannite. The massive body replaces mainly an Upper Triassic-Lower Jurassic carbonate sequence (Pucará Group), along the eastern contact of the diatreme-dome complex, as well as, subordinately, the diatreme-dome complex itself (Fig. 1). A quartz-sericite alteration halo is observed in the diatreme rocks along the pyrite-quartz body. The pyrrhotite pipes are known to replace only the carbonate sequence. The second mineralization stage took place, in the western part of the deposit, as a set of E-W–trending Cu-Ag-(Au-Zn-Pb) enargite-pyrite veins hosted by the diatreme breccia, and, in the eastern part, as large well-zoned Zn-Pb-(Bi-Ag-Cu) carbonate replacement bodies (Fig. 1).

Recent studies by Baumgartner (2007) and Baumgartner et al. (2008) characterized the second stage of mineralization. However, no comprehensive study has been done on the first mineralization stage since seminal Einaudi's work (1968, 1977). According to previous studies, the pyrite-quartz body was thought to have been first emplaced, followed by the pyrrhotite pipes and their outer zone of sphalerite and galena. However, this study had access to new mining areas and drill cores, allowing observations that have led to the alternative interpretation that the massive pyrite-quartz body is emplaced after the pyrrhotite pipes and belongs to the second stage.

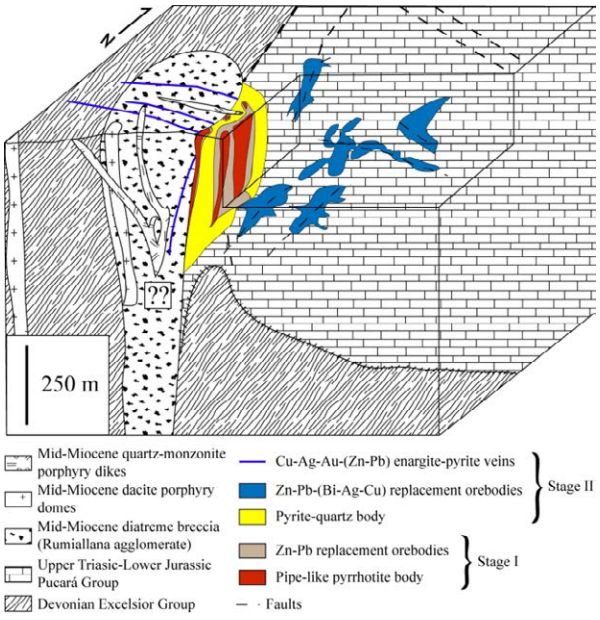

Figure 1: Block diagram, showing the Cerro de Pasco deposit (modified after Baumgartner et al., 2008).

2 Pyrrhotite-pyrite relationships

This study focuses on the contact of the pyrrhotite pipes with the pyrite-quartz body. At the meter scale, a replacement front of pyrrhotite by pyrite is observable. From the pyrrhotite pipes to the pyrite-quartz body the following main textural patterns are seen. Inside the pyrrhotite pipes, near the contact, patches of porous fine-grained pyrite occur (Fig. 2 A-C). Follows a part of

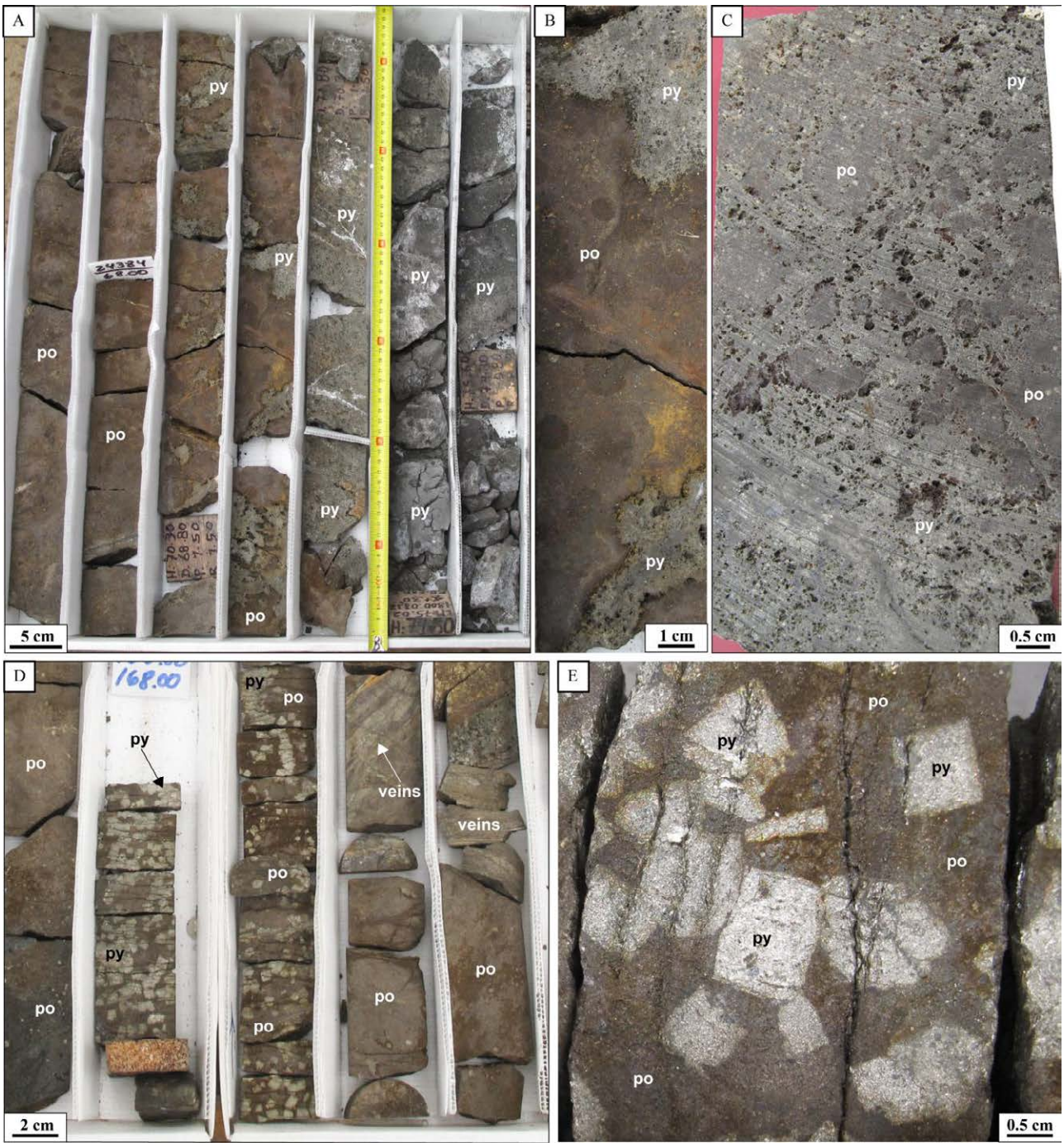

Figure 2: A) Cores of the contact between a pyrrhotite pipe and the pyrite-quartz body (borehole n°1800-08-18). B) Progressive replacement of pyrrhotite by pyrite C) Part of a core where pyrrhotite is replaced by pyrite (sample CP-12-BR-46), note the spongy replacement texture of pyrite. D) Large euhedral pyrite crystals and centimetric veins of pyrite, marcasite, sphalerite, and minor galena in pyrrhotite (borehole n°1600-08-12). E) Large euhedral pyrite in pyrrhotite (sample CP-12-BR-63) *Abbreviations:* po – pyrrhotite, py – pyrite.

pyrrhotite-free porous fine-grained pyrite with some euhedral pyrite that grades to the pyrite-quartz body. In the places where an outer zone, mainly constituted by Fe-rich sphalerite and galena, exist, it is observed that pyrite also partly replaces galena, (Fig. 3E) but the replacement front is less clear than in the pyrrothite pipes. Sphalerite remains systematically unaffected.

Centimeter-scale euhedral pyrite is present throughout all parts of the pyrrhotite pipes. These crystals are spatially related to numerous veins (up to 15 mm thick) of pyrite, marcasite, Fe-rich sphalerite, and minor galena (Fig. 2 D-E, Fig. 3 G-H) that crosscut the pyrrhotite pipes.

The up to 1-1.5 cm in size euhedral pyrite (Fig. 3 A, C-D), is rich in inclusions, mainly pyrrhotite, minor amounts of arsenopyrite, chalcopyrite, Fe-rich sphalerite, galena, and stannite, reflecting the initial mineralogy of the pyrrhotite pipe. Groups of pyrrhotite inclusions present synchronous extinction evidencing that they are relicts of larger pyrrhotite grains. Euhedral pyrite crystals are randomly oriented and commonly show a rim of fine-grained mixture of pyrite and marcasite (Fig. 3D). Lacy (1949) and Einaudi (1968, 1977) designated

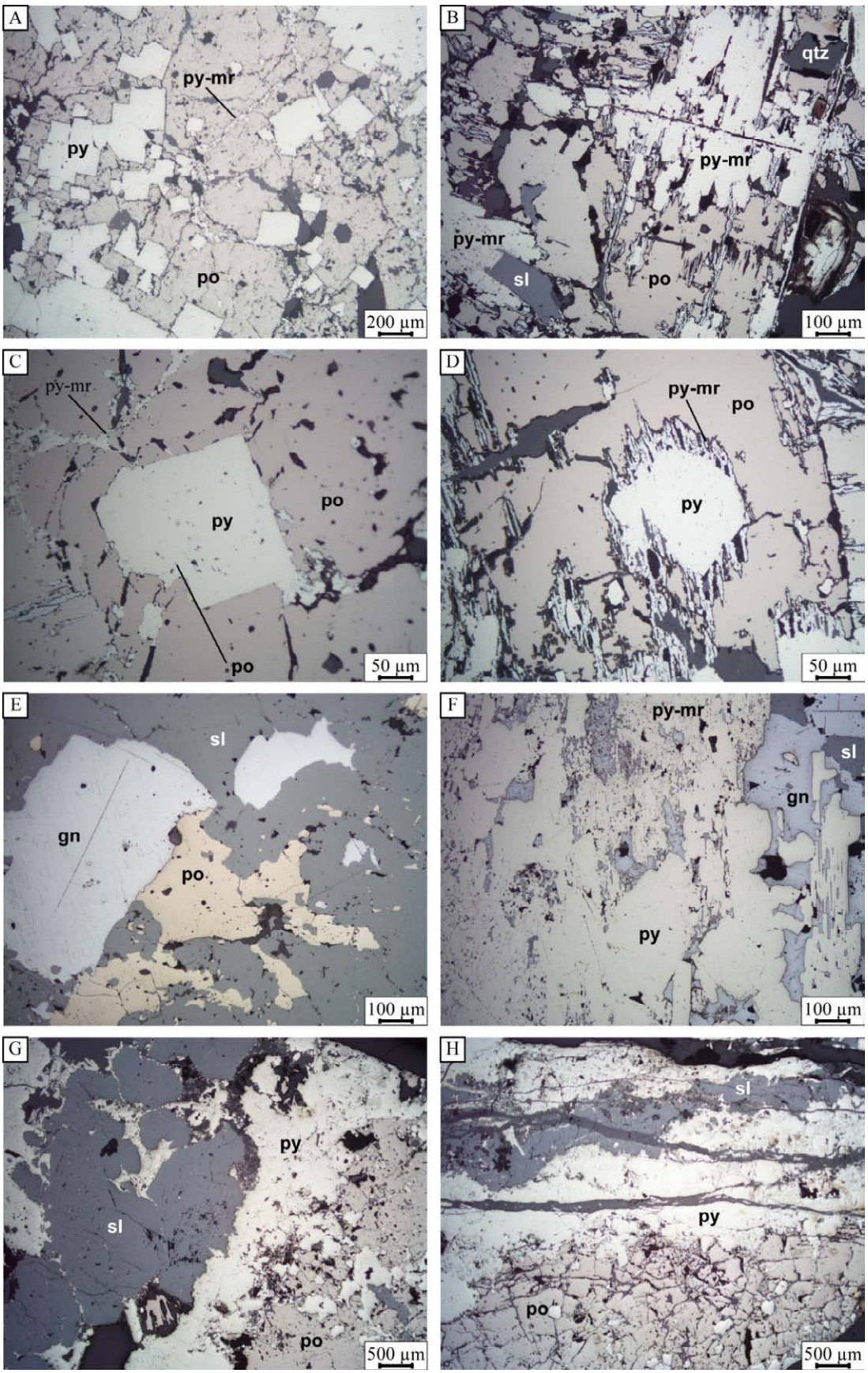

Figure 3: Typical textural patterns observed in pyrrhotite pipes and their outer Fe-rich sphalerite galena zone. A-D) Euhedral pyrite and fine-grained mixture of pyrite and marcasite replacing pyrrhotite, (A-sample CP-12-BR-53, B-sample CP-12-BR-56, C-sample CP-12-BR-118 and D-sample CP-12-BR-56); E) Pyrrhotite-sphalerite-galena assemblage from an Fe-rich sphalerite-galena body (sample CP-12-BR-41) not affected by pyrite replacement; F) Pyrite and marcasite replacing galena in a Fe-rich sphalerite-galena body (sample CP-12-BR-73); G) Pyrite-sphalerite vein within pyrrhotite (sample CP-12-BR-44); H) Pyrite-sphalerite vein crosscutting pyrrhotite crosscut by late siderite veins (sample CP-12-BR-46). *Abbreviations:* gn – galena, mr – marcasite, po – pyrrhotite, py – pyrite, qtz – quartz, sl – sphalerite.

this euhedral pyrite as "pyrite 1". They reported pyrrhotite crosscutting this euhedral pyrite and used this observation to support the interpretation that the euhedral pyrite and by inference the massive pyrite-quartz body were previous to the pyrrhotite pipes. During the present study, the observation of pyrrhotite crosscutting euhedral pyrite could not be reproduced despite careful search. Moreover, as explained above, all studied textures strongly suggest that euhedral pyrite postdates pyrrothite.

Fine-grained mixture of pyrite and marcasite also replaces pyrrhotite. This mixture is generally present along cracks, grain boundaries, and also inside the pyrrhotite grains where they replace the pyrrhotite and form the typical "intermediate product" texture (Fig. 3 A-D; Ramdohr, 1980).

Transformation of pyrrhotite in non-porous pyrite is a low-temperature replacement process indicative of input of additional reduced sulfur and more acidic conditions, according to Murowchick (1992) and Quian et al (2011).

3 Conclusions

The new data suggest an early emplacement of the pyrrhotite pipes inside the Pucará carbonate sequence. These pipes evolve outward to Pb-Zn replacement bodies. Similar pipe morphology and mineral associations are known in other polymetallic nearby deposits with low-sulfidation assemblages like Vinchos (Lavado and Farfán 2008) and Atacocha, located 20 and 10 km north of Cerro de Pasco. A N¬S corridor is recognized in the field. The three deposits of Vinchos, Atacocha, Cerro de Pasco and other similar deposit are within this corridor along major N-S and NNW-SSE faults.

Cordilleran deposits with high-sulfidation assemblages like Colquijirca and Morococha (Bendezú Juarez 2007, Bendezú and Fontboté 2009, Catchpole et al., 2011) show an early mineralization stage of pyrite-quartz replacement bodies and veins. The pyrite-quartz body of Cerro de Pasco has characteristics similar to the first stage of these deposits. It can be interpreted as the early expression of the magmato-hydrothermal system that subsequently produces the Cu-Ag-(Au-Zn-Pb) enargite-pyrite veins and Zn-Pb-(Bi-Ag-Cu) carbonate replacement bodies.

The large Cerro de Pasco deposit is a product of two distinct superimposed mineralizing events. A first low-sulfidation event formed the pyrrhotite pipes and the associated Fe rich sphalerite and galena replacement bodies; and a second event, with up to high-sulfidation assemblages, gave rise to the emplacement of the pyrite-quartz body, enargite-pyrite veins and Zn-Pb-(Bi-Ag-Cu) carbonate replacement bodies.

Acknowledgements

This research is supported by the Swiss National Science Foundation (grant 200020_134872). The authors are grateful to the Volcan Compania Minera S.A.A. for the logistic support in the field.

References

Baumgartner R (2007) Sources and evolution in space and time of hydrothermal fluids at the Cerro de Pasco Cordilleran base metal deposit, Central Peru: Terre & Environnement 66: 167 p.

Baumgartner R, Fontboté L, Vennemann T (2008) Mineral zoning and geochemistry of epithermal polymetallic Zn-Pb-Ag-Cu-Bi mineralization at Cerro de Pasco, Peru. Economic Geology 103: 493-537.

Baumgartner R, Fontboté L, Spikings R, Ovtcharova M, Schneider J, Pace L, Gutjahr M (2009) Bracketing the age of magmatic-hydrothermal activity at the Cerro de Pasco epithermal polymetallic deposit, central Peru: a U-Pb and $^{40}Ar/^{39}Ar$ study. Economic Geology 104: 479-504.

Bendezú R (2007) Shallow polymetallic and precious metal mineralization associated with a Miocene diatreme-dome complex: the Colquijirca district in the Peruvian Andes. Terre & Environnement 64: 221 p.

Bendezú R, Fontboté L (2009) Cordilleran epithermal Cu-Zn-Pb-(Au-Ag) mineralization in the Colquijirca District, Central Peru: deposit-scale mineralogical patterns. Economic Geology 104: 905-944.

Catchpole H, Kouzmanov K, Fontboté L, Guillong M, Heinrich C.A (2011) Fluid evolution in zoned Cordilleran polymetallic veins - Insights from microthermometry and LA-ICP-MS of fluid inclusions: Chemical Geology 281: 293-304.

Einaudi M (1968) Pyrrhotite-pyrite-sphalerite relations at Cerro de Pasco, Peru. Unpublished Ph.D. thesis, Cambridge, MA, Harvard University, 381 p.

Einaudi M (1977) Environment of ore deposition at Cerro de Pasco, Peru. Economic Geology 72: 893–924.

Lacy W (1949) Types of pyrite and their relations to mineralization at Cerro de Pasco, Peru: Unpublished Ph.D. thesis, Cambridge, MA, Harvard University, 193 p.

Lavado M, Farfán C (2008) Reinterpretación geológica; aspectos geo-económicos; retros y logros en la explaración del yacimiento Vinchos. XIII Congreso Latinoamericano de Geología y XIV Congreso Peruano de Geología, Lima-Perú, 2008.

Murowchick J (1992) Marcasite inversion and the petrographic determination of pyrite ancestry. Economic Geology 87: 1141–1152.

Qian G, Xia F, Brugger J, Skinner W, Bei J, Chen G, Pring A (2011) Replacement of pyrrhotite by pyrite and marcasite under hydrothermal conditions up to 220 °C: An experimental study of reaction textures and mechanisms. American Mineralogist 96: 1878-1893.

Ramdohr P (1980) The ore minerals and their intergrowths Pergamon (Oxford), 1205 p.

Ward H (1961) The pyrite body and copper orebodies, Cerro de Pasco mine, central Peru. Economic Geology 56: 402-422.

Transport and deposition of metallic nanoparticles and the origin of bonanza epithermal ores

James A. Saunders
Dept. of Geology and Geography, Auburn University, AL, USA, 36849 (saundja@auburn,edu)

George D. Kamenov
Dept. of Geological Sciences, University of Florida, 241 241 Williamson Hall, P.O. Box 112120, FL 32611, USA

Ryan Mathur
Dept. of Geology, Juniata College, 1700 Moore Street, Huntingdon, PA 16652, USA

Toru Shimizu
Magma-hydrothermal deposits Research Group, Geological Survey of Japan, AIST1-1-1 Higashi, Tsukuba 305-8567, Japan

Matthew E. Brueseke
Dept. of Geology, Kansas State University, Manhattan, Kansas 66506

Abstract. Two principal textures exhibited by metallic ore minerals indicate deposition of metallic nanoparticles during bonanza epithermal ore formation in USA and Japan. These include: 1) 3-dimensional self-organized fractal dendrites that apparently formed by aggregation of metallic nanoparticles under chaotic conditions; and 2) evidence of physical transport and deposition of nanoparticles ("sluice box textures") caused by perturbations along vein walls. To date we have recognized such fractal dendritic nanoparticles aggregates composed of electrum, "naumannite" (various Ag-Se-S phases), and mixed chalcopyrite and naumannite. Naumannite commonly exhibits the transport textures. Previously, nucleation of nanoparticles in these bonanza epithermal ores was interpreted by us to have formed in response to boiling in the shallow epithermal setting. However, new Pb-, Re-Os-, and Cu-isotope data indicate that all three of the aforementioned mineral phases have isotopic signatures consistent with a deep and primitive magmatic source. This implies nanoparticles must have formed deep in the "porphyry to epithermal" environment and then have been transported up to their point of deposition in the epithermal setting.

Keywords. Nanoparticles, bonanza epithermal ores, copper, lead isotopes

1 Introduction

Nanoparticles are particles $<10^{-7}$m (100nm) in diameter, and may have different chemical and physical properties than the bulk mineral phases. Lindgren (1934), originally from Sweden, first proposed that electrum nanoparticles ("colloids") were important in forming some bonanza epithermal ores in the western USA. Saunders (1990, 1994) confirmed this, and also showed that silica colloids were important in forming some bonanza epithermal ores in the western USA. Here we review textural features of these ores and present new isotopic data that address the origin of the metallic nanoparticles.

Some of the most spectacularly high-grade ("bonanza") low sulphidation (LS) epithermal Au-Ag ores occur in the northern Great Basin of western USA and on the islands of Kyushu and Hokkaido, Japan. These deposits occur in extensional environments formed by subduction-related back-arc extension in Japan or caused by the Northern Nevada Rift and emergence of the Yellowstone Hotspot in the USA (John, 2001; Silllitoe and Hedenquist, 2003; Saunders et al., 2008; Saunders and Brueseke, 2012). Our summary observations here are based on Hsihikari, Koryu, and Kushikino deposits, Japan; Midas, Sleeper, National, Ivanhoe, and Jumbo deposits of NV, McLaughlin, CA, Republic district (WA), multiple deposits in the Silver City district (ID), and the Haile deposit (SC) in USA. Besides their high Au-Ag grades and evidence of nanoparticle aggregation, these Japanese and USA epithermal ore share a number of characteristics: 1) banded encrustation textures indicating numerous different and episodic ore-formation events; 2) Se-rich nature caused by abundance of Ag-Se(S) phases; 3) common silica textures suggesting the former presence of amorphous silica; 4) contain abundant adularia; 5) commonly contain bladed calcite replaced by silica or locally preserved (as at Midas, NV); 5) have chalcopyrite as the principal sulphide phase in highest-grade bands; and 6) O- and H-isotopes and fluid inclusion data indicating ore forming solutions were largely heated meteoric waters that underwent some isotopic exchange with country rocks and may contain a small contribution of magmatic water. Older genetic concepts involving leaching of metals from country rocks by heated meteoric water have recently been called into question by recent Pb-isotope data (Kamenov et al., 2007; Saunders et al., 2008; this study) and Cu-isotope data presented here.

Detailed petrography and petrogenetic interpretations are perhaps possible (and less ambiguous) due to the presence of abundant Au-Ag minerals in the ores, and the chrono-stratigraphic nature of the banded ores. This has provided the firm basis for the important decisions about *which* minerals to collect isotopic data from. Some of these textures are described below and in more detail in Saunders (2004), Saunders and Schoenly (2005) and Saunders (2012).

2 Ore Mineralogy and Petrography

The most abundant ore minerals in the bonanza ores are electrum (~40-70 wt. % Au), "naumannite" (Ag_2Se), and chalcopyrite. We suspect much of what has been labelled naumannite in USA deposits in the pre-1920s literature may actually be aguilarite and Se-rich acanthite; naumannite would have been largely identified by optical properties and blow-pipe analysis prior to the use of X-ray diffraction. Our recent (unpublished) detailed study on Ag minerals from Silver City (ID) and Midas (NV) indicate aguilarite>Se-rich acanthite are the most abundant Ag minerals in those deposits, but more work is needed on silver minerals in other NGB epithermal deposits. In addition to these, much less abundant pyrite, galena, sphalerite, pyrargyrite, proustite, tetrahedrite, miargyrite, and rare tellurides also occur. Although many of these minerals occur in most of the deposits, there does appear to be two end member types of ore in terms of mineralogy: 1) almost mono-mineralogic electrum-rich ores like Sleeper, National, and Jumbo NV, and 2) those containing predominantly dark-coloured "ginguro" (silver-black) bands rich in naumannite (Fig. 1), like Hishikari, Koryu, Midas, Ivanhoe, Silver City, Buckskin National, and Republic.

Multiple precious metal-rich bands are common in many of the deposits (Fig. 1) indicating many ore deposition events over time (Saunders, 2012). Fractal dendrites point toward the vein center or younging direction. These dendrites are 3-dimensionsal features (Fig. 2) and can easily be overlooked in a 2-dimensional surface in a polished section or a polished thin section. For example, earlier ore petrology investigations at Hishikari (Izawa et al., 1992) and Koryu (Shimizu, 1998) did not recognize these features, but they have now been identified in this study (Fig. 3).

In addition to the fractal dendrites formed by nanoparticle aggregation, we have observed physical transport textures (Figs. 4, 5) in the bonanza epithermal ores. These are not as abundant as the fractal dendrites, but perhaps are conclusive proof that metallic nanoparticles can be transported and deposited by hydrothermal solutions. We have observed these features at Republic, Sleeper, Midas, Ivanhoe, and Silver City (USA). Typically naumannite is the principal phase exhibiting this texture, but disseminated electrum can occur in that naumannite, or actually be deposited with silica colloids as at Sleeper.

The protrusions emanating from the vein wall that can cause these textures include quartz crystals, coliform silica growths (Fig. 4), platy calcite crystals, silica pseudomorphs after platy calcite, and even large electrum dendrites (Fig. 5). Another feature that suggests hydrothermal transport of phases even larger than nanoparticles are doubly terminated, euhedral, quartz crystals (Figs. 2, 3) that only occur in the highest grade bands in both the Japanese and western USA epithermal ores. They are as large as 0.75 mm in length, and we propose that their doubly terminated, euhedral nature suggests that they grew in, and were transported by, the hydrothermal ore-forming solutions and were deposited in the same location as silica and metallic

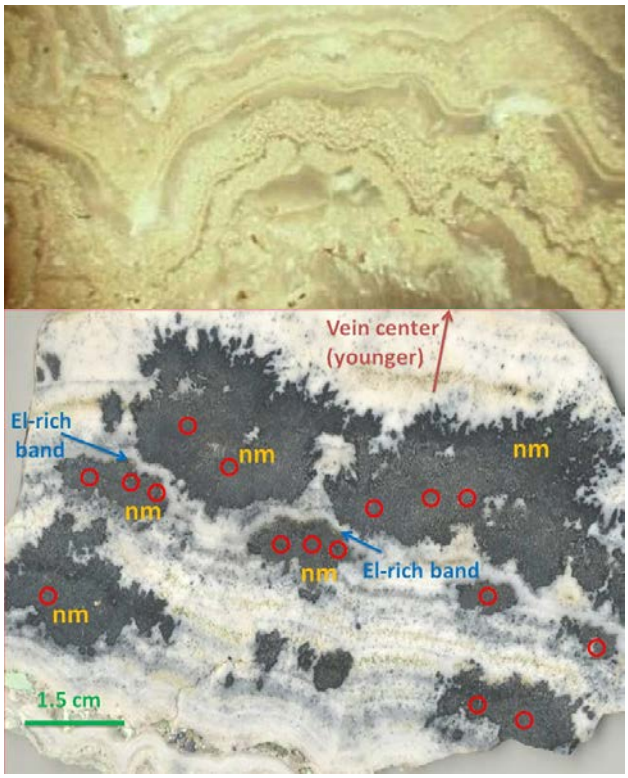

Figure 1. (Top) Multiple electrum-opal bands from Sleeper (NV). Electrum bands are composed of "forests" of fractal electrum dendrites. For more details see Saunders (1994) and Saunders and Schoenly (1995). **(Bottom)** Multiple bands containing large naumannite (nm) fractal dendrites and minor electrum (in red circles), for more details see Vikre (1995) and Saunders (2012).

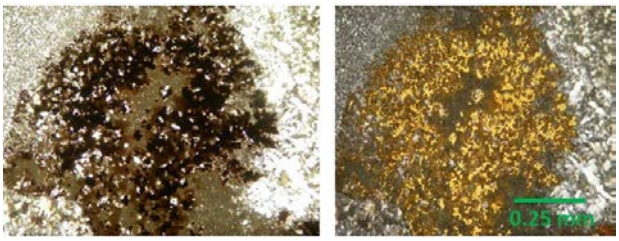

Figure 2. Fractal electrum dendrite from the Sleeper deposit imbedded in slightly recrystallized opal in transmitted light (left) and transmitted and reflected light (right) formed from the aggregation of both silica and electrum nanoparticles simultaneously. Note some doubly terminated quartz euhedra (seen best in left image) are also present in the dendrite; these are discussed in the text.

nanoparticles. Note that most silica in the fractal electrum dendrite from the Sleeper deposit (Fig. 2) is opal which encapsulates both the quartz euhedra and electrum branches. This clearly indicates that the two silica phases are not in equilibrium with each other. Another observation we have made at Sleeper is that locally the quartz euhedra contain electrum nanoparticle inclusions deep in their interiors. This could be the result of growing quartz trapping metallic nanoparticles (apparently formed much deeper, as the hydrothermal discussed below) as they both travelled entrained in the

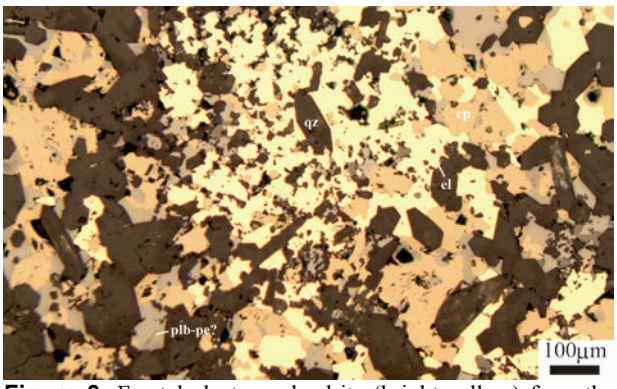

Figure 3. Fractal electrum dendrite (bright yellow) from the Hishikari deposit, associated with naumannite (light grey) and chalcopyrite, (pale yellow). The orientation of this dendrite is a right angle to the one shown in Fig 2 from the Sleeper deposit. Also note some doubly terminated quartz euhedra (dark grey) here as well, and compare to Fig. 2.

Figure 4. Physical transport ("sluice box") textures from the Ivanhoe-Hollister deposit (NV) showing deposition of black naumannite particles along the "lee" side of silica protrusions along the vein wall (current direction was from right to left).

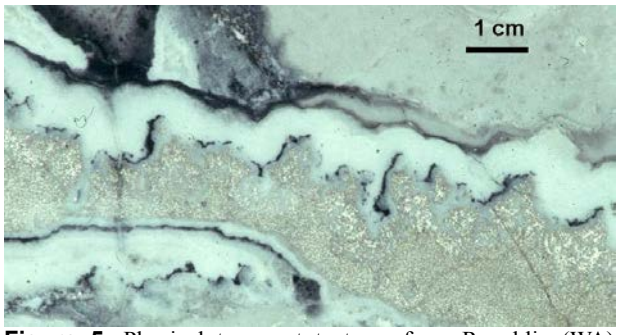

Figure 5. Physical transport textures from Republic (WA) showing deposition of black naumannite particles along the "lee" side of fractal electrum dendrites protrusions that lined the then vein wall (current direction was from right to left).

ore-forming fluids.

We have seen evidence of at least one other euhedral phase that may have formed similarly to the quartz euhedra: sphalerite. Euhedral, equant, sphalerite crystals at the Trade Dollar deposit, Silver City district (ID) occur within coarse naumannite dendrites along with the aforementioned quartz euhedra and may have a similar origin. We have only recently recognized these textures and will investigate them further.

The textures described from western USA and Japan are all in ores of Eocene age or younger. However, similar textures occur in epithermal ores as old as at least the Cambrian (Fig. 6).

Figure 6. Electrum-rich bands containing fractal electrum dendrites from the Cambrian Haile, (SC) deposit, SE USA.

3 Pb- and Cu-Isotope data

In order to address the origin of metals in the bonanza epithermal ores from western USA, we initially measured Pb-isotopic composition of electrum and naumannite using MC-ICP-MS. Initial Pb-isotope results from Sleeper, Jumbo, Seven Troughs, and National (NV) indicated that gold and silver were sourced from the mafic magmas that were part of the bimodal volcanism associated with the initial emergence of the Yellowstone Hotspot (Kamenov, 2007, Saunders et al., 2008). Pb-isotope data of Au-Ag minerals from additional deposits in the northern Great Basin (NGB) of western USA support this earlier interpretation (Fig. 7). The additional Pb-isotope data raises an interesting question: why should such shallow deposits contain Au-

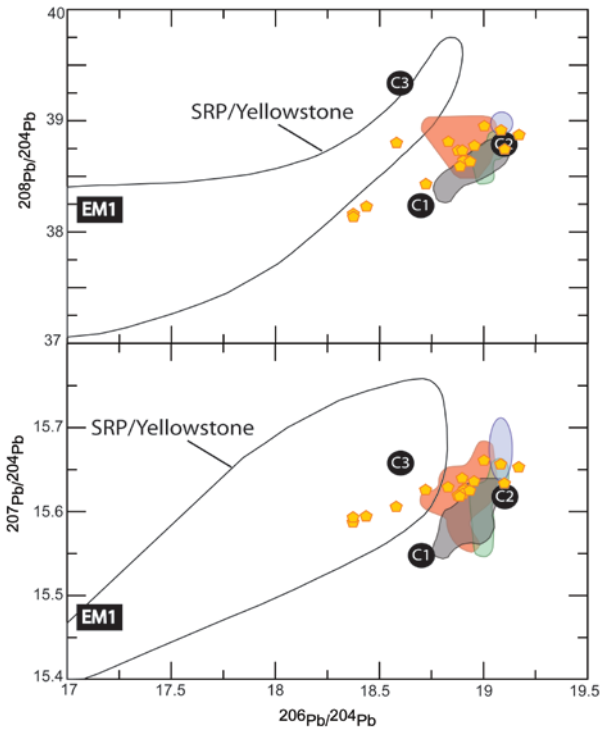

Figure 7. Pb-isotope data from Au-Ag minerals in NGB epithermal ores (gold pentagons) from Hasten (2012). The large outlined field includes Miocene to present basalt in the Yellowstone/Snake River Plain volcanic province; red and green fields = Miocene Columbia River Basalt lavas, grey field = Miocene Steens Basalt lavas, and blue field = regional continental felsic basement rocks. Note epithermal Au-Ag minerals have similar Pb isotopic composition as coeval regional basalt flows. Other symbols are discussed in Hasten (2012).

Ag minerals with such primitive (deep) magmatic signatures? Thus we conducted some reconnaissance Re-Os analyses of electrum at Sleeper and National, and initial $^{187}Os/^{188}Os$ ratios suggested a deep primitive magmatic signature of the electrum (Saunders et al., 2011).

We have conducted some reconnaissance Cu-isotope analyses of both ore minerals (electrum, naumannite, and chalcopyrite) and basalts in the NGB of western USA. All three of the ore minerals yield similar Cu-isotope values suggesting they were in isotopic equilibrium, and all are close to the standard value of 0‰ for $\partial^{65}Cu$ (Fig. 8). Shown in Fig. 8 are our new data from epithermal ores and basalts, the typical range of chalcopyrite in porphyry copper ores, along with published data (Bishop et al., 2012) for metallic meteorites and mantle rocks. Results confirm previous Pb- and Re-Os-isotope data indicating a primitive (mafic?) source of Au-Ag and now Cu in these epithermal ores.

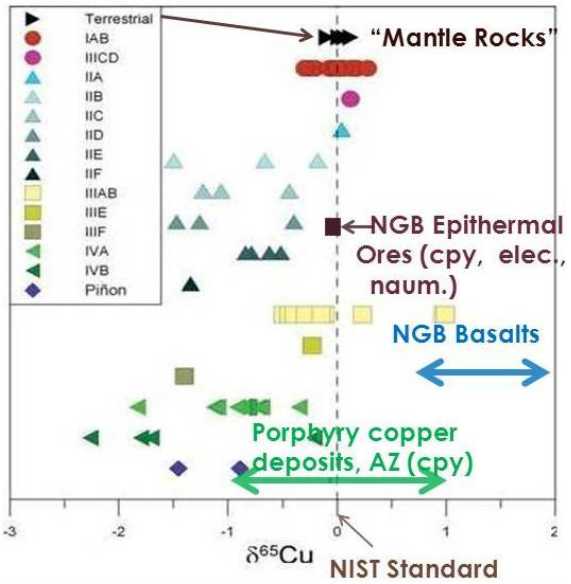

Figure 8. Cu-isotope data on ore minerals from northern Great Basin (NGB) USA epithermal ores in comparison to metallic meteorites (bulk of data), mantle-like rocks, NGB basalts, and typical porphyry copper deposits. Data on Cu-isotopes in meteorites and mantle-like rocks from Bishop et al. (2102).

4 Discussion and Conclusions

Finally, we return to the question posed above about how could bonanza epithermal ores that formed as shallow as a few hundred meters below the surface, with temperatures of deposition in the range of ~150-250°C, preserve such primitive isotopic signatures? Our current working hypothesis is that metallic nanoparticles of chalcopyrite, electrum, and Ag-Se-S phases nucleated from low-density magmatic fluids deep near the host magma chamber and were entrained in upward moving ore-forming solutions. This caused the nanoparticles to lock in a deep primitive isotopic signature, and then they were entrained in upward-moving ore-forming fluids, where they were deposited in the shallow, often boiling, epithermal setting by the process of nanoparticle aggregation. In contrast, the doubly terminated quartz euhedra also formed deeper than the epithermal setting (but not as deep as metallic nanoparticles), and grew as they moved upward, locally trapping some of the metallic nanoparticles as solid inclusions in them. They too were deposited as nanoparticles of silica and ore minerals aggregated.

Acknowledgements

This work was partially supported by grants from the USGS-MRERP program to Saunders (0HQGR0153) and the U.S. NSF to Brueseke (EAR-0838139) and Saunders (EAR-0838208).

References

Bishop, MC, Moynier F, Weinstein C, Fraboulet, JG, Wang, K, Foriel, J. (2012) The Cu isotopic composition of iron meteorites. Meteoritics & Plan Sci 47:68-276

Hasten, ZEL (2012) Mid-Miocene magmatism in the Owyhee Mountains, ID: origin and petrogenesis of volcanic rocks in the Silver City district. [M.S. thesis] Manhattan, Kansas State University, 222 pp.

Izawa E, Urashima Y, Ibaraki K, Suzuki R, Yokohama T, Kawasaki K, Koga, A, Taguchi S (1992) The Hishikari gold deposit: High-grade epithermal veins in Quaternary volcanics of Southern Kyushu, Japan. J. Geochem Explor 36:1–56

John DA (2001) Miocene and early Pliocene epithermal gold silver deposits in the in the northern Great Basin, western USA: Characteristics, distribution, and relationship to magmatism. Econ Geol 96:1827–1853

Kamenov GD, Saunders JA, Hames WE, Unger D (2007) Mafic magmas as sources for gold in Middle-Miocene epithermal deposits of Northern Great Basin, USA: evidence from Pb isotopic compositions of native gold. Econ Geol 102:1191–1195

Lindgren, W (1934) Mineral Deposits: McGraw Hill Book Company, New York, 930 pp.

Saunders JA (1990) Colloidal transport of gold and silica in epithermal precious metal systems: Evidence from the Sleeper deposit, Humboldt County, Nevada. Geology 18:757–760

Saunders JA (1994) Silica and gold textures at the Sleeper deposit, Humboldt County, Nevada: evidence for colloids and implications for ore-forming processes. Econ Geol 89:628–638

Saunders JA, Schoenly PA (1995) Boiling, colloid nucleation and aggregation, and the genesis of bonanza gold mineralization at the Sleeper Deposit, Nevada. Miner Depos 30:199–211

Saunders, JA, Unger DL, Kamenov GD, Fayek M., Hames W, Utterback WC (2008) Genesis of Middle Miocene Yellowstone-hotspot-related bonanza epithermal Au-Ag deposits, Northern Great Basin Region, USA. Miner Depos 43: 715-734

Saunders, JA, Kamenov GD, Hofstra AH, Unger, DL, Creaser RA, Barra, F (2011) "Forensic" geochemical approaches to constrain the source of Au-Ag in low-sulfidation epithermal ores. In Steininger R and Pennell W (eds.): Great Basin evolution and metallogeny. Geol Soc of Nevada, Reno, pp 693-700

Saunders JA (2012) Textural evidence of episodic introduction of metallic nanoparticles into bonanza epithermal ores. Minerals 2: 228-243

Saunders JA, Brueseke ME (2012) Volatility of Se and Te during subduction-related "distillation" and the geochemistry of epithermal ores of western USA. Econ Geol 107:165-172

Shimizu T, Matsueda H, Ishiyama D, Matsubaya O (1998) Genesis of epithermal Au–Ag mineralization of the Koryu Mine, Hokkaido, Japan. Econ Geol 93:303–325

Sillitoe RH, Hedenquist JW (2003) Linkages between volcanotectonic settings, ore-fluid compositions, and epithermal precious metal deposits. Soc Econ Geol Sp Publication 10:315–343

Vikre PG (1985) Precious metal vein system in the National district, Humboldt County, Nevada. Econ Geol 80:360–393.

Porphyry Cu-Au/Mo deposits of Central Eurasia: geodynamics and metallogeny

Reimar Seltmann, Alla Dolgopolova
Centre for Russian and Central EurAsian Mineral Studies (CERCAMS), Department of Earth Sciences, Natural History Museum, London, United Kingdom

T. Mike Porter
Porter GeoConsultancy Pty Ltd, Adelaide, South Australia

Franco Pirajno
Centre for Exploration Targeting, The University of Western Australia, Perth, Western Australia

Abstract. Tectonic activity within the Central Asian Orogenic Belt commenced in the early Palaeozoic, when micro-continental slivers were rifted from the palaeo-Tethys Ocean margin of the combined Eastern Europe and Siberian cratons, to form a wide, intervening oceanic back-arc basin. Throughout the Palaeozoic, and into the Mesozoic, subduction below the microcontinents, and parallel intraoceanic subduction both within the back-arc basin, and continuous along trend with that below the micro-continental slivers, respectively produced a series of long-lived, ensialic and ensimatic magmatic arcs. A diverse suite of porphyry Cu-Au/Mo, Mo and Au-Cu, other intrusive-related Cu-Au, and epithermal Au mineralised systems, were developed throughout these arcs, both temporally and spatially. In sections of the belt, the waning stages of orogenesis, collapse and post-collisional crustal extension, were accompanied by the development of giant, intrusion-related gold deposits. The formation and location of most of the mineralised systems was influenced by tectonic elements that cross-cut the hosting arcs, and by processes both within the crust and the subcrustal lithospheric mantle.

Keywords. Porphyry deposits, central Eurasia

1 Introduction

Major porphyry Cu-Au and Cu-Mo deposits (e.g. *Oyu Tolgoi* in Mongolia (6.54 Gt @ 0.70% Cu, 0.29 g/t Au; AMC Consultants, 2013) and *Kal'makyr-Dalnee* in Uzbekistan (6 Gt @ 0.39% Cu, 0.37 g/t Au; Singer et al., 2008) are distributed over an interval of almost 5000 km across central Eurasia, from the Urals Mountains in Russia in the west, to Inner Mongolia in north-eastern China, to the east (Seltmann and Porter 2005). These deposits were formed during a range of magmatic episodes from the Ordovician to the Jurassic. They evolved as magmatic arcs within the extensive subduction-accretion complex of the Altaid and Transbaikal-Mongolian Orogenic Collages (Fig. 1), which developed from the late Neoproterozoic, through the Palaeozoic orogeneses to the Jurassic intra-cratonic extension. These arcs are predominantly located on the palaeo-Tethys Ocean margin of the proto-Asian continent, but are also associated with the closure of two rifted back-arc basins behind that ocean facing margin. The complex now comprises collages of fragments of sedimentary basins, island arcs, accretionary wedges and tectonically bounded terranes composed of Neoproterozoic to Cenozoic rocks. The development of these collages commenced when slivers of an earlier Proterozoic subduction complex, accreted to the palaeo-Tethys Ocean margin of the combined Eastern Europe and Siberian cratons, were rifted from the main cratonic mass. These slivers were the contiguous Karakum and Altai-Tarim micro-continents, which became separated from the main cratonic mass by oceanic spreading that created the Khanty-Mansi back arc basin. Subduction of the palaeo-Tethys Ocean beneath these micro-continents and the adjacent back-arc basin produced the overlapping late Neoproterozoic to early Palaeozoic Tuva-Mongol and Kipchak magmatic arcs. Contemporaneous intra-oceanic subduction within the back-arc basin, from the Late Ordovician, produced the parallel Urals-Zharma magmatic arc, and separated the main Khanty-Mansi back-arc basin from the inboard Sakmara marginal sea. By the Late Devonian, the Tuva-Mongol and Kipchak arcs had amalgamated to form the Kazakh-Mongol arc, which extended over the whole palaeo-Tethys Ocean margin of the combined cratonic mass, while magmatic activity continued on the Urals-Zharma arc. During the mid Palaeozoic, the two main cratonic components of the proto-Asian continent, the Siberian and Eastern European cratons (Fig. 1), began to rotate relative to each other, "drawing-in" the two sets of parallel arcs to form the Kazakh Orocline between the two cratons. During the Late Devonian to Early Carboniferous, the Khanty-Mansi back-arc basin began subducting beneath the oroclinally infolded outer island arc mass to form the Valerianov-Beltau-Kurama arc. At the same time, the palaeo-Pacific Ocean began subducting below the Siberian craton to form the Sayan-Transbaikal arc, which expanded by the Permian to become the Selanga-Gobi-Khanka arc, and for a period was continuous with the Kazakh-Mongol arc. By the Mid to Late Permian, as the Kazakh Orocline had continued to develop, both the Sakmara and Khanty-Mansi back-arc basins had been closed and the collage of cratons and arcs were sutured by accretionary complexes. During the Permian and Triassic, the North China craton approached and docked with the continent, closing the Mongol-Okhotsk sea (an embayment on the palaeo-Pacific margin) to form the Mongolian Orocline. Subduction and arc building activity on the palaeo-Pacific Ocean margin continued to the Mid Mesozoic as the Indo-Sinian and Yanshanian orogenic cycles (Seltmann and Porter 2005, and references cited therein).

2 Key deposits in space and time

Significant porphyry Cu-Au/Mo and Au-Cu, other

intrusive-related Cu-Au, and epithermal Au mineralised systems (Table 1, Fig. 1 – updated after Seltmann and Porter 2005) were formed during the: Ordovician in the Kipchak arc (e.g. *Bozshakol* Cu-Au in Kazakhstan, *Taldy Bulak* porphyry Au-Cu in Kyrgyzstan); Silurian to Devonian in the Kazakh-Mongol arc (e.g. *Nurkazgan* Cu-Au in Kazakhstan; *Taldy Bulak-Levoberezhny* Au in Kyrgyzstan); Devonian in the Urals-Zharma arc (e.g. *Yubileinoe* Au-Cu in Russia); Devonian in the Kazakh-Mongol arc (e.g. *Oyu Tolgoi* Cu-Au, and *Tsagaan Suvarga* Cu-Au, both in Mongolia); Carboniferous in the Kazakh-Mongol arc (e.g. *Kharmagtai* Au-Cu in Mongolia, *Tuwu-Yandong* Cu-Au in Xinjiang, China; *Koksai* Cu-Au, *Sayak* skarn Cu-Au, *Kounrad* Cu-Au and the *Aktogai Group* of Cu-Au deposits, all in Kazakhstan); Carboniferous in the Valerianov-Beltau-Kurama arc (e.g. *Kal'makyr-Dalnee* Cu-Au and *Kochbulak* epithermal Au, both in Uzbekistan; *Benqala* Cu-Au in the southeast Urals of Kazakhstan); Triassic in the Selanga-Gobi-Khanka arc (e.g. *Erdenet* Cu-Mo in Mongolia); and Jurassic in the Selanga-Gobi-Khanka arc (e.g. *Wunugetushan* Cu-Mo in Inner Mongolia, China). In addition to the tectonic, geologic and metallogenic setting, and the distribution of the mineralised systems listed above, descriptions of the setting, geology, alteration and mineralisation recorded at each provides important insights into their metallogenic significance (Seltmann and Porter 2005; Pirajno et al., 2009; Seltmann et al., 2013).

Recent research has furthered controversial discussions on the formation of mineral deposits in accretionary orogens. If we review, compare and contrast the linked geodynamic and metallogenic evolution of older accretionary orogens, such as the Central Asian Orogenic Belt (or Altaids), with more recent settings, e.g., the western Pacific, all have a large endowment of different types of mineral systems. The diversity in styles and timing of mineralisation appears to be a direct consequence of differing lithosphere-asthenosphere processes during the evolution of accretionary orogens, where variations in arc architecture and position in the cycle influences the mineral endowment (Fig. 2). Over the last decade, progressive specialisation has caused the knowledge gap between lithospheric and asthenospheric processes to widen, which interdisciplinary research has failed to bridge adequately and to keep pace. The necessary holistic view of crustal growth processes, mantle dynamics and crust-mantle interaction has suffered in the specialised literature, from some degree of decoupling between plate tectonic processes (rifting – spreading – subduction – accretion – collision cycles) on the one hand, and (post-collisional, within-plate) anorogenic or plume tectonics on the other (Dalimov 2007; Xiao et al. 2008; Pirajno et al. 2009). Too little attention has been given to interconnecting studies, facts and processes, and some concepts developed two to three decades ago, thereby hindering, rather than helping successful mineral exploration targeting for a variety of deposit types. For instance, some mineral deposits classified as "orogenic", e.g., Bakyrchik (Rafailovich, 2009) and Muruntau (De Boorder et al., 2010), may instead be controlled by non-orogenic magmatism, trans-crustal shear zones and dilational jogs, related by processes in the subcrustal lithospheric mantle.

3 Conclusions

The location of giant, arc-related, mineralised systems within the Altaids (e.g., Oyu Tolgoi in Mongolia, Aktogai in Kazakhstan or Almalyk in Uzbekistan), and other orogenic belts elsewhere in the world (e.g., in the Andes of South America) are controlled by tectonic elements that cross-cut the hosting arc.

Post-collisional crustal extension, following orogenic collapse, is related to the close, to contemporaneous, temporal and spatial development of giant intrusion-related gold deposits in the Southern Tienshan (e.g., Muruntau, Zarmitan) and diamondiferous lamproites and carbonatites (e.g., Karashokho, Chagatai; Seltmann et al. 2010, 2011). High-heat flow (thermal aureoles) and noble gas data, indicate a mantle influence in the formation of these systems (Graupner et al. 2010). Both Aktogai and Muruntau, are reportedly located above zones of seismic transparency interpreted to indicate heat-matter flux from the mantle, causing the generation of giant, though crustal-dominated, magma-ore systems (S. Cherkasov, pers. comm. 2006). As such, some giant mineral deposits appear to be influenced by atypical orogenic and anorogenic processes.

Further research, based on robust facts from modern micro-analytical, thermo-chronology, noble gas and isotope studies, as well as geophysical data, is required to address these relationships.

Acknowledgements

Cooperation and inspiring discussions with numerous associated CERCAMS researchers are appreciated. This is a contribution to project IGCP-592 funded by IUGS-UNESCO.

References

AMC Consultants Pty Ltd (2013) Oyu Tolgoi Project, IDOP Technical Report for Turquoise Hill Resources Ltd, March, 2013, www.turquoisehill.com/s/financials_tech_reports.asp

Dalimov TN (2007) Evolution and genetic model of the Chatkal-Kurama plume. Geology and Mineral Resources. Tashkent, 3:3-18 (in Russian).

Gerel O, Munkhtsengel B (2005) Erdenetiin Ovoo Porphyry Copper-Molybdenum Deposit in Northern Mongolia. In: Porter TM (ed.) Super Porphyry Copper & Gold Deposits: A Global Perspective, PGC Publ., Adelaide, v. 2, pp. 525-543.

Graupner T, Niedermann S, Rhede D, Kempe U, Seltmann R, Williams T, Klemd R (2010) Multiple sources for mineralizing fluids in the Charmitan gold (-tungsten) mineralization (Uzbekistan). Mineralium Deposita, 45:667-682.

Groves DI, Goldfarb RJ, Gebre-Mariam M, Hagemann SG, Robert F (1998) Orogenic gold deposits: a proposed classification in the context of their crustal distribution and relationship to other gold deposit types. Ore Geol. Rev. 13:7-27

Han C, Rui Z, Mao J, Yang J, Wang Z, Yuan W (2003) Geological characteristics of the Tuwu copper deposit, Hami, Xianjiang. In: Mao, Goldfarb, Seltmann, Wang, Xiao and Hart, (Eds.), Tectonic Evolution and Metallogenesis of the Chinese Altay and Tianshan, Proceedings Volume of the International Symposium of the IGCI – 473 Project in Urumqi, *IAGOD Guidebook Series 10: CERCAMS/NHM,* London, pp. 249-260.

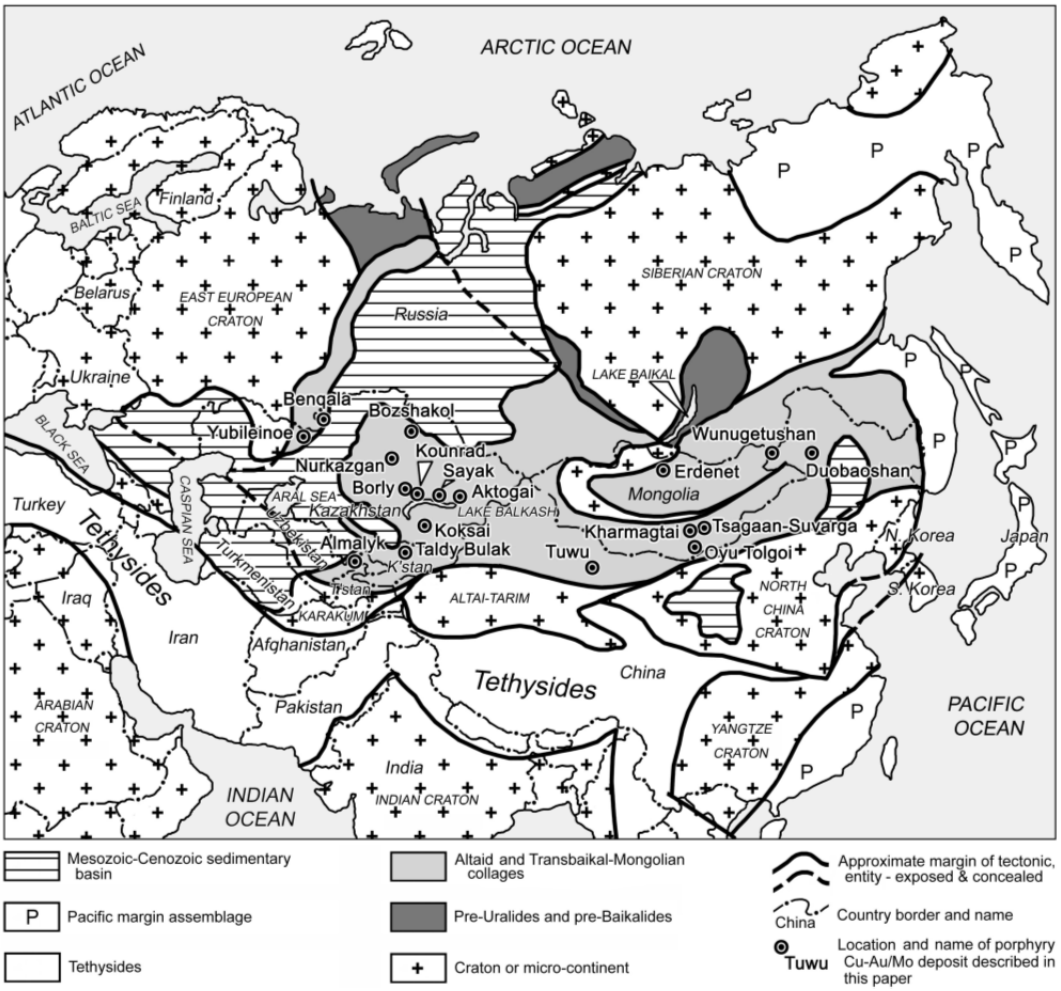

Figure 1. Location plan showing the tectonic elements of Eurasia and key porphyry Cu-Au/Mo deposits (Seltmann and Porter 2005). T'stan = Tajikistan, K'stan = Kyrgyzstan. Tectonic subdivisions in part after Yakubchuk (2005) and a variety of other sources cited in Seltmann and Porter (2005)

IMC Group Consulting Limited (2011) Competent Persons Report on the Mining Assets of Kazakhmys Plc, Kazakhstan and Kyrgyzstan, Appendix III, 342p.

Kirwin DJ, Wilson CC, Turmagnai D, Wolfe R (2005) Exploration History, Geology and Mineralisation of the Kharmagtai Gold-Copper Porphyry District, South Gobi Region, Mongolia. In: Seltmann, Gerel, and Kirwin, (Eds.), Geodynamics and Metallogeny of Mongolia with a Special Emphasis on Copper and Gold Deposits, *IAGOD Guidebook Series 10: CERCAMS/NHM,* London, pp. 175-191.

Mutschler FE, Ludington S, Bookstrom, AA (2000) Giant porphyry-related metal camps of the world - a database; *U.S. Geological Survey* Open-File Report 99-556, Online Version 1.0, http://geopubs.wr.usgs.gov/open-file/of99-556/world_ppy.xls

Pirajno F, Seltmann R, Cook NJ, Borisenko AS (eds., 2009) Intraplate magmatism and associated metallogeny in Central Asia, China and Siberia. Special Issue. Ore Geology Reviews, 35:111-261.

Seltmann R, Konopelko D, Biske G, Divaev F, Sergeev S (2011) Hercynian post-collisional magmatism in the context of Paleozoic magmatic evolution of the Tien Shan orogenic belt. Journal of Asian Earth Sciences, 42-5:821-838.

Seltmann R, Shatov V, Yakubchuk A (2004) Mineral Deposits Database and Thematic Maps of Central Asia, Scale 1.5 million: ArcView 3.2 and MapInfo 6.0(7.0) GIS Packages, Explanatory Notes, *CERCAMS, Natural History Museum,* London, UK., 117p.

Seltmann R, Porter TM (2005) The Porphyry Cu-Au/Mo Deposits of Central Eurasia: 1. Tectonic, Geologic & Metallogenic Setting and Significant Deposits. In: Porter TM (ed) Super Porphyry Copper & Gold Deposits: A Global Perspective, vol. 2. PGC Publishing, Adelaide, pp. 467-512.

Seltmann R, Soloviev S, Shatov V, Pirajno F, Naumov E, Cherkasov S (2010) Metallogeny of Siberia: Tectonic, Geologic and Metallogenic Settings of Selected Significant Deposits. Australian Journal of Earth Sciences, 57:655-706.

Seltmann R, Porter TM, Pirajno F (2013) Geodynamics and metallogeny of the central Eurasian porphyry (and related epithermal) mineral systems: a review. Journal of Asian Earth Sciences, (in press).

Singer DA, Berger VI, Moring BC (2008) Porphyry Copper Deposits of the World: Database and Grade and Tonnage Models, US Geological Survey, Open-File Report 2008-1155.

Watanabe Y, Stein HJ (2000) Re-Os ages for the Erdenet and Tsagaan Suvarga porphyry Cu-Mo deposits, Mongolia, and tectonic implications. Economic Geology, 95:1537-1542.

Wu HY, Zhang LC, Wan B, Chen ZG, Xiang P, Pirajno F, Du A, Qu WJ (2011) Re-Os and 40Ar/39Ar ages of the Jiguanshan porphyry Mo deposit, Xilamulun metallolgenic belt, NE China, and constraints on mineralization events. Mineralium Deposita, 46:171-186.

Xiao W, Pirajno F, Seltmann R (Eds., 2008) Geodynamics and metallogeny of the Altaid Orogen. Special Issue. Journal of Asian Earth Sciences, 32–2-4:77-300.

Yakubchuk AS (2005) Geodynamic evolution of accreted terranes of Mongolia against the background of the Altaids and Transbaikal-Mongolian collages. In: Seltmann R, Gerel O, Kirwin DJ (eds) Geodynamics and Metallogeny of Mongolia; NHM London: IAGOD Guidebook Series, 11, pp. 13-24.

Table 1. Tonnage, grade and age statistics of a selection of the more significant porphyry Cu-Au/Mo and related epithermal Au deposits of the Altaids and Transbaikal-Mongolian Orogenic Collages in central Eurasia, (from Seltmann et al., 2013, updated after Seltmann and Porter 2005; locations are shown in Fig. 1)

Deposit	Location	Tonnage	Grade			Contained Metal		Age
Bozshakol (i)	Kazakhstan	1.17 Gt	0.35% Cu	0.004% Mo	0.14 g/t Au	4.1 Mt Cu	163 t Au	481 Ma
Andash (j)	Kyrgyzstan	19.2 Mt	0.4% Cu		1.10 g/t Au		21 t Au	Ordovician
Taldy Bulak (k)	Kyrgyzstan	423 Mt	0.17% Cu	0.01% Mo	0.46 g/t Au	0.7 Mt Cu	196 t Au	Ordovician
Duobaoshan (m)	China, (I.M.)	951 Mt	0.46% Cu	0.02% Mo	0.13 g/t Au	4.4 Mt Cu	120 t Au	476 Ma
Tongshan (b)	China, (I.M.)	180 Mt	0.47% Cu	0.023% Mo		0.9 Mt Cu	0.04 Mt Mo	~476 Ma ?
Nurkazgan (l)	Kazakhstan	200 Mt.	0.89% Cu	0.1% Mo	0.38 g/t Au	1.8 Mt Cu	76 t Au	410 Ma
TB Lev.$^{Mesoth\text{-}Porph}$ (a,f)	Kyrgyzstan	18.7 Mt	0.2 - 0.3% Cu		6.9 g/t Au		129 t Au	Devonian
Yubileinoe (a)	Kazakhstan	~ 10 Mt	0.42% Cu		4 - 5 g/t Au		45 t Au	~380 Ma
Oyu Tolgoi (c)	Mongolia	6.54 Gt	0.70% Cu		0.29 g/t Au	45 Mt Cu	1920 t Au	370 Ma
Tsagaan Suvarga (b,e)	Mongolia	240 Mt	0.53% Cu	0.02% Mo	0.08 g/t Au	1.3 Mt Cu	19 t Au	365-325 Ma
Kharmagtai (m,n)	Mongolia	229 Mt	0.35% Cu		n.a.	0.8 Mt Cu		~330 Ma
Tuwu-Yandong Grp (g)	China, (Xin.)							330 Ma
Tuwu (m)		280 Mt	0.75% Cu		0.16 g/t Au	2.1 Mt Cu	44 t Au	
Yandong (m)		372 Mt	0.58% Cu		0.06 g/t Au	2.1 Mt Cu	22 t Au	
Koksai (a,b,m)	Kazakhstan	320 Mt	0.52% Cu		0.12 g/t Au	1.6 Mt Cu	37 t Au	Carbonifrs
Sayak ^{Sk} (a) - original	Kazakhstan	55 Mt	1.1 - 3.2% Cu		0.2-2.1 g/t Au	1 Mt Cu	30 t Au	330 Ma
Kounrad (a,b) - original	Kazakhstan	>800 Mt	0.62% Cu		0.1-0.76 g/t Au	>5 Mt Cu	>600 t Au	330 Ma
remaining 2010 (l)		169 Mt	0.32% Cu		0.02 g/t Au	0.5 Mt Cu	3 t Au	
Aktogai Group (a)	Kazakhstan							~320 Ma
Aktogai (l)		1.72 Gt	0.34% Cu	0.009% Mo	0.04 g/t Au	5.8 Mt Cu	68 t Au	
Aidarly (l)		1.53 Gt	0.38% Cu	0.010% Mo	0.01 g/t Au	5.8 Mt Cu	15 t Au	
Benqala (a,m)	Kazakhstan	309 Mt	0.42 % Cu	0.003% Mo	0.07 g/t Au	1.3 Mt Cu	21 t Au	Carbonifrs
Kal'makyr-Dalnee(a)	Uzbekistan	>5 Gt	0.47-0.51% Cu		0.35-0.6 g/t Au	>21 Mt Cu	>2000 t Au	~315 Ma
or (m)		6.1 Gt	0.39% Cu	0.0023% Mo	0.37 g/t Au	24 Mt Cu	2250 t Au	
Kochbulak ^{Epith} (a)	Uzbekistan	~11 Mt			12 g/t Au		135 t Au	290-280 Ma
Erdenet (d,e)	Mongolia	1.78 Gt	0.62% Cu	0.025% Mo		11 Mt Cu	0.45 Mt Mo	240 Ma
Wunugetushan (b,m)	China, (I.M.)	495 Mt	0.45% Cu	0.09% Mo		2.2 Mt Cu	0.45 Mt Mo	188 -182 Ma
Jiguanshan (h)	China, (I.M.)	100 Mt	n.a.	0.08 - 0.11 Mo		n.a.		155 Ma

Abbreviations: Gt = billion tonnes; Mt = million tonnes; t = tonnes; g/t = grams per tonne; ^{Sk} = skarn; ^{Epith} = epithermal; $^{Mesoth\text{-}Porph}$ = mesothermal to porphyry Au; Carbonifrs = Carboniferous; Xin = Xinjiang; I.M. = Inner Mongolia; TB Lev. = Taldy Bulak Levoberezhny; n.a. = not available.
Source: (a) Seltmann et al. (2004) and references cited therein; (b) Mutschler et al. (2000) and references cited therein; (c) AMC Consultants report to Turquoise Hill Resources - total resource, at 0.37% CuEq. cut-off (2013); (d) Gerel & Munkhtsengel (2005); (e) Watanabe & Stein (2000); (f) Central Asia Gold (2005): (g) Han et al. (2003); (h) Wu et al. (2011); (i) Kazakhmys plc website (2012); (j) Kentor Gold Ltd Annual Report (2011) - measured+indicated resource; (k) Gold Fields of South Africa website (2012) - indicated+inferred resources in 2010; (l) IMC Group Consulting Competent Persons report to Kazakhmys plc (2011) - remaining measured+indicated resources; (m) Singer et al. (2008) and references cited therein; (n) Kirwin et al. (2005).

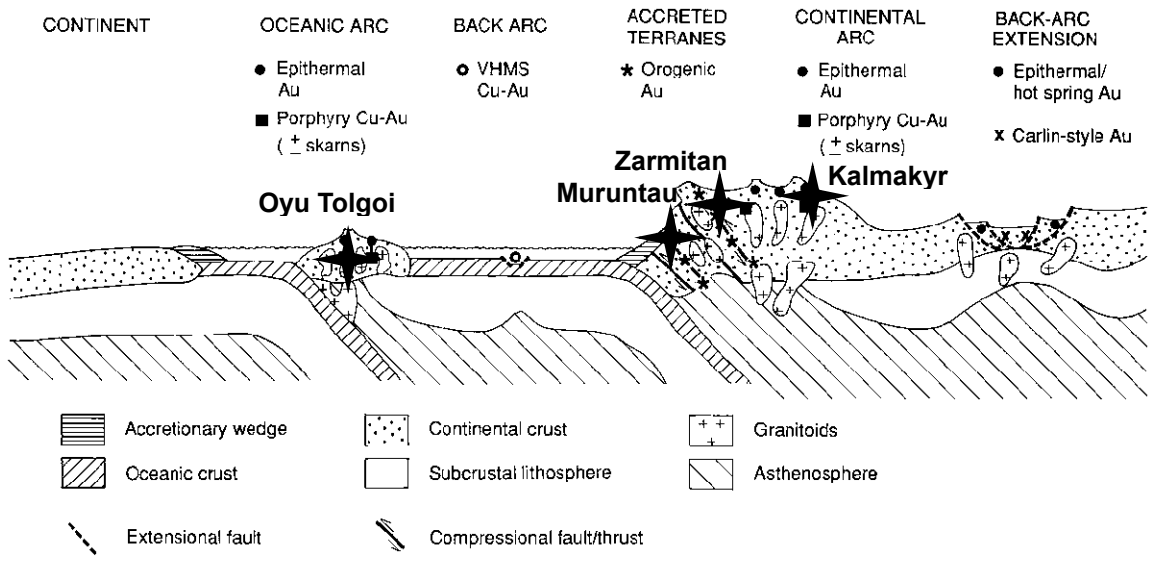

Figure 2. Tectonic setting of gold-rich mineral deposits (modified after Groves et al., 1998) and schematic location of study sites

Au-Pd bearing pyrites and chalcopyrites from the Buchim porphyry copper deposit, Eastern Macedonia

Todor Serafimovski, Krsto Blažev, Goran Tasev
Faculty of Natural and Technical Sciences, University "Goce Delčev"-Štip, R. Macedonia

Kosta Pockov
Buchim Mine, Radoviš, R. Macedonia

Abstract. Interesting chemical compositions have been determined from the study of pyrite and chalcopyrite samples from the active Buchim open pit mine. Namely, beside the standard Fe, S, and Cu, increased concentrations of gold and palladium always followed by some amounts of arsenic were determined. In all the analysed pyrites, gold concentrations were within the range 0.027÷7.746% while the palladium concentrations were within the range 0.010–6.784%. Gold concentrations in all analysed chalcopyrites were within the range 0.009–9.095% while the palladium concentrations were within the range 0.020–8.110%. It is evident that concentrations of gold and palladium in the studied pyrite and chalcopyrite are almost always accompanied by increased concentrations of arsenic in the range of 0.002–0.761%. Increased gold and palladium concentrations have been determined in particular phases, especially in pyrite; in chalcopyrite they are due to metal substitution in the mineral lattice.

Keywords. gold-palladium phases, pyrite, chalcopyrite, Buchim mine

1 Introduction

The Buchim porphyry copper deposit is situated in the border area between the Serbo-Macedonian massif and the Vardar zone. In terms of its metallogeny it belongs to the Lece-Chalkidiki metallogenic zone (Serafimovski, 1993), where manifestations of porphyry copper and epithermal ore are developed. On a more local scale the Buchim copper mine is located in eastern central Macedonia, 10 km west of the town of Radovis. The mine started production in 1980 and produced four million tonnes of ore annually with 0.25% Cu, 0.27% Au, and 1 g/t Ag. Estimated reserves are approximately 100 million tonnes of low grade Cu-Au ores with some Ag and Mo and include primary (the most important Cu-Au resources) as well as secondary (related to the zone of oxidation-cementation enrichment) and mixed types of ores. The deposit is a porphyry copper type deposit (Serafimovski et al., 1996) and mineralization is related to Tertiary sub-volcanic intrusions of andesite and latite in a host of Pre-Cambrian gneisses and amphibolites (Čifliganec, 1993).

Basic ore paragenesis was studied by Pavičević and Rakić (1983), Čifliganec (1993), Serafimovski et al. (2006), and others. Beside the basic ore paragenesis (pyrite, chalcopyrite, magnetite, bornite, enargite, etc.), Bi-Se mineral phases and especially Au-Pd mineral phases were also determined. Petrunov et al. (2001) published preliminary microscopic and microprobe data of the occurrence of the platinum group elements (PGEs) within the Buchim porphyry copper deposit for the first time. An increased content of Pd as well as Pd-mineralization (PGM) was established in the Cu-Au ores of the deposit in Buchim, Macedonia. Thus, this is the fourth case in the territory of the Balkan Peninsula after Bor-Majdanpek, Serbia (Janković, 1990), Skouries, Greece (Tarkian et al., 1991), and Elatsite, Bulgaria (Petrunov et al., 1992) where the Cu-porphyry style of hydrothermal PGM has been found.

As an alkaline porphyry deposit, the Buchim deposit represents, beside copper, a significant gold resource for Macedonia and fits quite well into the recently reported elevated levels of PGEs, particularly Pd and Pt, described in the Cordillera of British Columbia (Copper Mountain, Galore Creek), Allard Stock, La Plana Mountains, and Copper King Mine in the USA, Skouries porphyry deposit in Greece, Elatsite in Bulgaria, and so on (Economou-Eliopoulos, 2010). With the latest studies, results were obtained for Au-Pd-bearing pyrite and chalcopyrite, which are the subject of this particular paper.

2 General features of the Buchim porphyry copper deposit

The ore deposition is genetically connected with the intrusion of Tertiary, Oligocene-Miocene (27.5–24.5 m.y., Serafimovski, 1993, or 24.5–24.0 m.y., Barcikowski et al., 2012), subvolcanic latitic and latite-andesitic bodies within Precambrian metamorphic rocks-gneisses, micas-hists, and amphibolites. Primary Cu-Au mineralization occurs around the subvolcanic bodies, being most abundant amid the hosting gneisses. Four ring-shaped ore bodies are located within and around the magmatic bodies (Figure 1). The main (Central) ore body is approximately 500 m in diameter and 250 m in vertical extent and has been worked in a large open pit. The ore consists of 0.25% Cu, 0.27g/t Au, 1g/t Ag, 13g/t Mo, and 1-4% pyrite. The igneous rocks have been altered to clays and micas. Important metallic minerals are chalcopyrite, pyrite, and bornite, with small amounts of galena, sphalerite, magnetite, haematite, and cubanite. According to the results of exploration, the copper mineralization covers an area of 1.5–2.0 km^2 and is traced to a depth of 300 m.

The Central, Bunardzik, Vrsnik, and Cukar ore bodies are contoured (Figure 1); the Central ore body has the largest copper reserves. Three ore bodies are morphologically related to stocks, and the fourth body is presumably a fragment of a previously existing sheetlike layer of manto-type oxidized and redeposited ore (Figure 1).

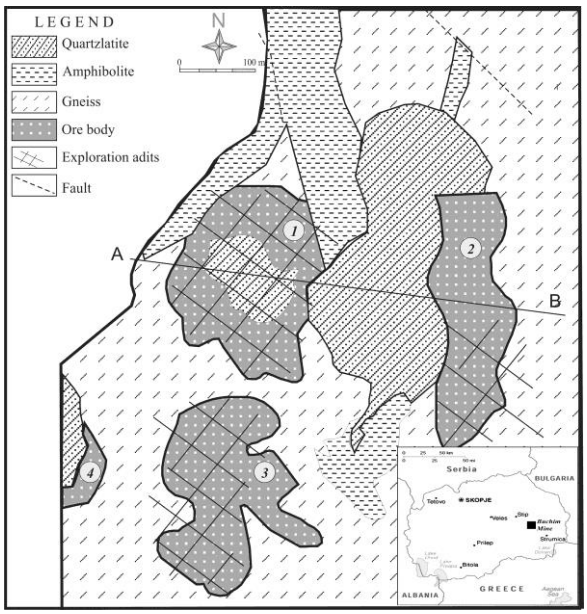

Figure 1. Simplified geological map of the Buchim porphyry copper deposit (Serafimovski, 1993).
1. Central ore body; 2. Vršnik ore body; 3. Čukar ore body; 4. Bunardžik ore body

The country rocks adjoining the porphyry stocks are silicified, chloritized, and sericitized, and underwent argillic alteration. Early potassic alteration developed as well.

Titanite, rutile, magnetite, haematite, chalcopyrite, pyrite, bornite, gold, molybdenite, petzite, calaverite, and argentite were identified as ore minerals. Enargite, tetrahydrite, galena, and sphalerite are less abundant. Chalcocite and covellite are predominant in the Cukar ore body, being accompanied by pyrite, tenorite, and occasional native copper, malachite, and azurite. The ore mineralization was formed in the following sequence: titanite, rutile, and magnetite crystallized first, followed by pyrrhotite, cubanite, vallerite, and the early generation of chalcopyrite. After deposition of these minerals, the hydrothermal ore-forming solution became enriched in sulfur, giving rise to pyrite crystallization. The late chalcopyrite and galena formed at the final stage of ore deposition (Serafimovski, 1993).

3 Methodology

The field sampling took place within the boundaries of an active Buchim open pit mine. Samples were taken from the Central ore body, between levels of 580 m and 540 m, for microscopic and microprobe study. In total 40 ore samples were studied under a Zeiss Axiolab Pol reflected light polarized microscope (at magnifications of 100 to 500) in the optical laboratory of the Faculty of Natural and Technical Sciences, University "Goce Delčev"-Štip, R. Macedonia. Quantitative elemental analyses of ten of the most interesting samples were performed under a JEOL JXA-8200 Electron Probe Micro-Analyser WD/ED Combined Microanalyser (equipped with a SE- and BSE-detector, five-WDS crystal spectrometer and an EDS analyser) in the analytical facilities at the Institute of Geochemistry and Petrology, ETH-Zurich, Switzerland. The selected electron beam conditions were a beam current of 20 nA at an acceleration voltage of 15 kV. Beside the analysis of elements, microphotographs were also taken.

4 Results and discussion

Our preliminary microscope and microprobe investigations determined two main mineral assemblages: magnetite-pyrite-chalcopyrite (Mt-Py-Cp) and pyrite-chalcopyrite (Py-Cp) as major hosts of Au and Pd.

Characteristic for the Mt-Py-Cp assemblage (earlier and high-temperature) is the geochemical association Fe-Cu-Ni, Co-As-O-S+Au, Ag, and Pd, with magnetite, chalcopyrite, pyrite, and cobaltite, Ni-Co-Fe-sulfides, and native Au (subordinate and rare). Pd is included in the structure of the main, subordinate, and rare minerals.

Later enrichment of the hydrothermal fluids with Cu, Bi, Se, Te, Pb, As, Au, and Ag led to the formation of a py-cp assemblages overprinting Mt-Py-Cp aggregates. New minerals were formed, partly as a result of the inclusion of elements "*in situ*": aikinite, bismuthinite, friedrichite, wittichenite, soucekite, emplectite, paderaite, merenskyite, michenerite (Serafimovski et al., 2006), other Pd-Bi-Te phases, tennantite (including. Pd-, Co-, and Ni-bearing), Ni-Co pyrite, Ni-Te phases, Bi-Pb-Ag-S phases, Cu-Fe-Bi-S phases, galena, clausthalite, sphalerite, native gold, and electrum, and (in the uppermost levels) enargite, luzonite, and pearceite (Petrunov et al., 2001).

Au-Pd association has been determined within the pyrite and chalcopyrite of the major ore-bearing phase in the Central ore body in the Buchim mine. It should be stressed that this Au-Pd association occupies certain levels (580–540 m) within the Buchim open pit. There, ore-bearing pyrite and chalcopyrite are in association with magnetite and are usually massive and coarse grained. The studied pyrites are of four different generations and increased concentrations of Au and Pd were determined in so-called block pyrites or massive pyrites with emphasized crystallinity and sizes up to 0.5 mm. Au-Pd phase occurs as a separate mineral phase, which is distinguished by a special colour (gull grey to pink grey; Figure 2). That mineral phase in the composition mostly corresponds to the pyrite (Table 1), but as can be seen from the table, increased gold (7.746% Au, Table 1, analysis 10) and palladium (6.784% Pd, Table 1, Analysis 11) concentrations are directly associated with decreased concentrations of iron and sulfur as major constituents of pyrite.

In practice this means that there is substitution of major pyrite constituents by gold and palladium. The fact that gold and palladium form such a mixture in the main mineral phase in pyrite and chalcopyrite equally (temperatures around 250 ºC) and their absence in later phases of the ore-bearing process could indicate stabilization of the crystal lattice of the pyrite in the later evolution of the process.

From the table it can be seen that, among the 12 analyses shown, gold is present in concentrations within the range of 0.027–7.746% and increased gold concentrations are usually accompanied by increased concentrations of palladium, except in analysis No. 3.

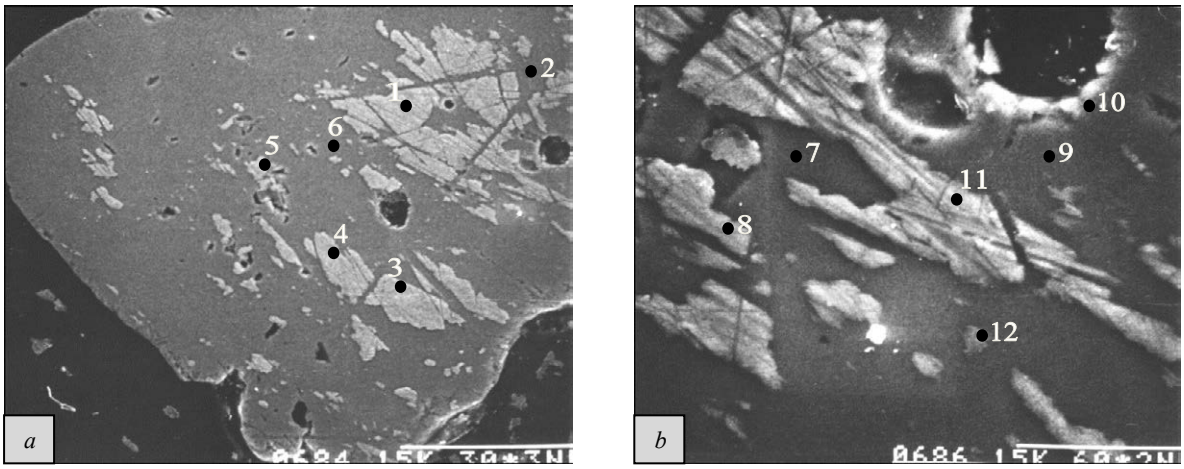

Figure 2. Electron microprobe photographs of pyrites (dark) and Au-Pd phases (light grey), from the Buchim porhyry copper deposit, with analysis points. *a) primary photograph, b) detail*

Palladium concentrations were within the range of 0.040–6.784%. Increased concentrations of gold and palladium caused reductions of Fe and S from their ideal values for pyrite, which should be around 45.55% Fe and 53.45% S. It should be mentioned that increased concentrations of arsenic were found in all analyses where gold and palladium showed increased values (0.019–0.761% As), too. The relation between concentrations of gold, palladium, and arsenic in pyrite and chalcopyrite from the Buchim deposit showed a high degree of geochemical correlation (Pockov, 1997). This probably points to the wide range of physicochemical conditions and the interplay between magmatic and hydrothermal processes during the formation of the deposit.

Figure 1. Electron probe microanalyses of pyrites

Analysis	**1**	**2**	**3**	**4**	**5**	**6**	**7**	**8**	**9**	**10**	**11**	**12**
Au (%)	6,979	0,21	7,627	6,512	0,12	7,54	0,22	0,027	0,1	7,746	6,47	0,033
Fe (%)	39,228	43,636	40,575	39,976	45,458	43,556	43,854	45,438	45,123	39,177	38,932	45,531
S (%)	44,438	53,503	47,352	44,398	53,534	47,342	52,668	51,818	53,265	46,169	45,452	53,926
Cu (%)	0	0	0,01	0,022	0,062	0,012	0	0	0,02	0,034	0	0,024
As (%)	0,157	0	0,019	0,684	0,141	0,02	0,02	0,761	0	0,028	0,042	0,157
Ag (%)	0	0	0,21	0	0	0,73	0,04	0	0,02	0	0	0
Pd (%)	6,33	0,01	1,25	5,65	1,23	0,04	0	2,34	0	6,02	6,784	0,28
Ge (%)	0,31	0,35	-	-	-	0,21				0,25	0,38	
Zn (%)	0,22		-	-	-		0,37			0,26	0,35	
V (%)	0,33	0,25	0,27	0,21	-	0,22	0,41			0,21	0,32	
Ni (%)	0,24	0,47	-		-	0,21	0,54			0,15	0,28	
Se (%)	-	-	0,74	0,52	-	-						
Bi (%)	-	-	0,48	0,65	-	-						
Te (%)	-	-	0,35	0,39	-	-	0,21					
Σ sum	**98,232**	**98,429**	**98,883**	**99,012**	**100,545**	**99,88**	**98,332**	**100,384**	**98,528**	**100,044**	**99,01**	**99,951**

The studies of chalcopyrite from the Buchim deposit were performed on numerous ore samples, and different types of chalcopyrites were analysed. This was possible because the chalcopyrite is the major ore mineral within the Buchim deposit and the main bearer of copper. Its presence in the Buchim ore is around 1%. Our detailed studies confirmed the microscopy findings of some former authors, but some new phases were also found. Beside the already determined Bi-Se mineralization, the mineral paragenesis py-mgt-chp, which is the bearer of increased concentrations of Au and Pd, was confirmed. We would like to stress that the determined concentrations of Au and Pd were related to only one type of chalcopyrite (massive and coarse grained, Figure 3) of the so-called major ore-bearing phase of the Cu-mineralization within the Buchim mine or second generation chalcopyrite.

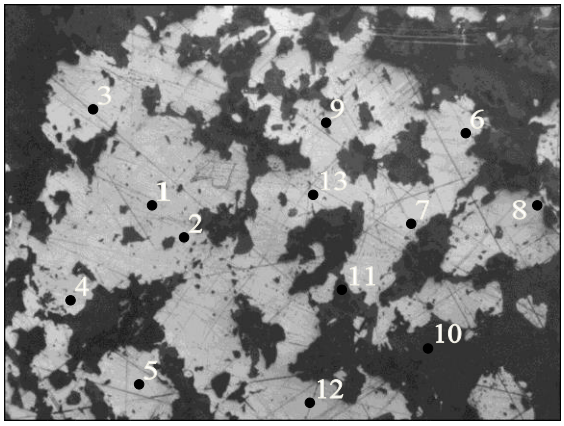

Figure 3. Microprobe photograph of chalcopyrite from the Buchim porhyry copper deposit, with analysis points.

This type of chalcopyrite mainly occurs in veins, veinlets and massive impregnations in association with magnetite and medium-to-high temperature pyrite.

The results of the microprobe analysis are shown in Table 2, where it can be seen that increased concentrations of Au and Pd were determined in 13 microprobe analyses. Gold concentrations were within the range 0.009–9.095%, while the palladium concentrations were 0.020–8.111%. By analogy with the studied pyrite, increased concentrations of As were determined here, too. However arsenic showed lower values here compared to those in pyrite. In chalcopyrite the Au-Pd concentrations are probably related to the mixed mineral phases that we were unable to fully determine, but with the noted presence of Au-Pd in chalcopyrite we have confirmed that there are numerous mineral phases such as Bi-Se minerals (laitakarite, friedrichite, cosalite, etc.), already determined previously by Serafimovski (1993) and Serafimovski et al., (2006).

Additional studies are needed to determine the stages of the Au-Pd pair. Within our latest studies particular phases that have resulted from the deformation of the chalcopyrite crystal lattice were determined, but their definite separation was not possible at the moment.

Figure 2. Electron probe microanalyses of chalcopyrites

Analysis	1	2	3	4	5	6	7	8	9	10	12	13
Au (%)	6,335	0	6,457	0,286	9,095	7,29	6,923	0,14	0,116	0,23	7,159	0,009
Fe (%)	25,923	29,08	25,128	29,112	25,972	25,728	26,679	29,775	29,707	29,52	25,729	29,346
S (%)	28,737	34,324	29,736	33,595	26,964	28,643	27,884	34,371	35,299	35,577	28,66	34,882
Cu (%)	29,463	33,675	28,678	33,514	26,638	28,912	29,824	34,211	34,153	34,225	27,942	33,692
As (%)	0	0,022	0,048	0	0,045	0,005	0,108	0	0,055	0,074	0,002	0,005
Pd (%)	7,38	0,02	8,11	0,3	7,97	6,81	5,98	1,33	0,42	0,28	7,46	1,43
Ge (%)	0,22	-	-	0,38	0,42	0,35	-	-	-	-	0,29	-
Zn (%)	0,35	-	-	0,44	0,36	0,41	-	-	-	-	0,35	-
V (%)	0,38	0,37	-	0,42	0,44	0,45	0,22	-	-	-	0,42	-
Ni (%)	0,33	-	-	0,35	0,41	0,48	-	-	-	-	0,35	-
Se (%)	-	0,33	0,22	-	-	-	0,49	-	-	-	-	-
Bi (%)	-	0,42	0,31	-	-	-	0,52	-	-	-	-	-
Te (%)	-	0,35	0,25	-	0,22	-	0,42	-	-	-	-	-
Σ sum	**99,118**	**98,591**	**98,937**	**98,397**	**98,534**	**99,078**	**99,048**	**99,827**	**99,75**	**99,906**	**98,362**	**99,364**

We would also like to point out that significant concentrations of the standard geochemical association of elements for the Buchim chalcopyrite, such as Ni, Co, Pb, Zn, Ag, and so on, were not determined in these studies.

5 Conclusion

The studied mineral association in the Buchim porphyry copper deposit confirmed that the most common mineral is pyrite with a presence of 3%, while chalcopyrite is the major bearer of copper mineralization with a presence of 1%. Microscope and microprobe investigations have determined two main mineral assemblages: magnetite-pyrite-chalcopyrite (mt-py-cp) and pyrite-chalcopyrite (py-cp), as major hosts of Au and Pd. The gold content in the studied pyrite is within the range of 0.027–7.746% while the palladium content is within the range 0.040–6.784%, and they are related with the special mixture mineral phases characterized by gull gray colour.

Increased concentrations of Au-Pd in chalcopyrite are related to the massive medium-to-high temperature chalcopyrite, which constitutes the major ore phase within the Buchim deposit and occupies a certain level within the deposit (580–540 m). For more detailed definition of the PGM, additional studies are needed

References

Barcikowski, J., Lehmann, S., von Quadt, A., Heinrich, A. C. and Serafimovski, T., 2012. The magmatic evolution of the Buchim-Damjan-Borov Dol ore district. (Eds. A. von Quadt & T. Serafimovski) Diversity of copper and gold deposits in the Eastern Europe Balkan, Carpathian and Rhodopean belts: tectonic, magmatic and geochronological investigations; SCOPES Project–International Conference, Stip, Macedonia, pp. 16

Economou-Eliopoulos, M., 2010. Platinum-group elements (PGE) in various geotectonic settings: Opportunities and risks. *Hellenic Journal of Geosciences, vol. 45, 65-82*

Janković, S., 1990. Ore deposit of Serbia. Faculty of Mining and Geology, Belgrade, p.765.

Pavičević, M. and Rakić, S., 1983. Study of occurence of gold, silver and other rare elements in ores from the Central ore body, Buchim. ULEMA, Belgrade, 202 p. (in Serbian)

Petrunov, R., Dragov, P., Ignatov, G., Heykov, H., Iliev, Ts., Vassileva, N., Tzatzov, V., Djunakov, S. and Doncheva, K., 1992. Hydrothermal PGE-mineralization in the Elatsite porphyry-copper deposit (Sredna Gora metallogenic zone, Bulgaria). Comptes Rendu Academie Bulg. Sci, Vol. 45, No. 4, pp. 37-40.

Petrunov, R., Serafimovski, T., Dragov, P., 2001: New finding of PGE-mineralisation in porphyry-copper environment-the Buchim deposit, Macedonia: preliminary microscope and microprobe data. ABCD-GEODE 2001 WORKSHOP VATA BAI, ROMANIA. Vol. 79, suppl. 2, pp 79-80

Pockov, K., 1997. Geochemical types of pyrites in the porphyry copper deposit Buchim. Master thesis, Faculty of Mining and Geology, Štip, Macedonia, 125 p. (in Macedonian)

Serafimovski, T. (1993). Types of Mineral Deposits and Distribution. Special edition of RGF Stip, No \,p. 328. Structural metallogenetic characteristics of the Lece-Chakidiki zone:

Serafimovski, T., Tasev, G. and Lazarov, P., 2006. Au-Ag-Te-Bi-Se minerals associated with porphyry copper mineralization in the Buchim copper mine, R. Macedonia. Au-Ag-Te-Se deposits IGCP-486, Field Workshop, Izmir, Turkey, pp. 154-158.

Tarkian, M., Eliopoulos, D.G. and Economou-Eliopoulos, M., 1991.Mineralogy of precious metals in the Skouries porphyry copper deposit, N. Greece. Neues Jahrbuch fur Mineralogie Abhandlungen, 12, 529-537

Čifliganec, V., 1993. Copper Mineralization in the Republic of Macedonia: Types and Distribution Pattern. Geol. Dept., Faculty Min. Geol., Spec. Issue, Vol.1., 303 p. (in Macedonian with extended summary in English)

LA-ICP-MS pyrite chemistry, evidences for mineralizing stages at Chahnaly low sulfidation epithermal gold deposit, SE Iran

Ali Sholeh, Ebrahim Rastad
Department of Geology, Faculty of Basic Sciences, Tarbiat Modares University, Tehran, Iran

David Huston
Geoscience Australia, Canberra, Australia

Bruce Gemmell
ARC Centre of Excellence in Ore Deposits (CODES), University of Tasmania, Hobart, Australia

Abstract. The Chahnaly low sulfidation epithermal Au deposit and adjacent Au prospects are located to the northwest of the Bazman semi-active strato-volcano at the western end of Makran volcanic arc. The host rocks include early Miocene volcanic and volcaniclastic rocks. Gold mineralization is related to chalcedony-adularia alteration assemblages and occurs within altered volcaniclastic rocks as a series of 030° trending sub-vertical siliceous veins. Pyrite is the most abundant ore mineral and occurs in all types of altered volcanic/volcaniclastic rocks. Based on LA-ICP-MS analysis supported by mineralographical studies, pyrite minerals have been grouped into 6 different classes from which gold and silver have strong affinities with the first and second types. At least 3 generations of pyrites can be observed with the second and third generations carrying high gold contents. The first generation of barren pyrite in regional scale altered wall rocks is mainly of type 3. The second generation occurred after remobilization of pre-existing pyrite minerals along sub-vertical structures. It shows zoned characteristics (type 5) and in some cases shows overgrowth feature (type 6) suggesting more than one stage of mineralizing hydrothermal activity. The third generation of pyrite mineralization is brecciated pyrite (type 2) occurring in hydrothermal breccia.
Keywords. Epithermal gold, LA-ICP-MS, Chahnaly, Bazman

1 Introduction

The Chahnaly low sulfidation type epithermal Au deposit and adjacent Au prospects are located to the northwest of the Bazman semi-active strato-volcano at the western end of Makran volcanic arc (Fig.1). This arc formed as the result of subduction of the remnant Neotethyan oceanic crust beneath southeastern Central Iran (Lut block).

The Makran volcanic arc hosts several porphyry-epithermal deposits, including the Siah Jangal deposit, the Bidster and Kharestan prospects (near Taftan volcano) as well as the Saindak Cu-Au porphyry deposit (Richards, 2011) and the giant Reko Diq Cu-Au porphyry-epithermal deposit (near the Kuh-i-Sultan volcano in Pakistan) (Fig.2). An internal report of the Geological Survey of Iran indicates a resource of more than 3 Mt grading 1.04 ppm Au for Chahnally and significant potential for gold mineralization in four other prospects in the area.

2 Geology

The Chahnaly deposit and nearby prospects are located at the western end of Makran arc, a 300-km-long volcanic arc that extends from the Bazman volcano at the western end to the Kuh-i-Sultan volcano and Chagai belt in Pakistan at the eastern end. The Makran arc resulted from shallow dipping (~5 degrees, Jacob and Quittmeyer, 1979; Byrne et al., 1992; Carbon, 1996 ; Dolati, 2010) subduction of the Oman Sea beneath the Lut block of the Central Iran zone (Berberian and King, 1981; Harms et al., 1984; Kopp et al., 2000). The subduction initiated during the Paleocene (Platt et al., 1988) or late Cretaceous (Farhoudi and Karig, 1977; Arthurton et al. 1982; Berberian et al. 1982). To the south of Bazman and Kuh-i-Soltan there are two large depressions, Jaz Murian and Hamun-i-Mashkel that are interpreted as forearc basins (Farhoudi and Karig, 1977).

Regional magmatism includes intrusive bodies of Late Cretaceous age to the south of Bazman, and Miocene-Quaternary volcanic and volcaniclastic rocks to the north of Bazman. The intrusive bodies include inner felsic phases (hornblende granite, biotite granite and porphyritic granite), and outer mafic phases (gabbro, olivine gabro and diorite bodies). The volcanic rocks are mainly of andesitic to dacitic composition but include a minor amount of rhyolite. Younger basalts are also present.

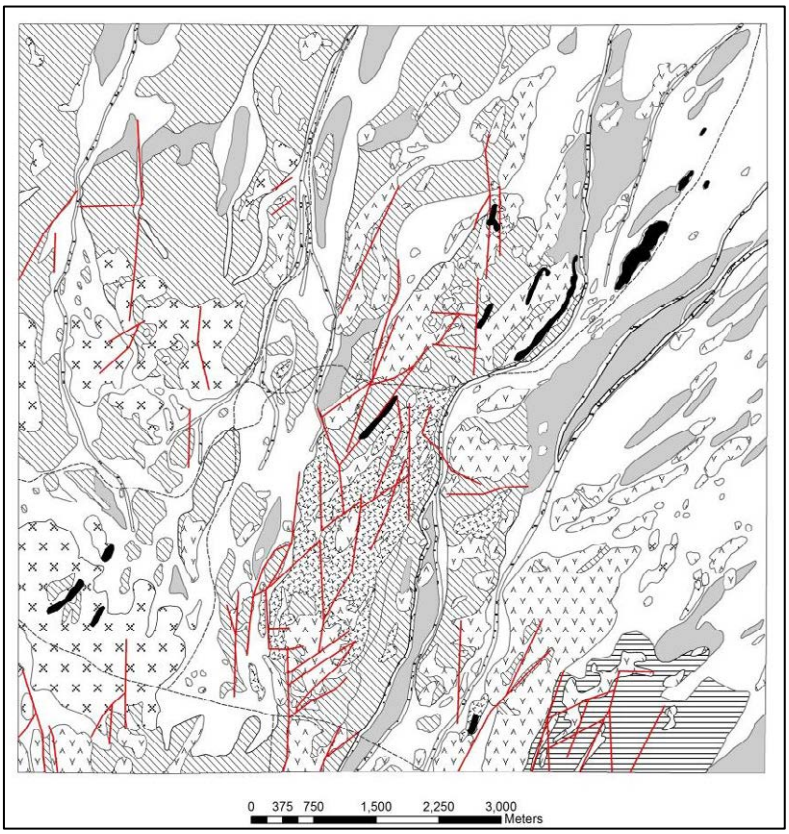

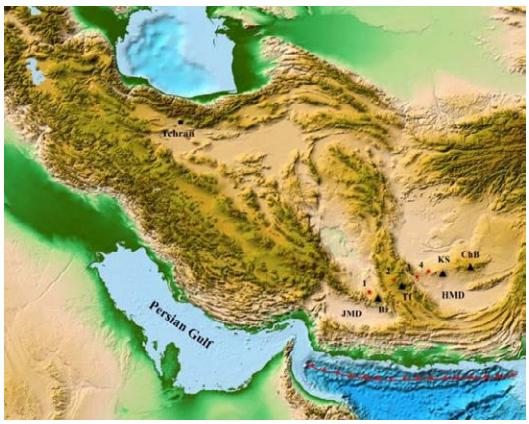

Figure 1. Main tectonic units and mineral deposits of Makran Volcanic Arc. Main volcanos include Bazman (Bz), Taftan (Tf), Kuh-i-Sultan (KS) and Chagai belt (ChB). Forearc basins (Farhoudi and Karig, 1977) include the Jaz Murian (JMD) and Hamun-i-Mashkel (HMD) depressions. Main mineral deposits are the Chahnaly (1), Siah Jangal (2), Saindak (3) and Reko Diq (4) deposits (background image from ETOPO1).

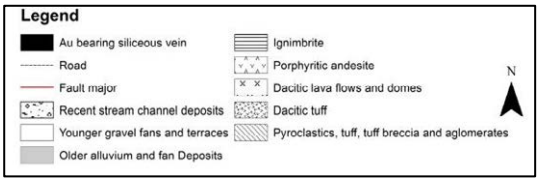

Figure 2. Geological map of the area (modified from Pars Kani unpublished report, 2004).

Chahnaly is hosted by volcanic rocks of Bazman stratovolcano. These rocks include an early Miocene phase of andesite, rhyolite and dacite volcanic and volcaniclastic rocks that are intruded by younger dacitic domes. Unaltered Late Miocene dacitic ignimbrites overlie the older volcanic rocks. There are also several small Quaternary parasitic mafic cones around the Bazman stratovolcano (Saadat & Stern, 2011) with K-Ar ages of 4.6 to 0.6 Ma (Conrad et al., 1981).

LA-ICP-MS U–Pb zircon geochronology yielded ages between 21.78 and 9.93 Ma which suggests a Miocene age for felsic-intermediate volcanism (Sholeh et al, 2012). The last volcanic activity of Bazman stratovolcano involved a basic (olivine basalt) phase with Pliocene to Quaternary ages (Conrad et al., 1981).

3 Mineralization

Gold mineralization is temporally and spatially related to chalcedony-adularia assemblages and occurs within altered volcaniclastic rocks as a series of 030° trending sub-vertical siliceous veins. Gold minerals, which include free gold, Au-rich electrum and petzite, are hosted by hydrothermal breccias. In primary ores, they are associated with pyrite, and in supergene ores, they are associated with iron-oxides and hydroxides.

Silver minerals include Ag-rich electrum and rare petzite, acanthite, naumannite, iodargyrite, stromeyerite, hessite and cupro-iodargyrite. Sulfide minerals include wide spread pyrite as well as less abundant sphalerite, chalcopyrite, galena, chalcocite and covelite. Other scarce ore minerals are cuprite, Fe oxides and hydroxides, powellite, molybdenite, melanothallite, monazite, anglesite and plattnerite.

4 LA-ICP-MS analysis of pyrite

Samples were analyzed at the CODES laser ablation analytical facility with a New Wave UP-213 Nd:YAG Q-switched Laser Ablation System coupled with an Agilent 7500a Quadrapole ICP-MS. Samples were ablated in a constant geometry cell, in an atmosphere of an ultra-high purity He which was mixed with Ar before flowing into the ICP-MS.

Spot analyses in pyrite were analysed with a beam size of 32 µm and laser energy of ~3.5 Jcm^{-2}. The in-house standard STDGL2b-2 (Danyushevsky et al., 2011) was used as the primary standard to calculate concentrations and to correct for instrument drift. The distribution of trace elements was determined using a series of line rasters across the pyrite grains of interest, with a spot size of 10-15 µm travelling at a speed of 10 µm/s, and laser energy of ~3.5 Jcm^{-2}. Each line was pre-ablated immediately before analysis to remove contamination from previously ablated lines. Pyrite as the most abundant ore mineral occurs in all types of altered rock including andesitic tuff, volcaniclastic breccia, porphyry andesite as well as hydrothermal breccia. Based on LA-ICP-MS analysis of about 150 spots of different types of pyrites supported by microscopic studies, pyrite minerals have been grouped into 6 different classes (table 1). The main chemical differences between these 6 classes have been summarized in table 2.

Table 1. Main characteristics of 6 classes of pyrites.

Py. Types	Host	Description
Type 1	Siliceous vein	Clean euhedral pyrite in siliceous vein
Type 2	Hydrothermal breccia	Brecciated pyrite in hydrothermal breccia
Type 3	Volcaniclastic wall rock	Fine-medium size pyrite in wall rock alteration
Type 4	Siliceous vein and hydrothermal breccia	Spongy pyrite with internal fractures
Type 5	hydrothermal breccia	Zoned pyrite
Type 6	Siliceous vein and hydrothermal breccia	Pyrite with overgrowth feature

Table 2: Statistical parameters of selected variables in different types of pyrites.

Pyrite type	Parameter	Au	Ag	As	Se	Te	Cu	Zn	Pb
Type 1	Min	0.02	1.7	119.3	4.8	0.03	79.5	1.7	6.9
	Max	139.5	674.9	6617.5	585.5	178	17690	87168	9199
	Mean	21.7	98.4	1998.3	166.0	21.8	1846	5761	945
Type 2	Min	0.1	2.2	17.6	11.8	0.03	43	1.0	6.3
	Max	42.8	400.2	18519.9	1430.6	151.2	2039	505	2117
	Mean	10.0	81.1	2571.8	189.3	69.4	499	62.3	322
Type 3	Min	0.01	1.3	5.5	2.1	0.03	10	0.1	8.6
	Max	10.0	1931.3	19253.9	594.1	8.8	5331	7702	8214
	Mean	1.3	218.5	3755.7	74.4	0.8	567	226	382
Type 4	Min	0.01	0.3	17.3	2.3	0.03	19	1.8	16.1
	Max	4.2	569.2	11077.9	282.4	84.9	954	2591	1019
	Mean	0.7	48.1	1381.0	39.0	4.7	232	202	242
Type 5	Min	0.1	0.2	6.8	9.0	1.0	7.4	0.2	0.8
	Max	16.0	687.1	12497.6	298.0	362.7	11593	168	433
	Mean	3.9	88.2	3613.8	63.7	72.8	2922	23	92
Type 6	Min	0.04	0.2	51.6	10.7	0.03	0.8	0.1	0.5
	Max	6.8	276.5	11989.4	443.6	65.3	1990	570	3764
	Mean	2.1	40.3	2275.6	60.0	15.2	462	86	528

5 Discussion

Laser ablation-inductively coupled plasma mass spectrometry (LA-ICP-MS) is a strong in situ analytical tool for studying trace element distribution especially in sulfide minerals. The Chahnaly Au-(Ag) deposit is a low sulfidation type epithermal deposit (Sholeh et al, 2012) located on an active geothermal system to the northwest of the Bazman volcano at the western end of Makran volcanic arc. In the area, gold originally occurred in pyrite minerals of chalcedony-adularia bearing siliceous veins. Gold bearing and barren pyrites were classified into 6 groups using detailed mineralogy, texture, structure, SEM analysis followed by laser ablation studies. The current study documents trace and precious element variation in previously classified pyrites using LA-ICP-MS spot analysis and image to determine gold mineralization stages.

6 Conclusions

In the Chahnaly epithermal Au-(Ag) deposit, gold and silver have strong affinities with the first and second type of pyrite and the assemblage Cu-As-Te-Mo has a strong affinity to the fifth type of pyrite (Sholeh et al, 2012).

At least 3 generations of pyrites can be observed from which second and third generations carry gold at high concentrations. The first generation of barren pyrite is widespread and is present in regional scale altered wall rocks. It is mainly of type 3 with euhedral-subhedral form.

The second generation occurred when siliceous solutions remobilized pre-existing pyrite minerals along sub-vertical structures forming ore bearing siliceous veins. These are clean euhedral pyrites of mainly type 1. It shows zoned characteristics (type 5) and in some cases shows overgrowth feature (type 6) suggesting more than one stages of gold forming pulses of hydrothermal activity. The third generation of pyrite mineralization is breciated pyrites (type 2) occurring in hydrothermal breccias.

Acknowledgments

This paper is a part of first author's PhD thesis at Tarbiat Modares University, Tehran, Iran in collaboration with University of Tasmania, Hobart, Australia and Geosciences Australia, Canberra, Australia. The authors would like to thank Geological Survey of Iran for providing access to exploration data and core logs. Particular thanks go to M. Karimi and B. Borna. B. Rashidi and H. Moosazadeh. The LA-ICP-MS analyses were supported by 2012 SEG research grant.

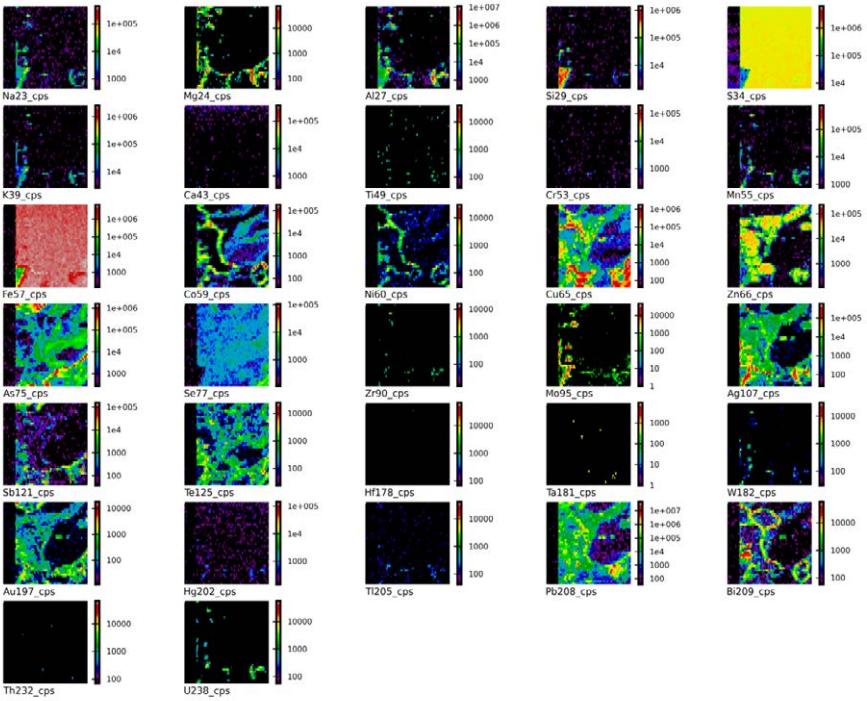

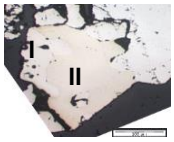

Figure 3. LA-ICP-MS pyrite images showing the different metal zonation pattern in pyrite with overgrowth feature (Type 6). It shows 2 phases of pyrite mineralization from which the first phase (I) caries Au, Cu, Sb, Te, Zn, Ag, Bi, Pb while the second phase (II) has no gold, silver and other metal elements.

References

Arthurton, R. S. Farah, A. Wahiduddin, A. 1982. The Late Cretaceous-Cenozoic history of western Baluchistan Pakistan—the northern margin of the Makran subduction complex. Geological Society, London 10: 373-385.

Berberian, M. and King, G.C. 1981. Towards a Paleogeography and tectonic evolution of Iran. National research council of Canada: 210-265.

Berberian, F. Muir, I. D. Pankhurst, R. J. Berberian, M.1982. Late Cretaceous and early Miocene Andean-type plutonic activity in northern Makran and central Iran. Journal of the Geological Society of London 139 Part 5: 605-614.

Byrne, D. E. Sykes, L.R. Davis, D.M. 1992. Great Thrust Earthquakes and aseismic Slip Along the Plate Boundary of the Makran Subduction Zone. Geophysical research 97(No. B1): 449-478.

Carbon, D. 1996. Tectonique post-obduction des montagnes d'Oman dans le cadre de la convergence Arabie-Iran. Montpellier II.

Compston, W. 1999. Geological age by instrumental analysis: the 29th Hallimond Lecture. Mineralogical Magazine 63: 297-311.

Conrad, G., Montignary, R., Thuizat, R., Westphal, M. 1981. Tertiary and Quaternary geodynamics of southern Lut (Iran) as deduced from palaeomagnetic, isotopic and structural data. Tectonophysics 75: 11–17.

Danyushevsky, L. V. and Plechov P. Petrolog3: Integrated software for modeling crystallization processes, Geochem. Geophys. Geosyst., doi:10.1029/2011GC003516.

Dowlati, A. 2010. Stratigraphy, structural geology and low-temperature thermochronology across the Makran accretionary wedge in Iran. PhD thesis: Swiss Institute of Technology Zurich.

ETOPO 1, (http://www.ngdc.noaa.gov/mgg/global/relief/ETOPO1/image/color_etopo1_ice_full.tif.gz).

Farhoudi, G., Karig, D.E. 1977. Makran of Iran and Pakistan as an active arc system. Geology 5: 664–668.

Harms, J. C. Cappel, H. N. Francis, D. C. 1984. The Makran coast of Pakistan; its stratigraphy and hydrocarbon potential. Marine geology and oceanography of Arabian Sea and coastal Pakistan. U. Haq Bilal, Milliman John, D. New York, NY, United States, Van Nostrand Reinhold Co.: 3-26.

Jacob, K. H. and Quittmeyer R. L. 1979. The Makran region of Pakistan and Iran: Trench-arc system with active plate subduction. Geodynamics of Pakistan. A. Farah and K. A. de Jong. Quetta, Pakistan: 305-317.

Jeremy P. Richards, Terry Spell, Esmaeil Rameh, Abdul Razique & Tim Flether, 2011. High Sr/Y Magmas Reflect Arc Maturity, High Magmatic Water Content, and Porphyry Cu ± Mo ± Au Potential: Examples from the Tethyan Arcs of Central and Eastern Iran and Western Pakistan; Economic Geology V. 107 No. 2 : 295-332.

Kopp, C. Fruehn, J. Flueh, E. R. Reichert, C. Kukowski, N. Bialas, J. Klaeschen, D. 2000. Structure of the Makran subduction zone from wide-angle and reflection seismic data. Deep seismic profiling of the continents and their margins. R. Carbonell, Gallart, J. Torne, M. Elsevier. Amsterdam, Netherlands.

Platt, J. P., Leggett, J. K., and Alam, S. 1988. Slip vectors and fault mechanics in the Makran accretionary wedge, southwest Pakistan. J. Geophys. Res. 93: 7955-7973.

Saadat, S., Stern, C.R. 2011, Petrochemistry and genesis of olivine basalts from small monogenetic parasitic cones of Bazman stratovolcano, Makran arc, southeastern Iran, Lithos, doi:10.1016.

Sholeh, A., Rastad, E., Huston, D., Gemmell, B. 2012, Geology, texture, structure and fluid inclusion studies of Bazman epithermal Au deposits, north of Bazman volcano, southeastern Iran (abstract), SEG 2012 Annual Meeting, Lima, Peru.

Investigating the controls on critical metal distribution in porphyry deposits

K.A. Sullivan, S. Roberts, D.A.H. Teagle
Ocean and Earth Science, National Oceanography Centre, University of Southampton, Southampton, SO14 3ZH, U.K.
k.sullivan@noc.soton.ac.uk

J. Naden, P.A.J. Lusty
British Geological Survey, Environmental Science Centre, Nicker Hill, Keyworth, Nottingham, NG12 5GG, U.K.

Abstract. Investigations of critical metal enrichment in the Muratdere Cu-Au porphyry deposit, Western Turkey, suggests that the enhanced levels of Re and Te in this porphyry system results from the interaction between the porphyry magmas, fluids and pre-existing mafic and ultramafic rocks, rather than from mantle derived melts. An initial quartz-pyrite vein set is associated with the majority of the Cu-Au mineralisation, along with a later disseminated pyrite-chalcopyrite phase. Molybdenite is disseminated within the host rock, and in quartz veins which cross-cut the earlier quartz-pyrite veins. High Re concentrations, up to 2.37 ppm from assay, correlate with increased molybdenite content, which suggests it was introduced during the same mineralisation phase. A later faulting event generated a series of breccias which are also associated with increased Re. The Muratdere deposit also contains up to 5.9 ppm Te, which is associated with a late polymetallic quartz vein generation, characterised by abundant sphalerite, pyrite and molybdenite and containing significant lead and zinc content. This suggests that the critical metal enrichment occurred during a series of discrete mineralising events and is the result of interactions between ore forming fluids and the ultramafic country rocks.

Keywords.
Porphyry, Critical metals, PGE, Rhenium, Tellurium, Turkey

1 Introduction

European industry requires specialist metals for the production and development of green technologies – for example platinum group elements (PGE) for fuel cells and catalytic converters; Te and Se for photovoltaic electricity generation; Ag for high performance mirrors and Re in the new generation of energy efficient jet engines. Recent studies in the USA and EU have highlighted the supply risk associated with some of these metals (Bauer et al. 2011; Catinat et al. 2010; Jaffe et al. 2011). In some cases this results from concentration of production in a limited number of countries (e.g. about 77% of platinum is produced in South Africa). Few of these metals occur as the main target element in a mineral deposit and they are typically derived as by-products from the production of major industrial metals, for example Te and Se are by-products of Cu refining. However, some of them (e.g. PGE, Ag, Te, Se, Re) are enriched in mineralization associated with high-level potassic and calc-alkaline magmatism more commonly noted for its Cu, Mo or Au potential.

Te is common within porphyry systems (Watterson et al. 1977) with telluride minerals often associated with chalcopyrite (Tarkian and Koopmann 1995). Rhenium enrichment is often associated with molybdenum, as it substitutes for Mo in molybdenite (Voudouris et al. 2009). The predominate wall rock alteration in Re enriched porphyries tends to be quartz-sericite and propylitic (Berzina et al. 2005), as opposed to the potassic alteration associated with PGE mineralisation (Economou-Eliopoulos & Eliopoulos 2000), and the alkalinity of the source magmas also differs between PGE and Re enriched intrusions.

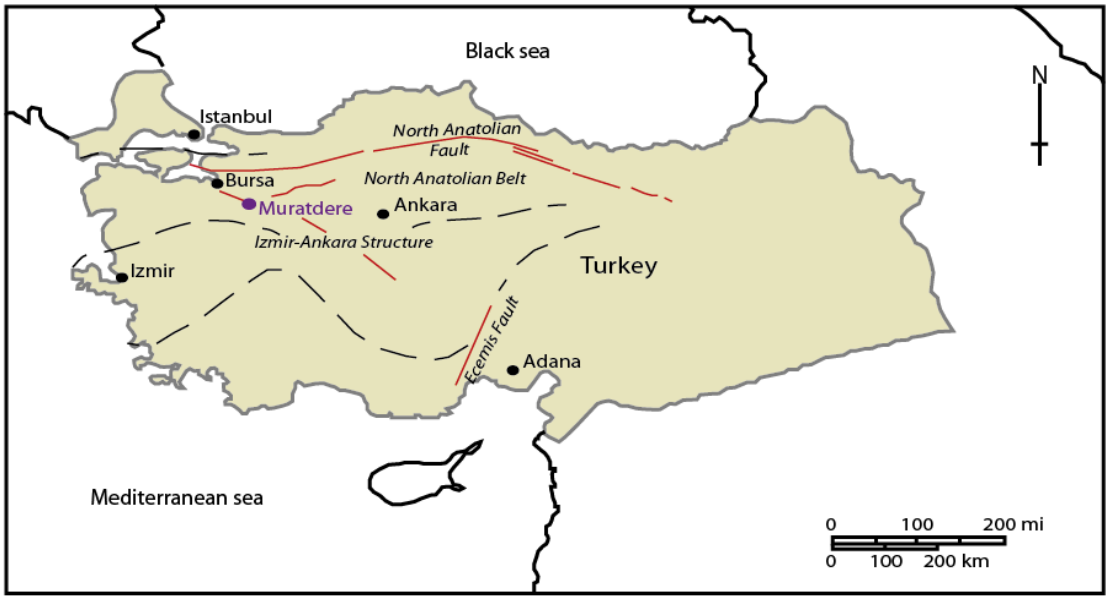

Figure 1. Map showing the location of the Muratdere deposit and the main structural features of the region. (Adapted from Okay 2000)

In particular, Re-enriched porphyries have been linked with a higher Cu/Mo ratio, lower $\delta^{34}S$ and $^{87}Sr/^{86}Sr$ values, decreased alkalinity and more mafic composition of host rocks, along with an oxidised source magma (Voudouris et al. 2009).

PGE mineralisation is often related to potassic alteration (Economou-Eliopoulos 1996) at the core of deposits, and experimental work has shown PGE to be mobile as chloride complexes in 400–700°C saline fluids (Xiong & Wood 2000). Field studies have shown that PGE enriched deposits tend to be associated with hydrous, oxidised source magma (shown by the presence of magnetite), alkaline magma with SiO_2 <65% and high REE, as well as crustal components (Economou-Eliopoulos 2005).

As PGE and Re are both associated with oxidised source magmas and crustal components PGE and Re enrichment can occur in the same deposit, as seen in the Skouries deposit in Greece (Economou-Eliopoulos 1996). Experimental work on Re mobility has mainly focussed on the conditions found in supergene and surficial environments (Xiong et al. 2006), and has shown that Re can be readily leached from molybdenite under these conditions. However little work has been undertaken on Re mobility in hypogene environments.

2 Geological Setting

The Muratdere deposit is a Cu-Au porphyry system in western Turkey with significant Mo, Ag, Te and Re credits. The deposit is located in the Sakarya Zone, a continental fragment to the north of the Izmir-Ankara Suture (Okay 2000), within the North Anatolian Belt (Fig. 1). The North Anatolian Belt is a pre-Jurassic subduction complex associated with the closure of the Tethyan Ocean (Tekeli 1981), which contains ophiolitic melange units, incorporating limestone blocks and ultramafic lenses.

The Muratdere deposit is hosted in a suite of Palaeocene-Eocene granodiorite and quartz-feldspar porphyry intrusions. These have a strike length of 4000 m, a width of 200 m, and intrude an ophiolite melange, considered to be Cretaceous in age. The deposit is covered by Pliocene conglomerates and Quaternary alluvium and is intersected by a north-south-trending fault, which uplifts the eastern side of the system, revealing potassic alteration. The western side of the deposit is characterised by predominately phyllic alteration and is only weakly mineralized. The whole area is cut by east-west-trending faults.

3 Results

3.1 Paragenesis

Core logging and optical microscopy revealed several generations of veins and mineralization (Fig. 3), associated with extensive potassic alteration and a grade destructive propyllitic overprint at depth. The first vein set (V1) comprises barren quartz veins 2–10 mm in width, predominantly composed of microcrystalline quartz. V2 veins are composed of quartz with pyrite cores, varying between 5–30 mm in width. The V3 veinset is composed of quartz-molybdenite, consisting of equigranular medium-grained quartz and dendritic molybdenite (Fig. 4), while V4 veins consists of barren equigranular quartz, often with clay selvages. V5 is a set of polymetallic quartz veins contain sphalerite, molybdenite and pyrite, with the sphalerite growing interstitially between quartz crystals. The most recent vein sets, V6 and V7, are grey and pink anhydrite veins, respectively with V7 being the only veinset to crosscut the fault breccias.

3.2 Mineralisation

The majority of the Cu-Au mineralisation is associated with V2 veins, with chalcopyrite replacing pyrite, in disseminated sulfides within the host rock. Molybdenite is also disseminated within the host rock. However, most of the molybdenum appears to be associated with V3. High Re concentrations, up to 2.37 ppm (from whole rock assay), are associated with an increase in modal

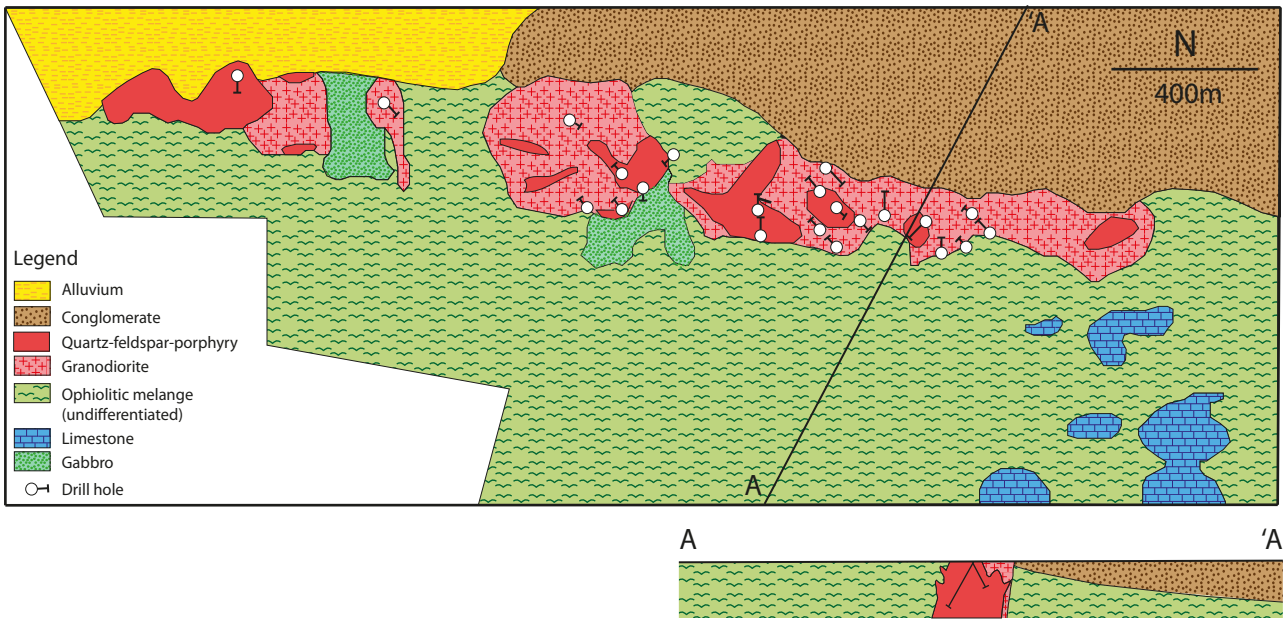

Figure 2. Sketch geological map and cross section of the Muratdere deposit.

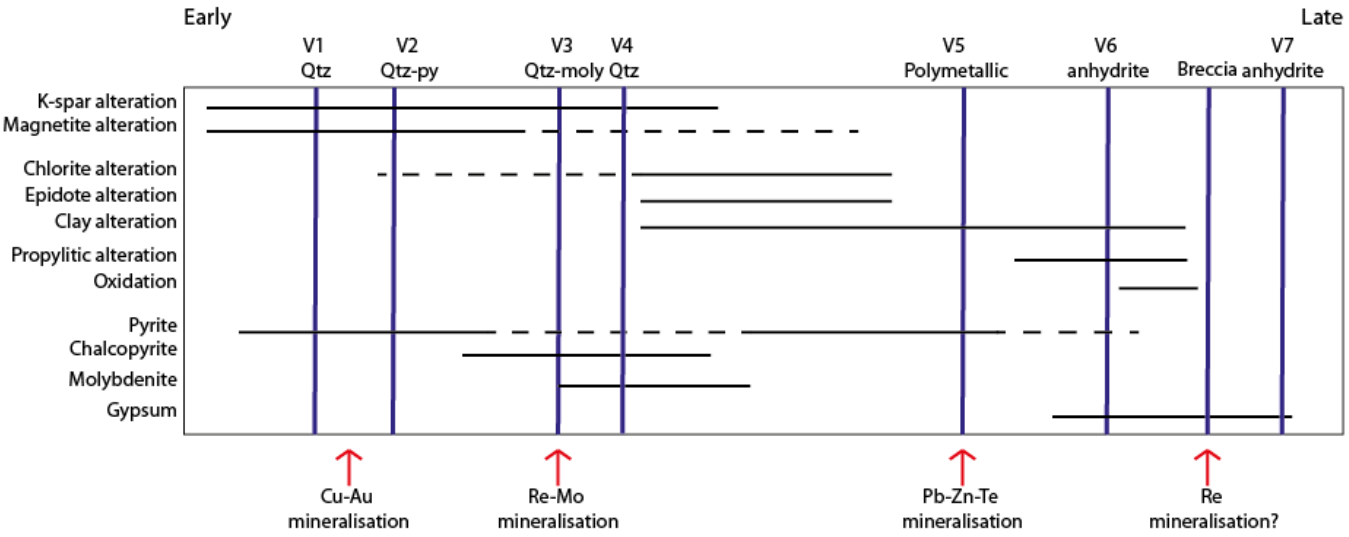

Figure 3. Diagram to show the paragenesis and alteration phases of the Muratdere deposit

percent molybdenite, suggesting it was introduced during the same mineralisation phase. This is supported by the geochemical data which shows a Re-Mo correlation of 0.87. Two different textures of molybdenite were observed – dendritic molybdenite (Fig. 4), which is only seen in those samples with whole rock Re values greater than 1 ppm, and spherical disseminated molybdenite which dominates the samples containing less than 1 ppm Re. This is reflected in the geochemical data as some core sections contain high Mo values but only trace Re. A later faulting event generated a series of breccias which are also associated with elevated Re levels.

The Muratdere deposit also contains Te, up to 5.9 ppm, associated with the late polymetallic quartz vein generation (V5) which is characterised by abundant sphalerite, pyrite and molybdenite, with a significant lead and zinc content.

4 Discussion

The Muratdere deposit shows rhenium enrichment at depth (80–250 m), and associated potassic alteration. This suggests that the rhenium mineralisation developed as part of the hypogene ore formation, rather than during a later supergene event. This is consistent with the rhenium mineralisation developing from primary ore forming hydrothermal/magmatic fluids. However, the rhenium mineralisation appears to have formed later than the main stage hypogene Cu-Au mineralization as it is associated with the dendritic molybdenite in the V3 veins, and does not seem to be associated with the disseminated spherical molybdenite in the host rock. This suggests that there were two discrete phases of molybdenite deposition, only one of which was Re bearing. This hypothesis is supported by the geochemical data, which indicates the strong Re-Mo relationship in

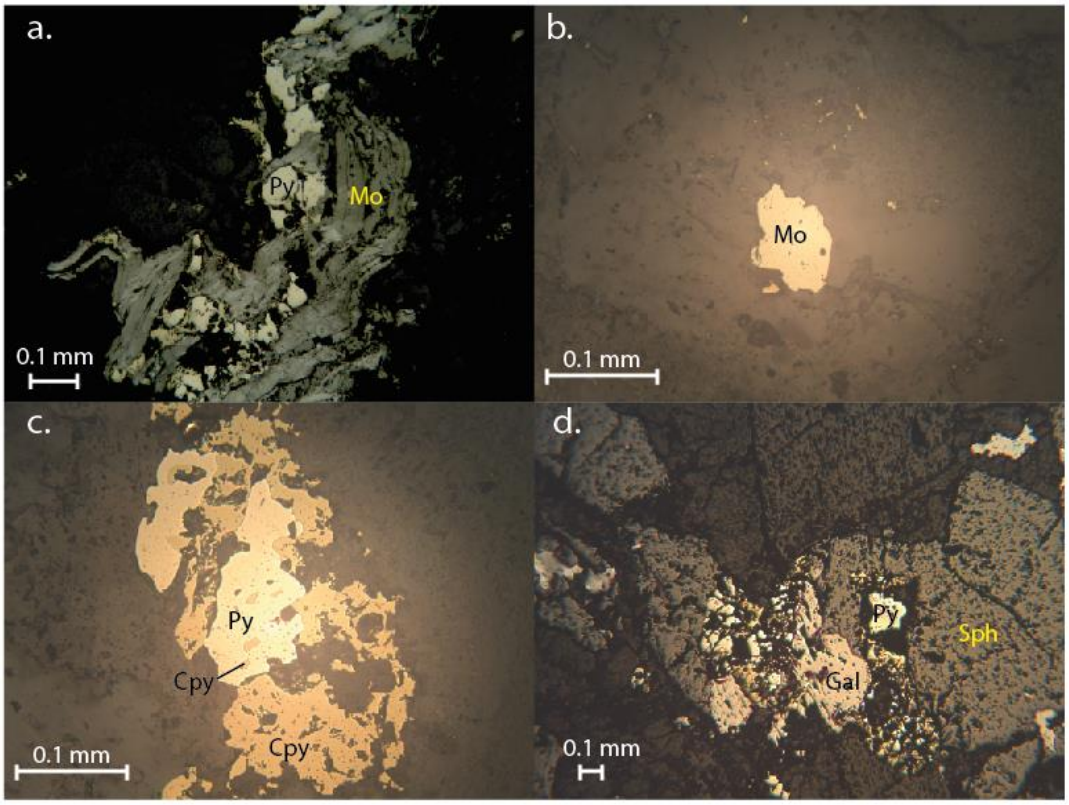

Figure 4. Photomicrographs of mineralogy in the Muratdere deposit
a.) Dendritic molybdenite (Mo) surrounding earlier pyrite (Py)
b.) Primary disseminated molybdenite
c.) Pyrite-chalcopyrite (Cpy) assemblage
d.) Polymetallic vein assemblage including galena (Gal), pyrite and sphalerite (Sph).

some areas, as well as sections which contain substantial Mo but only trace levels of Re. This raises the possibility that the Re is associated with a later phase of ore formation, resulting from fluids circulated through the surrounding country rock, scavenging Re.

Some of the fault breccias also show elevated rhenium values. This may indicate either that the fault zones acted as conduits for a second Re bearing fluid, or, as not all the breccias show this enrichment, the faults may simply be intersecting previously enriched Re-rich areas of the system. As the tellurium in this system is only associated with the later polymetallic vein set it is likely that this was also derived from the surrounding country rocks by circulating fluids.

5 Conclusions

These preliminary studies recognise a series of vein events, each with discrete mineralogy and chemistry, indicating that the rhenium mineralisation is part of the multiphase evolution of this porphyry system. The Re-Mo event postdates the main Cu-Au mineralisation and is associated with potassic alteration, magnetite and a dendritic molybdenite phase. The Te-Pb-Zn event postdates the main Re-Mo deposition, but predates the breccia formation which may constitute a second phase of Re deposition. It is therefore suggested that the critical metal enrichment in this system is due to interactions between ore forming fluids and the ophiolitic melange surrounding the intrusions.

Acknowledgements

Many thanks to Lodos Madencilik and Stratex International Plc. for providing samples and hospitality while in the field.

References

Bauer D et al (2011) Critical Materials Strategy. U.S. Department of Energy

Berzina AN et al (2005) Distribution of rhenium in molybdenite from porphyry Cu-Mo and Mo-Cu deposits of Russia (Siberia) and Mongolia. Ore Geol Rev 26:91-113

Catinat M et al (2010) Critical raw materials for the EU: Report of the Ad-Hoc Working Group on defining critical raw materials. European Commission of Enterprise and Industry

Economou-Eliopoulos M (1996) Platinum-group elements (PGE) in various geotectonic settings: Opportunities and risks. Hell J Geosci 45:65-82

Economou-Eliopoulos M (2005) Exploration for Deposits of Platinum-Group Elements. In: Mungall JE (ed) Mineralogical Association of Canada Short Course 35. Mineralogical Association of Canada, Oulu, pp 203-246

Economou-Eliopoulos M, Eliopoulos DG (2000) Palladium, platinum and gold concentration in porphyry copper systems of Greece and their genetic significance. Ore Geol Rev 16:59-70

Jaffe R et al (2011) Energy Critical Elements: Securing Materials for Emerging Technologies, Washington, DC

Okay AI (2000) Was the Late Triassic orogeny in Turkey caused by the collision of an oceanic plateau? Geol Soc Lond Spec Publ 173:25-41

Tarkian M, Koopmann G (1995) Platinum-group minerals in the Santo Tomas II (Philex) porphyry copper-gold deposit, Luzon Island, Philippines. Min Dep 47:49-47

Tekeli O (1981) Subduction complex of pre-Jurassic age, northern Anatolia, Turkey. Geol 9:68-72

Voudouris PC, Moritz R, Elissa M (2009) Rhenium-rich molybdenite and rheniite in the Pagoni Rachi Mo-Cu-Te-Ag-Au prospect, northern Greece: implications for the Re geochemistry of porphyry-style Cu-Mo and Mo mineralization. Can Mineral 47:1013-1036

Watterson ET et al (1977) Tellurium, a guide to mineral deposits. J Geochem Explor 8:31-48

Xiong Y, Wood S, Kruszewski J (2006) Hydrothermal transport and deposition of rhenium under subcritical conditions revisited. Econ Geol 2:471-478

Xiong YA, Wood SA (2000) Experimental quantification of hydrothermal solubility of platinum-group elements with special reference to porphyry copper environments. Mineral & Petrol 68:1-28

Ore mineralogy of a high sulphidation type epithermal Cu-Au-Ag deposit in the Recsk ore complex, Hungary

Ágnes Takács, and Judit Turi
Department of Mineralogy, Eötvös Loránd University, Pázmány Péter street 1/C, H-1117 Budapest, Hungary

Ferenc Molnár
Geological Survey of Finland, P.O. Box 96, FI-02151, Espoo, Finland

Aberra Mogessie
Institute of Mineralogy and Petrology, University of Graz, Universitätsplatz 2, A-8010 Graz, Austria

Abstarct. The Recsk Ore Complex (NE Hungary) is an intrusive-volcanic system of Palaeogene age in Central Europe, where the conditions are suitable for studying the relationship among deep porphyry ore genesis and different epithermal mineralization styles. The characteristics of ore mineralogy in the high sulphidation type epithermal Cu-Au-Ag deposit at Recsk reflect a slight fluctuation in the system's sulphidation state at the early stages, which was followed by a Te-enrichment. The easternmost ore body has mineralogical and geochemical similarities with both high and intermediate sulphidation type epithermal mineralization, thus representing the transition state between them. The coupled fluid inclusion studies on both opaque and transparent minerals outline the temporal and spatial evolution (NNW-SSE fluid flow path) of the high sulphidation type epithermal system and suggest enhanced magmatic brine influx into the shallow hydrothermal system.

Keywords. high sulpidation type epithermal mineralization, Au-Ag-Te minerals, fluid inclusions, Lahóca Cu-Au deposit, Recsk Ore Complex, Hungary

1 Introduction

The Recsk Ore Complex is one of the largest porphyry-skarn-epithermal systems in the Alp-Carpathian region. The first ore discoveries in the area are dated back to the end of the 18th century and the exploitation of the shallow epithermal Au-Ag-Cu ore was carried out until the 1970s. The porphyry Cu-(Mo-Au), Cu-Zn-Fe skarn and Pb-Zn metasomatic ores at depth were recognized by an intense drilling program in the 1950-80s. Mine development started in the 1980's by construction of 1100m deep shafts and interconnecting adits between them, but exploitation of the deep-seated ore bodies has not been started yet. The further gold potential of the shallow epithermal zones has been recognised at the end of the 1990's (Földessy 2008). The current known resources are summarized in the Table 1.

Due to the former mining activity and extensive mineral exploration in the area, a large amount of representative samples are available from the high sulphidation (HS) type epithermal Cu-Au deposits and also from the related intermediate sulphidation type (IS) epithermal Au-base metal, as well as the Cu- (Mo-Au) porphyry and Cu-Zn-Fe skarn deposits.

This paper presents new results on mineralogy of the HS type ore mineralization with reference to the importance of precious metal tellurides and other tellurium-bearing sulphides in understanding ore forming processes.

Ore types	Resources [mill. t]	Grade [%] (cut-off)	Reference
Cu-porphyry	109.4	0.96 (@ 0.8) Cu	Fodor et al. 1998
Cu-skarn	36	2.19 (@ 1.5) Cu	Fodor et al. 1998
Copper ore (porphyry+skarn)	779.3	0.65 (@ 0.4) Cu 0.19 g/t Au	Kontsek et al. 2006
Zn-skarn	11.5	4.98 Zn	Fodor et al. 1998
Pb-Zn metasomatic ore	36.6	3.15-3.56 Zn 1.19-2.15 Pb	Fodor et al. 1998
Pb-Zn ore Recsk Deep	48.9	1.26 Pb (+Ag content) 3.02 Zn (+0.44 % Cu)	Kontsek et al. 2006
HS-type ore	36.5	1.47g/t (@ 0.59g/t) Au	Kontsek et al. 2006

Table 1. The estimated resources for the Recsk Deep and shallow epithermal mineralization (according to the refered authors).

2 Geological background

The Recsk Ore Complex is hosted by an intrusive-volcanic structure of Palaeogene age which intruded and overlays a carbonate and siliceous shale dominated sedimentary basement of Triassic and Jurassic age. The intermediate volcanic and subvolcanic units of the complex are part of the Palaeogene Volcanic Belt of Hungary (Fig. 1), which can be correlated with other post-syncollisional Palaeogene igneous belts along the Periadritic Lineament in the Alps and in the NW Sava-Vardar belt of the Dinarides (Benedek 2002; Pamic et al. 2002; Molnár, 2007).

Dioritic cupolas elongated in NNE-SSW direction at depth (min. 400-500 m below the surface) contain Cu-(Mo-Au) porphyry ores at Recsk (Fig. 2). Cu-Zn-Fe-skarn mineralization along the contacts with the host sedimentary units and metasomatic Pb-Zn ores in proximal setting to the intrusions also occur at depth. Above the mineralized dioritic intrusion, the dacitic volcanic cover contains IS type epithermal Au-Ag-Pb-Zn ores. The HS type epithermal Cu-Au-Ag-Te mineralization is located in andesitic tuff units, in a peripheral setting in relation to the northernmost apex of the deep intrusion. Several HS type ore bodies occur in one cluster on the Lahóca Hill, whereas a single HS type ore body occur at Lejtakna (Fig.2).

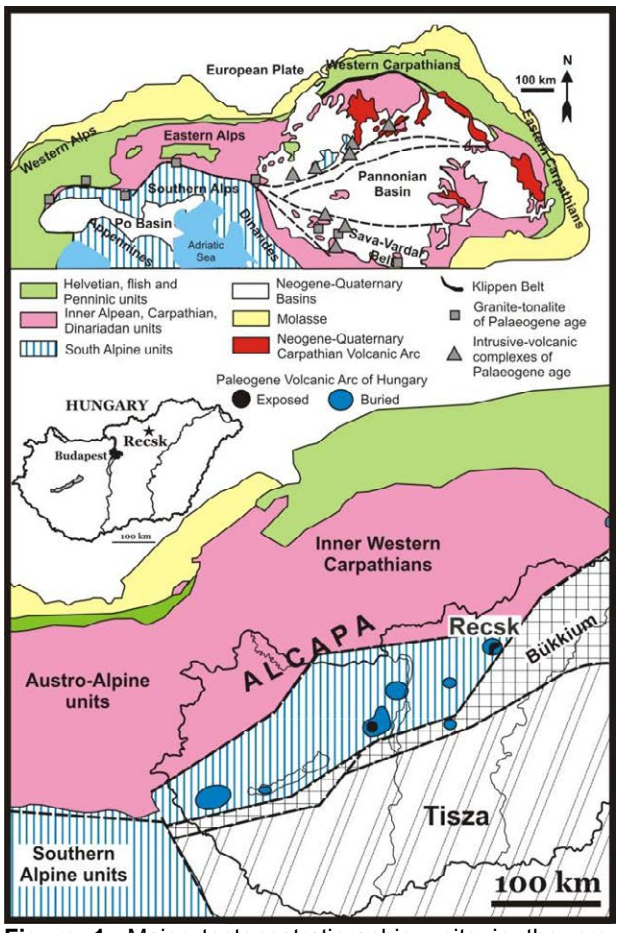

Figure 1. Major tectonostratigraphic units in the pre-Tertiary basement of the Circum-Pannonian domain with the location of Recsk in the displaced Neotethyan fragment. The displacement took place after the formation of the intrusive-volcanic and ore complex at Recsk.

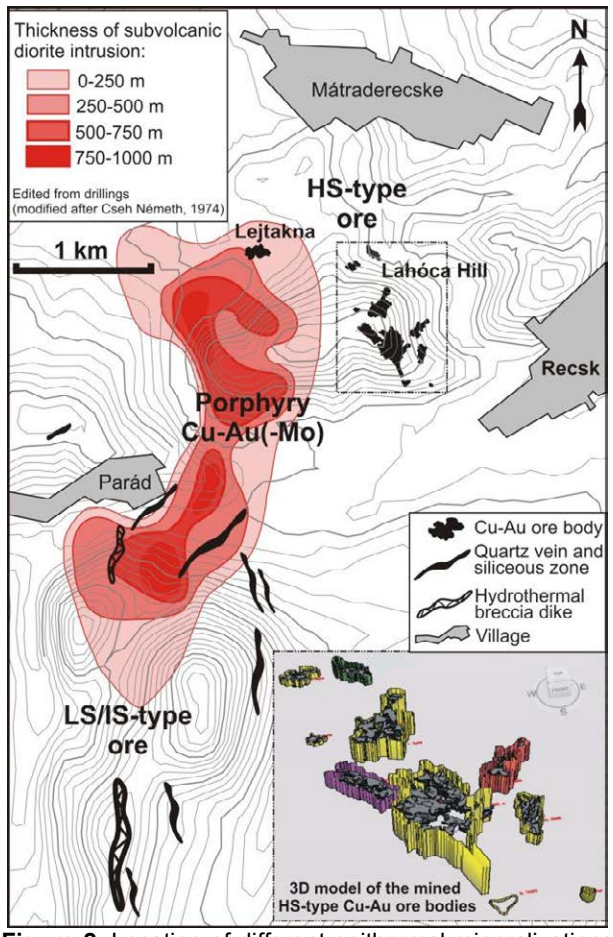

Figure 2. Location of different epithermal mineralizations related to the porphyry Cu-bearing deep intrusion (reconstructed after Baksa, 1975) and the 3 dimensional model of the historically mined ore stocks.

3 Mineralogy of the ore bodies on the Lahóca Hill

The HS type ore mineralization occurs in 11 irregular breccia bodies. These bodies follow a NNW-SSE oriented trend which presumably outlines a synvolcanic structure because diatreme breccias also cut through the host andesitic tuff unit along the same structure. The breccias of ore bodies usually consist of angular to round fragments of variably altered, mostly silicified host rock in the matrix of massive enargite and luzonite. The andesitic tuff unit is also host different types of hydrothermal breccia veins which contain fragments of the enargite-luzonite rich ore. The andesitic tuff is characterised by advanced argillic alteration (dickite-kaolinite-quartz) with disseminations of pyrite.

The early stage of mineralization in the enargite-luzonite rich ore bodies consists of a pyrite-tennantite-sphalerite-galena-chalcopyrite assemblage (stage I.) with coexisting quartz. Pyrite usually shows As-zoning, while galena grains always contain various amount of Se. The selenium rich end member of the PbS-PbSe series (clausthalite) is locally also present. This assemblage usually occurs as remnant after partial replacement by minerals of the next ore stage.

Stage II is characterized by the massive deposition of enargite and luzonite. Precipitation of these minerals was accompanied by the crystallisation of emplectite-wittichenite ($CuBiS_2$-Cu_3BiS_3) and aikinite-bismuthinite ($PbCuBiS_3$-Bi_2S_3) group minerals, as well as famatinite, bournonite, stibnite, bohdanowiczite (AgBiSe2), pyrite and native gold (with appr. 0.19-0.27 mol% Ag content). The first generation of Au- and Ag-tellurides, calaverite and hessite also precipitated at this stage (Figure 3).

In the third stage of ore formation, grey ore minerals (tennantite-goldfieldite) locally replaced enargite and luzonite. Empressite (AgTe), krennerite-sylvanite ($[Au,Ag]Te_2$-$[Au,Ag]_2Te_4$), petzite (Ag_3AuTe_2) and native tellurium are associated with these minerals. The composition of the grey ore crystals gradually developed from tennantite to goldfieldite during growth. The composition of Au-Ag tellurides follows the same Te-enrichment trend as the composition of the grey ore crystals and ended up with the formation of the native tellurium. The above mentioned mineral succession was accompanied by the local formation of kawazulite (Bi_2Te_2Se) and Sn-bearing minerals (e.g. kesterite ($Cu_2[Zn,Fe]SnS_4$)). Crystallisation of pyrite also continued in this stage and many euhedral crystals exhibit zoning in the distribution of copper in their structures.

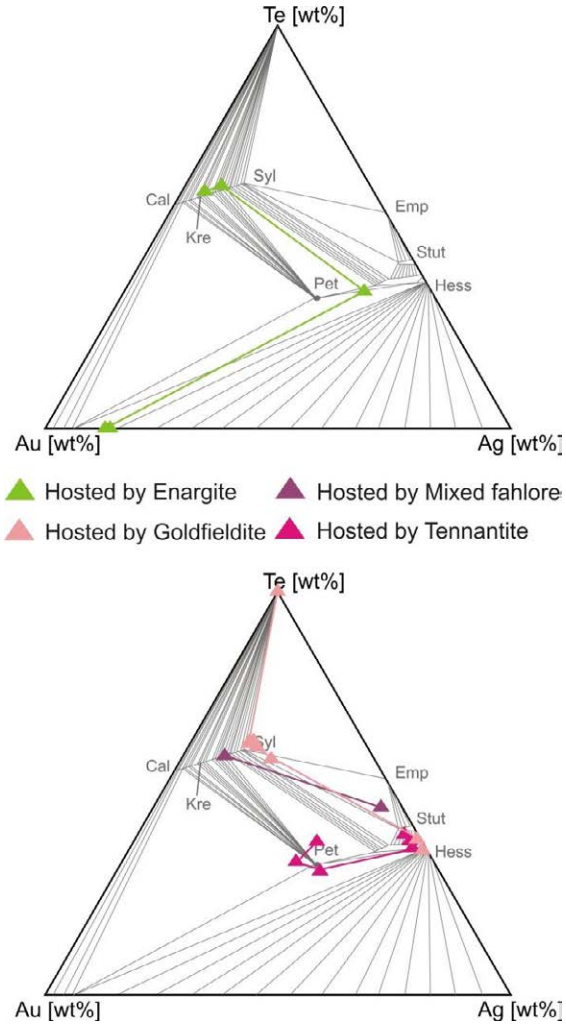

Figure 3. Ternary Au-Ag-Te diagram showing the phase relationships among Au-Ag tellurides in the temperature range 120-300°C according to experimental data, microprobe analysis of natural assemblages (after Zhang and Spry, 1994) and the Au-Ag-Te minerals of Lahóca, hosted by different Cu-bearing minerals. Abbrevations: Cal: calaverite; Emp: empressite; Hess: hessite; Kre: krennerite; Pet: petzite; Stut: stuetzite; Syl: sylvanite;

The fourth stage of the ore mineralization is dominated by the formation of fine grained and collomorph pyrite, which contains significant amount of gold. This type of pyrite also characterises gold enrichments in the late hydrothermal breccias.

4. Mineralogy of the Lejtakna ore body

The early stage of mineralization in the Lejtakna ore body is similar to the Stage I and II of the Lahóca stocks but the stage II is poorer in mineral diversity. The main ore minerals are almost the same (enargite-luzonite-famatinite) and they are also accompanied by emplectite-wittichenite, bismuthinite and pyrite, but Au- and Ag-tellurides are very rare. During the third ore forming stage the precipitation of the grey ore does not just follow the precipitation of enargite and luzonite but also resorbs them. In the deeper part of the deposit (+92 m above sea level) the replacement is not significant, but above that (+133 ab. sea level) it becomes dominant and only rare fragments of enargite-luzonite crystals occur in a pyrite-chalcopyrite-grey ore matrix. The Au-Ag-Te mineralization is rare or absent and the composition of the grey ore crystals do not show such enrichment in Te as in the first mentioned ore bodies. The grey ore usually consists of Mn-(Ag)-bearing tennantite and tetrahedrite. The shallowest part of the Lejtakna ore body (+152 m above sea level) contains a pyrite-chalcopyrite-tennantite-tetrahedrite-galena-sphalerite assemblage with rare enargite-luzonite crystal fragments. The framboidal pyrite is common, where the cubic pyrite crystals are cemented by galena.

4 Fluid inclusion studies

Fluid inclusion microthermometry studies were carried out in samples from the ore bodies of the Lahóca Hill. Data for quartz from the stage I indicate low salinity (0.5-2.5 NaCl equivalent wt%) and 260-235°C temperature of mineral forming fluids, while fluid inclusions in late quartz, which was precipitated in one of the multiple late hydrothermal brecciation event, suggest lower temperature (140-170°C) and higher salinity (6.5 – 8.0 NaCl equv. wt%) of fluids (Figure 4).

Results of the near-infrared microthermometry of the enargite-hosted fluid inclusions indicate cooling ore forming fluid from 245 to 170°C with increase of fluid salinity (from ~1.0 to 9.5 NaCl equv. wt%) during the ore stage II (Fig. 4). Spatial distribution of homogenization temperature data in the ore bodies suggests that the main direction of the fluid-flow path did not point toward the closest apex of the porphyry Cu-bearing intrusion. The outlined NNW-SSE trend confirms the lateral flow of fluids, as previously described by Molnár (2007).The large increase of salinity coupled with cooling of hydrothermal fluids may suggest enhanced magmatic brine influx into the shallow hydrothermal system, since adiabatic boiling is unable to explain such a significant (~4X) increase in salinity. As salinity and temperature data systematically varies among different orebodies (Fig. 4) local boiling towards dryness appears to be an unlikely process to explain increase of salinities.

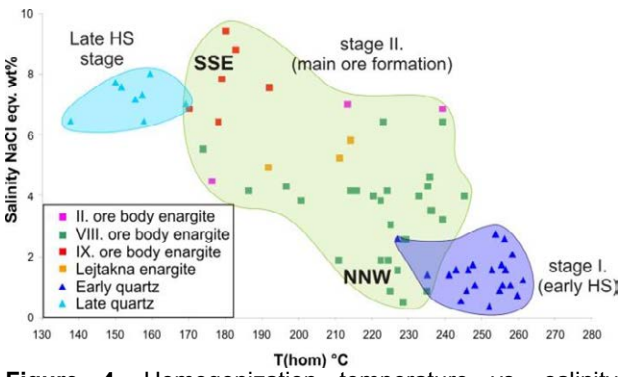

Figure 4. Homogenization temperature vs. salinity diagram for data from the enargite (squares) and quartz-hosted (triangles) fluid inclusions.

5 Discussion

The observed succession of mineral assemblages outlines the evolution of the epithermal system at the ore

forming stages. The mineralization stage I and II exhibit the first changes in the chemistry of the epithermal activity, which are interpreted to be a slight fluctuation in the system's sulphidation state. The Te-enrichment trend of the stage III ores started in stage II with the formation of hessite and calaverite indicating the increase of fTe_2, as a consequence of cooling in the epithermal system or by magmatic input of tellurium from the associated intrusion (Afifi et al. 1988). The absence of tellurides in stage I and their variable presence in stage II and III suggest that both cooling of fluids and magmatic input are needed to interpret the observed mineral sequence. We suggest that a Te-bearing magmatic input caused the appearance of tellurides in stage II and the decreasing temperature induced the changes in the futher formation of Au-Ag tellurides in stage III. In the observed mineral assemblage, Ag-content of gold can be used to estimate the tellurium fugacity (Affifi et al., 1988). Thus the log fTe_2 values are between -10.5 and -15.7 in the temperature range of 250-150°C for the ore forming stage II (Fig.5-). The presence of petzite or other Ag-telluride minerals in the assemblage of stage II is not documented, but calaverite is a significant mineral in this stage. The Te-bearing mineralizion of the deposit plays an important role in the occurrence and distribution of gold and silver in the ore bodies. The evolution of the Au-Ag-Te mineralization is pointing toward to the Te-enrichment, which implies that significant Au precipitation is rather related to the stage II, while the precipitation of Ag is more related to the stage III.

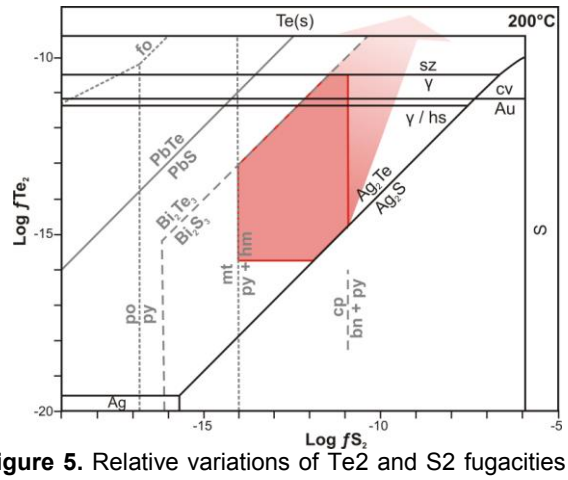

Figure 5. Relative variations of Te2 and S2 fugacities in the mineralization stage II-III with respect to selected ore minerals equilibria (modified after Afifi et al. 1988).

The different composition of the post-enargite grey ore between the 11 ore bodies of Lahóca and the Lejtakna ore body suggest spatial evolution of the system. The occurrence of post-enargite Mn-(Ag)-bearing tennantite-tetrahedrite in the Lejtakna ore body suggests a lower sulphidation state of the hydrothermal system compared to the ore bodies in the Lahóca Hill. The Mn-(Ag)-bearing grey ore is a typical mineral of the IS type epithermal ore mineralization around Parád. The mineralogical and geochemical characteristics of the Lejtakna ore body and the differences and similarities between Lejtakna and other epithermal mineralization at Recsk, suggest that the Lejtakna orebody represents the transition state between the IS mineralization styles around Parád and the HS type ore zone on the Lahóca Hill (Fig.2).

6 Conclusions

The detailed mineralogical study of HS type epithermal ore bodies of the Recsk Ore Complex accompanied with VIS/NIR fluid inclusion microthermometry outline the temporal and spatial evolution of the epithermal system related to the Cu-porphyry-bearing deep intrusion. The ore bodies of Lahóca Hill are hosted by a diatreme breccia structure, which had direct connection to the deep-seated intrusions, thus this structure acted as the primary conduit for magmatic fluids. The observed mineralogical and geochemical changes among the ore bodies of the Lahóca Hill and Lejtakna and the defined NNW-SSE main direction of fluid flow path indicate lateral flow of fluids, which were associated with the decreasing sulphidation state of fluids in the Lahóca-Lejtakna and Parád direction (Fig.2).

Acknowledgement

The project was supported by the European Union and the European Social Fund (grant agreement no. TÁMOP 4.2.1./B-09/KMR-2010-0003) and CEEPUS (Mobility grant no.CIII-RO-0038).

References

Afifi AM, Kelly WC, Essene EJ (1988) Phase relations among tellurides, sulphides, and oxides: I. Thermochmeical data and calculated equilibria. Economic Geology 83:377-394

Afifi AM, Kelly WC, Essene EJ (1988) Phase relations among tellurides, sulphides, and oxides: II. Application to telluride-bearing ore deposits. Economic Geology 83:395-404

Baksa Cs. (1975) The subvolcanic andesite body of Recsk and its dikes. Bull. of the Hungarian Geological Society 105:612-622

Benedek K (2002) Palaeogene igneous activity along the easternmost segment of the Periadriatic-Balaton Lineament. Acta Geol. Hung. 45:359-371

Földessy J, Zelenka T, Benedek K, Pécskay Z, Mádai F (2008) The Recsk Palaeogene magmatism in a regional context. In Földessy J, Hartai É, (eds) Recsk and Lahóca Geology of the Paleogene Ore Complex. Pub. of the Univ. of Miskolc Series A 73:7-20

Molnár F (2007) The Cu-Au-Ag-Zn-Pb ore complex at recsk, Hungary: a uniquely preserved and explored porphyry-skarn-epithermal system in the Palaeogene magmatic belt of the Alp-Carpathian-Dinaride system. Digging deeper, Proc. of the 9. Biennal SGA Symposium, Dublin 1:153-157

Molnár F, Jung P, Kupi L, Pogány A, Vágó E, Viktorik O, Pécskay Z, Hurai V (2008) Epithermal zones of the porphyry-skarn-epithermal ore complex at Recsk. In Földessy J, Hartai É, (eds) Recsk and Lahóca Geology of the Paleogene Ore Complex. Pub. of the Univ. of Miskolc Series A 73:99-128

Pamic J, Balen D, Herak M (2002) Origin and geodynamic evolution of Late Paleogene magmatic associations along the Periadriatic-Sava-Vardar magmatic belt. Geodinamica Acta 15:209-231

Fodor B, Forgács-Gombár G, Káli Z (1998) Mineral resources and reserves of Hungary. Annual Report of the Hungarian Geological Survey (in Hungarian)

Kontsek T (eds. 2006) Mineral resources and reserves of Hungary. Annual Report of the Hungarian Geological Survey (in Hungarian)

Zhang X., Spry P.G. (1994) Calculated stability of aqueous tellurium species, calaverite and hessite at elevated temperatures. Economic Geology 89:1152-1166.

The Cu-Mo-Au mineralization of the Paleoproterozoic Kedonojankulma intrusion, Häme Belt, Southern Finland

Markku Tiainen, Ferenc Molnár, Esko Koistinen
Geological Survey of Finland, Espoo

Abstract. The paper presents new data for age, petrochemistry and mineralisation of the Kedonojankulma intrusion in Southern Finland. The Cu-Mo mineralisation and its host rock have several features which are comparable to porphyry copper systems, and observations also support epithermal gold potential for the volcanic units next to the intrusion. However, Au mineralisation appears to be connected to overprinting shear structures in the intrusion.

Keywords: porphyry copper, Paleoproterozoic volcanic arc, Häme Belt

1. Introduction

The Forssa-Jokioinen ore province, which is located in the Häme Belt, (Fig.1) contains granitoid-hosted Cu, Mo and Au ore occurrences. The first indications of the ore potential of the area were found as a result of systematic till geochemical exploration in the Forssa-Huittinen area in the years 2003-2005 (Kärkkäinen et al 2012). An ongoing follow-up exploration program to assess the ore potential of the area was initiated in 2004. Exploration has included till geochemistry, geological mapping, boulder tracing, geophysics and diamond drilling. Target scale geochemistry of the basal till was applied in two phases, reducing the target area and increasing sampling density from 16 samples per one km^2 to 50 meters grid in the most interesting areas. The target at Kedonojankulma included till geochemical anomalies of specific suites of elements, namely Cu-Au-Ag-As-Sb(-Te).

The Cu mineralization at Kedonojankulma was observed in a few outcrop only, but bedrock mineralization in the area has subsequently been confirmed by drilling. The Kedonojankulma ore occurrence is the best studied target in the Kuuma-Kedonojankulma-Arolanmäki area in the eastern part of the Häme Belt (Kärkkäinen et al 2012; Tiainen et al., 2011; 2012). So far, 58 drill holes, totalling 4561 meters drill core, have been drilled within the poorly exposed Kedonojankulma intrusion. The ore resources of the drilled part of the mineralization are 1.8 Mt, including 0.4 % Cu, 11 ppm Ag, 0.12 ppm Au and 18 ppm Mo.

The occurrence is open at least to depth and it may

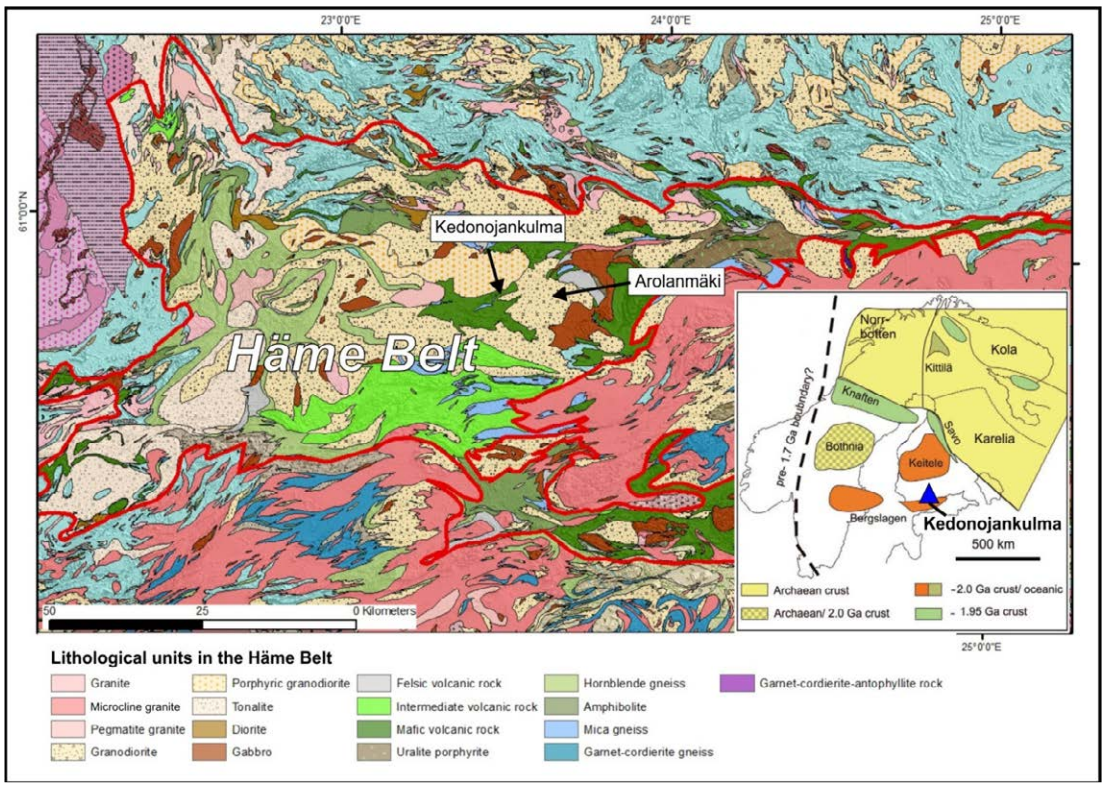

Figure 1: geological map of the Häme Belt with location of the Kedonojankulma intrusion. Inset drawing shows tectonic reconstruction at around 1.9 Ga and inferred location of the Kedonojankulma intrusion in the soutward oriented subductiopn zone between the Keitele and Bergsladen microcontinents (modified after Lahtinen et al., 2005).

also continue several hundred meters further to the south-west from the northern contact of the intrusion.

In this paper we summarise characteristics of the mineralization and its host intrusion and present arguments for classification of the ore occurrence as a porphyry-copper type ore deposit.

2. Regional and local geology

The Häme Belt forms a part of the Palaeoproterozoic Southern Finland Supersuite and predominantly consists of volcanic sequences erupted in a subduction related volcanic arc. According to Lahtinen et al., (2005), southward oriented subduction existed between the Bergsladen microcontinent to the south and the Keitele microcontinent to the north at around 1.89-1.87 Ga in the southern part of Svecofennia (Fig. 1). Subduction generated back-arc magmatism in the Bergsladen Belt and island arc magmatism in the Häme Belt.

Volcanic rocks in the Häme belt comprise two main units; the lower Forssa suite is dominated by calc-alkaline medium-K intermediate-acidic lavas and pyroclastics, while the upper Häme suite is dominated by tholeiitic basalts (Hakkarainen 1994; Lahtinen 1996). The volcanic rocks of the Forssa suite are related to stratovolcanoes whereas eruption of the Häme suite basalts are related to E-W trending fissure systems. Both suites also contain voluminous batholiths and intrusions from granitoid to grabbroic compositions (Fig. 1).

Rocks in the Häme belt underwent amphibolite facies metamorphism at around 1.88-1.86 Ga. The Häme Belt was also affected by a high T event at around 1.83-1.81 Ga (Nironen, 1999; Väisänen et al., 2002).

The Kedonojankulma intrusion was mapped as a multiphase tonalitic intrusion, including equigranular and porphyritic tonalite – quartz-plagioclase porphyrite, aplitic veins and mafic veins. The mineralized intrusion appears to be connected to the large Arolanmäki granodiorite batholith via the Koijärvi intrusion to the East (Fig. 2). The contact zones of the Kedonojankulma intrusion to the surrounding volcanic-sedimentary sequence are not exposed, but intrusive breccias, as well as highly silicified alteration zones in the intermediate volcanic rocks near to the inferred contact (within tens of meters) have been recognized in outcrops. The contact zone was drilled through in the northern part of the intrusion where it is also characterized by strong silicification and brecciation.

3. Petrochemistry

The unmineralized samples from the Kedonojankulma intrusion have peraluminous-metaluminous granodiorite-granite compositions with medium to high-K calc-alkaline character. These compositions correspond to arc related granitoids. The Sr/Y ratios are higher than 20 and the chondrite normalized REE-patterns show no Eu anomaly, and it is characterised by

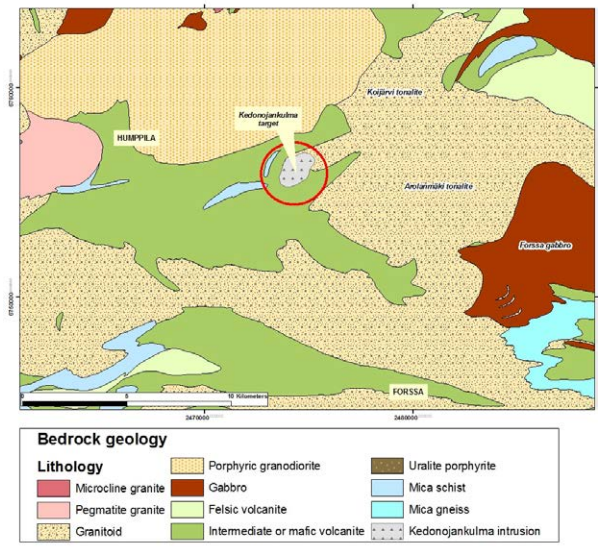

Figure 2. The location of the Kedonojankulma intrusion in relation to the volcanic units and other tonalitic-granodioritic intrusion in the eastern part of the Häme Belt.

enrichment in LREE and depletion in HREE (e.g. La/Yb ratios are from 15 to 27 with less than 2 ppm Yb contents; Fig.3). Some samples from the Arolanmaki tonalite, and especially from the Koijärvi intrusion east of Kedonojankulma (Fig. 2) share similar geochemical characteristics. Moreover, there also are granitoids in the western and northern parts of the Häme belt which show petrochemical characteristics comparable to those for the Kedonojankulma intrusion.

4. Geochronology

U-Pb analyses have been carried out on zircon grains from the Kedonojankulma intrusion by LA MC-ICPMS technique. Results suggest that the age of intrusion is 1883±5 Ma (Fig. 4). This age is coincident with the 1.89-1.88 age of the felsic volcanism in the Häme belt (Vaasjoki 1994) confirming that emplacement of Kedonojakulma intrusion is coeval with the andesitic-dacitic Forssa suite.

5. Hydrothermal alteration

Classification of alteration is based on observations on drill cores, thin sections and geochemical analyses. The major mass of the intrusion is characterized by sericitisation of plagioclase and biotitisation of amphibole and pyroxene phenocrysts. Epidotization with biotitization was detected in the outer zone of the intrusion. Intense silicification characterizes the zones with Cu- and Mo-enrichments. In addition, a strongly siliceous zone along the northern contact of the intrusion was mapped out by observations in drillcores. The texture of rocks is completely obscured by the intense alteration and the siliceous rock contains carbonate mineral filled 1-2 mm large vugs at some places. The outline of these vugs resembles to rock forming silicate phenocrysts. This alteration zone may be interpreted as a lower part of a lithocap.

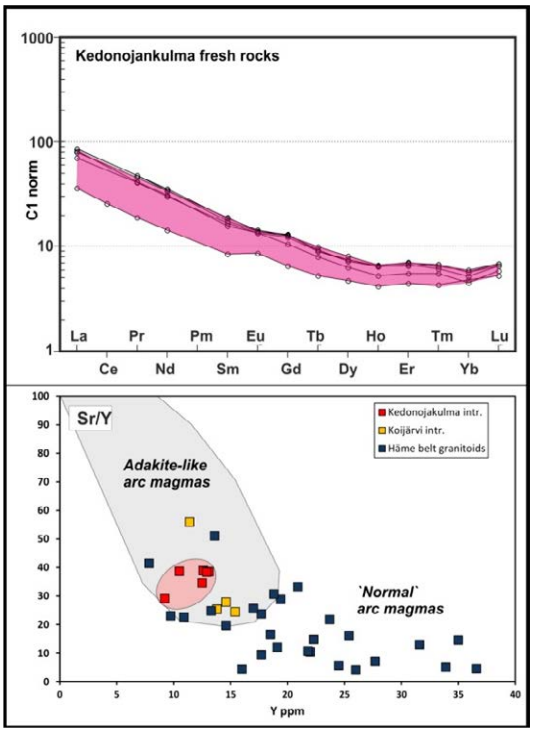

Figure 3: C1 chondrite normalized REE pattern for unmineralised geanodiorite-granite of the Kedonojakulma intrusion (upper chart) and Sr/Y vs Y diagram for granitoid intrusions of the Häme belt.

The alteration types described above are overprinted by a alteration, which is present in several intersections in all drillcores. Macroscopically, those alteration zones show pinkish colour. The most intense colouring occur along open fractures with chlorite coatings on the walls of fractures and around carbonate veins and carbonate cemented tectonic breccias. The pinkish colour of these alteration zones is due to the presence of finely distributed microscopic hematite after alteration of feldspars and alteration of mafic minerals under oxidatized conditions. These zones are characterised by 7-9 wt % Na_2O. This kind of alteration overprints unmineralized, weakly altered and strongly mineralized rocks, as well as shear zones, therefore it is related to a superimposing alteration process unrelated to the formation of the deposit.

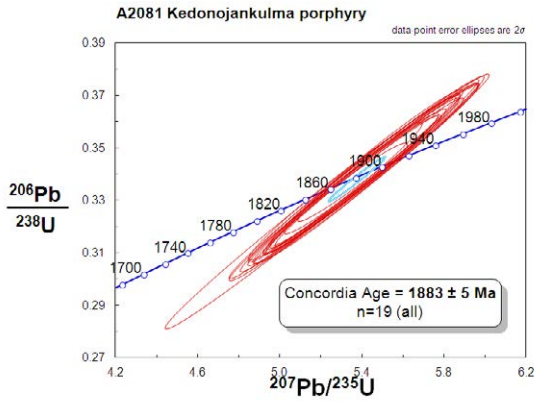

Figure 3: Concordia diagram of U-Pb analyses on zircon crystals from the Kedonojankulma intrusion.

Mineralized parts (>300 ppm Cu) of the Kedonojankulma intrusion are characterized by slightly elevated SiO_2-contents due to silicification associated with the ore forming processes. Mineralizing processes also resulted in slight enrichment in LILE in altered rocks. Parallel with increase of copper content in the altered rocks, a pronounced negative Eu anomaly appears in the REE patterns. The post-mineralization Na-metasomatic alteration under oxidatized and alkaline conditions also resulted in desilification (decrease of SiO2 content to around 63-65 wt%), and depletion of potassium and barium, as well as enrichment in HREE and development of more pronounced negative Eu anomalies.

6. Vein system

Detailed vein-system characterization has been carried out on drillcores from the Kedonojankulma intrusion in order to better constrain structures controlling distribution of metals and to understand the importance of superimposing processes in distribution of metals.

The earliest hydrothermal veins are filled with fine grained-equigranular dark grey/black quartz with fine grained pyrite, chalcopyrite and locally molybdenite disseminations. Their thicknesses are usually less than 5 mm. In thicker veins, sulphides are locally arranged along the centreline of the vein. The vein contact to the host rock is sharp and selvaged by fracture parallel biotite flakes. The opposite walls of veins are often not parallel to each other and the thicknesses of veins are variable along their strike. There is no preferred orientation for these veins and they often form dense stockwork especially in silicified parts of the intrusion.

A second type of early veins also contain fine grained quartz infillings but 1-3 cm thick feldspar-desctructive alteration halo with epidote and pyrite dissemination surrounds them. However, these veins are rare in drillcores.

The early quartz veins are cut by 0.1-1m wide shear zones in several drillcore intersections. Post-shearing veins commonly have breccia textures and they are filled up by chlorite+pyrite or carbonate minerals. Na-metasomatic alteration with finely disseminated hematite are associated with these veins.

The number/meter (abundance) parameters for each type of veins were measured in five drillholes. The results confirm that copper grades correlate well with the abundance of early veins filled up by massive dark-grey to black silica. However, it was also observed that in zones with elevated molybdenum content, the abundance of early veins also increases, although it is always smaller than in the copper rich zones. This suggests that molybdenite precipitated during the early stages of fracture system development and chalcopyrite started to crystallize at more evolved stages of fracture propagation. Abundance parameters for other types of veins do not show correlation with metal contents. Gold is associated with shear zones in the eastern part of the drilled area.

7. Mineralogy and geochemistry of ore

The major ore minerals are pyrite, chalcopyrite and molybdenite and their diesseminations are confined to the early quartz veins and silicified zones. Minor ore minerals include sphalerite, galena, mackinawite, marcasite, ilmenite, rutile, scheelite and gold. Bornite, chalcocite and covellite commonly replace chalcopyrite in the overprinting pinkish alteration zones. Native bismuth inclusions with Cu-Bi-sulphide reaction rim and Bi-, Ag-tellurides locally occur in chalcopyrite and in chalcocite replacing chalcopyrite. Arsenopyrite with Co-Ni-arsenides is locally abundant in some rare late veins.

Among the metallic elements of sulphide minerals, copper shows good correlation (Pearson corr. coeff = 0.819) with silver only. Silver is enriched in the fractures of chalcopyrite, therefore this correlation is probably the result of superimposing processes. Copper is not correlated with molybdenum, confirming the observations on the different timing of veins with molybdenite and chalcopyrite. Significant additional correlation exists among concentrations of Bi, Te and Au. The Au-Bi and Au-Te correlation coefficients are 0.861 and 0.883, respectively. Since Au is connected to superimposing shear zones, these correlations suggest that occurrence of Bi-minerals are also secondary in relation to the formation of copper ores.

8. Discussion and conclusions

The discovery of the Cu-Mo-Au mineralisation of the Kedonojakulma intrusion was mostly based on geochemical and geophysical exploration methods in a strongly covered area. Characteristics of mineralisation could be evaluated on the basis of drillcores only.

Geochemical and geochronological data confirms that the Kedonojakulma intrusion was formed during the subduction related igneous activity of the Svecofennian orogeny. Geochemical features (REE patterns, Sr/Y and La/Yb ratios) of the intrusion reflect suppression of plagioclase fractionation and/or relatively oxidizing conditions with high water contents in its parent melt. Thus the Kedonojankulma intrusion shows adakite-like geochemistry, which is a rather common, though not exclusive attribute of host rocks to porphyry-copper systems (Richards et al., 2012). Occurrences of rocks with similar geochemistry in the Koijärvi and Arolanmäki granodiorite batholith east to Kedonojakulma suggest common origin of parent melts and support the hypothesis that the Koijärvi intrusion may be a conduit between the deep batholitic level (Arolanmäki intrusion) and the shallow subvolcanic level (Kedonojankulma intrusion) Accepting this hypothesis also means that the Kedonojakulma-Koijärvi-Arolanmäki magmatic system is in a tilted position.

The vein system of the Kedonojankulma intrusion shows similarities to, but not fully comparable with those in Phanerozoic porphyry copper systems. The early veins appear to correspond to type A, B and D veins known in young, unmetamorphosed porphyry-copper systems (Sillitoe, 2010 and references therein), however the most notable difference is the absence of magnetite in the early veins and the very low abundance of later veins with feldspar-destructive alteration haloes. However, it should also be considered that current information is available from a relatively small volume (about250x100x100 m^3) of a much larger porphyry intrusion and outcrop observations indicate that drill holes have only intersected the marginal zone of a more extensive hydrothermal system. The presence of a lithocap like siliceous zone along the contact of the intrusion opens up exploration potential of epithermal systems in the volcanic units next to the Kedonojankulma intrusion.

Elevated concentrations of gold in the Kedonojankulma intrusion occur in certain cross-cutting shear zones. Thus the gold enrichment does not have genetic association with the formation of the Cu(-Mo) ore.

Acknowledgements

We express our thanks to Niilo Kärkkäinen (GTK) for discussions on the subject and Hahnu Huhma (GTK) for U-Pb age dating of zircon. SEM-EDS analyses of minerals were done by Bo Johanson and Lassi Pakanen (GTK).

References

Hakkarainen G (1994) Geology and geochemistry of the Mämeenlina-Somero volcanic belt, southwestern Finland: a Paleoproterozoic island arc. Geol Sorv Finland Spec. Paper 19:85-100.

Kärkkäinen N, Huhta P, Lehto T, Tiainen M, Vuori S, Pelkkala M (2012) New geochemical data for gold exploration in southern Finland. Geol Surv Finland Spec Paper 52:23-46.

Lahtinen R, Korja A, Nitonen M (2005) Paleoproterozoic tectonic evolution. In:Lehtinen M, Nurmi P, Rämö OT (eds) Precambrian geology of Finland – Key to evolution of the Fennoscandian shield. Elsevier BV Amsterdam pp 481-532.

Nironen M (1999) Structural and magmatic evolution in the Loimaa area, southwestern Finland. Bull Geol Soc Finland 71:57-71.

Richards JP, Spell T, Raameh E, Razique A, Fletcher T (2012) High Sr/Y magmas reclect arc maturity, high magmatic water content and poephyry Cu±Mo±Au ptential: examples from the Tethyan arc of Central and Eastern Iran and Western Pakistan. Econ Geol 107:295-332.

Sillitoe RH (2010) Porphyry copper systems. Econ Geol 105:3-41.

Tiainen M, Kärkkäinen N, Koistinen E, Pakkanen L, Sipilä P (2011) Kedonojankulma, a recently discovered Palaeoproterozoic porphyry-type Cu-Au deposit in Southern Finland. Proc. Eleventh Biennal SGA Meeting, 393-395.

Tiainen M., Kärkkäinen N, Koistinen E, Lohva J, Sipilä P, Huhta P (2012) Discovery of the Kedonojankulma Cu-Au occurrence, hosted by a Svecofennian porphyritic granitoid in Southern Finland. Geol Surv Finland Spec Paper 52: 73-90.

Vaasjoki M (1994) Valijärven hapan vulkaniitti: minimi Hämeen liuskejakson iäski. Geologi 46:91-92

Väisänen M., Mänttäri I., Hölttä P (2002) Svecofennian magmatic and metamorphic evolution in southwestern Finland as revealed by U-Pb zircon SIMS geochronology. Precamb Res 116:111-127.

The Laver 1.9 Ga large volume, low grade, porphyry-style Cu-Au-Mo-Ag mineralization

Annika Wasström & Sebastian Knipfer
Exploration, Boliden Mines, SE 936 81 Boliden, Sweden

Lina Åberg
Ore Reserves and Project Evaluation, Boliden Mines, SE 936 81 Boliden, Sweden

Abstract. The Laver mineralization is a large volume, low grade, porphyry-style Cu-Au-Mo-Ag mineralization, located in Norrbotten, northern Sweden. The mineralization is located 1 km south of the old Laver Mine on Lill-Laverberget. The Laver old mine operated between 1938 and 1946. The ore consisted of narrow zones with "high" Cu-grade. In total 1.3 Mt @ 1.5% Cu, 0.2 g/t Au and 36 g/t Ag was mined.
The host rocks in Laver are c. 1.9 Ga in age and lie north of the Skellefte District in the Fennoscandian Shield. The host rocks to the Laver mineralization consist of metamorphosed porphyries, volcaniclastic rocks and minor reworked sediments. The mineralization comprise mainly of sulphides in dissemination and veins. The main ore minerals are pyrite, chalcopyrite, pyrrhotite, molybdenite, magnetite and sphalerite. Arsenopyrite, galena, hematite, bornite and some native copper are also observed. The mineralized rocks are strongly altered, mainly by pervasive silicification but also by quartz-veining.
A Mineral Resource estimation was completed in late 2012, which gave an Inferred Mineral Resource of 690 Mt @ 0.20% Cu, 0.12 g/t Au, 2.8 g/t Ag and 35 g/t Mo. A conceptual study has recently started.

Keywords. Porphyry Cu deposit, Au, Sweden, Palaeoproterozoic

1 Introduction

Boliden Mineral is exploring for a large scale, low grade copper-mineralization in Laver. The mineralization is located in Älvsbyn Municipality, Norrbotten, Sweden (Figure 1). Laver lies <50 km north of the Skellefte District in the Fennoscandian Shield in an area which is dominated by 1.88-1.86 Ga (Kathol et al 2005) old Arvidsjaur Group rocks.

1.1 Old Laver Mine

In 1929, a chalcopyrite rich boulder was found on Nattberget about 10 km south east of Laver by Boliden Exploration. The boulder trace was followed in the ice direction and an outcropping mineralization was found in 1930. Electromagnetic surveys resulted in a number of indications, which were tested by drilling. The Laver deposit was discovered in 1930.

The old Laver Mine operated between 1938 and 1946. The ore consisted of narrow zones with "high" Cu-grade. In total 1.3 Mt @ 1.5% Cu, 0.2 g/t Au and 36 g/t Ag was mined. Mining was done both in open pit and underground. The average grade of the Laver deposit was in fact too low, but the company needed Cu-concentrate to recover more gold in the newly built smelter at Rönnskär.

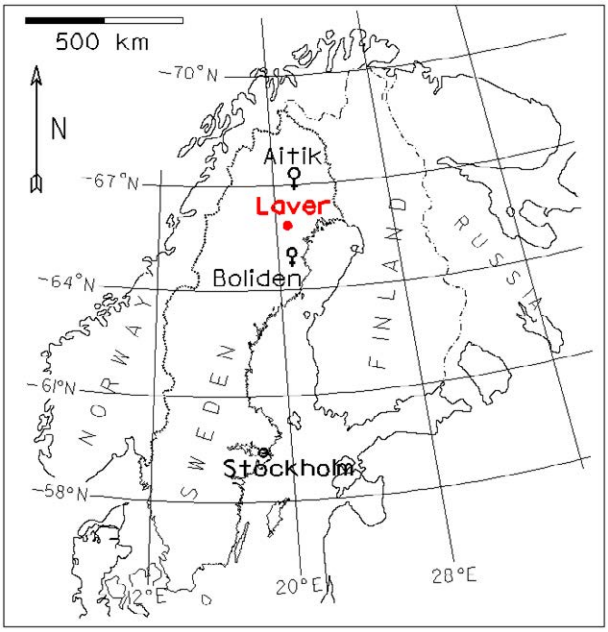

Figure 1. Location of Laver.

The bedrock around the deposit is composed of felsic and mafic volcanic rocks of the Arvidsjaur porphyry series. Pyroclastic sediments, in part waterlaid, are intercalated with the volcanic rocks (Ödman 1943). The rocks around the mine are tilted and strike NW-SE and dip vertically or steeply to the W or SW. The axis of the fold dips steeply to SSE.

Ödman (1943) described four different ore zone types from the old mine; breccia ore, ore "dykes", ore-bearing fault zones and sphalerite impregnation. He also described three different alteration types; hydrothermal brecciation, silicification (with minor zones of chlorite and sericite alteration) and garnet and skarn alteration. Chalcopyrite, pyrrhotite, pyrite, traces of sphalerite were common ore minerals, while vallerite ($Cu_3Fe_4S_7$), cubanite ($CuFe_2S_3$), marcasite, arsenopyrite and molybdenite were considered as rare. Du Rietz (1944) described the alteration in the Laver deposit more in detail. Ödman (1945) described a Ni-Co-Ag mineral paragenensis close to the chalcopyrite ore.

No modern study on the genesis and origin of the deposit has been made. However, according to Weihed (2001) it is possible that the mineralization is epigenetic

in character and that a structural control or magmatic relationship cannot be excluded.

1.2 New Discovery

Boliden did exploration in Laver in 1970-1972 and 1997. From these exploration campaigns the Laver area was known to have anomalous Cu-grades at surface.

New ideas made Boliden apply for an exploration license in 2007. The exploration target was a large volume, low grade, porphyry-style Cu-mineralization (Aitik-type). In 2008, compilation and reconnaissance work was done in the field, and in 2009, drilling and surveying started. More than 36 000 m and almost 100 diamond drill holes have been drilled since 2009. In November 2012 the first Resource Estimation was done. The new discovery the Laver mineralization is located 1 km south of the old Laver Mine.

2 Geology

2.1 Regional Geology

The Laver area is located north of the Skellefte District in the Fennoscandian Shield. Laver is surrounded by reddish, terrestrial, felsic (rhyolitic to dacitic) flows, ignimbrites, intrusions, dykes and volcaniclastic rock as well as mafic to intermediate (basaltic to andesitic) flows, tuffs, intrusions, dykes and volcaniclastic rocks of the Arvidsjaur Group (1.88-1.86 Ga). Sediments cover only minor parts of the region. Their metamorphic grade is normally upper greenschist to lower amphibole facies. The supracrustal rocks are intruded by Early Svecofennian granitoids (ca. 1.88-1.86 Ga, Kathol et al. 2005) also of Arvidsjaur type.

2.2 Local Rock Types

The host rocks in Laver are various ca 1.9 Ga old porphyries of felsic to mafic composition. Most of them are feldspar porphyritic with fine grained matrix and a dacitic-andesitic composition, but rhyolites and basalts occur too. The volcanic rocks consist of lava flows, pyroclastic rocks, sub-volcanic intrusions and dykes. Porphyritic texture and flow-banding are common. Associated with these porphyries there are breccias, volcaniclastic rocks and mass flows derived from the above mentioned porphyries, some of these also contain pumice clasts. There are also some minor reworked sedimentary rocks in which grading and slumping can be observed. Younger dykes and fault cross-cut the porphyries, volcaniclastic rocks and sedimentary rocks.

The mineralized rocks are strongly altered, mainly by pervasive silicification but also by quartz-veining. Minor biotite, epidote, chlorite, garnet, sericite, K-feldspar, skarn and carbonate alterations were observed too.

The metamorphic grade is probably of upper greenschist to lower amphibole facies as biotite, amphiboles and garnets are quite common. The rock types are in part very well-preserved (pumice clasts, volcanic breccias, slumping etc.), but are strongly deformed, altered and brecciated in other zones.

2.3 Mineralization

The Laver mineralization is a large volume, low grade, porphyry-style Cu-Au-Mo-Ag mineralization (Figure 2 & 3). The mineralization comprise mainly of sulphides in dissemination and veins. The main minerals (visually) are pyrite, chalcopyrite, pyrrhotite, molybdenite, magnetite and sphalerite. Arsenopyrite, galena, hematite, bornite and some native copper were also observed. The mineralization is not defined at depth and strike extension.

The host rocks are normally strongly silicified when mineralized and the edge of the mineralization cross cuts the rock type contacts.

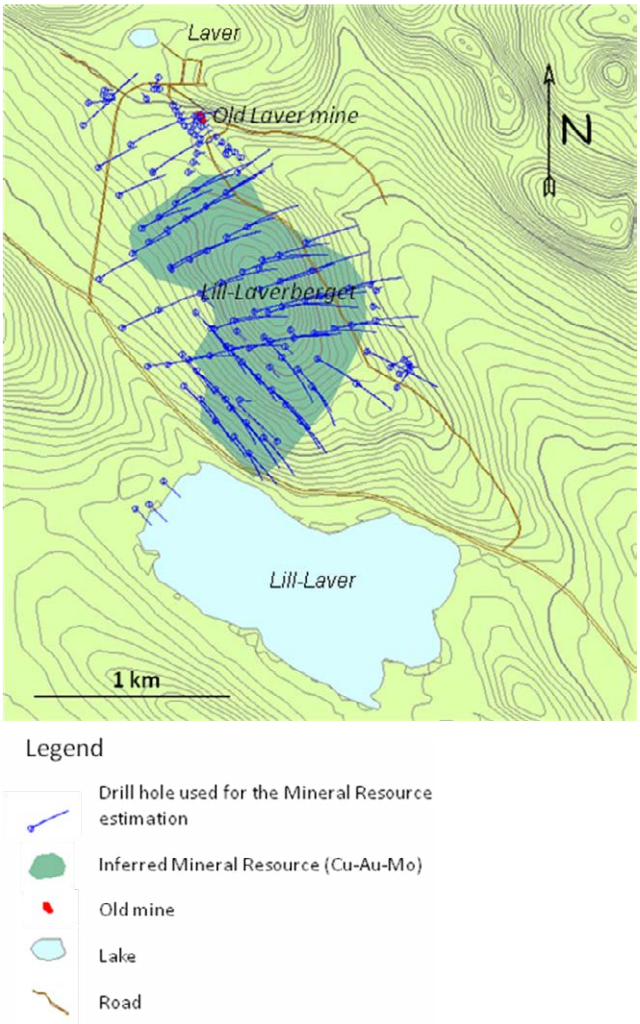

Figure 2. The Laver mineralization, surface map.

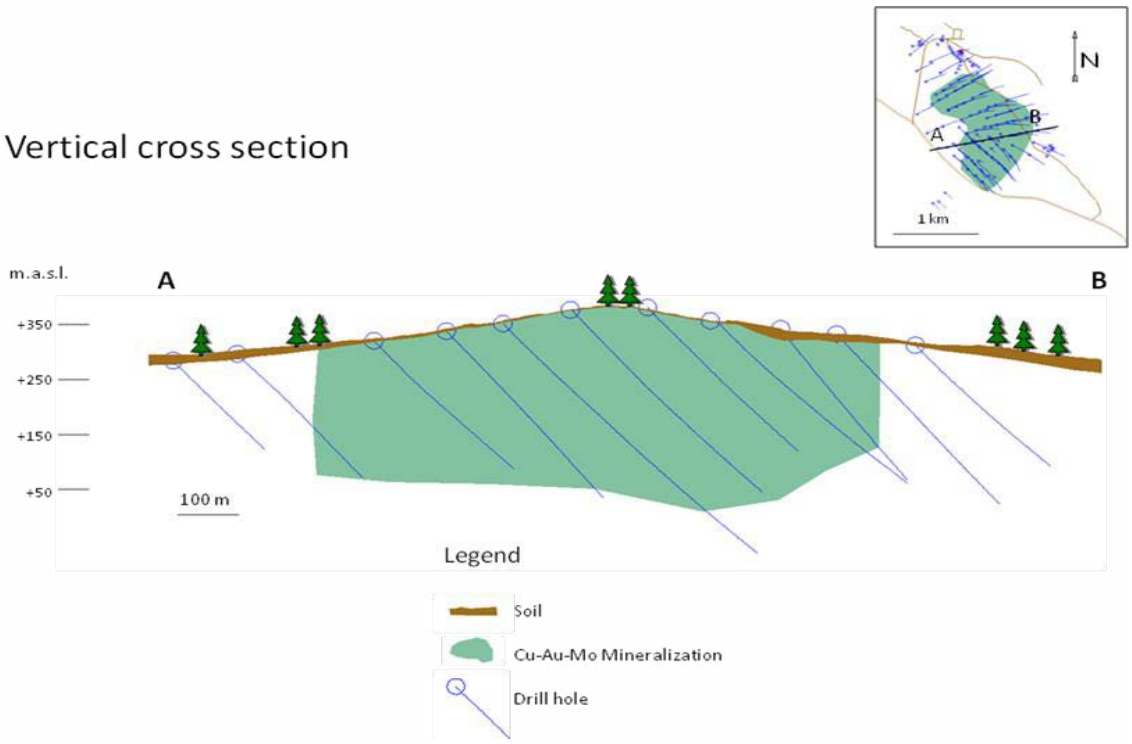

Figure 3. Vertical cross section of the Laver mineralization.

3 Mineral Resource Estimate

A Mineral Resource estimate was recently completed and was published on November 22nd 2012. This gave an Inferred Mineral Resource of 690 Mt @ 0.20% Cu, 0.12 g/t Au, 2.8 g/t Ag and 35 g/t Mo.

The estimation is based on 16 geological 2D interpretations and analysed grades in drill hole sections in 62 diamond drill holes. A 3D model was made to define the volume for the estimation (Figure 4). The grades were estimated in blocks by Ordinary Kriging. Dynamic anisotropy along the strike and dip of the mineralization was used to control the interpolation.

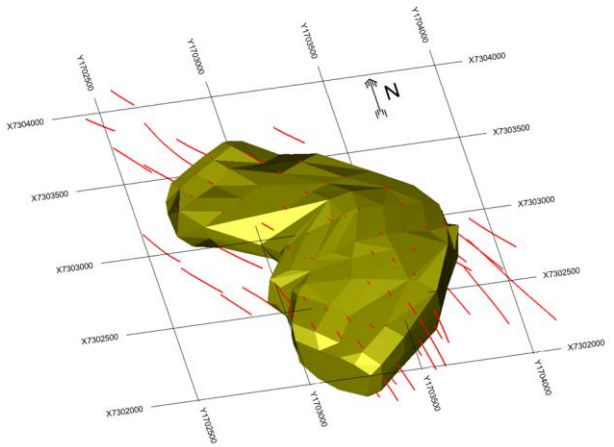

Figure 4. 3D picture of the Laver mineralization (RT 90, 500 m grid).

4 Plans

The Inferred Mineral Resource estimation is a milestone for the new Laver deposit and Boliden intends to continue the exploration and evaluation of the deposit. A conceptual study has recently started.

Acknowledgements

Thanks to Boliden Mineral AB and all other persons who have contributed to our present knowledge about the Laver mineralization.

References

Du Rietz, T. (1945) The alteration of the rocks in the copper deposit at Laver in N. Sweden SGU Ser. C 467

Kathol, B., Weihed, P., Antal Lundin, I., Bark, G., Bergman Weihed, J., Bergström, U., Billström, K., Björk, L., Claesson, L., Daniels, J., Eliasson, T., Frumerie, M., Kero, L., Kumpulainen, R.A., Lundström, H., Lundström, I., Mellqvist, C., Pettersson, J., Sköld, T., Sträng, T., Stølen, L.-K., Söderman, J., Triumf, C.-A., Wikström, A., Wikström, T. & Årebäck, H. (2005) Regional geological and geophysical maps of the Skellefte District and surrounding areas: Bedrock map. Sveriges geologiska undersökning Ba 57:1

Ödman, O. H. (1943) Geology of the copper deposit at Laver, N. Sweden. SGU Ser. C 452

Ödman, O. H. (1945) - A nickel-cobalt-silver-mineralization in the Laver copper mine, N. Sweden. SGU Ser. C 470

Weihed, P. (2001) A review of Palaeoproterozoic intrusive hosted Cu-Au-Fe-oxide deposits in northern Sweden. In Weihed, P. (ed.): Economic geology research. Vol. 1, 1999–2000. Uppsala 2001. Sveriges geologiska undersökning C 833, pp. 4–32

The Muine-Toyoha magmatic-hydrothermal system: Pliocene–Pleistocene base-metal mineralization related to magmatic intrusion beneath an andesite volcano

Yasushi Watanabe
Geological Survey of Japan, AIST
Higashi 1-1-1, Tsukuba, Japan

Eijun Ohta
Geological Survey of Japan ,AIST
Odori Nishi 5, Chuo-ku, Sapporo, Japan

Abstract. Studies on geology, hydrothermal alteration and mineralization, geochronology and geophysics are synthesized to propose an evolutionary model of the Muine-Toyoha magmatic hydrothermal system in the Northeast Japan arc. A magmatic intrusion subsequent to volcanic eruption at Muine at about 3 Ma exsolved immiscible vapour and brine phases, the latter of which was enriched in base metals and silver. The vapour phase ascended and condensed to form acid fluids that caused advanced argillic alteration near the volcanic centre and associated smectite alteration at the margin. The brine phase flowed northwards to the fracture zone at the Toyoha deposit where the brine mixed with meteoric water, resulting in precipitation of base metals and silver. Boiling of the hydrothermal fluids after the deposition of the sulfide minerals released vapour including H_2S, which was oxidized above the water table, resulting in the formation of steam heated alteration near the surface.

.

Keywords. Muine, Toyoha, magmatic-hydrothermal system, alteration, brine, vapour

1 Introduction

A link between intermediate, calc-alkaline volcanism and hydrothermal mineralization has been recognized in subduction-related magmatic arcs. This link is reflected in stratovocanoes associated with porphyry Cu deposits as well as base metal and precious metal deposits (Sillitoe, 1973; Lexa et al., 1999).

Association of epithermal base metal and precious metal deposits with Pliocene andesite volcanoes is observed in a northern part of the Northeast Japan arc (Figure 1). The best studied example in the region is the Toyoha polymetallic Pb-Zn-Ag-In deposit, a vein type epithermal deposit, which is related to the magmatic activity at a calc-alkaline Muine andesite volcano of Pliocene age. This magmatic-hydrothermal system is young and has been only slightly eroded, resulting in the preservation of surface expression of the hydrothermal alteration. This paper revisits the relationship among the magmatism, hydrothermal alteration and mineralization, based on the compilation of the previously reported data and recently obtained results of magnetotelluric surveys (Takakura and Matsushima, 2003, NEDO, 2011).

2 Geology and mineralization

2.1 Geology in the Muine-Toyoha area

The Muine volcano is located in a Late Pliocene NW-striking volcanic chain composed of polygenetic andesite volcanoes in the northern part of the Northeast Japan arc.

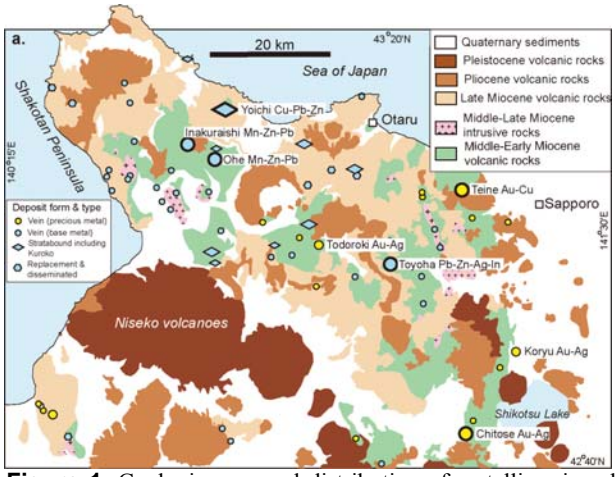

Figure 1. Geologic map and distribution of metallic mineral deposits and occurrences in northern part of Northeast Japan arc (Watanabe, 2002).

The basement rocks in the Muine-Toyoha area are pre-Miocene flysh sequence of the Usubetsu Formation, which consists of alternating beds of sandstone and mudstone. Late Oligocene and Miocene granodiorite intrusion into the basement rocks resulted in widespread biotite hornfels metamorphism in the basement rocks. This metamorphism lowered the porosity of the basement rocks (1.3%), which is significantly lower than Miocene volcanic (4.4%) and sedimentary rocks (15.6%). The basement rocks are covered by 1,000-1,500 m thick Miocene rocks, which are composed of Early-Middle Miocene volcanic and sedimentary rocks accumulated in a submarine environment and overlying Late Miocene andesite lavas erupted in a subaerial environment.

The Pliocene Muine volcano is a N-S elongated body consisting of two-pyroxene andesite lavas with a flat ridge. Several phreatic craters, 250-500m in diameter, are present in landslide deposits and andesite lavas in the volcano. These craters cluster mainly in two areas (the northern and southern centres) (Figure 2). Lacustrine breccia, sandstone and siltstone composed of volcanic fragments are observed in these craters. Present-day geothermal activity is not recognized in these craters. Landslide and debris flow deposits originated mainly in

the northern and southern centres of these phreatic craters. Several arsenic occurrences present at the margin of the Muine andesite lavas.

2.2 Mineralization at the Toyoha deposit

The Toyoha deposit is located about 4 km north from the top of Mt. Muine (Figure 2). The deposit consists of E-striking and NW-striking veins. The major E-striking Tajima and Harima composite vein system is about 2km long parallel to the Shiraigawa River. Two stages of vein formation are recognized in the deposit. The ore minerals of the early stage veins are characterized by an assemblage of sphalerite, galena and pyrite in gangue quartz whereas those of the late stage by the presence of various kinds of Sn, In and Ag minerals in addition to the assemblage of the early stage (Ohta, 1991). Fluid inclusion studies show that the salinity of the fluids in the inclusions hosted in quartz and sphalerite decreases from 9 to 0.5 NaCl equivalent wt.% with decreasing temperature from 300°C to 150°C (Yajima and Ohta, 1979; Sanga et al., 1992; Ono and Sato, 1994; Masuda et al., 1996). This suggests that the saline ore solutions were diluted by low temperature meteoric water in the deposit. Fluid boiling is suggested locally by the vein texture that changes from lower sulfide ore to upper illite-rich clay through breccia in the Shinano vein (Sanga et al., 1992), and co-existence of vapour-rich and liquid-rich inclusions in quartz from the Nagato vein of the deposit (Shimizu and Aoki, 2001a).

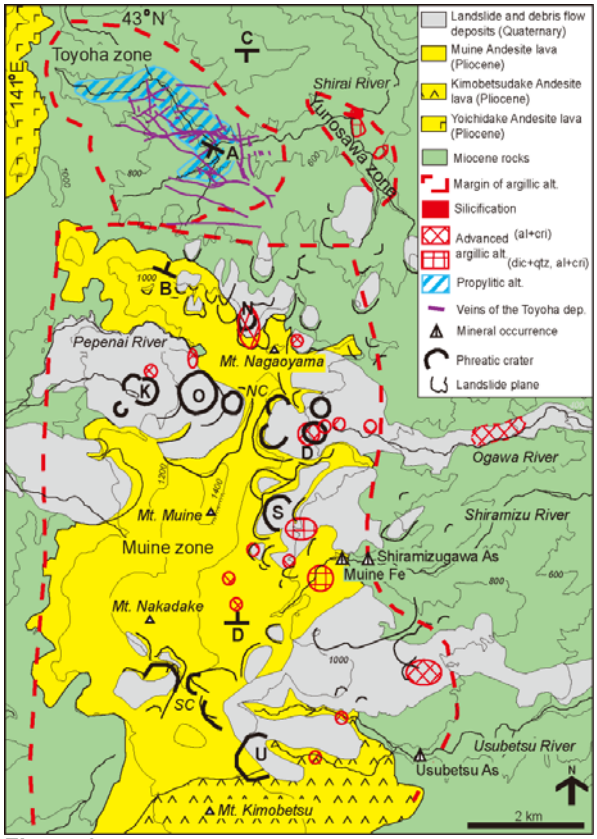

Figure 2. Geologic map and hydrothermal alteration zones of the Muine-Toyoha area. Abbreviations of phreatic craters and crater centres are; D: Daijagahara, K: Konuma, N: Nagaoyama, O: Ohnuma, S: Shiramizugawa and U: Usubetsu, NC: northern centre, SC: southern centre.

3 Hydrothermal alteration

Three major hydrothermal alteration zones are recognized in the Muine-Toyoha area (Figure 2). Muine zone, about 10 km by 6 km in plan occurs in and around the Pliocene Muine andesite lavas. This zone is characterized by sporadic occurrences of advanced argillic assemblage near the phreatic craters and extensive smectite fringing the andesite lavas. Arsenic occurrences are included within the smectite zone. The advanced argillic alteration is hosted by hydrothermal breccia, massive andesite lavas and crater-filling sedimentary rocks. Porous and massive silicification formed by cristobalite and tridymite are common. Alunite is generally cryptocrystalline and is associated with cristobalite and tridymite, but phanerocrystalline alunite is also present in some places. The sulfur isotopic value of alunite varies mainly from 9 to 32‰. There is a slight variation in individual phreatic craters; 9.1-15.9‰ in the Konuma, Ohnuma and Usubetsu craters, 15.3 and 16.7‰ in an extinct fumarole located between Muine and Nakadake, 17.4-21.5‰ in the Nagaoyama and Daijagahara craters, and 26.7 and 31.1‰ in the Shiramizugawa crater. The relatively low sulfur isotopic range (9-15‰) at the Konuma, Ohnuma and Usubetsu craters is similar to that of volcanic SO_2 erupted from Usu volcano (6-17‰) during the eruption in 1977-1978 (Sakai and Uyeda, 1984).

Toyoha Zone, 4 by 2.5 km in size, fringes the veins of the Toyoha deposit. The alteration zone is thickest in the mine site (>800 m) and decreases in thickness to 300 m at the eastern margin of the zone. The host rocks of this zone are Middle-Early Miocene andesite and sedimentary rocks. The alteration zone is divided into shallow argillic and deeper propylitic and sericitic alteration. The propylitic-sericitic alteration changes in assemblage form quartz-illite-pyrite to quartz-chlorite-calcite-albite as the distance from the ore veins increases (Sawai, 1984). A quartz-epidote-K-feldspar assemblage becomes dominant at the southern margin of the deposit where the present rock temperature exceeds 100°C (Masuda et al., 1996). Sulfur isotopic value of sulfides in the deposit is limited mostly to a narrow range between 4 and 10‰ (average 7‰) irrespective of the mineral species, sample elevations and mineralization stage (Hamada and Imai, 2000). This sulfur isotope range is similar to that of volcanic H_2S erupted from Usu volcano (3-8‰) in 1977 and 1978 (Sakai and Ueda, 1984).

The Yunosawa zone is exposed in a 2 x 1 km area at the eastern extension of the Toyoha zone. This zone corresponds to the area of present high rock temperature, where geothermal energy has been explored. This zone is 300-350 m thick and was formed in steam-heated environment near the surface. An advanced argillic assemblage mixed with an argillic assemblage is widespread on the surface. Dickite becomes dominant at depth (185-350m from the surface) and pyrophyllite occurs at the base of this zone (300-350m from the surface). A cristobalite-alunite assemblage occurs in a sulfate-rich low-temperature fumarole with a halo of cristobalite and sublimation sulfur. A sulfur isotopic value, -2.8‰ of alunite, together with 3.2‰ of SO_4^{2-} in

the present spring water is reported (NEDO, 1988).

4 Temporal relationship

A compilation of K-Ar age dates of the Muine andesite lavas and hydrothermal illite in the Toyoha deposit shows that the andesite volcanism at the Muine volcano occurred at 3.2-2.9 Ma, which was followed by the hydrothermal activity in the Toyoha zone (Figure 3). These hydrothermal activities continued over two million years. This temporal relationship suggests that the hydrothermal mineralization at Toyoha was not directly related to the magmatic eruption at Muine.

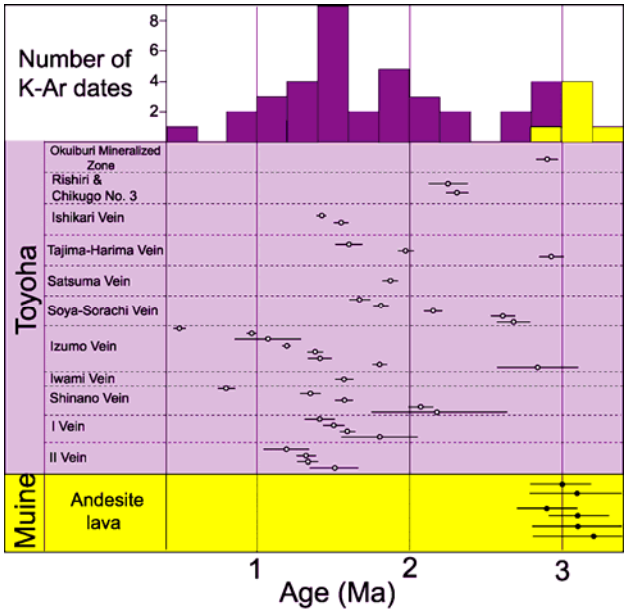

Figure 3. K-Ar dates of the Muine andesite lavas and hydrothermal illite associated with ore veins in the Toyoha deposit (Sawai et al., 1989; Masuda et al., 1996; Shimizu and Aoki, 2001b) and hydrothermal illite in the Yunosawa zone (Sawai et al., 1989)..

5 Magnetotelluric survey results

An E-W magnetotelluric survey conducted in the area (Takakura and Matsushima, 2003) shows that an extremely conductive zone is present beneath the Muine volcano, in addition to a conductive zone near the surface (Figure 4). The near-surface conductive zone corresponds to hydrothermal alteration at Muine. The deep conductive zone, the top of which is approximately 2 km below the surface, is interpreted as a large hydrothermal reservoir with abundant hot water or melted magma (Takakura and Matsushima, 2003), because the zone corresponds to zone of elastic wave attenuation detected by a seismic survey (Ohminato and Takakura, 1999). A new N-W profile by NEDO (2011) shows that this extremely low conductive zone extends northwards near the base of the Toyoha zone. This new profile also shows two separated low resistivity zones, corresponding to the locations of the Daijagahara-Ohnuma-Konuma craters and Nagaoyama crater above the extremely low conductivity zone.

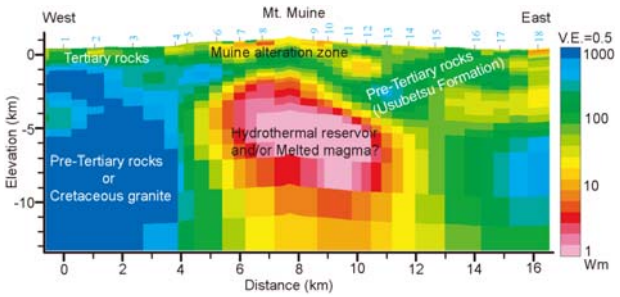

Figure 4. 2D resistivity model for the E-W profile of the Muine-Toyoha area from the Magnetotelluric survey (Takakura and Matsushima, 2003). V.E.: vertical exaggeration.

6 Model proposed for the Muine-Toyoha magmatic-hydrothermal system

The studies on geology, hydrothermal alteration and mineralization, geochronology and geophysics mentioned above are synthesized to propose an evolutionary model of the Muine-Toyoha magmatic hydrothermal system described below (Figure 5).

A magmatic intrusion subsequent to volcanic eruption at Muine at about 3 Ma exsolved immiscible vapour and brine phases, the latter of which was enriched in base metals and silver. The aqueous vapour that contained CO_2, SO_2, H_2S, HCl and other species (Hedenquist, 1995) ascended due to its low density and either discharged to the surface as volcanic fumaroles or was condensed at depth, forming acid fluids that caused the advanced argillic alteration in a magmatic-steam environment on the northern centre (Ohnuma, Konuma, Daijyagahara) and a magmatic hydrothermal environment on the margin of the northern centre (Nagaoyama, Shiramizugawa) in the Muine alteration zone. The acid fluids then flowed along the contact of the Muine andesite lavas and underlying Miocene formations, and were neutralized by reaction with host rock and precipitated smectite and arsenic on the margin of the hydrothermal system (Figure 5).

The brine phase that may have been enriched in base metals and silver (Heinrich et al., 1999) flowed northwards near the Shiraigawa River, where E-trending strike-slip fractures were present (Watanabe, 1990). The impermeable hornfels of the Usubetsu Formation above the intrusive body together with the density of the brine may have promoted this lateral flow by providing a hydrologic cap to the fluids; the brine ascended through fractures near the Shiraigawa River and mixed with meteoric water within the permeable Miocene volcanic rocks above the Usubetsu Formation, as indicated by the fluid inclusion data. This mixing reduced the salinity and temperature of the fluids, resulting in precipitation of base metals and silver in the Toyoha deposit.

Boiling of hydrothermal fluids after the deposition of the sulfide minerals in the Toyoha deposit released vapour including H_2S, which was oxidized above the water table, resulting in the formation of steam heated alteration at Yunosawa.

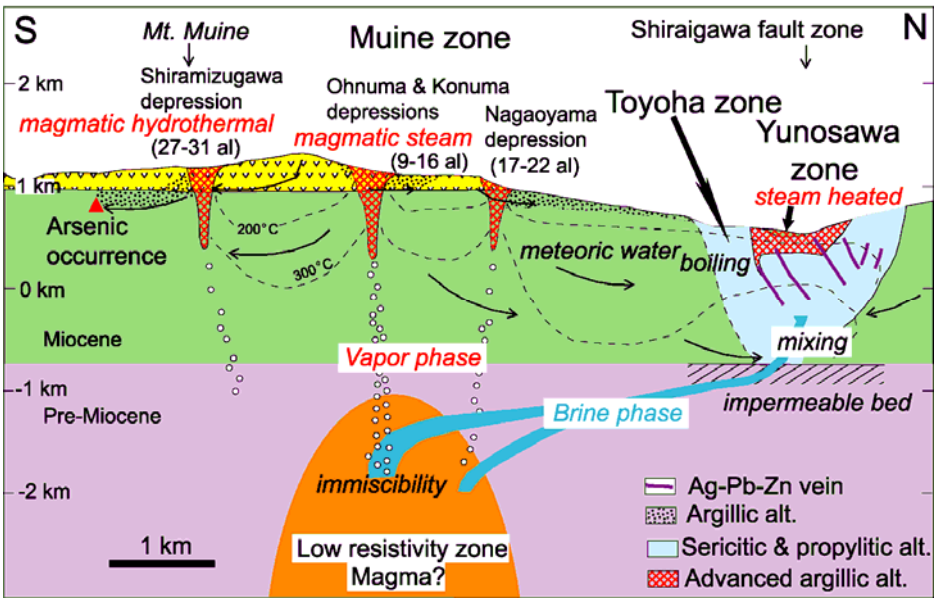

Figure 5. N-S section of the Muine-Toyoha magmatic hydrothermal system. Locations of the low resistivity zone, Yunosawa alteration zone and arsenic occurrence are projected on this section. Number within parenthesis is sulfur isotopic range of alunite. The location of this section is shown in Figure 2 as C-D.

References

Hamada M, Imai A (2000) Sulfur isotopic study of the Toyoha deposit, Hokkaido, Japan-Comparison between the earlier-stage and the later-stage veins-. Resource Geology 50: 113-122

Hedenquist JW (1995) The ascent of magmatic fluid: Discharge versus mineralization. Mineralogical Association of Canada, Short Course 23: 263-289

Heinrich CA., Gunther D, Audetat A, Ulrich T, Frischknecht R (1999) Metal fractionation between magmatic brine and vapor, determined by microanalysis of fluid inclusions. Geology 27: 755-758

Lexa J, Stohl J, Konecny V (1999) The Banska Stiavnica ore district: relationship between metallogenetic processes and the geological evolution of a stratovolcano. Mineralium Deposita 34: 639-654

Masuda K, Kamiki T, Narui E (1996) Polymetallic mineralization at the Toyoha south district, Hokkaido, Japan. Resource Geology 46: 45-61 (in Japanese)

NEDO (1988) Report on Geothermal Development Promotion Survey, No. 12 Toyoha area. Tokyo, New Energy Development Organization: 1156p (in Japanese)

NEDO (2011) Report on Geothermal Development Promotion Survey in the Toyoha Area during the fiscal year Heisei 22. Tokyo, New Energy Development Organization: 656p (in Japanese with English abstract)

Ohminato T, Takakura S (1999) Seismic survey around Mt. Muine. Report of Regional Geological Structure Survey during the Fiscal Year Heisei 10: Southern Hokkaido Area. Ministry of International Trade and Industry: 125-145 (in Japanese)

Ohta E (1991) Polymetallic mineralization at the Toyoha Mine, Hokkaido, Japan. Mining Geology 41: 279-295

Ono S, Sato J (1994) Ore minerals and fluid inclusions from the veins in the northwestern part of the Toyoha Pb-Zn-Ag minng district, Hokkaido, Japan. Resource Geologu 44: 369-379

Sakai H, Ueda H (1984) Sulfur isotopic values of volcanic gases, in Ossako, J., ed., Fundamental Research for Predicting Volcanic Eruption through Observation of Volcanic Gases

Sanga T, Kanbara H, Shoji T, Takeyama T. (1992) Characteristic feature of the late stage mineralization and its vein system at the Toyoha polymetallic vein deposits, Hokkaido, Japan. Mining Geology 42: 85-100 (in Japanese with English abstract)

Sawai O (1984) Wall rock alteration around the Motoyama deposits, Toyoha mine, Hokkaido, Japan. Mining Geology 34: 173-186 (in Japanese with English abstract)

Sawai O, Okada T, Itaya T (1989) K-Ar ages of sericite in hydrothermally altered rocks around the Toyoha deposits, Hokkaido, Japan. Mining Geology 39: 191-204

Shimizu T, Aoki M (2001a) Fluid inclusion and oxygen isotope studies of hydrothermal quartz from Yunosawa Stream and Nagatozawa Stream near the Toyoha Ag-Pb-Zn deposit, Hokkaido. Shigen-Chishitsu 51: 133-144 (in Japanese with English abstract)

Shimizu T, Aoki M (2001b) Overprinted Cenozoic hydrothermal activities at the Toyoha Ag-Pb-Zn deposit, Japan. In Cidu, ed., Water Rock Interaction 2001: 757-760

Sillitoe RH (1973) The tops and bottoms of porphyry copper deposits. Economic Geology 63: 799-815

Takakura S, Matsushima N (2003) Magnetotelluric investigation of hydrothermal system and heat source in the Muine-Toyoha geothermal area, Japan. Resource Geology 53: 213-220

Watanabe Y. (1990) Pull-apart vein system of the Toyoha deposit, the most productive Ag-Pb-Zn vein-type deposit in Japan. Mining Geology 40: 269-278

Watanabe Y (2002) Late Cenozoic metallogeny of Souothwest Hokkaido, Japan. Resource Geology 52: 191-210

Yajima J, Ohta E (1979) Two-stage mineralization and formation process of the Toyoha deposits, Hokkaido, Japan. Mining Geology 29: 291-306.

Temporal and spatial relationships between porphyry and epithermal systems: a hydrological perspective

Philipp Weis, Thomas Driesner and Christoph A. Heinrich
Institute of Geochemistry and Petrology, ETH Zurich, Switzerland

Abstract. Porphyry and epithermal systems are believed to be genetically linked and formed by fluids expelled from crystallizing hydrous magma chambers in the Upper Crust. Numerical simulations of the physical hydrology of porphyry copper systems demonstrate that metal enrichment to economic grades occurs at a hydrological divide between areas of ductile and brittle rock behaviour. A dynamic permeability model responding to changes in temperature and fluid pressure representing hydraulic fracturing and the brittle-ductile transition in a geologically realistic way proved to be essential to explain a precipitation mechanism in agreement with observations. The resulting self-organizing hydrothermal system stabilised a temperature-pressure front along an inner part dominated by near-lithostatically pressured hot magmatic fluids that is cooled from the outside by meteoric fluids under hyrdostatic conditions. With inward crystallization of the pluton, fluid production decreases and the front gradually retreats to greater depths, allowing earlier intense but barren quartz veining to be overprinted by copper precipitation. The simulations also provide a physical explanation for the transition to epithermal conditions at shallower levels with pulses of magmatic fluids mixing with convecting ambient fluids.

Keywords. Magmatic-hydrothermal systems, porphyry deposits, epithermal deposits, numerical simulations, permeability, hydraulic fracturing, brittle-ductile transition.

1 Introduction

Porphyry copper and epithermal gold systems are major economic resources, located above active and ancient subduction zones with intermediate to felsic magmatic activity (Sillitoe 2010; Henley and Ellis 1983). Fluids expelled from cooling hydrous magma chambers in the Upper Crust are believed to be the transport medium from a solidifying source pluton at depth to the site of metal precipitation at shallower levels (Hedenquist and Lowenstern 1994).

The similarities among a large number of deposits call for a comparatively simple and uniform formation mechanism, and a close relationship between the evolution of porphyry and epithermal systems has been proposed by several studies (e.g. Sillitoe 2010). Comprehensive conceptual models should therefore attempt to explain mineralization, alteration patterns and vein sequences in accordance with heat and mass balance calculations and plausible transport processes.

Here, we present new insights that have emerged from numerical simulations with a geologically-constraint model describing the physical hydrology of porphyry copper systems (Weis et al. 2012).

2 Numerical Method

The model configuration has been kept as simple as possible to quantify the first-order controls on the hydrothermal system (Fig. 1). Our numeric process model is an implementation of the CSMP++ software and solves for heat and mass advection as well as heat conduction in a continuum, porous medium approach (see Weis et al. 2012 for details).

Numerous fluid inclusion studies document the state, temperature, pressure and composition of the fluid at the time of entrapment and show that the presence of NaCl has a significant influence on phase separation from a single-phase intermediate-density fluid to a high-salinity, high-density brine and a low-salinity, low-density vapour phase during ascent through fractured rock (Redmond et al. 2004). The model therefore incorporates a thermodynamic module that accurately represents fluid properties of the system H_2O-NaCl for the relevant temperature and pressure range (Driesner and Heinrich 2007; Driesner 2007). Fluid and rock are assumed to be in thermal equilibrium at every modelling time step (Coumou et al. 2009).

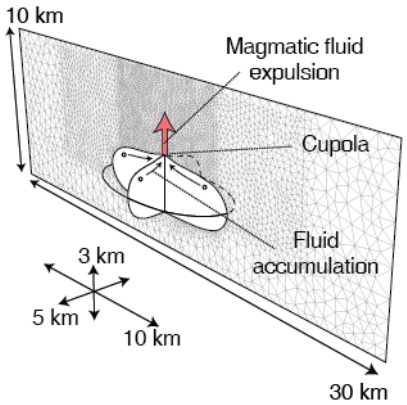

Figure 1. An initially hot pluton with the dimensions of the Yerington Batholith (Dilles 1987) gets successively cooled by heat conduction to the surrounding host rock and heat advection by convecting meteoric fluids. Magmatic fluids are injected through a cupola in the roof the magma chamber at about 5 km depth and the rate of fluid production is calculated to be proportional to the rate of crystallization. We consider accumulation effects of a 3-dimensional pluton into our 2-dimensional model (modified from Weis et al. 2012).

3 Dynamic Permeability

First simulations with different static system-scale permeabilities neither produced characteristic fluid states nor an efficient precipitation mechanism. We

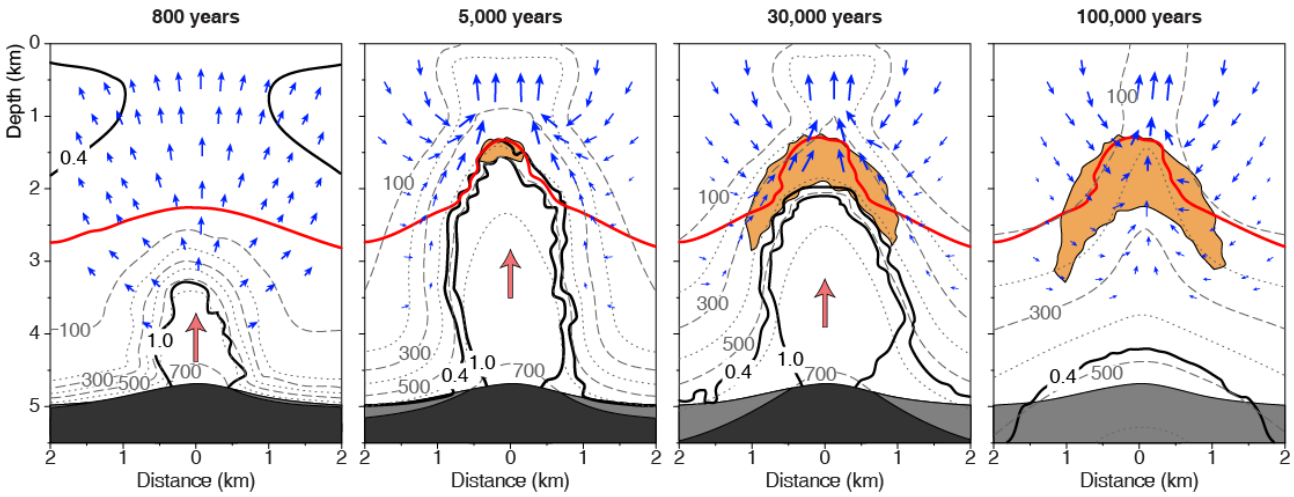

Figure 2. Temporal and spatial evolution of a porphyry system. Fluid pressure is shown in relation to lithostatic pressure (solid black lines): values above 0.4 and 1.0 denote fluid pressures above hydrostatic and lithostatic, respectively. Temperature is given in degrees Celsius (dashed and dotted grey lines). Ascending magmatic fluids are illustrated with schematic red arrows and fluid flow of cooler predominantly meteoric fluids are shown with blue arrows. The area of most intense fracturing is shown with the contour line of the 10% vein volume potential (red line) and the area of metal precipitation with the outline of a copper enrichment potential of 500 (orange field), which relates to an upper limit of about 1.25 wt% copper ore grade (modified from Weis et al. 2012).

therefore assembled a dynamic permeability model by mapping existing models describing the permeability, stress state and failure conditions of the Upper Crust to our continuum, porous media approach.

Only the implementation of this module lead to simulations that could reproduce observations and identifies the following hydrological key parameters for metal enrichment to economic grades:

a) Permeability generally follows a characteristic depth-dependent profile of tectonically active crust (Ingebritsen and Manning 2010).
b) This permeability profile is related to a critically stressed brittle crust (Zoback et al. 2002), leading to a failure criterion at near-hydrostatic fluid pressures (Cox 2010).
c) Permeability closes and stress state relaxes at elevated temperatures due to increasingly ductile behaviour of the rock (Fournier 1999), resulting in a near-lithostatic failure criterion (Cox 2010). In our simulations, we assume the brittle-ductile transition to happen between 370° and 500°C (Hayba and Ingebritsen 1997).
d) Permeability is temporarily increased to values of up to two orders of magnitude higher (Ingebritsen and Manning 2010) whenever fluid pressures exceed a stress-state dependent failure criterion.

4 Hydrology of Copper Porphyry Systems

The hydrothermal system self-organizes into a fluid plume with two distinct hydrological regions (see Weis et al. 2012). The inner part is dominated by magmatic fluids at high temperatures (>600°C) and near-lithostatic pressures (Fig. 2). The elevated temperatures tend to close permeability while high fluid pressures keep interconnected pore space open or hydrofracture the rock as soon as the near-lithostatic failure criterion is exceeded. This mechanism creates fracturing-sealing cycles and magmatic volatiles move through the inner part in overpressure-permeability waves.

From the outside, meteoric waters convecting under near-hydrostatic conditions cool the system and help stabilizing a sharp temperature-pressure front dividing the rock into areas of brittle and ductile rock behaviour. The temperature and pressure drop experienced by the pulses agrees with the conditions for copper mineralisation in porphyry systems as inferred from fluid inclusion studies and experiments (Hezarkhani et al. 1999; Landtwing et al. 2005). Assuming copper precipitation within the temperature interval of 350° to 450°C allows estimating the potential ore grade. Scaling the accumulated amount of permeability increase to a potential quartz vein volume serves as a proxy for comparisons with observed vein densities (Weis et al. 2012).

5 Temporal and Spatial Evolution

The simulation starts with an instantaneous intrusion of a 900°C hot magma chamber into a host rock with temperatures of a normal geothermal gradient. As soon as the outer rim of the pluton reaches an assumed solidus temperature of 700°C, the pluton starts to crystallize and to exsolve saline, metal-bearing volatiles that are injected at the cupola (Fig. 1). Due to the large surface area of the initial pluton, fluid production rates during the early stage are high, leading to a strong overpressuring in response to the forced injection of additional fluid mass (Fig. 2; 800 years). As the cold brittle crust is near-critically stressed, permeability is readily increased by hydrofracturing, allowing the magmatic volatiles to escape rapidly.

On ascent, the hot magmatic volatiles will eventually heat the surrounding rock to temperatures above the brittle-ductile transition. This change establishes the fracturing-healing cycles and overpressure-permeability

waves in the region of near-magmatic temperatures and near-lithostatic fluid pressures. During this early phase, magmatic fluids are able to locally move the brittle-ductile transition up to depths as shallow as 2 km. There, the depth-dependent background permeability increases and meteoric convection can cool more efficiently from the outside (Fig. 2; 5,000 years).

This early phase produces intense quartz veining with no significant copper precipitation process in place yet. Tentatively, this is the stage of stockwork veining and most intense potassic alteration. The duration of the early barren stage approaches the relatively short time scales that have been inferred from analysis of potassic alteration halos in porphyry deposits (Cathles and Shannon 2007).

Once the sharp temperature-pressure front is stabilized, copper can start to be efficiently enriched at a depth of about 2km. At the same time, conditions favourable for epithermal gold deposits develop above the porphyry system. Pulses of magmatic fluids that episodically cross the brittle-ductile transition mix with the ambient fluids in variable proportions. Temperatures are between 100° and 350°C and follow a boiling curve with depth profile. With the incoming surges of magmatic fluids, this region fluctuates between a two-phase zone spanning the whole distance from porphyry system to surface and a slightly cooler state with phase separation being limited to the uppermost part. Episodic boiling events have been inferred for several epithermal deposits and gold mineralization is usually limited to thin layers (Izawa et al. 1990). Pressure and temperature conditions of this region are also characteristic for lithocaps of advanced argillic alteration that are located above or overprinting the tops of porphyry deposits (Sillitoe 2010).

In the following few thousands of years, the hydrological divide stays intact and its location gradually retreats as the remaining source pluton gets smaller in volume and hence produces magmatic fluids at a decreasing rate (Fig. 2; 30,000 years). During this phase, copper-bearing veins are overprinting areas that had previously been intensely fractured.

The process continues until all magmatic fluids have been released and convection of meteroric fluids removes the remaining heat of the cooling pluton (Fig. 2; 100,000 years). This phase could be related to overprinting sodic alteration in some deposits and can potentially lead to redistribution of copper.

6 Discussion

The generic numerical simulations reproduce key observations of porphyry and epithermal systems and explain their formation from a hydrological perspective. However, the chemical consequences of this hydrology and potential feedbacks from fluid-rock interactions are currently only implemented in a very simple form. Integrating a geochemical perspective to the model in order to predict transport and precipitation of gold will require more insight from measurements and observations and further development of the numerical tools.

The same holds for the addition of a magmatic perspective. We adopted the classical second-boiling scenario of a crystallizing pluton (Burnham and Ohmoto 1980), which possibly neglects internal dynamics within the magma chamber that may have an impact on fluid production rates and the hydrological system. However, unless these dynamics lead to volcanic eruptions, the general mechanism of the self-organizing magmatic-hydrothermal system will presumably still be in place.

References

Burnham CW, Ohmoto H (1980) Late-stage processes of felsic magmatism. Mining Geology Special Issue:1-11.

Cathles LM, Shannon R (2007) How potassium silicate alteration suggests the formation of porphyry ore deposits begins with the nearly explosive but barren expulsion of large volumes of magmatic water. Earth Planet Sci Lett 262:92-108.

Coumou D, Driesner T, Weis P, Heinrich CA (2009) Phase separation, brine formation, and salinity variation at Black Smoker hydrothermal systems. J Geoph Res 114:B03212.

Cox SF (2010) The application of failure mode diagrams for exploring the roles of fluid pressure and stress states in controlling styles of fracture-controlled permeability enhancement in faults and shear zones. Geofluids 10:217-233.

Dilles JH (1987) The petrology of the Yerington Batholith, Nevada: evidence for the evolution of porphyry copper ore fluids. Econ Geol 82:1750-1789.

Driesner T (2007) The system H2O-NaCl. Part II: Correlations for molar volume, enthalpy, and isobaric heat capacity from 0 to 1000 degrees C, 1 to 5000 bar, and 0 to 1 X-NaCl. Geochim Cosmochim Acta 71:4902-4919.

Driesner T, Heinrich CA (2007) The system H2O-NaCl. Part I: Correlation formulae for phase relations in temperature-pressure-composition space from 0 to 1000 degrees C, 0 to 5000 bar, and 0 to 1 X-NaCl. Geochim Cosmochim Acta 71:4880-4901.

Fournier RO (1999) Hydrothermal processes related to movement of fluid from plastic into brittle rock in the magmatic-epithermal environment. Econ Geol 94:1193-1211.

Hayba DO, Ingebritsen SE (1997) Multiphase groundwater flow near cooling plutons. J Geophys Res 102:12235-12252.

Hedenquist JW, Lowenstern JB (1994) The role of magmas in the formation of hydrothermal ore-deposits. Nature 370:519-527.

Henley RW, Ellis AJ (1983) Geothermal systems ancient and modern – a geochemical review. Earth-Sci Rev 19:1-50.

Hezarkhani A, Williams-Jones AE, Gammons CH (1999) Factors controlling copper solubility and chalcopyrite deposition in the Sungun porphyry copper deposit, Iran. Miner Depos 34:770-783.

Ingebritsen SE, Manning CE (2010) Permeability of the continental crust: dynamic variations inferred from seismicity and metamorphism. Geofluids 10:193-205.

Izawa E et al. (1990) The Hishikari gold deposit – high-grade epithermal veins in quaternary volcanics of Southern Kyushu, Japan. J Geochem Explor 36:1-56.

Landtwing MR et al. (2005) Copper deposition during quartz dissolution by cooling magmatic-hydrothermal fluids: The Bingham porphyry. Earth Planet Sci Lett 235:229-243.

Redmond PB et al. (2004) Copper deposition by fluid cooling in intrusion-centered systems: New insights from the Bingham porphyry ore deposit, Utah. Geology 32:217-220.

Sillitoe RH (2010) Porphyry Copper Systems. Econ Geol 105:3-41.

Weis P, Driesner T, Heinrich CA (2012) Porphyry-Copper Ore Shells Form at Stable Pressure-Temperature Fronts Within Dynamic Fluid Plumes. Science 338:1613-1616.

Zoback MD, Townend J, Grollimund B (2002) Steady-state failure equilibrium and deformation of intraplate lithosphere. Int Geol Rev 44:383-401.

Fluid evolution in a super-giant porphyry Cu-Mo deposit: El Teniente, Chile

Jamie J. Wilkinson, Victoria H. Vry and Edward T. Spencer
Department of Earth Science & Engineering, Imperial College London, Exhibition Road, London, SW7 2AZ, UK

José Seguel
Superintendencia de Geología División El Teniente, CODELCO-Chile, Rancagua, Chile

Abstract. The magmatic-hydrothermal evolution at El Teniente has been deduced based on detailed description of field relationships, fluid inclusion petrography, scanning electron microscopy-cathodoluminescence (SEM-CL), microthermometry and laser ablation ICP-MS analysis (LA-ICP-MS). The P-T-X fluid evolution is characterized by early, high pressure exsolution of high salinity brines relating to pre- to early mineralization veining and potassic alteration, recognized most clearly in the A-porphyry complex. At the onset of the main mineralization stage a change in fluid properties occurred, characterized by a switch to lower density (liquid-like), low salinity fluids. It is interpreted that this is related to major brecciation that allowed rapid degassing, pressure-quench crystallization and migration of the locus of fluid exsolution to deeper in the melt column. In copper-rich mineralization stages, local P-T fluctuations led to the appearance of vapour-like fluids, probably by upward expansion of supercritical liquids in the one-phase field. Molybdenite-rich veins appear to show a contrasting behaviour with a transition from vapour-like to liquid-like fluids with decreasing depth, implying contraction of fluids in the one-phase field. The later reappearance of brines is linked to phase separation at lower pressures. LA-ICP-MS data highlight chemical heterogeneities between fluid types and individual intrusion-centred systems, indicating significant variations in melt-fluid partitioning of metals during the life of the deposit.

porphyry, fluid inclusions, copper, molybdenum

1 Introduction

The supergiant El Teniente porphyry Cu-Mo deposit is located in the Central Chilean porphyry-belt and is one of the world's largest deposits of its kind, hosting a pre-mining resource of over 12 billion metric tons of ore with grades averaging 0.65% Cu and 0.019 % Mo. Previous fluid models (Cannell, 2004; Cannell et al., 2005; Klemm et al., 2007) proposed a single, deposit-scale fluid evolutionary sequence that is perhaps surprising given the geological complexity and ~2 My history (Fig. 1). Much of the previous work was limited to fluid inclusions within quartz-dominated veins in and around the Teniente Dacite Porphyry Complex and thus did not incorporate data from earlier vein types recognized elsewhere (Vry et al., 2010). This study aims to understand the deposit-scale hydrothermal fluid evolution of the El Teniente system, building on geological observations that constrain a multistage formation model (Vry et al., 2010). In particular, we focus on veins sampled at depth within the early A-Porphyry system as these provide a record of the earliest mineralizing fluids at El Teniente and also preserve fluids trapped close to the magmatic interface.

2 Vein chronology

A new vein classification at El Teniente has defined thirteen vein types (Vry et al., 2010) that can be divided into three distinct stages, with stages 1-2 repeated with each renewed magmatic cycle. Pre-mineralization vein types (1-3) comprise biotite – K-feldspar – magnetite – actinolite ± minor quartz – anhydrite with biotite – plagioclase ± quartz alteration halos. Main mineralization stage veins evolve from quartz –anhydrite ± minor sulphide veins with biotite or no alteration halos in the Teniente Mafic Complex and K-feldspar alteration in felsic hosts (types 5-6) to later, sulphide-dominated veins with no alteration halos (7) and finally sulphide-rich veins (8) that are distinctive because of the first appearance of intense phyllic alteration halos. The early main stage veins are related to the formation of intrusion-hydrothermal breccia complexes which comprise magmatic (deep and early), K-feldspar-, biotite-, anhydrite- and tourmaline-cemented types. These are progressively overprinted by the later vein generations. Late mineralization stage veins (9-10) are distinct with their tourmaline-carbonate-anhydrite-gypsum-sulphide assemblages and phyllic alteration halos, interpreted to be related to the emplacement of the large Braden Breccia Pipe that marked the cessation of mineralization in the deposit.

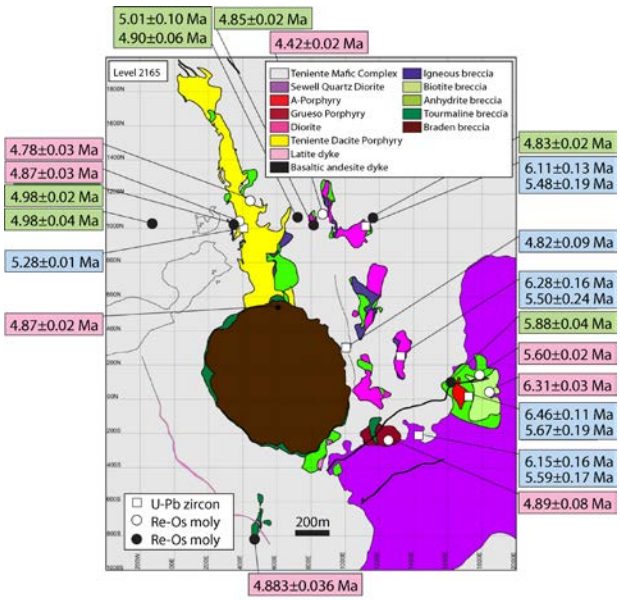

Figure 1. Simplified geology of El Teniente, showing U-Pb zircon ages (light blue; Maksaev et al., 2004), and Re-Os molybdenite ages from Cannell et al. (2003; pink) and Maksaev et al. (2004; light green).

3 Fluid inclusion types

Fluid inclusions were divided into 8 types based on their appearance at room temperature (Fig. 2).

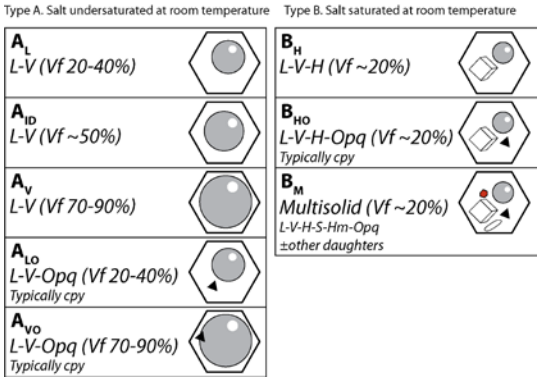

Figure 2. Fluid inclusion types observed. A = aqueous, B = brine. Subscripts: L = liquid, ID = intermediate density, V = vapor, O = opaque daughter, H = halite daughter, S = sylvite, Hm = hematite, M = multiple daughters. Vf = volumetric fraction of vapor phase.

Due to the long life of the system at El Teniente and complex overprinting of earlier veins by later fluids, determining which inclusions are genetically related to particular vein generations is not straightforward. As is the case in most porphyry systems, unequivocal evidence for a primary origin is rarely observed. Consequently, inclusion types were linked to specific vein generations (Table 1) based on: (1) fluid inclusion mode of occurrence (secondary, possibly primary, definitely primary) derived from transmitted light and SEM-CL observations; (2) compositional similarities; and (3) likely overprinting sequences derived from (1) and (2). SEM-CL imaging is one of the most useful techniques because if fluid inclusions can be spatially related to a specific type of quartz then they become primary with respect to that quartz (Wilkinson, 2001), irrespective of the textural feature concerned (e.g. microfracture, growth zone, vug infill).

Fluid inc. type	Interpreted primary assemblage in vein type
B_M	1, 2, 3, early anhydrite breccia (≡5)
B_{HO}	1, 2, 3, 6b, 8
A_{LO}	6a
A_{ID}	6a
A_{VO}	6a, 8
A_L	6a, 6b
A_V	6a, 6b, 8
B_H	6b (Mo-rich), 8

Table 1. Interpreted inclusion types associated with different vein generations.

4 Fluid evolution

The presence of high salinity brine inclusions that lack coexisting vapor in stage 1 through to early stage 5 veins associated with the A-Porphyry complex is best explained by direct exsolution of brine from an underlying melt at high pressure (Fig. 4). Previous depth estimates for El Teniente suggest maximum depths of ~5 km, implying maximum lithostatic pressures of 120-140 MPa. Using experimental data for a 40 wt% NaCl fluid (e.g. Bodnar, 1994) in combination with homogenization temperature data yields trapping temperatures of around 500°C at inferred near-magmatic conditions. This is consistent with the mutual crosscutting relationships between veins, magmatic breccias and the A-Porphyry intrusion that indicate a close spatial and temporal association between stage 1-5 veins and magma emplacement at the current level of exposure (Vry et al., 2010).

A distinct change in fluid properties appears to have accompanied the formation of anhydrite-cemented breccias in stage 5 (Fig. 4). This is characterised by a switch from dominantly dense (~1.1 g/cm^3), high salinity (~40 wt% NaCl equivalent) fluids to abundant, much lower density (~0.6 g/cm^3), low salinity (~6 wt% NaCl equivalent) liquid-like fluids (late stage 5 - stage 6a). Estimated P-T conditions suggest that this change is accompanied by a pressure drop of ~70 MPa, which could be explained by decompression from lithostatic to near-hydrostatic pressure at an approximately constant depth. Trapping of fluids at ~450-350°C at variable pressures but generally fairly close to the critical density in the supercritical field is inferred to explain the rare presence in type 6a veins of A_{ID} and A_V/A_{VO} inclusions in addition to the predominant A_L type (Table 1).

Consideration of the bulk density of type A_L/A_{LO} inclusions in type 6a veins as a function of location within the system (Fig. 3) shows that the deeper vein samples contain the densest, liquid-like fluids and that these appear to decrease in bulk density upwards. This pattern is supported by the appearance of A_{ID} and A_V/A_{VO} inclusions mostly in shallower samples. These relationships imply that A_L/A_{LO} inclusions represent the parent fluids for these veins, and that these underwent expansion as they migrated upwards, following a steep path in P-T space (decreasing pressure at fairly constant temperature) in the one-phase field, crossing the critical isochore.

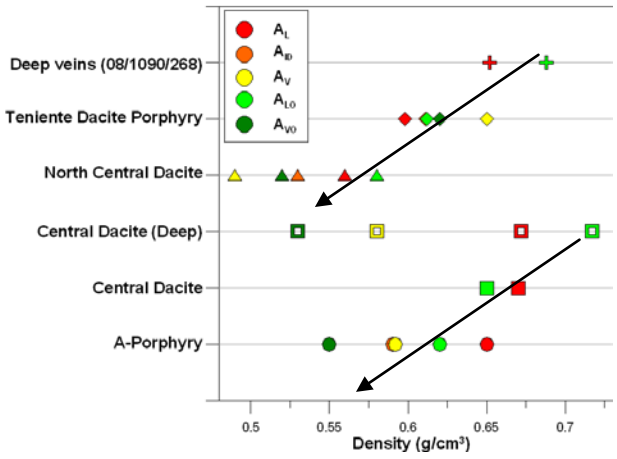

Figure 3. Variation in average bulk density of fluid inclusions in type 6a veins from different parts of El Teniente (see Fig. 1 for locations).

Perhaps significantly, fluid inclusions associated with the type 6a (and related type 7) molybdenite-rich vein

generation show the opposite behaviour with the deepest vein samples being dominated by type A_V and A_{ID} inclusions and the shallower samples by A_L inclusions. This suggests that molybdenite mineralizing solutions were vapour-like at depth and followed a flatter P-T path (decreasing temperature at fairly constant pressure), contracting as they migrated upwards, crossing the critical isochore to the liquid-like side.

Type 7 quartz-poor, sulphide-rich veins mark the onset of intense, fracture-controlled sulphide precipitation. The contrast in vein compositions from the type 6a-6b quartz–(anhydrite–sulphide) veins implies an evolution in fluid properties at this time. Although no inclusion data are available, the general lack of quartz precipitation is taken to indicate that fluids underwent cooling at ~450-350°C at approximately constant pressure (≤50 MPa), allowing them to enter the zone of retrograde quartz solubility. The lower pressures also allowed fluids to increasingly cross into the two-phase field, as indicated by the increasing abundance of brine inclusions in type 6b veins.

Cooling below ~350°C and dissociation of acid species led to the development of the prominent sericitic alteration halos around type 8 veins. These are thought to be directly linked to the type 6/6a and type 7 veins, forming above and outboard of them as fluids migrated upwards (Fig. 4).

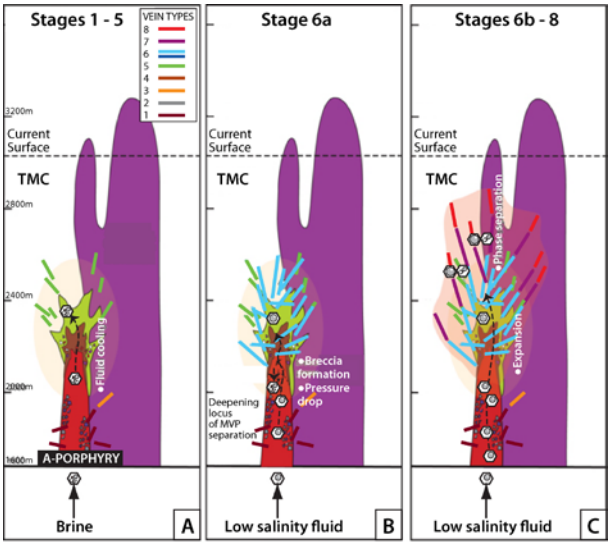

Figure 4. Cartoon illustrating the evolution of the A-Porphyry system. A. Brines exsolve early from magma to form magnetite and biotite/K-feldspar alteration with limited mineralization. B. Anhydrite breccia development coincides with switch to deeper-sourced, low salinity, supercritical, liquid-like fluids that formed abundant, quartz-rich, type 6 veins. C. Fluids continue to migrate upwards, depressurizing, cooling slightly and undergoing local phase separation to produce sulphide-rich type 7 and eventually type 8 veins with sericitic halos.

It is considered likely that this cycle of fluid evolution was repeated several times through the remaining life of the El Teniente system, associated with the multiple magmatic pulses documented by geochronology. A significant hiatus is then inferred before type 9-10 veins formed during emplacement of the Braden Breccia at ~5.0-4.5 Ma. The lower pressures at this stage resulted in the increased incidence of fluid boiling as indicated by more abundant coexisting brine and vapor inclusions. These constrain the P-T conditions fairly tightly at 340-380°C and 10-20 MPa corresponding to a depth of ~2.5 ± 1 km at hydrostatic pressure. This implies exhumation by approximately 2.5 km in ~1 My, consistent with estimates by Cannell (2004).

5 Fluid chemistry

The A-Porphyry system provides the best opportunity to determine fluid chemistry variations throughout the vein paragenesis owing to the good preservation of the widest variety of vein types. Early alteration in the A-Porphyry complex is dominated by quartz–magnetite–feldspar at depth and with no significant or systematic variation in Na, Fe(– K) observed this has been interpreted to reflect a high magmatic fluid flux at this stage giving fluid dominated conditions during alteration. SO_2 is interpreted as the main oxidation agent in this system, forming magnetite by the reaction:

$$9FeCl_2 + SO_2 + 10H_2O \rightarrow 3Fe_3O_4 + H_2S + 18HCl$$

The H_2S produced could act to drive sulphide saturation; however, the inferred high temperatures of these brines (~500°C) and a lack of fluid boiling acted to prevent significant Cu- and Mo-sulphide precipitation at this stage. Cooling of these brines into stage 4a appears to correspond to a slight drop in both Cu and Mo concentrations and stage 4a brines show a more pronounced variation in Cu, Fe and Mo concentrations than stage 1 brines, implying some sulphide precipitation in the late pre-mineralization stage, consistent with the vein mineralogy. Primary brine inclusions in type 4a veins show a systematic variation in K/Na ratios that is interpreted to reflect replacement of plagioclase by K-feldspar:

$$2Na_{0.5}Ca_{0.5}Al_{1.5}Si_{2.5}O_8 + 4SiO_2 + 3K^+ \rightarrow 3KAlSi_3O_8 + Na^+ + Ca^{2+}$$

Stage 4a brines also show a decrease in Zn(+As) concentrations from stage 1. Microprobe analysis of biotite alteration halos on type 4a veins show that biotite contains on average 0.02 wt% ZnO, suggesting that this could account for the drop. Zinc and As concentrations show a marked increase in interpreted primary stage 8 brines, this may partly be due to preferential partitioning of Zn into high salinity fluids during phase separation, but may also relate to breakdown of biotite releasing Zn and As to these later fluids. A relative increase in both Sr and Ca in later stage 8 brines compared to stage 6a brines could be related to phase separation or release of Ca(–Sr) by alteration of plagioclase to sericite and quartz producing the characteristic alteration halos at this stage. The presence of high concentrations of As, Zn, Pb in late stage 8 fluids may explain the presence of base metal and As-bearing sulphosalts such as tennantite in subsequent late mineralization stage veins.

Fluid chemistry data indicate subtle spatial variations between the multiple intrusive centres. Cu/Fe ratios in A_{LO} fluids are generally high due to high concentrations

of Cu in this fluid type, with the highest Cu/Fe ratio obtained from fluids associated with deep type 6a veins. The exception to this are A_{LO} fluids associated with the A-Porphyry complex which show generally lower Cu/Fe ratios most likely linked to higher Fe concentrations in these fluids. Mn concentrations are also generally higher in fluids associated with the A-Porphyry. This may be a result of early development of the A-Porphyry complex depleting the underlying melt in Fe and Mn due to exsolution of early brines and high, Cl dependent, fluid-melt partition coefficients for Fe and Mn.

All fluid inclusion types from the North Central Dacite vein samples show a distinctive enrichment in Mo(+Ba, Sr) indicating that this represents a system characteristic rather than element fractionation between different fluid types. This distinct fluid chemistry corresponds to anomalously high Mo concentrations in whole rock analysis of the dacite finger porphyries, high Mo grades associated with the North Central Dacite intrusion particularly at level 1890 m.a.s.l, and the observation that Mo-bearing veins are particularly abundant associated with the dacite finger porphyries.

6 Conclusions

Geological observations at El Teniente suggest multiple mineralization events linked to the development of multiple intrusion-breccia-vein complexes (Vry et al., 2010), a model that is supported by earlier geochronology (e.g. Maksaev et al., 2004) and recent paleomagnetic data (Astudillo et al., 2010). In contrast to previous models (Cannell et al., 2005; Klemm et al., 2007) fluid inclusion petrography, microthermometry and fluid chemistry analysis in the present study indicates that mineralization at El Teniente is not linked to one major, temporally extended event (~0.7 m.y.; Klemm, 2005) involving constant degassing of a low salinity, intermediate density fluid from an underlying magma reservoir (Klemm, 2005), neither is mineralization explicitly related to the intrusion of the Teniente Dacite Porphyry (e.g. Klemm et al., 2007). Instead, it is suggested that distinct degassing events from a deep, underlying magma chamber were channelled through multiple high-level intermediate-felsic stocks that were emplaced at the level of the deposit. This multistage character is typical for Late Miocene copper deposits in the central Andes, and at El Teniente the repeated episodes of porphyry emplacement have been suggested to be triggered by localised dilation caused by reverse and/or strike slip faulting (e.g. within the Teniente Fault Zone; section 5.4.5) related to regional shortening at the time of formation (Garrido et al., 2002). It is likely that porphyry emplacement was associated with discrete degassing events releasing magmatic volatiles rich in Cu, Mo and S. The nature of the fluid exsolved varied as a function of pressure fluctuations linked to extensive breccia formation at the level of the deposit, immediately above and surrounding porphyry intrusions.

High Cu concentrations in all fluid types relate to the ability of Cu to complex with a variety of ligands and indicate high melt-fluid partition coefficients. The high Cu concentrations observed in low salinity fluids suggest volatile sulphur ligands. Differential complexation behaviour of Cu and Mo in hydrothermal fluids is likely to be the overriding control on selective precipitation of chalcopyrite and molybdenite in the El Teniente system resulting in segregation of these minerals in different vein types.

Acknowledgements

We would like to thank the members of the Superintendencia de Geología of the El Teniente mine, particularly Patricio Zuñiga, for granting access to the mine. David Benado, Miguel Letelier, Roberto González, Juan Carlos Roa, Rodrigo Morel, and Ricardo Floody provided assistance, guidance, and useful discussions and debate. Thanks to the Natural History Museum, London, particularly Anton Kearsley, John Spratt, Terry Williams, and Tony Wighton, and to CODES, particularly Karsten Göemann, for SEM laboratory support. Simon Stephens at CODES assisted with sample preparation. Funding for this project was obtained from multiple sources, including Imperial College London Janet Watson Scholarship, the Society of Economic Geologists Hugh McKinstry Student Research Grant and Graduate Student Fellowship, CODES, University of Tasmania, the Institute of Materials, Minerals and Mining G Vernon Hobson Bequest and Edgar Pam Fellowships, the Geological Society of London Elspeth Matthews Grant, the University of London Central Research Fund, the UK Resource Centre for Women Student Travel Bursary, and the Mineralogical Society Postgraduate Travel Bursary.

References

Bodnar, R.J., 1994. Synthetic fluid inclusions. XII. Experimental determination of the liquidus and isochores for a 40 wt% H_2O-NaCl solution. Geochimica et Cosmochimica Acta, 58: 1053-1063.

Cannell, J., 2004. The El Teniente porphyry copper-molybdenum deposit, central Chile. Unpublished PhD thesis, University of Tasmania, 317 p.

Cannell, J., Cooke, D. R., Stein, H. J., and Markey, R., 2003. New paragenetically constrained Re-Os molybdenite ages for El Teniente Cu-Mo porphyry deposit, central Chile. Mineral Exploration and Sustainable Development, Proceedings of the 7th Biennial SGA meeting, Athens, Greece, Extended Abstracts: 255-258.

Cannell, J., Cooke, D. R., Walshe, J. L., and Stein, H., 2005. Geology, mineralization, alteration, and structural evolution of the El Teniente porphyry Cu-Mo deposit. Economic Geology, 100: 979-1003.

Klemm, L. M., Pettke, T., Heinrich, C. A., and Campos, E., 2007. Hydrothermal evolution of the El Teninete deposit, Chile: Porphyry Cu-Mo ore deposition from low-salinity magmatic fluids. Economic Geology, 102: 1021-1045.

Maksaev, V., Munizaga, F., McWilliams, M., Fannning, M., Mathur, R., Ruiz, J., and Zentilli, M., 2004. New chronology for El Teniente, Chilean Andes, from U-Pb, 40Ar/39Ar, Re-Os, and fission-track dating: Implications for the evolution of a supergiant porphyry Cu-Mo deposit. Special Publication of the Society of Economic Geologists, 11: 15-54.

Vry, V.H., Wilkinson, J.J., Seguel, J., and Millán, J., 2010. Multistage intrusion, brecciation and veining at El Teniente, Chile: Evolution of a nested porphyry system. Economic Geology, 105: 119-153.

Wilkinson, J.J., 2001. Fluid inclusions in hydrothermal ore deposits. Lithos, 55: 229-272.

Comparing anatomy of mineralization of Tongcun porphyry molybdenum deposit in western Zhejiang Province with that of Dexing porphyry copper deposit in Jiangxi Province

Dehui Zhang, Yudi Zhu, Lili Wang, Keqiang Wang
School of Earth Sciences and Resources, China University of Geosciences (Beijing), Beijing 100083, China

Abstract. The Dexing porphyry copper deposit and Tongcun porphyry molybdenum deposit are both located in the southeast margin of the Yangtze block. However, they have different ore-forming elements, and disparities in the size and grade of the deposits. The authors suggest from geochemical features of the two deposits that the differences are caused by the different tectonic units hosting these two deposits; and different depths of the magmatic emplacement controlling the time of the exsolution and the volume of the volatile in magma. Therefore, different mineralization in the deposits reflects discrepancies in mineralization efficiency.

Keywords. Porphyry molybdenum deposit; porphyry copper deposit; Comparative anatomy of mineralization; Dexing; Tongcun

1 Introduction

The Tongcun porphyry molybdenum deposit (TPD) discovered in Kaihua county, west Zhejiang province has proven molybdenum resource of about 50,000 tons recently, and copper of approximately 30,000 tons, indicating potential porphyry Mo-Cu mineralization in western Zhejiang (Zhu et al., 2009). The famous Dexing porphyry copper deposit (DPD) in Jiangxi Province, west to TPD, with a distance of 60 km from TPD. DPD has Cu of nearly 10 million tons and associated Au of about 200 tons (Zhu et al., 1983). Despite distance between these two deposits being close (Fig. 1), why are the ore-forming elements, size and grade of these two deposits quite different? In this paper, we study main geological and geochemical characteristics of these two deposits to answer this question and provide theoretical support for geological prospecting in western Zhejiang.

2 Geological structure backgrounds of Tongcun and Dexing deposits

Both DPD and TPD are located in southeast margin of the Yangtze block and northern part of Jiangshan-Shaoxing suture, but they lie in different sub-tectonic units of this zone. Separated by the deep fault in the northeastern Jiangxi, TPD is situated in Qiangtang depression to the east of Jiangshan-Shaoxing suture, with thick Paleozoic sediments. DPD is situated in the southeastern margin of Jiangnan uplift where Proterozoic sediments is exposed. The difference in sediment thickness between the subtectonic units is more than 15,000 m (Zhu et al., 1983; Fig. 1).

The $\varepsilon_{Nd}(t)$ values range from -1.52 to 0.59, averaging -0.2976, and initial $^{87}Sr/^{86}Sr$ ratios range from 0.7044 to 0.70725, averaging 0.70527 for DPD, whereas, $\varepsilon_{Nd}(t)$ values range from -6.7 to -3.4, averaging -4.75, and initial $^{87}Sr/^{86}Sr$ ratios range from 0.70925 to 0.78116, averaging 0.71741 for TPD. $(^{87}Sr/^{86}Sr)_i$ versus $\varepsilon_{Nd}(t)$ plot (Fig. 2) shows that Sr-Nd isotope values of DPD distribute basically along the Chondritic Meteorites Uniform Reservoir (CHUR) from the Bulk Silicate Earth (BSE) close to the primitive mantle, and fall within the South China area and partly within the I-type granites of Australia, indicating that mantle-derived materials are a major contribution to the porphyry source of DPD. On the other hand, TPD has low Nd values, some of which fall into the I-type and S-type granites of South China, indicating that both mantle- and crust-derived materials can be correlated to the formation of Tongcun granite magma; the latter plays a main role in the granitic magma formation of TPD. Nd isotopic variation ranges of both deposits are narrow, while Sr ranges wide, which could be attributed to AFC process of magmatic assimilation of country rocks (De Paolo, 1985; Chen et al., 1994). The SiO_2 diagram by Frost et al. (2001) also provided evidence of assimilation or contamination of crust materials in the magma formation of these two deposits (Fig. 3).

3 Comparison of magmatic rocks and magmatic evolution between the two deposits

The ore-bearing rocks of DPD are small granodiorite porphyry rock stocks, whereas TPD are small monzonitic granite (porphyry) stocks, both of which contain three small rock bodies with similar outcrops. Geological and geochemical characteristics of DPD and TPD are listed in Table 1.

DPD has pleocrystalline porphyritic texture, and phenocrysts are composed of andesine, hornblende, biotite, K-feldspar and a few amount of dissolution round shaped quartzes; the matrixes have micro-fine grained anhedral granular structure, and are mainly composed of oligoclase, quartz, K-feldspar, a few hornblende and biotite. While ore-bearing rocks of TPD are of porphyritic polycrystalline texture, and the phenocrysts consist of plagioclase, K-feldspar, quartz partly corroded, biotite and little amphibole; the components of matrixes are similar to the phenocrysts with fine-grained texture (Zhu et al., 1983). The zircon

U-Pb age of Dexing porphyry using LA-ICP-MS is 171±2 Ma (Zhou et al., 2012), while the zircon U-Pb age of Tongcun granite using LA-ICP-MS and SHRIMP is 164±2.5 Ma, both of which were formed in the early Yanshannian during mid-late Jurassic, however, Tongcun granite intrusion occurred later than Dexing porphyry.

Compared with Dexing porphyry, Tongcun granite is characterised by more acidic and higher alkalinity, belonging to monzogranite, whereas Dexing porphyry is granodiorite. The SiO_2 contents of Dexing porphyry deposit range from 63.1% to 73.1%, averaging 67.9%; while the SiO_2 contents of Tongcun ore-bearing magma range from 68.7% to 79.9%, averaging 71.7%. Fig. 3 shows (Na_2O+K_2O-CaO)-SiO_2 (Fig. 3a) and FeO_{tot}/(FeO_{tot}+MgO)-SiO_2 (Fig. 3b) of the deposits (Frost et al., 2001), indicating that DPD falls into I-type granites, magnesian calc-alkaline - calcium granite; while TPD also falls into I-type granites, but partly into S-type granites, showing ferruginous calc-alkalic—calcic- alkali-calcic granite.

Blevin (2004) has discussed the ore-bearing characteristics of magmatic rocks from the granitoids of eastern Australia, and proposed 4 parameters for evaluating mineralization potential of granites, including the oxidation state of magma, rock type-composition-alkalinity of magmatic rocks, evolution degree of magma, and fractional crystallization of magma. According to granites in eastern Australia related to Cu-Au mineralization lying in strong oxidizing zone and un-evolution zone, Dexing granites are categorized into from un- to moderate-evolution zones, whereas Tongcun granites are fallen into moderate- to strong-evolution and strong-fractionation zones (Fig. 4).

4 Comparison of mineralization

Table 1 shows that the mineralization characteristics between DPD and TPD are quite different, including weak potassic feldspathization and sericitization of TPD; the differences on ore-bearing fissure development between both deposits are also much greater, for example, the ore-bearing fracture density of DPD is more than 25/m, while that of TPD is only 2.3/m; ore-forming fluid systems of both deposits are also different: the homogenization temperatures of fluid inclusions in DPD range from 150 to 575 ℃, salinities range from 1% to 21% NaCl, while the fluid salinity during the ore-forming phase is up to 40% ~ 55% NaCl, indicating a high-medium temperature, and high salinity NaCl-KCl-H_2O system which has a typical porphyry ore-forming fluid characteristics with boiling (Zhu et al., 1983). On the other hand, the ore fluid system of TPD is NaCl-H_2O-CO_2 containing CH_4 in low temperature and low salinity without boiling. Diagenetic mineralization for DPD is at depths of 2 to 3 km, whereas that for TPD is greater than 6 km, indicating the latter has significantly greater mineralization depth (Xu and Zhang, 2012).

5 Discussion and conclusion

Factors causing the difference between DPD and TPD are suggested as follows.

5.1 Environment forming the magma

Ore-bearing porphyries of DPD and TPD were formed in active continental margin environment related to the subduction of paleo-Pacific plate in the early mid-Jurassic (171 Ma); magmatic rocks of both deposits are high-K calc-alkaline series with adakite features (Zhu et al., 2012). The interaction between the lithospheric mantle and crustal materials by partial melting ultimately led to the formation of ore-bearing magma of TPD and DPD. The difference between both deposits is environment forming magma: DPD is located in the southeast margin of Jiangnan uplift; because of thinner lithospheric mantle and deep fracture cutting of the northeastern Jiangxi Province, more mantle materials are involved in the partial melting magma source area (Xiao et al., 2002); whereas TPD is located in Qiantang depression with large thickness of lithospheric and minor cutting depth associated with the fault zone, leading to more crustal materials involved in magma source to form I-S type magma. As a result, the participation ratio of mantle- and crust-derived materials in magma source lead to DPD mainly with Cu-Au, and TPD mainly with Mo.

5.2 Effective mineralization process

The study has shown that if there is no effective mineralization process, even in the best tectonic and crustal structure environment, can only form large-scale and low-grade geochemical anomalies rather than large deposits (Cook et al., 2005). Seedorff et al. (2005) has discussed the prerequisites for the formation of large porphyry copper deposits and the main reason for causing the different geochemical characteristics and different evolution of deposits in details. Blevin (2004) has proposed 4 parameters for evaluating mineralization potential of granites, including the oxidation state of magma, rock composition of magmatic rocks, evolution degree of magma, and fractional crystallization of magma.

5.3 Difference in minerals

Differences in minerals between Dexing and Tongcun deposits can be analyzed as follows: the ore-bearing porphyry of DPD is granodiorite porphyry, belonging to reduction high-temperature I type magnesian and calc-alkaline magma series, and there are a large number of mantle-derived materials involved in the magma source region; while the ore-bearing porphyry of TPD is monzogranite, belonging to reduction low-temperature I-S type calc-alkaline magma series, and the magma source is mainly composed of crustal materials. Different contribution ratios of the magma source cause large ranges of ore-bearing magma composition. Cu, Au and Pt group elements of TPD are mainly derived from mantle resource, while Mo and Pb may be derived from subtractive plate or crust (Seedorff et al., 2005). Furthermore, high degree of magmatic evolution also produces Mo instead of Cu mineralization (Blevin, 2004).

5.4 Factors leading to metallogenic scale and grade

The factors that led to extreme variation in the metalogenic scale and grade of DPD and TPD are more complicated, in which the time of the exsolution and the volume of the volatile in magma directly impact on metal extraction and subsequent enrichment, while the depths of the magmatic emplacement directly restrain the time of the exsolution and the volume of the volatile in magma (Strong, 1988). From the study, the magma emplacement depth of DPD is shallow and only 2-3 km, which causes magmatic volatiles reached saturation and exsolution earlier, and larger volume of dissolved fluid, forming cryptoexplosive breccia pipe and developing large-scale diffusion-like hydraulic fractures. On contrast to DPD, the magmatic emplacement and mineralization of TPD are deeper, which are very unfavorable for the exsolution hydrothermal fluids; furthermore, natural fluids subsequently exsolved from the magma, unfavorable for Cu (compatible element) enrichment, caused less exsolved fluids, lower ore-bearing fracture density, weaker hydrothermal alteration intensity, and lower salinity fluid without boiling.

Acknowledgements

We thank Professors Xinqi Yu and Wei Shen for helpful advice and discussion, and senior engineers Xudong Jin, Jinsheng Jia and Xifang Ye of number 3 geological party of Zhejiang Province at Jinhua city for their support and permission to publish the data.

References

Blevin, P.L., 2004. Redox and compositional parameters for interpreting the granitoid metallogeny of Eastern Australia: implications for gold-rich ore systems. Resource Geology 54(3), 241–252.

Chen, J., Zhou, T., Xing, F., et al., 1994. Pb, Sr and Nd isotope characteristics of copper-bearing rocks from middle-low area of Yantze. Acta Geoscientia Sinia (1-2), 111-116.

Cooke, D.R., Hollings, P., Walshe, J.L., 2005. Giant porphyry deposits: characteristics, distribution, and tectonic controls. Economic Geology 100(5), 801-818.

De Paolo, D.J., 1985. Isotopic studies of processes in mafic magma chambrers. I. The Kiglapait intrusion, Labradoc. Journal of Petrology, 26, 925-951.

Frost BR, Barnes CG, Cllins WJ, Arculus RJ, Ellis DJ, Frost CD(2001) A geochemical classification for granitic rocks. Journal of Petrology 42(11):2033-2048

McCuloch, M.T., Chappell, B.W., 1982. Nd isotopic characteristics of S- and I-type granites. Earth Planet Science Letter 58, 51-64.

Seedorff, E ., Dilles, J.H., Proffett, J.R., et al., 2005. Porphyry deposits: Characteristics and origin of hypogene features. Economic Geology 100th Anniversary Volume. Society of Economic Geologists, 251-298.

Strong, D.F., 1988. A review and model for granite-related mineral deposits. In: Taylor R P and Strong D F(Editors): Recent advances in the geology of granite-related mineral deposits. The Canadian Institute of Mining and Metallurgy, Special Volume 39, 2988.

Xiao, Q.H, Deng, J.F., Ma, D.Q., 2002. The ways of investigation of granitoids. Geological Publishing House, Beijing, 71-101(in Chinese).

Xing, F., Xu, X., 1995. The essential features of magmatic rocks along the Yangtze River in Anhui Province. Acta Geoscientia Sinia 11(4), 409-422(in Chinese with English abstract).

Xu, W.G., Zhang, D.H., 2012. An interpretation of the role of reduced fluid in porphyry metallogenesis. Acta Geoscientia Sinia 86(3), 495-502(in Chinese with English abstract).

Zhou, Q., Jiang, Y.H., Zhao, P., Liao, S., Jin, G., 2012. Origin of the Dexing Cu-bearing porphyries, SE China: elemental and Sr–Nd–Pb–Hf isotopic constraints. International Geology Review 54, 572–592.

Zhou, X., Chen, P., Xu, X. et al., 2007. The origin of Late Mesozoic granitoids and dynamic evolution of lithosphere in Nanling region, China. Science Press, Beijing, 123-198(in Chinese).

Zhu, A.Q., Zhang, Y.S., Lu, Z.D., Zhang, C.L., 2009. The metallogenic series and metallogenic province of metal and nonmetal mineral deposits in Zhejiang Province. Geological Publishing House, Beijing, 1-433 (in Chinese).

Zhu, X., Huang, C.K., Rui, Z.Y., Zhu, X.J., Hu, C.S., Mei, Z.K., 1983. Geology of the Dexing porphyry copper ore field. Geological Publishing House, Beijing, 1983 (in Chinese with English abstract).

Zhu, Y.D., Ye, X.F., Zhang, D.H., et al., 2012. A comparative study of granites in Tongcun porphyry molybdenum-copper deposit in West of Zhejiang Province and Dexing Porphyry copper deposit. Advances in Earth Science 27(10), 1043-1053(in Chinese with English abstract).

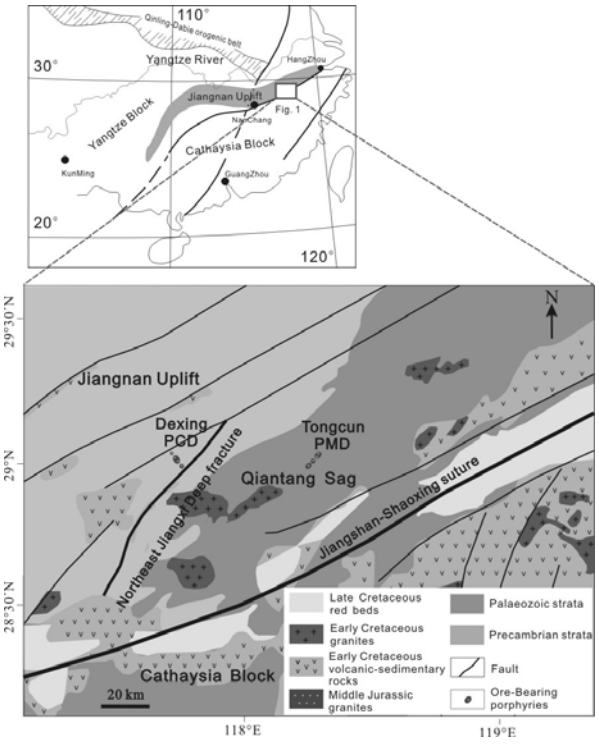

Figure 1. Regional tectonic sketches of Dexing and Tongcun deposits (after Jiang et al., 2011)
PCD-porphyry copper deposit; PMD-porphyry molybdenum deposit

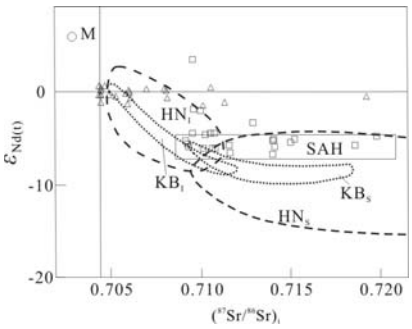

Figure 2. Sr-Nd isotopic compositions of Dexing and Tongcun deposits
KBI and KBS are data from the batholith granites and inclusions of Berridale and Kosciusko in the southeastern Australia (McCulloch and Chappell, 1982); HNI: early I-type granites of Yanshan in South China, HNS: early S-type granite of Yanshan in South China (Zhou et al., 2007); SAH: Mesozoic magmatic rocks of Wannan (Xing and Xu, 1995). M: depleted mantle, LC: lower crust. Triangle means Dexing copper deposit, box is Tongcun molybdenum deposit

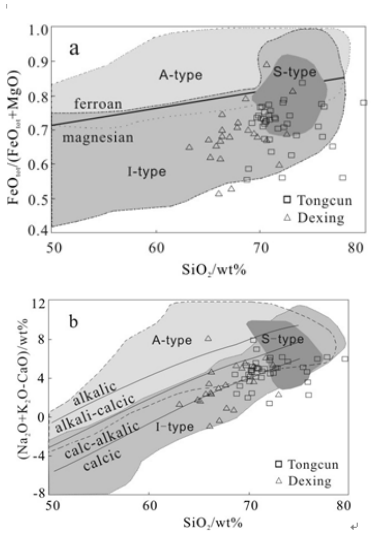

Figure 3. a: $FeO_{tot}/(FeO_{tot}+MgO)$ versus SiO_2; b: (Na_2O+K_2O-CaO) versus SiO_2 diagram (after Frost and Frost, 2011).
Straight lines are boundary between ferroan and magnesian granites, or between A type and I type granites.

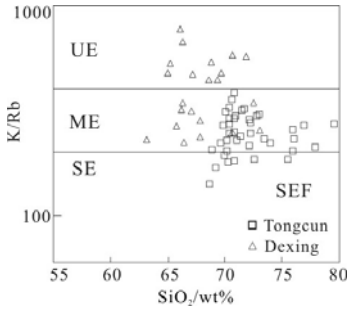

Figure 4. Evolution degree classification based on K/Rb ratios (Blevin, 2004)
UE: unevolution zones, ME: moderate evolution zones, SE: strong evolution zones, SEF: strong evolution and strong fractionation zones. See previous figure for legend. VSO: very strong oxidation, SO: strong oxidation, MO: moderate oxidation, MR: moderate reduction, SR: strong reduction.

Table 1. Comparison of characteristics between Dexing and Tongcun deposits

		DPD	TPD
Ore-bearing bodies	Rock assemblage	Granodiorite porphyry	Monzonitic granite porphyry
	Outcrop area (km^2)	0.7, 0.2, 0.06	0.5, 0.4, 0.3
	Breccia pipe	Crypto-explosive breccia pipe	-
	Rock series	Calc-alkaline—high K calc-alkaline	high K calc-alkaline —Tephrite
	Petrogenesis type	High-temperature I type	Low temperature I-S type
	SiO_2(wt%)	63.1%—73.1%/**67.9%**(23)	68.7%—79.9%/**71.7%**(40)
	A/CNK	0.7—1.9/**1.2**(20)	0.9—1.6/**1.1**(36)
	Emplacement age	Zircon U-Pb 171±2 Ma	Zircon U-Pb 164±2.5 Ma
	Ore-controlling structure	Main NW-trending fracture	Main NE-trending fracture
Surrounding rocks	country rock	Proterozoic metamorphic volcanic-sedimentary	Paleozoic clastic-carbonatite
Metallogenic charateristics	Stage of mineralizaiton	Biotite-K-feldspar—anhydrite-quartz-oxide—chlorite-oxide—carbonatite-fluorite—sulfate	Skarn—potassic-sulfide—quartz-sericite-sulphide—molybdenite-quartz—quartz-carbonatite
	Alteration zoning	Contact zone from the center to the margin: quartz with sericitization →chlorite(epidote) with hydromuscovitized→ illite with potassic feldspathization	upward: weak potassic feldspathization→sericitization→argillization
Ore-bearing fissures	Fracture density	> 25/m	Average 2.3/m
Metallo-genic depth		2-3 km	> 6 km

Au-porphyry mineralisation at Kráľova – Western Carpathians, Slovakia

Juraj Žitňan, Peter Koděra
Department of Geology of Mineral Deposits, Faculty of Natural Sciences, Comenius University, Bratislava, Slovakia

Andrej Biroň
Geological Institute, Slovak Academy of Sciences, Banská Bystrica, Slovakia

Jaroslav Lexa
Geological Institute, Slovak Academy of Sciences, Bratislava, Slovakia

Anthony E. Fallick
Scottish Universities Environmental Research Centre, East Kilbride, Glasgow, UK

Abstract. Kráľova is a new subeconomic Au porphyry deposit in the Western Carpathians. The deposit is located in the Neogene Javorie stratovolcano associated with altered diorite to andesite porphyry. Prevailing intermediate argillic alteration variably overprints earlier K-silicate and Ca-Na silicate alteration patterns. Propylitisation forms an outer alteration zone. The vein system is dominated by A-type and banded quartz veins. Compared to other Au porphyry systems in the district, the deposit shows increase in Cu, Fe, Na, Ca and Mn. Positive correlation between Au and Cu has been also observed. Gold grain shows increased concentration of Ag (18 wt. %). Vein quartz hosts dominant vapour-rich fluid inclusions, locally accompanied by salt melts inclusions. Stable isotope data from vein quartz and magnetite are consistent with magmatic origin of hydrothermal fluids.

Keywords. Au-porphyry, Javorie stratovolcano, fluid inclusions, stable isotopes, alteration

1 Introduction

Au porphyries are a relatively new type of porphyry deposit of increasing importance. The most important deposits belts occur in Maricunga (Chile) and Middle Cauca (Columbia). Common properties of these systems are significantly lower Cu content (< 0.25%) than Cu-Au porphyries, low amounts of sulphides, enrichment in magnetite and association exclusively with highly oxidized I-type (magnetite series) intrusives (diorite, quartz-diorite to granodiorite). Au porphyries are thought to originate at shallow depths (< 1 km) from magmatic fluids affected by decompression (Muntean and Einaudi 2000, 2001).

Au porphyry mineralization in Western Carpathians have been discovered recently by EMED Slovakia, Ltd. Porphyry gold mineralization was found on several localities in the Javorie and Štiavnica stratovolcanoes, however only one locality (Biely vrch deposit; Hanes et al. 2010) reaches economic accumulation of the gold ore. Kráľová is located in western part of the Javorie stratovolcano, hosted by Central Slovakia Volcanic Field of Neogene age on the inner side of the Carpathian arc. Initial Mineral Resource estimate totals 47.8 Mt at 0.29 g/t Au (Hanes et al. 2010).

In this contribution we present new data about mineral composition, alterations patterns and isotope composition of minerals and fluid from Kráľová Au-porphyry deposit. Despite this locality does not have economic resources of ore; it is important for understanding differences between mineralized and non-mineralized systems.

2 Methods

Description of rocks, alteration patterns and mineralogy is based on macroscopic and microscopic observations, and analytical data from samples from boreholes KVE-1 to KVE-5 drilled by EMED Slovakia, Ltd. That also kindly provided whole-rock geochemistry data from all drill holes. Microprobe analyses and cathodoluminiscence imaging were performed at the State Geological Institute of Dionýz Štúr on the electron microprobe CAMECA SX 100. XRD analyses of whole rocks and clay fractions were performed at the Slovak Academy of Science in Bratislava and Banská Bystrica and at Comenius University in Bratislava. Oxygen isotope analyses of monomineral separates of quartz and magnetite were performed by laser flourination at SUERC (Glasgow, UK). Mineral abbreviations used in this paper: biotite - Bt, calcite - Cal, galenite – Gn, chalcopyrite – Ccp, chlorite – Chl, K-feldspar – Kfs, plagioclase – Pl, magnetite – Mag, quartz – Qtz, zeolite – Zeo.

3 Results and discussion

3.1 Host rocks

Au-porphyry mineralization at the locality Kráľová is hosted by a stock-like intrusion of andesite porphyry changing to diorite porphyry in about 200 m depth. Porphyry contains phenocrysts of zonal plagioclase, subordinate pyroxenes, amphibole, rare biotite and garnet. Groundmass is represented by Kfs, subordinate quartz and biotite that show increasing grain size towards depth.

The ore body is locally cut by younger porphyry dykes which are maximum several meters thick. At least three generations of breccias have been recognized here, including pre-mineralization, inter-mineralization and post-mineralization breccias (Hanes et al. 2010).

3.2 Hydrothermal alterations and their

succession

Parental intrusion of the Kráľová deposit and its host rock are affected by various types of alteration. Alteration took place during several stages with changing PTX properties of fluids, resulting in overprinting of earlier mineral associations. Resulting assemblages of secondary minerals are very complex and mineral associations characteristic of individual alteration types were difficult to determine in practice.

Early high-temperature Ca-Na-silicate alteration is represented by Ca-plagioclase anorthite and actinolite and probably corresponds to earliest stages of hydrothermal alteration (Sillitoe 2000). Ca-Na-silicate alteration is poor in sulphides but contains common magnetite. Frequent association of these minerals with biotite and K-feldspar points to a hybrid Ca-Na silicate/K-silicate alteration type (Sillitoe 2000). K-silicate type of alteration is represented by biotitization and magnetitization of dark minerals and groundmass. Magnetite is often accompanied by ilmenite.

Late intermediate argillic alteration is the most widespread type of alteration, overprinting partially or completely mineral assemblages of the Ca-Na- and K-silicate alterations. Characteristic minerals are smectite (montmorillonite, saponite), corrensite, illite?, chlorite and pyrite. Saponite is replacing mafic minerals and forms irregular aggregates in groundmass and rare short veinlets. Silicification occurs in surroundings of quartz veinlets. Typical are tile-like pattern of quartz grains and variable grain size. In contrast to other localities of the Javorie stratovolcano, advanced argillic alteration is absent at Kráľová. Konečný et al. (1998) described propylitic alteration in outer zones of this porphyry system.

3.3 Vein types and their succession

Porphyry intrusion at Kráľová contains several generations of veinlets. Most of them are closely associated with the alteration patterns presented above, containing similar mineral assemblages. The oldest types of veinlets are rare biotite veinlets (Fig. 1) with magnetite and sporadic quartz. Locally, only magnetite is present. These veinlets are short and narrow, mostly < 0.2 mm in diameter, typically irregular in shape and lack internal symmetry. Sometimes they have alteration halos with K-feldspar. Based on their appearance, mineral content, relative age and association with potassic and Ca-Na alteration they can be classified as EB veinlets, based on the terminology of Gustafson and Quiroga (1995) and Sillitoe (2000).

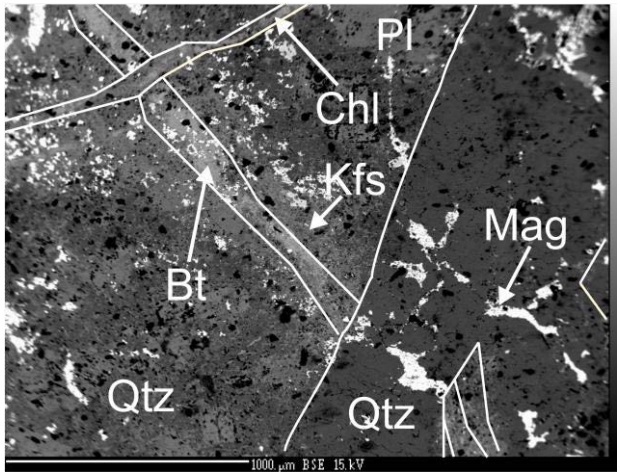

Figure 1. BSE image of biotite veinlet surrounded by K-feldspar, that is cut by younger chlorite and quartz veinlets.

Quartz veinlets are the most common type of veinlets at the deposit, forming a distinct stockwork within the porphyry intrusion. Several generations of quartz veinlets have been recognized with clear crosscutting relationships in some samples. A-type of veinlets form early generations of quartz veinlets. Their average thickness is 0.2 to 0.7 cm, but some of them reach up to 1.5 cm. Later grey veinlets show a clear banding. The dark coloration is due to a high content of vapor-rich fluid inclusions and micrometer-sized magnetite and ilmenite grains. In addition to magnetite, dark bands contain rare micrometer-sized chalcopyrite, pyrite and sphalerite encapsulated in quartz. Dark bands locally show botryoidal textures that continue along quartz veinlets suggesting that the quartz recrystallized from silica gel (Muntean and Einaudi 2000; Koděra et al.,2010). Central part of some quartz veinlets is filled by various later stage minerals that are elsewhere forming individual younger veinlets. They include calcite, less frequent zeolite (chabazite), sulphides (pyrite, chalcopyrite, molybdenite), and rare corrensite. These minerals either occur disseminated or in discontinuous clusters in cavities among individual quartz grains or in individual bands within the quartz veinlets. Other types of veinlets recognized at the Kráľová deposit are chlorite-saponite veinlets. They are very rare, short, narrow, and discontinuous around 1 mm thick and younger than quartz veinlets. The youngest veinlets present at Kráľová are calcite-zeolite veinlets (Fig. 2) with zeolite older than calcite. Saponite and chlorite are rarely present on their margins.

Monazite, apatite and zircon were locally identified as accessoric minerals hosted by altered rock.

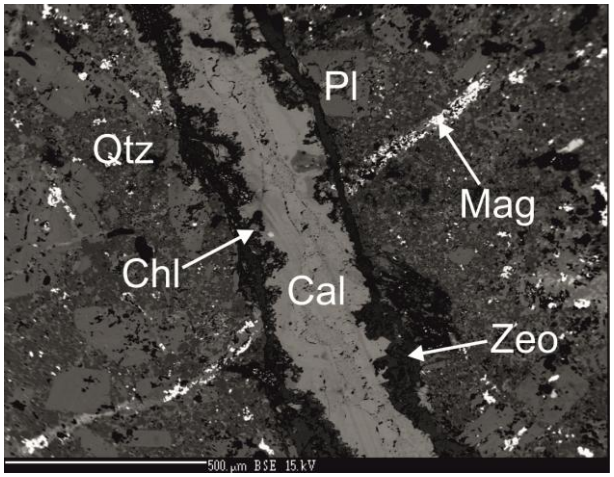

Figure 2. BSE image of a calcite–zeolute-chlorite veinlet cuting older magnetite veinlet.

3.4 Gold mineralization

Extent of Au mineralization at the Kráľová deposit roughly corresponds to the extent of quartz veinlets. The same feature was recognized in other porphyry gold deposits - at the Biely vrch, Slovakia (Koděra et al. 2010) and in Refugio district in the Maricunga belt, Chile (Muntean and Einaudi 2000). The average content of Cu in all drillholes is only 0.026 % and the Cu/Au ratio is 0.09 (wt% Cu, ppm Au). This is similar to other Au-porphyry systems in the Maricunga belt (0.07 to 0.114; Camus 2003), but it is significantly higher than Biely vrch deposit (0.018). In contrast to Biely vrch a positive correlation between Au and Cu has been observed (0.74; Hanes et al. 2010). Only one grain of gold has been indentified yet in a sample affected by K-silicate and intermediate argillic alteration with quartz, A-type and EB-type of veinlets. The gold grain was of isometric shape, enclosed in chalcopyrite (Fig. 3). Microprobe analyses of gold showed increased concentration of Ag up to 18 wt. % and Cu up to 4 wt. % (Cu is probably from surrounding chalcopyrite). One grain of hessite (Ag_2Te) was also identified in this sample.

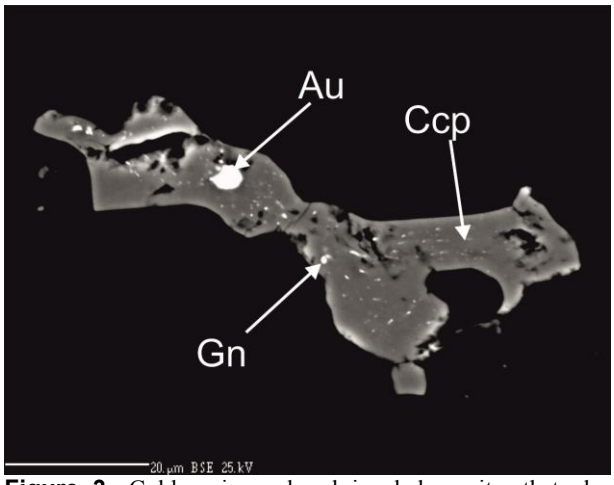

Figure 3. Gold grain enclosed in chalcopyrite, that also contains galena inclusion (KVE-2/125.3).

3.5 Geochemical aspects

Whole rock geochemistry data from the Kráľová deposit do not show significant variation along the limited amount of available drill holes. Some variation can be observed only in sections affected by post-mineralization brecciation that show increased concentrations of Mg and Fe (more chlorite and biotite), decreased Na contents, lack of quartz veinlets and significantly decreased Au and Cu contents. Compared to the Biely vrch deposit Kráľová has slightly different geochemical properties including increased average contents of Fe (5.2 vs. 4.4 wt%), Ca (3.2 vs. 1.2 wt%), Na (1.3 vs. 0.3 wt%) and Mn (1494 vs. 221 ppm). Increased Ca, Na contents at Kráľová are probably caused by the presence widespread Ca-Na silicate alteration in all drillholes. The high content of Mn is manifested by the presence ranceite and rhodocrosite in cavities of calcite and by increased presence of Mn in some silicate and oxide minerals (chlorite, clay minerals, magnetite, less in biotite and pyroxene).

3.6 Fluid inclusions

Over 99 percent of fluid inclusions at the Kráľová deposit are vapour-rich inclusions without visible liquid. These inclusions were abundant in all generations of quartz veinlets and were also observed as rare secondary inclusions in magmatic plagioclase, pyroxene and amphibole. Less than 1 percent of the fluid inclusions in quartz veinlets are liquid rich inclusions of mainly secondary origin, recognized. A-types quartz veinlets also contain salt melt inclusions with a green anisotropic solid phase coexisting with variable proportions of vapour, but no visible aqueous liquid (Fig. 4).

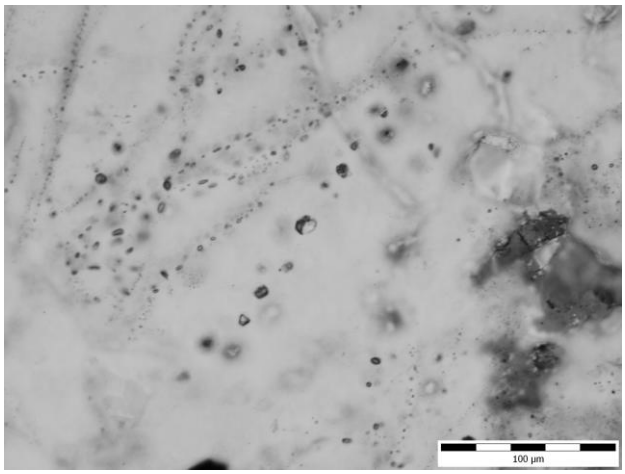

Figure 4. Trail of secondary salt melt + vapor inclusions (KR-5).

3.7 Stable isotopes

Oxygen isotopic composition was measured on quartz from veinlets and on magnetite from altered rock. Vein quartz showed a narrow range of data from 7.9 to 9.1 ‰ $\delta^{18}O$ that show a slight increase with depth (Fig. 5). Magnetite from altered rock had a relatively wide range

of $\delta^{18}O$ values from -1.1 to 3.0 ‰. Assuming that vein quartz and magnetite crystallized from the same fluid the quartz-magnetite isotopic geotermometer could be applied to calculate crystallization temperatures (Clayton and Keiffer 1991). Both minerals were in isotopic equilibrium with the fluid at ~600°C. At this temperature, the fluid in isotopic equilibrium would achieve 5.4 to 9.5 ‰ $\delta^{18}O$, which are values typical for purely magmatic fluid source. Slightly different values of the isotopic composition were obtained from the Biely vrch deposit (quartz 9.4 ± 0.5 ‰ $\delta^{18}O$, magnetite 2.6 ± 0.6 ‰; Koděra et al. 2011). High temperature of quartz veins on the locality Kráľova is also supported by the presence of minor pyroxene needles enclosed in vein quartz.

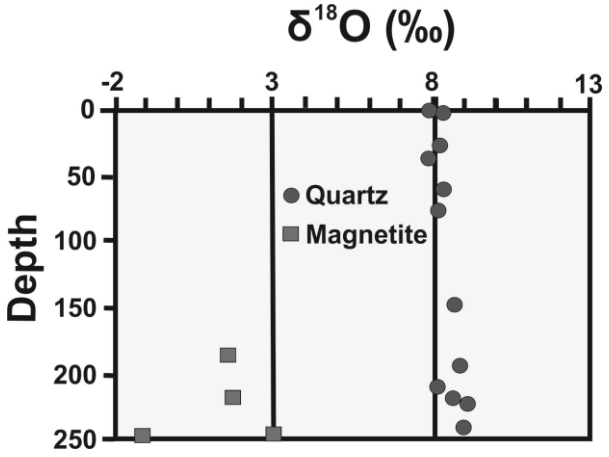

Figure 5. Oxygen isotopic composition of vein quartz and magnetite from the Kráľová deposit.

4 Conclusions

Kráľova deposit is a typical Au-porphyry system, displaying all major characteristics of this type of porphyry deposit worldwide (Sillitoe 2000). Quartz veinlets mark the area of economic Au mineralisation and are inferred to be associated with input of magmatic fluids. Parental intrusion of the Kráľová deposit and its host rock are affected by various types of alteration: higher temperature Ca-Na- and K-silicate alterations and the most widespread intermediate argillic alteration. Propylitization is present in outer zone of porphyry system. Porphyry intrusion contains several generations of veinlets (oldest biotite and magnetite, most common quartz, younger chlorite-saponite, youngest calcite-zeolite). Extent of Au mineralization deposit roughly corresponds to the extent of quartz veinlets. The dominant fluids in quartz veinlets were low density vapors, accompanied by extreme "brines" approaching some kind of salt melts. Oxygen isotope data from quartz and magnetite showed purely magmatic fluid source a isotopically equilibriated at high temperature (~600°C). Compared to the Biely vrch deposit the porphyry system Kráľová has many similar features but some distinct differences also have been observed. Whole geochemistry data deposit show different composition of some elements compared to the Biely vrch deposit, including increase in Cu, Fe, Na, Ca and Mn. Kráľová also showed absence of advanced argillic alteration and specific association of alteration minerals of intermediate argillic alteration including three-octaedric smectite. Slightly different isotopic composition of vein quartz has been also found out. The different features of the system may be associated with different properties of the parental intrusion and associated fluids and/or with significantly different, probably deeper erosion level of this locality.

Acknowledgements

Support by APVV grant 0537-10 and EMED – Slovakia, Ltd. is acknowledged.

References

Camus, F (2003) Geología de los sistemas porfíricos en los Andes de Chile. Servicio Nacional de Geología y Minería 267

Clayton, RN., Keifer, SW (1991) Oxygen isotopic thermometer calibtations. In: Taylor HP., O'Neil JR., Kaplan IR. (eds.): Stable Isotope Geochemistry: A tribute to Samuel Epstein, The Geochemical Society, Special Publ 3: 3-10

Gustafson, LB, Quiroga, J (1995) Patterns of mineralization and alteration below the porphyry copper orebody at El Salvador,Chile. Econ Geol 90: 2−16

Hanes R, Bakos F, Fuchs P, Žitňan P, Konečný V (2010) Exploration results of Au porphyry mineralizations in the Javorie Stratovolcano. Miner Slovaca 42:15-3

Koděra P, Lexa J, Biroň A, Žitňan J (2010) Gold mineralization and associated alteration zones of the Biely vrch Au-porphyry deposit, Slovakia. Miner Slovaca 42:33-56

Konečný, V. Bezák, V., Halouzka, R., Konečný, P., Mihaliková, A., Marcin, D.,Igkárová, Ľ., Panáček, A., Štohl, J., Žáková, E., Galko, I., Rojkovičová, Ľ., Onačila, D. (1998) Explanations to the geological map of the Štiavnické vrchy and Považský Inovec mountain ranges (Štiavnica stratovolcano). Bratislava, GS SR, 473 (In Slovak with English summary)

Muntean JL, Einaudi MT (2000) Porphyry gold deposits of the Refugio district, Maricunga belt, northern Chile. Econ Geol 95:1445-1472

Muntean JL, Einaudi MT (2001) Porphyry-epithermal transition: Maricunga belt, northern Chile. Econ Geol 96:743-772

Seedorf E, Dilles JH, Phoffett Jr, JM, Einaudi MT, Zurcher L, Stavast WJA, Johnson DA, Barton MD, 2005: Porphyry deposits: Characteristics and origin of hypogene features. Econ Geol 100: 251-298

Sillitoe, RH (2000) Gold-rich porphyry deposits: Descriptive and genetic models and their role in exploration and discovery: Reviews in Econ Geol 13: 315-345

SGU
Sveriges geologiska undersökning
Geological Survey of Sweden

Box 670
SE-751 28 Uppsala, Sweden
www.sgu.se

Uppsala 2013
ISBN 978-91-7403-207-9
Print: Elanders Sverige AB